SPRINGER NATURE
Reference

GUY BEN SIMON
GAHL GREENBERG
DAPHNA LANDAU PRAT
EDITORS

Atlas of Orbital Imaging



Springer

Atlas of Orbital Imaging

Guy Ben Simon • Gahl Greenberg •
Daphna Landau Prat
Editors

Atlas of Orbital Imaging

With 1275 Figures and 5 Tables

Springer

Editors
Guy Ben Simon
Ophthalmic Plastic and Lacrimal
Surgery Institute
Department of Ophthalmology
The Goldschleger Eye Institute
Sheba Medical Center
Tel Hashomer, Israel

Daphna Landau Prat
Ophthalmic Plastic and Lacrimal
Surgery Institute
Department of Ophthalmology
The Goldschleger Eye Institute
Sheba Medical Center
Tel Hashomer, Israel

Gahl Greenberg
Department of Diagnostic Imaging
Sheba Medical Center
Tel Hashomer, Israel

ISBN 978-3-030-62425-5 ISBN 978-3-030-62426-2 (eBook)
ISBN 978-3-030-62427-9 (print and electronic bundle)
https://doi.org/10.1007/978-3-030-62426-2

© Springer Nature Switzerland AG 2022
This work is subject to copyright. All rights are reserved by the Publisher, whether the whole or part of the material is concerned, specifically the rights of translation, reprinting, reuse of illustrations, recitation, broadcasting, reproduction on microfilms or in any other physical way, and transmission or information storage and retrieval, electronic adaptation, computer software, or by similar or dissimilar methodology now known or hereafter developed.
The use of general descriptive names, registered names, trademarks, service marks, etc. in this publication does not imply, even in the absence of a specific statement, that such names are exempt from the relevant protective laws and regulations and therefore free for general use.
The publisher, the authors, and the editors are safe to assume that the advice and information in this book are believed to be true and accurate at the date of publication. Neither the publisher nor the authors or the editors give a warranty, expressed or implied, with respect to the material contained herein or for any errors or omissions that may have been made. The publisher remains neutral with regard to jurisdictional claims in published maps and institutional affiliations.

This Springer imprint is published by the registered company Springer Nature Switzerland AG.
The registered company address is: Gewerbestrasse 11, 6330 Cham, Switzerland

Foreword 1

Inspired perhaps by my mentor Jack Rootman, I have been studying art. More, I am making my fellows take drawing classes during their training. The discipline of learning to draw is all about increasing one's skill in observation. And careful observation is the heart of learning to interpret orbital imaging.

As much as looking at a photo of some breathtaking vista, or the mesmerizing photomicrographic patterns of some wonder of nature, I view orbital images with certain sense of artistic awe. Nature's art is revealed in the intricate anatomic patterns, fascinating contour changes that occur with orbital pathology, and nuances of shape and shading that are created with different imaging techniques.

In this atlas, Professor Ben Simon, Drs. Greenberg, and Landau Prat have put together a masterful collection of images that will provide an ideal tool for both the beginning student and the experienced practitioner, to increase their skills of careful observation and pattern recognition. The more one looks at orbital images, the more one sees. I hope that the readers of this atlas can appreciate the amount of dedication and effort that the editors and authors have applied to produce this outstanding product. I am optimistic that it will improve our ability to optimally understand orbital disease and help our patients. And perhaps the readers will, as well, be better able to appreciate the intrinsic artistic beauty of orbital imaging.

Sincerely,
Robert Alan Goldberg, M.D. F.A.C.S.
Karen and Frank Dabby Endowed Chair in Ophthalmology
Chief, Orbital and Ophthalmic Plastic Surgery
Stein Eye, David Geffen School of Medicine at UCLA



Foreword 2

Orbital disease is uncommon, and, in a relatively small part of the body, there is a very broad range of pathologies that can occur. This makes the diagnosis and management of orbital disease challenging. Improvements in imaging over a number of decades have helped the clinician enormously in establishing a diagnosis or a short list of differential diagnoses. However, even with this additional information, experience in the interpretation of orbital images is important, and correlating these images with the clinical presentation is vital in order to optimally manage each patient with orbital disease.

This atlas fills an important niche by comprehensively documenting the appearances on orbital imaging (largely computerized tomography (CT) and magnetic resonance imaging (MRI)) of the broad range of orbital pathologies encountered in clinical practice. Drs Ben Simon and Landau Prat have assembled a large international group of experienced orbital specialists to author these chapters. The chapters and their numerous images have been carefully selected, edited, and described with the aid of specialist radiologist Dr Gahl Greenberg. The atlas should therefore provide invaluable information to those clinicians managing patients with orbital disease, especially as the majority of such patients will be first seen by doctors with limited experience in managing the broad range of diseases affecting the orbit.

This atlas will be a useful reference tool for all those clinicians managing patients with orbital disease for many years to come. Drs Ben Simon, Greenberg, and Landau Prat should be congratulated for putting together such a useful resource.

Alan A. Mcnab
Associate Professor
Consultant, Orbital Plastic and Lacrimal Clinic
Royal Victorian Eye and Ear Hospital
Melbourne, Australia



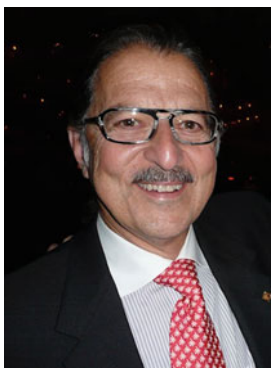
Foreword 3

The foundation for the management of orbital disorders requires a multidisciplinary approach. In addition, the approach is based on knowledge of the anatomical territory of the orbit as well as the diversity of the complex tissues within and surrounding it. Indeed, the orbit is also affected by many systemic and neurological disorders as well. Clinical practice includes structural lesions, inflammations, vascular anomalies, benign and malignant neoplasms, both regional and metastatic, as well as lymphoproliferative disorders. In addition, an orbital specialist has to interact with colleagues in many related disciplines and collate the clinical observations, imaging, and pathology to arrive at a diagnosis and treatment plan in the context of evolving knowledge and techniques.

The authors of this book have focused on the imaging of orbital disorders derived from their own cases and from outstanding institutions that focus on orbital disorders throughout the world. The many cases are critically organized with contemporary imaging technology and cover a wide range of disorders.

I am pleased to be part of this publication along with my colleague, Mr. Bruce Stewart, to provide our anatomical drawings of the orbit as a foundation for evaluation of disorders requiring surgery. These images define the territory within and surrounding the orbit. When paired with modern imaging, they will be useful for planning diagnostic, interventional, and new surgical approaches.

Jack Rootman MD FRCSC
Professor Emeritus
Ophthalmology and Vision Science
Pathology and Laboratory
University of British Columbia
Vancouver Canada



Preface

Every journey begins with a dream. Ours was clear, figuring out how to decipher orbital imaging. Throughout the years as orbital surgeons, every case has brought us a little closer to this goal. Yet, the more you learn, the more you realize that there is an endless amount of knowledge to acquire. As is so well put by our mentors, orbital imaging is more art than science.

We have been fortunate to know all these great teachers – world experts in oculoplastic and orbital surgery. Not only have they set a path for excellence in patients care, but also their kindness and generosity have been irreproachable. Such an atlas could never stand alone based on the work of one person. It is a collaborative effort of many. We cannot fully express our gratitude to all authors who have made a tremendous effort in establishing guidelines to orbital imaging, using their personal experience, know-how, and sharing their knowledge.

We have the honor and privilege to include Jack Rootman's and Bruce Stewart's anatomy illustrations which have become inalienable assets for the ophthalmic literature. This is somewhat symbolic as they started off with the anatomy atlas and have now merged into the imaging atlas, constituting a single continuum in oculoplastic database. An irreplaceable tool in the understanding and teaching this wonderful world of orbital surgery.

The *Atlas of Orbital Imaging* is a joint venture of ophthalmologists, oculoplastic surgeons, anatomists, and neuroradiologists, facing the everlasting challenge of combining their clinical and imaging interpretation skills. It is a known fact that imaging has captured a pivotal role in both surgical planning and medical management of our patients, necessitating close and efficient collaborations between physicians, either through daily communications, timely consultations as well as structured tumor boards and in the form of multidisciplinary meetings.

We hope that the orbital imaging atlas will bring us a small step toward diagnosis and enhanced patient care.

Tel Hashomer, Israel
October 2021

Guy Ben Simon
Gahl Greenberg
Daphna Landau Prat

Contents

Part I Orbital Anatomy 1

1 Bones of the Orbit 3
Jack Rootman, Daniel B. Rootman, Bruce Stewart, Stefania B. Diniz, Kelsey A. Roelofs, Liza M. Cohen, Claire S. Smith, Ayelet Eran, Ben Kaplan, and Assaf Marom

2 Vascular Anatomy 25
Daniel B. Rootman, Bruce Stewart, and Jack Rootman

3 Ocular Adnexa, Soft Tissue, and Extraocular Muscles 33
Jack Rootman, Daniel B. Rootman, Bruce Stewart, Stefania B. Diniz, Kelsey A. Roelofs, Liza M. Cohen, Claire S. Smith, Ayelet Eran, Ben Kaplan, and Assaf Marom

4 Paranasal Sinuses 47
Jack Rootman, Daniel B. Rootman, Bruce Stewart, Stefania B. Diniz, Kelsey A. Roelofs, Liza M. Cohen, Claire S. Smith, Ayelet Eran, Ben Kaplan, and Assaf Marom

5 Orbital Fissures 63
Jack Rootman, Daniel B. Rootman, Bruce Stewart, Stefania B. Diniz, Kelsey A. Roelofs, Liza M. Cohen, Claire S. Smith, Ayelet Eran, Ben Kaplan, and Assaf Marom

6 Orbital Fissures: Inferior Orbital Fissure 69
Jack Rootman, Daniel B. Rootman, Bruce Stewart, Stefania B. Diniz, Kelsey A. Roelofs, Liza M. Cohen, Claire S. Smith, Ayelet Eran, Ben Kaplan, and Assaf Marom

7 Orbital Fissures: Pterygopalatine Fossa 75
Jack Rootman, Daniel B. Rootman, Bruce Stewart, Stefania B. Diniz, Kelsey A. Roelofs, Liza M. Cohen, Claire S. Smith, Ayelet Eran, Ben Kaplan, and Assaf Marom

8 Orbital Fissures: Infratemporal Fossa 79
Jack Rootman, Daniel B. Rootman, Bruce Stewart, Stefania B. Diniz, Kelsey A. Roelofs, Liza M. Cohen, Claire S. Smith, Ayelet Eran, Ben Kaplan, and Assaf Marom

9 Cavernous Sinus 85
Jack Rootman, Daniel B. Rootman, Bruce Stewart, Stefania B. Diniz, Kelsey A. Roelofs, Liza M. Cohen, Claire S. Smith, Ayelet Eran, Ben Kaplan, and Assaf Marom

10 Meckel's Cave 91
Jack Rootman, Daniel B. Rootman, Bruce Stewart, Stefania B. Diniz, Kelsey A. Roelofs, Liza M. Cohen, Claire S. Smith, Ayelet Eran, Ben Kaplan, and Assaf Marom

Part II Orbital Imaging Modalities 97

11 Orbital CT 99
Denise S. Kim, Remy R. Lobo, and Alon Kahana

12 Orbital MRI 103
Arnaldo Mayer and Gahl Greenberg

13 Orbital CTA/CTV 113
Denise S. Kim, Remy R. Lobo, and Alon Kahana

14 Orbital MRA/MRV 117
Denise S. Kim, Remy R. Lobo, and Alon Kahana

15 Intraoperative Dynamic Imaging 121
Denise S. Kim, Remy R. Lobo, Neeraj Chaudhary, and Alon Kahana

16 Ultrasound of Orbit Tumors and Tumorlike Lesions 127
Bernadete Ayres and Alon Kahana

17 Orbital Ultrasound with Doppler 149
Stefania B. Diniz and Robert A. Goldberg

18 Orbital Positron Emission Tomography/Computed Tomography (PET/CT) 155
J. Matthew Debnam and Bita Esmaeli

19 Orbital Imaging Pearls 179
Gahl Greenberg, Daphna Landau Prat, and Guy Ben Simon

Part III Congenital Malformations/Anomalies 189

20 Craniofacial Dystosis 191
William R. Katowitz

21 Neurofibromatosis 199
William R. Katowitz

22 Anophthalmia and Microphthalmia 209
William R. Katowitz

23 Cystic Lesions of the Orbit: Dermoid and Epidermoid Cysts 215
William R. Katowitz

24 Cystic Lesions of the Orbit: Teratomas 221
William R. Katowitz

25 Other Cystic Lesions of the Orbit: Encephalocele 225
William R. Katowitz

26 Congenital Lacrimal Pathologies: Dacryocystocele 233
William R. Katowitz

27 Pediatric Orbital Vascular Tumors: Infantile Hemangioma 239
William R. Katowitz

Part IV Lacrimal Gland Tumors 247

28 Lacrimal Gland Prolapse and Dacryops 249
Oded Sagiv, J. Matthew Debnam, and Bita Esmaeli

29 Pleomorphic Adenoma of the Lacrimal Gland 253
Oded Sagiv, J. Matthew Debnam, and Bita Esmaeli

30 Recurrent Pleomorphic Adenoma of the Lacrimal Gland (RLGPA) 259
Oded Sagiv, J. Matthew Debnam, and Bita Esmaeli

31 Lacrimal Gland Carcinoma: Primary 263
Oded Sagiv, J. Matthew Debnam, and Bita Esmaeli

32 Carcinoma Ex-Pleomorphic Adenoma of the Lacrimal Gland 267
Oded Sagiv, J. Matthew Debnam, and Bita Esmaeli

33 Benign (Reactive) Lymphoid Hyperplasia and Lymphoma 271
Oded Sagiv, J. Matthew Debnam, and Bita Esmaeli

Part V Lacrimal Pathways 277

34 Normal Anatomy of the Lacrimal System 279
Swati Singh and Mohammad Javed Ali

35 Imaging in Lacrimal Drainage Obstruction and Acute Dacryocystitis 283
Swati Singh and Mohammad Javed Ali

36 Lacrimal Sac Tumors Imaging 289
Swati Singh and Mohammad Javed Ali

Part VI Primary Orbital Tumors 295

37 Orbital Lymphoma 297
Jaskirat Aujla, Valerie Juniat, Sandy Patel, and Dinesh Selva

38 Orbital Multiple Myeloma 307
Jaskirat Aujla, Valerie Juniat, Sandy Patel, and Dinesh Selva

39 Orbital Soft Tissues Sarcomas/Liposarcoma 313
Jaskirat Aujla, Valerie Juniat, Sandy Patel, and Dinesh Selva

40 Orbital Rhabdomyosarcoma 319
Ran Ben Cnaan, Dana Niry, and Igal Leibovitch

41 Orbital Lipoma 325
Ran Ben Cnaan, Dana Niry, and Igal Leibovitch

42 Solitary Fibrous Tumor of the Orbit 331
Ran Ben Cnaan, Justin N. Karlin, Dana Niry, Igal Leibovitch, and Robert A. Goldberg

43 Granulomatous Orbital Inflammation: Orbital Langerhans Cell Histiocytosis 339
Alan A. McNab

Part VII Eye and Ocular Adnexa Tumors with Orbital Extension 347

44 Periocular Basal Cell Carcinoma (BCC) 349
Alon Tiosano, Natalia Michaeli, and Iftach Yassur

45 Periocular Squamous Cell Carcinoma (SCC) 353
Alon Tiosano, Natalia Michaeli, and Iftach Yassur

46 Periocular Sebaceous Cell Carcinoma 359
Alon Tiosano, Natalia Michaeli, and Iftach Yassur

47 Ocular Surface Squamous Neoplasia with Orbital Extension 365
Swathi Kaliki and Ido Didi Fabian

48 Uveal Melanoma with Extraocular Spread 369
Andrew W. Stacey, Mahmud Mossa-Basha, and Ido Didi Fabian

49 Retinoblastoma 375
Vikas Khetan, Pim de Graaf, Devjyoti Tripathy, and Ido Didi Fabian

50 Metastatic Orbital Lesions: Breast Cancer 385
Oded Sagiv, J. Matthew Debnam, and Bita Esmaeli

51 Metastatic Orbital Lesions: Lung Cancer, Prostate Cancer, and Renal Cell Carcinoma (RCC) 389
Oded Sagiv, J. Matthew Debnam, and Bita Esmaeli

52 Metastatic Orbital Lesions: Melanoma 395
Oded Sagiv, J. Matthew Debnam, and Bita Esmaeli

53 Orbital Extension of Tumors from the Paranasal Sinuses: Squamous Cell Carcinoma 399
Oded Sagiv, J. Matthew Debnam, and Bita Esmaeli

54 Differential Diagnosis of Malignant Tumors of the Lacrimal Sac 403
Oded Sagiv, J. Matthew Debnam, and Bita Esmaeli

55 Merkel Cell Carcinoma of Eyelid (MCC) 407
Soltan Khalaila, Rosa Novoa, Benzion Samueli, and Erez Tsumi

Part VIII Osseous and Meninges Lesions 415

56 Imaging of Orbital Osteoma and Osteosarcoma 417
Alexandra Manta, Stefania B. Diniz, and Robert A. Goldberg

57 Ossifying Fibroma and Chondromyxoid Fibroma of the Orbit 423
Alexandra Manta, Stefania B. Diniz, and Robert A. Goldberg

58 Fibrous Dysplasia 427
Stefania B. Diniz and Robert A. Goldberg

59 Intraosseous Hemangioma and Cholesterol Granuloma of the Orbit 433
Liza M. Cohen, Stefania B. Diniz, and Robert A. Goldberg

60 Aneurysmal Bone Cyst and Ewing Sarcoma of the Orbit 439
Stefania B. Diniz, Liza M. Cohen, and Robert A. Goldberg

61 Meningioma of the Orbit and Orbital Vicinity 445
Justin N. Karlin and Robert A. Goldberg

Part IX Optic Nerve 453

62 Optic Nerve Glioma: Pilocytic Astrocytoma 455
Yoon-Duck Kim

63 Optic Nerve Sheath Meningioma 467
Yoon-Duck Kim

64 Intrinsic and Extrinsic Etiologies of Optic Nerve Damage 475
Ofira Zloto, Nina Borissovsky, Judith Luckman, and Nitza Goldenberg Cohen

Part X Vascular Malformations 489

65 Lymphatic Malformations 491
Kasturi Bhattacharjee, Nirod Medhi, and Shyam Sundar Das Mohapatra

66 Venous Malformations (VM) Distensible/Lymphatico-Venous Malformations (LVM) 499
Kasturi Bhattacharjee, Shyam Sundar Das Mohapatra, and Aditi Mehta

67 Orbital Venous Malformations (VM): Nondistensible 507
Kasturi Bhattacharjee, Nirod Medhi, and Shyam Sundar Das Mohapatra

68 Carotid-Cavernous Fistula 513
Kasturi Bhattacharjee, Nirod Medhi, and Shyam Sundar Das Mohapatra

69 Arteriovenous Malformations of the Orbit 521
Kasturi Bhattacharjee and Aditi Mehta

70 Other Rare Vascular Tumors of the Orbit 529
Kasturi Bhattacharjee and Vatsalya Venkatraman

Part XI Orbital Inflammation 537

71 Idiopathic Orbital Inflammation (IOI) 539
Alan A. McNab

72 Orbital Myositis 545
Alan A. McNab

73 Dacryoadenitis 551
Alan A. McNab

74 Scleritis 557
Alan A. McNab

75 Orbital Manifestations of Granulomatosis with Polyangiitis 561
Alan A. McNab

76 IgG-4 Related Orbital Disease 567
Alan A. McNab

77 Granulomatous Orbital Inflammation: Orbital Sarcoidosis 573
Alan A. McNab

78 Xanthogranulomatous Disease of the Orbit 577
Alan A. McNab

79 Thyroid Eye Disease 581
Kelsey A. Roelofs and Ezekiel Weis

Part XII Orbital Infection 589

80 Pre-septal Orbital Cellulitis 591
Kelsey A. Roelofs and Ezekiel Weis

81 Orbital Cellulitis 599
Kelsey A. Roelofs and Ezekiel Weis

82 Mucocele with Orbital Involvement 605
Kelsey A. Roelofs and Ezekiel Weis

83 Subperiosteal Orbital Abscess 611
Kelsey A. Roelofs and Ezekiel Weis

84 Aspergillosis 615
Kelsey A. Roelofs, Erin D. Wright, and Ezekiel Weis

85 Mucormycosis 623
Kelsey A. Roelofs and Ezekiel Weis

86 Orbital Hydatid Cysts 629
Milind N. Naik and Dilip K. Mishra

87 Orbital Cysticercosis 633
Jaee M. Naik and Milind N. Naik

88 Granulomatous Orbital Inflammation: Orbital Tuberculosis (TB) 637
Milind N. Naik and Joveeta Joseph

Part XIII Orbital Trauma and Other Inferred Changes 647

89 Orbital Trauma: Orbital Soft Tissue Injuries and Intraorbital Foreign Bodies 649
Gangadhara Sundar

90 Orbital Trauma: Orbital and Orbitofacial Fractures 661
Kavya Sundar and Gangadhara Sundar

91 Ocular Trauma and Intrinsic Pathology 677
Ofira Zloto

92 Nontraumatic Orbital Hemorrhage (NTOH) 683
Daphna Landau Prat, Gahl Greenberg, Alan A. McNab, and Guy Ben Simon

93 Postoperative Changes 695
Ofira Zloto

94 Periocular Fillers 705
Ayelet Priel, Don Kikkawa, Gahl Greenberg, Dana Niry, and S. Cohen

95 Periocular Fillers–Related Complications: Imaging Features 713
S. Cohen, Dana Niry, and Ayelet Priel

96 Acquired Anophthalmus 719
Yoav Vardizer, Nina Borissovsky, and Daphna Landau Prat

Index 727

About the Editors



Guy Ben Simon
Ophthalmic Plastic and Lacrimal Surgery Institute
Department of Ophthalmology
The Goldschleger Eye Institute
Sheba Medical Center
Tel Hashomer, Israel

Guy Ben Simon, MD, is Professor of Ophthalmology, Master of Health Administration and Chairman of the Institute of Orbital, Ophthalmic Plastic and Lacrimal Surgery at the Sheba Medical Center, Tel Hashomer, Israel. He has international standing in the field of oculoplastics and has published over 130 peer-reviewed scientific papers, also serving as reviewer for leading ophthalmology journals. Prof. Ben Simon is a much sought-after speaker at international conferences. He has also chaired many international conferences in Israel. Much of his scientific work is in collaboration with world-renowned researchers. He has been awarded numerous research grants and prizes for excellence in research. He established the Oculoplastics Fellowship Training Program at Sheba Medical Center and has trained many fellows and postdoctorate students. Prof. Ben Simon served as course instructor in orbital surgery in the American Academy of Ophthalmology and as a member of the Ophthalmology News and Education Committee (O.N.E. network). He was the Chairman of the Israeli Oculoplastic Society and the Chairman of the Ophthalmology Board Exams Committee, Israel Medical Association. His main fields of interest are orbital imaging, vascular malformations, thyroid eye disease, and orbital anatomy. He regularly participates in and directs voluntary missions to many third world countries to perform oculoplastic surgeries. He is a member of the Talpiot Medical Leadership program at the Sheba Medical Center.



Gahl Greenberg
Department of Diagnostic Imaging
Sheba Medical Center
Tel Hashomer, Israel

Gahl Greenberg is a Senior Staff Neuroradiologist and the current Head of the Head and Neck Imaging Service at the Department of Diagnostic Imaging, Sheba Medical Center, Israel. Dr. Greenberg serves as the primary consultant for the Maxillo-Facial, ENT, and Ophthalmology units and the chief advisor in multidisciplinary head and neck tumor boards. He is also the designated Safety Officer for MRI and a regular instructor in Continuing Medical Education courses at the Sackler Faculty of Medicine, Tel Aviv University. Dr. Greenberg is a graduate of the Hebrew University's medical school in Jerusalem and completed a two-year Diagnostic Neuroradiology Fellowship program in Toronto, Canada. His main fields of interest are craniofacial, orbit and paranasal sinuses oncology, temporomandibular joint and odontogenic disorders, and skull base pathology, and he has co-authored several publications in the field.



Daphna Landau Prat
Ophthalmic Plastic and Lacrimal Surgery Institute
Department of Ophthalmology
The Goldschleger Eye Institute
Sheba Medical Center
Tel Hashomer, Israel

Daphna Landau Prat is an orbital and oculoplastic surgeon at the Goldschleger Eye Institute, Sheba Medical Center, Israel, and a research affiliate at the Division of Ophthalmology, Children's Hospital of Philadelphia (CHOP). She has an MD degree from Tel Aviv University and a BSc in Mathematics with Computer Science from the Technion – Israel Institute of Technology, and is a graduate of the Rothschild Scholars Program, the Technion Program for Excellence. Dr. Landau was trained in oculoplastic surgery at CHOP. She participated in several humanitarian delegations, performing oculoplastic surgeries. Dr. Landau is a member of the "Sheba Talpiot Medical Leadership" program for excellence in medicine and medical research and is leading various academic and innovative projects.

Contributors

Mohammad Javed Ali Govindram Seksaria Institute of Dacryology, L.V. Prasad Eye Institute, Hyderabad, Telangana, India

Center for Ocular Regeneration, L.V. Prasad Eye Institute, Hyderabad, Telangana, India

Jaskirat Aujla South Australian Institute of Ophthalmology, Adelaide, SA, Australia

Bernadete Ayres Department of Ophthalmology, University of Michigan Medical School, Ann Arbor, MI, USA

Ran Ben Cnaan Oculoplastic and Orbital Institute, Division of Ophthalmology, Sourasky Medical Center, Sackler Faculty of Medicine, Tel Aviv University, Tel Aviv, Israel

Guy Ben Simon Ophthalmic Plastic and Lacrimal Surgery Institute, Department of Ophthalmology, The Goldschleger Eye Institute, Sheba Medical Center, Tel Hashomer, Israel

Kasturi Bhattacharjee Department of Ophthalmic Plastic and Reconstructive Surgery, Sri Sankaradeva Nethralaya, Guwahati, India

Nina Borissovsky Imaging Department, Bnai-Zion Medical Center, Rappaport Faculty of Medicine, Technion, Haifa, Israel

Neeraj Chaudhary Department of Radiology, University of Michigan Medical School, Ann Arbor, MI, USA

Department of Neurosurgery, University of Michigan Medical School, Ann Arbor, MI, USA

Department of Neurology, University of Michigan Medical School, Ann Arbor, MI, USA

Department of Otorhinolaryngology, University of Michigan Medical School, Ann Arbor, MI, USA

Liza M. Cohen Division of Orbital and Ophthalmic Plastic Surgery, Stein Eye Institute, University of California, Los Angeles, CA, USA

S. Cohen Department of Plastic and Reconstructive Surgery, Assaf Harofeh Medical Center, Zerifin, Israel

Nitza Goldenberg Cohen Krieger Eye Research Laboratory, Bnai-Zion Medical Center, Haifa, Israel

Department of Ophthalmology, Bnai-Zion Medical Center, Haifa, Israel

Rappaport Faculty of Medicine, Technion, Israel Institute of Technology, Haifa, Israel

J. Matthew Debnam Department of Neuroradiology, The University of Texas MD Anderson Cancer Center, Houston, TX, USA

Pim de Graaf Department of Radiology and Nuclear Medicine, Amsterdam UMC, Vrije Universiteit Amsterdam, Cancer Center Amsterdam, Amsterdam, The Netherlands

Stefania B. Diniz Division of Orbital and Ophthalmic Plastic Surgery, Stein and Doheny Eye Institutes, University of California, Los Angeles, CA, USA

Ayelet Eran Neuroradiology Unit, Radiology Department, Rambam Healthcare Medical Center, Haifa, Israel

Department of Anatomy, Rappaport Faculty of Medicine, Technion – Israel Institute of Technology, Haifa, Israel

Bita Esmaeli Ophthalmic Plastic Surgery, Department of Plastic Surgery, The University of Texas MD Anderson Cancer Center, Houston, TX, USA

Ido Didi Fabian Ocular Oncology Service, The Goldschleger Eye Institute, Sheba Medical Center, Tel Hashomer, Tel Aviv University, Tel Aviv, Israel

Robert A. Goldberg Division of Orbital and Ophthalmic Plastic Surgery, Stein and Doheny Eye Institutes, University of California, Los Angeles, CA, USA

Gahl Greenberg Department of Diagnostic Imaging, Sheba Medical Center, Tel Hashomer, Israel

Joveeta Joseph LV Prasad Eye Institute, Hyderabad, India

Valerie Juniat South Australian Institute of Ophthalmology, Adelaide, SA, Australia

Alon Kahana Ophthalmology Department, Oakland University William Beaumont School of Medicine, Rochester, MI, USA

Attending Surgeon, Consultants in Ophthalmic and Facial Plastic Surgery, Southfield, MI, USA

Swathi Kaliki Operation Eyesight Universal Institute for Eye Cancer, LV Prasad Eye Institute, Hyderabad, India

Ben Kaplan Department of Anatomy, Rappaport Faculty of Medicine, Technion – Israel Institute of Technology, Haifa, Israel

Justin N. Karlin Division of Orbital and Ophthalmic Plastic Surgery, Stein Eye Institute, University of California, Los Angeles, CA, USA

William R. Katowitz The Children's Hospital of Philadelphia, Philadelphia, PA, USA

Soltan Khalaila Ophthalmology, Soroka University Medical Center, Beer-Sheva, Israel

Vikas Khetan Sankara Nethralaya, Chennai, India

Don Kikkawa Division of Oculofacial Plastic and Reconstructive Surgery, Department of Ophthalmology, University of California San Diego, La Jolla, CA, USA

Denise S. Kim Department of Ophthalmology and Visual Sciences, University of Michigan Medical School, Ann Arbor, MI, USA

Yoon-Duck Kim Oculoplastic and Orbital Surgery Division, Nune Eye Hospital, Seoul, South Korea

Daphna Landau Prat Ophthalmic Plastic and Lacrimal Surgery Institute, Department of Ophthalmology, The Goldschleger Eye Institute, Sheba Medical Center, Tel Hashomer, Israel

Igal Leibovitch Oculoplastic and Orbital Institute, Division of Ophthalmology, Sourasky Medical Center, Sackler Faculty of Medicine, Tel Aviv University, Tel Aviv, Israel

Remy R. Lobo Department of Radiology, University of Michigan Medical School, Ann Arbor, MI, USA

Judith Luckman Radiology Department, Rabin Medical Center-Beilinson Hospital, Petah Tikva, Israel

Alexandra Manta Division of Orbital and Ophthalmic Plastic Surgery, Jules Stein Eye Institute, University of California, Los Angeles, CA, USA

Assaf Marom Department of Anatomy, Rappaport Faculty of Medicine, Technion – Israel Institute of Technology, Haifa, Israel

Arnaldo Mayer PI at the Computational imaging lab (Cilab), Sheba Medical Center, Ramat Gan, Israel

Alan A. McNab Orbital Plastic and Lacrimal Clinic, Royal Victorian Eye and Ear Hospital, Melbourne, VIC, Australia

Nirod Medhi Primus Imaging, Guwahati, India

Aditi Mehta Department of Ophthalmic Plastic and Reconstructive Surgery, Sri Sankaradeva Nethralaya, Guwahati, India

Natalia Michaeli Sackler Faculty of Medicine, Tel Aviv University, Tel Aviv, Israel
Department of Radiology, Rabin Medical Center, Petah Tikva, Israel

Dilip K. Mishra LV Prasad Eye Institute, Hyderabad, India

Shyam Sundar Das Mohapatra Sri Sankaradeva Nethralaya, Guwahati, India

Mahmud Mossa-Basha Department of Radiology, University of Washington, Seattle, WA, USA

Milind N. Naik LV Prasad Eye Institute, Hyderabad, India

Jaee M. Naik St. John's Medical College, Bangalore, India

Dana Niry Department of Radiology, Sourasky Medical Center, Tel Aviv University, Tel Aviv, Israel

Rosa Novoa Diagnostic Imaging, Soroka University Medical Center, Beer-Sheva, Israel

Sandy Patel Department of Radiology, Royal Adelaide Hospital, Adelaide, SA, Australia

Ayelet Priel Department of Ophthalmology, Goldschleger Eye Institute, Sheba Medical Center, Ramat-Gan, Israel
Sackler Faculty of Medicine, Tel Aviv University, Tel Aviv, Israel

Kelsey A. Roelofs Division of Orbital and Ophthalmic Plastic Surgery, Stein and Doheny Eye Institutes, University of California, Los Angeles, CA, USA

Daniel B. Rootman Division of Orbital and Ophthalmic Plastic Surgery, Stein and Doheny Eye Institutes, University of California, Los Angeles, CA, USA

Jack Rootman University of British Columbia, Vancouver, BC, Canada

Oded Sagiv The Goldschleger Eye Institute, Sheba Medical Center, affiliated to the Sackler Faculty of Medicine, Tel-Aviv University, Tel Aviv, Israel

Benzion Samueli Pathology, Soroka University Medical Center, Beer-Sheva, Israel

Dinesh Selva South Australian Institute of Ophthalmology, Adelaide, SA, Australia

Swati Singh Center for Ocular Regeneration, L.V. Prasad Eye Institute, Hyderabad, Telangana, India

Claire S. Smith Division of Orbital and Ophthalmic Plastic Surgery, Stein and Doheny Eye Institutes, University of California, Los Angeles, CA, USA

Andrew W. Stacey Department of Ophthalmology, University of Washington, Seattle, WA, USA

Bruce Stewart BFA Art Center College of Design, UBC Faculty of Medicine, Kelowna, BC, Canada

Kavya Sundar Faculty of Dentistry, National University Centre for Oral Health, National University of Singapore, Singapore, Singapore

Gangadhara Sundar Orbit & Oculofacial Surgery, Department of Ophthalmology, National University Hospital, National University of Singapore, Singapore, Singapore

Alon Tiosano Department of Ophthalmology, Rabin Medical Center – Beilinson Hospital, Petach Tikva, Israel

Department of Radiology, Rabin Medical Center, Petah Tikva, Israel

Devjyoti Tripathy Ophthalmic Plastics, Orbit & Ocular Oncology Services, MTC Campus, LV Prasad Eye Institute, Bhubaneswar, India

Erez Tsumi Ophthalmology, Soroka University Medical Center, Beer-Sheva, Israel

Yoav Vardizer Ophthalmology Department, Bnai-Zion Medical Center, Rappaport Faculty of Medicine, Technion, Haifa, Israel

Vatsalya Venkatraman Sri Sankaradeva Nethralaya, Guwahati, India

Ezekiel Weis Department of Ophthalmology and Visual Sciences, University of Alberta, Edmonton, AB, Canada

Department of Surgery, University of Calgary, Calgary, AB, Canada

Erin D. Wright Department of Surgery, University of Alberta, Edmonton, AB, Canada

Iftach Yassur Department of Ophthalmology, Rabin Medical Center – Beilinson Hospital, Petach Tikva, Israel

Department of Radiology, Rabin Medical Center, Petah Tikva, Israel

Ofira Zloto Department of Ophthalmology, Créteil, France

Goldschleger Eye Institute, Sheba Medical Center, Tel Hashomer, Israel

Sackler Faculty of Medicine, Tel Aviv University, Tel Aviv, Israel

Part I

Orbital Anatomy

Bones of the Orbit

1

Jack Rootman, Daniel B. Rootman, Bruce Stewart, Stefania B. Diniz, Kelsey A. Roelofs, Liza M. Cohen, Claire S. Smith, Ayelet Eran, Ben Kaplan, and Assaf Marom

Contents

1 **Introduction** 3

2 **Figures with Captions** 5

References 23

Abstract

The facial skeleton comprises two orbital cavities. Each of them is an elongated square pyramidal cavity with its base facing anteriorly as the orbital opening, and its axis is directed posteromedially towards the orbital apex. Supported within the orbital cavity by a sizable amount of adipose tissue, the main orbital constituents are the bulbus oculi (the eyeball) and the second cranial (optic) nerve; the extraocular muscles; the third (oculomotor), fourth (trochlear), and sixth (abducens) cranial nerves; the ophthalmic and maxillary divisions of the fifth (trigeminal) cranial nerve; the lacrimal gland and nasolacrimal system; and the ciliary (parasympathetic) ganglion.

The bony orbit and ocular adnexa provide globe protection, allowing normal function and vision. The orbit is comprised of seven distinct cranial bones. CT is the modality of choice for orbital bone imaging; however, MRI can be a valuable adjunct in certain osseous pathologies especially in determining bone marrow involvement.

Keywords

Orbital bones · Frontal bone · Sphenoid bone · Zygomatic bone · Lacrimal bone · Maxillary bone · Ethmoidal bone · Palatine bone

J. Rootman
University of British Columbia, Vancouver, BC, Canada

D. B. Rootman · S. B. Diniz · K. A. Roelofs · C. S. Smith
Division of Orbital and Ophthalmic Plastic Surgery, Stein and Doheny Eye Institutes, University of California, Los Angeles, CA, USA

B. Stewart
BFA Art Center College of Design, UBC Faculty of Medicine, Kelowna, BC, Canada

L. M. Cohen
Division of Orbital and Ophthalmic Plastic Surgery, Stein Eye Institute, University of California, Los Angeles, CA, USA

A. Eran
Neuroradiology Unit, Radiology Department, Rambam Healthcare Medical Center, Haifa, Israel

Department of Anatomy, Rappaport Faculty of Medicine, Technion – Israel Institute of Technology, Haifa, Israel

B. Kaplan · A. Marom (✉)
Department of Anatomy, Rappaport Faculty of Medicine, Technion – Israel Institute of Technology, Haifa, Israel
e-mail: assafma@technion.ac.il

1 Introduction

Each orbital cavity has a roof and a floor, a medial wall, and a lateral wall. Several cranial bones contribute to the formation of these bony boundaries.

The orbital roof is mainly formed by the orbital surface of the frontal bone, which also serves as the floor for the anterior cranial fossa. Anteromedially the orbital roof relates to the frontal sinus, where there is also a trochlear spine where the trochlea (pulley) of the superior oblique muscle attaches. Situated anterolaterally is the lacrimal fossa for the lacrimal gland. Posteriorly there is a short horizontal suture with the lesser wing of the sphenoid bone, the inferior surface of which contributes a small portion to the orbital roof. Lastly, the optic canal is situated posteriorly at the apex, bounded between the roots of the lesser wing of the sphenoid bone.

© Springer Nature Switzerland AG 2022
G. Ben Simon et al. (eds.), *Atlas of Orbital Imaging*,
https://doi.org/10.1007/978-3-030-62426-2_1

From anterior to posterior, the thin medial wall of the orbital cavity consists of the frontal process of the maxilla, the lacrimal bone, and the orbital surface of the ethmoid labyrinth. The latter forms a vertical suture with the sphenoid body. The groove for the lacrimal sac (the superior blind widening of the vertical nasolacrimal duct) is situated between the frontal process of the maxilla and the lacrimal bone, and it is bounded anteriorly and posteriorly by the anterior and posterior lacrimal crests of these bones, respectively. The maxillo-lacrimal suture lies at the floor of this fossa, and the lacrimal part of the orbicularis oculi muscle attaches to the posterior lacrimal crest and bridges the groove. The vertical nasolacrimal canal opens inferiorly into the inferior nasal meatus. Posterior to the lacrimal groove, most of the medial orbital wall is mostly formed by the rectangular orbital surface of the ethmoid bone. Anteriorly, it articulates with the lacrimal bone; posteriorly, with a small portion of the sphenoid body that forms the most posterior part of the medial orbital wall; inferiorly, with the orbital surface of the maxilla and the triangular orbital surface of the palatine bone; and superiorly, it articulates with the orbital surface of the frontal bone at the fronto-ethmoidal suture. Along the latter, the anterior and posterior ethmoidal foramina are situated.

The orbital floor is formed by the orbital surfaces of the maxilla (medially) and zygomatic bone (anterolaterally) and the palatine bone.

The lateral orbital wall is formed posteriorly by the orbital surface of the sphenoid bone and anteriorly by the orbital surface of the zygomatic bone, where the openings of the canals for the zygomaticotemporal (higher) and the zygomaticofacial (lower) nerves are situated. The lateral wall and the floor are separated by the inferior orbital fissure, which connects the orbital cavity with the pterygopalatine and infratemporal fossae. This fissure is bounded superiorly by the greater wing of the sphenoid and inferiorly mostly by the maxilla. Posteriorly, the lateral wall and the roof are separated by the superior orbital fissure, which is the gap between the greater and lesser wings of the sphenoid bone. This fissure, which allows the communication between the orbital cavity and the middle cranial fossa, is widest medially and tapers laterally.

The apex of the orbit is situated at the medial end of the superior orbital fissure, above which is the optic canal. The optic canal lies between the flat anterior (thin) root and the posterior (thick) root that connect the lesser wing to the body of the sphenoid bone.

2 Figures with Captions

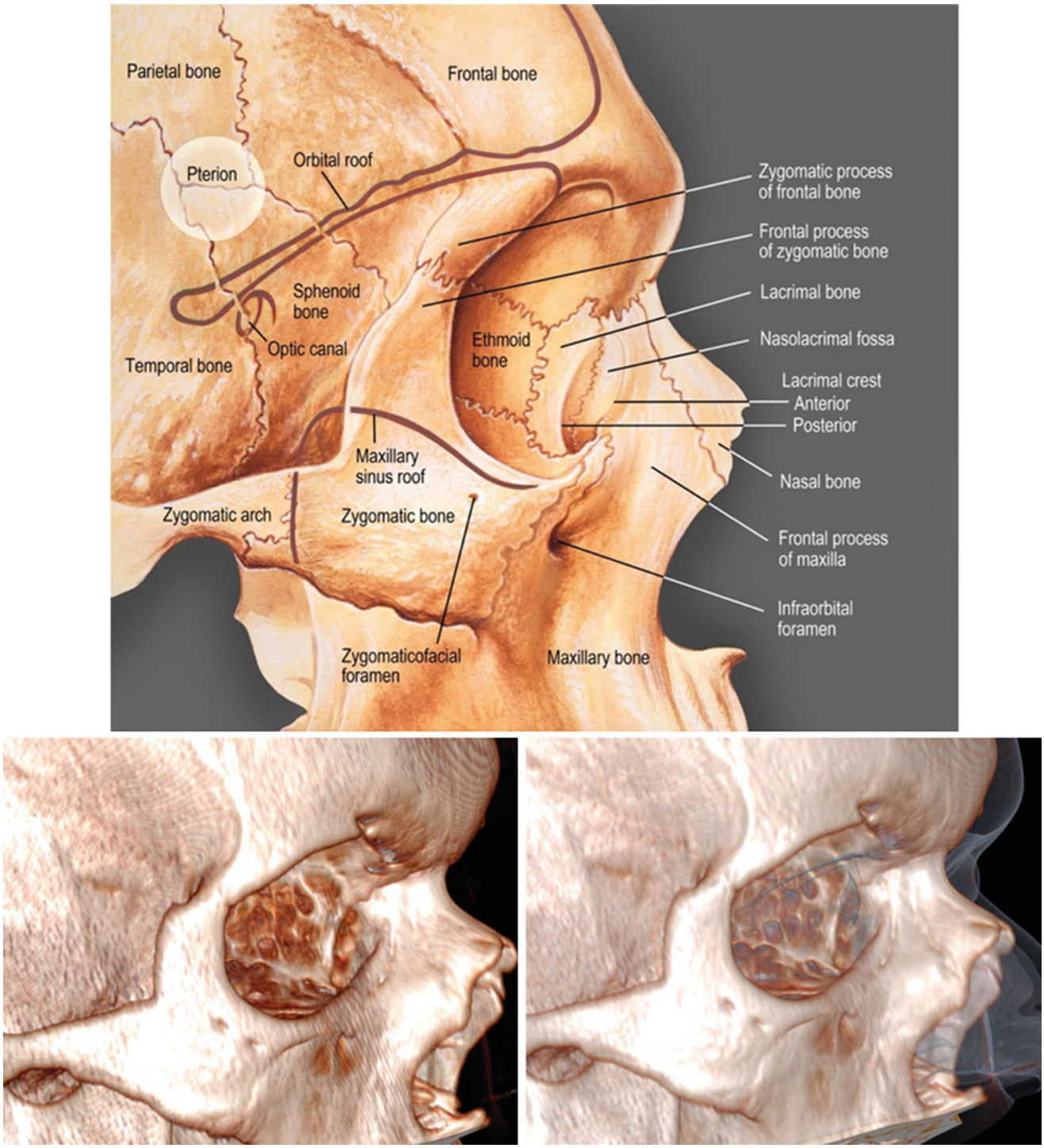


Fig. 1 Lateral view – drawing (*upper*) and corresponding 3D CT reconstruction (*lower left* plain, and *lower right* with surface rendering) of constituents of the orbital bony structures and adjacent spaces

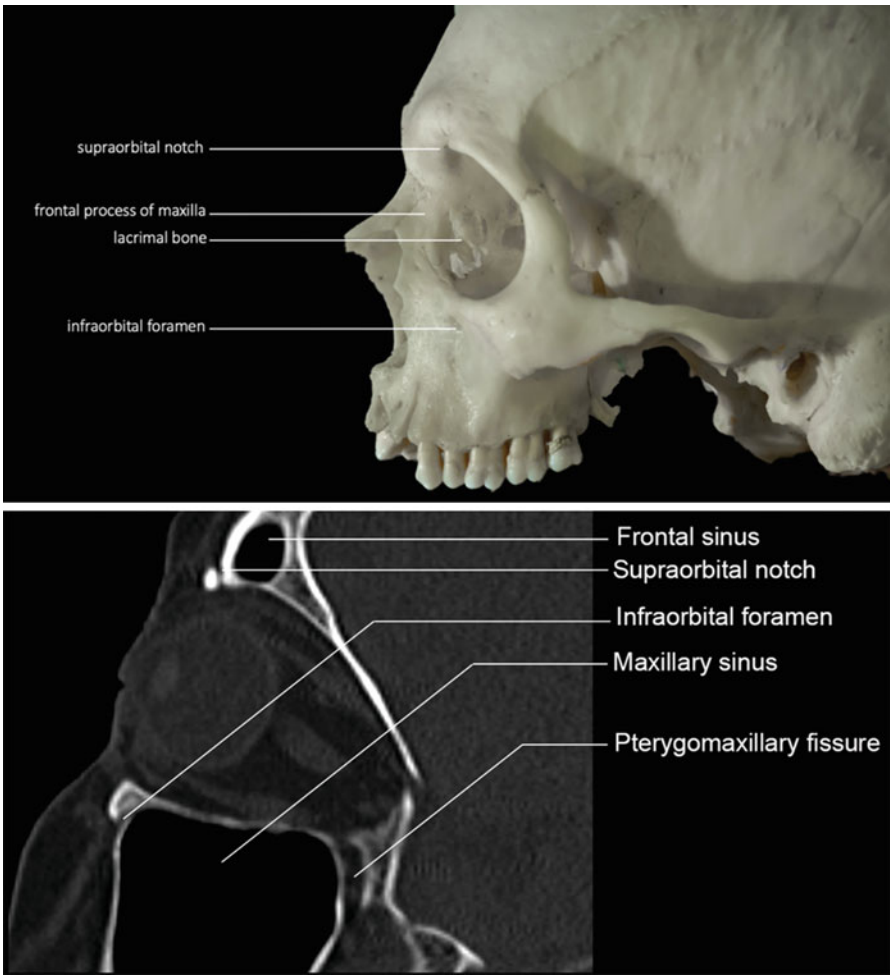


Fig. 2 Lateral view of the orbital cavity, human skull (*upper*), and CT bone window sagittal oblique MPR (*lower*)

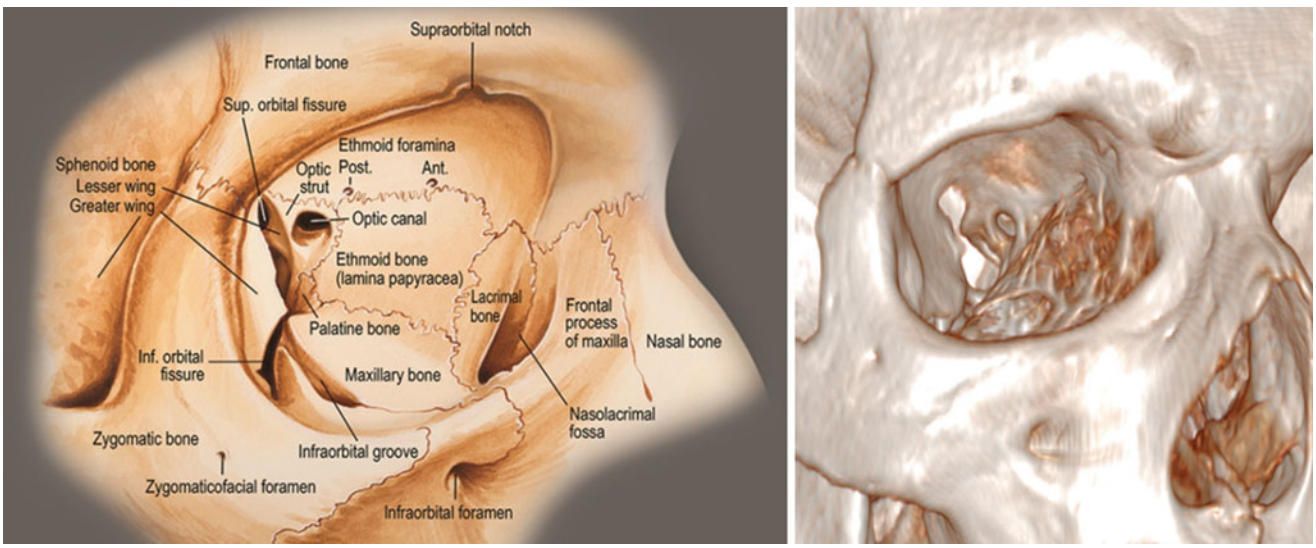


Fig. 3 Anterior-medial view of orbital bony and adjacent skeletal structures, drawing (*left*) and matching 3D CT reformat (*right*)

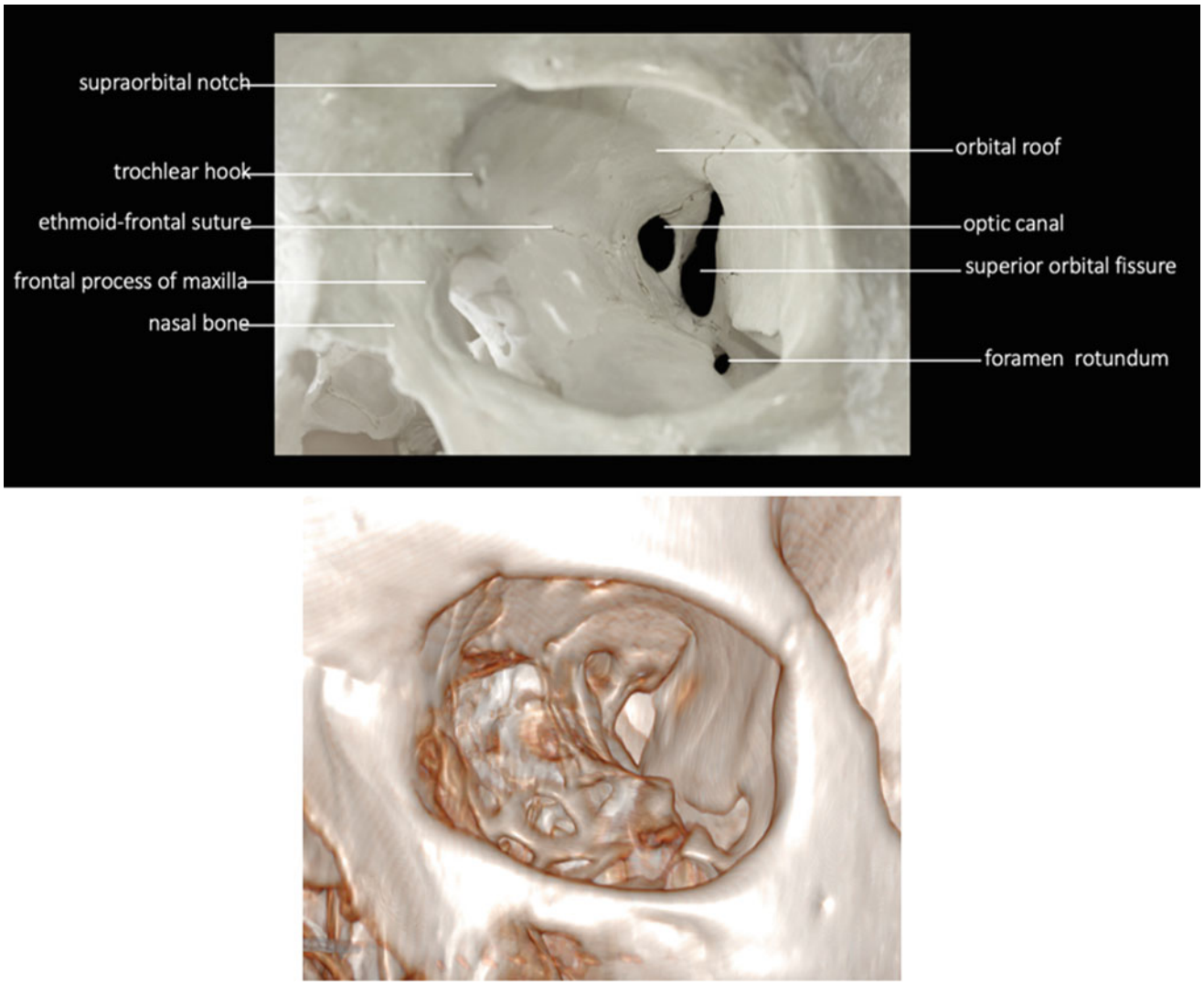


Fig. 4 Anterior view of the left orbital cavity – human skull (*upper* image) with 3D reconstruction (*lower* image)

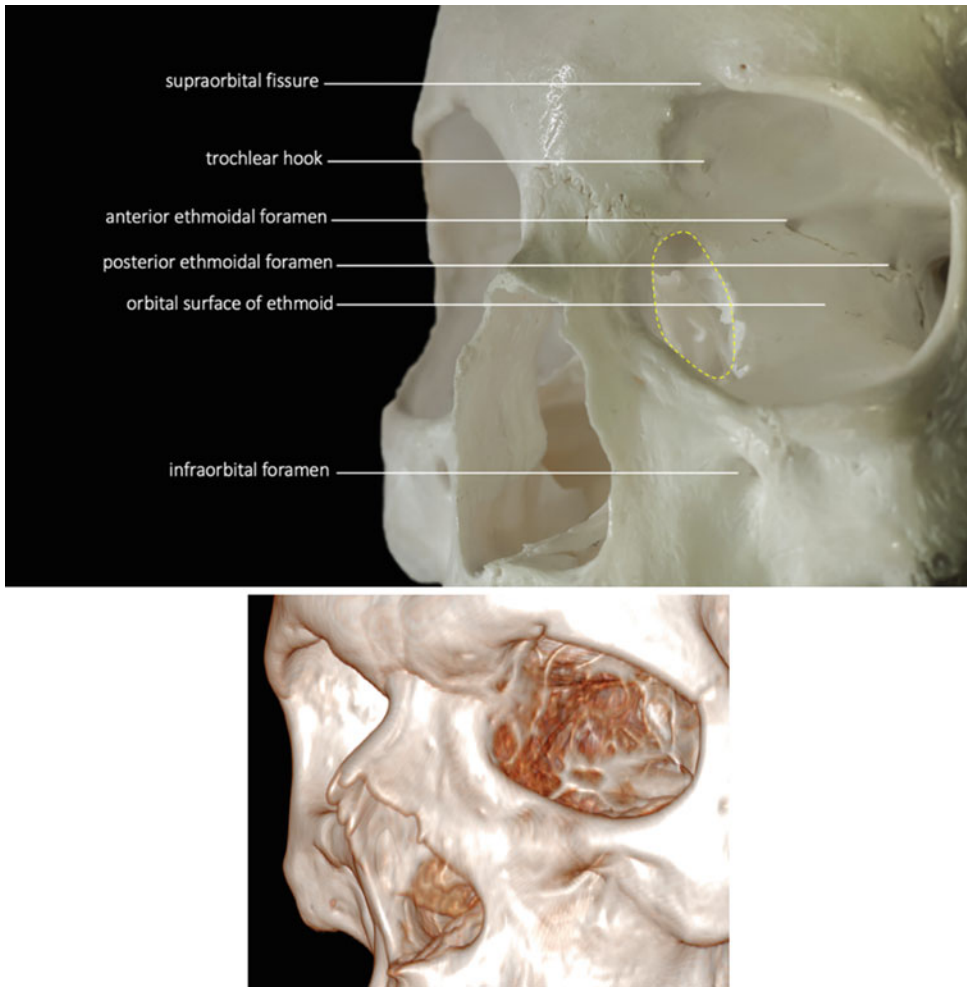


Fig. 5 Anterolateral view of the orbital cavity. The dashed yellow line indicates the borders of the missing lacrimal bone; human skull (*upper*) with corresponding 3D reformat (*lower*)

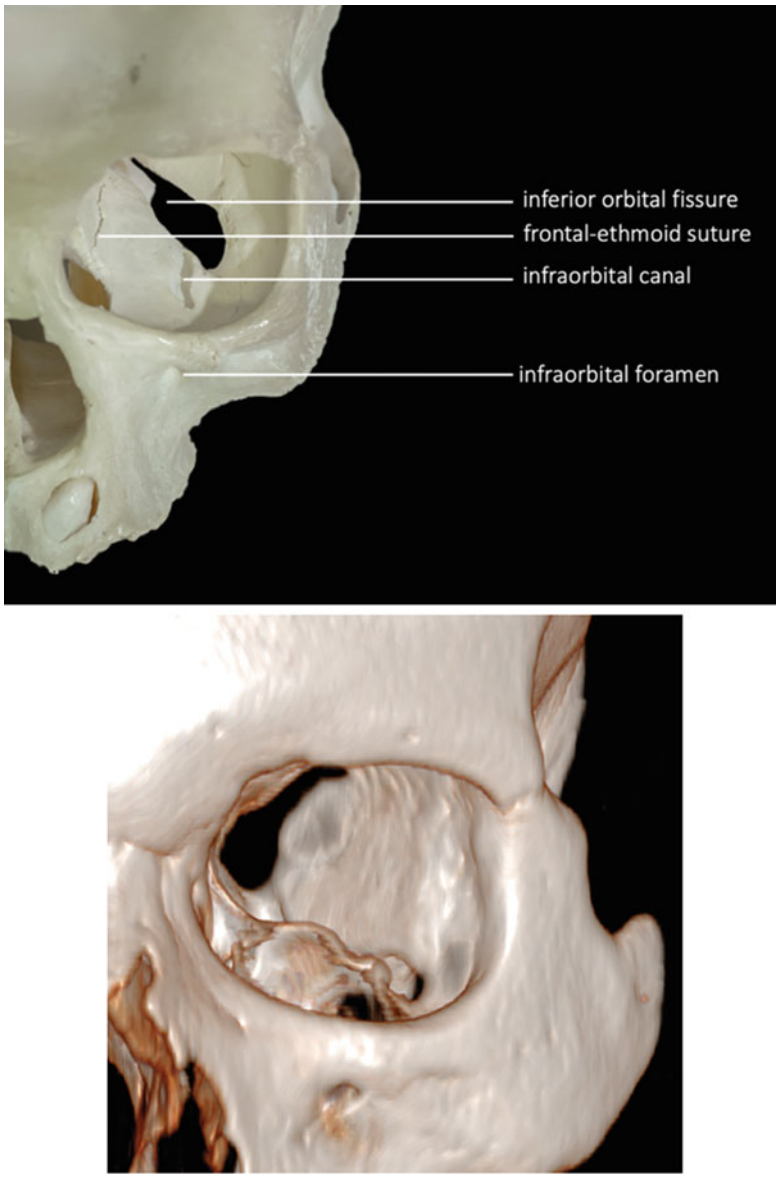


Fig. 6 Anterosuperior view of the orbital cavity, human skull (*upper*), and corresponding 3D reconstruction (*lower*)

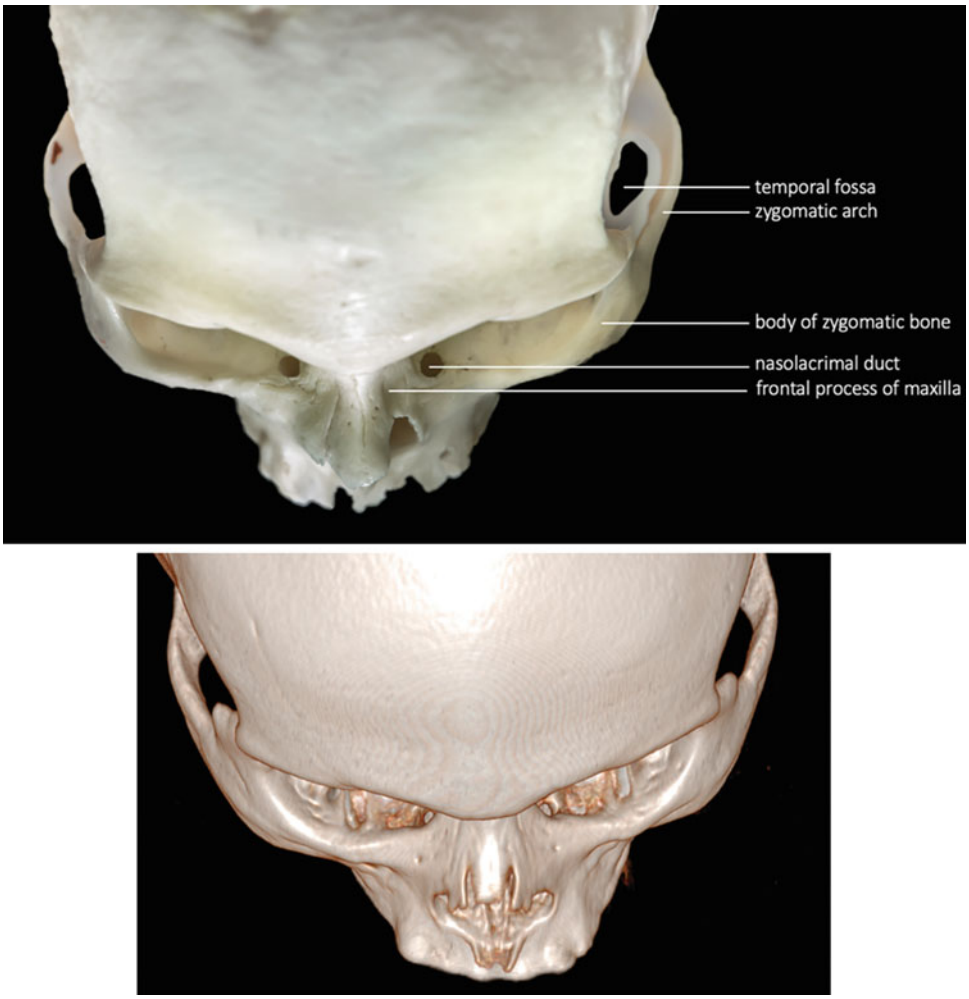


Fig. 7 Superior view of the orbital rim, human skull (*upper*), and 3D reconstruction (*lower*)

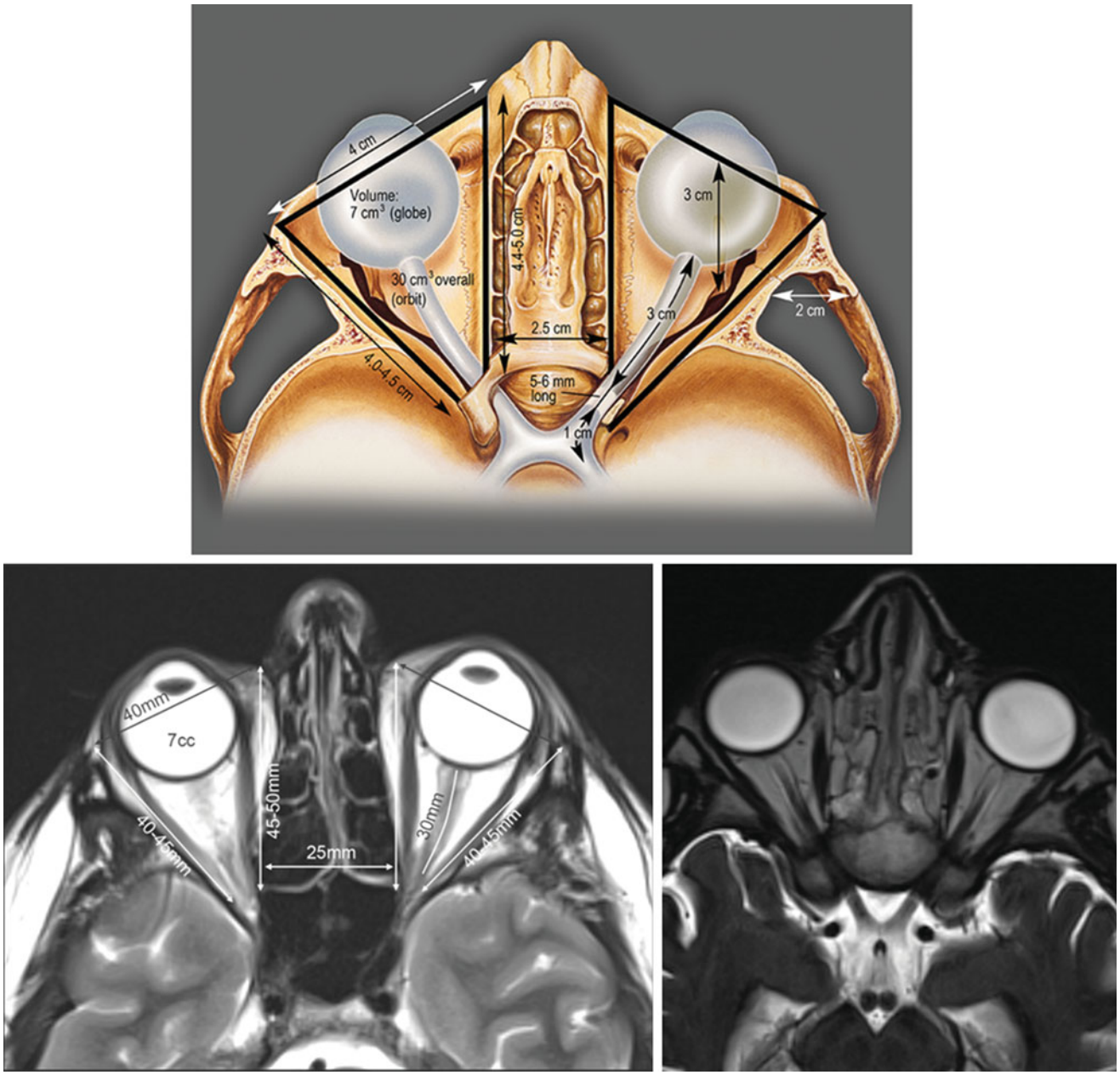


Fig. 8 Transview of the globe and optic nerves with the major orbital dimensions and relationships, drawing (*upper*) and axial T2W MRI (*lower left*). Note the relationship of the globe to the infraorbital canal. T2 space (*lower right*) better demonstrates the entire length of the anterior visual pathway

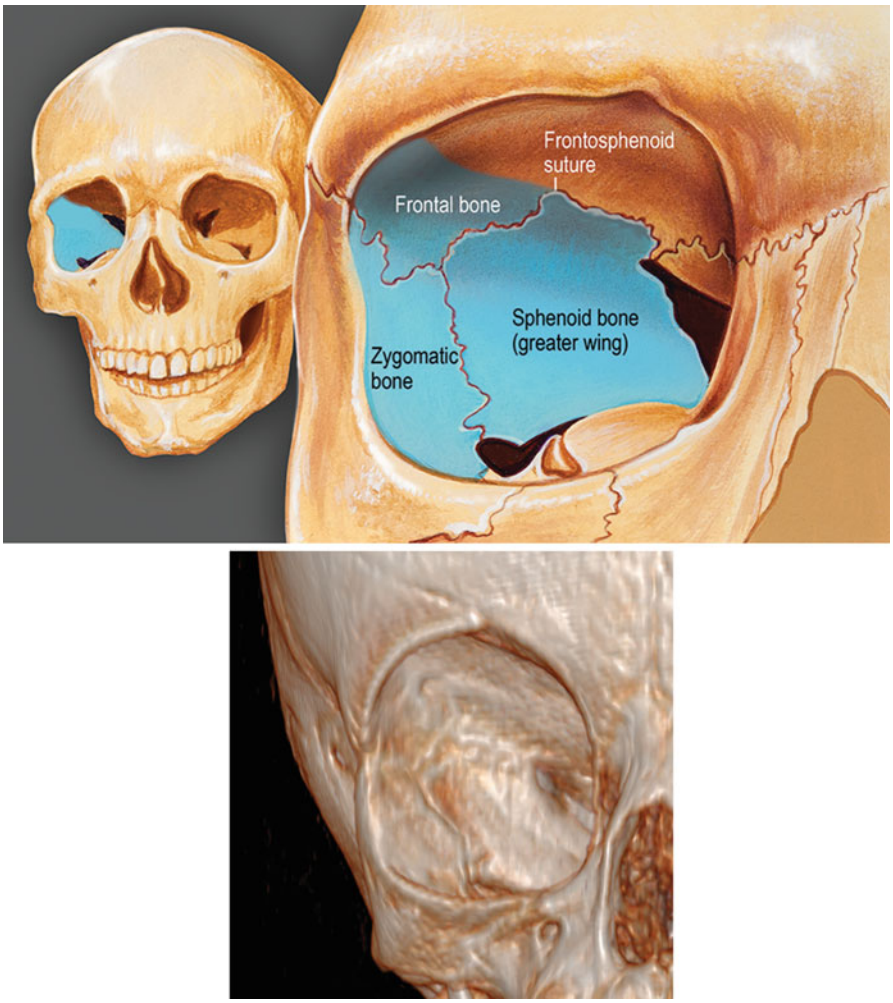


Fig. 9 Constituents of the lateral orbital wall drawing (*upper*) with corresponding 3D CT reformat of a 6-month-old boy (*lower*). A pediatric scan was chosen in order to accentuate the suture lines of the lateral orbital wall

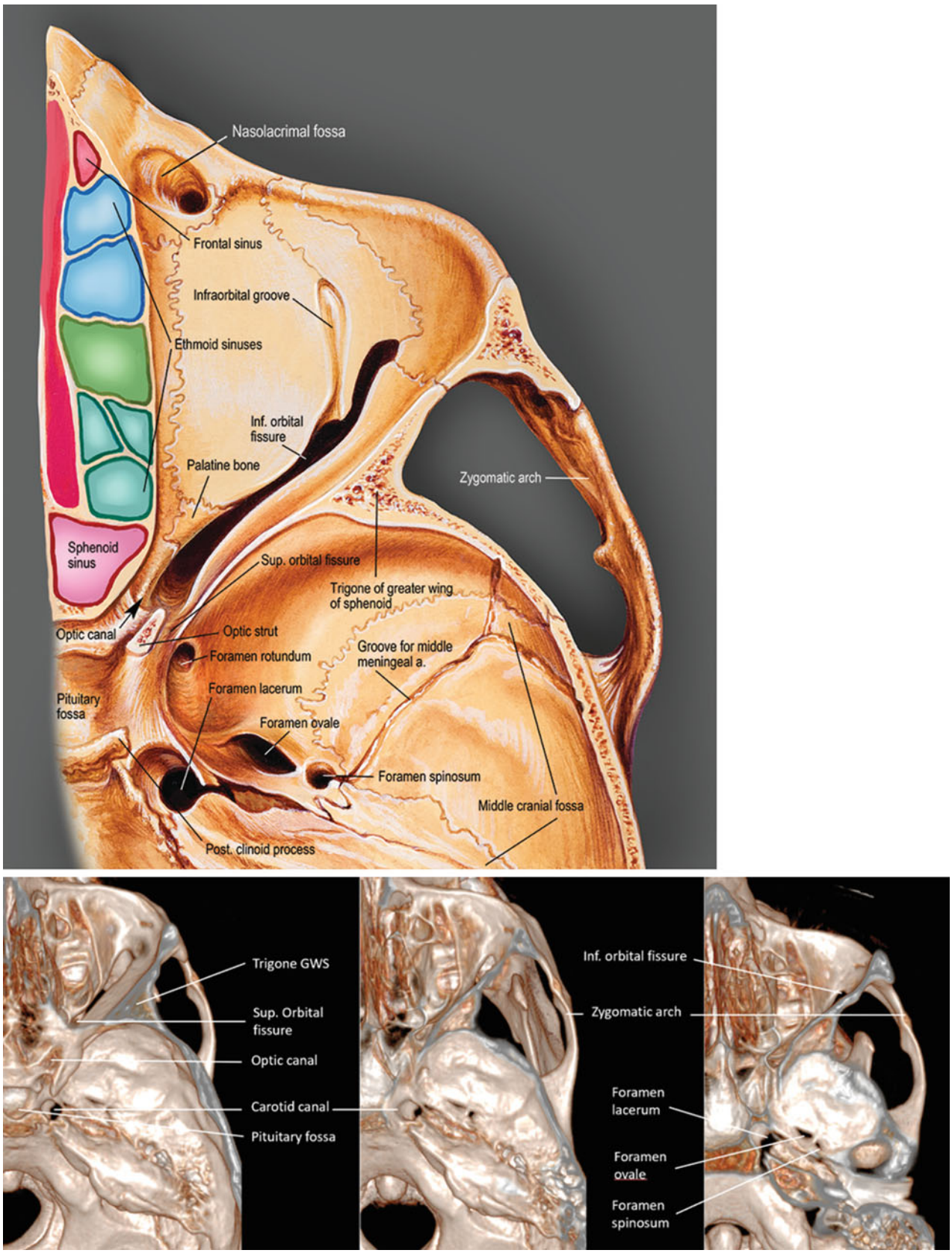


Fig. 10 The lateral wall and floor of the orbit as seen from above showing relationships of adjacent spaces (sinuses, temporalis fossa, and middle cranial fossa) as well as canals and fissures. Note the marrow at the trigone of the sphenoid wing. Drawing (*upper*) and sequential upper to lower 3D axial reformat CT images (*lower*)

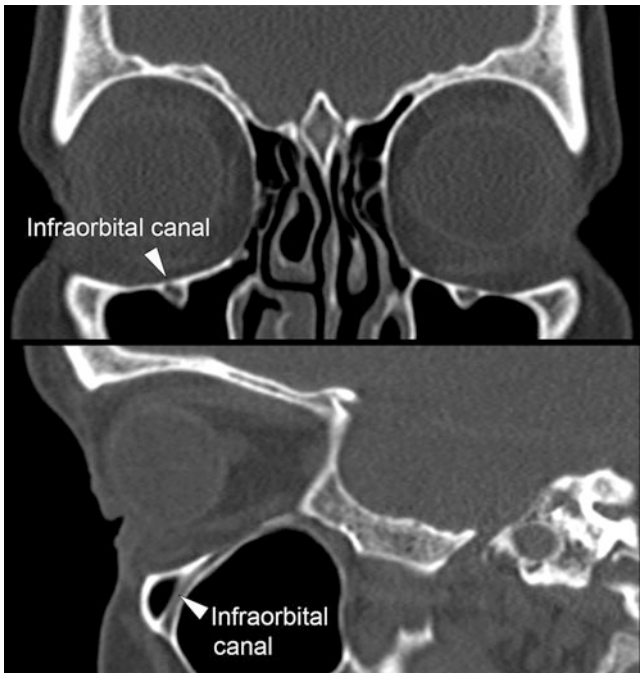


Fig. 11 The infraorbital canal as depicted in coronal and sagittal bone window CT images

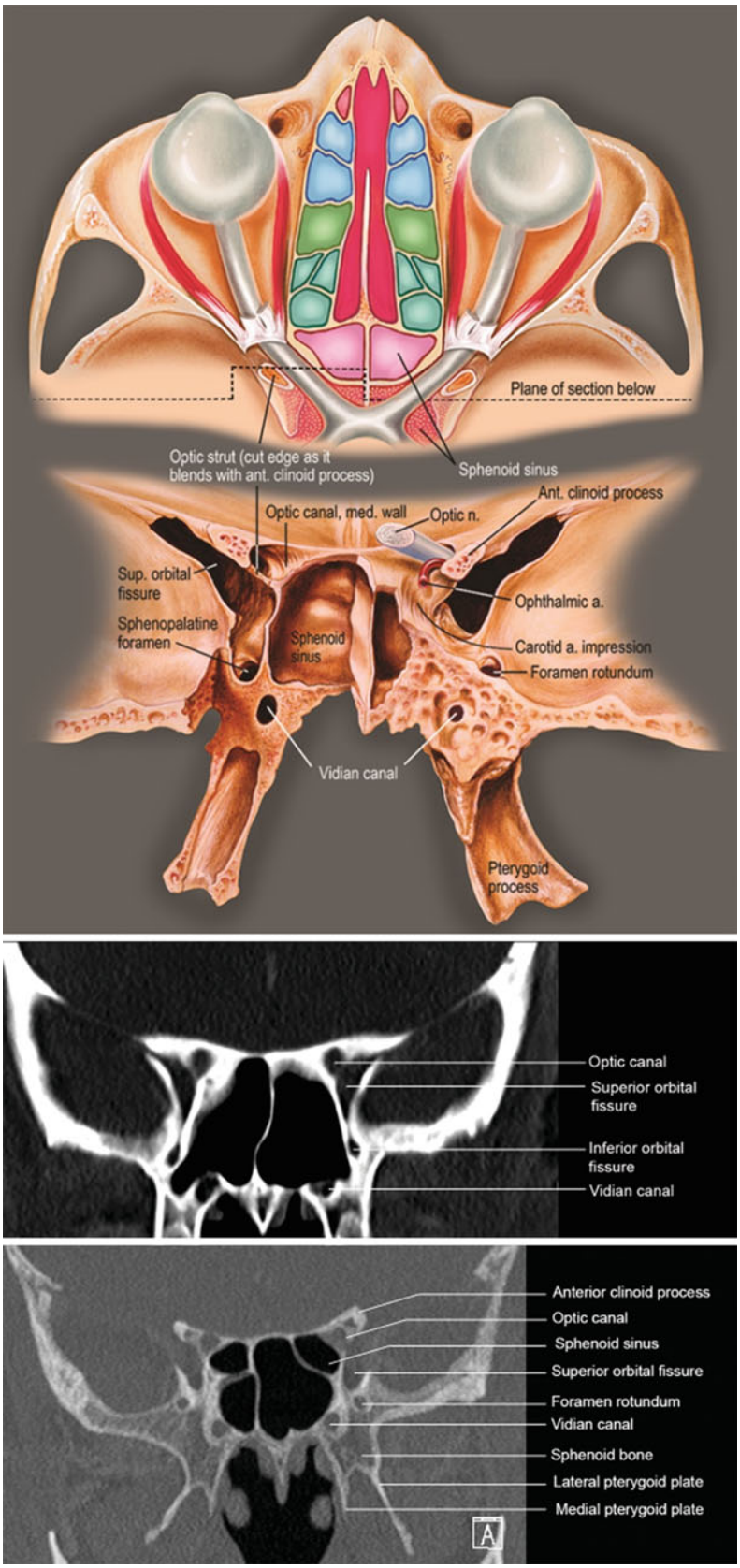


Fig. 12 Major relationships of the optic canal to the sphenoid sinus and sphenoid bone. Lower drawing is a view from behind with a block of bone excised (level indicated as dotted line) to demonstrate relationships at the anterior and posterior ends of the optic canal and superior orbital fissure. Corresponding coronal CT scans are shown below (*lower* images)

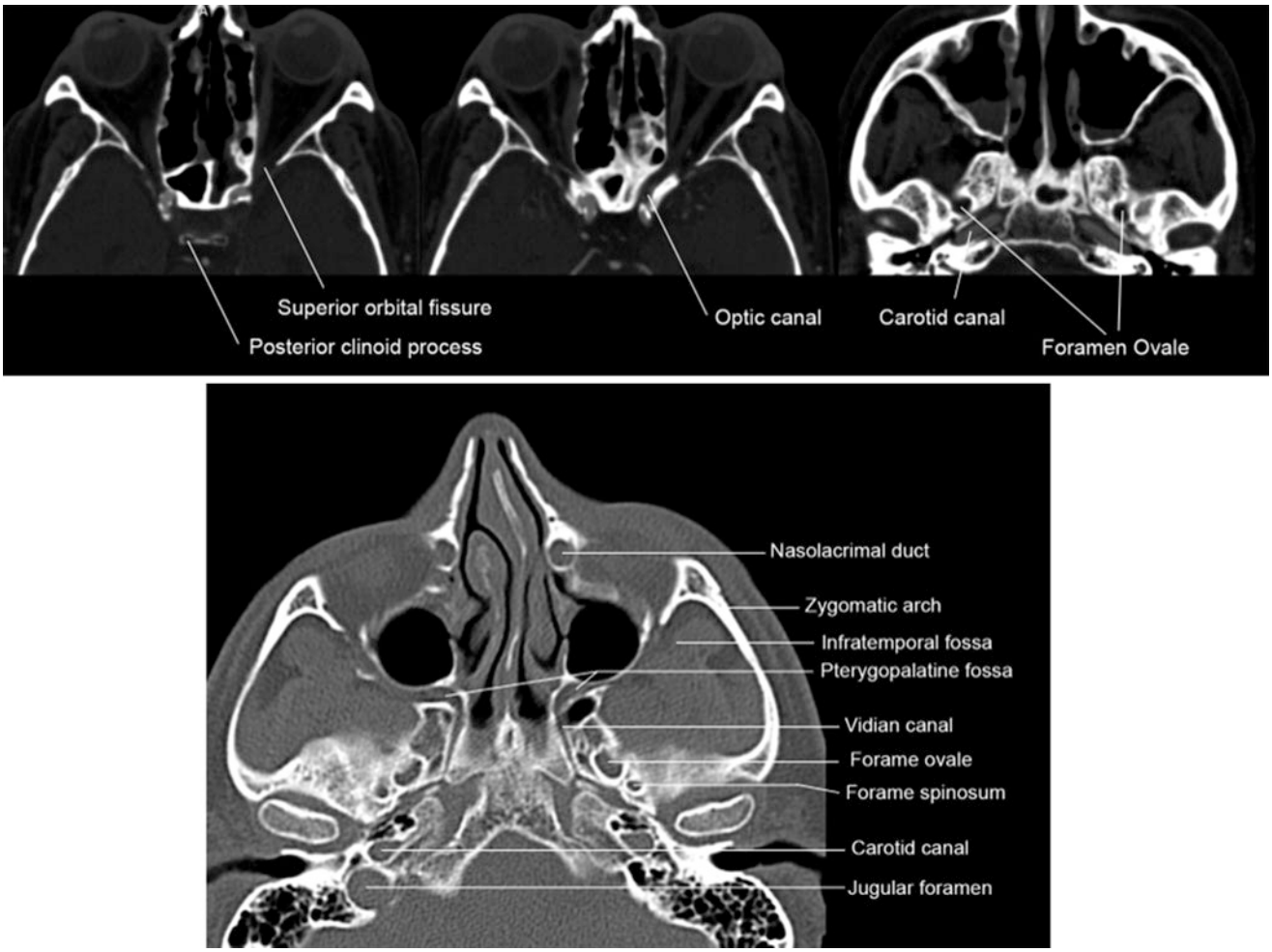


Fig. 13 Sequential axial CT images of the skull base at the level of the orbital fissures and neural foramina

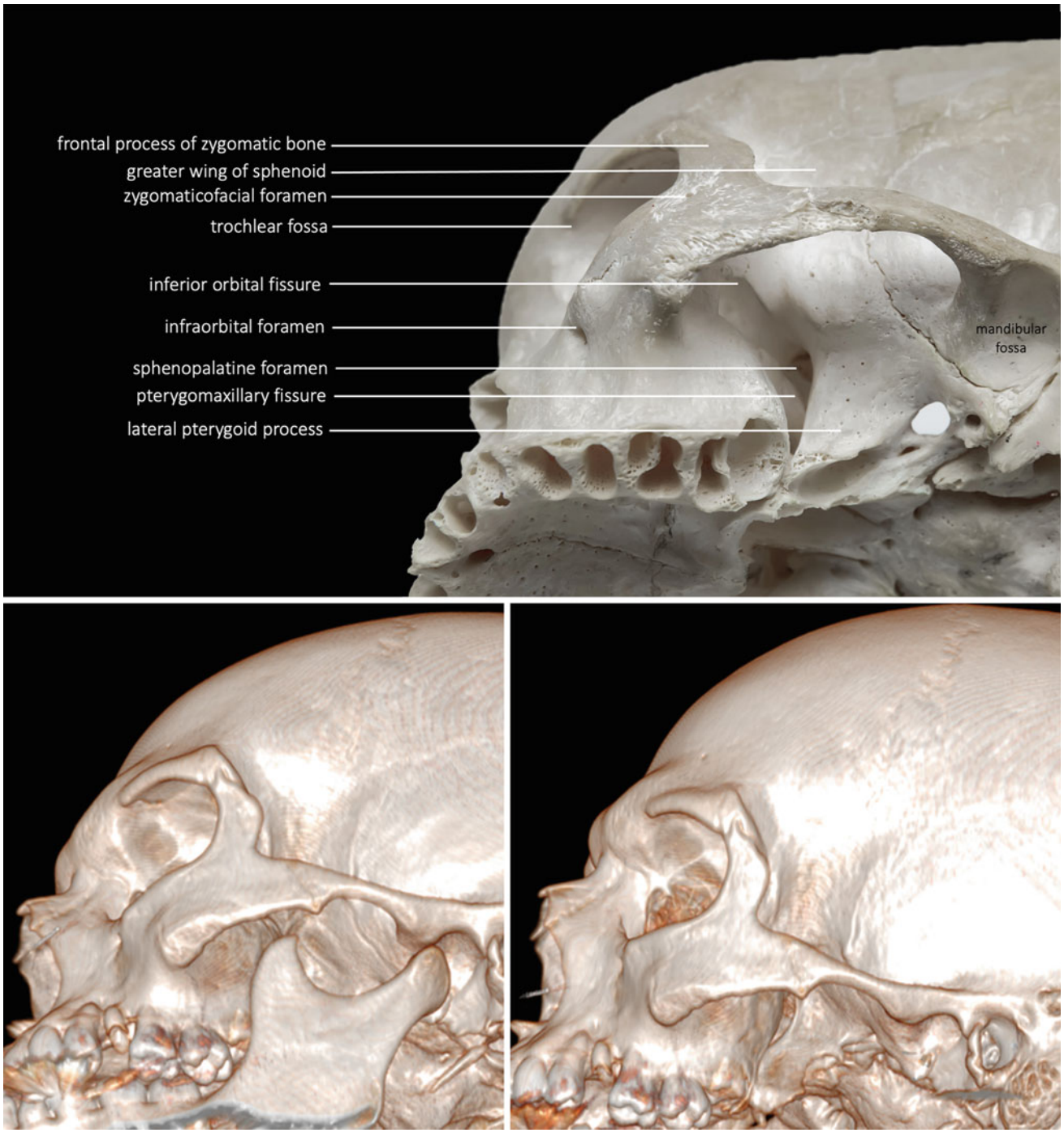


Fig. 14 The infratemporal fossa. *Upper* image – human skull, note the mandible is disarticulated, with corresponding 3D CT reformat (*lower* image, *left* with mandible, *right* – mandible disarticulated)

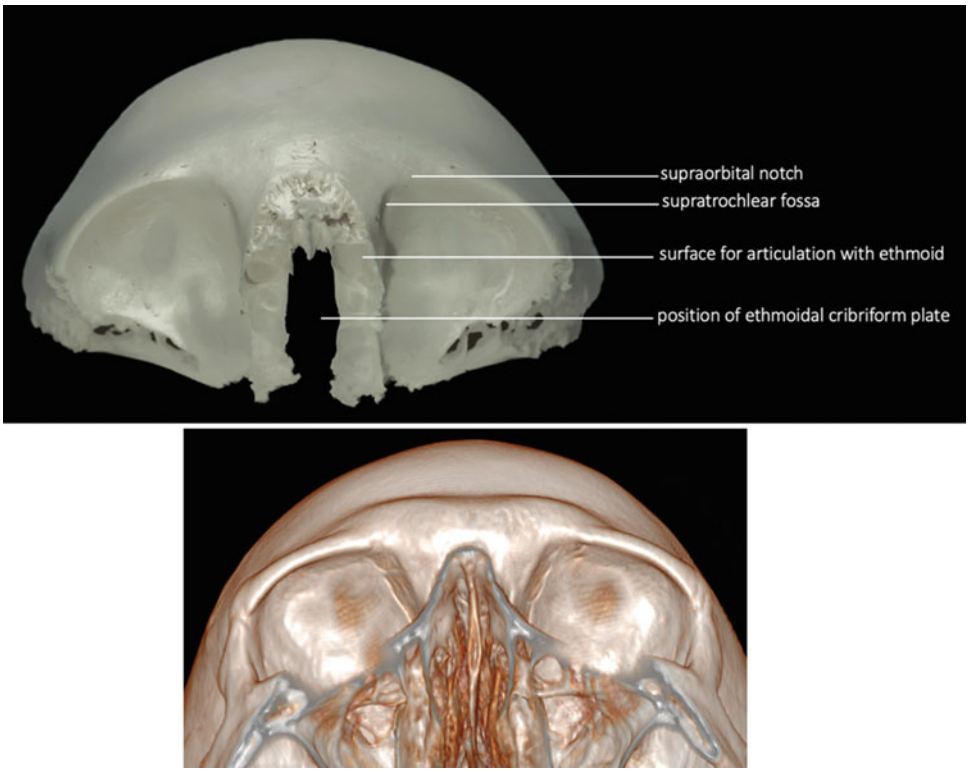


Fig. 15 Inferior view of the frontal bone. Skull, *upper* image; 3D CT reconstruction, *lower* image

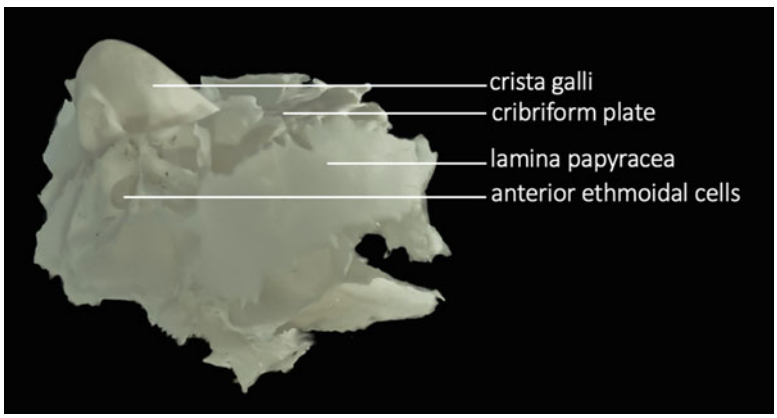


Fig. 16 Anterolateral view of the ethmoid bone

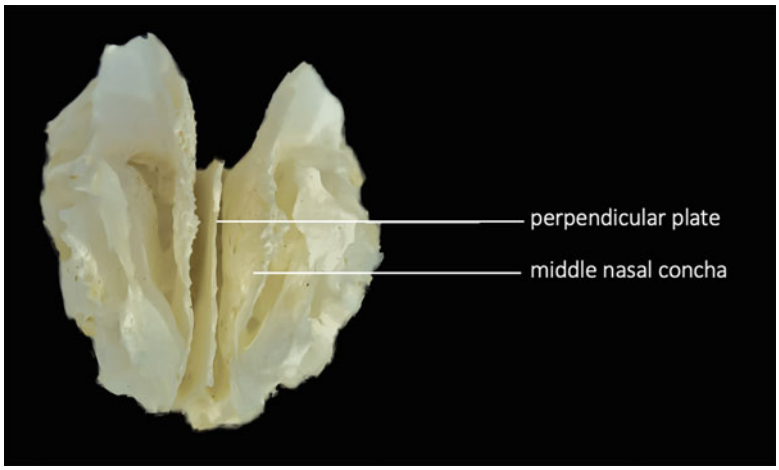


Fig. 17 Inferior view of ethmoid bone

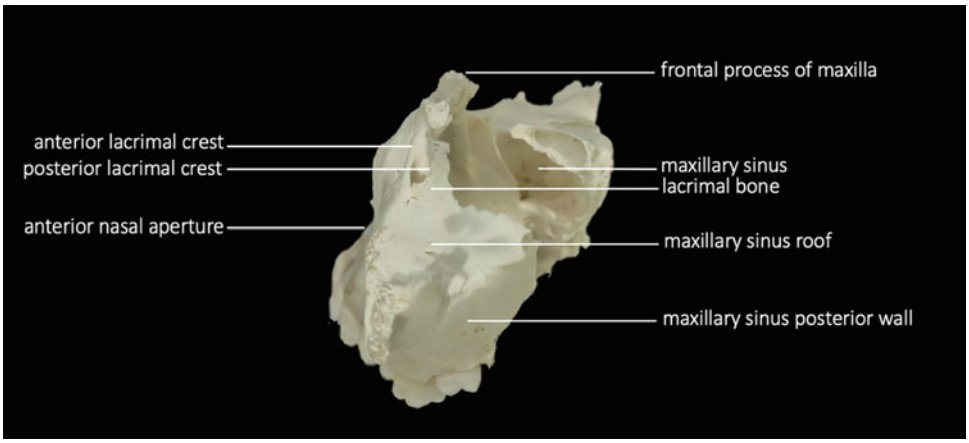


Fig. 18 Posterolateral view of maxillae and lacrimal bones

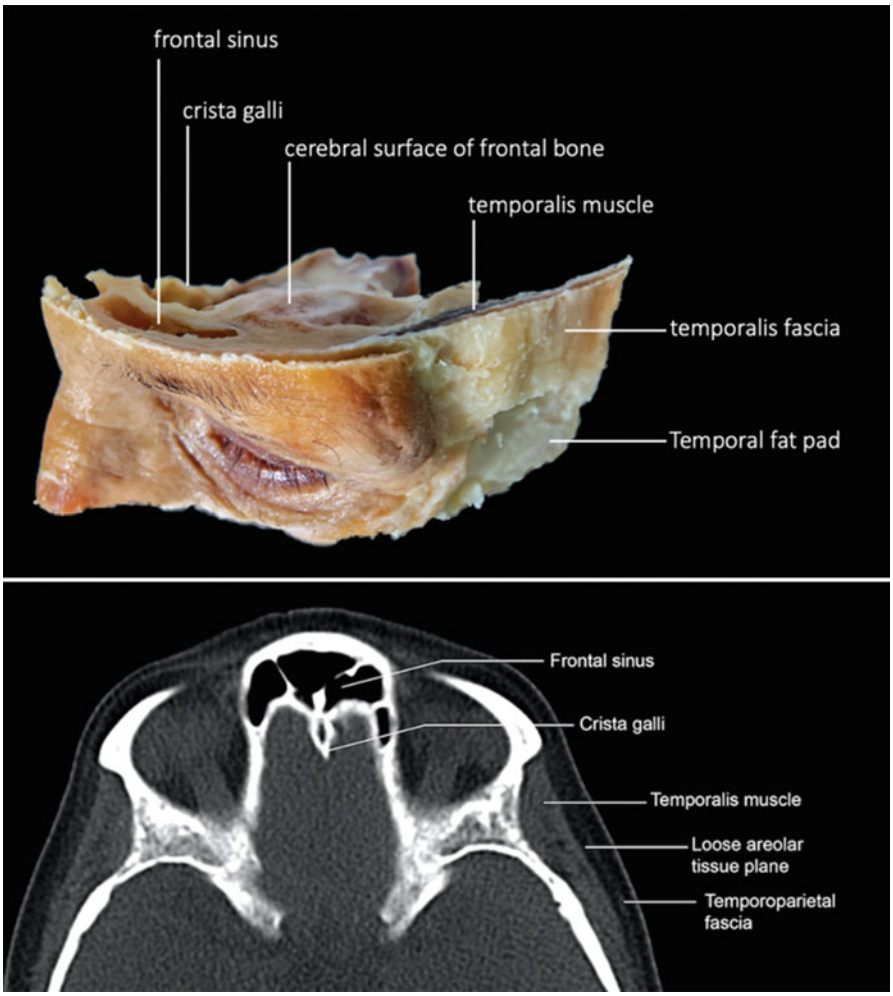


Fig. 19 Orbital roof and related structures. Left orbit, anterolateral view, cadaver dissection (*upper*), and axial CT bone window (*lower*)

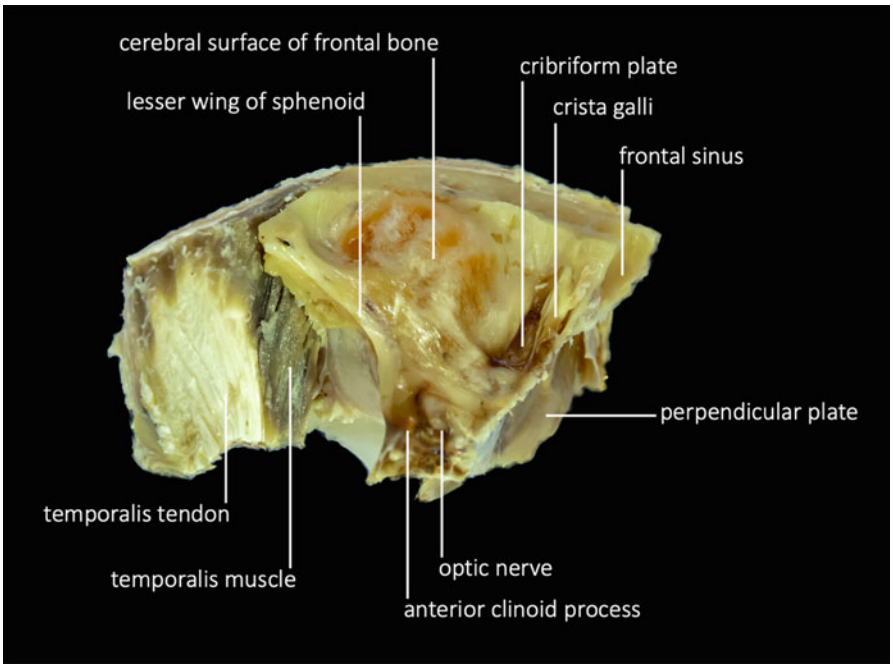


Fig. 20 Orbital roof and related structures. Left orbit, posterolateral view

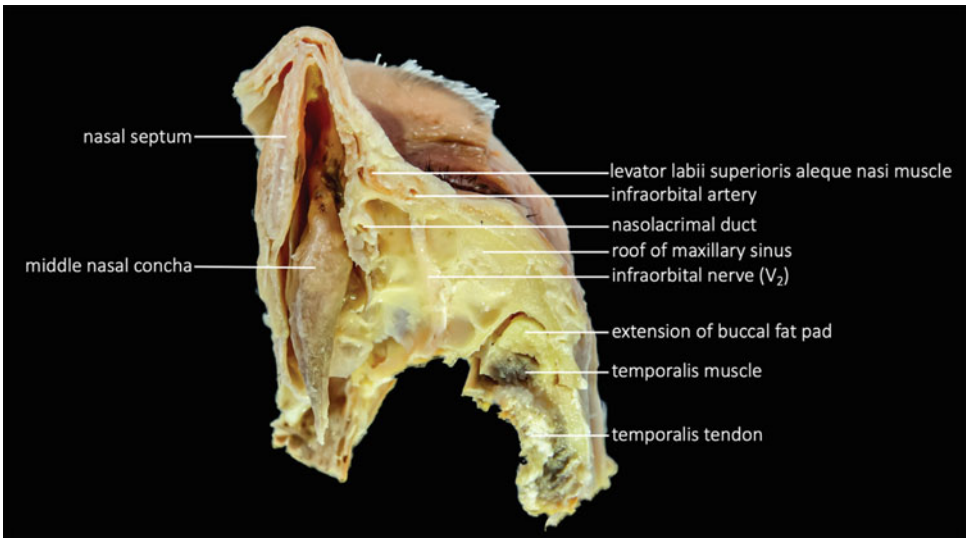


Fig. 21 Orbital floor and related structures. Left orbit, inferior view (horizontal section at the level of the middle nasal concha)

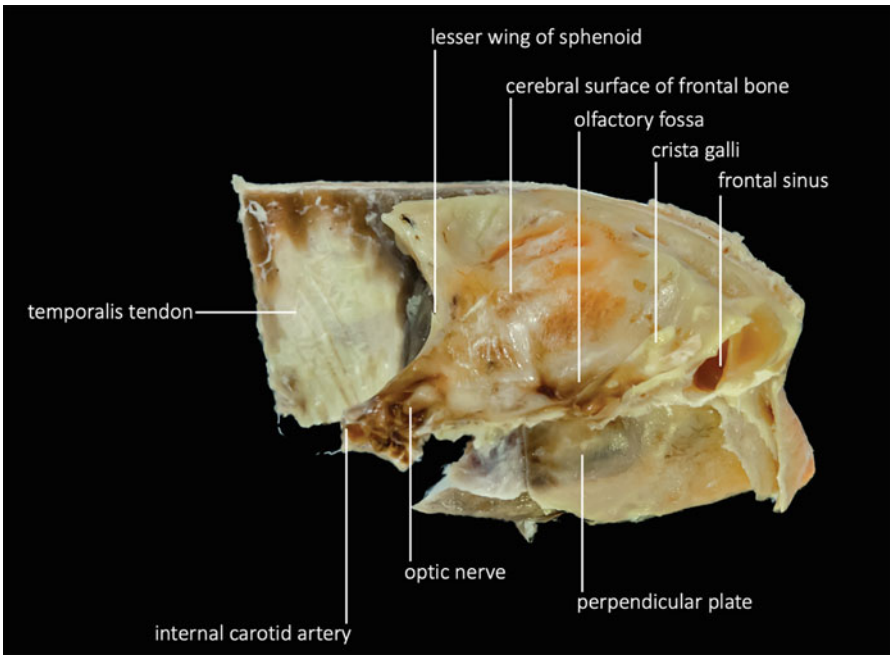


Fig. 22 Orbital roof and related structures. Left orbit, posteromedial view

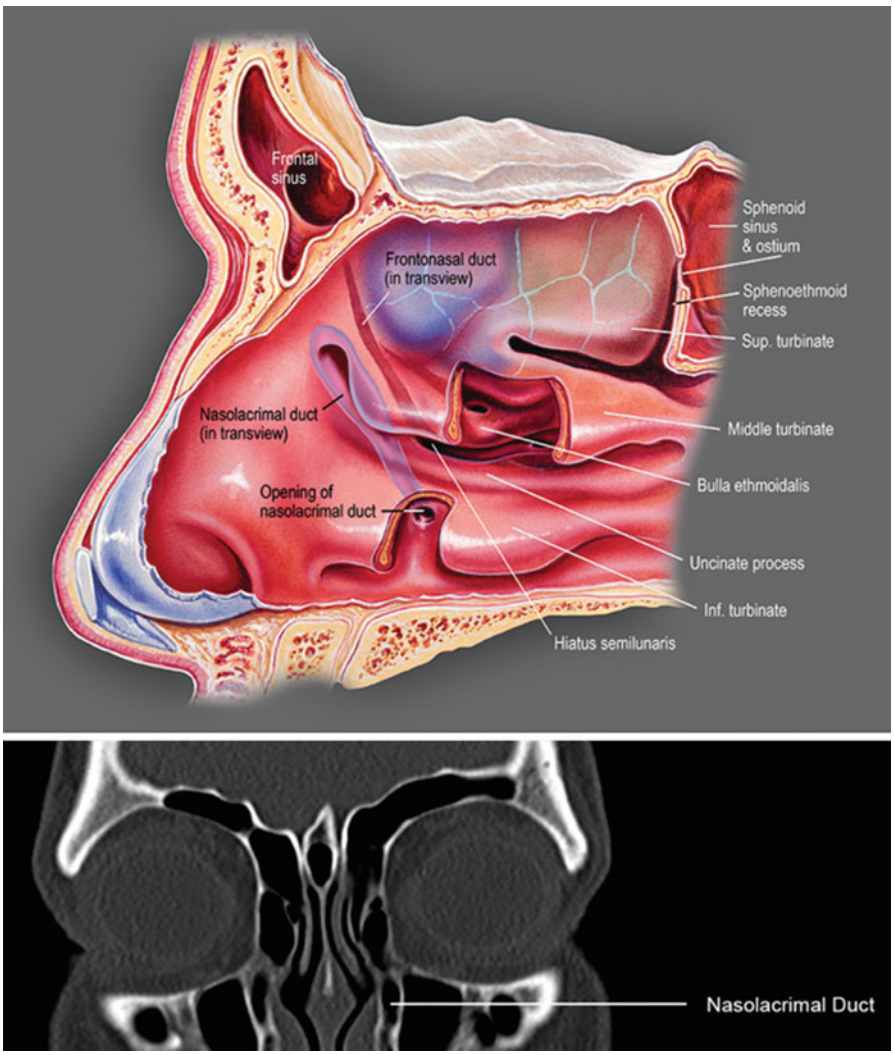


Fig. 23 Trans-nasal view (drawing, *upper*) and coronal view (CT, *lower*) of the inferior medial orbital wall and the lacrimal drainage apparatus

References

1. Gray H, Standring S, Ellis H, Berkovitz BKB. Gray's anatomy: the anatomical basis of clinical practice. 39th ed. Edinburgh/New York: Elsevier Churchill Livingstone; 2005.
2. Most SP, Mobley SR, Larrabee WF. Anatomy of the eyelids. Facial Plast Surg Clin North Am. 2005;13:487–92.
3. Sicher H, DuBrul EL. Oral anatomy. 6th ed. Saint Louis: The CV Mosby; 1975.
4. Kanagalingam S, Miller NR. Horner syndrome: clinical perspectives. Eye Brain. 2015;7:35–46.
5. Meybodi AT, et al. The oculomotor-tentorial triangle. Part 1: microsurgical anatomy and techniques to enhance exposure. J Neurosurg. 2019;130:1426–34.
6. Malhotra A, et al. Neuroimaging of Meckel's cave in normal and disease conditions. Insights Imaging. 2018;9:499–510.
7. Zhuang W, et al. Anatomical study of the extraocular check ligament system. J Plast Reconstr Aesthet Surg. 2019;72(12): 2017–26.
8. Marom A. A new look at an old canal. Skull Base. 2011;21(1): 53–8.
9. Voirol JR, Vilensky JA. The normal and variant clinical anatomy of the sensory supply of the orbit. Clin Anat. 2014;27: 169–75.
10. Wolfram-Gabel R, Kahn JL. Adipose body of the orbit. Clin Anat. 2002;15:186–92.
11. Goh PS, et al. Review of orbital imaging. Eur J Radiol. 2008;66: 387–95.

Vascular Anatomy

2

Daniel B. Rootman, Bruce Stewart, and Jack Rootman

Contents

1 Introduction 25
1.1 Arterial Anatomy 25
1.2 Venous Anatomy 27
2 Figures with Captions 27
References 32

Abstract

The orbit and ocular adnexa are highly vascularized, receiving arterial flow from both the extremal (ECA) and internal (ICA) carotid circulations. Likewise, the venous outflow network is extensive, draining to the cavernous sinus and through the intracerebral circulation, the pterygoid plexus and temporal veins to the external jugular, and the facial veins to the internal jugular. True shunt vessels likely exist between vascular territories, creating anastomotic flow networks on the arterial side and similarly multiple bridging veins create direct connection between venous territories. These anatomic relationships allow for dynamic changes in regional flow and evolutionarily emphasize the critical nature of the ocular structures, demonstrating extensive circulatory redundancy.

The modalities of choice would include CTA, MRA – either nonenhanced time-of-flight (TOF) scans, or contrast-enhanced single-phase/multi-phasic scans – and DSA.

Keywords

Vascular anatomy · Orbital arterial supply · Orbital venous drainage

1 Introduction

1.1 Arterial Anatomy

1.1.1 Internal Carotid Circulation

The carotid artery enters the cranial vault via the carotid canal. It then travels anteriorly within the cavernous sinus and loops back to exit the sinus creating an overlapping configuration described as the carotid siphon (Fig. 2). The anterior most vertical component of the carotid forms a vertical indentation within the lateral wall of the sphenoid sinus. This vertical indentation meets superiorly near the roof of the sphenoid sinus with the inferolateral component of the optic canal creating a triangular space known as the opticocarotid recess (Fig. 3).

Immediately after emerging from the cavernous sinus, the ophthalmic artery branches from the ICA. The ophthalmic artery joins the optic nerve inferiorly as it enters the optic canal and emerges inferolaterally in the orbit (Fig. 4). Some variation in this configuration can be encountered rarely with certain individuals demonstrating a separate ophthalmic artery canal in the sphenoid and others in which the ophthalmic artery is derived from the recurrent meningeal passing through the superior orbital fissure. In the orbit, the

D. B. Rootman (✉)
Division of Orbital and Ophthalmic Plastic Surgery, Stein and Doheny Eye Institutes, University of California, Los Angeles, CA, USA

B. Stewart
BFA Art Center College of Design, UBC Faculty of Medicine, Kelowna, BC, Canada

J. Rootman
University of British Columbia, Vancouver, BC, Canada

© Springer Nature Switzerland AG 2022
G. Ben Simon et al. (eds.), *Atlas of Orbital Imaging*,
https://doi.org/10.1007/978-3-030-62426-2_2

ophthalmic artery then crosses from lateral to medial over the optic nerve in 80% of cases and under the nerve in the remaining (Fig. 5).

The first major branch of the ophthalmic is the central retinal artery, piercing the optic nerve sheath near the apex, and passing forward to supply the inner retina. Two or three long posterior ciliary arteries also branch in the apex, following the surface of the optic nerve sheath towards the globe where a number of short posterior ciliary arteries branch off to supply the choroid and optic nerve head before eventually penetrating the sclera and terminating as supply to the anterior ocular structures.

Ophthalmic branching patterns are quite variable after this point; however, two main trunks form in the posterior orbit. The lacrimal artery forms the lateral branch and the nasofrontal artery forms a similar supply to the medial orbit. Multiple muscular branches are variably derived from these major trunks and pass forward in pairs to supply each rectus muscle and terminate in an anastomotic fashion with the long posterior ciliary arteries in the anterior segment. The exception is the lateral rectus, which is typically supplied by a single muscular branch.

The lacrimal artery passes anterolaterally, where an anastomosis is formed with the recurrent branch of the middle meningeal artery (ECA), passing typically through the superior orbital fissure. The lacrimal artery supplies two branches that exit the orbit through foramina in the zygoma: the zygomaticofacial and zygomaicofrontal arteries, respectively. The lacrimal artery continues to supply the lacrimal gland and terminates as the lateral palpebral artery.

The nasofrontal artery passes forward in the superomedial orbit roughly along the axis of the frontoethmoidal suture. Before reaching the medial wall, the supraorbital artery branches off and follows the roof to exit through the supraorbital notch or foramen. The (typically) two ethmoidal arteries branch off of the nasofrontal artery, 6 mm and 12 mm anteriorly to the optic canal classically. There is however considerable variation in the number and position of these branches. Both arteries pass through the similarly named foramina in the medial wall as the nasofrontal artery passes forward in the orbit to terminate as the supratrochlear, dorsal nasal, and medial palpebral arteries (Figs. 2 and 6).

1.1.2 External Carotid Circulation

The external carotid supplies the orbit both anteriorly and posteriorly. Posteriorly, branches of the internal maxillary artery supply the inferior and lateral orbit. The meningeal artery branches off the first segment of the maxillary artery and enters the skull base through the foramen spinosum. A recurrent branch then typically passes back out of the calvarium through the superior orbital fissure to anastomose with the lacrimal artery as noted above (Fig. 7).

The infraorbital artery branches off the third segment of the maxillary artery and passes through the inferior orbital fissure to join the infraorbital nerve in the infraorbital groove before passing through the infraorbital canal and foramen and terminating in the midface.

Anteriorly two main branches of the ECA, the superficial temporal and the facial arteries, supply the lateral and medial orbit, respectively. The superficial temporal artery travels within the superficial temporalis fascia branching posteriorly and anteriorly approximately 5 cm above the zygomatic arch as the parietal and frontal branches, respectively. The frontal branch continues medially and forms ECA-ICA anastomoses with the supraorbital and supratrochlear arteries.

The facial artery branches off the ECA in the carotid triangle and travels tortuously through the anterior facial structures providing a number of branches in the cervical and facial region. The angular artery is the terminal branch of the facial artery and travels along the nasolabial fold where it has a variable course and then passes along the lateral base of the nose up to the medial orbit. Extensive anastomoses between the angular artery and the dorsal nasal, medial palpebral, and supratrochlear arteries are found in this region.

1.1.3 Anastomoses

As noted in previous sections there are rich anastomoses between the ECA and ICA circulation in the periorbital region. Superiorly, the superficial temporal provides ECA supply and merges with the supraorbital and supratrochlear ICA branches medially and the lateral palpebral branches of the ICA laterally.

Posteriorly, internal maxillary branches of the ECA anastomose with the ICA supply of the lacrimal artery via the recurrent meningeal, the muscular branches of the ICA supplied ophthalmic artery via the ECA infraorbital artery, and the ethmoidal branches of the ICA supplied nasofrontal via the ECA sphenopalatine artery in the nasal cavity.

Anteriorly, the facial artery provides ECA flow through the angular artery to anastomose with the supratrochlear, medial palpebral, and dorsal nasal terminal branches of the ophthalmic artery (ICA). Additionally, anterior ECA to ICA anastomotic regions can be found in the territory of the infraorbital artery (ECA) and the inferior medial palpebral vessels (ICA).

Virtually the entire orbit and ocular adnexa can be supplied by the ECA through these anastomoses. In conditions such as internal carotid occlusion, flow can be dynamically directed through the ECA circulation and ocular ischemia is uncommon. Similarly, contralateral to ipsilateral ICA flow can be diverted through the circle of Willis in such cases. These redundancies again underscore the vital nature of the ocular apparatus and multiple adaptative states that can be dynamically marshalled in the case of vascular occlusive pathology, whether pathologic or iatrogenic.

1.2 Venous Anatomy

Venous drainage is again highly variable and redundant in the periorbital region, utilizing intracranial and extracranial outflow pathways. The main drainage from the superior orbit is the superior ophthalmic vein. This vein begins as a confluence of the supraorbital, supratrochlear, and angular veins anteriorly. It travels in three sections through the orbit: superomedially in the anterior orbit, transverse from medial to lateral under the superior muscle group in the mid orbit, and lateral passing through the superior orbital fissure in the posterior orbit. Primary drainage is to the cavernous sinus. There are many intraorbital tributaries to the superior ophthalmic vein including muscular, vortex, and lacrimal sources (Fig. 9).

The inferior ophthalmic vein forms as a confluence of the medial and lateral orbital plexi and travels posteriorly, superior to the inferior rectus before passing through the inferior orbital fissure and draining to the pterygoid plexus and the retromandibular vein of the external jugular circulation. There are multiple bridging vessels between the inferior and superior ophthalmic veins. In the anterior orbit the medial and lateral collateral veins connect these drainage pathways, and in the posterior orbit the inferior ophthalmic vein continues after partially draining to the pterygoid plexus to join the superior ophthalmic vein in draining to the cavernous sinus. Other posteriorly located unnamed bridging vessels are additionally described.

Anteriorly, the venous drainage follows a similar pattern to the arterial supply. Inferomedially, drainage is via the angular and facial veins to the internal jugular vein. Superiorly, venous drainage passes through the superficial temporal vein egress route and drains to the common facial vein before entering the internal jugular. The veins of the orbit are thought to be valveless and thus can flow in either direction if higher pressure is generated downstream by an arterial fistula or venous obstruction.

2 Figures with Captions

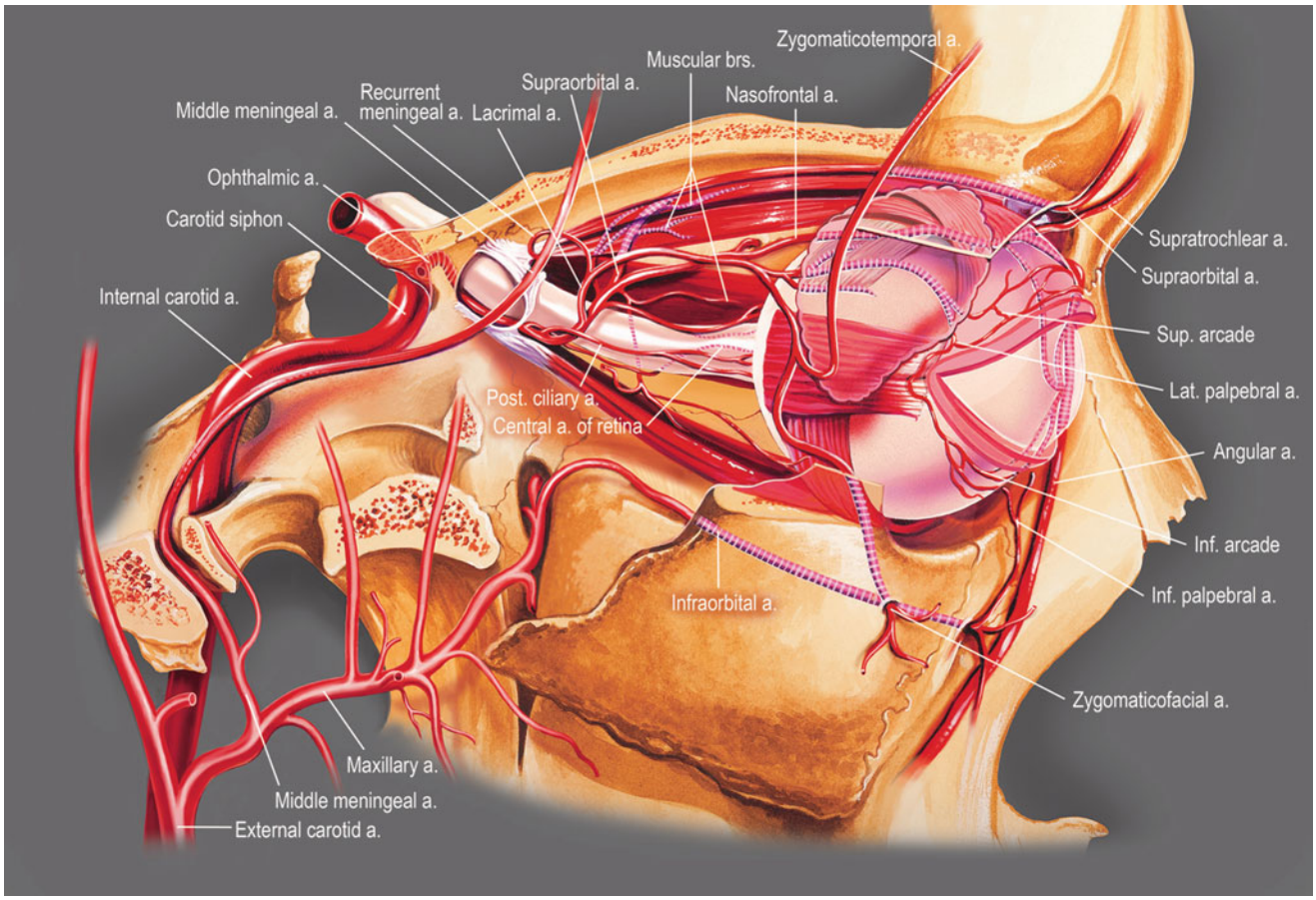


Fig. 1 Arterial supply to the orbit

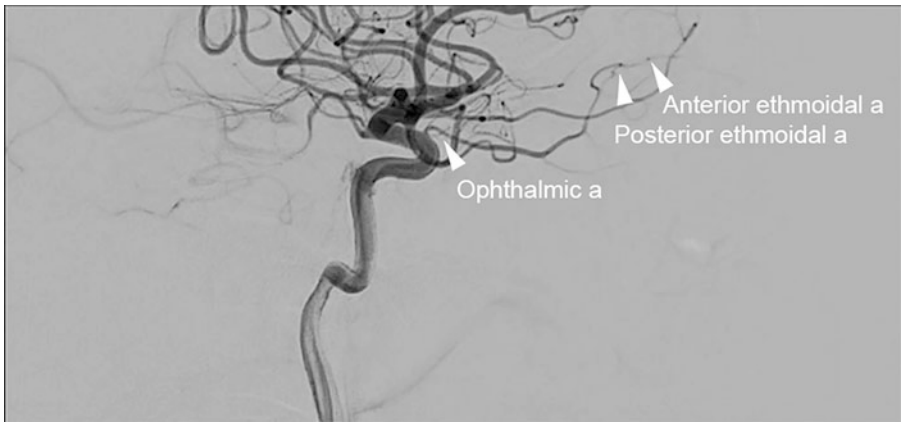


Fig. 2 Digital subtraction angiography (DSA), lateral view, showing the ophthalmic and ethmoidal branches of the internal carotid artery circulation

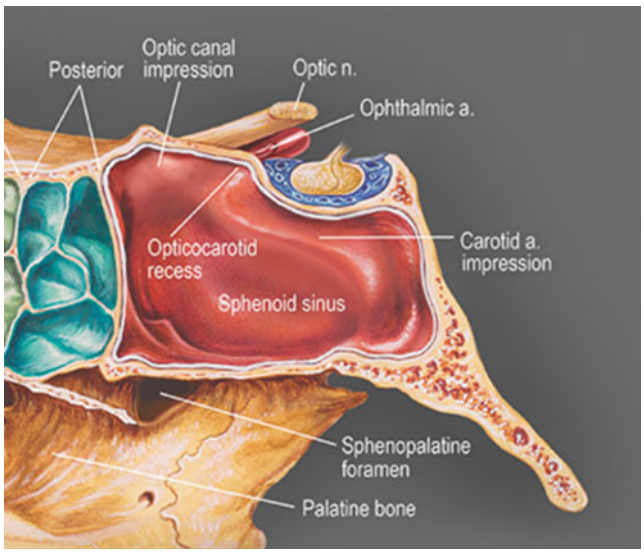


Fig. 3 Sagittal view of the sphenoid sinus. Note the bony impressions on the lateral wall of the sinus, formed by the optic nerve, carotid siphon, and pituitary gland

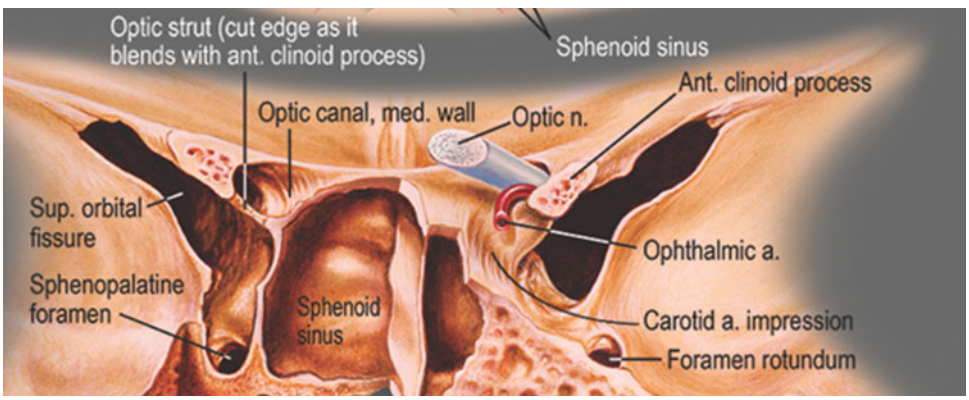
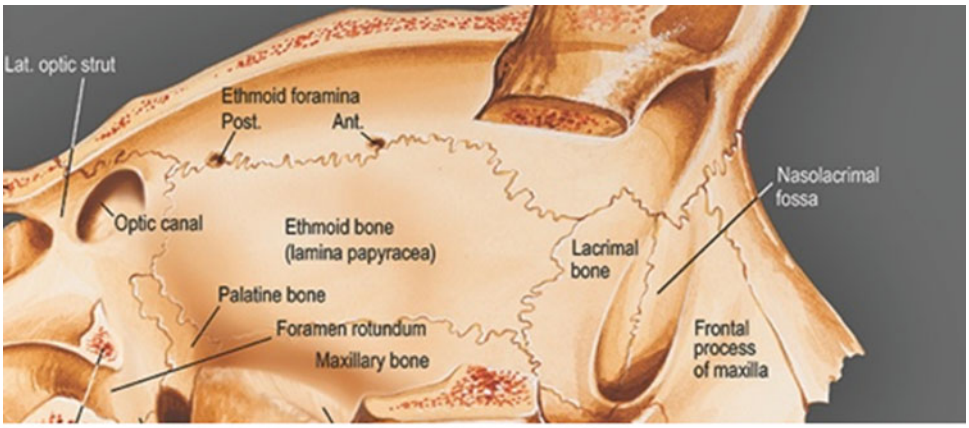


Fig. 4 Major relationships of the ophthalmic artery to the optic nerve and adjacent structures (sphenoid sinus, clinoid, and orbital fissures)



Fig. 5 CTA demonstrating the course of the ophthalmic artery and its relation to the optic nerve



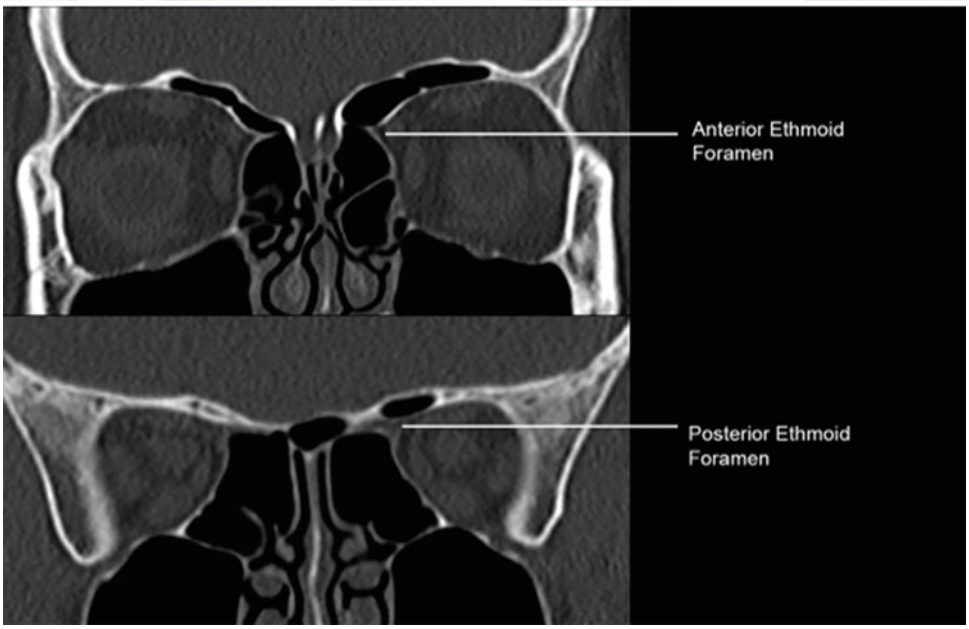


Fig. 6 Direct lateral view of the medial wall of the orbit showing the ethmoidal foramina at the superior border of the lamina papyracea (drawing, *upper*). Coronal CT scans showing the anterior and posterior ethmoidal foramina housing the anterior and posterior ethmoidal arteries, respectively (*middle* and *lower*)

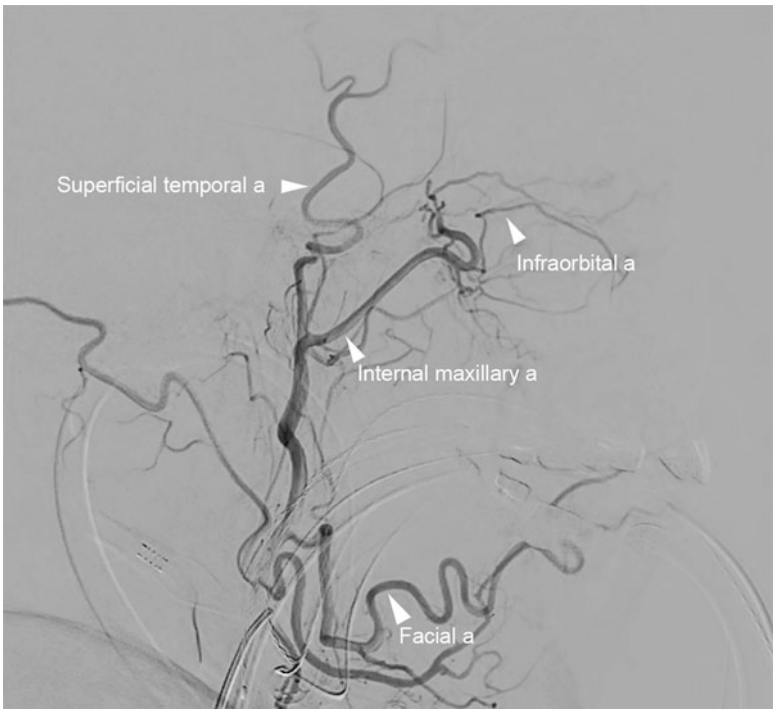


Fig. 7 DSA demonstrating selected branches of the external carotid artery circulation

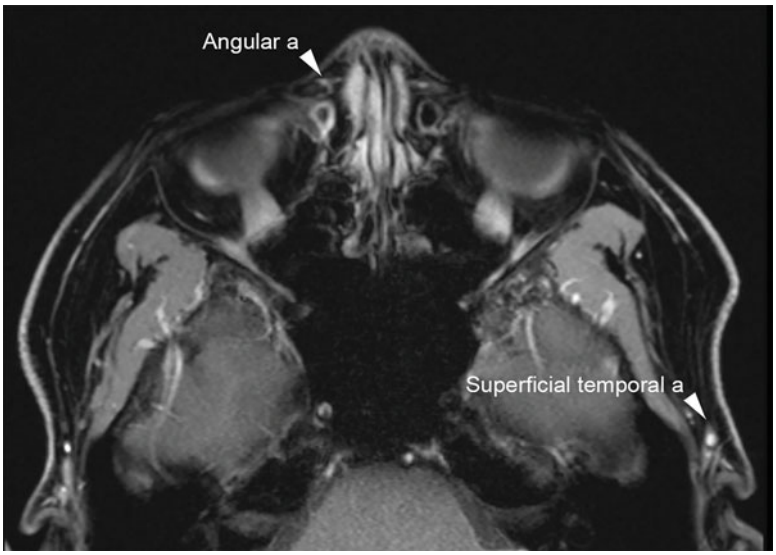


Fig. 8 Post-contrast T1 MRI with fat suppression showing enhancement of the angular and superficial temporal arteries

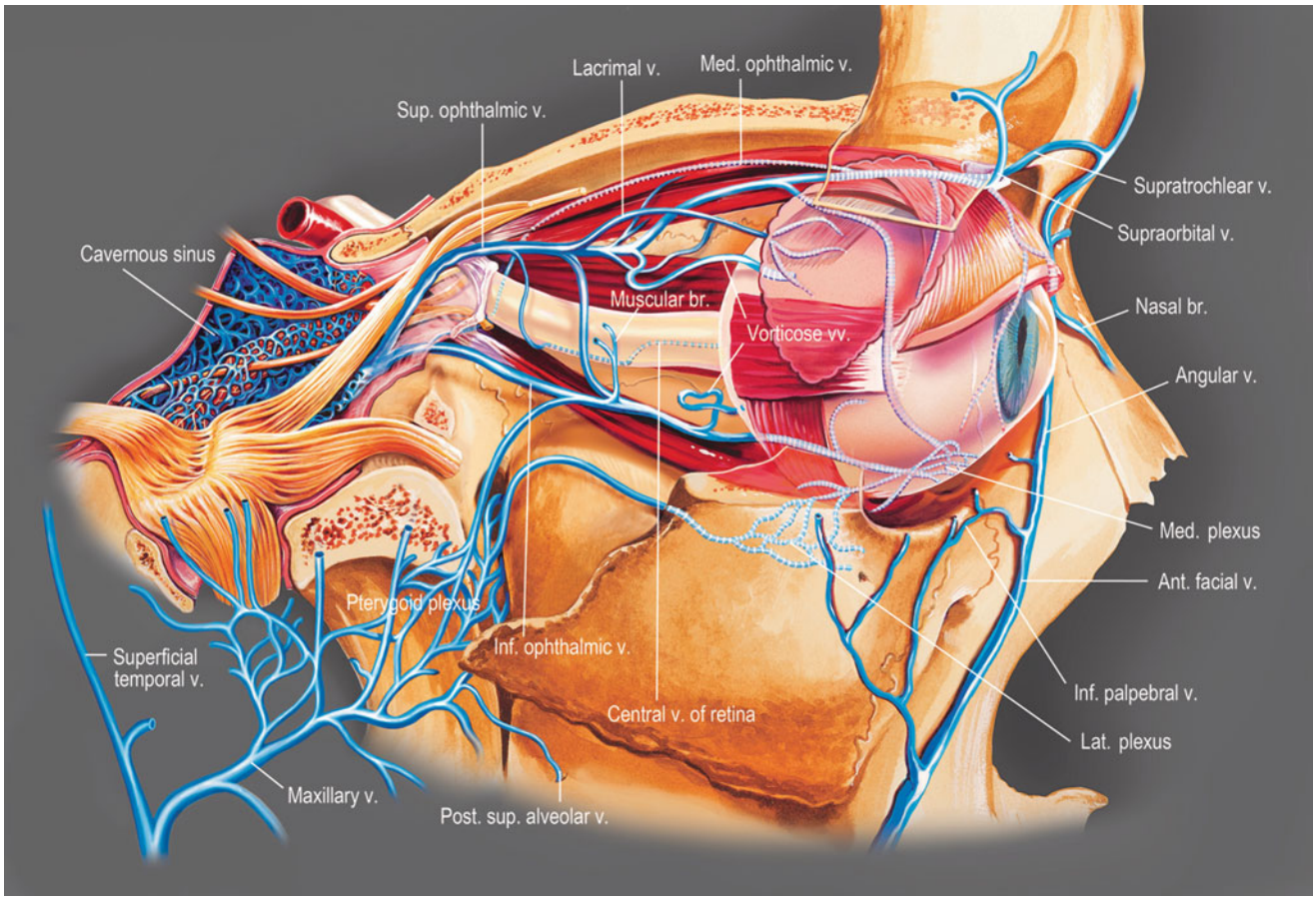


Fig. 9 Venous drainage pathways

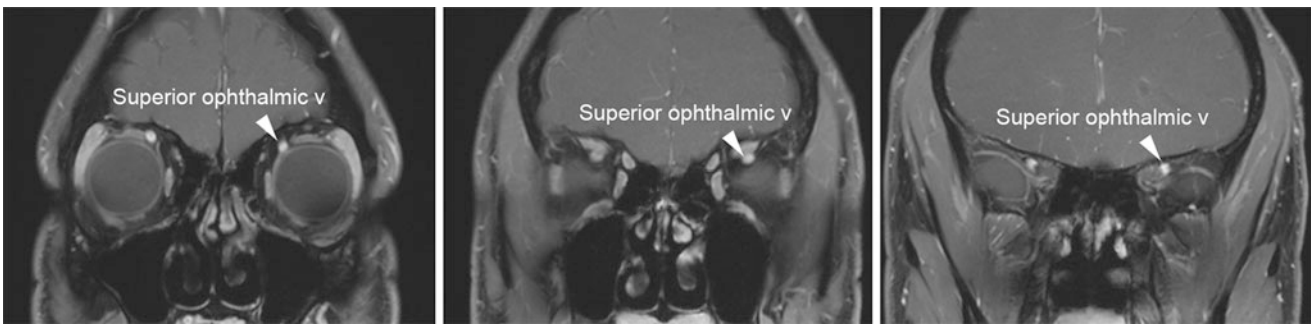


Fig. 10 Coronal T1 FS CE MRI scan showing the course of the superior ophthalmic vein

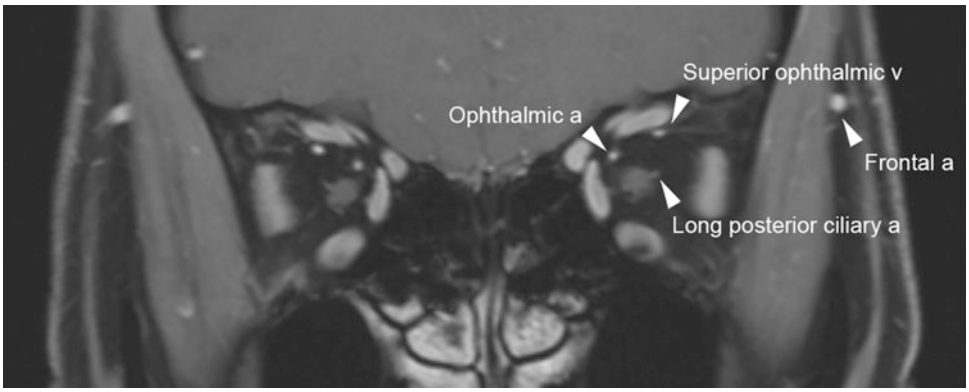


Fig. 11 Coronal T1 FS CE MR showing the vasculature of the orbit

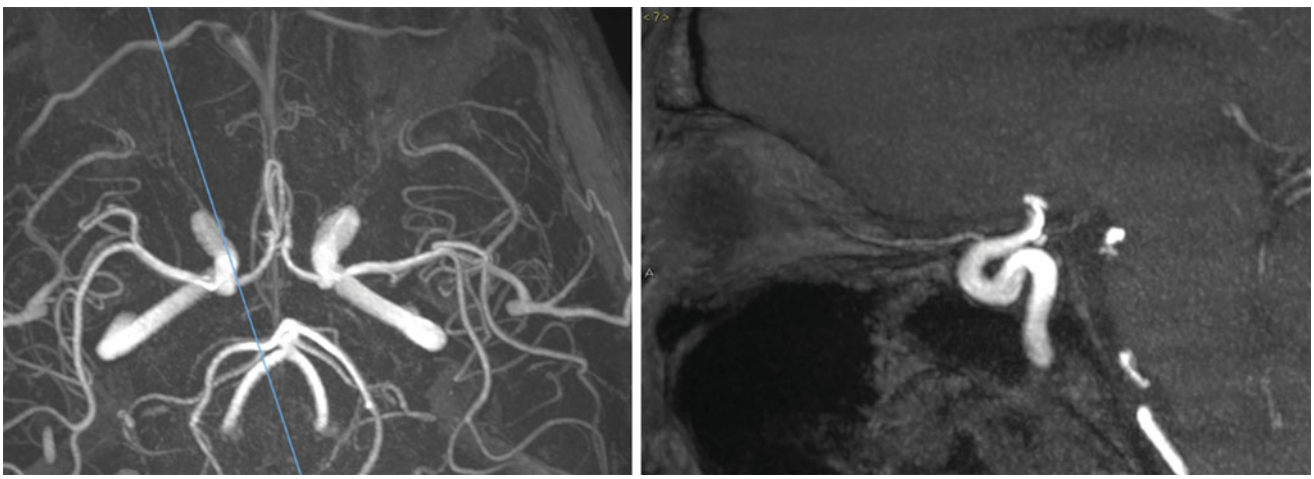


Fig. 12 MRA time-of-flight (TOF) sagittal oblique reformat depicting the origin of the ophthalmic arteries. Corresponding 3D MIP reconstruction showing the reference line (*blue line*)

References

1. Cheung N, McNab AA. Venous anatomy of the orbit. Invest Ophthalmol Vis Sci. 2003;44:988–95.
2. Hayreh SS. Orbital vascular anatomy. Eye (Lond). 2006;20: 1130–44.
3. Rootman J. Orbital surgery: a conceptual approach. Second edition. Ed. Philadelphia: Wolters Kluwer Health/Lippincott Williams & Wilkins; 2014.
4. Taylor GI, Shoukath S, Gascoigne A, Corlett RJ, Ashton MW. The functional anatomy of the ophthalmic angiosome and its implications in blindness as a complication of cosmetic facial filler procedures. Plast Reconstr Surg. 2020;146:745.

Ocular Adnexa, Soft Tissue, and Extraocular Muscles

3

Jack Rootman, Daniel B. Rootman, Bruce Stewart, Stefania B. Diniz, Kelsey A. Roelofs, Liza M. Cohen, Claire S. Smith, Ayelet Eran, Ben Kaplan, and Assaf Marom

Contents

1 Introduction 33
1.1 Eyelids 33
1.2 Fascia of the Eyeball 34
1.3 Extraocular Muscles 34

2 Figures with Captions 36

References 46

Abstract

The orbital soft tissues consist of the eyelids, lacrimal gland, extraocular muscles, fascia, and orbital fat. These support the globe, thus allowing normal ocular function, motility, and vision, and also form a mechanical barrier which provides protection from infection and trauma. The adnexa can be assessed on different modalities; however, MRI is the imaging modality of choice for delineating the orbital soft tissue content, due to its enhanced capabilities and superiority over CT in demonstrating the complex normal anatomy and a wide range of pathological conditions such as inflammation, tumors, and malformations.

Keywords

Ocular adnexa · Extraocular muscles · Lacrimal gland

1 Introduction

1.1 Eyelids

The superior and inferior eyelids are thin, movable, protective coverings of the anterior surface of the globe. Their external surface is covered by the skin, and the internal surface by the conjunctiva. The gap between the eyelids is referred to as the palpebral fissure. Blinking of the eyelids maintains a thin layer of tear fluid over the cornea. The upper

J. Rootman
University of British Columbia, Vancouver, BC, Canada

D. B. Rootman · S. B. Diniz · K. A. Roelofs · C. S. Smith
Division of Orbital and Ophthalmic Plastic Surgery, Stein and Doheny Eye Institutes, University of California, Los Angeles, CA, USA

B. Stewart
BFA Art Center College of Design, UBC Faculty of Medicine, Kelowna, BC, Canada

L. M. Cohen
Division of Orbital and Ophthalmic Plastic Surgery, Stein Eye Institute, University of California, Los Angeles, CA, USA

A. Eran
Neuroradiology Unit, Radiology Department, Rambam Healthcare Medical Center, Haifa, Israel

Department of Anatomy, Rappaport Faculty of Medicine, Technion – Israel Institute of Technology, Haifa, Israel

B. Kaplan · A. Marom (✉)
Department of Anatomy, Rappaport Faculty of Medicine, Technion – Israel Institute of Technology, Haifa, Israel
e-mail: assafma@technion.ac.il

© Springer Nature Switzerland AG 2022
G. Ben Simon et al. (eds.), *Atlas of Orbital Imaging*,
https://doi.org/10.1007/978-3-030-62426-2_3

eyelid is larger, and when it moves down the palpebral fissure is closed. An elevator muscle, the levator palpebrae superioris, is attached to the upper eyelid. The mucocutaneous border in each eyelid is marked by the "gray line," anterior to which the eyelashes emerge, and posterior to this line the tarsal (meibomian) glands open.

The skeleton of the eyelids is provided by the orbital septum and the tarsal plates (tarsi). The orbital septum is a fibrous membrane that arises from the periosteum of the orbital rim as the arcus marginalis, and blends with the levator aponeurosis superiorly and the palpebral fascia inferiorly. The orbital septum separates between the orbital contents (postseptal) from the external structures (preseptal). The superior and inferior tarsi are thin, crescent-shaped and anteriorly convex plates of dense fibrous tissue about 2.5 cm long, attached to the orbital margin by the orbital septum and by the medial and lateral palpebral (canthal) ligaments. The medial canthal ligament connects the medial ends of the tarsi with the anterior lacrimal crest and the frontal process of the maxilla. The lateral canthal ligament runs from the lateral ends of the tarsal plates to the zygomatic margin of the orbital rim.

Medially, each eyelid has an elevation, the lacrimal papilla. At its center is the opening of the lacrimal canaliculus, the lacrimal punctum. The medial and lateral angles of the eye are referred to as the medial canthus and lateral canthus. While the lateral one does not feature any special anatomical structures, the medial one contains a small triangular space, the lacrimal lake, in which the typically red lacrimal caruncle is situated. Situated lateral to the caruncle is a conjunctival fold, the plica semilunaris. The conjunctiva, a transparent mucous membrane, covers the internal palpebral surfaces, and is continuous onto the sclera at the superior and inferior conjunctival fornix. Embedded in the tarsi are the tarsal glands, which may be visible when the eyelids are everted.

1.2 Fascia of the Eyeball

From the optic nerve to the corneoscleral junction (limbus), the eyeball is covered by thin fascia, referred to as Tenon's capsule, which insulates it from the orbital adipose tissue and is loosely connected to the sclera by episcleral connective tissue. This sheath is perforated by the tendons of the extraocular muscles and is continuous with their muscular fascia. The fascia of the extraocular muscles has extensions that are important for the movements of the eyeball. The medial and lateral recti have strong triangular expansions that attach to the lacrimal and zygomatic bones. They are termed "check ligaments" because they limit the movement range of these muscles. The sheath of the inferior rectus is thicker on the inferior aspect of the muscle and is connected to the sheath of the inferior oblique. Anteriorly, the sheath is inserted into the inferior tarsus, such that a suspensory ligament is formed below the eyeball. This extends into the lower eyelid. For this reason, contraction of the inferior rectus muscle in downward gaze also draws the inferior eyelid downwards. The shared fascial sheath of the superior rectus and the levator palpebrae superioris muscles is referred to as Whitnall's ligament.

The orbital periosteum is loosely attached to the bone. Posteriorly, it is continuous with the dural sleeve of the optic nerve, and anteriorly with the orbital septum. Lastly, the spaces between the ocular structures are occupied by a considerable amount of orbital adipose tissue, particularly between the optic nerve and the muscular cone. The orbital fat stabilizes the eyeball and forms a socket within which it rotates.

1.3 Extraocular Muscles

Seven extrinsic (extraocular) muscles are associated with the eyeball. The levator palpebrae superioris elevates the upper eyelid, while the other six muscles enable the wide range of ocular movements. These muscles belong to two groups: the four recti muscles (superior, inferior, medial, and lateral) and the two oblique muscles (superior and inferior).

Levator palpebrae superioris originates as a short tendon from the inferior aspect of the lesser wing of the sphenoid and broadens anteriorly to form a wide tendon at its anterior end. Some of the fibers run into the anterior surface of the superior tarsus, while others terminate in the skin of the upper eyelid. The fascia between the levator palpebrae superioris and the superior rectus forms a thick mass to which the superior conjunctival fornix is attached. Laterally, the wide tendon of the levator passes between the orbital and palpebral parts of the lacrimal gland into Whitnall's tubercle on the zygomatic bone. Medially, it forms loose connective tissue that is continuous with the medial palpebral ligament. The muscle is supplied by a branch of the superior division of the superior division of the oculomotor nerve, which penetrates the inferior surface of the muscle.

The four strap-shaped recti muscles originate from the common tendinous ring. This fibrous ring attaches to the superior and middle surroundings of the optic canal and

also extends across the medial part of the superior orbital fissure. It contains the optic nerve with its dural sheath, and divides the superior orbital fissure into two compartments, as the lateral rectus muscle bridges the fissure. The lateral compartment is external to the common tendinous ring, and the medial one contains vessels that pass through the superior orbital fissure and through the ring. In the lateral compartment pass the lacrimal, frontal, and trochlear nerves, as well as the superior ophthalmic vein. In the medial compartment, the superior and inferior divisions of the oculomotor nerve, the abducens, and the nasociliary nerves are found. Lastly, the inferior orbital fissure is situated below the ring, and contains the zygomatic nerve, infraorbital nerve and artery, and the inferior ophthalmic vein.

The tendons of the rectus muscles originate from the ring, and the muscular fibers run forwards and attach by tendinous expansions into the sclera, each as implied by its name: superior, inferior, medial, and lateral recti muscles. The geometric basis for movements of these muscles (which will not be discussed here) is the discrepancy between the axis of the orbit, which is determined by the orientation of its bony walls, and the anteroposterior axis of the eyeball. With the eyes in primary position, the angle between these axes is approximately 25°.

In addition to the four recti muscles, tendons of two oblique muscles attach to the sclera. The superior oblique arises from the common tendinous ring and passes forwards, parallel to the superomedial border of the orbit, to terminate as a round tendon that passes through a pulley (trochlea) attached to the trochlear fossa of the frontal bone. The tendon then passes inferior to the superior rectus, and attaches to the sclera at the superolateral part of the posterior quadrant. The inferior oblique muscle arises from a small tendon that attaches to the orbital surface of the maxilla, lateral to the nasolacrimal fossa, and runs posterolaterally. At first, it passes between the orbital floor and the inferior rectus muscle, then between the eyeball and lateral rectus. The tendon attaches to the inferolateral part of the posterior quadrant near the insertion area of the superior oblique. The extrinsic ocular muscles receive their motor innervation from the superior division of the oculomotor nerve (superior rectus), from the inferior division of the oculomotor nerve (medial and inferior recti and the inferior oblique), from the abducens nerve (lateral rectus), and from the trochlear nerve (superior oblique).

In addition to the muscle of the superior eyelid and extrinsic muscles of the eyeball, the orbit also contains three minor smooth muscles that are innervated by the autonomic nervous system (i.e., by the superior cervical ganglion via the carotid sympathetic plexus). Two of them – the superior (Müller) and inferior tarsal muscles – are associated with the tarsal plates, and function as eyelid retractors. Loss of sympathetic supply in patients with Horner syndrome causes ptosis of the upper eyelid and elevation of the lower eyelid (also referred to as reverse ptosis). The combination of these symptoms lends an appearance of enophthalmos in these patients. The third smooth muscle is the orbitalis muscle that spans the inferior orbital fissure. This muscle may produce some elevation and protrusion of the eyeball.

2 Figures with Captions

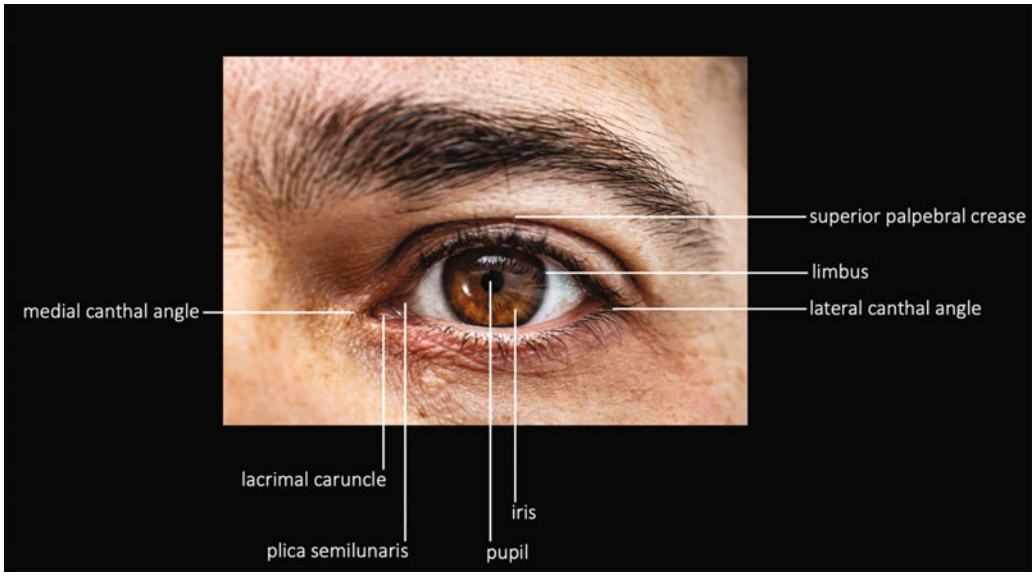


Fig. 1 Anterior view of the (open) palpebral fissure and adnexa

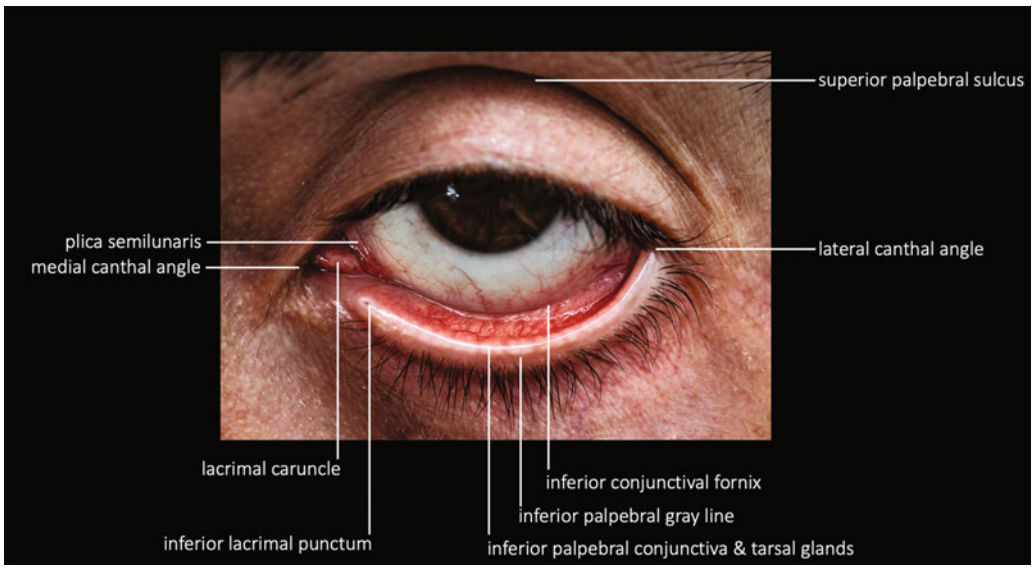


Fig. 2 Anterior view of the (open) palpebral fissure and adnexa, inferior eyelid inverted

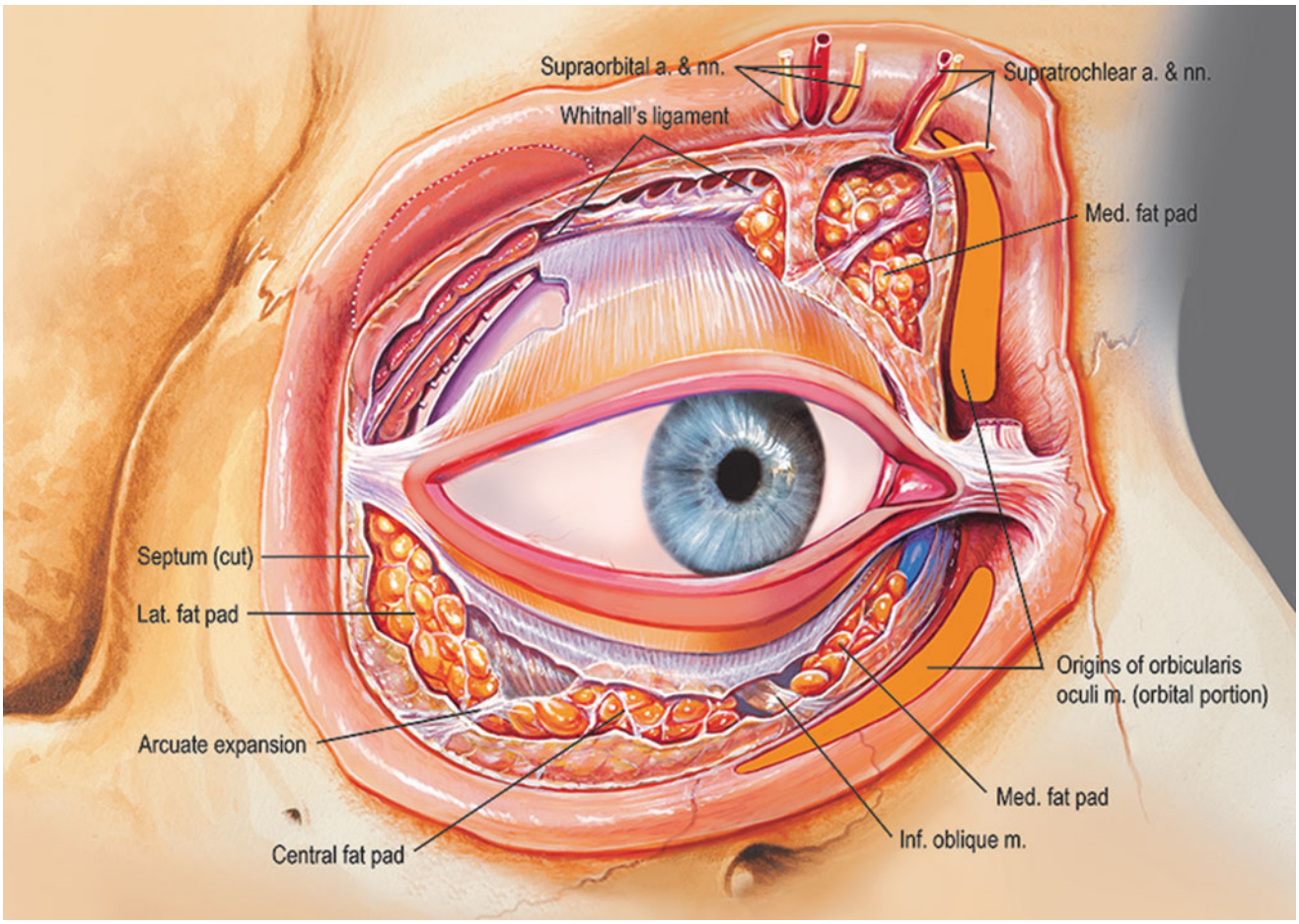


Fig. 3 Dissection of entire upper and lower lids posterior to orbicularis with part of the septum removed

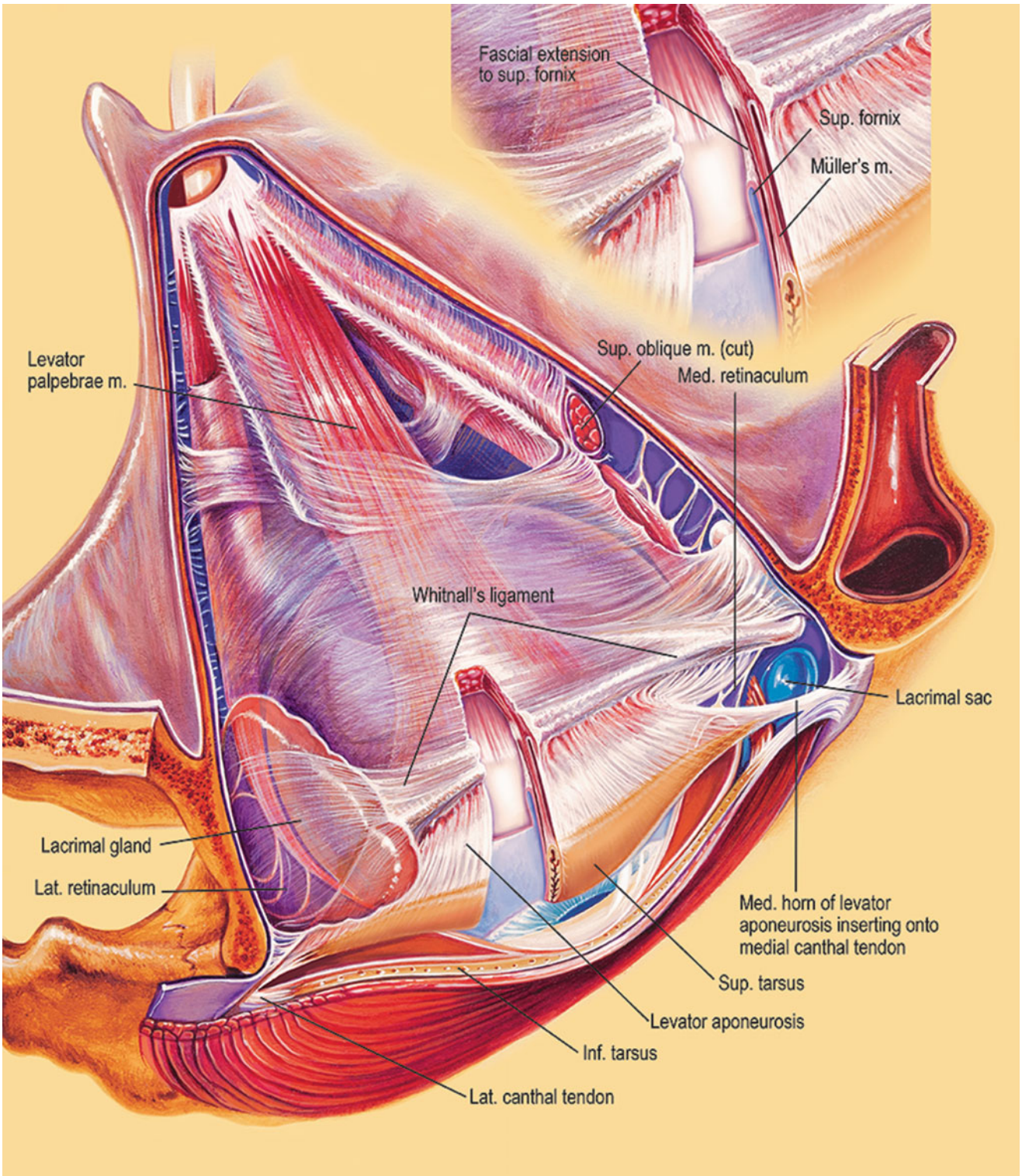


Fig. 4 Superior transview of the major orbital septa and soft tissues

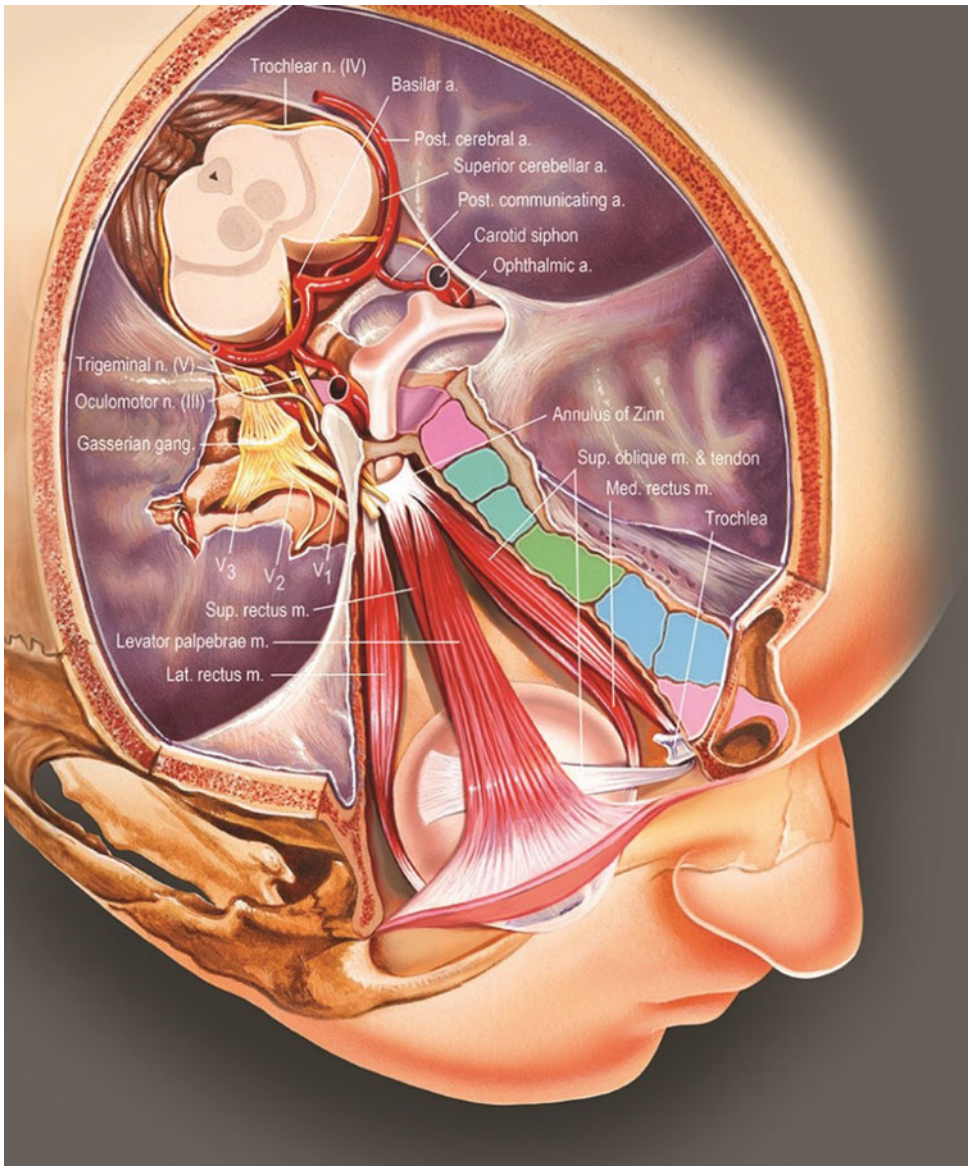


Fig. 5 Superior panoramic view of the extraocular muscles and intracranial structures; the orbital septa are not illustrated

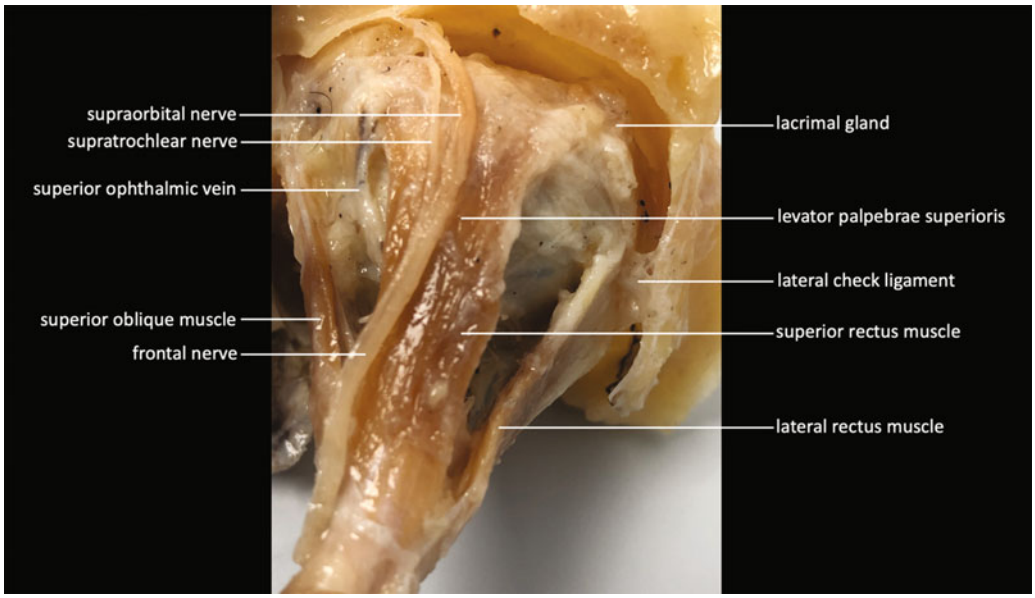


Fig. 6 Extraocular muscles, right orbit, superior view

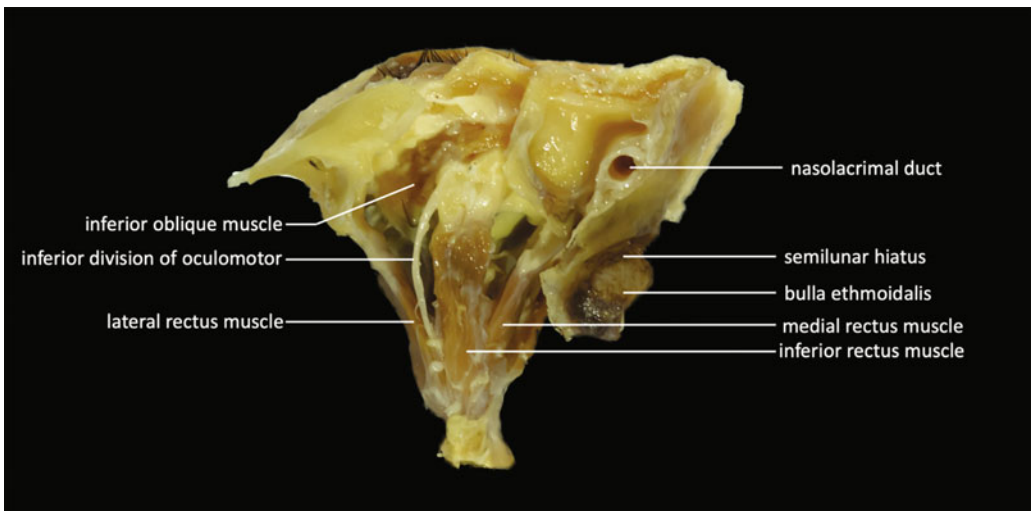


Fig. 7 Extraocular muscles, right orbit, inferior view

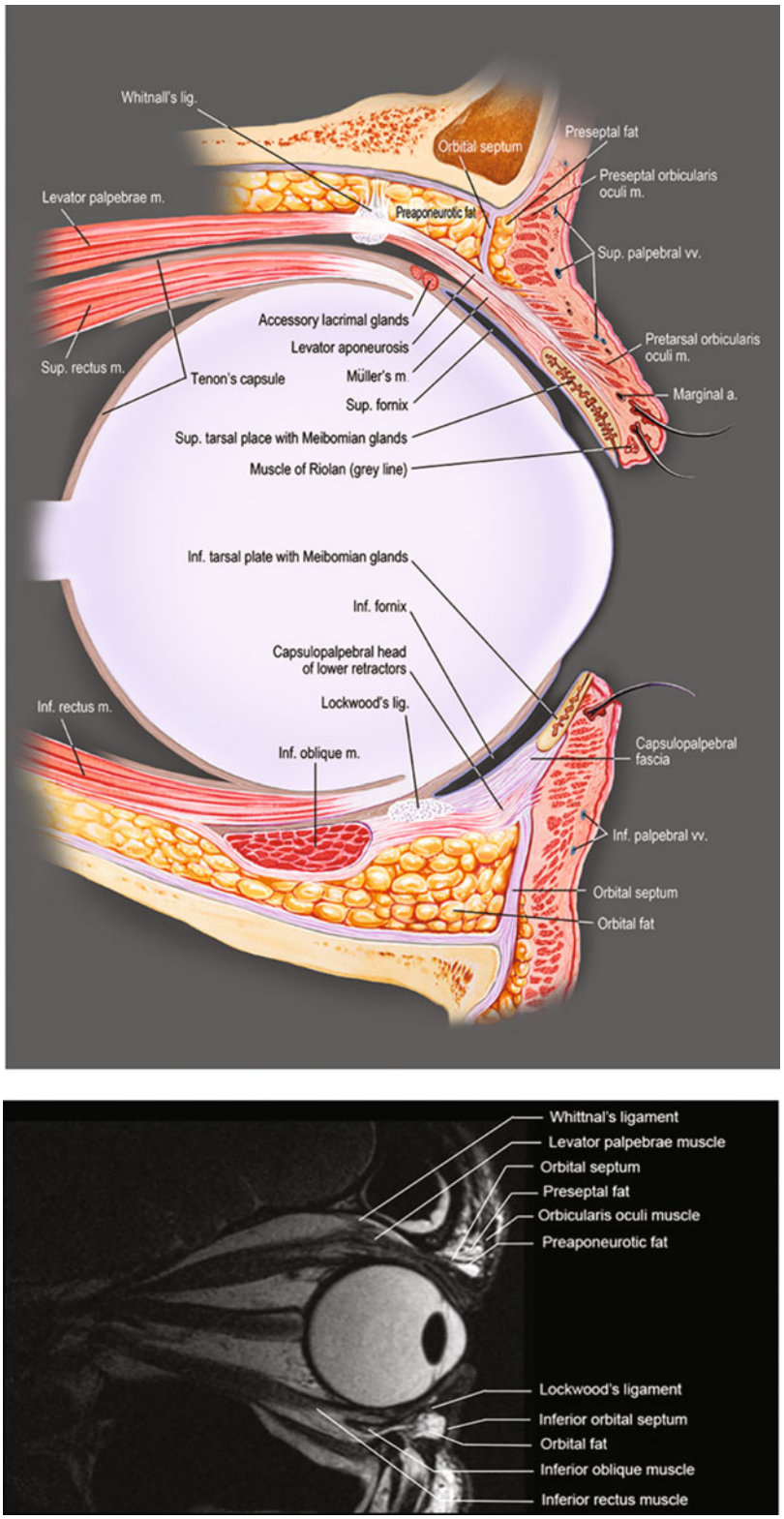


Fig. 8 Sagittal view of the upper lid and lower lids and adjacent ocular and orbital structures. Drawing (*upper*) and corresponding T2W MRI (*lower*)

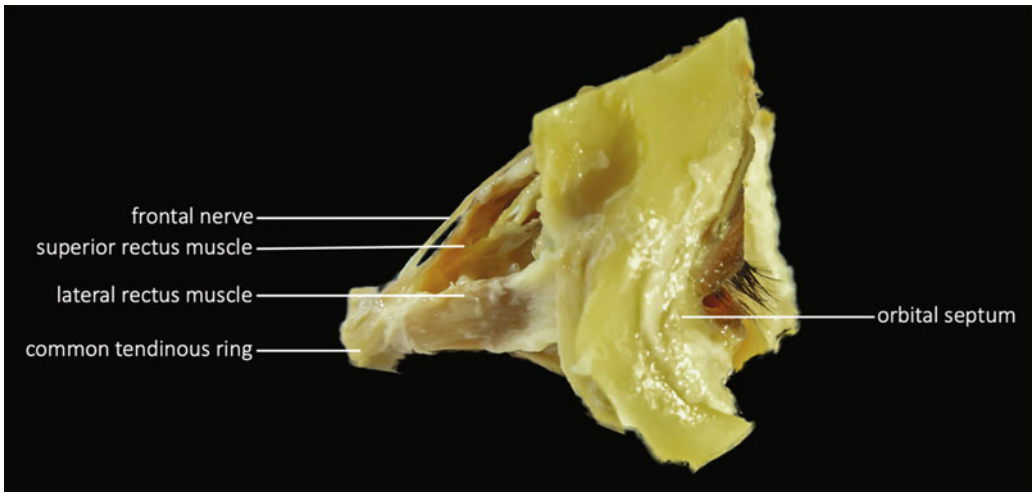


Fig. 9 Extraocular muscles, right orbit, lateral view

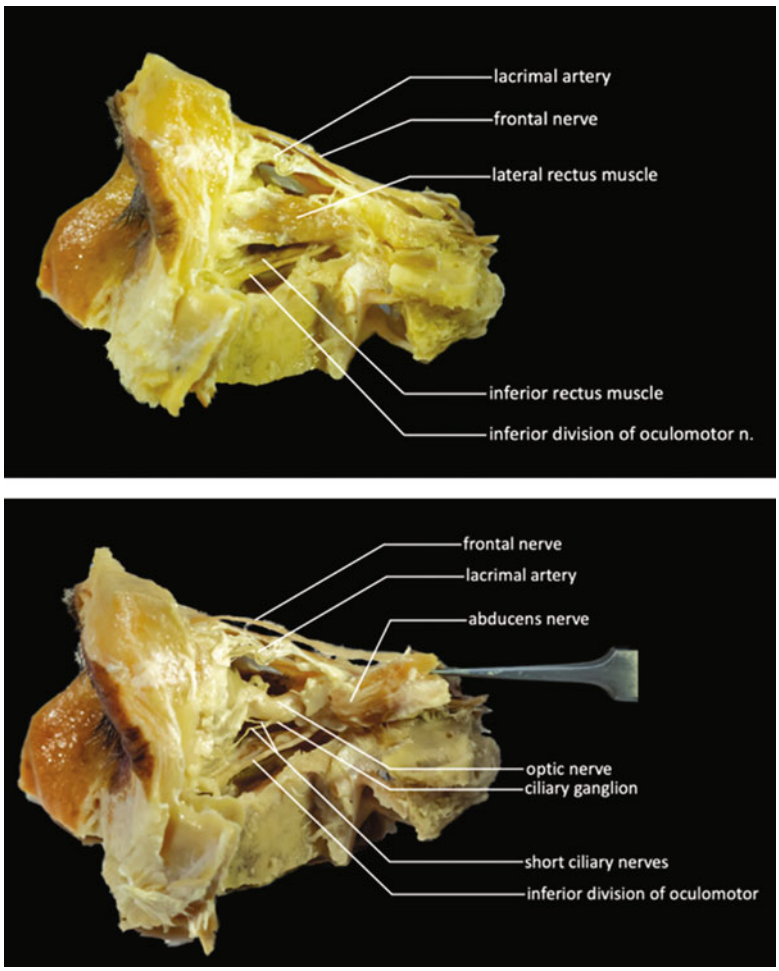


Fig. 10 Extraocular muscles, left orbit, lateral view (*upper*); lateral rectus reflected posteriorly (*lower*)

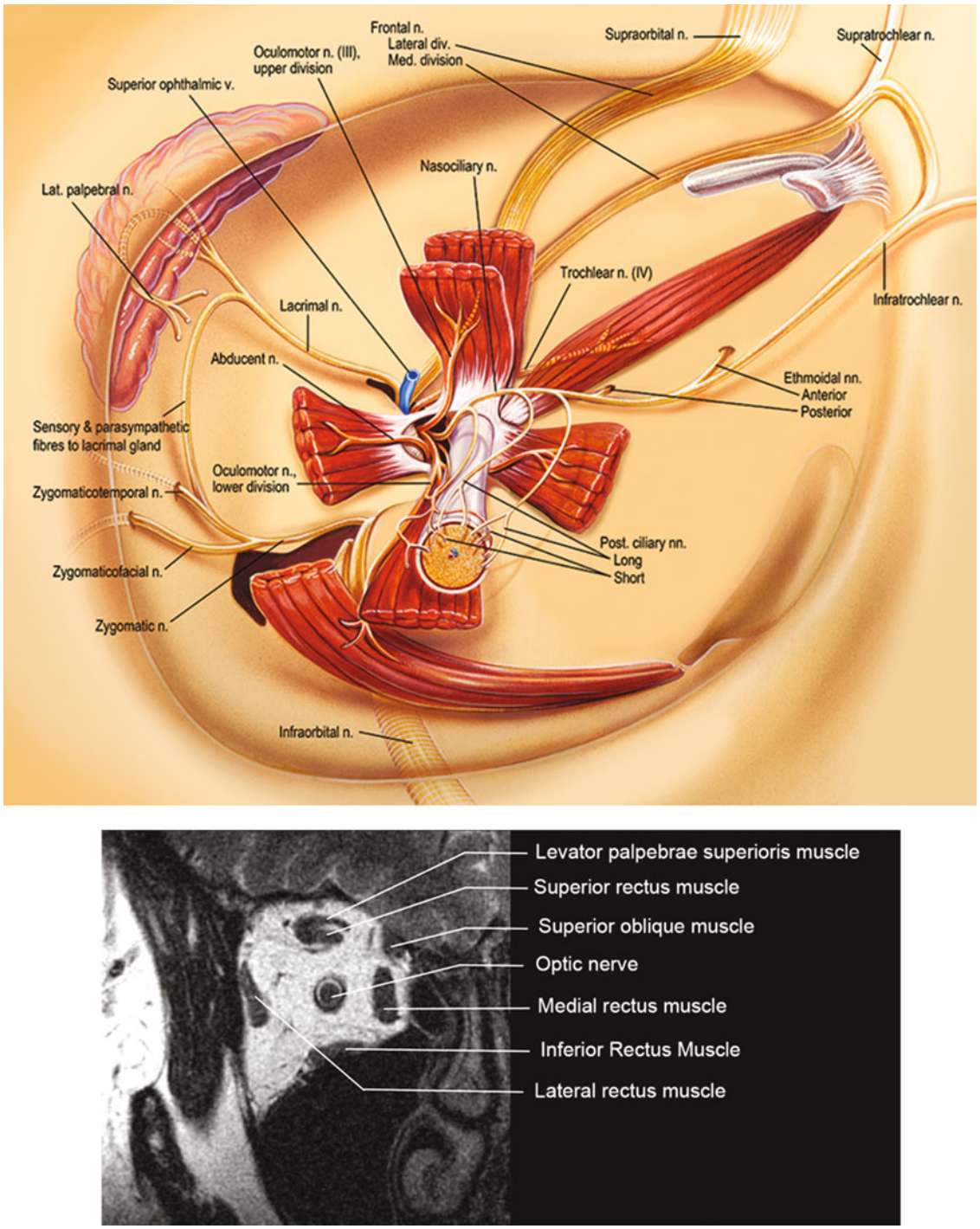


Fig. 11 Foreshortened view emphasizing the major relationships of the nerves and extraocular muscles in the orbital apex, superior orbital fissure, and annulus. Drawing (*upper*), mid orbit coronal MR T2WI (*lower* image)

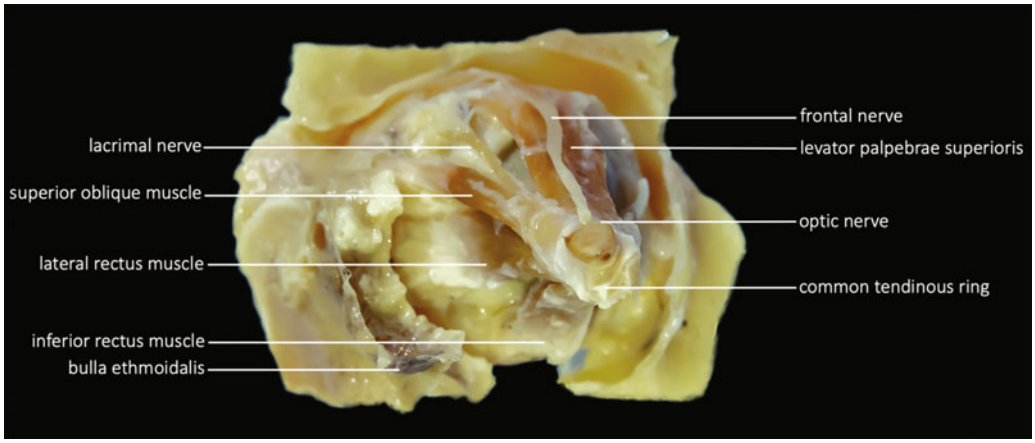


Fig. 12 Extraocular muscles, right orbit, posterior view

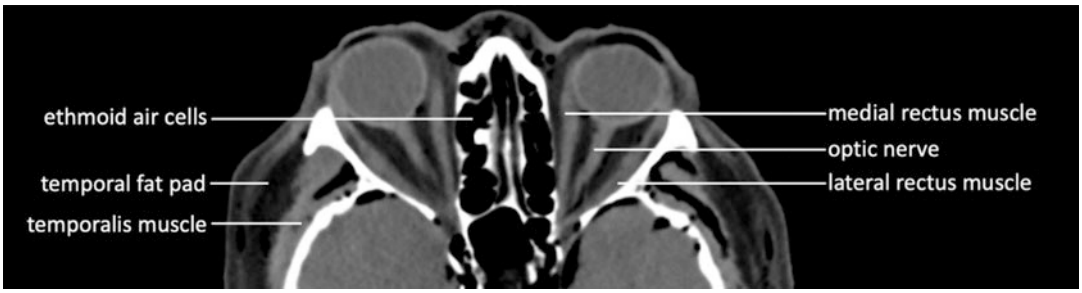


Fig. 13 PM HRCT scan (soft tissue window), extraocular muscles. Note the artifacts typical of PM scans (air replacing blood and CSF, emphysematous changes in the subcutaneous tissues)

Fig. 14 Axial and sagittal MR T1WI demonstrating the four recti muscles and a cross-section through the inferior oblique (*lower*)



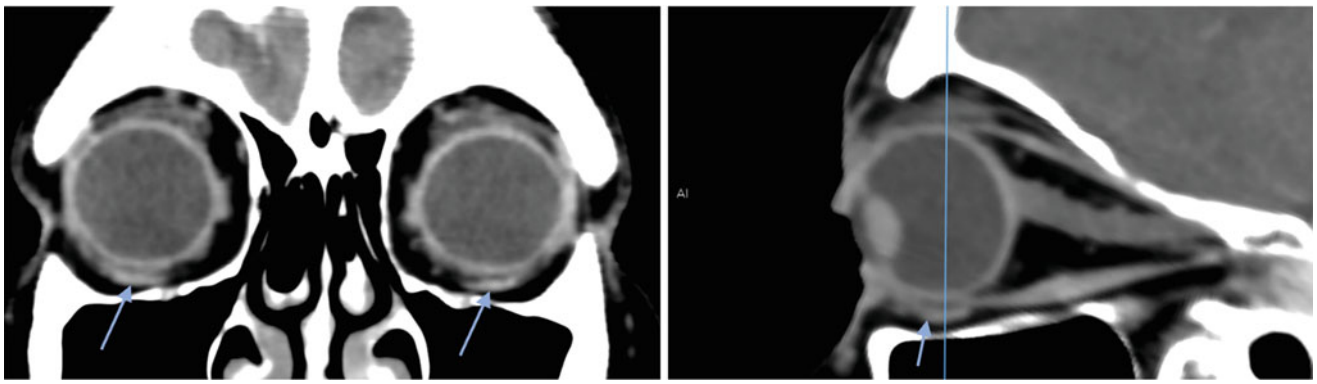


Fig. 15 Coronal and corresponding sagittal oblique CT scan showing the inferior oblique muscle and its attachment to the inferior eyelid

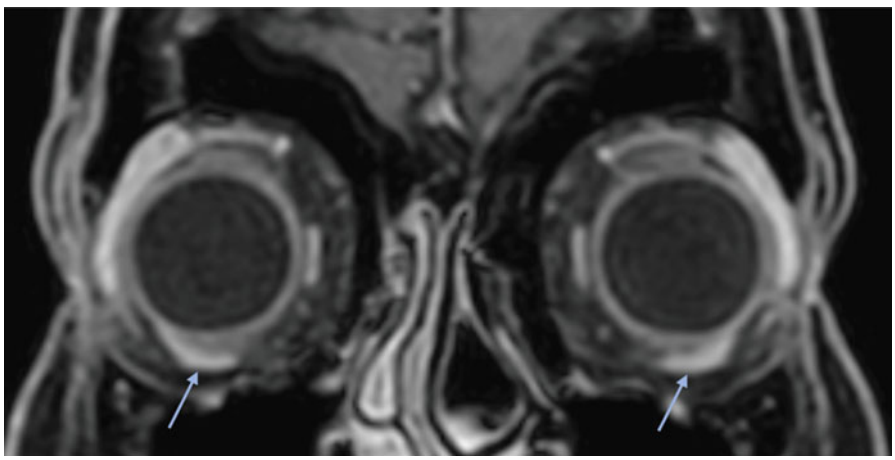


Fig. 16 Coronal T1 FS post gad showing the inferior oblique. Note the normal enhancing lacrimal glands

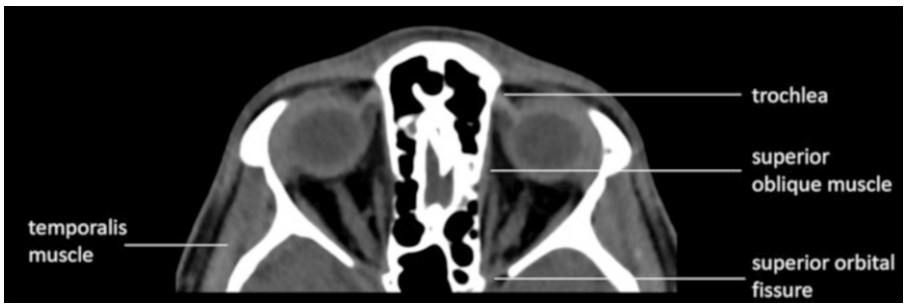


Fig. 17 Axial CT demonstrating the course of the superior oblique muscle

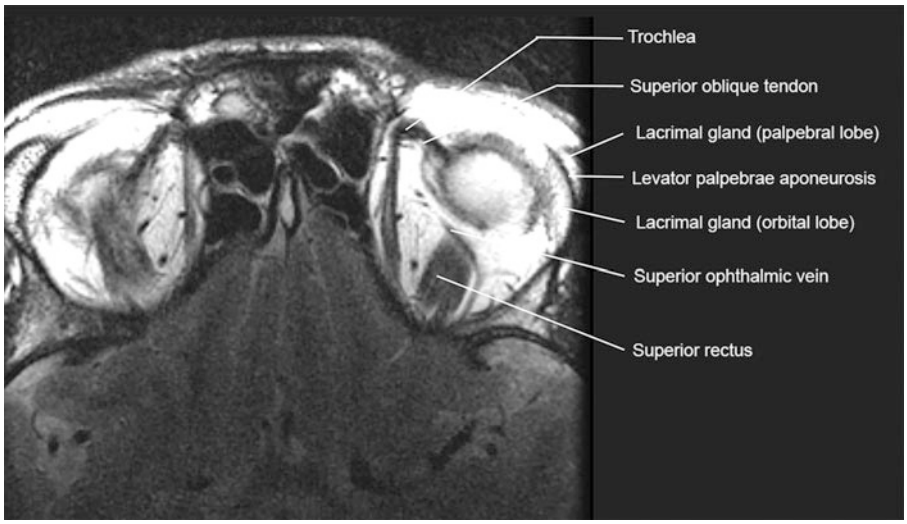


Fig. 18 Axial T2WI at the level of the orbital roof, demonstrating the superior rectus and the superior oblique muscles. Note the course of the superior ophthalmic vein as it traverses the orbit from medial anteriorly to lateral posteriorly

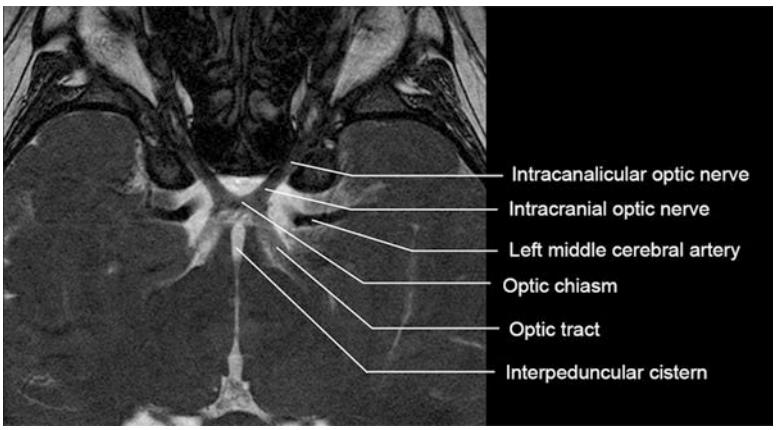


Fig. 19 Axial high-resolution T2 WI at the level of the optic chiasm. Note the intraorbital optic nerve within the hyperintense intraconal fat, as opposed to the hypointense vicinity of the intracanalicular segment

References

1. Gray H, Standring S, Ellis H, Berkovitz BKB. Gray's anatomy: the anatomical basis of clinical practice. 39th ed. Edinburgh/New York: Elsevier Churchill Livingstone; 2005.
2. Most SP, Mobley SR, Larrabee WF. Anatomy of the eyelids. Facial Plast Surg Clin North Am. 2005;13:487–92.
3. Sicher H, DuBrul EL. Oral anatomy. 6th ed. Saint Louis: The CV Mosby; 1975.
4. Kanagalingam S, Miller NR. Horner syndrome: clinical perspectives. Eye Brain. 2015;7:35–46.
5. Meybodi AT, et al. The oculomotor-tentorial triangle. Part 1: microsurgical anatomy and techniques to enhance exposure. J Neurosurg. 2019;130:1426–34.
6. Malhotra A, et al. Neuroimaging of Meckel's cave in normal and disease conditions. Insights Imaging. 2018;9:499–510.
7. Zhuang W, et al. Anatomical study of the extraocular check ligament system. J Plast Reconstr Aesthet Surg. 2019;72(12): 2017–26.
8. Marom A. A new look at an old canal. Skull Base. 2011;21(1): 53–8.
9. Voirol JR, Vilensky JA. The normal and variant clinical anatomy of the sensory supply of the orbit. Clin Anat. 2014;27: 169–75.
10. Wolfram-Gabel R, Kahn JL. Adipose body of the orbit. Clin Anat. 2002;15:186–92.
11. Goh PS, et al. Review of orbital imaging. Eur J Radiol. 2008;66: 387–95.

Paranasal Sinuses

4

Jack Rootman, Daniel B. Rootman, Bruce Stewart, Stefania B. Diniz, Kelsey A. Roelofs, Liza M. Cohen, Claire S. Smith, Ayelet Eran, Ben Kaplan, and Assaf Marom

Contents

1 Introduction 47

2 Figures with Captions 48

References 61

Abstract

The cranial bones that relate to the nasal cavity bear air-filled cavities: the frontal, ethmoidal, maxillary, and sphenoidal sinuses. These cavities open into the lateral nasal wall by small and substantially variable apertures, which allow pressure equilibration and mucus drainage. The mucosa that lines the sinuses is continuous with that of the nasal cavity (thus allowing the spread of infection). While most sinuses are rudimentary at birth, they enlarge during childhood and puberty and thus contribute substantially to shaping the morphology of the face.

Keywords

Frontal sinus · Ethmoid sinus · Sphenoid sinus · Maxillary sinus · Bulla ethmoidalis

1 Introduction

The frontal sinus is paired, and lies posterior to the superciliary arch. They are frequently asymmetrical, and the septum between them often deviates from the midline. The frontal sinus extends superiorly and laterally and may be appreciably developed in the elderly; however, the prominence of the superciliary arch does not correlate with the size of the sinus. The frontal sinus usually drains into the middle nasal

J. Rootman
University of British Columbia, Vancouver, BC, Canada

D. B. Rootman · S. B. Diniz · K. A. Roelofs · C. S. Smith
Division of Orbital and Ophthalmic Plastic Surgery, Stein and Doheny Eye Institutes, University of California, Los Angeles, CA, USA

B. Stewart
BFA Art Center College of Design, UBC Faculty of Medicine, Kelowna, BC, Canada

L. M. Cohen
Division of Orbital and Ophthalmic Plastic Surgery, Stein Eye Institute, University of California, Los Angeles, CA, USA

A. Eran
Neuroradiology Unit, Radiology Department, Rambam Healthcare Medical Center, Haifa, Israel

Department of Anatomy, Rappaport Faculty of Medicine, Technion – Israel Institute of Technology, Haifa, Israel

B. Kaplan · A. Marom (✉)
Department of Anatomy, Rappaport Faculty of Medicine, Technion – Israel Institute of Technology, Haifa, Israel
e-mail: assafma@technion.ac.il

© Springer Nature Switzerland AG 2022
G. Ben Simon et al. (eds.), *Atlas of Orbital Imaging*,
https://doi.org/10.1007/978-3-030-62426-2_4

meatus (medial to the middle nasal turbinate) via an elongated frontonasal duct, occasionally medial to the semilunar hiatus. The frontal sinus is supplied by branches of the supraorbital and anterior ethmoidal arteries, and its mucus is innervated by the supraorbital nerve.

The sphenoidal sinuses are paired and lie posterior to the upper part of the nasal cavity, within the sphenoid body. The septum between them often deviates from the midline, and there may frequently be additional minor septa. The sphenoid sinus may invade the lesser and greater wings of the sphenoid and also the basilar part of the occipital bone. Important relations of this sinus are the optic nerve and the hypophysis cerebri (above), and the carotid siphon and cavernous venous sinus (laterally). The sphenoid sinus drains via an opening in its anterior wall into the spheno-ethmoidal recess of the nasal cavity, and is supplied by the posterior ethmoidal branch of the ophthalmic artery and by the nasal branch of the sphenopalatine artery. The sensory innervation is given by the posterior ethmoidal nerve, and the parasympathetic innervation by orbital branches of the pterygopalatine ganglion.

The ethmoidal sinuses are small multiple cavities that form an ethmoidal labyrinth medial to the orbital surface of the ethmoid (the extremely thin lamina papyracea), with variable drainage pathways into the nasal cavity. They are usually categorized into anterior, middle, and posterior groups, but in other divisions the middle group is considered part of the anterior group.

The anterior ethmoidal air cells open into the ethmoidal infundibulum or the frontonasal duct. The middle ethmoidal air cells bulge into the middle nasal meatus as the bulla ethmoidalis, and are thus referred to as the bullar sinuses. They drain via one or more openings on the ethmoidal bulla. The posterior ethmoidal air cells lie in close proximity to the optic canal and nerve, and usually drain into the superior nasal meatus. The ethmoidal sinuses are supplied by branches of the ethmoidal and ophthalmic arteries; their sensory innervation is given by the anterior and posterior ethmoidal nerves, and the parasympathetic supply by the orbital branches of the pterygopalatine ganglion.

The maxillary sinus is the largest of the paranasal sinuses, and fills the body of the maxilla. Its thin walls form a pyramid with its base facing medially:

- The roof corresponds to the orbital surface of the maxilla, where a ridge is formed by the infraorbital canal and nerve.
- The floor corresponds to the alveolar aspect of the maxilla and often relates to the roots of the premolar and molar teeth.
- The anterior wall corresponds to the facial surface of the maxilla.
- The apex extends into the zygomatic bone.
- Its base faces medially as the lateral wall of the nasal cavity that contains the ostiomeatal complex for drainage of the sinuses.

The maxillary sinus may contain incomplete septa. Its ostium is usually in the semilunar hiatus. The mucosa is supplied by several branches of the maxillary artery, and innervation is given by the infraorbital and superior alveolar nerves.

2 Figures with Captions



Fig. 1 CT 3D reconstruction with soft tissue rendering beautifully demonstrating the frontal and maxillary paranasal sinuses. Note the mastoid air cells on both sides. The ethmoid and sphenoid air cells are superimposed and are partially obscured by the superior and middle nasal conchae. The supraglottic structures and the superior tracheal opening are demonstrated inferiorly

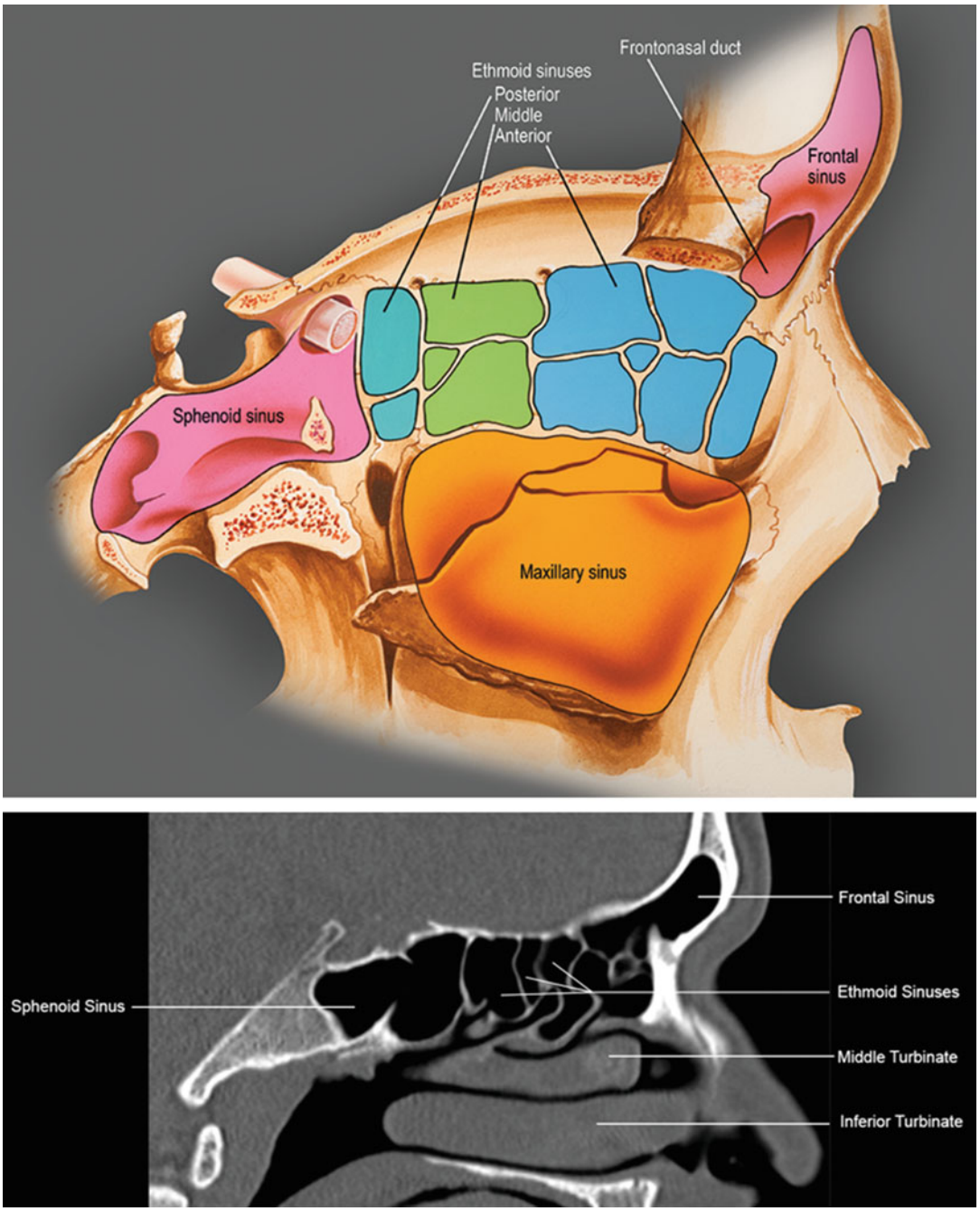


Fig. 2 Transview of major sinus structures. Drawing (*upper*) and sagittal CT scan bone window (*lower*)

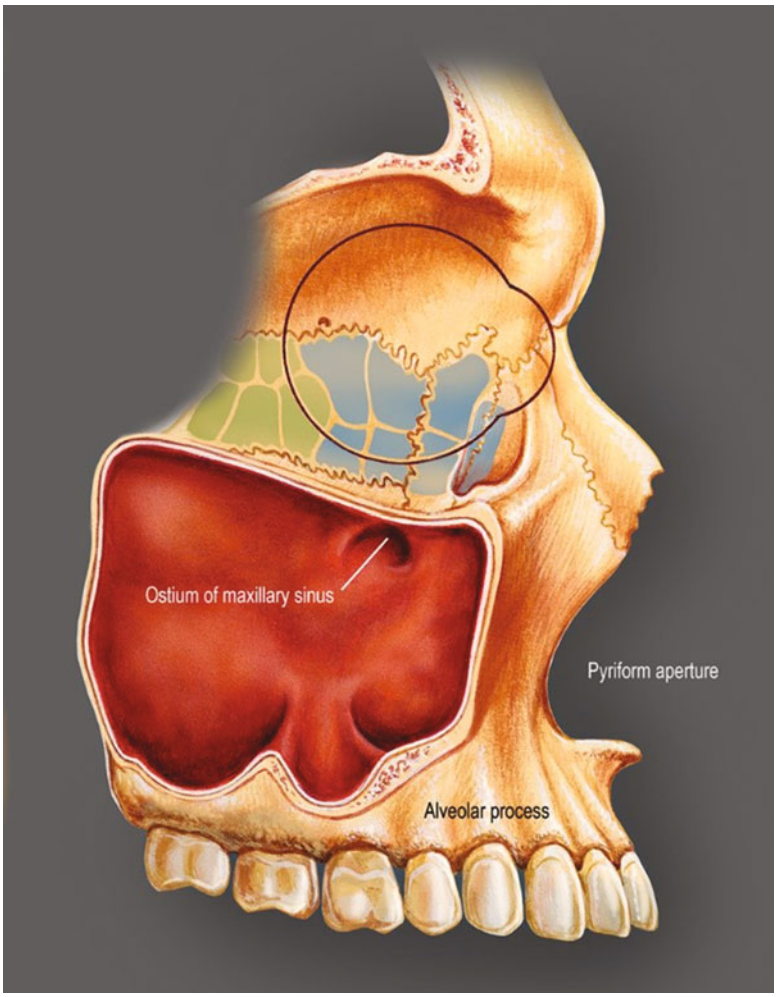


Fig. 3 Medial wall of the right maxillary sinus and its relationship to ethmoids and the orbit

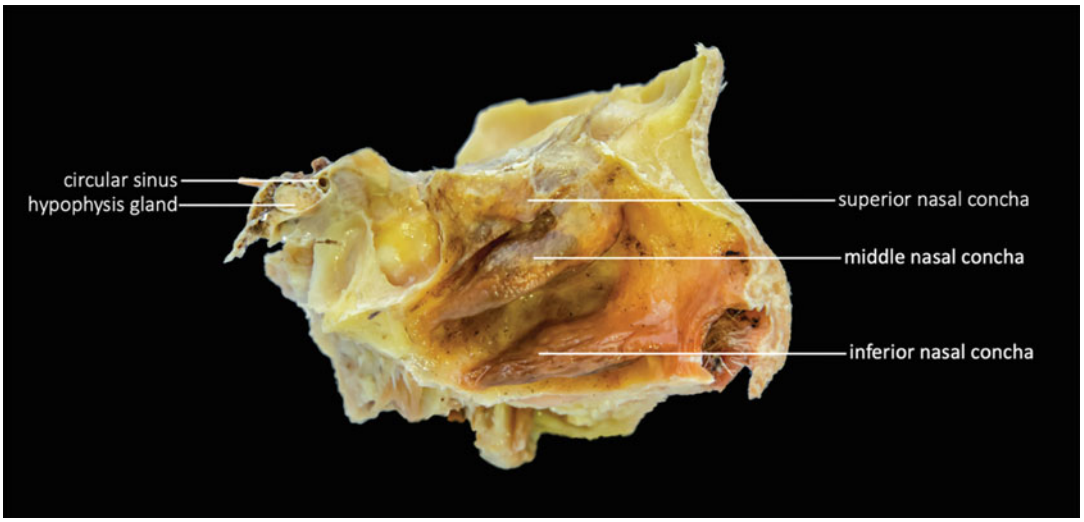


Fig. 4 Medial view of nasal (ethmoidal) turbinates

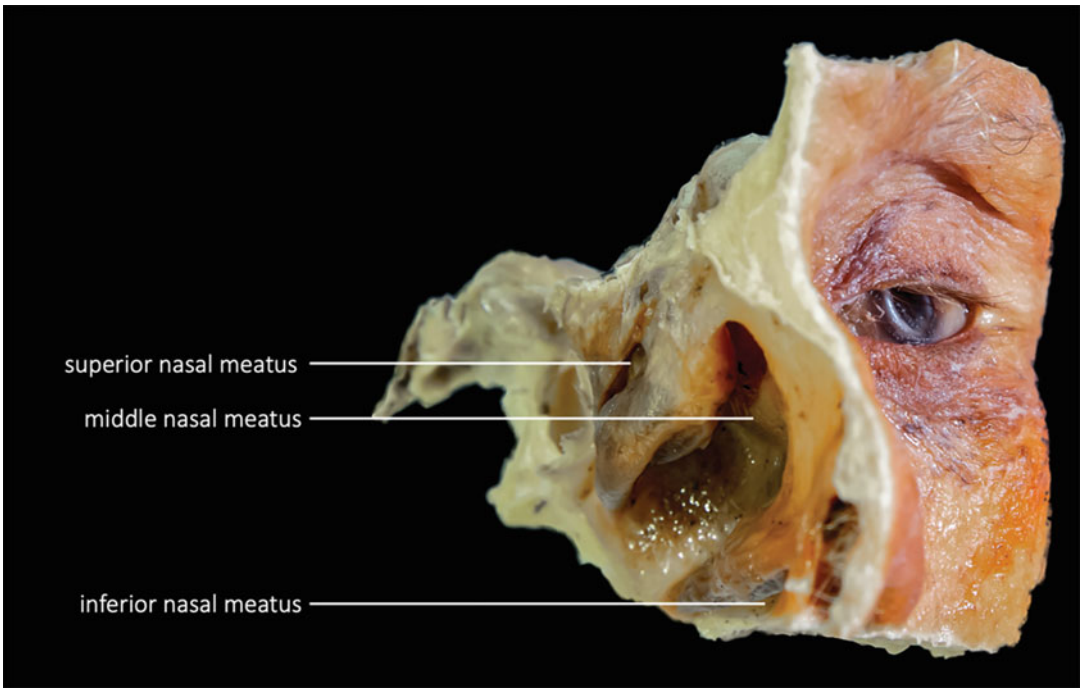


Fig. 5 Left orbit, mediolateral view of nasal (ethmoidal) turbinates



Fig. 6 Coronal section through the bones of the midface and orbit just behind the orbital rim. Drawing (*upper*), corresponding CT slab reformat (*middle*), and coronal bone window CT (*lower*)

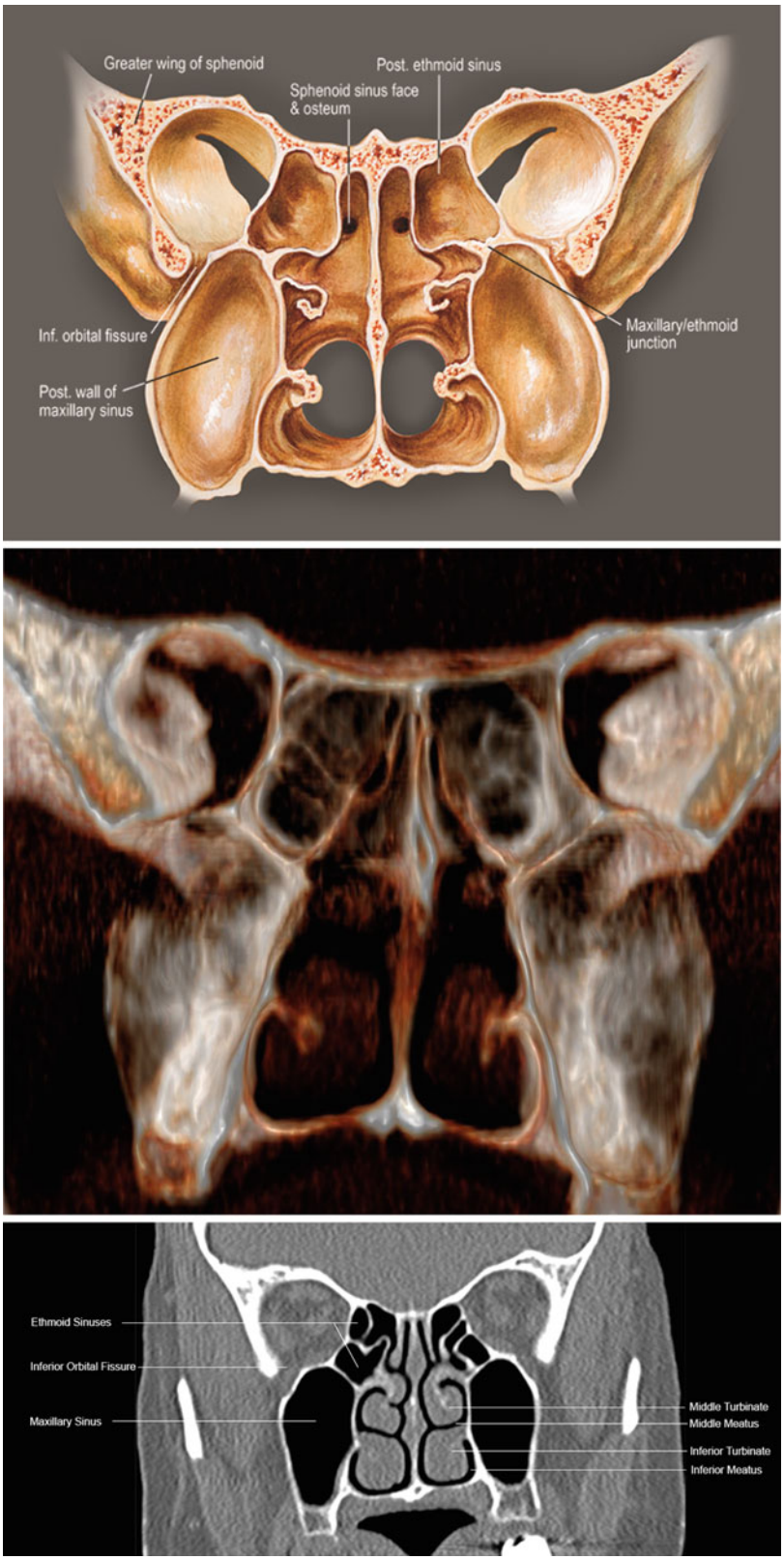


Fig. 7 Coronal section through the bones of the midface and orbit posterior to the midorbital plane. Drawing (*upper*), corresponding CT slab reformat (*middle*), and coronal soft tissue CT (*lower*)

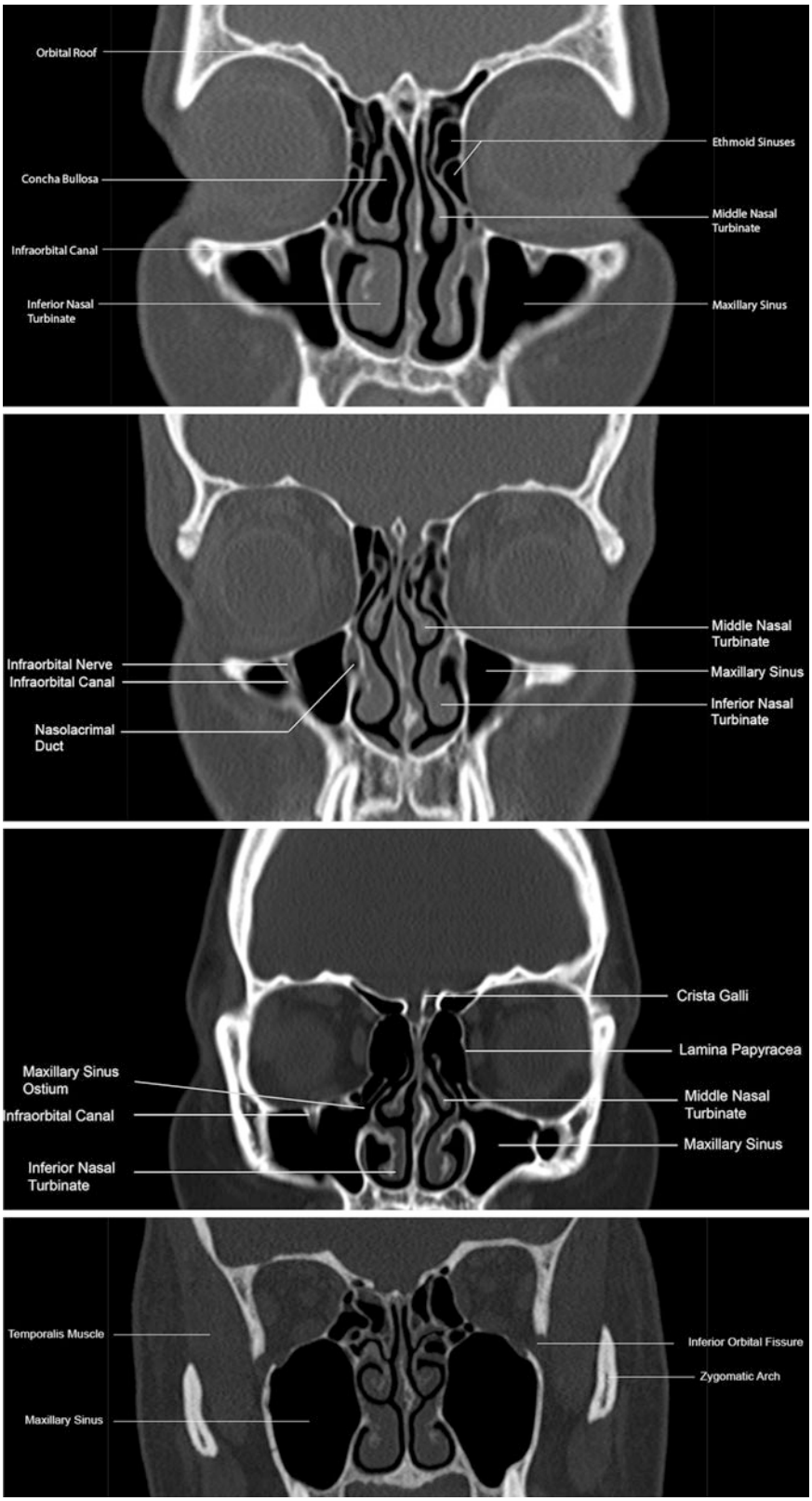


Fig. 8 Successive coronal scans (*upper* – anterior to *lower* – posterior) through the maxillary sinuses and the lacrimal drainage system

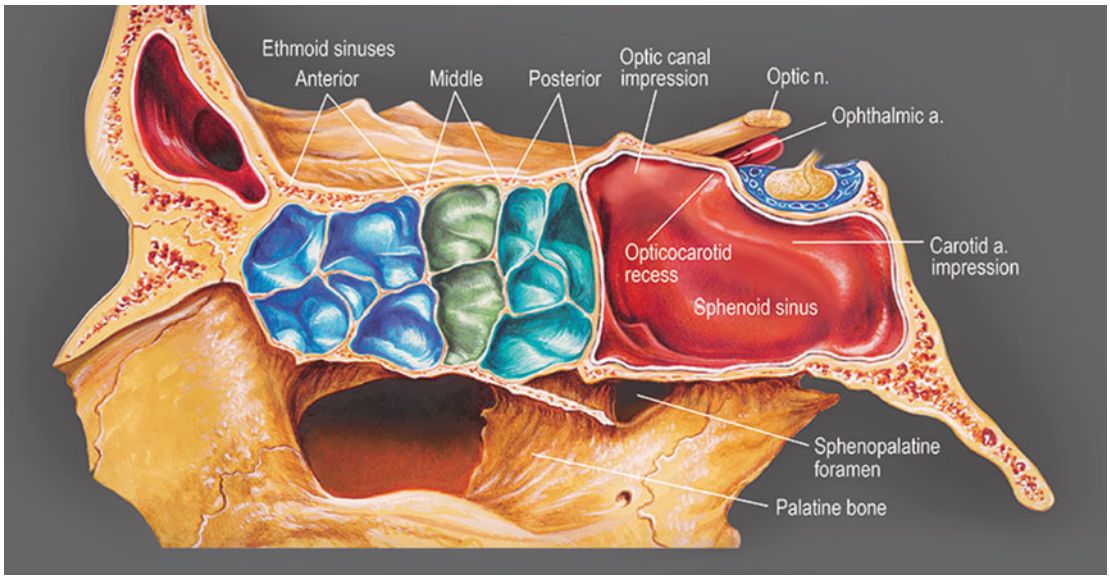


Fig. 9 Sagittal view of sinuses. Note the lateral wall of the sphenoid sinus with bony impressions formed by the optic nerve, carotid siphon, and pituitary gland. Bottom drawings show coronal view of the relationship of neurovascular structures to the lateral wall of sphenoid sinus

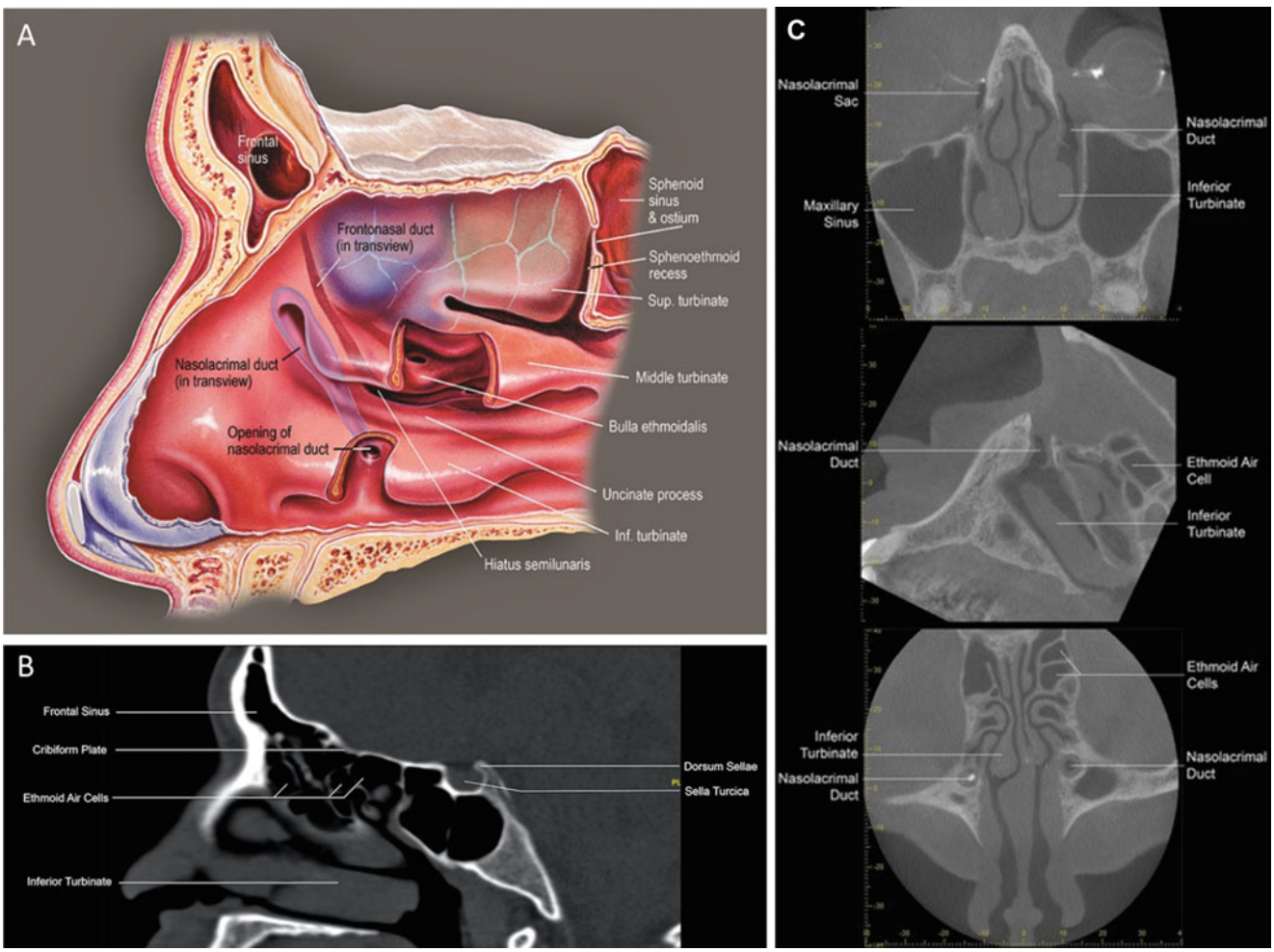


Fig. 10 Drawing (**a**) of the right lateral wall of the nose with sinuses, ostia, frontonasal duct, and lacrimal system. Corresponding parasagittal bone window CT (**b**). Cone beam CT DCG (**c**) demonstrating passage of contrast through the lacrimal system on the right

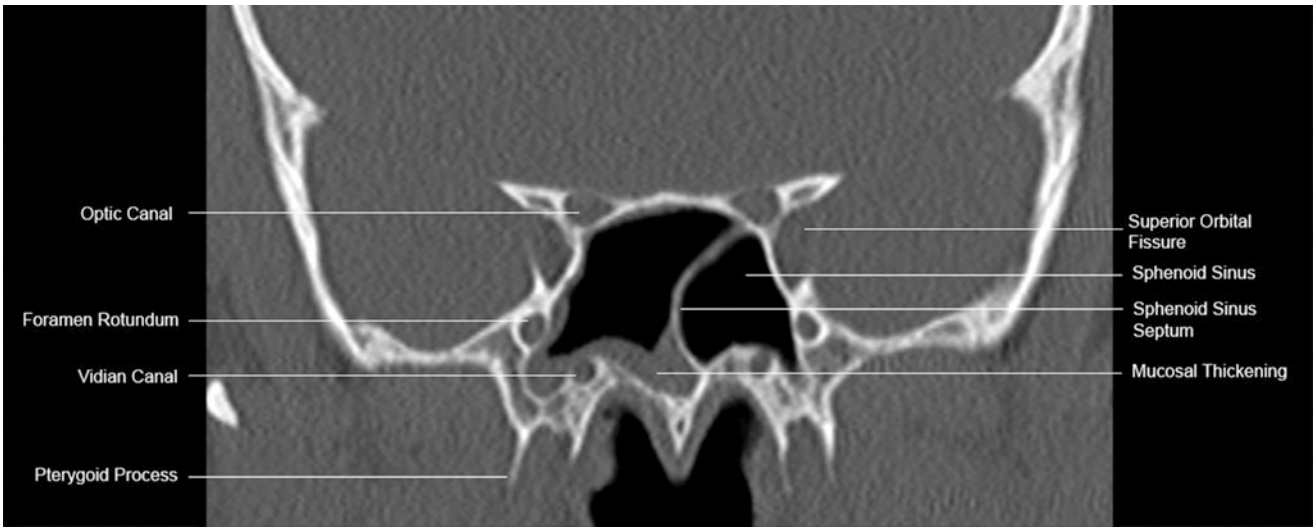


Fig. 11 Coronal CT scan through the sphenoid sinus

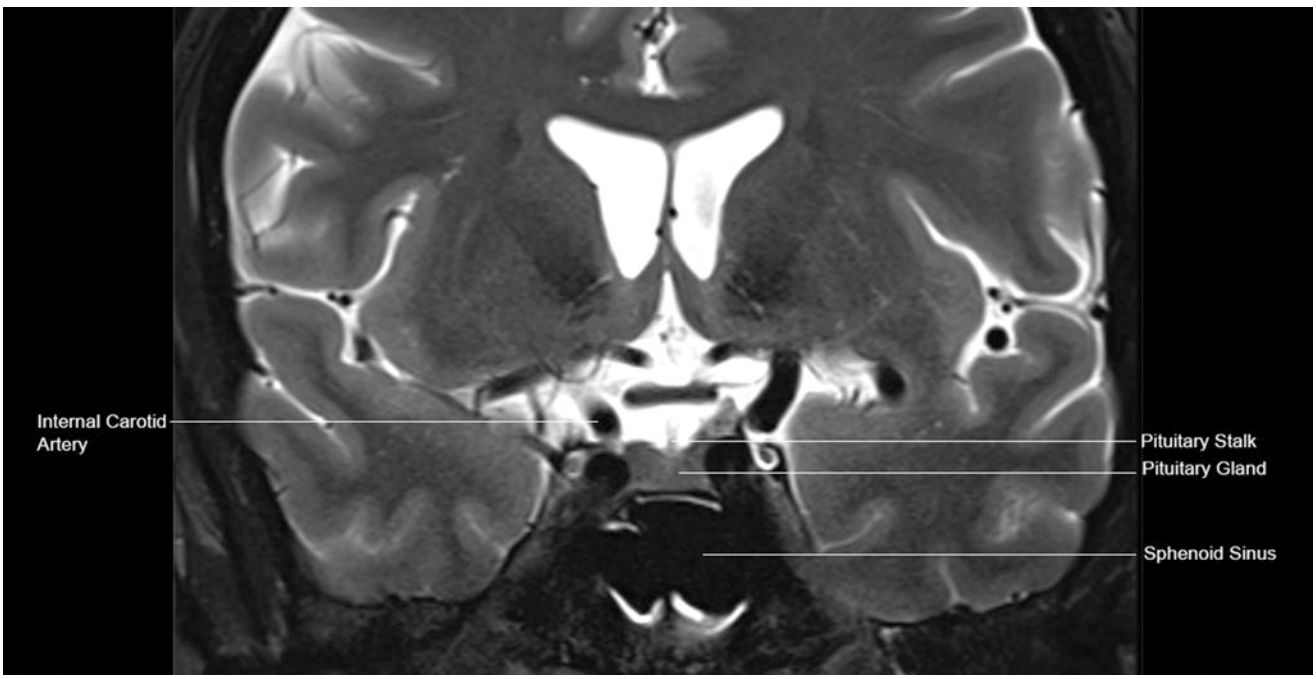


Fig. 12 Coronal T2W MR scan through the sphenoid sinus

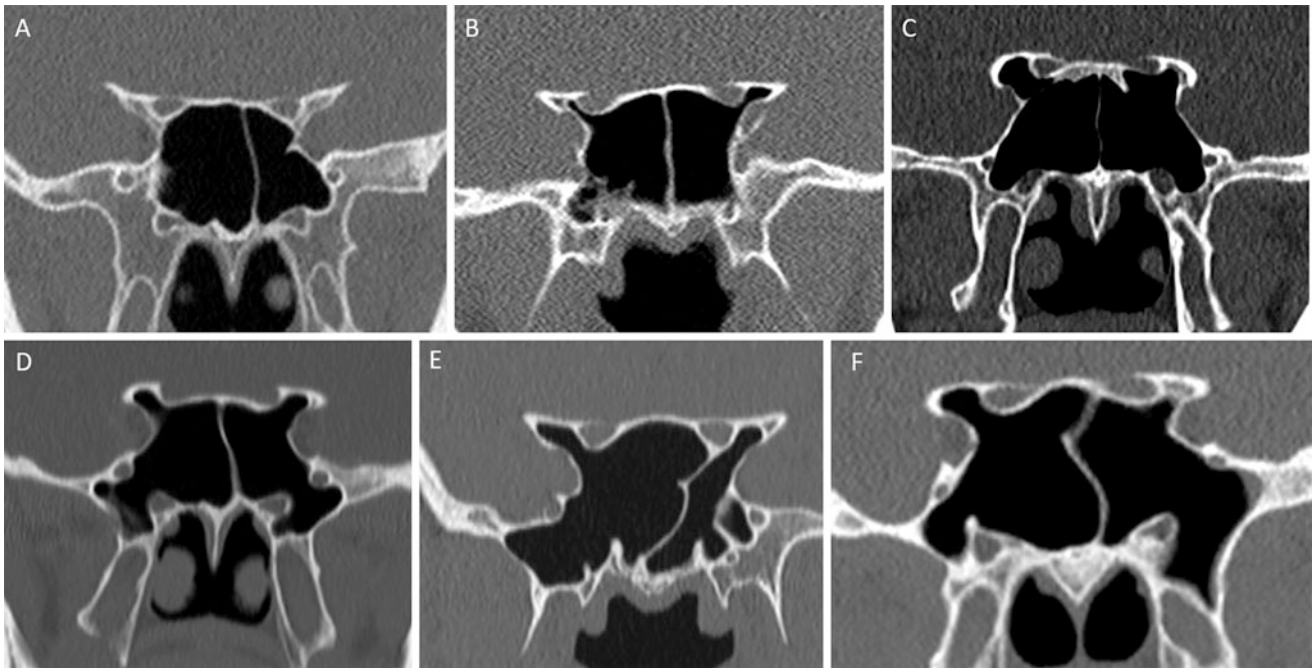


Fig. 13 Coronal CT sections (**a**–**f**) of different patients representing the incremental pneumatization of the sphenoid sinus and anterior clinoids surrounding the optic canals; there are numerous variants including asymmetric variations as shown in the last image. Note that in image ***e***, the inter sphenoidal septum attaches to the floor of the optic canal. Delano et al. suggested four different anatomical configurations depending on the level of pneumatization, depth of indentation into the sinus wall, and degree of bony dehiscence. These anatomical relations should be detected and recorded in order to avoid serious sinus surgery complications

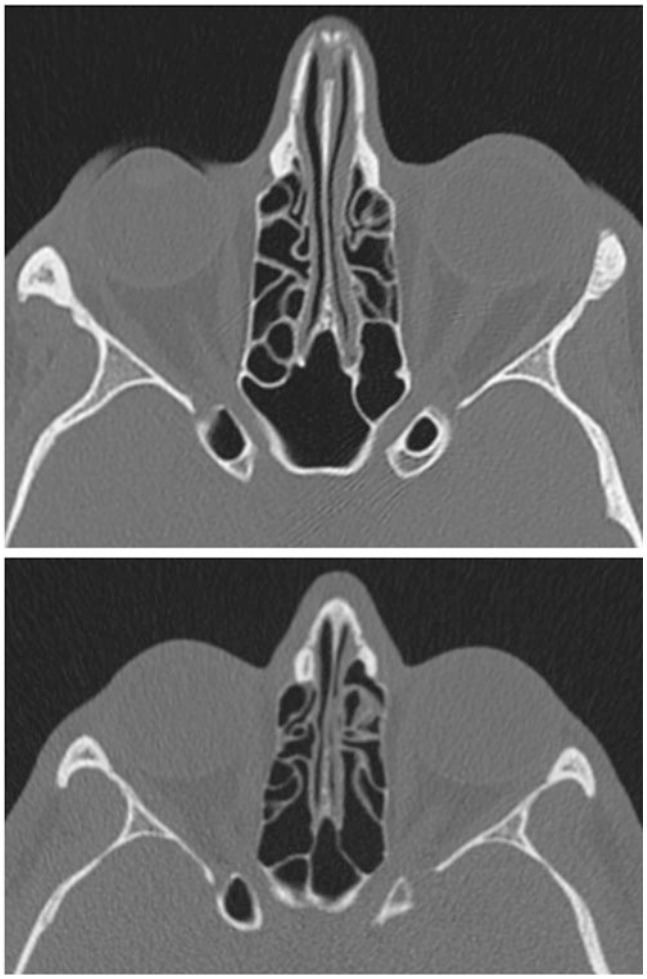


Fig. 14 Axial CT sections demonstrating pneumatized anterior clinoid. Upper, bilateral, lower, and unilateral



Fig. 15 Axial CT bone window through the maxillary sinuses

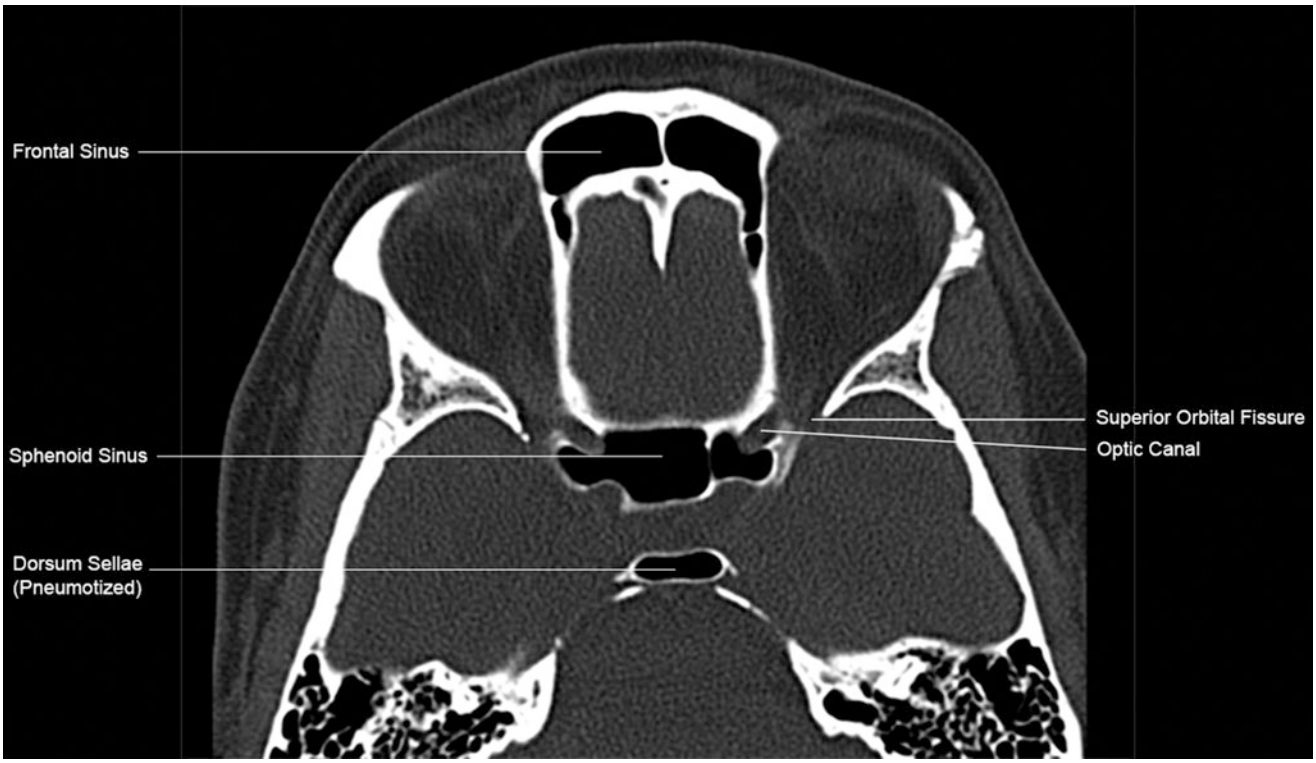


Fig. 16 Axial CT scan bone window through the sphenoid and frontal sinuses

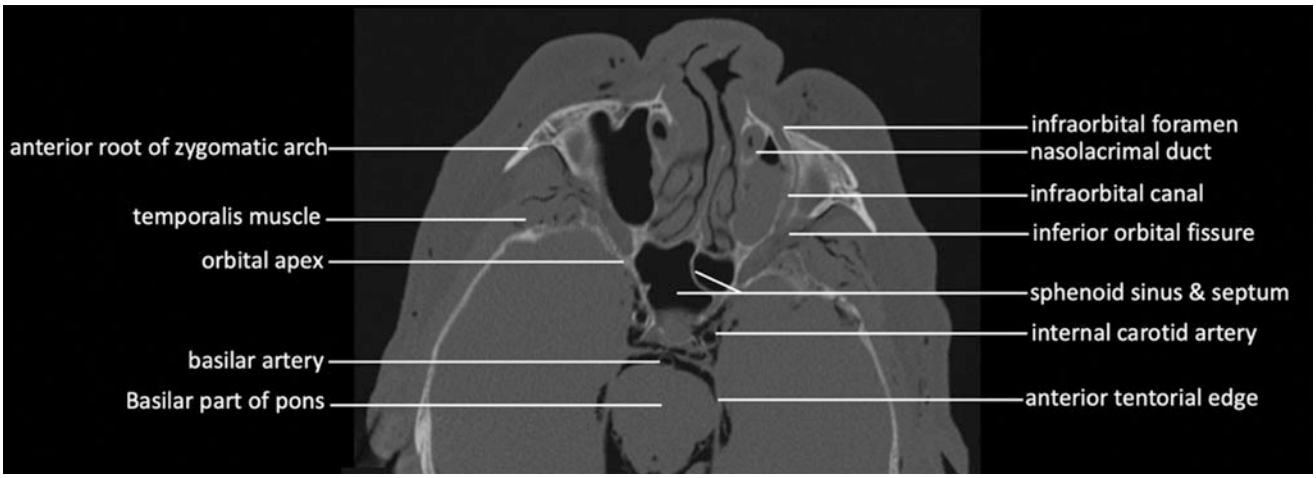


Fig. 17 Postmortem (PM) HRCT scan, horizontal section through sphenoid sinuses

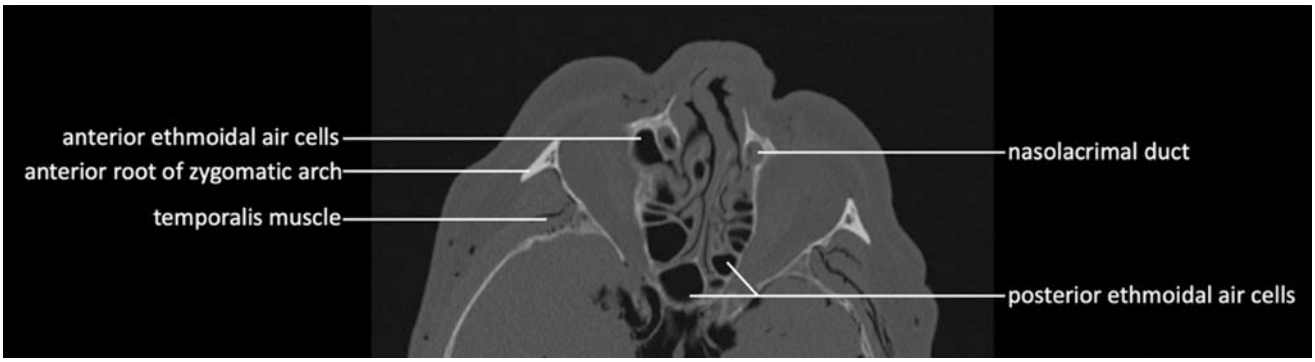


Fig. 18 PM HRCT scan, horizontal section through ethmoidal sinuses

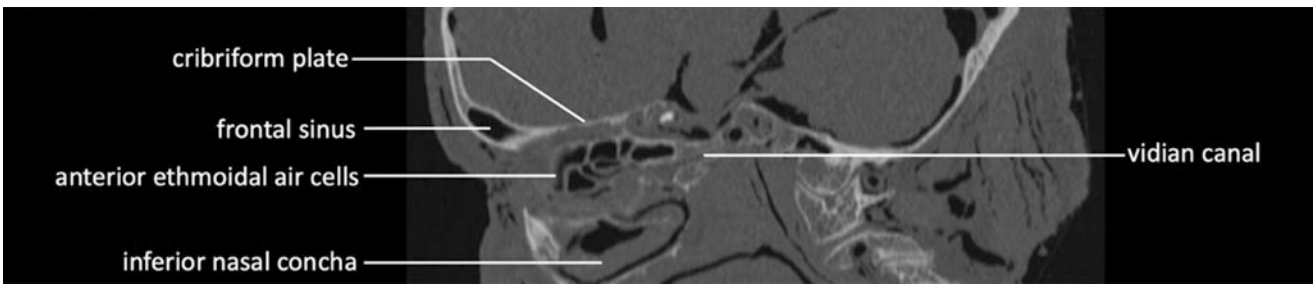


Fig. 19 PM HRCT scan, sagittal section through ethmoid sinuses

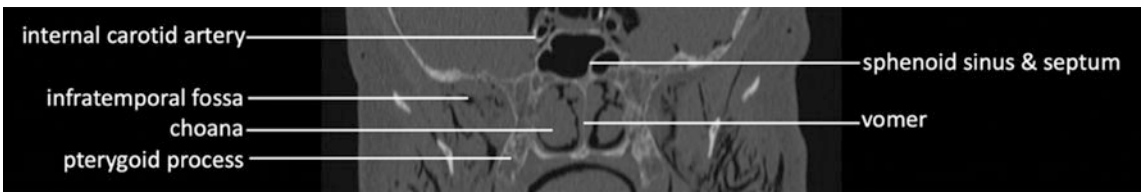


Fig. 20 PM HRCT scan, coronal section through sphenoid sinuses

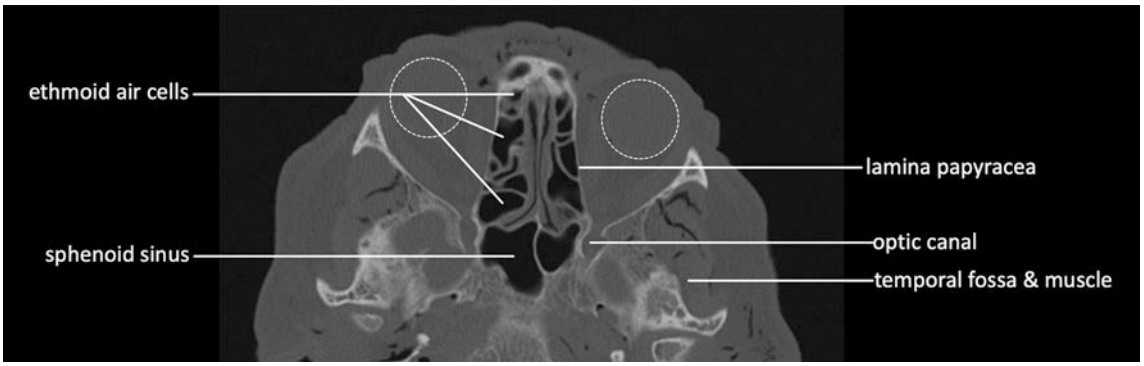


Fig. 21 PM HRCT scan, horizontal section through ethmoid sinuses. Dashed circles circumscribe eyeballs

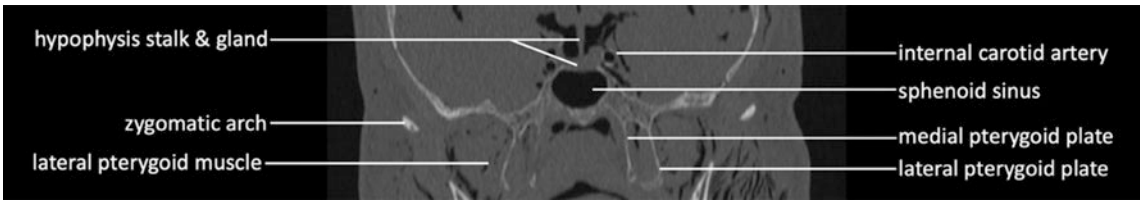


Fig. 22 PM HRCT scan, coronal section through sella turcica

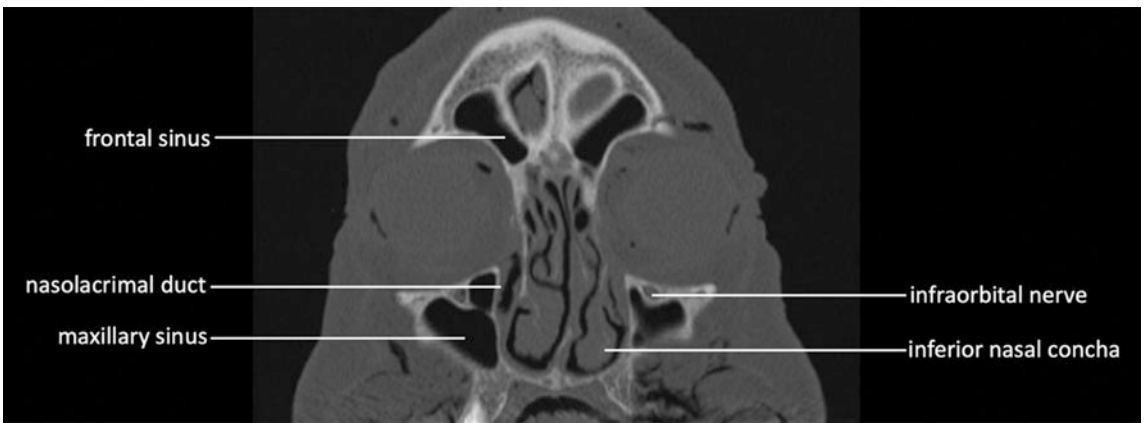


Fig. 23 PM HRCT scan, coronal section through frontal sinuses and lacrimal drainage apparatus

References

1. Gray H, Standring S, Ellis H, Berkovitz BKB. Gray's anatomy: the anatomical basis of clinical practice. 39th ed. Edinburgh/New York: Elsevier Churchill Livingstone; 2005.
1. Most SP, Mobley SR, Larrabee WF. Anatomy of the eyelids. Facial Plast Surg Clin North Am. 2005;13:487–92.
2. Sicher H, DuBrul EL. Oral anatomy. 6th ed. Saint Louis: The CV Mosby; 1975.
3. Kanagalingam S, Miller NR. Horner syndrome: clinical perspectives. Eye Brain. 2015;7:35–46.
4. Meybodi AT, et al. The oculomotor-tentorial triangle. Part 1: microsurgical anatomy and techniques to enhance exposure. J Neurosurg. 2019;130:1426–34.
5. Malhotra A, et al. Neuroimaging of Meckel's cave in normal and disease conditions. Insights Imaging. 2018;9:499–510.
6. Zhuang W, et al. Anatomical study of the extraocular check ligament system. J Plast Reconstr Aesthet Surg. 2019;72(12):2017–26.
7. Marom A. A new look at an old canal. Skull Base. 2011;21(1): 53–8.
8. Voirol JR, Vilensky JA. The normal and variant clinical anatomy of the sensory supply of the orbit. Clin Anat. 2014;27:169–75.
9. Wolfram-Gabel R, Kahn JL. Adipose body of the orbit. Clin Anat. 2002;15:186–92.
10. Goh PS, et al. Review of orbital imaging. Eur J Radiol. 2008;66: 387–95.
11. DeLano MC, Fun FY, Zinreich SJ. Relationship of the optic nerve to the posterior paranasal sinuses: a CT anatomic study. AJNR Am J Neuroradiol. 1996;17(4):669–75.

Orbital Fissures

5

Superior Orbital Fissure

Jack Rootman, Daniel B. Rootman, Bruce Stewart, Stefania B. Diniz, Kelsey A. Roelofs, Liza M. Cohen, Claire S. Smith, Ayelet Eran, Ben Kaplan, and Assaf Marom

Contents

1 Introduction 63

2 Figures and Captions 64

References 67

Abstract

The gap between the lesser wing and greater wing is the superior orbital fissure, an elongated comma-shaped opening that tapers laterally with the following borders: medially, the sphenoid body; laterally, the frontal bone; above, the lesser wing of the sphenoid; and below, the medial edge of the orbital surface of the greater wing. This chapter discusses the normal anatomy of the superior orbital fissure and its relation to the orbital vicinity. CT and MRI serve as conjoined modalities for depicting the region of the orbital fissures.

J. Rootman
University of British Columbia, Vancouver, BC, Canada

D. B. Rootman · S. B. Diniz · K. A. Roelofs · C. S. Smith
Division of Orbital and Ophthalmic Plastic Surgery, Stein and Doheny Eye Institutes, University of California, Los Angeles, CA, USA

B. Stewart
BFA Art Center College of Design, UBC Faculty of Medicine, Kelowna, BC, Canada

L. M. Cohen
Division of Orbital and Ophthalmic Plastic Surgery, Stein Eye Institute, University of California, Los Angeles, CA, USA

A. Eran
Neuroradiology Unit, Radiology Department, Rambam Healthcare Medical Center, Haifa, Israel

Department of Anatomy, Rappaport Faculty of Medicine, Technion – Israel Institute of Technology, Haifa, Israel

B. Kaplan · A. Marom (✉)
Department of Anatomy, Rappaport Faculty of Medicine, Technion – Israel Institute of Technology, Haifa, Israel
e-mail: assafma@technion.ac.il

Keywords

Superior orbital fissure · SOF

1 Introduction

The cuboidal body of the sphenoid bone contains two sphenoidal air sinuses, separated by a septum. The jugum sphenoidale is smooth and lies anteriorly and articulates with the ethmoidal cribriform plate. Posteriorly is the sulcus for the optic chiasm, which leads laterally to the optic canals. Posteriorly is the sella turcica that houses the hypophysis gland. It is bounded posteriorly by the dorsum sellae, in the superior border of which are the posterior clinoid processes. The body of the sphenoid bone articulates with the occipital bone and together they form the clivus. The greater wings of the sphenoid project superolaterally from its body. The trapezoid orbital surface of the greater wing faces anteromedially, and forms the posterior part of the lateral orbital wall.

The lesser wings are triangular extensions that project laterally from the anterior part of the body. The superior surface of the lesser wing is smooth and forms part of the cerebral surface that relates to the frontal lobe. The inferior surface forms the posterior part of the orbital roof. The lesser wing is connected to the sphenoid body by two roots: a thin anterior root and a thick (triangular) posterior root – the interval between which is the optic canal that houses the optic nerve, its dural sleeve, and the ophthalmic artery.

The gap between the lesser wing and greater wing is the superior orbital fissure, an elongated comma-shaped opening that tapers laterally with the following borders: medially, the

© Springer Nature Switzerland AG 2022
G. Ben Simon et al. (eds.), *Atlas of Orbital Imaging*,
https://doi.org/10.1007/978-3-030-62426-2_5

sphenoid body; laterally, the frontal bone; above, the lesser wing of the sphenoid; and below, the medial edge of the orbital surface of the greater wing. The superior orbital fissure connects the endocranial cavity with the orbital cavity, and transmits the superior and inferior divisions of cranial nerve III (oculomotor); cranial nerve IV (trochlear); several branches of cranial nerve V_1 (ophthalmic nerve): the lacrimal, frontal, and nasociliary nerves; the recurrent meningeal artery; and the superior ophthalmic vein. The lateral and inferior parts of the common tendinous ring divide the superior orbital fissure (and bridges the inferior orbital fissure) such that two compartments are formed: a medial one that contains vessels that pass through the superior orbital fissure and the common tendinous ring, and a lateral one that transmits vessels lateral to the common tendinous ring.

2 Figures and Captions

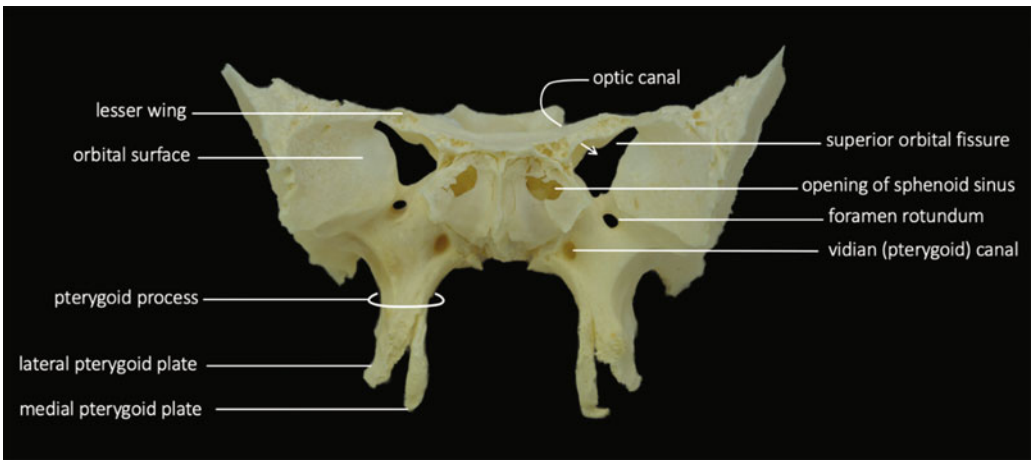


Fig. 1 Anterior view of the sphenoid bone

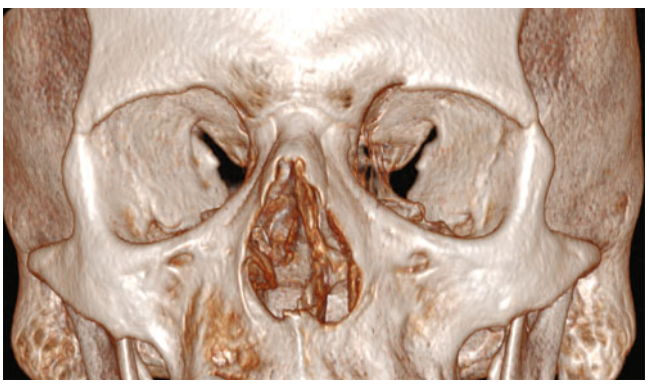


Fig. 2 3D volume rendering of the skull demonstrating the oblique fashion of the SOF

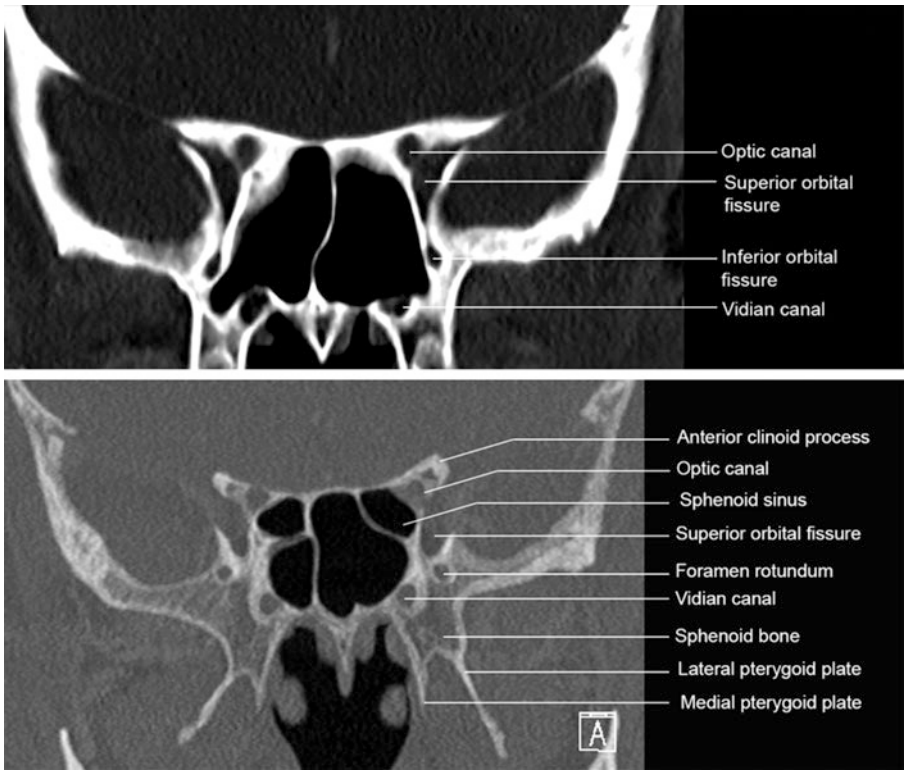


Fig. 3 CT scan, bone window, coronal sections through the superior orbital fissure (SOF)

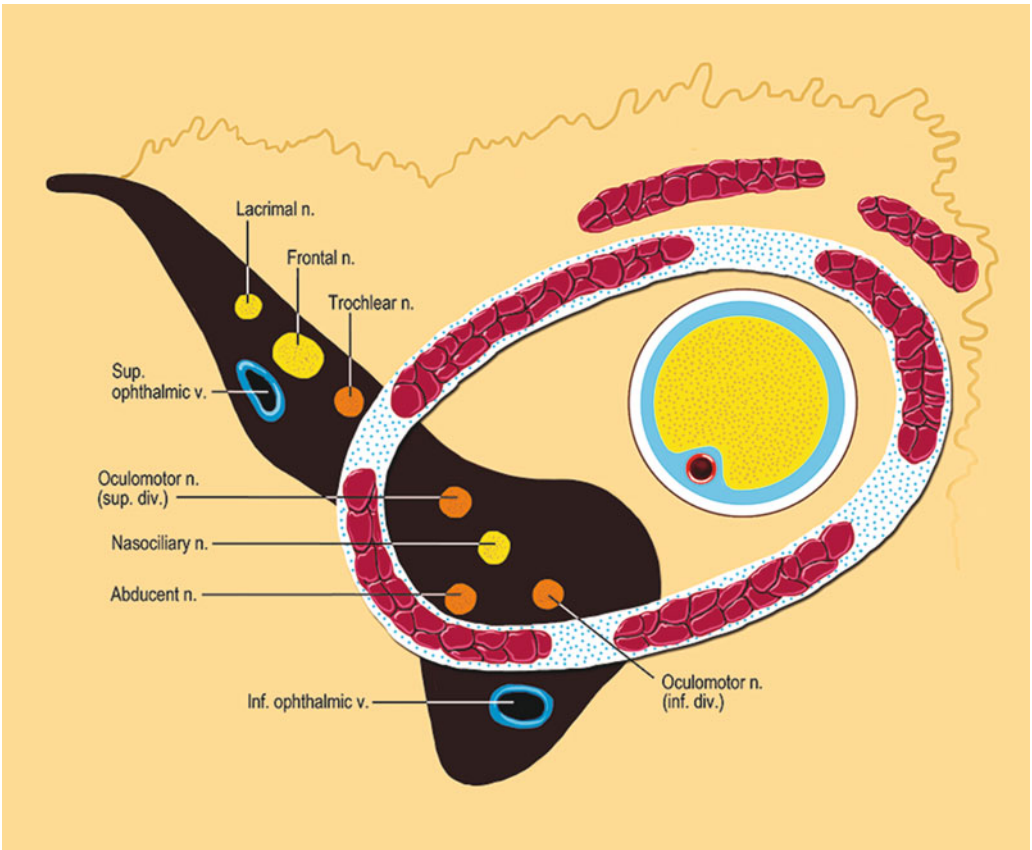


Fig. 4 Diagram of the superior orbital fissure and annulus and relationships to the neurovascular structures

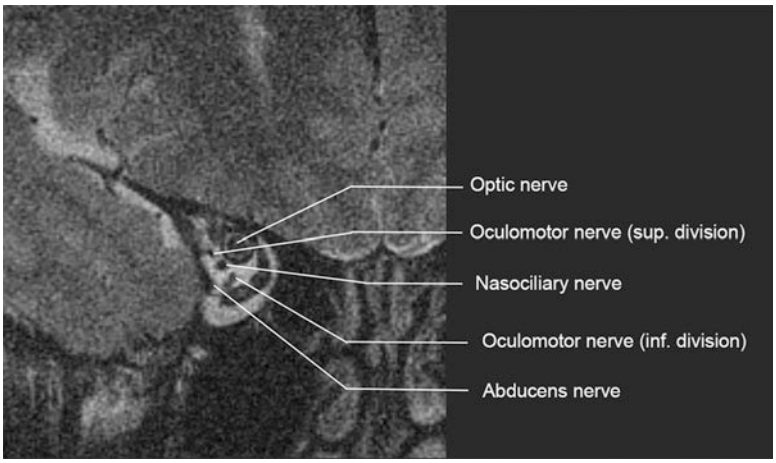


Fig. 5 Coronal T2WI non-FS MR demonstrating the contents of the SOF and their relation to the optic nerve



Fig. 6 CT scan, axial view, bone window, through the SOF

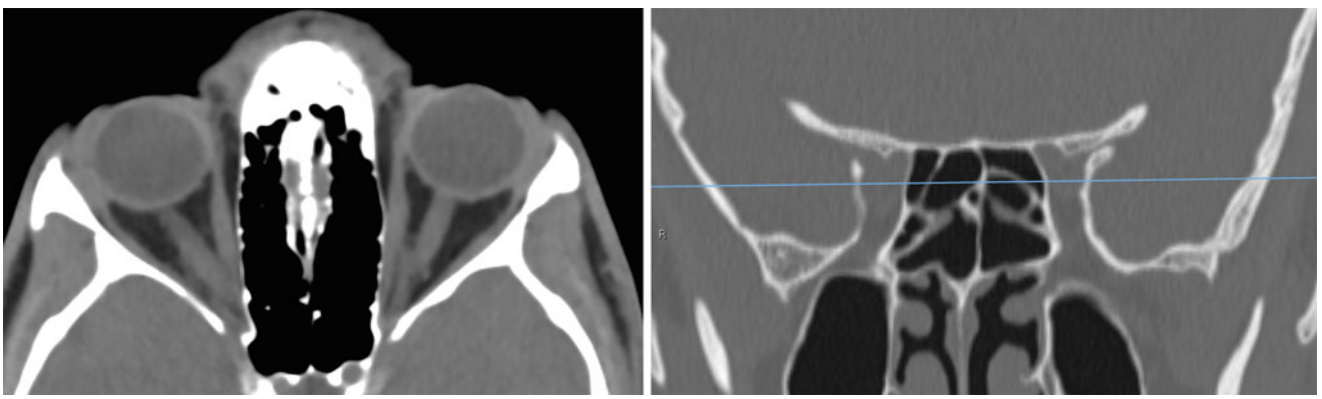


Fig. 7 CT scan axial view (*left*), with corresponding coronal view (*right*), through the SOF, at a lower level in comparison with Fig. 6. The blue line is the reference line for the axial section



Fig. 8 Consecutive axial T1-weighted images through the SOF (*arrows*), the fissure is mainly depicted by the bright fatty content

References

1. Gray H, Standring S, Ellis H, Berkovitz BKB. Gray's anatomy: the anatomical basis of clinical practice. 39th ed. Edinburgh/New York: Elsevier Churchill Livingstone; 2005.
2. Most SP, Mobley SR, Larrabee WF. Anatomy of the eyelids. Facial Plast Surg Clin North Am. 2005;13:487–92.
3. Sicher H, DuBrul EL. Oral anatomy. 6th ed. Saint Louis: The CV Mosby; 1975.
4. Kanagalingam S, Miller NR. Horner syndrome: clinical perspectives. Eye Brain. 2015;7:35–46.
5. Meybodi AT, et al. The oculomotor-tentorial triangle. Part 1: microsurgical anatomy and techniques to enhance exposure. J Neurosurg. 2019;130:1426–34.
6. Malhotra A, et al. Neuroimaging of Meckel's cave in normal and disease conditions. Insights Imaging. 2018;9:499–510.
7. Zhuang W, et al. Anatomical study of the extraocular check ligament system. J Plast Reconstr Aesthet Surg. 2019;72(12):2017–26.
8. Marom A. A new look at an old canal. Skull Base. 2011;21(1):53–8.
9. Voirol JR, Vilensky JA. The normal and variant clinical anatomy of the sensory supply of the orbit. Clin Anat. 2014;27:169–75.
10. Wolfram-Gabel R, Kahn JL. Adipose body of the orbit. Clin Anat. 2002;15:186–92.
11. Goh PS, et al. Review of orbital imaging. Eur J Radiol. 2008;66:387–95.

Orbital Fissures: Inferior Orbital Fissure

6

Jack Rootman, Daniel B. Rootman, Bruce Stewart, Stefania B. Diniz, Kelsey A. Roelofs, Liza M. Cohen, Claire S. Smith, Ayelet Eran, Ben Kaplan, and Assaf Marom

Contents

1 **Introduction** 69

2 **Figures and Captions** 70

References 74

Abstract

The inferior orbital fissure is an elongated opening between the orbital floor and lateral wall that projects and widens anterolaterally. Its borders are as follows: above, the orbital surface of the sphenoid bone, below, the maxilla (anteriorly) and the orbital process of the palatine (posteriorly), and laterally, the zygomatic bone and zygomaticomaxillary suture. The maxilla and sphenoid may join anteriorly to exclude the zygomatic bone from the borders of the fissure.

Keywords

Inferior orbital fissure · Infratemporal fossa · Pterygopalatine fossa · Maxillary nerve (V2)

1 Introduction

The inferior orbital fissure establishes the communication between the orbital cavity and the pterygopalatine and infratemporal fossae, and houses the zygomatic and infraorbital branches of cranial nerve V_2 (maxillary nerve), and the inferior ophthalmic vein and its connection to the pterygoid venous plexus. In addition, the inferior orbital fissure is bridged by the orbitalis muscle, a minor smooth muscle that is innervated by the autonomic nervous system (i.e., by the superior cervical ganglion via the carotid sympathetic plexus). This muscle may produce some elevation and protrusion of the eyeball.

J. Rootman
University of British Columbia, Vancouver, BC, Canada

D. B. Rootman · S. B. Diniz · K. A. Roelofs · C. S. Smith
Division of Orbital and Ophthalmic Plastic Surgery, Stein and Doheny Eye Institutes, University of California, Los Angeles, CA, USA

B. Stewart
BFA Art Center College of Design, UBC Faculty of Medicine, Kelowna, BC, Canada

L. M. Cohen
Division of Orbital and Ophthalmic Plastic Surgery, Stein Eye Institute, University of California, Los Angeles, CA, USA

A. Eran
Neuroradiology Unit, Radiology Department, Rambam Healthcare Medical Center, Haifa, Israel

Department of Anatomy, Rappaport Faculty of Medicine, Technion – Israel Institute of Technology, Haifa, Israel

B. Kaplan · A. Marom (✉)
Department of Anatomy, Rappaport Faculty of Medicine, Technion – Israel Institute of Technology, Haifa, Israel
e-mail: assafma@technion.ac.il

© Springer Nature Switzerland AG 2022
G. Ben Simon et al. (eds.), *Atlas of Orbital Imaging*,
https://doi.org/10.1007/978-3-030-62426-2_91

2 Figures and Captions

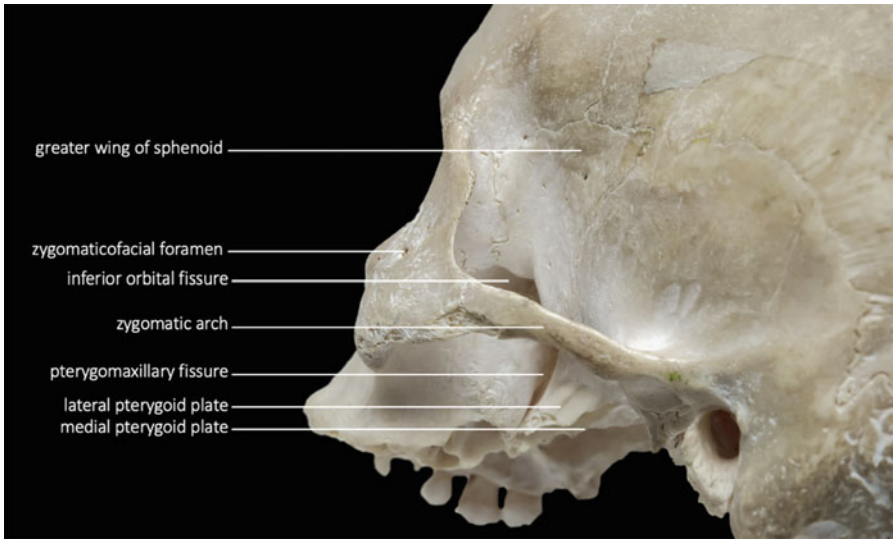


Fig. 1 Posterior view of the lateral orbital wall and temporal fossa

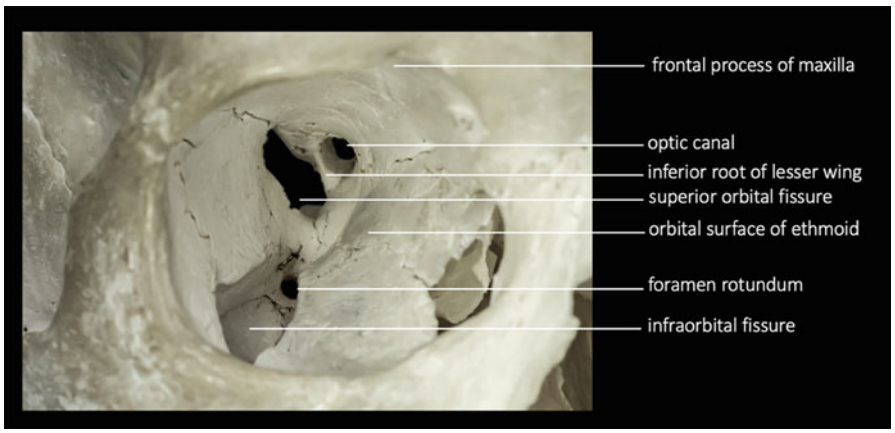


Fig. 2 Main orbital foramina, right orbit

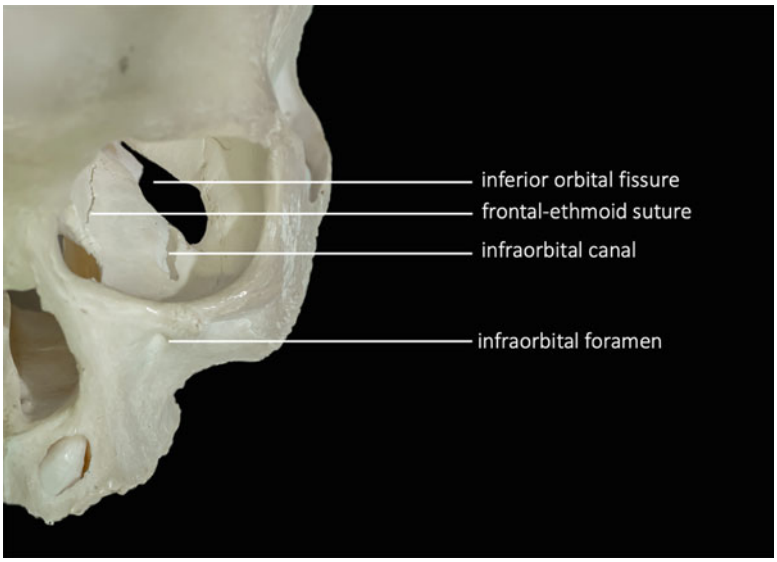


Fig. 3 The orbital floor and inferior orbital fissure, left orbit

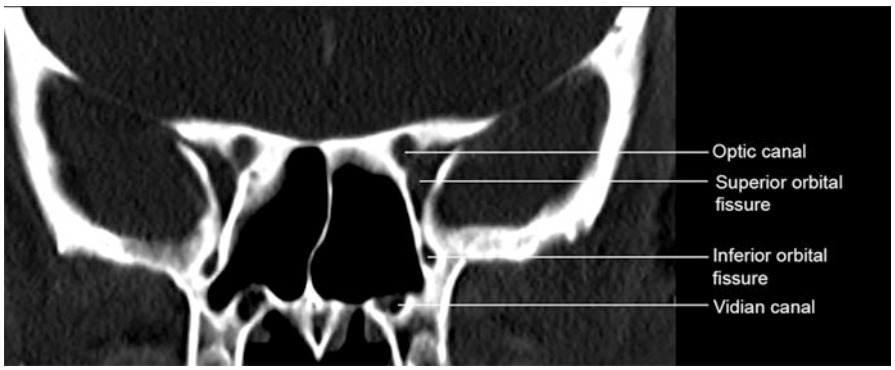


Fig. 4 CT coronal section demonstrating the relations between the optic canal, and superior and inferior orbital fissures

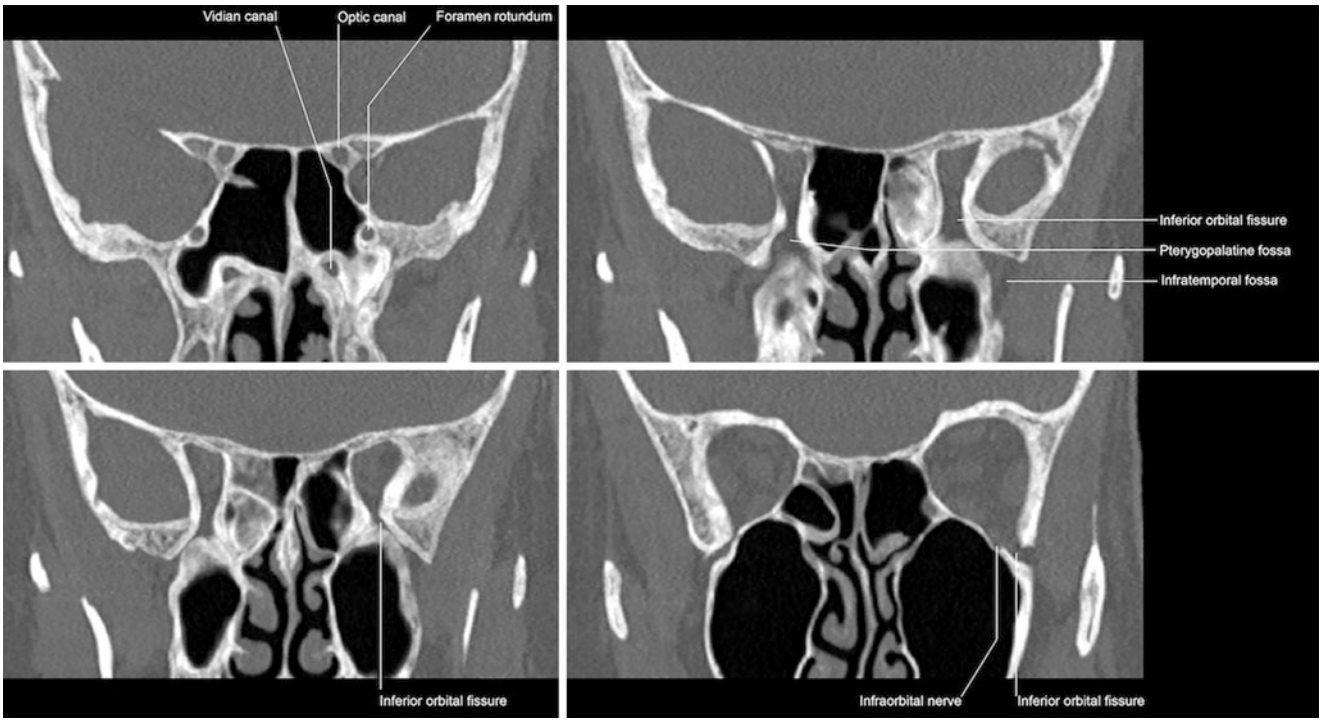


Fig. 5 Sequential CT scans, coronal view, bone window showing the extent of the fissure from posterior to anterior orbit (*left upper* ➔ *right upper*➔ *left lower* ➔ *right lower*)

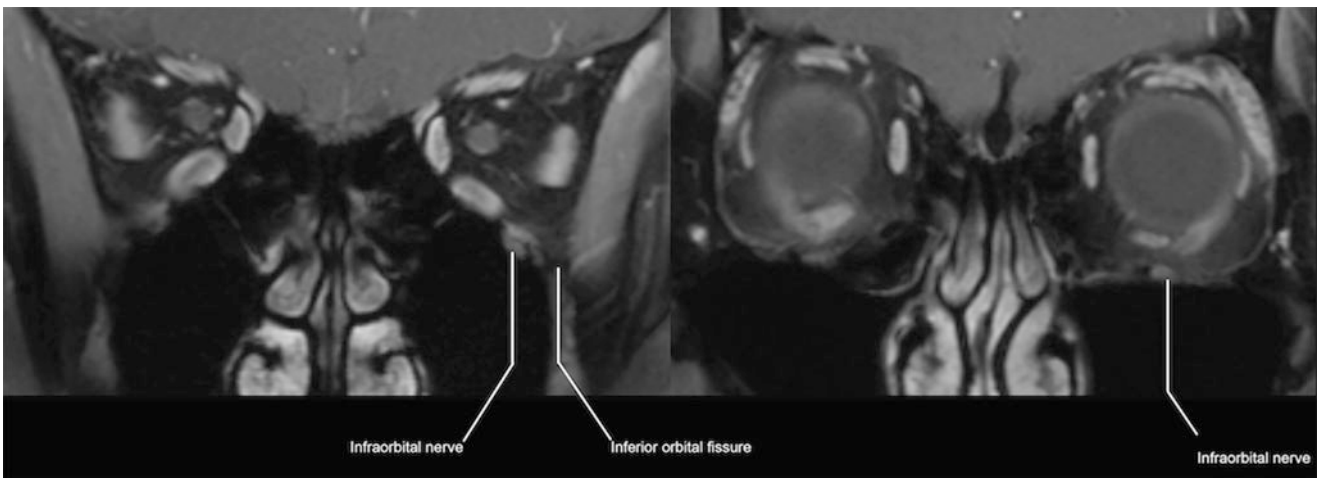


Fig. 6 Sequential MR scans, coronal view, T1WI FS CE showing the relation of the infraorbital nerve canal and the IOF

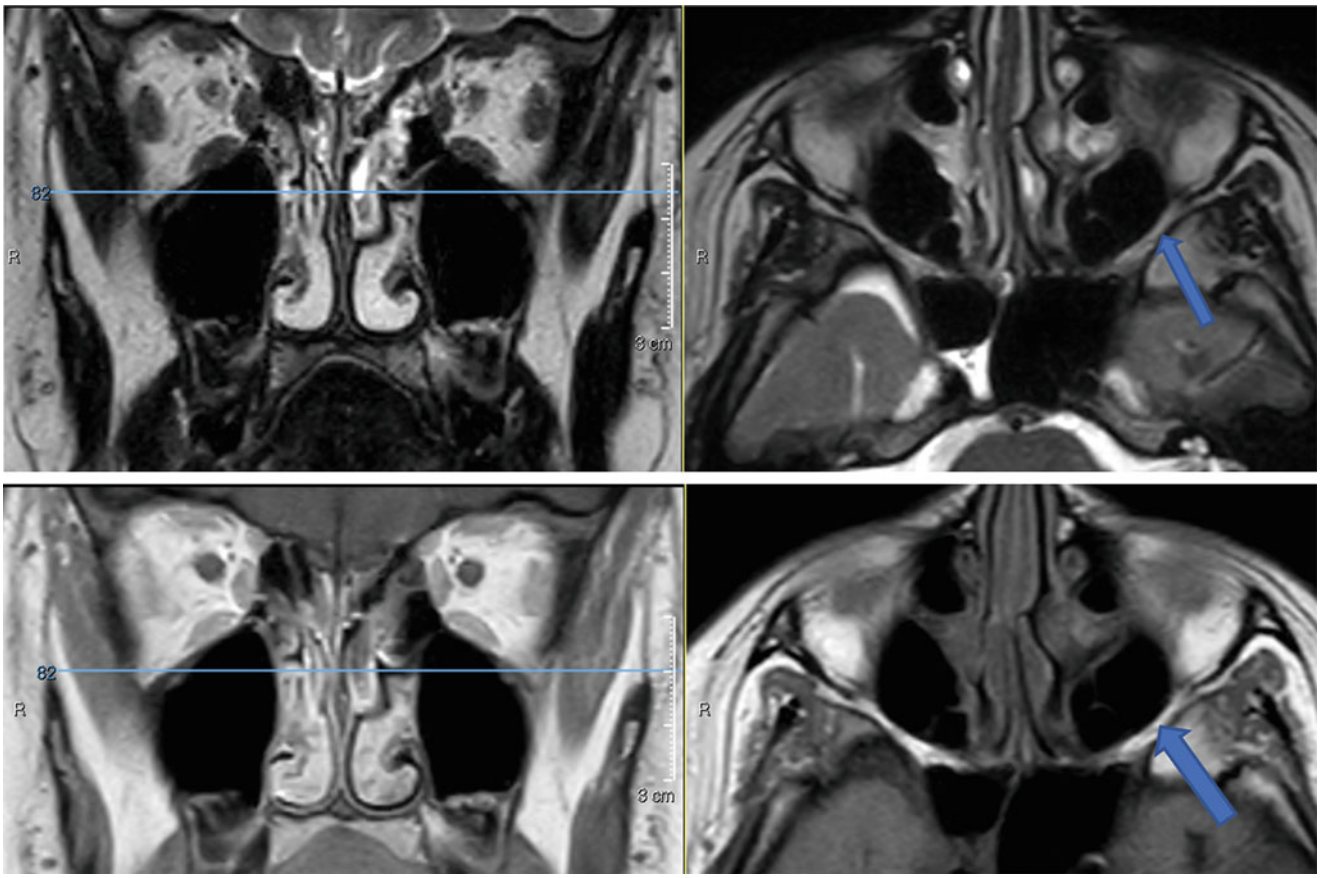


Fig. 7 Axial and coronal MR images through the IOF (*upper* T2W, *lower* T1W scans). The reference line corresponds to the lower aspect of the inferior orbital fissure on both sequences (arrows)

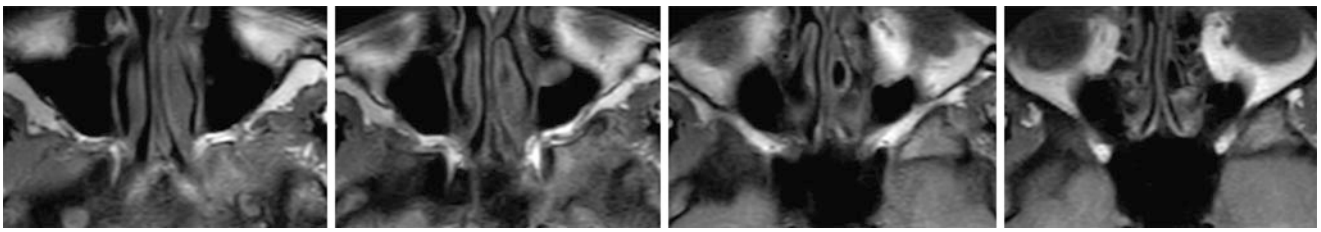


Fig. 8 Sequential axial T1 images through the IOF (*left* to *right* from lower to upper)

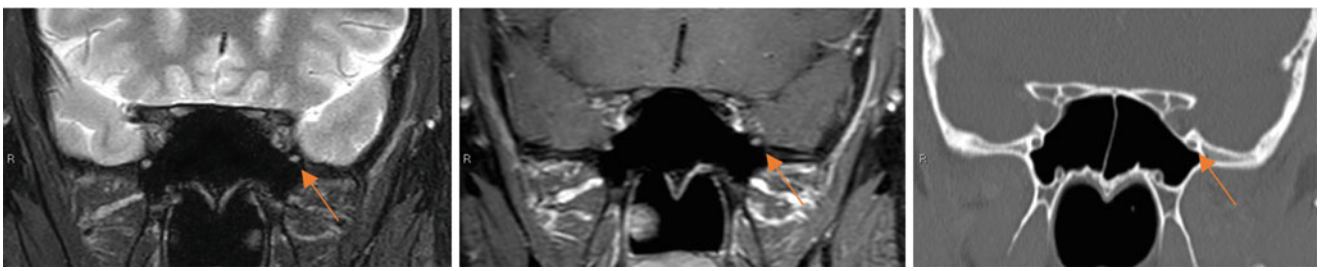


Fig. 9 Coronal views of foramen rotundum on both modalities (l*eft* – Cor T2 FS, *middle* – Cor T1 FS post-contrast, *right* – Cor CT reformat)

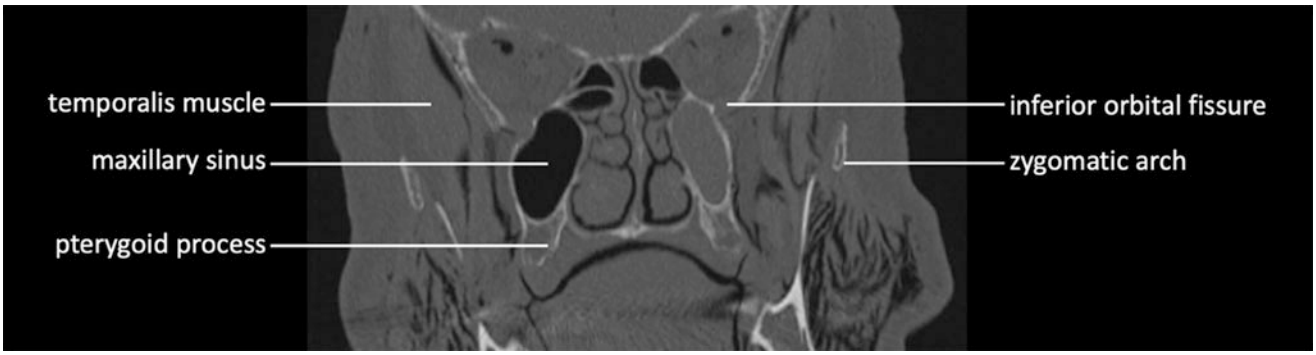


Fig. 10 Postmortem HRCT scan, coronal section through the inferior orbital fissure

References

1. Gray H, Standring S, Ellis H, Berkovitz BKB. Gray's anatomy: the anatomical basis of clinical practice. 39th ed. Edinburgh/New York: Elsevier Churchill Livingstone; 2005.
2. Most SP, Mobley SR, Larrabee WF. Anatomy of the eyelids. Facial Plast Surg Clin North Am. 2005;13:487–92.
3. Sicher H, DuBrul EL. Oral anatomy. 6th ed. Saint Louis: The CV Mosby; 1975.
4. Kanagalingam S, Miller NR. Horner syndrome: clinical perspectives. Eye Brain. 2015;7:35–46.
5. Meybodi AT, et al. The oculomotor-tentorial triangle. Part 1: microsurgical anatomy and techniques to enhance exposure. J Neurosurg. 2019;130:1426–34.
6. Malhotra A, et al. Neuroimaging of Meckel's cave in normal and disease conditions. Insights Imaging. 2018;9:499–510.
7. Zhuang W, et al. Anatomical study of the extraocular check ligament system. J Plast Reconstr Aesthet Surg. 2019;72(12): 2017–26.
8. Marom A. A new look at an old canal. Skull Base. 2011;21(1): 53–8.
9. Voirol JR, Vilensky JA. The normal and variant clinical anatomy of the sensory supply of the orbit. Clin Anat. 2014;27: 169–75.
10. Wolfram-Gabel R, Kahn JL. Adipose body of the orbit. Clin Anat. 2002;15:186–92.
11. Goh PS, et al. Review of orbital imaging. Eur J Radiol. 2008;66: 387–95.

Orbital Fissures: Pterygopalatine Fossa

7

Jack Rootman, Daniel B. Rootman, Bruce Stewart, Stefania B. Diniz, Kelsey A. Roelofs, Liza M. Cohen, Claire S. Smith, Ayelet Eran, Ben Kaplan, and Assaf Marom

Contents

1 **Introduction** 75
2 **Figures and Captions** 76
References 78

Abstract

The pterygopalatine fossa is a small gap below the orbital apex, with the following boundaries:

- Posteriorly, the pterygoid process and greater wing of the sphenoid bone.
- Anteriorly, the infratemporal surface of the maxilla.
- Medially, the orbital process of the palatine bone and its perpendicular plate.
- Laterally, the pterygopalatine fossa communicates with the pterygomaxillary fissure which is situated between the posterior surface of the maxilla and the pterygoid process.

The pterygopalatine fossa communicates with other cranial cavities, as follows:

- With the orbital cavity, via the medial end of the inferior orbital fissure.
- With the nasal cavity, via the sphenopalatine foramen.
- With the infratemporal fossa, via the pterygomaxillary fissure.

Keywords

Pterygopalatine fossa · Pterygomaxillary fissure · Infratemporal fossa · Inferior orbital fissure

1 Introduction

In the posterior wall of the pterygopalatine fossa there are two openings into the middle cranial fossa: the foramen rotundum (which transmits the maxillary nerve) and the vidian (pterygoid) canal (which transmits the nerve of the pterygoid canal).

The main contents of the pterygopalatine fossa are the maxillary division of the trigeminal nerve (V_2), the pterygopalatine ganglion – the largest of the autonomic (parasympathetic) ganglia – and the terminal part of the maxillary artery.

The purely sensory maxillary nerve exits the middle cranial fossa via the foramen rotundum. It gives rise to two ganglionic branches that passively pass through the

J. Rootman
University of British Columbia, Vancouver, BC, Canada

D. B. Rootman · S. B. Diniz · K. A. Roelofs · C. S. Smith
Division of Orbital and Ophthalmic Plastic Surgery, Stein and Doheny Eye Institutes, University of California, Los Angeles, CA, USA

B. Stewart
BFA Art Center College of Design, UBC Faculty of Medicine, Kelowna, BC, Canada

L. M. Cohen
Division of Orbital and Ophthalmic Plastic Surgery, Stein Eye Institute, University of California, Los Angeles, CA, USA

A. Eran
Neuroradiology Unit, Radiology Department, Rambam Healthcare Medical Center, Haifa, Israel

Department of Anatomy, Rappaport Faculty of Medicine, Technion – Israel Institute of Technology, Haifa, Israel

B. Kaplan · A. Marom (✉)
Department of Anatomy, Rappaport Faculty of Medicine, Technion – Israel Institute of Technology, Haifa, Israel
e-mail: assafma@technion.ac.il

© Springer Nature Switzerland AG 2022
G. Ben Simon et al. (eds.), *Atlas of Orbital Imaging*,
https://doi.org/10.1007/978-3-030-62426-2_92

pterygopalatine ganglion, and then turns laterally on the posterior surface of the maxilla (and external to the orbital periosteum), where the zygomatic and superior alveolar branches exit its trunk. Subsequently, it turns medially to enter the infraorbital canal as the infraorbital nerve.

The pterygopalatine ganglion is morphologically but not functionally connected to the maxillary nerve, since these sensory connections do not synapse in the ganglion. This ganglion is the synapse site for preganglionic parasympathetic fibers (axons) that travel through the greater petrosal nerve. When the latter is joined by the deep petrosal nerve (which carries postganglionic sympathetic axons from the carotid plexus), the nerve of the pterygoid canal (vidian nerve) is formed. Sensory fibers leave the ganglion without synapsing via its orbital, nasopalatine, palatine (greater and lesser palatine nerves), and pharyngeal branches.

The maxillary artery travels through the infratemporal fossa, and then into the pterygomaxillary fissure to enter the pterygopalatine fossa. Here it gives off several branches: the posterior superior alveolar artery; the infraorbital artery that runs in the infraorbital groove of the orbital floor, supplies part of the maxillary sinus and surfaces in the face via the infraorbital foramen; the vidian artery; pharyngeal and palatine branches; and the sphenopalatine artery that enters the nasal cavity posterior to the superior meatus.

2 Figures and Captions

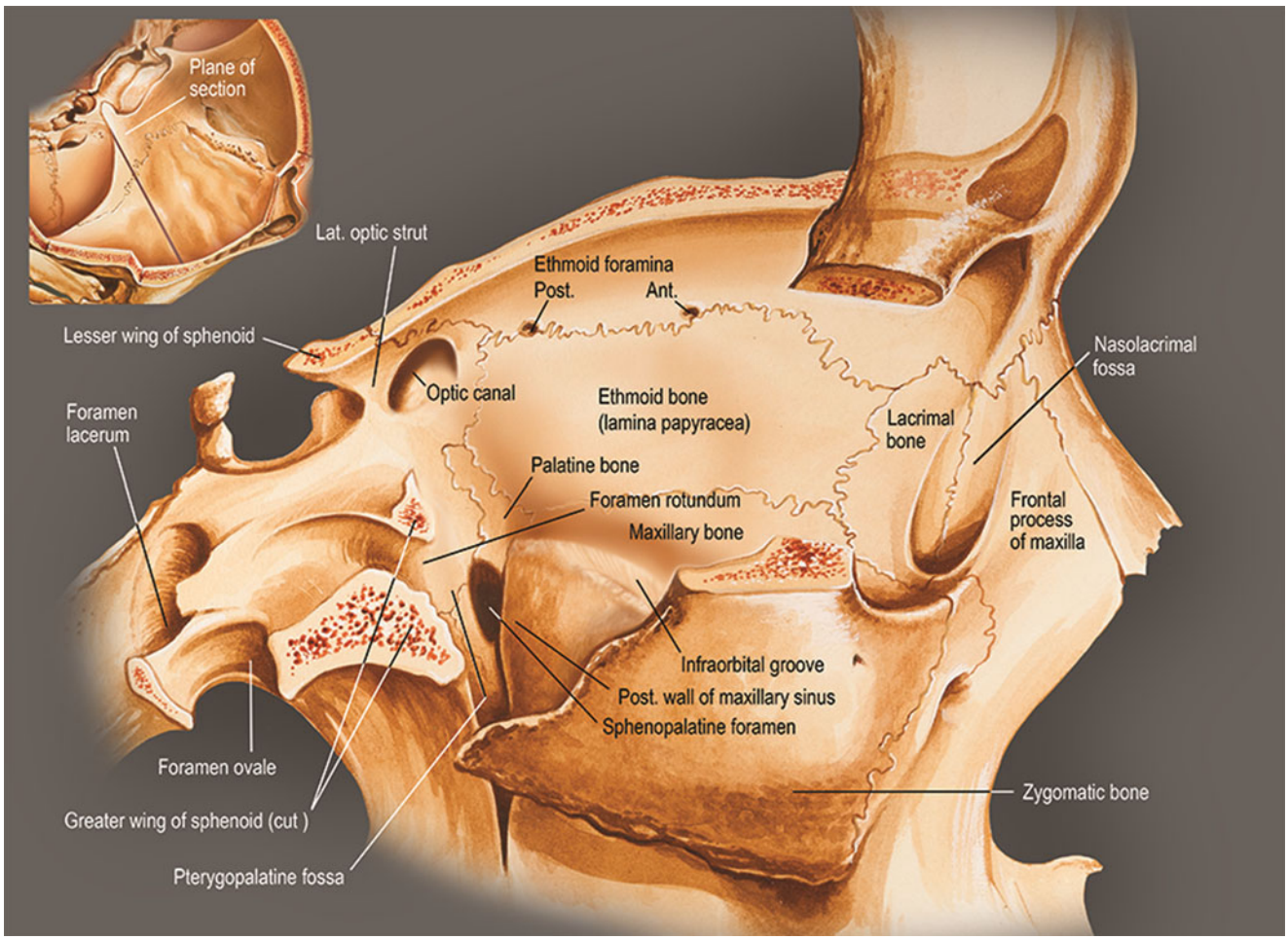


Fig. 1 Direct lateral view of the medial wall of the orbit with excision of part of the zygomaticofrontal process, the wing of the zygoma, the root of the greater wing of sphenoid, and the orbital roof. The pterygopalatine fossa is exposed

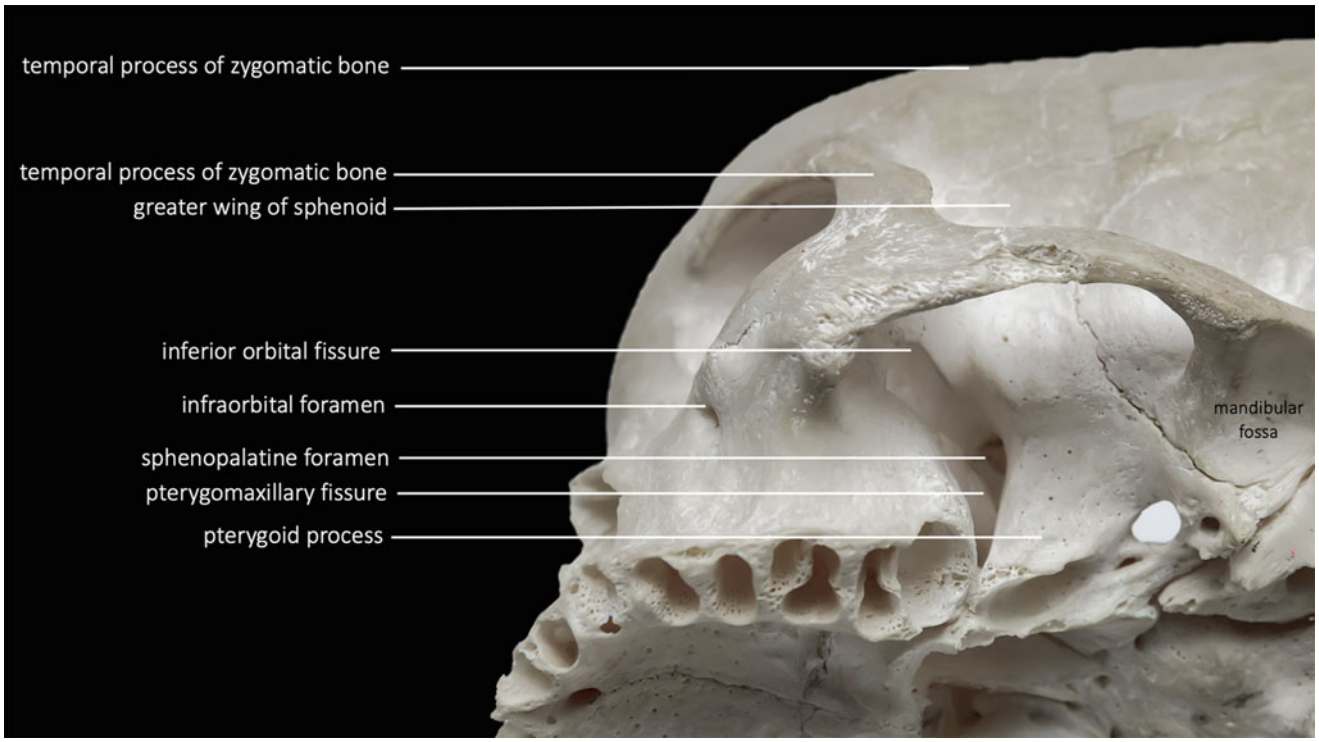


Fig. 2 Inferior view of the infratemporal and pterygopalatine fossae

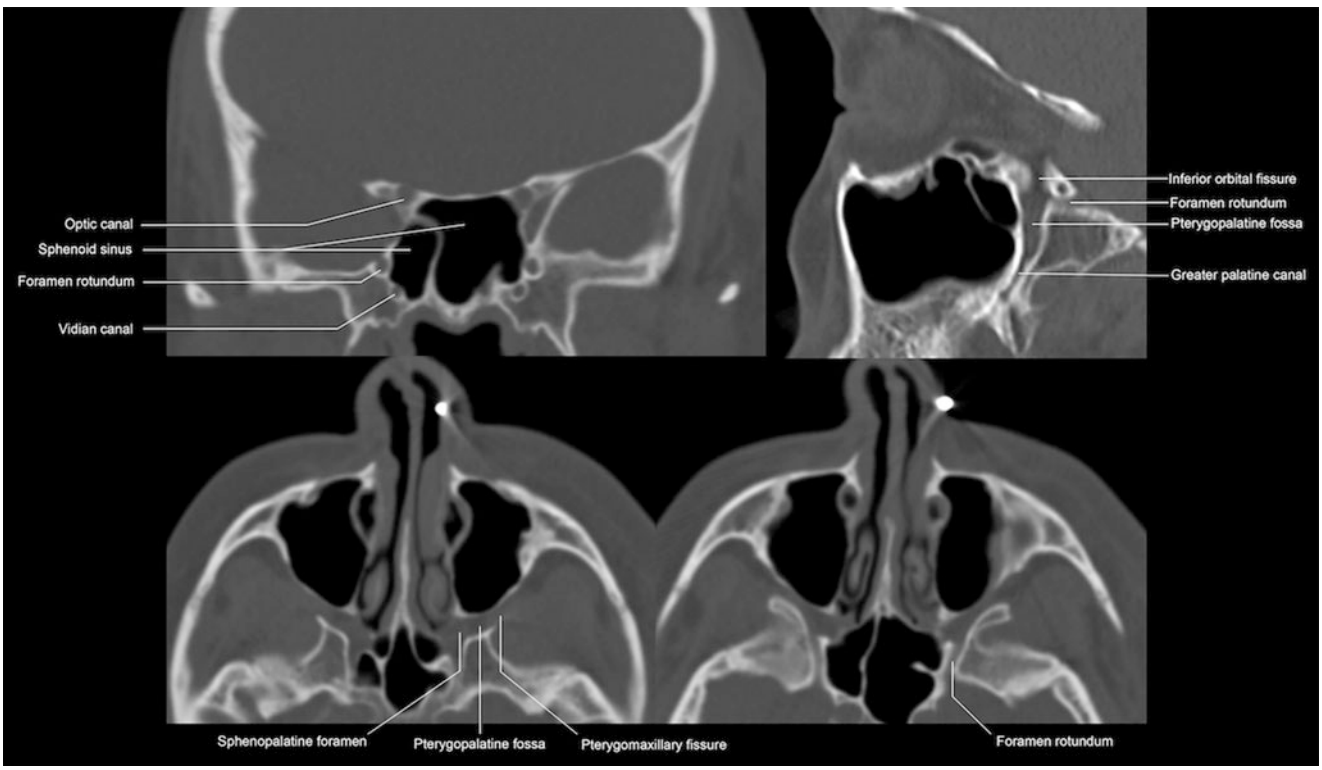


Fig. 3 CT images, bone window, demonstrating the relations between the fissures at the orbital apex



Fig. 4 The PPF and related openings, PPF – pterygopalatine fossa, SPF – sphenopalatine foramen, FR – foramen rotundum, and PMF – pterygomaxillary fissure

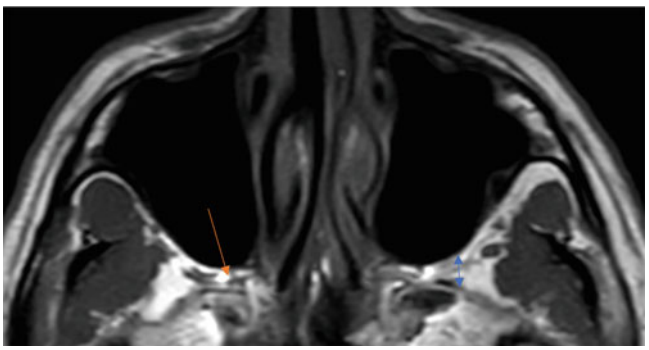


Fig. 5 Ax T1W scan at the level of the pterygopalatine fossa, demonstrating the fatty content and traversing vessels in the right PPF (*orange arrow*). The left pterygomaxillary fissure opening is depicted by the double blue arrow

References

1. Gray H, Standring S, Ellis H, Berkovitz BKB. Gray's anatomy: the anatomical basis of clinical practice. 39th ed. Edinburgh/New York: Elsevier Churchill Livingstone; 2005.
2. Most SP, Mobley SR, Larrabee WF. Anatomy of the eyelids. Facial Plast Surg Clin North Am. 2005;13:487–92.
3. Sicher H, DuBrul EL. Oral anatomy. 6th ed. Saint Louis: The CV Mosby; 1975.
4. Kanagalingam S, Miller NR. Horner syndrome: clinical perspectives. Eye Brain. 2015;7:35–46.
5. Meybodi AT, et al. The oculomotor-tentorial triangle. Part 1: microsurgical anatomy and techniques to enhance exposure. J Neurosurg. 2019;130:1426–34.
6. Malhotra A, et al. Neuroimaging of Meckel's cave in normal and disease conditions. Insights Imaging. 2018;9:499–510.
7. Zhuang W, et al. Anatomical study of the extraocular check ligament system. J Plast Reconstr Aesthet Surg. 2019;72(12): 2017–26.
8. Marom A. A new look at an old canal. Skull Base. 2011;21(1): 53–8.
9. Voirol JR, Vilensky JA. The normal and variant clinical anatomy of the sensory supply of the orbit. Clin Anat. 2014;27: 169–75.
10. Wolfram-Gabel R, Kahn JL. Adipose body of the orbit. Clin Anat. 2002;15:186–92.
11. Goh PS, et al. Review of orbital imaging. Eur J Radiol. 2008;66: 387–95.

Orbital Fissures: Infratemporal Fossa

8

Jack Rootman, Daniel B. Rootman, Bruce Stewart, Stefania B. Diniz, Kelsey A. Roelofs, Liza M. Cohen, Claire S. Smith, Ayelet Eran, Ben Kaplan, and Assaf Marom

Contents

1 Introduction 79

2 Figures and Captions 80

References 84

Abstract

The infratemporal fossa is a space located medial to the zygomatic bone and zygomatic arch. It communicates with the temporal fossa and with the pterygopalatine fossa via the pterygomaxillary fissure. The boundaries of the infratemporal fossa are as follows:

- Superiorly, the infratemporal aspect of the sphenoidal greater wing
- Laterally, the mandibular ramus
- Medially, the lateral surface of the lateral pterygoid plate (that serves as the origin for the lateral pterygoid muscle)
- The fossa has no anatomical floor

Some refer to the temporal fossa as the suprazygomatic infratemporal fossa.

Both CT and MRI are complementary in the assessment of the infratemporal fossa. CT provides superb bony detail and serves well in trauma and infectious/inflammatory processes; however, MR surpasses CT in delineating soft tissue masses, as well as in perineural and bone marrow assessment.

Keywords

Infratemporal fossa · ITF · Lateral pterygoid muscle (LPM) · Medial pterygoid muscle (MPM) · Temporal fossa

1 Introduction

The major anatomical structures included in this space are the medial and lateral pterygoid muscles, the maxillary artery and pterygoid venous plexus, the mandibular (V_3) division of the trigeminal nerve, the otic (parasympathetic) ganglion, and the chorda tympani branch of the facial nerve.

J. Rootman
University of British Columbia, Vancouver, BC, Canada

D. B. Rootman · S. B. Diniz · K. A. Roelofs · C. S. Smith
Division of Orbital and Ophthalmic Plastic Surgery, Stein and Doheny Eye Institutes, University of California, Los Angeles, CA, USA

B. Stewart
BFA Art Center College of Design, UBC Faculty of Medicine, Kelowna, BC, Canada

L. M. Cohen
Division of Orbital and Ophthalmic Plastic Surgery, Stein Eye Institute, University of California, Los Angeles, CA, USA

A. Eran
Neuroradiology Unit, Radiology Department, Rambam Healthcare Medical Center, Haifa, Israel

Department of Anatomy, Rappaport Faculty of Medicine, Technion – Israel Institute of Technology, Haifa, Israel

B. Kaplan · A. Marom (✉)
Department of Anatomy, Rappaport Faculty of Medicine, Technion – Israel Institute of Technology, Haifa, Israel
e-mail: assafma@technion.ac.il

© Springer Nature Switzerland AG 2022
G. Ben Simon et al. (eds.), *Atlas of Orbital Imaging*,
https://doi.org/10.1007/978-3-030-62426-2_93

A key structure in this fossa is the lateral pterygoid muscle, the prime mover for jaw opening. This muscle is comprised of a superior and an inferior head, fibers of which originate from the lateral surface of the lateral pterygoid plate and run anteroposteriorly on a horizontal plane. While the main divisions of the mandibular nerve (the anterior division, which is mostly motor for the muscles of mastication, and the posterior division which is mostly sensory) and origin of the medial pterygoid muscle are deep, the maxillary artery is superficial. The maxillary artery is a terminal branch of the external carotid artery that arises behind the neck of the mandibular condyle that passes anteriorly into the infratemporal fossa to enter the pterygomaxillary fissure and subsequently into the pterygopalatine fossa. The artery commonly passes lateral to the inferior alveolar and lingual branches of the mandibular nerve.

A pterygoid venous network lies around the lateral pterygoid muscle and between its heads. This venous plexus receives contributions from the sphenopalatine, deep temporal, pterygoid, masseteric, buccal, alveolar, palatine, and inferior ophthalmic veins. It communicates with the facial vein through the deep facial vein, and with the cavernous sinus through veins that pass through the foramen ovale and foramen lacerum at the floor of the carotid canal.

In addition to the medial and lateral pterygoid muscles, the infratemporal fossa also includes the temporalis muscle tendon, which attaches to the coronoid process of the mandibular ramus.

2 Figures and Captions

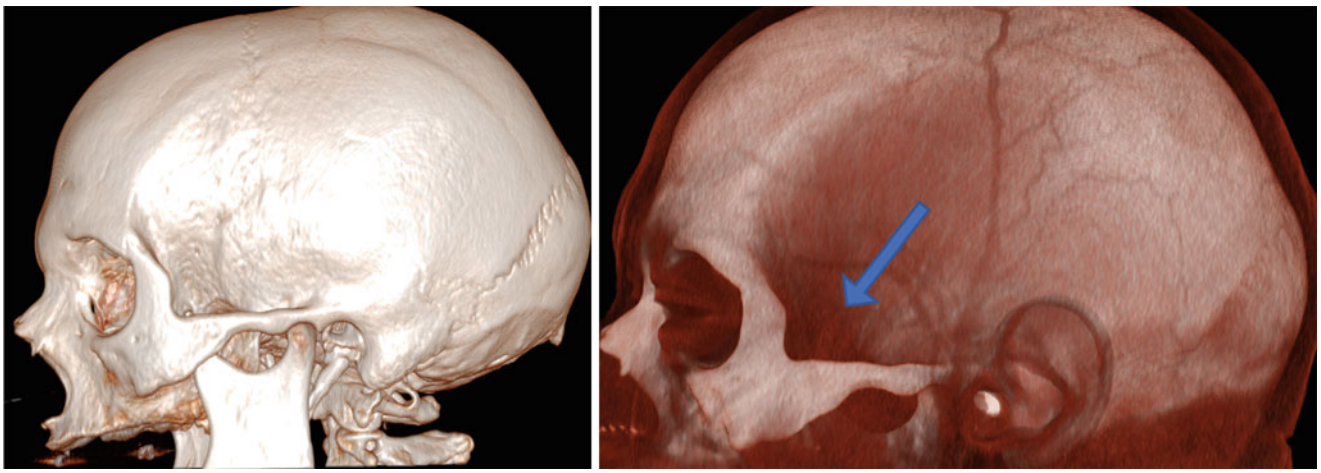


Fig. 1 3D CT volume rendering (bone – *left*, bone and soft tissue – *right*). The arrow pointing at the anatomical infratemporal fossa

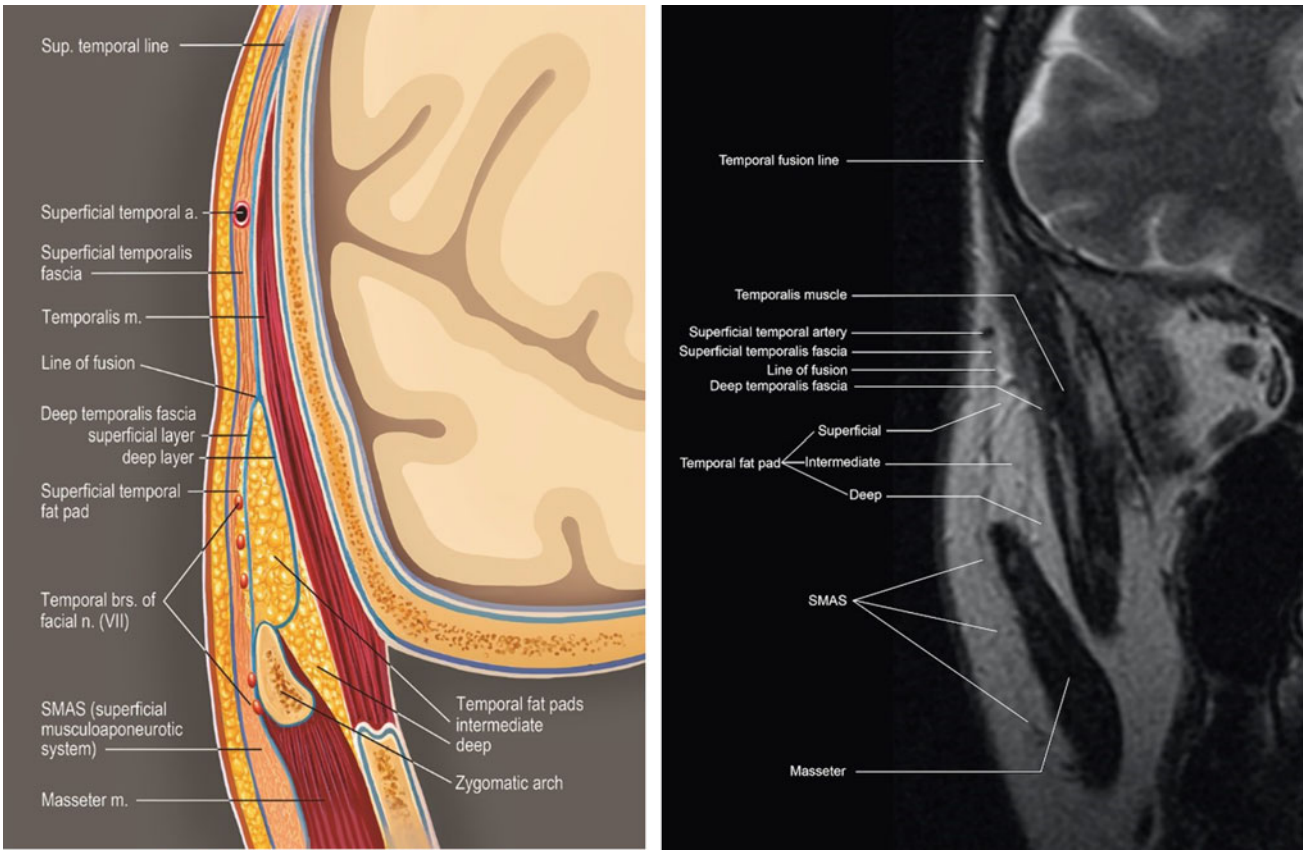


Fig. 2 Coronal cross-section of temporalis fascia and zygomatic arch. Drawing (*left*), MRI T2WI (*right*)

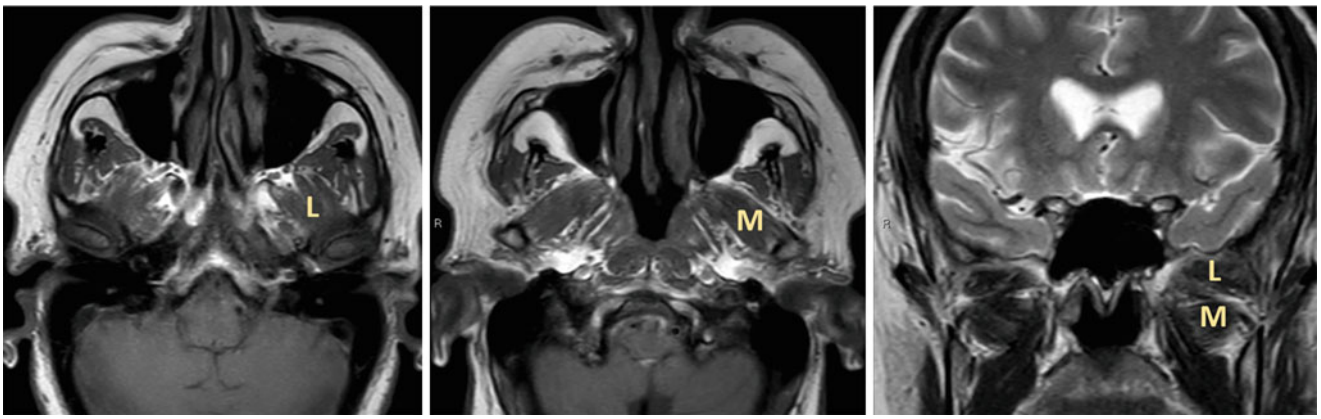


Fig. 3 MR views of the Infratemporal fossa. Axial T1W (*left*) and T2W (*middle*) images, and a corresponding Cor T2W scan, demonstrating the orientation of the lateral (L) and medial (M) pterygoid muscles

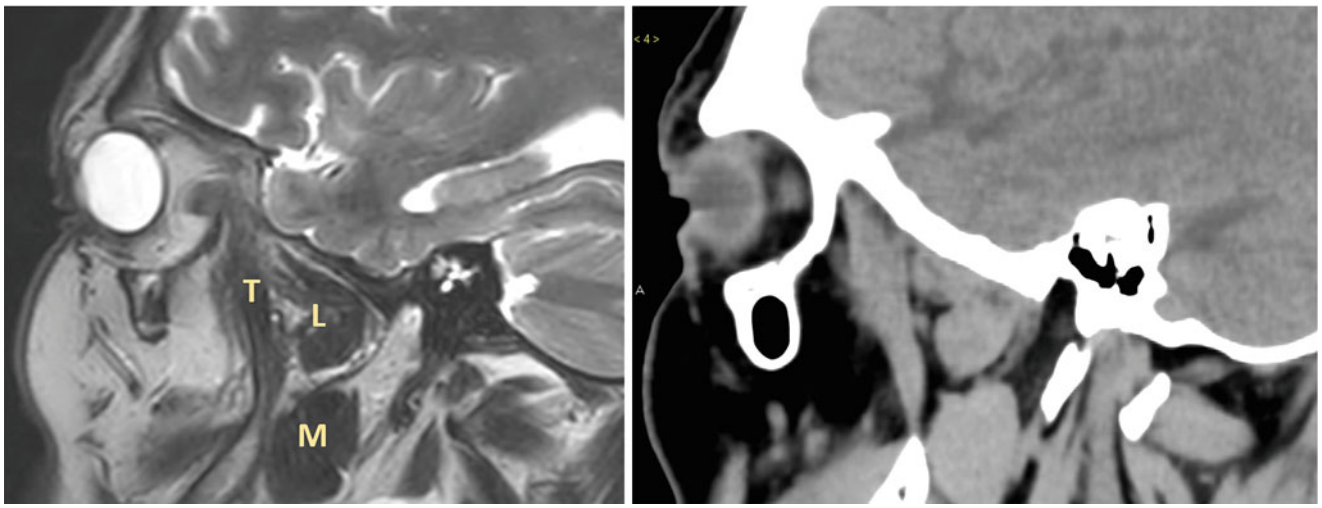


Fig. 4 Lateral views of the ITF, Sag T2W (*left*), and an equivalent Sag CT reformat (*right*) of the same patient, portraying the location of the LPM (L), MPM (M), and temporalis muscle tendon (T)

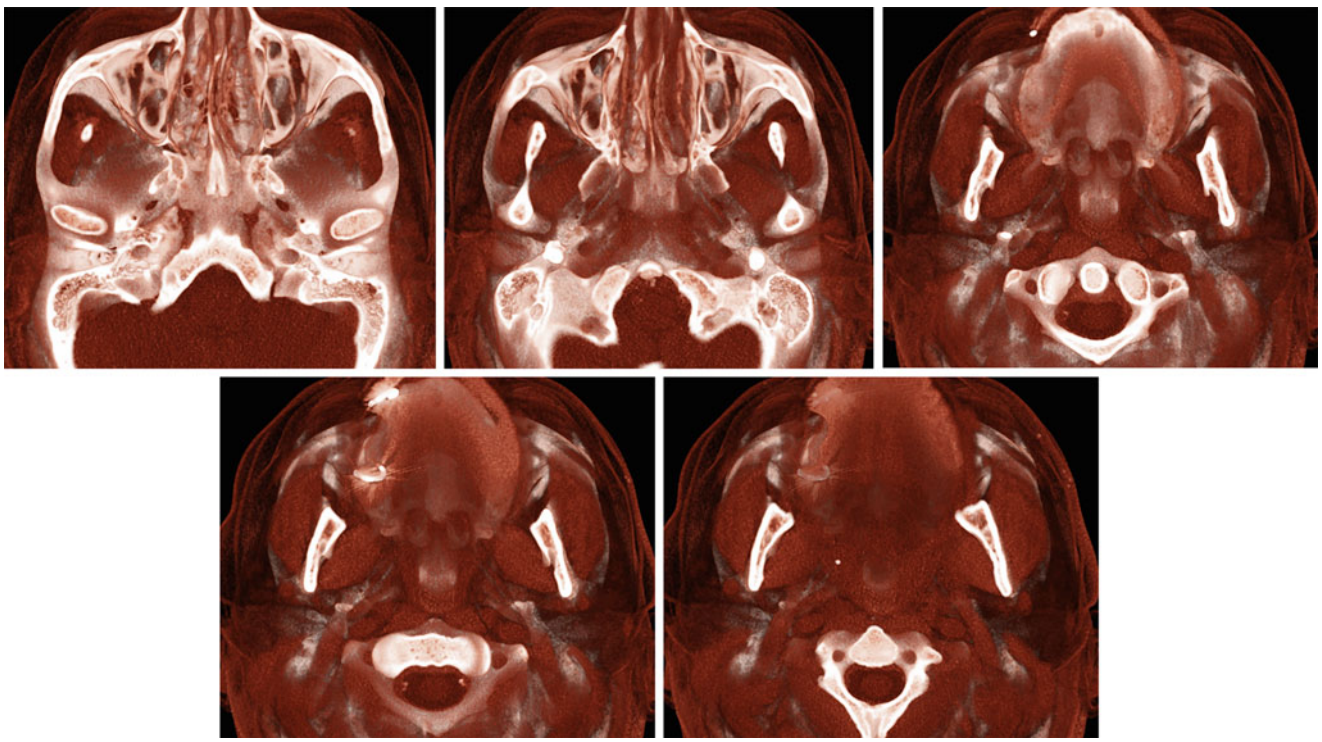


Fig. 5 CT Volume rendering protocol windowing (Carestream© Vue PACS) allow a "hybrid" view of bone and soft tissue. Consecutive axial views of the ITF

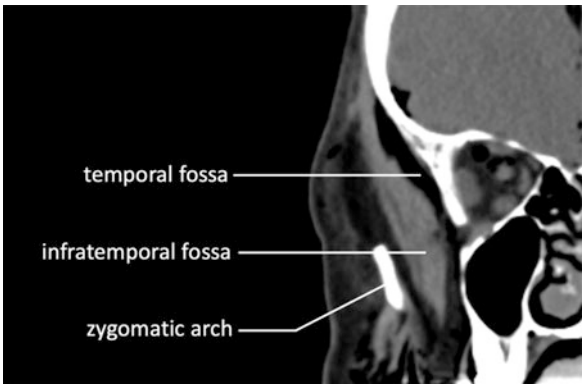


Fig. 6 Postmortem HRCT scan, coronal section through the right infratemporal fossa

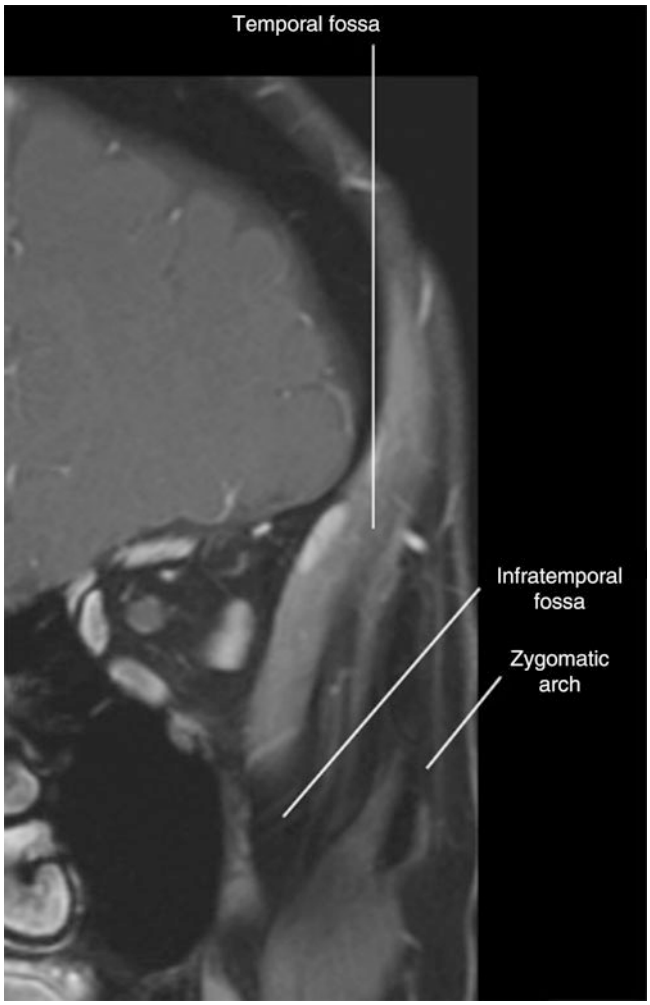


Fig. 7 Coronal T1 FS with contrast MR image demonstrating the left temporal and infratemporal fossa

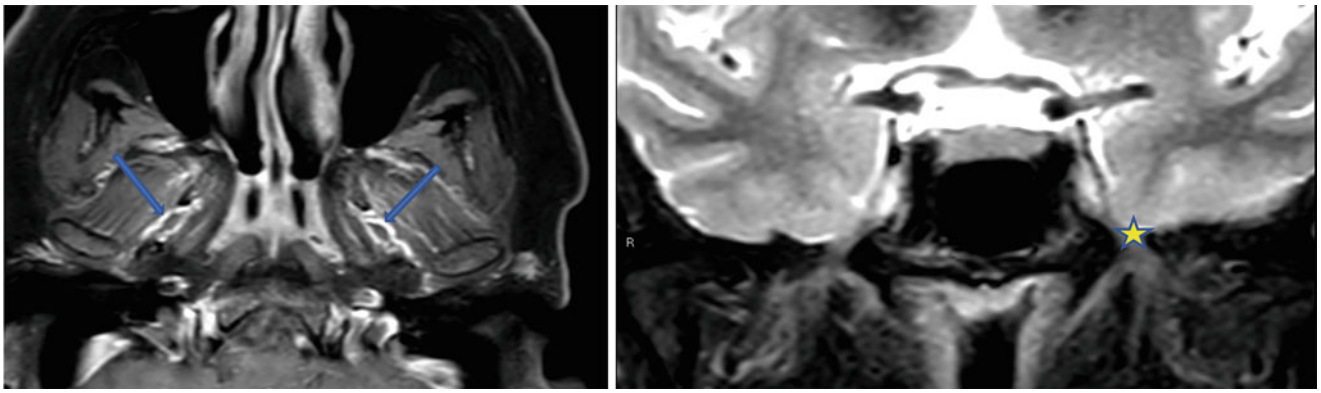


Fig. 8 Axial T1 FS post contrast (*left*) depicting the extracranial Mandibular division of the Trigeminal Nerve (*arrows*). Note how the nerve is surrounded by the enhancing pterygoid venous network. A Cor T2-weighted image shows V3 course through foramen ovale (*star*)

References

1. Gray H, Standring S, Ellis H, Berkovitz BKB. Gray's anatomy: the anatomical basis of clinical practice. 39th ed. Edinburgh/New York: Elsevier Churchill Livingstone; 2005.
2. Most SP, Mobley SR, Larrabee WF. Anatomy of the eyelids. Facial Plast Surg Clin North Am. 2005;13:487–92.
3. Sicher H, DuBrul EL. Oral anatomy. 6th ed. Saint Louis: The CV Mosby; 1975.
4. Kanagalingam S, Miller NR. Horner syndrome: clinical perspectives. Eye Brain. 2015;7:35–46.
5. Meybodi AT, et al. The oculomotor-tentorial triangle. Part 1: microsurgical anatomy and techniques to enhance exposure. J Neurosurg. 2019;130:1426–34.
6. Malhotra A, et al. Neuroimaging of Meckel's cave in normal and disease conditions. Insights Imaging. 2018;9:499–510.
7. Zhuang W, et al. Anatomical study of the extraocular check ligament system. J Plast Reconstr Aesthet Surg. 2019;72(12):2017–26.
8. Marom A. A new look at an old canal. Skull Base. 2011;21(1):53–8.
9. Voirol JR, Vilensky JA. The normal and variant clinical anatomy of the sensory supply of the orbit. Clin Anat. 2014;27:169–75.
10. Wolfram-Gabel R, Kahn JL. Adipose body of the orbit. Clin Anat. 2002;15:186–92.
11. Goh PS, et al. Review of orbital imaging. Eur J Radiol. 2008;66:387–95.

Cavernous Sinus

9

Jack Rootman, Daniel B. Rootman, Bruce Stewart, Stefania B. Diniz, Kelsey A. Roelofs, Liza M. Cohen, Claire S. Smith, Ayelet Eran, Ben Kaplan, and Assaf Marom

Contents

1 Figures and Captions 86

References 89

Abstract

The cavernous sinus is a large venous cavity that lies on both sides of the sella turcica of the sphenoid bone. It extends from the petrous apex posteriorly to the superior orbital fissure anteriorly, and the sphenoidal sinus and the hypophyseal fossa are medial to it. In the inferoposterior part of its lateral wall lies Meckel's cave and the trigeminal ganglion. Among the major contents of the sinus are the cavernous segment of the internal carotid artery and carotid sympathetic nervous plexus, and several cranial nerves.

The oculomotor nerve lies most superior in the lateral wall of the sinus, followed by the trochlear nerve. Having exited Meckel's cave, the ophthalmic (V_1) and maxillary (V_2) divisions of the trigeminal nerve pass in the lateral wall in this order, inferior to the trochlear nerve. The abducens nerve begins its cavernous segment after having passed through Dorello's canal under the petrosphenoidal ligament of Grüber. In this segment, the abducens nerve passes lateral to the artery within the sinus' cavity.

The cavernous sinus is richly connected to other venous systems. It receives tributaries from the superior and inferior ophthalmic veins, from the sphenoparietal sinus that follows the edge of the sphenoid lesser wing, and from several cerebral veins. The sinus communicates with the transverse sinus and the internal jugular vein via the superior and inferior petrosal sinuses, respectively, and also with the laterally situated pterygoid venous plexus.

MRI is the imaging of choice to evaluate most pathologies although most cranial nerves may not be readily demonstrated in the normal cavernous sinus. CT angiography and DSA are essential in vascular anomalies (e.g., carotid aneurysm and CC fistula).

Keywords

Cavernous sinus · Dorello's canal

J. Rootman
University of British Columbia, Vancouver, BC, Canada

D. B. Rootman · S. B. Diniz · K. A. Roelofs · C. S. Smith
Division of Orbital and Ophthalmic Plastic Surgery, Stein and Doheny Eye Institutes, University of California, Los Angeles, CA, USA

B. Stewart
BFA Art Center College of Design, UBC Faculty of Medicine, Kelowna, BC, Canada

L. M. Cohen
Division of Orbital and Ophthalmic Plastic Surgery, Stein Eye Institute, University of California, Los Angeles, CA, USA

A. Eran
Neuroradiology Unit, Radiology Department, Rambam Healthcare Medical Center, Haifa, Israel

Department of Anatomy, Rappaport Faculty of Medicine, Technion – Israel Institute of Technology, Haifa, Israel

B. Kaplan · A. Marom (✉)
Department of Anatomy, Rappaport Faculty of Medicine, Technion – Israel Institute of Technology, Haifa, Israel
e-mail: assafma@technion.ac.il

© Springer Nature Switzerland AG 2022
G. Ben Simon et al. (eds.), *Atlas of Orbital Imaging*,
https://doi.org/10.1007/978-3-030-62426-2_6

1 Figures and Captions

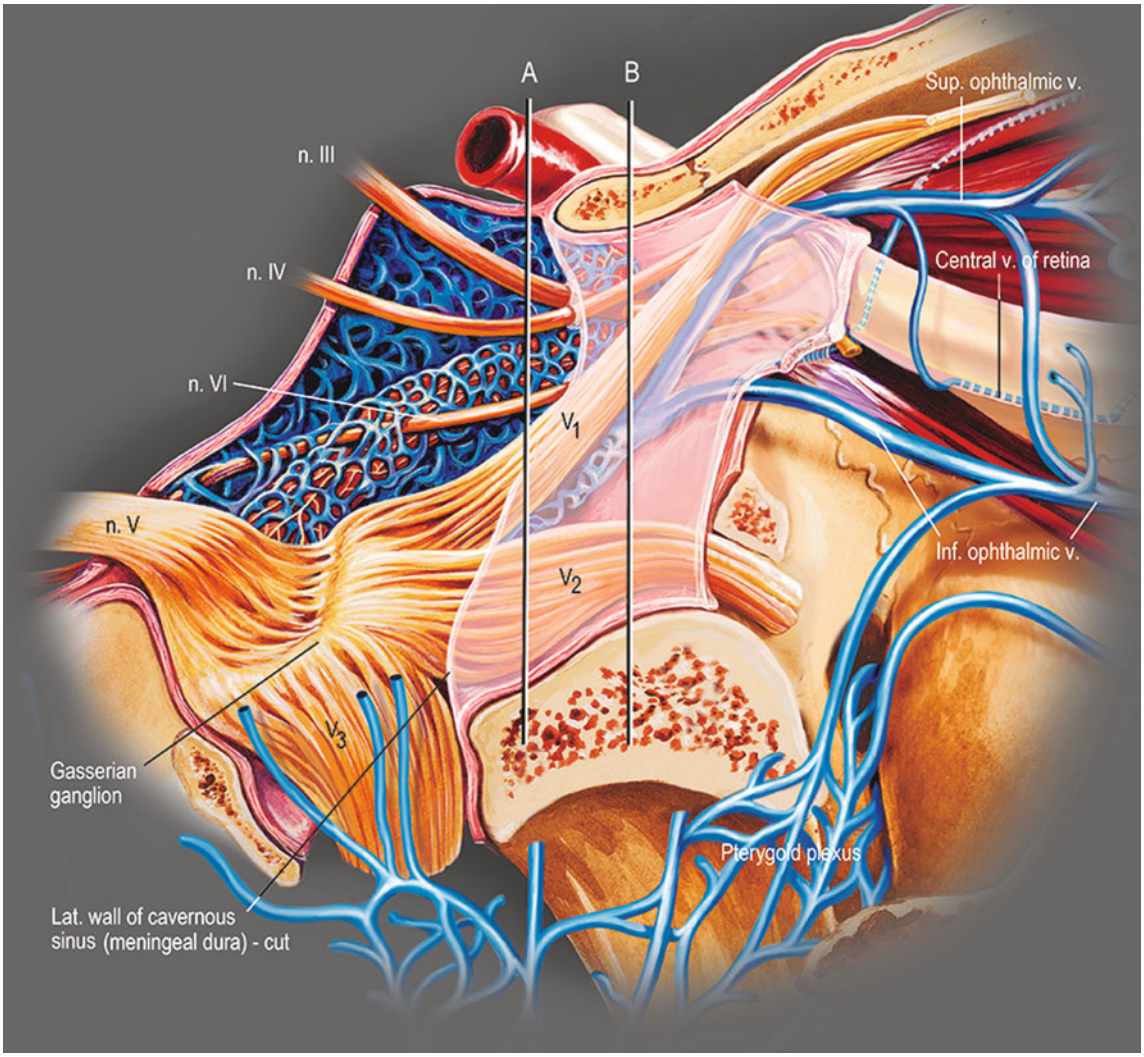


Fig. 1 Artist's drawing of the lateral view of the cavernous sinus (lateral sellar compartment), with the outer leaf partially removed, and orbital apex. The vertical lines (A and B) correspond to the planes of coronal section in the cavernous sinus in Fig. 2. Posterolaterally, the three branches of the trigeminal nerve, (V1, V2, and V3) are contiguous with the outer wall of the cavernous sinus (in Meckel's cave)

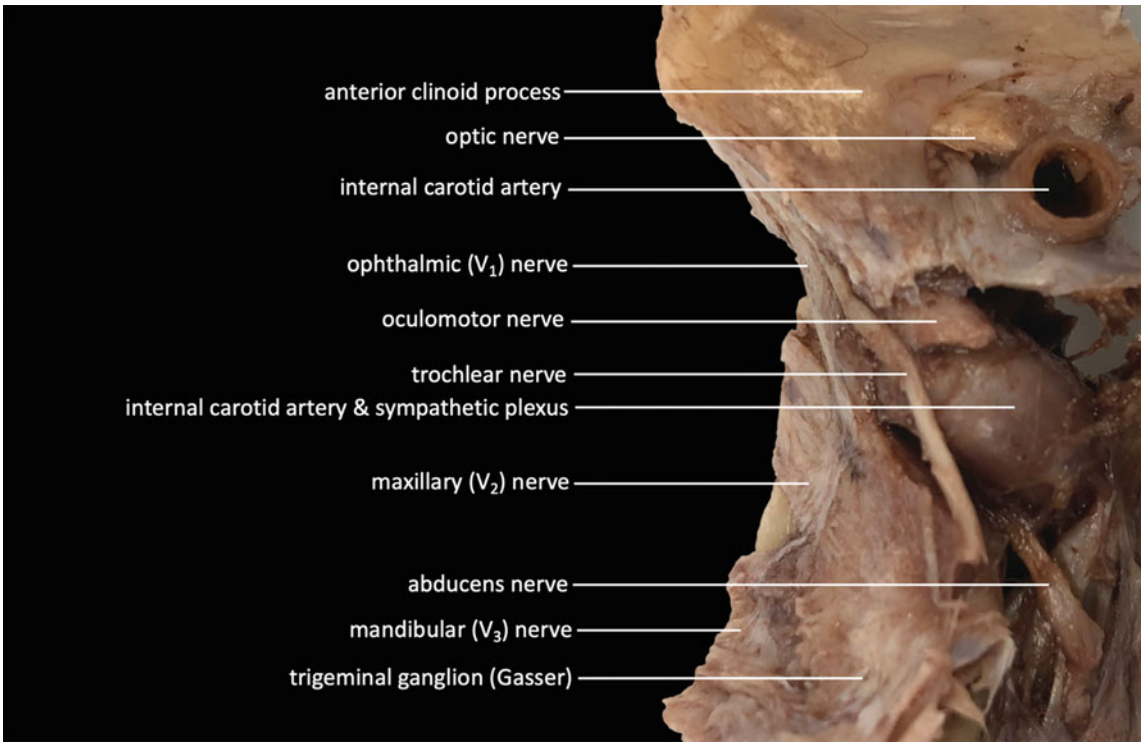


Fig. 2 The cavernous sinus and related structures. Posterior view, right cavernous sinus, cadaver dissection

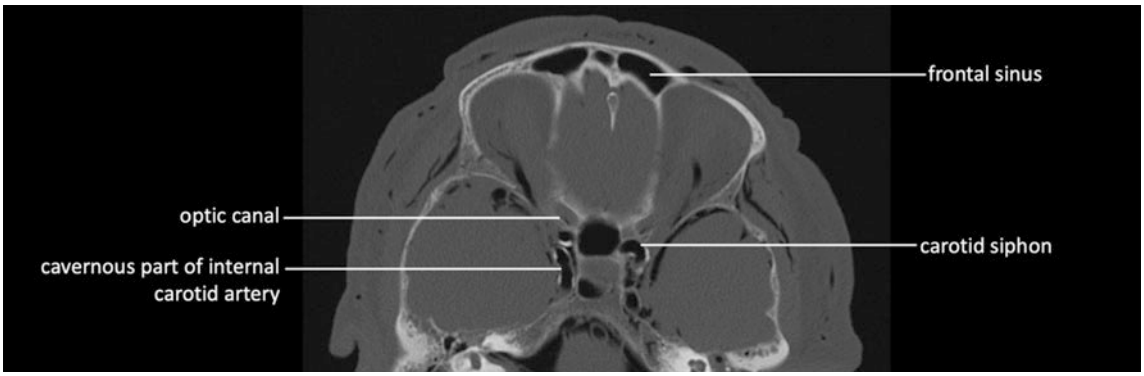


Fig. 3 Postmortem (PM) HRCT scan, the cavernous sinus and related structures

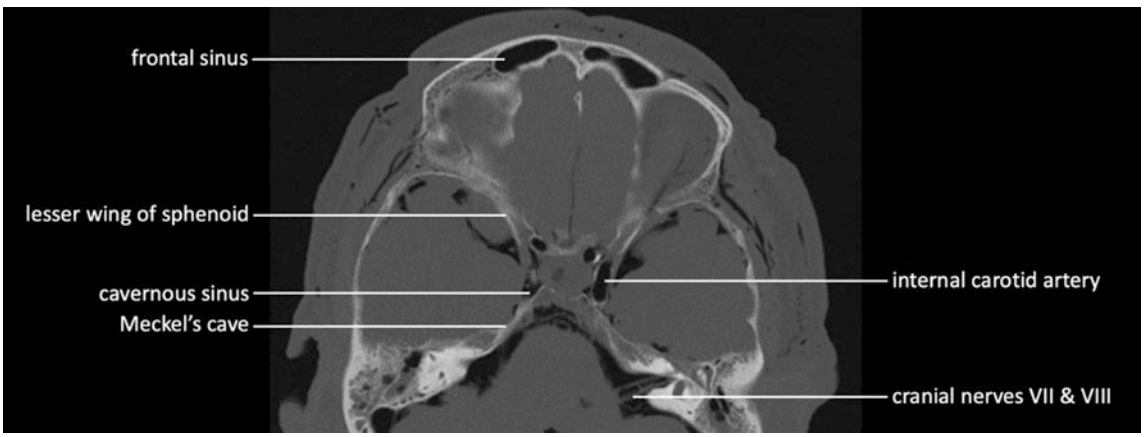


Fig. 4 PM HRCT scan, the cavernous sinus and related structures

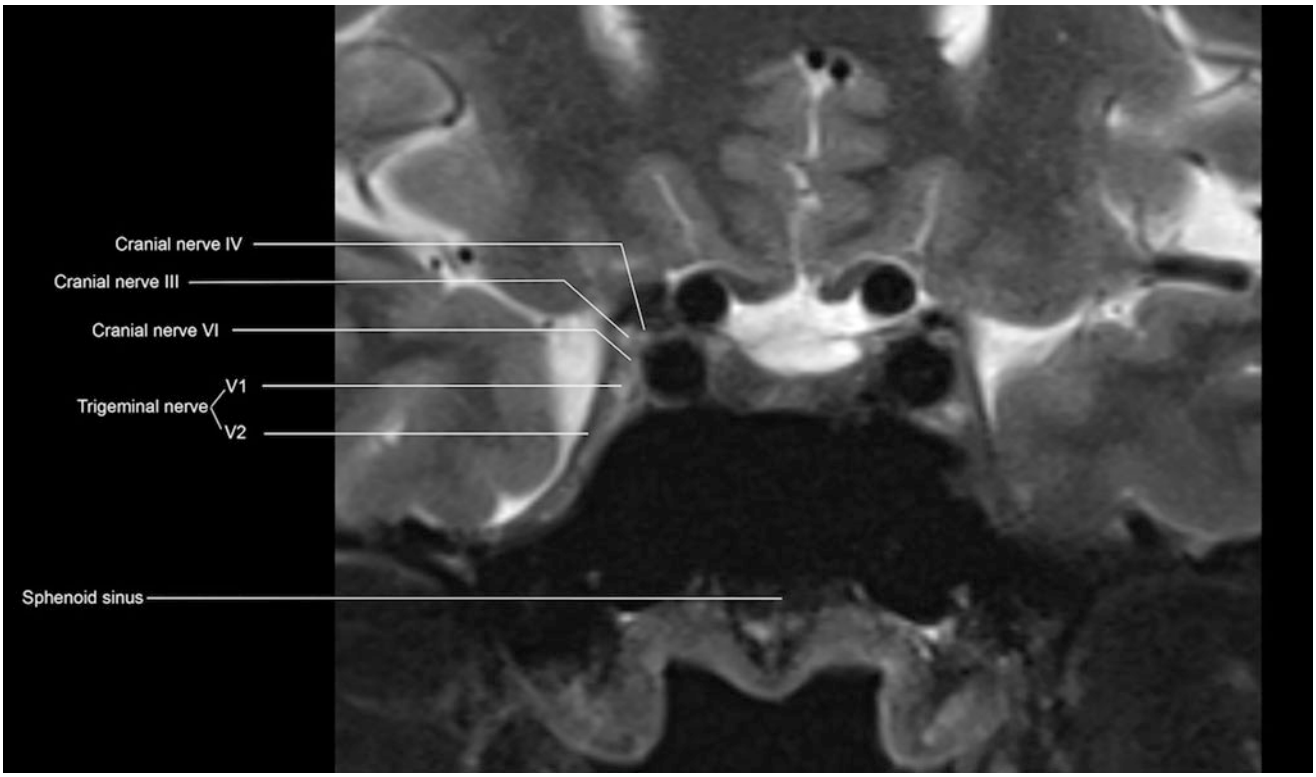


Fig. 5 T2W MR, coronal view, at the level of the cavernous sinus



Fig. 6 MR T1W FS contrast-enhanced, axial view, through the cavernous sinuses

References

1. Gray H, Standring S, Ellis H, Berkovitz BKB. Gray's anatomy: the anatomical basis of clinical practice. 39th ed. Edinburgh/New York: Elsevier Churchill Livingstone; 2005.
2. Most SP, Mobley SR, Larrabee WF. Anatomy of the eyelids. Facial Plast Surg Clin North Am. 2005;13:487–92.
3. Sicher H, DuBrul EL. Oral anatomy. 6th ed. Saint Louis: The CV Mosby; 1975.
4. Kanagalingam S, Miller NR. Horner syndrome: clinical perspectives. Eye Brain. 2015;7:35–46.
5. Meybodi AT, et al. The oculomotor-tentorial triangle. Part 1: microsurgical anatomy and techniques to enhance exposure. J Neurosurg. 2019;130:1426–34.
6. Malhotra A, et al. Neuroimaging of Meckel's cave in normal and disease conditions. Insights Imaging. 2018;9:499–510.
7. Zhuang W, et al. Anatomical study of the extraocular check ligament system. J Plast Reconstr Aesthet Surg. 2019;72(12):2017–26.
8. Marom A. A new look at an old canal. Skull Base. 2011;21(1):53–8.
9. Voirol JR, Vilensky JA. The normal and variant clinical anatomy of the sensory supply of the orbit. Clin Anat. 2014;27:169–75.
10. Wolfram-Gabel R, Kahn JL. Adipose body of the orbit. Clin Anat. 2002;15:186–92.
11. Goh PS, et al. Review of orbital imaging. Eur J Radiol. 2008;66:387–95.

Meckel's Cave

10

Jack Rootman, Daniel B. Rootman, Bruce Stewart, Stefania B. Diniz, Kelsey A. Roelofs, Liza M. Cohen, Claire S. Smith, Ayelet Eran, Ben Kaplan, and Assaf Marom

Contents

1 **Introduction** 91

2 **Figures and Captions** 92

References 96

Abstract

Meckel's cave establishes the connection between the prepontine cistern of the posterior cranial fossa and the cavernous sinus. The sleeve-like dural extension divides into three separate sleeves that contain the ophthalmic (V_1), maxillary (V_2), and mandibular (V_3) divisions of the trigeminal ganglion which carry the sensory innervation of the face and provide motor innervation mainly to the muscles of mastication. Importantly, the precavernous segment of the internal carotid artery passes inferomedial to Meckel's cave.

MRI is the modality of choice for depicting intradural involvement of Meckel's caves. CT can assist in demonstrating possible osseous changes occurring at the petroclival bone. CT angiography is also of major value for evaluating vascular anomalies of the carotid and cavernous sinus.

Keywords

Meckel's cave · Trigeminal nerve · Trigeminal ganglion · Gasserian ganglion · Semilunar ganglion · Gasser's ganglion

1 Introduction

The dura mater is a thick membrane of dense connective tissue (and some fibroblasts) that lines the cranial and spinal cavities. It consists of two layers: an outer endosteal layer and an inner meningeal layer. The two layers are fused, except for areas where they enclose the venous sinuses that drain the cerebral veins. The endosteal layer is continuous with the pericranium through cranial sutures and skull base foramina,

J. Rootman
University of British Columbia, Vancouver, BC, Canada

D. B. Rootman · S. B. Diniz · K. A. Roelofs · C. S. Smith
Division of Orbital and Ophthalmic Plastic Surgery, Stein and Doheny Eye Institutes, University of California, Los Angeles, CA, USA

B. Stewart
BFA Art Center College of Design, UBC Faculty of Medicine, Kelowna, BC, Canada

L. M. Cohen
Division of Orbital and Ophthalmic Plastic Surgery, Stein Eye Institute, University of California, Los Angeles, CA, USA

A. Eran
Neuroradiology Unit, Radiology Department, Rambam Healthcare Medical Center, Haifa, Israel

Department of Anatomy, Rappaport Faculty of Medicine, Technion – Israel Institute of Technology, Haifa, Israel

B. Kaplan · A. Marom (✉)
Department of Anatomy, Rappaport Faculty of Medicine, Technion – Israel Institute of Technology, Haifa, Israel
e-mail: assafma@technion.ac.il

© Springer Nature Switzerland AG 2022
G. Ben Simon et al. (eds.), *Atlas of Orbital Imaging*,
https://doi.org/10.1007/978-3-030-62426-2_7

and with the orbital periosteum through the superior orbital fissure. The meningeal layer also forms tubular envelopes ("sleeves") for cranial nerves as they exit the endocranial cavity through the skull base foramina. These fibrous sheaths are continuous with the epineurium as the nerves emerge from the skull. The dural sheath of the optic nerve is continuous with the ocular sclera.

The tentorium cerebelli is a lamina of dura mater that covers the cerebellum, with a lateral attachment to the petrous part of the temporal bone and an anterior free border. Along the lateral attachment, the superior petrosal venous sinus is formed. The anterior free margin forms the tentorial incisura (notch) that houses the upper part of the brainstem. Near the apex of the petrous temporal bone the lower layer of the tentorium forms an extension that evaginates anterolaterally under the superior petrosal sinus into the middle cranial fosse. This para-sellar recess is located between the two dural layers and is referred to as Meckel's cave (or the trigeminal cave), because it acts as a conduit to the root and Gasserian ganglion of the trigeminal nerve. The meningeal layer of the dura is firmly attached to the ganglion. Meckel's cave establishes the connection between the prepontine cistern of the posterior cranial fossa and the cavernous sinus. The sleeve-like dural extension divides into three separate sleeves that contain the ophthalmic (V_1), maxillary (V_2), and mandibular (V_3) divisions of the trigeminal ganglion which carry the sensory innervation of the face, and provide motor innervation mainly to the muscles of mastication. Importantly, the precavernous segment of the internal carotid artery passes inferomedial to Meckel's cave.

The free (anterior) tentorial border continues anteriorly and attaches to the anterior clinoid process. It is crossed by the anterior extension of the tentorial lateral attachment, which attaches to the posterior clinoid process. The "triangular field" that forms at this crossing is where the oculomotor nerve pierces the dura mater into the cavernous sinus.

2 Figures and Captions

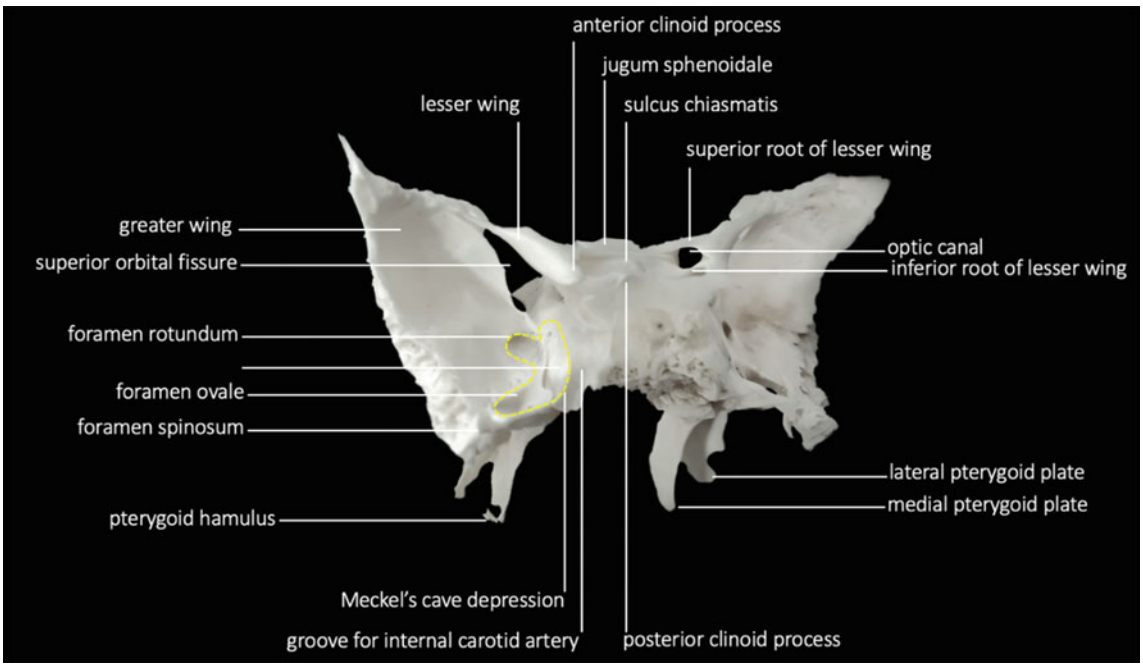


Fig. 1 Posterolateral view of the sphenoid bone. The dashed yellow line marks the location of Meckel's cave

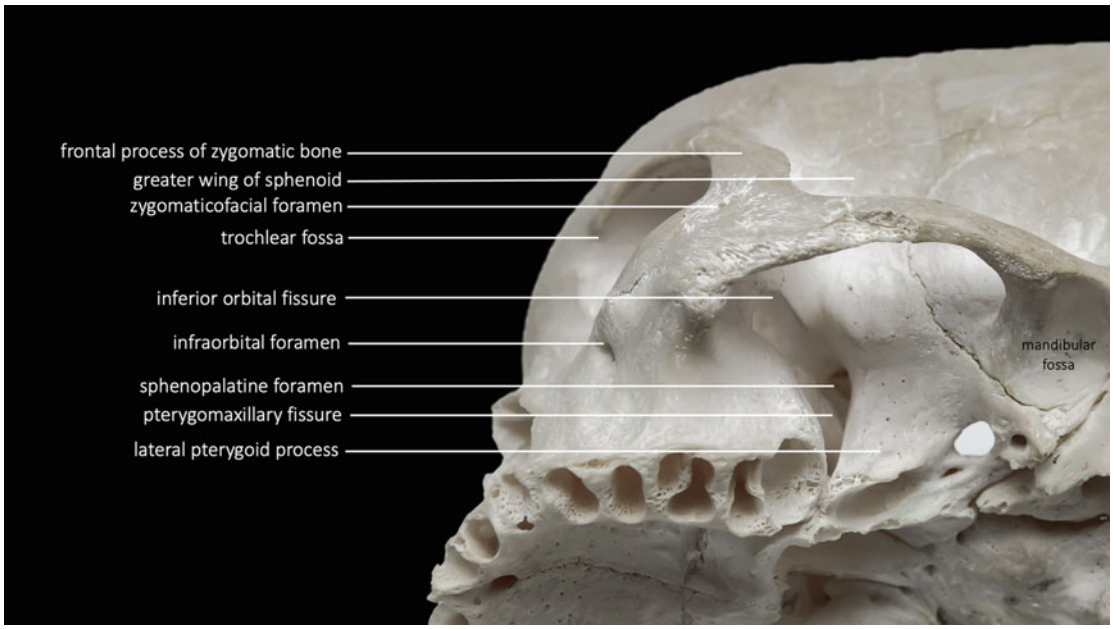


Fig. 2 Posterior view of the left middle cranial fossa, with dural lining

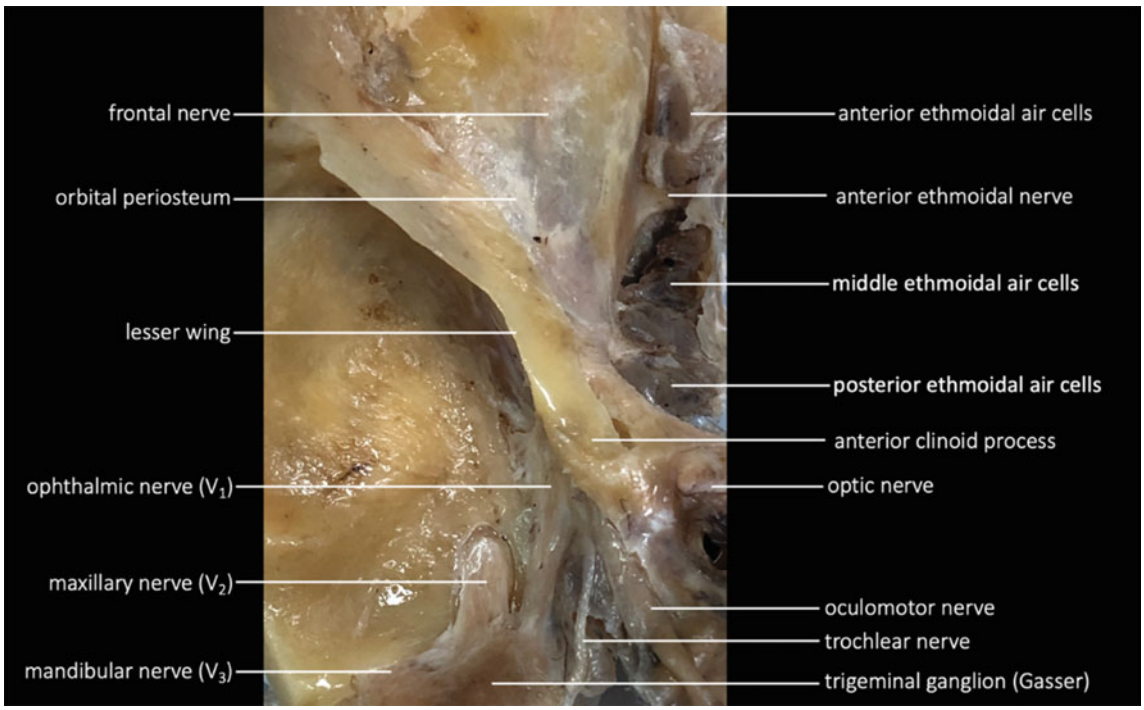


Fig. 3 Posterior view of the left middle cranial fossa and Meckel's cave after the dural lining was removed

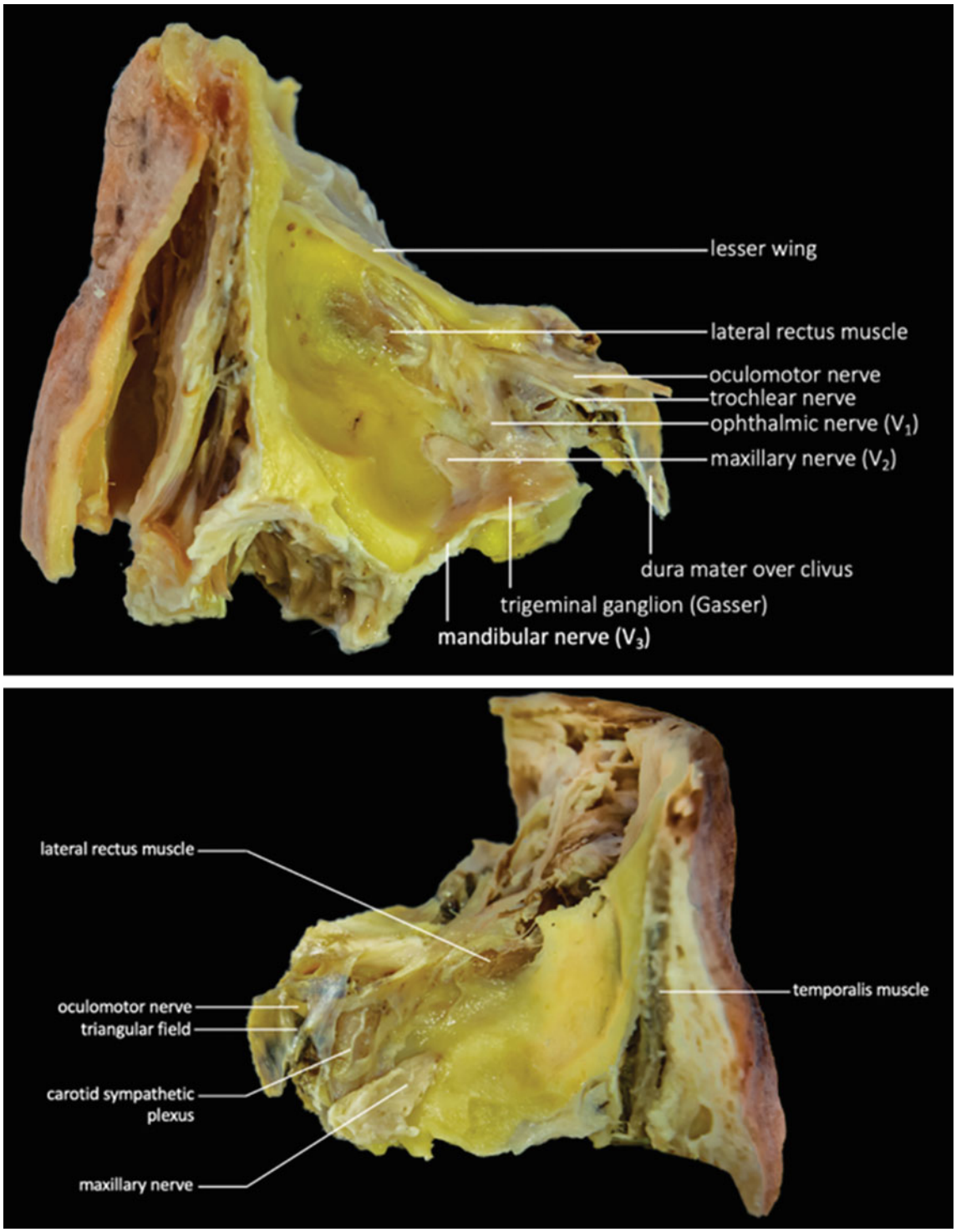


Fig. 4 Lateral view of Meckel's cave – left (*upper*) and right (*lower*)

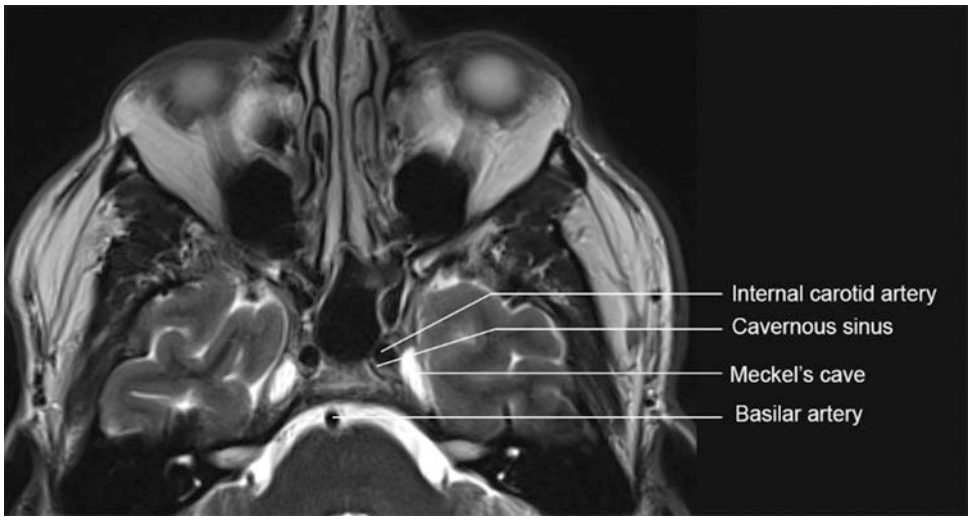


Fig. 5 Axial T2W MR non-FS at the level of Meckel's cave and caudal portions of the cavernous sinuses

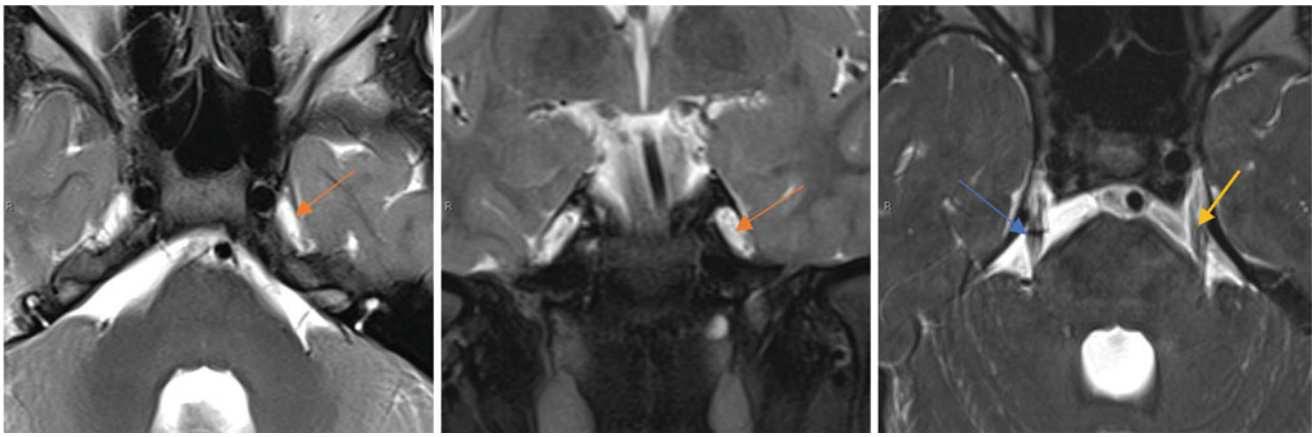


Fig. 6 Axial and coronal T2-weighted scans through the Meckel's cave (*orange arrows*, *left* and *middle*). The reformatted thin slice T2 Space (0.7 mm) scan on the right better demonstrates the passage of the trigeminal rootlets through the CSF space (*yellow arrow*). Note a small vessel is crossing the right cisternal trigeminal nerve (*blue arrow*), a common imaging finding, generally of no clinical significance unless true signs of neurovascular conflict (trigeminal neuralgia)

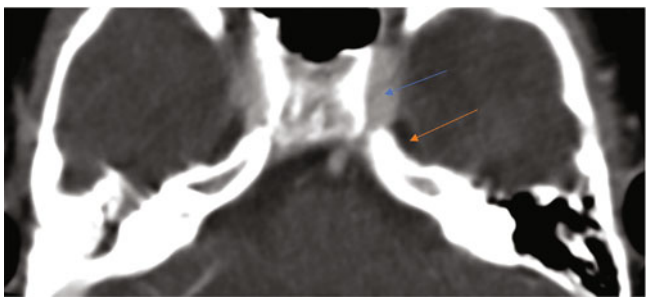


Fig. 7 Axial contrast-enhanced CT scan shows the CSF filled cavities (*orange arrow*) and the enhancing structures of the cavernous sinus medially (*blue arrow*)

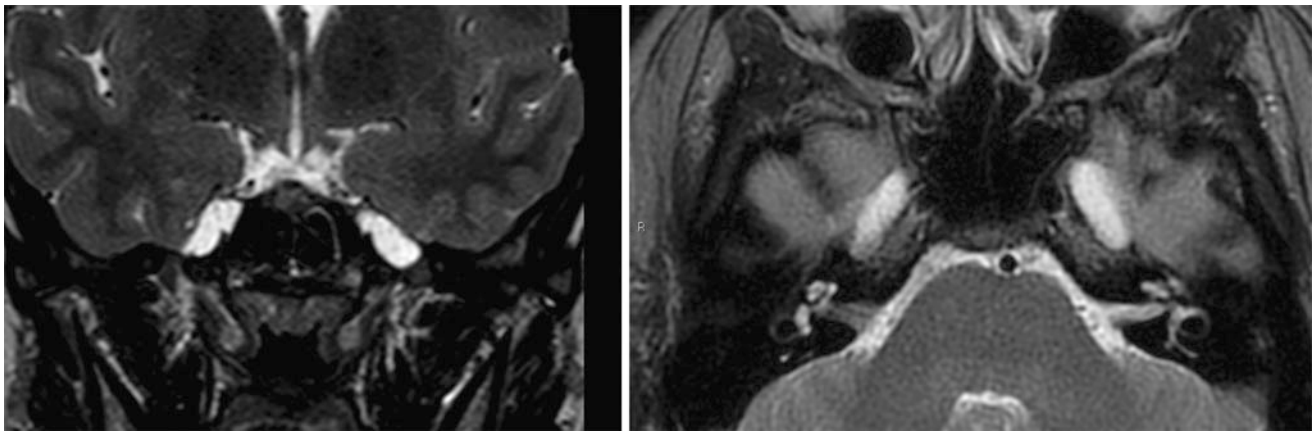


Fig. 8 Coronal and axial T2-weighted images showing cystic enlargement of Meckel's caves in a 23-year-old female with pseudo-tumor cerebri. According to the literature Meckel's caves may indeed appear more prominent in patients with idiopathic intracranial hypertension (IIH) [12]

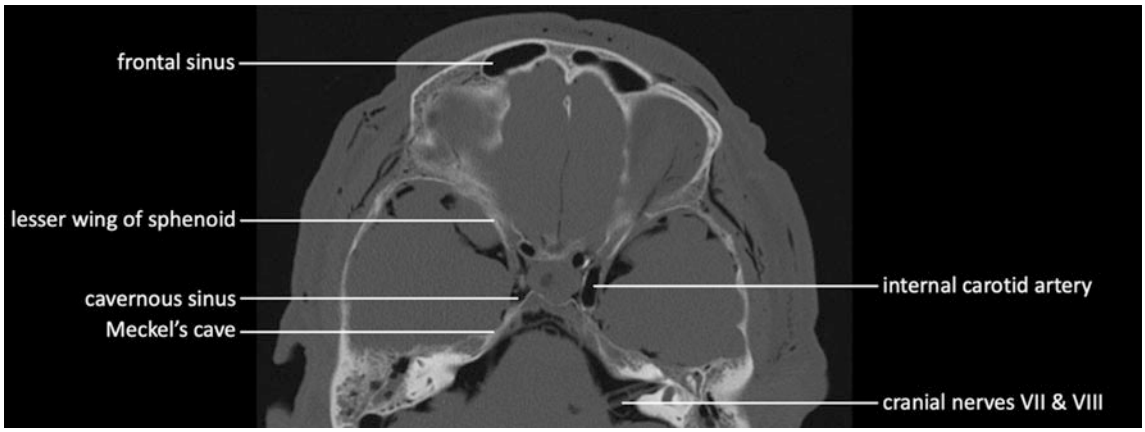


Fig. 9 Postmortem (PM) HRCT scan, horizontal section at the level of the cavernous sinus, showing the air-filled cavernous carotid and other relevant anatomy of the skull base

References

1. Gray H, Standring S, Ellis H, Berkovitz BKB. Gray's anatomy: the anatomical basis of clinical practice. 39th ed. Edinburgh/New York: Elsevier Churchill Livingstone; 2005.
2. Most SP, Mobley SR, Larrabee WF. Anatomy of the eyelids. Facial Plast Surg Clin North Am. 2005;13:487–92.
3. Sicher H, DuBrul EL. Oral anatomy. 6th ed. Saint Louis: The CV Mosby; 1975.
4. Kanagalingam S, Miller NR. Horner syndrome: clinical perspectives. Eye Brain. 2015;7:35–46.
5. Meybodi AT, et al. The oculomotor-tentorial triangle. Part 1: microsurgical anatomy and techniques to enhance exposure. J Neurosurg. 2019;130:1426–34.
6. Malhotra A, et al. Neuroimaging of Meckel's cave in normal and disease conditions. Insights Imaging. 2018;9:499–510.
7. Zhuang W, et al. Anatomical study of the extraocular check ligament system. J Plast Reconstr Aesthet Surg. 2019;72(12):2017–26.
8. Marom A. A new look at an old canal. Skull Base. 2011;21(1):53–8.
9. Voirol JR, Vilensky JA. The normal and variant clinical anatomy of the sensory supply of the orbit. Clin Anat. 2014;27:169–75.
10. Wolfram-Gabel R, Kahn JL. Adipose body of the orbit. Clin Anat. 2002;15:186–92.
11. Goh PS, et al. Review of orbital imaging. Eur J Radiol. 2008;66: 387–95.
12. Bialer OY, Rueda MP, Bruce BB, Newman NJ, Biousse V, Saindane AM. Meningoceles in idiopathic intracranial hypertension. AJR Am J Roentgenol. 2014;202(3):608–13.

Part II

Orbital Imaging Modalities

Orbital CT

11

Denise S. Kim, Remy R. Lobo, and Alon Kahana

Contents

1 **Overview** 99
2 **Indications** 100
3 **Technique and Protocol Considerations** 100
4 **Figures with Captions** 100
References 102

Abstract

Computed tomography (CT) is a noninvasive, diagnostic imaging modality with high spatial resolution. It is rapid, amenable to claustrophobic patients, and provides excellent examination of bone anatomy with adequate soft tissue evaluation.

Keywords

Computed tomography · Orbit · Imaging · Iodine contrast

1 Overview

Computed tomography (CT) is a noninvasive, diagnostic imaging modality with high spatial resolution [1]. It provides excellent examination of bone anatomy with adequate soft tissue evaluation. Ionizing radiation is passed in a radial pattern through a patient and residual radiation is detected on the opposing side. The sequential radiographic images are reconstructed to create cross-sectional images of varying attenuation in Hounsfield units (HU) through structures.

In the interpretation of CT imaging, the relative density rather than absolute density is used to characterize various tissues, with 0 HU representing water. Dense or hyperdense objects attenuate the X-rays and appear brighter; examples include acute hemorrhage, bone, and metallic foreign objects. Hypodense objects allow X-rays to pass through more freely and appear relatively dark; examples include air, fat, and water. Tissues containing relatively excess water will appear hypodense, a marker of edema or inflammation. Iodinated contrast, which appears dense, can be administered intravenously to better evaluate certain pathologies.

D. S. Kim
Department of Ophthalmology and Visual Sciences, University of Michigan Medical School, Ann Arbor, MI, USA
e-mail: kimden@med.umich.edu

R. R. Lobo
Department of Radiology, University of Michigan Medical School, Ann Arbor, MI, USA
e-mail: remylobo@med.umich.edu

A. Kahana (✉)
Ophthalmology Department, Oakland University William Beaumont School of Medicine, Rochester, MI, USA

Attending Surgeon, Consultants in Ophthalmic and Facial Plastic Surgery, Southfield, MI, USA

© Springer Nature Switzerland AG 2022
G. Ben Simon et al. (eds.), *Atlas of Orbital Imaging*,
https://doi.org/10.1007/978-3-030-62426-2_111

2 Indications

- Trauma
- Foreign body
- Acute infection
- Preoperative planning (assessment of anatomy, navigation protocols)
- Postoperative outcomes assessment
- Orbital masses (often in conjunction with MRI)
- Thyroid eye disease (without iodinated contrast)

3 Technique and Protocol Considerations

A scout radiograph is obtained to orient the patient and define the region of acquisition. The reformatted images of an orbital CT typically extend from the mid-maxillary sinus to the mid-frontal sinus, and from the eyelid skin anteriorly to the brain stem posteriorly. Data is acquired in a helical fashion, usually in the z-axis (craniocaudal direction). Images are then reconstructed into standard anatomical planes (axial, coronal, and sagittal). Since the data is volumetric, images can be reconstructed in any direction, and contoured to create special oblique planes as needed for problem solving. Separate filters are applied to accentuate different structures (e.g., soft tissue algorithm vs bone algorithm). While the scan is usually obtained with the patient laying supine, distensible venous anomalies may only show with the patient in prone position [2].

Contrast is primarily used to evaluate infectious processes, for example, differentiating between abscess vs phlegmon. Contrast may be used in the evaluation of vascular lesions but CT has limited temporal resolution. Administration of contrast is not necessary to evaluate fractures or to assess bony anatomy and healing. Possible contraindications to use of contrast include past history of reaction to contrast agents, renal impairment, and pregnancy.

CT is advantageous over other imaging modalities in that it is noninvasive, widely available, rapidly acquired, and relatively inexpensive when compared to MRI. Thus, it is the favored imaging modality in the emergency room setting. CT is also a more practical choice for imaging patients with significant claustrophobia, altered mental status, or difficulty lying flat.

The main disadvantage of CT is the use of ionizing radiation, of particular concern in the pediatric population. Another limitation is the lack of soft tissue detail and inability to differentiate between isodense structures. CT does carry a risk of motion artifact, but it is relatively reduced given the speed of acquisition. Finally, dense objects such as metallic foreign bodies will cause streak artifact, as they attenuate X-rays thereby limiting the resolution of adjacent structures.

4 Figures with Captions

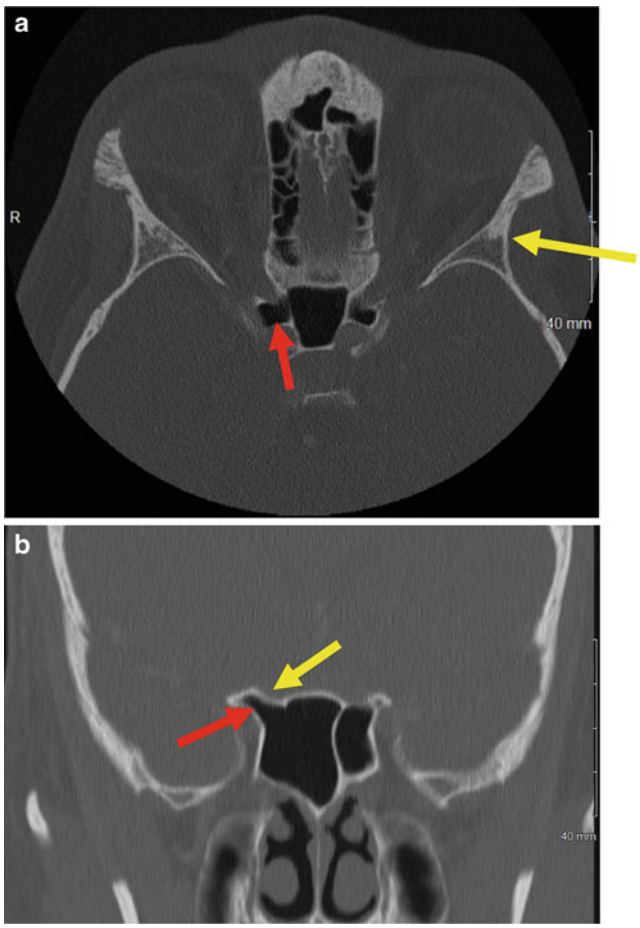


Fig. 1 (**a**) Axial bone algorithm CT at the mid-orbit shows excellent osseous detail, including left lateral orbital wall (yellow arrow) contiguous to the sphenoid trigone (greater wing) posteriorly. Note the aerated clinoid process (red arrow) along the optic canal. (**b**) Coronal bone algorithm CT at the posterior optic canal shows aeration of the right clinoid (red arrow), with superior medial positioning of the optic nerve (yellow arrow) at the posterior optic canal. This case shows aeration from the posterior sphenoid. When the ethmoid aerates above the sphenoid, it is considered an "Onodi" cell (which can also aerate the clinoid)

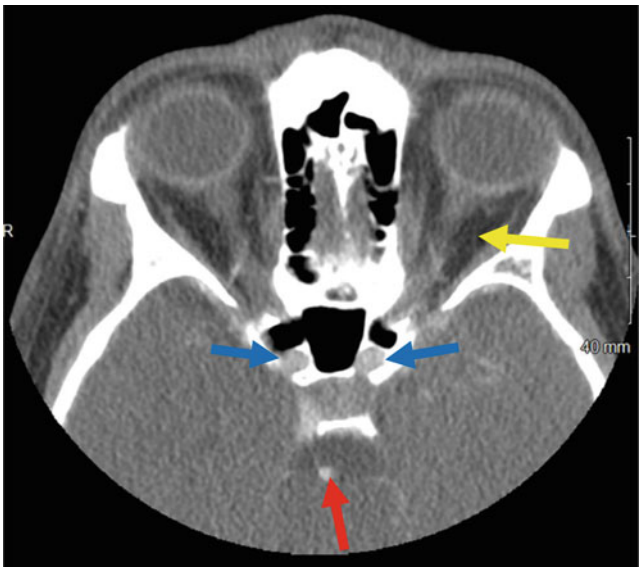


Fig. 2 Axial soft tissue CT with contrast. Note the opacified vascular structures, including internal carotid arteries (blue arrows) and basilar artery (red arrow). This window provides adequate soft tissue detail (yellow arrow: intraconal fat), but limits resolution in the bone

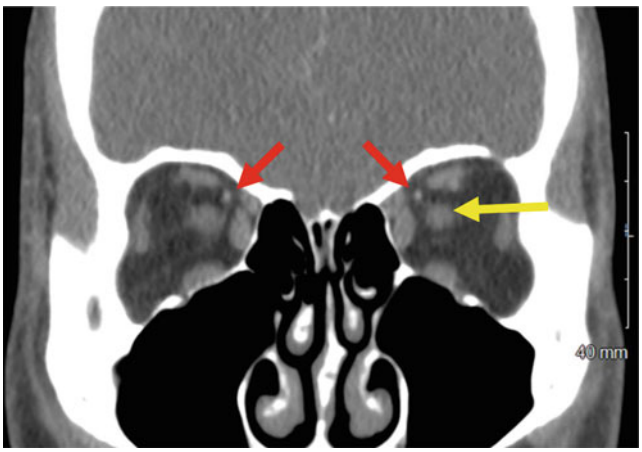


Fig. 3 Coronal soft tissue CT with contrast, at the mid-orbit, normal morphology optic nerves (yellow arrow) and extraocular muscles. Bilateral small, normally opacified superior ophthalmic veins (red arrows)

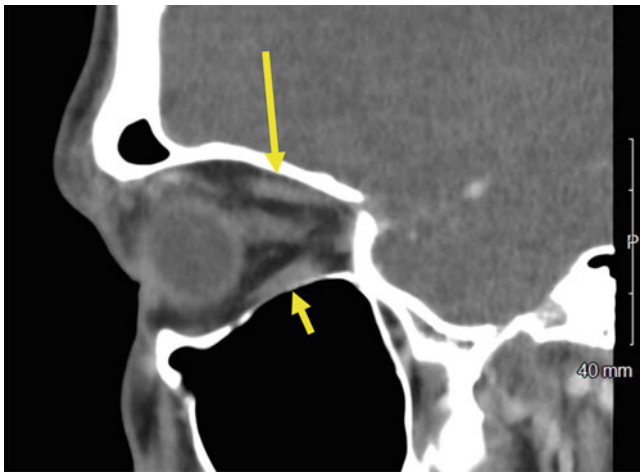


Fig. 4 Sagittal soft tissue CT with contrast, at the mid-orbit, shows normal superior and inferior muscle complexes (long and short yellow arrows, respectively). Figure also shows a natural sloping orbital floor (short arrow)

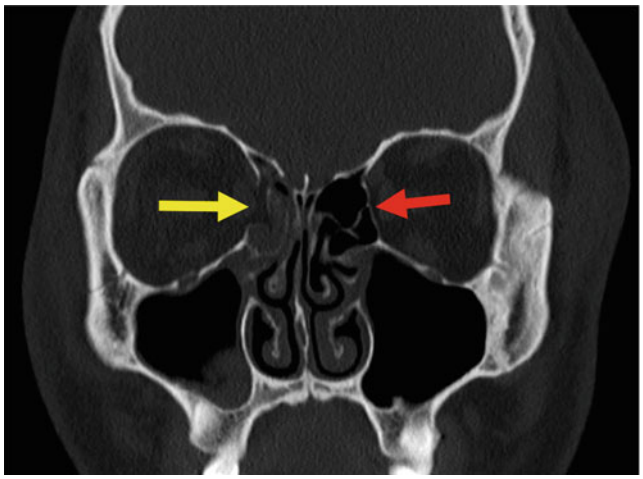


Fig. 5 Coronal CT without contrast, bone algorithm shows the disrupted contour of the right lamina papyracea (yellow arrow), sometimes described as a blow-out fracture. Notice how it compares to the normal left orbital contour (red arrow)

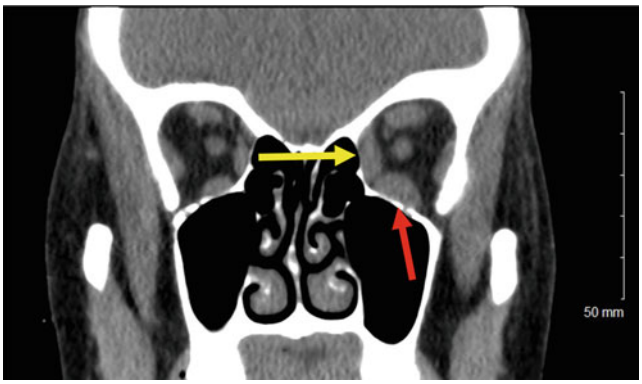


Fig. 6 Coronal CT without contrast, soft tissue algorithm at the mid-orbit showing asymmetric enlargement of the inferior (red arrow) and medial (yellow arrow) recti, consistent with thyroid-associated ophthalmopathy

References

1. ACR-ASNR-SPR. ACR–ASNR–SPR practice parameter for the performance of computed tomography (CT) of the extracranial head and neck Res. 14 – 2016. Available from http://www.acr.org. Accessed 7 July 2020.
2. Kiang L, Kahana A. Images in clinical medicine. Orbital varix. N Engl J Med. 2015;372(7):e9. https://doi.org/10.1056/NEJMicm1314101.

Orbital MRI

12

Arnaldo Mayer and Gahl Greenberg

Contents

1 **Introduction** 103
2 **Figures and Captions** 105
References 111

Abstract

MRI is a powerful medical imaging technique that provides 3D and sectional images with high anatomical resolution and unrivalled contrast between soft tissues. MRI is noninvasive and does not expose the patient to ionizing radiation. MRI is widely used in orbital imaging for various indications, especially those requiring soft tissue inspection, while CT is preferable for assessment of orbital bony structure, intralesional calcifications, etc. As discussed in a different chapter, CT is faster, and is the imaging modality of choice for orbital trauma and bony tumors; MRI, however, better evaluates most types of orbital tumors and malformations. The versatility of MR sequences enables us to portray anatomical detail to much greater extent, especially when dealing with intraocular or optic nerve/sheath pathologies, inflammatory nerve conditions, perineural spread, as well as bone marrow infiltration, skull base involvement, or cavernous sinus invasion. The current chapter discusses some of the basic principles of MR imaging and its commonly used modalities and sequences.

Keywords

MRI · MR imaging · Magnetic resonance imaging · Voxel · T1 · T2 · FLAIR · FIESTA · CISS · DWI · Diffusion weighted imaging

1 Introduction

MRI is based on the physical phenomenon of nuclear magnetic resonance of the hydrogen protons (nuclei) distributed in the human body tissues as part of the water molecules. The resonance signal is the response of these nuclei subjected to a strong permanent (static) magnetic field, and a sequence of radio frequency (RF) electromagnetic pulses.

The signal intensity collected at a given element of volume (voxel) depends on the local concentration of hydrogen protons, resulting in a 3D image of the hydrogen protons density in the body of the patient. In addition, it is possible to generate images wherein the local contrast is provided by the spatial variation of protons relaxation time, during which protons recover their initial energy level (i.e., reaching resting state), following excitation by an RF pulse sequence.

A. Mayer
PI at the Computational imaging lab (Cilab), Sheba Medical Center, Ramat Gan, Israel

G. Greenberg (✉)
Department of Diagnostic Imaging, Sheba Medical Center, Tel Hashomer, Israel
e-mail: gahl.greenberg@sheba.health.gov.il

© Springer Nature Switzerland AG 2022
G. Ben Simon et al. (eds.), *Atlas of Orbital Imaging*,
https://doi.org/10.1007/978-3-030-62426-2_126

Two main relaxations are used in MRI:

1. Longitudinal relaxation (Fig. 1, blue): Also known as T1 relaxation or "spin-lattice" relaxation [1], it corresponds to the return to energy balance of the spins after excitation, by energy transfer from spins to the surrounding molecules (lattice). The time constant T1 is the time required for protons to recover two-thirds of their magnetization [1]. T1 depends on the mobility of hydrogen protons or that of the molecules they occupy. In a nutshell, the larger these molecules, the shorter is their T1 property.
2. Transversal relaxation or "spin-spin" (Fig. 1, red): Usually denoted by T2, it characterizes the progressive dephasing of the transverse magnetization component of spins, following excitation by an RF pule sequence.

The T2 relaxation time is always shorter than the T1 relaxation time [1]. It also depends on the mobility of the atoms or molecules to which these protons are attributed.

These relaxation times will vary for a given tissue according to the physicochemical organization of the water in this tissue, and it is on these variations that we rely to detect the related modifications within a tissue caused by the presence of a lesion.

In practice, the MRI signal is acquired in a Fourier space, called k-space (Fig. 2, left) from which the final image (right) is derived by computing a 2D or 3D Fourier transformation of the acquired signal [2].

Over the years, many pulse sequences were developed allowing to obtain many types of complementary contrasts between the tissues. This led to specific multi-sequence scan protocols, optimized to provide an accurate answer for the targeted radiological query.

For example, specific pulse sequences were developed to capture the random diffusion motion of water molecules (Fig. 3). This led to diffusion-weighted images (DWI) from which the voxel-wise apparent diffusion coefficients (ADC) can be computed [3]. The ADC proved extremely sensitive to the presence of highly cellular tumors, as the associated abnormal cell growth and high nucleus-to-cytoplasm ratio restrict water molecules motion, thus decreasing the local ADC values. DWI sequences were also found useful in depicting pus material in infectious processes and are similarly known for picking up epidermoids due to the laminated keratin layers within the cyst.

Furthermore, fitting tensor models (Fig. 4, top) to DWI enables the association of a main direction of diffusion at each voxel that can be used to track white matter tracts from end to end (bottom, left) [4]. The resulting diffusion tensor imaging (DTI) tractography (bottom, right) is routinely used for neurosurgical navigation [5].

Pulse sequences have also been developed to remove undesired signal from the images. An important example is given by fat suppression pulses that may be added to existing pulse sequences to eliminate the contribution of fat when undesirable [6]. Any dedicated head and neck protocol, including those directed at orbits, sino-nasal cavities, facial structures, skull base, infratemporal fossa, and mucosal spaces, must include fat-saturated images in order to pick up the contrast-enhanced pathology while suppressing the intrinsic bright signal of the surrounding fat planes and fatty marrow in the background.

Another commonly used feature is the fluid-attenuated inversion recovery (FLAIR). It is up to the operator to apply it to either a T1- or T2-weighted sequences, but the most common weighting is T2 FLAIR. This essentially suppresses free water movement (i.e., CSF and vitreous fluid), thus reversing the bright signal of free-flowing fluid and highlighting all that is abnormal; for example, areas of edema, inflammation, and demyelination. Post-contrast FLAIR sequences are also highly sensitive for detecting leptomeningeal involvement (e.g., infectious, granulomatous disease or carcinomatous spread) [7].

Clinicians should also familiarize themselves with high-resolution submillimeter sequences, with high T1/T2 contrast, capable of demonstrating intraocular content, cranial nerves, CSF cisterns, and cavernous sinuses in high detail. These include, among others: constructive interference in steady state (CISS) on Siemens, balanced fast field echo (BFFE) on Philips, and FIESTA (fast imaging employing steady-state acquisition) on GE [8]. Vendors also provide 3D-fast (turbo) spin echo "isotropic" acquisitions, in which the voxels measure the same in all three vectors, allowing reformats of equal resolution in every direction (for example, SPACE (Siemens), CUBE (GE), and DRIVE (Philips)).

2 Figures and Captions

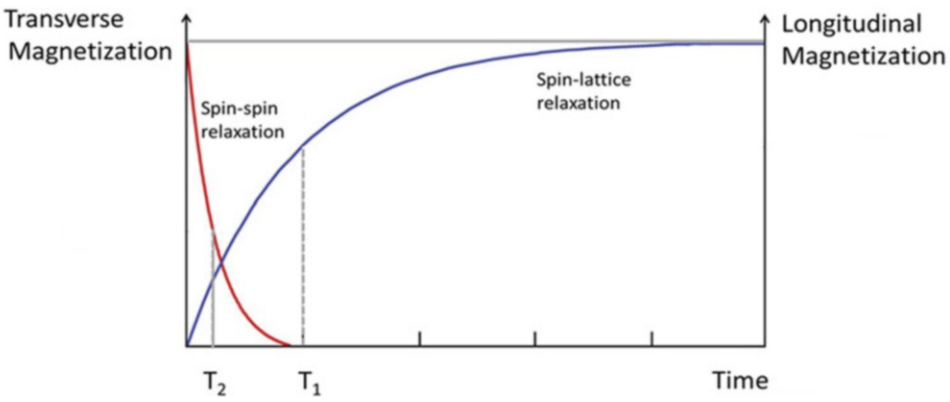


Fig. 1 T1 and T2 relaxation curves

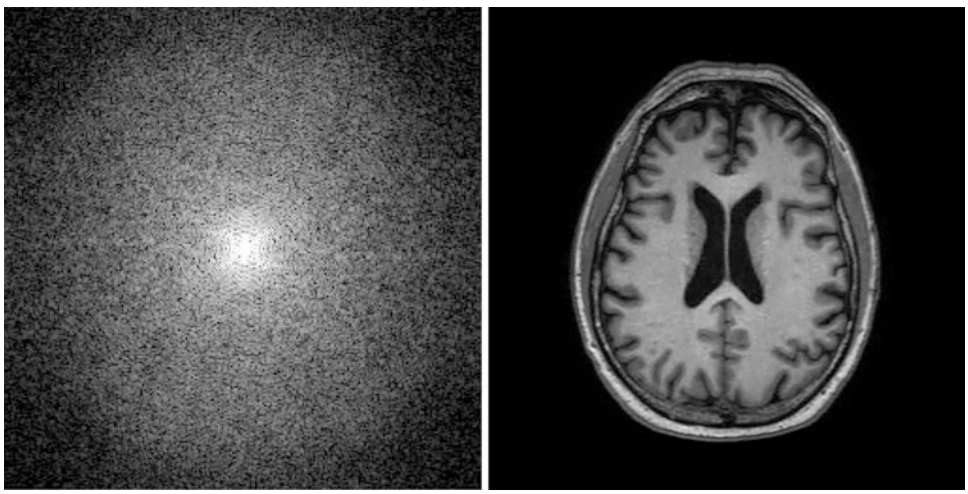


Fig. 2 (left) K-space acquisition and (right) corresponding image obtained by 2D fourier transform computation

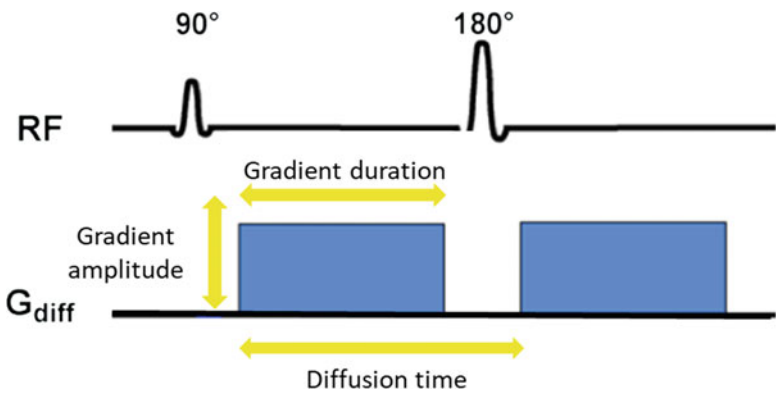


Fig. 3 Gradient pulse pair used for diffusion-weighted imaging

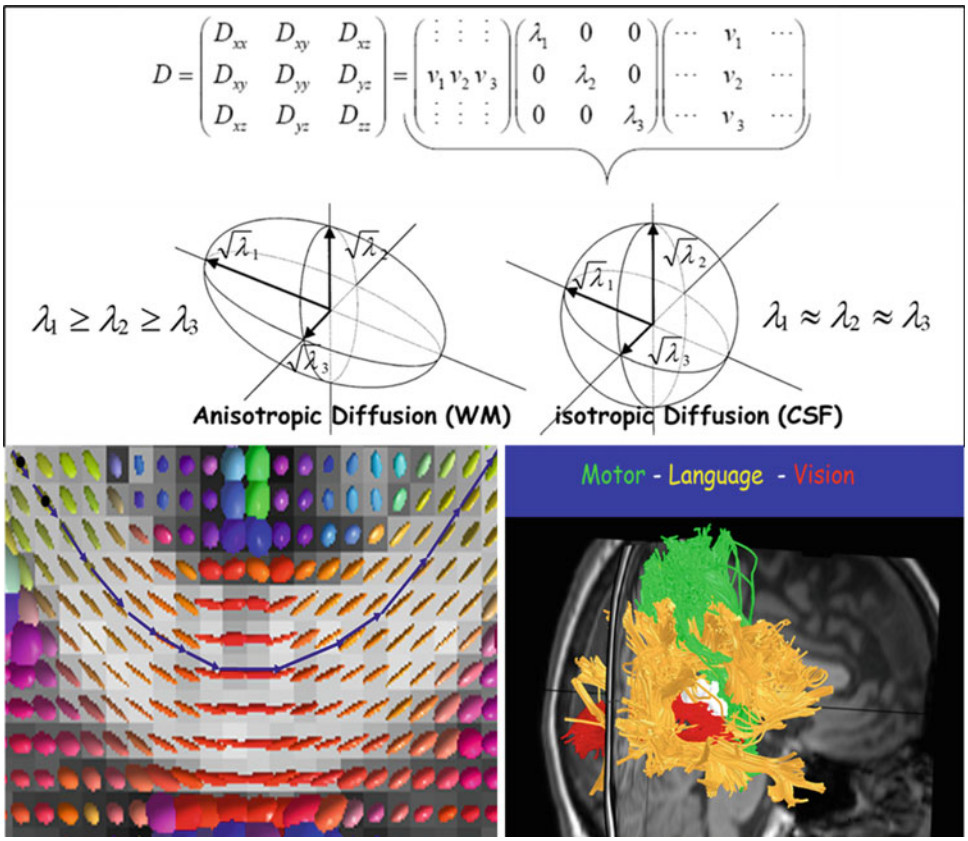


Fig. 4 The diffusion tensor model (top) can be fitted at each voxel (bottom, left), providing a principal direction of diffusion (long axis of the colored ellipsoids) that can be tracked to reconstruct white matter tracts. The resulting diffusion tensor imaging tractography (bottom, right) is used for neurosurgical navigation: motor tracts (green), arcuate tracts (gold), and optic radiation tracts (red), surrounding the target lesion (white)

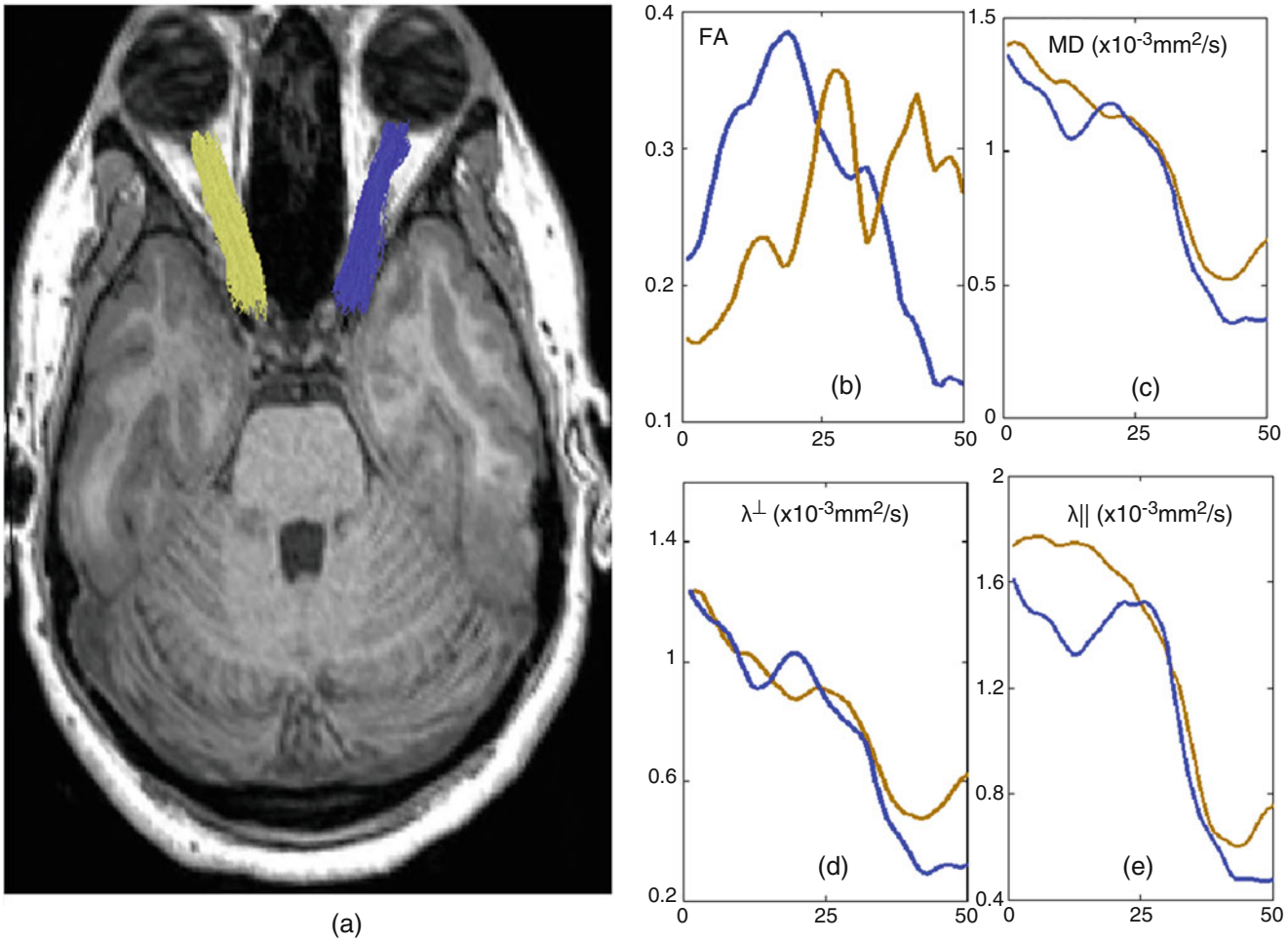


Fig. 5 A preliminary result for the full-length tractography of the optic nerves by probabilistic tractography on a single subject: (**a**) Left (blue) and right (yellow) optic nerves from the optic bulb to the optic chiasm; (**b**)–(**e**) DTI signal sampled along the optic nerves at 50 equidistant points. Applications such as this hold the potential to detect axonal atrophy and demyelination processes in the optic nerve. (Courtesy of Arnaldo Mayer)

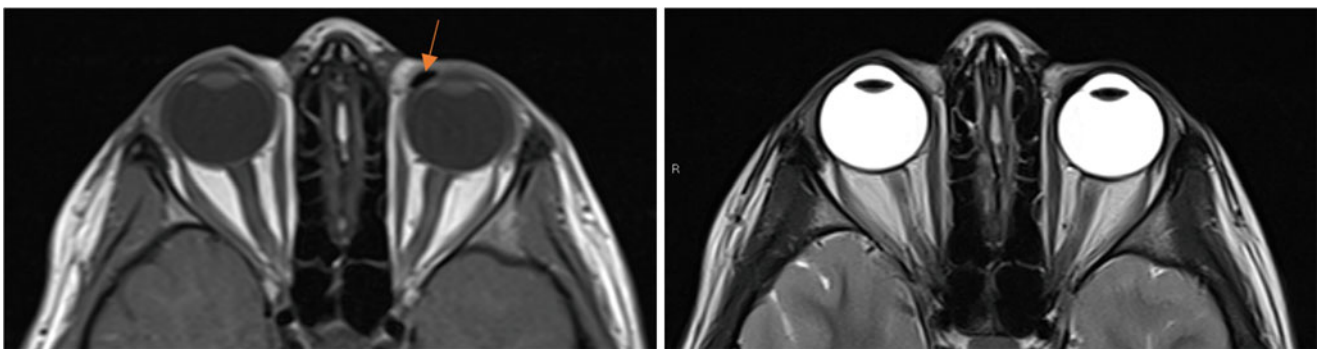


Fig. 6 Axial T1W (left) and T2W (right) images of the orbits. Note the optic nerves are isointense to brain WM. Occasionally trapped air under the eyelid may appear as a focus of "signal void" (arrow)

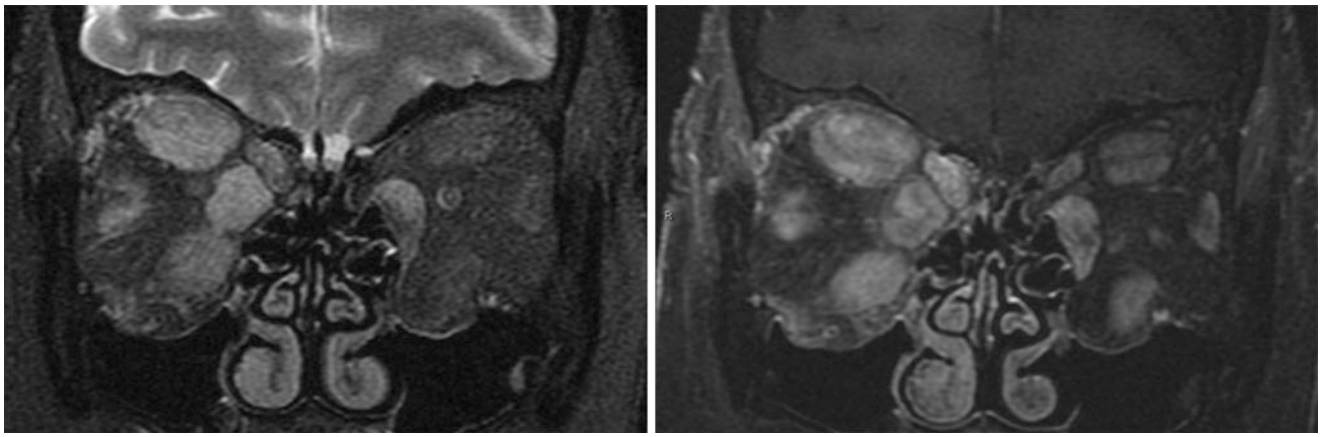


Fig. 7 A 70-year-old female patient with active TED. Cor T2 FS (left) and T1 post-contrast FS (right). The fat suppression augments the edematous and enhancing muscle groups on both sides, more remarkable in the right orbit



Fig. 8 Axial T1w non-enhanced, non-FS image (left), followed by early (middle) and late (right) post-contrast T1 FS images. The lesion at the right orbital apex shows the classical appearance of a venous malformation with typical incremental contrast opacification (this lesion is erroneously termed cavernous hemangioma which is a misnomer). The suppression of the orbital fat allows a nice delineation of the lesion and keeps it from "blending in" with the surrounding bright fatty content

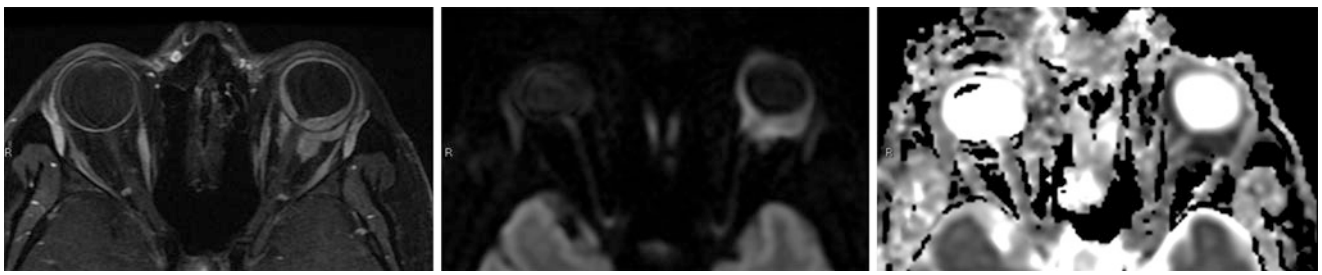


Fig. 9 Orbital lymphoma. Ax T1 post-contrast FS image (left) portraying left sided diffuse choroidal thickening mainly in the posterior globe with retrobulbar involvement. The high signal on the diffusion image (middle) and corresponding low signal on the ADC map (right) indicate restriction of water molecular diffusion in keeping with a highly cellular tumor mass

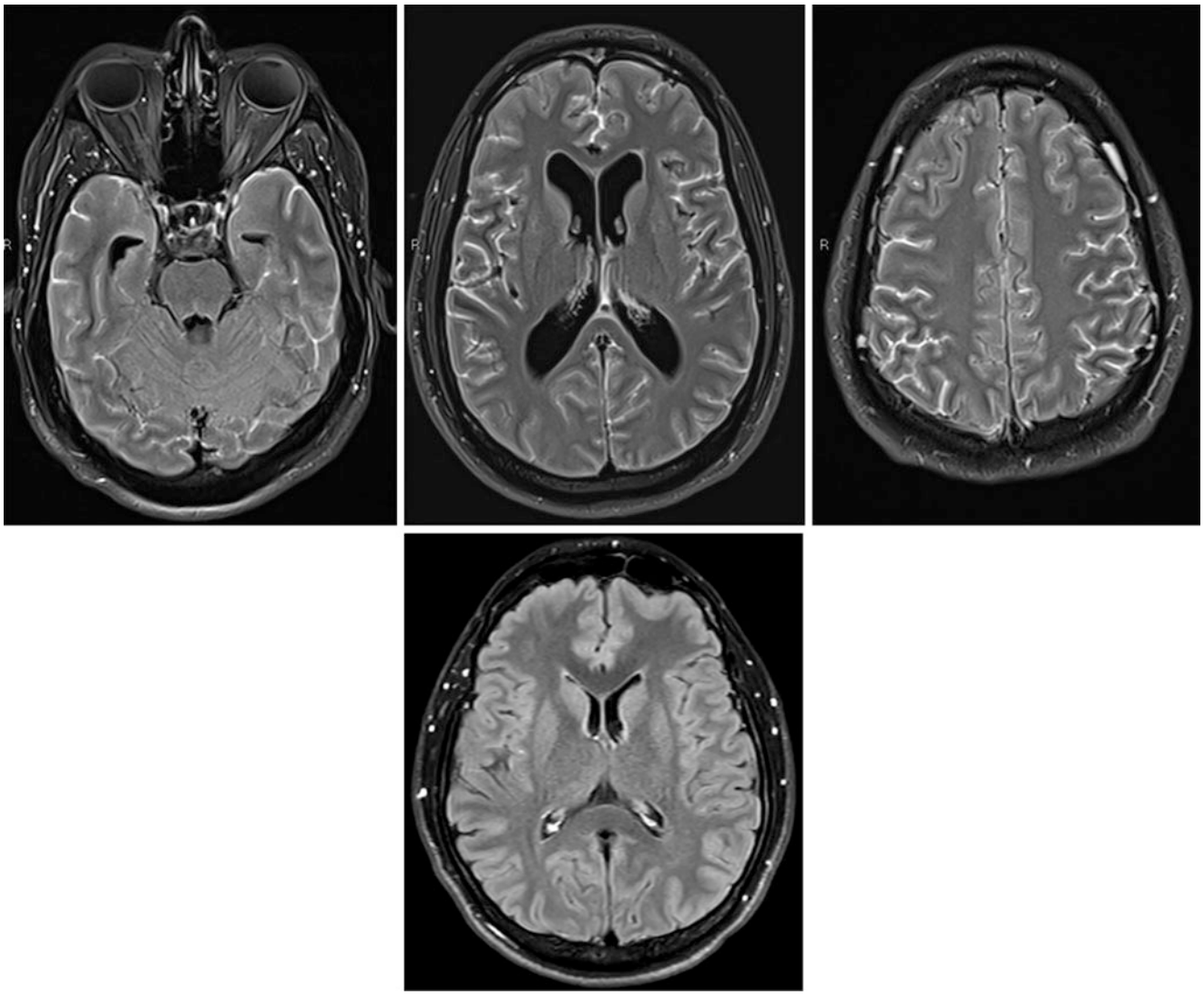


Fig. 10 T2 FLAIR post-contrast images of a melanoma patient with leptomeningeal spread (top). Note diffuse hyperintensity of the brain sulci representing massive pial involvement. Brain ventricles are also mildly dilated. Compare with a normal T2 FLAIR image (bottom)

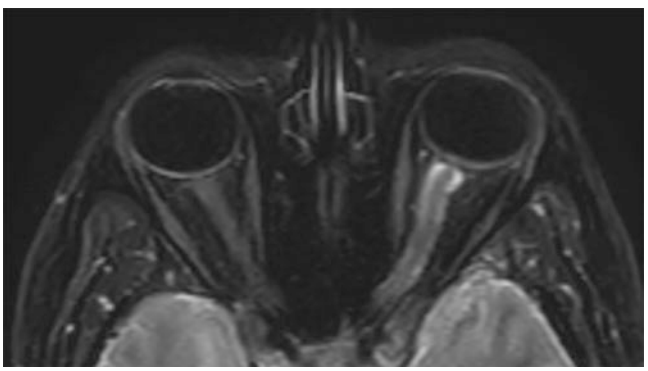


Fig. 11 T2 FLAIR post-contrast image (same patient as above), 9 months later there is obvious seeding of the left optic nerve sheath with associated proptosis

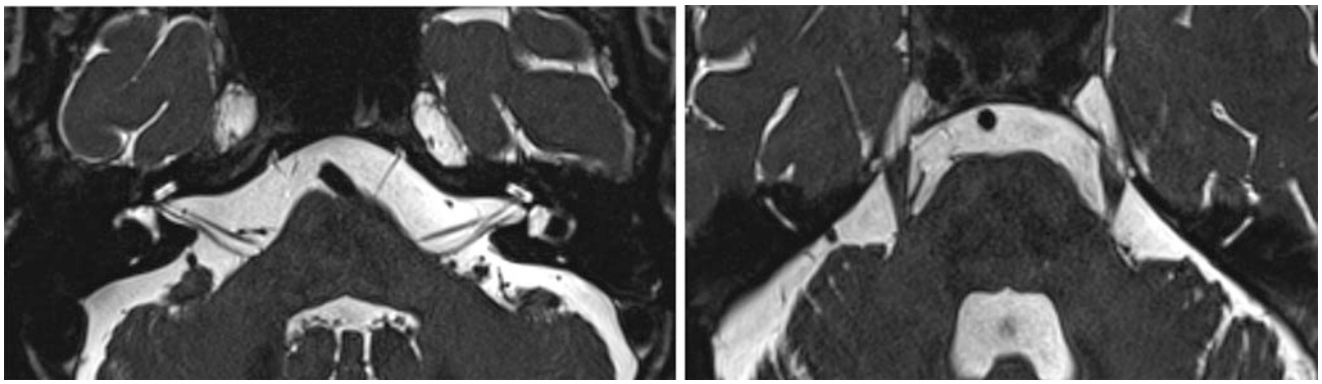


Fig. 12 T2 SPACE_tra_iso 0.5 mm. The CSF provides a great contrast for depicting the cisternal portion of the cranial nerves. Right – trigeminal nerves, Left – abducens, facial, and vestibulocochlear nerves

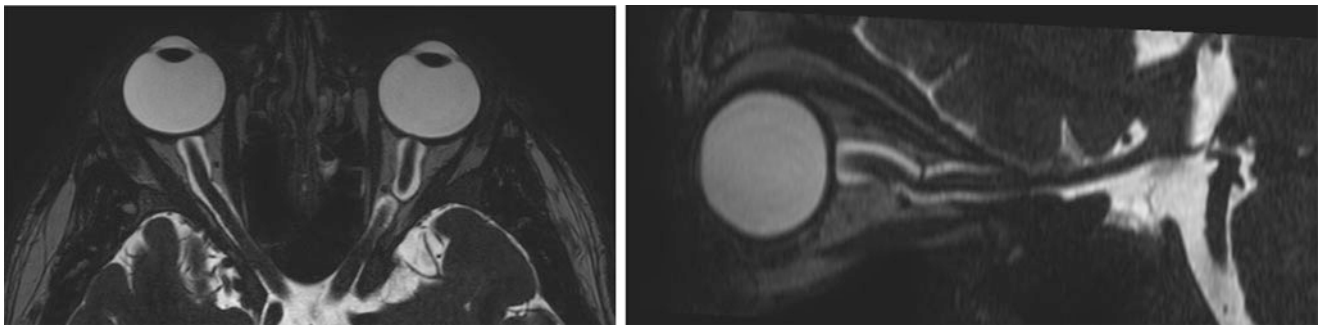


Fig. 13 3D DRIVE axial 1 mm image of the optic nerves (left). The apparent "interrupted" nerve on the left is merely an artifact, resulting from a convoluted sheath. Using MPR tools one can generate a full length reformat of the tortuous optic complex (right)

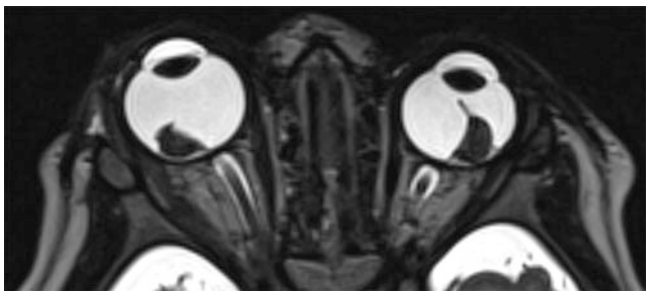


Fig. 14 Ax T2 SPACE. A 6-month-old male with bilateral retinoblastomas. The 0.5 mm slices provide superb detail of the ocular masses and their relation to the choroid and optic discs

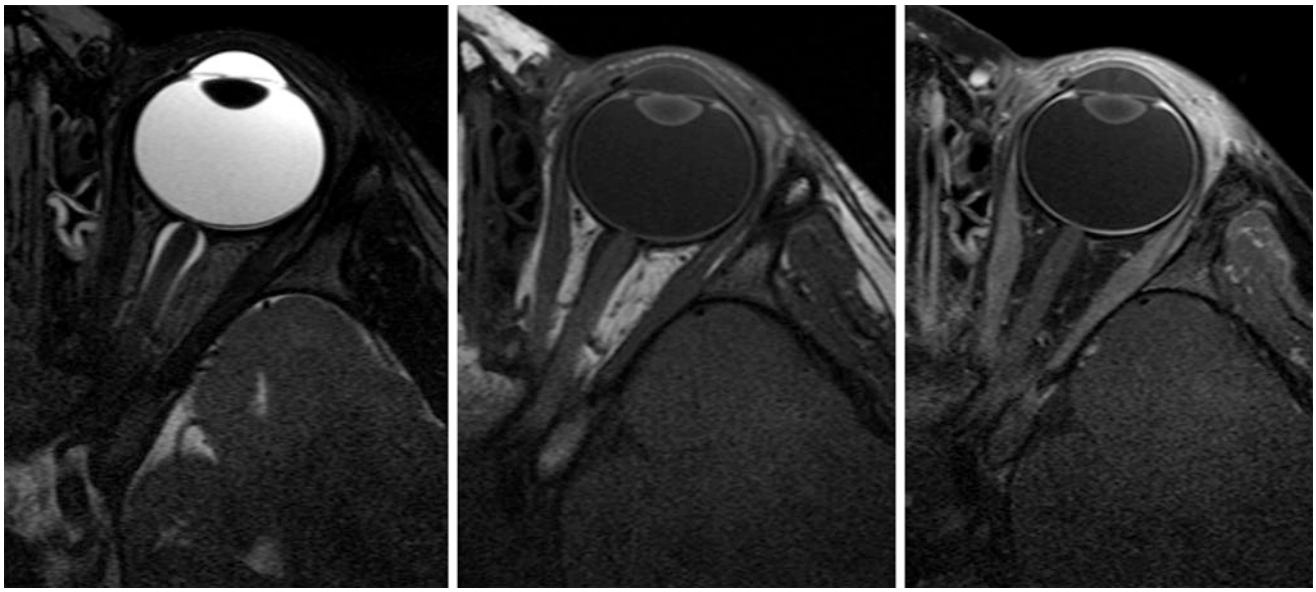


Fig. 15 Axial high-res scans of the left orbit using a surface coil, featuring T2W (left), T1W (middle), and T1W FS post-contrast images (right). The proximity of the coil allows exquisite delineation of the ocular content including the anterior chamber, ciliary bodies, vitreous, choroid/retina surfaces, optic nerve, and adjacent structures. (Courtesy Dr. Graaf P)

References

1. Vlaardingerbroek MT, Boer JA. Magnetic resonance imaging: theory and practice: Springer Science & Business Media; 2013.
2. Liang ZP, Lauterbur PC. Principles of magnetic resonance imaging: a signal processing perspective: SPIE Optical Engineering Press; 2000.
3. Le Bihan D, Turner R, Douek P, Patronas N. Diffusion MR imaging: clinical applications. AJR Am J Roentgenol. 1992;159(3):591–9.
4. Le Bihan D, Mangin JF, Poupon C, Clark CA, Pappata S, Molko N, Chabriat H. Diffusion tensor imaging: concepts and applications. J Magn Reson Imaging. 2001;13(4):534–46.
5. Basser PJ, Pajevic S, Pierpaoli C, Duda J, Aldroubi A. In vivo fiber tractography using DT-MRI data. Magn Reson Med. 2000;44(4): 625–32.
6. Guy J, Mao J, Bidgood WD Jr, Mancuso A, Quisling RG. Enhancement and demyefination of the intraorbital optic nerve: fat suppression magnetic resonance imaging. Ophthalmology. 1992;99(5):713–9.
7. Fukuoka H, Hirai T, Okuda T, Shigematsu Y, Sasao A, Kimura E, Hirano T, Yano S, Murakami R, Yamashita Y. Comparison of the added value of contrast-enhanced 3D fluid-attenuated inversion recovery and magnetization-prepared rapid acquisition of gradient echo sequences in relation to conventional postcontrast T1-weighted images for the evaluation of leptomeningeal diseases at 3T. AJNR Am J Neuroradiol. 2010;31(5):868–73.
8. Chavhan GB, Babyn PS, Jankharia BG, Cheng HL, Shroff MM. Steady-state MR imaging sequences: physics, classification, and clinical applications. Radiographics. 2008;28(4):1147–60.

Orbital CTA/CTV

13

Denise S. Kim, Remy R. Lobo, and Alon Kahana

Contents

1 **Overview** 113
2 **Indications** 113
3 **Technique and Protocol Considerations** 113
4 **Figures with Captions** 114
References 116

Abstract

Computed tomography angiography (CTA) and venography (CTV) provide a noninvasive approach to evaluating arterial and venous blood flow in the characterization of normal and abnormal tissue vascular beds. The use of these imaging modalities has become more powerful over the years, providing not only outstanding resolution of vascular channels but also concomitant assessment of surrounding human tissue. An understanding of these modalities and their utility can improve patient care.

Keywords

Computed · Tomography · Angiography · Venography · Aneurysm · Orbit · Vascular malformation · AVM

D. S. Kim
Department of Ophthalmology and Visual Sciences, University of Michigan Medical School, Ann Arbor, MI, USA
e-mail: kimden@med.umich.edu

R. R. Lobo
Department of Radiology, University of Michigan Medical School, Ann Arbor, MI, USA
e-mail: remylobo@med.umich.edu

A. Kahana (✉)
Ophthalmology Department, Oakland University William Beaumont School of Medicine, Rochester, MI, USA

Attending Surgeon, Consultants in Ophthalmic and Facial Plastic Surgery, Southfield, MI, USA

1 Overview

Computed tomography angiography (CTA) and computed tomography venography (CTV) utilize ionizing radiation and intravascular contrast to obtain sequential radiographic images timed to evaluate arterial and venous structures, respectively. These techniques can be used as a non-invasive alternative to digital subtraction angiography (DSA) for evaluation of aneurysms, orbital vascular malformations, and arteriovenous fistulas.

2 Indications

- Aneurysms, pseudoaneurysms, varices
- Orbital vascular malformations
- Arteriovenous fistulas
- Acute complications of trauma
- Venous and dural sinus thrombosis (CTV)
- Vascular anatomic variants
- Pre- and Post- intervention surveillance

3 Technique and Protocol Considerations

To obtain CTA or CTV imaging, a thin section spiral CT is acquired with a power injection of intravenous iodinated contrast medium through a catheter capable of

© Springer Nature Switzerland AG 2022
G. Ben Simon et al. (eds.), *Atlas of Orbital Imaging*,
https://doi.org/10.1007/978-3-030-62426-2_86

accommodating a rate of 4–5 mL/s. During CTA, a test bolus of contrast is injected to identify the carotid arteries and a region of interest is designated over the selected artery. Further contrast is injected at a set rate; when the attenuation within the selected artery rises to a predetermined level, the acquisition of images is triggered so that contrast is optimized for the evaluation of arterial structures. During CTV, the acquisition of images is generally a set timed-delay of 90–120 s after injection of contrast. For both CTA and CTV, acquisition of images is completed rapidly, within seconds.

With CTA [1], evaluation of vascular structures can be obtained non-invasively, rapidly, and with high spatial resolution. CTA has an added benefit of evaluation of intracranial vasculature abnormalities such as atherosclerosis, aneurysms, and vasculitis. CTA is limited by less soft tissue detail in comparison to magnetic resonance angiography (MRA).

4 Figures with Captions

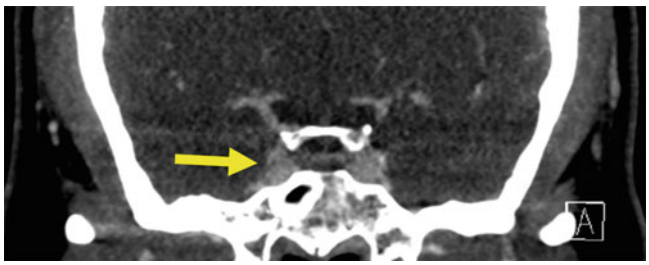


Fig. 1 Coronal CT with contrast (venous phase) at the level of the cavernous sinus, showing an example of a normal cavernous sinus. Cranial nerves III, IV, V1, and V2 positioned along the lateral wall (yellow arrow), usually not visible on CT. Cavernous sinus opacifies well in the venous phase

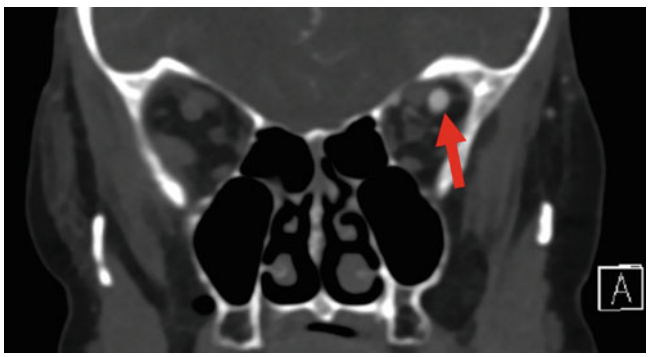


Fig. 2a Coronal CTA at the mid orbit shows arterialized flow in the left SOV (red arrow). This 61-year-old female patient was struck by a deer

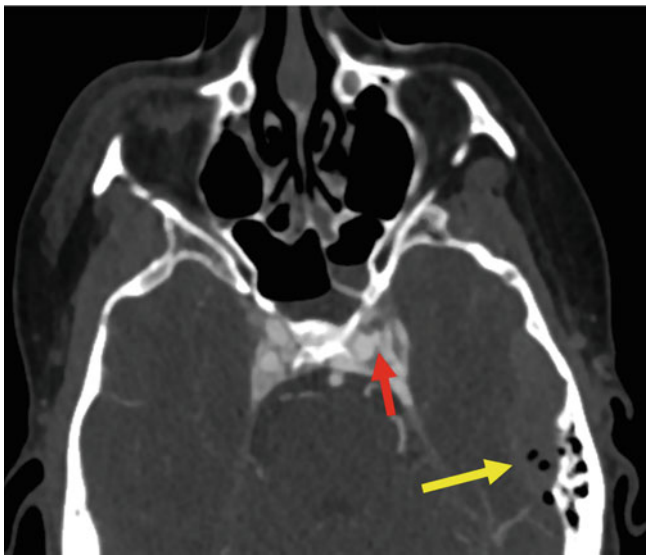


Fig. 2b Axial CTA at the inferior orbit level in the same trauma patient shows the direct left carotid cavernous fistula, CCF (red arrow). Note additional post trauma sequela, left convexity extra-axial blood and gas (yellow arrow)

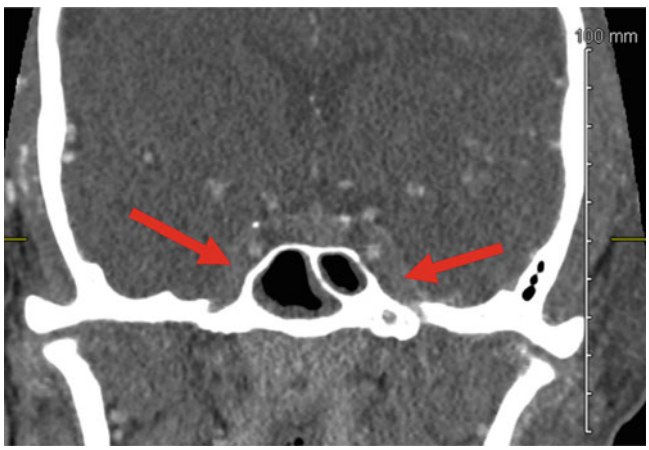


Fig. 3 Coronal CTV showing non-opacification of both cavernous sinuses in keeping with bilateral cavernous sinus thromboses (red arrows) in an immunocompromised patient with sinusitis (compare with Fig. 1)

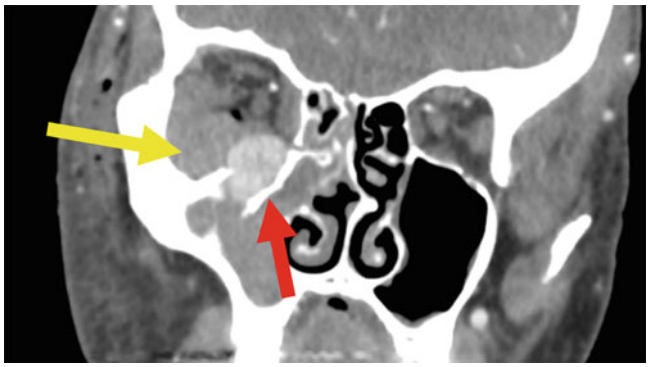


Fig. 4 Coronal CTA at the mid right orbit level in a trauma patient shows an orbital floor defect, adjacent hematoma (yellow arrow), and round enhancing lesion (red arrow) which was found to be a pseudoaneurysm

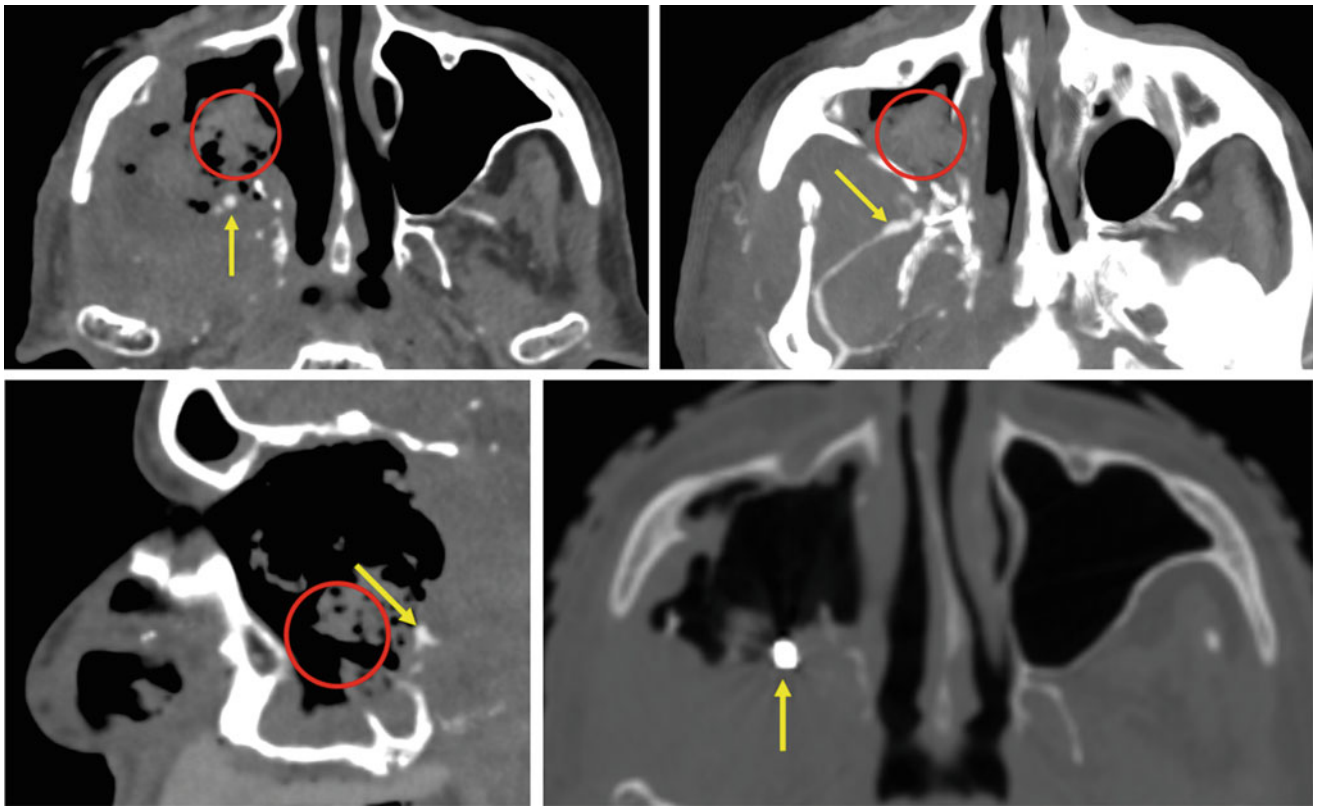


Fig. 5 CTA of a 77-year-old male post extended right orbital exenteration for recurrent sphenoid wing meningioma. The patient had episodes of brisk bleeding. *Left* images demonstrate the pseudoaneurysm at the surgical site (*yellow arrows*) behind a bandage (*red circles*). MIP CTA (*upper right*) showing the pseudoaneurysm is related to the right internal maxillary artery. The patient underwent endovascular coiling with closure of the pseudoaneurysm and resolution of symptoms as demonstrated on non-ontrast enhanced axial CT (*lower right, arrow*); note the radiotherapy mask as the patient was prepared for additional treatment for tumor recurrence

References

1. ACR-ASNR-SPR (2014) ACR–ASNR–SPR practice parameter for the performance and interpretation of cervicocerebral computed tomography angiography (CTA) Res. 20—2010, Amended 2014 (Res. 39). Available from www.acr.org Accessed: 7 July 2020.

Orbital MRA/MRV

14

Denise S. Kim, Remy R. Lobo, and Alon Kahana

Contents

1 **Indications** 117
2 **Technique and Protocol Considerations** 117
3 **Figures with Captions** 118
References 120

Abstract

Magnetic resonance angiography (MRA) and magnetic resonance venography (MRV) enable noninvasive imaging of vascular structures without using ionizing radiation. Pulse sequences are constructed to generate signal from blood flow by taking advantage of variable magnetic relaxation properties and magnetic susceptibilities. MRA/MRV in conjunction with MRI offer excellent soft tissue detail while utilizing vascular characteristics to help identify different lesions. Both sequences can be performed either with or without contrast.

Keywords

Magnetic resonance · Angiography · Venography · Orbit · Vascular anomaly

D. S. Kim
Department of Ophthalmology and Visual Sciences, University of Michigan Medical School, Ann Arbor, MI, USA
e-mail: kimden@med.umich.edu

R. R. Lobo
Department of Radiology, University of Michigan Medical School, Ann Arbor, MI, USA
e-mail: remylobo@med.umich.edu

A. Kahana (✉)
Ophthalmology Department, Oakland University William Beaumont School of Medicine, Rochester, MI, USA

Attending Surgeon, Consultants in Ophthalmic and Facial Plastic Surgery, Southfield, MI, USA

1 Indications

- Aneurysms, pseudoaneurysms, varices
- Orbital vascular malformations in the pre- and post-intervention setting
- Arteriovenous fistulas
- Arterial or venous occlusive processes
- Vascular anatomy in the perioperative setting of tumor resection
- Complications of trauma
- Vascular anatomic variants

2 Technique and Protocol Considerations

MRA is a broad term referencing multiple techniques [1]. These can be separated into two categories: techniques in which blood appears brighter than surrounding tissue and those in which blood appears relatively darker. Bright blood sequences are numerous and commonly used in orbital imaging; these can be either contrast enhanced or non-contrast enhanced. Dark blood sequences include Fast Spin Echo (FSE), Inversion Recovery (IR), and Susceptibility-Weighted Imaging (SWI), which are rarely used in orbital imaging (possibly in elucidating orbital vessel wall thickening in the context of vasculitis) [2].

Contrast-enhanced (CE) MRA uses injected gadolinium to increase conspicuity of vascular structures by shortening the T1 relaxation time. Images can be acquired before, during,

© Springer Nature Switzerland AG 2022
G. Ben Simon et al. (eds.), *Atlas of Orbital Imaging*,
https://doi.org/10.1007/978-3-030-62426-2_87

and after injection of gadolinium, and subtraction maps can be created to isolate vascular structures.

Non-contrast-enhanced MRA techniques are more numerous and more commonly used. The most popular of these is Time-of-Flight (TOF) MRA, in which radiofrequency pulses are used to saturate a slab of tissue, after which imaging can track the flow of fresh, unsaturated blood (that is aligned to the magnetic field) into the saturated tissue. Arterial Spin Labeling (ASL) MRA is a non-contrast technique used to assess relative perfusion of tissue. Steady-State Free Precession (SSFP) MRA, like True FISP, is a gradient-based technique with limited application in the orbit. Phase-contrast (PC) MRA and Fast Spin Echo (FSE) MRA are rarely used in the orbit.

MRV of the orbit can be performed using TOF, CE, and, less commonly, PC imaging techniques, modified to focus on the venous structures.

Time-resolved imaging techniques – such as TWIST (Siemens), TRICKS (GE), 4D-TRAK (Philips), TRAQ (Hitachi), and Freeze Frame (Toshiba) – are contrast-enhanced techniques in which serial images are rapidly obtained through a volume of tissue, enabling a temporal examination of both arterial and venous anatomy. The resulting images appear similar to those acquired with digital subtraction angiography (DSA), but without the associated risks of invasive access, and with the added benefit of soft tissue imaging. These dynamic imaging techniques are useful for evaluating arteriovenous malformations and assessing collateralization. It is helpful for the ordering clinician to share the expected flow velocity characteristics of the lesion so that the study can be timed correctly, using triggering techniques with relatively low contrast dose.

Benefits of MRA include: concurrent performance of MRI allowing excellent soft tissue detail, spatial resolution of less than 1 mm enabling volumetric data, which can be used for navigation or creating reformats, and the ability to acquire images directly in any plane as well as in a supine or prone position. MRA is advantageous over DSA in that it is noninvasive, avoiding the small risks of neurologic deficits or circulatory compromise, and provides concurrent soft tissue imaging. MRA is advantageous over both DSA and CTA in that it avoids ionizing radiation and the use of iodinated contrast. Because MRA techniques do not utilize ionizing radiation, serial imaging can be performed rapidly and safely over a volume of tissue to show changes in vascular patterns of enhancement. MRA (like MRI) is limited by artifacts due to patient motion, vascular flow, and metal. MRA may not be a practical choice for patients with significant claustrophobia, altered mental status, or difficulty lying flat. In children, MRA of diagnostic quality often requires sedation. Clinicians should also be aware of the possibility of nephrogenic systemic fibrosis with administration of gadolinium for CE MRA in at-risk patients.

3 Figures with Captions

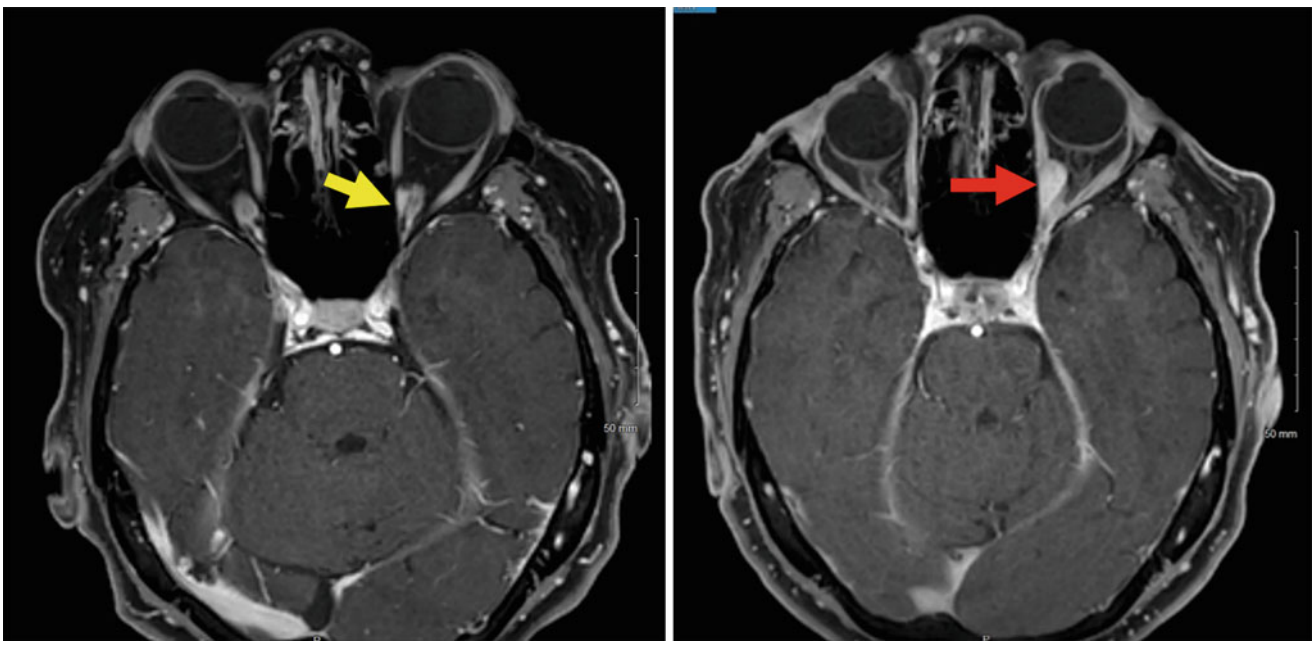


Fig. 1 Orbital varix. Left axial T1 + C FS supine, right T1 + CFS prone. Intraconal lesion (yellow arrow) near the left orbital apex while supine. The lesion (red arrow) increases in size with prone imaging

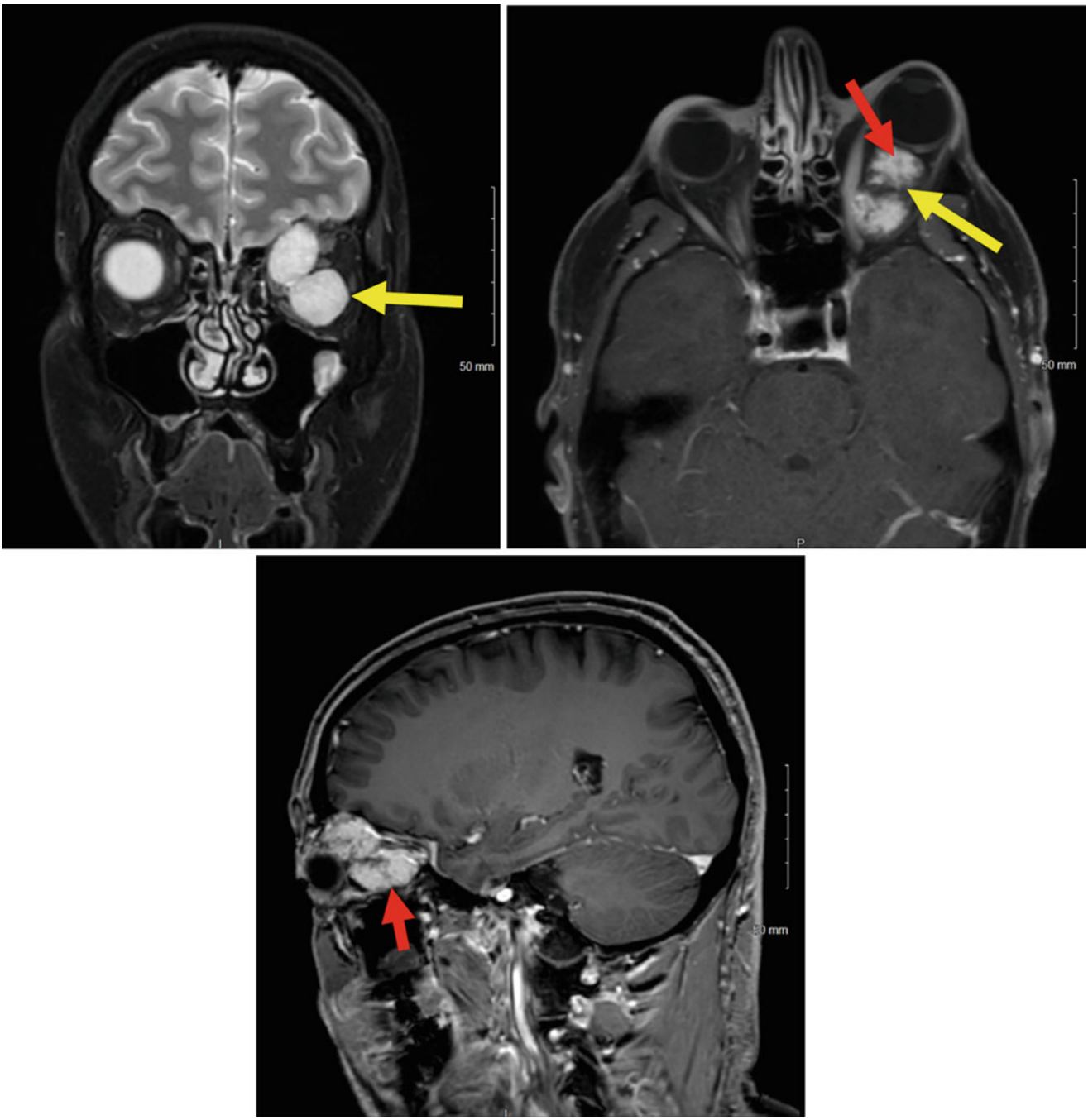


Fig. 2 Orbital cavernous venous vascular malformation (cavernous hemangioma). *Upper left* – coronal T2 FS shows the bilobed T2 hyperintense intraconal lesion (yellow arrow). *Upper right* – axial T1 + C FS shows primarily central enhancement of the lesion (red arrow) and incomplete peripheral filling (yellow arrow). *Lower image* – sagittal delayed SPGR post-contrast T1 shows more complete (now peripheral) filling in of contrast at the left intraconal bilobed lesion (red arrow)

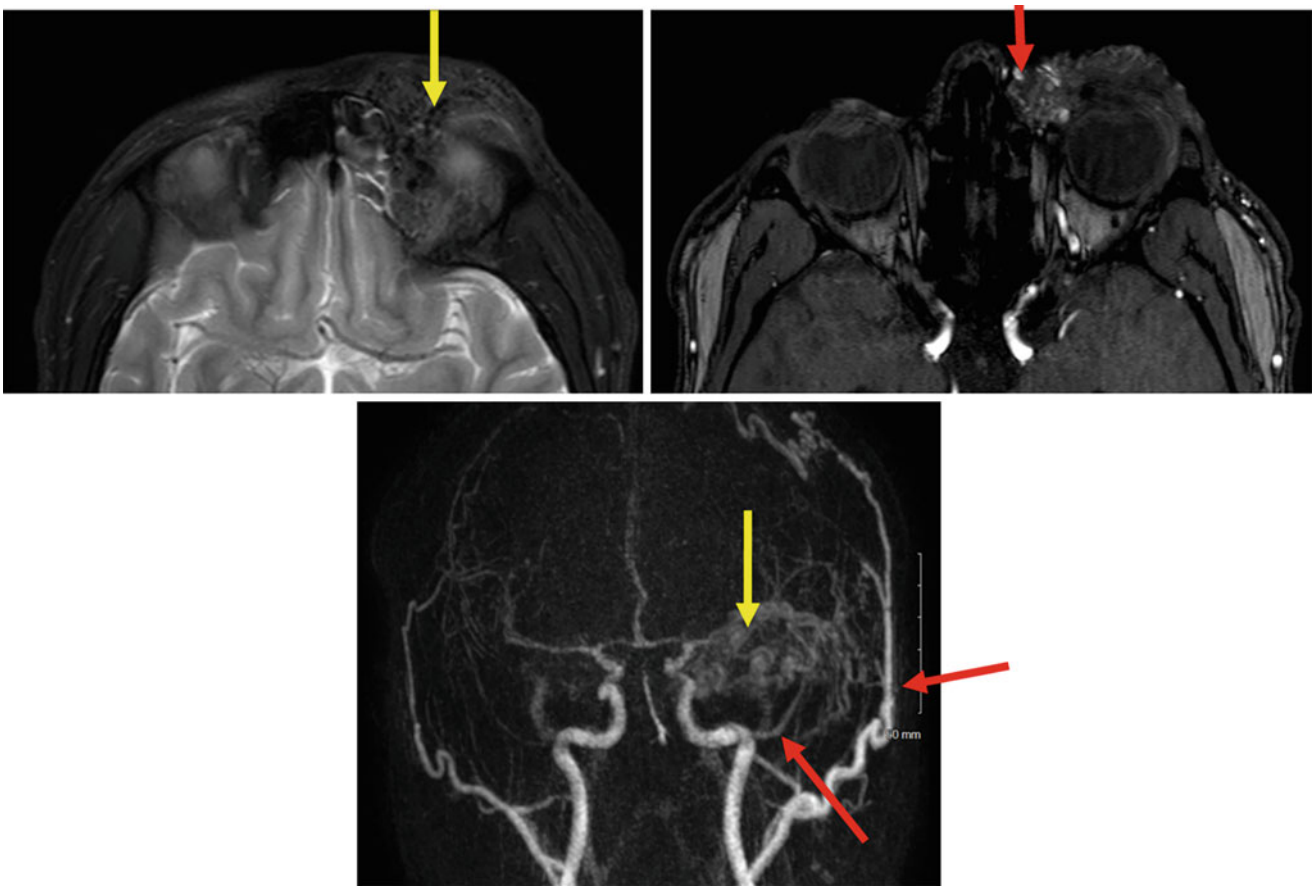


Fig. 3 Orbital arteriovenous malformation. *Upper left* – axial T2 FS at the level of the superior orbit, shows expanded left upper lid and frontal brow soft tissue with tubular T2 hypointense flow voids (yellow arrow). *Upper right* – axial non-contrast TOF MRA at the level of the lenses shows flow-related enhancement within the left medial canthal region, suggesting an arterial component (red arrow). *Lower image* – coronal MIP from time-resolved MRA shows multiple regions of enhancement. This image is from the early arterial phase and shows the early arterial component (yellow arrow). The lesion is supplied from hypertrophied ophthalmic and superficial temporal arteries (red arrows); i.e., the lesion is supplied from both the internal and external carotid artery branches

References

1. ACR–ASNR–SNIS–SPR. ACR–ASNR–SNIS–SPR practice parameter for the performance of cervicocerebral magnetic resonance angiography (MRA) Res. 10 – 2015. Available from http://www.acr.org. Accessed 7 July 2020.
2. Stacey AW, Gemmete JJ, Kahana A. Management of orbital and periocular vascular anomalies. Ophthalmic Plast Reconstr Surg. 2015;31(6):427–36. https://doi.org/10.1097/IOP.0000000000000504.

Intraoperative Dynamic Imaging

15

Denise S. Kim, Remy R. Lobo, Neeraj Chaudhary, and Alon Kahana

Contents

1 **Overview** 121
2 **Indications** 122
3 **Technique and Protocol Considerations** 122
4 **Figures with Captions** 123
References 125

Abstract

Intraoperative imaging is a cornerstone of interventional vascular procedures and is becoming increasingly important in functional neurosurgery and tumor excision surgery. Dynamic intraoperative imaging is particularly useful for vascular procedures, enabling a real-time delineation of vascular channels and blood flow characteristics. Because of the lack of tissue resolution in the majority of dynamic intraoperative vascular imaging techniques, a thorough knowledge of anatomy is essential. Having a preexisting MRI or CT for clinic-radiologic correlation is helpful.

Keywords

Dynamic · MRA · CTA · Angiogram · Vascular anomaly · Orbit · Orbital

1 Overview

Dynamic, real-time intraoperative imaging utilizing angiography and/or fluoroscopy facilitates performance of minimally invasive techniques to treat a variety of orbital lesions. Angiography and fluoroscopy use ionizing radiation (X-rays) which are passed through the patient and absorbed on a detector,

D. S. Kim
Department of Ophthalmology and Visual Sciences, University of Michigan Medical School, Ann Arbor, MI, USA
e-mail: kimden@med.umich.edu

R. R. Lobo
Department of Radiology, University of Michigan Medical School, Ann Arbor, MI, USA
e-mail: remylobo@med.umich.edu

N. Chaudhary
Department of Radiology, University of Michigan Medical School, Ann Arbor, MI, USA

Department of Neurosurgery, University of Michigan Medical School, Ann Arbor, MI, USA

Department of Neurology, University of Michigan Medical School, Ann Arbor, MI, USA

Department of Otorhinolaryngology, University of Michigan Medical School, Ann Arbor, MI, USA
e-mail: neerajc@med.umich.edu

A. Kahana (✉)
Ophthalmology Department, Oakland University William Beaumont School of Medicine, Rochester, MI, USA

Attending Surgeon, Consultants in Ophthalmic and Facial Plastic Surgery, Southfield, MI, USA

© Springer Nature Switzerland AG 2022
G. Ben Simon et al. (eds.), *Atlas of Orbital Imaging*,
https://doi.org/10.1007/978-3-030-62426-2_112

generating a series of images in real time which the neurointerventional radiologist interprets to guide the procedure [1].

Catheter-based angiography, most commonly achieved through femoral access and passage of small catheters/wires into the orbital vasculature, can provide exquisite anatomical detail of facial and orbital vascular malformations. Angiography requires contrast media to visualize structures of interest and their relation to pathology, to characterize the arterial and venous components of lesions, and to identify pathways for treatment. In addition to its diagnostic use, angiography is also used to treat arteriovenous shunt malformations, aneurysms, venous varices, neoplasms (via intra-arterial targeted chemotherapy), and other processes [2–4].

Dynamic fluoroscopy allows the safe percutaneous placement of a needle directly into orbital vascular malformations. Navigating a safe tract requires knowledge of bony landmarks and expected locations of vulnerable structures, such as the optic nerve. Fluoroscopy is primarily utilized for percutaneous sclerotherapy of low flow lesions (e.g., lymphatic and venolymphatic malformations). During sclerotherapy, contrast media is used to confirm the needle location prior to injection of sclerosants.

Cone-beam CT is a supplemental imaging technology that provides intraoperative CT-like images in the angiography suite. It is acquired by rapidly rotating the flat panel fluoroscopy detector around the patient. Acquisition of images in multiple planes allows visualization in three dimensions rather than the static plane of angiography or fluoroscopy, which is useful for problem-solving in complex cases.

2 Indications

- Angiography: Diagnosis and treatment of high-flow vascular malformations such as arteriovenous shunts (arteriovenous fistula and arteriovenous malformation), treatment of aneurysms, sclerosing of varices, presurgical or therapeutic embolization of vascular neoplasms, and intra-arterial targeted chemotherapy of orbital malignancy such as retinoblastoma.
- Fluoroscopy: Sclerosing of lymphatic or venolymphatic malformations and presurgical embolization (injection of glue prior to surgical removal of lesion).

3 Technique and Protocol Considerations

Scout images are obtained to orient the patient and define the regions of acquisition, most commonly in the supine position. Images are usually acquired in anterior-posterior and medial-lateral planes, though the detectors can rotate freely to create oblique angles of approach. Physical exam identifies the access points such as femoral artery for angiography. Fluoroscopic procedures are often guided by established bony landmarks, which correlate with other noninvasive imaging modalities. Sterile technique is employed for all procedures. Attention is also paid to cumulative exposure time given use of ionizing radiation in image acquisition.

Angiography begins with femoral access, after which small catheters and wires are passed retrograde up the aorta to the carotid artery, with subselection into the orbital vessels. Roadmaps are obtained to define the vasculature and subsequent safe placement of microcatheters. These catheters are employed to embolize lesions with intravascular sclerosants (doxycycline, bleomycin, ethanol, and sodium tetradecyl sulfate), particulate material (polyvinyl alcohol), or liquid embolics (ethylene vinyl alcohol and n-butyl cyanoacrylate glue). Micro-balloons can be floated to a particular spot where they are inflated just prior to treatment, to limit treatment to a particular anatomic location and minimize outflow.

Fluoroscopy uses real-time image acquisition to guide needle placement into the expected location of a lesion. Contrast media is injected to confirm positioning. Once positioning is adequate, sclerosants can be injected to treat the target. On occasion, a two-needle technique is employed where one needle is placed and used to allow egress of contents of a lesion, while the second needle is used to inject/treat the lesion.

Benefits of these techniques stem mainly from directed therapeutic responses that cause specific cicatrization of pathologies, which obviates the need for aggressive surgical intervention. When used as an adjuvant prior to surgery, these techniques can decrease blood loss and optimize a more complete resection with smaller exposure. Drawbacks stem mainly from the risks of intervention, specifically nontarget embolization. This includes a small-stroke risk from catheter angiography, and other inadvertent vascular insults, particularly around the eye and ophthalmic artery.

4 Figures with Captions

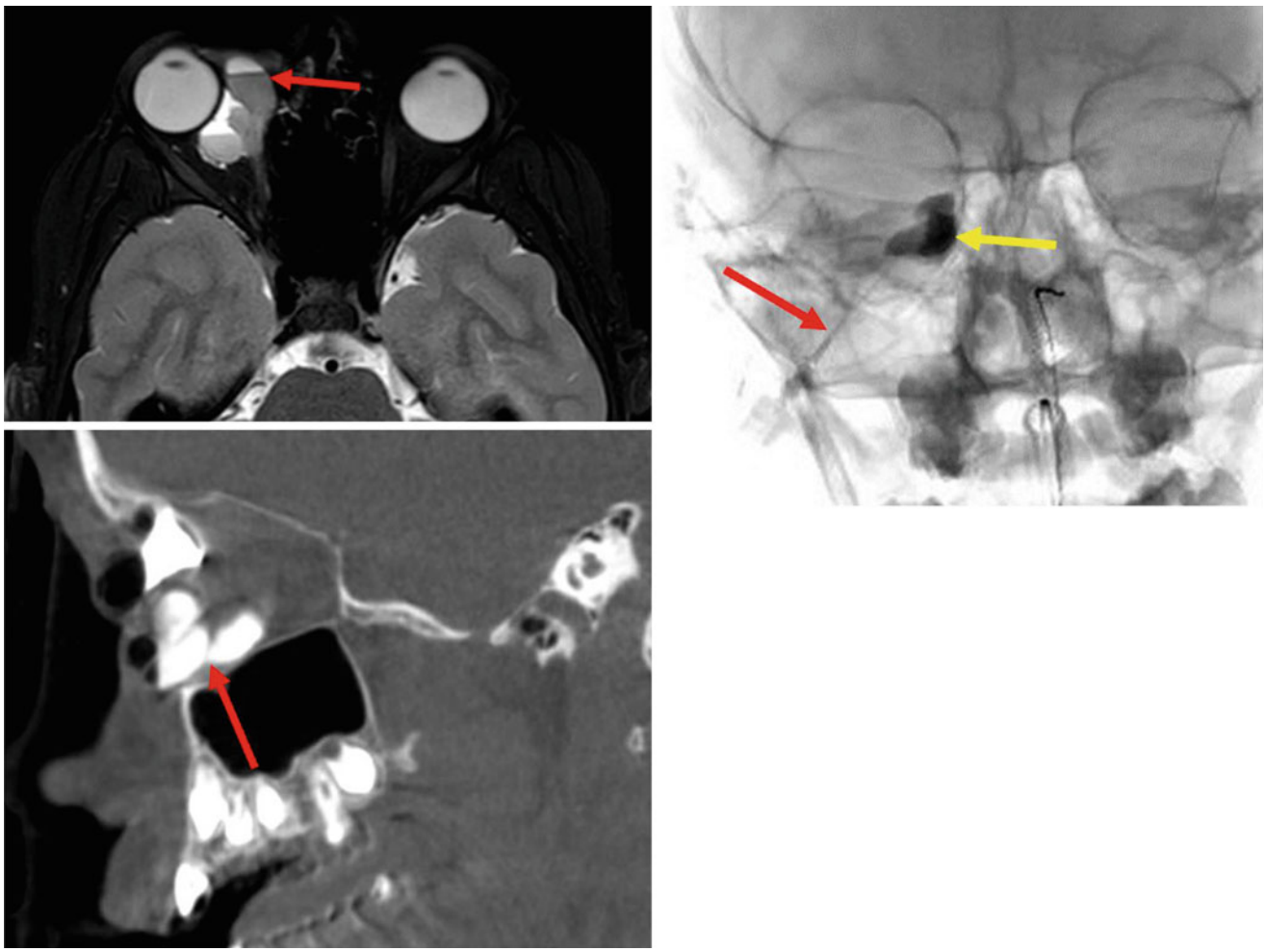


Fig. 1 Orbital venolymphatic malformation. (**a**) Axial T2 FS shows a right orbital lesion with fluid-fluid levels (red arrow), most suggestive of lymphatic malformation. (**b**) Intraoperative fluoroscopic image showing right infraorbital (red arrow) approach and contrast placement in the target lesion (yellow arrow). (**c**) Intraoperative dynamic CT, sagittal reformat, confirms contrast within the target lesion (red arrow) prior to sclerosis

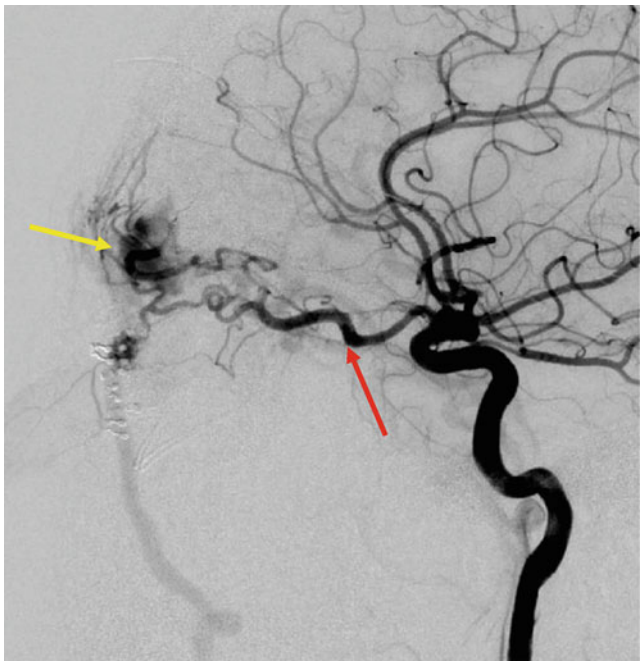


Fig. 2 Lateral projection DSA (digital subtraction angiography) from right internal carotid artery injection shows hypertrophied ophthalmic artery (red arrow) as the primary supply to an upper eyelid arteriovenous malformation (yellow arrow)

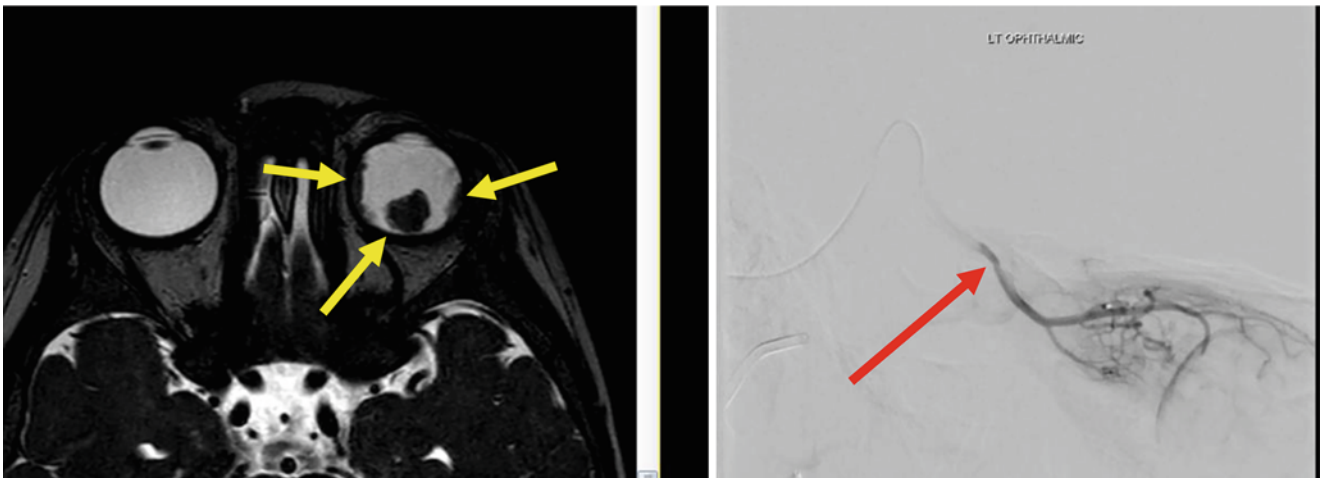


Fig. 3 T2 WI axial view of a 1.7 YO boy with left eye multifocal retinoblastoma (left image, yellow arrows) and intra-arterial neoadjuvant chemotherapy (right image DSA) with direct ophthalmic artery catheterization (red arrow)

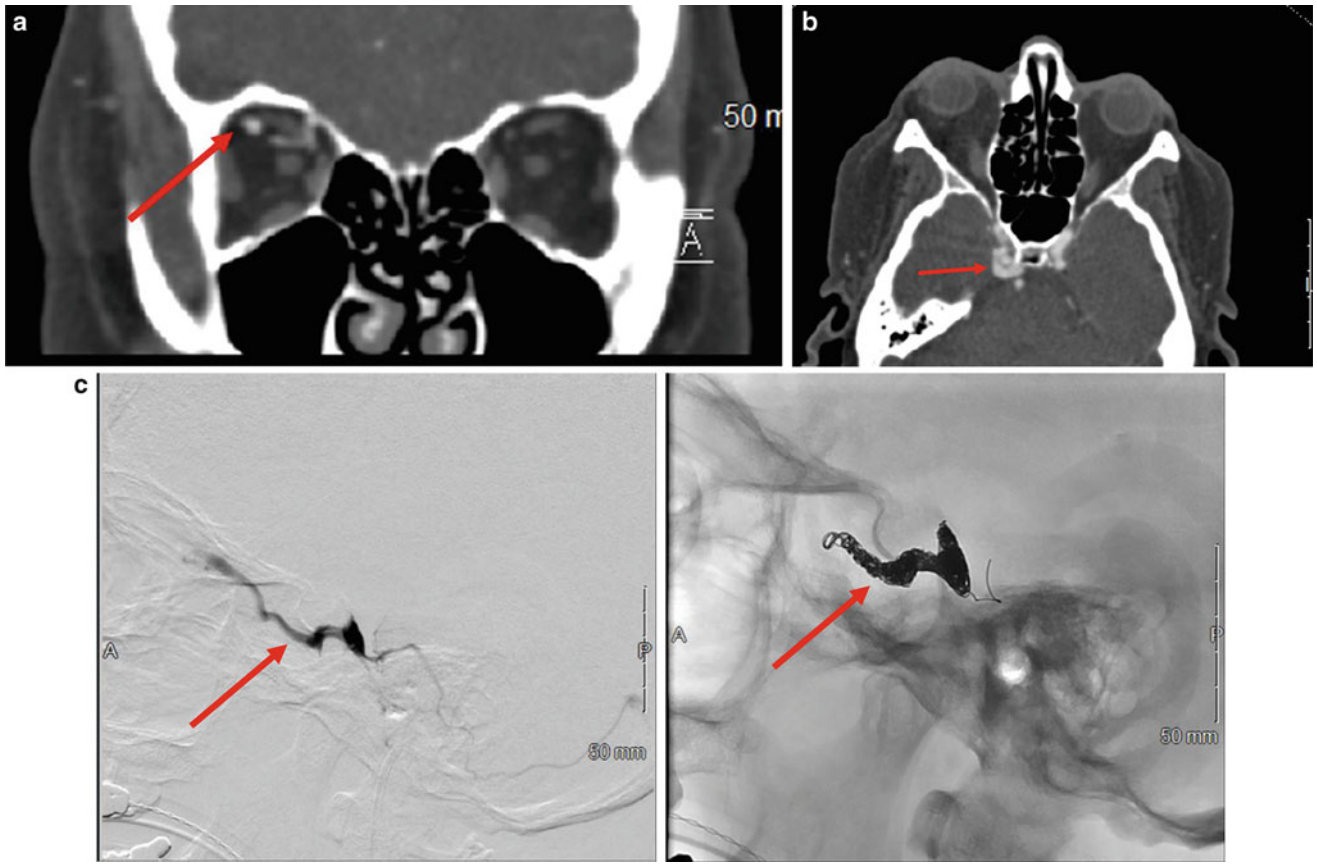


Fig. 4 (**a**) Coronal CTA in a 67-year-old female with right proptosis, note the arterialized flow in the right SOV (red arrow) (**b**) Axial CTA in the same patient shows asymmetric arterialized flow in the right cavernous sinus (red arrow) (**c**) Pretreatment lateral projection DSA image, venous injection, showing enlarged SOV (red arrow). (**d**) Posttreatment unsubtracted lateral fluoroscopic image showing the coil pack (red arrow) used to embolize the CCF

References

1. ACR–ASNR–SIR–SNIS. ACR–ASNR–SIR–SNIS practice parameter for the performance of diagnostic cervicocerebral catheter angiography in adults Res. 5–1999, Amended 2018 (Res. 44). 2018. Available from http://www.acr.org. Accessed 7 July 2020.
2. Stacey AW, Gemmete JJ, Kahana A. Management of orbital and periocular vascular anomalies. Ophthalmic Plast Reconstr Surg. 2015;31(6):427–36. https://doi.org/10.1097/IOP.0000000000000504.
3. Ozgonul C, Chaudhary N, Hutchinson R, Archer SM, Demirci H. Fluorescein angiography findings in both eyes of a unilateral retinoblastoma case during intra-arterial chemotherapy with melphalan. Int J Ophthalmol. 2019;12(12):1987–9. https://doi.org/10.18240/ijo.2019.12.24.
4. Vadlamudi V, Gemmete JJ, Chaudhary N, Pandey AS, Kahana A. Transvenous sclerotherapy of a large symptomatic orbital venous varix using a microcatheter balloon and bleomycin. BMJ Case Rep. 2015;2015:bcr2015011777. https://doi.org/10.1136/bcr-2015-011777.

Ultrasound of Orbit Tumors and Tumorlike Lesions

16

Bernadete Ayres and Alon Kahana

Contents

1 Introduction 128

2 Transducers and Frequencies 128

3 Technique of Examination 129

4 Probe Orientation 129

5 Probe Position 130

6 B-Scan Screening Exam 130

7 Normal Ultrasound Anatomy of the Orbit and Periorbital Region 130

8 Cysts and Celes 131
8.1 Microphthalmos with Orbital Cyst 131
8.2 Respiratory Epithelial Cysts of the Orbit 132
8.3 Dermoid Cyst 133
8.4 Orbital Mucocele 134

9 Vascular Anomalies 134
9.1 Infantile Hemangioma (Former Capillary Hemangioma) 134
9.2 Cavernous Venous Malformation (Former Cavernous Hemangioma) 135
9.3 Orbital Venous-Lymphatic Malformation (Former Lymphangioma) 135

10 Orbital Inflammatory Diseases 137
10.1 Thyroid Eye Disease 137
10.2 Idiopathic Orbital Inflammation (Orbital Pseudotumor) 138

11 Tumors of Lymphoid and Hematopoietic Tissues 140
11.1 Orbital Lymphoma 140
11.2 Orbital Plasmacytoma 140

12 Epithelial Tumors of the Lacrimal Gland 140
12.1 Pleomorphic Adenoma (Benign Mixed Tumor) 140
12.2 Adenoid Cystic Carcinoma 141

13 Tumors of Primitive Mesoderm 142
13.1 Rhabdomyosarcoma 142

B. Ayres
Department of Ophthalmology, University of Michigan Medical School, Ann Arbor, MI, USA
e-mail: mbayres@med.umich.edu

A. Kahana (✉)
Ophthalmology Department, Oakland University William Beaumont School of Medicine, Rochester, MI, USA

Attending Surgeon, Consultants in Ophthalmic and Facial Plastic Surgery, Southfield, MI, USA

© Springer Nature Switzerland AG 2022
G. Ben Simon et al. (eds.), *Atlas of Orbital Imaging*,
https://doi.org/10.1007/978-3-030-62426-2_113

14 Primitive Neuroectodermal Tumors 145
14.1 Neuroblastoma 145

References 146

Abstract

Ultrasound is a noninvasive, first-line imaging method for orbital disease, providing accurate detection and tissue differentiation of orbital and periorbital pathologies. The dynamic nature of the exam allows to establish the kinetic characteristics of the lesions such as its consistency and vascularity. Moreover, ultrasound is a nonionizing, cost-effective, and readily available imaging technique. However, it requires a high level of expertise to perform and interpret.

Keywords

Acoustic impedance · Adenoid cystic carcinoma · A-scan · B-scan · Cavernous venous malformation · Dermoid cyst · Frequency · Gain · Idiopathic orbital inflammation · Infantile hemangioma · Malignant glaucoma · Microphthalmos with orbital cyst · Neuroblastoma · Orbital cavernous hemangioma · Orbital lymphoma · Orbital mucocele · Orbital plasmacytoma · Orbital rhabdomyosarcoma · Orbital venous-lymphatic malformation · Pleomorphic adenoma · Probe · Reflectivity · Respiratory epithelial cysts of the orbit · Rhabdomyosarcoma · Thyroid eye disease · Transducer · Ultrasound

1 Introduction

Due to its anatomical and histological composition, the orbit and ocular adnexal areas have a wide spectrum of juxtaposed tissues, including skin, bone, ocular globe, muscles, nerves, meninges, fat, vessels, lacrimal gland, and others. This diversity of tissues is a key reason of the multiplicity of orbital disease processes comprising congenital, inflammatory, and neoplastic disorders.

The in-depth history and comprehensive systemic and ophthalmic examinations are essential in the assessment of a patient with orbital pathology. Of course, the histopathological exam, either by fine needle aspiration or incisional/excisional biopsy, is the gold standard in the definitive diagnosis of orbital lesions of unknown etiology. In both straightforward or challenging diagnosis, complementary imaging techniques involving computed tomography (CT), magnetic resonance (MR), and ultrasonography can provide crucial information for differential diagnosis, medical therapy, and surgical planning.

Ultrasound is a noninvasive, first-line imaging method, which can provide accurate detection and tissue differentiation of orbital and periorbital pathologies. The dynamic nature of the exam allows to establish the kinetic characteristics of the lesions such as its consistency and vascularity. Moreover, ultrasound is a nonionizing, cost-effective, and readily available imaging technique.

2 Transducers and Frequencies

Ultrasound uses high frequency sound waves, which are reflected, deflected, or absorbed in the tissues. The returning waves (echoes) are processed by the instrument and displaying two types of images: A-scan or B-scan, as shown in Fig. 1.

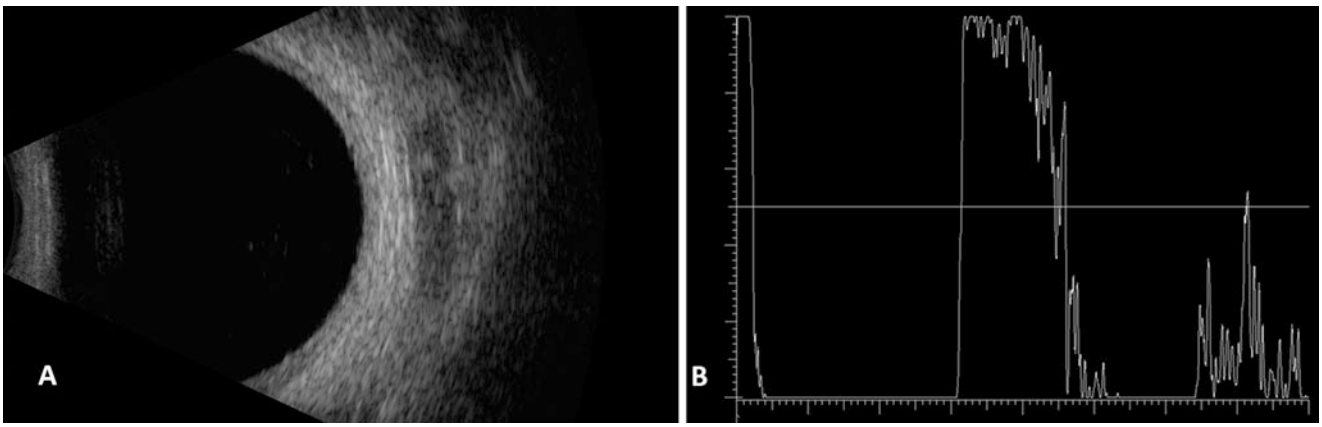


Fig. 1 Normal eye ultrasound images: (**a**) B-scan echogram; (**b**) A-scan echogram

In ocular imaging, the most commonly used frequency in B-scan transducers is 10 MHz, which can provide an axial resolution of 100 μm. More recently, higher frequency B-probes have been introduced allowing for better imaging resolution at the posterior pole and orbit. A standardized A-scan probe commonly operates at a frequency of 8 MHz. A lower frequency of 8 MHz is used to obtain the penetration needed to reach the orbital apex.

3 Technique of Examination

The exam can be conducted with the patient in supine or sitting position. A methylcellulose-based gel, used as coupling agent, is applied to the probe face. The probe is placed opposite to the area being examined, and the exam can be performed either with the open eye under topical anesthesia, or conducting the exam through the lids. The latter is more comfortable for the patient, particularly when the patient experiences pain in contact between the eye and the probe, and also allows a somewhat greater range of probe movement.

The B-scan probe has a white mark near the tip that indicates the top of the screen display. Because the lens produces considerable sound absorption, it can be avoided by placing the probe face at the limbal area.

4 Probe Orientation

There are three basic B probe orientations used to evaluate the globe, orbit, and periorbital regions:

- ***Transverse scan***, which produces a circumferential slice through a certain quadrant (Fig. 2)
- ***Longitudinal scan***, which produces a radial (or anteroposterior) slice along a certain meridian (Fig. 3)
- ***Axial scan***, where the probe is placed on the cornea of a patient in primary gaze, and the sound beam sweeps along the two opposites meridians (e.g., 12 and 6 on axial vertical scan, or 3 and 9 on axial horizontal scan)

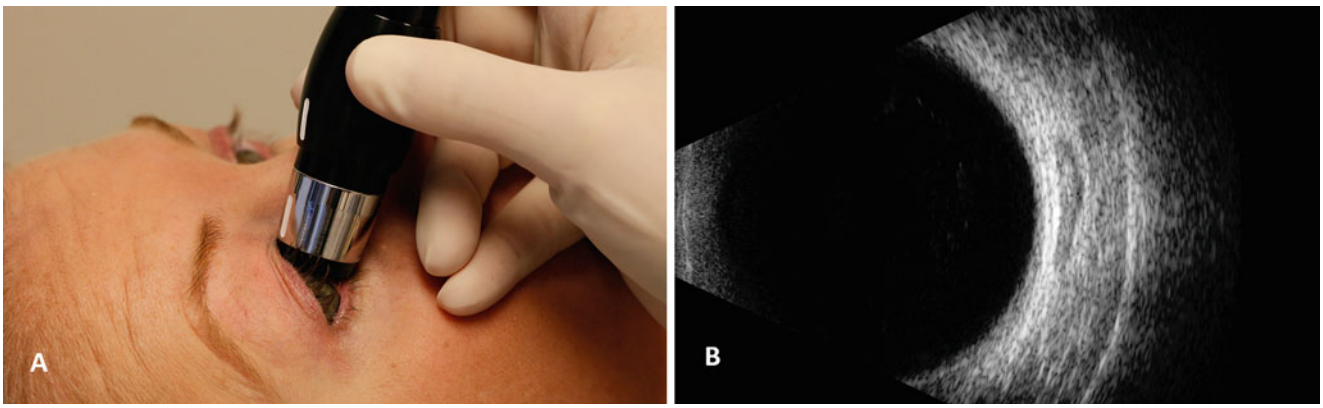


Fig. 2 Transverse B-scan: (**a**) the probe is placed at the nasal limbus with the mark oriented upright; (**b**) resulting echogram of the temporal quadrants

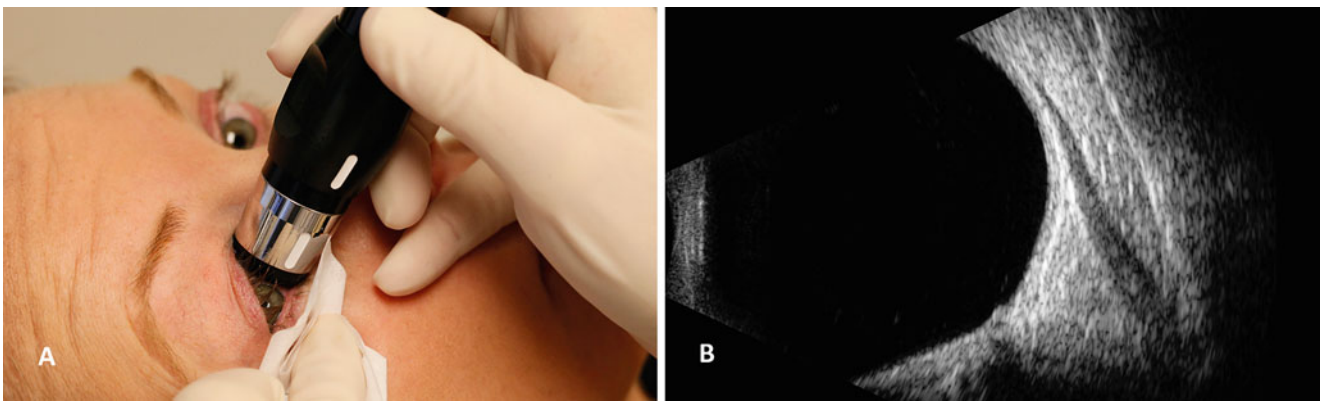


Fig. 3 Longitudinal B-scan: (**a**) the probe is placed at the nasal limbus with the mark oriented toward the center of the cornea; (**b**) resulting echogram of the 9 o'clock meridian

By convention, for transverse scan, the probe mark is oriented:

- ***Upright*** for transverse vertical scans (nasal or temporal fundus image)
- ***Nasally*** for transverse horizontal scans (superior or inferior fundus image)
- ***Upright*** for transverse oblique scans in superonasal, inferonasal, inferotemporal, and superotemporal fundus images
- ***Toward the center of the cornea*** for longitudinal scans, in any meridian

5 Probe Position

The orbit and periorbit are assessed using two basic ultrasound exam techniques:

- ***Transocular approach***, in which the sound travels through the globe (Figs. 2, 3, and 4).
- ***Paraocular approach***, in which the sound beam is aimed surrounding the eye, assessing the anterior region (Fig. 5). The paraocular-modified immersion technique using a finger of glove filled with water allows images of superficial lesions located within the eyelid or the anterior margin of an orbital lesion.

6 B-Scan Screening Exam

A comprehensive ultrasound exam of the orbit is initiated with a transocular transverse B-scan at medium gain setting. The optic nerve is initially identified, providing a landmark to characterize the position of any pathologic condition. The probe is then shifted from the limbus toward the fornix, repeatedly screening all quadrants. If any pathologic condition is detected, a longitudinal scan evaluation must be performed.

The lesion is characterized by the echogenicity, shape, borders, location, extension, and size. Having the patient's eye steady allows the examiner to assess the internal vascularity of a lesion or tumor. An A-scan through the area of greatest interest can complement the B-scan exam to further define internal tissue characteristics such us reflectivity, structure, and sound attenuation.

7 Normal Ultrasound Anatomy of the Orbit and Periorbital Region

The ***soft tissues*** contained in the orbit are primarily fat and connective tissues (fascia and septa) and appear as high reflective images surrounding the globe (Fig. 6). Sound attenuation is observed in the posterior area of the echogram.

The echo-density of ***extraocular muscles*** is lower and is clearly distinct from the surrounding fat. The longitudinal scan can display most of the muscle extension, with a thin inserting tendon and gradual thickening of the muscle belly (Fig. 6a). On a transverse view, the muscles have an ellipsoid shape (Fig. 6b) and the muscle cone demarcates the intraconal and extraconal spaces.

The ***orbital bony walls*** are imaged as an extremely hyperechoic, smooth, linear image at the posterior region of the echogram, and it is followed by an area of acoustic shadow. Expansive periorbital or orbital mass lesions can be associated with bone remodeling or bone erosion.

Ultrasound is a fast diagnostic tool to assess the ***retrobulbar optic nerve*** and serves as a screening method before more invasive tests. In general, on transverse or axial B-scans, the retrobulbar optic nerve appears as a hypoechoic

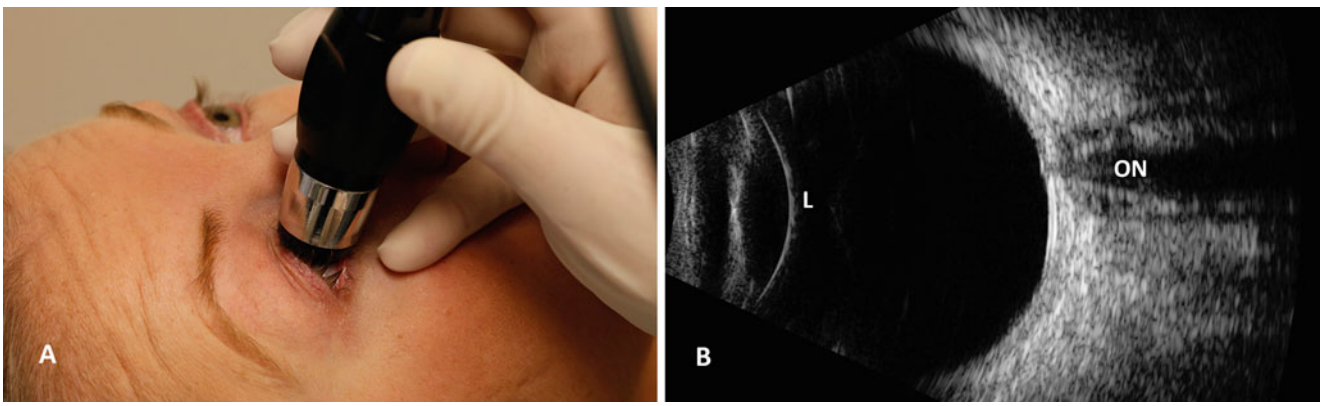


Fig. 4 Axial B-scan: (**a**) the probe is placed on the center of the cornea with patient fixating in primary gaze; (**b**) resulting image of the posterior pole, with two opposing meridians crossed by the optic disc: *L*, posterior lens capsule; *ON*, optic nerve

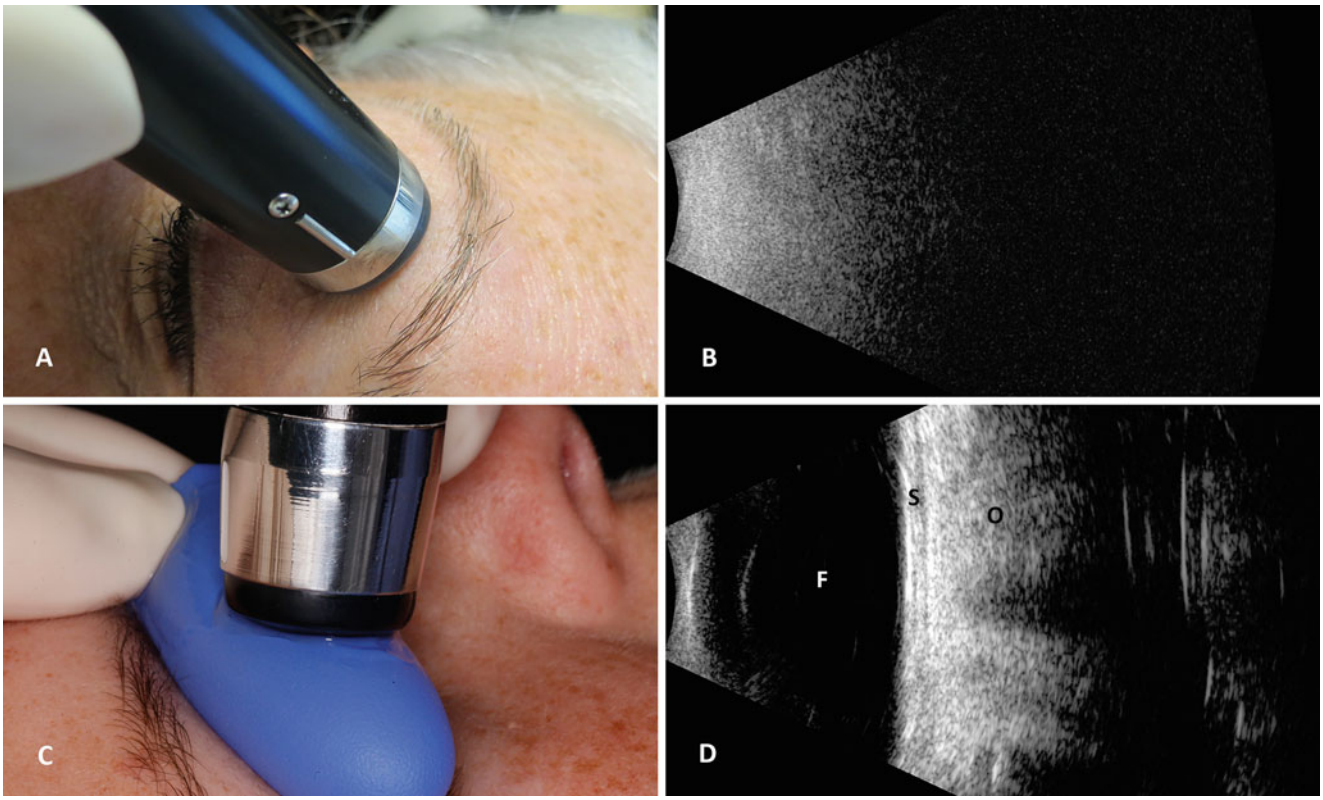


Fig. 5 Paraocular approach: (**a**) the probe is placed on the eyelid, away from the globe, imaging the anterior region of the orbit; (**b**) normal echogram of the soft orbital tissue; (**c**) paraocular-modified immersion using a finger of glove filled with water; and (**d**), resulting echogram; *F*, fluid; *S*, skin; and *O*, soft orbital tissue

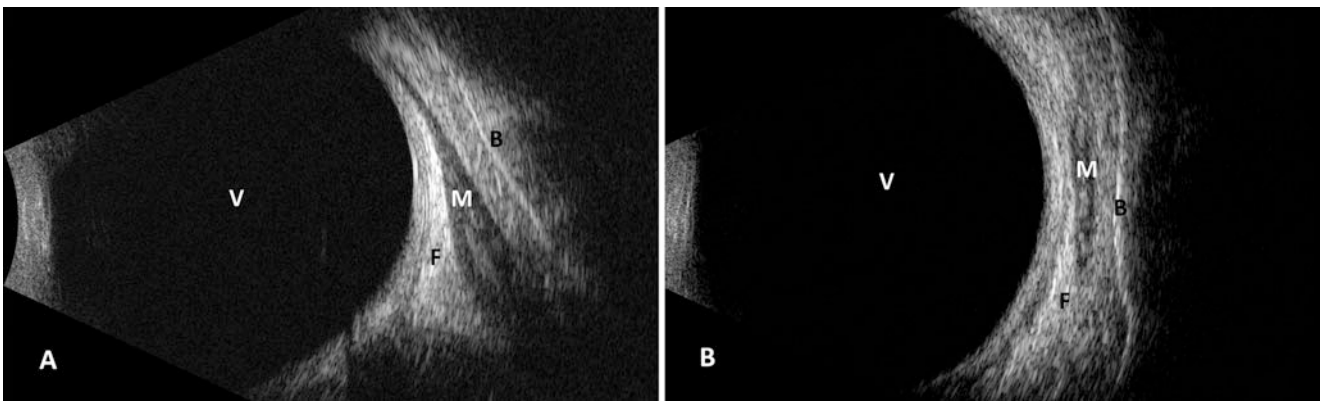


Fig. 6 Normal eye and orbit: (**a**) longitudinal B-scan; (**b**) transverse B-scan; *V*, vitreous cavity; *F*, orbital fat; *M*, muscle; and *B*, bony wall

strip area that comprises the homogeneous nerve parenchyma, lined by hyperechoic perineural meningeal sheaths (Fig. 7a). On A-scan exams, the optic nerve appears as a distinct low-reflective defect bounded by the hyper-reflective perineural sheaths (Fig. 7b).

The normal ***lacrimal gland*** and the adjacent soft orbital tissue have similar levels of acoustic impedance; therefore, these tissues cannot be differentiated from each other under their normal states.

8 Cysts and Celes

8.1 Microphthalmos with Orbital Cyst

Microphthalmos with orbital cyst is a rare, severe congenital anomaly of the globe caused by a defective closure of the embryonic fissure at an early stage and is usually detected in the early neonatal period. The

condition is usually unilateral and may appear either as an isolated finding or in association with other systemic abnormalities [1].

8.1.1 Ultrasonography

Cysts appear as a well-outlined, smooth, low-reflective cavity, usually located inferiorly within the orbit, and displacing the microglobe superiorly (Fig. 8).

8.1.2 Differential Diagnosis

The differential diagnosis of microphthalmos with orbital cyst includes congenital cystic eye, microphthalmia with cystic teratoma, and meningoencephalocele.

8.2 Respiratory Epithelial Cysts of the Orbit

Most commonly, respiratory epithelial cysts are generated orbital trauma or developed as choristomas. Rarely,

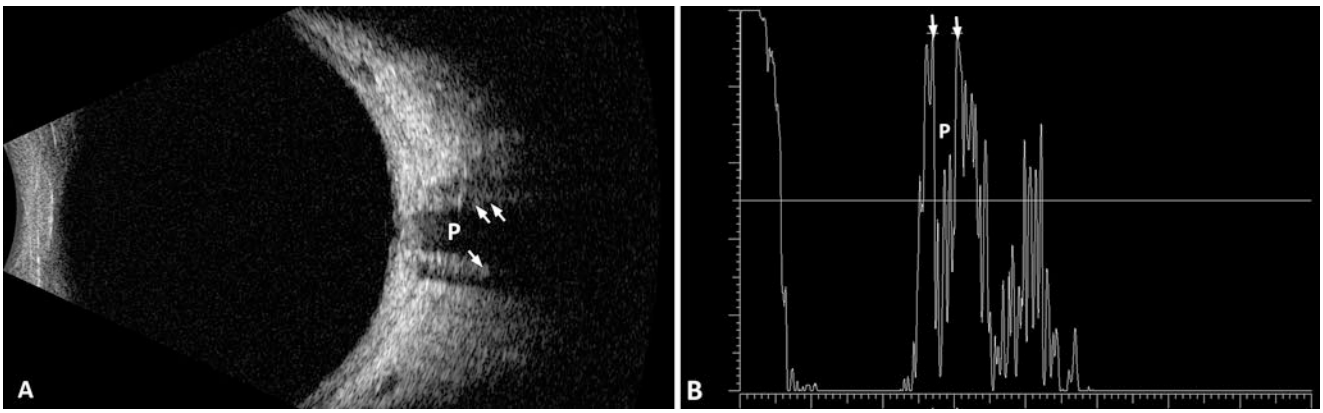


Fig. 7 Normal optic nerve: (**a**) vertical transverse B-scan of retrobulbar optic nerve; (**b**) A-scan echogram of retrobulbar optic nerve; *P*, parenchima; *arrows*, perineural meningeal sheaths

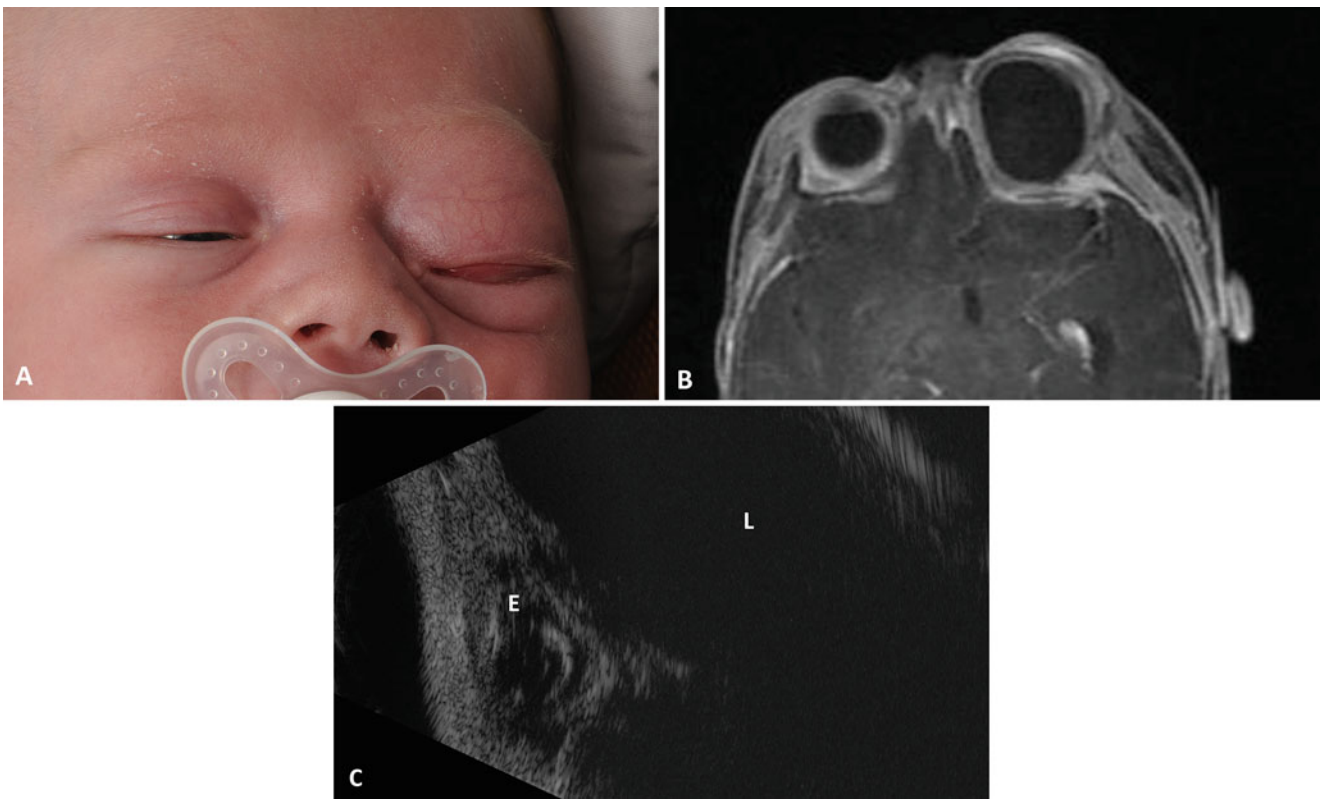


Fig. 8 Microphthalmos with orbital cyst: (**a**) clinical picture; (**b**) T1-weighted axial MR image showing a large left orbital cyst; and (**c**) paraocular immersion B-scan showing a large orbital cystic lesion (*L*) and a rudimentary eye (*E*)

primary orbital cysts lined by the respiratory epithelium will occur without extension from the nasal cavity or paranasal sinuses.

Post-traumatic respiratory epithelial cysts are formed by the proliferation of respiratory epithelium deposited into the orbit through a fracture from previous orbital trauma or following orbital surgery [2].

8.2.1 Ultrasound Features

Respiratory epithelial cysts are typically well-circumscribed, smooth, round-, or oval-shaped lesions. Depending on the amount of mucoid contents, the internal appearance can vary from regularly homogeneous and low-reflective lesions to more heterogeneous images with increased reflectivity (Fig. 9).

8.2.2 Differential Diagnosis

The differential diagnosis of choristomatous respiratory cyst includes dermoid cyst and microphtalmos with orbital cyst. Acquired respiratory cysts must be distinguished from mucocele and hematic cyst.

8.3 Dermoid Cyst

Dermoid cyst is the most frequent orbital tumor, accounting for near 14% of all orbital lesions [3], and it is generated from epithelial sequestration [4]. Clinically, dermoids cysts can be divided into two groups: superficial and deep. They are slow-growing benign lesions; however, they may occasionally rupture and mimic acute inflammation.

8.3.1 Ultrasonography

B-scan will characterize a well-outlined lesion, with a smooth margin and oval or round shape. The internal structure is usually homogeneous and low reflective; however, cysts that are rich of epidermal appendages have a more heterogeneous structure and higher reflectivity (Fig. 10).

8.3.2 Differential Diagnosis

Medial lesions in infants can be confused with congenital encephaloceles, dacryoceles, and mucoceles. Differential diagnosis of lateral lesions includes orbital hemangioma and lacrimal tumors.

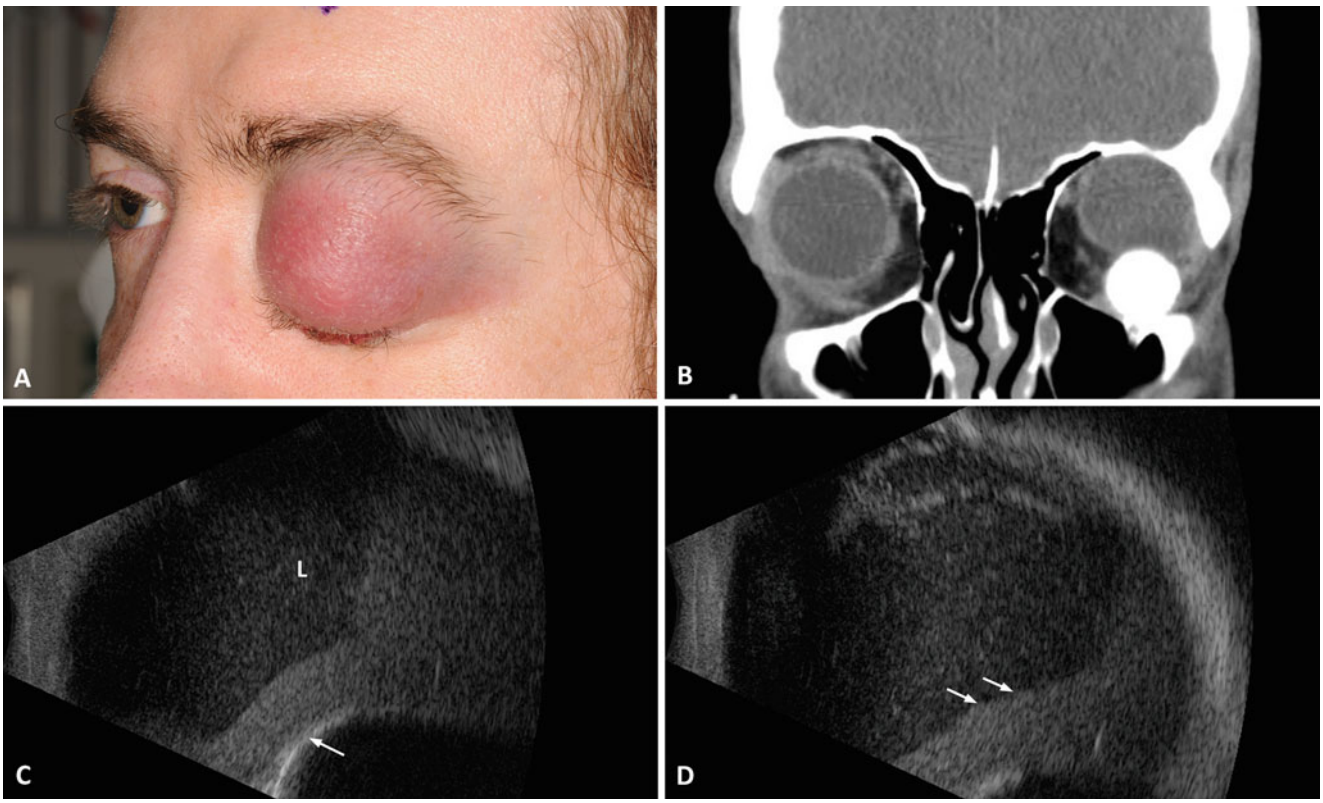


Fig. 9 Respiratory orbital cyst: (**a**) clinical picture of a 34-year-old male with a history of congenital anophthalmia and orbital surgery; (**b**) coronal CT scan showing an orbital cystic lesion and spherical hyperattenuating orbital implant; (**c**) paraocular B-scan shows a large orbital lesion (*L*) with moderately dense mucoid content. Note the edge of an orbital implant inferior to the cyst (*arrow*); and (**d**), Paraocular B-scan of a respiratory cyst. Shifting of the mucoid contents can be detected with a head changing position under the kinetic ultrasound exam (*arrow*)

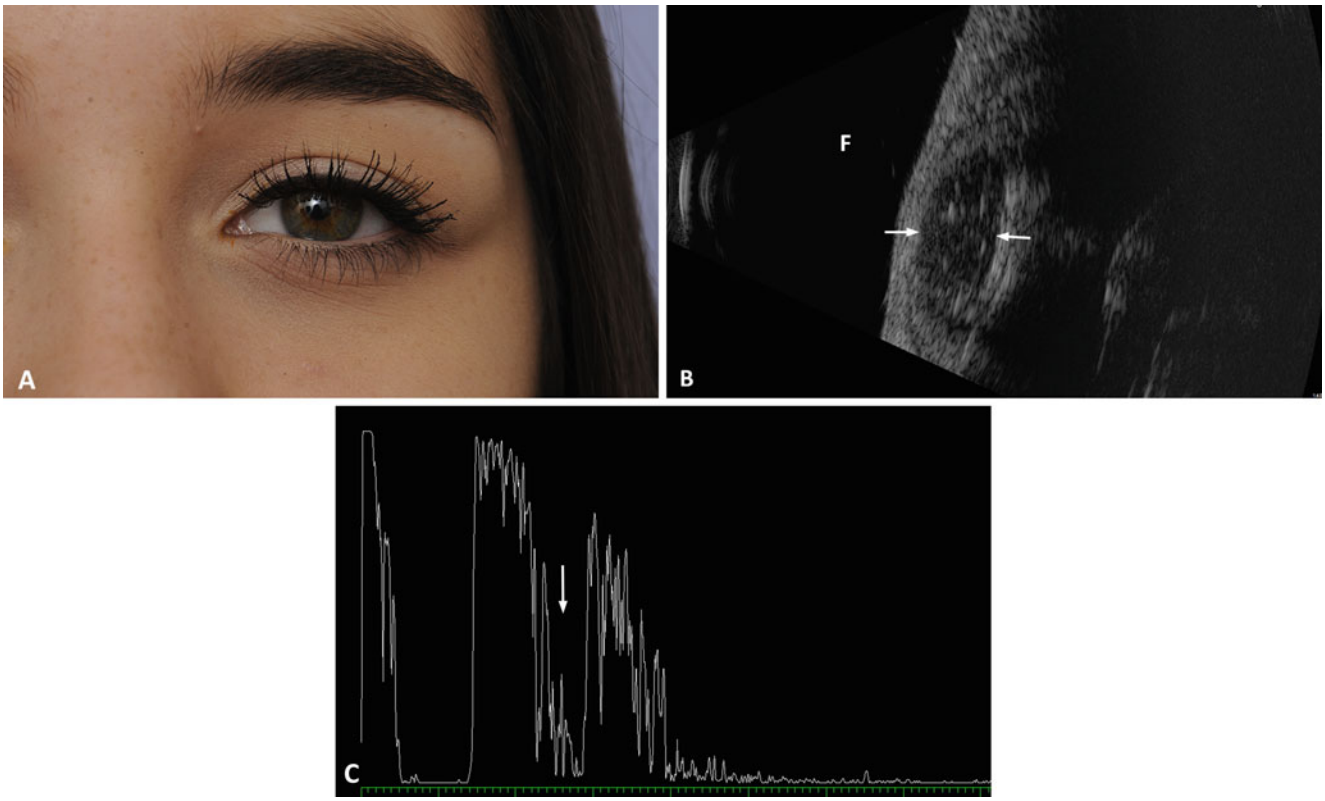


Fig. 10 Dermoid cyst: (**a**) clinical image of a superotemporal dermoid cyst that was present since birth; (**b**) paraocular immersion B-scan showing a well-circumscribed, oval-shaped, mainly low-reflective cyst (*arrows*); *F*, fluid; and (**c**), corresponding paraocular A-scan showing the cyst's low reflectivity internal structure (*arrow*)

8.4 Orbital Mucocele

Obstruction of the paranasal sinus may lead to mucocele that can erode through the orbit. The lesion can occur in any phase of life; however, it is most frequent within the fifth to seventh decades. The frontal and frontoethmoidal sinus are the most frequent site of source of mucoceles [5].

8.4.1 Ultrasonography

On sonography, mucoceles are identified on B-scan as large, well-outlined, extraconal, round-, or oval-shaped, low-reflective masses that extend to the sinus. Sometimes, a bone defect associated to the mucocele can be detected. A-scan displays a low-reflective, regular internal structure (Fig. 11).

8.4.2 Differential Diagnosis

The differential diagnosis of orbital mucocele includes paranasal sinus tumors, e.g., inverted papilloma, orbital malignant lesions, e.g., lymphoma and plasmacytoma. In kids' group, rhabdomyosarcoma and orbital cysts are considered in the differential diagnosis.

9 Vascular Anomalies

9.1 Infantile Hemangioma (Former Capillary Hemangioma)

Infantile hemangiomas are classified as vascular hamartomas, predominately of capillary size. Infantile hemangioma is the most common tumor of the orbit and periorbital areas in childhood. The benign lesions can be superficial in the eyelid or can extend deep into the orbit. Presentation often occurs after birth, and usually within the first 6 months of life [6].

9.1.1 Ultrasonography

On B-scan, infantile hemangiomas are usually poorly outlined, irregularly shaped lesions with heterogeneous internal structure. On dynamic exam, the masses are compressible and exhibit marked vascularity.

On A-can exam, infantile hemangiomas exhibit irregular structure and mainly medium-high to high amplitude spikes (Fig. 12).

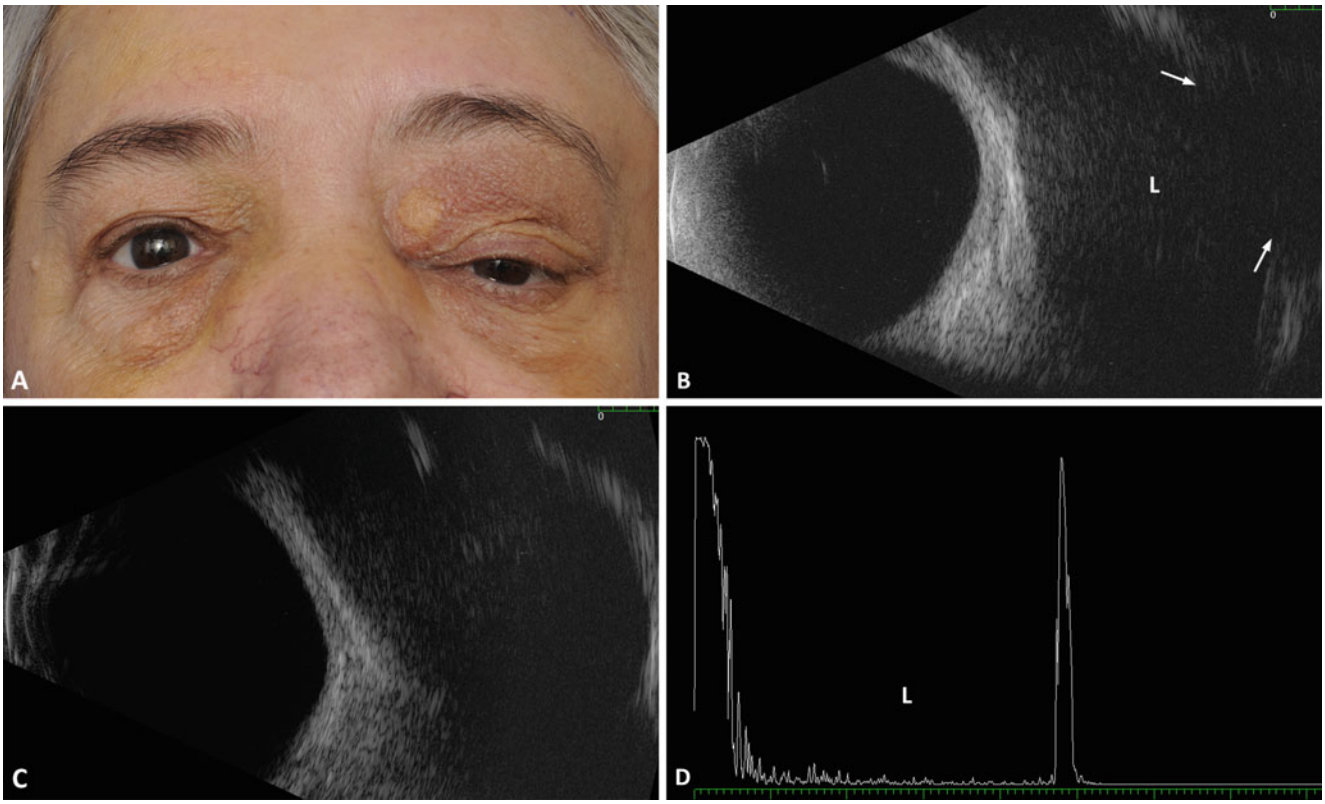


Fig. 11 Orbital mucocele: (**a**) clinical picture of a 64-year-old female presented with a left proptosis and inferior displacement of the eye in case of frontal mucocele; (**b**) longitudinal B-scan aimed superiorly, through a mucocele, shows a large well-outlined, low-reflective lesion (*L*) with associated bone defect (*arrows*); (**c**) transverse B-scan shows homogeneous, low-reflective orbital mass; and (**d**), corresponding A-scan showing cyst's extremely low internal reflectivity; *L*, lesion

9.1.2 Differential Diagnosis

The differential diagnosis of infantile hemangioma includes rhabdomyosarcoma, lymphangioma, neuroblastoma, and orbital cysts.

9.2 Cavernous Venous Malformation (Former Cavernous Hemangioma)

The cavernous venous malformation is a common primary orbital lesion of adults. Cavernous venous malformation occurs more often in women and typically evolves with progressive proptosis during the fourth and fifth decades of life [7].

Histologically, cavernous venous malformation is composed of multiple, dilated blood-filled channels lined by endothelium and separated by fibrous septa of variable thicknesses. The lesion is surrounded by a fibrous pseudocapsule.

9.2.1 Ultrasonography

Cavernous venous malformations appear as a well-outlined, smooth, round-, or oval-shaped lesion. The lesion is homogeneous, hyper-reflective, and has firm consistency. In cases of large lesions, flattening of the globe, or optic nerve, and muscle deviation can be observed. A-scan typically shows a regular internal structure with medium-high to high reflectivity, moderate to intense sound attenuation, and mild internal vascularity (Fig. 13).

9.2.2 Differential Diagnosis

Cavernous venous malformation should be distinguished from well-circumscribed lesions that cause slowly progressive proptosis such as schwannoma, solitary fibrous tumor, and hemangiopericytoma.

9.3 Orbital Venous-Lymphatic Malformation (Former Lymphangioma)

Venous-lymphatic malformations are nonmalignant embryonic malformations consisting of fluid-filled channels and spaces due to abnormal development of the lymphatic system. Most patients develop symptoms in the first or second decade [8]. Typically, patients have progressive swelling or a

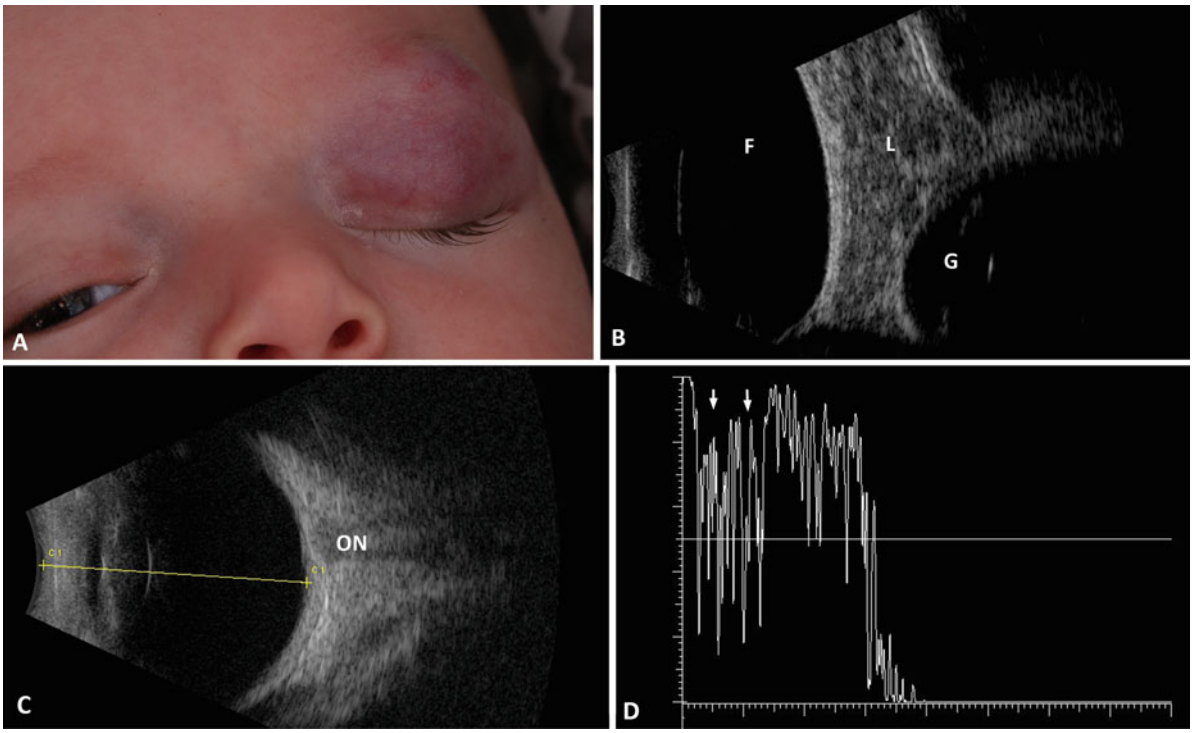


Fig. 12 Orbital infantile hemangioma: (**a**) clinical picture of an 8-week infant with infantile hemangioma; (**b**) immersion B-scan through the lids displays a large, irregular structure, hyperechoic, anterior orbital lesion (*L*) adjacent to globe (*G*); *F*, fluid; (**c**), axial B-scan showing no extension of the lesion to the retrobulbar space. *ON*, optic nerve; and (**d**), paraocular A-scan shows the high reflectivity of the lesion (*arrows*)

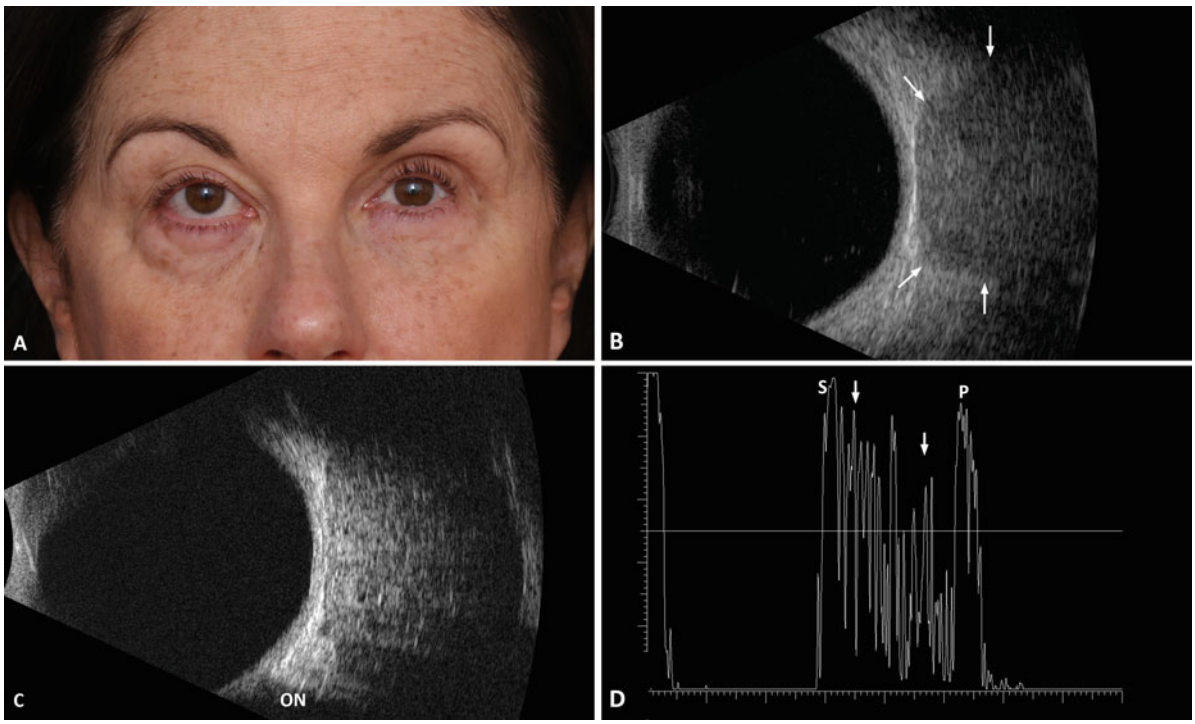


Fig. 13 Orbital cavernous venous malformation: (**a**) clinical picture of a 61-year-old female with cavernous venous malformation, showing right-sided proptosis and lower lid swelling; (**b**) transverse B-scan shows well-outlined lesion with smooth contour (*arrows*) and regular, hyperechoic internal structure; (**c**) longitudinal B-scan showing the proximity of the lesion to the optic nerve (*ON*); and (**d**) A-scan exhibits high reflectivity and moderate sound attenuation (*arrows*); *S* sclera; and *P*, posterior lesion margin spike

mass affecting the eyelids, leading to proptosis, and restricted eye mobility. Hemorrhage can occur leading to painful proptosis and compressive neuropathy.

9.3.1 Ultrasonography

The lesion is irregularly shaped and has poorly defined borders infiltrating to the adjacent orbital tissues. The internal architecture is heterogeneous with low-reflective, lymph-filled, channel-like spaces separated by connective tissue and vessel walls with high amplitude echoes. On the lesion pressure test, venous-lymphatic malformations are soft in consistency.

In case of intralesional hemorrhage, the cystic spaces become dilated, and occasionally a level of fluid can be observed.

A-scan demonstrates a lesion of irregular internal structure, with multiple low-reflective spaces intercalated by high amplitude spikes corresponding to septations and vascular walls (Fig. 14).

9.3.2 Differential Diagnosis

Orbital venous-lymphatic malformation should be differentiated from other conditions resulting in unilateral proptosis, including orbital cellulitis, idiopathic orbital inflammation, ruptured dermoid cyst, thyroid eye disease, and primary or metastatic neoplasm (e.g., neuroblastoma, leukemia, and rhabdomyosarcoma).

10 Orbital Inflammatory Diseases

10.1 Thyroid Eye Disease

Thyroid eye disease results from an autoimmune process closely associated with Grave's disease. Nearly 90% of cases occur in hyperthyroidism, with the remaining 10% associated to euthyroidism or hypothyroidism.

Enlargement of the orbital soft tissues is the fundamental process that underlies most of the clinical manifestations. Common clinical findings of thyroid eye disease include exophthalmos, eyelid retraction, and strabismus. Based on the level of disease activity, thyroid eye disease can be classified in two phases: an active phase characterized by soft tissue inflammation, and an inactive phase associated with orbital fibrosis (Fig. 15) [9].

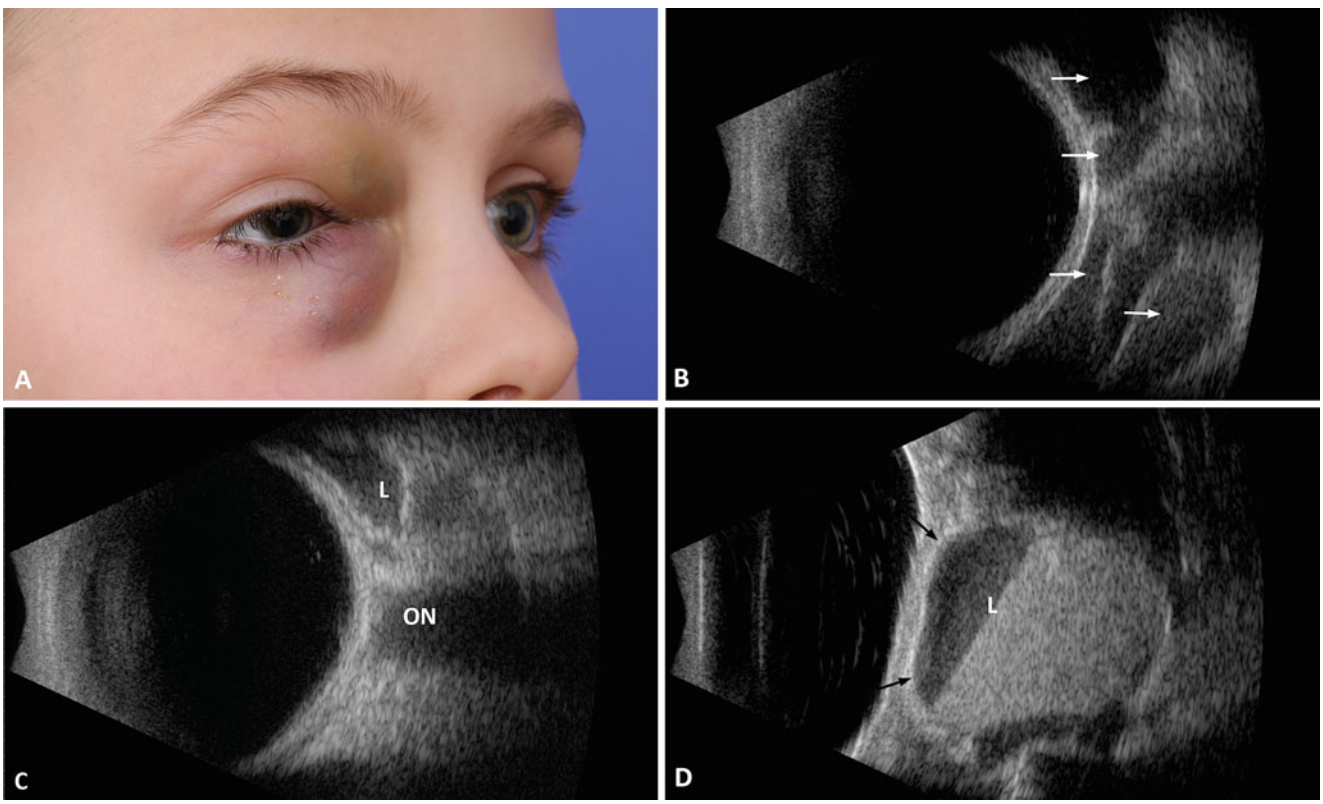


Fig. 14 Orbital venous-lymphatic malformation: (**a**) clinical picture of a 9-year-old girl with orbital venous-lymphatic malformation with bleeding, characterized by a bluish subcutaneous eyelid mass for 1 week; (**b**) transverse B-scan of infiltrative, multicystic mass (*arrows*); (**c**) transverse B-scan aimed to the optic nerve (*ON*) area showing close proximity of the lesion (*L*) to the optic nerve; and (**d**) paraocular B-scan, with the probe positioned on the lower eyelid, displays large blood-filled space (*arrows*) with fluid level (*L*)

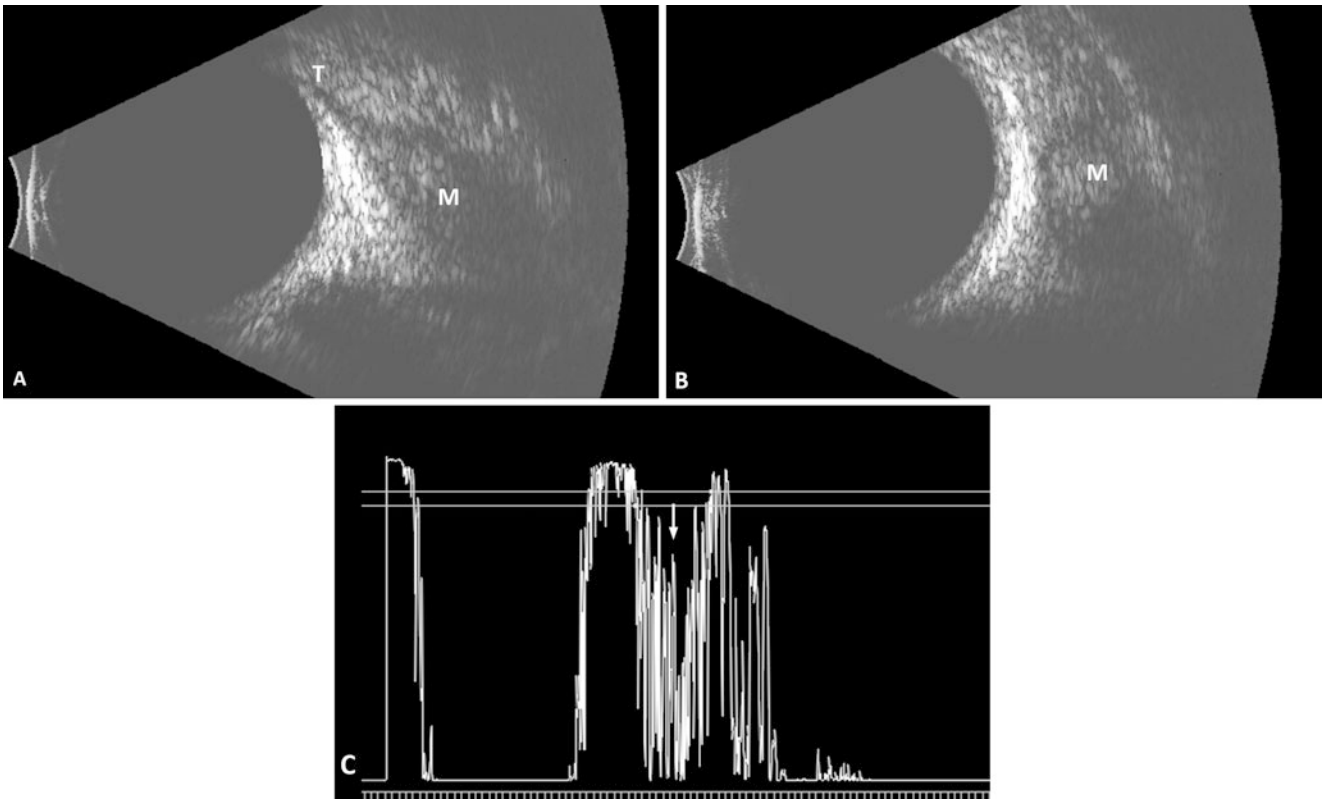


Fig. 15 Thyroid eye disease: (**a**) longitudinal B-scan of enlarged medial rectus (*M*) with spared tendon (*T*); (**b**) transverse B-scan shows cross section of the posterior aspect of an enlarged muscle (*M*) in fibrotic phase; and (**c**) corresponding A-scan shows medium internal reflectivity (*arrow*) typical of inactive fibrotic phase of thyroid eye disease

10.1.1 Ultrasonography

Muscle enlargement in thyroid eye disease usually affects multiple muscles with bilateral involvement. Usually, the muscle belly is enlarged, whereas the tendon is within normal limits. The internal reflectivity of an enlarged muscle can be low in the active phase, and then become more reflective in fibrotic phase.

10.1.2 Differential Diagnosis

The differential diagnosis for thyroid eye disease includes infectious and inflammatory orbital conditions such as orbital idiopathic orbital inflammatory syndrome, and orbital cellulitis. Rarer conditions include orbital neoplasms and carotid cavernous sinus fistulas.

10.2 Idiopathic Orbital Inflammation (Orbital Pseudotumor)

Idiopathic orbital inflammation is a noninfection, possibly immunopathologic dysfunction, without underlying local or systemic etiology. It accounts for 5–10% of orbital lesions. Mixed inflammatory infiltration can be seen in any area of the orbit; however, most commonly, it involves the retrobulbar region and takes the form of a mass [10].

Depending on the orbital site of involvement, idiopathic orbital inflammation can be classified into different categories, including anterior, diffuse, apical or posterior, myositis, dacryoadenitis, and optic neuritis.

The most common presentation is a middle-aged male or female with acute or subacute onset of orbital pain inflammation, swelling, and restricted motility.

10.2.1 Ultrasonography

The lesion can be focal or multifocal, well-outlined, or infiltrative, usually as a regular structure with low to medium internal reflectivity. Internal vascularity sometimes is positive, and the lesion has firm consistency under the probe pressure test (Fig. 16).

The myositic type is usually unilateral and involves single or multiple extraocular muscles, including the tendinous insertion (Fig. 17).

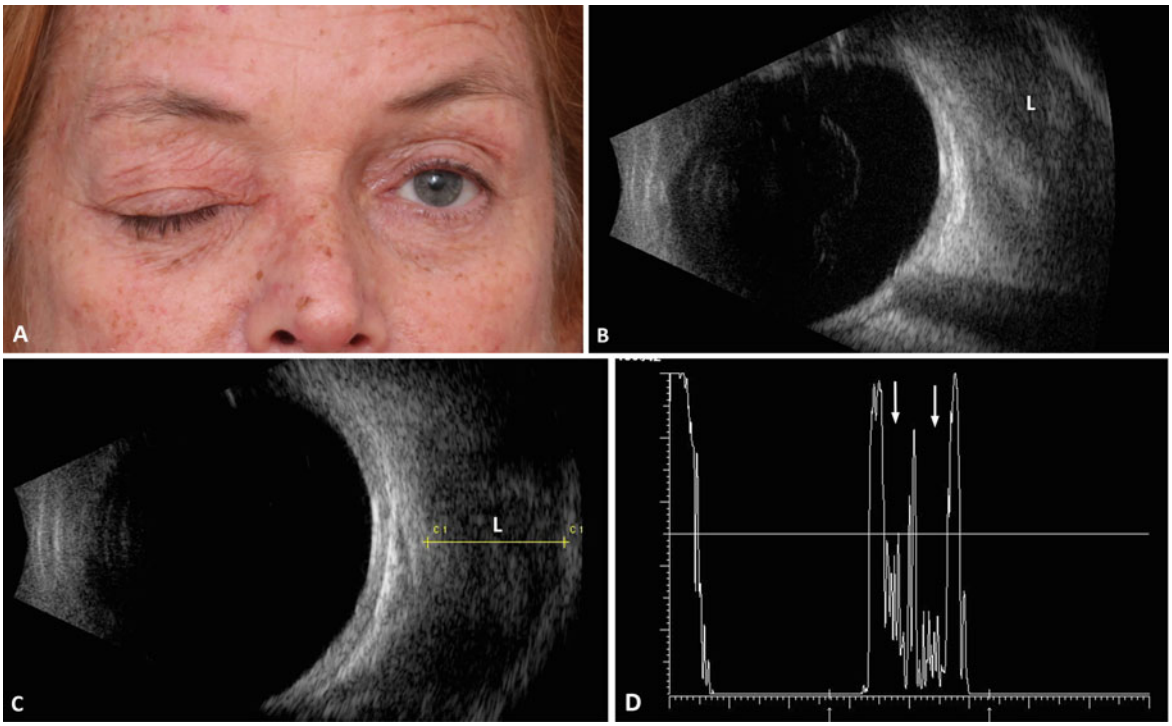


Fig. 16 Idiopathic orbital inflammation: (**a**) clinical picture of a 57-year-old female patient with eyelid swelling and palpable orbital mass superiorly. Histopathologic exam revealed an inflammatory sclerosing lesion; (**b**) longitudinal B-scan through superior orbit demonstrates a well-outlined, extraconal, low-reflective lesion (*L*); (**c**) transverse B-scan through the superior orbit region displays a large low-reflective mass lesion (*L*); and (**d**) corresponding A-scan demonstrating a homogeneous, low-reflective orbital lesion (*arrows*)

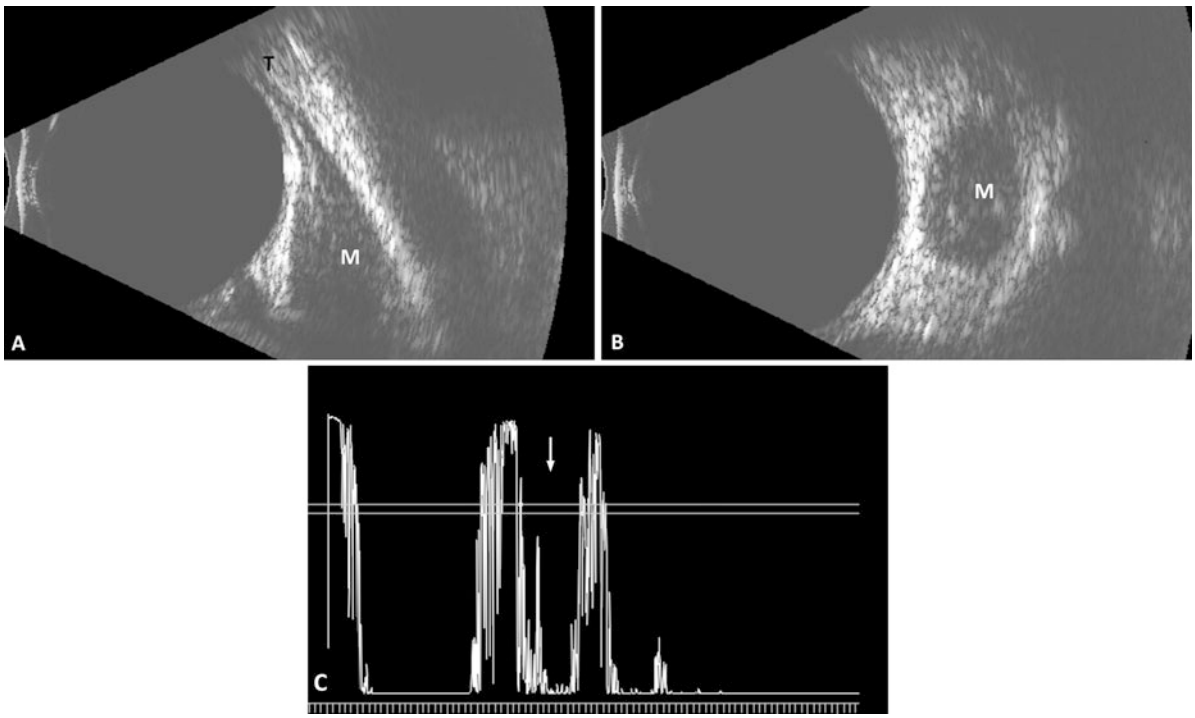


Fig. 17 Myositis: (**a**) longitudinal B-scan through the medial rectus shows a marked muscle (*M*) enlargement with tendon (*T*) involvement; (**b**) transverse view of enlarged medial rectus muscle (*M*); and (**c**) corresponding A-scan of enlarged muscle (*arrow*) demonstrates regular internal structure with low reflectivity

10.2.2 Differential Diagnosis

The differential diagnosis of idiopathic orbital inflammation includes orbital cellulitis, thyroid eye disease, lymphoproliferative disorders, ruptured dermoid cyst, and carotid cavernous sinus fistula.

11 Tumors of Lymphoid and Hematopoietic Tissues

11.1 Orbital Lymphoma

Lymphoma is the most frequent neoplasm of the orbit. Ocular adnexal lymphoma can arise in the conjunctiva, eyelids, and the orbit, including the lacrimal gland. Most orbital lymphomas are of B-cell origin and affect patients older than 50 years with a slight predominance of males. The majority of B-cell lymphomas arise as a primary orbital disease and less frequently occur secondarily, either as a metastatic spread or as a local invasion from adjacent periorbital structures [11, 12].

Most of the tumors present as slowly, growing painless masses. At presentation, lid swelling, proptosis, and a palpable mass are common findings. Red-salmon color conjunctival infiltration can be present in the fornix. The involvement is usually unilateral.

11.1.1 Ultrasound

Orbital lymphomas are usually well-outlined with smooth borders, extraconal mass molding to the globe. The lesion is homogeneous and occasionally contains connective tissue septa. The tumor is soft in consistency. On A-scan, orbital lymphoma presents regular internal structure with low to medium reflectivity and weak sound attenuation.

Orbital lymphoma and idiopathic orbital inflammation share common echographic findings. The idiopathic orbital inflammation has a relatively short, aggressive onset, and pain is usually present (Fig. 18).

11.1.2 Differential Diagnosis

Orbital lymphoma should be differentiated from masses or lesions involving the intra- and extraconal compartment, including idiopathic orbital inflammation, thyroid eye disease, sarcoidosis, tumors of the lacrimal gland, and metastasis.

11.2 Orbital Plasmacytoma

Plasmacytoma is a monoclonal proliferation of the plasma cells. It may grow within osseous structures or soft tissues.

Orbital plasmacytoma is usually associated with multiple myeloma, which has been diagnosed before or immediately after the initial orbital presentation. Solitary primary plasmacytoma, without evidence of systemic disease, is extremely rare. Thuro et al. [13] found that the median age of patients at diagnosis was 57 years, with similar distribution among male and female patients. The study also revealed that the most common pattern of orbital plasmacytoma is a bony lesion originating from the frontal bone or sphenoid bone causing a mass effect on the orbital contents.

11.2.1 Ultrasound

On B-scan, plasmacytomas are well-outlined, firm in consistency, and internal vascularity can be visible within the mass. Histologically, plasmacytoma is comprised of a dense, monotonous population of plasma cells which produces a regular structured lesion. On A-scan, plasmacytomas exhibit low internal reflectivity (Fig. 19).

11.2.2 Differential Diagnosis

Differential diagnosis of orbital plasmacytomas includes other lymphoproliferative disorders, orbital inflammation, lacrimal gland tumors, and mesenchymal tumors.

12 Epithelial Tumors of the Lacrimal Gland

12.1 Pleomorphic Adenoma (Benign Mixed Tumor)

Pleomorphic adenoma is the most common benign tumor of the lacrimal gland, constituting 20% of all lacrimal gland tumors [14].

The initial presenting scenario is a painless, firm enlargement of the lacrimal gland that indents the eye resulting in a downward and inward displacement of the globe, and with some degree of proptosis. The duration of the symptoms at the time of presentation is normally between 1 and 2 years.

12.1.1 Ultrasound

Ultrasound can show either a round or oval-shaped, smooth, well-outlined mass. The tumor is firm and can cause indentation in the contiguous eye wall and bone remodeling. Medium reflectivity with moderate sound attenuation is typically seen on A-scan (Fig. 20).

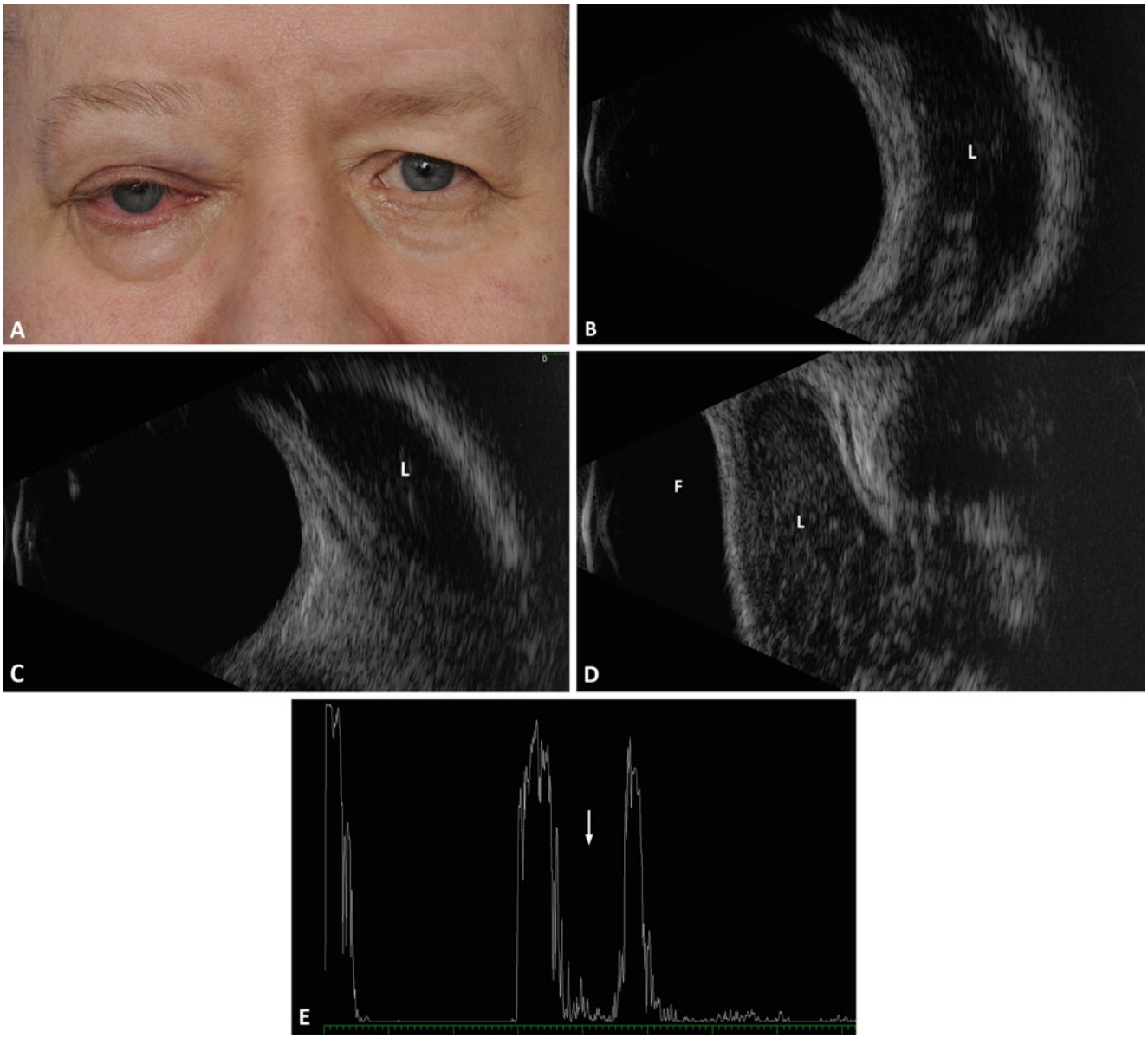


Fig. 18 Orbital lymphoma: (**a**) a 66-year-old male presented with upper lid swelling and inferior displacement of the eye that progressed over a 6-month period. The patient underwent incisional biopsy, and pathology demonstrated B-cell lymphoma; (**b**) transverse B-scan shows a well-outlined lesion (*L*) molding the globe; (**c**) longitudinal B-scan shows a well-outlined, extraconal, homogeneous, and low-reflective lesion (*L*); (**d**) paraocular immersion technique B-scan through closed lids shows the well-circumscribed anterior margin of a large lesion (*L*); *F*, fluid; and (**e**) A-scan shows low-medium internal reflectivity (*arrow*)

12.2 Adenoid Cystic Carcinoma

Adenoid cystic carcinoma is the most common malignant epithelial tumor of the lacrimal gland. It occurs in either sex, with a peak in the fifth decade of life [14].

Patients typically present painful eyelid swelling, ptosis, and palpable mass superotemporally. The lesion has rapid growth, usually with approximately 6 months of history. Pain is the major symptom, and it can be secondary to perineural invasion.

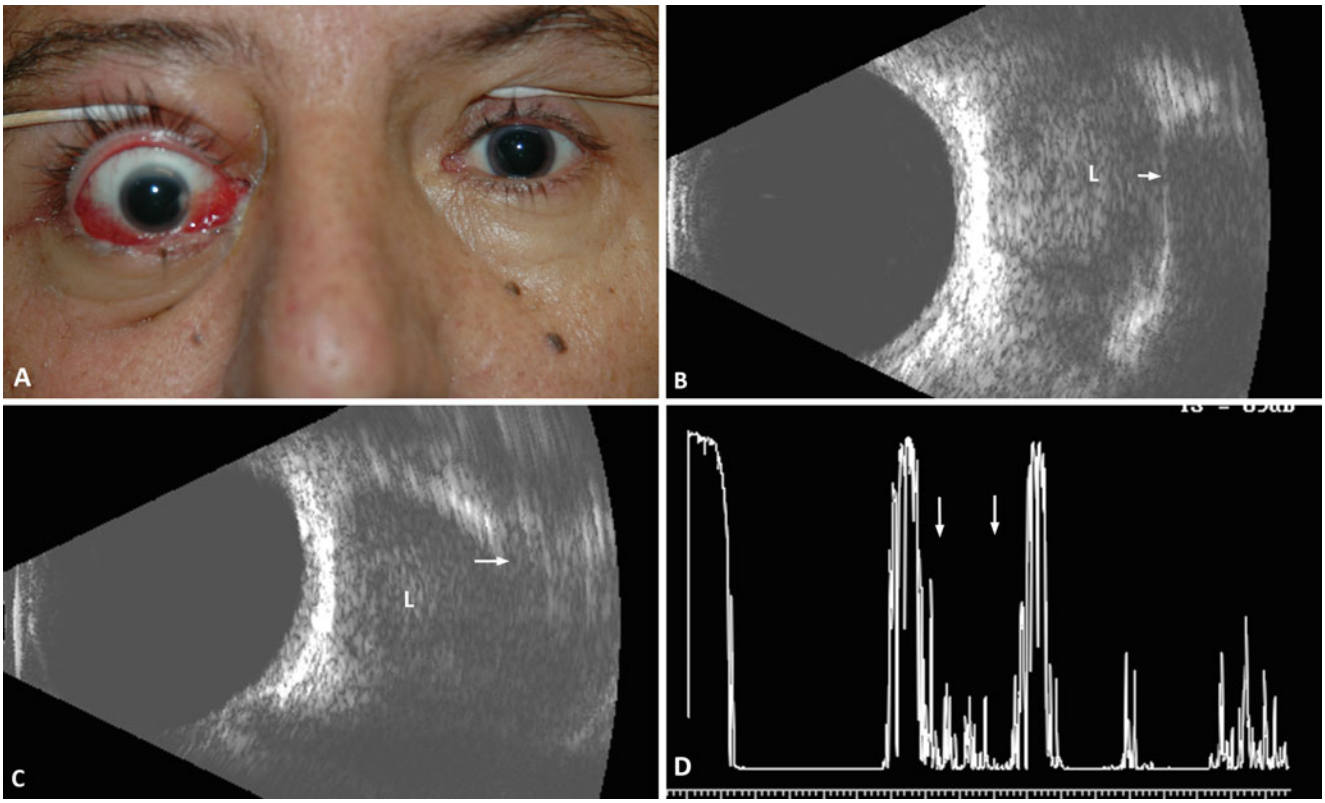


Fig. 19 Orbital plasmacytoma: (**a**) clinical picture of a 54-year-old male with history of multiple myelomas and a large mass extending from the sphenoid through the orbit on radiologic exams; (**b**) transverse B-scan exhibits a well-outlined, homogeneous orbital lesion (*L*) with associated bone erosion (*arrow*); (**c**) longitudinal B-scan aimed superotemporally exhibits a large orbital lesion (*L*) adjacent to a bone defect (*arrow*); and (**d**) A-scan echogram shows very low reflectivity (*arrows*)

12.2.1 Ultrasound

On B-scan, adenoid cystic carcinoma can be well outlined at the early stages. In more advanced cases, the lesion can have irregular borders. On the probe pressure maneuver, the lesion is firm to hard in consistency. Often, bone erosion can be present. A-scan image exhibits medium to medium-high internal reflectivity with marked sound attenuation (Fig. 21).

The differential diagnosis of this type of palpable mass in the lacrimal fossa includes pleomorphic adenoma and adenoid cystic carcinoma. A rapid progressive history and presence of bone erosion on imaging studies is a hallmark of adenoid cystic carcinoma.

12.2.2 Differential Diagnosis

Epithelial tumors of the lacrimal gland must be distinguished from other causes of enlargement of the lacrimal gland, including lymphoproliferative processes, sarcoidosis, and dacryoadenitis.

13 Tumors of Primitive Mesoderm

13.1 Rhabdomyosarcoma

Rhabdomyosarcoma is the most prevalent primary orbital malignancy of childhood. Orbital rhabdomyosarcoma probably arises from primitive pluripotent mesenchymal cells with a propensity to differentiate toward the skeletal muscle.

It most commonly occurs in the first decade of life, with a mean age at diagnosis at 8 years, when the patient develops a rapidly progressive proptosis and displacement of the eye. Other common characteristics include ptosis, conjunctival and eyelid swelling, and pain. The tumor is always unilateral and is usually located superiorly or superonasally in the anterior region of the orbit [15].

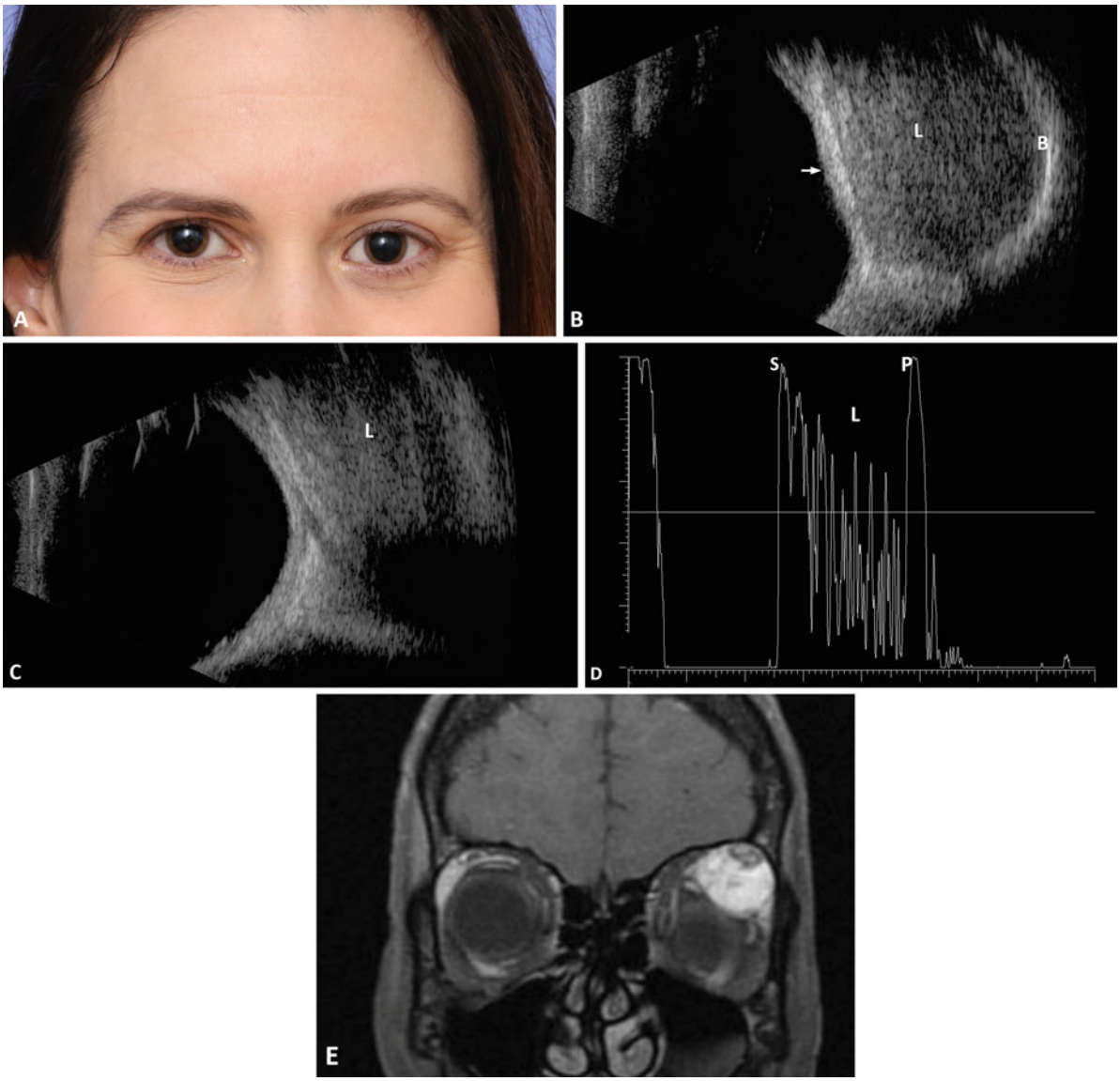


Fig. 20 Pleomorphic adenoma of the lacrimal gland: (**a**) clinical picture of a 36-year-old female with pleomorphic adenoma causing left upper eyelid swelling and downward displacement of the eye during a period of 12 months; (**b**) transverse B-scan shows a large orbital lesion (*L*) indenting the eye (*arrow*) and causing orbital bone excavation (*B*); (**c**) longitudinal B-scan shows the anteroposterior extension of the lesion (*L*); (**d**) corresponding A-scan predominantly shows medium internal reflectivity and moderate sound attenuation; *S* sclera; *L*, lesion; *P*, posterior lesion margin spike; and (**e**) coronal postcontrast T1-weighted MRI displays a heterogeneously enhanced mass superotemporally

13.1.1 Ultrasound

On echographic images, rhabdomyosarcoma appears as an extraconal, well-outlined, oval-shaped, homogeneous mass. The lesion is firm in consistency and can cause globe indentation. Larger tumors have less well-defined margins and can be associated with bone erosion. A-scan demonstrates a regular internal structure with low to medium reflectivity. At times, the internal structure is more irregular and the reflectivity varies from low to medium-high.

Ultrasound images of a 9-year-old girl presented for a 3-week history of anterior, superonasal orbital mass are illustrated in Fig. 22. The patient underwent excisional biopsy, and pathology was consistent with embryonal rhabdomyosarcoma.

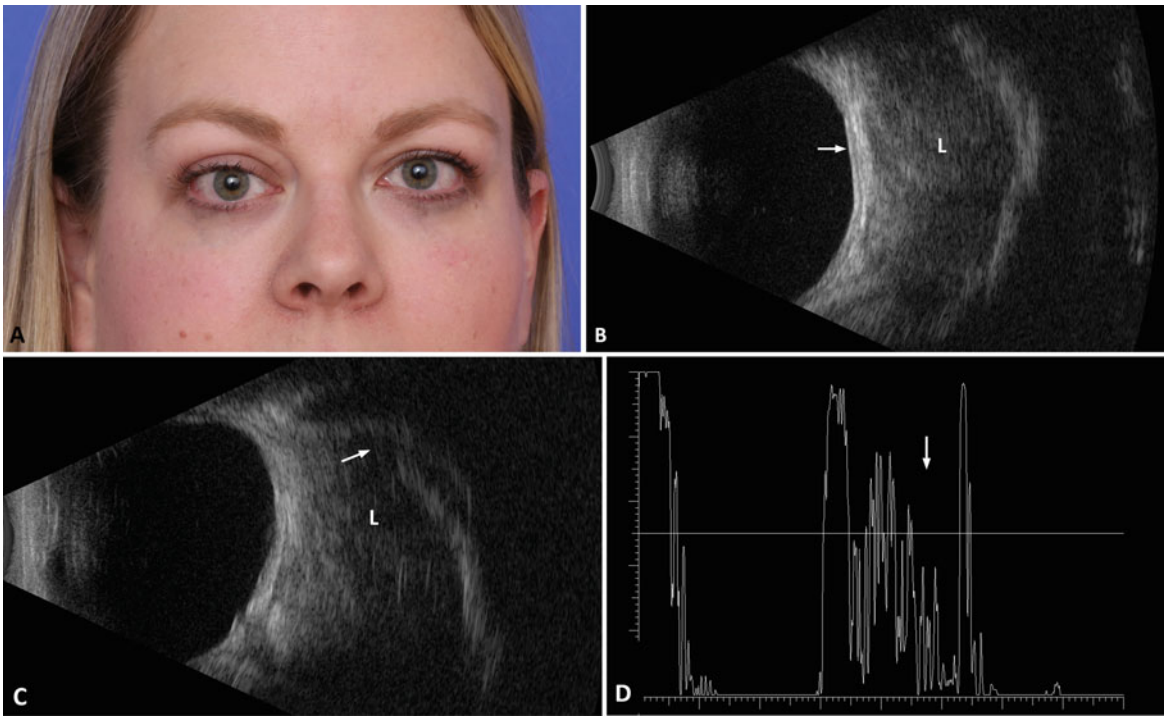


Fig. 21 Adenoid cystic carcinoma of the lacrimal gland: (**a**) clinical picture of a 38-year-old female with adenoid cystic carcinoma of the right lacrimal gland displacing the globe inferiorly; (**b**) transverse B-scan view of adenoid cystic carcinoma indenting the globe (*arrow*); *L*, lesion; (**c**) longitudinal B-scan through superior orbit showing large mass extending posteriorly with associated bone defect (*arrow*); *L*, lesion; and (**d**) corresponding A-scan predominantly showing medium-high internal reflectivity with sound attenuation (*arrow*)

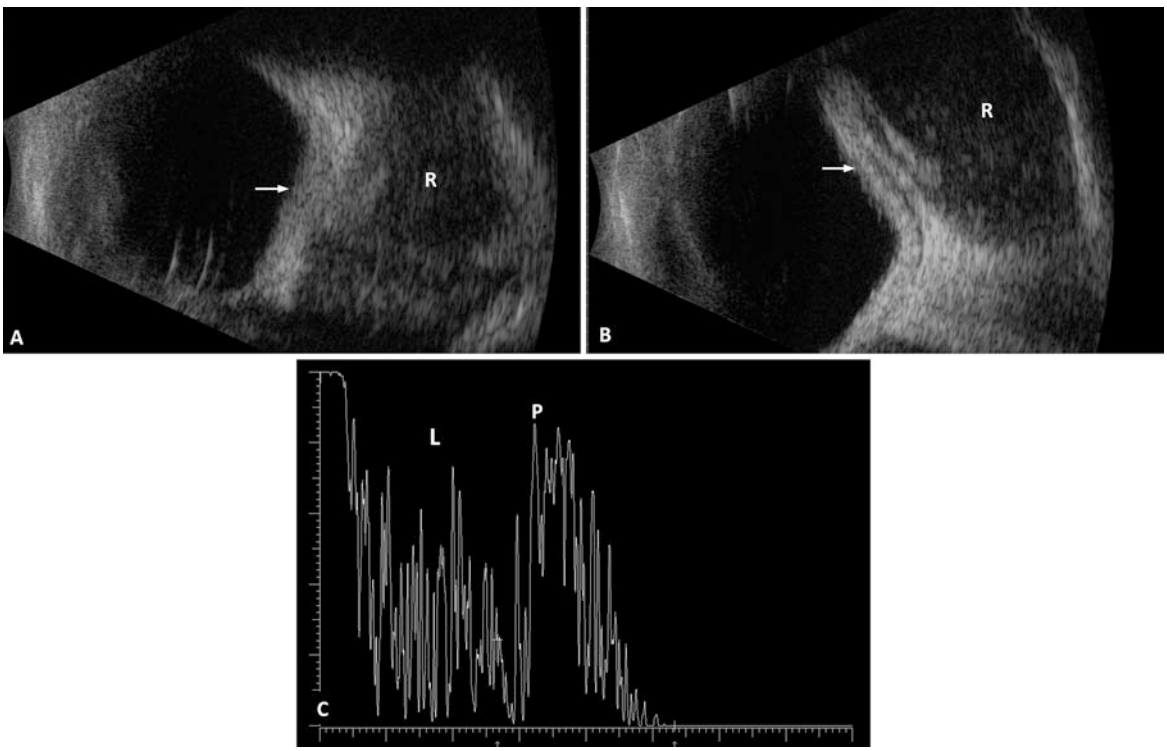


Fig. 22 Orbital rhabdomyosarcoma: (**a**) transverse B-scan shows a large rhabdomyosarcoma (*R*) indenting the globe (*arrow*); (**b**) longitudinal B-scan shows a large, homogeneous orbital rhabdomyosarcoma (*R*) indenting the globe (*arrow*) with anteroposterior extension; and (**c**) corresponding paraocular A-scan predominantly shows medium internal reflectivity; *L*, lesion; and *P*, posterior lesion margin spike

13.1.2 Differential Diagnosis

The differential diagnosis of orbital rhabdomyosarcoma includes a group of childhood neoplastic, vascular, inflammatory, and infectious conditions that result in proptosis.

These include the following: lymphangioma, infantile hemangioma, orbital cellulitis, idiopathic orbital inflammation, dermoid cyst, leukemia, lymphoma, and neuroblastoma.

14 Primitive Neuroectodermal Tumors

14.1 Neuroblastoma

Neuroblastoma originates from neural crest cells and can arise anywhere along the sympathetic chain, most commonly affecting the adrenal glands. Neuroblastoma is the most common extracranial solid tumor of early childhood, and between 10% and 20% of cases there is ophthalmic involvement. Orbital metastasis is the most common ocular manifestation. Proptosis, periorbital swelling, and periorbital ecchymosis ("raccoon eyes") are common ocular manifestations [16].

14.1.1 Ultrasound

In our experience, based on the examination of one patient with orbital neuroblastoma, ultrasound demonstrated a well-circumscribed, irregularly shaped, extraconal, lateral, homogeneous, medium reflective mass with a defect of the lateral bone wall (Fig. 23).

14.1.2 Differential Diagnosis

The differential diagnosis should include rhabdomyosarcoma, vascular malformations, leukemia, and other metastatic tumors such as Ewing's sarcoma or Wilms' tumor.

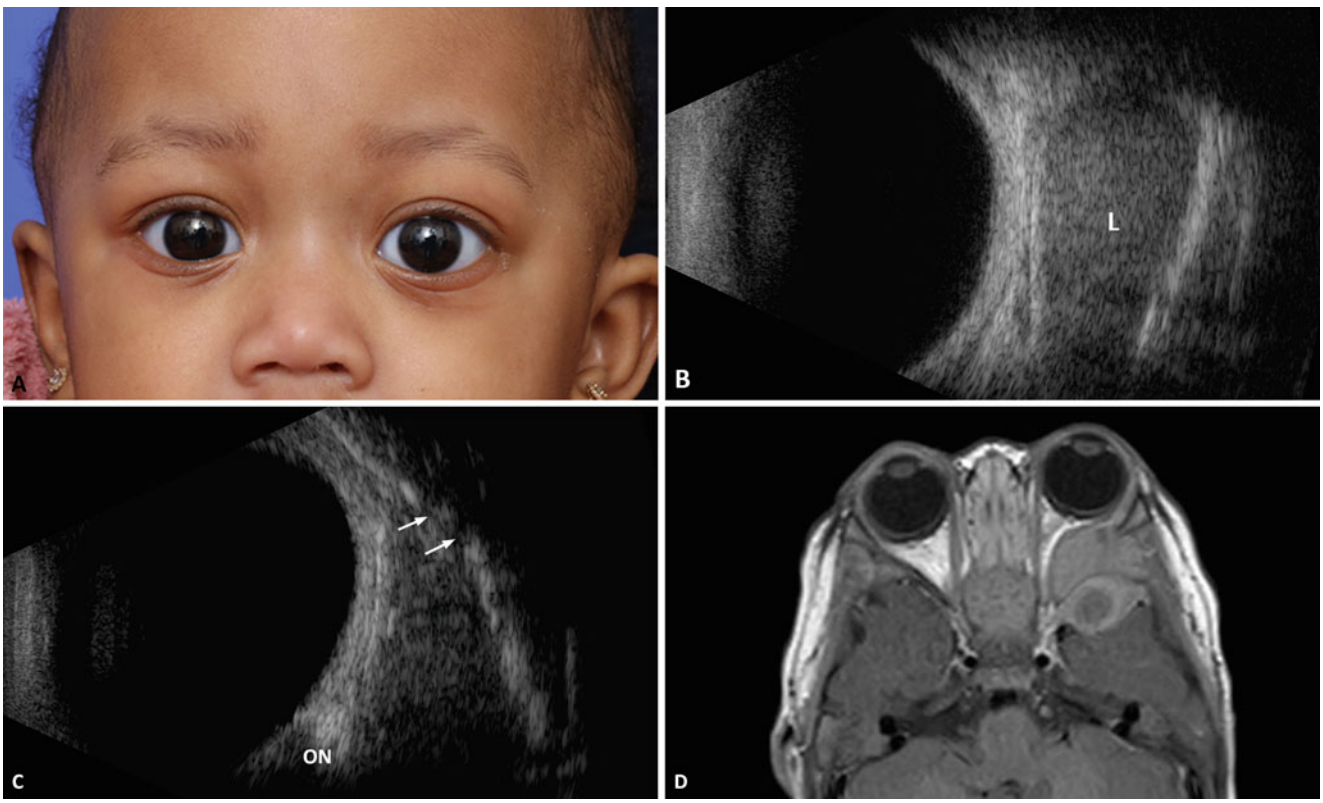


Fig. 23 Orbital neuroblastoma: (**a**) an 8-month-old girl presented a left-sided proptosis that developed during 1 week. Systemic workup revealed a primary retroperitoneal abdominal neuroblastoma; (**b**) transverse B-scan revealed a well-outlined, extraconal, homogeneous medium-reflective lesion (*L*); (**c**) longitudinal B-scan demonstrates the posterior extension of the orbital mass to the area of the optic nerve (*ON*) and a defect in the bony orbital wall (*arrows*); and (**d**) axial T1-weighted postcontrast MRI showing a mass lesion centered in the greater wing of the left sphenoid bone with an orbital extension

Summary of orbit tumors and tumorlike lesions

Orbital lesion	Age group (years)	Clinical hallmark	Echographic features
Microphthalmos with cyst	<10	Infant with small globe and cyst-like orbital mass	Well-outlined, low-reflective cavity, usually located inferiorly dislocating microglobe
Respiratory epithelial cyst (congenital or acquired)	Any age	Slow onset, progressive lid swelling and proptosis. Usually temporal in congenital cases	Well circumscribed, smooth, round/oval shaped, low reflective, compressible
Dermoid cyst	<20	Slow growing, superotemporal, subcutaneous palpable mass	Circumscribed, round/oval, variable internal structure, low to medium reflectivity, firm consistency
Mucocele	40–70	Periorbital swelling, palpable mass, orbital pain or headache, and previous history of sinusitis	Well-outlined, extraconal, round/oval, homogeneous, low-reflective, hard, often bone defect
Infantile hemangioma	<10	Rapid onset within first months of life; strawberry or bluish lid mass	Poorly outlined, irregularly shaped heterogeneous structure, medium/high reflectivity, compressible
Cavernous venous malformation	30–50	Slow-onset and progressive proptosis	Well outlined, smooth, round/oval, intraconal, homogeneous, hyper-reflective, firm consistency
Venous-lymphatic malformation	<10	Proptosis and periorbital swelling. Pain in case of sudden intralesional hemorrhage	Poorly outlined, heterogeneous, low-reflective channel-like spaces separated by highly reflective connective tissue, soft in consistency
Thyroid eye disease	40–50	Slow-onset, exophthalmos, lid retraction, and restrictive strabismus	Extraocular muscles enlargement with normal tendons
Idiopathic inflammation	20–70	Acute or subacute onset of periocular pain and swelling, chemosis, and restricted motility	Focal or multifocal, well/poorly outlined or infiltrative, usually regularly structured with internal low to medium reflectivity
Lymphoma	50–70	Painless, slowly progressive periorbital swelling, palpable anterior mass	Well-outlined, smooth borders, extraconal, homogeneous, low to medium reflectivity, molding to the globe, compressible
Plasmacytoma	50–70	Painless, slowly progressive periorbital swelling. Usually secondary to multiple myeloma	Circumscribed, homogeneous, low reflective, firm, bone defect
Pleomorphic adenoma	20–50	Slow-onset, palpable mass in the superotemporal quadrant	Anterosuperotemporal, round/oval, well-outlined smooth, homogeneous, and medium reflective, firm can cause indentation of the eye
Adenoid cystic carcinoma	30–60	Palpable mass in the superotemporal quadrant, often painful	Circumscribed or irregular borders, irregular structure, medium to high reflectivity, firm, bone defect
Rhabdomyosarcoma	<20	Rapid onset of progressive proptosis and displacement of the eye	Well-outlined, oval, homogeneous, regular internal structure, low to medium reflectivity, firm
Neuroblastoma	<10	Proptosis, periorbital swelling, and periorbital ecchymosis	Circumscribed, irregularly shaped, extraconal, homogeneous, medium reflective, with a bone defect

(continued)

References

1. Chaudhry IA, Arat YO, Shamsi FA, Boniuk M. Congenital microphthalmos with orbital cysts: distinct diagnostic features and management. Ophthalmic Plast Reconstr Surg. 2004;20:452–7.
2. Goh RL, Hardy TG, Williams RA, McNab AA. Respiratory epithelial cysts of the orbit. Orbit. 2016;35:245–9.
3. Bonavolontà G, Strianese D, Grassi P, Comune C, Tranfa F, Uccello G, Iuliano A. An analysis of 2,480 space-occupying lesions of the orbit from 1976 to 2011. Ophthalmic Plast Reconstr Surg. 2013;29:79–86.
4. Purohit BS, Vargas MI, Ailianou A, Merlini L, Poletti PA, Platon A, Delattre BM, Rager O, Burkhardt K, Becker M. Orbital tumours and tumour-like lesions: exploring the armamentarium of multiparametric imaging. Insights Imaging. 2016;7:43–68.
5. Garrity JA. Henderson's orbital tumors. 4th ed. Philadelphia: Lippincott Williams & Wilkin; 2007. p. 33.
6. Reem RE, Golden RP. Periocular hemangiomas and lymphangiomas. Pediatr Clin N Am. 2014;61:541–53.
7. Calandriello L, Grimaldi G, Petrone G, Rigante M, Petroni S, Riso M, Savino G. Cavernous venous malformation (cavernous hemangioma) of the orbit: current concepts and a review of the literature. Surv Ophthalmol. 2017;62:393–403.
8. Tunç M, Sadri E, Char DH. Orbital lymphangioma: an analysis of 26 patients. Br J Ophthalmol. 1999;83:76–80.
9. Joseph S, Douglas R. Thyroid eye disease: a comprehensive review. In: Demirci H, editor. Orbital inflammatory diseases and their differential diagnosis. Heidelberg: Springer; 2015. p. 73.
10. Aygun N, Shah G, Gandhi D. Idiopathic orbital pseudotumor. In: Pearls and pitfalls in head and neck and neuroimaging: variants and other difficult diagnoses. Cambridge: Cambridge University Press; 2013. p. 331.
11. Olsen TG, Heegaard S. Orbital lymphoma. Surv Ophthalmol. 2019;64:45–66.
12. Demirci H, Shields CL, Karatza EC, Shields JA. Orbital lymphoproliferative tumors: analysis of clinical features and systemic involvement in 160 cases. Ophthalmology. 2008;115:1626–31.

13. Thuro BA, Sagiv O, Shinder R, Debnam JM, Ozgur O, Ng JD, Rootman D, Thomas SK, Esmaeli B. Clinical presentation and anatomical location of orbital plasmacytomas. Ophthalmic Plast Reconstr Surg. 2018;34:258–61.
14. Andreasen S, Esmaeli B, Holstein SL, Mikkelsen LH, Rasmussen PK, Heegaard S. An update on tumors of the lacrimal gland. Asia Pac J Ophthalmol. 2017;6:159–72.
15. Shields JA, Shields CL. Rhabdomyosarcoma: review for the ophthalmologist. Surv Ophthalmol. 2003;48:39–57.
16. Graef S, Irwin MS, Wan MJ. Incidence and prognostic role of the ocular manifestations of Neuroblastoma in children. Am J Ophthalmol. 2020;213:145–52.

Orbital Ultrasound with Doppler

17

Stefania B. Diniz and Robert A. Goldberg

Contents

1 **Probe and Image Conventions** 149
2 **Arteriovenous Malformation** 150
3 **Venolymphatic Malformation** 151
4 **Cavernous Venous Malformation** 152
5 **Solitary Fibrous Tumor (Hemangiopericytoma)** 153
6 **Dermoid Cysts** 153
References 154

Abstract

In the era of high resolution MR and CT imaging, orbital ultrasonography has a limited role. There are two areas in which it can give additional information: assessment of Doppler flow, and dynamic imaging. Doppler flow can be helpful in determining the vascularity of tumors, particularly in the case of active vascular processes such as lymphaticovenous malformations. Dynamic imaging can be helpful in assessing the relationship of a tumor to the optic nerve: with eye movements, if the nerve is separate from the tumor, the two structures can be seen to move independently. Finally, dynamic imaging can be used to assess the compressibility of cystic tumors or varices, and to observe the effect of Valsalva. Representative cases are shown in this chapter.

Keywords

Ultrasonography · Orbit · Neoplasm

1 Probe and Image Conventions

There are two main considerations regarding the orientation of anatomic structures as they are viewed on the ultrasound display. "Indicator-to-screen" is the relationship of the probe indicator to the image on the screen and "indicator-to-patient" is the relationship of the probe indicator to the patient's head. The probe indicator (a bump or groove) corresponds to the left side of the screen as it is viewed, whereas the top of the screen typically represents the probe face. On the other hand, the anatomic orientation is based on where the indicator is directed on the patient. Therefore, to acquire images in a sagittal/longitudinal plane, the probe indicator is turned towards the patients' head (Fig. 1a, b) and, for the transverse plane, the indicator is turned horizontally (Fig. 1c, d).

S. B. Diniz (✉) · R. A. Goldberg
Division of Orbital and Ophthalmic Plastic Surgery, Stein and Doheny Eye Institutes, University of California, Los Angeles, CA, USA
e-mail: contato@stefaniadiniz.com; goldberg@jsei.ucla.edu

© Springer Nature Switzerland AG 2022
G. Ben Simon et al. (eds.), *Atlas of Orbital Imaging*,
https://doi.org/10.1007/978-3-030-62426-2_124

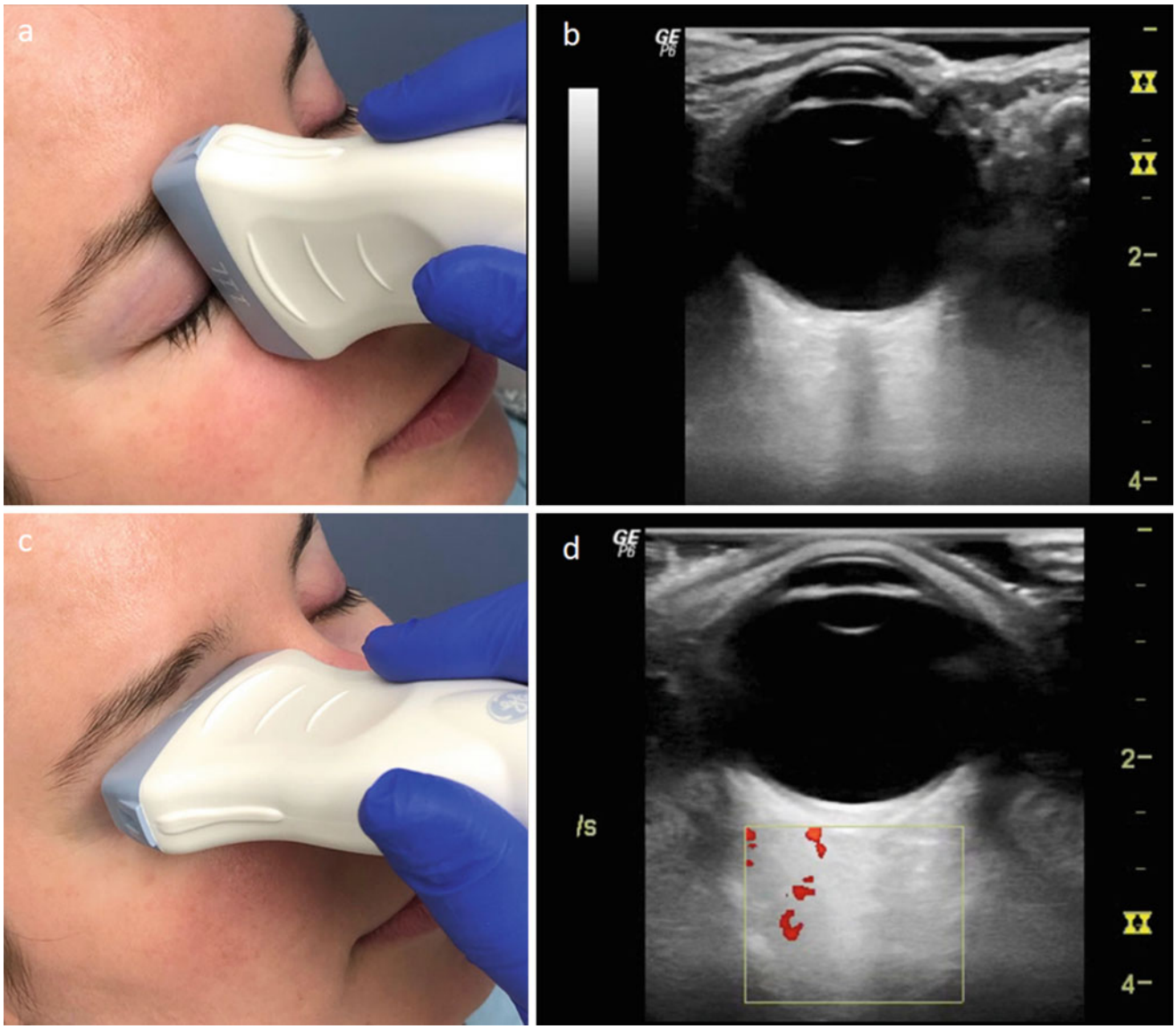


Fig. 1 External representation and normal ultrasound anatomy of the orbit in sagittal (**a**, **b**) and transversal view (**c**, **d**)

2 Arteriovenous Malformation

Orbital sonography can often be the initial screening study performed in the setting of suspected orbital AVM and should include the use of color Doppler with flow velocity measurements. Gray-scale sonographic findings can be non-specific and may have a range of manifestations including areas of subtle orbital inhomogeneity, thickened extraocular muscles, tubular spaces within the orbital cavity and enlarged vessels. Color Doppler evaluation should be used to document the presence of multiple serpiginous vessels and apparent flow reversal indicative of turbulent high-velocity pattern. Valsalva maneuver can promote dilation of the vessels and decrease of the flow. Dynamic ultrasound reveals an intimate relation of the tumor to the optic nerve and globe, without anatomical invasion.

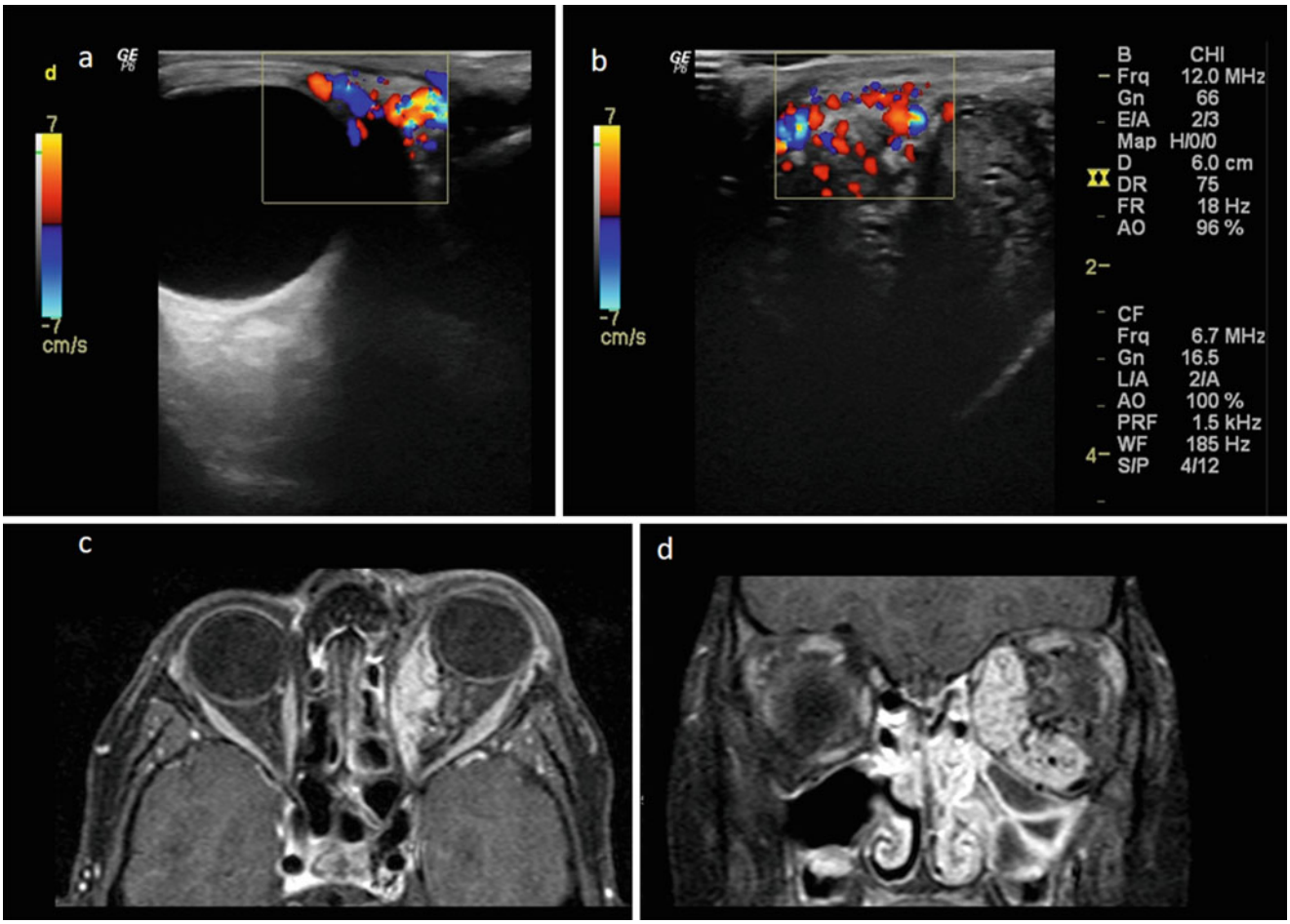


Fig. 2 A 9-year-old male with a complex left orbital AVM. (**a**) Sagittal color Doppler ultrasound demonstrates a hyperechoic lesion surrounding the globe with markedly increased flow. (**b**) Gain was increased, and amplification of the display was adjusted, depicting dilated vessels and turbulent flow in the mass. T1WI MR axial (**c**) and coronal (**d**) elucidating the mass-occupying AVM in the left orbit

3 Venolymphatic Malformation

Typically, a venolymphatic malformation of the orbit is seen as a hypoechoic lesion of heterogeneous echotexture and multiple cystic spaces within. On color Doppler, there may be a weak or undetectable signal. When present, arterial and venous flow are found within the septa. Phleboliths, fluid-fluid levels and internal debris may also be noted in the cystic spaces. Size of the cysts and vascular flow usually do not change with Valsalva.

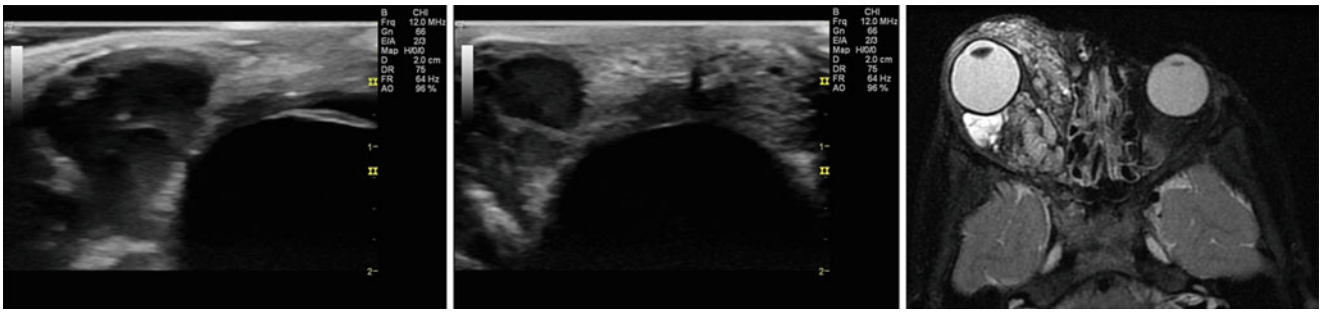


Fig. 3 A 4-year-old girl with right orbital VLM. (**a**, **b**) Sagittal sonograms reveal large cystic cavities separated by septa, surrounding the globe. (**c**) T2WI MR depicts a mass-occupying hyperintense heterogeneous lesion in the right orbit with marked proptosis and globe dystopia

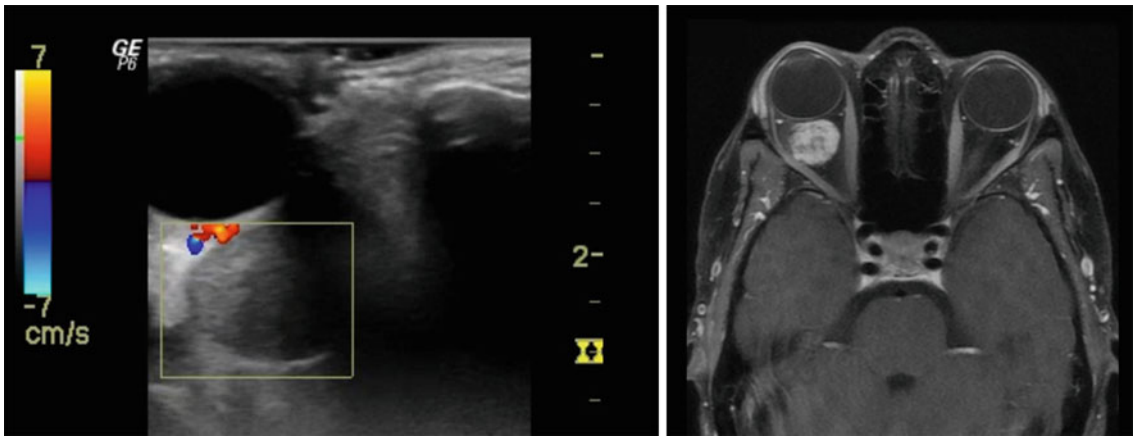


Fig. 4 Sagittal ultrasonography on a 43-year-old female with orbital cavernous hemangioma, showing a heterogeneous, slightly hyperechoic oval lesion (**a**). Posterior sound attenuation from the inferior rectus creates a dark interface to the lower aspect of the lesion. The mass showed heterogeneous signal intensity with inhomogeneous enhancement on axial T1WI (**b**)

4 Cavernous Venous Malformation

The diagnosis of a cavernous venous malformation can be highly suggested on well-defined intraconal lesions in adult patients with painless progressive proptosis. Not rarely, they are discovered incidentally, since they are slow-growing and often asymptomatic. Ultrasonographic features include well-circumscribed lesions with homogeneous and slightly hyperechoic patterns. Small areas of slow blood flow can also be found. The increased echogenicity has been postulated to be caused by multiple interfaces between the walls of the cavernous spaces and the blood within them [1, 2].

5 Solitary Fibrous Tumor (Hemangiopericytoma)

Hemangiopericytomas should be considered as a differential diagnosis if the ultrasonographic findings demonstrate a hypoechoic, well-defined mass displacing the adjacent structures and with large collateral feeding vessels [3].

6 Dermoid Cysts

Ultrasonography is particularly useful in younger patients with painless subcutaneous lesions along the zygomaticofrontal or frontoethmoidal sutures. Dermoid cysts account for 46% of childhood orbital neoplasms and, therefore, its clinical features combined with US findings can often provide enough information for diagnosis and management of the lesion [4]. Dermoids are normally non-vascularized cysts with a well-defined linen, hyperechoic walls and hypoechoic content mostly formed by fluid. Possible additional findings include echogenic components in the cyst's cavity and fluid-fluid levels. CT or MR is reserved for recurrent lesions or in deeper cysts, to rule out intradiploic components or dumbbell configuration.

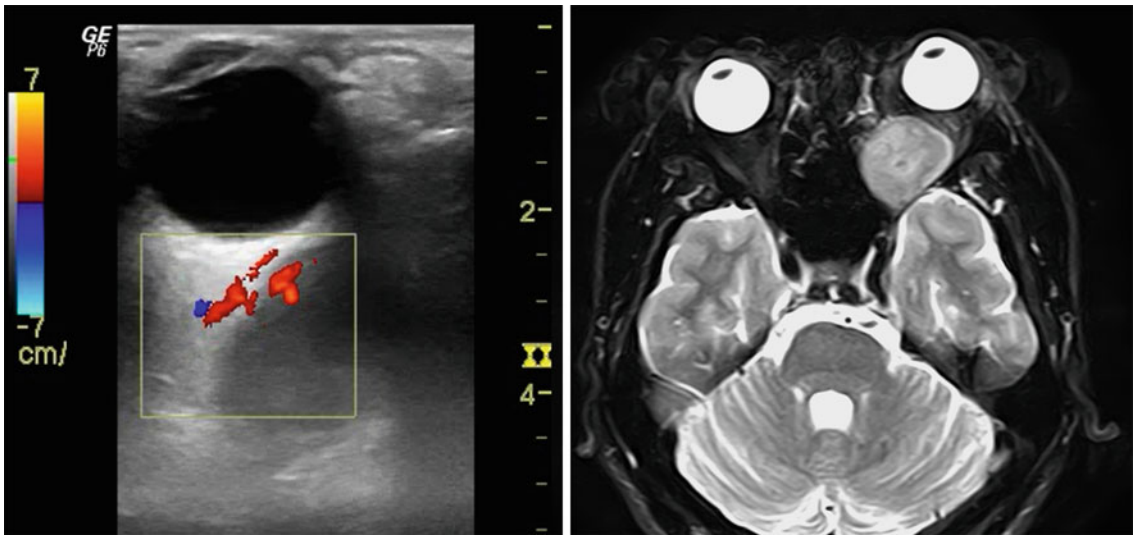


Fig. 5 A 29-year-old male with progressive left proptosis and blurred vision over the course of 4 years. (**a**) Sagittal US with color Doppler depicts an oval well-defined hypoechoic retrobulbar mass with intense peripheral hypervascular activity in the hyperechoic area. (**b**) Axial T2W MRI reveals a heterogeneously enhanced left orbital lesion. These findings were consistent with orbital malignancy and histopathologic exam confirmed hemangiopericytoma

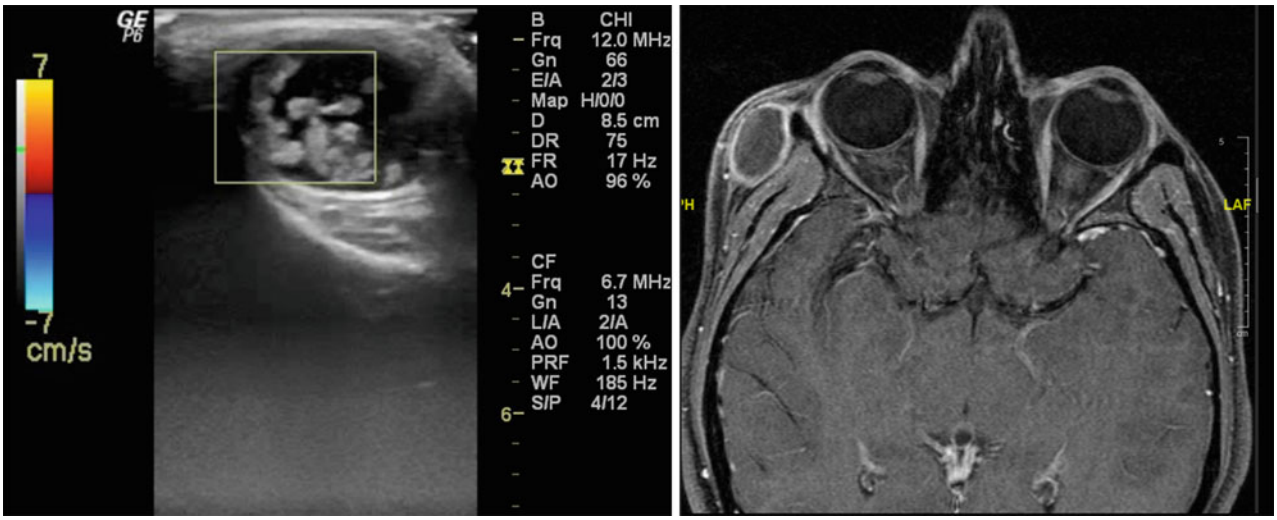


Fig. 6 A 23-year-old female with a recurrent, painless, slow-growing mass in the supero-lateral aspect of the right periorbital region. (**a**) US image depicts a unilocular cystic lesion with smooth contours, full of multiple echogenic components floating within the fluid matrix. (**b**) Axial T1WI MR depicts a hyperintense lesion with peripheral enhancement

References

1. Keng C-Y, Lan HH-C, Chen CC-C, Gueng M-K, Su Y-G, Lee S-K. Soft tissue Hemangiomas: high-resolution grayscale and color Doppler ultrasonographic features in 43 patients. J Med Ultrasound. 2008;16(3):223–30.
2. Diamantopoulou A, Damianidis C, Kyriakou V, et al. Orbital cavernous hemangiomas: ultrasound and magnetic resonance imaging evaluation. Neuroradiol J. 2010;23(1):99–108.
3. Kantilaras AP. Role of ultrasound in the diagnosis approach of malignant solitary fibrous tumor. J Diagn Med Sonography. 2018;34(5):391–5.
4. Shields JA, Shields CL. Orbital cysts of childhood – classification, clinical features, and management. Surv Ophthalmol. 2004;49(3):281–99.

Orbital Positron Emission Tomography/ Computed Tomography (PET/CT)

18

J. Matthew Debnam and Bita Esmaeli

Contents

1 Squamous Cell Carcinoma 156
1.1 Signs and Symptoms 156
1.2 Differential Diagnosis 156
1.3 Diagnosis 156
1.4 Treatment 156
1.5 Figures with Captions 157

2 Melanoma 160
2.1 Signs and Symptoms 160
2.2 Differential Diagnosis 160
2.3 Diagnosis 160
2.4 Treatment 160
2.5 Figures with Captions 160

3 Lymphoma 163
3.1 Signs and Symptoms 163
3.2 Differential Diagnosis 164
3.3 Diagnosis 164
3.4 Treatment 164
3.5 Figures with Captions 164

4 Adenoid Cystic Carcinoma 168
4.1 Signs and Symptoms 168
4.2 Differential Diagnosis 168
4.3 Diagnosis 168
4.4 Treatment 168
4.5 Figures with Captions 169

5 Orbital Metastases 170
5.1 Signs and Symptoms 170
5.2 Differential Diagnosis 170
5.3 Diagnosis 170
5.4 Treatment 170
5.5 Figures with Captions 171

6 Orbital Inflammatory Syndrome ("Pseudotumor") 172
6.1 Signs and Symptoms 172

J. M. Debnam (✉)
Department of Neuroradiology, The University of Texas MD Anderson Cancer Center, Houston, TX, USA
e-mail: Matthew.Debnam@mdanderson.org

B. Esmaeli
Ophthalmic Plastic Surgery, Department of Plastic Surgery, The University of Texas MD Anderson Cancer Center, Houston, TX, USA
e-mail: besmaeli@mdanderson.org

© Springer Nature Switzerland AG 2022
G. Ben Simon et al. (eds.), *Atlas of Orbital Imaging*,
https://doi.org/10.1007/978-3-030-62426-2_84

6.2 Differential Diagnosis 172
6.3 Diagnosis 172
6.4 Treatment 172
6.5 Figures with Captions 173

7 IgG4-Related Disease 174
7.1 Signs and Symptoms 174
7.2 Differential Diagnosis 175
7.3 Diagnosis 175
7.4 Treatment 175
7.5 Figures with Captions 175

References 176

Abstract

Positron Emission Tomography/Computed Tomography (PET/CT) utilizes a radio-labeled tracer, such as glucose, that is accumulated in cells in the body, including cancer cells that have high chemical or metabolic activity. For example, as cancer cells have a higher metabolic rate compared to other cells in the body, radiolabeled glucose will accumulate in cancer cells and show the disease location and degree of activity. Different markers can be used to identify certain tumors including meningiomas and neuroendocrine tumors. PET/CT can be used for detection, to define the extent of locoregional and distant sites of disease, guide biopsies, and monitor treatment response.

Keywords

Squamous cell carcinoma (SCC) · Positron Emission Tomography/Computed Tomography (PET/CT) · Melanoma · Cutaneous · Sinonasal · Orbital lymphoma · Ocular adnexal lymphoma · MALT lymphoma · Adenoid cystic carcinoma · ^{68}Ga-dotatate PET/CT · Metastasis · Inflammatory orbital pseudotumor · IgG4 related disease

1 Squamous Cell Carcinoma

Abstract

- Squamous cell carcinoma about the orbit is usually encountered in the medial canthus and lower eyelid
- ^{18}Fluoride-fluorodeoxyglucose (^{18}F-FDG) is glucose radiolabeled with fluorine-18.
- Glucose uptake in tumors can be visualized with ^{18}F-FDG PET/CT.
- PET/CT may aid in defining the location for biopsy.

1.1 Signs and Symptoms

Squamous cell carcinoma (SCC) may present clinically as an erythematous patch or a larger ulcerative lesion. Sinonasal SCC invading the orbit can cause signs such as nasal obstruction, epistaxis, pain, paresthesia, and trismus. Mass effect on the globe may lead to eyelid fullness, diplopia, ophthamoplegia, and decreased vision.

Periocular SCC larger than T2C by AJCC eighth edition has some risk of metastasis to regional lymph nodes and rarely distant metastases. The most common regional metastatic sites include the pre-auricular, parotid, and submandibular lymph nodes.

1.2 Differential Diagnosis

Differential considerations include other skin cancers such as basal cell carcinoma (BCC) and melanoma. Larger lesions may appear radiographically similar to adenoid cystic carcinoma, melanoma, and lymphoma.

1.3 Diagnosis

Diagnosis is made by clinical examination and biopsy. ^{18}F-FDG PET/CT may aid in defining the location for biopsy and aid in identification of metastatic sites. Orbital imaging may be necessary in larger lesions to define involvement of the skin surface, orbit, intracranial compartment, and paranasal sinuses.

1.4 Treatment

Smaller lesions can be treated with surgical excision. Larger lesions with more extensive involvement may require exenteration, craniotomy or maxillectomy and adjuvant radiation therapy or systemic chemotherapy or immunotherapy. ^{18}F-FDG PET/CT can be used to monitor treatment.

1.5 Figures with Captions



Fig. 1 Axial T1 post-contrast fat-saturated image of a 75-year-old man with recurrent eyelid SCC and orbital extension (same patient in Figs. 2, 3, 4, and 5). An enhancing mass is present in the left orbit and periorbital soft tissue with compression upon the globe and proptosis (arrows)

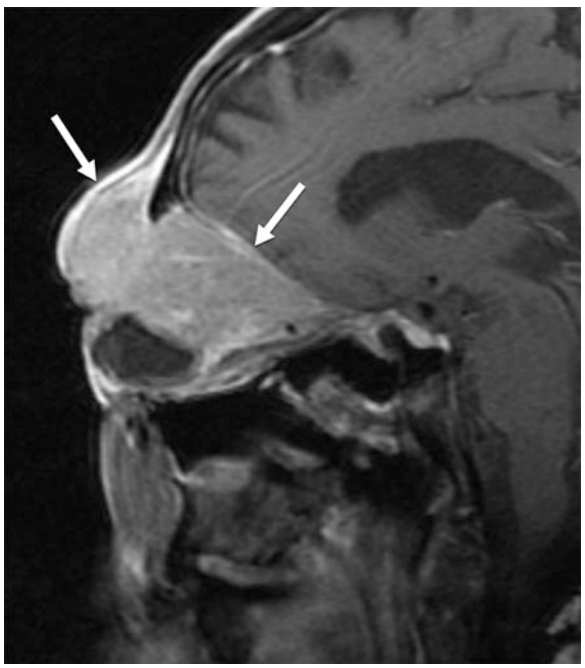


Fig. 2 Sagittal T1 post-contrast fat-saturated image shows the left orbital mass with involvement of the inferior frontal subcutaneous soft tissues and the intracranial, extradural compartment (arrows)

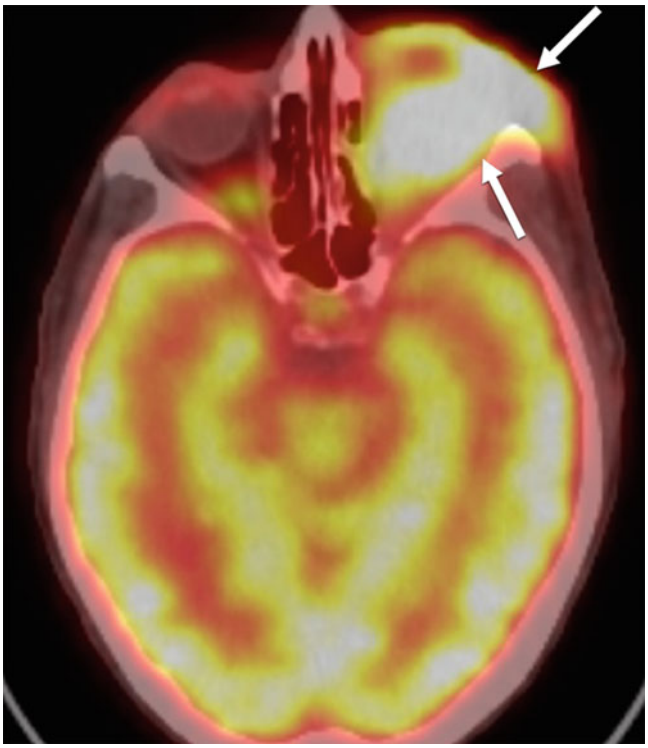


Fig. 3 Axial PET/CT image shows the FDG-avid mass in the left orbit with proptosis and extension into the periorbital soft tissues (arrows)

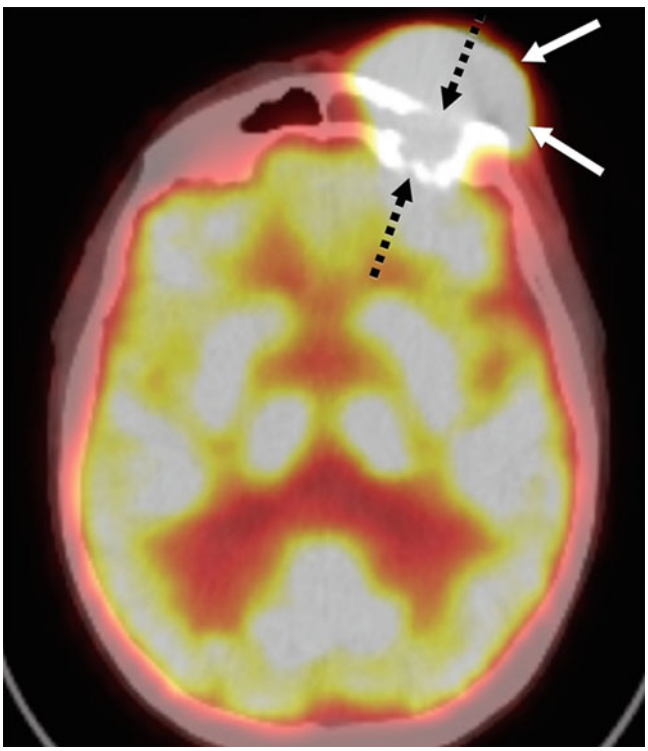


Fig. 4 Axial PET/CT image with an FDG-avid mass in the left inferior frontal soft tissues (white arrows) The CT portion of the study demonstrates destruction of the left frontal sinus (dotted black arrows)

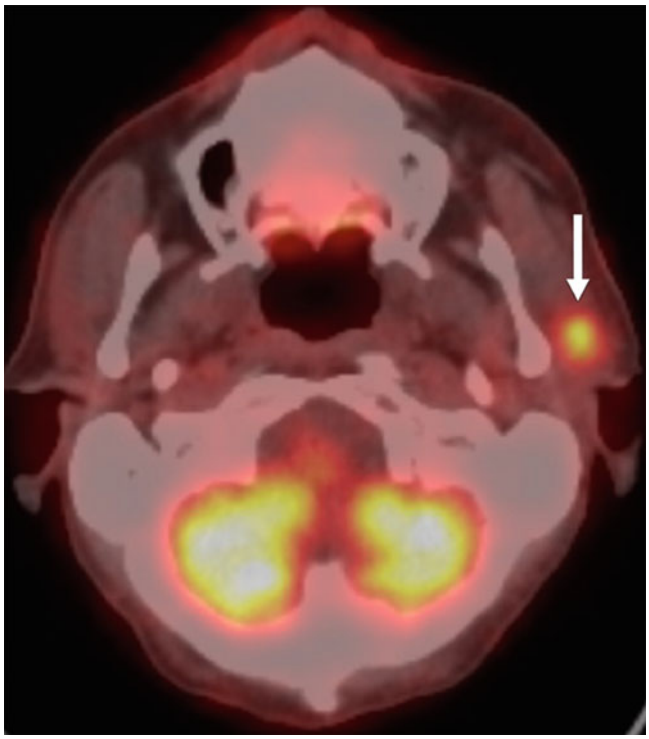


Fig. 5 Axial PET/CT image showed regional spread, with an FDG-avid left parotid nodal metastasis (arrow)

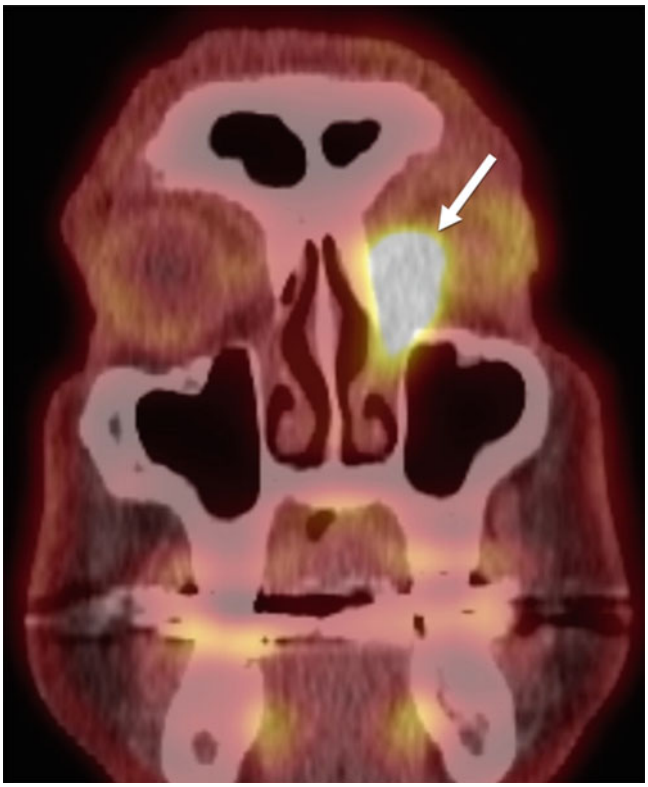


Fig. 7 Coronal PET/CT image shows an FDG-avid mass in the left medial canthus and lacrimal sac (arrow)

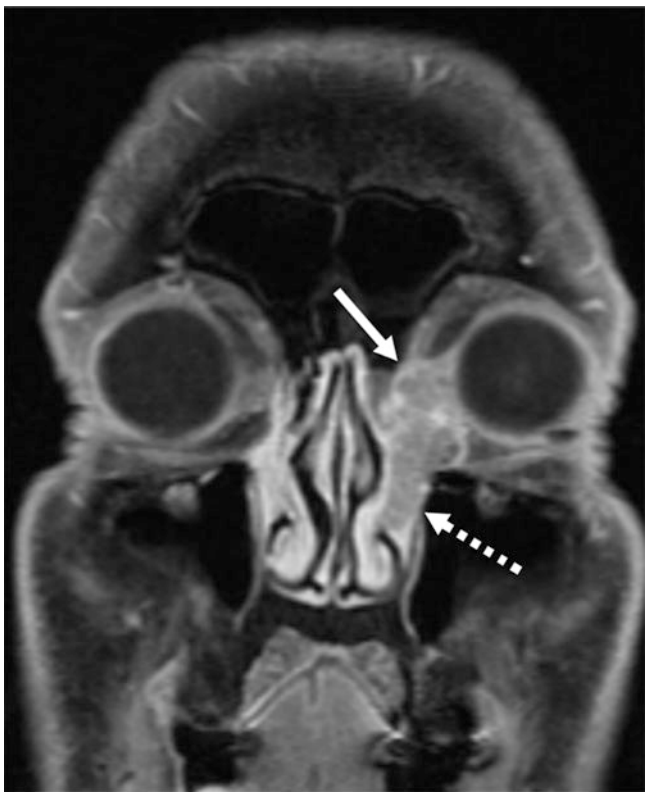


Fig. 6 Coronal T1 post-contrast fat-saturated image of a 75-year-old man (same patient in Figs. 6, 7, and 8) with an enhancing mass in the left medial canthus (arrow) with involvement of the lacrimal sac and likely the lacrimal duct (dotted arrow)

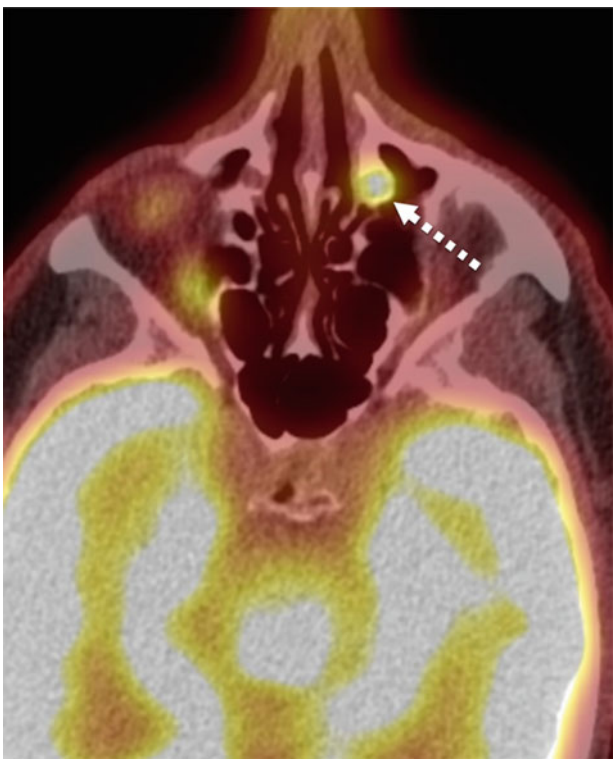


Fig. 8 Axial PET/CT image with FDG activity in the left lacrimal duct (arrow). Due to involvement of the lacrimal duct the surgical resection included a medial maxillectomy

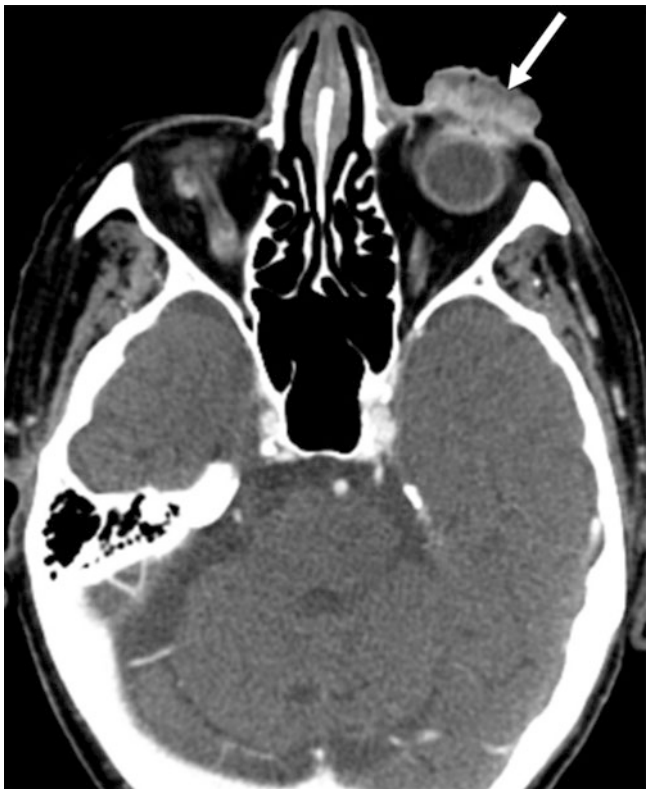


Fig. 9 Axial post-contrast CT orbit, soft tissue window image of an 89-year-old man (same patient in Figs. 9, 10, 11, and 12) with an exophytic SCC of the left lower eyelid (arrow)

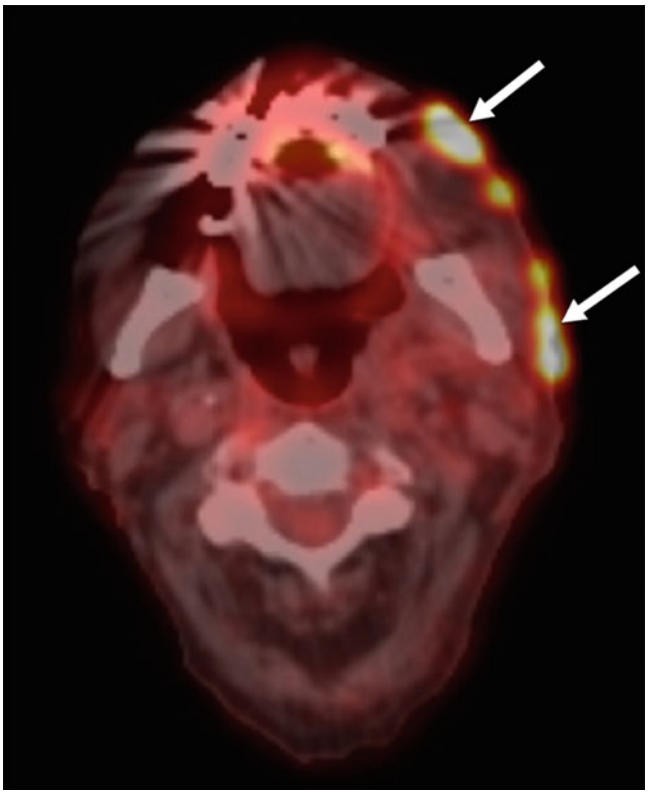


Fig. 11 Axial PET/CT image shows further involvement of the FDG-avid squamous cell carcinoma more inferiorly in the left face (arrows)

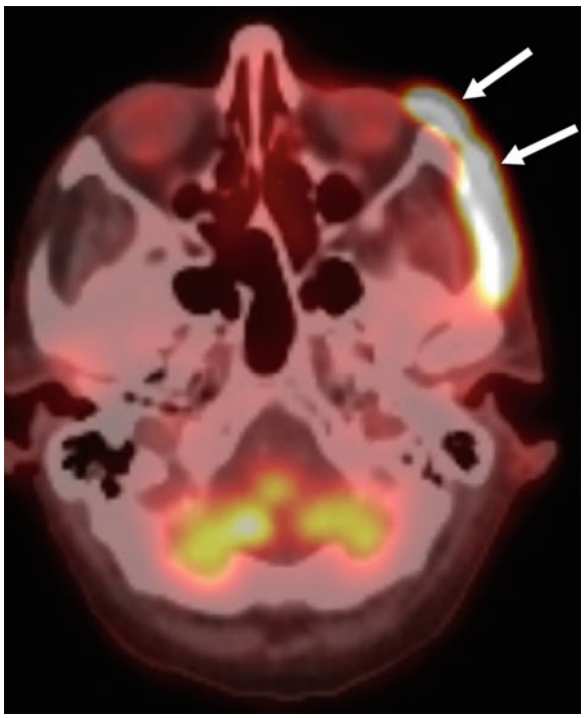


Fig. 10 Axial PET/CT image. Follow-up PET/CT examination at a later date shows a new FDG-avid SCC in the left face (arrows) consistent with multifocal disease progression. The location of FDG-avid tumor can be used to guide biopsy



Fig. 12 Coronal PET/CT image shows the ulcerative mass in the left face and tumor in the left chin (arrows)

2 Melanoma

Abstract
- The annual incidence in cutaneous melanoma has been increasing at a faster rate than any other cancer.
- Most patients with newly diagnosed cutaneous melanoma present with early stage disease.
- Sinonasal melanoma is a rare but aggressive tumor associated with a poor prognosis. Extension may occur though the orbital floor.
- ^{18}F-FDG PET/CT can be used to detect metastasis and monitor treatment response.

2.1 Signs and Symptoms

Cutaneous melanoma in the periocular region can present as a new or enlarging mass on the eyelid or periocular skin. Larger tumors may extend directly into the orbit. Sinonasal melanoma may present with nasal obstruction, epistaxis, pain, paresthesia, and trismus. Mass effect on the globe may lead to eyelid fullness, diplopia, ophthalmoplegia, and decreased vision.

Metastatic sites include the regional lymph nodes, lungs, liver, gastrointestinal track, and central nervous system.

2.2 Differential Diagnosis

For cutaneous melanoma the differential diagnosis includes other skin cancers such as squamous cell and basal cell carcinoma. Other sinonasal tumors would include squamous cell carcinomas, sinonasal undifferentiated carcinoma, and lymphoma.

2.3 Diagnosis

Diagnosis is made by clinical examination and biopsy. CT and MR imaging show local extent. Ultrasonography can be used for detection of regional nodal metastasis. ^{18}F-FDG PET/CT can be used to guide biopsy and detect regional nodal or distant metastasis.

2.4 Treatment

For cutaneous melanoma in the periocular region surgical excision is the primary treatment and is curative for the majority of patients. Immunotherapy has gained popularity for metastatic or locally advanced cases that would otherwise require orbital exenteration as a surgical option. Sinonasal melanoma can also be treated with surgical resection, radiation, and chemotherapy for control of local disease and distant metastasis. ^{18}F-FDG PET/CT can be used to monitor treatment response.

2.5 Figures with Captions



Fig. 13 Axial post-contrast CT orbit, soft tissue window image of an 84-year-old woman with a history of recurrent melanoma in the left lower eyelid who presented with a rapidly growing mass in that region. The CT shows a heterogeneously enhancing mass in the left lower eyelid (arrow)

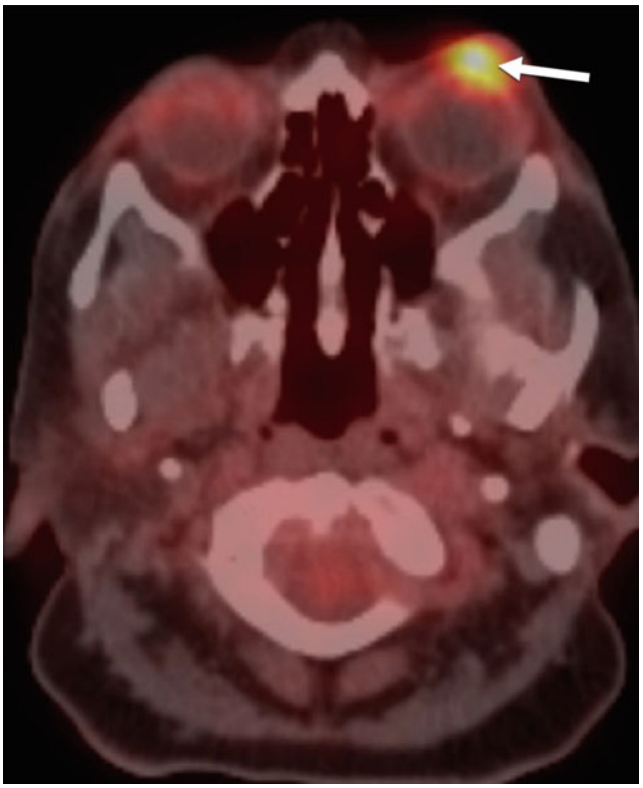


Fig. 14 Axial PET/CT image shows FDG-avidity of the left lower eyelid mass (arrow)

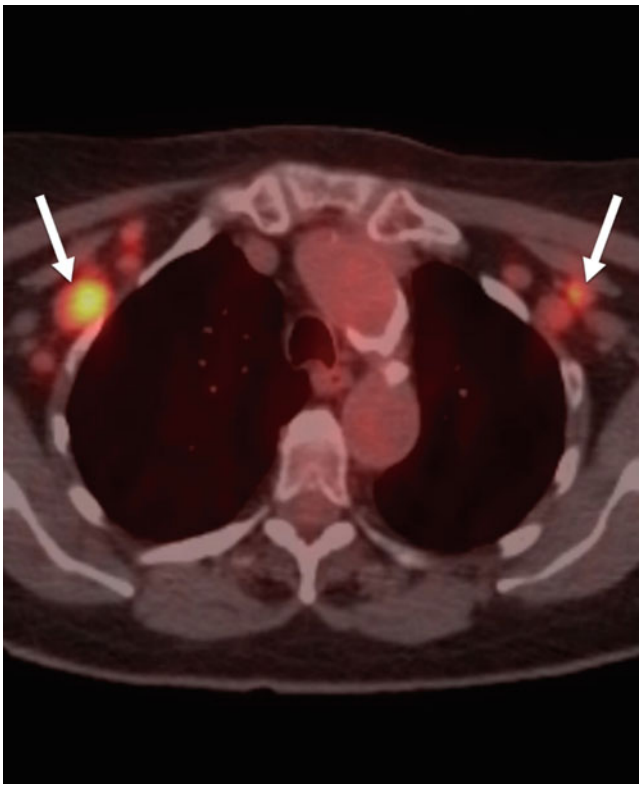


Fig. 16 Axial PET/CT image shows nodal metastases in the axilla bilaterally (arrows)

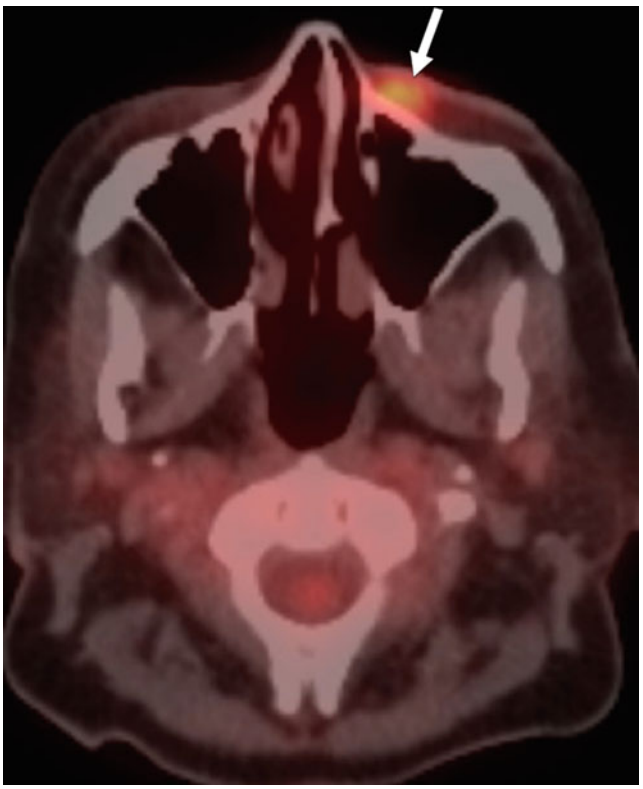


Fig. 15 Axial PET/CT image demonstrates a second FDG-avid focus in a clinically evident left premaxillary soft tissue lesion (arrow)

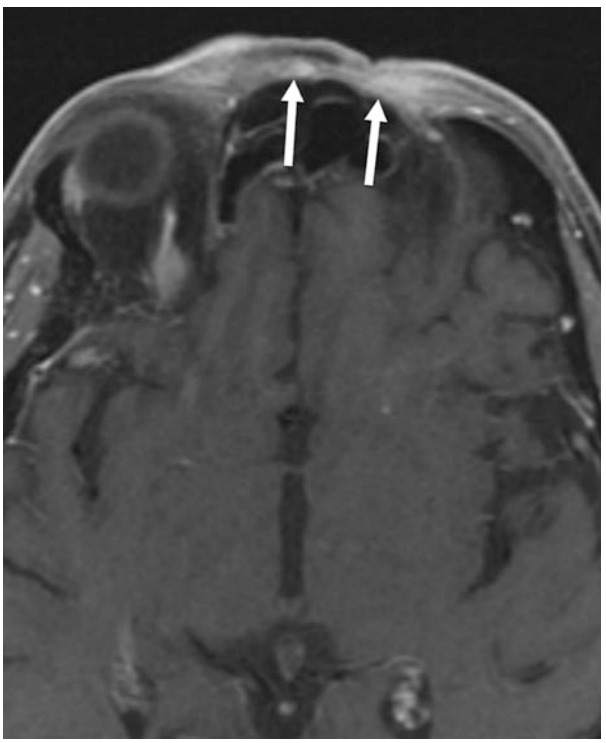


Fig. 17 Axial T1 post-contrast fat-saturated image of an 88-year-old male (different patient) who underwent resection of a forehead melanoma at an outside institution. Heterogeneously enhancing tissue is present without a definite mass and may represent postoperative change (arrows)

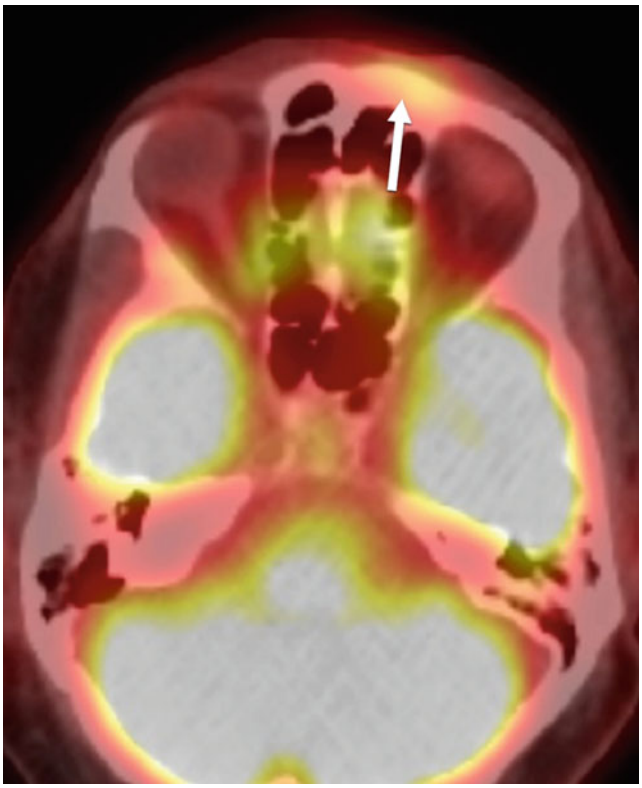


Fig. 18 **Axial PET/CT image** shows an FDG-avid lesion in the left supraorbital region that was subsequently resected and confirmed to be melanoma (arrow)

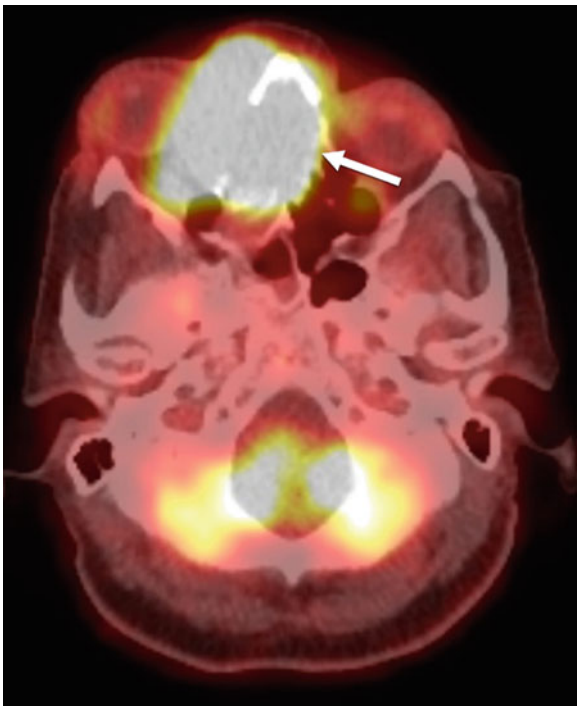


Fig. 19 **Axial PET/CT image** of a 68-year-old woman (different patient) with sinonasal melanoma. The PET/CT demonstrates an FDG-avid mass in the right maxillary sinus with involvement of the nasal cavity and inferomedial right orbit (arrow)

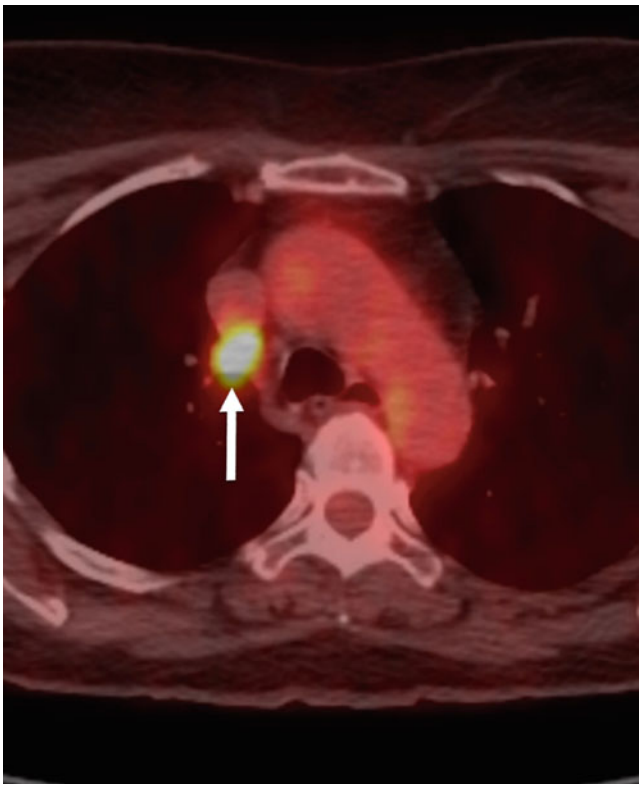


Fig. 20 **Axial PET/CT image** shows an FDG-avid mediastinal nodal metastasis (arrow)

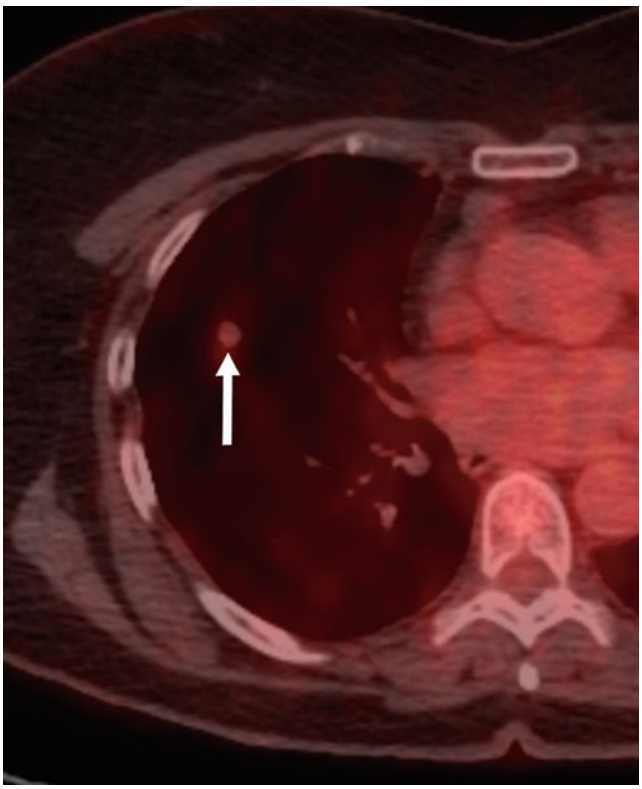


Fig. 21 **Axial PET/CT image** demonstrates FDG-avidity of a right lung nodule (arrow)

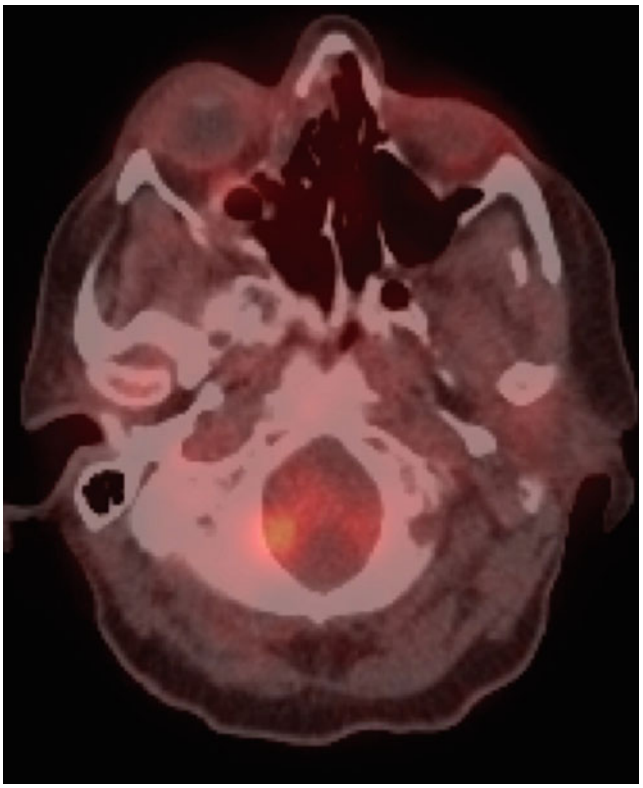


Fig. 22 Axial PET/CT image shows resolution of the FDG-avid sinonasal and orbital melanoma following chemotherapy

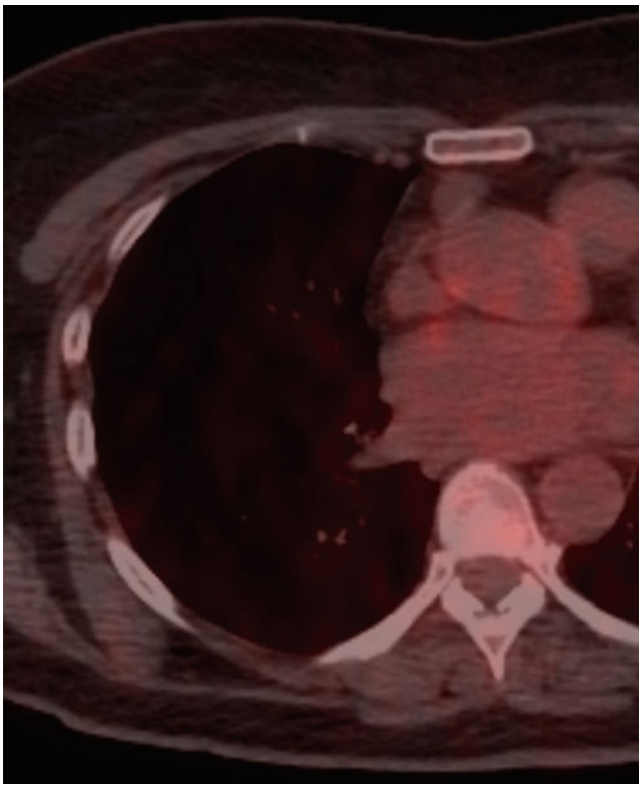


Fig. 24 Axial PET/CT image. The FDG-avid pulmonary metastasis has also resolved after chemotherapy

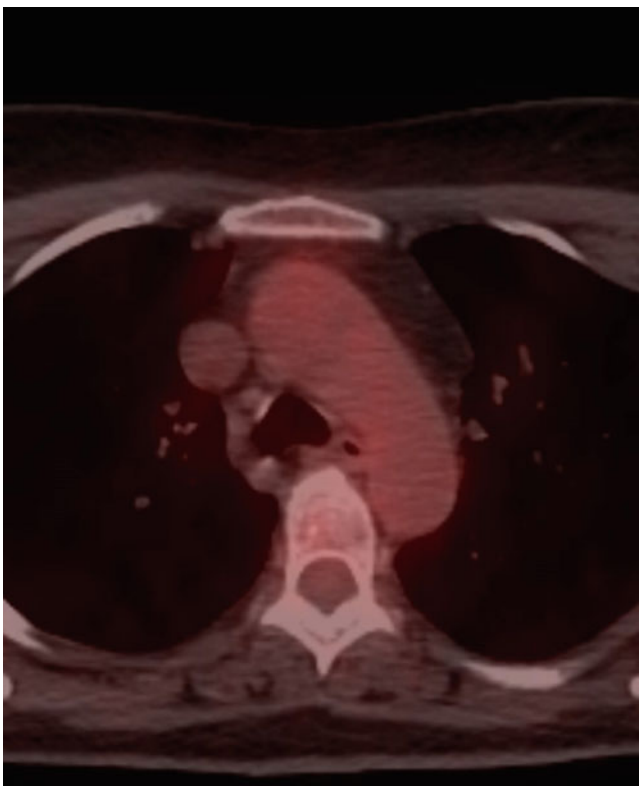


Fig. 23 Axial PET/CT image. The previously seen FDG-avid mediastinal node is no longer present following treatment with chemotherapy

3 Lymphoma

Abstract

- Most common primary malignant orbital tumor in adults
- Whole-body PET/CT with ^{18}F-FDG is utilized for initial staging and posttreatment assessment for orbital lymphoma and ocular adnexal lymphoma.
- Low-grade MALT lymphoma may have low metabolic activity and thus low ^{18}F-FDG uptake possibly leading to a false negative study. However, ^{18}F-FDG PET/CT is highly sensitive in the detection of extraorbital sites of involvement with lymphoma. Diffuse large B cell lymphoma or mantle cell lymphoma of orbit are expected to have high FDG uptake both in the orbit and in extraocular sites.

3.1 Signs and Symptoms

Orbital and ocular adnexal lymphoma can present as unilateral or bilateral involvement of orbital soft tissue with involvement of lacrimal gland in approximately 50% of cases. Conjunctival involvement may present as a "salmon patch" infiltrate. Proptosis, a painless slow growing mass,

upper eyelid ptosis, or a palpable nodule are all possible presentations of ocular adnexal lymphoma. Most lesions are in the anterior orbit but occasionally the posterior orbital apical structures and extraocular muscles can be involved.

3.2 Differential Diagnosis

The differential diagnosis includes benign lymphoid hyperplasia, IgG4 disease, and orbital inflammatory syndrome. Other causes of lacrimal gland enlargement include epithelial tumors, thyroid eye disease, orbital pseudotumor, and infection.

3.3 Diagnosis

Tissue biopsy is required to diagnose lymphoma and lymphoma studies such as flow cytometry to help establish the diagnosis and guide treatments. Once the diagnosis is established, the staging work-up includes whole-body ^{18}F-FDG PET/CT.

3.4 Treatment

The treatment varies depending on the histological subtype and stage and may include radiation therapy, chemotherapy, and/or immunotherapy. Whole-body PET/CT with ^{18}F-FDG can be used for posttreatment surveillance.

3.5 Figures with Captions

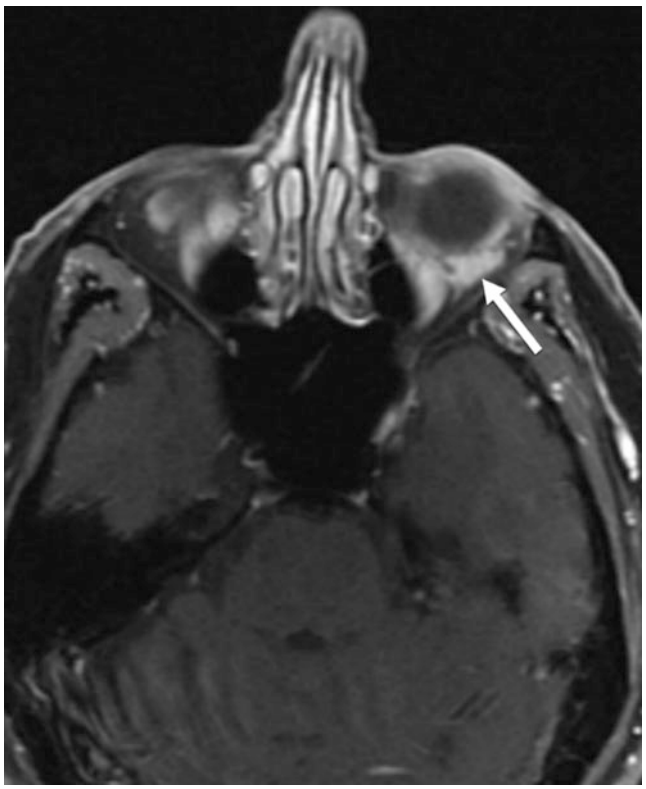


Fig. 25 Axial T1 post-contrast fat-saturated image in a 59-year-old man with marginal zone lymphoma involving the left orbit. The MRI examination shows homogeneously enhancing tissue in the left retro-orbital space (arrow)

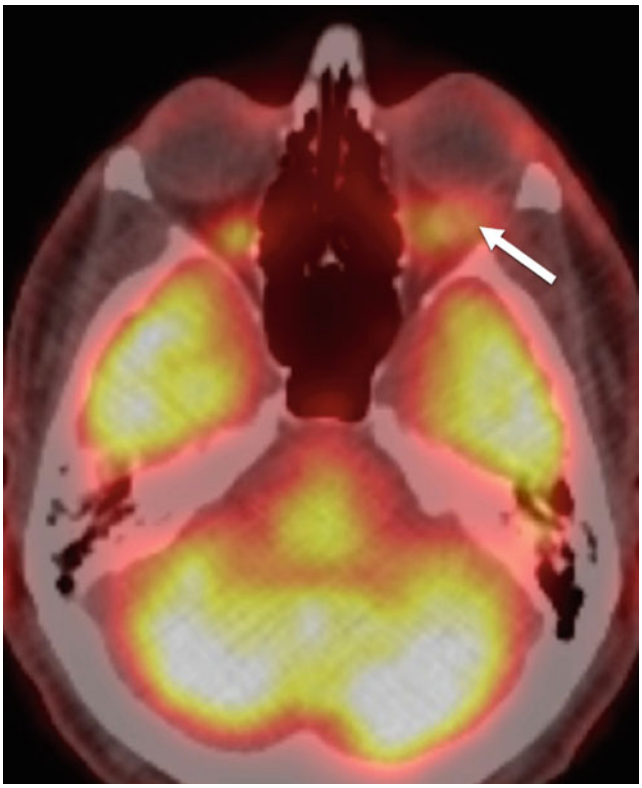


Fig. 26 Axial PET/CT image. The left retro-orbital lesion is FDG-avid (arrow)



Fig. 28 Coronal T1 post-contrast fat-saturated image of a 74-year-old female (different patient) with Hodgkin lymphoma. The MRI examination shows a large mass in the left face and inferolateral left orbit (arrows)

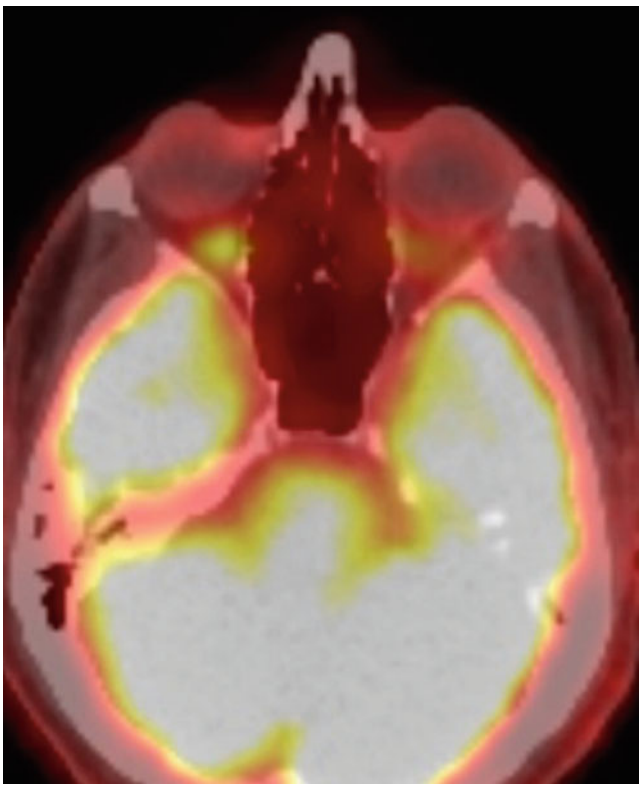


Fig. 27 Axial PET/CT image shows resolution of the FDG-avid left retro-orbital mass following low-dose radiation treatment

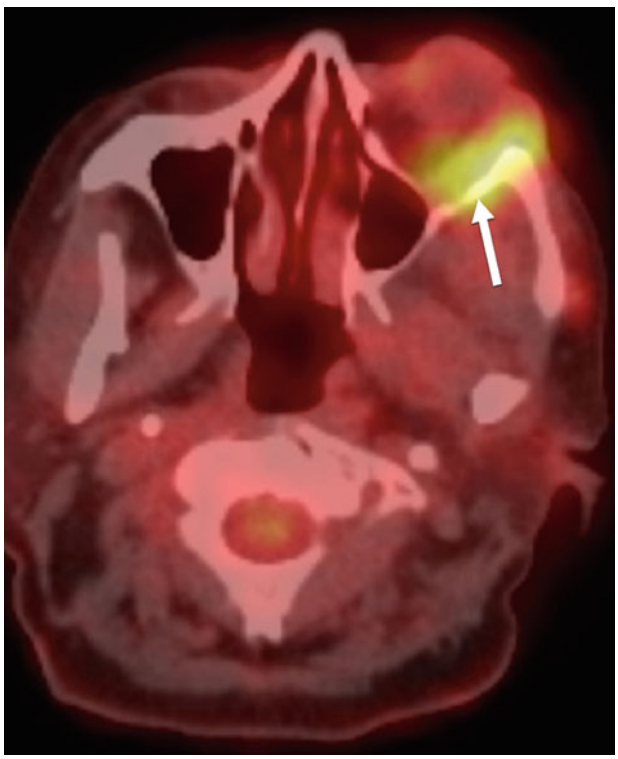


Fig. 29 Axial PET/CT image shows FDG-avidity of the inferolateral left orbital component of the mass (arrow)

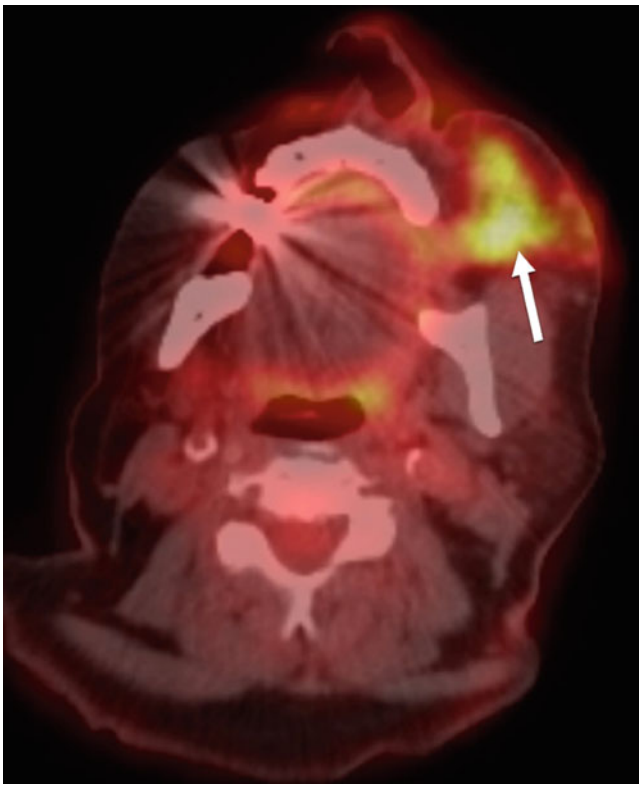


Fig. 30 **Axial PET/CT image** demonstrates FDG-avidity in the mass involving the left face (arrow)

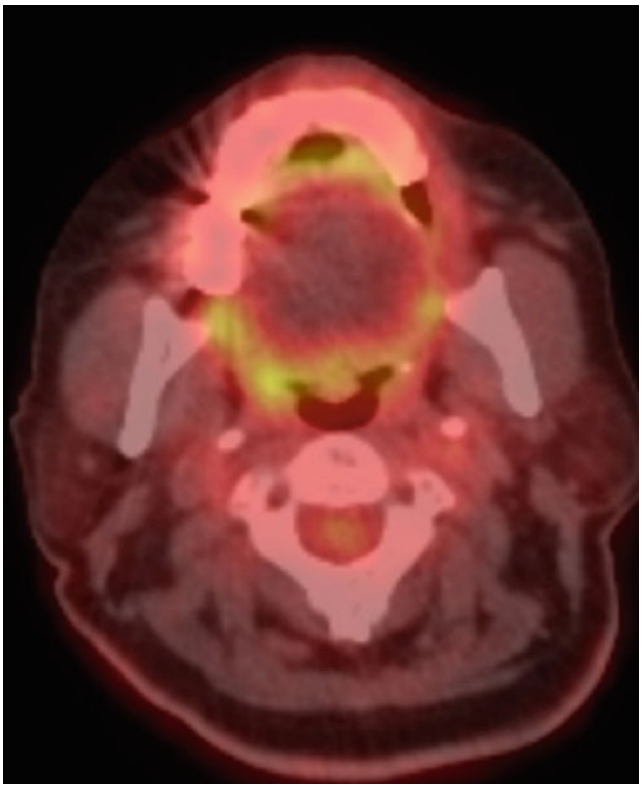


Fig. 32 **Axial PET/CT image** also demonstrates resolution of the FDG-avid left facial mass after chemotherapy

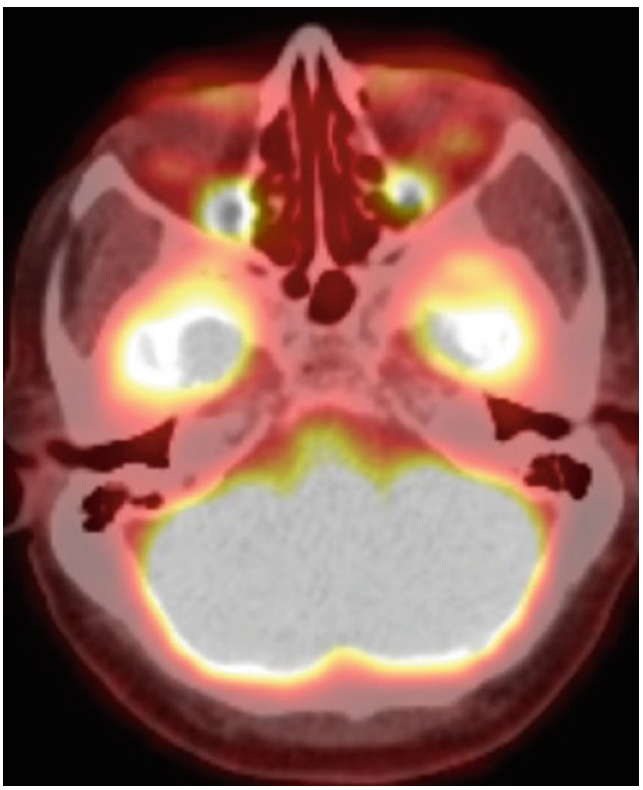


Fig. 31 **Axial PET/CT image** shows resolution of FDG-avidity in the inferolateral left orbit following treatment with chemotherapy

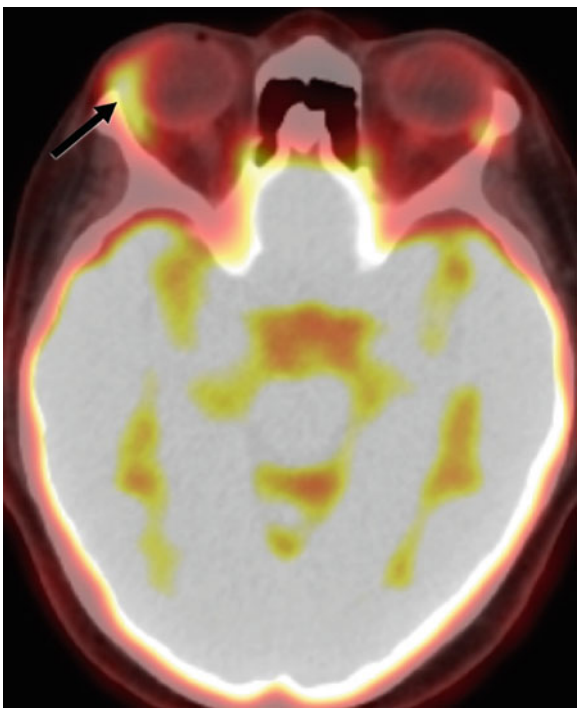


Fig. 33 **Axial PET/CT image** in a 61-year-old female (different patient) with chronic enlargement of the right lacrimal gland who underwent biopsy demonstrating follicular lymphoma. The PET/CT examination shows FDG-avidity in the right lacrimal gland (arrow)

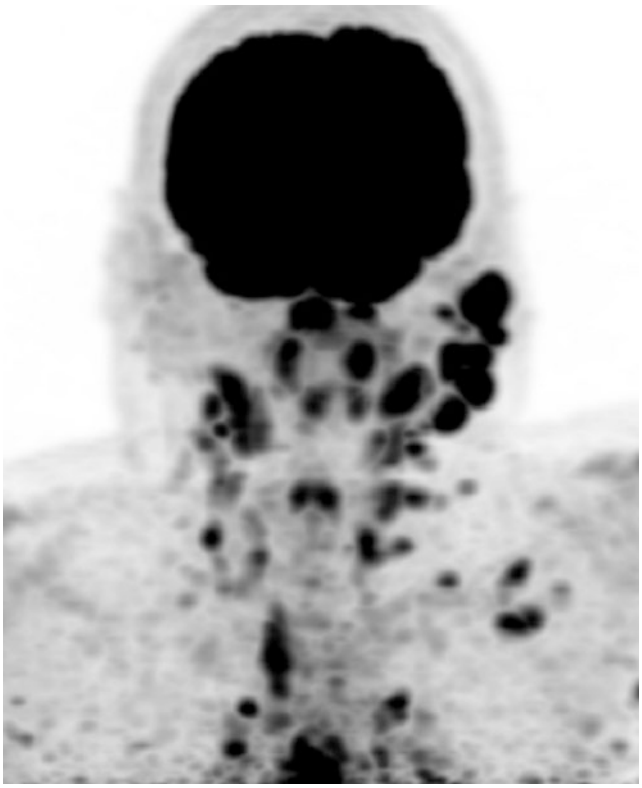


Fig. 34 Three-dimensional PET/CT image reveals further disease involvement of multiple lymph nodes throughout the neck and chest

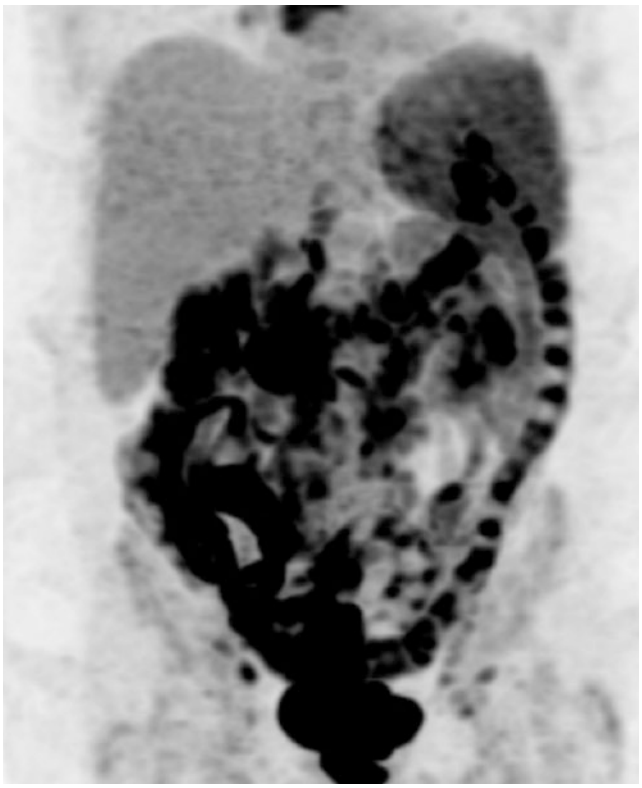


Fig. 35 Three-dimensional PET/CT image demonstrates FDG activity in the small and large intestine

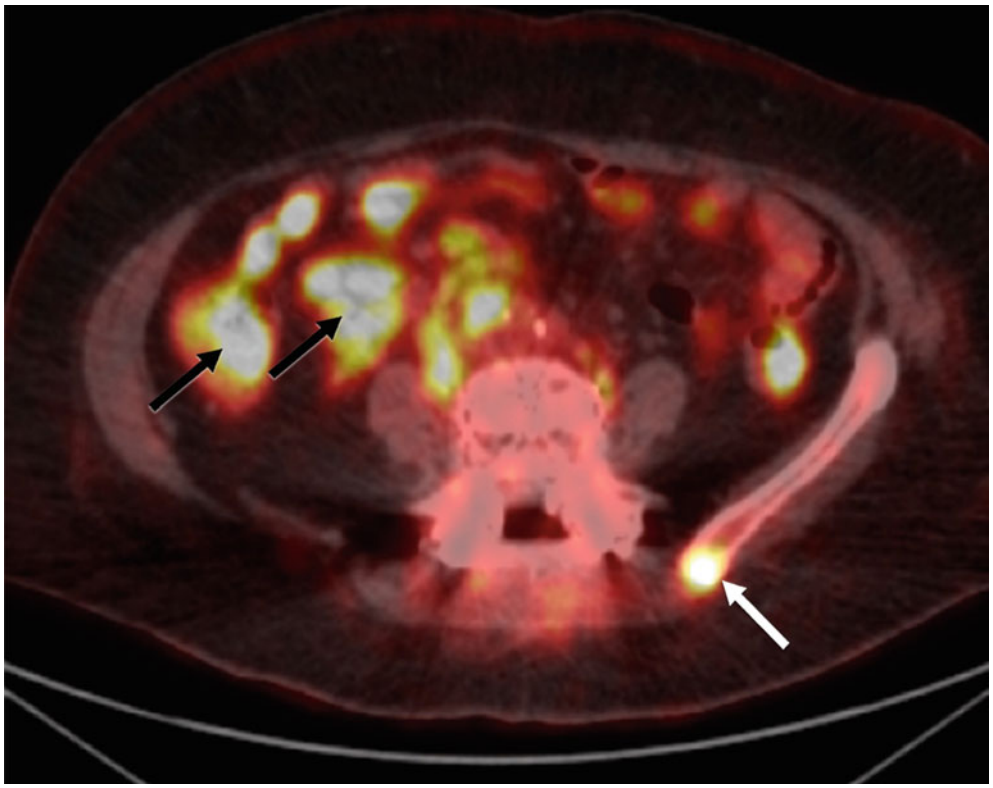


Fig. 36 **Axial PET/CT** with FDG-avidity in the bowl (black arrows) and involving the left iliac bone (white arrow)

4 Adenoid Cystic Carcinoma

Abstract

- Most common lacrimal gland primary malignant epithelial tumor, yet a very rare cancer.
- Whole-body PET/CT with 18F-FDG is utilized for initial staging and posttreatment assessment for lacrimal adenoid cystic carcinoma.

4.1 Signs and Symptoms

Symptoms of adenoid cystic carcinoma (ACC) include periocular pain, ptosis, diplopia, and paresthesia. As ACC arises from the lacrimal gland, the globe may be displaced inferomedially and is usually proptotic. Local spread including bone invasion may be present. There is a high rate of recurrence, distant metastases most commonly to the lungs and bony metastasis; lymph node metastasis is quite rare.

4.2 Differential Diagnosis

Differential consideration would include other epithelial cancers of the lacrimal gland such as pleomorphic-ex and lymphoproliferative disorders and benign epithelial lacrimal gland tumors such as pleomorphic adenoma. Other malignant epithelial lacrimal gland tumors include adenocarcinoma, mucoepidermoid carcinoma, and squamous cell carcinoma.

4.3 Diagnosis

If ACC is suspected both clinically and radiographically then an incisional biopsy is performed to establish the diagnosis before definitive treatments. Whole-body ^{18}F-FDG PET/CT can be used for initial staging to exclude distant metastases.

4.4 Treatment

Treatment varies among institutions depending on the extent of the tumor. Complete surgical resection with negative margins followed by adjuvant radiation therapy or concurrent radiation and chemotherapy is the preferred treatment at our institution for cases in which gross total resection can be done with eye sparing surgery. The choice between eye-sparing surgery or orbital exenteration with removal of the orbital wall and radiotherapy ± chemotherapy depends on tumor extension. Whole-body ^{18}F-FDG PET/CT can be used for posttreatment assessment.

4.5 Figures with Captions



Fig. 37 Axial T1 post-contrast fat-saturated image in a 46-year-old female right lacrimal gland adenoid cystic carcinoma. This image shows an enhancing lesion in the superotemporal right orbit (arrow)

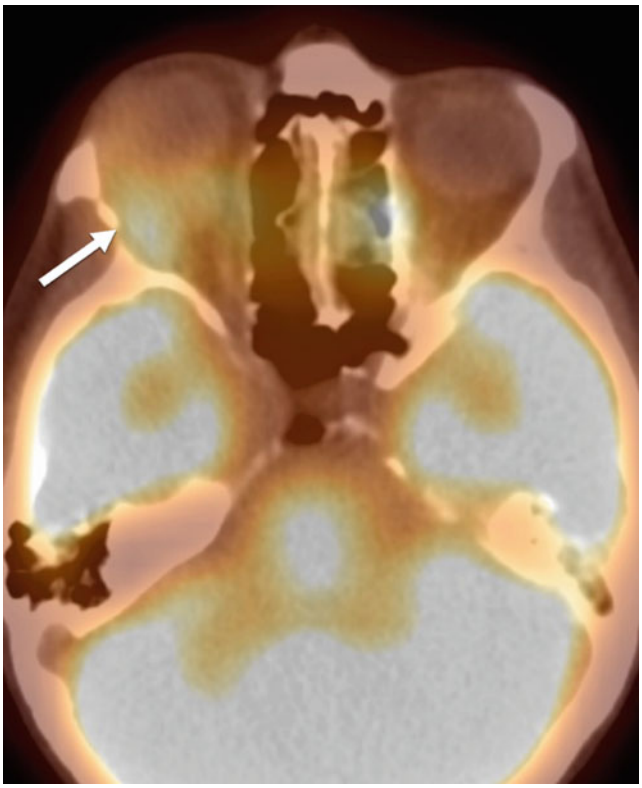


Fig. 38 Axial PET/CT image. The lesion in superotemporal right orbit is FDG-avid (arrow)

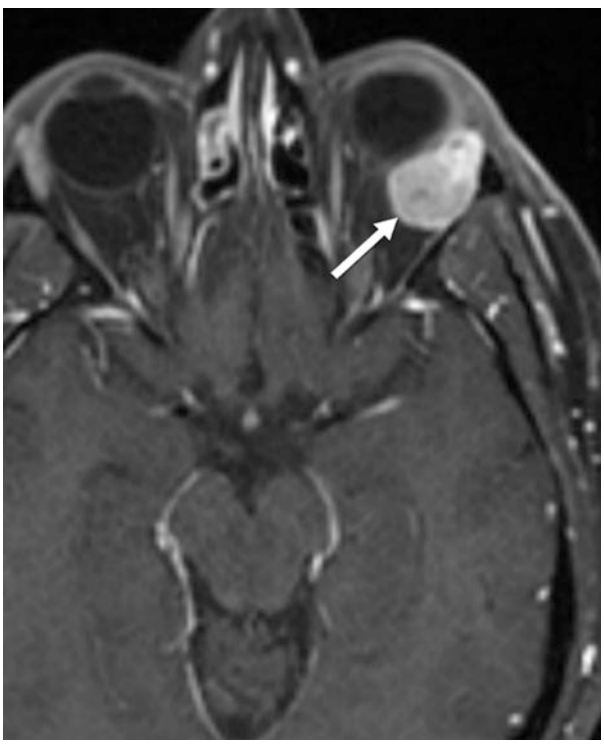


Fig. 39 Axial T1 post-contrast fat-saturated image of a 51-year-old male (different patient) with left lacrimal adenoid cystic carcinoma. The MRI examination shows an enhancing mass in the superotemporal left orbit (arrow)



Fig. 40 Axial PET/CT image. After resection of the mass and chemoradiation, the follow-up PET/CT showed no activity in the left orbit



Fig. 41 Coronal PET/CT image. The follow-up PET examination shows FDG-avid metastases in the cervical spine and right humerus (arrows)

5 Orbital Metastases

Abstract

- Metastases to the orbit may occur from primary tumors in any anatomic site; most commonly breast, lung, melanoma, prostate, and gastrointestinal tumors in adults and neuroblastoma in pediatric patients.
- Neuroendocrine tumors arise from endocrine cells and are usually seen in the gastrointestinal or bronchopulmonary tracts.
- (Gallium-68) ^{68}Ga-dotatate has an affinity for somatostatin receptors in neuroendocrine tumors.

5.1 Signs and Symptoms

Metastases to the orbit are usually unilateral but can also be bilateral in presentation and present with rapid progression of symptoms over weeks to months. Symptoms include the presence of a palpable mass or may be related to mass effect upon the globe causing displacement and proptosis, diplopia, pain, inflammation, eyelid swelling, chemosis, and erythema. Tumors may be mass-like or infiltrative. Extraocular muscle involvement is seen in about 50% of cases.

In 19–25% of cases of orbital metastases there is no preexisting known cancer diagnosis.

5.2 Differential Diagnosis

Differential consideration include benign and malignant lesions arising from the orbital contents. Scirrhous breast carcinoma may be infiltrative and mimic inflammation/infection.

5.3 Diagnosis

Orbital biopsy is required for diagnosis unless there is widespread disease present and/or clinical history is suggestive of metastasis. Once the diagnosis is established, staging work-up includes whole-body ^{18}F-FDG PET/CT.

5.4 Treatment

Metastases to the orbit may be treated with various combinations of chemotherapy, biologic, hormonal, and immunotherapies, and with palliative radiation therapy. Rarely palliative surgical resection can be performed but surgery most often is for a diagnostic biopsy.

5.5 Figures with Captions



Fig. 42 Axial post-contrast CT orbit, soft tissue window image of a 50-year-old woman with metastatic breast cancer and a right orbital infiltrative lesion (arrows). The associated enophthalmos is typical for scirrhous breast metastasis

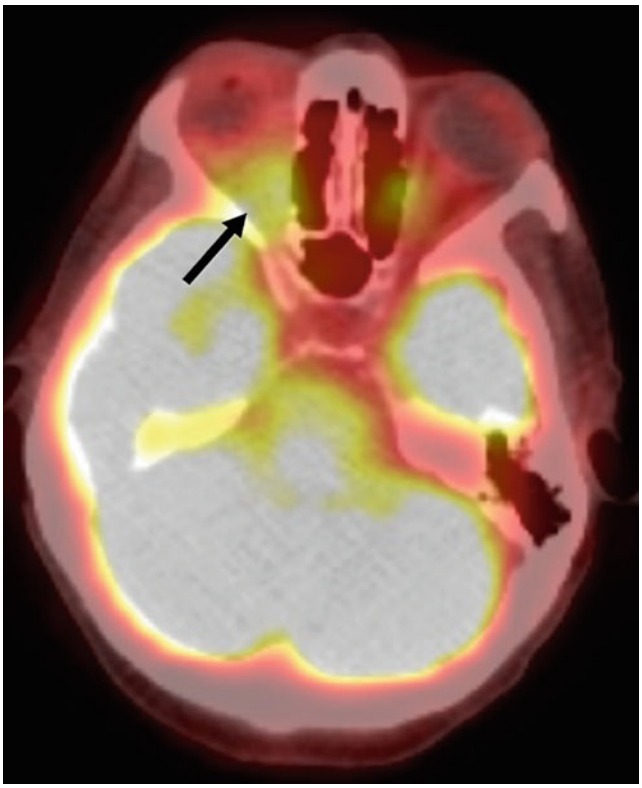


Fig. 43 Axial PET/CT image shows asymmetric uptake in the right orbit (arrow)

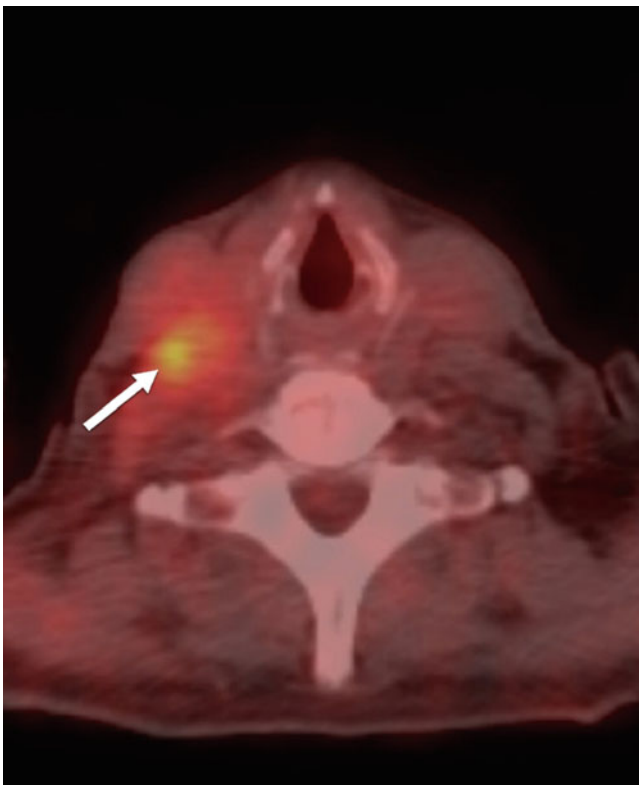


Fig. 44 Axial PET/CT image reveals an FDG-avid right neck node (arrow)

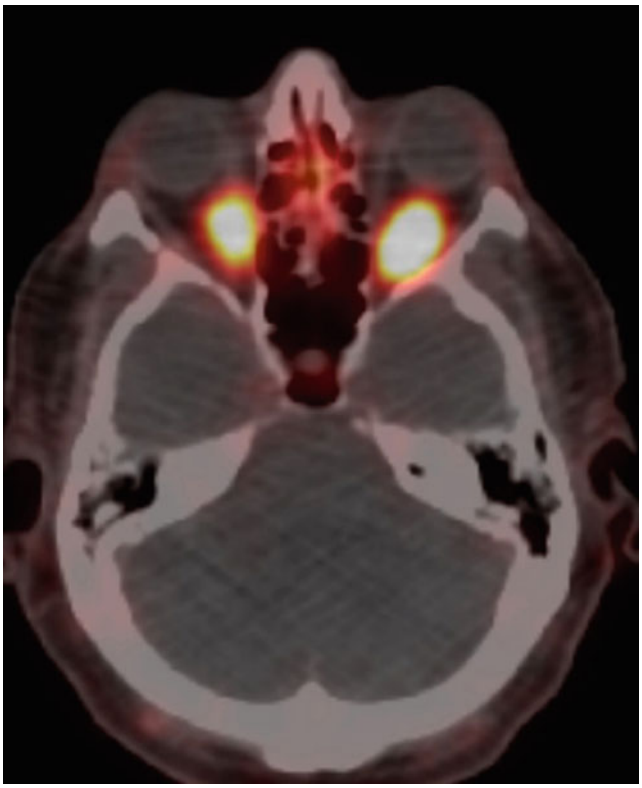


Fig. 45 Axial ^{68}Ga-DOTATATE PET/CT image of a 67-year-old male (different patient) with neuroendocrine carcinoma. This image shows avid metastases in bilateral orbits



Fig. 46 Three-dimensional ^{68}Ga-DOTATATE PET/CT image shows bilateral orbital masses and diffuse metastases throughout the body

6 Orbital Inflammatory Syndrome ("Pseudotumor")

Abstract

- Orbital inflammatory syndrome ("orbital pseudotumor") is a noninfectious, inflammatory disorder of the orbit thought to be of autoimmune nature.
- Most common etiology of a painful orbital mass.
- Represents an inflammatory infiltrate consisting of a mixture of histiocytes, plasma cells, and small lymphocytes. Fibrosis is frequently present.
- ^{18}F-FDG PET/CT may be used for diagnosis and monitoring treatment.

6.1 Signs and Symptoms

In the pediatric population, bilateral disease may be present with disc edema and uveitis. Adult patients may present with unilateral painful opthalmoplegia, impaired ocular movement, lid erythema, and proptosis.

6.2 Differential Diagnosis

The primary differential consideration in children is orbital rhabdomyosarcoma. In adults, Grave's disease may appear similarly when the extraocular muscles and lacrimal gland are involved. The tendinous insertion of the muscles is spared in Grave's disease and this may serve as a distinguishing finding from myositis caused by orbital pseudotumor. Larger lesions may simulate lymphoma or other malignant processes in the orbit.

6.3 Diagnosis

Clinical history and imaging aid in the differential diagnosis. A surgical biopsy is recommended to confirm the diagnosis and rule out malignancy. The diagnosis is confirmed with a positive response to steroids. ^{18}F-FDG PET scans show high levels of FDG activity.

6.4 Treatment

First-line treatment for orbital inflammatory syndrome is oral steroids with a very slow taper over the course of several months. Steroid sparing drugs such as Methotrexate can be considered in recurrent or refractory cases. Other treatments may include surgical resection and radiation. ^{18}F-FDG PET can be used to monitor treatment.

6.5 Figures with Captions

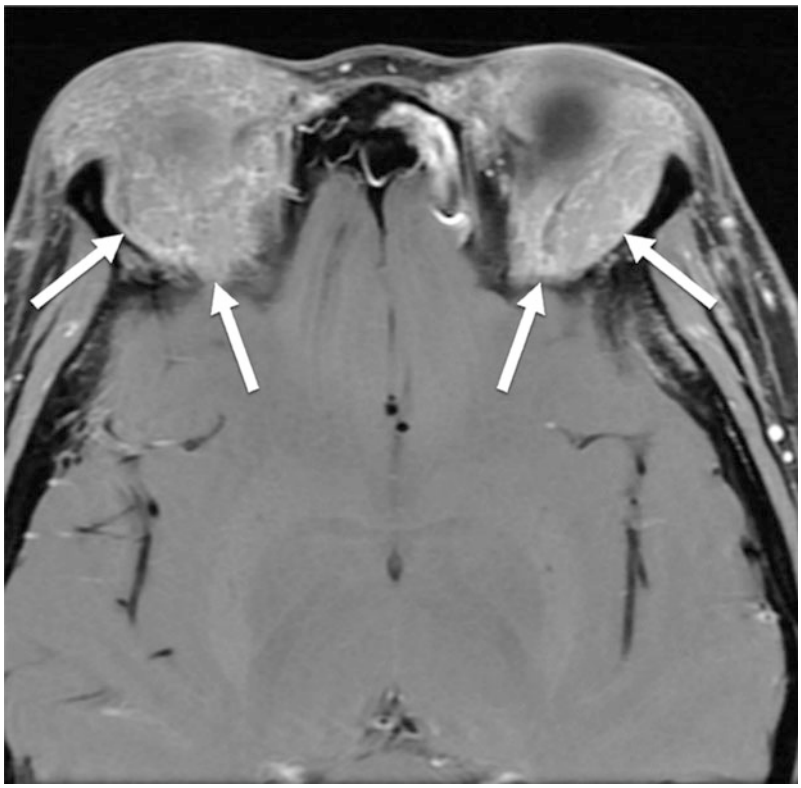


Fig. 47 Axial T1 post-contrast fat-saturated image in a 21-year-old female with painless right upper eyelid swelling and bilateral palpable orbital masses. MRI examination shows enhancing infiltrative disease in both orbits with involvement of the right eyelid and periorbital soft tissues (arrows). Pathology demonstrated reactive follicular hyperplasia with chronic granulomatous inflammation, no evidence of malignant neoplasm, no acid-fast bacilli or fungal microorganisms, and no amyloid deposition

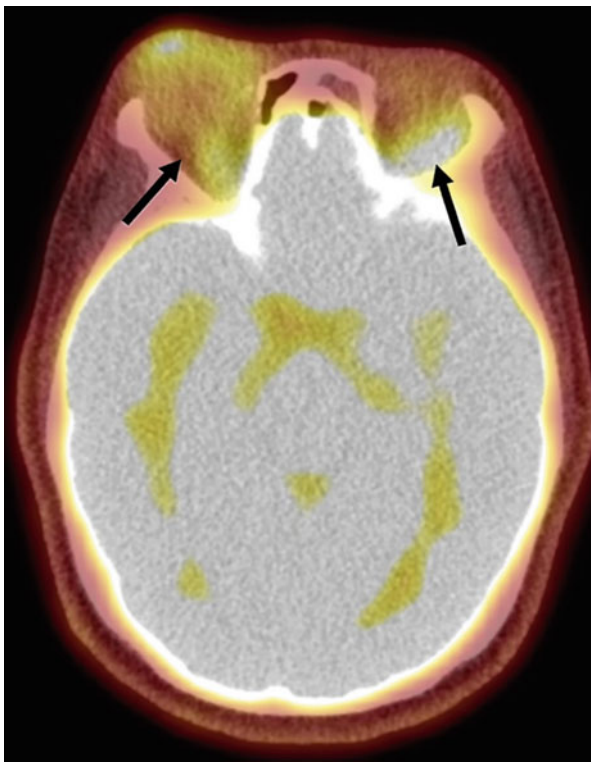


Fig. 48 Axial PET/CT image demonstrates FDG-avidity of both orbital masses (arrow)

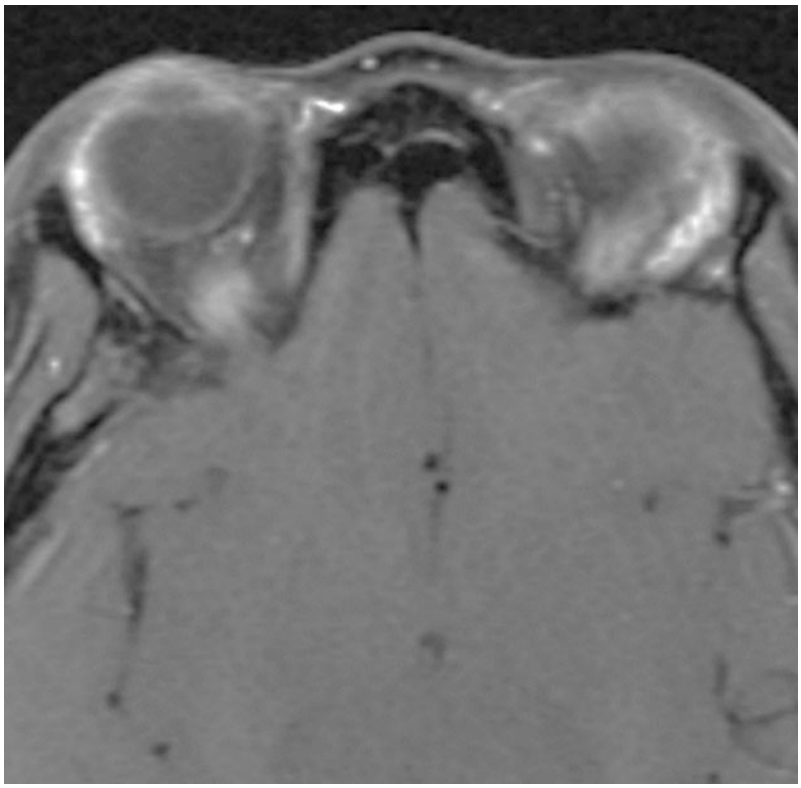


Fig. 49 Axial T1 post-contrast fat-saturated image shows near complete resolution of the orbital masses after treatment with steroids

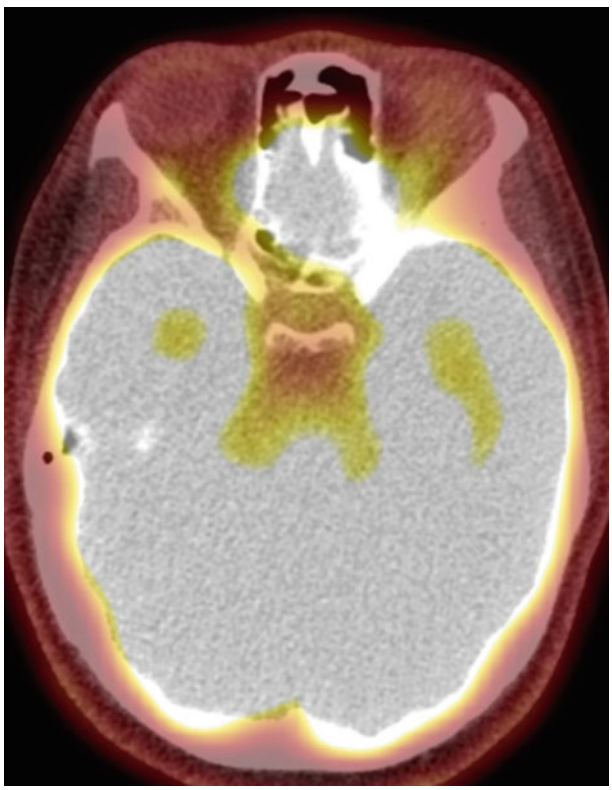


Fig. 50 Axial PET/CT image demonstrates no FDG activity in either orbit

7 IgG4-Related Disease

Abstract

- Systemic autoimmune condition characterized by lymphoplasmacytic infiltrates
- Tissue infiltration by IgG4-positive plasma cells with sclerosing inflammation.
- Lesions may be ^{18}FDG PET/CT or (68-Gallium) ^{68}Ga-DOTANOC avid

7.1 Signs and Symptoms

As IgG4-related disease is a systemic condition in which multiple organ system can be involved. This is a subclass of what previously was lumped together as orbital inflammatory syndrome. In the orbits IgG4-related disease may appear similar to orbital pseudotumor and may also involve the lacrimal glands and the trigeminal nerve. Other symptoms may include hypophysitis, thyroiditis, asthma and pneumonitis, autoimmune pancreatitis, retroperitoneal fibrosis, nephritis, and erythematous papules.

7.2 Differential Diagnosis

Lacrimal gland involvement needs to be differentiated from lymphoma and other lacrimal gland neoplasms, dacryoadenitis, and Sjogren syndrome. Perineural disease can appear similar to that arising from tumors such as SCC, ACC, and lymphoma. When the extraocular muscles are involved, orbital pseudotumor, thyroid orbitopathy (Grave's disease), lymphoma, metastases, and infection are in the differential diagnosis.

7.3 Diagnosis

IgG4-related disease is often difficult to distinguish from lymphoma on imaging. In addition, lymphoma may complicate IgG4-related orbital disease. Tissue biopsy is required for definitive diagnosis. PET/CT aids in defining the extent of disease.

7.4 Treatment

IgG4-related disease responds to steroids but may be incomplete and relapse is common. Maintenance treatment with rituxamab (Rituxan and MabThera), a monoclonal antibody against the B-cell protein CD20, following initial treatment with prednisone has been described as being effective in treating patients with refractory IgG4-related disease.

7.5 Figures with Captions



Fig. 51 Axial T1 post-contrast fat-saturated image of a 35-year-old woman who presented with enlarged bilateral lacrimal glands and cervical adenopathy**.** MRI shows enlargement of bilateral lacrimal glands (arrows)

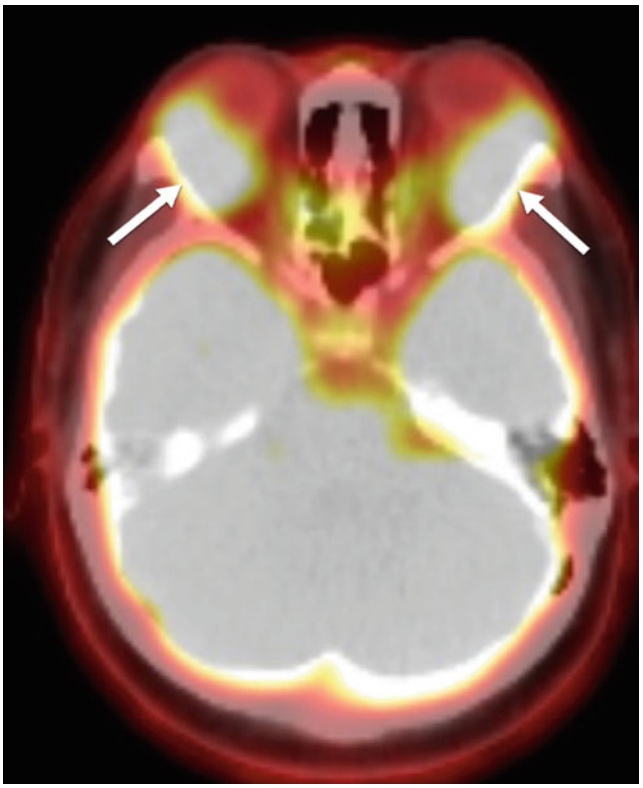


Fig. 52 **Axial PET/CT image** demonstrated FDG-avidity of bilateral lacrimal glands (arrows)

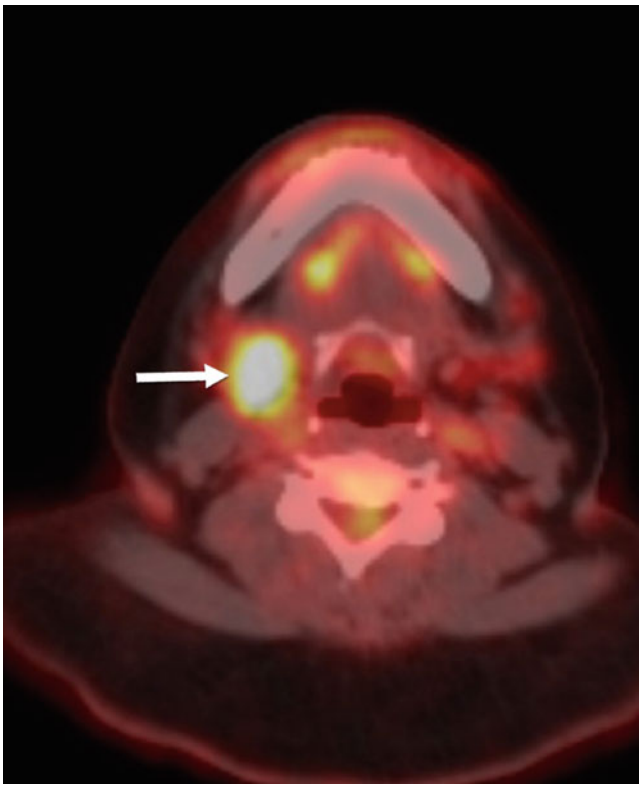


Fig. 54 **Axial PET/CT image** demonstrating an enlarged right submandibular gland that is FDG-avid (arrow)

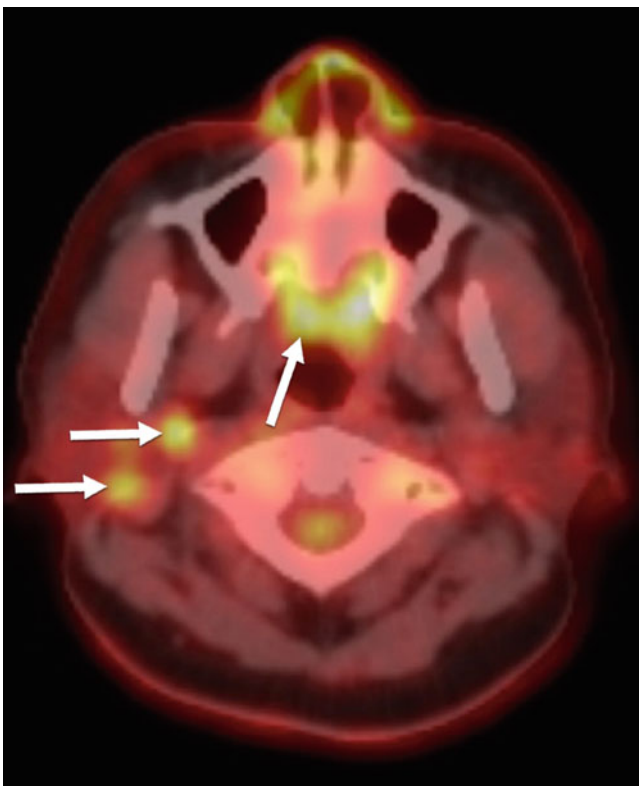


Fig. 53 **Axial PET/CT image** show FDG-avidity of right upper neck nodes and presumably the soft palate (arrows) that decreased on follow-up imaging

References

1. Donaldson MJ, Sullivan TJ, Whitehead KJ, Williamson RM. Squamous cell carcinoma of the eyelids. Br J Ophthalmol. 2002;86(10):1161–5.
2. Faustina M, Diba R, Ahmadi MA, Esmaeli B. Patterns of regional and distant metastasis in patients with eyelid and periocular squamous cell carcinoma. Ophthalmology. 2004;111(10):1930–2.
3. Esmaeli, B., Ophthalmic oncology, vol. 6. Springer Science & Business Media; 2011.
4. Yin VT, Merritt HA, Sniegowski M, Esmaeli B. Eyelid and ocular surface carcinoma: diagnosis and management. Clin Dermatol. 2015;33(2):159–69.
5. Lee SP, Shimizu KT, Tran LM, Juillard G, Calcaterra TC. Mucosal melanoma of the head and neck: the impact of local control on survival. Laryngoscope. 1994;104(2):121–6.
6. Ross MI, Gershenwald JE. Evidence-based treatment of early-stage melanoma. J Surg Oncol. 2011;104(4):341–53.
7. Ali Z, Yousaf N, Larkin J. Melanoma epidemiology, biology and prognosis. EJC Suppl. 2013;11(2):81–91.
8. Hui KH, Pfeiffer ML, Esmaeli B. Value of positron emission tomography/computed tomography in diagnosis and staging of primary ocular and orbital tumors. Saudi J Ophthalmol. 2012;26(4):365–71.
9. English JF, Sullivan TJ. The role of FDG-PET in the diagnosis and staging of ocular adnexal lymphoproliferative disease. Orbit. 2015;34(5):284–91.
10. Pinnix CC, Dabaja BS, Milgrom SA, Smith GL, Abou Z, Nastoupil L, Romaguera J, Turturro F, Fowler N, Fayad L, Westin J, Neelapu S, Fanale MA, Rodriguez MA, Hagemeister F, Lee HJ, Oki Y, Wang M, Samaniego F, Chi L, Esmaeli B. Ultra-low-

dose radiotherapy for definitive management of ocular adnexal B-cell lymphoma. Head Neck. 2017;39(6):1095–100.
11. Williams MD, Al-Zubidi N, Debnam JM, Shinder R, DeMonte F, Esmaeli B. Bone invasion by adenoid cystic carcinoma of the lacrimal gland: preoperative imaging assessment and surgical considerations. Ophthalmic Plast Reconstr Surg. 2010;26(6): 403–8.
12. Crown A, Rocha FG, Raghu P, Lin B, Funk G, Alseidi A, Hubka M, Rosales J, Lee M, Kennecke H. Impact of initial imaging with gallium-68 dotatate PET/CT on diagnosis and management of patients with neuroendocrine tumors. J Surg Oncol. 2020;121(3): 480–5.
13. Das S, Pineda G, Goff L, Sobel R, Berlin J, Fisher G. The eye of the beholder: orbital metastases from midgut neuroendocrine tumors, a two institution experience. Cancer Imaging. 2018;18(1):47.
14. Weber AL, Romo LV, Sabates NR. Pseudotumor of the orbit. Clinical, pathologic, and radiologic evaluation. Radiol Clin N Am. 1999;37(1):151–68.
15. Purohit BS, Vargas MI, Ailianou A, Merlini L, Poletti PA, Platon A, Delattre BM, Rager O, Burkhardt K, Becker M. Orbital tumours and tumour-like lesions: exploring the armamentarium of multiparametric imaging. Insights Imaging. 2016;7(1):43–68.
16. Ginat DT, Freitag SK, Kieff D, Grove A, Fay A, Cunnane M, Moonis G. Radiographic patterns of orbital involvement in IgG4-related disease. Ophthalmic Plast Reconstr Surg. 2013;29(4):261.
17. Arora S, Damle NA, Meel R, Sharma S, Sen S, Bal C, Lata K, Prakash S, Yadav D, Angamuthu M. Orbital IgG4 disease: imaging findings on 68Ga-DOTANOC PET/CT. Nucl Med Mol Imaging. 2019;53(6):432–5.
18. Chwalisz BK, Stone JH. Neuro-ophthalmic complications of IgG4-related disease. Curr Opin Ophthalmol. 2018;29(6):485–94.

Orbital Imaging Pearls

19

Gahl Greenberg, Daphna Landau Prat, and Guy Ben Simon

Contents

1 **Introduction** 179
2 **Figures with Captions** 180

Abstract

While constructing the book I had played with the idea of providing, a "behind the scenes" chapter on the structured interpretation of images, namely CT and MRI. Obviously, it is beyond the scope of this book to elaborate on the machinery and physics behind these miraculous anatomical aids; however, readers should be aware of the basic differences between these modalities.

Keywords

Orbital imaging tips · Imaging check list · Imaging pearls

1 Introduction

Before reading a scan, build yourself a structured check list and remember to cover your own "blind spots."

A suggested list would include (pick your own order):

Periorbital/Preseptal tissues including Lacrimal apparatus
Bony walls
Globe shape, position, intraocular findings
Optic nerve/sheath complex
Extraocular muscles
Intra/extra conal spaces (composition of the orbital fat)
Ophthalmic veins
Orbital apex
SOF and IOF
Cavernous sinus
Suprasellar cistern including Prechiasmatic ON and optic chiasm
Posterior optic pathways
Paranasal sinuses/skull base

As a simplification, CT is a rotating X- Ray equipment producing a "density scan," that is, a "single shot in time" of all the range of densities within the scanned object. It is essentially a freeze image, lacking functional information per se. However, some functional data can be obtained through phasic scans (e.g., noncontrast, arterial, venous, and late scans). These allow evaluation of the properties of both vascular and tumoral masses based on their enhancement patterns and wash-out behavior.

The final product may be considered as a "what you see is what you get" image, since it features a density map, readily measurable by applying an ROI (region of interest) tool which should measure the same on all PACS systems and on any office computer. These measurements are based on Hounsfield units and surprisingly will not alter while "windowing" the image since the intrinsic density of a tissue is independent of the on-screen product (see below).

G. Greenberg (✉)
Department of Diagnostic Imaging, Sheba Medical Center, Tel Hashomer, Israel
e-mail: gahl.greenberg@sheba.health.gov.il

D. Landau Prat · G. Ben Simon
Ophthalmic Plastic and Lacrimal Surgery Institute, Department of Ophthalmology, The Goldschleger Eye Institute, Sheba Medical Center, Tel Hashomer, Israel

© Springer Nature Switzerland AG 2022
G. Ben Simon et al. (eds.), *Atlas of Orbital Imaging*,
https://doi.org/10.1007/978-3-030-62426-2_127

2 Figures with Captions

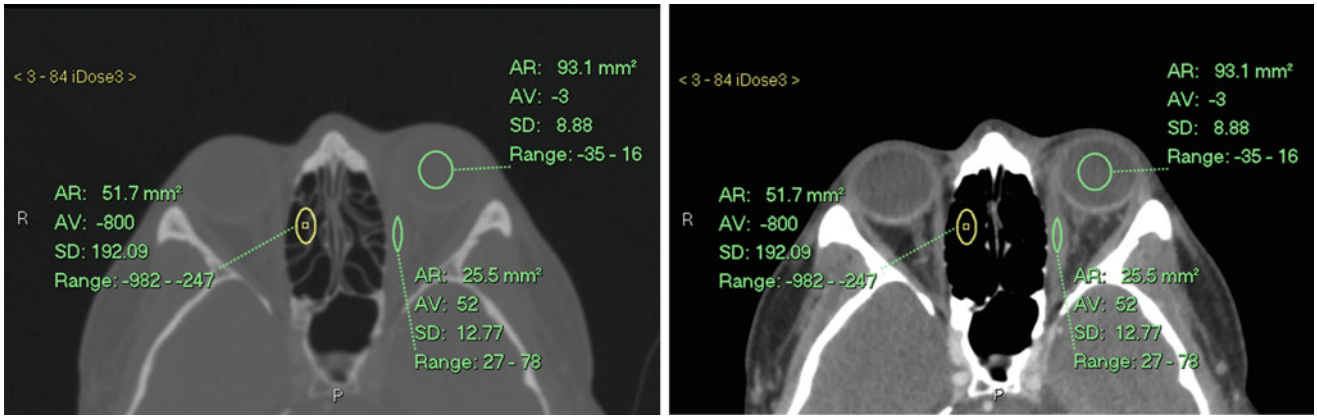


Fig. 1 Axial CE CT scan of the orbits portraying 3 measurements utilizing bone window (*left*) and soft tissue (*right*). Measurements of the inflamed MR, the vitreous, and the ethmoidal air cells are unchanged (AR – area, AV – average HU, SD – standard deviation, Range – range of densities within the ROI)

- Remember CT is best at demonstrating the bony properties of a lesion (Internal Matrix, pressure erosions vs. frank lytic destruction, sclerotic borders, periosteal reaction, etc.)
- Don't be shy to order a CT following the "comprehensive and aristocratic" MRI, you'll be surprised at how this "inferior" modality will change your idea on aggressive-looking lesions on MR, such as Fibrous dysplasia (FD).

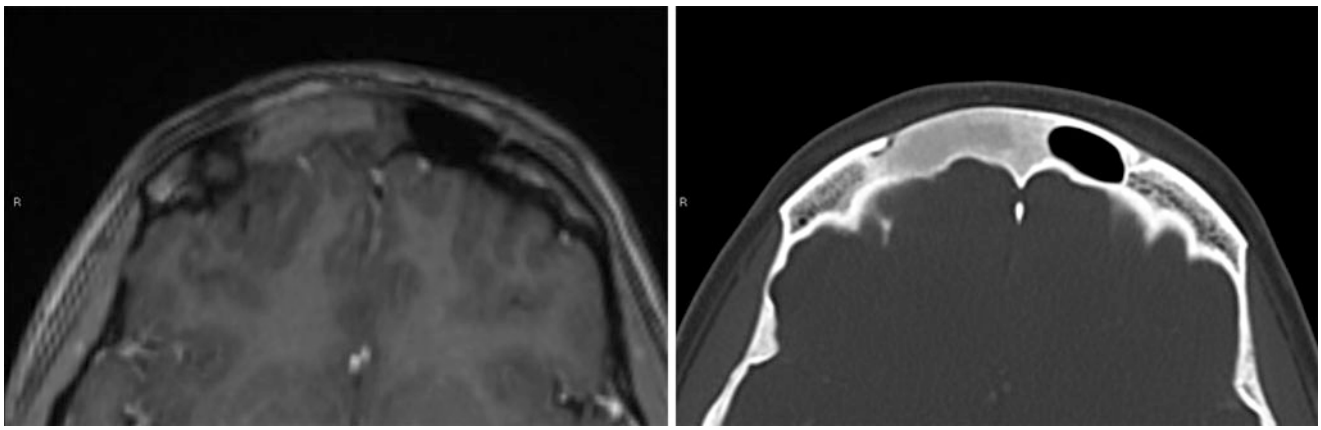


Fig. 2 Left Ax T1 postcontrast image, Right Ax CE CT (*bone window*). This 18-year-old patient was referred for a suspected frontal bone/orbital roof infiltrating lesion. CT ordered 2 months later confirms the typical Ground Glass appearances of FD

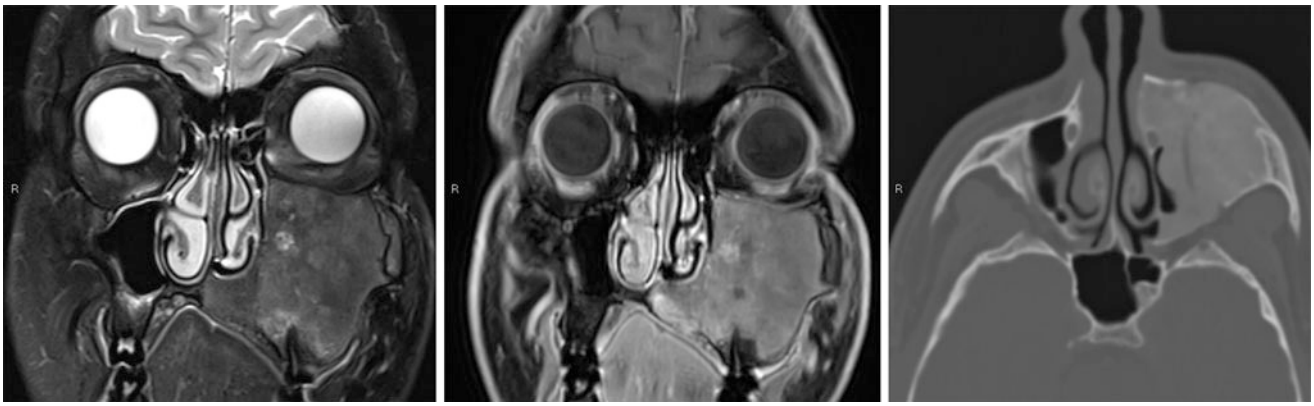


Fig. 3 Left Cor T2 FS, center Cor T1 CE FS, right Ax CE CT (*bone window*). Again, this expansile heterogeneous appearing lesion in the left maxilla may be mistaken for other aggressive tumors but the CT reassures us of the diagnosis (FD)

- CT will also beat MR in your search for subtle calcifications, stones, radiopaque foreign bodies, or "phleboliths" within a slow flow vascular malformation.

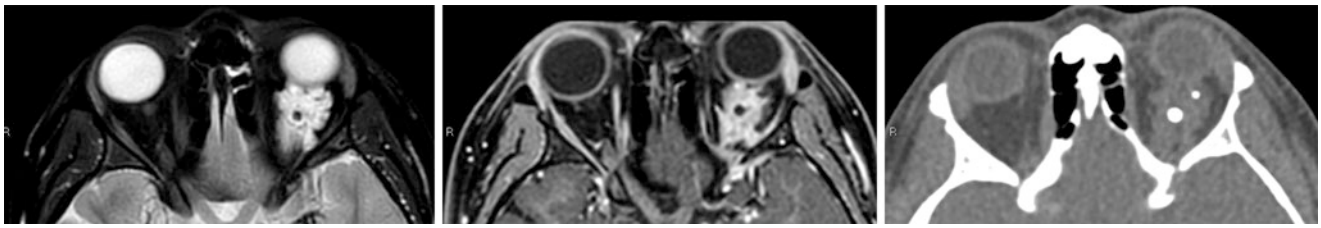


Fig. 4 *Left* Ax T2 FS, *Center* Ax T1 CE FS, *Right* Ax NC CT (*soft tissue window*). Venous malformation. Some phleboliths may be picked up as "signal voids" on an MR scan but may be confused with vessels, therefore better appreciated on CT



Fig. 5 NECT. Bone window. Axial view – Senile calcific scleral plaques – A 95-year-old female after a fall. An incidental finding of bilateral ovoid calcification is seen consistent with senile calcific scleral plaques also known as limbic calcifications. This finding usually occurs medially and/or laterally, anterior to the insertion of respective rectus muscle. Not to be confused with postoperative changes (i.e., band/scleral buckle) especially in the unilateral cases

- Consider MR as a "Proton image" portrayed in a scale of intensities. In a nutshell, this modality harbors a very strong static magnet and applies Radiofrequencies directed at the precession speeds of protons and Gradients to localize their faint signals. As opposed to a CT scan, one cannot and should never interpret a finding based on a single sequence. Hence, a standard MR protocol includes a series of sequences (e.g., T1, T2 "weighted" images) representing our choice of timing and flipping of the protons, thus representing different elements of the examined tissue.
- Safety and Technical issues in MRI – All patients who are scheduled for an MR scan are screened for possible metallic foreign material residing near the globe/orbit, as these objects may be influenced by the strong static field of the magnet and result in serious injury due to translational and rotational forces. The Radiofrequencies applied during a scan may also cause some local heating effect as well.
- Aside from safety, any paramagnetic object will cause local susceptibility artifacts. This is a common issue with

orthodontic hardware/braces in the young (see below!). Removing braces prior to scanning is strongly advised if possible; however, we must bear in mind that this may become a financial burden for the parents. Consult the radiologist whether this is mandatory, some brackets may cause a much weaker distortion. Also remember that dental implants are forever!

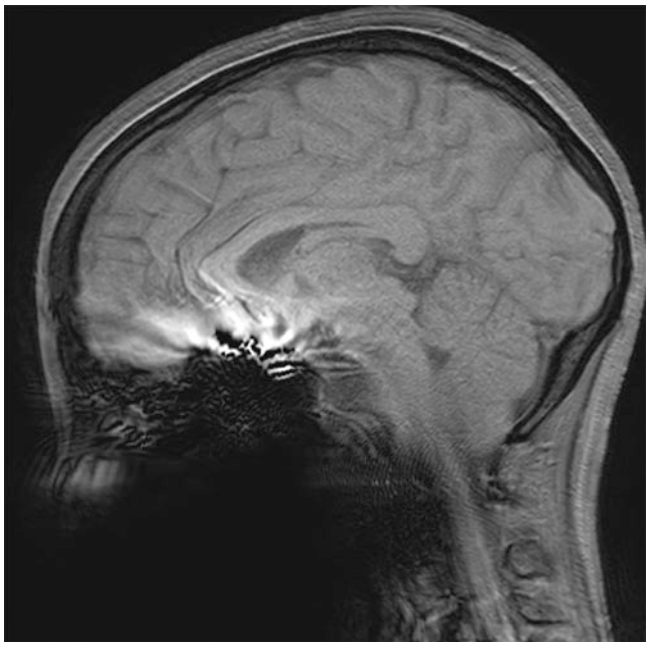


Fig. 6 Dental braces causing a significant distortion due to metal-induced artifact rendering the exam unreadable

- Do not neglect your basic T1 weighted nonenhanced, nonfat-suppressed images, as they are the backbone of your study!

Some important T1 pearls:

- T1 serves as a preview of all that shortens T1 signal, that is, "T1 bright." Of mention are fat, blood (methemoglobin products), melanin, proteinaceous material, and contrast. A common mistake is to assume a lesion is enhancing while it was bright precontrast! (Check out Fig. 7)

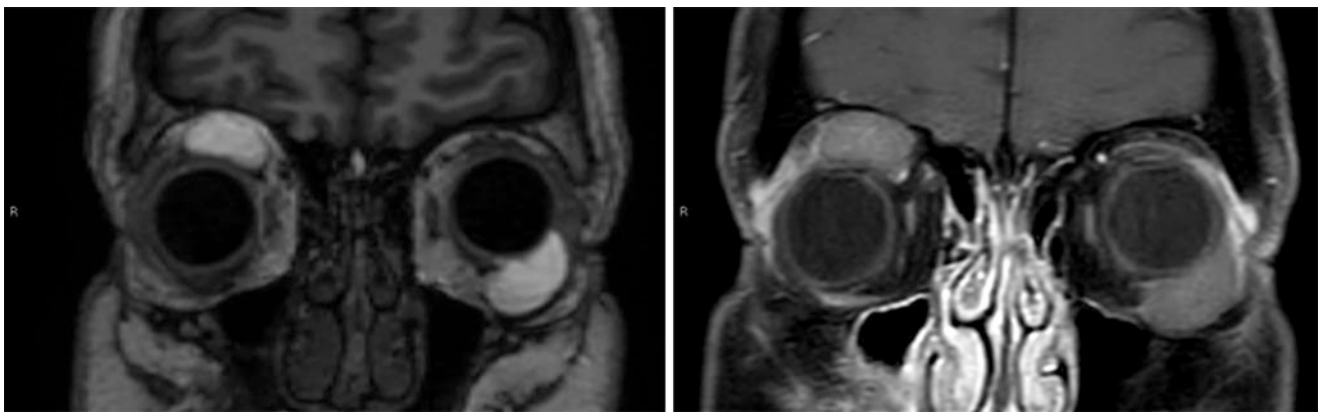


Fig. 7 Cor T1W images (*left* nonenhanced, *right* postcontrast FS). These prominent extraconal melanotic deposits may be mistaken for enhancing lesions unless you checked out the "boring" T1's at the beginning of the study

- T1 pulses give you a good outline of the bones, typically the bright interior signal of the fatty bone marrow and the outlining hypointense "water-poor" cortex. Bear in mind, of course, that the amount of fatty tissue varies according to age and general bone density. Bone marrow will also be affected by treatment changes (e.g., chemoradiation). However, if the fatty marrow is maintained, a sclerotic lesion will stand out relative to the "white" background. Use this to assess greater sphenoid wing (GSW) lesions and infiltrations

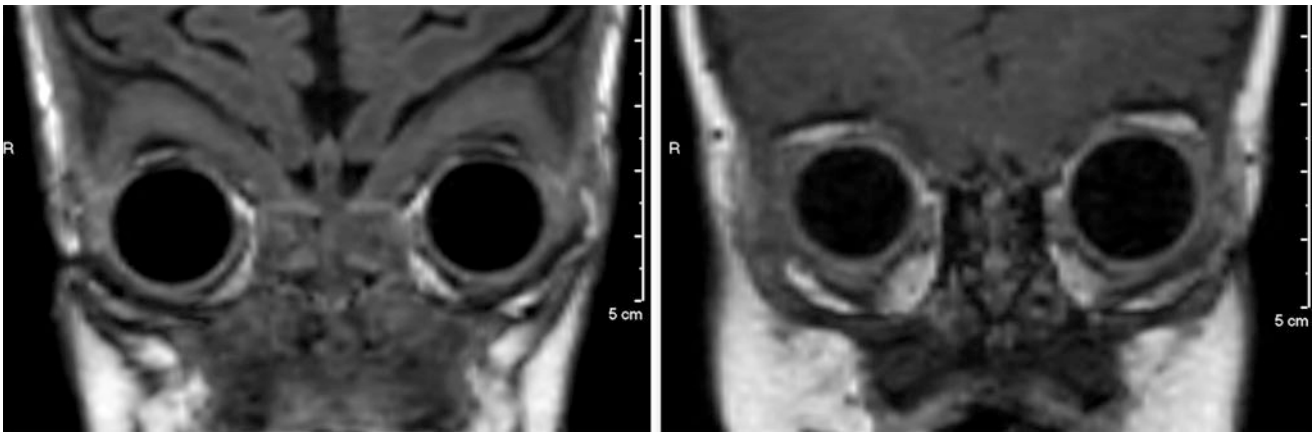


Fig. 8 Cor T1 3D TFE no-enhanced, nonfat-saturated images demonstrating bony abnormality. *Left* a 6 month old child with osteopetrosis, note the thickening of the orbital roof bilaterally. *Right* normal age-matched control.

- A thorough orbital scan (and practically any face/skull base directed scan) should include Fat Saturated images to suppress the bright signal of the orbital fat and fatty marrow of the adjacent bone, thus allowing to pick up any enhanced tissue which may be obscured by the inherent hyperintensity of fatty tissue. However, beware the fat saturated pre contrast T1W images! Keep in mind that the saturation changes the intrinsic T1 properties of the tissues. Check out the next figure.

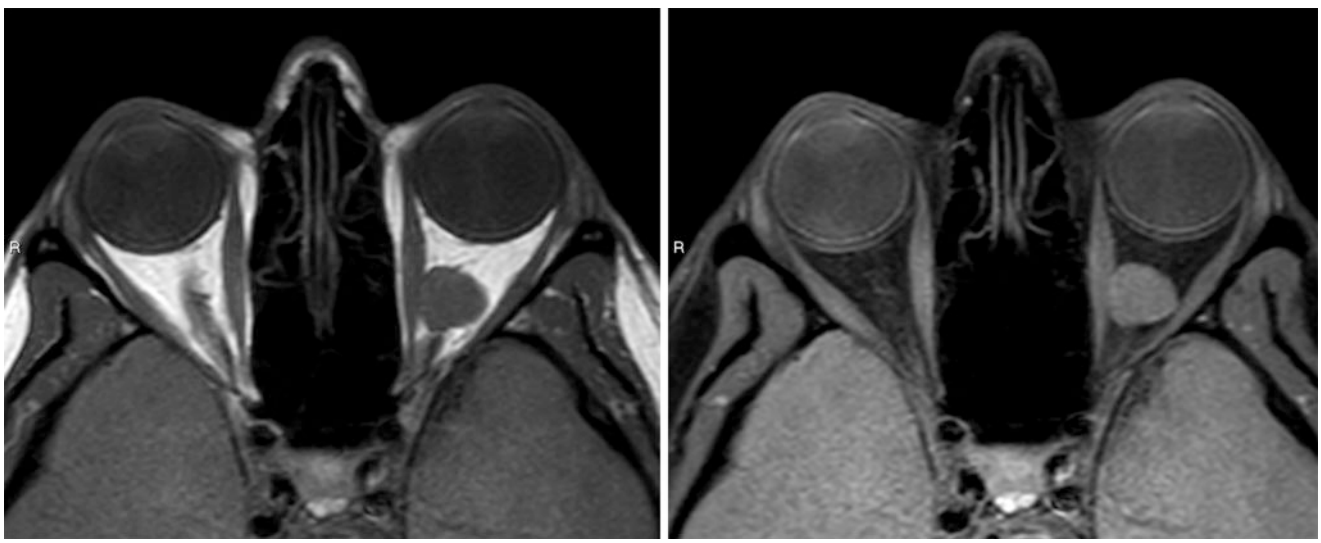


Fig. 9 Axial T1w mDixon images (left nonsuppressed T1, right fat-suppressed image). Compare the intensities of the vitreous, muscles, and the mass itself between both sequences

- Dural reaction – Not all dural enhancements indicate tumoral infiltration, occasionally this phenomenon may represent reactive changes which can resolve following treatment.



Fig. 10 Metastatic RCC, axial T1W postcontrast FS image shows a large destructive enhancing mass centered about the greater wing of sphenoid, with classical "Trilateral" involvement. The white arrows are pointing at the intraorbital and infratemporal fossa components of the lesion. Note the thickening and enhancement of the dural lining adjacent to the lesion in the left middle cranial fossa (blue arrow)

- Fat-saturating sequences are also essential in depicting skull base, neural foramina, cavernous sinus, and meningeal involvement.

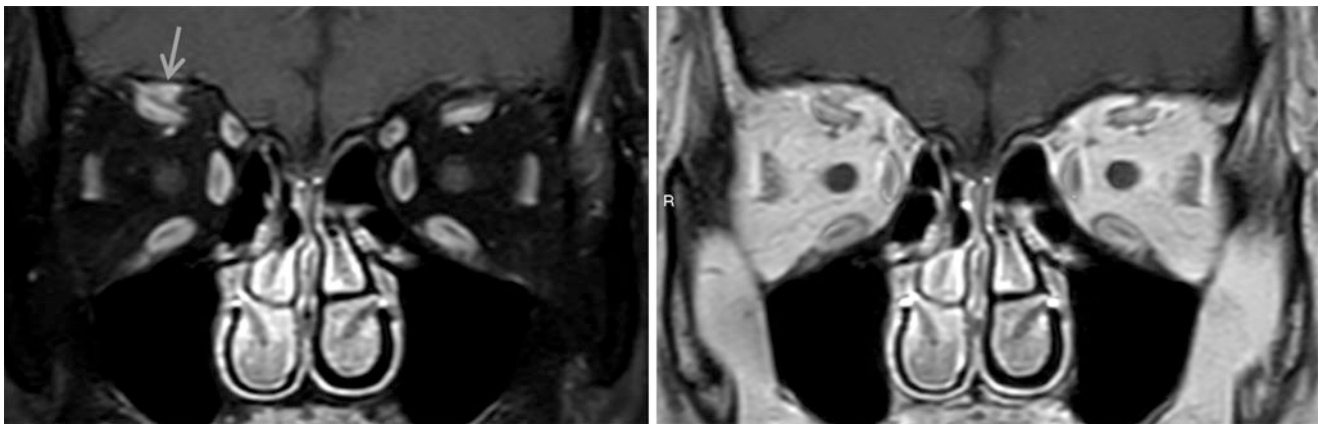


Fig. 11 Cor T1W mDixon postcontrast images (*left* fat saturated, *right* non Fat saturated), the perineural invasion along V1 in the roof of the right orbit (arrow) is much better seen when the background is suppressed

- T2 Fat Saturated images are best for depicting optic nerve intrinsic signal alterations ranging from acute inflammatory changes/neuritis, to atrophy and denervation (next image).

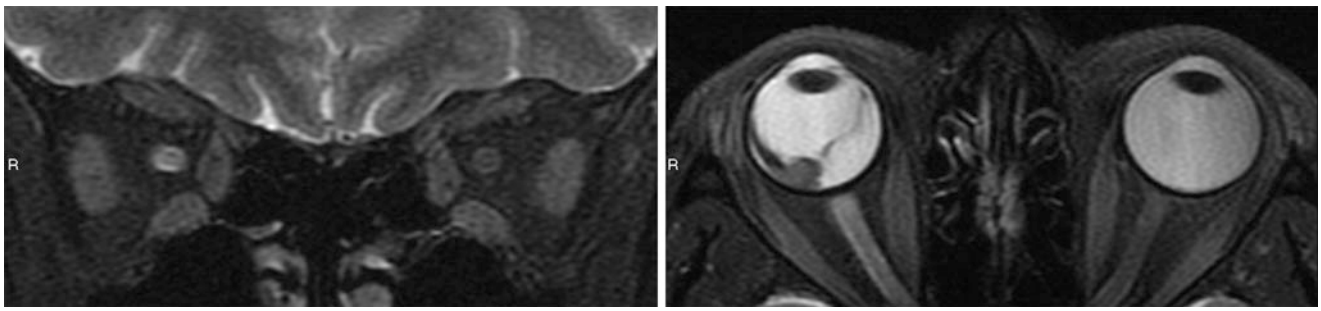


Fig. 12 Coronal (*left*) and Axial (*right*) T2W Fat saturated images of a patient with right eye choroidal melanoma demonstrating atrophy and "T2 pallor" secondary to antegrade denervation

- Use steady-state gradient echo sequence (e.g., FIESTA/CISS) or isotropic 3D imaging (TSE/SPACE depending on vendor). These are your sequences of choice when assessing choroidal masses, cranial nerves, or structures surrounded by CSF due to the high T2 contrast. The submillimeter slice thickness and high spatial resolution also allow great 3D reconstructions.

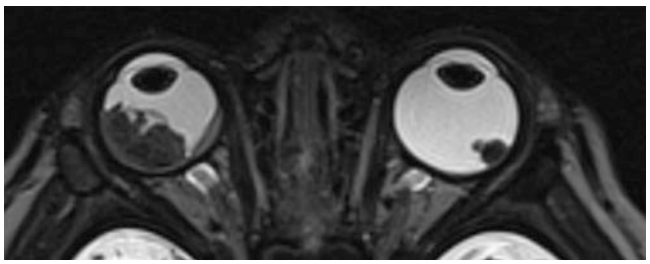


Fig. 13 Ax T2 SPACE (tra iso 0.5 mm slices) allow visualization of bilateral retinoblastomas in great detail including choroidal separations

- Contrast enhanced T2 FLAIR is your sequence of choice for neuritis/leptomeningeal enhancement. This may not be performed as a routine at all centers. Many places do 3D MPRAGE T1 or similar sequences postcontrast.

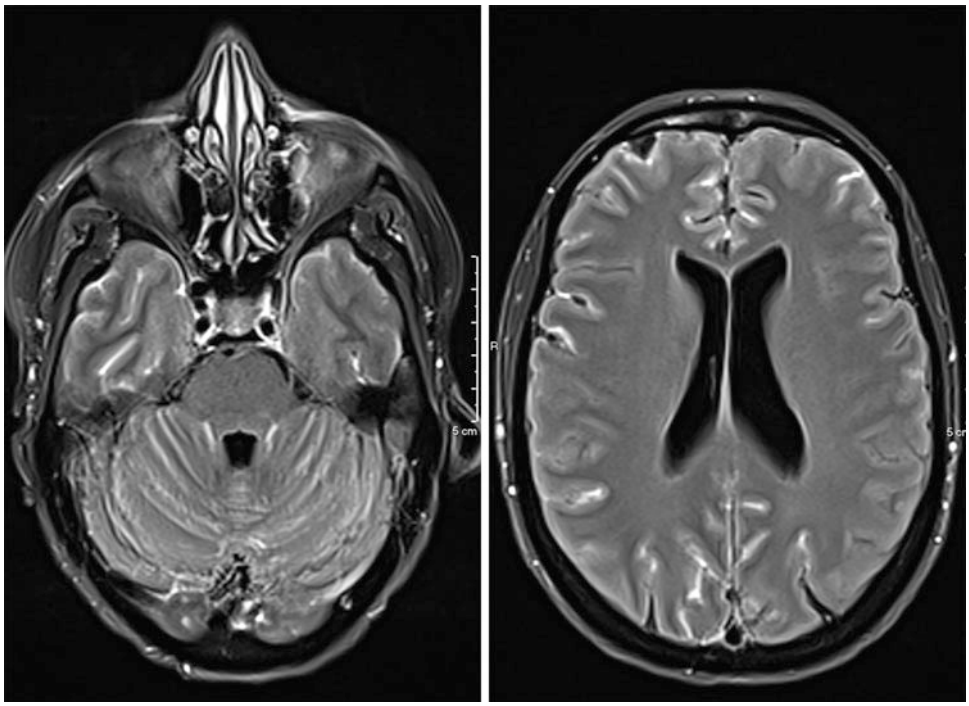


Fig. 14 Axial T2 FLAIR postcontrast images at the level of the lateral ventricles (*right*) and posterior fossa (*left*), demonstrating diffuse pial enhancement within the sulci and cerebellar folia, respectively, in keeping with leptomeningeal carcinomatous spread

- Papilla elevation (true disc edema) vs papillitis – search for signs of increased intracranial pressure including convoluted and widened optic nerve sheaths with abundant perioptic fluid.

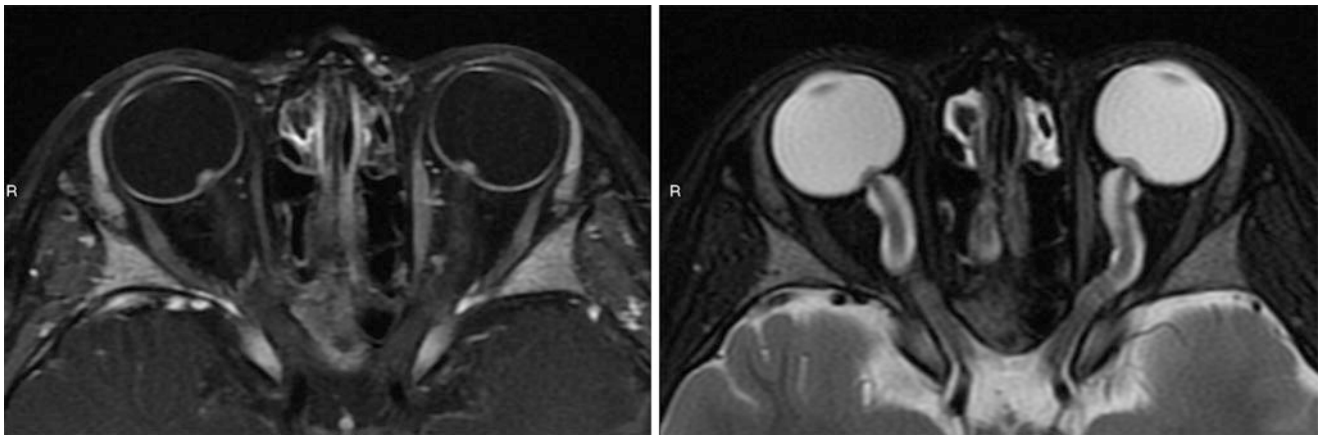


Fig. 15 Ax T2 FS (*right*) T1 FS postcontrast (*left*), showing tortuous and expanded optic nerve sleeves with bilateral enhancing swollen discs in a child with ALL, leptomeningeal involvement, and elevated ICP

- Chemical shift artifact and misleading SWI signal in fatty lesions (e.g., lipoma)

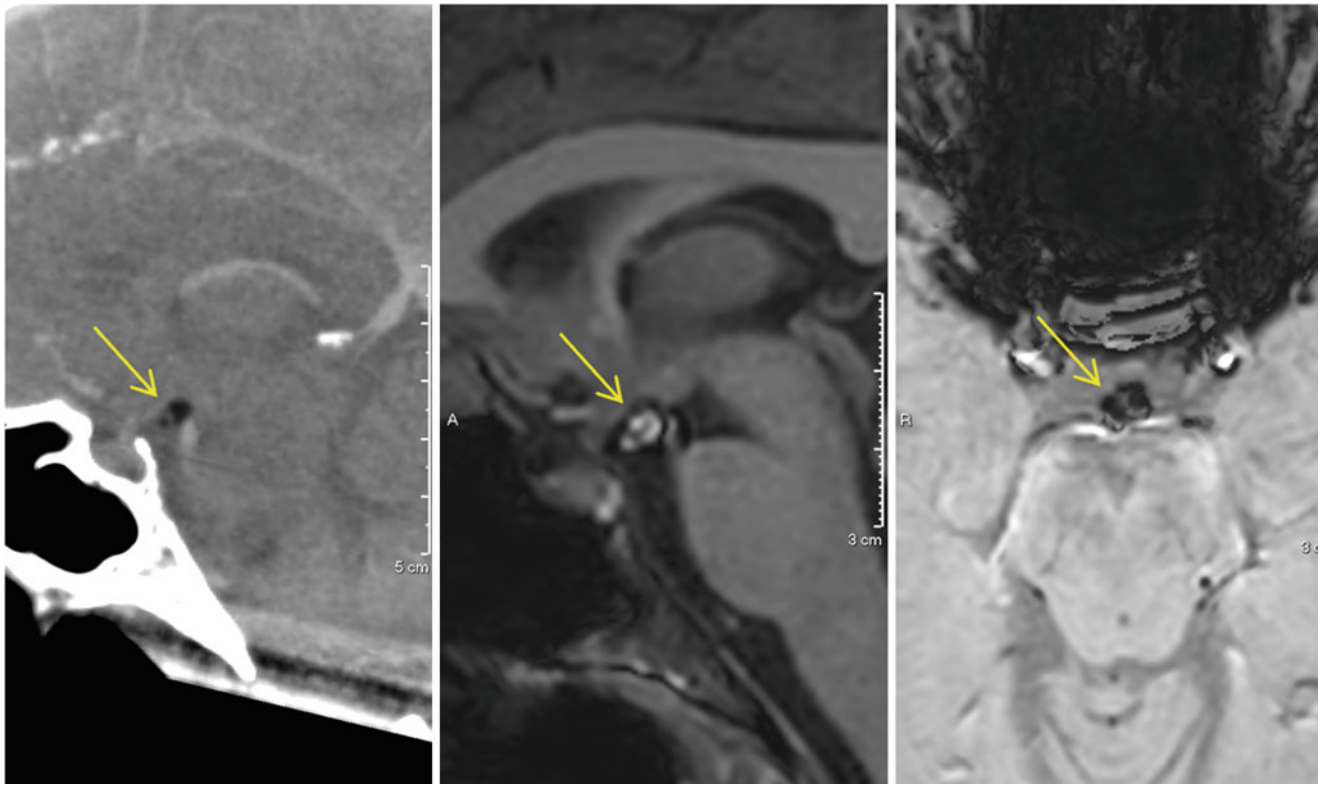


Fig. 16 Sag CT reformat (*left*), Sag T1 3D TFE nonenhanced (*middle*), Ax SWI (*right*). Be aware of the chemical shift artifact occurring at the interface of lipomatous lesions, appearing as bright/dark bands (*middle image*). These occur in the frequency encoding direction due to slight differences of resonance frequencies between water and fat, typically not fully concentric around the fat, but rather in one axis only. Remember that a fatty lesion may masquerade as hemorrhage or calcification on SWI sequences (*far right image*) due to the intrinsic fat suppression

Part III

Congenital Malformations/Anomalies

Craniofacial Dystosis

20

William R. Katowitz

Contents

1 **Signs and Symptoms** 192
2 **Differential Diagnosis** 192
3 **Diagnosis** 192
4 **Treatment** 192
5 **Figures with Captions** 192
References 198

Abstract

- Craniosynostosis describes the early closure of a cranial vault or skull base suture.
- The craniosynostoses may be syndromic or nonsyndromic.
- The most common syndromic synostoses include Apert syndrome, Crouzon syndrome, Pfeiffer syndrome, and Saethre–Chotzen syndrome and are associated with other dysmorphic features.
- Over 190 congenital syndromes of the head and neck have been identified.
- Approximately 85% of patients with craniosynostosis are nonsyndromic. Premature closing of the sagittal suture is one of the most common forms of nonsyndromic synostosis. It is more common in male infants and is easily diagnosed by observing the classic scaphocephalic appearance of the head with frontal bossing.
- The American Cleft Palate-Craniofacial Association (ACPA) classification is a simple way to classify the diverse group of craniofacial anomalies:
  - 1. Rare craniofacial clefts using the Tessier classification system
  - 2. Craniosynostosis: (a) syndromic, (b) nonsyndromic
  - 3. Atrophy and hypoplasia
  - 4. Neoplasia, hypertrophy, and hyperplasia
  - 5. Unclassified craniofacial deformities
- Figure 1.0 depicts the normal sutures and fontanelles of the fetal skull.
- A scaphoid skull involves closure of the sagittal suture.
- Suture involvement in Crouzon syndrome is variable; coronal and sagittal synostoses are most common, followed by lambdoidal synostosis. This pattern leads to the typical features of a shortened calvarium, steep forehead, and flattened occiput.
- Apert calvaria at birth is characterized by coronal synostosis and a widely gaping midline defect. The midfrontal region of the brain may not be covered with bone during early infancy, which often produces a prominent frontal pseudoencephalocele. Patients with Pfeiffer syndrome have premature fusion of the coronal and lambdoid sutures and occasionally the sagittal sutures. In more severe phenotypes, a cloverleaf skull can develop.
- Hypertelorism is typically defined as a widening of the medial canthal bones with the anterior lacrimal crest and corresponding medial canthi inter-distance that is

W. R. Katowitz (✉)
The Children's Hospital of Philadelphia, Philadelphia, PA, USA
e-mail: katowitzw@email.chop.edu

© Springer Nature Switzerland AG 2022
G. Ben Simon et al. (eds.), *Atlas of Orbital Imaging*,
https://doi.org/10.1007/978-3-030-62426-2_9

clinically appreciable as over ½ of the interpupillary distance.

Keywords

Craniosynostosis · Syndromic · Nonsyndromic · Apert syndrome · Crouzon syndrome · Pfeiffer syndrome · Saethre-Chotzen syndrome · Plagiocephaly · Suture closure · Coronal suture · Sagittal suture · Treacher-Collin syndrome

1 Signs and Symptoms

Dysmorphic facial features, proptosis, hypertelorism, eyelid retraction, eyelid coloboma, lagophthalmos, other systemic anomalies [1–4].

2 Differential Diagnosis

There are over 190 congenital syndromes of the head and neck which have been identified. The diagnosis of a craniodysmorphic syndrome is best performed by a multidisciplinary craniofacial team. Genetic testing and counseling is rudimentary in the diagnosis, identification of other systemic abnormalities, and treatment plan. Cranio-orbital imaging with 3-D CT imaging is critical in diagnosis and treatment planning.

3 Diagnosis

Clinical characteristics and radiologic findings. CT of orbits is the radiologic study of choice, and contrast material may be useful in delineating vascular structures especially in surgical planning. Diagnosis is confirmed sometimes with genetic testing.

4 Treatment

Surgical reconstruction is performed when necessary. Hydrocephalus will require early intervention. Sometimes, developmental delay will also inspire early intervention. Oculoplastic interventions may include fronto-orbital advancement, eyelid malposition surgery, and lacrimal surgery.

5 Figures with Captions

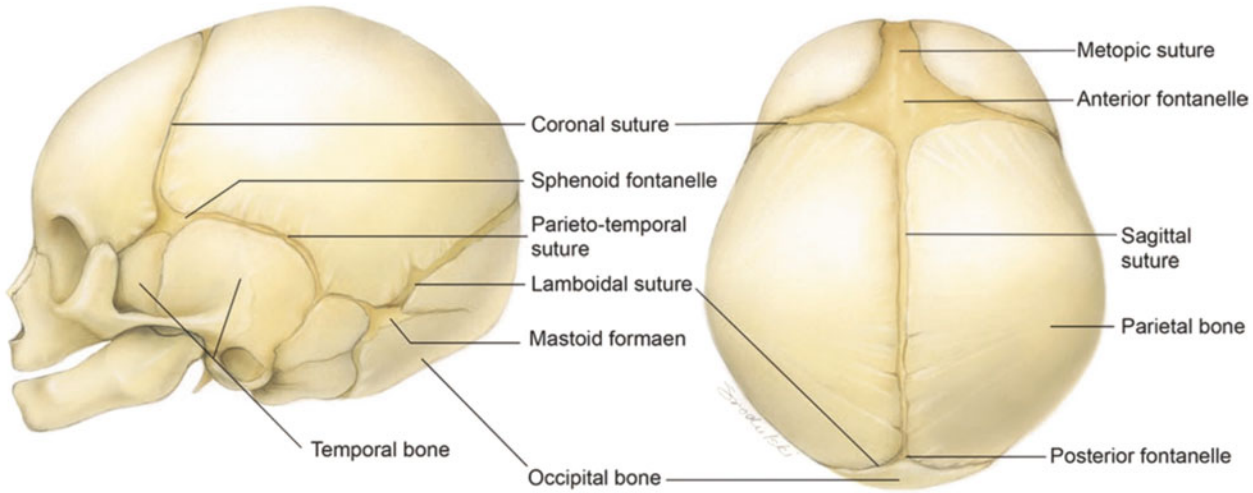


Fig. 1 Normal sutures and fontanelles of the fetal skull. With permission from Oculoplastic Considerations in Pediatric Craniofacial Surgery (2018). In Katowitz JA, Katowitz WR eds, Pediatric oculoplastic surgery 2nd edition, Springer, Switzerland



Fig. 2 Patient with Treacher-Collins syndrome. The major features of Treacher-Collins syndrome are external ear malformations, conductive hearing loss, hypo-plastic zygoma, lateral canthal dystopia with an antimongoloid slant of the palpebral fissures, pseudocoloboma or true coloboma (usually of the lateral lower eyelid), flattening of the nasofrontal angle, micrognathia with macrostomia, abnormal dentition, and malocclusion. The flattened nasofrontal angle, together with macrostomia and receding chin, produces the characteristic bird- or fishlike facies of the Treacher–Collins patient. In this axial CT, hypoplasia of the zygoma is seen



Fig. 3 Axial CT of the same patient shows hypertelorism and shallow orbits

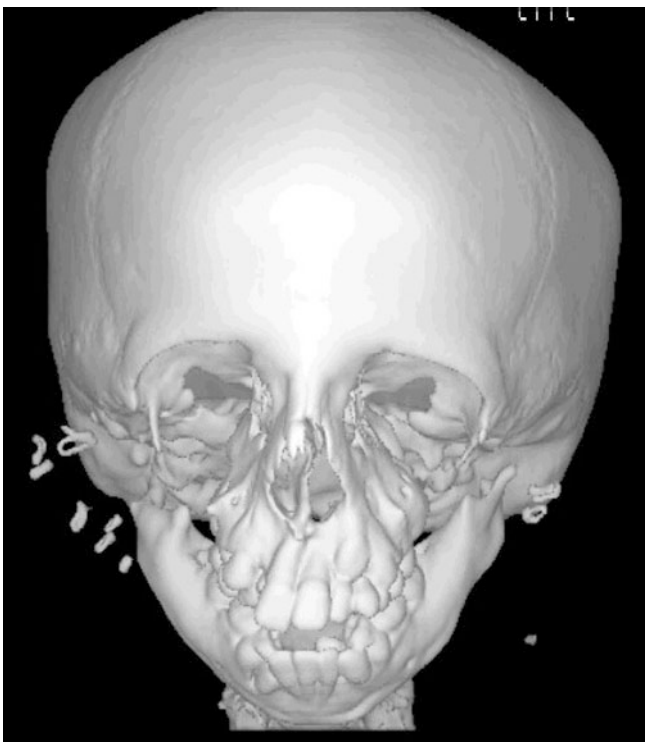


Fig. 4 3-D CT imaging. In this same patient with Treacher-Collins, the hypoplasia of the mandible, maxilla, and orbits is very evident. There is secondary abnormality in dentition. There are also bilateral malformations and hypoplasia of the auditory canals



Fig. 5 Nonsyndromic sagittal craniosynostosis is a child. The clinical image of the scalp, superior view, shows scaphocepahly (boatlike appearance)



Fig. 6 Plain film x-ray (lateral view) showing the appearance of the head with elongation due to early closure of the sagittal suture of the skull. The orbits are not involved

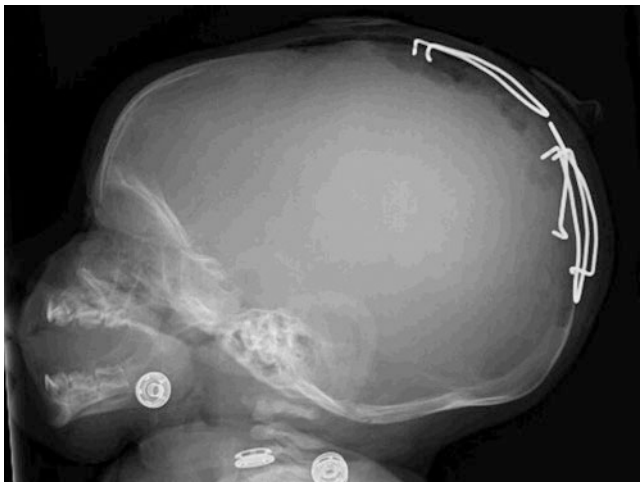


Fig. 7 Plain film x-ray (lateral view) of the same patient after surgery where distractors were placed to allow gradual expansion of the skull



Fig. 8 Hemifacial microsomia in a 7-year-old female. The right half of the calvarium is asymmetrically smaller than the left. The right orbit, right maxillary bone, and to a lesser degree the right mandible are all smaller compared to their left counterpart. There is also asymmetry of the soft tissues of the nose and right face. There is leftward deviation of the nasal septum with slightly smaller right naris. The right pinna is slightly smaller than the left, but the external auditory canal, middle, and the inner ear structures appear normal and symmetric

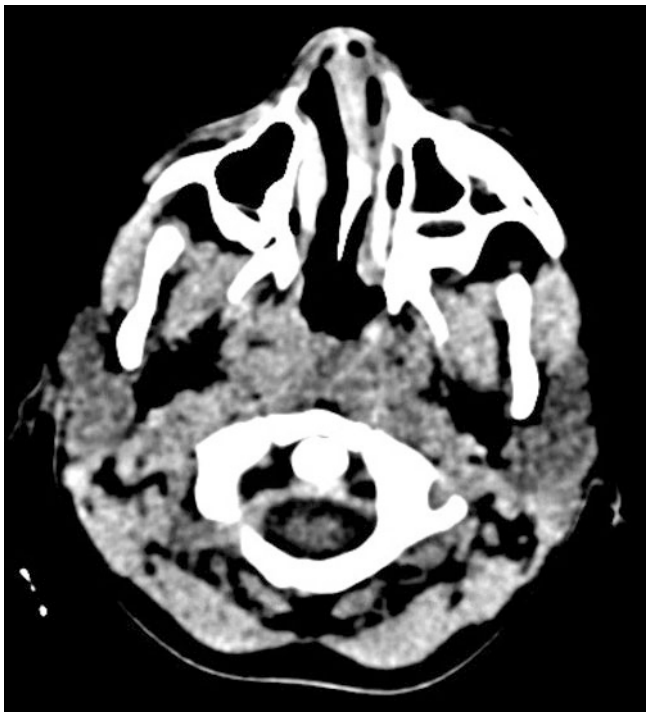


Fig. 9 Axial CT (soft tissue window) at the same level of the maxilla. The septal deviation is well appreciated



Fig. 10 Axial CT (bone window) of the orbits in the same patient. The right orbit is markedly smaller relative to the left side

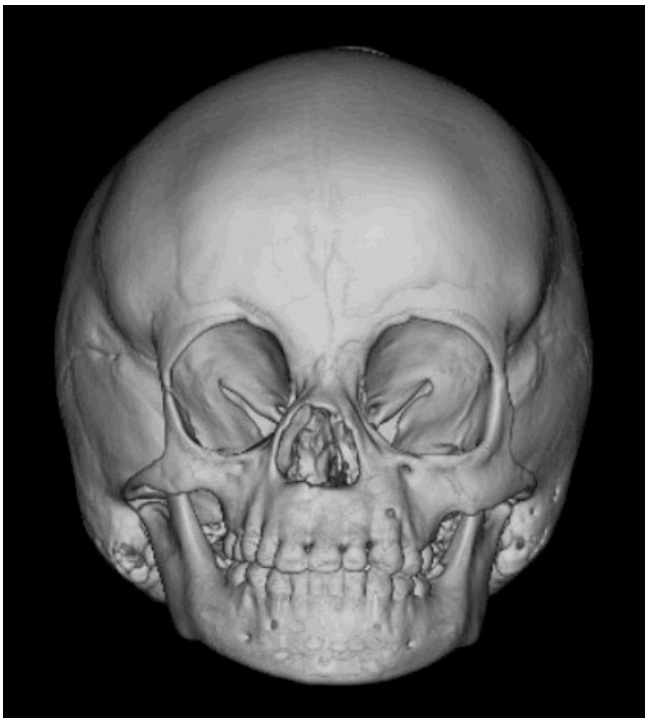


Fig. 11 3-D CT of the same patient with hemifacial microsomia. The right orbit is smaller. This patient did not have any ocular abnormalities, such as limbal dermoids or strabismus, which is seen in Goldenhar syndrome (a more severe variant of hemifacial microsomia also known as oculo-auriculo-vertebral syndrome)



Fig. 12 3-D soft tissue reconstruction of the same patient. There is a right-sided nasal deviation. The right side of the face as a whole appears smaller

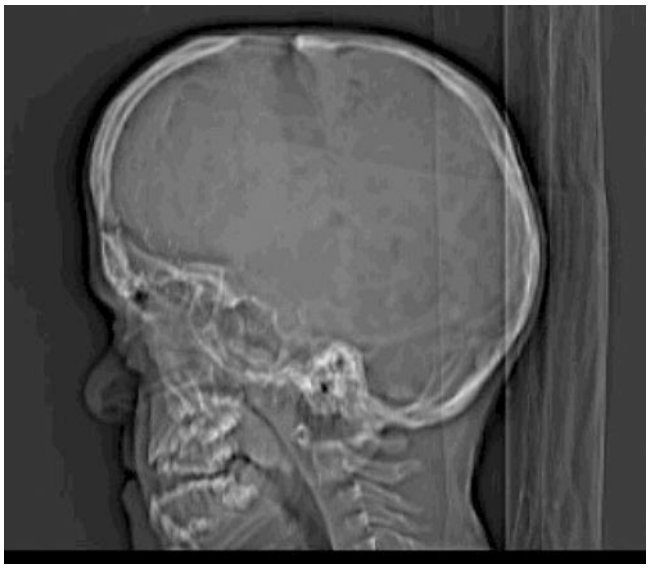


Fig. 13 Lateral x-ray of an infant with Apert syndrome. The skull morphology is abnormal with elongation of the upper frontal portion of the skull and shortening of the anterior cranial fossa; this is called turribrachycephaly (high and prominent forehead) with a foreshortened anterior–posterior dimension to the skull and exorbitism. Also seen is the diminutive nose. There is hypoplasia of the midface. Not shown is the syndactyly of the hands and feet characteristic of this disease. Individuals with Apert syndrome typically have a flat, elongated forehead, prominent or bulging eyes due to shallow orbits (eye sockets), recession or underdevelopment of the midface (maxillary hypoplasia), and syndactyly or fusion of the digits

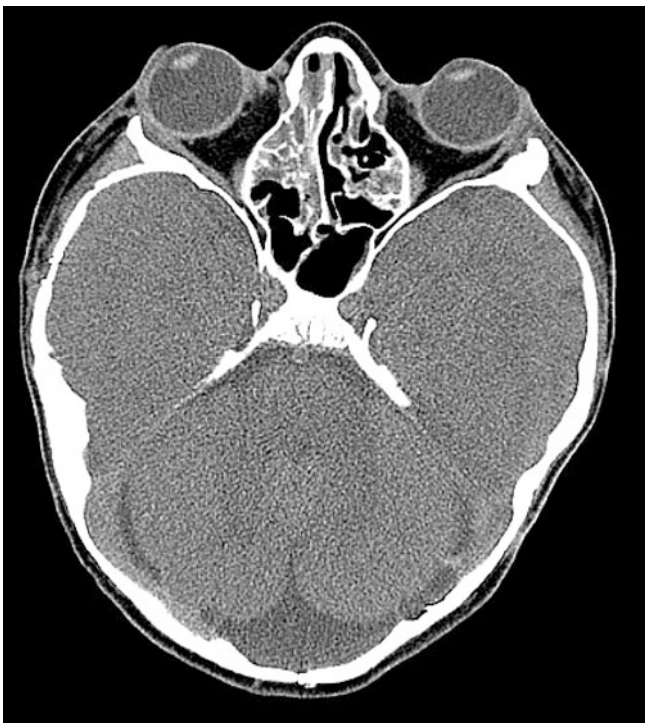


Fig. 14 Axial CT of the same patient with Apert syndrome. There is bilateral exorbitism due to shallow orbits

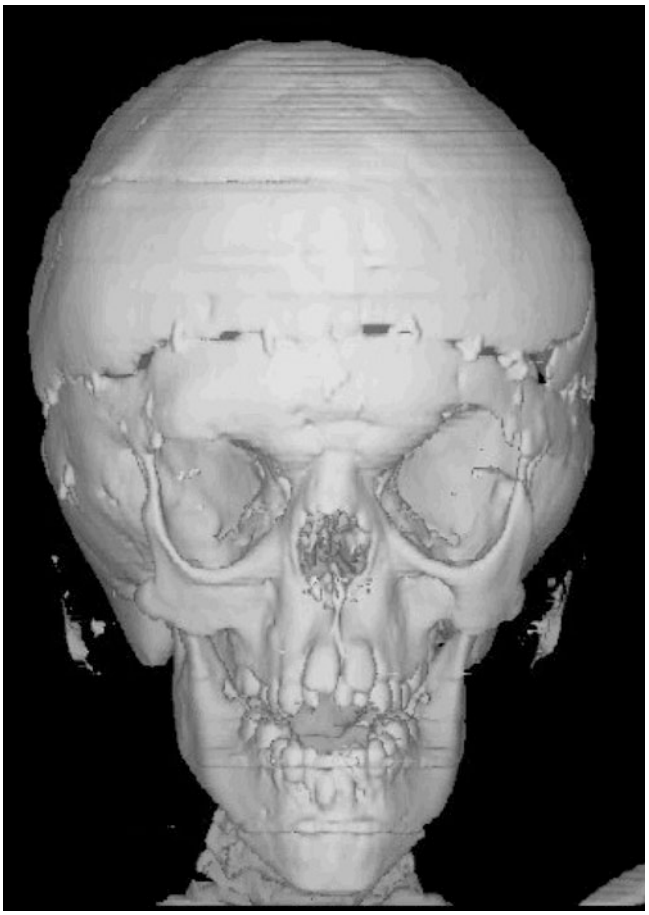


Fig. 15 3-D CT imaging of the same patient with Apert syndrome. Multiple strip craniectomies are noted within the axial, sagittal, and coronal planes within the frontal bone which are partially open

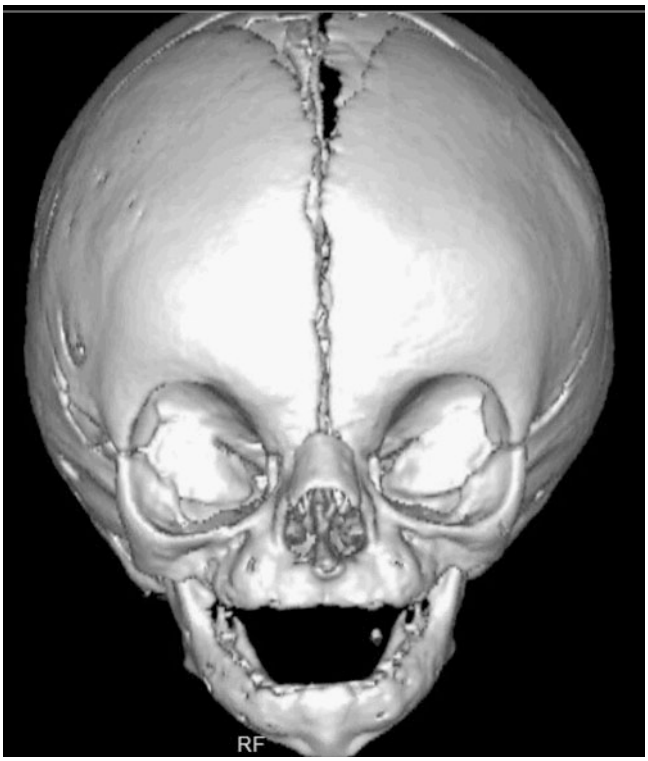


Fig. 16 3-D CT imaging in a patient with Pfeiffer syndrome. Please note the clover leaf skull appearance that is typical of more severely impacted patients with this syndrome. In addition, there is midface hypoplasia. Findings in Pfeiffer syndrome include ocular hypertelorism, down-slanting palpebral fissure, midface hypoplasia, broad thumbs and great toes, and variable cutaneous syndactyly

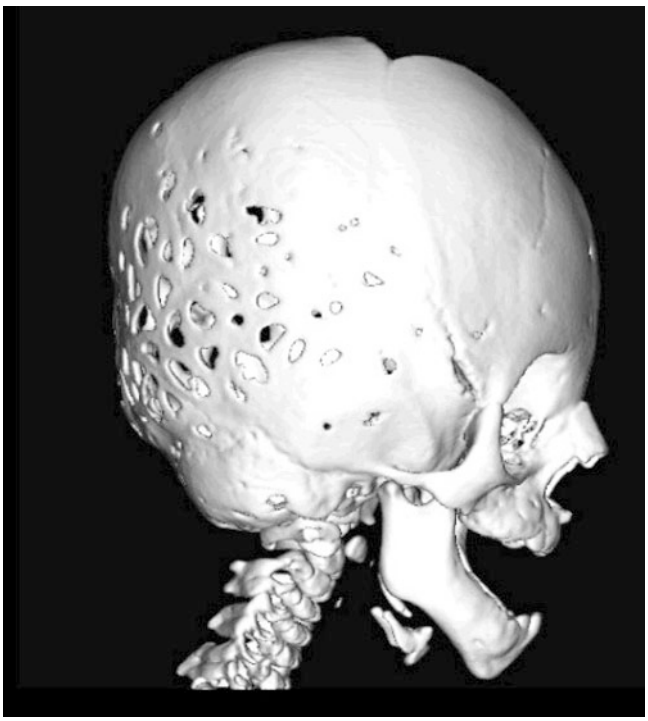


Fig. 17 3-D CT scan of the same patient (lateral view) showing brachycephaly, which is a flattening of the back of the head



Fig. 18 3-D CT with facial reconstruction displays the small nose, midface hypoplasia. The skull deformity is less easy to appreciate compared to the bony imaging. There is relative exophthalmos, hypertelorism, a small mandible, "parrot-beaked" nose, recessed supraorbital ridges, and increased forehead height



Fig. 19 Axial CT of the same patient. The midface hypoplasia is evident in the small nonaerated maxilla and zygoma bones



Fig. 20 Plain x-ray of a patient with Saethre-Chotzen syndrome; there is a relative a-p shortening of the vault relative to the skull base. There is premature closure of the right coronal suture. Saethre-Chotzen syndrome, in addition to craniosynostosis, includes a low-set frontal hairline, ptosis of the eyelids, deviated nasal septum, and variable syndactyly of fingers and toes



Fig. 21 Axial CT of the same patient showing facial asymmetry impacting the orbits

References

1. Whitaker L, Pashayan H, Reichman J. A proposed new classification of craniofacial anomalies. Cleft Palate J. 1981;18:161–4.
2. Naran S, Spadola MF, Storm PB, Bartlett SP. Oculoplastic considerations in pediatric craniofacial surgery. In: Katowitz JA, Katowitz WR, editors. Pediatric oculoplastic surgery. 2nd ed. Cham: Springer; 2018.
3. Gorlin R, Cohen M, Levin S. Syndromes of the head and neck. 3rd ed. New York: Oxford University Press; 1990.
4. Rogers BO. Berry–Treacher–Collins syndrome: a review of 200 cases. Br J Plast Surg. 1979;17:109–13.

Neurofibromatosis

21

William R. Katowitz

Contents

1 **Signs and Symptoms** 200
2 **Differential Diagnosis** 200
3 **Diagnosis** 200
4 **Treatment** 200
5 **Figures with Captions** 201
References 208

Abstract

- Neurofibromatosis is associated with tumors of the nervous system.
- There are three types NF-1, NF-2, and schwanommatosis.
- Neurofibromatosis can cause optic pathway gliomas and plexiform neurofibromas.
- Patients with NF-1 can have optic pathway gliomas that are bilateral, with intracranial involvement, and the optic nerve/sheath complex shows tubular or lobulated enlargement with elongation and kinking. These optic nerve gliomas tend to have a heterogeneous appearance.
- This is in contrast to optic nerve gliomas in patients without NF-1, who more often have unilateral, large fusiform tumors with more severe vision loss.
- Plexiform neurofibromas (PF) are complex nerve sheath tumors that follow multiple nerve branches.
- They occur in roughly 10% of patients with NF-1.
- Plexiform neurofibromas can cause pain, functional impairment, disfigurement, and can undergo malignant transformation.
- Plexiform neurofibromas of the orbit and face frequently cause vision loss secondary to deprivational or anisometropic amblyopia as well as glaucoma.
- Plexiform neurofibromas are composed of neoplastic Schwann cells, fibroblasts, perineural cells, and mast cells.
- Neoplastic Schwann cells lack NF1 gene expression.
- Loss of neurofibromin is associated with elevated levels of activated Ras.
- Activated Ras results in the initiation of a cascade of signaling events such as activation of Raf and mitogen-activated protein kinase (MAPK) that lead to increased cell proliferation.
- Discrete neurofibromas should be distinguished clinically from plexiform neurofibromas.
- Discrete neurofibromas arise from small nerves or nerve endings, and include dermal neurofibromas that protrude from the surface of the skin, or subcutaneous neurofibromas that present as firm nodules just below the surface of the skin.
- These tumors tend to be small and generally appear in the second decade of life, becoming more frequent as the patient ages. They have no risk of malignant transformation and rarely cause neurologic deficits.

W. R. Katowitz (✉)
The Children's Hospital of Philadelphia, Philadelphia, PA, USA
e-mail: katowitzw@email.chop.edu

© Springer Nature Switzerland AG 2022
G. Ben Simon et al. (eds.), *Atlas of Orbital Imaging*,
https://doi.org/10.1007/978-3-030-62426-2_10

Imaging Features

- Since plexiform neurofibromas lack a capsule and are infiltrative, they appear on images as serpiginous, cordlike masses that course through orbital fat and produce enlargement and irregularity of orbital structures.
- Plexiform neurofibromas are most often isointense on T1-weighted images and typically hyperintense on T2-weighted images. Areas of central low signal can frequently be seen on T2-weighted images. Tumors demonstrate variable contrast enhancement.
- A very large defect or absence of the greater wing of the sphenoid bone in NF-1 may produce pulsatile exophthalmos due to brain tissue abutting orbital soft tissue ("Orphan Annie sign.").
- Frequently, plexiform neurofibroma extends through the superior orbital fissure and produces enlargement of the cavernous sinus.
- Plexiform neurofibromas may be difficult to distinguish from schwannomas, but they are generally more infiltrative. In addition, when there is clinical suspicion, PET imaging can help to detect sarcomatous transformation of the plexiform neurofibroma.
- Neurofibromatosis type 2 is associated with central nervous system meningiomas and schwannomas, especially of the vestibular nerve.
- Small schwannomas of the cranial nerves may be difficult to visualize, leading to diagnostic dilemmas in children presenting with cranial nerve palsies and "normal" neuroimaging.
- MRI is particularly useful in imaging of cranial nerves and associated abnormalities in the cisternal spaces and the cavernous sinus [1–5].

Keywords

Neurofibromatosis · NF-1 · NF-2 · Neuoribroma · Plexiform neurofibrama · Glioma · Optic pathway glioma · Shwanomma

1 Signs and Symptoms

Proptosis, buphthalmos, pediatric glaucoma, facial dysmorphism, pulsatile proptosis, vision loss, hearing loss, strabismus, lagophthalmos, corneal exposure, and sphenoid wing dysplasia.

2 Differential Diagnosis

Neurofibromatosis type 1, neurofibromatosis type 2, plexiform neurofibroma, discreet neurofibroma, glioma, schwannoma, and schwannomatosis.

3 Diagnosis

There is diagnostic criteria for NF-1: Patients must have two or more of the following findings:

1. More than 5 café au lait macules over 5 mm in diameter if prepubertal or 15 mm if postpubert
2. Axillary or inguinal freckling (armpit or groin freckling)
3. More than 2 neurofibromas of any type or 1 plexiform neurofibroma
4. Optic glioma
5. Over 2 Lisch nodules
6. Distinctive osseous lesions such as sphenoid dysplasia or thinning of long bone cortex with/without pseudoarthrosis
7. Affected first degree relative by 1–6

There is diagnostic criteria for NF-2. Patients must meet one of the following criteria:

1. Bilateral vestibular schwannomas (VS)
2. First-degree relative with NF2 and unilateral
3. First-degree relative with NF2 or unilateral VS and two of:
   - meningioma, cataract, glioma, and neurofibroma
   - schwannoma and cerebral calcification
4. Multiple meningioma (two or more) and two of: unilateral VS, cataract, glioma, neurofibroma, schwannoma, and cerebral calcification

The diagnostic criteria for schwannomatosis is two or more non-intradermal schwannomas, one with pathological confirmation, including no bilateral vestibular schwannoma by high-quality MRI.

4 Treatment

Complete surgical excision of plexiform neurofibromas is nearly impossible. There is no standard of care, but an individualized approach with surgical debulking when needed has often been the approach. More recently MEK pathway inhibitors have shown great promise in minimizing the growth of plexiform neurofibromas. Serial MRI imaging is the modality of choice for disease monitoring.

5 Figures with Captions

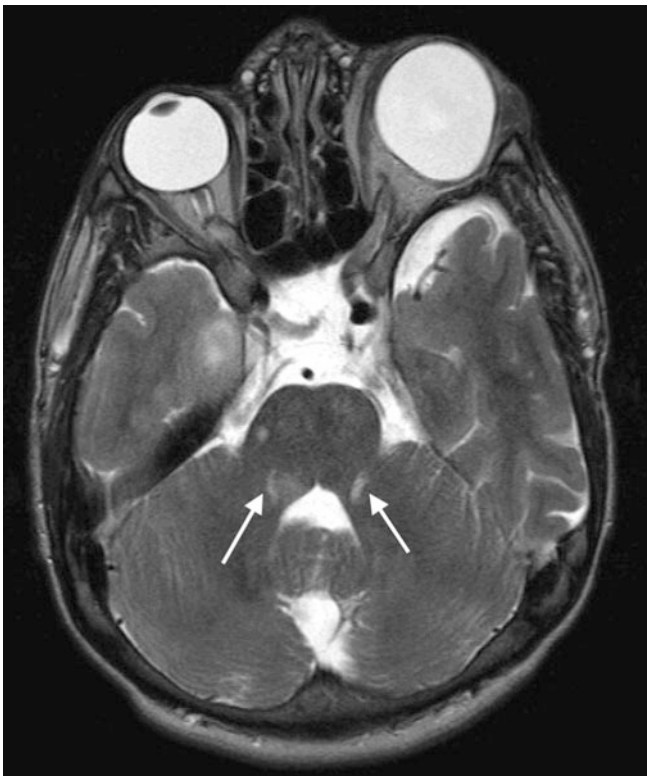


Fig. 1 Axial T2-weighted FS MRI in a 21-year-old patient with neurofibromatosis type 1. His MRI is significant for left sphenoid wing dysplasia, left optic nerve glioma, and buphthalmos due to glaucoma. The enlarged pre-chiasmatic/pre-canalicular portions of the left optic nerve, left optic chiasm, and left optic tract remain stable with mild enhancement. The intraorbital portion of the left optic nerve seems atrophic. There is stable deformity and enlargement of left globe consistent with buphthalmos. There is left sphenoid wing dysplasia also. Note hyperintense signals on the dorsolateral pons – FASI (focal areas of signal intensity) part of NF-1

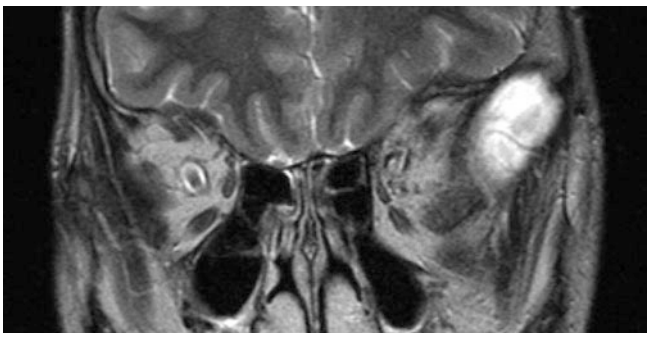


Fig. 2 Coronal T1-weighted MRI of the same patient. The left orbital portion of the optic nerve shows atrophy

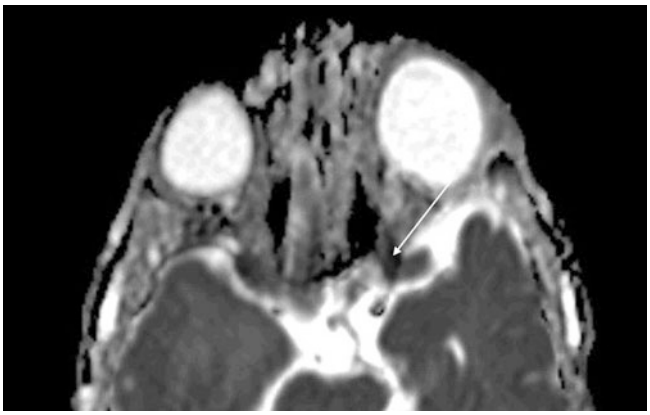


Fig. 3 Diffusion weighted imaging. There is mild restricted diffusion (arrow) on the ADC map at the pre-chiasmatic portion of the left optic nerve

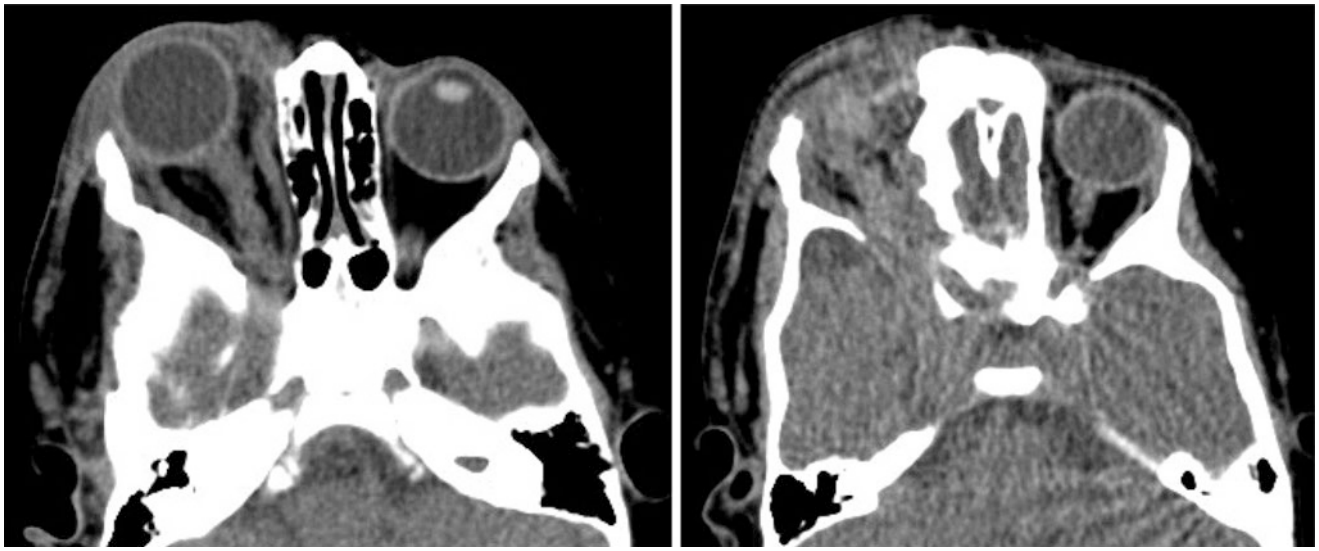


Fig. 4 Axial CT of a 2-year-old male with neurofibromatosis type 1. There is a plexiform neurofibroma ensheathing the right optic nerve (*left*). Also notable is dysplasia of the right sphenoid wing (*right*). The left orbit and optic nerve are normal

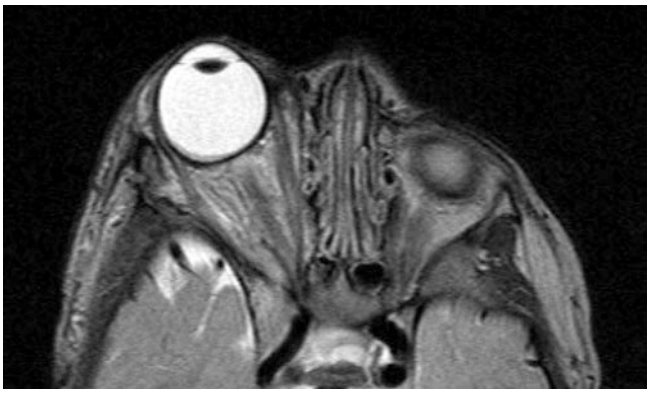


Fig. 5 T2-weighted axial MRI of the same patient age 2 years and 2 months before debulking surgery. There is gross right proptosis. The orbital plexiform fibroma is seen filling the intraconal space

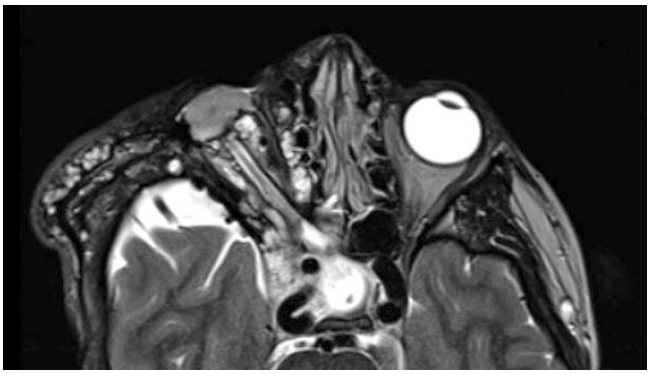


Fig. 6 Axial T2-weighted MRI of the same patient now age 14 status post a right enucleation (performed at age 2) with a dermis fat graft placed in the right orbit and post-tumor debulking. Twelve year late at age 14 there has been significant tumor growth. There is a persistent large infiltrative heterogenously enhancing plexiform neurofibroma centered in the right orbit with extension into the right superior and inferior fissures and orbital apex into the cavernous sinus, right face, right temporomandibular joint, and the external auditory canal (not shown). The lesion continues to encase the right cavernous carotid which is slightly smaller than the left but the flow void is maintained. There is persistent stretching and thinning of the right optic nerve complex with intrinsic T2 hyperintense signal. There is mild tortuosity of the left optic nerve without contrast enhancement. The left orbital soft tissues and left globe are otherwise unremarkable

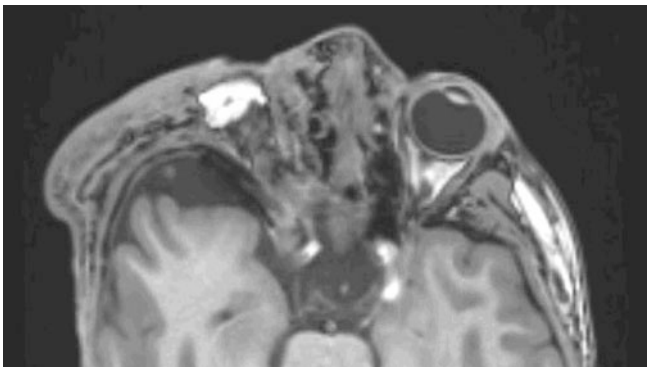


Fig. 7 Axial T1-weighted MRI of the same patient with NF1 now 14. The dermis fat graft is appreciated in the anterior orbit

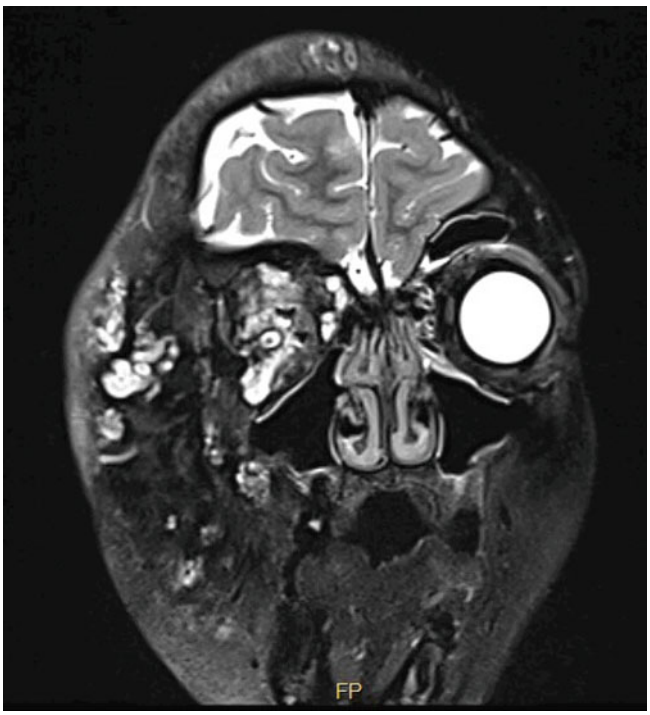


Fig. 8 Axial T2-weighted MRI of the same patient with NF1 age 14. There is extensive facial involvement of plexiform neurofibromas in the temporalis fossa

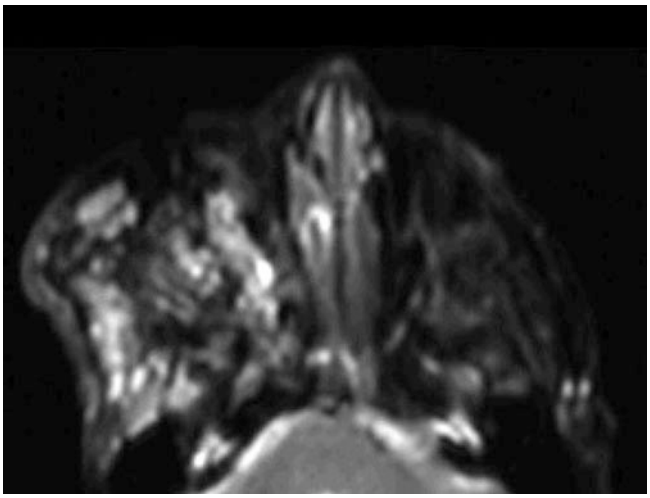


Fig. 9 Diffusion weighted image of the same patient with NF1 age 14. There is extensive tumor seen in the right orbit

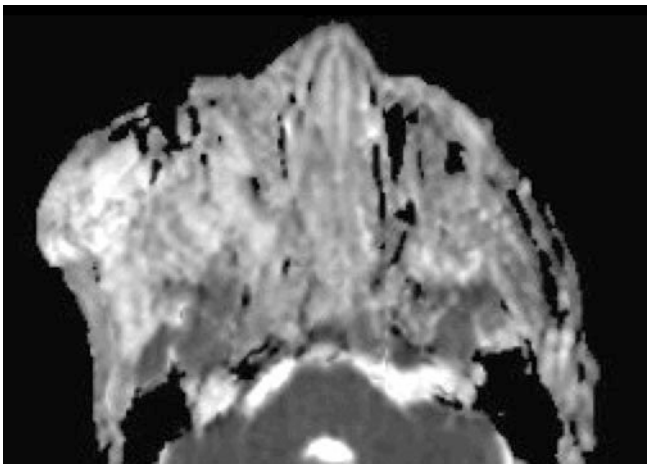


Fig. 10 Apparent diffusion coefficient (ADC) map of the same patient with NF1 age 14. The signal intensity is bright with no restriction in the right orbit

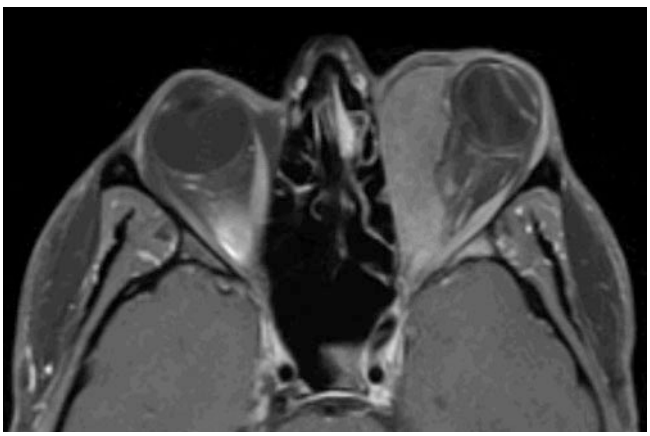


Fig. 11 Axial T1-weighted post-contrast fat-saturated MRI image of a 21-year-old male with NF2. There is a left intramuscular schwanomma involving the left medial rectus

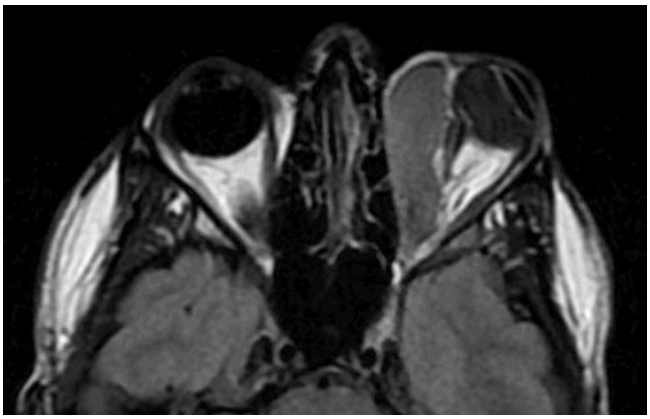


Fig. 12 Axial T2-weighted flair MRI. The schwanomma is relatively hyperintense when compared to the uninvolved extraocular muscles

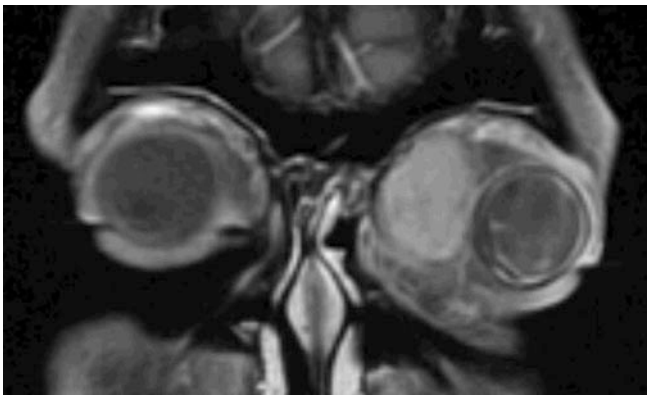


Fig. 13 Coronal T1-weighted fat-saturated post-contrast MRI of the same 21-year-old patient with NF2. The schwannoma involving the left medial rectus is causing lateral displacement of the globe in the left orbit

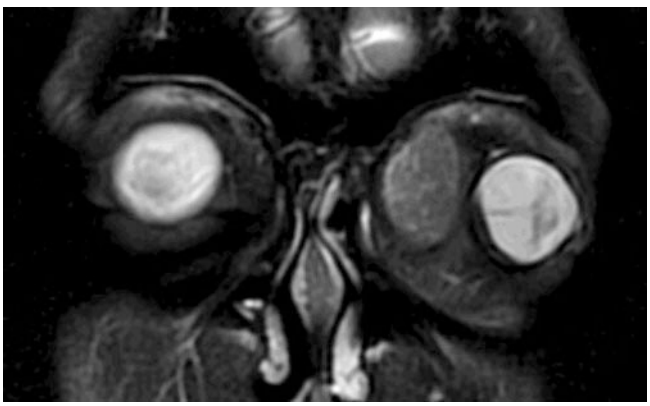


Fig. 14 Coronal T2-weighted fat saturation MRI of the same patient

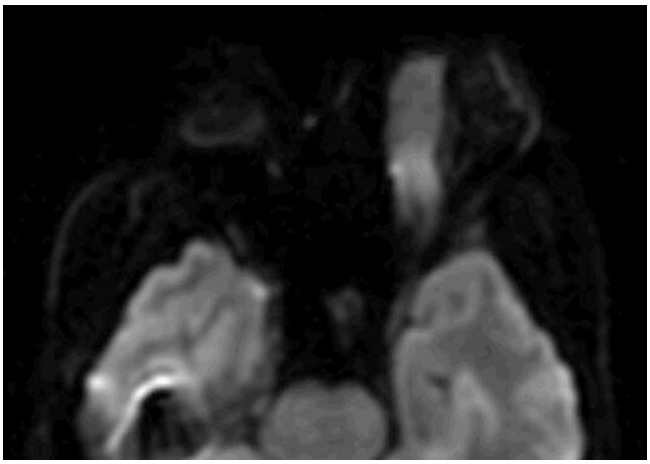


Fig. 15 DWI showing brightness in the left medial rectus infiltrated by a large schwannoma

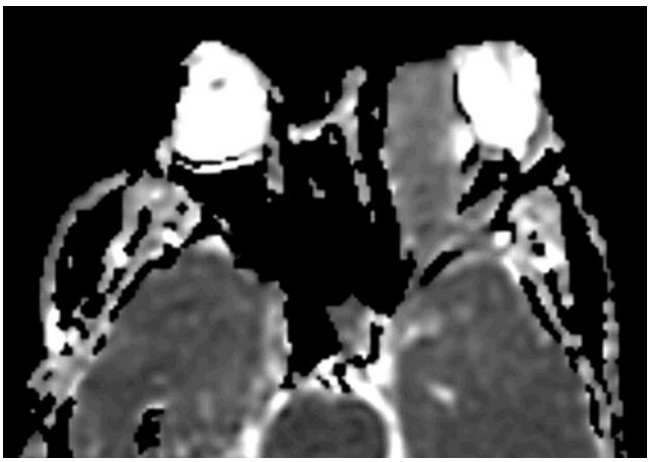


Fig. 16 ADC map of the same patient showing no diffusion restriction

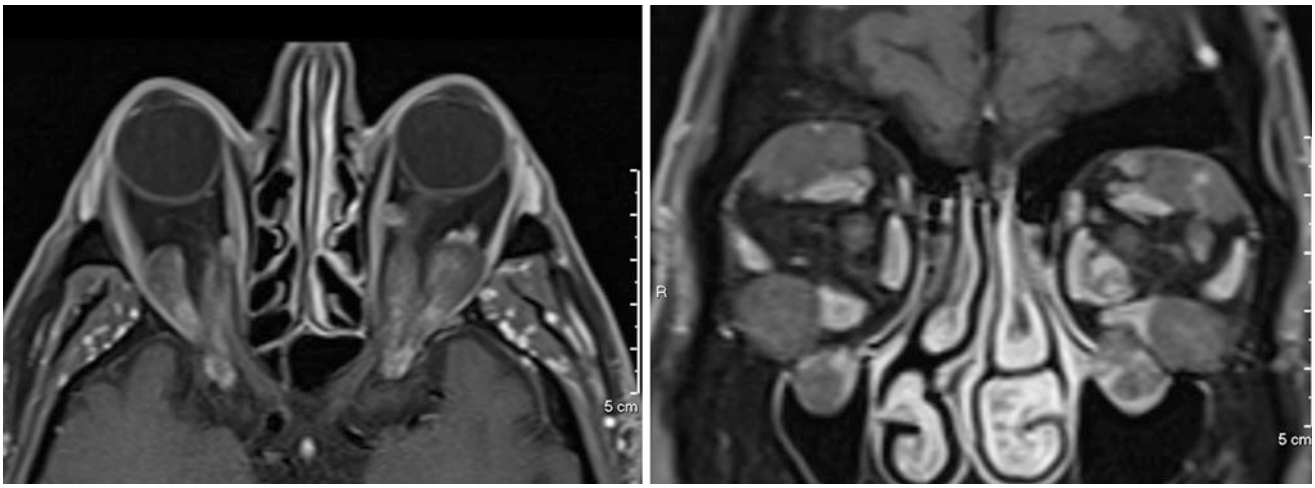


Fig. 17 T1WI FS CE, MRI, axial (*left*), and coronal (*right*) of a 71-year-old male with presumed multiple cranial nerve schwannomas involving both orbits. The patient presented with bilateral painless proptosis and normal optic nerve function

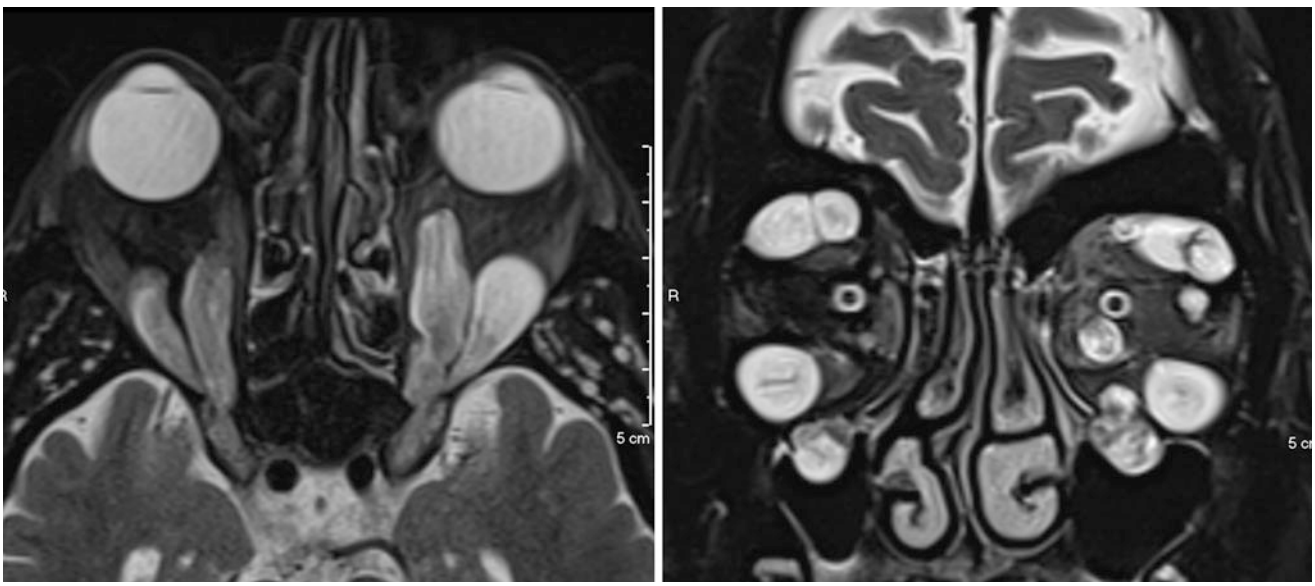


Fig. 18 T2 WI FS MR of the same patient showing the multiple tumors are isointense and follow cranial nerve course

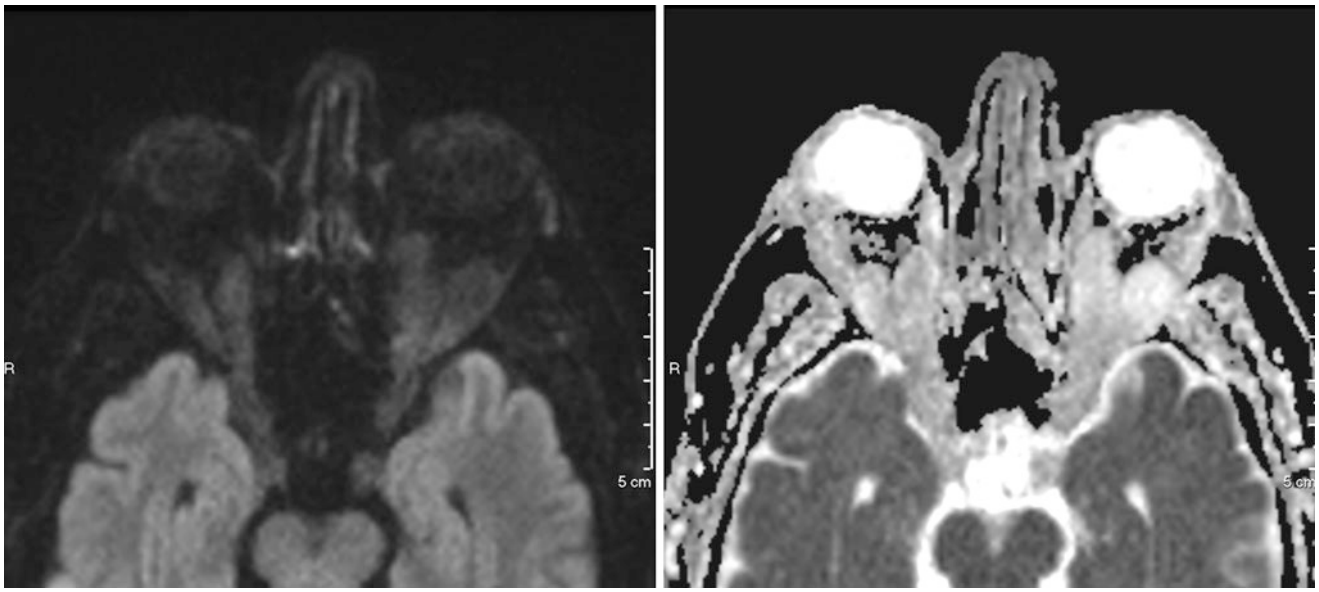


Fig. 19 DWI (*left*) with corresponding ADC map (*right*) shows no restrictive features

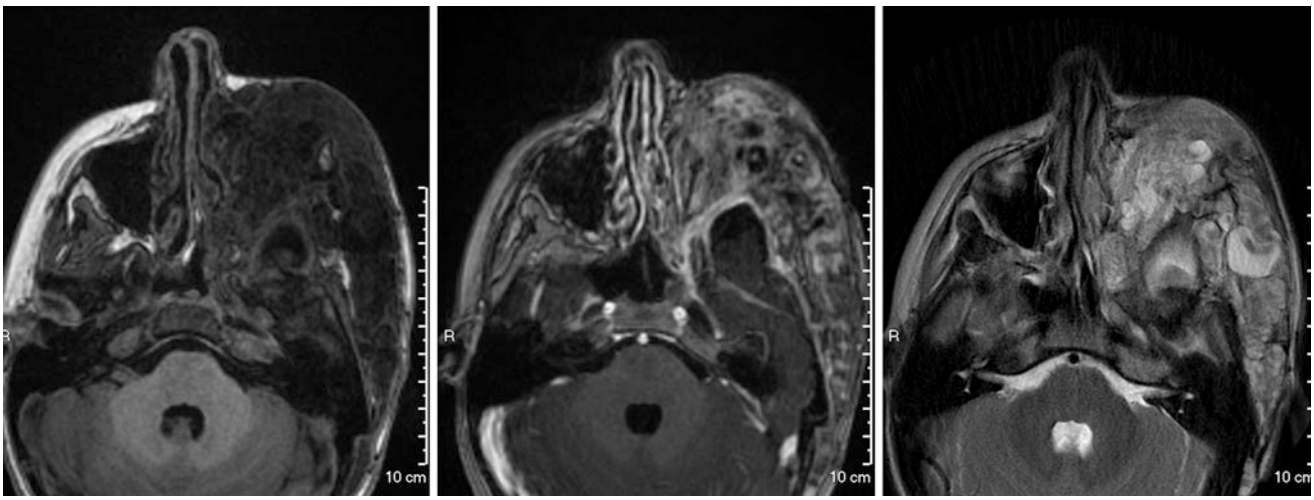


Fig. 20 Axial MR scan of a 9-year-old female with left orbital plexiform neurofibroma and sphenoid wing dysplasia. T1 WI (*left*), with FS and CE (*middle*) and T2 WI (*right*) showing the serpiginous nature of the tumor, with heterogenous intensity and contrast enhancement. The tumor is extending into the right temporal fossa

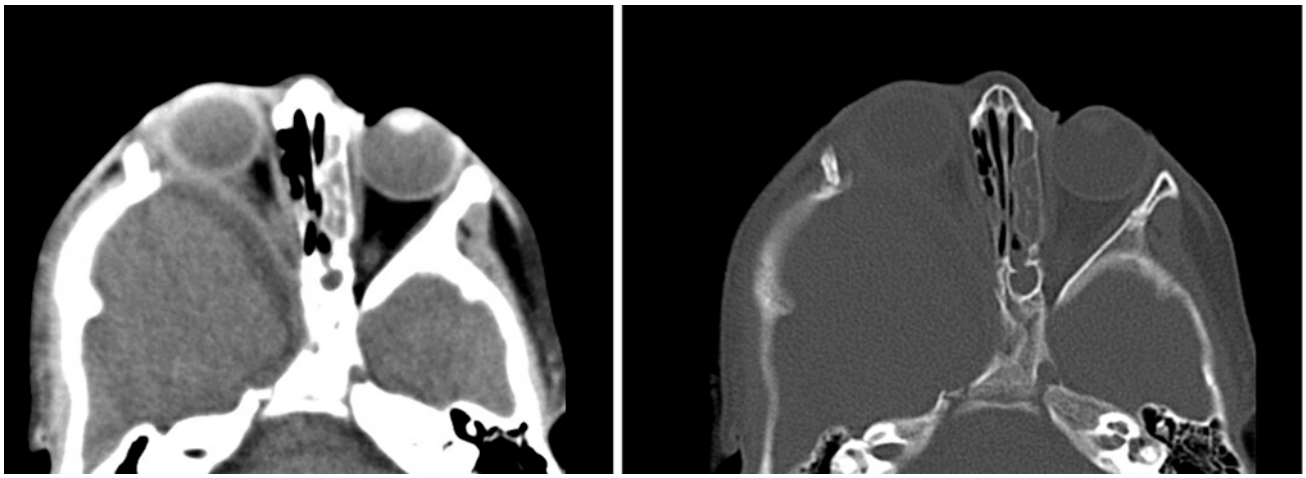


Fig. 21 NECT of a 5-year-old female with left sphenoid wing aplasia second to NF-1. The patient presented with pulsating exophthalmos on the right side. Soft tissue window (*left*) and bone window (*right*) better demonstrating lack of bony sphenoid wing

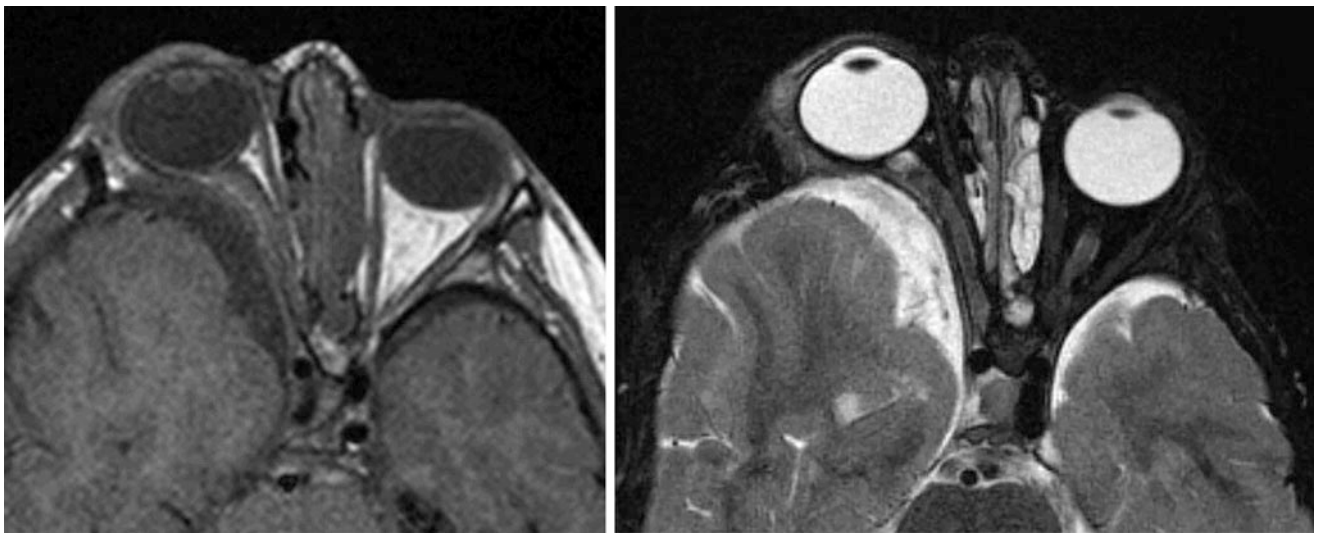


Fig. 22 T1WI (*left*) of the same patient showing no obvious sphenoid wing with the middle cranial fossa pushing the globe forward but not invading the orbit; T2 WI (*right*) demonstrating relative larger amount of CSF at the posterior-lateral orbit

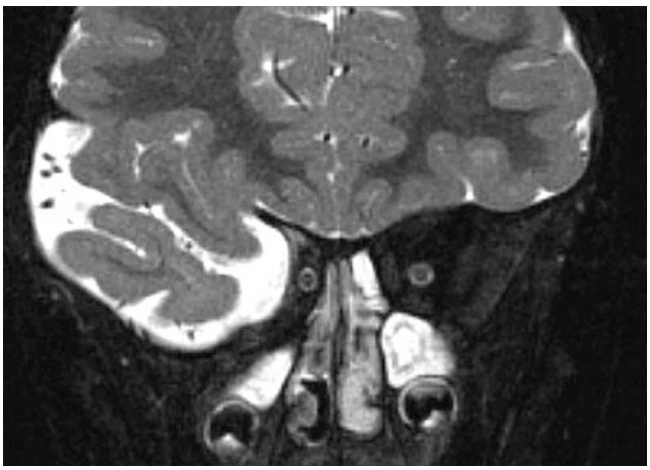


Fig. 23 T2 WI of the same patient, coronal view beautifully demonstrating how the orbital content is being displaced by the right temporal lobe. The periorbita is intact

References

1. Jackson IT, Laws ER Jr, Martin RO. The surgical management of orbital neurofibromatosis. Plast Reconstr Surg. 1983;71:751–8.
2. Bilaniuk LT, Murchison AP, Bilyk JR. Imaging of the pediatric orbit. In: Katowitz JA, Katowitz WR, editors. Pediatric oculoplastic surgery. 2nd ed. Cham: Springer; 2018.
3. Wright JE, McNab AA, McDonald WI. Optic nerve glioma and the management of optic nerve tumours in theyoung. Br J Ophthalmol. 1989;73(12):967–74.
4. Stern J, Jakobiec FA, Housepian EM. The architecture of optic nerve gliomas with and without neurofibromatosis. Arch Ophthalmol. 1980;98(3):505–11.
5. Evans DG, Huson SM, Donnai D, et al. A clinical study of type 2 neurofibromatosis. Q J Med. 1992;84(304):603–18.

Anophthalmia and Microphthalmia

22

William R. Katowitz

Contents

1 **Signs and Symptoms** 209
2 **Differential Diagnosis** 210
3 **Diagnosis** 210
4 **Treatment** 210
5 **Figures with Captions** 210
References 213

Abstract

- Congenital anophthalmia is rare and refers to a complete absence of ocular tissue.
- Congenital anophthalmia occurs when there is a failure of the optic vesicle to bud or early arrest of its development with subsequent degeneration.
- Microphthalmia is a small and malformed eye.
- Persistent primary hyperplastic primary vitreous (PHPV)/persistent fetal vasculature (PFV) may result in a microphthalmic eye.
- A microphthalmic eye may be associated with a cyst. This is usually due to a coloboma of the uveal tissue of the eye.
- A small orbit or orbits may be present due to poor bony growth. This may result in facial asymmetry.
- Abnormalities of the eyelid occurring in association with microphthalmia include eyelid coloboma, decreased horizontal and vertical palpebral fissure length, and decreased conjunctival surface area with relative shortening of the posterior lamellae with or without congenital entropion.
- Associated systemic abnormalities may involve the central nervous system, face (cleft lip or palate, hemifacial microsomia, facial hypoplasia, and micrognathia), skeletal system (anomalous limbs), ear (pre-auricular skin tags and deafness), heart (ventricular septal defects, tetralogy of Fallot, and coarctation of the aorta), genitourinary system, and gastrointestinal system
- Imaging key points:
  - Look for the presence of an eye not visible clinically.
  - Are there extraocular muscles present? These can be utilized for a blood supply and possibly for motility if a dermis fat graft were to be placed.
  - Is a cyst present associated with a microphthalmic eye? At times a cyst may be large or expand resulting in overexpansion of the bony orbit with or without proptosis causing disfigurement with possible corneal exposure.

Keywords

Anophthalmia · Microphthalmia · Coloboma

1 Signs and Symptoms

Small or missing eye with associated small appearing orbit. This may be unilateral or bilateral. Facial asymmetry may be present due to poor facial growth [1–3].

W. R. Katowitz (✉)
The Children's Hospital of Philadelphia, Philadelphia, PA, USA
e-mail: katowitzw@email.chop.edu

© Springer Nature Switzerland AG 2022
G. Ben Simon et al. (eds.), *Atlas of Orbital Imaging*,
https://doi.org/10.1007/978-3-030-62426-2_12

2 Differential Diagnosis

Persistent hyperplastic primary vitreous, phthisis bulbi, a socket post-enucleation (acquired clinical anophthalmos).

3 Diagnosis

The presence of a small appearing eye (or eyes) with a corneal diameter under 10 mm and an axial length under 20 mm. The absence of an eye confirms the diagnosis of clinical anophthalmos; however, a small microphthalmic eye is often revealed on imaging.

4 Treatment

Early intervention to expand the orbit is needed to allow for proper orbital and facial growth. This can be accomplished via serial prosthetic conformers or with osmotic expanders. Ultimately, an ocular implant may be placed, such as a dermis fat graft.

5 Figures with Captions

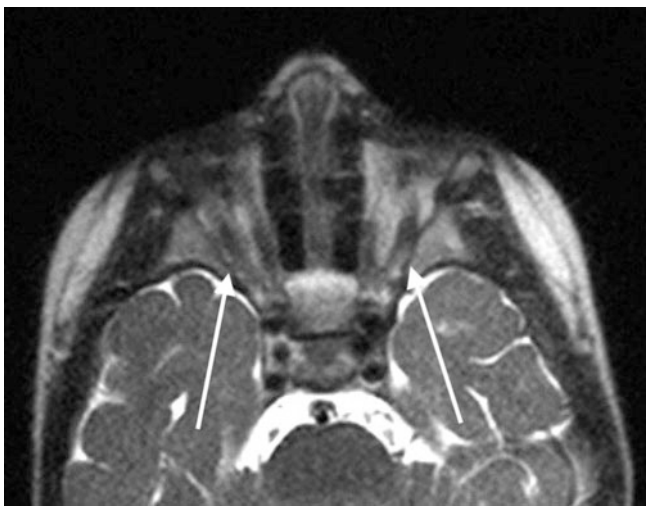


Fig. 1 Axial T2-weighted MRI of a 3-year-old with bilateral anophthalmia. The orbits are somewhat narrow with hypotelorism (reduced inter-orbital distance). There is bilateral anophthalmia: no globe, optic nerve, or optic nerve sheath is present (white arrows). However, the orbits do contain normal fat, lacrimal glands, and extraocular muscles. The periorbital soft tissues show no evidence of inflammation

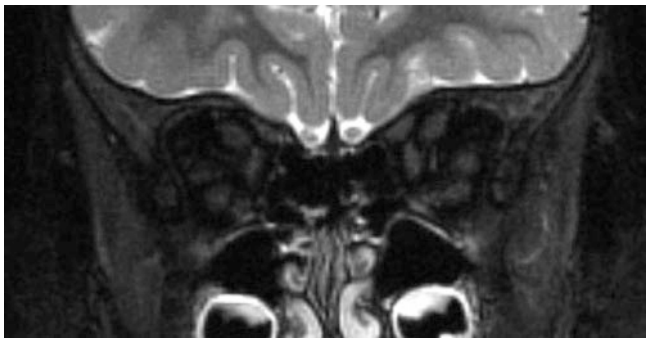


Fig. 2 Coronal T2-weighted MRI, fat sat of the same patient showing normal appearing extraocular muscles



Fig. 3 Bilateral anophthalmia in a 10-month-old with osmotic expanders in place for orbital expansion. T2-weighted axial MRI showing bilateral hypo-development of the orbits. Bilateral ocular hydrogel hemispheres are seen, with small areas of associated susceptibility (white arrows). No definite optic pathway is seen, the left orbit shows two extraocular muscles with no optic nerve. The extraocular muscles are diminutive

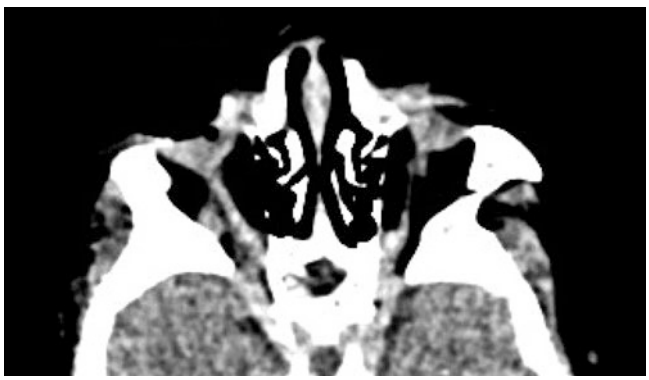


Fig. 4 Axial CT imaging of the same patient. The orbits are very small. There are no expanders present in this patient during imaging



Fig. 5 3D reconstruction of the same patient with bilateral anophthalmia. The orbits are small relative to the facial bones



Fig. 6 3D reconstruction with tissue rendering of the same patient. Eyelid phimosis noted in addition to the small and sunken appearing orbits. There are no colobomas to the eyelids

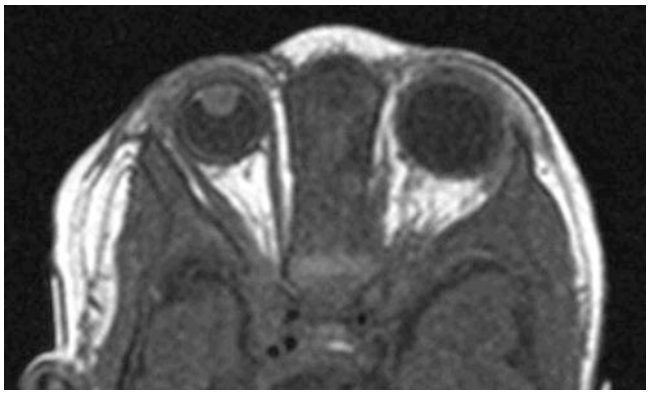


Fig. 7 Right microphthalmia in a 2-month-old. T1-weighted axial MRI showing the right globe is hypoplastic relative to the left. There is no visible optic nerve attached to the right globe. The vitreous humor on the right has normal signal intensity, without significant asymmetry of the posterior globe to suggest underlying neoplasm. The extraocular muscles are bilaterally symmetric

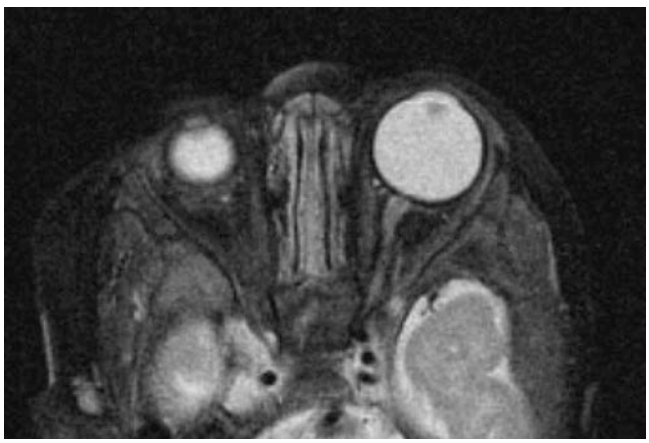


Fig. 8 T2 imaging with fat saturation in the same patient. The right eye is noticeably smaller. The left optic nerve is normally sized and courses to the midline

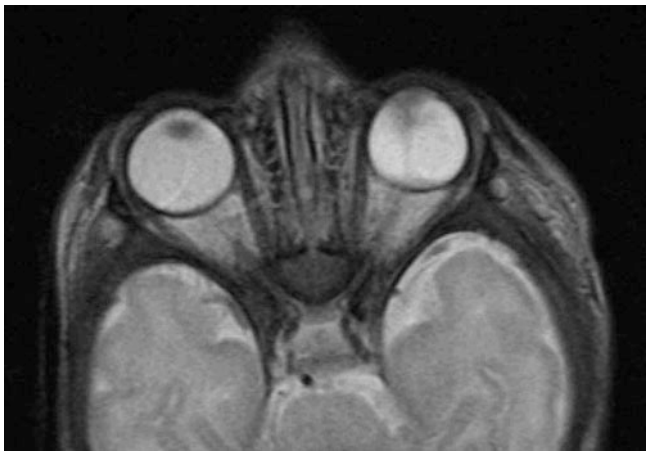


Fig. 9 Left persistent hyperplastic primary vitreous with microphthalmia in an 8-day-old infant. T2-weighted MRI imaging shows slight asymmetry of the globes, smaller on the left side. There is likely proteinaceous fluid within the left ocular globe content. A linear tract is seen along the midline that represents Cloquet's (hyaloid) canal

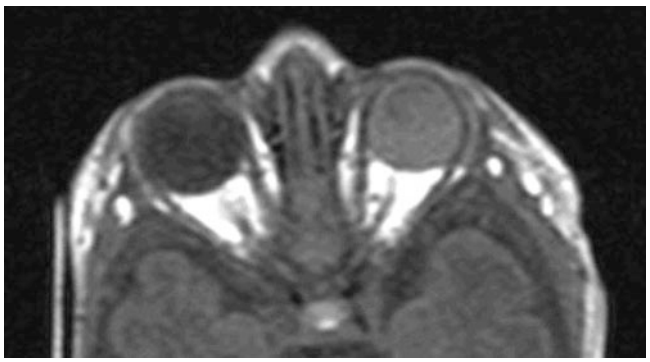


Fig. 10 T1-weighted MRI imaging. The smaller left optic nerve within the orbit is noted. Note the hyperintense content of the left globe evident of PFV

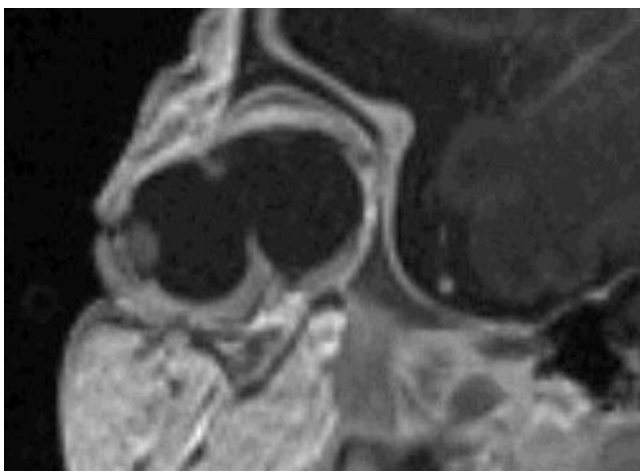


Fig. 11 A large ocular cyst associated with a chorioretinal coloboma. T1-weighted post-contrast sagittal MRI showing the large posterior ocular cyst

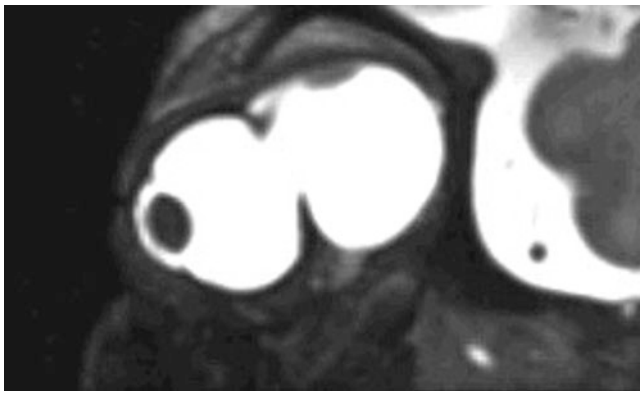


Fig. 12 T2-weighted fat sat MRI sagittal imaging showing this large posterior cyst. The globe is flattened due to mass effect of the congenital cyst



Fig. 13 T2-weighted fat sat coronal MRI imaging in the same patient

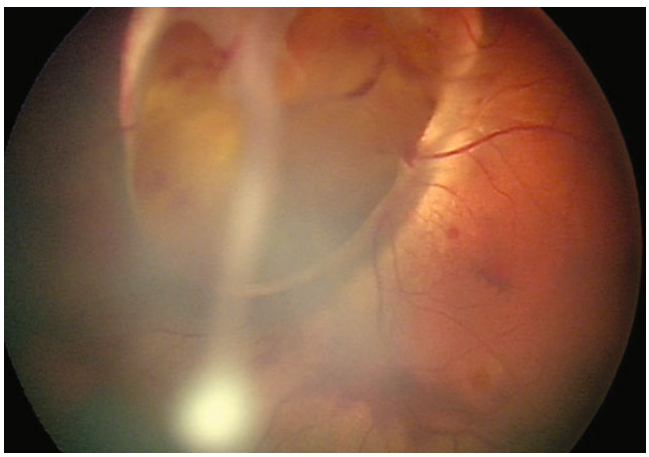


Fig. 14 Color fundus photo of the same patient's left eye. A large posterior chorioretinal coloboma can be appreciated with an anomalous appearing optic nerve. The cyst is visualized containing presumed vitreous

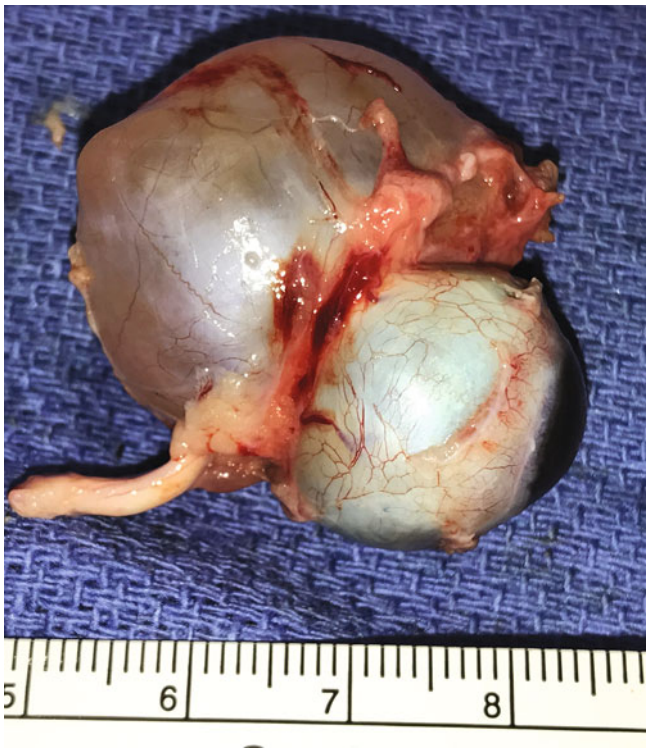


Fig. 15 Left eye with colobomatous cyst after enucleation due to excessive orbital expansion, proptosis, and lagophthalmos resulting is patient discomfort and disfigurement



Fig. 16 Bilateral colobomas and microphthalmia in a patient with CHARGE syndrome (coloboma, heart defects, choanal atresia, growth retardation, genital abnormalities, and ear abnormalities). T2-weighted MRI showing both optic globes are small and misshapen. They are lobulated posteriorly, indicating colobomas. The right globe is small and the left globe is enlarged. There appears to be a thin membrane in the posterior medial aspect of the left globe. There are multiple cystic outpouchings around the posterior aspect of the right globe in the region of the proximal aspect of the optic nerve and seem to be separate from the globe. No hemorrhage is seen within the globes. Both globes are medially deviated



Fig. 17 T2-weighted MRI imaging with fat saturation in the same patient. The lenses appear globular in shape (black arrows), particularly on the right with partial dislocation. Bilateral intra-orbital optic nerves are thin and atrophic (white arrows). The intracranial optic nerves appear slightly small, right more than the left

References

1. Moore KL, TVN P, Torchia MG. The developing human clinically oriented embryology. Philadelphia: Elsevier; 2016. p. 1. online resource.
2. Handler L, Heher K, Katowitz J. Congenital and acquired anophthalmia. Curr Opin Ophthalmol. 1994;5:84–90.
3. Kennedy RE. The effect of early enucleation on the orbit in animals and humans. Adv Ophthalmic Plast Reconstr Surg. 1992;9:1–39.

Cystic Lesions of the Orbit: Dermoid and Epidermoid Cysts

23

William R. Katowitz

Contents

1 **Signs and Symptoms** 215
2 **Differential Diagnosis** 216
3 **Diagnosis** 216
4 **Treatment** 216
5 **Figures with Captions** 216
References 220

Abstract

- Dermoid and epidermoid cysts are congenital malformations of ectodermal origin; epithelial cysts can be acquired.
- Both are lined with squamous epithelium; epidermoid cysts do not contain other tissues from mesodermal origin.
- Dermoid cysts may contain skin appendages including hair, as well as bone and teeth.
- These can present as a palpable periocular or periorbital mass.
- May fistulize to the skin, or be dumbbell through the orbital bones to be intranasal, intracranial, or intraorbital spaces. In rare cases, spontaneous or post-traumatic rupture may occur.
- CT imaging will show a well-defined mass that may be heterogenous due to various content material. The lesion content normally does not enhance with contrast material, unlike the rim which typically enhances. It may cause bone remodeling with pressure erosion. The presence of adipose tissue within the lesion is not mandatory for diagnosis.
- MR shows inhomogeneous mass with mixed signal on T1 and T2 WI depending on the content. The content of the lesion does not enhance with contrast; it may show rim enhancement.
- Diffusion-weighted imaging (DWI) is useful to differentiate epidermoid from dermoid cyst by showing restricted diffusion (low ADC) in dermoid cysts.

Keywords

Dermoid · Cyst · Dermoid cyst · Epidermoid cyst · Choristoma · Dumbbell shape

1 Signs and Symptoms

A painless mass may be present around the eye or orbital bones; this may be soft, firm, moveable, or fixed to the deeper tissue. Orbital dermoid cysts may induce proptosis and strabismus. Leaking or ruptured dermoid cysts may present as orbital cellulitis. Lesions may also fistulize to the skin [1–3].

W. R. Katowitz (✉)
The Children's Hospital of Philadelphia, Philadelphia, PA, USA
e-mail: katowitzw@chop.edu

© Springer Nature Switzerland AG 2022
G. Ben Simon et al. (eds.), *Atlas of Orbital Imaging*,
https://doi.org/10.1007/978-3-030-62426-2_13

2 Differential Diagnosis

Infection: orbital cellulitis. Malformation: epidermoid cyst, dermolipoma, and lipoma. Benign vascular tumor: hemangioma. Vascular malformation: lymphatic, venous, or lyphatico-venous. Neoplasm: rhabdomyosarcoma, other sarcomas.

3 Diagnosis

Patients may present with either a visible mass in the ocular adnexa or with proptosis or some other vertical or horizontal globe displacement. Some orbital dermoid cysts are completely asymptomatic and are only discovered inadvertently on orbital imaging for some other indication. Dermoid cysts are typically in the region of a bony suture. The mass can be palpable firm (or sometimes soft) and sometimes fixed to the periosteal tissue. A skin fistula may be present that can drain a foul-smelling substance. Rarely a patient will present with peri-ocular or preseptal cellulitis or orbital cellulitis.

4 Treatment

Observation is always an option; however, the natural history of dermoid cysts carries a risk of rupture and cellulitis and should eventually be removed. When diagnosed in an infant, surgery can be deferred to after the age of 6 months when general surgery is considered safer. Orbital imaging should always be considered but can be avoided when the lesion is freely mobile. Any atypical location of a suspected dermoid cyst that is not over a bony suture should be imaged (central orbital rim). Lesion in the medial location and lesions that are very adherent to the periosteum should raise the concern for extension through the underlying bony suture. This may represent a dumbbell configuration to the dermoid cyst with a portion below the skin and extension to the other side of the underlying bone. Lesions may extend into the intraorbital, intranasal, or intracranial space.

5 Figures with Captions



Fig. 1 A 4-year-old girl with a progressive right noncomitant esotropia. Mild proptosis was noted. The esotropia was persistent after the dermoid removal; however, the angle of strabismus was smaller, and the patient was managed with glasses alone for the accommodative component to her strabismus



Fig. 2 Axial CT (soft tissue window) showing a right-sided hypodense oval nonhomogenous mass-inducing proptosis. Note smooth remodeling of lateral orbital wall denoting long-standing lesion. The mass appears to be both intra- and extraconal abutting the ON sheath complex and causing mild proptosis



Fig. 3 Axial CT (bone window). The mass results in right-sided proptosis. There is associated remodeling, thinning, and outward bowing of the right superolateral orbital wall. There is no osseous invasion

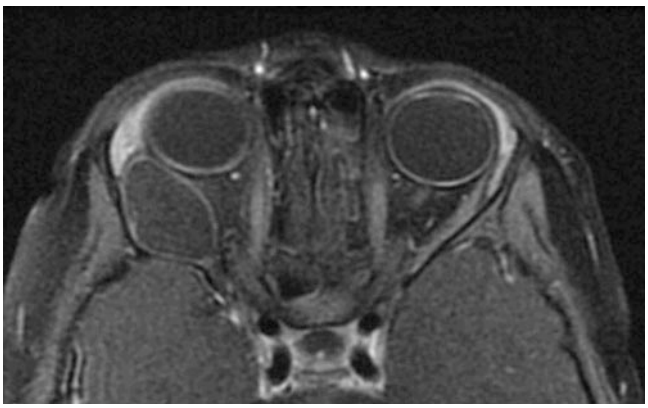


Fig. 4 Axial T1-weighted postcontrast MRI with fat saturation shows a large hypointense lesion in the lateral right orbit with faint peripheral enhancement

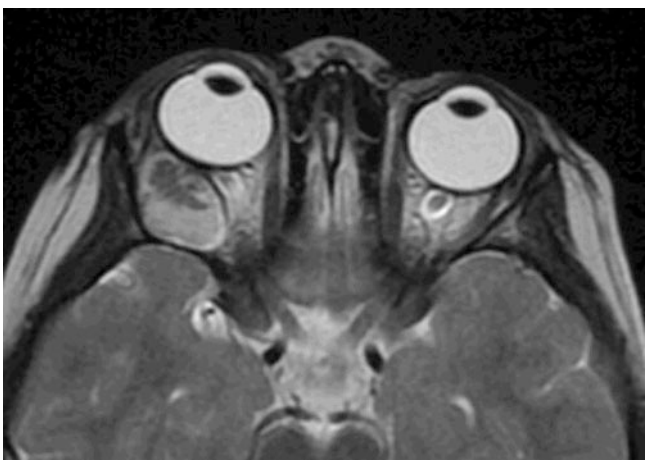


Fig. 5 Axial T2-weighted fast recovery fast spin echo (FRFSE) MRI. The lesion is cystic and heterogenous. There is a hypointense component within the lesion

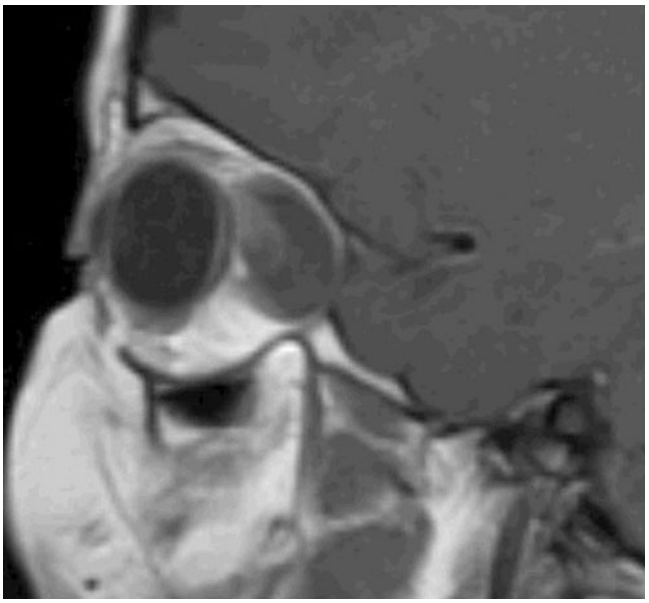


Fig. 6 Sagittal postcontrast T1-weighted MRI. On this series, the cyst is causing a mass effect on the posterior right eye

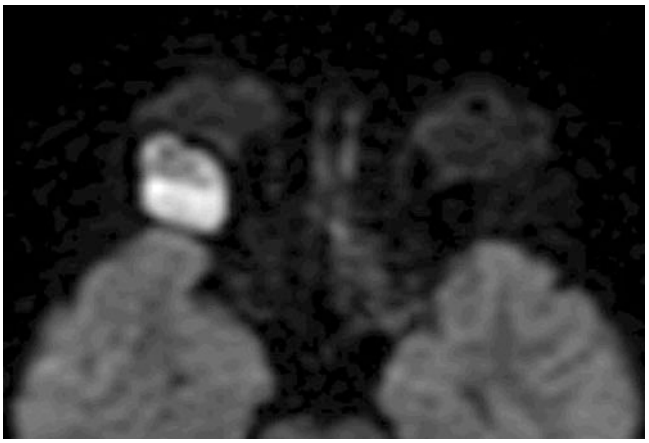


Fig. 7 Diffusion-weighted imaging showing a bright signal on the cyst typical to epi-dermoid

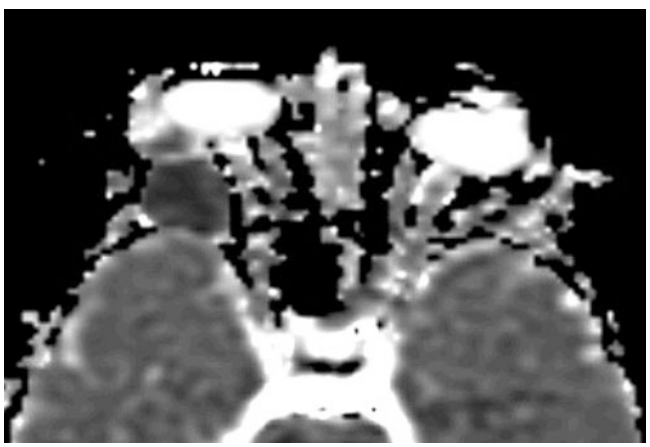


Fig. 8 Apparent diffusion coefficient imaging showing restricted diffusion within the right-sided orbital lesion

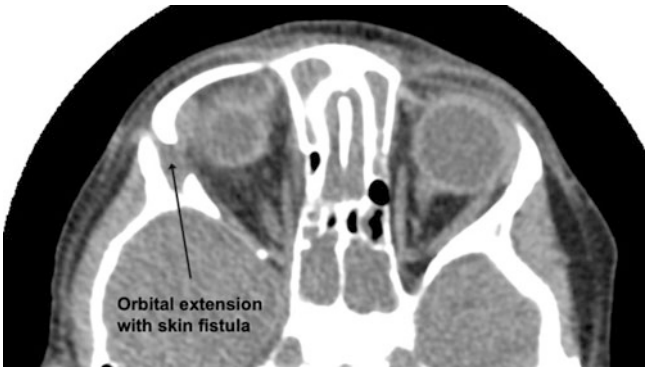


Fig. 9 Axial CT (soft tissue window) of a different patient with an orbital dermoid with a fistula to the skin in the temporalis region. The lesion is present within the sphenoid bone at the sphenoid zygomatic suture. There is a bony defect in the lateral orbital wall through which the cyst extends from the orbit, into the temporalis fossa. The next Fig. 10 shows the intracranial extension of the lesion



Fig. 10 Axial CT (soft tissue window) of the same patient in Fig. 9 showing extension of the fistula into the cranial fossa

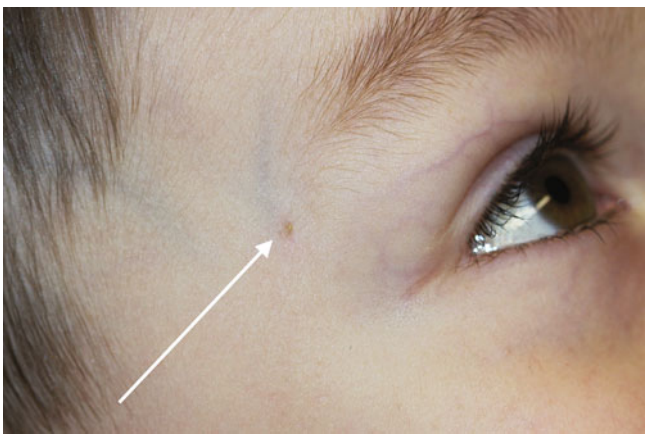


Fig. 11 External color photograph of the right temporal skin fistula. The white arrow shows the location of the fistula, which was actively leaking a keratinous exudate

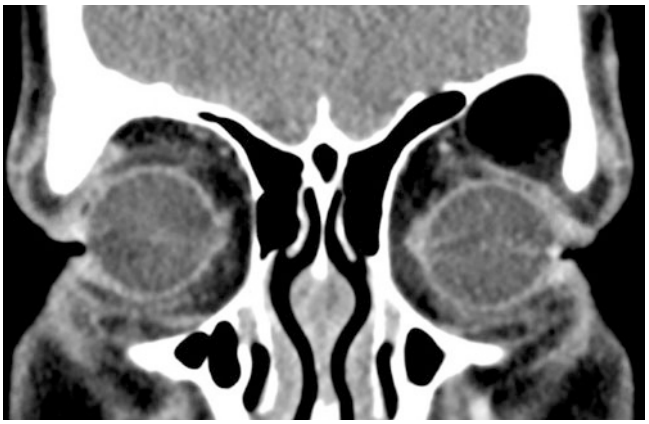


Fig. 12 Orbital dermoid cyst of the superior orbit with orbital roof thinning in a 14-year-old male. The coronal CT image shows a fluid-filled mass that has remodeled the orbital roof

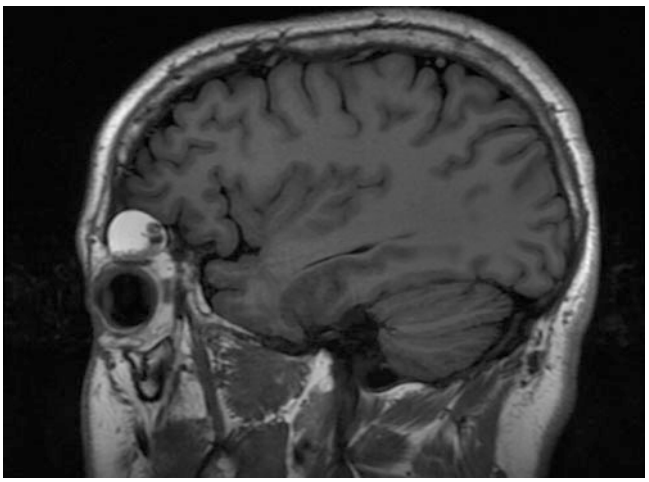


Fig. 13 Sagittal T1-weighted MRI showing heterogeneity of the lesion

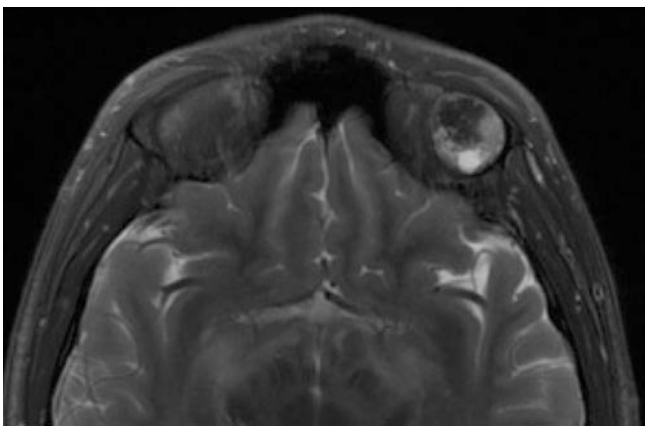


Fig. 14 Axial T1-weighted MRI showing the position of the lesion near the orbital roof



Fig. 15 External color photograph of a 7-year-old female with a medial left orbital mass. The lesion was firm in the medial orbit and was adherent to the periosteum on palpation

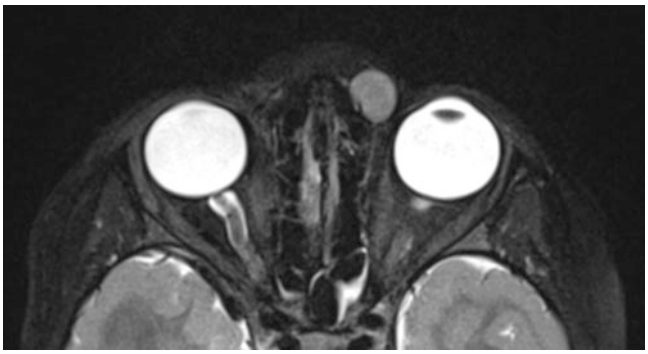


Fig. 16 T2-weighted MRI of the same patient showing the medial location of the left orbital dermoid without intranasal extension



Fig. 17 External color photograph of an 8-year-old male with a left-sided suprabrow cyst (black arrow) that was firm and fixed to palpation

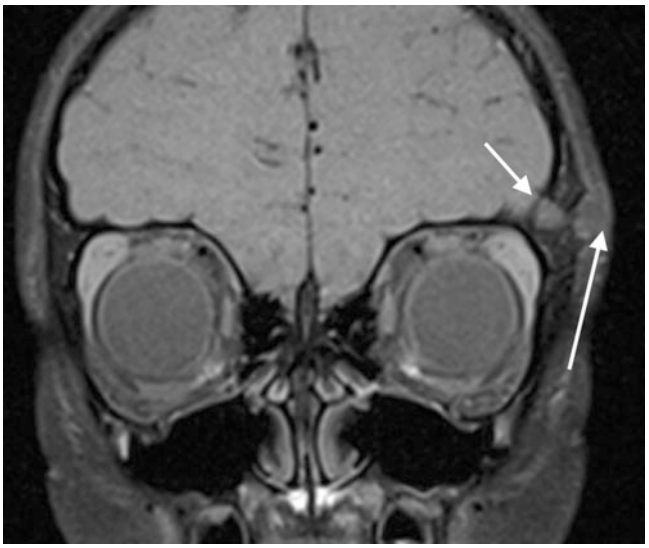


Fig. 18 Coronal T1-weighted MRI with fat saturation shows a mass with both an external component (long white arrow) that dumbbells through a bony defect into the epidural space (short white arrow). The lesion was removed, via a hairline coronal incision, and was a dermoid cyst

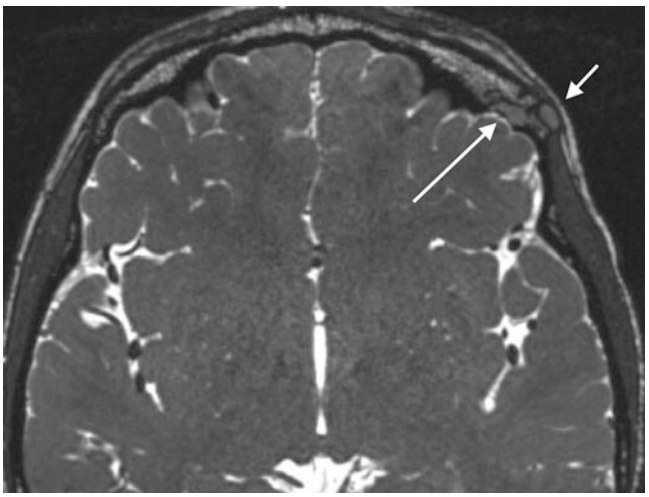


Fig. 19 Axial T2-weighted MRI reveals the extension of the mass with the intracranial/extradural component (long white arrow), the bony defect with the subcutaneous extension (short white arrow)

References

1. Lucas LT, Shams P, Shriver EM, Allen RC. Dermoid cysts: clinical predictors of complex lesions and surgical complications. J AAPOS. 2017;21:44–7.
2. Siah WF, Al-Muhaylib AA, Rajak S, Ziahosseini K, Selva D, Malhotra R, Alsuhaibani AH. Clinical outcomes of ruptured periorbital and orbital dermoid cysts. Ophthal Plast Reconstr Surg. 2017;33:264–7.
3. Shah NB, Chang WY, White VA, Heran MK, Rootman J. Orbital lipoma: 2 cases and review of literature. Ophthal Plast Reconstr Surg. 2007;23(3):202–5.

Cystic Lesions of the Orbit: Teratomas

24

William R. Katowitz

Contents

1 **Signs and Symptoms** 221
2 **Differential Diagnosis** 221
3 **Diagnosis** 222
4 **Treatment** 222
5 **Figures with Captions** 222
References 223

Abstract

- Orbital teratomas are composed of tissue from two to three germ cell layers. While in the orbit, they are typically benign and they do carry a risk for malignant transformation. A classification system was modified to describe teratomas as:
  - A complete fetus implanted in the orbit (orbitopagus parasiticus)
  - A portion of a second fetus in the orbit
  - A tumor consisting of all three germinal layers
  - Tumors containing representatives of two germinal cell layers only
- These congenital tumors typically contain disorganized tissues but, rarely, may have fetal features.
- Located adjacent to the globe instead of near the site of bony closures, some may be as large as 10 cm in diameter on presentation, creating a rather alarming appearance made even more grotesque if the face, sinuses, or cranium are also involved.
- CT and MR demonstrate the teratomas as large multicystic masses that cause prominent expansion of the bony orbit.
- On MR, heterogenous signals T1/T2 may show proteinaceous material, calcifications, and cystic components representative evident of all three germlines.
- Imaging studies are important in delineating teratomas and identifying their vascularity, deter- mining whether there is an intracranial component [1–10].

Keywords

Teratoma · Choristoma

1 Signs and Symptoms

Proptosis (often severe), usually noted at birth, lagophthalmos, and corneal exposure.

2 Differential Diagnosis

Microphthalmos with a cyst, dermoid cyst, meningoencephalocele, infantile hemangioma, congenital hemangioma, and lymphatico-venous malformation (lymphangioma) located deep within the orbit.

W. R. Katowitz (✉)
The Children's Hospital of Philadelphia, Philadelphia, PA, USA
e-mail: katowitzw@chop.edu

© Springer Nature Switzerland AG 2022
G. Ben Simon et al. (eds.), *Atlas of Orbital Imaging*,
https://doi.org/10.1007/978-3-030-62426-2_94

3 Diagnosis

MR (or CT) imaging is critical to make the diagnosis and differentiate a teratoma from other possible lesions.

4 Treatment

Treatment for these lesions is based on the size of the teratoma, presence of vision in the affected globe, and involvement of other orbital, sinus, or cranial structures. If vision is present, attempts can be made to separate the teratoma from the globe and optic nerve during orbitotomy. Successful preservation of vision is possible in some cases but is frequently not possible with large teratomas.

5 Figures with Captions

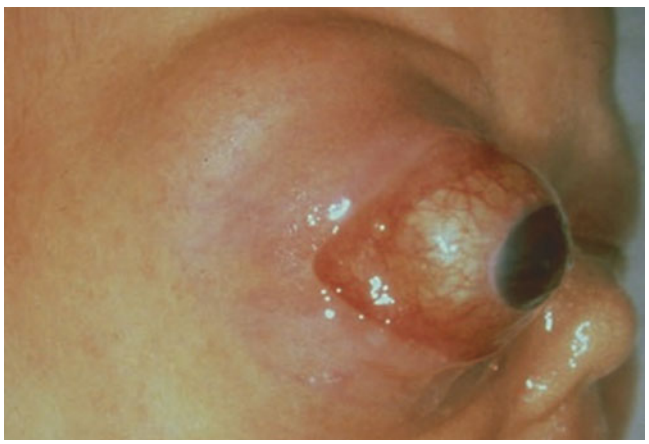


Fig. 1 Cranio-orbital teratoma. Clinical photograph of a newborn with marked right exophthalmos. (Used with permission from Pediatric Oculoplastic Surgery, 2nd edition, eds Katowitz JA, Katowitz WR, Springer)

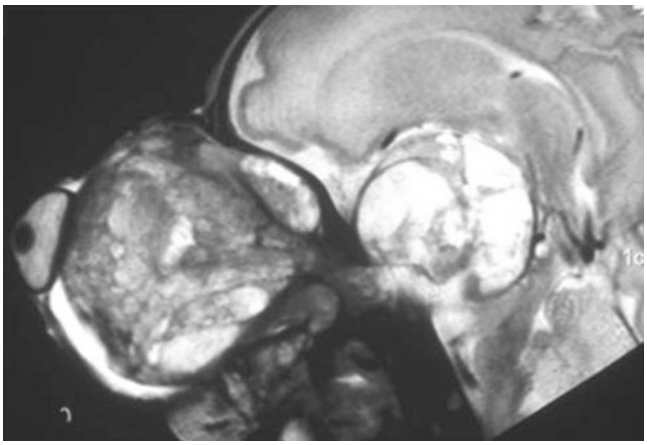


Fig. 2 Sagittal T2-weighted MRI reveals a heterogeneous solid cystic mass with internal septations filling the right orbit and extending through the skull base intracranially. The lesion is occupying the orbital cavity causing marked orbital expansion with proptosis and flattening of the posterior globe. There are fluid collections at the anterior vicinity of the tumor. The intracranial component confers mass effect upon the upper brainstem and basal aspect of the frontal lobe. (Used with permission from Pediatric Oculoplastic Surgery, 2nd edition, eds Katowitz JA, Katowitz WR, Springer)

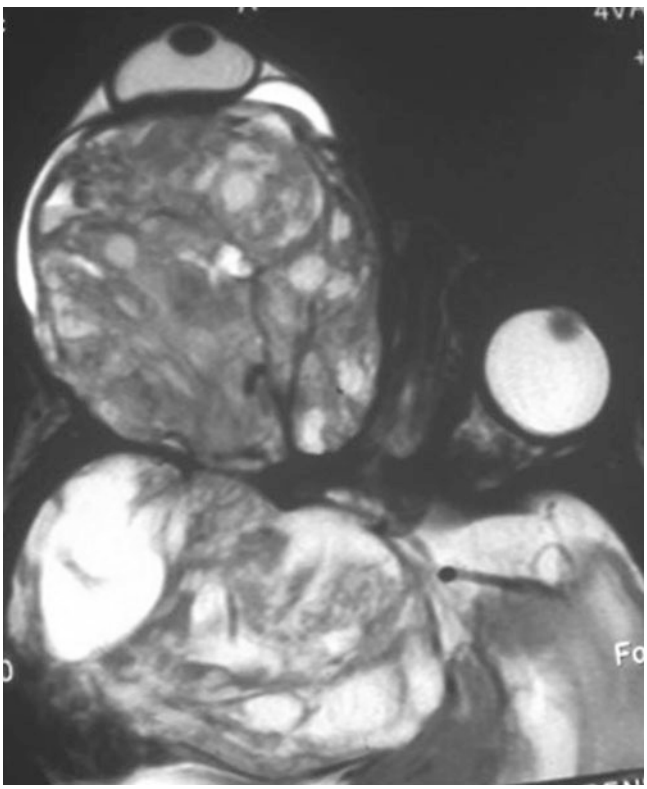


Fig. 3 Axial T2-weighted MRI of the same patient further demonstrates the extent of the lesion with marked orbital widening and globe proptosis. The teratoma is compressing the midface and causing sino-nasal cavity narrowing. Note the intracranial part displaces the midbrain to the left side. (Used with permission from Pediatric Oculoplastic Surgery, 2nd edition, eds Katowitz JA, Katowitz WR, Springer)

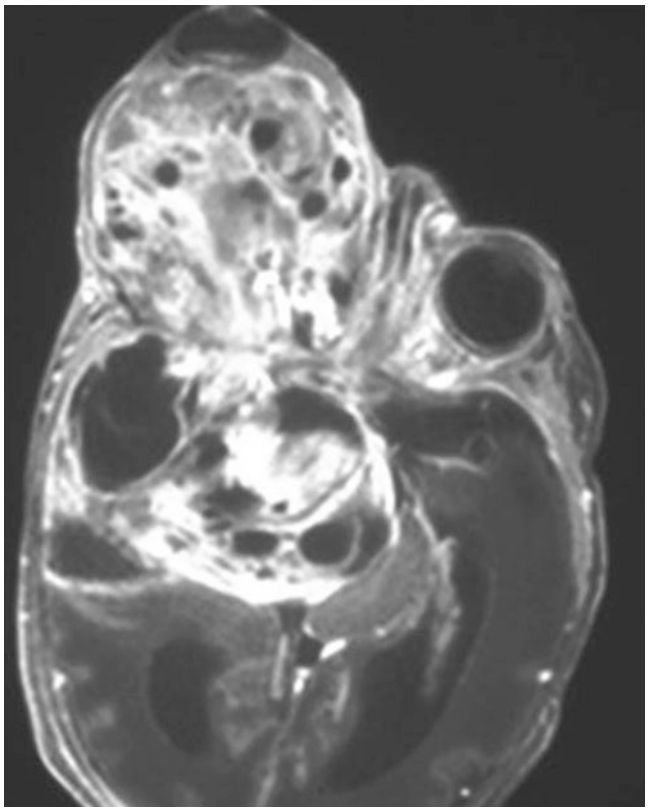


Fig. 4 Axial, postcontrast T1-weighted image, with fat suppression, demonstrates the enhancement of the solid components emphasizing the inhomogeneous nature of the lesion. Note the marked distortion of the right globe and the displacement of the native intracranial anatomy. The teratoma parasitized the brain's blood supply, resulting in a large stroke and death. (Used with permission from Pediatric Oculoplastic Surgery, 2nd edition, eds Katowitz JA, Katowitz WR, Springer)

References

1. Alkemade PP. Congenital teratoma of the orbit. Ophthalmologica. 1976;173(3–4):274–85.
2. Levin ML, Leone CR Jr, Kincaid MC. Congenital orbital teratomas. Am J Ophthalmol. 1986;102(4):476–81.
3. Bilaniuk LT, Murchison AP, Bilyk JR. Imaging of the pediatric orbit. In: Katowitz JA, Katowitz WR, editors. Pediatric oculoplastic surgery. 2nd ed. Springer: Switzerland; 2018.
4. Bojino A, Zavattero E, Gambella A, Gerbino G. Surgical treatment of massive teratoma of the orbit. Ophthalmic Plast Reconstr Surg. 2020;36(3):e68–70. https://doi.org/10.1097/IOP.0000000000001581. PMID: 32022750.
5. Nair AG, Mulay K, Honavar SG. Congenital teratoma of the orbit: a rare tumor. J Pediatr Ophthalmol Strabismus. 2015;52(2):128. https://doi.org/10.3928/01913913-20150313-12. PMID: 25798710.
6. Aiyub S, Chan W, Szetu J, Sullivan LJ, Pater J, Cooper P, Selva D. Congenital orbital teratoma. Indian J Ophthalmol. 2013;61(12):767–9. https://doi.org/10.4103/0301-4738.111219. PMID: 23619505; PMCID: PMC3917402.
7. Damato PJ, Damato FJ. Neonatal orbital teratoma. Br J Ophthalmol. 1962;46(11):685–91. https://doi.org/10.1136/bjo.46.11.685. PMID: 18170834; PMCID: PMC510268.
8. Gnanaraj L, Skibell BC, Coret-Simon J, Halliday W, Forrest C, DeAngelis DD. Massive congenital orbital teratoma. Ophthalmic Plast Reconstr Surg. 2005;21(6):445–7. https://doi.org/10.1097/01.iop.0000189222.20693.ff. PMID: 16304523.
9. Singh M, Singh U, Gupta A, Zadeng Z. Primary orbital teratoma with tooth in an adult: a rare association with cataract and corectopia. Orbit. 2013;32(5):327–9. https://doi.org/10.3109/01676830.2013.814682. Epub 2013 Jul 29. PMID: 23895389.
10. Kivelä T, Tarkkanen A. Orbital germ cell tumors revisited: a clinicopathological approach to classification. Surv Ophthalmol. 1994;38(6):541–54. https://doi.org/10.1016/0039-6257(94)90147-3. PMID: 8066543.

Other Cystic Lesions of the Orbit: Encephalocele 25

William R. Katowitz

Contents

1 **Signs and Symptoms** 225
2 **Differential Diagnosis** 226
3 **Diagnosis** 226
4 **Treatment** 226
5 **Figures with Captions** 226
References 232

Abstract

- An encephalocele is a sac-like protrusion (herniation) or projection of the brain and the membranes that cover it through an opening in the skull [2].
- Meningoceles are protrusions that contain meninges alone, without actual brain tissue herniating through the defect. If both brain and meninges are contained in the mass, the term meningoencephalocele is used.
- The malformation can be congenital, but also may be acquired following trauma or postoperative/craniofacial reconstruction.
- The congenital forms can occur when the neural tube does not close completely during intrauterine development.
- It can present as proptosis or orbital dystopia.
- Skull base and orbital imaging is critical to make the diagnosis.
- CT is essential to demonstrate the bony defect. It should be able to show the bony avenue through which the sinus contents herniate into the cranium and orbit.
- MR imaging shows the content of these prolapses with more detail than CT allowing identification of brain tissue.
- The appearances of the herniated brain tissue may vary upon the ischemic liquification. Variations in the viscosity of the cyst contents along with breakdown and desiccation of solid components are the proposed explanations for the variable MR features, which are usually hypointense on T1-weighted images and hyperintense on T2-weighted images.
- Mucoceles have a fairly characteristic appearance, but congenital encephaloceles may present with similar clinical signs.

Keywords

Encephalocele · Congenital · Meningocele · Meningoencephalocele · Mucocele

1 Signs and Symptoms

Painless orbital dystopia. For encephaloceles, these are present at birth. A mucocele is usually acquired. Both cause orbital dystopia with or without relative proptosis.

W. R. Katowitz (✉)
The Children's Hospital of Philadelphia, Philadelphia, PA, USA
e-mail: katowitzw@chop.edu

© Springer Nature Switzerland AG 2022
G. Ben Simon et al. (eds.), *Atlas of Orbital Imaging*,
https://doi.org/10.1007/978-3-030-62426-2_95

2 Differential Diagnosis

Encephalocele, meningocele, meningoencephalocele, sinus mucocele, ossifying fibroma, and dacryocystocele.

3 Diagnosis

Clinical characteristics and radiologic findings. Combination of CT and MRI are necessary for accurate diagnosis.

4 Treatment

Once the diagnosis has been made via imaging surgery is usually warranted to reduce the orbital dystopia and repair the skull base or sinus defect.

5 Figures with Captions



Fig. 1 A 1-month-old female with a right-sided mass below the medial canthus, but lateral to the lacrimal sac



Fig. 2 There is a complex cystic mass with septations which demonstrates mild rim enhancement within the inferior medial aspect of the right orbit. The lesion measures 2.3 × 1.6 cm, and causes superior lateral deviation of the globe and flattening of the medial aspect of the globe. There is also lateral displacement of the medial rectus muscle as well as mass effect on the superior ophthalmic vein. The mass appears to be communicating with the brain through a frontoethmoidal bony defect. The medial inferior aspect of the right frontal lobe demonstrates irregular hypodensity, which may represent dysplastic tissue versus gliosis

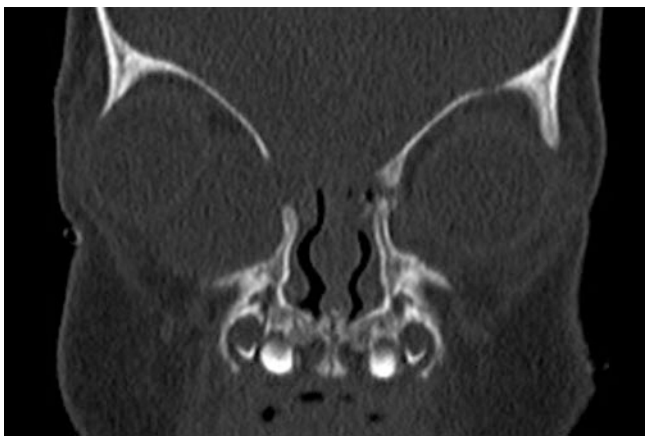


Fig. 3 Coronal bone window CT. The aforementioned bony defect appears to be between the frontal, ethmoidal, and nasal bones; the anterior portion of the cribriform plate appears irregular and crista galli is small



Fig. 4 Coronal bone window CT. In addition, there is a midline cleft in the planum sphenoidale, which is usually ossified at 6 months of age. The appearance is in keeping with frontonasal encephalocele



Fig. 5 The white arrow depicts the mass effect of the encephalocele on the right eye



Fig. 6 The encephalocele (white arrow) is flattening the globe

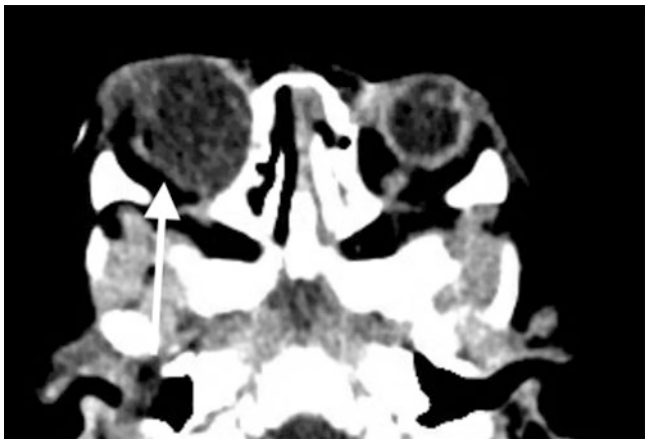


Fig. 7 The encephalocele is large enough to fill the superior orbit (white arrow)



Fig. 8 Three-dimensional CT rendering showing right orbital dysptopia due to the encephalocele



Fig. 9 Axial T-2 weighted MRI of this patient preoperative at 2 months of age. There is right orbital T2 hyperintense complex cystic mass with internal septations and small solid component with minimal peripheral edema (white arrow) in keeping with meningo-encephalocele (encelphalomalatic brain tissue together with meninges). The lesion mostly occupies inferior medial aspect of the right orbit. The lesion causes right-sided proptosis and superior lateral displacement of the globe and flattening of the medial aspect of the globe. There is also lateral displacement of the medial and inferior rectus muscles as well as mass effect on the superior ophthalmic vein (better appreciated when scrolling through the whole scan). The optic nerve appeared intact. This lesion extends infero-laterally through the bony defect in the lateral lamella at the anterior skull base (see the following coronal image)



Fig. 10 Coronal T2-weighted MRI. The most inferior portion of the right frontal lobe is markedly dysmorphic and apparently fused with left frontal lobe (which might reflect forme fruste variant of syntelencephaly). There is a well-defined T2 hyperintense lesion within the white matter (black arrow), which might represent dysplastic tissue or a sequela of remote insult and adjacent irregular cortex in keeping with polymicrogyria

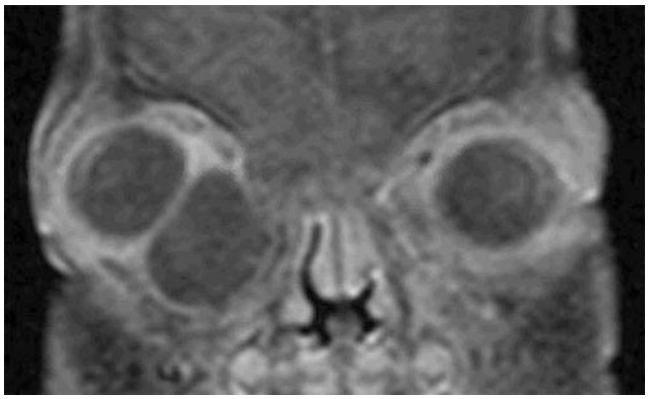


Fig. 11 Coronal T1-weighted MRI FS CE. The lesion causes right-sided proptosis and superior lateral displacement of the globe and flattening of the medial aspect of the globe. There is delicate smooth peripheral enhancement

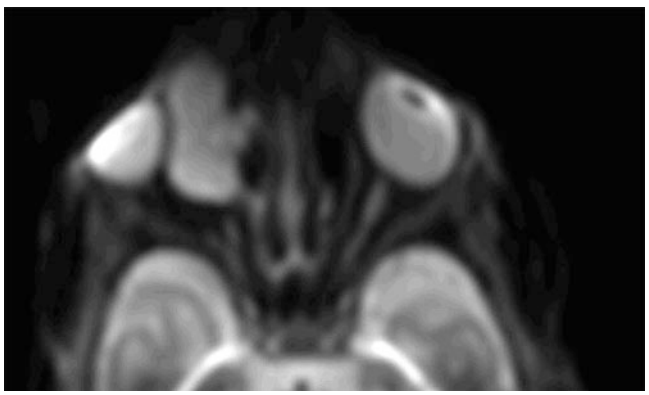


Fig. 12 Diffusion-weighted imaging B0. The eneceophalocele is isointense to the globe

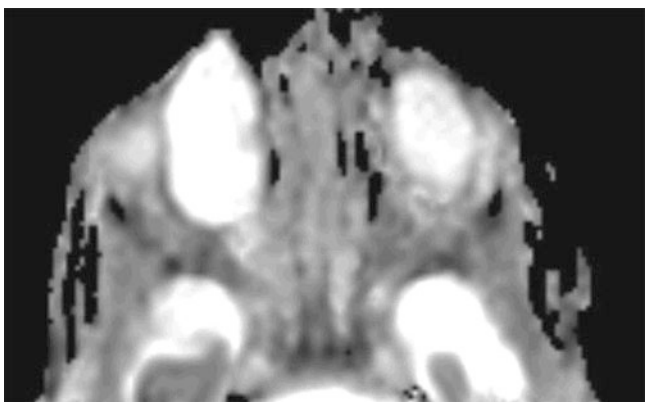


Fig. 13 Apparent diffusion coefficient (ADC) map. The encephalocele shows no restricted diffusion and is bright

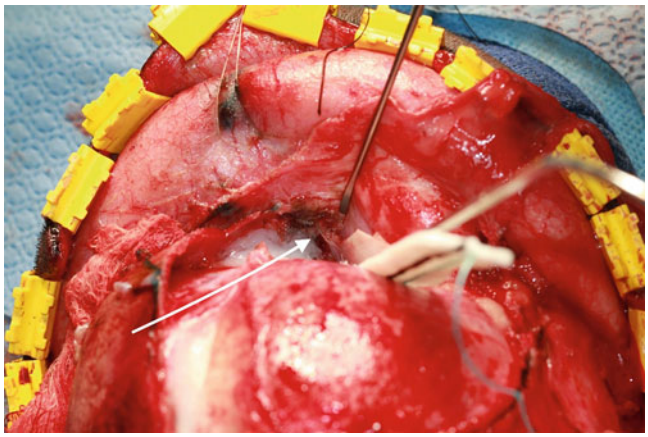


Fig. 14 Neurosurgical repair of the anterior skull base defect (white arrow). The bicoronal craniotomy approach was needed for the repair that was performed at 2 months of age



Fig. 15 Coronal T2-weighted MRI of the same patient at age 18 months. The white arrow shows the bone graft used for repair of the skull base defect



Fig. 16 Axial CT image (bone window) of the same patient with a nasal encephalocele (white arrow). Note widening of the foramen cecum

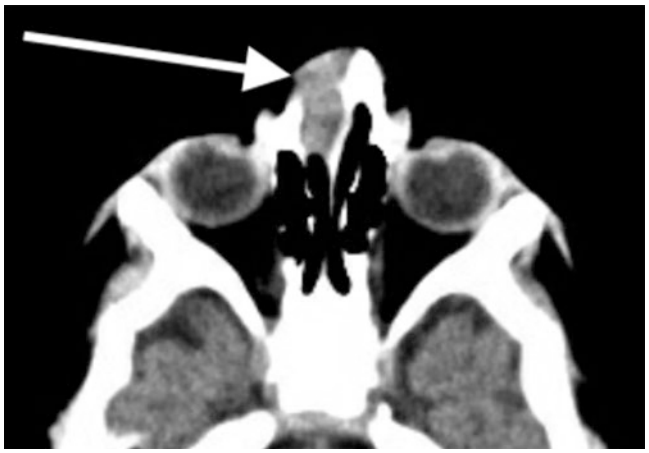


Fig. 17 Soft tissue window showing the anterior extension of the encephalocele (white arrow). The heterogeneity of the lesion on CT may imply both soft tissue and meninges and the diagnosis of encephalocele



Fig. 18 Coronal CT (soft tissue window) showing the defect in the skull base (white arrow). There is a subcutaneous soft tissue mass at the nasal roof, slightly off the midline towards the right. The lesion seemingly represents herniation of the brain tissue from the most inferior right frontal lobe through the area of foramen cecum and through the anterior skull base defect into the right nasal cavity. The lesion extends along the nasal septum and markedly expands the right nasal cavity; it extends through a defect in the thin right nasal bone and protruding from the right nostril, through a cleft in the right nares

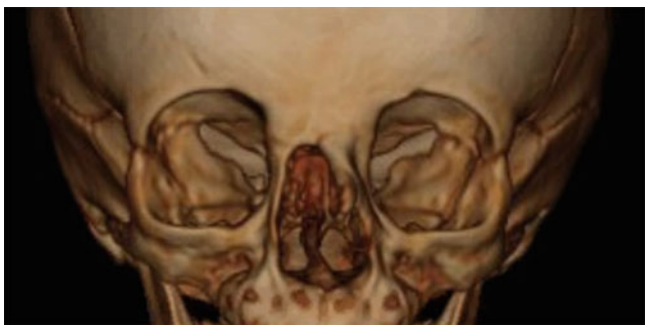


Fig. 19 CT 3D imaging showing the anterior nasal defect of the nasal encephalocele

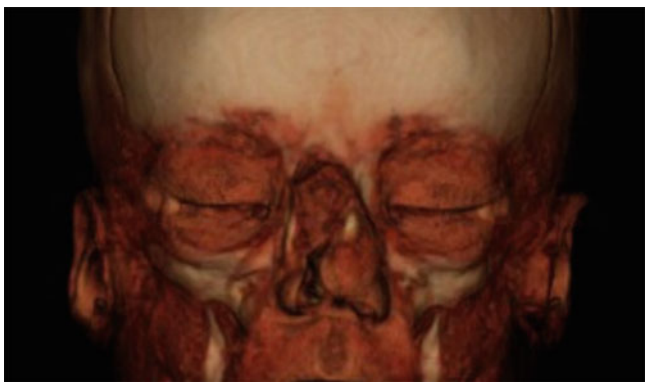


Fig. 20 Soft tissue rendering the same patient



Fig. 21 Facial reconstruction via CT 3D imaging showing the extent of the nasal defect due to poor bony fusion and subsequent nasal encephalocele



Fig. 22 A 13-year-old male with right orbital dystopia. Right-sided relative hypertelorism is present

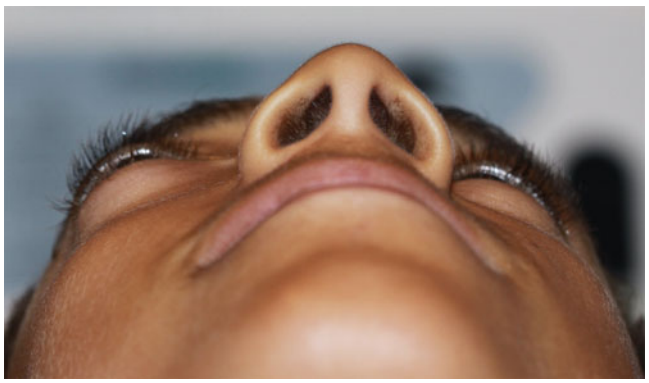


Fig. 23 Chin-up worm's eye view of the same patient showing right-sided relative proptosis



Fig. 24 Axial CT (soft tissue window) showing a large right cyst (white arrow). The sinus mass is filling an anterior ethmoidal air cell. There is significant bony remodeling of the right orbit with induced hypertelorism. CT with intravenous contrast was performed. The right orbital contents are displaced laterally and anteriorly by an expansile soft tissue mass that is most likely a mucocele, but could represent a dermoid. The epicenter of this lesion is either in the right lacrimal duct or the right ethmoid sinus projecting anteromedially and posteriorly. The mass measures 2.7 × 2 cm and causes marked thinning of the medial wall of the right bony orbit and roof of the right maxillary sinus, which is partially deformed by this finding (better shown on the following coronal sections). Because there is no intrinsic air fluid level or debris within the mass the diagnosis of a mucocele is most likely. An MRI would have been helpful to differentiate the mass; however, surgery was performed on this patient, who was found to have a mucocele in a right anterior air cell of the right ethmoid sinus. The right lacrimal system was patent on probing and irrigation [1]

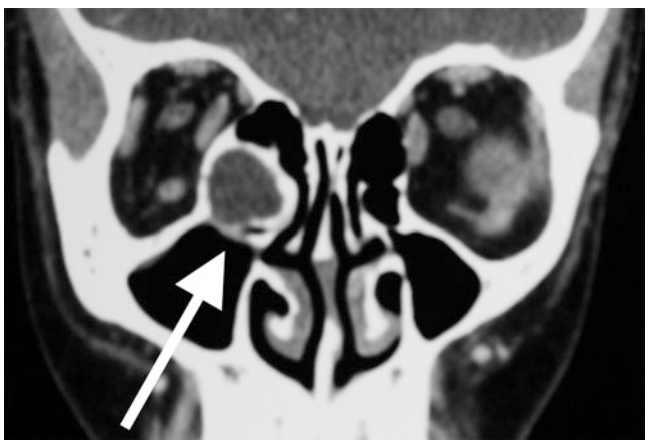


Fig. 25 Coronal (soft tissue window) CT showing the posterior extent of the mucocele (white arrow)

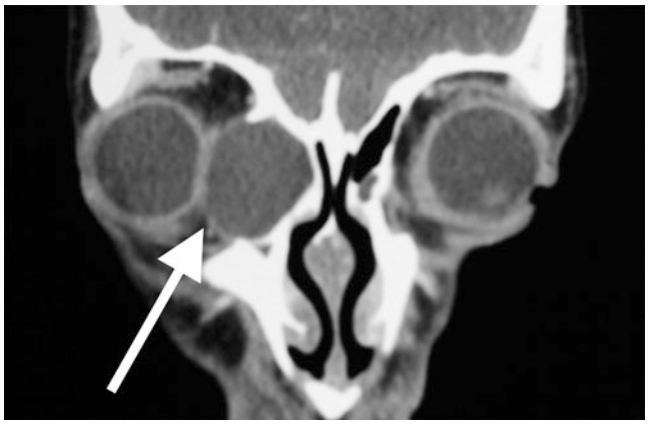


Fig. 26 Coronal CT (soft tissue window) showing the mass effect on the right globe

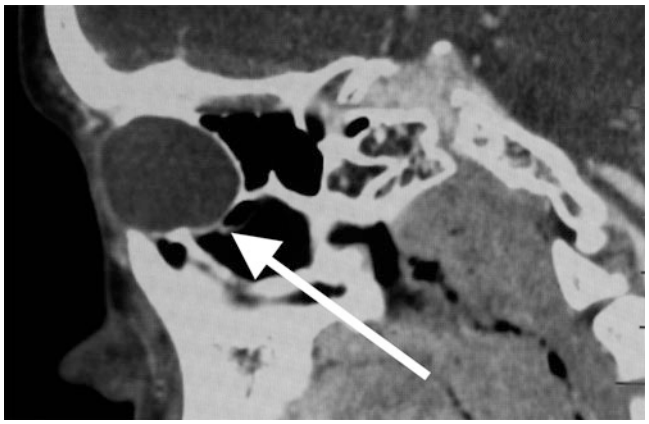


Fig. 27 Sagittal (soft tissue window) of the right ethmoidal mucocele



Fig. 28 Mimicker of an enceophalocle: A 4-month-old girl with a medial mass above the medial canthus concerning for an enceophalocele

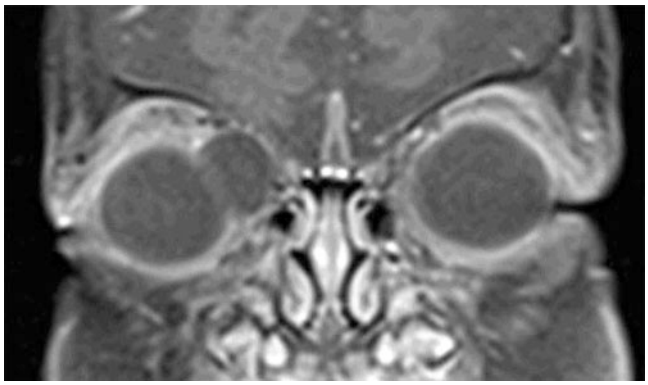


Fig. 29 Coronal T-1 weighted MRI. There is a well-circumscribed cystic lesion, located superomedial to the right globe. There is very mild mass effect on the adjacent globe with minimal infero-lateral displacement. No solid component is identified within aforementioned cystic lesion. Some thinning and remodeling of adjacent frontal bone is noted

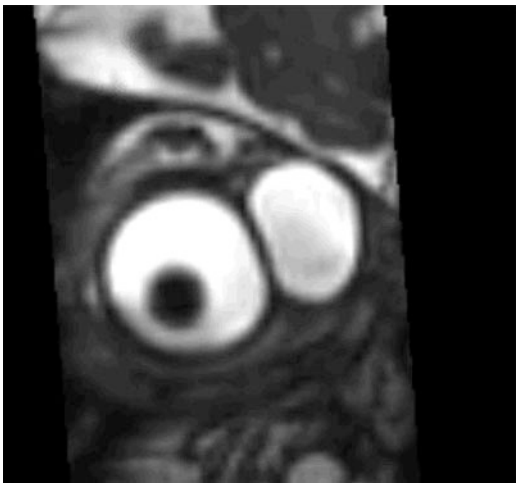


Fig. 30 Oblique coronal T2-weighted MRI. There is frontal bone thinning, but no dehiscence or communication with the intracranial space. Some thinning and remodeling of adjacent frontal bone is noted. No connection between this lesion and intracranial subarachnoid CSF space can be seen

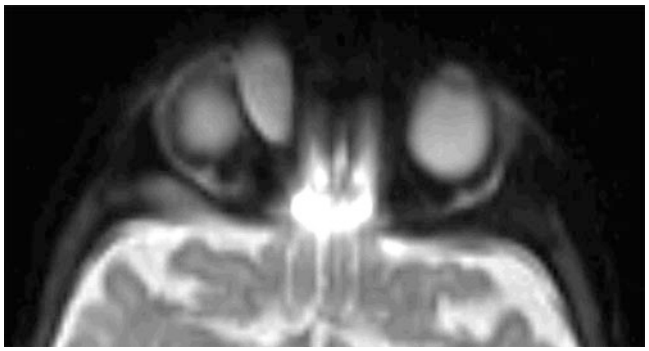


Fig. 31 Diffusion-weighted imaging (B0) showing the lesion is isointense to vitreous body

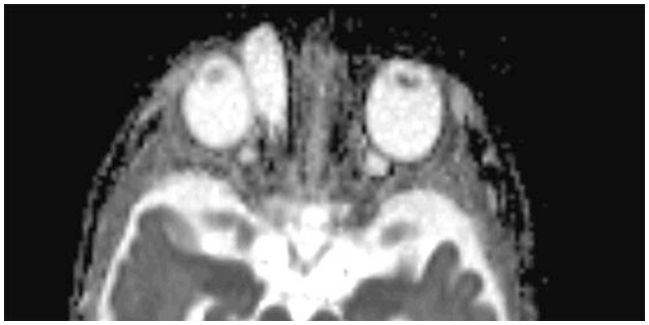


Fig. 32 Apparent diffusion coefficient (ADC) map. No solid diffusion restriction is demonstrated

The patient underwent anterior orbitotomy surgery, and a simple orbital epithelial cyst was removed and confirmed by pathology

References

1. Katowitz WR, Fries PD, Kazim M. Benign pediatric orbital tumors. In: Katowitz JA, Katowitz WR, editors. Pediatric oculoplastic surgery. 2nd ed. Cham: Springer; 2018.
2. https://www.cdc.gov/ncbddd/birthdefects/encephalocele.html

Congenital Lacrimal Pathologies: Dacryocystocele

26

William R. Katowitz

Contents

1 **Signs and Symptoms** 233
2 **Differential Diagnosis** 234
3 **Diagnosis** 234
4 **Treatment** 234
5 **Figures with Captions** 234
References 238

Abstract

- Persistent membrane at the valve of Hasner in utero results in amniotic fluid filling the lacrimal sac.
- This may result in a cyst formation in the nose that may persist at birth.
- Patients may present with respiratory distress if there are bilateral intranasal cysts.
- Significant risk for infection (dacryocystitis) warrants urgent treatment.
- CT should be avoided as an imaging modality in infants due to radiation exposure.
- MR imaging can also be avoided unless there is an increased suspicion for a tumor or encephalocele.
- Nasal endoscopy is diagnostic if an intranasal cyst is identified below the inferior turbinate.
- On CT imaging, hypodense homogenous cystic expansion of the lacrimal sac was found. There was no enhancement of the sac content with normal enhancement of the native epithelial lying of the duct.
- On MRI, in uncomplicated cases, lesions resemble clear fluid, i.e., hypointense signal on T1 and hyperintense on T2 with no fluid level.
- In infected cases the lesions may be more heterogenous and contain fluid-fluid levels, proteinaceous material with associated restricted diffusion. Post contrast they show more pronounced rim enhancement that may extend to adjacent tissue.
- Any mass of the orbit in a location not over the lacrimal sac should be considered for orbital imaging [1–4].

Keywords

Dacryocystocele · Dacryocele · Amniotocele · Lacrimal mucocele · Dacryocystitis · Intranasal cyst · Nasal endoscopy · Congenital nasolacrimal duct obstruction

1 Signs and Symptoms

A painless mass is usually present that is medial to the eye and inferior to the medial canthal tendon. This may appear blue in hue with no overlying skin erythema and no fever. Mucus discharge may be present. Mucus can sometimes be expressed from the punctum with mild massage over the lacrimal sac. Respiratory distress is a sign of the presence of an intranasal cyst.

W. R. Katowitz (✉)
The Children's Hospital of Philadelphia, Philadelphia, PA, USA
e-mail: katowitzw@chop.edu

© Springer Nature Switzerland AG 2022
G. Ben Simon et al. (eds.), *Atlas of Orbital Imaging*,
https://doi.org/10.1007/978-3-030-62426-2_14

2 Differential Diagnosis

Infection: dacryocystitis, skin abscess. Vascular tumor: infantile hemangioma, rapidly involuting capillary hemanigoma, non-involuting capillary hemangioma. Vascular malformation: venous, lymphatic, lyphatico-venous (lymphangioma). Other malformation: encephalocele, phacomatous choristoma (Zimmerman's tumor), dermoid cyst. Other malignancy: neuroblastoma, rhabdomyosarcoma, rhabdoid tumor.

3 Diagnosis

Firm mass below the medial canthal tendon that may be decompressed with mild massage (take care not press too hard to cause skin trauma or lacrimal sac trauma). With sac decompression clear or colored mucus may be visible at the ipsilateral eyelid puncta or from the nostril. Nasal endoscopy is useful to diagnose the presence of an intranasal cyst. Beware of a lesion that extends above the medial canthal tendon making the diagnosis much less likely to be of lacrimal origin. Beware of a mass that is not just below the canthal tendon but instead is more lateral under the eye. Any atypical location of the medial mass next to the eye warrants imaging.

4 Treatment

The presence of a dacryocystocele in an infant represents a very high likelihood of an intranasal cyst. Thus, in- office probing must be accompanied by a period of observation to screen for respiratory distress. Bilateral dacryocsytoceles should not be probed in the office due to the risk for respiratory distress. Unilateral dacryocsystoceles that are compressible may be managed with Crigler massage and topical antibiotics with a low threshold surgery with persistent symptoms or with signs of infection. Dacryocystoceles that cannot be reduced should be treated with in-office endoscopy if possible to identify a nasal cyst or with close observation with our without in-office probing. If the cyst persists surgery is warranted. An intransal cyst may be removed with a microdebrider.

5 Figures with Captions

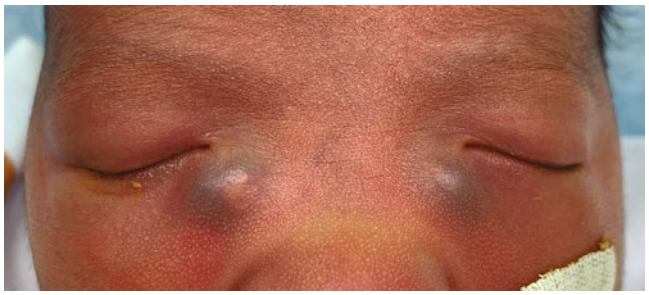


Fig. 1 A 4-day-old girl with bilateral dacryocystoceles. Both tear sacs are obstructed with amniotic fluid and are visible as blue-hued masses below the medial canthi

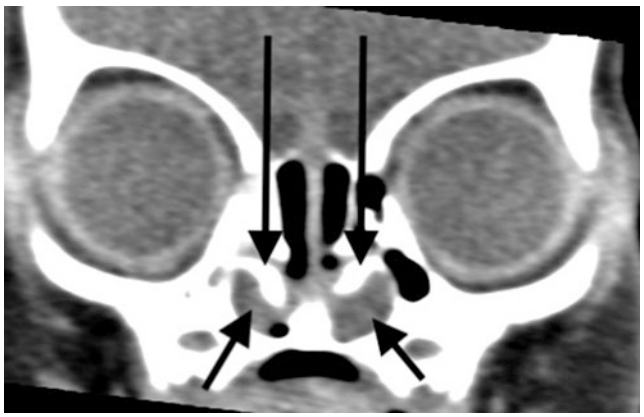


Fig. 2 Coronal CT scan of the same patient showing bilateral intranasal cysts filling the inferior meatus of both nasal cavities. The short black arrows point to the right and left intranasal cysts. The overlying inferior turbinates (long black arrows) are pushed upwards and toward the nasal septum

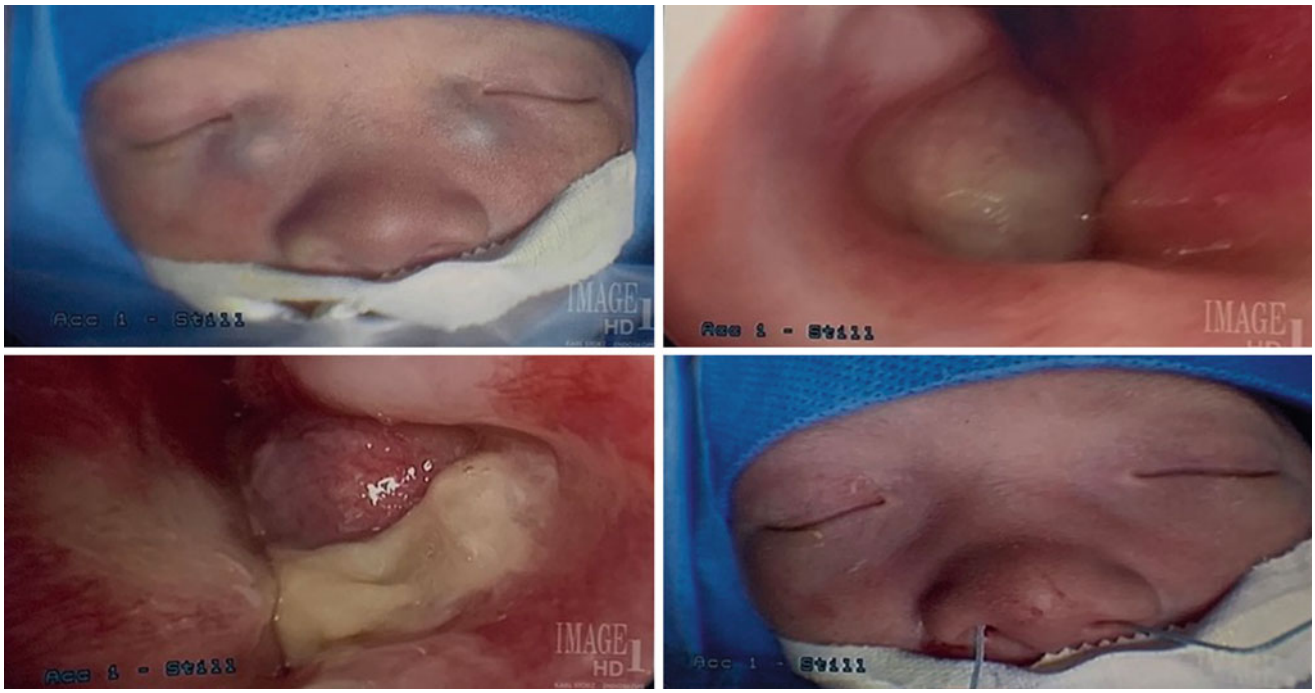


Fig. 3 Images taken with an endoscope. (Top left) Bilateral dacryocystoceles, (top right) right intranasal cyst, (bottom left) left intranasal cyst, and (bottom right) status post bilateral nasal cyst microdebridement with drainage of both dacryocystoceles

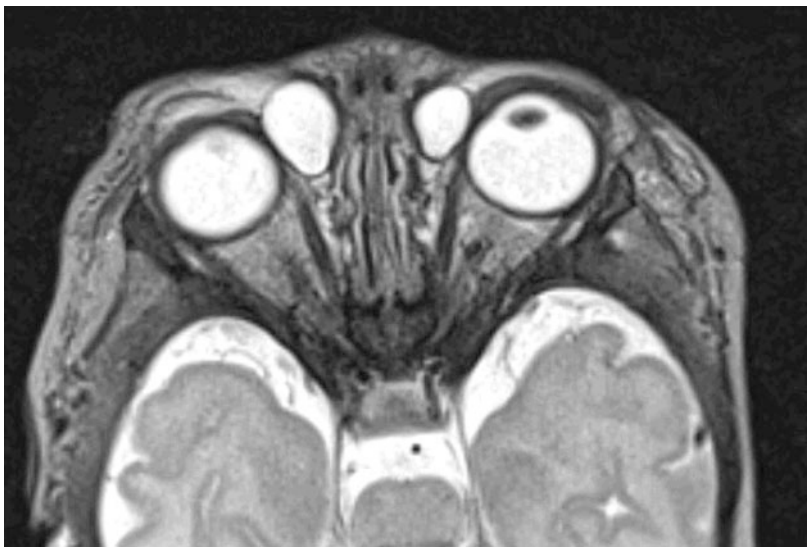


Fig. 4 Axial T2 MRI in a different patient with bilateral asymmetric dacryocystoceles. The lacrimal sacs are dilated and are isointense to the vitreous/csf (representing fluid)



Fig. 5 Axial T2 MRI in a same patient showing bilateral dilation of the nasolacrimal ducts with bilateral cysts (short white arrows) extending into the nasal space. Note the remodeling of the inferior turbinates (long white arrows) and nasal obstruction due to the nasal cysts

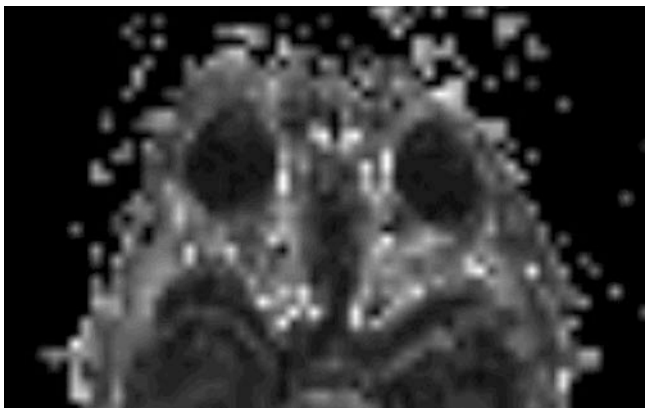


Fig. 6 Diffusion weighted MR imaging showing bilateral dacryocystoceles, which are isointense to the vitreous.

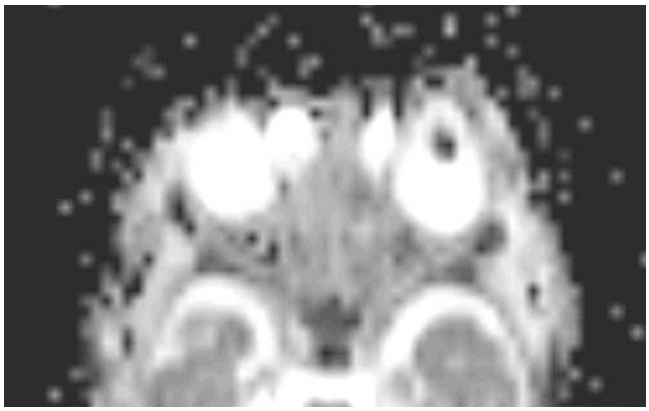


Fig. 7 Apparent diffusion coefficient (ADC) MR imaging shows bilateral bright signals at the site of the dacryocystoceles. The bright signal denotes there is no restriction in diffusion making the cystic lesions more likely fluid filled rather than hyper-cellular/infected cyst

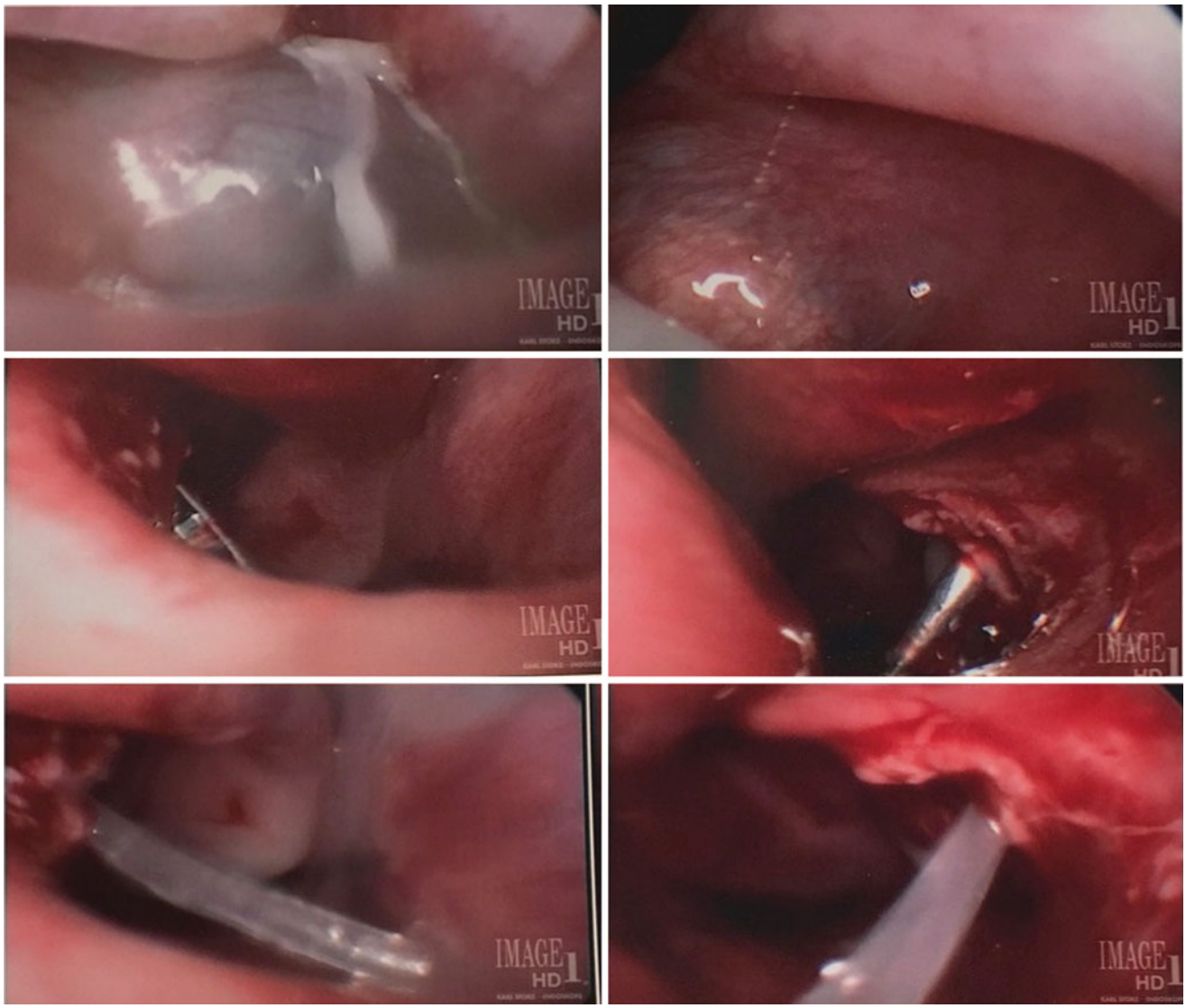


Fig. 8 Intraoperative endonasal images of the same patient. Bilateral endonasal cysts are present on the top right and left images. The middle set of images are of the inferior right and left meatus status post cyst excision via microdebridement. A lacrimal probe is visible at the opening of each nasolacrimal duct. The bottom right and left images show the position of a monocanalicular stent that was placed in each tear system

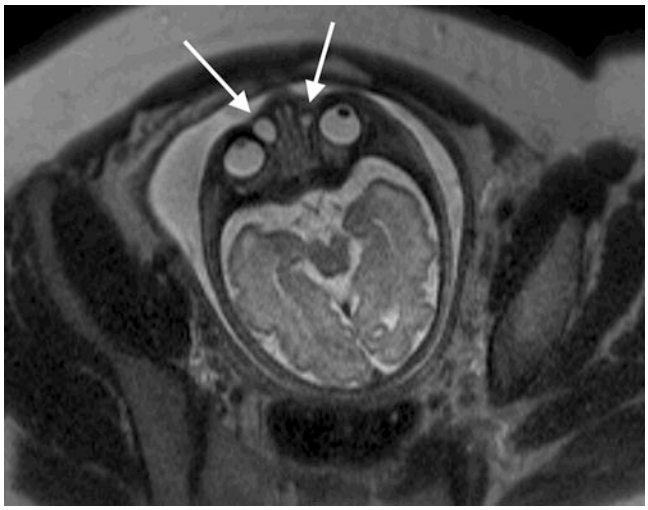


Fig. 9 Axial T2 MRI of a third patient via a prenatal MRI showing a fetus at 30 weeks gestation. Bilateral asymmetric dacryocystoceles (white arrows) are present with dilated lacrimal sacs isointense to the vitreous

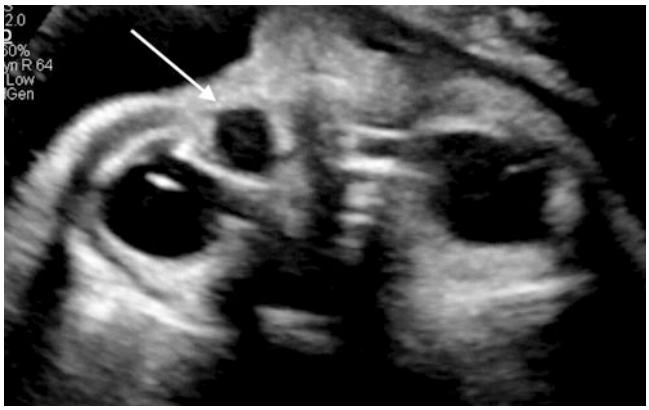


Fig. 10 Ultrasound of a dacryocystocele (white arrow) in a fourth patient. A fluid and dilated lacrimal sac is identified medial to the right eye

References

1. Levin AV, Wygnanski-Jaffe T, Forte V, Buckwalter JA, Buncic JR. Nasal endoscopy in the treatment of congenital lacrimal sac mucoceles. Int J Pediatr Otorhinolaryngol. 2003;67(3):255–61.
2. Lueder GT. The association of neonatal dacryocystoceles and infantile dacryocystitis with nasolacrimal duct cysts (an American Ophthalmological Society thesis). Trans Am Ophthalmol Soc. 2012;110:74–93.
3. Miranda-Rivas A, Villegas VM, Nieves-Melendez JR, De La Vega. Congenital dacryocystocele: sonographic evaluation of 11 cases. J AAPOS. 2018;22(5):390–2.
4. Durrani J. Crigler massage for congenital blockade of nasolacrimal duct. J Coll Physicians Surg Pak. 2017;27(3):145–8.

Pediatric Orbital Vascular Tumors: Infantile Hemangioma

27

William R. Katowitz

Contents

1 **Signs and Symptoms** 240
2 **Differential Diagnosis** 240
3 **Diagnosis** 240
4 **Treatment** 240
5 **Figures with Captions** 240
References 246

Abstract

- Vascular tumor of infancy
- History of presentation is critical: Not present at birth, but typically appearing days to weeks after birth
- Rapid growth until 10 months of age with slow involution over the next 5–9 years
- Can be difficult to distinguish from other vascular tumors such as malformations on MRI and CT imaging modalities, however with contrast and fat suppression on MR the lesion can be better delineated
- Orbital ultrasound with doppler flow studies can best differentiate from other vascular tumors often making more expensive and time intensive imaging such as MRI unnecessary
- Large facial hemanigomas (>20 cm^2) are associated with an increased risk of other systemic abnormalities (PHACE syndrome)
- CT shows a non-specific not well-defined soft tissue stranding, with contrast enhancement
- MRI is the best technique for characterization of hemangiomas
- Infantile hemangiomas have slightly higher intensity than muscle on T1-weighted images and are typically hyperintense relative to fat and muscles on T2-weighted images.
- On both T1- and T2-weighted images, the characteristic heterogeneity caused by the interlobular vessels and septa is seen. To demonstrate and delineate the lesion best, it is necessary to have a contrast-enhanced T1 image where the fat is suppressed and a T2-weighted image that is also fat suppressed.
- Suppression of signal from fat leads to much greater conspicuity of the infantile hemangioma.

Keywords

Infantile hemangioma, Vascular tumor, PHACE syndrome, Mechanical ptosis, Proptosis

W. R. Katowitz (✉)
The Children's Hospital of Philadelphia, Philadelphia, PA, USA
e-mail: katowitzw@chop.edu

© Springer Nature Switzerland AG 2022
G. Ben Simon et al. (eds.), *Atlas of Orbital Imaging*,
https://doi.org/10.1007/978-3-030-62426-2_15

1 Signs and Symptoms

Painless eyelid mass with or without proptosis. The tumor can be strawberry colored, dark blue, or associated with no color changes. Mechanical ptosis may be present.

2 Differential Diagnosis

Other vascular tumors of infancy: non-involuting capillary hemangioma (NICH), rapidly involuting capillary hemangioma (RICH), nevus simplex, angel's kiss. Vascular malformations: lymphatic malformation, venous malformation, lymphatico-venous malformation (formerly known as lymphangioma), nevus flammeus (capillary malformation). Orbital malformations: orbital dermoid, phacomatous choristoma, lacrimal mucocele (or dacryocystocele), encephalocele. Malignant tumors: neuroblastoma, rhabdomyosarcoma, rhabdoid tumor, juvenile sarcoma.

3 Diagnosis

Usually soft lesion around the eye that may involve the skin surface or be deep to the skin with or without proptosis. The lesion is almost never present at birth. Infantile hemangiomas are high flow lesions that can be identified with doppler flow studies. On MR imaging, flow voids are very common for large orbital lesions.

4 Treatment

Topical beta blockers for very superficial lesions, oral beta blockers for deep and large lesions (PHACE screening is necessary for large lesions on the face to rule out cardiac and large intracranial vascular malformations association with PHACE syndrome). Oral steroids are a treatment option, but less favorable due to side effects. Surgery is necessary only for very large lesions that respond poorly to medical treatments or for persistent lesions with fibro-fatty infiltration that have failed to fully involute [1–5].

5 Figures with Captions



Fig. 1 Three-month-old male with large orbital mass that is inducing proptosis and hyperglobus (same patient as in Figs. 2, 3, 4, 5, 6, 7, 8, 9, and 10). The lesion is deep to the skin but visible a blue mass under the eyelid



Fig. 2 Post contrast axial T1WIFS MRI showing a diffuse right-sided intra- and extra-conal mass along with supra-zygomatic infra-temporal/soft tissue involvement. There is diffuse infiltration of the intraconal and extraconal spaces of the right orbit by enhancing soft tissue



Fig. 3 Post contrast sagittal T1 MR imaging. The soft tissue mass (infantile hemangioma) extends up to but not through the orbital apex. There is also infiltration of the overlying right eyelid, right frontal scalp (non-contiguous), right cheek (non-contiguous), right frontotemporal scalp, and (through the inferior orbital foramen) the right pterygopalatine fossa and masticator space. Skull base involvement includes extension from the pterygopalatine fossa through the right foramen rotundum into Meckel's cave. Enhancement in the right maxilla is consistent with osseous involvement by the pterygopalatine fossa portion of the mass versus perineural extension along the greater palatine nerve



Fig. 4 Axial T1-weighted MRI with fat saturation allows for better appreciation of the flow voids within the infantile hemangioma. This helps differentiate this lesion from a microcystic lymphatico-venous malformation (lymphangioma), which can sometimes have a similar appearance



Fig. 5 T2-weighted MR imaging. As a result of the right orbital mass, there is marked right eye proptosis. While the individual extraocular muscles are discretely seen, the right inferior rectus appears somewhat atrophic. The right optic nerve is discretely identified and demonstrates no definite enhancement or signal abnormality. However, the right optic nerve is slightly thinned along its intraorbital segment



Fig. 6 Coronal T1-weighted MR imaging showing a markedly enlarged right ophthalmic artery and draining superior ophthalmic vein. There are also numerous tiny smaller vessels seen in association with the intraconal lesion

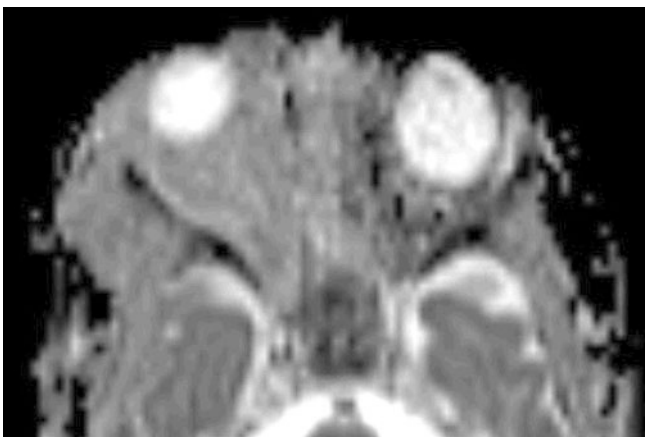


Fig. 7 Diffusion weighted imaging (DWI) showing moderate signal intensity within the infantile hemangioma, which is isointense to the rest of the orbital fat

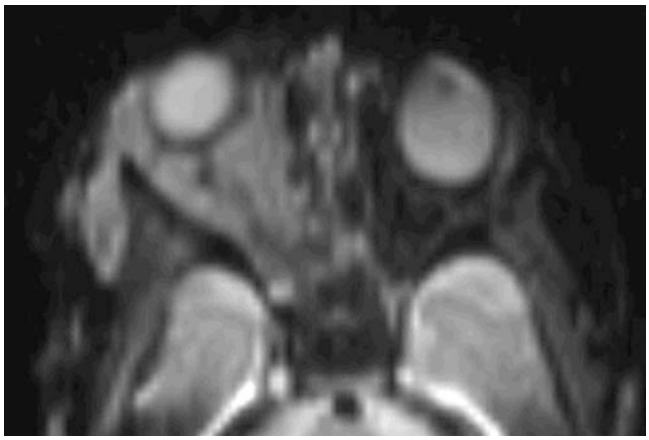


Fig. 8 ADC Map showing no restriction and therefore a low suspicion for malignancy



Fig. 9 MRA image demonstrates prominent right ophthalmic vein (small arrow) and internal maxillary arteries (large arrow) feeding the right orbital/pterygopalatine fossa mass



Fig. 10 After 6 months of oral beta blocker treatment

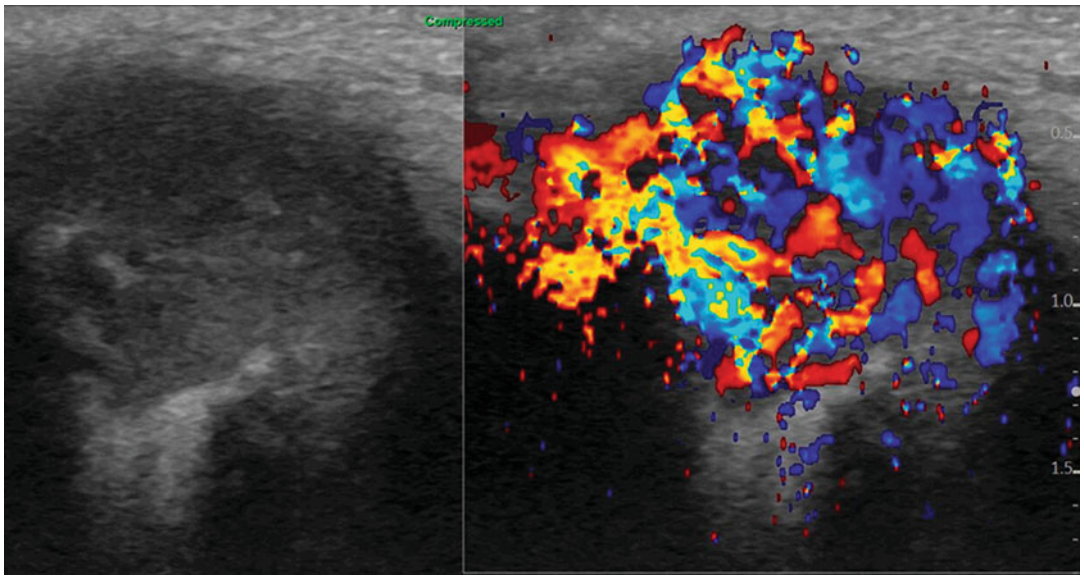


Fig. 11 Ultrasound with doppler flow studies in a different patient with a left upper eyelid infantile hemangioma. The left supraorbital soft tissues is a 0.7 × 0.9 × 1.6 cm well-defined, hypoechoic mass with marked vascularity



Fig. 12 Large facial hemangioma (segmental) in a patient (same patient as in Figs. 13, 14, and 15). This large facial lesion measures over 20 cm^2 (4 × 5 cm), which great increase the risk for additional abnormalities of the heart, brain vasculature and eyes (PHACES syndrome). The hemangioma in PHACES will often span a zone a facial development and not a dermatome, which is more often the case in the hemangioma associated with Sturge Weber. This patient had a normal MRI of the brain and echocardiogram, as well as a normal eye exam and did not have PHACES

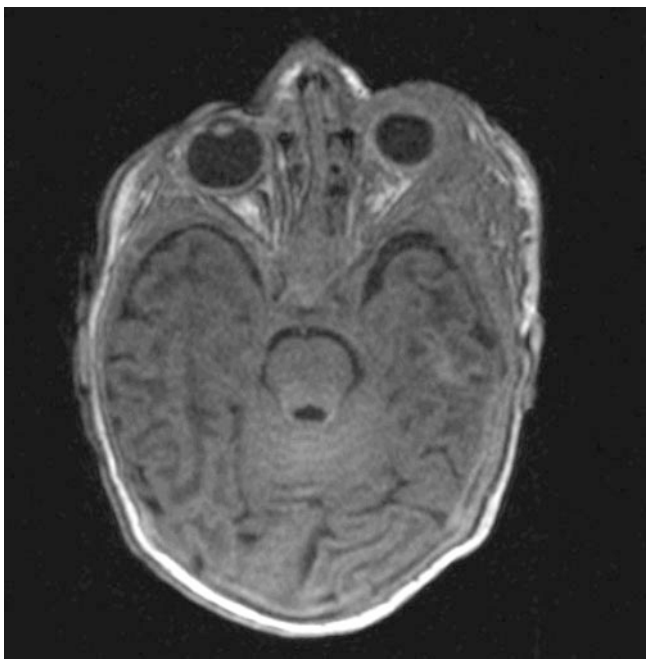


Fig. 13 Axial T1-weighted MRI. There are multiple soft tissue hemangiomas (at least 4) in the left side of the face and orbit. They exhibit heterogeneous intermediate signal on T1-weighted images and high signal on T2 weighted images (Figs. 14 and 15). After contrast administration, they show intense enhancement. The margins of these hemangiomas appear to merge/overlap with the others. The first hemangioma is seen in the left cheek anterior to the left masseter muscle and measures about 13 × 18 mm along its maximum AP and TR dimensions. Another hemangioma is seen in the left infratemporal fossa and measures 27 × 18 mm along its AP and TR dimensions. A superficial hemangioma is seen as a plaque-like enhancing lesion along the skin of the forehead and temporal region on the left. A preseptal orbital hemangioma with deep post-septal extension is seen on the left. This hemangioma is inseparable from the left lateral rectus muscle and may have an intraconal component



Fig. 14 Coronal T2-weighted MRI showing the large cheek component of the lesion

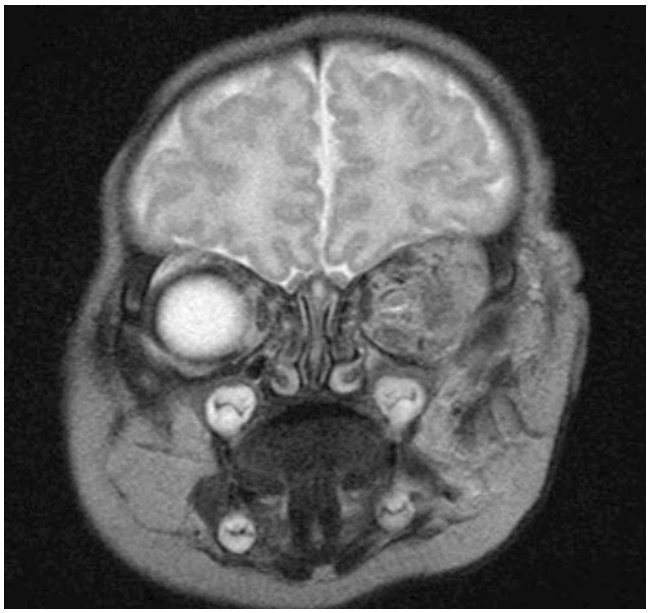


Fig. 15 Coronal T2-weighted MRI (more posterior) showing the orbital component of an infantile hemangioma



Fig. 16 PHACES syndrome with brain and neck vasculature abnormalities seen on this T2-weighted axial MRI. Posterior fossa anomalies with small dysplastic left cerebellar hemisphere and hypoplastic vermis. The left cerebellar hemisphere is abnormally rotated and dysplastic appearing with lack of the normal appearing cerebellar folia and fissures. Medial to the left cerebellar hemisphere, there is a region of dysplastic tissue in continuity with the right cerebellar hemisphere. This tissue presumably represents an abnormal and small appearing vermis. The right cerebellar hemisphere is more normal in size and appearance but also lacks the expected cerebellar sulcation. The foramen of Magendie is widened and in direct communication with a large retrocerebellar CSF space. There are only very small hemangiomas of the face. One hemangioma can be seen in the lateral orbital and lateral canthus



Fig. 17 Axial MR angiography without contrast of the head, neck and chest in an infant with PHACES. An unnamed vessel arises from the cavernous portion of the distal left ICA extending medially and supplying both A2 segments. There is no A1 segment seen bilaterally. The anterior communicating artery is absent. The right posterior cerebral artery is extremely irregular and small demonstrating less than expected flow related enhancement. The posterior communicating artery appear present but are small. No areas of aneurysmal outpouching are appreciated

References

1. Bilaniuk LT, Murchison AP, Bilyk JR. Imaging of the pediatric orbit. In: Katowitz JA, Katowitz WR, editors. Pediatric oculoplastic surgery. 2nd ed. Cham: Springer; 2018.
2. Katowitz WR, Fries PD, Kazim M. Benign pediatric orbital tumors. In: Katowitz JA, Katowitz WR, editors. Pediatric oculoplastic surgery. 2nd ed. Cham: Springer; 2018.
3. Frieden IJ, Reese V, Cohen D. PHACE syndrome. 2. The association of posterior fossa brain malformations, hemangiomas, arterial anomalies, coarctation of the aorta and cardiac defects, and eye abnormalities. Arch Dermatol. 1996;132(3):307–11.
4. Léauté-Labrèze C, Hoeger P, Mazereeuw-Hautier J, et al. A randomized, controlled trial of oral propranolol in infantile hemangioma. N Engl J Med. 2015;372(8):735–46.
5. Chambers CB, Katowitz WR, Katowitz JA, Binenbaum G. A controlled study of topical 0.25% timolol maleate gel for the treatment of cutaneous infantile capillary hemangiomas. Ophthalmic Plast Reconstr Surg. 2012;28(2):103–6.

Part IV

Lacrimal Gland Tumors

Lacrimal Gland Prolapse and Dacryops

28

Oded Sagiv, J. Matthew Debnam, and Bita Esmaeli

Contents

1 **Signs and Symptoms** 249
2 **Differential Diagnosis** 250
3 **Diagnosis** 250
4 **Treatment** 250
5 **Figures with Captions** 250
References 252

Abstract

- Lacrimal gland prolapse:
  - Inferotemporal and anterior prolapse of the lacrimal gland without enlargement
  - Post-contrast T1 shows normal lacrimal gland enhancement pattern
- Dacryops:
  - Well-circumscribed cyst in the lacrimal gland
  - Bright T2 signal consistent with fluid content
  - Post-contract T1 may show peripheral enhancement

Keywords

Lacrimal gland prolapse · Dacryops · Lacrimal gland cyst

1 Signs and Symptoms

Lacrimal gland prolapse typically presents as a palpable, soft, and nontender mass in the temporal aspect of the upper eyelid or superotemporal orbit. Eversion or distraction of the upper eyelid will show a prolapsed lacrimal gland.

Dacryops (lacrimal gland ductal cysts) are relatively uncommon, arising from any lacrimal gland tissue. Multifactorial mechanism leads to dacryops including chronic inflammation, immune response, and IgA hypersecretion with an osmotic effect, all contributing to the cyst formation. Although the exact etiology of dacryops remains unclear, associated

O. Sagiv
The Goldschleger Eye Institute, Sheba Medical Center, affiliated to the Sackler Faculty of Medicine, Tel-Aviv University, Tel Aviv, Israel
e-mail: Oded.sagiv@sheba.health.gov.il

J. M. Debnam
Department of Neuroradiology, The University of Texas MD Anderson Cancer Center, Houston, TX, USA
e-mail: Matthew.Debnam@mdanderson.org

B. Esmaeli (✉)
Ophthalmic Plastic Surgery, Department of Plastic Surgery, The University of Texas MD Anderson Cancer Center, Houston, TX, USA
e-mail: besmaeli@mdanderson.org.il

© Springer Nature Switzerland AG 2022
G. Ben Simon et al. (eds.), *Atlas of Orbital Imaging*,
https://doi.org/10.1007/978-3-030-62426-2_16

conditions have been described. Chronic conjunctival inflammation, trauma, chemical injury, ocular surface reconstruction surgery, and ocular trachoma infection have been associated with the development of lacrimal ductal cyst. Dacryops may be associated with an underlying benign tumor or malignancy. However, they often occur in the absence of any predisposing factor. Histopathological examination showed immunoreactivity to IgA on the luminal surface of the epithelial ductal cyst and mild chronic inflammation in the underlying stroma or lacrimal gland.

A dacryops typically presents as a painless, cystic, slowly growing mass, most commonly in the temporal eyelid. On eversion of the eyelid a forniceal purple-blue cyst in the area of the openings of the lacrimal gland ductules is seen. Rarely these cysts can form in the orbital lobe of the lacrimal gland, or in the accessory lacrimal glands of Krause or Wolfring.

2 Differential Diagnosis

For lacrimal gland prolapse the differential includes prolapsed orbital fat, enlarged lacrimal gland, or dacryops.

For dacryops, on external examination one could suspect a lacrimal gland prolapse or a chalazion, but on eversion of the eyelid the appearance is typical for a dacryops.

3 Diagnosis

Diagnosis is made by clinical examination. For a typical dacryops there is usually no need for a biopsy. Orbital imaging may be prudent in larger lesions, or if proptosis or tenderness to palpation exists.

4 Treatment

Prolapsed lacrimal gland is usually regarded as an aesthetic issue that could be addressed surgically on its own or as part of a blepharoplasty surgery. The gland is reattached to the periosteum of the lacrimal gland fossa using a nonabsorbable suture.

Small asymptomatic dacryops can be observed. Nonspecific anti-inflammatory therapy can be helpful in symptomatic cases. Larger or nonresolving symptomatic lesions can be marsupialized or completely excised using a direct forniceal/eyelid crease approach and avoiding damage to the adjacent lacrimal ductules. Fibrin sealant and trypan blue mixture can facilitate en bloc surgical excision.

5 Figures with Captions



Fig. 1 **Clinical photograph** of a 39-year-old female with 3-months history of right upper eyelid painless swelling more noticebale with her eyes closed (left image). She has medical history of nonactive lupus (*courtesy of the editors*)

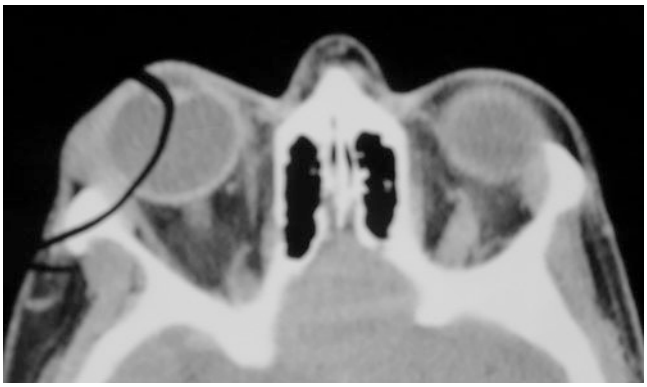


Fig. 2 Noncontrast-enhanced CT of the same patient, axial view, showing homogenous enlargement of the right palpebral lacrimal gland consistent with dacryops (black solid line is markup on X-ray film)

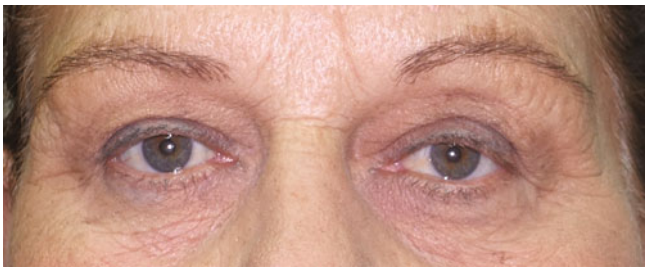


Fig. 3 Clinical photograph of a 68-year-old woman with left upper eyelid nontender fullness, causing mild temporal ptosis (*courtesy of the editors*)

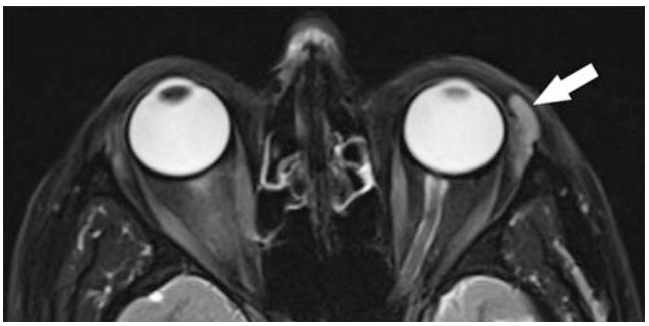


Fig. 4 Axial T2 fat-saturated image of the same patient shows inferotemporal and anterior prolapse of the palpebral segment of the left lacrimal gland (arrow). This portion of the gland appears thickened in comparison to the right lacrimal gland

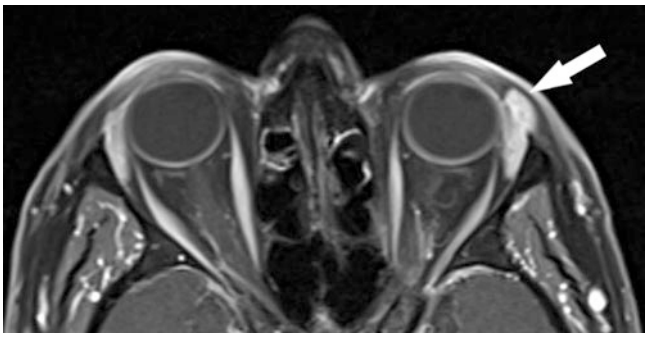


Fig. 5 Axial T1 post-contrast fat-saturated image normal diffuse enhancement of the prolapsed lacrimal gland (arrow)

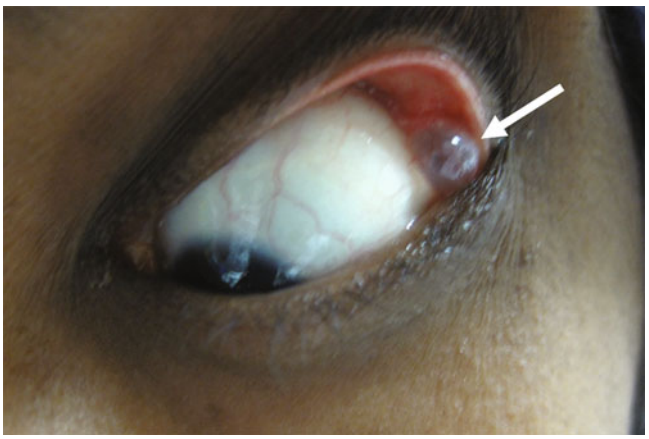


Fig. 6 Clinical photograph of a left dacryops in the superotemporal fornix seen with upper eyelid eversion (arrow)

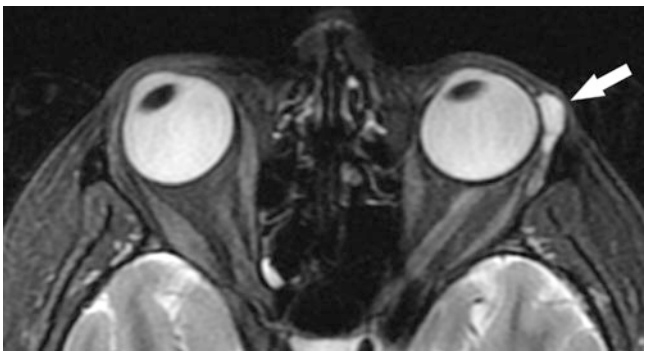


Fig. 7 Axial T2 fat-saturated image of the same patient shows a well-circumscribed cystic lesion in the palpebral segment of the left lacrimal gland with a posterior septum probably delineating the cyst from the orbital component of the gland. Bright signal in the central portion of the cyst is consistent with fluid (arrow)

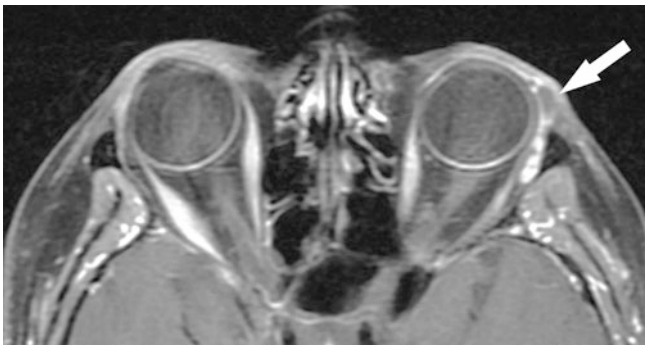


Fig. 8 Axial T1 post-contrast fat-saturated image with peripheral enhancement of the cyst's margin (arrow)

References

1. Tanaboonyawat S, et al. Dacryops - a review. Orbit. 2020;39(2):128–34.
2. Ozgonul C, et al. Clinical features and management of dacryops. Orbit. 2018;37(4):262–5.
3. Massry GG. Prevalence of lacrimal gland prolapse in the functional blepharoplasty population. Ophthalmic Plast Reconstr Surg. 2011;27(6):410–3.
4. Brownstein S, Belin MW, Krohel GB, Smith RS, Condon G, Codere F. Orbital dacryops. Ophthalmology. 1984;91(11):1424–8. https://doi.org/10.1016/s0161-6420(84)34133-1. PMID: 6514311.
5. Nerad JA, Carter K, Folberg R. Simple dacryops. Arch Ophthalmol. 1988;106(8):1129. https://doi.org/10.1001/archopht.1988.01060140285042. PMID: 3401142.
6. Lam K, Brownstein S, Jordan DR, Jastrzebski A. Dacryops: a series of 5 cases and a proposed pathogenesis. JAMA Ophthalmol. 2013;131(7):929–32. https://doi.org/10.1001/jamaophthalmol.2013.1885. PMID: 23846204.
7. Men CJ, Yang P, Gur Z, Paik JS, Kikkawa DO, Korn BS. Complete excision of a simple Dacryops using fibrin sealant and trypan blue mixture. Ophthalmic Plast Reconstr Surg. 2019;35(1):e16–8. https://doi.org/10.1097/IOP.0000000000001283. PMID: 30562335.
8. Pornseth A, Charukamnoetkanok P, Uiprasertkul M, Sintuwong S. Large Dacryops mimicking lacrimal gland tumor with secondary corneal ulcer. Ophthalmic Plast Reconstr Surg. 2020. https://doi.org/10.1097/IOP.0000000000001735. Epub ahead of print. PMID: 32732534.
9. Andrew NH, AA MN, Selva D. Review of 268 lacrimal gland biopsies in an Australian cohort. Clin Exp Ophthalmol. 2015;43(1):5–11. https://doi.org/10.1111/ceo.12371. Epub 2014 Aug 19. PMID: 24923880.
10. Jakobiec FA, Zakka FR, Perry LP. The cytologic composition of dacryops: an immunohistochemical investigation of 15 lesions compared to the normal lacrimal gland. Am J Ophthalmol. 2013;155(2):380–396.e1. https://doi.org/10.1016/j.ajo.2012.07.028. Epub 2012 Oct 28. PMID: 23114708.

Pleomorphic Adenoma of the Lacrimal Gland

29

Oded Sagiv, J. Matthew Debnam, and Bita Esmaeli

Contents

1 **Signs and Symptoms** 253
2 **Differential Diagnosis** 253
3 **Diagnosis** 254
4 **Treatment** 254
5 **Figures with Captions** 254
References 257

Abstract

- Anterior superolateral extraconal mass, originating predominantly in the orbital lobe of the lacrimal gland.
- Usually a well-defined solid mass lesion, mostly ovoid but lobular when large; may have a cystic component.
- Slightly hyperdense (though heterogenous) on non-enhanced CT, possible small foci of calcification.
- Causes smooth remodeling of the adjacent orbital rim on bone windowing.
- Intermediate signal on T1 and T2 weighted images, usually diffuse, marked, albeit heterogeneous, enhancement. T1 shows iso- to hypo-intense signal while the signal is iso- to hyper-intense on T2.
- Usually high diffusivity on ADC maps indicative of a hypocellular mass.

Keywords

Lacrimal gland pleomorphic adenoma · Benign mixed tumor · Benign epithelial tumors of the lacrimal gland

1 Signs and Symptoms

Unilateral proptosis, usually painless, slowly progressing over months to years. The lesion usually displaces the globe inferomedially and may cause a mass effect in the temporal upper eyelid. However, atypical presentation may include pain and rapidly progressive symptoms.

2 Differential Diagnosis

Other diseases causing enlargement of the lacrimal gland: other epithelial lesions, such as myoepithelioma, oncocytoma; malignant epithelial tumors such as adenoid cystic carcinoma, primary adenocarcinoma, pleomorphic adenocarcinoma, mucoepidermoid carcinoma, acinic cell carcinoma, squamous cell carcinoma, malignant myoepithelial carcinoma, lymphoproliferative lesions of the lacrimal gland: benign lymphoid hyperplasia, atypical lymphoid hyperplasia, lymphoma. Other lesions that can involve the lacrimal fossa such as dermoid cyst.

O. Sagiv
The Goldschleger Eye Institute, Sheba Medical Center, affiliated to the Sackler Faculty of Medicine, Tel-Aviv University, Tel Aviv, Israel
e-mail: Oded.sagiv@sheba.health.gov.il

J. M. Debnam
Department of Neuroradiology, The University of Texas MD Anderson Cancer Center, Houston, TX, USA
e-mail: Matthew.Debnam@mdanderson.org

B. Esmaeli (✉)
Ophthalmic Plastic Surgery, Department of Plastic Surgery, The University of Texas MD Anderson Cancer Center, Houston, TX, USA
e-mail: besmaeli@mdanderson.org.il

© Springer Nature Switzerland AG 2022
G. Ben Simon et al. (eds.), *Atlas of Orbital Imaging*,
https://doi.org/10.1007/978-3-030-62426-2_18

3 Diagnosis

Clinical suspicion is based on typical findings on imaging and clinical course. If a pleomorphic adenoma is clinically suspected, excisional biopsy is the treatment of choice and will provide the diagnosis.

4 Treatment

Complete excision is curative. Partial excision can result in multiple recurrences, dissemination of the tumor in the orbit, and rarely even malignant transformation.

5 Figures with Captions



Fig. 1 Axial postcontrast CT orbit, soft tissue window. This image shows a well-circumscribed, slightly enhancing lesion in the superotemporal left orbit (arrow)



Fig. 2 Coronal postcontrast CT orbit, bone window, same patient. The lesion in the superotemporal left orbit is associated with smooth remodeling of the orbital roof (arrow)

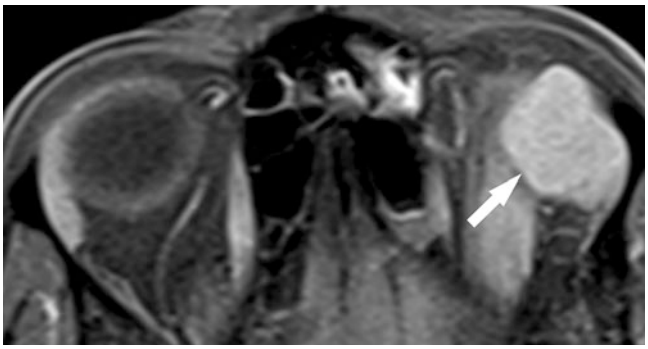


Fig. 3 Axial T1 postcontrast fat-saturated image shows homogeneous enhancement of the well-circumscribed orbital mass (arrow)

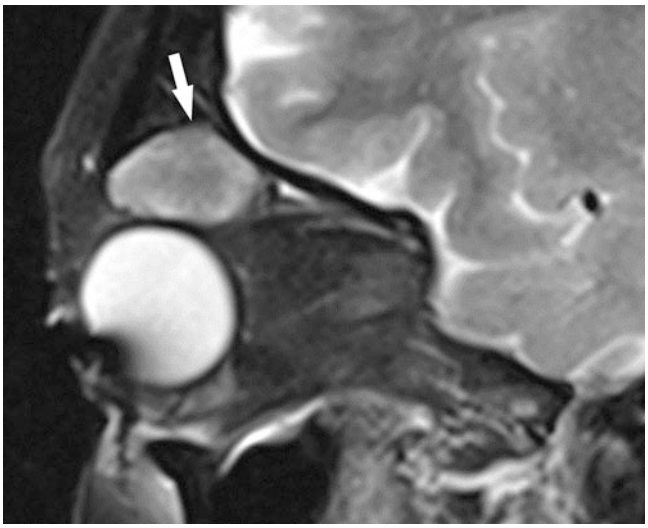


Fig. 4 Sagittal T2 fat-saturated image shows the position of the mass superior to the globe with intermediate signal intensity and erosion into the orbital roof (arrow)



Fig. 5 Axial T2 fat-saturated image (different patient) demonstrates a more heterogenous appearance of the tumors. There are cystic (dark arrow) and solid (white arrow) components within the superior lateral orbital tumor. Mass effect upon the globe causes proptosis. There is also relative orbital expansion

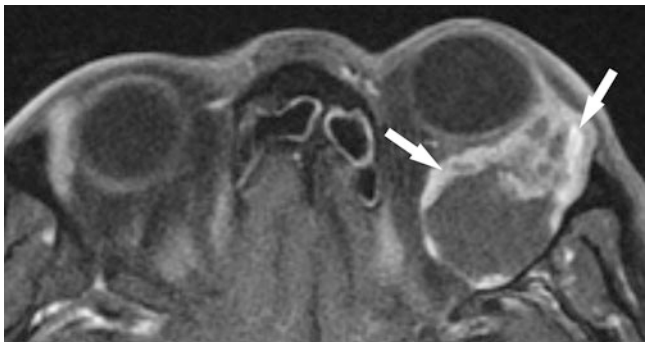


Fig. 6 **Axial T1 postcontrast fat-saturated image** shows enhancement of the solid components of the mass (arrows). Note expansion of the orbit secondary to thinning and temporal deviation of the lateral wall

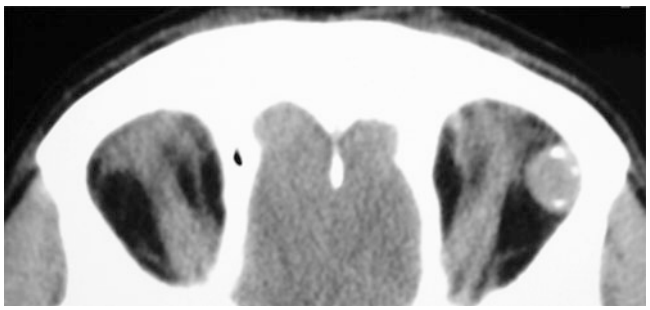


Fig. 7 CT scan of a different patient shows a few calcific deposits within the tumor

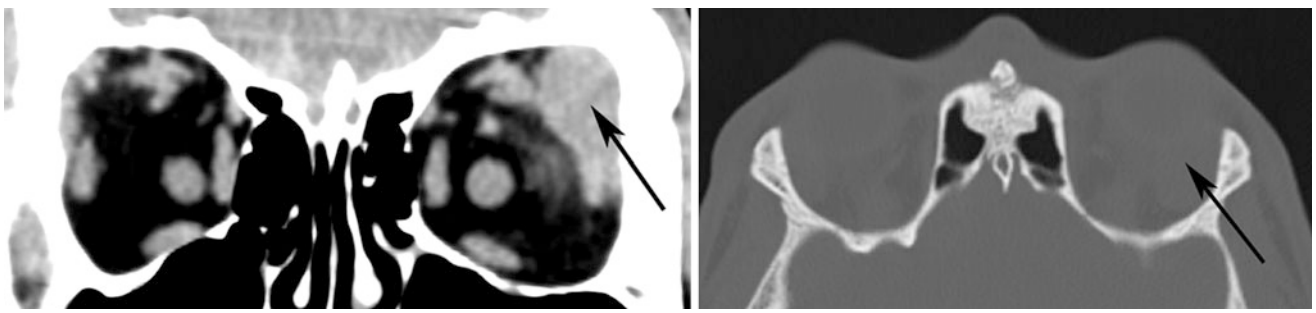


Fig. 8 **Postcontrast orbit CT. Soft tissue window, coronal view (*left*).** A slightly enhancing well-defined extraconal mass residing in the superior temporal region of the left orbit, inseparable from the lacrimal gland, most likely originating from the orbital segment of the gland. There are no obvious calcifications, and no cystic or fatty elements. **Bone window, axial view *(right).*** The extraconal mass residing in the superior temporal region of the left orbit causing minimal smooth remodeling of the bony contour with no evidence of sclerosis or bony destruction

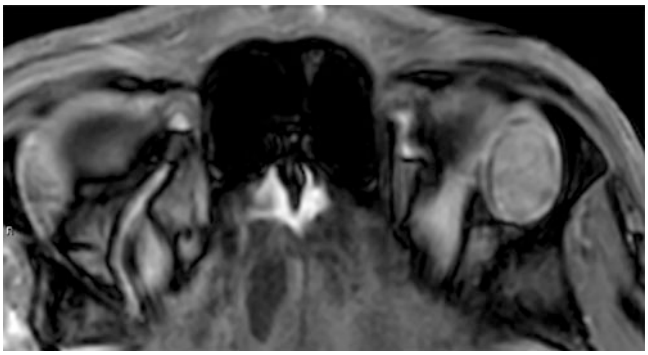


Fig. 9 Postcontrast axial T1 fat-saturated image at the level of the orbital roof depicting a well-defined enhancing oval extraconal mass. The enhancement pattern is heterogeneous

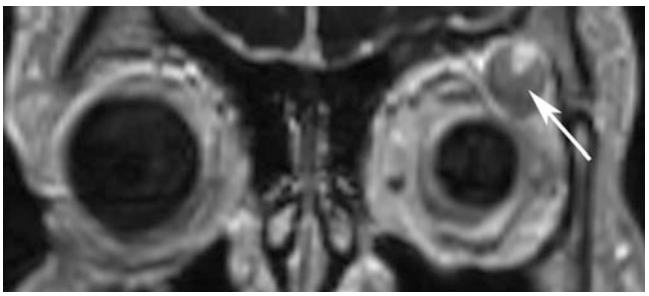


Fig. 10 Early postcontrast coronal FSPGR T1 partially saturated image through the middle third of the orbit depicting a well-defined oval extraconal mass, located at the anatomical lacrimal apparatus. The image reveals a focal intramural focus of enhancement within the cranial portion of the lesion

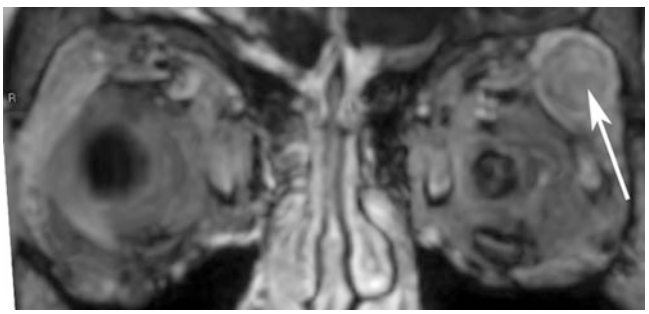


Fig. 11 Late postcontrast coronal FSPGR T1 partially saturated image showing a diffuse enhancement pattern. The enhancement is heterogeneous

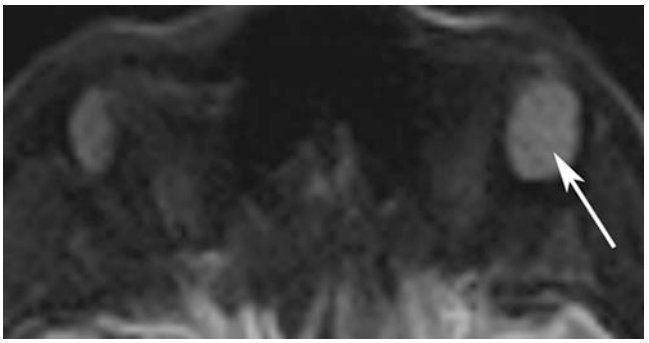


Fig. 12 Diffusion DWI image at the level of the lesion showing hypersignal, but there is no confirmatory restriction on the accompanying ADC map (Fig. 13)

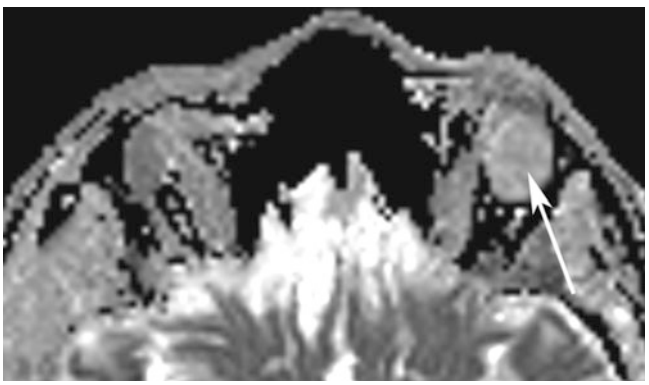


Fig. 13 Diffusion ADC map at the level of the lesion showing an iso-hyperdense signal with no obvious restriction, suggesting that the lesion has low cellularity

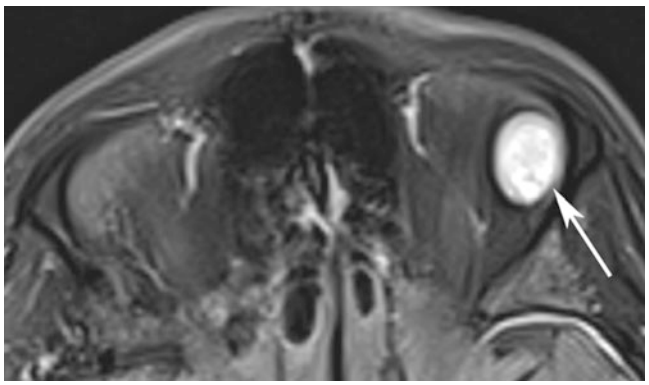


Fig. 14 Axial T2 fat-saturated image at the level of the lesion depicting a rather bright internal hyperintense signal with a rim of low intensity

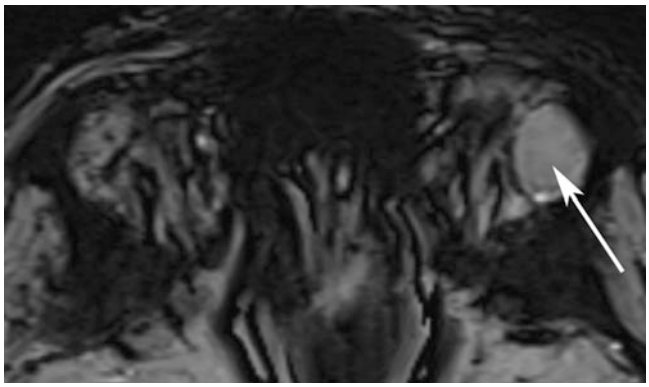


Fig. 15 Axial SWI image at the level of the lesion showing no evidence of internal blood products

References

1. Esmaeli B. Ophthalmic oncology, vol. 6: Springer Science & Business Media; 2011.
2. Black EH, et al. Smith and Nesi's ophthalmic plastic and reconstructive surgery: Springer Science & Business Media; 2012.
3. Gündüz AK, Yeşiltaş YS, Shields CL. Overview of benign and malignant lacrimal gland tumors. Curr Opin Ophthalmol. 2018;29(5):458–68.
4. Young SM, Kim Y-D, Shin HJ, Imagawa Y, Lang SS, Woo KI. Lacrimal gland pleomorphic adenoma and malignant epithelial tumours: clinical and imaging differences. Br J Ophthalmol. 2019;103(2):264–8.
5. Auran J, Jakobiec FA, Krebs W. Benign mixed tumor of the palpebral lobe of the lacrimal gland. Clinical diagnosis and appropriate surgical management. Ophthalmology. 1988;95(1):90–9. https://doi.org/10.1016/s0161-6420(88)33223-9. PMID: 3278262.
6. Rose GE. To crash or not to crash? Probability in the management of benign lacrimal gland tumours. Eye (Lond). 2009;23(8):1625–8. https://doi.org/10.1038/eye.2009.89. PMID: 19675571.
7. Parks SL, Glover AT. Benign mixed tumors arising in the palpebral lobe of the lacrimal gland. Ophthalmology. 1990;97(4):526–30. https://doi.org/10.1016/s0161-6420(90)32572-1. PMID: 2158030.

Recurrent Pleomorphic Adenoma of the Lacrimal Gland (RLGPA) 30

Oded Sagiv, J. Matthew Debnam, and Bita Esmaeli

Contents

1 **Signs and Symptoms** 259
2 **Differential Diagnosis** 259
3 **Diagnosis** 260
4 **Treatment** 260
5 **Figures with Captions** 260
References 262

Abstract

- Recurrent mass sharing the same imaging characteristics of the primary lesion including bony erosions/remodeling.
- In primary LGPA bone remodeling is smooth second to pressure erosion whereas RLGPA lesions may cause adjacent deep bone erosions and remodeling. These changes do not necessarily imply malignant transformation and are likely to occur second to direct effect of the neoplastic cells on bone formation/destruction.
- Tends to be multifocal with spreading into the operative field.

Keywords

Recurrent lacrimal gland pleomorphic adenoma · Recurrent benign mixed tumor · Benign epithelial tumors of the lacrimal gland

1 Signs and Symptoms

RLGPA can recur after incomplete excision of primary LG pleomorphic adenoma. If a biopsy is performed prior to initial surgery, the 5-year cumulative recurrence rate can be as high as 32% versus only 5% where the tumor is removed with its capsule intact. Recurrence can occur up to 44 years after the primary surgery.

A patient with a history of an incompletely excised pleomorphic adenoma, with worsening symptoms as described above, or progression on imaging. Seventy percent of patients develop second recurrence after surgery for first recurrence, and the average time interval to malignant transformation in one series was 17 years. The risk of malignant transformation increases with time.

2 Differential Diagnosis

Same as for primary, but mainly consider recurrent pleomorphic adenoma versus carcinoma ex-pleomorphic adenoma.

O. Sagiv
The Goldschleger Eye Institute, Sheba Medical Center, affiliated to the Sackler Faculty of Medicine, Tel-Aviv University, Tel Aviv, Israel
e-mail: Oded.sagiv@sheba.health.gov.il

J. M. Debnam
Department of Neuroradiology, The University of Texas MD Anderson Cancer Center, Houston, TX, USA
e-mail: Matthew.Debnam@mdanderson.org

B. Esmaeli (✉)
Ophthalmic Plastic Surgery, Department of Plastic Surgery, The University of Texas MD Anderson Cancer Center, Houston, TX, USA
e-mail: besmaeli@mdanderson.org.il

© Springer Nature Switzerland AG 2022
G. Ben Simon et al. (eds.), *Atlas of Orbital Imaging*,
https://doi.org/10.1007/978-3-030-62426-2_96

3 Diagnosis

Clinical suspicion is based on history and imaging. Pathological analysis of a completely excised tumor will give the diagnosis.

4 Treatment

Complete surgical excision is the treatment of choice when possible. Some recurrences tend to have multifocal disease in the orbit which may be surgically challenging. Many require multiple operations over the years with significant morbidity and remote chance of orbital exenteration for local tumor control.

5 Figures with Captions

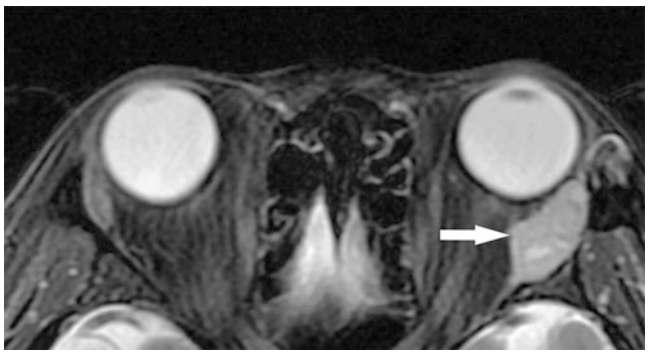


Fig. 1 Axial T2 fat-saturated image. This patient presented 4 years following resection of a left lacrimal gland pleomorphic adenoma at another institution. With slowly progressive proptosis and downward globe displacement, this scan shows a well-circumscribed lesion in left lacrimal fossa with extension into the intraconal space (arrow). No invasive features are noted

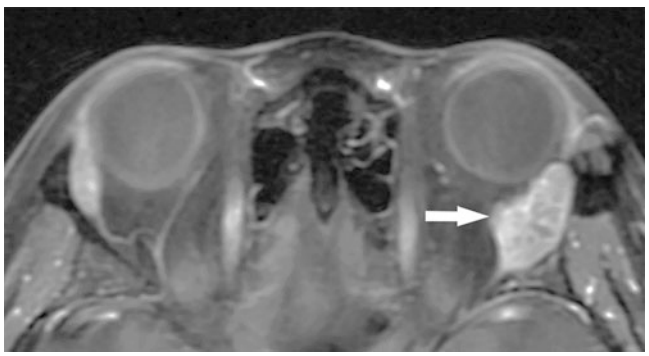


Fig. 2 Axial T1 post-contrast fat-saturated image (same patient as in Fig. 1) shows heterogeneous enhancement of the mass (arrow)

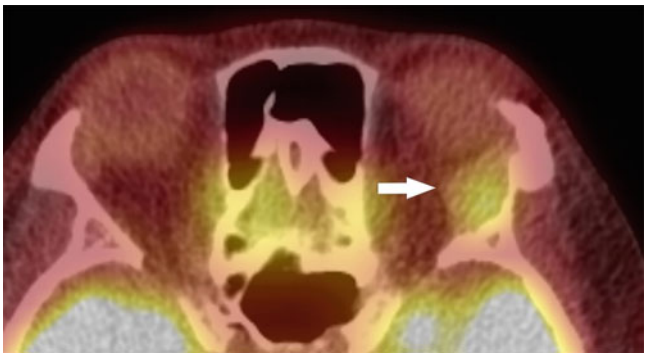


Fig. 3 Axial PET/CT image (same patient as in Fig. 1) shows FDG avidity of the mass (arrow). The lateral orbital wall is irregular post lateral orbitotomy surgery

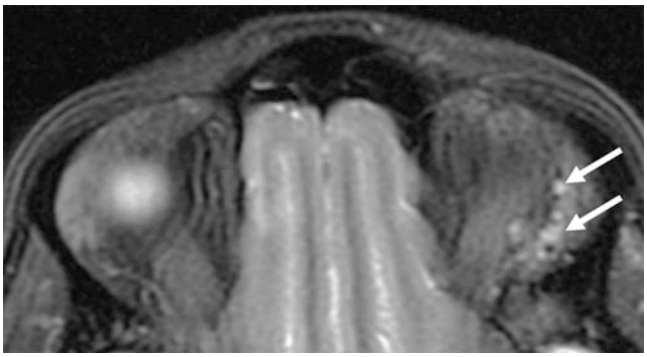


Fig. 4 Axial T2 fat-saturated image of a different patient, who underwent prior resection of a pleomorphic adenoma at an outside facility, shows multiple T2 hyperintense nodules in the superotemporal left orbit (arrows)

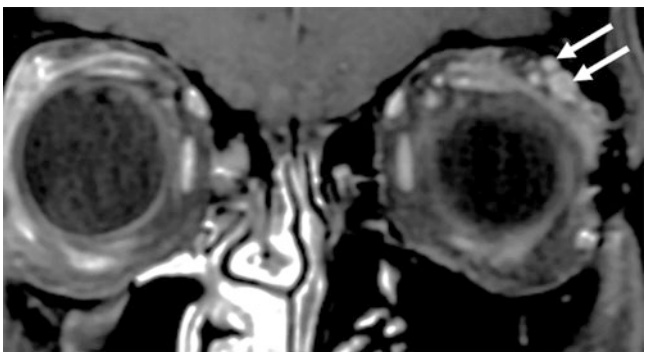


Fig. 5 Coronal T1 post-contrast fat-saturated image of the same patient as in Fig. 4 demonstrates enhancing nodules consistent with recurrent pleomorphic adenoma (arrows)



Fig. 6 NECT, (soft tissue window) axial view of a 52-year-old male with a history of right lacrimal gland pleomorphic adenoma removal 9 years prior to admission. The patient presented with periocular pain, mild proptosis, and inferior-medial globe dystopia. The scan shows an inhomogeneous soft tissue mass at the lacrimal gland fossa with bone scalloping and erosion adjacent to tumor nodules. Anterior bone fragment is related to prior lateral orbitotomy

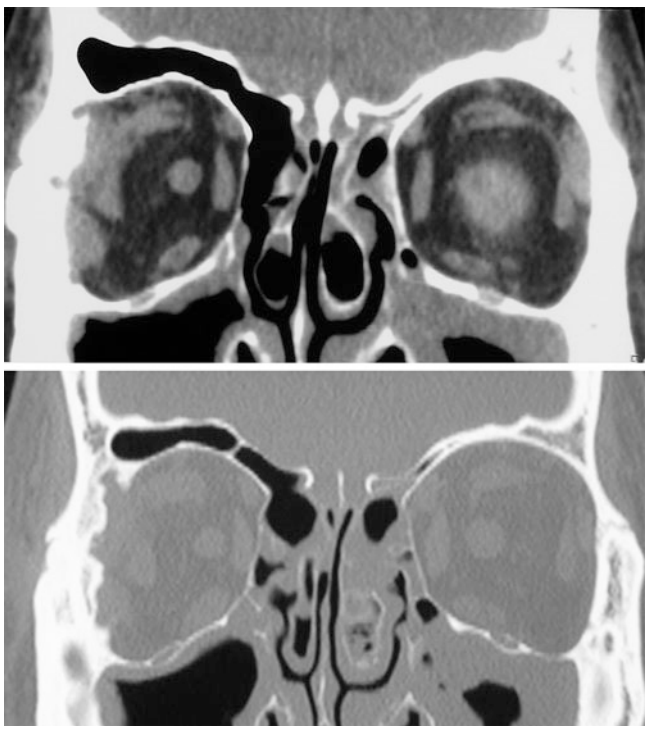


Fig. 7 NECT, coronal view soft tissue window (*upper*) and bone window (*lower*) of the same patient better demonstrates multiple areas of tumor recurrences along the lateral orbital wall with adjacent erosions or remodeling. Hyperostotic sclerotic changes are most likely related to previous lateral wall removal. Repeat surgical excision of the tumor disclosed RLGPA

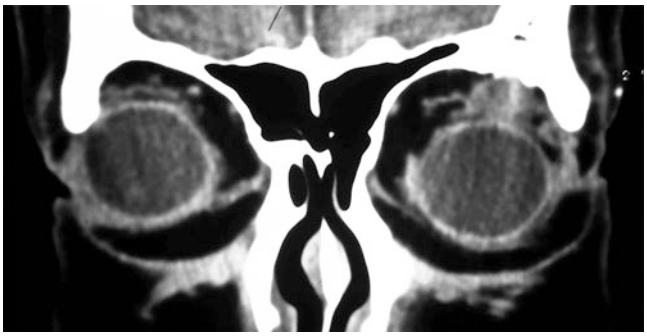


Fig. 8 NECT of a 52-year-old male (different patient) with a history of left lacrimal gland pleomorphic adenoma removal 19 years prior to admission. Note heterogenous superior orbital mass causing globe displacement, and although soft tissue window one can notice the irregularity of the temporal orbital roof indicative of erosive scalloping

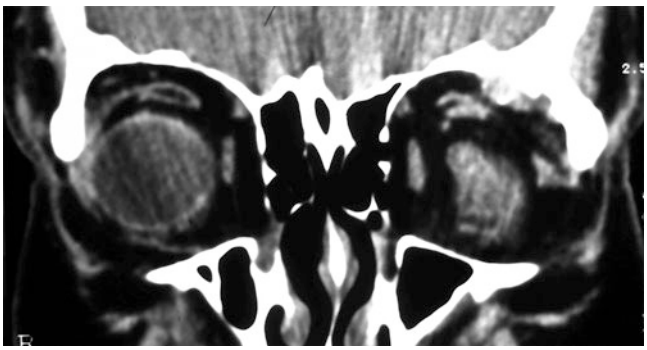


Fig. 9 CT coronal view of the same patient at a more posterior location showing deeper bone erosions at the lateral orbital roof filled by the tumor nodules. Both images (8 and 9) are affected by vertical streaks

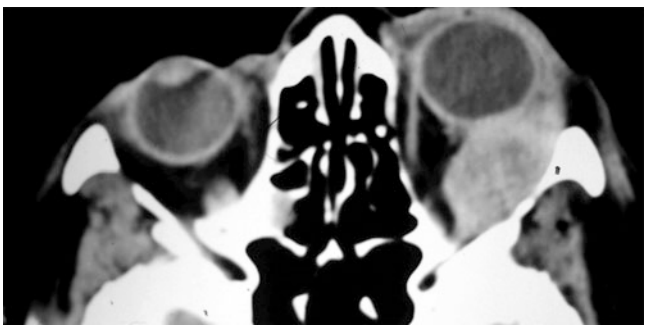


Fig. 10 Axial CT of a 74-year-old female who underwent partial removal of left lacrimal gland pleomorphic adenoma 22 years prior to admission. There is a left well-defined inhomogeneous lacrimal gland mass causing globe proptosis and posterior flattening

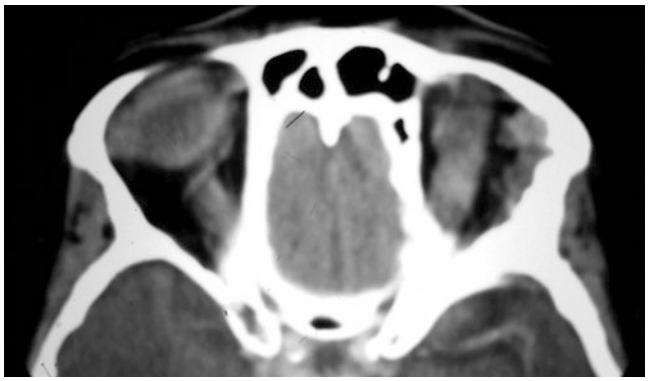


Fig. 11 NECT axial view of the same patient taken more superiorly showing tumor nodules with adjacent bone scalloping. En bloc tumor removal revealed malignant mixed tumor extending to the surgical margins, necessitating large cranio-facial resection with postoperative radiation. The patient remained disease free after 14 years of follow-up

(***Figures 6–11 courtesy of Alan. A. McNab, RVEEH, Melbourne, Australia***)

References

1. McNab AA, Satchi K. Recurrent lacrimal gland pleomorphic adenoma: clinical and computed tomography features. Ophthalmology. 2011;118(10):2088–92. https://doi.org/10.1016/j.ophtha.2011.03.014. PMID: 21684609.
2. Font RL, Gamel JW. Epithelial tumors of the lacrimal gland: an analysis of 265 cases. In: Jakobiec FA, editor. Ocular and adnexal tumors. Birmingham: Aesculapius; 1978. p. 787–805.
3. Currie ZI, Rose GE. Long-term risk of recurrence after intact excision of pleomorphic adenomas of the lacrimal gland. Arch Ophthalmol. 2007;125:1643–6.
4. Rose GE, Wright JE. Pleomorphic adenoma of the lacrimal gland. Br J Ophthalmol. 1992;76(7):395–400. https://doi.org/10.1136/bjo.76.7.395. PMID: 1320923; PMCID: PMC504299.
5. Esmaeli B. Ophthalmic oncology, vol. 6: Springer Science & Business Media; 2011.
6. Black EH, et al. Smith and Nesi's ophthalmic plastic and reconstructive surgery: Springer Science & Business Media; 2012.
7. Gündüz AK, Yeşiltaş YS, Shields CL. Overview of benign and malignant lacrimal gland tumors. Curr Opin Ophthalmol. 2018;29(5):458–68. https://doi.org/10.1097/ICU.0000000000000515. PMID: 30028745.
8. Henderson JW. Primary epithelial neoplasms. In: Orbital tumors. 3rd ed. New York: Raven Press; 1994. p. 324–9.
9. Yasumoto M, Sunaba K, Shibuya H, Kurabayashi T. Recurrent pleomorphic adenoma of the head and neck. Neuroradiology. 1999;41:300–4.
10. Kanatas A, Ho MWS, Mücke T. Current thinking about the management of recurrent pleomorphic adenoma of the parotid: a structured review. Br J Oral Maxillofac Surg. 2018;56(4):243–8. https://doi.org/10.1016/j.bjoms.2018.01.021. Epub 2018 Mar 8. PMID: 29526342.
11. Clarós P, Choffor-Nchinda E, Lopez-Fortuny M, Zofia Sobolewska A, Clarós A. Lacrimal gland pleomorphic adenoma: a review of 52 cases, 15-year experience. Acta Otolaryngol. 2019;139(1):100–4. https://doi.org/10.1080/00016489.2018.1541362. Epub 2019 Jan 10. PMID: 30628498.
12. Young SM, Kim YD, Shin HJ, Imagawa Y, Lang SS, Woo KI. Lacrimal gland pleomorphic adenoma and malignant epithelial tumours: clinical and imaging differences. Br J Ophthalmol. 2019;103(2):264–8. https://doi.org/10.1136/bjophthalmol-2017-311538. Epub 2018 Apr 21. PMID: 29680804.

Lacrimal Gland Carcinoma: Primary

31

Oded Sagiv, J. Matthew Debnam, and Bita Esmaeli

Contents

1 **Signs and Symptoms** 263
2 **Differential Diagnosis** 263
3 **Diagnosis** 264
4 **Treatment** 264
5 **Figures with Captions** 264
References 266

Abstract

- A well-circumscribed mass in the superotemporal orbit.
- Bone destruction can be seen in the orbital roof and lateral wall with tumor extension to adjacent periorbital spaces.
- Tumors can extend posteriorly (sometimes seen as a "wedge sign" as evidence of subperiostal involvement) in the orbit or to the intraconal space.
- Post-contrast T1 shows enhancement of the solid component. T2 bright cystic changes may represent areas of necrosis within the tumor.
- Perineural invasion can be seen.
- Restricted diffusion is a useful noninvasive tool in preoperative assessment. Lower ADC values are highly suggestive of malignancy.
- Staging includes PET imaging which shows an FDG-avid lesion.

Keywords

Lacrimal gland carcinoma · Adenoid cystic carcinoma · Malignant epithelial tumors of the lacrimal gland

1 Signs and Symptoms

Typical symptoms of carcinoma in the lacrimal gland include periocular pain, ptosis (mild and more temporal usually), and inferonasal displacement of the globe. Double vision and loss of sensation of the forehead and temporal region can also occur. Symptoms are usually present for less than 6–12 months prior to presentation.

2 Differential Diagnosis

Same as for pleomorphic adenoma. The most common type of malignant epithelial lacrimal gland tumor is adenoid cystic carcinoma, but the other carcinomas are also in the differential including: primary adenocarcinoma, carcinoma ex-pleomorphic

O. Sagiv
The Goldschleger Eye Institute, Sheba Medical Center, affiliated to the Sackler Faculty of Medicine, Tel-Aviv University, Tel Aviv, Israel
e-mail: Oded.sagiv@sheba.health.gov.il

J. M. Debnam
Department of Neuroradiology, The University of Texas MD Anderson Cancer Center, Houston, TX, USA
e-mail: Matthew.Debnam@mdanderson.org

B. Esmaeli (✉)
Ophthalmic Plastic Surgery, Department of Plastic Surgery, The University of Texas MD Anderson Cancer Center, Houston, TX, USA
e-mail: besmaeli@mdanderson.org.il

© Springer Nature Switzerland AG 2022
G. Ben Simon et al. (eds.), *Atlas of Orbital Imaging*,
https://doi.org/10.1007/978-3-030-62426-2_19

adenoma, mucoepidermoid carcinoma, acinic cell carcinoma, squamous cell carcinoma, and malignant myoepithelial carcinoma.

3 Diagnosis

Clinical suspicion is based on typical findings on imaging and clinical course. If a carcinoma of the lacrimal gland is suspected, an incisional biopsy is usually performed to establish diagnosis.

4 Treatment

Treatment is based on multiple factors including the extent of the tumor in the orbit, extension to adjacent structures, mainly the CNS, and existence of distant metastases. Generally, local control of the disease is achieved using a combination of surgery and radiotherapy with or without chemotherapy. For adenoid cystic carcinoma, when possible, complete surgical excision with frozen section control of margins is the preferred treatment, whether eye sparing or as part of an orbital exenteration. Some use neoadjuvant intra-arterial chemotherapy. Adjuvant chemoradiotherapy is used by the authors due to the high prevalence of perineural invasion.

5 Figures with Captions

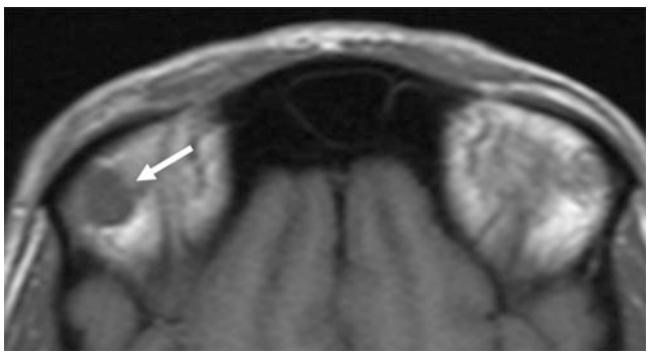


Fig. 1 Axial T1 pre-contrast image of a patient ("patient A") with a relatively small (TNM stage T1/T2) well-defined lacrimal gland adenoid cystic carcinoma, showing a well-circumscribed hypointense mass in the superotemporal right orbit (arrow)



Fig. 2 Axial T1 post-contrast fat-saturated image of patient A demonstrates heterogeneous enhancement of a mass arising from the orbital segment of the right lacrimal gland (arrow)

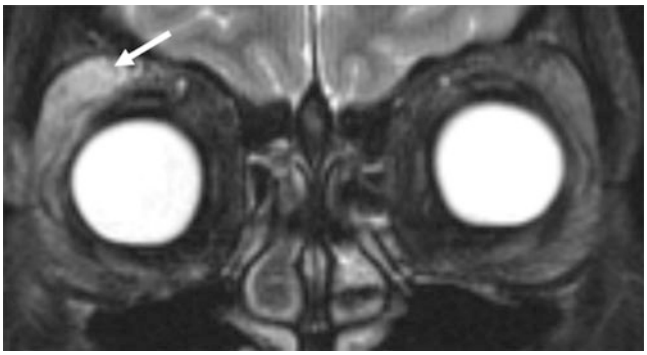


Fig. 3 Coronal T2 fat-saturated image of patient A shows intermediate high signal in the superotemporal right orbital mass with inferior displacement of the globe (arrow)



Fig. 4 Axial post-contrast CT orbit, soft tissue window of another patient ("patient B"). This image shows a heterogeneous mass in the superotemporal left orbit (large arrow). The defect in the lateral orbital wall (small arrow) is related to orbitotomy for biopsy that demonstrated adenoid cystic carcinoma

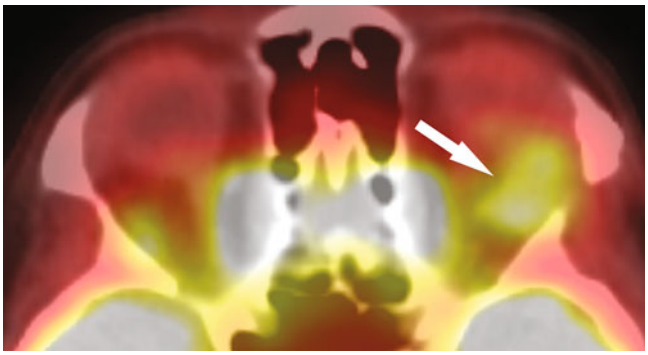


Fig. 5 Axial PET/CT image of patient B with FDG avidity of the mass (arrow)

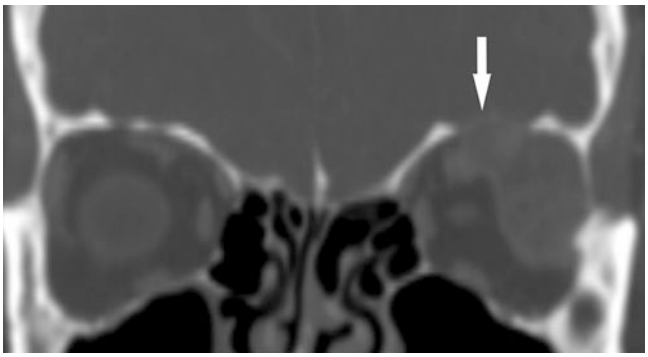


Fig. 6 Coronal post-contrast CT orbit, bone window of patient B**.** A defect is present in the left orbital roof superior to the tumor (arrow) related to bony destruction due to the aggressive nature of the lesion

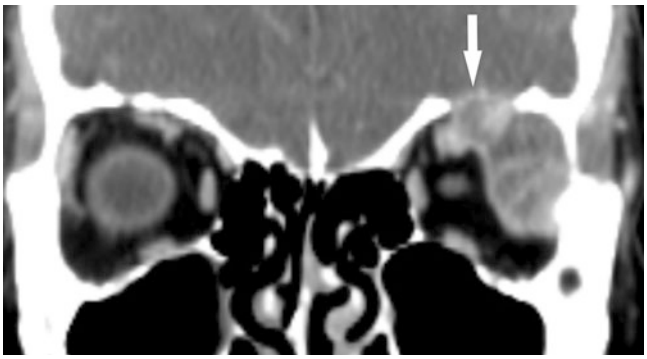


Fig. 7 Coronal post-contrast CT orbit, soft tissue window of patient B**.** The tumor in the superotemporal left orbit extends through the defect in the orbital roof into the intracranial compartment (arrow)

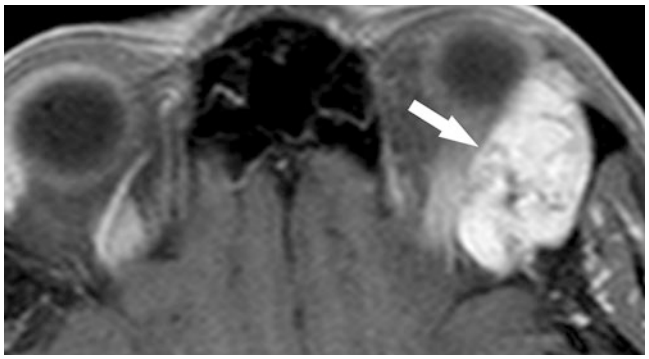


Fig. 8 Axial T1 post-contrast fat-saturated image of a different patient ("patient C") shows a brisk but heterogenous enhancing mass in the superotemporal left orbit

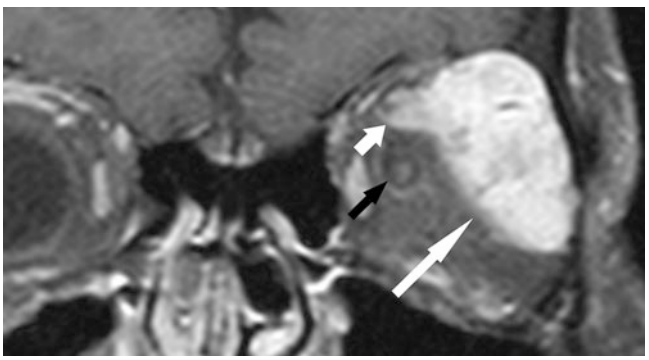


Fig. 9 Coronal T1 post-contrast fat-saturated image of patient C. The tumor in the superotemporal left orbit extends into the intraconal space superior (short white arrow) and inferior (long arrow) to the optic nerve (black arrow). Both the superior and lateral rectus muscles are inseparable from the tumor mass



Fig. 10 Axial T1 post-contrast fat-saturated image of a different patient ("patient D") who underwent a gross total resection of lacrimal gland adenoid cystic carcinoma and the lacrimal gland tissue. The image demonstrates a normal appearance of the orbits

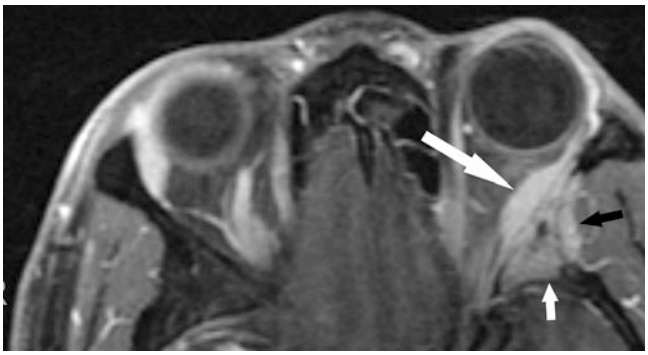


Fig. 11 This is an **axial T1 post-contrast fat-saturated image** of patient D, who underwent gross total resection of an adenoid cystic carcinoma followed by chemoradiation. This image represents tumor recurrence 2 years following treatment. The image shows a heterogeneously enhancing tumor recurrence in the lateral left orbit (long arrow) with both osseous and extra-osseous components. Note the posterior involvement of the sphenoid bone (short white arrow) as well as extension into the masticator space (black arrow)

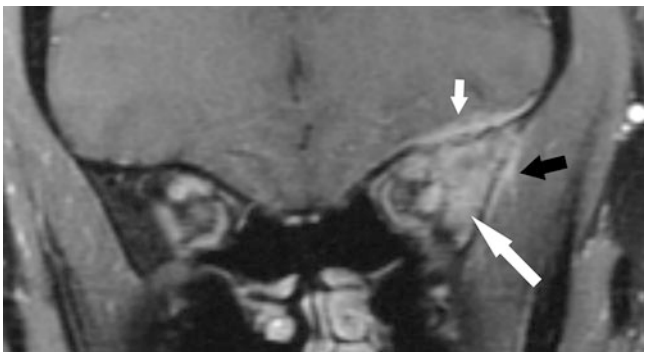


Fig. 12 Coronal T1 post-contrast fat-saturated image of patient D. The recurrent tumor in the superotemporal left orbit (long arrow) extends intracranially through the orbital roof with dural enhancement (short white arrow). Note tumor in the left masticator space (black arrow)



Fig. 13 Axial T1 post-contrast fat-saturated image of patient D. The image shows the recurrent tumor in the left orbit (long arrow) with V2 perineural invasion extending through the inferior orbital fissure (short, white arrow) and posteriorly to involve the cavernous sinus and Meckel's cave (black arrow)



Fig. 14 Coronal T1 post-contrast fat-saturated image of patient D. It demonstrates tumor in the left foramen rotundum (long arrow). Multiple foci of enhancement in the inferior left frontal (small arrows) and anterior temporal (black arrow) lobes are secondary to radiation necrosis

References

1. Esmaeli B. Ophthalmic oncology, vol. 6: Springer Science & Business Media; 2011.
2. Black EH, et al. Smith and Nesi's ophthalmic plastic and reconstructive surgery: Springer Science & Business Media; 2012.

Carcinoma Ex-Pleomorphic Adenoma of the Lacrimal Gland

32

Oded Sagiv, J. Matthew Debnam, and Bita Esmaeli

Contents

1 **Signs and Symptoms** 268
2 **Differential Diagnosis** 268
3 **Diagnosis** 268
4 **Treatment** 268
5 **Figures with Captions** 268
References 270

Abstract

- A heterogenous mass in the superotemporal orbit (may be well circumscribed)
- On CT, bone destruction can be seen in the orbital roof and lateral wall with tumor extension to adjacent peri-orbital spaces.
- MR images show a heterogenous mass that can extend posteriorly in the orbit or to the intraconal space.
- Post-contrast T1 shows nonhomogenous enhancement.
- Perineural invasion can be seen along V1 branches to the cavernous sinus
- FDG-avid on PET imaging

Keywords

Lacrimal gland carcinoma · Carcinoma ex-pleomorphic adenoma · Malignant epithelial tumors of the lacrimal gland · Myoepithelial carcinomas · Adenocarcinomas · Epithelial-myoepithelial carcinomas · Squamous cell carcinomas

O. Sagiv
The Goldschleger Eye Institute, Sheba Medical Center, affiliated to the Sackler Faculty of Medicine, Tel-Aviv University, Tel Aviv, Israel
e-mail: Oded.sagiv@sheba.health.gov.il

J. M. Debnam
Department of Neuroradiology, The University of Texas MD Anderson Cancer Center, Houston, TX, USA
e-mail: Matthew.Debnam@mdanderson.org

B. Esmaeli (✉)
Ophthalmic Plastic Surgery, Department of Plastic Surgery, The University of Texas MD Anderson Cancer Center, Houston, TX, USA
e-mail: besmaeli@mdanderson.org.il; besmaeli@mdanderson.org

© Springer Nature Switzerland AG 2022
G. Ben Simon et al. (eds.), *Atlas of Orbital Imaging*,
https://doi.org/10.1007/978-3-030-62426-2_97

1 Signs and Symptoms

Infiltrating carcinoma arising in a pleomorphic adenoma. A patient with a history of an incompletely excised pleomorphic adenoma, with worsening symptoms as described above, or progression on imaging. Pain may be present but its absence does not rule out malignancy. C-myc, a key protein in cell regulation, and the proliferation index Ki-67 were shown to be overexpressed in CA-Ex-PA. Recurrent chromosomal rearrangements of the PLAG1 and HMGA2 genes, a genetic feature retained in carcinoma ex pleomorphic adenoma (ca-ex-PA) that makes it possible to distinguish salivary gland ca-ex-PA from de novo carcinomas was also found in lacrimal ca-ex-PA. Overexpression of the IL-6/JAK/STAT3 pathways was also pronounced in Ca-ex-PA.

2 Differential Diagnosis

Same as for primary, but mainly consider: Recurrent pleomorphic adenoma vs. carcinoma ex-pleomorphic adenoma.

3 Diagnosis

Clinical suspicion is based on history and imaging. Diagnosis is based on pathological analysis. PET/CT can be used to determine FDG-avid areas of the tumor for biopsy and to assess for cervical and distant soft tissue and bone metastases.

4 Treatment

Same considerations as for other types of lacrimal gland carcinomas. Most cases can be treated with globe-sparing surgery followed by radiation; exenteration may be performed in non-resectable tumors confined to the orbit with no CNS involvement.

5 Figures with Captions



Fig. 1 Axial non-contrast CT orbit, soft tissue window shows a well-circumscribed mass in the right superotemporal orbit (arrow) in a patient who underwent prior resection of a "pleomorphic adenoma" at another facility several years earlier

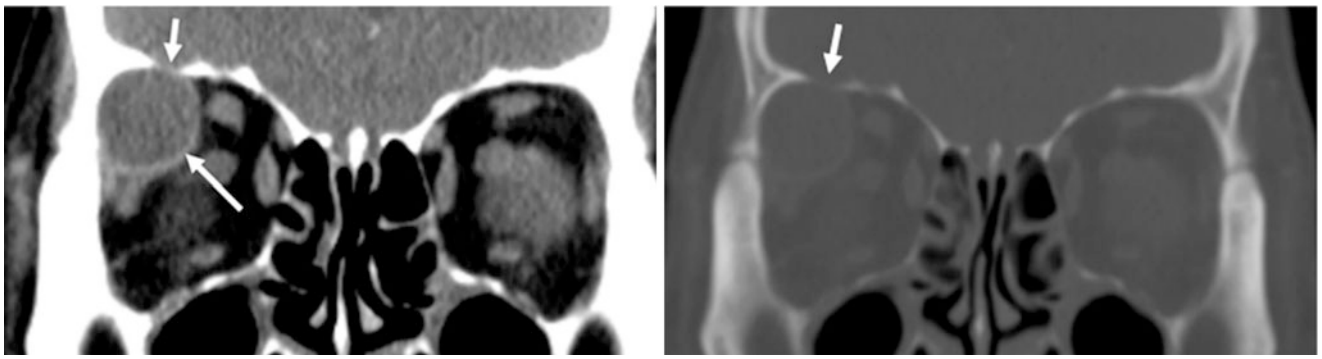


Fig. 2 Coronal non-contrast CT orbit, soft tissue window (left image) of the same patient as in Fig. 1 shows a well-circumscribed mass in the right superotemporal orbit (arrow) with thinning of the orbital roof (short arrow). Note the center of the lesion is somewhat nonhomogenous surrounded by iso-dense rim. Coronal non-contrast CT orbit bone window (right image) demonstrating thinning of the right orbital roof caused by the orbital mass (arrow)

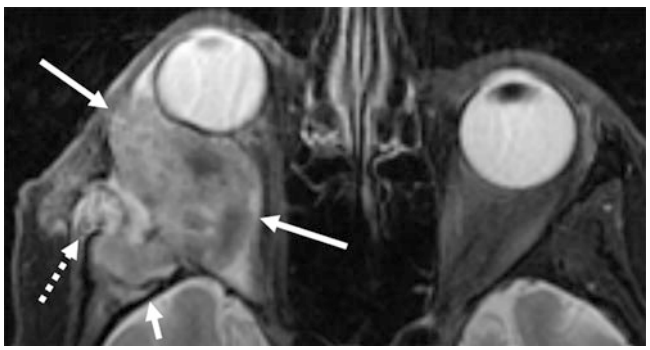


Fig. 3 Axial T2 fat-saturated image. This is a different patient after multiple previous resections of a pleomorphic adenoma at an outside facility who presented with a massive recurrence and transformation to carcinoma ex-pleomorphic adenoma. There is a large heterogeneous multi-lobulated mass (long arrows) in the lateral right orbit with posterior extension towards the apex extending through the sphenoid bone (short arrow) with extra-orbital lateral involvement of the masticator space (infra-temporal fossa) - dotted arrow. The lesion is occupying both intra- and extra-conal compartments. Note proptosis and posterior flattening of the right globe



Fig. 4 Axial T1 post-contrast fat-saturated image of the same patient as in Fig. 3 demonstrates heterogeneous enhancement of the mass (long arrows) with involvement of the sphenoid bone (short arrow) and masticator space (dotted arrow)

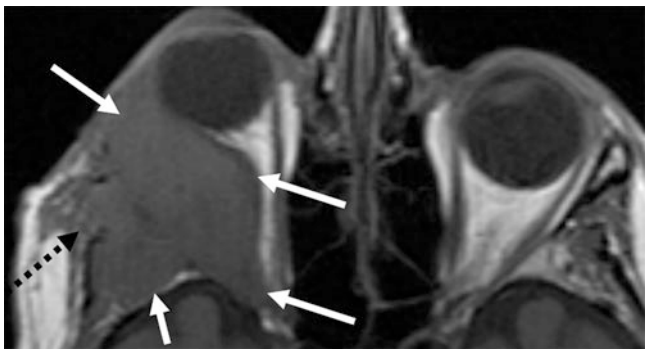


Fig. 5 Axial T1 pre-contrast without fat-saturated image of the same patient as in Fig. 3 demonstrates an isointense orbital mass with extension towards the optic canal (long white arrows) with involvement of the sphenoid bone (short white arrow) and masticator space (dotted black arrow)



Fig. 6 Coronal T1 post-contrast fat-saturated image of the same patient as in Fig. 3 shows extension of the orbital mass (long white arrow) into the orbital roof (short white arrow) and masticator space (dotted black arrow). The mass erodes into the orbital floor (dotted white arrow) but does not involve the maxillary sinus. The patient was treated with orbital exenteration, removal of the cranial extension of the mass, reconstruction with a free flap, and postoperative adjuvant chemoradiation. He is doing well 7 years after treatment

References

1. Esmaeli B. Ophthalmic oncology, vol. 6. Boston: Springer Science & Business Media; 2011.
2. Black EH, Nesi FA, Calvano CJ, Gladstone GJ, Levine MR, editors. Smith and Nesi's ophthalmic plastic and reconstructive surgery. Springer Science & Business Media; 2012. Springer Science+Business Media, LLC, New York, USA.
3. Zhang P, Tang LJ, Gao HH, Zhang WX, Lin JX, Yang HS. Immunohistochemical features of carcinoma ex pleomorphic adenoma and pleomorphic adenoma in the lacrimal gland. Int J Ophthalmol. 2019;12(8):1238–42. https://doi.org/10.18240/ijo.2019.08.02. PMID: 31456912; PMCID: PMC6694048.
4. von Holstein SL, Fehr A, Persson M, Nickelsen M, Therkildsen MH, Prause JU, Heegaard S, Stenman G. Lacrimal gland pleomorphic adenoma and carcinoma ex pleomorphic adenoma: genomic profiles, gene fusions, and clinical characteristics. Ophthalmology. 2014;121(5):1125–33. https://doi.org/10.1016/j.ophtha.2013.11.037. Epub 2014 Jan 24. PMID: 24468654.
5. Andreasen S, von Holstein SL, Homøe P, Heegaard S. Recurrent rearrangements of the PLAG1 and HMGA2 genes in lacrimal gland pleomorphic adenoma and carcinoma ex pleomorphic adenoma. Acta Ophthalmol. 2018;96(7):e768–71. https://doi.org/10.1111/aos.13667. Epub 2018 Feb 13. PMID: 29437290.
6. Andreasen S, Heegaard S, Grauslund M, Homøe P. The interleukin-6/Janus kinase/STAT3 pathway in pleomorphic adenoma and carcinoma ex pleomorphic adenoma of the lacrimal gland. Acta Ophthalmol. 2016;94(8):798–804. https://doi.org/10.1111/aos.13122. Epub 2016 June 11. PMID: 27286739.
7. Larbcharoensub N, Pangpunyakulchai D, Aroonroch R, Tuntiyatorn L, Mahaisavariya P. Lacrimal myoepithelial carcinoma ex recurrent pleomorphic adenoma: a clinicopathological report and review of the literature. Mol Clin Oncol. 2018;8(1):209–13. https://doi.org/10.3892/mco.2017.1488. Epub 2017 Nov 3. PMID: 29387416; PMCID: PMC5769277.
8. Tom A, Bell D, Ford JR, Debnam JM, Guo Y, Frank SJ, Esmaeli B. Malignant mixed tumor (carcinoma ex pleomorphic adenoma) of the lacrimal gland. Ophthalmic Plast Reconstr Surg. 2020;36(5):497–502. https://doi.org/10.1097/IOP.0000000000001625. PMID: 32282452.

Benign (Reactive) Lymphoid Hyperplasia and Lymphoma

33

Oded Sagiv, J. Matthew Debnam, and Bita Esmaeli

Contents

1 **Signs and Symptoms** 271

2 **Differential Diagnosis** 271

3 **Diagnosis** 272

4 **Treatment** 272

5 **Figures with Captions** 272
5.1 Benign (Reactive) Lymphoid Hyperplasia 272
5.2 Lymphoma 273

References 275

Abstract

- Unilateral or bilateral enlarged lacrimal glands
- Homogenous mass on both modalities CT and MR scans
- Post-contrast homogenously enhancing.
- Diffusion weighted imaging (DWI) image shows bright signal with restriction (low signal) on corresponding ADC map consistent with lymphoid tissue / hypercellular mass.
- PETCT may show an FDG-avid lesion.

Keywords

Benign lymphoid hyperplasia · Reactive lymphoid hyperplasia · Lymphoma · Lymphoproliferative disorders of the lacrimal gland

1 Signs and Symptoms

Lymphoproliferative disorders of the lacrimal gland are characteristically of insidious onset. The typical patient will experience gradually progressive painless proptosis over less than one year, with other signs of orbital dysfunction such as ptosis (temporal more than nasal), restriction in eye movements and double vision. Examination may reveal an enlarged lacrimal gland palpable in the superior sulcus as a firm rubbery and non-tender mass. Involvement of the conjunctival, eyelids or other ocular adnexa may also be present. About three-quarters of the cases are unilateral.

2 Differential Diagnosis

The differential diagnosis includes reactive (benign) lymphoid hyperplasia; lymphoma, with the vast majority (over 95%) being B-cell lymphomas, and the most common type

O. Sagiv
The Goldschleger Eye Institute, Sheba Medical Center, affiliated to the Sackler Faculty of Medicine, Tel-Aviv University, Tel Aviv, Israel
e-mail: Oded.sagiv@sheba.health.gov.il

J. M. Debnam
Department of Neuroradiology, The University of Texas MD Anderson Cancer Center, Houston, TX, USA
e-mail: Matthew.Debnam@mdanderson.org

B. Esmaeli (✉)
Ophthalmic Plastic Surgery, Department of Plastic Surgery, The University of Texas MD Anderson Cancer Center, Houston, TX, USA
e-mail: besmaeli@mdanderson.org; besmaeli@mdanderson.org.il

© Springer Nature Switzerland AG 2022
G. Ben Simon et al. (eds.), *Atlas of Orbital Imaging*,
https://doi.org/10.1007/978-3-030-62426-2_20

being extranodular marginal zone lymphoma (EMZL). Other common types include follicular lymphoma, diffuse large B-cell lymphoma, and Mantle cell lymphoma. Other causes for painless enlargement of the lacrimal gland include benign and malignant epithelial tumors as described above, and amyloidosis.

3 Diagnosis

Definitive diagnosis requires a tissue biopsy [1]. If a diagnosis of lymphoma is made, a systemic workup for staging is conducted and usually includes a total-body PET/CT and a bone marrow biopsy.

4 Treatment

Benign lymphoid hyperplasia can be treated with steroids. Treatment of lymphoma depends on the specific histologic type and clinical staging. Generally speaking, low-grade lymphoma localized to the orbit (stage 1E) can be treated with fractionated radiation therapy, with the usual dose being between 15–24 Gy, and with recent evidence that even an ultra-low-dose (4 Gy) is sufficient in most cases [2]. Alternative treatments for elderly patients with oral chlorambucil were also effective. High-grade lymphomas and systemic disease are treated systemically, sometime in combination with radiation therapy.

5 Figures with Captions

5.1 Benign (Reactive) Lymphoid Hyperplasia

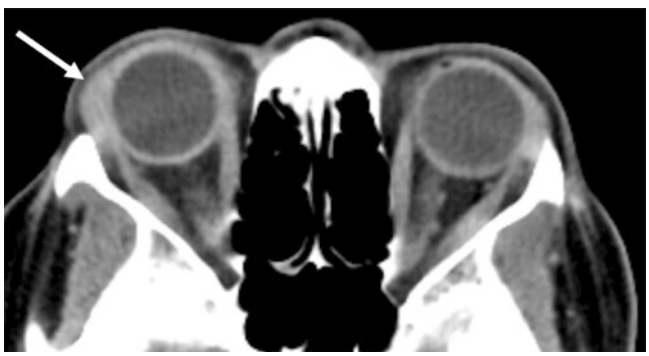


Fig. 1 Axial post-contrast CT orbit, soft tissue window shows asymmetric homogeneous enlargement of the right lacrimal gland, palpebral portion (arrow). The mass is abutting the globe with no indentation and causing mild proptosis

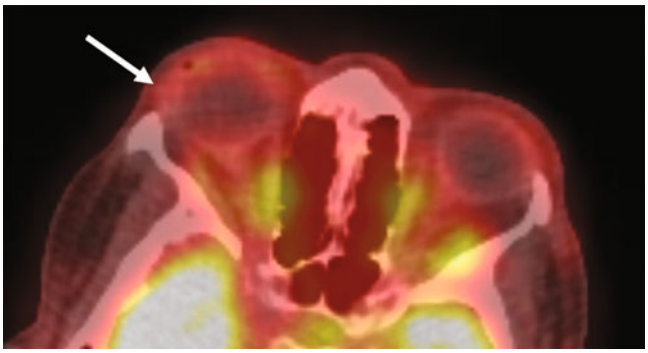


Fig. 2 Axial PET/CT image of the same patient as in Fig. 1.1 demonstrates no FDG activity in the right lacrimal gland (arrow)

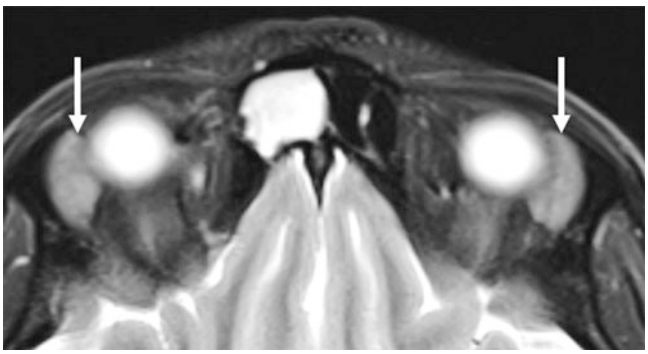


Fig. 3 Axial T2 fat-saturated image (different patient) shows homogeneous symmetrical enlargement of both lacrimal glands' orbital parts (arrows)

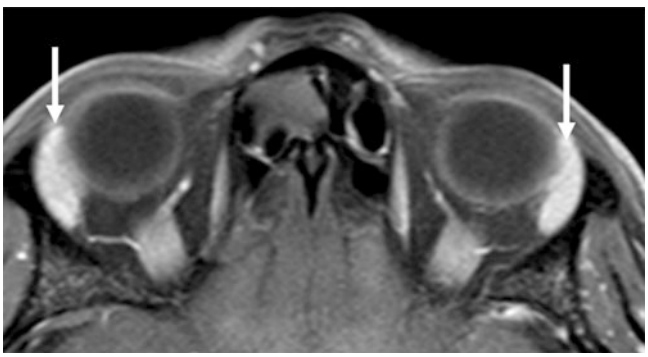


Fig. 4 Axial T1 post-contrast fat-saturated image of the same patient as in Fig. 1.3 shows homogeneous enhancement of enlarged but otherwise normal appearing lacrimal glands (arrows)

5.2 Lymphoma



Fig. 5 **Clinical photograph** of a 46-YOM with two-months history of left painless proptosis, hypoglobus, normal visual acuity and preserved ocular motility. (*courtesy of the editors*)

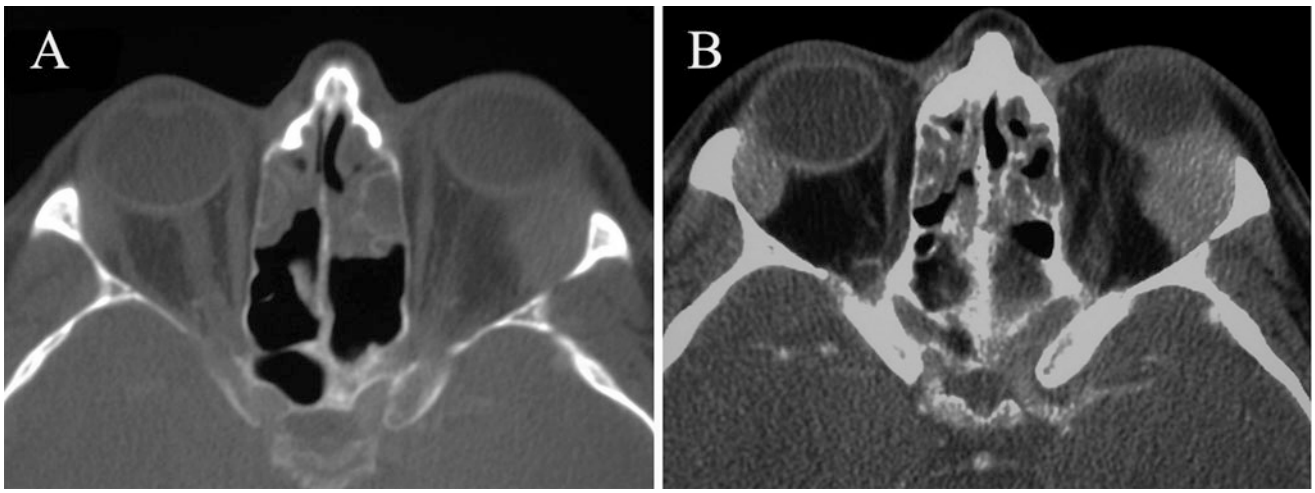


Fig. 6 **Axial CT**, same patient, showing homogenous enlargement of the left lacrimal gland (orbital portion), molding around the globe without indentation (**a**), post contrast scan (**b**) showing homogenous enhancement of the lacrimal gland. Biopsy consisted with the diagnosis of Mucosa Associated B Cell Lymphoma, or MALT. The patient was treated with orbital radiotherapy

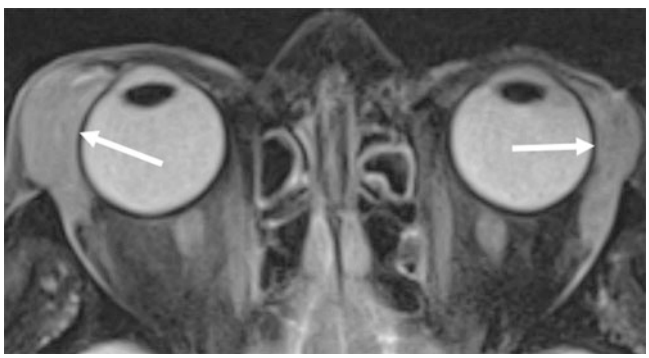


Fig. 7 **Axial T2 fat-saturated image** (different patient) shows homogenous enlargement of both palpebral and lacrimal segments of the lacrimal glands (arrows), right more than left

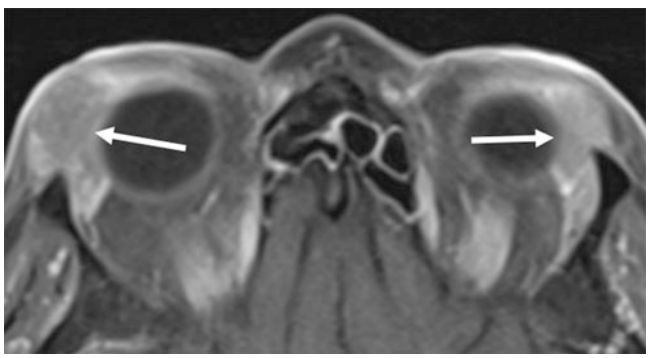


Fig. 8 **Axial T1 post-contrast fat-saturated image** of the same patient as in Fig. 2.1 demonstrates mild enhancement of the enlarged lacrimal glands (arrows)

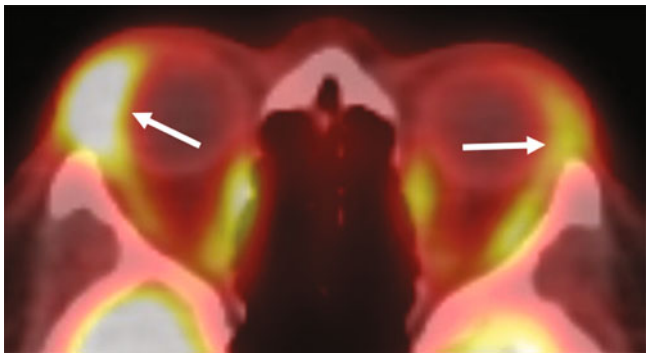


Fig. 9 **Axial PET/CT image** of the same patient as in Fig. 2.1 with increased FDG-avidity of the lacrimal glands (arrows)

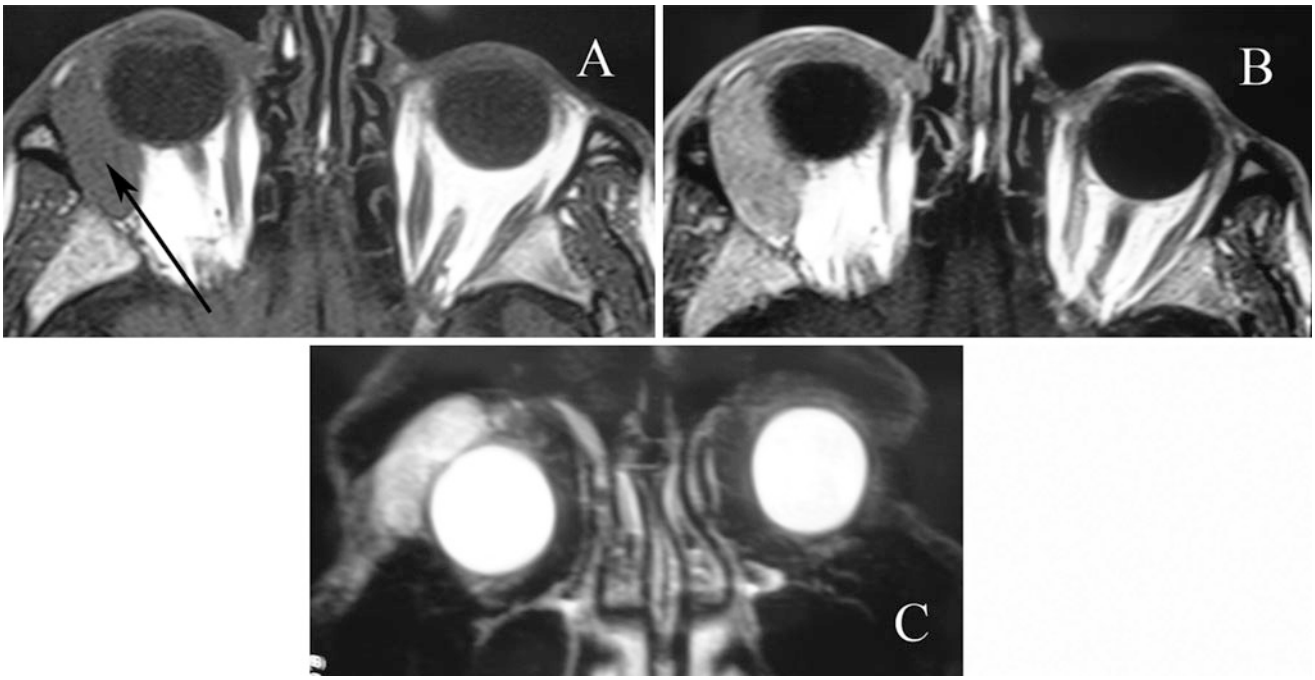


Fig. 10 **Magnetic resonance imaging** (MRI) scan of the orbit of an 80-year old patient presenting with right side proptosis. (**a**) T1 weighted sequence, pre-contrast, revealing a well-defined, circumscribed, supero-temporal orbital mass located in the lacrimal fossa (black arrow). The lesion is isointense to brain gray matter and is molding around orbital structures. No bone destruction or bone erosion is noticed. (**b**) Gadolinium enhanced T1 weighted sequence, axial section, showing homogeneous enhancement of the lesion. (**c**) The lesion is hyper-intense on T2-weighted sequence, coronal section. Orbital biopsy of the lesion demonstrated lymphoma. (Courtesy of the editors)

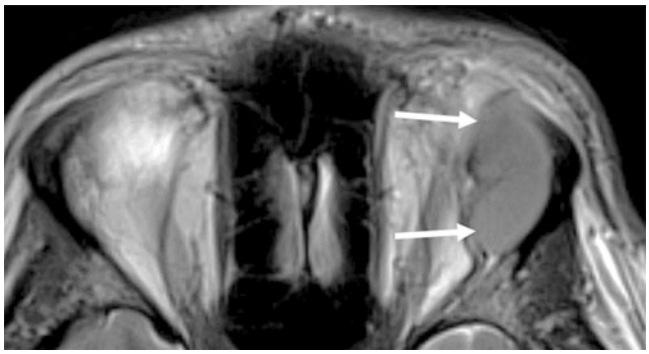


Fig. 11 Axial T2 image of a different patient shows an isointense, homogenous partially lobulated mass located at the left lacrimal gland fossa (arrows). The lesion appears well circumscribed

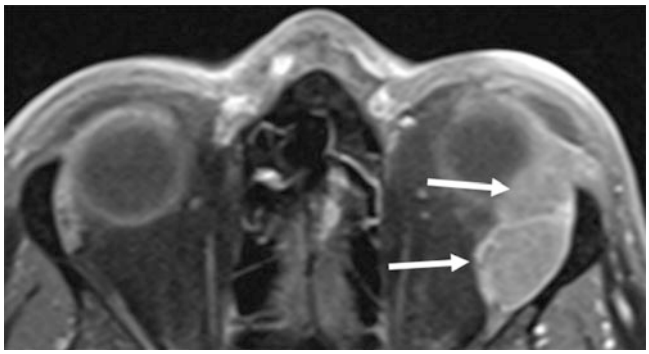


Fig. 12 Axial T1 post-contrast fat-saturated image of the same patient as in Fig. 11 with mild enhancement of the left lateral mass located within the orbital portion of the lacrimal gland (arrows)

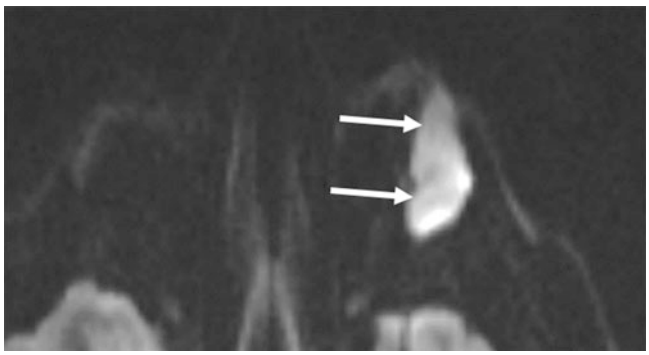


Fig. 13 Axial diffusion weighted (DWI) image of the same patient as in Fig. 11 shows bright signal throughout the left orbital mass (arrows)

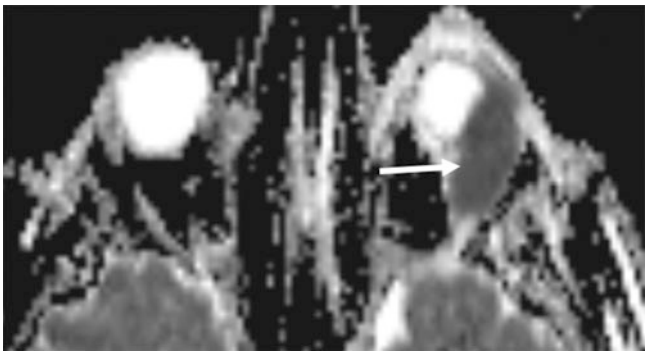


Fig. 14 Axial apparent diffusion coefficient (ADC) map of the same patient as in Fig. 11 shows low signal intensity in the left orbital mass consistent with restricted diffusion in a hypercellular mass (arrow)

References

1. Haradome K, et al. Orbital lymphoproliferative disorders (OLPDs): value of MR imaging for differentiating orbital lymphoma from benign OPLDs. AJNR Am J Neuroradiol. 2014;35(10):1976–82.
2. Pinnix CC, et al. Ultra-low-dose radiotherapy for definitive management of ocular adnexal B-cell lymphoma. Head Neck. 2017;39(6):1095–100.
3. Ben Simon GJ, Cheung N, McKelvie P, Fox R, McNab AA. Oral chlorambucil for extranodal, marginal zone, B-cell lymphoma of mucosa-associated lymphoid tissue of the orbit. Ophthalmology. 2006;113(7):1209–13. https://doi.org/10.1016/j.ophtha.2006.01.057. Epub 2006 Apr 27.
4. Olsen TG, Heegaard S. Orbital lymphoma. Surv Ophthalmol. 2019;64(1):45–66. https://doi.org/10.1016/j.survophthal.2018.08.002. Epub 2018 Aug 23.
5. Olsen TG, Holm F, Mikkelsen LH, Rasmussen PK, Coupland SE, Esmaeli B, Finger PT, Graue GF, Grossniklaus HE, Honavar SG, Khong JJ, McKelvie PA, Mulay K, Sjö LD, Vemuganti GK, Thuro BA, Heegaard S. Orbital lymphoma-An International Multicenter Retrospective Study. Am J Ophthalmol. 2019;199:44–57. https://doi.org/10.1016/j.ajo.2018.11.002. Epub 2018 Nov 10.
6. Briscoe D, Safieh C, Ton Y, Shapiro H, Assia EI, Kidron D. Characteristics of orbital lymphoma: a clinicopathological study of 26 cases. Int Ophthalmol. 2018;38(1):271–7. https://doi.org/10.1007/s10792-017-0457-y. Epub 2017 Mar 31.

Part V

Lacrimal Pathways

Normal Anatomy of the Lacrimal System

34

Swati Singh and Mohammad Javed Ali

Contents

1 **Introduction** 279
2 **Normal Anatomy** 279
3 **Figures with Captions** 280
References 282

Abstract

- Imaging modalities commonly used for assessing lacrimal drainage disorders include digital subtraction dacryocystography (DS-DCG), computed tomography dacryocystography (CT-DCG), and magnetic resonance dacryocystography (MR-DCG).
- CT-DCG can study the bony and soft tissue anatomy of the entire lacrimal drainage tract and is usually preferred over a plain DCG or DS-DCG.
- MR-DCG has superior resolution of soft-tissues of the lacrimal drainage and is usually preferred for functional studies of dye clearance or where soft tissue lesions are suspected.

Keywords

Lacrimal · Imaging · CT-DCG · MR-DCG · ASOCT

1 Introduction

Imaging modalities for clinical use in assessing and managing lacrimal drainage disorders are numerous and include ultrasound B-scan, ultrasound biomicroscopy (UBM), anterior segment optical coherence tomography (ASOCT), plain dacryocystography (DCG), digital subtraction dacryocystography (DS-DCG), computed tomography dacryocystography (CT-DCG), and magnetic resonance dacryocystography (MR-DCG). The mandate of the current section is to provide a brief overview of normal radiological lacrimal drainage anatomy, dacryocystitis, and lacrimal sac malignancies with their relevant radiological features.

2 Normal Anatomy

Lacrimal drainage system comprises of lacrimal punctum, ampulla, canaliculi, lacrimal sac, and nasolacrimal duct (NLD) with its bony and membranous components (Fig. 1) [1].

1. *Lacrimal punctum and canaliculi*: The diameter of lacrimal punctum is 0.2–0.6 mm measured with Fourier domain anterior segment optical coherence tomography (ASOCT) (Fig. 1) [2]. Vertical and horizontal lacrimal canaliculi can be visualized on dacryocystography (DCG) [3].
2. *Lacrimal fossa (LF):* Lacrimal fossa can be easily seen in anterior orbital cuts housing lacrimal sac visible as an isodense soft tissue continuing into NLD (Figs. 2, 3, and 4). Lacrimal fossa is constituted by frontal process of

S. Singh
Center for Ocular Regeneration, L.V. Prasad Eye Institute, Hyderabad, Telangana, India

M. J. Ali (✉)
Govindram Seksaria Institute of Dacryology, L.V. Prasad Eye Institute, Hyderabad, Telangana, India

Center for Ocular Regeneration, L.V. Prasad Eye Institute, Hyderabad, Telangana, India
e-mail: javed@lvpei.org

© Springer Nature Switzerland AG 2022
G. Ben Simon et al. (eds.), *Atlas of Orbital Imaging*,
https://doi.org/10.1007/978-3-030-62426-2_21

maxilla anteriorly, and lacrimal bone posteriorly, with varied contributions that vary across different races. The mean dimensions of the bony lacrimal sac fossa (on radiology) at superior, middle, and inferior levels were 4.1 ± 0.76 (range: 2.9–5.7 mm), 7.0 ± 1.15 (range: 4.9–9.3 mm), and 5.0 ± 0.93 mm (range: 3.4–6.9 mm), respectively. The longitudinal axes of bony LF and bony NLD subtend an average angle of 15° posteriorly, hence lacrimal sac and NLD are not visible initially in the same cuts [4].

3. *Bony NLD:* The walls of NLD are composed of posteromedial bony plate visible as very thin bone or dehiscent wall along the posterior aspect on coronal cuts (Figs. 5, 6, 7, 8, and 9) [5]. Anterolateral bony wall made of maxillary bone can be seen as thick bone that should be carefully looked for in maxillofacial fractures. The narrowest diameter of NLD reported radiologically is 3.8 +/−1 mm.
4. *Surgical anatomy:* Surgical implication of lacrimal fossa anatomy lies in removing the thick frontal process of maxilla (FPM), which tends to be difficult while creating osteotomy in DCR among Asians and Africans [6]. Naso-orbitoethmoid fractures involving lacrimal fossa and/or NLD usually present as displaced FPM, NLD discontinuity, and comminuted lacrimal bone (Fig. 10) [7, 8].

3 Figures with Captions

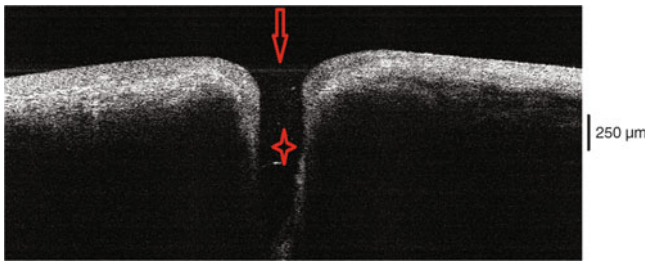


Fig. 1 Anterior segment optical coherence tomography demonstrating the punctum opening (arrow) and the vertical canaliculus (star)

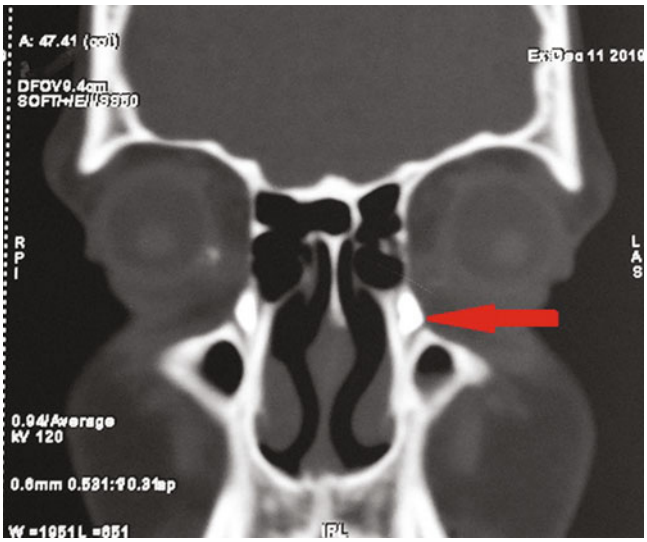


Fig. 2 CT-DCG, coronal cut, bone window demonstrating the bony lacrimal fossa and the dye within both the lacrimal sacs without sac dilation



Fig. 3 CT scan orbits and paranasal sinus, coronal cuts, bony window, demonstrating the bony lacrimal fossae (red arrow). Note the air shadows within the left lacrimal sac – which may be a normal finding

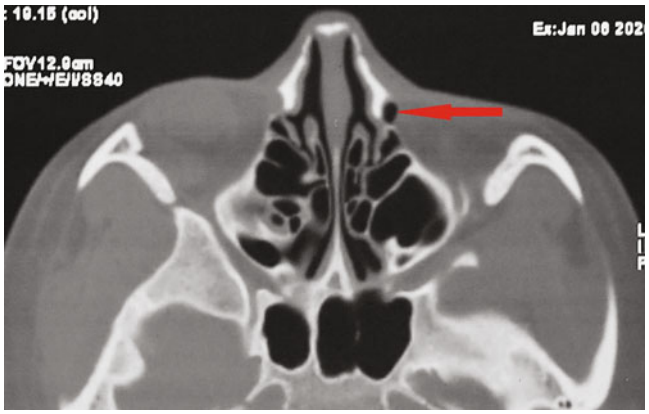


Fig. 4 CT scans, paranasal sinuses and orbits, axial cuts, bony window, demonstrating the axial view of the bony lacrimal fossae. Note the air shadows (red arrow) within the left normal-sized lacrimal sac and compare it with those in Fig. 3

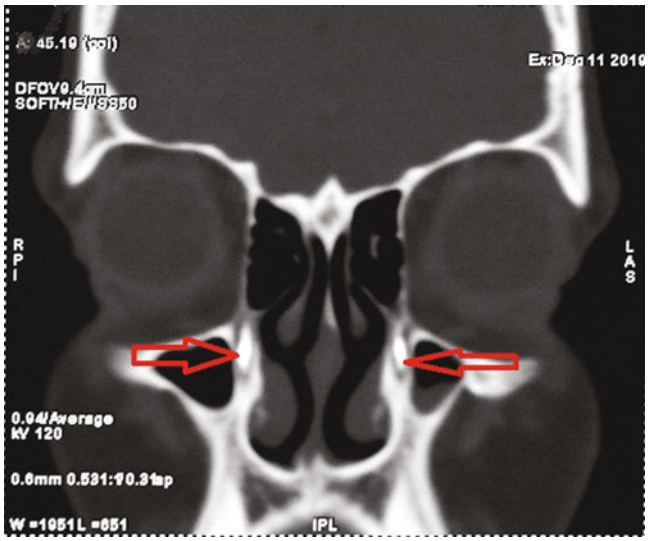


Fig. 5 CT-DCG, coronal cuts, bony tissue window of patient in Fig. 2. Note the dye in both the nasolacrimal ducts (red arrows) which reflect free flow from the sac into the NLD

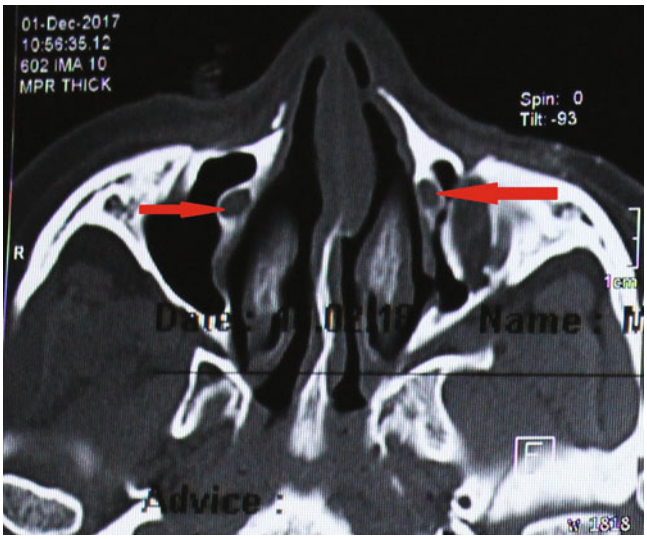


Fig. 6 CT scan, axial cuts, bony window, demonstrating the bony NLD (arrows) bilaterally. Note the normal contours of the bony NLD without any signs of dehiscence

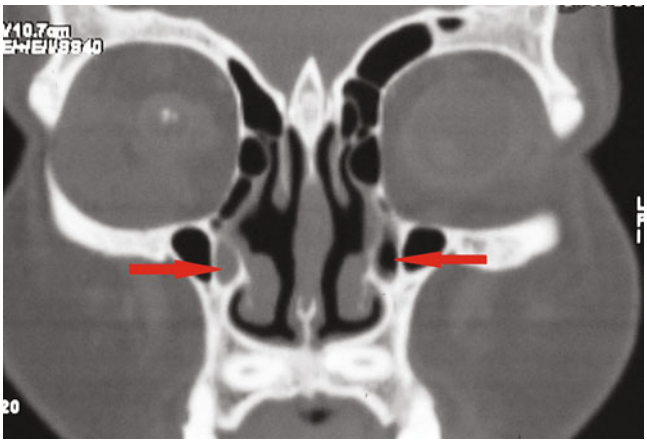


Fig. 7 CT scan orbits and paranasal sinus, coronal cuts, bony window, demonstrating the bony nasolacrimal ducts (NLD). Note the left NLD is aerated while the right is not and is usually secondary to secretions

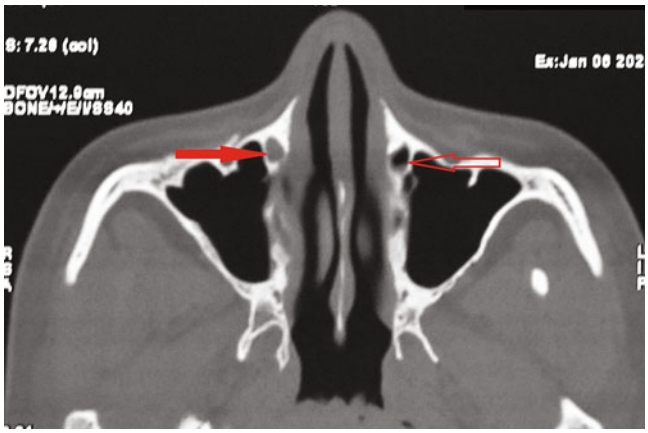


Fig. 8 CT scan, paranasal sinuses, axial cuts, bony window, demonstrating the bony NLDs traversing the maxillary sinus. Note the aerated left NLD (red outline arrow) as compared to the right (red solid arrow), corroborating with the coronal cuts in Fig. 6

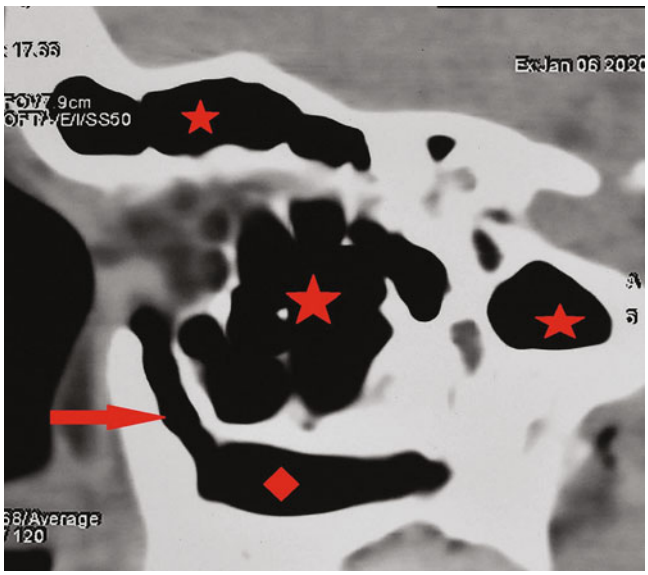


Fig. 9 CT scan, paranasal sinuses, soft tissue window, sagittal reconstruction image showing the bony nasolacrimal duct (red arrow). Also note the frontal, maxillary, and sphenoid sinuses (red stars) and the nasal cavity (red diamond)

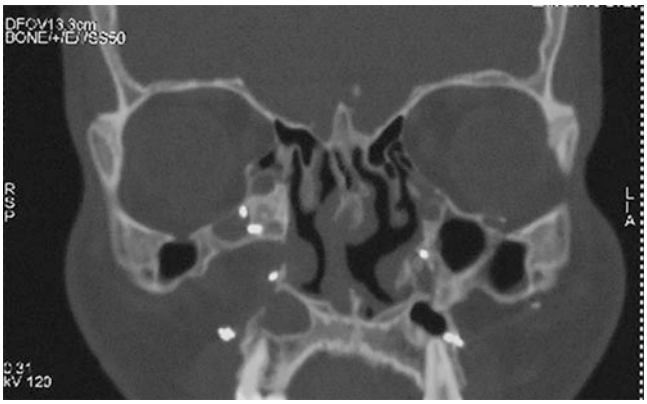


Fig. 10 CT scan, coronal image showing the involvement of the left bony lacrimal drainage apparatus in a trauma. Note the disruption of the normal lacrimal anatomical structures

References

1. Kakizaki H, Ali MJ. Anatomy, physiology and immunology of the lacrimal system. In: Ali MJ, editor. Principles and practice of lacrimal surgery. 2nd ed. Singapore: Springer; 2018. p. 19–39.
2. Kamal S, Ali MJ, Ali MH, Naik MN. Fourier domain optical coherence tomography with 3D and en face imaging of the punctum and vertical canaliculus: a step toward establishing a normative database. Ophthalmic Plast Reconstr Surg. 2016;32:170–3.
3. Singh S, Ali MJ, Paulsen F. Dacryocystography: from theory to current practice. Ann Anat. 2019;224:33–40.
4. Ali MJ, Schicht M, Paulsen F. Morphology and morphometry of lacrimal drainage system in relation to bony landmarks in Caucasian adults: a cadaveric study. Int Ophthalmol. 2018;38:2463–9.
5. Ali MJ. The lacrimal drainage anatomy. In: Atlas of lacrimal drainage disorders. Singapore: Springer; 2018. p. 7–38.
6. Ali MJ, Ganguly A, Ali MH, Naik MN. Time taken for superior osteotomy in primary powered endoscopic dacryocystorhinostomy: is there a difference between an ultrasonic aspirator and a mechanical burr? Int Forum Allergy Rhinol. 2015;5:764–7.
7. Ali MJ, Gupta H, Honavar SG, Naik MN. Acquired nasolacrimal duct obstructions secondary to naso-orbito-ethmoidal fractures: patterns and outcomes. Ophthalmic Plast Reconstr Surg. 2012;28:242–5.
8. Mahesh L, Ali MJ. Imaging modalities for lacrimal disorders. In: Ali MJ, editor. Principles and practice of lacrimal surgery. 2nd ed. Singapore: Springer; 2018. p. 111–22.

Imaging in Lacrimal Drainage Obstruction and Acute Dacryocystitis

35

Swati Singh and Mohammad Javed Ali

Contents

1 **Introduction** 283
2 **Signs and Symptoms** 284
3 **Differential Diagnosis** 284
4 **Diagnosis** 284
5 **Treatment** 284
6 **Image-Guided Dacryolocalization** 284
7 **Figures with Captions** 284
References 288

Abstract

- The AS-OCT is being increasingly used to assess the pre- and post-operative features of a number of proximal lacrimal disorders like incomplete punctal canalization, punctal keratin cyst, idiopathic canalicular inflammatory disease, canaliculops, and punctal stenosis.
- CT-DCG is one of the foremost investigations in lacrimal drainage trauma. It can delineate the trauma, locate the obstruction and position of the lacrimal sac, and other associated lesions.
- CT-DCG and MR-DCG guidance are being increasingly used for image-guided dacryolocalization (IGDL).

Keywords

Lacrimal · Imaging · CT-DCG · MR-DCG · ASOCT · Nasolacrimal duct obstruction

S. Singh
Center for Ocular Regeneration, L.V. Prasad Eye Institute, Hyderabad, Telangana, India

M. J. Ali (✉)
Govindram Seksaria Institute of Dacryology, L.V. Prasad Eye Institute, Hyderabad, Telangana, India

Center for Ocular Regeneration, L.V. Prasad Eye Institute, Hyderabad, Telangana, India

1 Introduction

Several modalities are routinely being used for imaging of the nasolacrimal system and its various pathologies. The AS-OCT is being increasingly used to assess the pre- and post-operative features of a number of proximal lacrimal disorders like incomplete punctal canalization, punctal keratin cyst, idiopathic canalicular inflammatory disease, and canaliculops and punctal stenosis (Figs. 1 and 2) [1–4]. In addition, en face imaging of the punctum provides detailed surface topography and may have potential clinical value (Fig. 3).

CT-DCG is one of the foremost investigations in lacrimal drainage imaging. Not only can it delineate the location of obstruction and position of the lacrimal sac (Figs. 4 and 5) and other associated lesions, it is also useful to study the anatomical flow of the dye through various part of the lacrimal drainage system (Fig. 6). Dilated lacrimal sac in often seen in nasolacrimal duct obstruction (NLDO), especially in cases of long-standing primary acquired nasolacrimal duct obstruction (PANDO) (Fig. 3).

The CT scan occasionally is also useful to assess the location of the mispositioned Lester-Jones tube (Fig. 7). However, information on most of the routinely used stents can be obtained with clinical evaluation alone.

© Springer Nature Switzerland AG 2022
G. Ben Simon et al. (eds.), *Atlas of Orbital Imaging*,
https://doi.org/10.1007/978-3-030-62426-2_22

2 Signs and Symptoms

Tearing with or without purulent discharge and increased tear lake are commonly seen. Patients with acute dacryocystitis present as a painful firm swelling in the region of medial canthus with overlying skin being erythematous and inflamed [5]. It can be infective or noninfective. Lacrimal sac mucoceles can be regurgitant or nonregurgitant with blocked lacrimal irrigation (soft stop). Similar signs may be noted in PANDO but without pain or inflammation.

3 Differential Diagnosis

Tearing can also be secondary to ocular surface abnormalities, mostly dry eye, blepharitis, or eyelid malposition. In an infant, congenital glaucoma should be ruled out. Encysted mucoceles can mimic lacrimal sac tumors and are differentiated based on history, lacrimal irrigation, and radiological findings.

4 Diagnosis

PANDO diagnosis is based on history, clinical examination, fluorescein dye disappearance test (FDDT), and lacrimal irrigation [6]. Diagnosis of dacryocystitis is often clinical, and imaging is performed in suspicious situations like atypical nonresponsive dacryocystitis, history of mass lesion extending above medial canthus, blood stained tears, and traumatic secondary NLD obstructions (Fig. 8). Acute dacryocystitis can present as an enlarged lacrimal sac with heterodense internal consistency, enhanced rim effect because of the well-demarcated lacrimal sac wall, and spill-over inflammation in the orbit (Figs. 9 and 10).

5 Treatment

Various lacrimal drainage procedures can be offered to patients with NLDO, depending on severity of symptoms and patients' preferences [7, 8].

However, in cases of acute dacryocystitis, early treatment is mandatory and includes systemic antibiotics, local warm compresses, and analgesics. Endoscopic dacryocystorhinostomy (DCR) can be performed in acute stage for primary and secondary NLD obstruction, however external DCR is performed once the acute stage resolves [9, 10]. In refractory canalicular obstruction, a bypass with Lester-Jones tube can be advised.

6 Image-Guided Dacryolocalization

Image-guided dacryolocalization is a technique of using intraoperative radiological assistance to localize the lacrimal sac or nasolacrimal ducts [11]. It involves either a plain CT or preferably a CT-DCG obtained using specific navigation protocols, which the computer then utilizes to guide the surgeons with regards to their locations intraoperatively (Figs. 11 and 12) [12]. It has good value in cases of trauma or gross craniofacial anomalies, where the normal clinical anatomy is disturbed and the surgeon would need to know the exact structures and their locations in an altered anatomical setting [13]. The computer can also guide the surgeon with regards to the anatomical structures behind a denoted point intraoperatively.

7 Figures with Captions

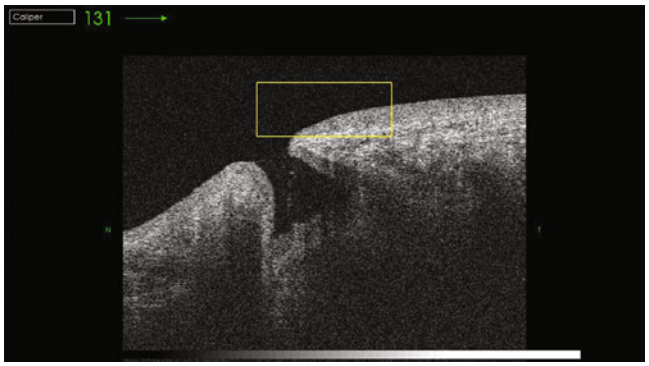


Fig. 1 AS-OCT of the punctum and vertical canaliculus following a 6-week monoka-stent dilatation in a case of punctal stenosis. Note the confirmation of the vertical canaliculus to the shape of the monoka head

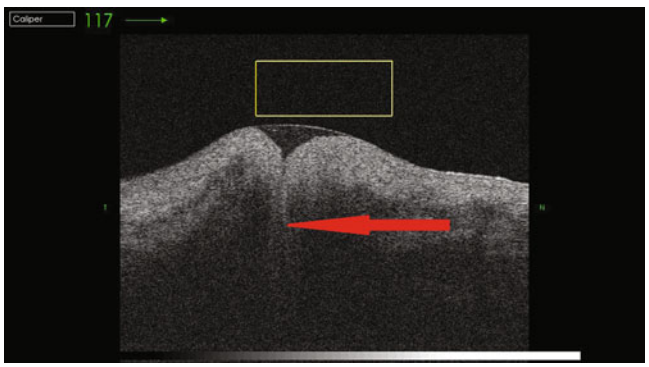


Fig. 2 AS-OCT in a case of idiopathic canalicular inflammatory disease (ICID) stage 1–2 demonstrating the approximated punctal orifice edges because of the mucosal edema and nearly occluded vertical canaliculus (red arrow)

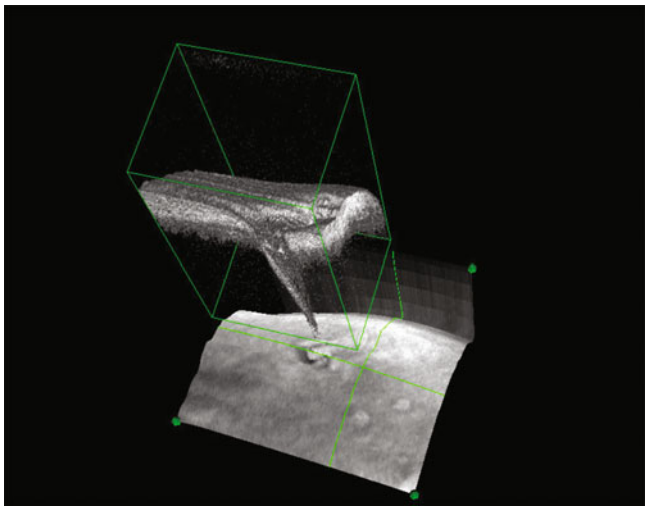


Fig. 3 En-Face AS-OCT imaging of the punctum demonstrating its topography. Note the 3D reconstruction of the punctum and peri-punctal area represented within the cube

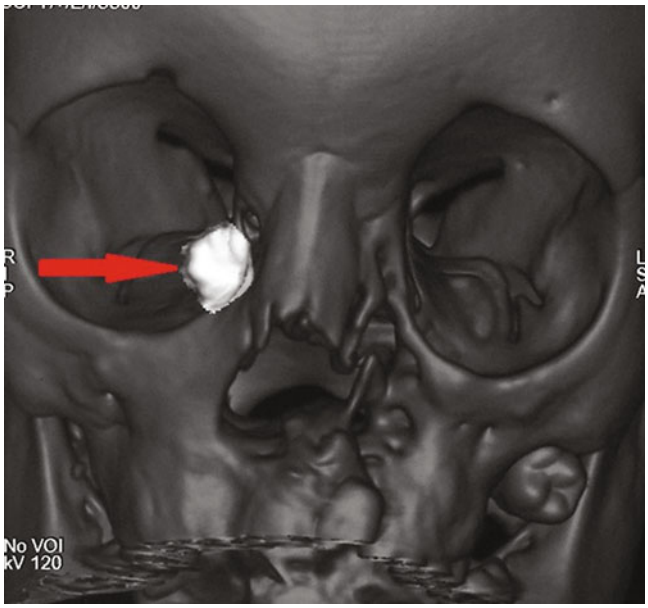


Fig. 4 3D volume rendered CT-DCG demonstrating a dilated lacrimal sac (red arrow) and obstruction at the sac duct junction in a case of PANDO

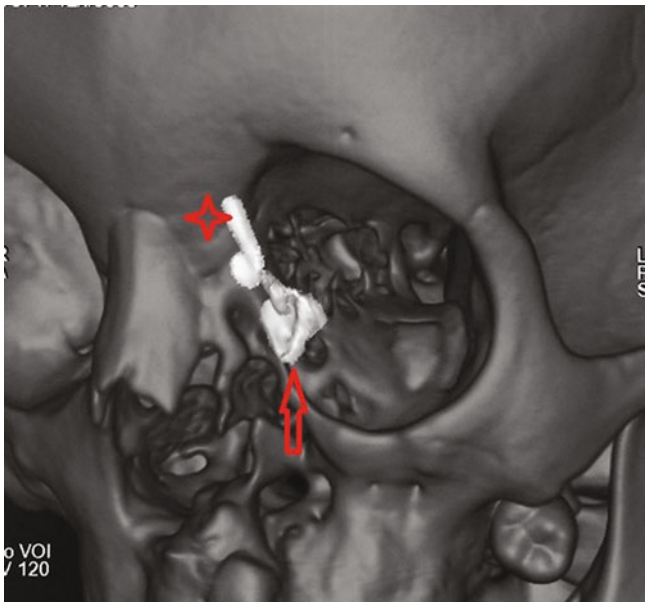


Fig. 5 3D volume rendered CT-DCG demonstrating an irregular lacrimal sac (arrow) and spill over from the superior canaliculus (red star)

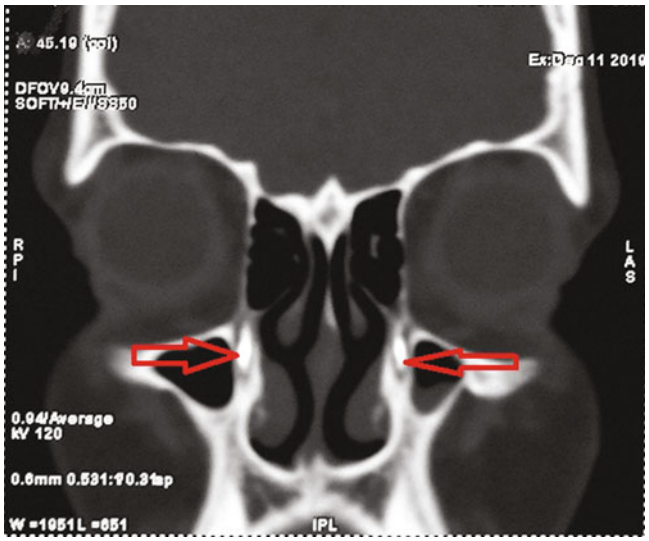


Fig. 6 CT scans, coronal cuts, and bone window demonstrating the flow of the dye from the lacrimal sac into the nasolacrimal ducts

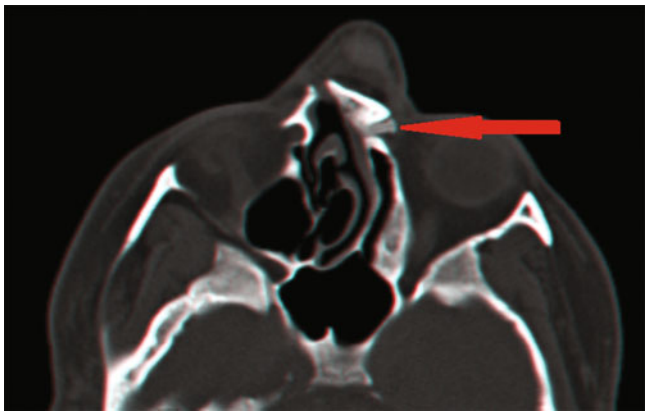


Fig. 7 CT scan, axial cut, and bony window, demonstrating the mis-positioned left-sided Lester-Jones tube (red arrow). Note the tube is displaced laterally and is not within the nasal cavity



Fig. 8 A 3D volume rendered CT scan of the skull demonstrating the lacrimal drainage trauma in a naso-orbitoethmoid fracture that was repaired. Note the numerous screws and plates



Fig. 9 Acute dacryocystitis with orbital cellulitis: CT scan, axial cut, and soft tissue window, showing an enlarged lacrimal sac (red border arrow) with variable internal density. Note the fuzzy borders and spill-over orbital inflammation (arrowhead)

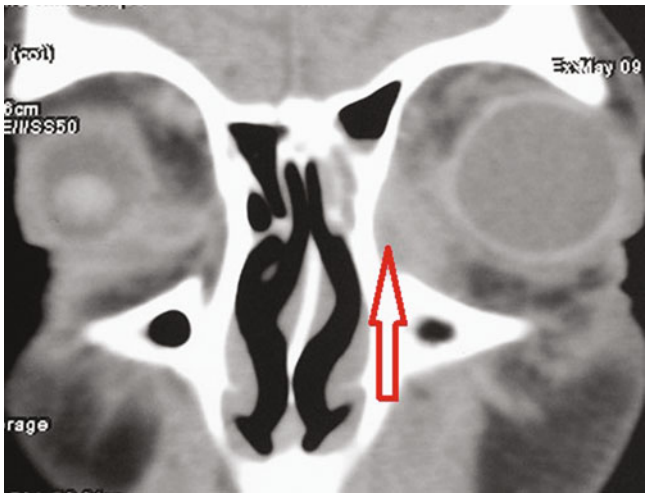


Fig. 10 Acute dacryocystitis with orbital cellulitis: CT scan, coronal cut, and soft tissue window of the patient in Fig. 9. Note the enlarged lacrimal sac (red arrow) with medial orbital haziness

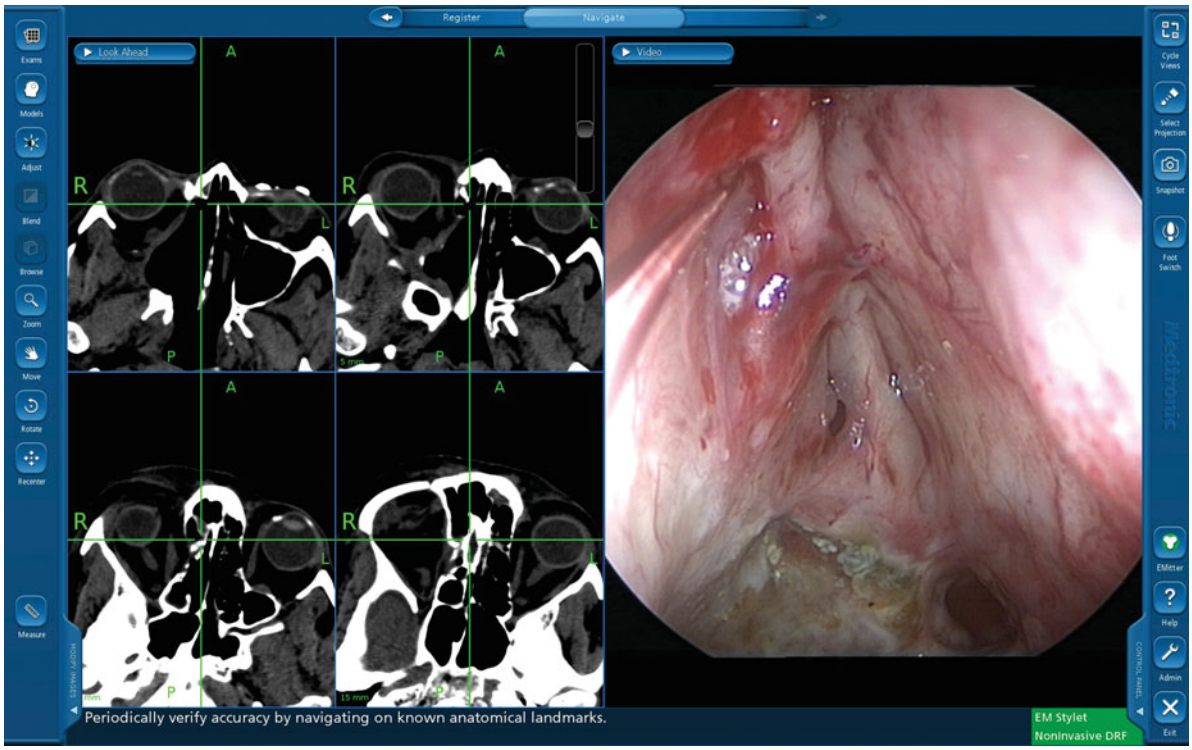


Fig. 11 Intraoperative navigation image showing the attempts at localizing the lacrimal sac (right panel endoscopy). The left panel is that of CT-DCG, axial cuts, demonstrating the exact location of the probe tip, live, intraoperatively. Note that the probe tip appears to be behind the lacrimal sac

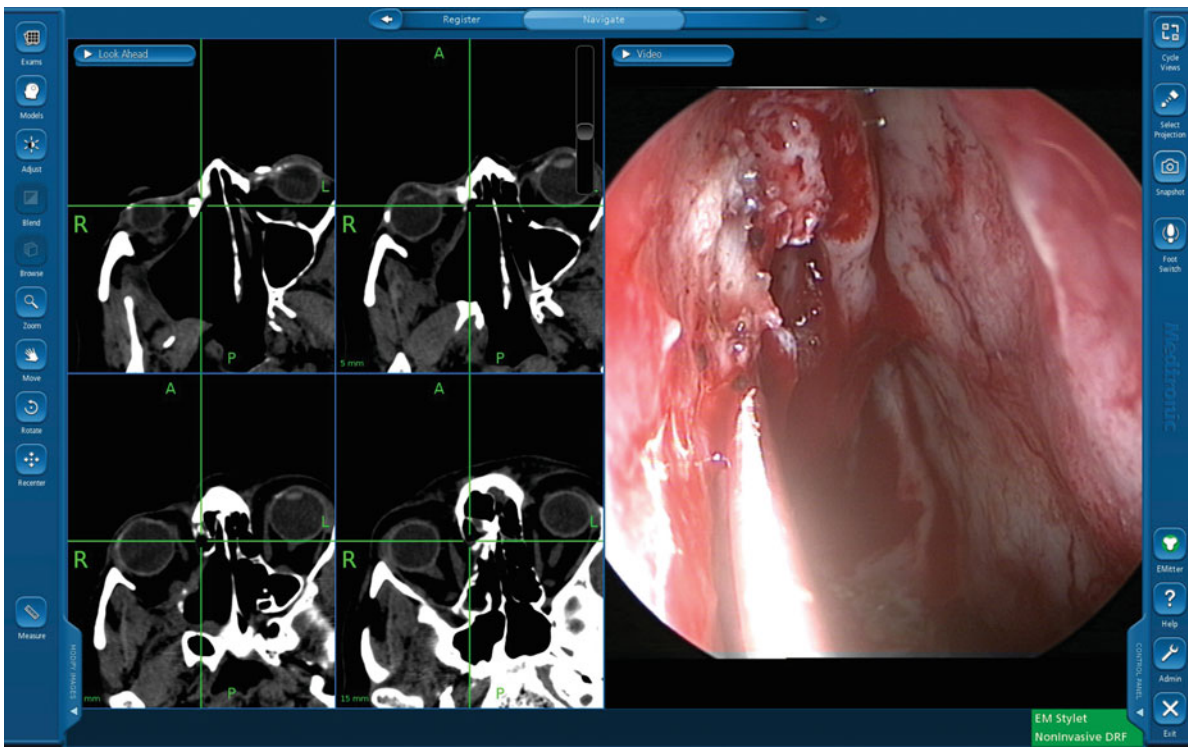


Fig. 12 Intraoperative navigation image of the same patient as in Fig. 11. Note now the accurate localization in the top right axial CT image. The subsequent CT images demonstrate the radiological structures the surgeon would encounter in 5, 10, and 15 mms from the probe tip in the same direction

References

1. Ali MJ. Idiopathic canalicular inflammatory disease: new disease description of clinical patterns, investigations, management, and outcomes. Ophthalmic Plast Reconstr Surg. 2018;34:528–32.
2. Singh S, Ali MJ, Naik MN. Familial incomplete punctal canalization: clinical and fourier domain optical coherence tomography features. Ophthalmic Plast Reconstr Surg. 2017;33:e66–9.
3. Kamal S, Ali MJ, Naik MN. Punctal keratinizing cyst: report in a pediatric patient with Fourier domain optical coherence tomography features. Ophthalmic Plast Reconstr Surg. 2015;31:161–3.
4. Singh S, Ali MJ, Peguda HK, Naik MN. Imaging the canaliculops with ultrasound biomicroscopy and anterior segment ocular coherence tomography. Ophthalmic Plast Reconstr Surg. 2017;33:e143–4.
5. Ali MJ, Joshi SD, Naik MN, Honavar SG. Clinical profile and management outcome of acute dacryocystitis: two decades of experience in a tertiary eye care center. Semin Ophthalmol. 2015;30: 118–23.
6. Kamal S, Ali MJ. Primary acquired nasolacrimal duct obstruction (PANDO) and secondary acquired lacrimal duct obstruction (SALDO). In: Ali MJ, editor. Principles and practice of lacrimal surgery. 2nd ed. Singapore: Springer; 2018. p. 165–74.
7. Ali MJ, Psaltis AJ, Murphy J, Wormald PJ. Powered endoscopic dacryocystorhinostomy: a decade of experience. Ophthalmic Plast Reconstr Surg. 2015;31:219–21.
8. Dave TV, Ezeanosike E, Naik MN, Ali MJ. Outcomes in pediatric external dacryocystorhinostomy: a single-center experience. Orbit. 2019;38:103–6.
9. Chong KK, Abdulla HAA, Ali MJ. An update on endoscopic mechanical and powered dacryocystorhinostomy in acute dacryocystitis and lacrimal abscess. Ann Anat. 2020;227:151408.
10. Kamal S, Ali MJ, Pujari A, Naik MN. Primary powered endoscopic dacryocystorhinostomy in the setting of acute dacryocystitis and lacrimal abscess. Ophthalmic Plast Reconstr Surg. 2015;31:293–5.
11. Ali MJ, Naik MN. Image-guided dacryolocalization (IGDL) in traumatic secondary acquired lacrimal drainage obstructions (SALDO). Ophthalmic Plast Reconstr Surg. 2015;31:406–9.
12. Ali MJ, Singh S, Naik MN, et al. Interactive navigation-guided ophthalmic plastic surgery: the utility of 3D CT-DCG-guided dacryolocalization in secondary acquired lacrimal duct obstructions. Clin Ophthalmol. 2016;11:127–33.
13. Ali MJ, Singh S, Naik MN. Image-guided lacrimal drainage surgery in congenital arrhinia-microphthalmia syndrome. Orbit. 2017;36: 137–43.

Lacrimal Sac Tumors Imaging

36

Swati Singh and Mohammad Javed Ali

Contents

1 **Introduction** 289
2 **Signs and Symptoms** 290
3 **Differential Diagnosis** 290
4 **Diagnosis** 290
5 **Treatment** 290
6 **Figures and Captions** 290
References 294

Abstract

- Lacrimal sac tumors are rare and can be benign or malignant.
- Contrast-enhanced computed tomography (CT) or magnetic resonance imaging (MRI) are the initial investigations of choice with variable contrast enhancement.
- Reported imaging features include expansion of the NLD, erosion of NLD, medial canthus involvement, and sino-nasal spread.
- MRI is the preferred modality for soft tissue assessment and may partly help in differentiating inflammatory lesions from malignant ones.
- Distant metastases are usually investigated with positron emission tomography.

Keywords

Lacrimal sac tumor · Sino-nasal malignancy · CT scan · MRI

1 Introduction

Lacrimal drainage tumors are not very common and can be both benign and malignant. The common malignancies include squamous cell carcinomas (most common), transitional cell carcinomas, mucoepidermoid carcinomas, lymphoproliferative tumors, and melanomas [1–3]. Radiological investigation is a keystone in diagnosis and surgical planning. Contrast-enhanced CT or MRI are investigations of choice (Figs. 1, 2, 3, 4, 5, 6, 7, and 8) [2–4]. CT imaging with thin slices (1.25 mm) helps in assessing the bony involvement and differentiating the expansion versus erosion of NLD canal (Figs. 4 and 5) [3, 4]. MRI is usually preferred for soft tissue assessment and local infiltration [4].

S. Singh
Center for Ocular Regeneration, L.V. Prasad Eye Institute, Hyderabad, Telangana, India

M. J. Ali (✉)
Govindram Seksaria Institute of Dacryology, L.V. Prasad Eye Institute, Hyderabad, Telangana, India

Center for Ocular Regeneration, L.V. Prasad Eye Institute, Hyderabad, Telangana, India

© Springer Nature Switzerland AG 2022
G. Ben Simon et al. (eds.), *Atlas of Orbital Imaging*,
https://doi.org/10.1007/978-3-030-62426-2_24

2 Signs and Symptoms

Typical clinical presentation includes epiphora with lacrimal fossa mass lesion with inconsistent presence of pain and blood-stained epiphora (hemolacria) [1–3]. Acute dacryocystitis can be the presenting sign of lacrimal sac tumors [5].

3 Differential Diagnosis

In early stages when a mass lesion is not apparent, dacryocystitis due to NLD obstruction can be confused with tumors. Necrotizing sialmetaplasia of lacrimal sac can closely mimic undifferentiated lacrimal sac tumor. Radiology (CT and MRI) helps in not only differentiating the lacrimal sac tumors from infective dacryocystitis but also for assessing the details of the tumor dimensions and extension which would help in surgical planning (Figs. 1, 2, 3, 4, and 5) [4].

4 Diagnosis

Tissue biopsy is necessary for the accurate diagnosis and differentiating benign tumors from the malignant ones. Almost 33–40% are detected incidentally during a dacryocystorhinostomy (DCR) surgery [2, 3].

5 Treatment

It depends upon the type of tumors. For benign lesions, complete excision of the tumorous lesion/lacrimal sac is sufficient whereas malignant lacrimal tumors require en-bloc surgical excision of the lacrimal system followed by radiotherapy and/or chemotherapy [1–3].

6 Figures and Captions

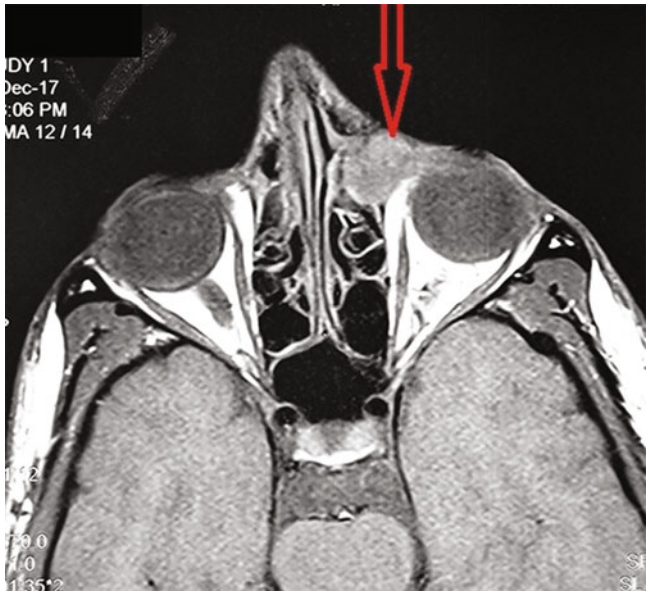


Fig. 1 Lacrimal sac malignancy: T1-weighted MRI orbits, axial cut, showing an isointense mass lesion in the lacrimal fossa (red arrow), which later proved to be an evolving transitional cell carcinoma

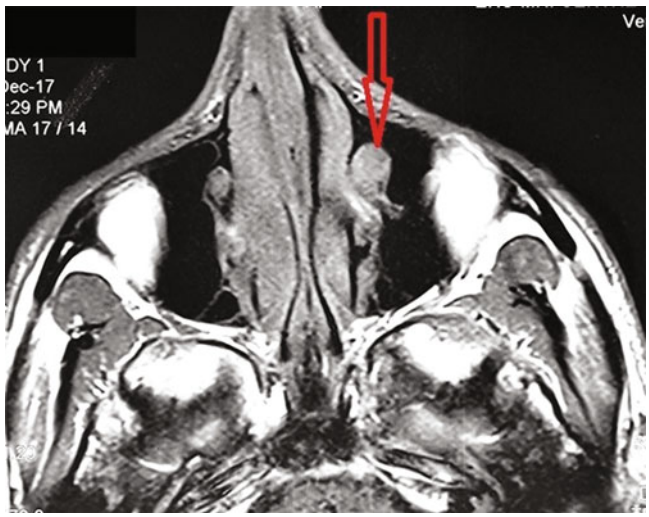


Fig. 2 Lacrimal sac malignancy: T1-weighted MRI, nasal cavity, of the patient in Fig. 1. Note the intranasal extension of the tumor (red arrow)

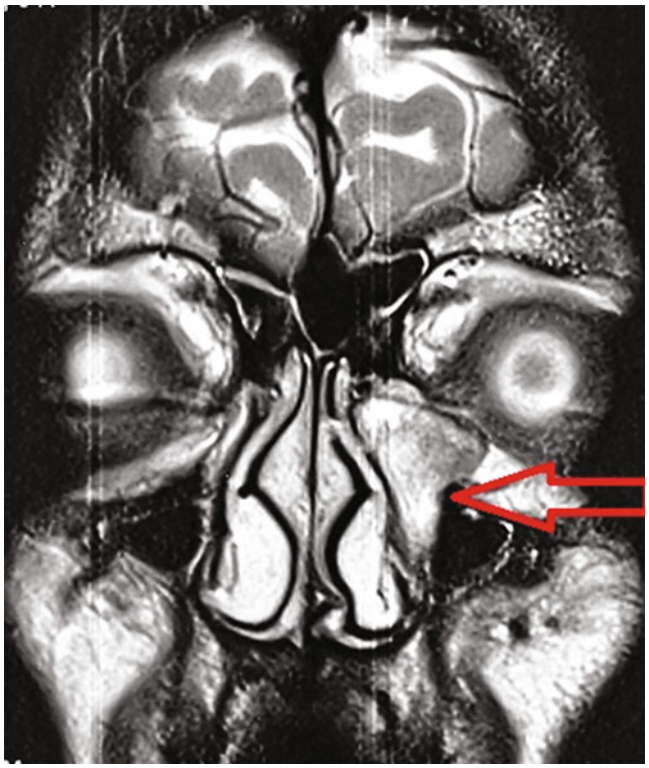


Fig. 3 Lacrimal sac malignancy: T1-weighted MRI orbits, coronal cut demonstrating the tumor extension into the nasolacrimal ducts. This was later proved to be a solitary fibrous tumor

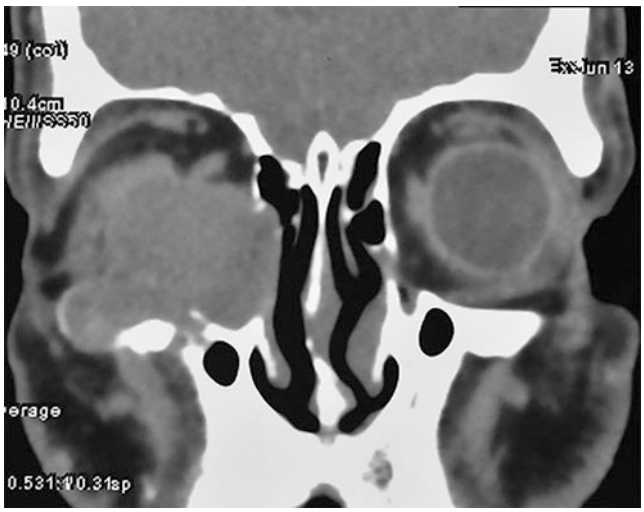


Fig. 4 Lacrimal sac malignancy: CT scan orbits, coronal cut, soft tissue window, demonstrating the orbital extension of the tumor with bony erosion of the floor but without intranasal extension. Histopathology proved it to be a case of a long-standing solitary fibrous tumor

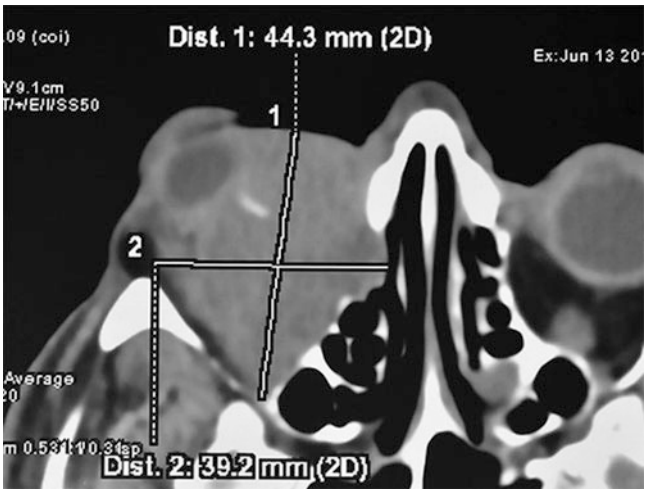


Fig. 5 Lacrimal sac malignancy: CT scan orbits, axial cut, of the patient in Fig. 4. Note the massive orbital extension with gross proptosis and dystopia

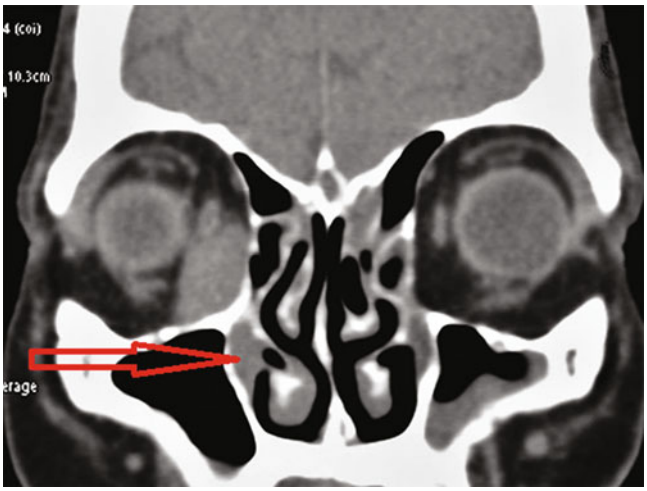


Fig. 6 CT scans, coronal cuts, soft tissue window demonstrating a large right lacrimal sac mass with extension into the inferior meatus (red arrow). Histopathology proved it to be a case of primary adenocarcinoma of the lacrimal sac

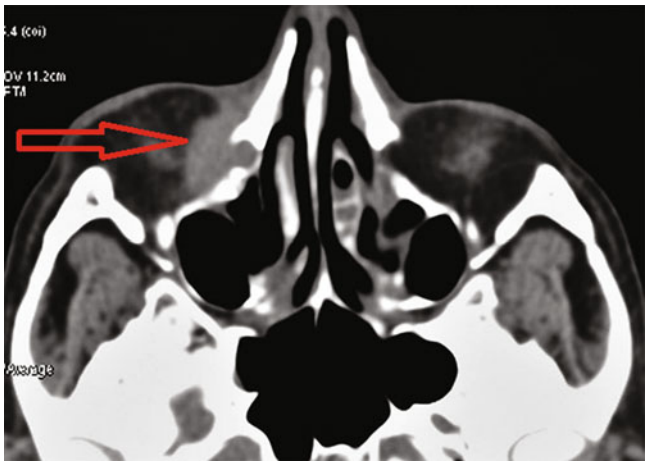


Fig. 7 CT scans, axial cuts, soft tissue window of the patient in Fig. 6, demonstrating the orbital extensions of the adenocarcinoma (red arrow)

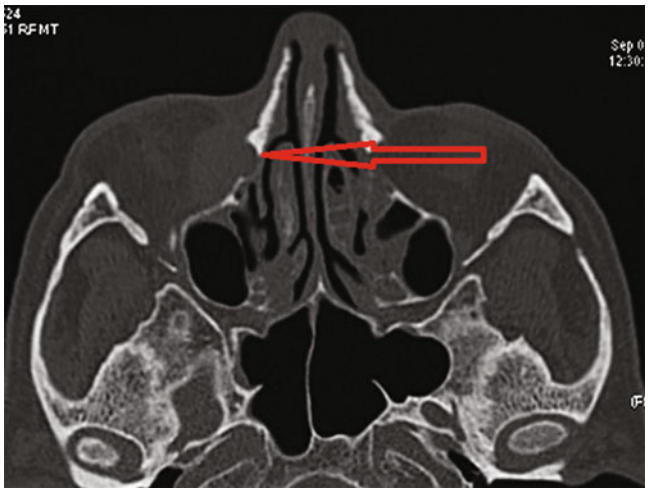


Fig. 8 CT scans, axial cuts, bony window of the patient in Figs. 6 and 7 demonstrating the bony involvement (red arrow)



Fig. 9 Clinical photograph of a young male with right lacrimal sac adenocarcinoma. Note superior and temporal displacement of the right globe with mild proptosis

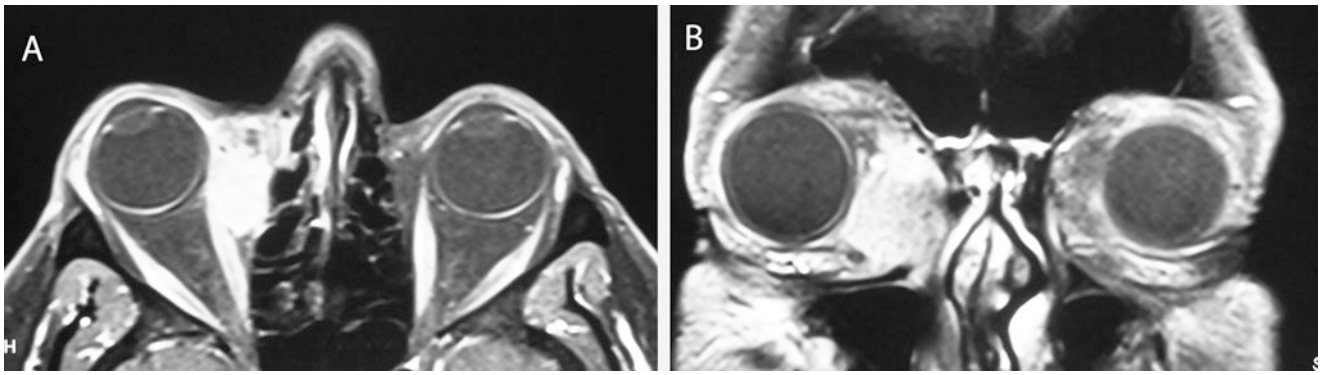


Fig. 10 CE-T1-FS MR axial scan of the same patient showing an infiltrative homogenously enhanced mass epi-centered at the right lacrimal sac fossa. The lesion is displacing the right globe and MR muscle temporally and anteriorly and infiltrating the right nasal space. There is no IC involvement. (Courtesy of Alan A. McNab, MD)

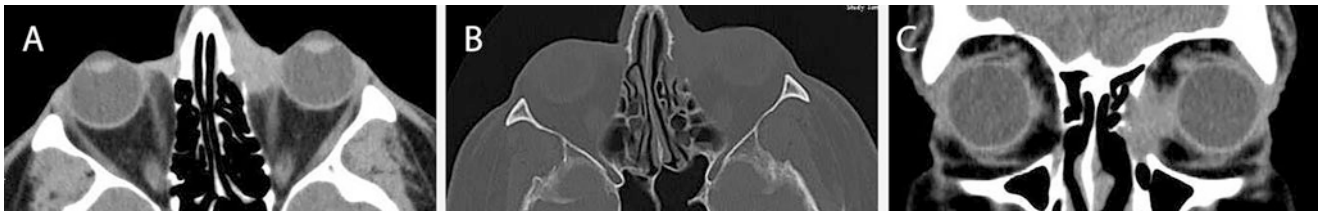


Fig. 11 NC-CT scan of a patient with muco-epidermoid carcinoma of the left lacrimal sac: (**a**) axial section, soft tissue window showing a homogenous mass centered at the left lacrimal sac infiltrating the anterior nasal space. The lesion is displacing the globe temporally and anteriorly; (**b**) axial section, bone window, better demonstrates left medial wall destruction; and (**c**) coronal section showing the vertical extent of the tumor. (Courtesy of Alan A. McNab, MD)



Fig. 12 Clinical photograph of an elderly male with left anterior-medial orbital mass proven to be squamous cell carcinoma of the lacrimal sac

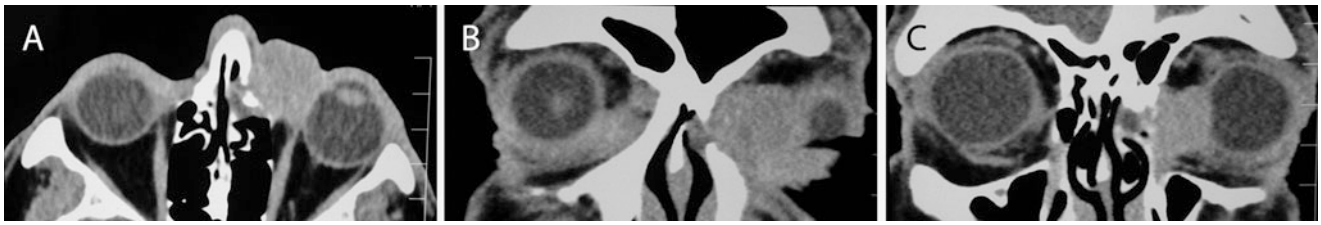


Fig. 13 NC-CT scan of the same patient: axial (**a**) and coronal (**b**, **c**) scans. There is a homogenous mass of the left lacrimal sac invading the anterior nasal space and the medial orbit. The lesion is displacing the globe temporally and anteriorly and causing marked globe indentation. The patient underwent en-bloc resection of the lacrimal drainage apparatus with good postoperative course. (Courtesy of Alan. A. McNab, MD)

References

1. Sundar G. Tumors of the lacrimal drainage system. In: Ali MJ, editor. Principles and practice of lacrimal surgery. 2nd ed. Singapore: Springer; 2018. p. 419–30.
2. Singh S, Ali MJ. Lymphoproliferative tumors involving the lacrimal drainage system: a major review. Orbit. 2019;3:1–9.
3. Singh S, Ali MJ. Primary malignant epithelial tumors of the lacrimal drainage system: a major review. Orbit. 2020;39:276–84.
4. Singh S, Ali MJ, Paulsen F. Dacryocystography: from theory to current practice. Ann Anat. 2019;224:33–40.
5. Mishra DK, Ali MJ, Bhargava A, Naik MN. Acute dacryocystitis as a presenting sign of chronic lymphocytic leukemia. Clin Exp Ophthalmol. 2016;44:67–9.

Part VI

Primary Orbital Tumors

Orbital Lymphoma

37

Jaskirat Aujla, Valerie Juniat, Sandy Patel, and Dinesh Selva

Contents

1 Signs and Symptoms 298

2 Differential Diagnosis 298

3 Diagnosis 298

4 Treatment 298

5 Figures with Captions 298
5.1 Case 1 298
5.2 Case 2 299
5.3 Case 3 301
5.4 Case 4 302
5.5 Case 5 302
5.6 Case 6 304
5.7 Case 7 305

References 305

Abstract

Most common features of orbital lymphoma:

- Presentation 5th–7th decade
- Primary orbital disease
- Approximately one quarter have systemic lymphoma
- Unilateral
- Extraconal, involving supero-temporal quadrant or lacrimal gland
- Anterior orbit
- Can be well circumscribed or diffuse
- Moulding to structures
- Other less common features include involvement of any orbital quadrant (including intraconal), extraocular muscle involvement, multifocal within the same orbit or bilateral
- Can be a trans-spatial/multi-compartment lesion (i.e., can involve adjacent compartments even though the separating bone appears intact)
- Bone involvement is atypical, but can occur and cause bony erosion

Computed tomography (CT) features include:

- Homogeneous mass
- Isodense or slightly hyperdense to extraocular muscles
- Mild to moderate contrast enhancement

Magnetic resonance imaging (MRI) features include:

- T1-weighted MRI signal which is iso- to hypointense to muscle
- T2-weighted MRI signal which is iso- to mildly hyperintense to muscle on fat sat, and iso- to mildly hypointense on conventional non-fat sat

J. Aujla · V. Juniat · D. Selva (✉)
South Australian Institute of Ophthalmology, Adelaide, SA, Australia
e-mail: Jaskirat.aujla@uqconnect.edu.au; vjuniat@doctors.org.uk

S. Patel
Department of Radiology, Royal Adelaide Hospital, Adelaide, SA, Australia

© Springer Nature Switzerland AG 2022
G. Ben Simon et al. (eds.), *Atlas of Orbital Imaging*,
https://doi.org/10.1007/978-3-030-62426-2_25

- Restricted diffusion-weighted MRI (due to increased tumor cellularity)
- Homogeneous contrast enhancement (variable intensity)

Keywords

Orbital lymphoma · Lymphoproliferative disease

1 Signs and Symptoms

- Progressive proptosis
- Palpable mass, swelling, and globe displacement
- Others include diplopia, decreased visual acuity, and ptosis
- Inflammatory signs of periorbital oedema and irritation/pain may occur
- Systemic symptoms such as fever, night sweats, and weight loss are uncommon [1–3]

2 Differential Diagnosis

Differentials are broad given the variability in appearance and location of orbital lymphoma. It can involve any orbital tissue [1, 4].

Differentials for lymphoma involving the lacrimal gland include:

- Inflammatory diseases, e.g., nonspecific orbital inflammation (NSOI), sarcoidosis, and IgG4-related disease
- Lacrimal gland tumors, e.g., pleomorphic adenoma, adenoid cystic carcinoma, and adenocarcinoma
- Metastases

Differentials for lymphoma involving muscle include:

- Inflammatory diseases, e.g., thyroid orbitopathy, NSOI, sarcoidosis, and IgG4-related disease
- Metastases

Differentials for lymphoma presenting as an infiltrative lesion include:

- Inflammatory diseases: NSOI, sarcoidosis, IgG4-related disease, granulomatosis with polyangiitis, histiocytosis, and infectious diseases
- Metastases

Differentials for lymphoma presenting as a well-circumscribed intraconal tumor include:

- Optic nerve sheath meningioma
- Solitary fibrous tumor
- Schwannoma
- Optic nerve glioma

Many differentials can be eliminated with comprehensive imaging [1, 4].

3 Diagnosis

Diagnosed by:

- Distinctive features on orbital MRI
- Biopsy: Histopathologic examination including haematoxylin-eosin staining and immuno-histochemical analysis
- Physician/oncologist systemic workup including full-body staging with CT and positron emission tomography (PET)
- Bone marrow biopsy [2, 3]

4 Treatment

Lymphoma treatment options include:

- Surgery – neoadjuvant treatment in cases with massive tumor load
- Radiotherapy – curative treatment for low-grade tumors
- Chemotherapy – common treatment choice for high-grade or disseminated orbital lymphoma
- Stem cell transplantation [2, 3]

5 Figures with Captions

5.1 Case 1

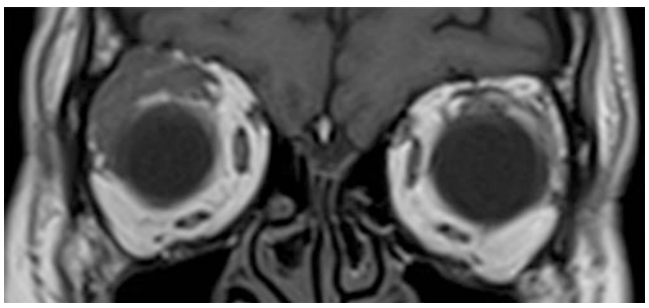


Fig. 1 Coronal noncontrast T1 MRI demonstrating a right supero-temporal orbital mass involving the lacrimal gland, superior rectus, and lateral rectus. The mass is homogeneous and isointense to muscle

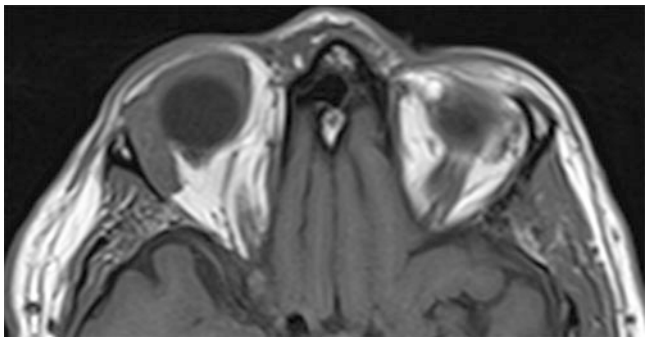


Fig. 2 Axial T1 MRI demonstrating the lacrimal gland mass moulding anteriorly to the globe

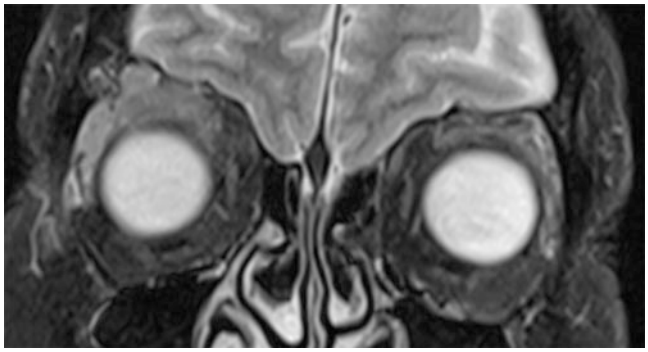


Fig. 3 Coronal fat-suppressed T2 MRI demonstrating the lacrimal gland lesion which is homogeneous and mildly hyperintense to muscle

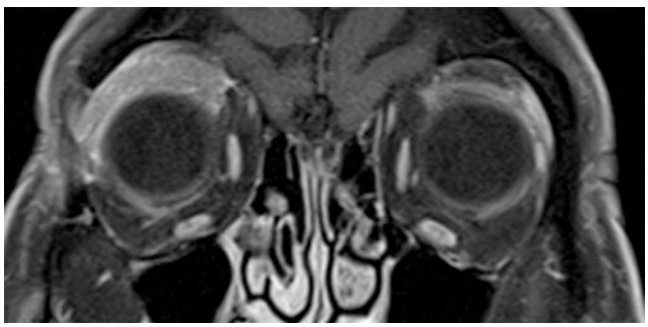


Fig. 4 Coronal postcontrast fat-suppressed T1 MRI revealing the homogeneously enhancing lesion which is moulding superolaterally to the globe

5.2 Case 2

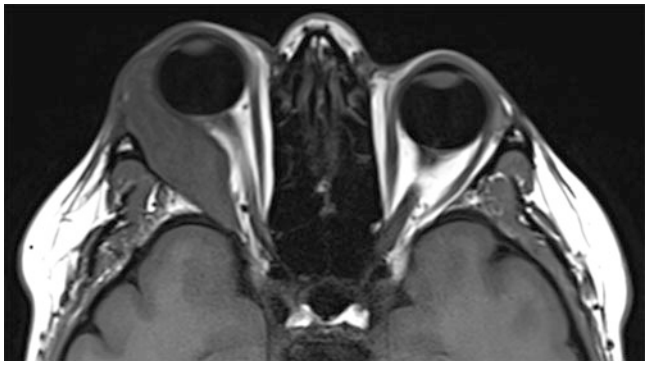


Fig. 5 Axial T1-weighted MRI demonstrating a well-defined right orbital mass that is isointense to muscle. It results in proptosis, extends posteriorly to the orbital apex and molds in a nonradial growth pattern to occupy the lateral orbit

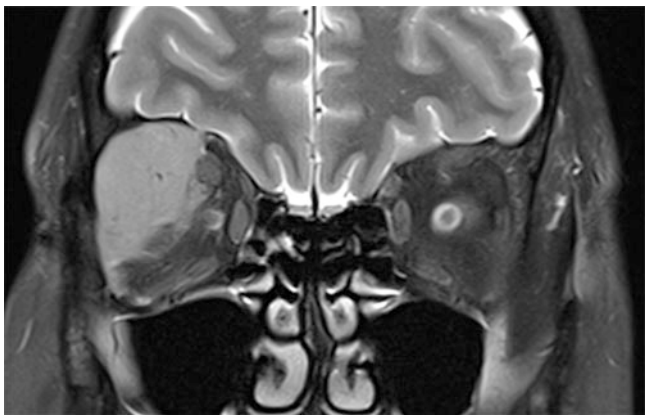


Fig. 6 Coronal fat-suppressed T2 MRI revealing a homogeneous mass at the superolateral right orbit, with a slightly ill-defined medial margin. The superior rectus, lateral rectus, and optic nerve are displaced medially. The signal intensity is mildly hyperintense to muscle, indicating a solid cellular mass with lymphoma being the most likely possibility. Metastases are also often hypercellular, depending upon tumor of origin, however the signal is usually more heterogeneous



Fig. 7 Axial diffusion weighted imaging (DWI) (**a**) and apparent diffusion coefficient (ADC) (**b**) MRI revealing a high DWI signal and low ADC signal (restricted diffusion) within the tumor

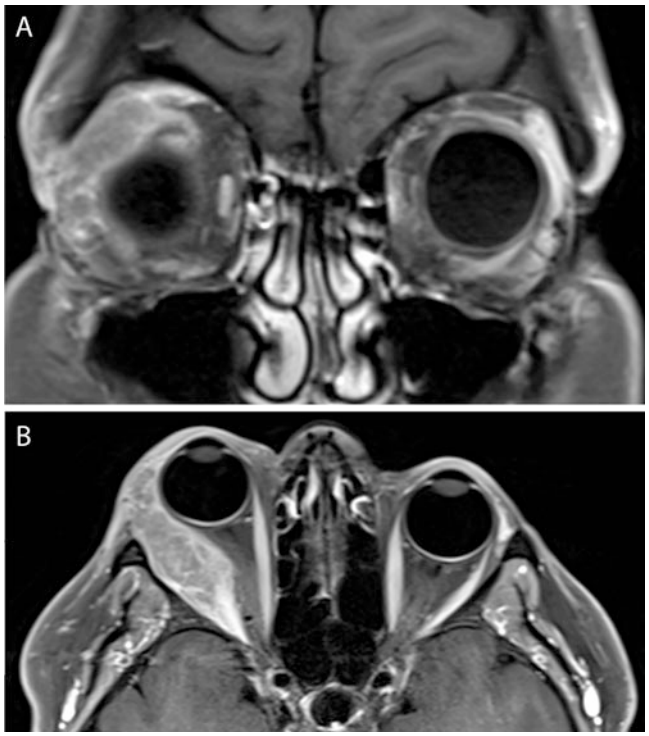


Fig. 8 Coronal (**a**) and axial (**b**) postcontrast fat-suppressed T1 MRI revealing involvement of the right lacrimal gland on the coronal image. Moderate enhancement is demonstrated with mild internal heterogeneity which is not usually seen in lymphoma. There may be some variation in the level of homogeneity between sequences, as each sequence depicts a slightly different characteristic of the tumor

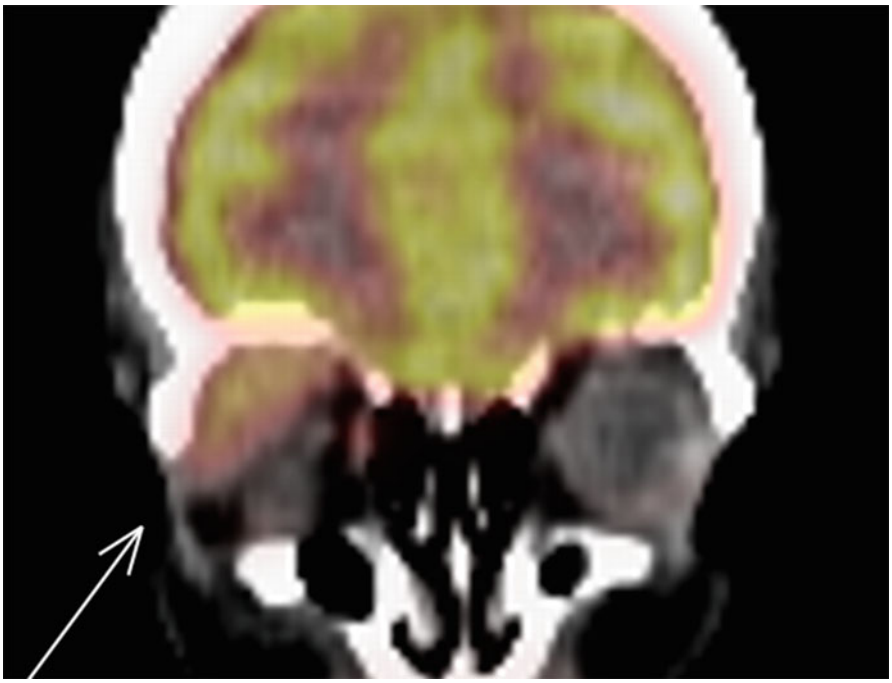


Fig. 9 Coronal FDG-PET scan demonstrating tracer uptake by the tumor (white arrow). FDG-PET is sensitive for lymphoma but nonspecific. This is an important investigation in systemic staging for lymphoma

5.3 Case 3



Fig. 10 Axial postcontrast CT demonstrating a homogeneous enhancing mass at the left lateral orbit, resulting in proptosis and subtle tenting of the globe. The adjacent orbital bone appeared intact on bone window (not shown). Subtle ill-defined changes in the right intraconal space are noted and better illustrated on subsequent MRI

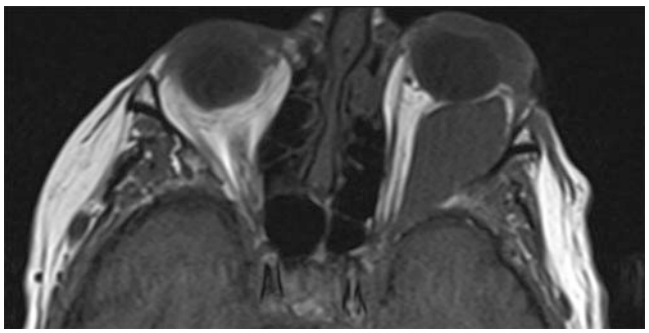


Fig. 11 On axial T1 MRI the mass is well defined in the left lateral orbit. The tumor extends to the orbital apex and has a preseptal component. The isointense T1 signal to muscle is nonspecific

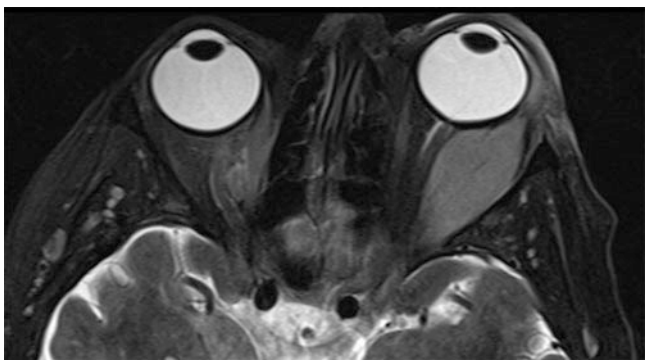


Fig. 12 On axial fat-suppressed T2 MRI, there is a homogeneous mass of intermediate signal in the left lateral orbit, which is typical for lymphoma. The optic nerve is medially displaced. The lateral rectus is involved. Additionally, there is a smaller mass adjacent to the right medial rectus. This patient had plasmablastic lymphoma. Metastasis is an important differential

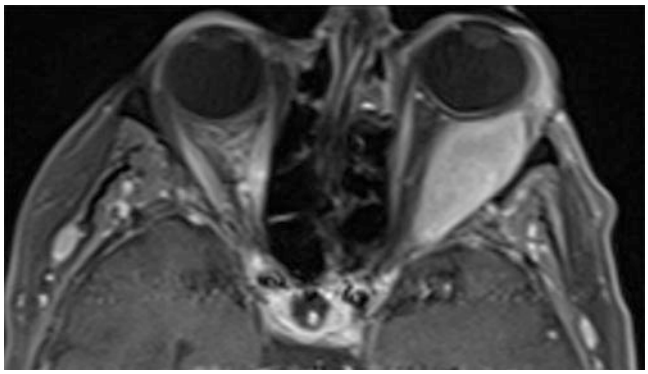


Fig. 13 On axial postcontrast fat-suppressed T1 MRI the left orbital and preseptal mass demonstrates homogeneous enhancement typical (but not specific) for lymphoma. The right orbital intraconal component is ill defined illustrating the variability in this pathology. This case demonstrates the potential bilateral and multifocal nature of lymphoma

5.4 Case 4



Fig. 14 Axial bone window CT revealing a bilateral anterior orbital mass, with attenuation (but not complete destruction) of the lamina papyracea anteriorly and the anterior ethmoid. While lymphoma frequently contacts bony structures, features such as bony destruction, hyperostosis, or scalloped remodeling of bone are atypical

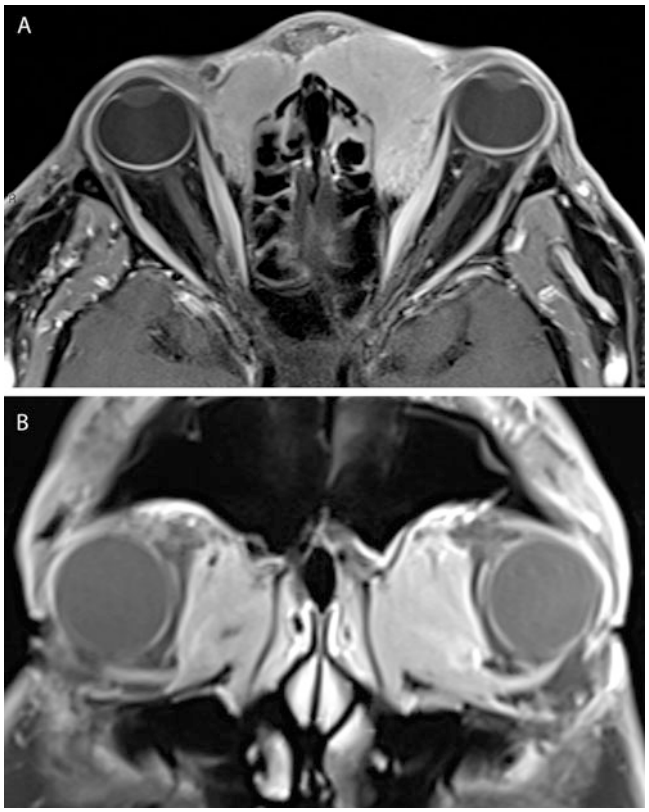


Fig. 15 Axial (**a**) and coronal (**b**) postcontrast fat-suppressed T1 MRI demonstrating a homogeneously enhancing mass at the medial anterior orbits. The globes are laterally displaced. The medial recti are well defined. The tumor involves the anterior ethmoid while preserving the bony architecture. The trans-spatial feature of lymphoma is highlighted

5.5 Case 5



Fig. 16 Axial CT revealing an intraconal mass with slightly ill-defined margins. The lesion is slightly hyperdense to the adjacent extraocular muscles prior to contrast, which is characteristic of lymphoma, being a highly cellular tumor

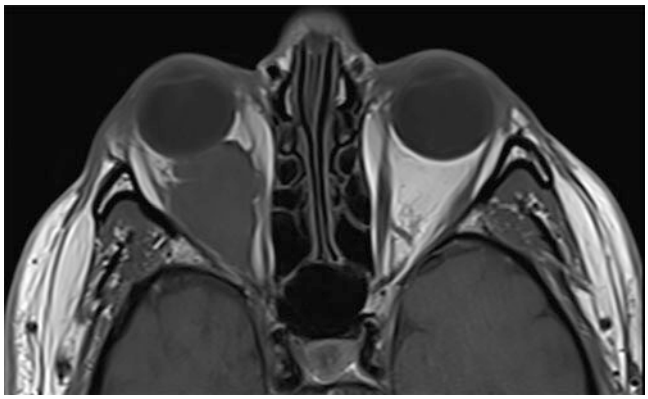


Fig. 17 Axial T1-weighted MRI revealing a well-defined hypointense right intraconal mass. There is mild globe indentation

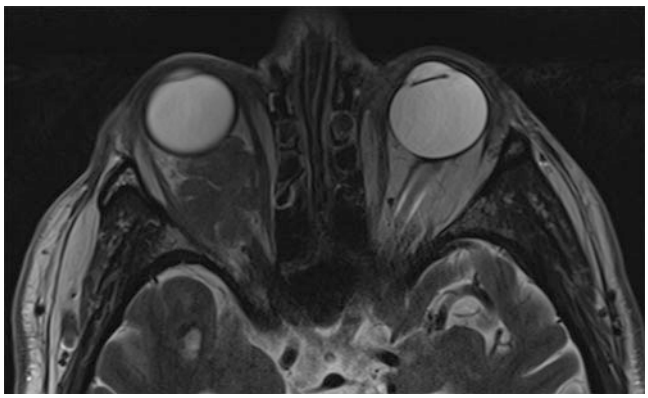


Fig. 18 Axial non-fat-suppressed T2 MRI revealing a lobulated heterogeneous and predominantly hypointense right intraconal orbital mass. The hypointense T2 signal implies a highly cellular tumor, such as lymphoma

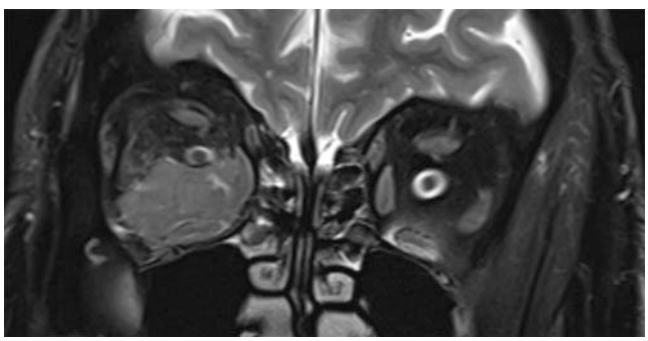


Fig. 19 On coronal fat-suppressed T2 MRI the right intraconal mass is isointense to muscle. The optic nerve can be identified separate to the lesion. Metastasis is a key differential for the radiological appearance, since these are often highly cellular tumors with a similar appearance

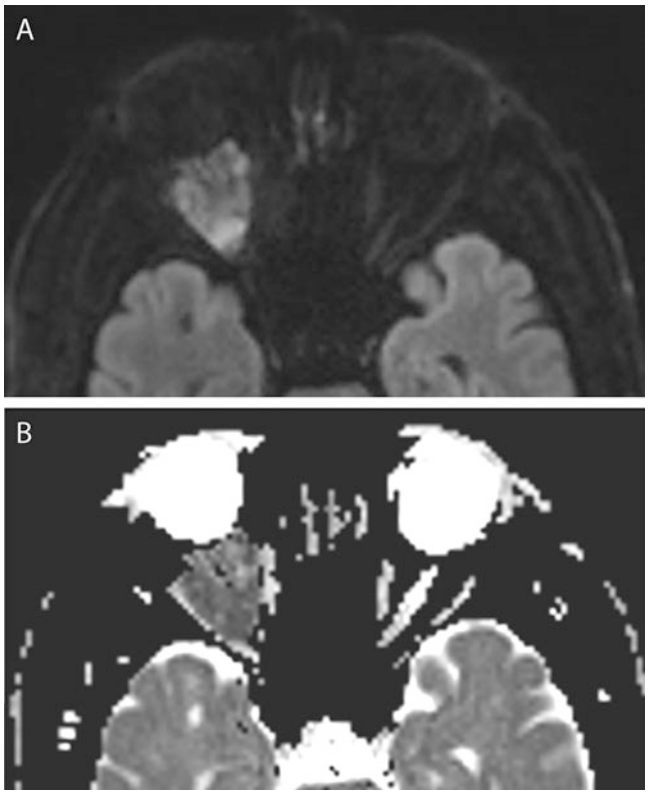


Fig. 20 DWI (**a**) and ADC (**b**) MRI revealing a high DWI, low ADC tumor, indicating restricted diffusion

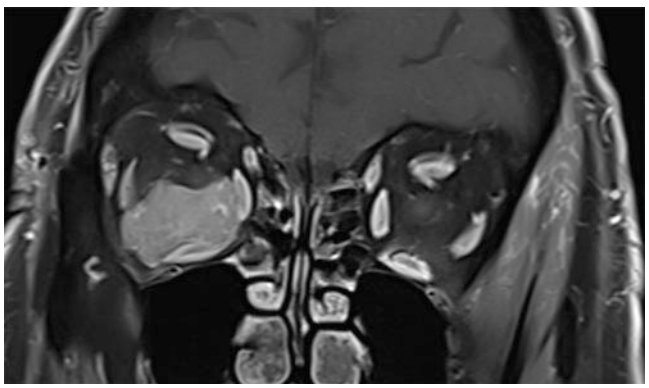


Fig. 21 Coronal postcontrast fat-suppressed T1 MRI demonstrating the intraconal enhancing mass which involves the inferior rectus

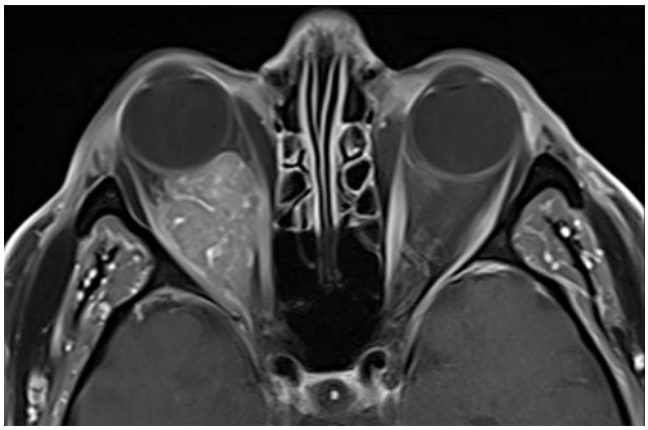


Fig. 22 On axial postcontrast fat-suppressed T1 MRI the intraconal mass demonstrates internal linear and punctate regions of more intense enhancement, which at least partly reflect displaced normal orbital vessels and nerves

5.6 Case 6

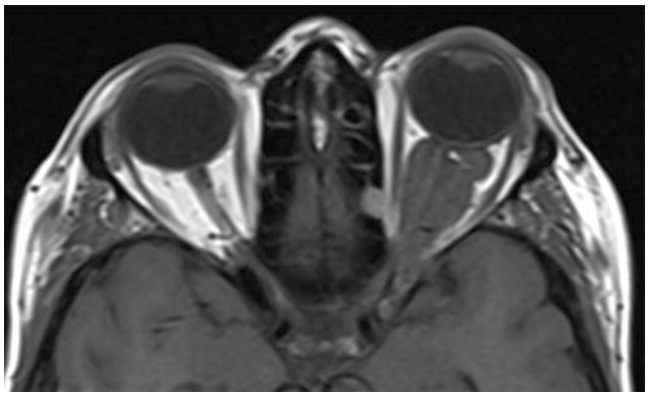


Fig. 23 Axial T1 MRI revealing a left orbital mass that is isointense to muscle. It demonstrates moulding and surrounds the optic nerve from the posterior globe to the orbital apex. There is left proptosis

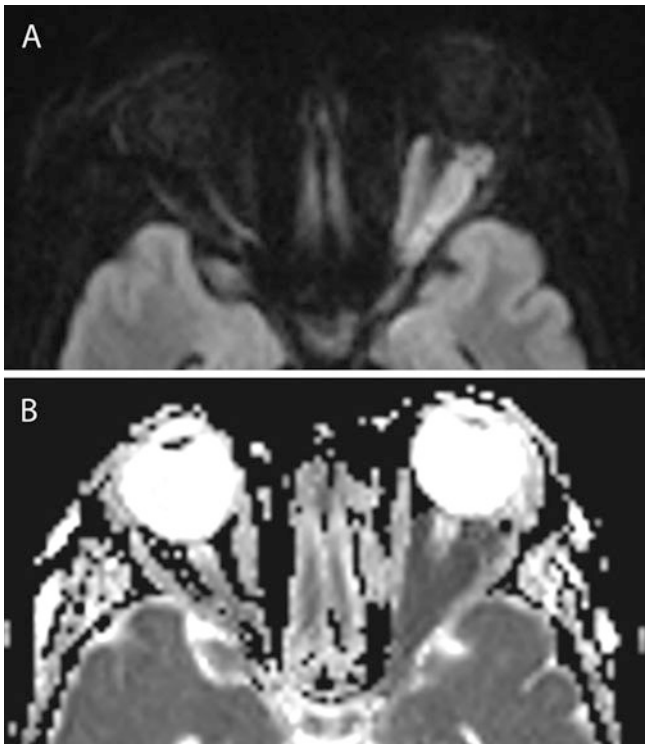


Fig. 24 Axial DWI (**a**) and ADC map (**b**) revealing high DWI signal and low ADC signal (restricted diffusion) typical of lymphoma

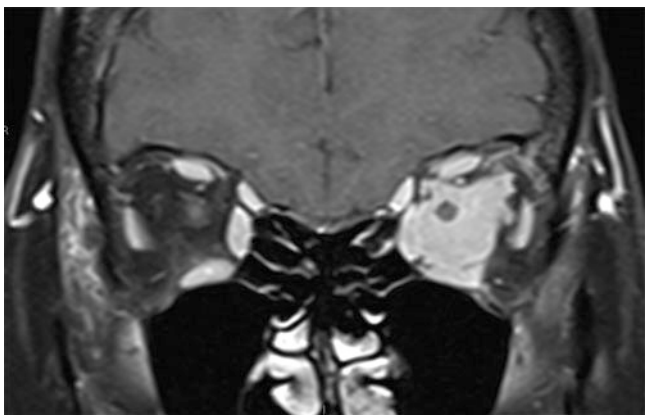


Fig. 25 Coronal postcontrast fat-suppressed T1 MRI of the mid orbits, demonstrating a moderately well-defined left intraconal mass surrounding the optic nerve, with homogeneous enhancement. The relative hypointense signal of the optic nerve can be well differentiated from that of the tumor. From this image alone, this lymphoma is indistinguishable from optic nerve sheath meningioma (ONSM)

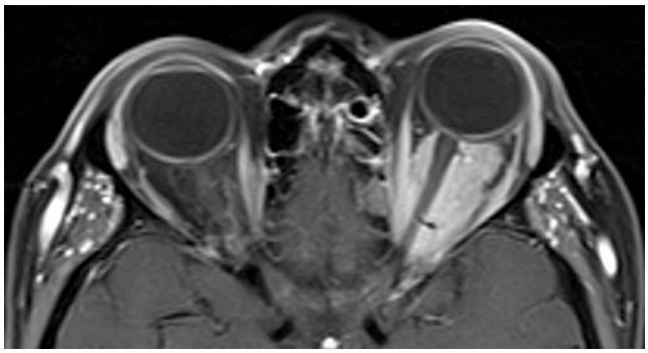


Fig. 26 Axial postcontrast fat-suppressed T1 MRI revealing homogeneous enhancement of the intraconal mass surrounding the optic nerve

5.7 Case 7



Fig. 27 Axial noncontrast CT revealing a bilateral infiltrative mass involving the posterior orbits. Lymphoma can present with an infiltrative pattern

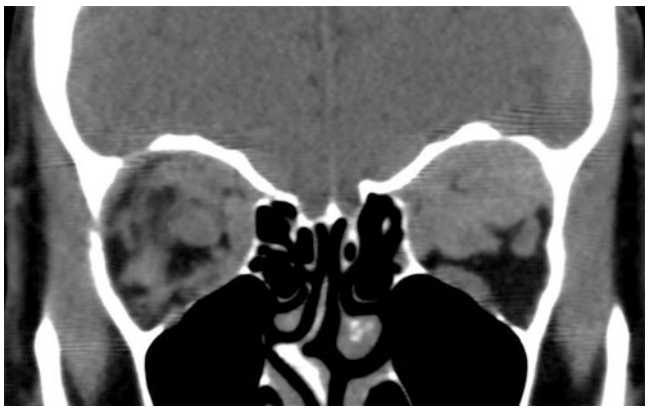


Fig. 28 Coronal CT at the level of the mid orbits demonstrating a bilateral infiltrative tumor, illustrating lymphoma can be multifocal and bilateral



Fig. 29 Axial bone window CT illustrating preservation of the adjacent bony structures

References

1. Priego G, Majos C, Climent F, Muntane A. Orbital lymphoma: imaging features and differential diagnosis. Insights Imaging. 2012;3(4):337–44. https://doi.org/10.1007/s13244-012-0156-1. [published Online First: Epub Date].
2. Olsen TG, Holm F, Mikkelsen LH, et al. Orbital lymphoma-an international multicenter retrospective study. Am J Ophthalmol. 2019;199:44–57. https://doi.org/10.1016/j.ajo.2018.11.002. [published Online First: Epub Date].
3. Olsen TG, Heegaard S. Orbital lymphoma. Surv Ophthalmol. 2019;64(1):45–66. https://doi.org/10.1016/j.survophthal.2018.08.002. [published Online First: Epub Date].
4. Mombaerts I, Ramberg I, Coupland SE, Heegaard S. Diagnosis of orbital mass lesions: clinical, radiological, and pathological recommendations. Surv Ophthalmol. 2019;64(6):741–56. https://doi.org/10.1016/j.survophthal.2019.06.006. [published Online First: Epub Date].

Orbital Multiple Myeloma

38

Jaskirat Aujla, Valerie Juniat, Sandy Patel, and Dinesh Selva

Contents

1 Signs and Symptoms 308

2 Differential Diagnosis 308

3 Diagnosis 308

4 Treatment 308

5 Figures with Captions 308
5.1 Case 1 308
5.2 Case 2 309
5.3 Case 3 310

References 311

Abstract

Key features of orbital multiple myeloma (MM):

- Median age at diagnosis: 70 years
- Equal gender distribution
- Majority already diagnosed with MM
- Unilateral bony tumors (involving the sphenoid or frontal bone with orbital extension into the superior and superotemporal orbit)
- Other anatomical patterns include:
  1. Discrete orbital tumors (mostly intraconal and adhering to an extraocular muscle)
  2. Trans-spatial/multi-compartment lesions (e.g., sinuses, eyelids and facial soft tissues)

Imaging features on CT and MRI are variable:

- The greatest value in imaging is staging the local extent
- Enhancing soft tissue mass on CT with possible bony erosion, destruction or expansion
- Nonspecific MRI signal characteristics:
  - T1-weighted images: isointense signal intensity to muscle
  - T2-weighted images: intermediate to high signal intensity, often homogenous
  - Post-contrast enhancement
  - Restricted diffusion due to hypercellularity

Keywords

Orbital multiple myeloma · plasmacytoma · primary extramedullary plasmacytoma · solitary extramedullary plasmacytoma

J. Aujla · V. Juniat · D. Selva (✉)
South Australian Institute of Ophthalmology, Adelaide, SA, Australia
e-mail: Jaskirat.aujla@uqconnect.edu.au; vjuniat@doctors.org.uk

S. Patel
Department of Radiology, Royal Adelaide Hospital, Adelaide, SA, Australia

© Springer Nature Switzerland AG 2022
G. Ben Simon et al. (eds.), *Atlas of Orbital Imaging*,
https://doi.org/10.1007/978-3-030-62426-2_26

1 Signs and Symptoms

Most common: Proptosis, decreased vision, diplopia, swelling, and ptosis. Uncommon presentations also include ecchymosis and cellulitis [1, 2].

2 Differential Diagnosis

The differential diagnosis is broad for lesions confined to the soft tissues due to the nonspecific radiological features and variable anatomical tumor locations [1–4].

Neoplastic differentials may include:

- Lymphoproliferative tumors
- Benign and malignant epithelial lacrimal gland neoplasms
- Schwannoma, solitary fibrous tumor
- Bony lesions such as cholesterol granuloma, giant cell granuloma, aneurysmal bone cyst, fibrous dysplasia, osteoma/osteosarcoma
- Metastases

Inflammatory differentials may include:

- Non-specific orbital inflammation, sarcoidosis, IgG4-related disease, granulomatosis with polyangiitis, amyloidosis

Spectrum of disease includes:

- Orbital MM
- Plasmacytoma
- Primary (or solitary) extramedullary plasmacytoma (PEP)

Many of the above could be eliminated from the differential with comprehensive imaging.

3 Diagnosis

Diagnosed by:

- Biopsy for histological examination and flow cytometry
- Full systemic work up by physicians for patients without a pre-existing diagnosis of MM [1]

4 Treatment

Treatment options include:

- Surgical resection (e.g., solitary plasmacytoma)
- Radiotherapy – low-dose for local palliation, high-dose for potential cure of localized plasmacytoma
- Chemotherapy – particularly for active MM
- Stem cell transplantation – following chemoradiation in patients achieving remission [1, 4, 5]

5 Figures with Captions

5.1 Case 1

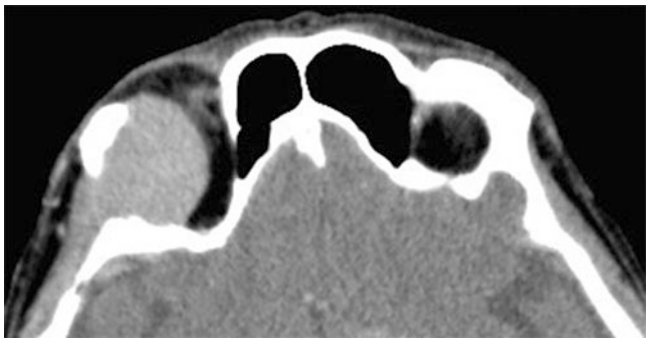


Fig. 1 Axial postcontrast CT through the superior orbits revealing a homogeneous enhancing mass at the lateral right orbit. MM is most commonly found in the superotemporal orbit

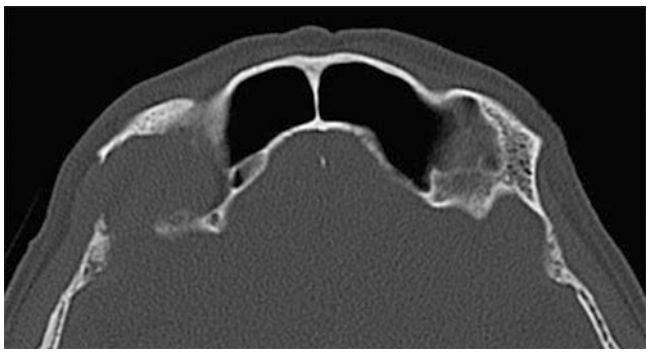


Fig. 2 Axial bone-window CT demonstrates bone destruction without sclerosis which is typical of myeloma. The bony destruction has a sharp bone margin anteriorly which is also typical of myeloma, as opposed to a more permeative margin usually seen in metastases

5.2 Case 2



Fig. 3 Axial non contrast CT demonstrating a homogeneous mass at the left posterior intraconal space. The mass is isodense to brain indicating a cellular tumor

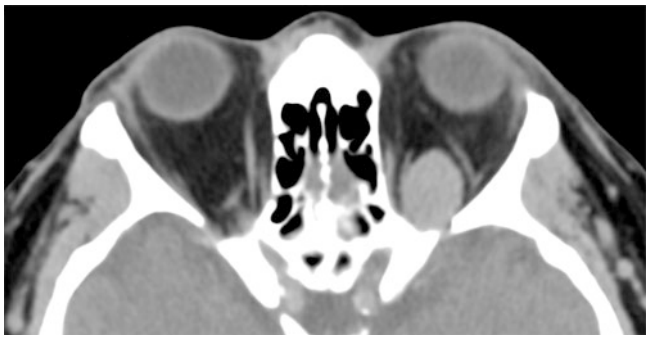


Fig. 4 Axial postcontrast CT reveals homogeneous enhancement of the left posterior intraconal mass

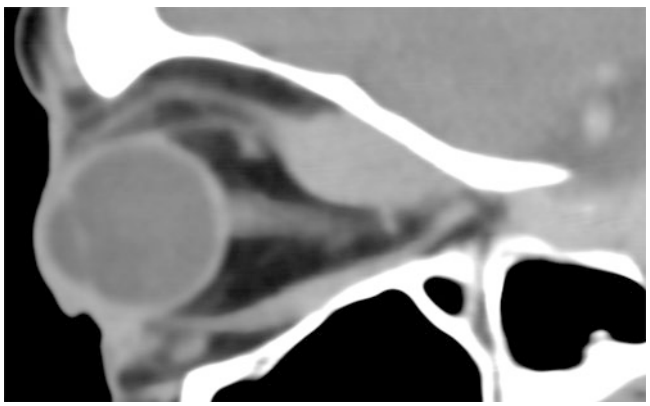


Fig. 5 Sagittal postcontrast CT reveals superior rectus involvement from mid orbit to the orbital apex

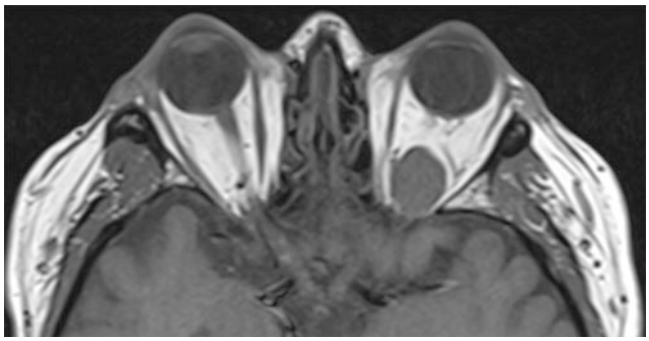


Fig. 6 Axial T1 MRI revealing a well-defined homogeneous mass at the left orbit with an isointense T1 signal to muscle, which is nonspecific and seen in a wide range of tumors

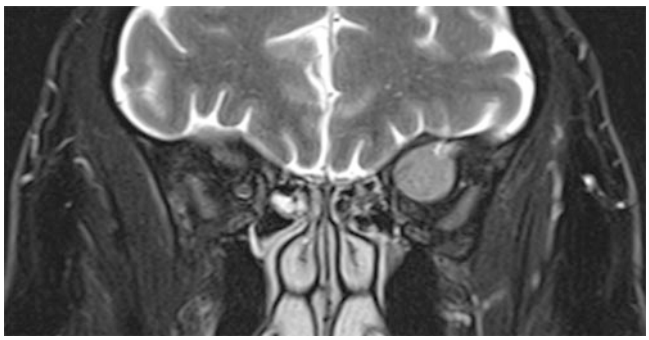


Fig. 7 Coronal fat-suppressed T2 MRI demonstrating the conspicuous intraconal lesion. The T2 signal intensity of the tumor is only slightly hyperintense to muscle reflecting hypercellularity (similar to lymphoma and some metastases). This implies a solid cellular tumor. Many other tumor types have less cellularity and a higher overall water content. Myeloma that presents as a discrete orbital soft tissue mass is often seen to involve or adhere to an extraocular muscle, as can be seen here

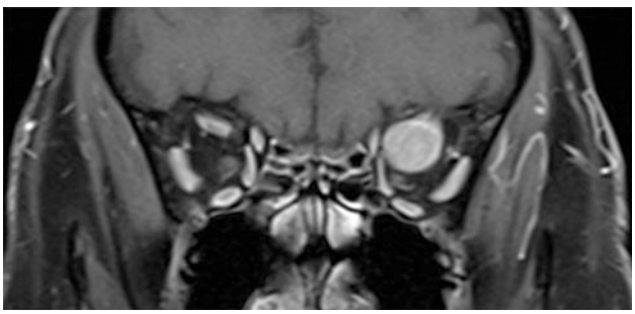


Fig. 8 Coronal postcontrast fat-suppressed T1 MRI indicating superior rectus involvement. Myeloma will invariably demonstrate homogeneous enhancement similar to lymphoma. This case illustrates one typical anatomical pattern of orbital myeloma – a discrete intraconal orbital mass

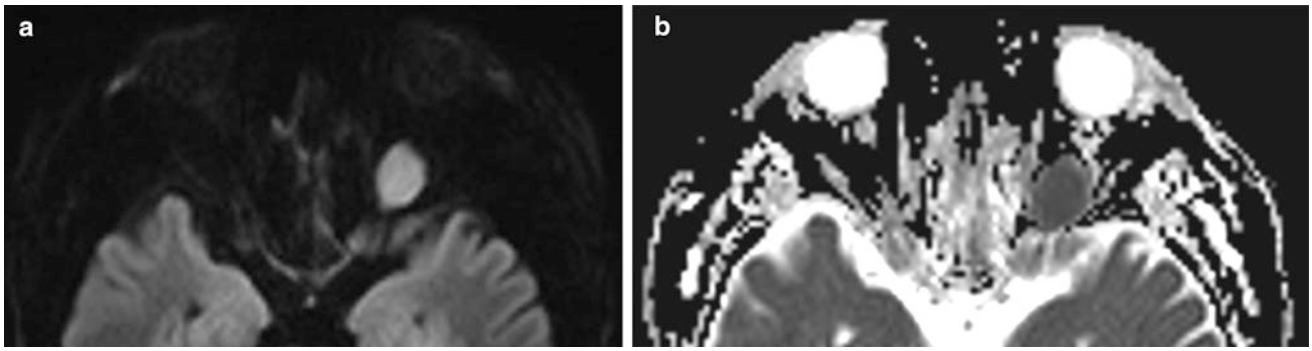


Fig. 9 Axial diffusion weighted imaging (DWI) (A) and apparent diffusion coefficient (ADC) (B) MRI. High signal on DWI and low signal on ADC, indicating restricted diffusion, a feature seen in hypercellular tumors such as lymphoma and myeloma

5.3 Case 3

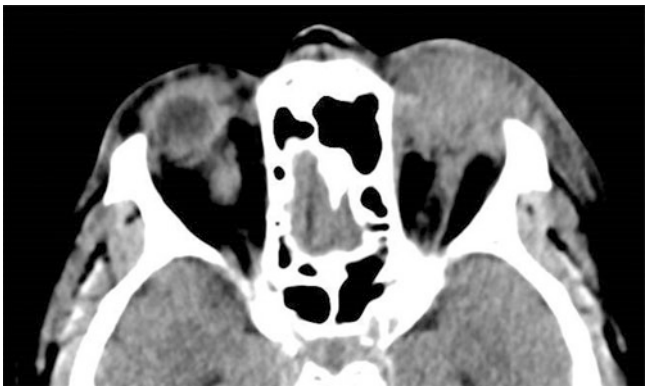


Fig. 10 Axial CT demonstrating an ill-defined left anterior orbital mass, isodense to brain. The density implies a solid cellular tumor

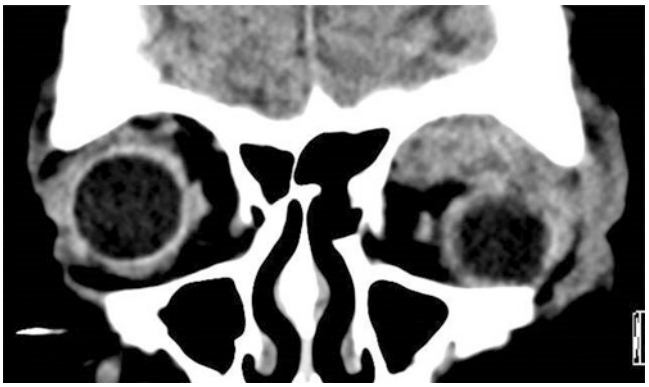


Fig. 11 On coronal CT, the mass at the left superior orbit results in inferolateral displacement of the globe

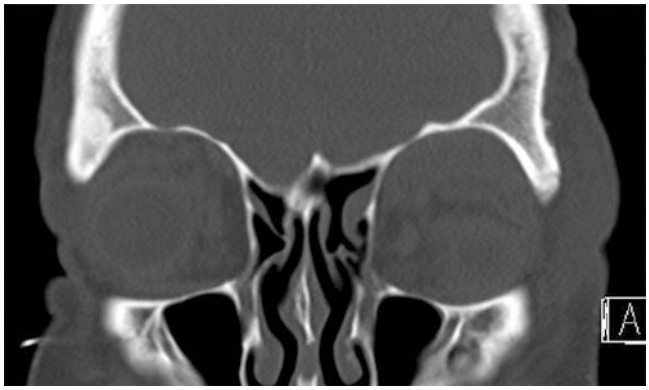


Fig. 12 Coronal bone-window CT revealing preservation of the adjacent bony orbit. While bony destruction can be seen with tumors arising as an osseous myelomatous deposit of the orbit, when arising as an extra-osseous soft tissue mass, bony destruction is atypical. In this setting myeloma may show an infiltrative soft tissue pattern

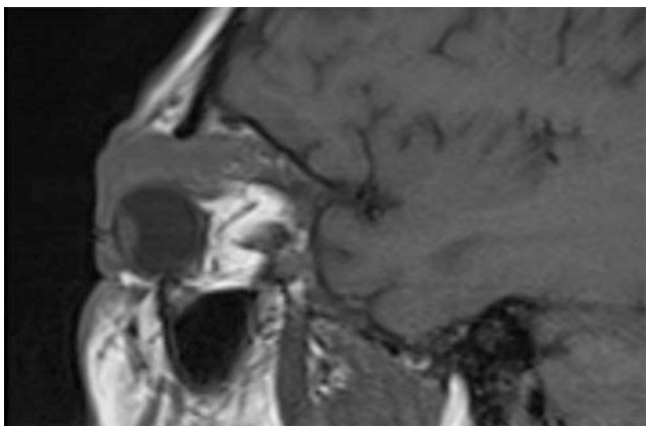


Fig. 13 Sagittal T1 MRI through the left orbit demonstrating an isointense mass to brain, at the superior orbit with involvement of the upper eyelid. The trans-spatial/multi-compartment nature of this tumor is demonstrated

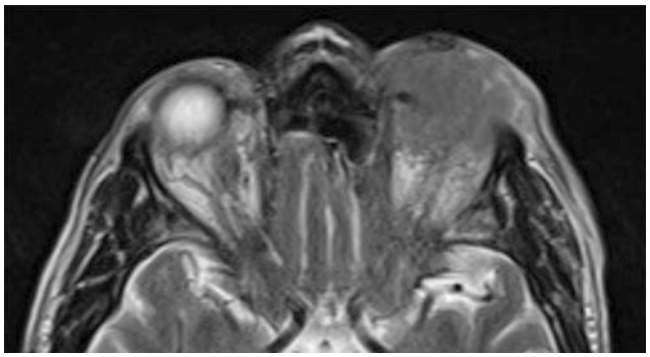


Fig. 14 Axial T2 MRI with some movement artefact. The lesion at the superior left orbit is ill-defined. The T2 signal is isointense to muscle indicating increased cellularity. Metastases have more variable T2 signal depending upon histology

References

1. Burkat CN, Van Buren JJ, Lucarelli MJ. Characteristics of orbital multiple myeloma: a case report and literature review. Surv Ophthalmol. 2009;54(6):697–704. https://doi.org/10.1016/j.survophthal.2009.04.012. [published Online First: Epub Date]|
2. Howling SJ, Tighe J, Patterson K, Shaw P. Case report: the CT features of orbital multiple myeloma. Clin Radiol. 1998;53(4):304–5. https://doi.org/10.1016/s0009-9260(98)80133-5. [published Online First: Epub Date]|
3. Mombaerts I, Ramberg I, Coupland SE, Heegaard S. Diagnosis of orbital mass lesions: clinical, radiological, and pathological recommendations. Surv Ophthalmol. 2019;64(6):741–56. https://doi.org/10.1016/j.survophthal.2019.06.006. [published Online First: Epub Date]|.
4. Tai E, Sim SK, Haron J, Wan Hitam WH. Orbital multiple myeloma: a diagnostic challenge. BMJ Case Rep. 2017;2017 https://doi.org/10.1136/bcr-2017-220895. [published Online First: Epub Date]|
5. Thuro BA, Sagiv O, Shinder R, et al. Clinical Presentation and Anatomical Location of Orbital Plasmacytomas. Ophthalmic Plast Reconstr Surg. 2018;34(3):258–61. https://doi.org/10.1097/IOP.0000000000000939. [published Online First: Epub Date]|

Orbital Soft Tissues Sarcomas/Liposarcoma

39

Jaskirat Aujla, Valerie Juniat, Sandy Patel, and Dinesh Selva

Contents

1 Signs and Symptoms 314
2 Differential Diagnosis 314
3 Diagnosis 314
4 Treatment 314
5 Figures with Captions 314
5.1 Case 1 314
5.2 Case 2 315
5.3 Case 3 316
5.4 Case 4 317
References 318

Abstract

Primary liposarcoma of the orbit is a rare tumor. Features include:

- Variable age at presentation: mean 4th–5th decade.
- Female preponderance.
- Predominantly intraconal or superior orbit.
- Variable tumor margin: some well-defined.
- Less commonly reported: tumors involving the medial, lateral, inferior orbit or the subconjunctival space.
- In general, imaging appearance depends on the tumor grade and the amount of fat component.

On computed tomography (CT):

- Nonspecific soft tissue density mass.
- Occasional fat density (measures in the range of negative HU [−50] to [−150]).
- Occasional calcification.
- Variable contrast enhancement: the fat density region usually does not enhance, while the soft tissue density component usually enhances.

Magnetic resonance imaging (MRI) reveals:

- Varied signal intensity on T1-weighted and T2-weighted images.
- If there is a pure fat component, it will follow fat signal, for example, at the contralateral orbit and subcutaneous fat on all (including fat suppressed) sequences.
- Large proportion show nonfatty soft tissue intensity; some can demonstrate fat component; chemical shift as a low intensity signal may appear at the periphery of the tumor (this misregistration stems from the difference in resonance between fat and water and is more prominent on older generation MRI sequences).

J. Aujla · V. Juniat · D. Selva (✉)
South Australian Institute of Ophthalmology, Adelaide, SA, Australia
e-mail: Jaskirat.aujla@uqconnect.edu.au; vjuniat@doctors.org.uk

S. Patel
Department of Radiology, Royal Adelaide Hospital, Adelaide, SA, Australia

© Springer Nature Switzerland AG 2022
G. Ben Simon et al. (eds.), *Atlas of Orbital Imaging*,
https://doi.org/10.1007/978-3-030-62426-2_27

- Without a fat component, the imaging is nonspecific.
- The soft tissue density component usually enhances following contrast; additional signs that may aid in differentiating from simple lipoma include inhomogeneity, thick septae, and prominent vessels.

Keywords

Orbital liposarcoma · Li-Fraumeni familial cancer syndrome

1 Signs and Symptoms

Most common:

- Painless proptosis
- Ophthalmoplegia
- Reduced vision
- Globe dystopia
- Lid swelling [1–3]

Systemic symptoms such as a change in weight (weight gain), malaise, and anosmia occur but are rare [1].

2 Differential Diagnosis

Differentials include, but may not be limited to:
Inflammatory causes:

- Nonspecific orbital inflammation, sarcoidosis, IgG4-related orbital disease, granulomatosis with polyangiitis, amyloidosis.

Neoplastic causes:

- Lymphoma
- Benign and malignant epithelial lacrimal gland neoplasms
- Schwannoma, solitary fibrous tumor, cavernous haemangioma, other sarcomas (e.g., rhabdomyosarcoma, fibrosarcoma), malignant peripheral nerve sheath tumor, neurofibroma, dermoid cyst
- Metastases

Many of the above could be eliminated from the differential with comprehensive imaging [1–5].

3 Diagnosis

Diagnosed by:

- Incisional biopsy targeted to the contrast-enhancing portion of the tumor and histopathological examination (including cytogenetic techniques such as fluorescent in situ hybridization) [1, 2]

May herald a diagnosis of Li-Fraumeni familial cancer syndrome [1, 2].

4 Treatment

Surgical excision, including:

- Local resection – including repeated local resections for recurrence
- Exenteration

Recurrence is common (10%) [1, 2].
Additional treatment with radiotherapy and chemotherapy may play a role [1].

5 Figures with Captions

5.1 Case 1

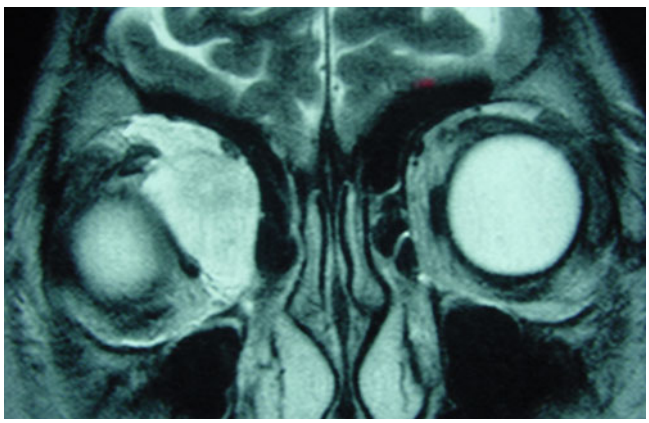


Fig. 1 Nonfat-suppressed coronal T2-weighted MRI at the anterior orbits revealing a well-circumscribed hyperintense mass at the superomedial right orbit, resulting in inferolateral globe displacement

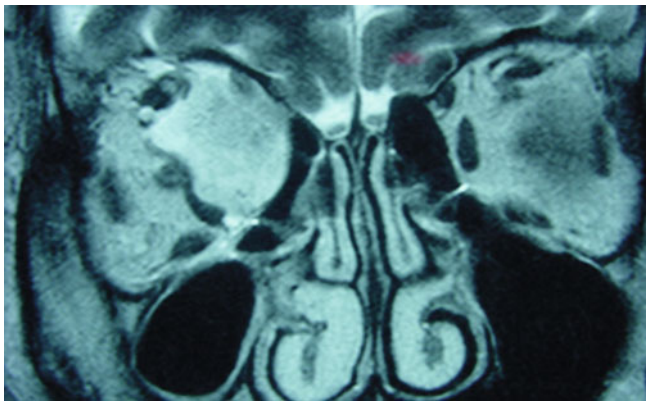


Fig. 2 Nonfat-suppressed coronal T2-weighted MRI at the mid orbits. The mass is seen abutting the optic nerve and displacing the medial rectus inferolaterally. The superior oblique is seen in a relatively normal anatomical position and can be differentiated from the tumor

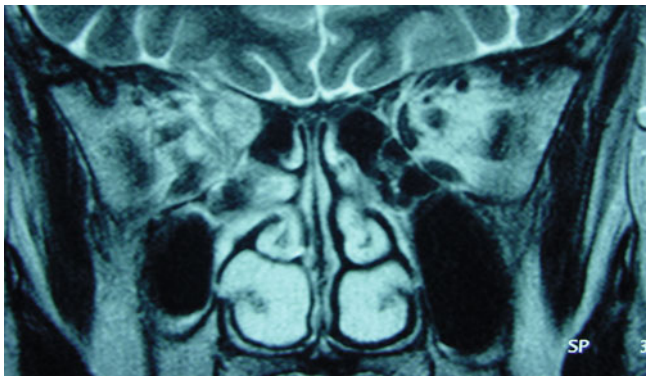


Fig. 3 Nonfat-suppressed coronal T2-weighted MRI at the posterior orbits. Without a fatty component, the T2 imaging alone is nonspecific. (Images courtesy of Dr Geoff Wilcsek, Sydney, Australia)

5.2 Case 2

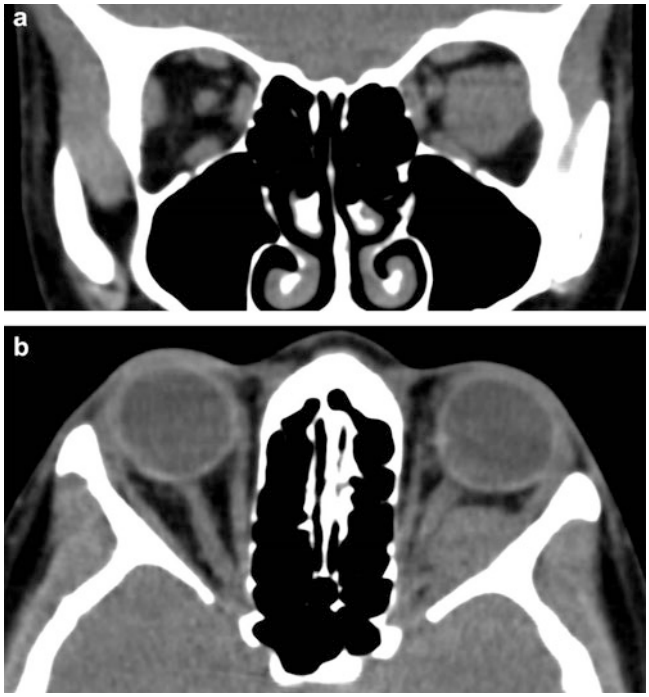


Fig. 4 Coronal (**a**) and axial (**b**) noncontrast CT scan revealing a well-circumscribed homogeneous intraconal mass at the left orbit without any calcification. The lateral rectus is involved. The tumor is isodense to muscle (nonspecific for differentiating between various soft tissue tumors). There was no extraorbital extension

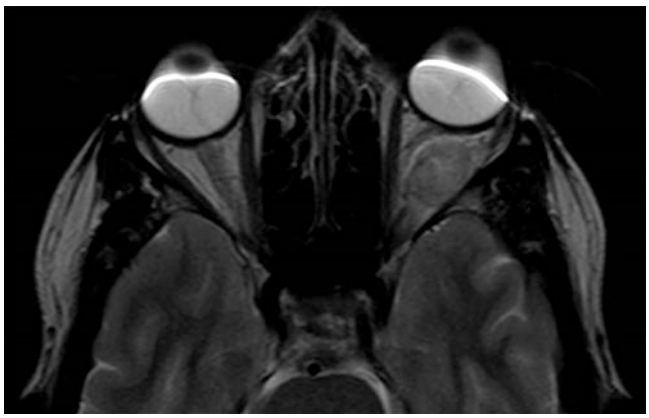


Fig. 5 Axial nonfat-suppressed T2 weighted MRI revealing a well-defined mass at the left intraconal space. The tumor is slightly hypointense to fat but hyperintense to muscle

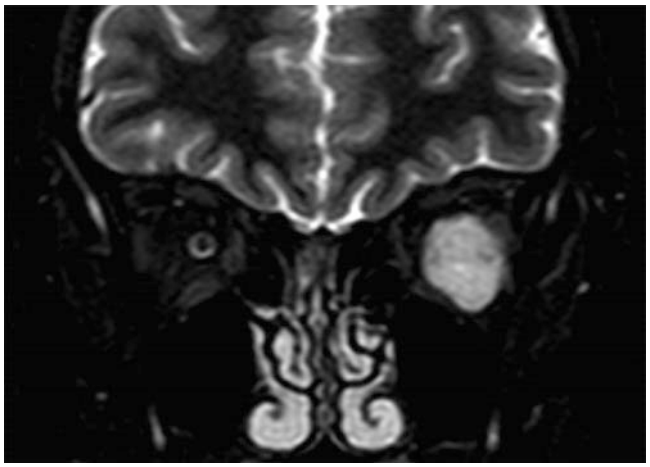


Fig. 6 Coronal STIR (short TI inversion recovery) MRI, which is similar to a T2-weighted fat-suppressed sequence, revealing a well-defined hyperintense mass at the left orbit. The lesion does not suppress like the adjacent fat, indicating a nonfatty solid soft tissue mass



Fig. 7 Axial postcontrast fat-suppressed T1 MRI revealing a well-defined, homogeneously enhancing mass at the left intraconal space, involving the lateral rectus and extending posteriorly towards the orbital apex. The mass does not follow fat signal at the contralateral orbit (lacking evidence of significant fatty component within the tumor)

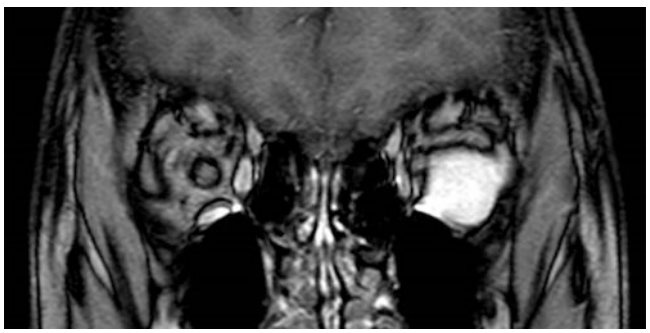


Fig. 8 Coronal postcontrast fat-suppressed T1 MRI confirming a predominantly intraconal lesion, with inferolateral extraconal extension. The optic nerve is displaced medially. The image reveals chemical shift artifact with low signal at the margin of orbital structures. Irrespective of the artifact, the lesion does not follow fat signal. Without a fatty component, the imaging alone is nonspecific. (Images courtesy of Dr. Iftach Yassur, MD, Rabin Medical Center, Petah Tikva, Israel)

5.3 Case 3

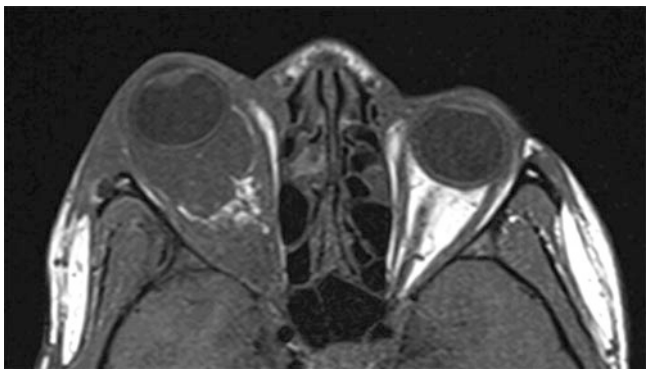


Fig. 9 Axial T1 MRI (non-FS, NE) revealing a large hypointense right orbital mass. Mild central hyperintensity is consistent with a fatty component. This was a recurrent mass following initial treatment and hence the central fat intensity could be residual orbital fat or tumor fat. There is prominent globe proptosis

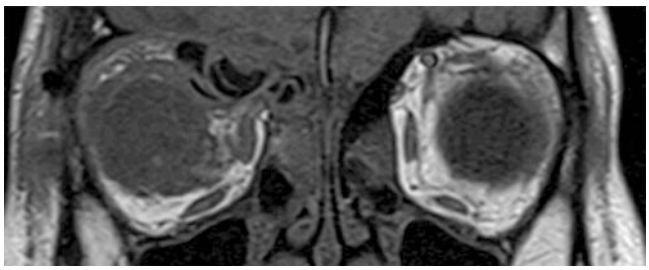


Fig. 10 Coronal noncontrast T1 MRI revealing the ill-defined intraconal mass isointense to muscle at the right orbit

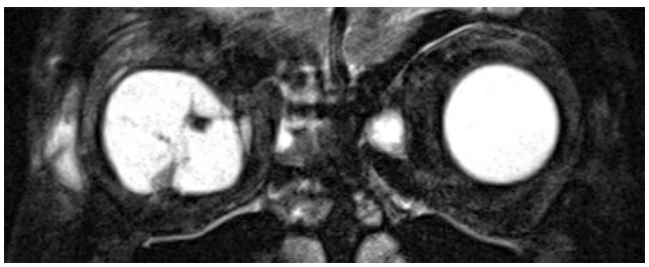


Fig. 11 Coronal fat-suppressed T2 MRI reveals a hyperintense retrobulbar mass at the right orbit demonstrating some internal low signal consistent with a suppressed fatty component – either tumor fat or residual orbital fat



Fig. 12 Axial postcontrast fat-suppressed T1 MRI demonstrating heterogeneous internal enhancement within the lesion. There is proptosis and involvement of virtually all retrobulbar orbital tissues. Liposarcomas usually reveal enhancement but this is not universal. Being a recurrent tumor, the nonenhancing regions of this mass may partly reflect treatment effect (such as increased fibrosis)

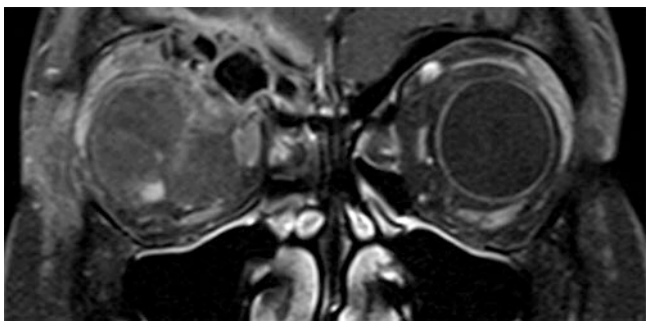


Fig. 13 Coronal postcontrast fat-suppressed T1 MRI. The patchy enhancement again demonstrating the heterogeneity of liposarcoma, especially in the setting of previous treatment. The added complexity in analyzing imaging in a recurrent tumor and with prior treatment is highlighted. (Images courtesy of Dr William Katowitz, Philadelphia, USA)

5.4 Case 4

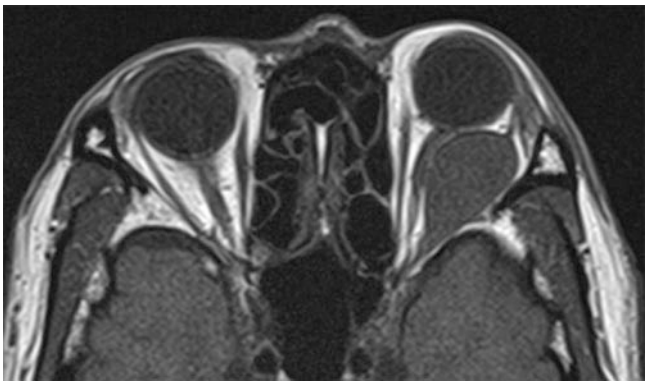


Fig. 14 Axial T1 MRI revealing a homogeneous mass isointense to muscle at the left lateral orbit. The tumor involves the lateral rectus



Fig. 15 Axial (**a**) and coronal (**b**) T2 MRI revealing a well-defined hyperintense homogeneous mass at the retrobulbar space of the left orbit, lateral to the optic nerve, confined to the lateral rectus muscle. The tumor signal appears isointense to fat. This could be misinterpreted as a significant fat component or a high-water content in the absence of further sequences, however in the current case is ruled out by the previous T1 sequences and the following T2 FS sequences

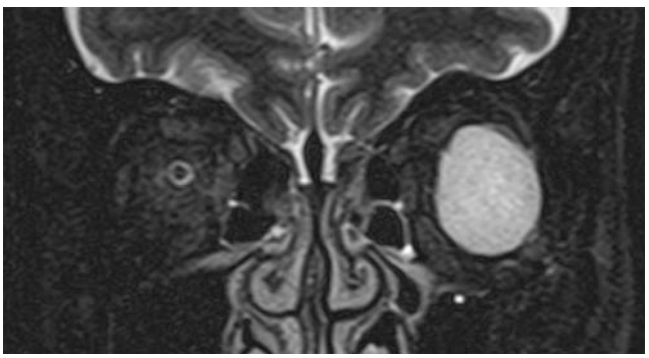


Fig. 16 Coronal Short-Tau Inversion Recovery (STIR) MRI, which is similar to a fat-suppressed T2-weighted sequence. The lesion signal does not follow suppressed orbital fat. Although it is quite hyperintense, it was not following fluid signal on the preceding T1 MRI

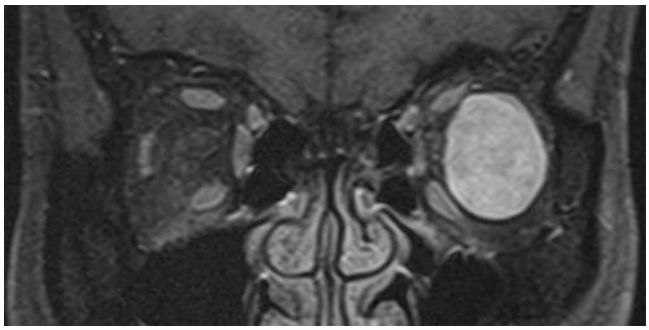


Fig. 17 Coronal postcontrast fat-suppressed T1 MRI. The mass demonstrates homogeneous enhancement. The combined imaging indicates a nonspecific soft tissue mass. (Images courtesy of Dr Akihide Watanabe, Kyoto Prefectural University of Medicine, Japan)

References

1. Madge SN, Tumuluri K, Strianese D, et al. Primary orbital liposarcoma. Ophthalmology. 2010;117(3):606–14. https://doi.org/10.1016/j.ophtha.2009.08.017. [published Online First: Epub Date].
2. Cai YC, McMenamin ME, Rose G, Sandy CJ, Cree IA, Fletcher CD. Primary liposarcoma of the orbit: a clinicopathologic study of seven cases. Ann Diagn Pathol. 2001;5(5):255–66. https://doi.org/10.1053/adpa.2001.27911. [published Online First: Epub Date].
3. Jakobiec FA, Rini F, Char D, et al. Primary liposarcoma of the orbit. Problems in the diagnosis and management of five cases. Ophthalmology. 1989;96(2):180–91. https://doi.org/10.1016/s0161-6420(89)32916-2. [published Online First: Epub Date].
4. Mombaerts I, Ramberg I, Coupland SE, Heegaard S. Diagnosis of orbital mass lesions: clinical, radiological, and pathological recommendations. Surv Ophthalmol. 2019;64(6):741–56. https://doi.org/10.1016/j.survophthal.2019.06.006. [published Online First: Epub Date].
5. Shinder R, Mostafavi D, Nasser QJ, Esmaeli B, Shore JW. Primary orbital liposarcoma misdiagnosed as thyroid associated orbitopathy. Orbit. 2012;31(4):264–6. https://doi.org/10.3109/01676830.2011.632112. [published Online First: Epub Date].

Orbital Rhabdomyosarcoma

40

Ran Ben Cnaan, Dana Niry, and Igal Leibovitch

Contents

1 **Signs and Symptoms** 320
2 **Differential Diagnosis** 320
3 **Diagnosis** 320
4 **Treatment** 320
5 **Figures with Captions** 320
References 323

Abstract

Rhabdomyosarcoma (RMS) is the most common soft tissue sarcoma in the pediatric population and infrequently occurs in adults. It is a malignant neoplasm that is composed of cells with histologic features of striated muscle in various stages of embryogenesis [1–4].

RMS can arise primarily in the orbit or as secondary extent from the sinuses and nasal cavity.

Among the histological subtypes, embryonal is most common in the head and neck region including the orbit while alveolar is more aggressive [1, 2].

Most alveolar rhabdomyosarcomas have translocations involving the PAX and the FOX01 genes, giving rise to fusion genes that contribute to lack of differentiation and proliferation of the tumor cells [3, 5].

May be both intraconal and extraconal.

CT shows homogenous soft tissue mass isodense to the extraocular muscles, no calcifications; invasive lesion commonly causing osseous erosion.

MRI – T1 signal isointense to normal muscle, hypointense to orbital fat; T2 signal hyperintense relative to the extraocular muscle.

Highly vascularized lesion with moderate to marked contrast enhancement.

Often low diffusivity on ADC maps indicative of a hypercellular mass [6].

Keywords

Rhabomyosarcoma · Soft tissue sarcoma · Orbital tumor

R. Ben Cnaan (✉) · I. Leibovitch
Oculoplastic and Orbital Institute, Division of Ophthalmology, Sourasky Medical Center, Sackler Faculty of Medicine, Tel Aviv University, Tel Aviv, Israel
e-mail: ran@drbencnaan.co.il

D. Niry
Department of Radiology, Sourasky Medical Center, Tel Aviv University, Tel Aviv, Israel

© Springer Nature Switzerland AG 2022
G. Ben Simon et al. (eds.), *Atlas of Orbital Imaging*,
https://doi.org/10.1007/978-3-030-62426-2_28

1 Signs and Symptoms

Usually rapid onset and progression of proptosis, globe displacement (most commonly inferotemporal), blepharoptosis, chemosis, eyelid swelling, palpable mass, visual impairment, and pain [1, 2, 6].

2 Differential Diagnosis

The differential diagnosis includes most causes for rapidly progressive proptosis in a child including Langerhans cell histiocytosis, orbital cellulitis, idiopathic orbital inflammation, and other "small round blue cell" malignancies such as neuroblastoma, acute leukemia, and Ewing's sarcoma [1, 2, 5].

3 Diagnosis

Clinical presentation includes typical age (8 years), painless proptosis, along with CT and MRI finding, histopathology combined with immunohistochemistry, and electron microscopy if necessary. Although histopathology remains the basis of diagnosis, cytogenetic features and molecular signatures are becoming part of the routine analysis of RMS to determine prognosis, management, and treatment regimens [1–3, 5, 6].

4 Treatment

Systemic chemotherapy and radiotherapy are the mainstay of treatment. Incisional biopsy is mandatory for tissue diagnosis. Orbital exenteration may be justified only for extremely advanced disease, or for very aggressive and resistant tumors. In residual disease, surgical debulking or orbital radiotherapy can be considered [1, 2, 5, 7, 8].

5 Figures with Captions

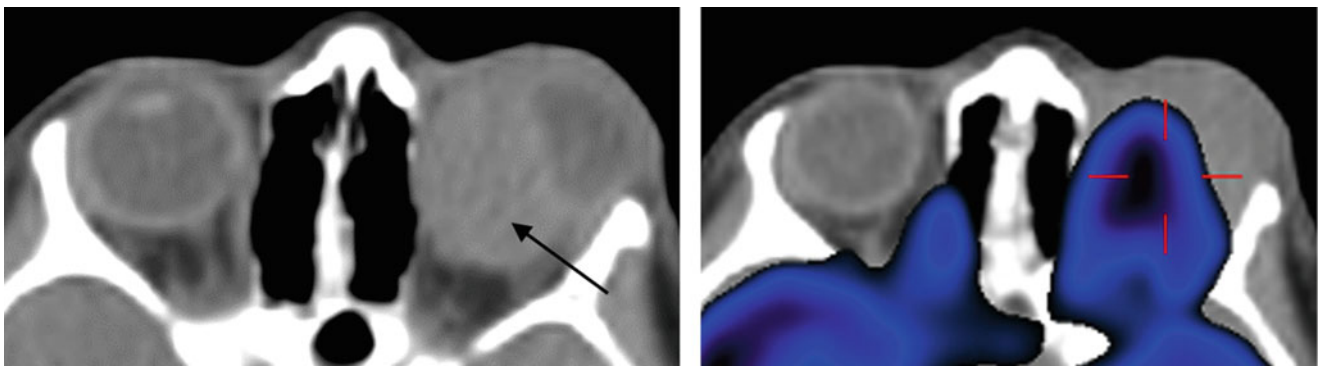


Fig. 1 **PET-CT. Low dose CT, soft tissue window, axial view (*left*),** demonstrates a homogenous soft tissue mass isodense to normal muscle in the left orbit. The mass results in proptosis and deforms the posterior aspect of the globe. There are no obvious calcifications. **Axial PET CT-fused image (*right*)** at the level of the lesion shows increased FDG uptake

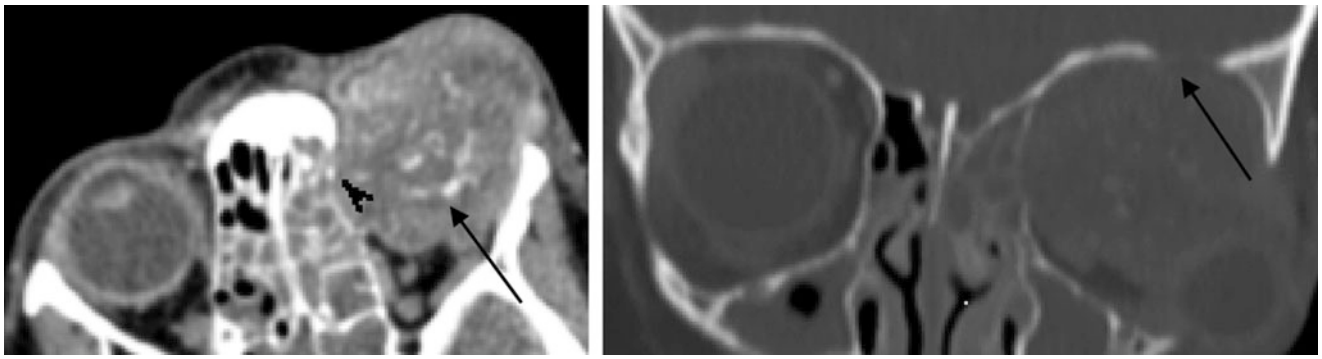


Fig. 2 **Postcontrast orbit CT. Soft tissue window, axial view *(left)***, performed 2 weeks later demonstrates rapid growth of the tumor, which involves both the intraconal and extraconal compartments. The mass shows heterogeneous enhancement and high vascularity (arrow). The lamina papyracea is thinned and deformed with concave margins (arrowhead). There is opacification of the ethmoid air cells. **Bone window, coronal view *(right)***, demonstrates lateral and inferior displacement of the globe. There is bony erosion, most evident in the orbital roof (arrow)

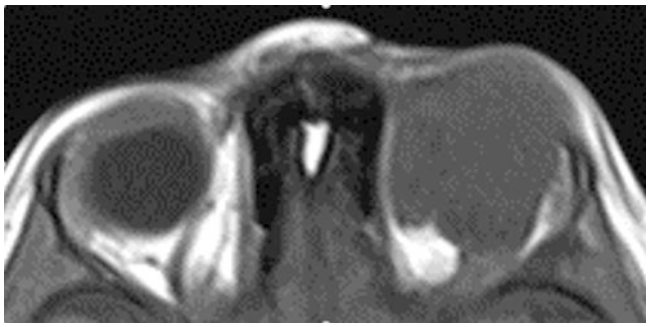


Fig. 3 **Axial unenhanced unsaturated T1 image** demonstrates a mass with irregular borders, with a T1 signal homogeneously isointense relative to extraocular muscles. The hyperintense orbital fat serves as contrast, allowing better delineation of the tumor

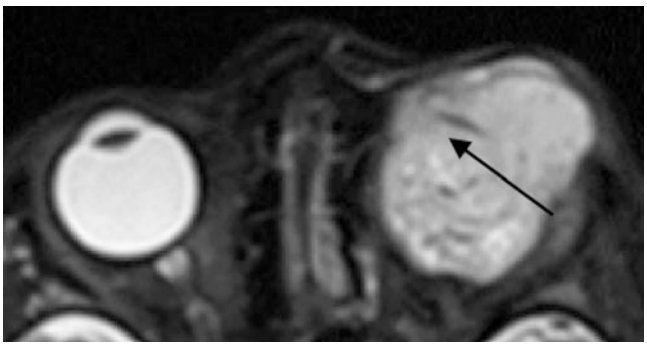


Fig. 4 **Axial STIR image** shows that the mass is of hyperintense T2 signal with flow voids within the lesion (arrow), compatible with high vascularity

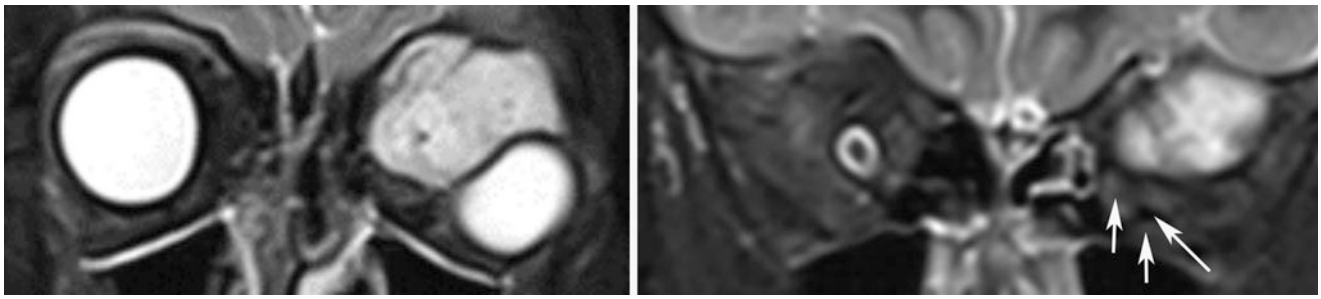


Fig. 5 **Coronal STIR image** ***(left)*** through the middle third of the orbit demonstrates that the epicenter of the mass is located in the superior nasal aspect of the orbit, distorting and markedly dislocating the globe. **Coronal STIR image** ***(right)*** at the level of the distal third of the intraorbital optic nerve shows that the tumor displaces and deforms the optic nerve (long arrow), causing effacement of the CSF space surrounding it. There is also mass effect exerted on the medial and inferior rectus muscles (short arrows) which are seen separate from the tumor. The superior rectus and superior oblique muscles are inseparable from the mass

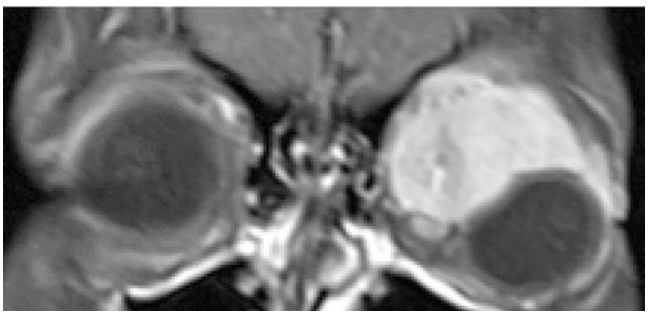


Fig. 6 **Enhanced fat-saturated T1 coronal image** reveals marked tumor enhancement. There is no evidence of intracranial extension

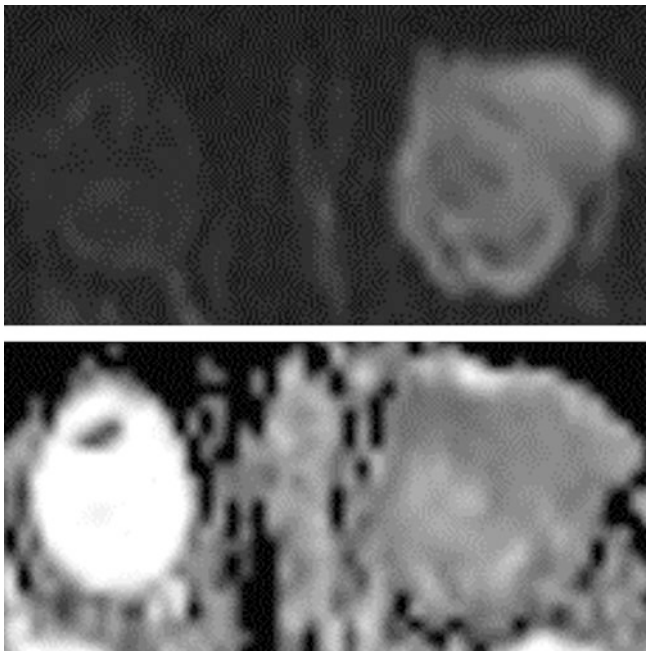


Fig. 7 **Diffusion-weighted imaging (upper image)** at the level of the lesion shows heterogenous hyperintense signal. **Axial apparent diffusion coefficient map (lower image)** reveals hypointense signal in the anterior aspect of the tumor, suggesting high cellularity

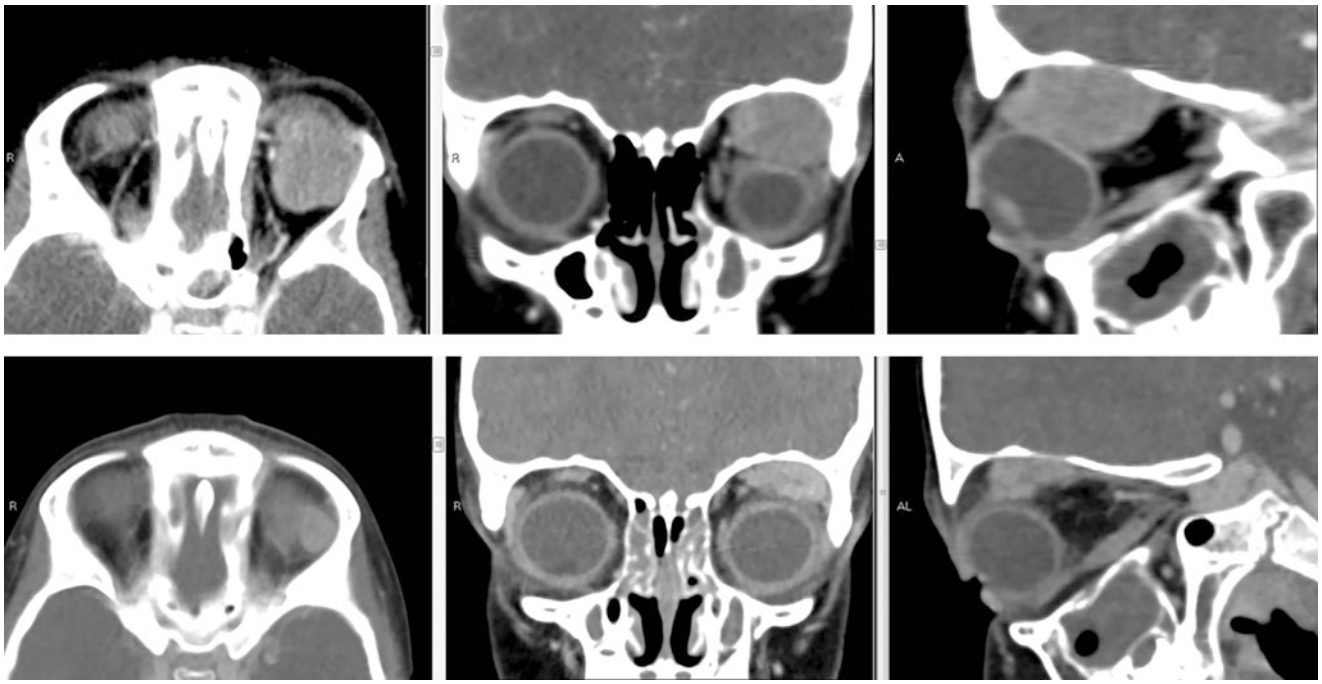


Fig. 8 Axial, coronal, and sagittal CT of a 5-YOM with left superior orbital RMS pre- (upper row) and post- (lower row) systemic treatment. There is marked improvement in tumor size, and globe indentation albeit small residual tumor

References

1. Shields JA, Shields CL. Rhabdomyosarcoma: review for the ophthalmologist. Surv Ophthalmol. 2003;48(1):39–57.
2. Karcioglu ZA, Hadjistilianou D, Rozans M, DeFrancesco S. Orbital Rhabdomyosarcoma. Cancer Control. 2004;11(5):328–33.
3. Leiner J, Le Loarer F. The current landscape of rhabdomyosarcomas: an update. Virchows Arch. 2020;476(1):97–108.
4. Spreafico F, Ferrari A, Mascarin M, Collini P, Morosi C, Biasoni D, Biassoni V, Schiavello E, Gandola L, Gattuso G, Chiaravalli S, Massimino M. Wilms tumor, medulloblastoma, and rhabdomyosarcoma in adult patients: lessons learned from the pediatric experience. Cancer Metastasis Rev. 2019;38(4):683–94.
5. Cortes Barrantes P, Jakobiec FA, Dryja TP. A review of the role of cytogenetics in the diagnosis of orbital rhabdomyosarcoma. Semin Ophthalmol. 2019;34(4):243–51.
6. Mu X, Wang H, Li Y, Hao Y, Wu C, Ma L. Magnetic resonance imaging and DWI features of orbital rhabdomyosarcoma. Eye Sci. 2014;29(1):6–11.
7. Crist WM, Anderson JR, Meza JL, Fryer C, Raney RB, Ruymann FB, Breneman J, Qualman SJ, Wiener E, Wharam M, Lobe T, Webber B, Maurer HM, Donaldson SS. Intergroup rhabdomyosarcoma study-IV: results for patients with nonmetastatic disease. J Clin Oncol. 2001;19(12):3091–102. https://doi.org/10.1200/JCO.2001.19.12.3091. PMID: 11408506.
8. Ingley KM, Cohen-Gogo S, Gupta AA. Systemic therapy in pediatric-type soft-tissue sarcoma. Curr Oncol. 2020;27(S1):6–16

Orbital Lipoma

41

Ran Ben Cnaan, Dana Niry, and Igal Leibovitch

Contents

1 **Signs and Symptoms** 326
2 **Differential Diagnosis** 326
3 **Diagnosis** 326
4 **Treatment** 326
5 **Figures with Captions** 326
References 329

Abstract

Lipomas are common mesenchymal neoplasms, usually occurring in the subcutaneous tissues of the extremities and trunk and less commonly occur within deeper tissues such as the retroperitoneum. Although fat is abundant in the orbit, lipomas and related variants (such as fibrolipoma, spindle cell lipoma, and angiolipoma) are rare in the orbital region, usually presenting as a well-circumscribed benign mass arising mainly from the anterior orbit [1–3]. Histologically they are composed of mature adipose tissue, lobulated and surrounded by fine capsule [1,4].

CT – Homogeneous, well-defined, low attenuation mass with fat density in Hounsfield units (range −50 to −150) and finely defined border. No calcifications or fluid-fluid levels. Long-term tumoral pressure may cause bone remodeling. MRI – Follows subcutaneous and intraorbital fat signal on T1 (hyperintense) and T2 (hypointense) weighted images with signal loss on fat-suppressed images.

Usually non-enhancing (significant enhancement, along with heterogeneity, hypervascularity, and rapid growth, raises concern for liposarcoma) [1–5].

Keywords

Lipoma · Benign mesenchymal tumor · Orbit

R. Ben Cnaan (✉) · I. Leibovitch
Oculoplastic and Orbital Institute, Division of Ophthalmology, Sourasky Medical Center, Sackler Faculty of Medicine, Tel Aviv University, Tel Aviv, Israel
e-mail: ran@drbencnaan.co.il

D. Niry
Department of Radiology, Sourasky Medical Center, Tel Aviv University, Tel Aviv, Israel

© Springer Nature Switzerland AG 2022
G. Ben Simon et al. (eds.), *Atlas of Orbital Imaging*,
https://doi.org/10.1007/978-3-030-62426-2_29

1 Signs and Symptoms

Orbital lipomas are well-circumscribed independent masses that displace rather than infiltrate surrounding tissue. The lesion is typically located in the anterior orbit and is thus clinically apparent at an early stage. Presentation includes a painless slowly growing mass, proptosis or eyelid swelling, diplopia, globe displacement, and eyelid ptosis, depending on size and location within the orbit [1–7].

2 Differential Diagnosis

Orbital fat, dermolipoma, dermoid/epidermoid, well-differentiated lipo-sarcoma or atypical lipomatous tumor [1, 6–11].

3 Diagnosis

The diagnosis can be based on radiological findings and if needed histological appearance.

4 Treatment

Conservative with regular clinical follow-up. In symptomatic cases or when suspecting malignant transformation, surgical excision is the treatment of choice [1], a subtotal removal may be acceptable in anatomically critical areas such as the orbital apex due to the rarity of local recurrence. Steroid injections are also described as an alternative option for treatment, through mechanism of local fat atrophy [5, 6, 8].

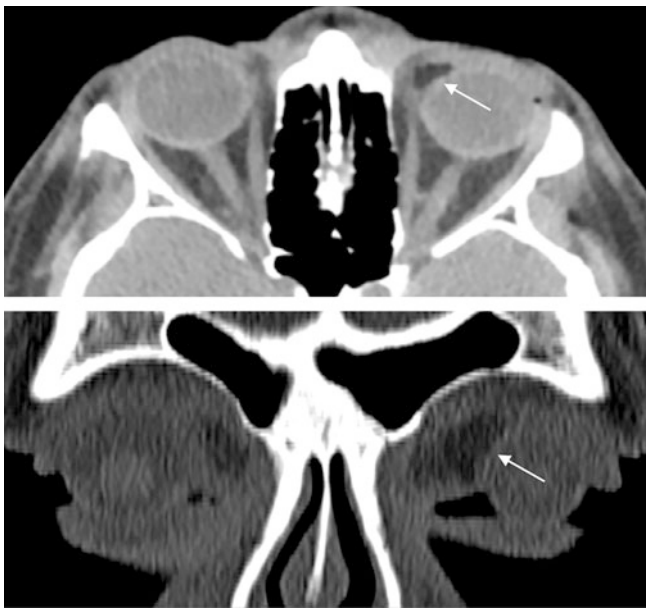


Fig. 1 Unenhanced orbit CT, soft tissue window, axial view (*upper*). A homogenous, well circumscribed, hypodense extraconal mass residing in the superonasal region of the left orbit. Attenuation values are consistent with fatty tissue. There is no continuity with the intraconal fat. **Bone window, coronal view (*lower*).** There are no calcifications within the mass

5 Figures with Captions

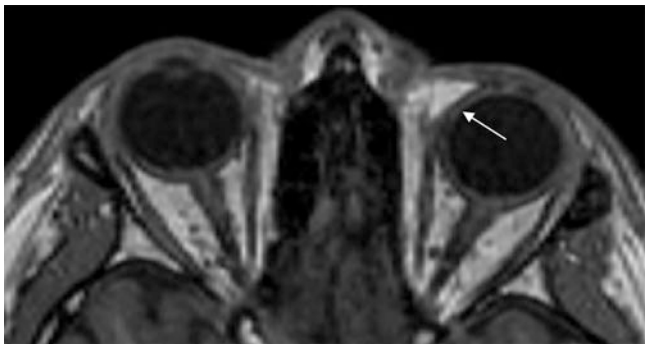


Fig. 2 Unenhanced unsaturated T1 axial image demonstrates the lesion abutting the medial wall of the eyeball, anterior to the insertion of the medial rectus muscle. It conforms to the contour of the eyeball. The mass returns hyperintense T1 signal

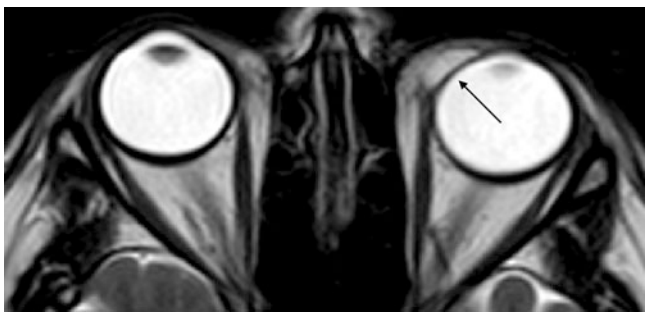


Fig. 3 T2 axial image nonfat saturated demonstrates that the mass is of high T2 signal, similar to that of the intraorbial and subcutaneous fat

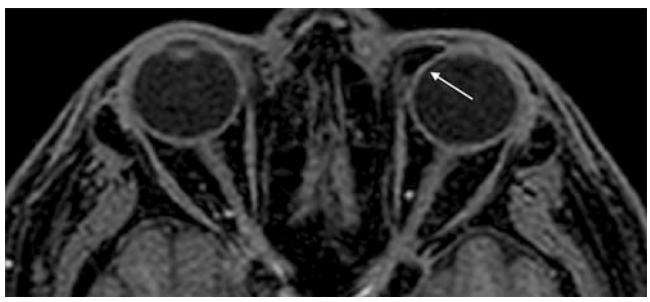


Fig. 4 Unenhanced fat-saturated T1 axial image shows that there is complete signal loss within the mass

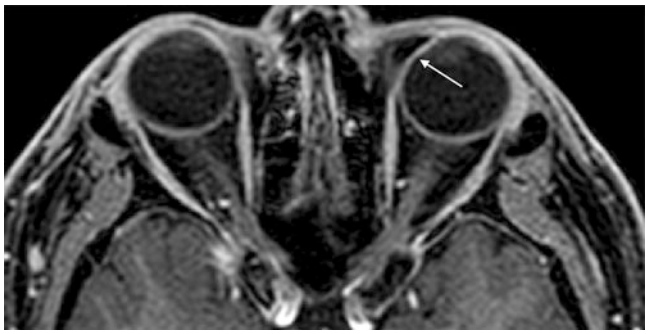


Fig. 5 Enhanced fat-saturated T1 axial image reveals no contrast enhancement of the lesion

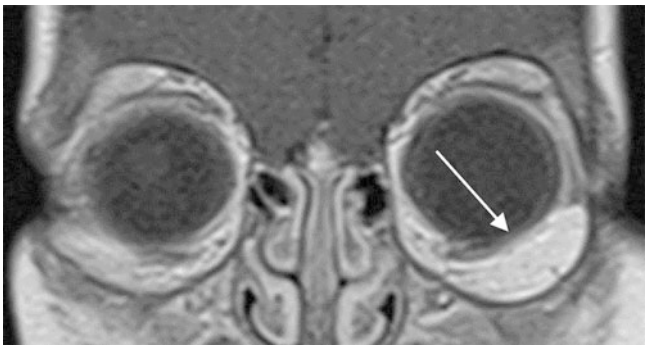


Fig. 8 Unenhanced unsaturated T1 coronal image of the same patient as in Fig. 7 shows that the lesion is of hyperintense T1 signal

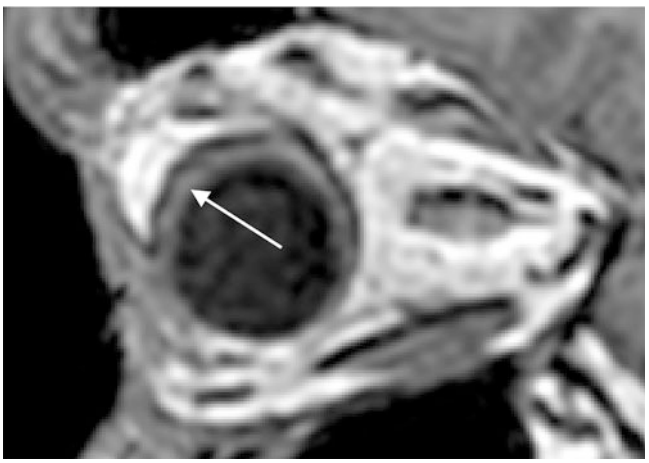


Fig. 6 Unenhanced unsaturated T1 sagittal image demonstrates the subconjuctival location of the crescent-shaped lesion of fat signal intensity

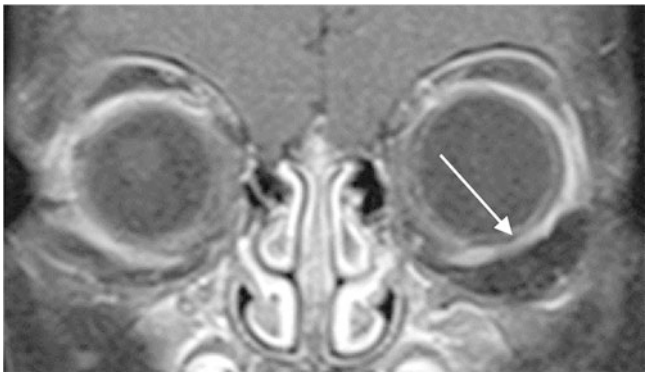


Fig. 9 Enhanced fat-saturated T1 coronal image demonstrates that the lesion is nonenhancing

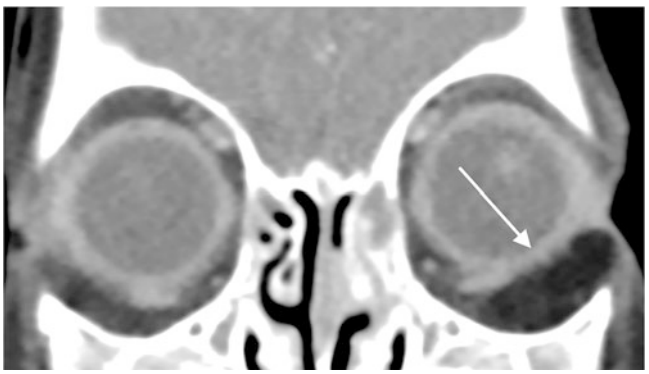


Fig. 7 Unenhanced orbit CT, soft tissue window, coronal view of a different patient demonstrates a well-defined hypodense lesion, of similar density to the orbital fat, in the inferior temporal aspect of the left orbit

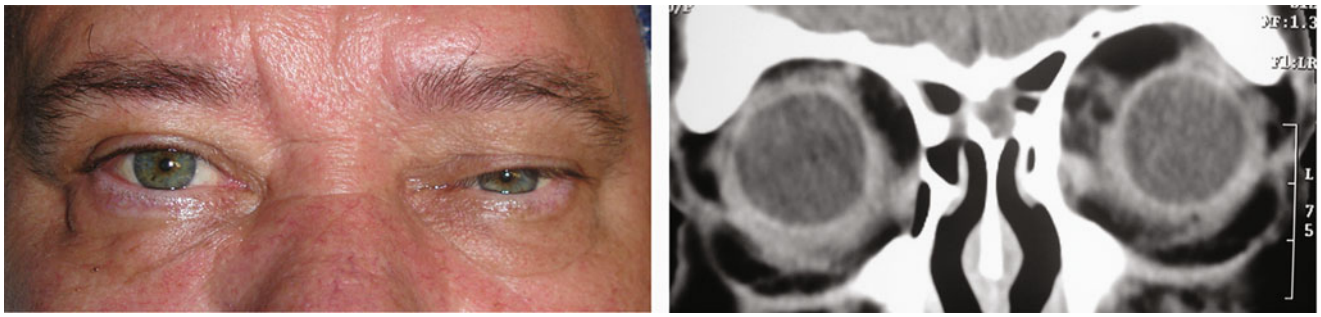


Fig. 10 Clinical photograph of an elderly male with slow growing mass on the left orbit causing mechanical ptosis and fullness of the left upper eyelid. NECT depicts fatty mass in the left anterior superior orbit, consistent with orbital lipoma. (Courtesy of the editors)

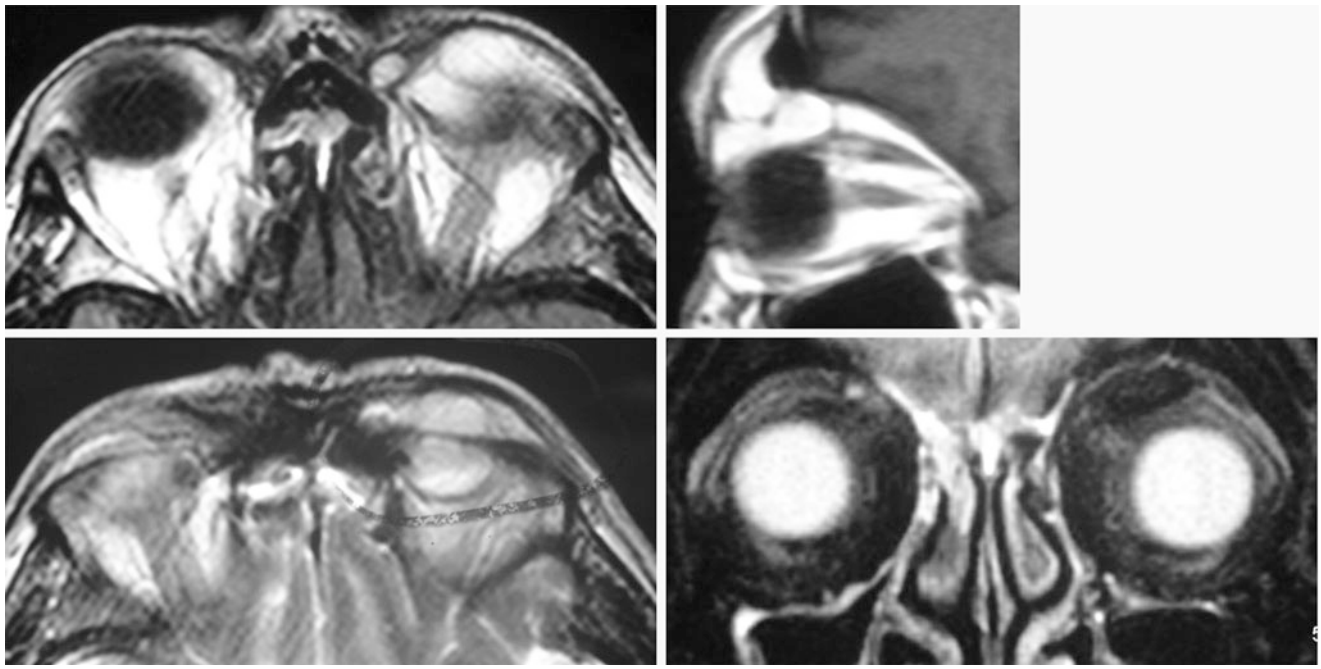


Fig. 11 MRI image of the same patient as in Fig. 10, showing a well-defined relatively homogenous mass in the left superior orbit, with bright hyperintense signal on T1 (axial upper left and sagittal upper right) and hypointense signal on T2 (axial lower left and coronal lower right). (courtesy of the editors)

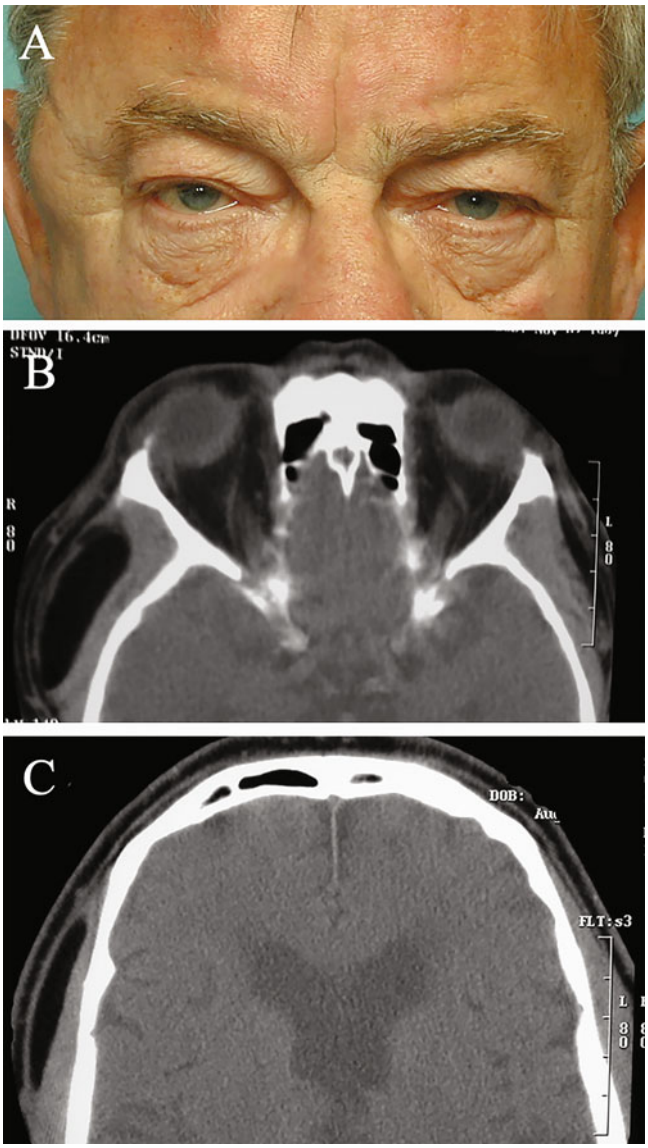


Fig. 12 A clinical photograph of 75-YOM with right temple soft tissue mass; B-C. NECT, axial sections showing a well-defined homogenous hypoindense mass in the right temple with fat tissue density, consistent with lipoma. (courtesy of the editors)

References

1. Shah NB, Chang WY, White VA, Heran MKS, Rootman J. Orbital lipoma: 2 cases and review of literature. Ophthalmic Plast Reconstr Surg. 2007;23(3):202–5.
2. Ong LY, Mercer B, Campbell LJ, McNab AA. Abnormal cytogenetic in orbital lipoma. Ophthalmic Plast Reconstr Surg. 2009;25(3):243–5.
3. Ali SF, Farber M, Meyer DR. Fibrolipoma of the orbit. Ophthalmic Plast Reconstr Surg. 2013;29(3):e79–81.
4. Kim MH, Sa HS, Woo KI, Kim YD. Fibrolipoma of the Orbit. Ophthalmic Plast Reconstr Surg, 2011; 27(1):e16–8
5. Corredor-Osorio R, Ramos-Pineda N, Orellana ME. Fibrolipoma on upper eyelid in child. GMC Ophthalmol cases 2016 Mar 17;6:Doc03
6. Hristodulopulos V, Medel R. Intramuscular lipoma of superior rectus muscle. Ophthalmic Plast Reconstr Surg 2016;32(3):e52–5.
7. McKey K, Zhang PJL, Shields CL, Lally SE, Eagle RC Jr, Milman T. Orbital atypical lipomatous tumor/well-differentiated liposarcoma masquerading as pleomorphic lipoma: a diagnostic challenge. Ophthalmic Plast Reconstr Surg 2019;35(3):e76–e80.
8. Tripathy D, Mittal R. Spindle cell lipoma of the orbit. Ophthalmic Plast Reconstr Surg 2015;31(3):e53–5.
9. Stacy RC, Bernardo LA, Nielsen GP. Absence of chromosomal abnormalities in herniated orbital fat. Histopathology. 2014;65(2):273–7. https://doi.org/10.1111/his.12404. Epub 2014 Apr 17. PMID: 24588545.
10. Schmack I, Patel RM, Folpe AL, Wojno T, Zaldivar RA, Balzer B, Kang SJ, Weiss SW, Grossniklaus HE. Subconjunctival herniated orbital fat: A benign adipocytic lesion that may mimic pleomorphic lipoma and atypical lipomatous tumor. Am J Surg Pathol. 2007;31(2):193–8. https://doi.org/10.1097/01.pas.0000213374.02171.0a. PMID: 17255763.
11. Daniel CS, Beaconsfield M, Rose GE, Luthert PJ, Heathcote JG, Clark BJ. Pleomorphic lipoma of the orbit: a case series and review of literature. Ophthalmology. 2003;110(1):101–5. https://doi.org/10.1016/s0161-6420(02)01450-1. PMID: 12511353.

Solitary Fibrous Tumor of the Orbit

42

Ran Ben Cnaan, Justin N. Karlin, Dana Niry, Igal Leibovitch, and Robert A. Goldberg

Contents

1 Signs and Symptoms 332
2 Differential Diagnosis 332
3 Diagnosis 332
4 Treatment 332
5 Figures with Captions 332
References 338

Abstract

Solitary fibrous tumor (SFT) is an uncommon spindle cell tumor of mesenchymal origin. SFT was first described as a pleural-based mass, but has since been identified in numerous extra-pleural sites including the orbit. Although generally benign, malignant variants have been identified and metastasis can rarely occur [1–3]. Ovoid, well-circumscribed, lobulated mass on noncontrast CT that may appear heterogeneous and may contain calcifications. MRI of benign lesions shows heterogeneous iso- to hypo-intensity on T1w and heterogeneous hypo- to iso-intensity on T2w sequences; hyperintense signal on T1 may suggest recent hemorrhage (methemoglobin). Heterogeneous hyperintensity on T2w sequences raises the possibility of cystic degeneration or hemorrhage. Tubular flow-void signals are occasionally seen, representing intra-tumoral vessels. Marked homogeneous or heterogeneous enhancement following contrast administration may have central cystic or necrotic changes in larger or malignant lesions. Regions of restricted diffusion may be seen [1–7].

Keywords

Solitary fibrous tumor · Hemangiopericytoma · Mesenchymal tumor · Spindle cell tumor · Soft tissue tumor

R. Ben Cnaan (✉) · I. Leibovitch
Oculoplastic and Orbital Institute, Division of Ophthalmology, Sourasky Medical Center, Sackler Faculty of Medicine, Tel Aviv University, Tel Aviv, Israel
e-mail: ran@drbencnaan.co.il

J. N. Karlin (✉)
Division of Orbital and Ophthalmic Plastic Surgery, Stein Eye Institute, University of California, Los Angeles, CA, USA
e-mail: jkarlin@mednet.ucla.edu

D. Niry
Department of Radiology, Sourasky Medical Center, Tel Aviv University, Tel Aviv, Israel

R. A. Goldberg
Division of Orbital and Ophthalmic Plastic Surgery, Stein and Doheny Eye Institutes, University of California, Los Angeles, CA, USA
e-mail: goldberg@jsei.ucla.edu

© Springer Nature Switzerland AG 2022
G. Ben Simon et al. (eds.), *Atlas of Orbital Imaging*,
https://doi.org/10.1007/978-3-030-62426-2_30

1 Signs and Symptoms

Painless slowly growing orbital mass, usually in the fifth decade of life but can also occur in childhood. There is a slight male or no sex predilection. Progressive proptosis, eyelid swelling, globe displacement, ocular motility restriction, vision disturbances, tearing, ptosis, and facial deformity, depending on tumor size and location in the orbit. Extrapleural cases seem less likely to run an aggressive course [1–5, 8].

Although generally benign, malignant variants have been identified and metastasis to the lung and parotid gland can rarely occur. It was first described as pleural based but has been identified in numerous extrapleural sites.

2 Differential Diagnosis

Cavernous hemangioma, meningioma, schwannoma, and other mesenchymal tumors (recognized as within the expanded spectrum of SFTs) as hemangiopericytoma, fibrous histiocytoma, and giant cell angiofibroma [1–7, 9].

3 Diagnosis

Radiologic features, particularly MRI findings combined with immunohistochemical activity analysis, are crucial for establishing the correct diagnosis. Immunohistochemical staining shows strong diffuse cytoplasmic positivity for CD34 and vimentin in almost all cases and variable positivity for CD99 and Bcl-2. SFTs are not immunoreactive for S-100, CK, and SMA [1, 7, 8, 10–12]. Staining for STAT 6 has high sensitivity and specificity for SFT [3, 9].

4 Treatment

Complete surgical resection with clear margins via orbitotomy is the definitive treatment for orbital SFT avoiding recurrence and potential malignant transformation [1]. Combined orbitotomy-craniotomy is required for larger or more complex lesions. Hemangiopericytoma spectrum lesions may be more likely to bleed intraoperatively, ostensibly due to the presence of vascular channels. Preoperative embolization can assist in preventing intraoperative bleeding, in large highly vascular SFTs [13]. Recurrence or malignant transformation of solitary fibrous tumor is possible with incomplete excision. Postoperative radiotherapy or chemotherapy can be used as an adjuvant therapy when the lesion is incompletely excised or in recurrent and malignant cases [1–4, 8]. Factors that may be associated with recurrence includes: tumor size, atypia, mitotic rate, necrosis, and epithelioid cytomorphology [9]. It remains unclear whether a subset of asymptomatic patients with histopathologically benign disease can be observed without negative sequelae [3]. Long-term follow-up including annual MRI scans is recommended in order to detect recurrences [5, 8, 14].

5 Figures with Captions

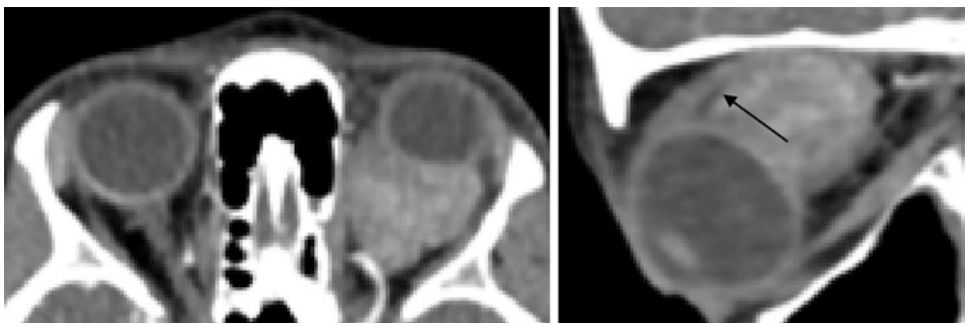


Fig. 1 **CT angiogram**. **Soft tissue window, axial view (*left*)** demonstrates a retrobulbar soft tissue mass with heterogeneous enhancement displacing the eyeball forward. There are no obvious calcifications, and no cystic or fatty elements. **Sagittal oblique view (*right*)** shows the mass residing in the superior intraconal region compressing the superior rectus muscle (arrow) and displacing it superiorly. There is mild flattening of the superior globe

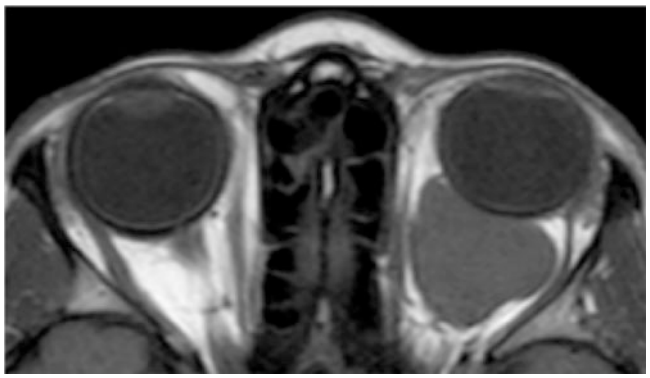


Fig. 2 Axial unenhanced unsaturated T1 image demonstrates a well-defined lobulated mass located in the superior aspect of the intraconal space, with a T1 signal homogeneously isointense to EOM

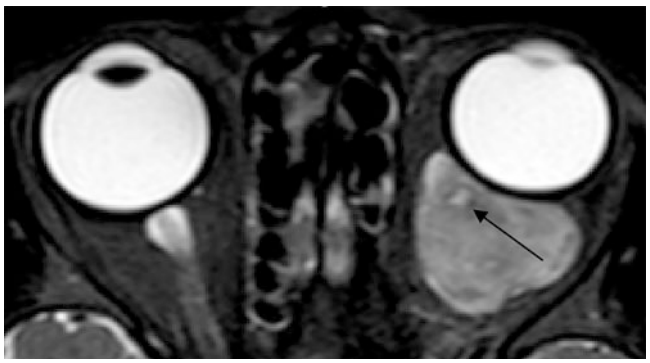


Fig. 3 Axial T2 fat-saturated view shows that the mass is of heterogeneous T2 signal with small areas of bright signal intensity (arrow) within the lesion

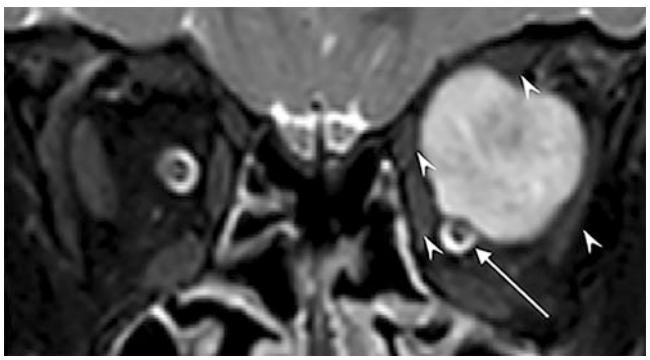


Fig. 4 Coronal T2 fat-saturated view demonstrates that the mass is abutting the superior margin of the left optic nerve sheath complex, exerting mass effect. The optic nerve (arrow) is displaced inferomedially, with effacement of the CSF space around its superior aspect. The superior rectus, superior oblique, medial and lateral recti muscles (arrowheads) are thinned and stretched around the mass

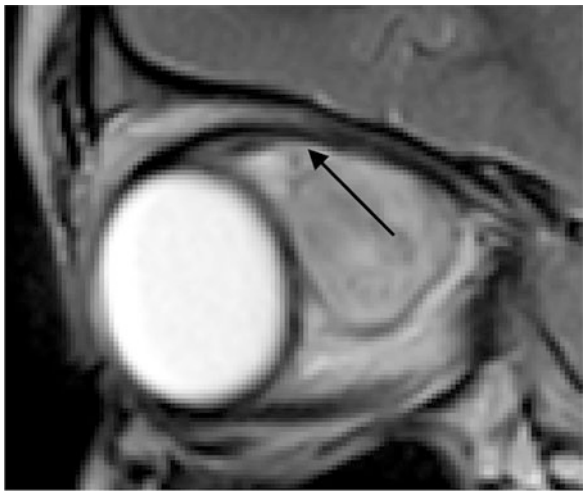


Fig. 5 Sagittal T2 view nicely shows the thinning and superior displacement of the superior rectus muscle (arrow)

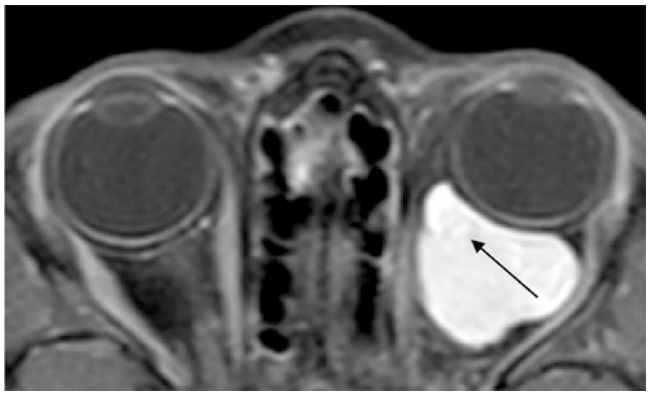


Fig. 6 Enhanced fat-saturated T1 axial image reveals homogeneous tumor enhancement. Note foci of more marked enhancement corresponding to the bright T2 signal areas (arrow)

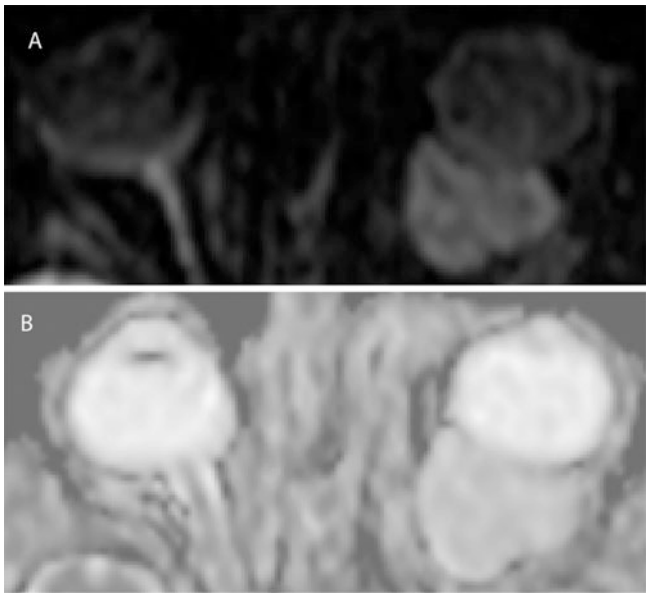


Fig. 7 **Axial diffusion-weighted image (A)** at the level of the lesion shows a slighlty heterogeneous isointense signal. **Axial apparent diffusion coefficient map (B)** reveals a heterogeneous isointense signal (nonrestrictive)

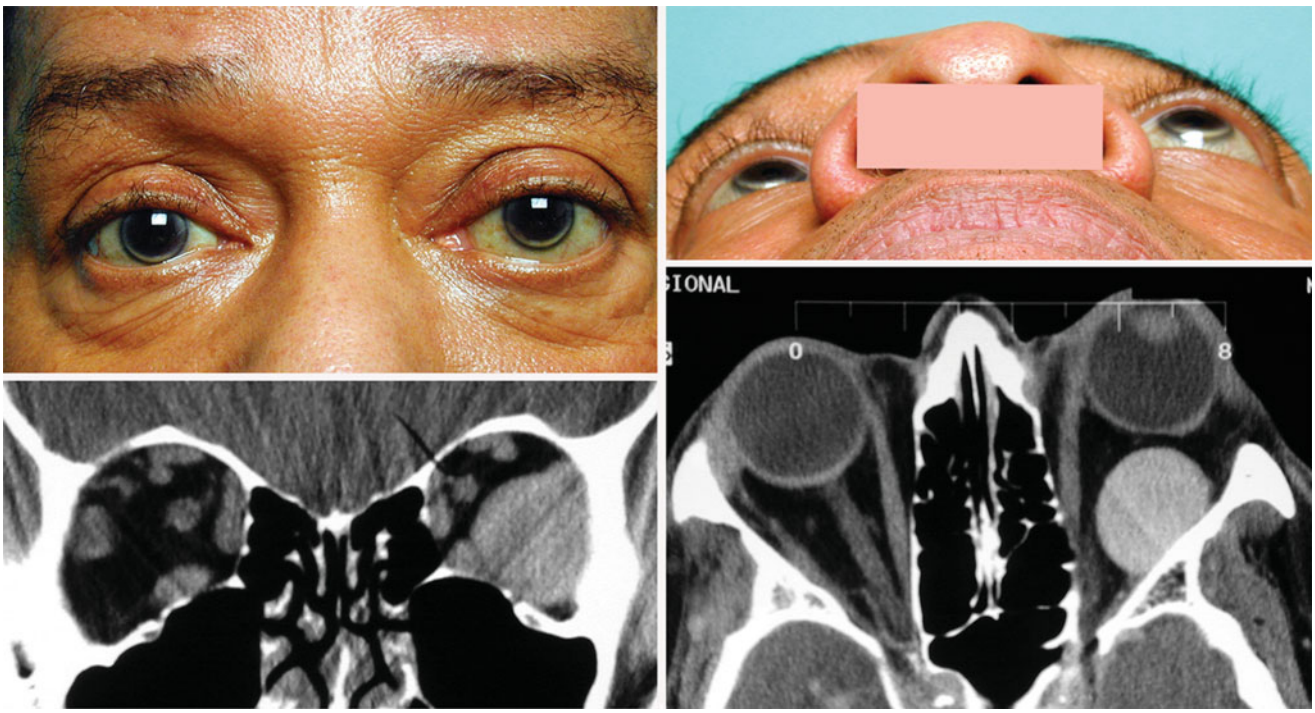


Fig. 8 Clinical photographs of an elderly male (upper row) with left eye axial proptosis and hyperglobus caused by orbital solitary fibrous tumor. CECT coronal and axial view (lower row) showing a well-defined oval mass in the lateral orbit, extra and intraconal, non-separable from the LR muscle. The lesion is displacing the optic nerve sheath complex medially and causing significant proptosis. The lesion is homogeneously enhancing. (Courtesy of the editors)

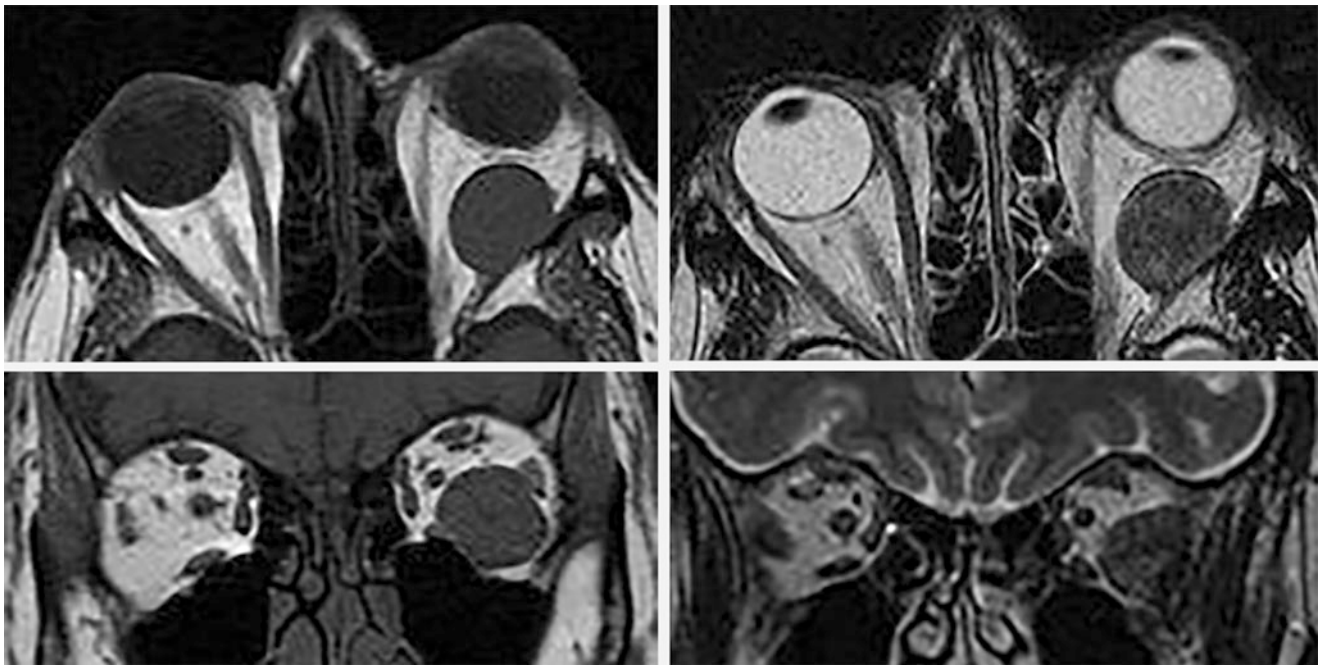


Fig. 9 MR scan of the same patient as in Fig. 8, NE T1WI axial and coronal (left column) and NE T2WI (non-FS) axial and coronal (right column) better demonstrating the homogeneity of the mass. The tumor is slightly hypointense on T1 and on T2 sequences. (Courtesy of the editors)

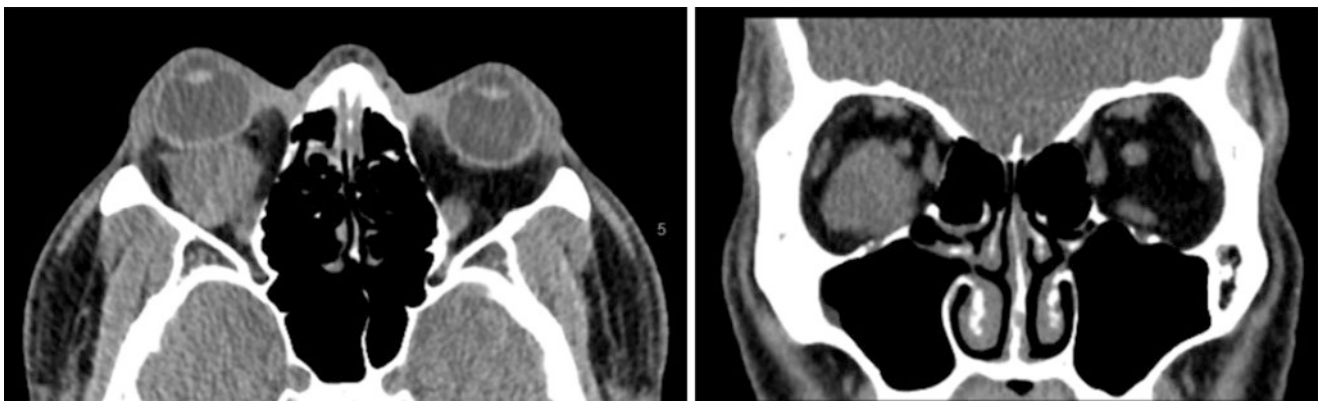


Fig. 10 **Left image – non-contrast axial CT orbit, soft tissue window (different patient),** shows isodense intraconal homogeneous lesion of the right orbit causing globe indentation and proptosis. **Right image – non-contrast coronal CT orbit** shows lobulated, smooth lesion occupying the caudal two-thirds of the intraconal space and displacing the optic nerve superomedially



Fig. 11 **Left image – non-contrast axial T2w MRI orbit without fat suppression (different patient)** shows a very large left orbital mass with intrinsic heterogeneous hypo- to isointensity replacing the orbital retrobulbar space inseparable from the orbital content and displacing the lamina papyracea. The lesion is causing significant proptosis and posterior globe indentation. **Middle image – non-contrast fat saturated axial T1w MRI orbit** demonstrates an isointense lesion of left orbit causing proptosis. **Right image – Gd contrast axial T1w MRI orbit** demonstrates diffuse, homogeneous enhancement. The lesion abuts the orbital apex and superior orbital fissure. Note the evidence of previous lateral orbitotomy. This lesion is a recurrent solitary fibrous tumour

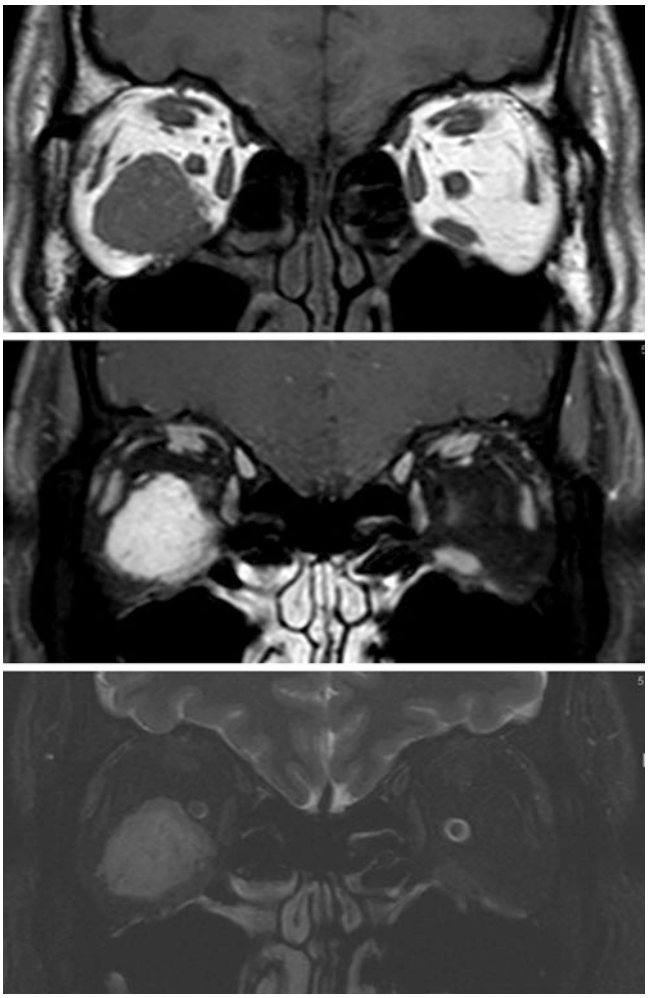


Fig. 12 **Top image – non-contrast coronal T1w MRI orbit (different patient)** shows an isointense right inferior orbital lesion with somewhat smooth borders displacing the optic nerve superomedially. **Middle image – Gd contrast fat saturated coronal T1w MRI orbit** demonstrates the same lesion with homogeneous contrast enhancement. **Lower image – coronal T2w MRI orbit shows** the same lesion, isointense

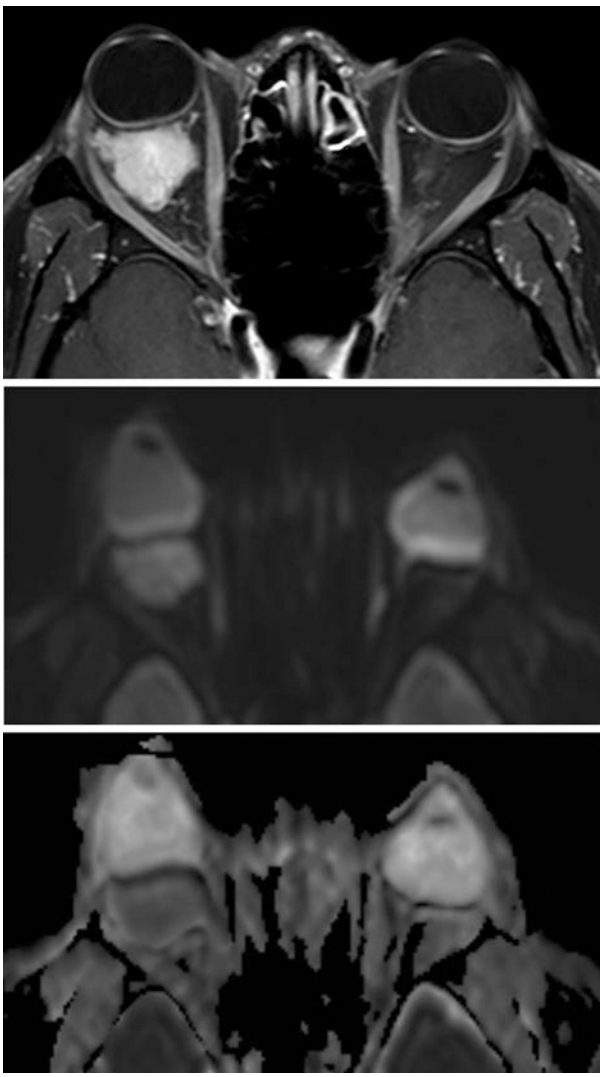


Fig. 13 **Top image – Gd contrast axial T1w MRI orbit with fat saturation** shows a contrast enhancing right orbital lesion with well-demarcated borders, which is indenting the globe. **Middle image – axial orbit MRI, diffusion-weighted imaging,** and **lower image – axial orbit MRI, apparent diffusion coefficient** show restricted diffusion of the right orbital lesion. Histopathology of this lesion demonstrated solitary fibrous tumor

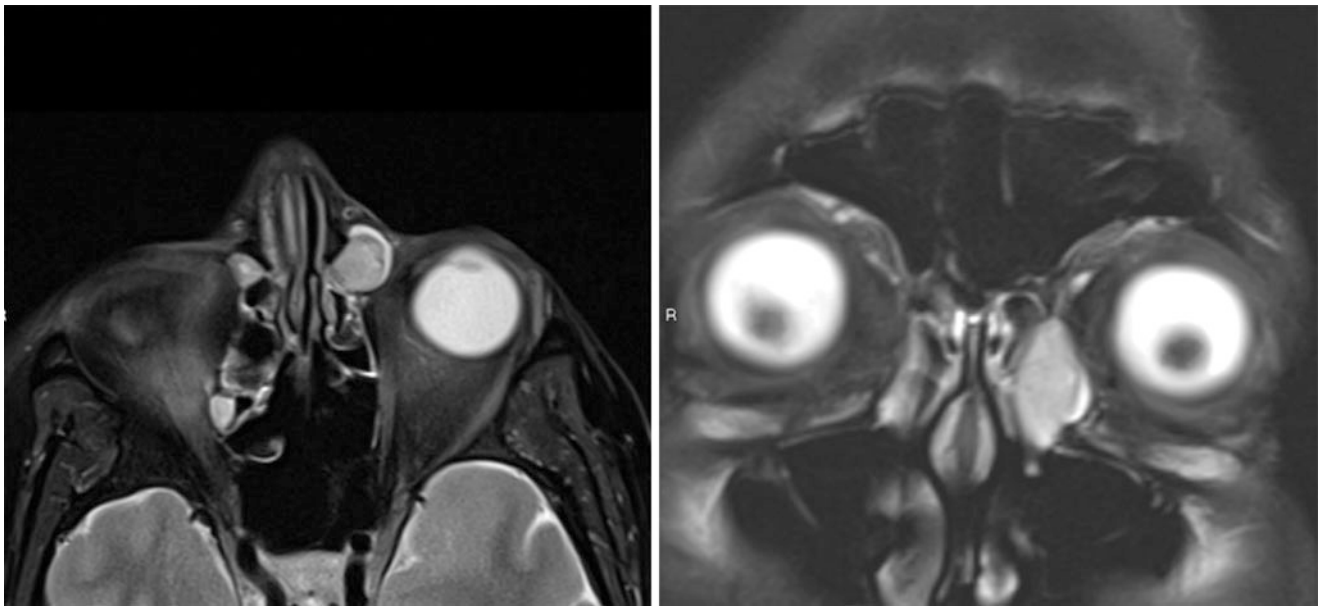


Fig. 14 A 50-YO female with a history of metastatic breast cancer presented with left-sided epiphora and punctal stenosis, presumed to be secondary to systemic chemotherapy. Conventional treatment with punctal dilation and stenting did not improve symptoms, hence, imaging was performed. **T2-FS-WI axial (left) and coronal (right)** views demonstrate an iso-hyper intense rather homogeneous mass expanding the left lacrimal sac. The tumor is surrounded by tear fluid. The coronal view better demonstrates the full extent of the lesion, which is confined to the lacrimal sac

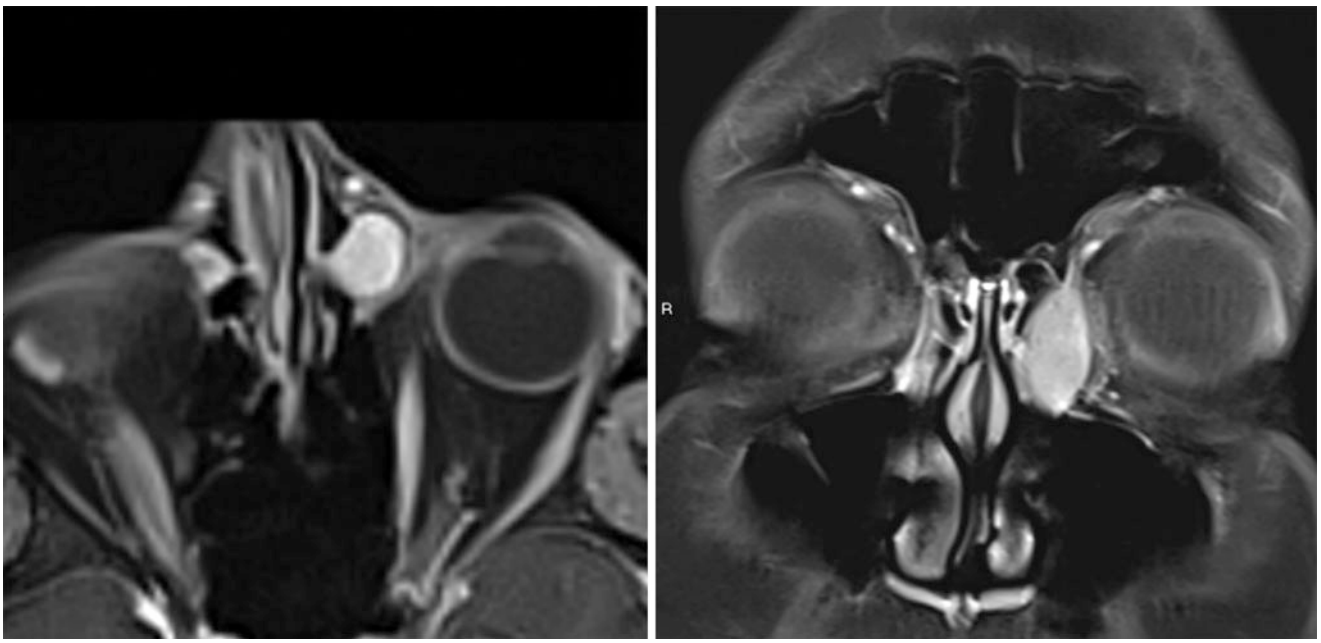


Fig. 15 **T1-WI-FS-CE of the same patient, axial (left) and coronal (right)** images, shows intense enhancement of the tumor, a typical feature of solitary fibrous tumor

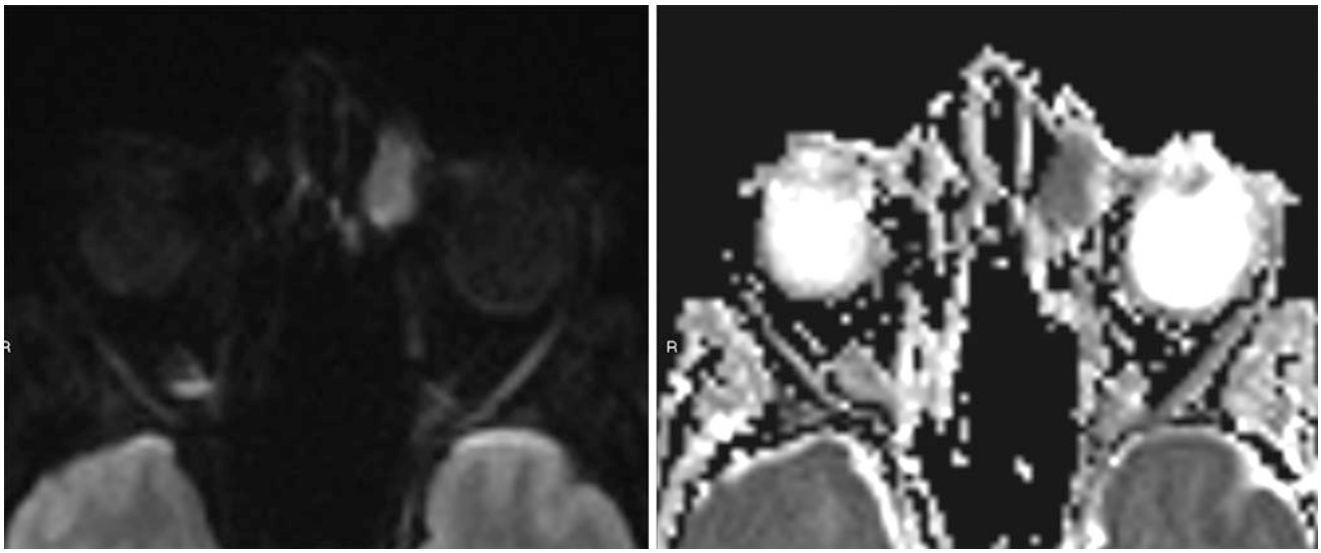


Fig. 16 DWI (left) and corresponding ADC map (right) showing restrictive diffusion. (Figs. 14, 15, and 16 courtesy of the editors)

References

1. Le CP, Jones S, Valenzuela AA. Orbital solitary fibrous tumor: a case series with review of the literature. Orbit. 2014;33(2):145–51.
2. Brum M, Nzwalo H, Oliveira E, Pelejão MR, Pereira P, Farias JP, Pimentel J. Solitary fibrous tumors of the orbit and central nervous system: a case series analysis. Asian J Neurosurg. 2018;13(2):336–40.
3. Blessing NW, Bermudez-Magner JA, Fernandez MP, Rosenberg AE, Dubovy SR, Johnson TE. Solitary fibrous tumor of the orbit: a case series with clinicopathologic correlation and evaluation of STAT6 as a diagnostic marker. Ophthalmic Plast Reconstr Surg. 2020;36(2):164–71.
4. Shen J, Li H, Feng S, Cui H. Orbital solitary fibrous tumor: a clinicopathologic study from a Chinese tertiary hospital with a literature review. Cancer Manag Res. 2018;10:1069–78.
5. Yang BT, Wang YZ, Dong JY, Wang XY, Wang ZC. MRI study of solitary fibrous tumor in the orbit. Am J Roentgenol. 2012;199(4): W506–11.
6. Kim HJ, Kim HJ, Kim YD, Yim YJ, Kim ST, Jeon P, Kim KH, Byun HS, Song HJ. Solitary fibrous tumor of the orbit: CT and MR imaging findings. Am J Neuroradiol. 2008;29(5):857–62.
7. Liu L, Li KC, Shi H, Tao XF. Solitary fibrous tumours in the extracranial head and neck region: correlation of CT and MR features with pathologic findings. Radiol Med. 2014;119:910–9.
8. Künzel J, Hainz M, Ziebart T, Pitz S, Ihler F, Strieth S, Matthias C. Head and neck solitary fibrous tumors: a rare and challenging entity. Eur Arch Otorhinolaryngol. 2016;273(6):1589–98.
9. Smith SC, Gooding WE, Elkins M, Patel RM, Harms PW, McDaniel AS, Palanisamy N, Uram-Tuculescu C, Balzer BB, Lucas DR, Seethala RR, McHugh JB. Solitary fibrous tumors of the head and neck: a multi- institutional clinicopathologic study. Am J Surg Pathol. 2017;41(12):1642–56.
10. Sayit AT, Elmali M, Gul A, Sullu Y. Solitary fibrous tumor of the orbit: computed tomography and histopathological findings. J Cancer Res Ther. 2019;15(3):719–21. https://doi.org/10.4103/jcrt.JCRT_1194_16.
11. Ali MJ, et al. Orbital solitary fibrous tumor: a clinicopathologic correlation and review of literature. Oman J Ophthalmol. 2011;4 (3):147–9.
12. Krishnakumar S, Subramanian N, Mohan ER, Mahesh L, Biswas J, Rao NA. Solitary fibrous tumor of the orbit: a clinicopathologic study of six cases with review of the literature. Surv Ophthalmol. 2003;48(5):544–54.
13. Demura M, Hayashi Y, Sasagawa Y, Mohri M, Takahira M, Nakada M. Intraorbital solitary fibrous tumor requiring preoperative embolization of feeding artery. Asian J Neurosurg. 2019 14 (2):593–7.
14. Chakrabartty H, Singhvi S, Purohit D, Mittal RS. Malignant solitary fibrous tumour of orbit. Asian J Neurosurg. 2017;12(1):55–7.

Granulomatous Orbital Inflammation: Orbital Langerhans Cell Histiocytosis

43

Alan A. McNab

Contents

1 **Symptoms and Signs** 339
2 **Differential Diagnosis** 339
3 **Diagnosis** 339
4 **Treatment** 340
5 **Figures with Captions** 340
References 345

Abstract

- Langerhans cell histiocytosis (LCH) is a histiocyte disorder occurring usually in childhood and manifesting as unifocal or multifocal disease.
- Orbital disease is most often unifocal and relatively benign.
- Bone erosion is characteristic, usually with beveled edges, and best seen on CT.
- T1-weighted MRI usually shows iso- to hypointense lesions with some heterogeneity, and mixed hyper- to hypo-intense signal on T2, with marked enhancement.
- Bone scans are useful for assessing systemic involvement, but PET-CT is more sensitive.
- Disease often involves the frontal bone adjacent to the lacrimal gland and may spread to involve the temporal and anterior cranial fossae.
- For unifocal orbital disease, curettage and local steroids may be curative.
- Compared to orbital rhabdomyosarcoma, there is usually far more bone erosion in LCH, and the lesion most often affects the area of the lacrimal fossa and adjacent bone.

Keywords

Langerhans cell histiocytosis · Bone erosion · Orbit

1 Symptoms and Signs

LCH usually affects children, and when the orbit is involved, the disease is most often unifocal, but in some cases, the disease may be multifocal, affecting other bones, soft tissue, and the central nervous system [1, 2]. The lacrimal gland fossa is frequently involved and the adjacent bone is often eroded with extension of soft tissue disease into the temporal fossa or anterior cranial fossa. Swelling of the upper eyelids and redness is typical.

2 Differential Diagnosis

Other soft tissue or bone tumors with osteolysis need to be excluded. This includes rhabdomyosarcoma and metastatic neuroblastoma.

3 Diagnosis

Typical erosive lesions of the lacrimal gland fossa are highly suggestive but a tissue diagnosis is essential.

A. A. McNab (✉)
Orbital Plastic and Lacrimal Clinic, Royal Victorian Eye and Ear Hospital, Melbourne, VIC, Australia

© Springer Nature Switzerland AG 2022
G. Ben Simon et al. (eds.), *Atlas of Orbital Imaging*,
https://doi.org/10.1007/978-3-030-62426-2_64

4 Treatment

For unifocal disease (the majority of orbital presentations of LCH), local measures such as curettage and local corticosteroids are usually curative [3]. Multifocal and CNS lesions require management with chemotherapeutic agents.

5 Figures with Captions

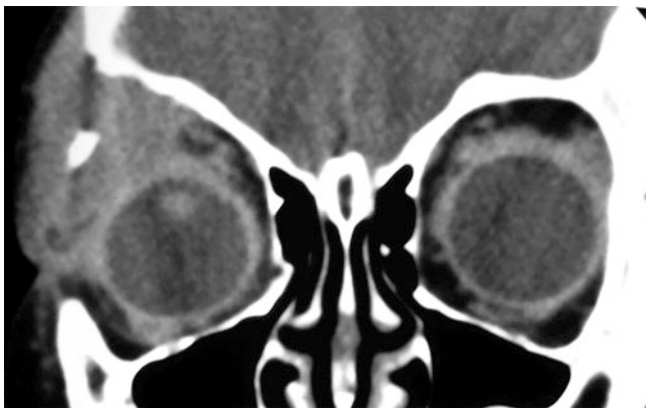


Fig. 1 A coronal noncontrast CT of a young child shows extensive soft tissue infiltration in the lacrimal fossa region with adjacent bone erosion and globe dystopia. LCH was diagnosed on biopsy

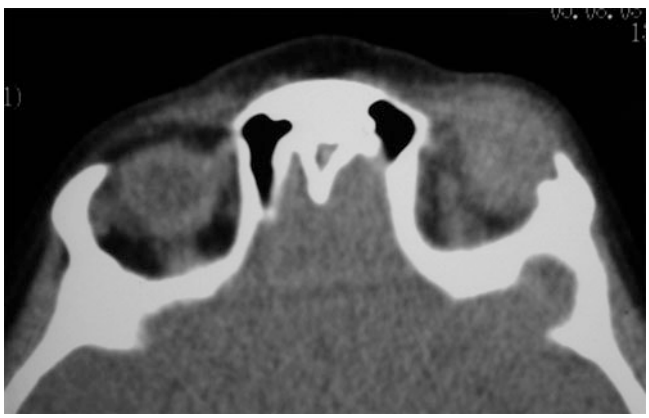


Fig. 2 An axial noncontrast CT shows a soft tissue lesion in the left superior orbit with some adjacent bone irregularity

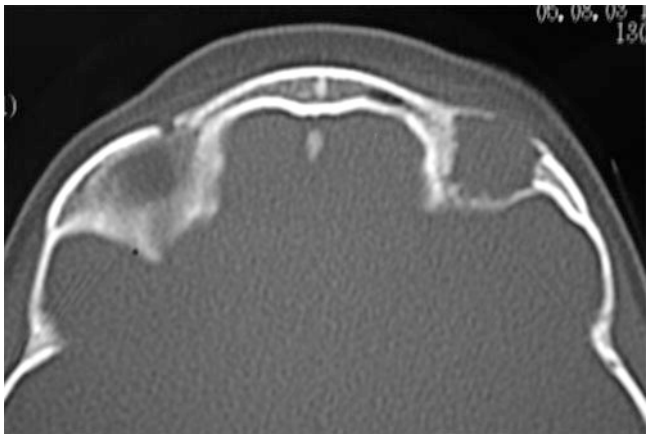


Fig. 3 An axial bone window setting CT shows irregular bone erosion of the left orbital roof (same patient as Figs. 2 and 4). Biopsy confirmed LCH

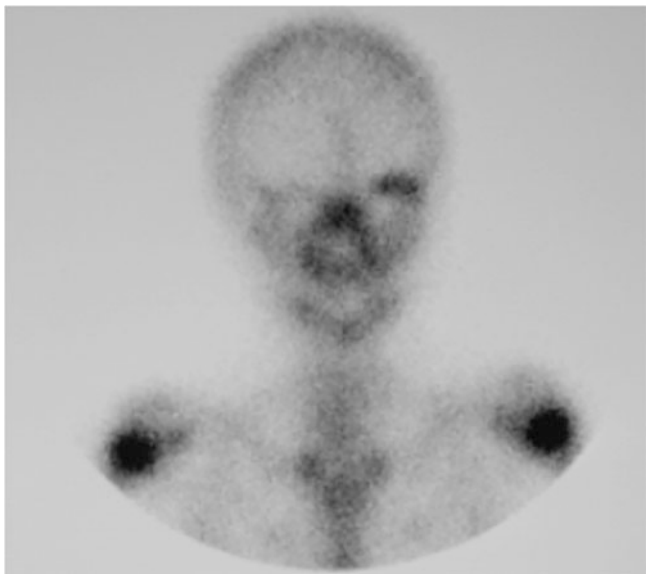


Fig. 4 A Technetium^{99} bone scan shows uptake in the left superior orbit (same patient as Figs. 2 and 3). No other lesions were identified in the entire skeleton, and the unifocal lesion was treated by curettage alone. PET-CT and whole-body MRI are more sensitive techniques for staging the disease

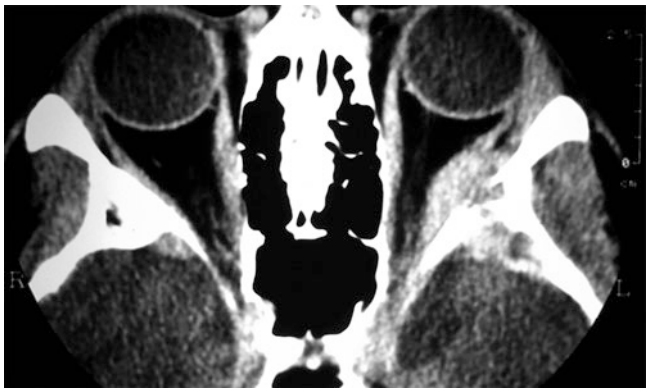


Fig. 5 An axial contrast-enhanced CT in a 14-year-old boy shows an enhancing soft tissue lesion in the left lateral orbit with extension into the middle cranial fossa and erosion of the greater wing of sphenoid. Biopsy confirmed LCH (unifocal). The left lateral rectus muscle is enlarged and possibly involved



Fig. 7 An axial contrast-enhanced T1 MRI with fat saturation shows extensive enhancing soft tissue in the postero-lateral orbit, middle cranial fossa, and temporal fossa with loss of bone in the greater wing of sphenoid (same patient as Figs. 5 and 6)

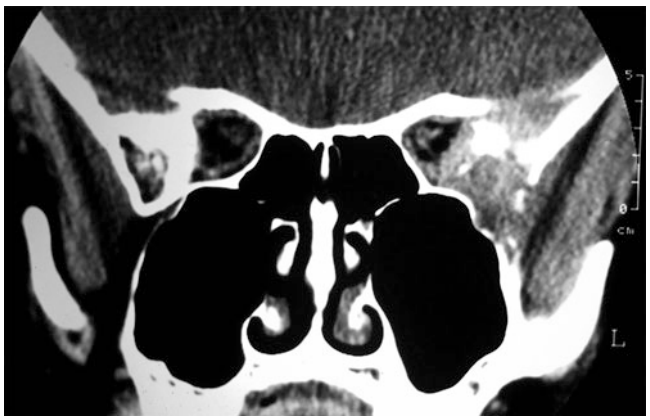


Fig. 6 A coronal contrast-enhanced CT shows soft tissue infiltration in the posterior lateral orbit extending into the middle cranial fossa and pterygopalatine fossa with associated bone erosion (same patient as in Figs. 5 and 7)



Fig. 8 An axial noncontrast CT in a young adult shows a soft tissue lesion involving the left postero-lateral orbit and middle cranial fossa with erosion of the posterior greater wing of sphenoid. Biopsy confirmed LCH

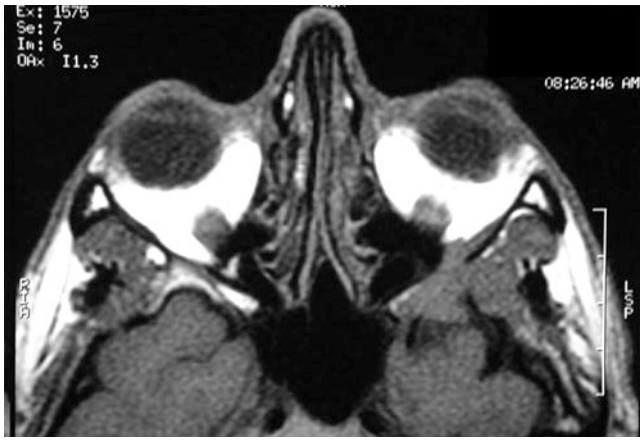


Fig. 9 An axial noncontrast T1 MRI shows a soft tissue lesion in the postero-lateral orbit, middle cranial fossa, and temporal fossa with some loss of bone (same patient as in Figs. 8 and 10). The lesion is iso-intense with brain

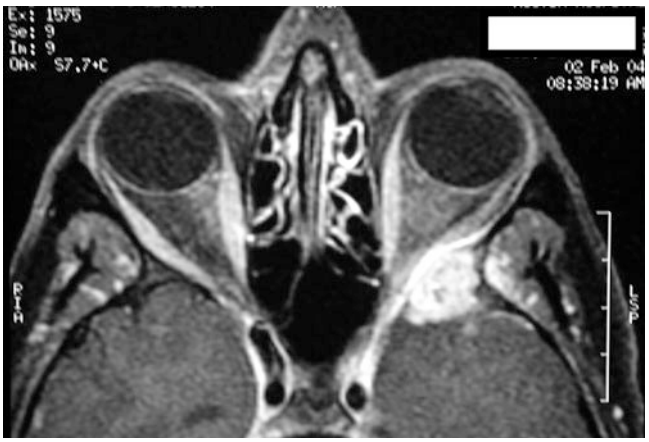


Fig. 10 An axial contrast-enhanced T1 MRI shows an enhancing soft tissue lesion in the postero-lateral orbit, middle cranial fossa, and temporal fossa with some loss of bone in the greater wing of sphenoid (same patient as in Figs. 8 and 9)

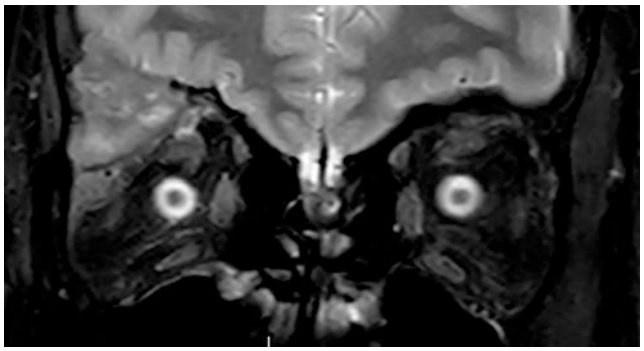


Fig. 11 Coronal T2WI FS image of a different patient with right lacrimal fossa LCH. This expansile soft tissue mass is causing local bone destruction at the superolateral orbital roof, with extraconal extension and moderate mass effect on the orbital content. There is thinning of the anterior skull base with no obvious intracranial extension. Note the heterogeneous signals within the lesion

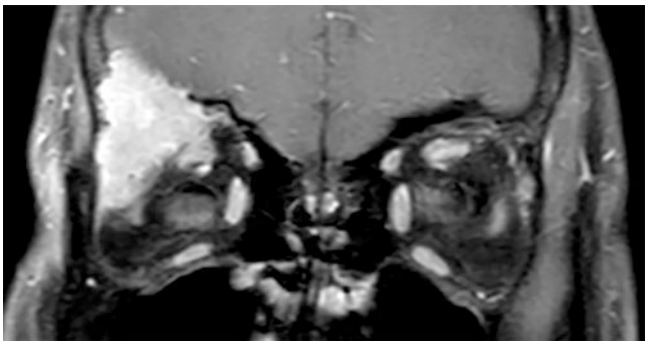


Fig. 12 Coronal T1WI FS contrast-enhanced image (same patient as Figs. 11, 13, and 14) showing relatively intense, however slight inhomogeneous, enhancement of the lesion

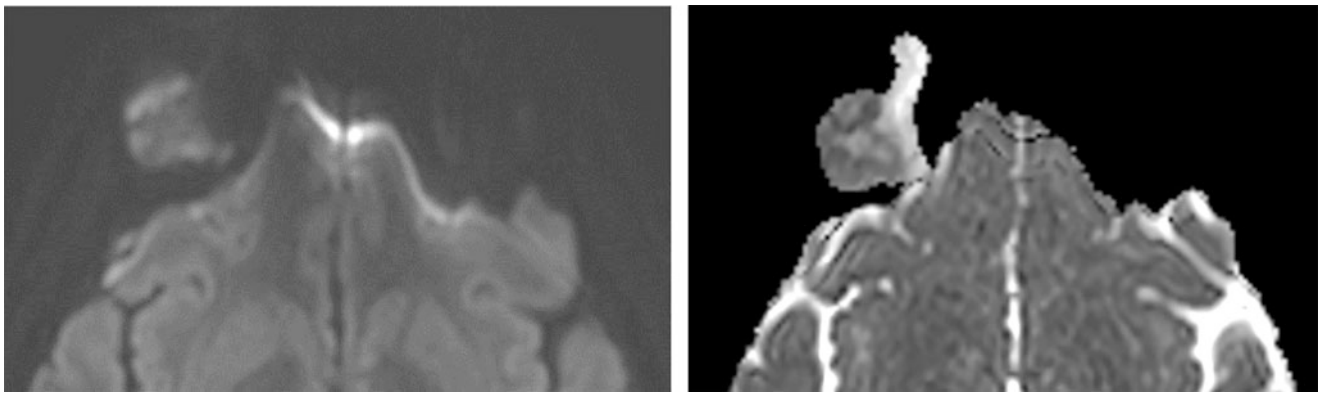


Fig. 13 The lesion showed mixed diffusivity signals on DWI, some of which are bright (left) with corresponding restrictive (dark) areas on the ADC map (right), consistent with regions of high cellular density



Fig. 14 Clinical photograph of a 2-year-old boy with recent onset left eyelid edema and mechanical ectropion, pain, and periocular swelling and inflammation

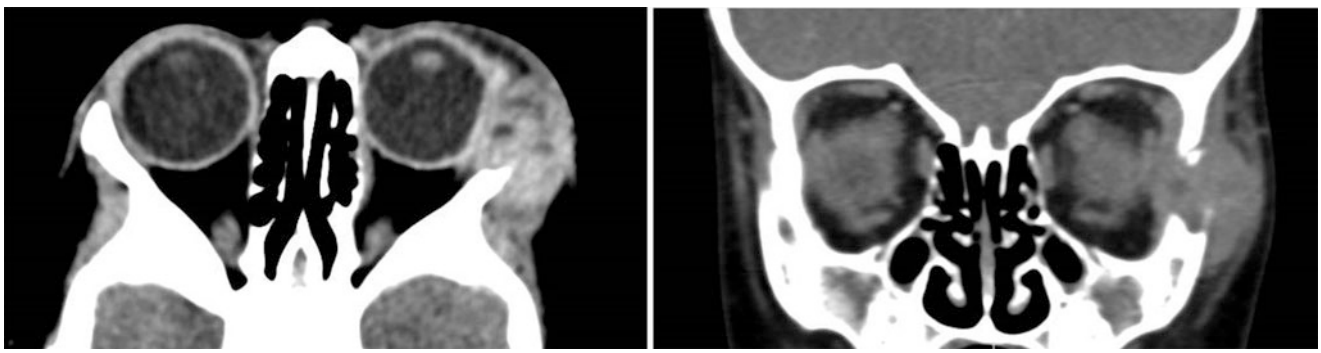


Fig. 15 NECT of the same patient, axial (*left*) and coronal (*right*), showing a poorly defined, mostly hyperdense, heterogenous bone destructive mass epi-centered in the left lateral wall with extra osseous extension into the temporal fossa. The extraconal orbital component is compressing the globe and displacing it medially. Orbital biopsy was consistent with LCH

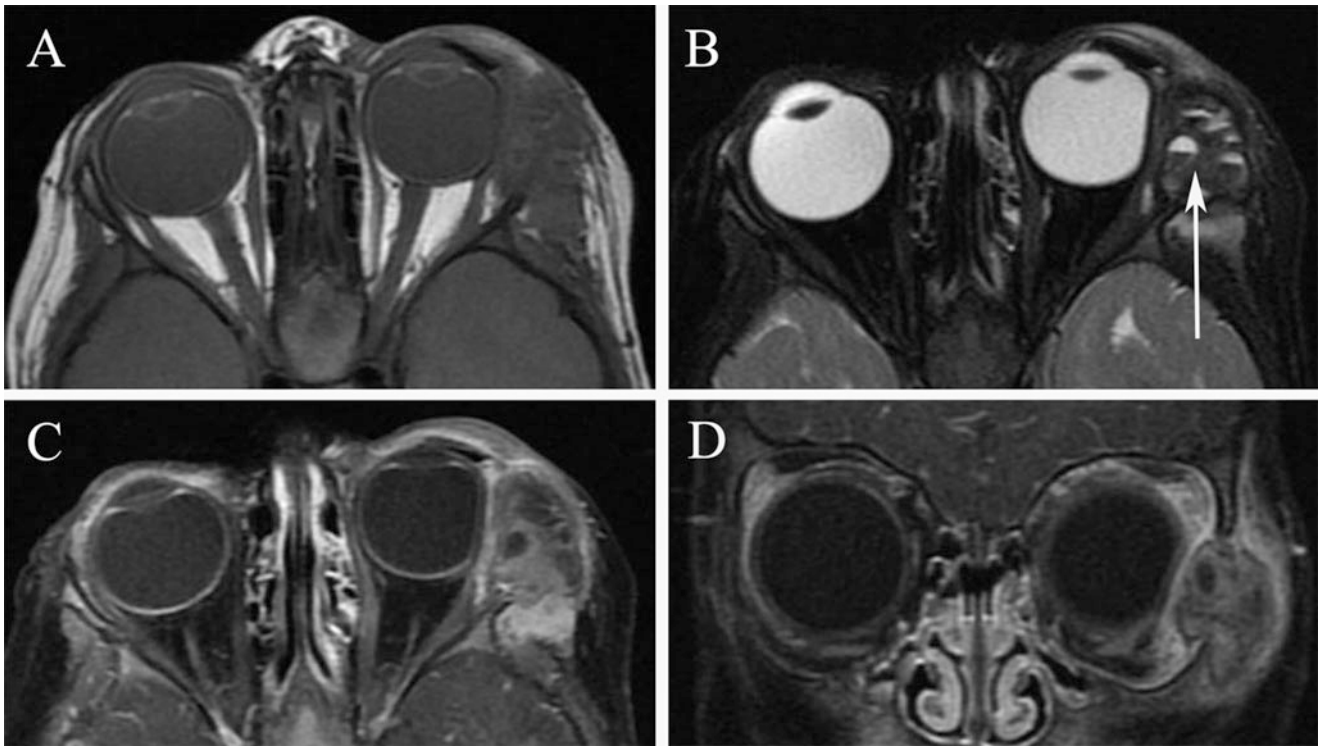


Fig. 16 MRI of the same patient, **a**–**c**, axial view (T1, T2-FS, and T1-FS-CE, respectively), and **d**, coronal view (T1-FS-CE), showing fluid-fluid levels in multiple cystic spaces within the mass, a distinctive but rather rare feature of aneurysmal bone cyst formation **(a**–**c)** within an LCH (white arrow). The tumor is displacing the LR muscle and compressing the left globe. Note the peritumoral edema **(b)** and enhancement **(c**, **d)** which may be reactive [4]

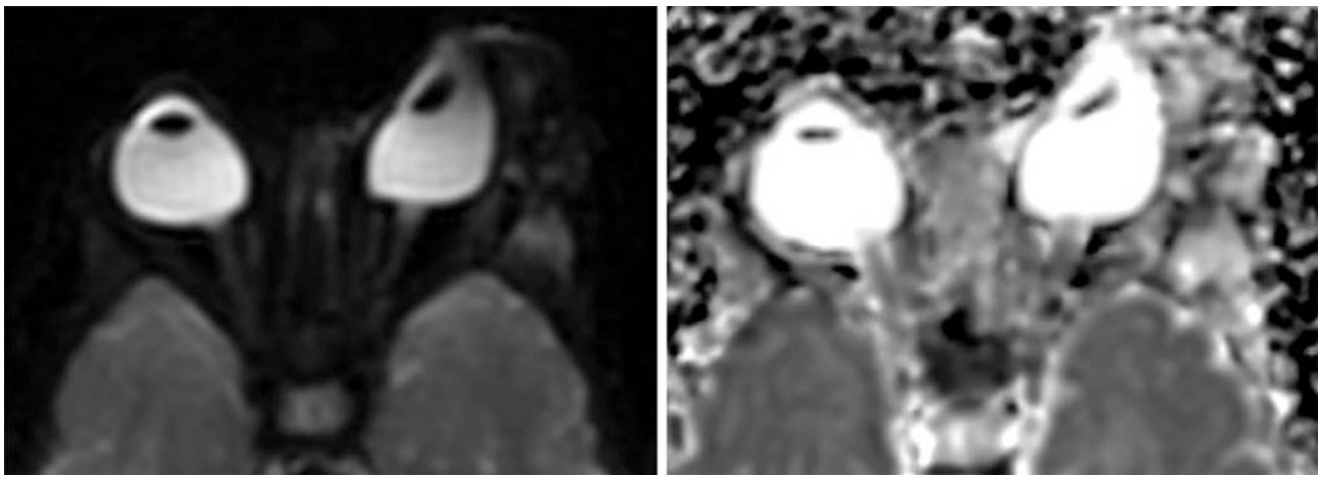


Fig. 17 DWI (left) showing mixed intensities of the lesion and corresponding ADC map (right) showing areas of mild central areas of restriction with surrounding high diffusivity; this may be related to the cystic component/ABC. Typical LCH are often restricted (Fig. 13)



Fig. 18 Clinical photographs of few months post-surgical curettage, steroids, and systemic chemotherapy, with complete clinical resolution of the inflammatory process (Figs. 14, 15, 16, 17, and 18 courtesy of the editors)

References

1. Maccheron LJ, McNab AA, Elder J, Selva D, Martin FJ, Clement CI, Sainani A, Sullivan TJ. Ocular adnexal Langerhans cell histiocytosis clinical features and management. Orbit. 2006;25:169–77.
2. Cheung N, Selva D, McNab AA. Orbital Langerhans cell histiocytosis in adults. Ophthalmology. 2007;114:1569–73.
3. Esmaili N, Harris GJ. Langerhans cell histiocytosis of the orbit: Spectrum of disease and risk of central nervous system sequelae in unifocal cases. Ophthalmic Plast Reconstr Surg. 2016;32:28–34.
4. Lomoro P, Simonetti I, Vinci G, Fichera V, Tarotto L, Trovato P, Prevedoni Gorone MS. Secondary aneurysmal bone cyst in Langerhans cell histiocytosis: case report, literature review. Eur J Radiol Open. 2019;6:97–100. https://doi.org/10.1016/j.ejro.2019.02.002. PMID: 30809556; PMCID: PMC6376152.

Part VII

Eye and Ocular Adnexa Tumors with Orbital Extension

Periocular Basal Cell Carcinoma (BCC)

44

Alon Tiosano, Natalia Michaeli, and Iftach Yassur

Contents

1 **Signs and Symptoms** 349
2 **Differential Diagnosis** 350
3 **Diagnosis** 350
4 **Treatment** 350
5 **Figures with Captions** 350
References 351

Abstract

- BCC is the most common eyelid malignancy, accounting for over 90% of malignant eyelid neoplasms.
- Risk factors: lightly pigmented individuals, sun exposure, radiation, immunosuppression, previous scar, and inherited syndromes.
- Treatment is guided by TNM classification for eyelid carcinomas according to AJCC Cancer Staging Manual 8th ed.
- BCC more often involves the lower eyelid, followed by the medial canthus.
- MRI with fat suppression sequences is the modality of choice to assess tumor extent including perineural invasion and is equivalent or superior to CT for bone marrow involvement.
- CT typically shows a slightly hyperdense lesion.
- MRI-T1-isointense or hyperintense, T2- and STIR – heterogenous hypo- to hyperintense [1]. Tumor enhancement postcontrast.
- DWI/ADC – Diffusion weighted imaging is not required and its contribution for tumor assessment is low; it may be appropriate for orbital lymphoma or abscess in specific cases.
- PET - Can be used for assessing tumor involvement postradiation treatment, or to identify distant metastasis.

Keywords

BCC · Basal cell carcinoma tumor

1 Signs and Symptoms

Painless raised area of skin with a shiny appearance with small blood vessels. Ulceration may appear, in some cases may be visually indistinguishable from other tumors. Gradual onset and progression, although distant spread in less common it can invade adjacent structures. Additional signs can be noticed as further anatomical structures are involved (e.g., ptosis, paresthesia or anesthesia, madarosis, distortion of tissue architecture)

A. Tiosano · I. Yassur (✉)
Department of Ophthalmology, Rabin Medical Center – Beilinson Hospital, Petach Tikva, Israel

Department of Radiology, Rabin Medical Center, Petah Tikva, Israel

N. Michaeli
Sackler Faculty of Medicine, Tel Aviv University, Tel Aviv, Israel

Department of Radiology, Rabin Medical Center, Petah Tikva, Israel

© Springer Nature Switzerland AG 2022
G. Ben Simon et al. (eds.), *Atlas of Orbital Imaging*,
https://doi.org/10.1007/978-3-030-62426-2_32

2 Differential Diagnosis

Malignant skin tumors mainly squamous cell carcinoma but also sebaceous cell carcinoma. Premalignant skin lesions (actinic keratosis, Keratoacanthoma, Bowen's disease) and inflammatory eyelid lesions (chalazion, chronic infection).

3 Diagnosis

Clinical characteristics and radiologic findings. MRI of orbit in STIR is the radiologic study of choice, if unavailable CT of orbits with contrast should be done. Diagnosis confirmed by tissue biopsy.

4 Treatment

Complete surgical excision with free margins is considered the best treatment option. For locally advanced BCC of which surgical excision is impossible, other treatment modalities should be considered, as radiation therapy, and recently biological treatment as Vismodegib or Sonidegib which inhibits the smoothened protein (SMO) of the hedgehog pathway [2].

5 Figures with Captions

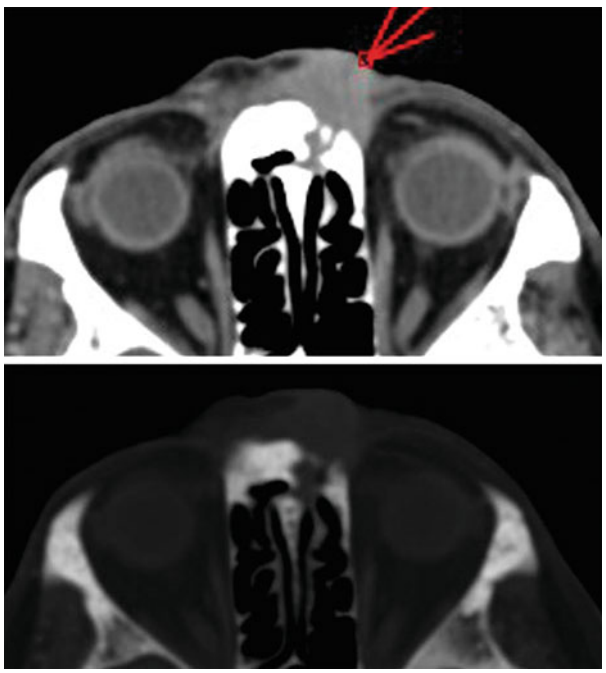


Fig. 1 Orbit CE CT, soft tissue window and bone window, Axial view. An enhancing soft tissue mass residing in the superior nasal region of the left orbit (marked in red arrow) penetrating the nasal bone; the lesion is involving all cutaneous layers. Bone window (lower image) better demonstrates nasal bone destruction

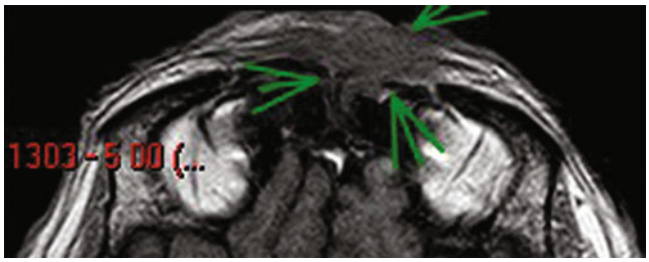


Fig. 2 Axial noncontrast, T1 (same patient) showing an iso-intense soft tissue mass at the left superior nasal area, involving skin, subcutis, bone invading the frontal sinus and crossing the midline

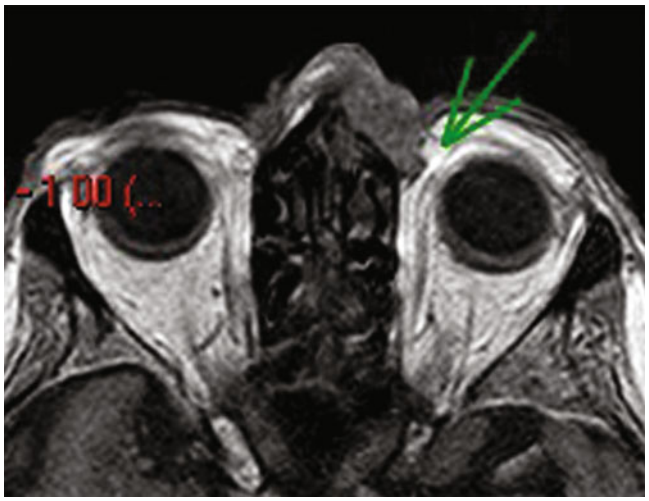


Fig. 3 Axial noncontrast, T1 (same patient) a more caudal image, showing the soft tissue mass at the left superior nasal area is slightly invading the extraconal fat (green arrow)

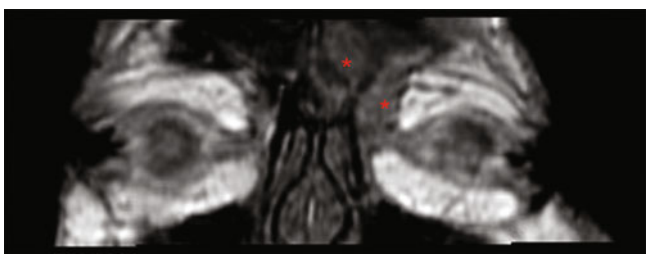


Fig. 4 Coronal noncontrast T1 showing a soft tissue mass at the medial canthus of left superior eyelid with bone and frontal sinus involvement (red asterisks)

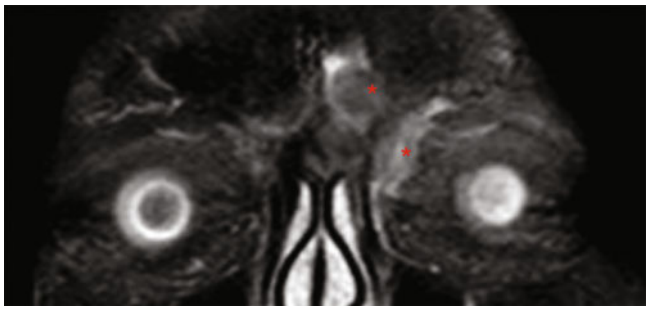


Fig. 5 Coronal STIR image at the medial canthus of left eye depicting a mixed signal mass with bone and frontal sinus involvement (red asterisks)



Fig. 6 3D reconstruction based on CT. Coronal view (same patient) on the left medial canthus with deep erosion of the bone

References

1. Baheti AD, Tirumani SH, Giardino A, Rosenthal MH, Tirumani H, Krajewski K, et al. Basal cell carcinoma: a comprehensive review for the radiologist. AJR Am J Roentgenol. 2015;204(2):W132–40.
2. Ben Ishai M, Tiosano A, Fenig E, Ben Simon G, Yassur I. Outcomes of vismodegib for periocular locally advanced basal cell carcinoma from an open-label trial. JAMA Ophthalmol. 2020;138:749.

Periocular Squamous Cell Carcinoma (SCC)

45

Alon Tiosano, Natalia Michaeli, and Iftach Yassur

Contents

1 **Signs and Symptoms** 354
2 **Differential Diagnosis** 354
3 **Diagnosis** 354
4 **Treatment** 354
5 **Figures with Captions** 357
References 357

Abstract

- Lesions usually originate from the skin of the eyelids, eyebrow, or canthal region.
- May present as a well-defined exophytic lesion with or without ulceration or as an infiltrative lesion with ill-defined borders invading the eye and orbit adnexa or bone via direct spread.
- Can invade the orbit and cavernous sinus via perineural spread (with or without skip lesions). Large lesions may metastasize to regional lymph nodes [1].
- A perineural invasion may rarely present with a cystic appearance which can be identified on CT and T1-weighted fat-suppressed MRI with a well-defined border and linear hyperintensity content [2].
- Treatment may be guided by TNM classification according to American Joint Committee on Cancer (AJCC) staging.
- On CT lesions are isodense relative to muscle tissue and are moderately enhanced following contrast material.
- MRI: T1 – low signal, T2 – intermediate to high signal, STIR – high signal.
- DWI/ADC – Diffusion-weighted imaging is emerging as a potential biomarker for tumor grading and detection of recurrences.
- PET can be used for assessing tumor involvement post radiation treatment, or to identify distant metastasis.

Keywords

SCC · Squamous cell carcinoma tumor

A. Tiosano · I. Yassur (✉)
Department of Ophthalmology, Rabin Medical Center – Beilinson Hospital, Petach Tikva, Israel

Department of Radiology, Rabin Medical Center, Petah Tikva, Israel

N. Michaeli
Sackler Faculty of Medicine, Tel Aviv University, Tel Aviv, Israel

Department of Radiology, Rabin Medical Center, Petah Tikva, Israel

© Springer Nature Switzerland AG 2022
G. Ben Simon et al. (eds.), *Atlas of Orbital Imaging*,
https://doi.org/10.1007/978-3-030-62426-2_33

1 Signs and Symptoms

Primarily effects elderly faired-skin individuals with a history of chronic sun exposure or younger individuals with a predisposing condition (immune suppression [organ transplant], carcinogenic factor [radiation], or genetic factor [albinism]). May arise in sun-damaged skin areas (actinic keratosis) or de novo. Clinical signs develop slowly (mean 1 y) but faster than BCC and include a painless lesion of nodular, ulcerative, placoid, and infiltrative cystic or papillomatous type. Ulceration, cicatricial ectropion, and madarosis commonly occur in SCC (as well as in other malignancies). Red skin with scale of keratin is more typical of SCC. Deep invasion (T4 AJCC Cancer Staging Manual, 8th edition) is associated with long-term neglect or recurrent failed treatment attempt. Sings of deep invasion include a nonmobile lesion, impaired ocular motility or blink, and exophthalmos or a sensory defect secondary to perineural spread. Larger lesions (T2c AJCC 8th edition) may result in metastasis, usually to regional lymph nodes.

2 Differential Diagnosis

Malignant skin tumors mainly basal cell carcinoma but also sebaceous cell carcinoma. Pre-malignant skin lesions (actinic keratosis, keratoacanthoma, and Bowen's disease) and inflammatory eyelid lesions (chalazion and chronic infection).

3 Diagnosis

Clinical characteristics are usually confirmed by tissue biopsy. Imaging by MRI or CT is recommended when deep invasion is suspected. MRI with fat-suppressed images is the radiologic study of choice. If unavailable CT of the orbits with contrast should be done.

4 Treatment

Complete surgical excision with free margin control is the treatment of choice. Locally advanced and nonoperable cases could be treated with radiation. Targeted therapy with biological treatment such as PD-1 inhibitors (Cemiplimab) is emerging as a new therapeutic option [3].

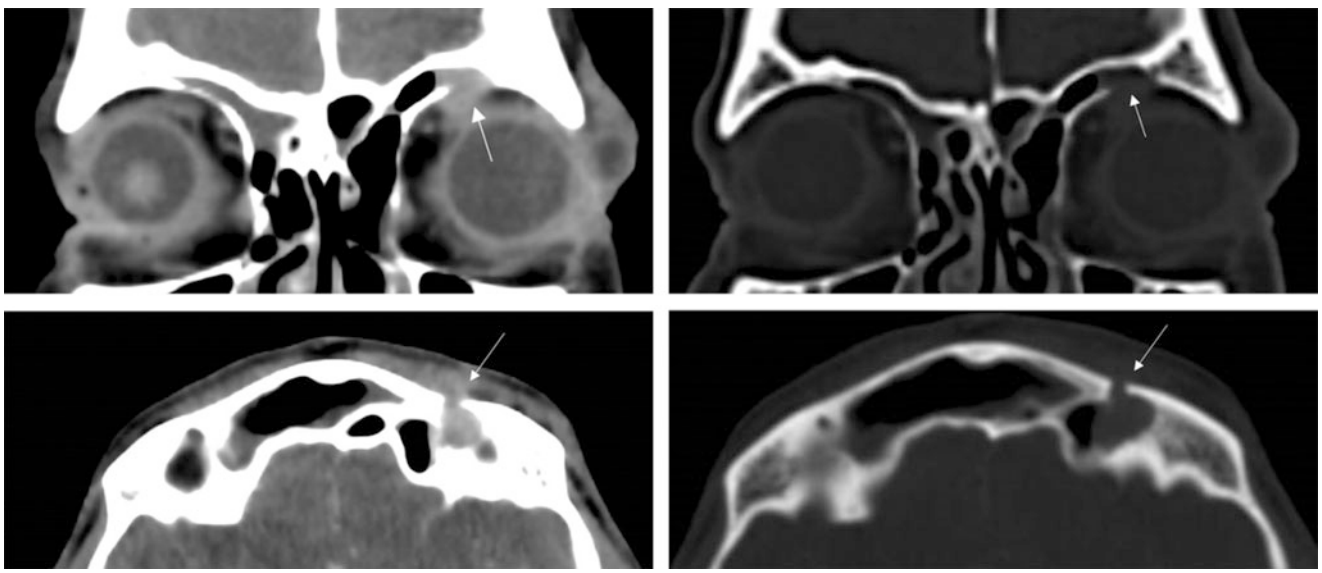


Fig. 1 CE CT, soft tissue window (*left*) and bone window (*right*) of a patient with left periocular SCC and orbital extension. There is a soft tissue mass residing in the supra orbit region of the left eye invading the bone and penetrating through the supraorbital foramen (*arrow*), originating from the superficial skin layers with perineural invasion (PNI). Bone windows (*right*) better demonstrate the bony involvement

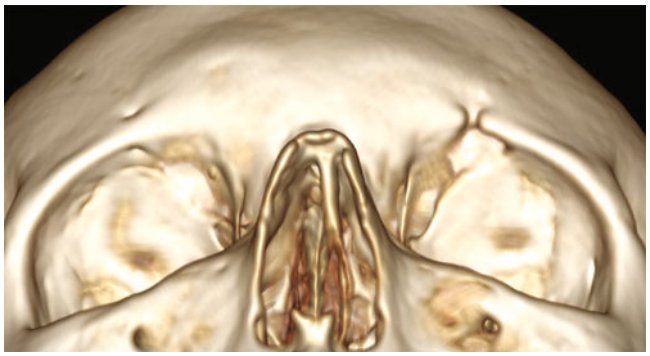


Fig. 2 CT 3D reconstruction, worms view of the same patient as in Fig. 1; note the bony erosion on the left supraorbital foramen, compared with an intact supraorbital foramen on the right

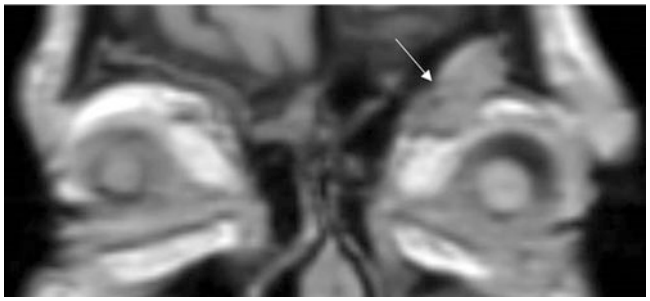


Fig. 3 MRI, noncontrast axial T1 image, showing an ill-defined mass penetrating the left frontal sinus along the supraorbital canal (*arrow*)

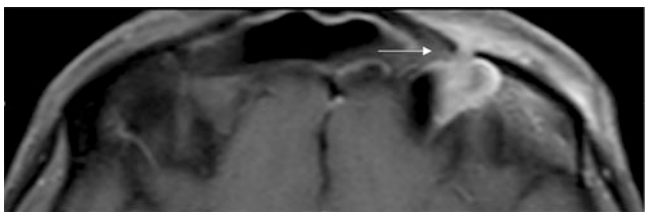


Fig. 4 MRI, post-contrast axial T1 fat-saturated image. An enhancing soft tissue mass eroding the bone and protruding the superior orbit through the supraorbital foramen

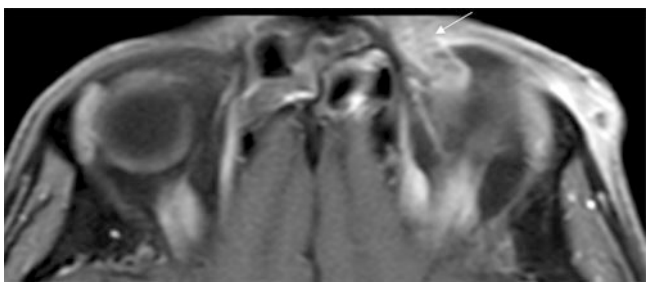


Fig. 5 MRI, post-contrast axial T1 fat-saturated image at a more caudal level. There is an extensive soft tissue periorbital infiltrative mass. The enhancing lesion appears to be invading the orbit at the trochlea level



Fig. 6 Post-contrast coronal T1 fat-saturated image showing an ill-defined enhancing mass penetrating the left frontal sinus along the supraorbital canal (A, arrows). Image B, at mid orbit, showing an enhancing soft tissue mass at the left superior orbit, advancing along the frontal nerve. Image C, further demonstrating deep PNI at the level of the orbital apex



Fig. 7 Noncontrast axial T1 image at the apex showing a soft tissue mass at the orbital apex lateral to the optic nerve, at the lateral side of left eye, at the superior orbital fissure, and at the cavernous sinus (*arrow*)



Fig. 8 Post-contrast axial T1 fat-saturated image showing an enhancing soft tissue mass at the orbital apex lateral to the optic nerve (*arrow*) penetrating through the SOF, abutting the cavernous carotid artery

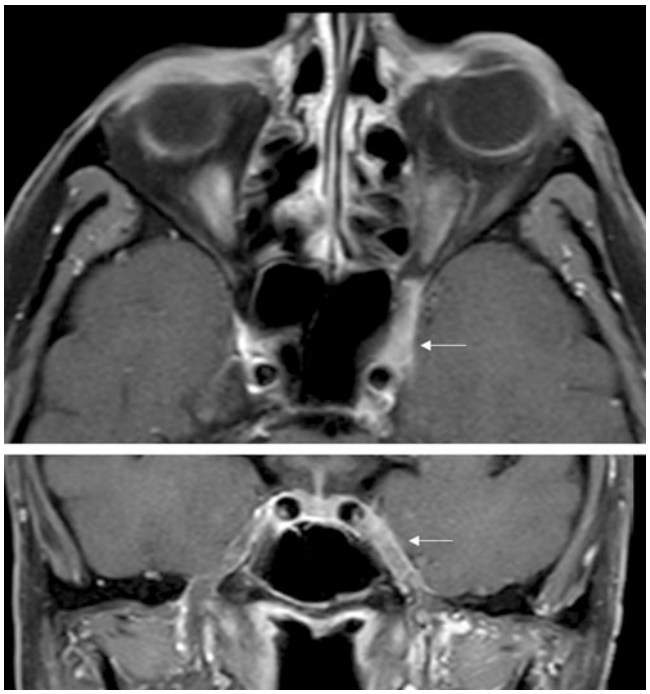


Fig. 9 Post-contrast axial and coronal T1 fat-saturated image showing the lesion is involving the left cavernous sinus (*arrows*)

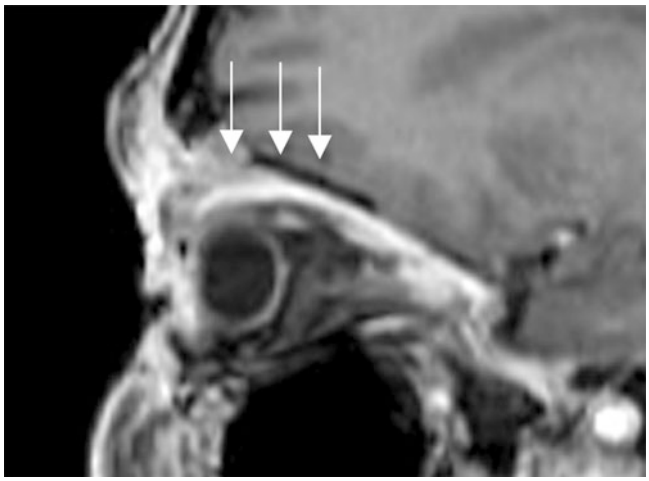


Fig. 10 Post-contrast sagittal T1 fat-saturated image showing the lesion to its full extent along orbital roof/SON, originating from the periocular skin to the orbital apex (*arrows*)

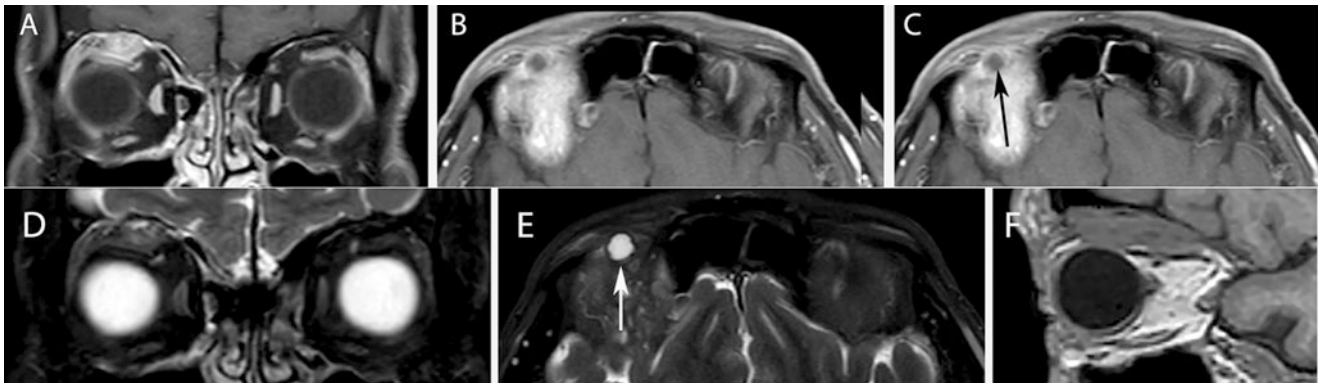


Fig. 11 MRI of a 61-year-old male (different patient) with recent history of RUL ptosis, and superior orbital mass proven to be SCC with PNI along the frontal branch. A–C: CE FS T1WI. D–E: STIR. Note typical cystic involvement (C, E) of the frontal branch (*black/white arrows*). The lesion is shown in its full extent in the T1WI sagittal section (F). There is secondary widening of the SO notch/canal (*arrows*) best seen on the following CT images (Fig. 12)

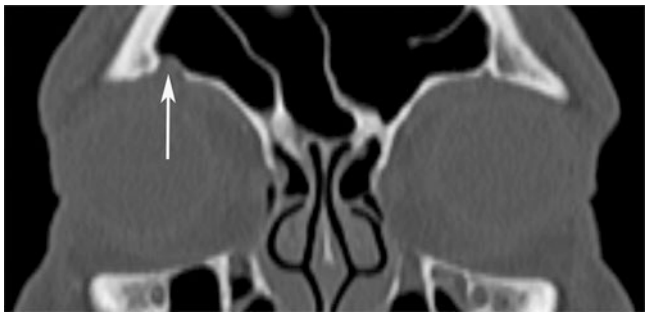


Fig. 12 CT scan coronal section of the same patient, showing widening of the SO notch/canal secondary to PNI of the tumor (*arrow*)

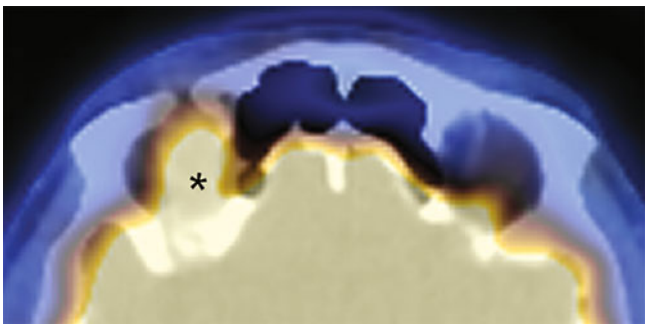


Fig. 13 PET scan showing the superior orbital SCC is FDG avid (asterix)

5 Figures with Captions

References

1. Karia PS, Morgan FC, Ruiz ES, Schmults CD. Clinical and incidental perineural invasion of cutaneous squamous cell carcinoma: a systematic review and pooled analysis of outcomes data. JAMA Dermatol. 2017;153(8):781–8.
2. Limawararut V, Hoyama E, Selva D, Davis G. Squamous cell carcinoma presenting as an orbital cyst with radiologic evidence of perineural invasion. Eur J Ophthalmol. 2007;17(6):970–2.
3. Migden MR, Rischin D, Schmults CD, Guminski A, Hauschild A, Lewis KD, et al. PD-1 blockade with Cemiplimab in advanced cutaneous squamous-cell carcinoma. N Engl J Med. 2018;379(4):341–51.

Periocular Sebaceous Cell Carcinoma

46

Alon Tiosano, Natalia Michaeli, and Iftach Yassur

Contents

1 **Signs and Symptoms** 360
2 **Differential Diagnosis** 360
3 **Diagnosis** 360
4 **Treatment** 360
5 **Figures with Captions** 360
References 363

Abstract

- Lesions usually originate from the sebaceous glands including meibomian glands and the Zeis glands.
- May present as a well-defined yellowish exophytic lesion at the lid margin and may extend to the palpebral conjunctiva.
- High index of suspicion is required as sebaceous cell carcinoma may mimic chronic eyelid inflammation such as blepharitis/chalazia, superior limbal keratitis (SLK), ocular cicatricial pemphigoid (OCP), or other eyelid tumors such as BCC and SCC.
- Pagetoid spread to adjacent eyelid or conjunctival tissue is not uncommon.
- Treatment is guided by TNM classification according to the American Joint Committee on Cancer (AJCC) staging.
- Sentinel lymph nodes biopsy are advised for tumors larger than 10 mm [1].
- On CT lesions are isodense relative to muscle tissue and enhance moderately following contrast material.
- MRI: T1 – low signal, T2 – intermediate to high signal, STIR – high signal
- DWI/ADC – Diffusion-weighted imaging is emerging as a potential biomarker for tumor grading and detection of recurrences. However, diffusion restriction may not distinguish between malignant tumors subtypes.
- PET-CT for evaluation of distant metastases should be considered only when nodal involvement is established.
- The roll of radiotherapy is not well established.

Keywords

Sebaceous cell carcinoma tumor

A. Tiosano · I. Yassur (✉)
Department of Ophthalmology, Rabin Medical Center – Beilinson Hospital, Petach Tikva, Israel

Department of Radiology, Rabin Medical Center, Petah Tikva, Israel

N. Michaeli
Sackler Faculty of Medicine, Tel Aviv University, Tel Aviv, Israel

Department of Radiology, Rabin Medical Center, Petah Tikva, Israel

© Springer Nature Switzerland AG 2022
G. Ben Simon et al. (eds.), *Atlas of Orbital Imaging*,
https://doi.org/10.1007/978-3-030-62426-2_34

1 Signs and Symptoms

Primarily affects elderly faired-skin females and patients of Asian ethnicity, and younger individuals with a predisposing condition (genetic factor [Muir-Torre syndrome] or carcinogenic factor [radiation]). Clinical signs can masquerade as other pathologies. Sebaceous cell carcinoma is a highly aggressive rare malignancy with high mortality rates. Recurrence is reported in up to 33% of cases, while distant metastasis can occur in up to 25%. Chalazia recurrence at the same location should raise the suspicion of sebaceous cell carcinoma, hence biopsy is mandatory. Sentinel lymph node biopsies are advised for tumors larger than 10 mm. Tumors larger than 20 mm are correlated with poor prognosis. Mortality rate varies from 9% to high as 40% with a 5-year survival rate of 33–50%. Larger lesions may metastasize usually to regional lymph node and are associated with high mortality rates (AJCC 8th edition) [2].

2 Differential Diagnosis

Malignant skin tumors mainly basal cell carcinoma but also squamous cell carcinoma. Premalignant skin lesions (actinic keratosis, keratoacanthoma, and Bowen's disease) and inflammatory eyelid or ocular surface lesions (chalazion, chronic infection, SLK, and OCP).

3 Diagnosis

Clinical characteristics are usually confirmed by tissue biopsy and map biopsies. Imaging by MRI or CT is recommended when deep invasion is suspected. A comprehensive MRI with fat suppression is the radiologic study of choice. DWI may aid in differentiating between a hypercellular malignant lesion to a more benign entity.

4 Treatment

Complete surgical excision with margin control is the treatment of choice. In selected cases chemotherapy eye drops may be considered. Locally advanced and nonoperable cases can be treated with radiation. PD-1 inhibitors (Pembrolizumab) is emerging as a new therapeutic modality [3].

5 Figures with Captions



Fig. 1 Color image of a patient with left recurrent sebaceous carcinoma. There is a soft tissue mass residing in the upper temporal eyelid invading the palpebral conjunctiva, protruding on eversion of the upper eyelid

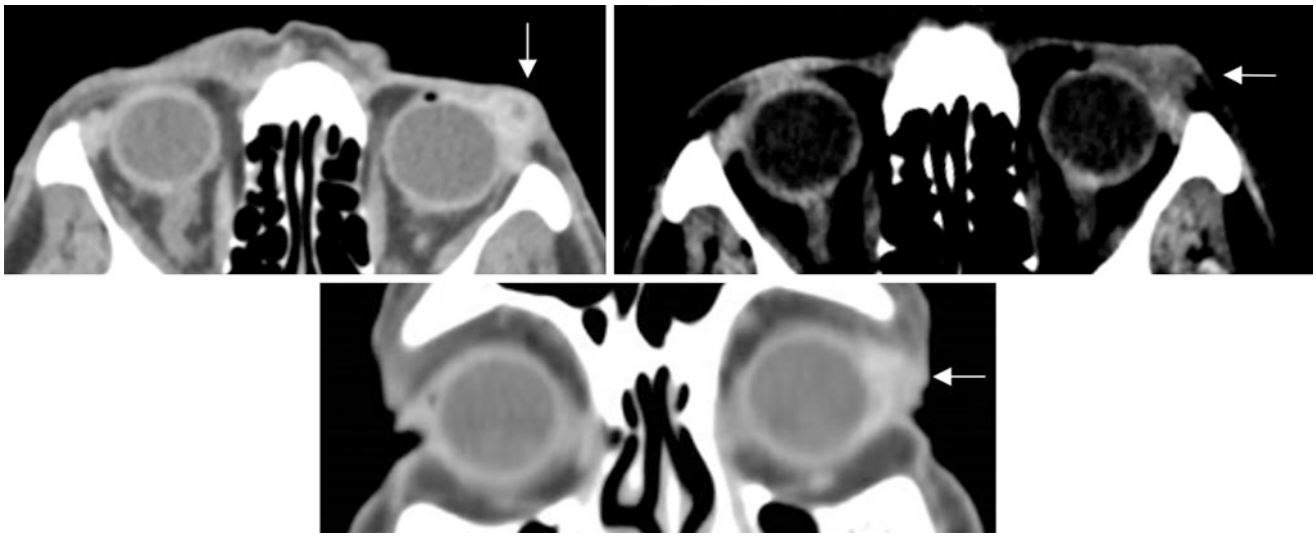


Fig. 2 CE CT, soft tissue window, of a different patient with left periocular sebaceous carcinoma. There is a soft tissue mass residing in the supra temporal region of the left eye. Two consecutive axial images (*upper*) and a coronal view (*lower*) demonstrate heterogeneously enhancing mass with suspected central necrosis abutting the globe

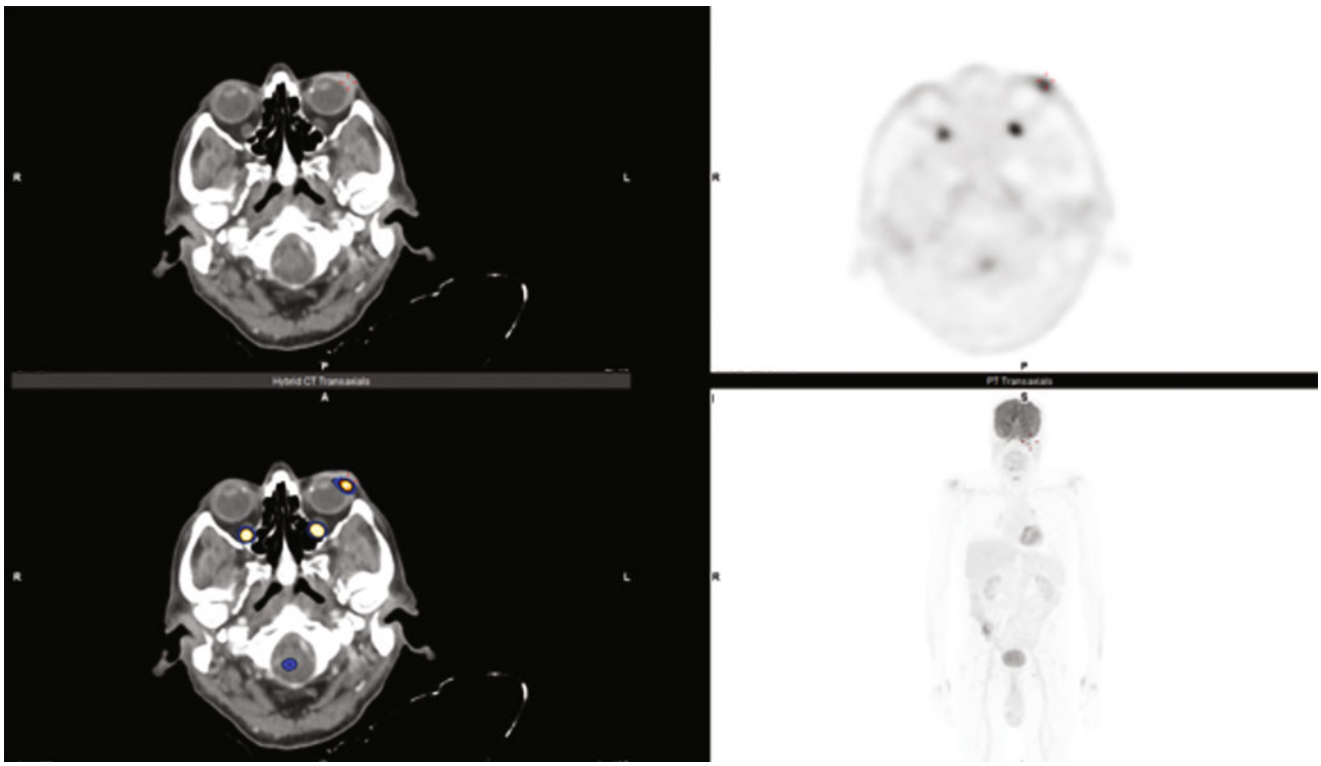


Fig. 3 PET CT, a transverse CT scan (*upper left*) showing the left upper eyelid tumor marked. A corresponding PET scan (*upper right*) showing the tumor FDG uptake. Combined PET CT image (*lower left*). Whole-body PET view (*lower right*) is negative for metastasis

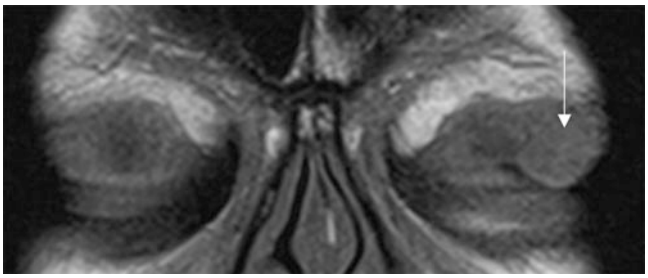


Fig. 4 MRI, NE coronal T1WI, showing an iso-intense mass epicentered at the left superior eyelid (*arrow*)

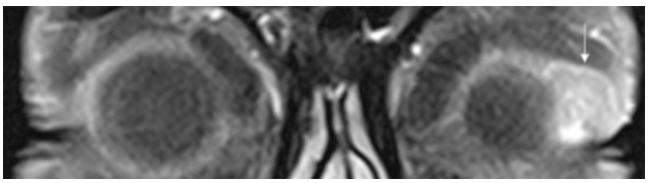


Fig. 5 Post-contrast coronal T1FS image showing an ill-defined enhancing mass at the left superior eyelid (*arrow*)

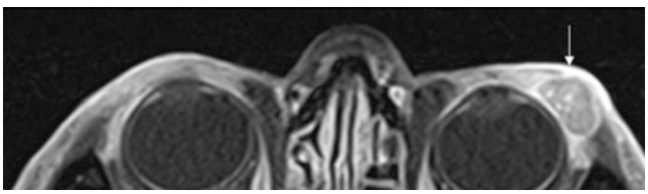


Fig. 6 MRI, post-contrast axial T1 fat-saturated image showing an enhancing soft tissue mass at the left superior temporal area (*arrow*)

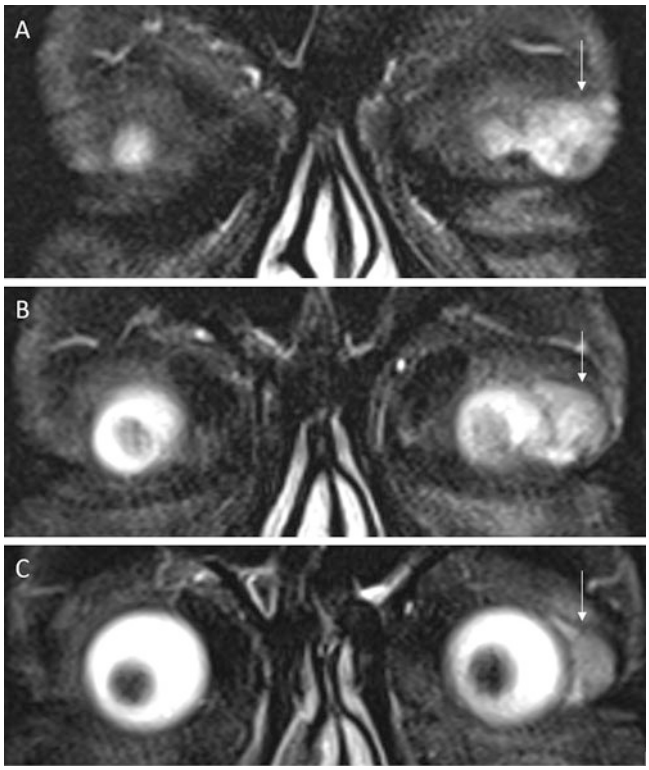


Fig. 7 MRI, coronal T2 STIR image. A relatively hyperintense soft tissue mass (*arrow*) at the superior temporal left eye at different depths (*A-anterior to C-posterior*)

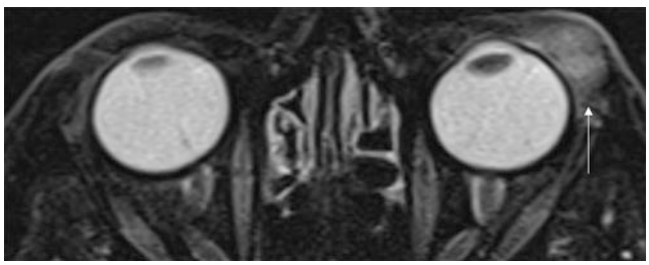


Fig. 8 MRI, axial T2 STIR image, again showing the lesion (*arrow*)

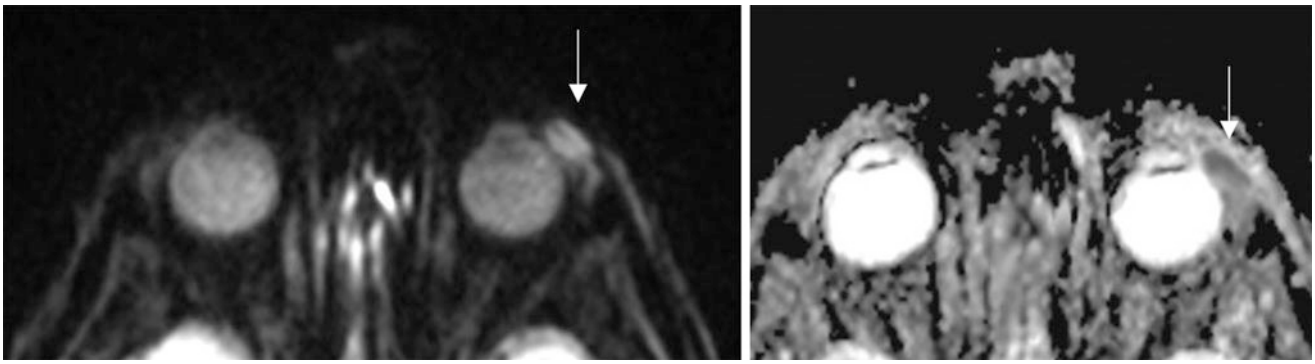


Fig. 9 MRI, axial DWI (*left*) and corresponding ADC map (*right*), showing restrictive diffusion (*arrow*)

References

1. Esmaeli B, Nasser QJ, Cruz H, Fellman M, Warneke CL, Ivan D. American Joint Committee on Cancer T category for eyelid sebaceous carcinoma correlates with nodal metastasis and survival. Ophthalmology. 2012;119(5):1078–82.
2. Hsia Y, Yeh CY, Wei YH, Chen LW, Liao SL. Eyelid sebaceous carcinoma: validation of the 8th edition of the American Joint Committee on cancer T staging system and the prognostic factors for local recurrence, nodal metastasis, and survival. Eye (Lond). 2019;33(6):887–95.
3. Domingo-Musibay E, Murugan P, Giubellino A, Sharma S, Steinberger D, Yuan J, et al. Near complete response to Pembrolizumab in microsatellite-stable metastatic sebaceous carcinoma. J Immunother Cancer. 2018;6(1):58.

Ocular Surface Squamous Neoplasia with Orbital Extension

47

Swathi Kaliki and Ido Didi Fabian

Contents

1 **Introduction** 365
2 **Signs and Symptoms** 365
3 **Differential Diagnosis** 366
4 **Diagnosis** 366
5 **Treatment** 366
6 **Figures with Caption** 366
References 368

Abstract

- Ocular surface squamous neoplasia is the most common ocular surface malignancy.
- Computed tomography or magnetic resonance imaging of the orbit are recommended in cases with a suspicion of intraocular or orbital tumor extension.
- Orbital imaging in OSSN aids in accurate staging of the disease.
- Orbital imaging in OSSN also helps to ascertain the tumor resolution in globe salvage treatment strategies.
- Orbital tumor extension of OSSN is seen as hyperdense mass on computed tomography or iso- to hyperintense mass or magnetic resonance imaging.

Keywords

Eye · Ocular surface squamous neoplasia · OSSN · Orbit

1 Introduction

- Orbital extension in a case of ocular surface squamous neoplasia (OSSN) is common in recurrent lesions, though can sometimes be noted in neglected nonstanding lesions. Orbital involvement is common in patients at risk for aggressive tumors, such as in patients with human immunodeficiency virus infection or those with noduloulcerative variant of OSSN [1, 2].

2 Signs and Symptoms

Painless unilateral ocular surface mass extending to the fornix and/or medially to the plicae semilunaris and caruncle. History of a previously excised ocular surface mass is common. Extraocular movement restriction may be noted in patients with tumor infiltration into the muscle. In recurrent lesions with orbital extension, the tumor epicenter may not always be the anterior ocular surface, and most of the lesion may be in the orbit.

S. Kaliki
Operation Eyesight Universal Institute for Eye Cancer, LV Prasad Eye Institute, Hyderabad, India
e-mail: swathikaliki@lvpei.org

I. D. Fabian (✉)
Ocular Oncology Service, The Goldschleger Eye Institute, Sheba Medical Center, Tel Hashomer, Tel Aviv University, Tel Aviv, Israel
e-mail: didi@didifabian.com

© Springer Nature Switzerland AG 2022
G. Ben Simon et al. (eds.), *Atlas of Orbital Imaging*,
https://doi.org/10.1007/978-3-030-62426-2_38

3 Differential Diagnosis

Other ocular surface masses, with orbital extension, include amelanotic melanoma, lymphoma, sebaceous gland carcinoma, metastasis of a nonocular neoplasm to the ocular surface, Kaposi sarcoma, and amyloidosis.

4 Diagnosis

Working diagnosis is based on clinical findings. Tissue biopsy and histopathology analysis remain the gold standard for tumor diagnosis [3]. Eye [4] and orbital imaging are important to demonstrate tumor extension and involvement of orbital structures.

5 Treatment

Systemic chemotherapy and radiotherapy can be attempted in selective cases [5, 6]. Orbital exenteration with or without adjuvant radiotherapy is required in most cases [7].

6 Figures with Caption

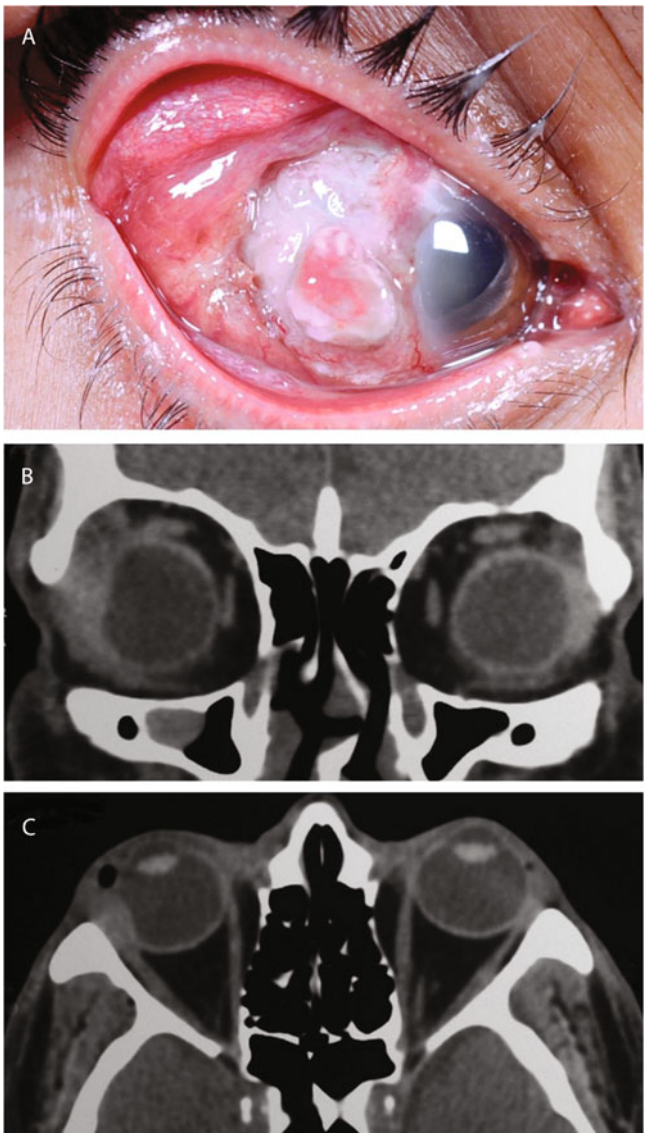


Fig. 1 **Clinical image** (**a**) showing a noduloulcerative ocular surface squamous neoplasia, with evidence of temporal scleral thinning and thickened surrounding conjunctiva. The patient had undergone a previous biopsy and Tenon's graft before current presentation. **Unenhanced orbital CT scan, soft tissue window of the patient described in Fig. 1a midaxial section** (**b**) shows a well-defined heterogeneous hyperdense mass on the lateral ocular surface of the right eye with mass extending into the anterior orbit. There is globe indentation in the adjoining region with possible intraocular tumor extension. The mass is not seen separately from the lateral rectus muscle at its insertion to the sclera. **Coronal section** scan (**c**) shows similar findings. Right lacrimal gland and lateral rectus muscle are not seen separately, suggesting tumor infiltration



Fig. 2 **Unenhanced orbital computed tomography (CT) scan, soft tissue window. Midaxial section** (**a**) shows an ill-defined diffuse heterogeneous mass involving the entire ocular surface and medial orbit of the left eye with tumor extension from the anterior orbit to the orbital apex. The entire length of the medial rectus muscle is not seen distinctly, suggestive of tumor infiltration. The lacrimal gland is seen in continuity with the ocular surface mass and is mildly enlarged, suggestive of possible tumor infiltration. The globe is irregular with hyperdense opacity intraocularly, suggestive of intraocular tumor extension. **Coronal section** scan (**b**) confirms the above findings and shows ill-defined diffuse mass in and around the left globe with possible infiltration of all recti muscles and lacrimal gland



Fig. 3 **MRI of the orbit, noncontrast-enhanced, nonfat-suppressed, T1-weighted axial section** (**a**) showing right intraconal ill-defined heterogenous isointense mass behind the hypointense orbital implant. A similar mass is seen anterior to the orbital implant. This patient had previously undergone right globe enucleation due to extensive ocular surface squamous neoplasia. **MRI orbit, contrast-enhanced, fat-suppressed, T1-weighted reconstructed sagittal section** (**b**) showing right intraconal heterogenous-enhancing lesion extending up to the midorbit

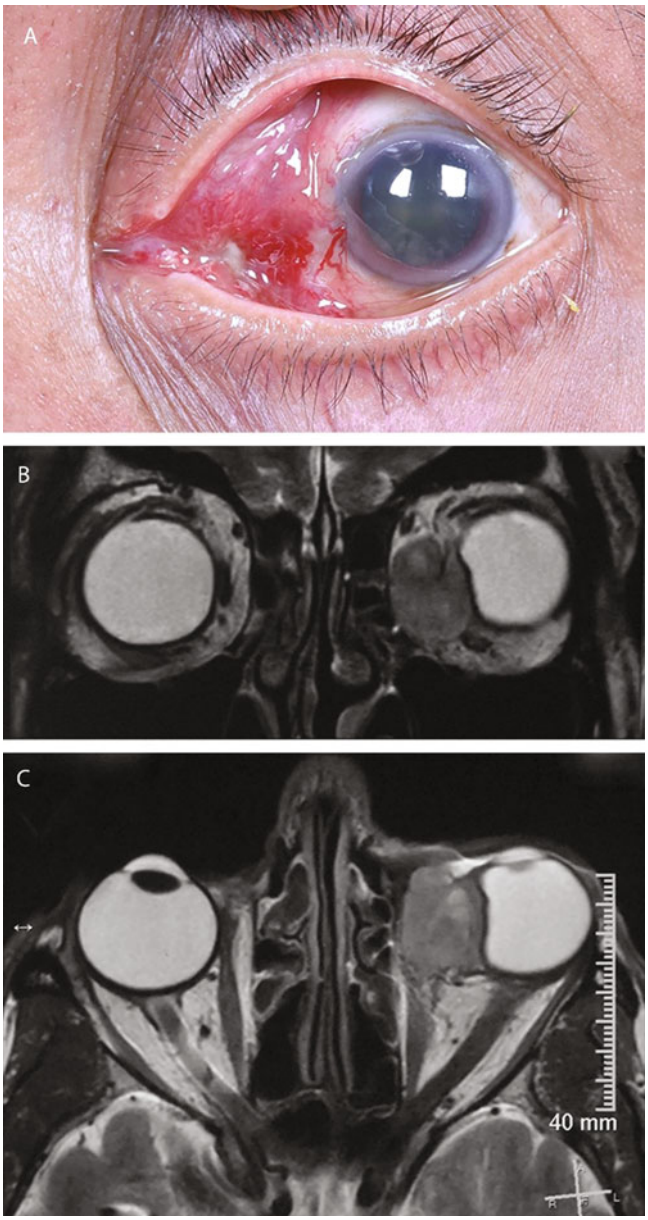


Fig. 4 **Clinical image** (**a**) showing left eye ocular surface squamous neoplasia involving the medial bulbar conjunctiva, plica semilunaris, and caruncle. The patient had a history of prior excisional biopsy of the conjunctival lesion that had recurred 6 years later. **MRI of the orbit, noncontrast-enhanced, nonfat-suppressed T2-weighted coronal section** (**b**) of the patient shown in Fig. 4a showing a well-defined, multilobulated, heterogenous, iso- to hyperintense lesion in the left medial orbit. Medial rectus is not seen separately, suggestive of tumor infiltration. Globe indentation is also noted medially. **T2-weighted axial section** (**b**) showing similar findings with extension of mass from the ocular surface to the midorbit. Proximal 1/3 of medial rectus is not seen separately, suggestive of muscle infiltration or compression

References

1. Kaliki S, Kamal S, Fatima S. Ocular surface squamous neoplasia as the initial presenting sign of immunodeficiency virus infection in 60 Asian Indian patients. Int Ophthalmol. 2017;37(5):1221–8.
2. Kaliki S, Freitag SK, Chodosh J. Nodulo-ulcerative ocular surface squamous neoplasia in 6 patients: a rare presentation. Cornea. 2017;36(3):322–6.
3. Lee GA, Hirst LW. Ocular surface squamous neoplasia. Surv Ophthalmol. 1995;39(6):429–50. https://doi.org/10.1016/s0039-6257(05)80054-2. PMID: 7660300.
4. Kaliki S, Jajapuram SD, Maniar A, Taneja S, Mishra DK. Ocular surface squamous neoplasia with intraocular tumour extension: a study of 23 patients. Eye (Lond). 2020;34(2):319–26. https://doi.org/10.1038/s41433-019-0503-2. Epub 2019 Jul 10. PMID: 31292522; PMCID: PMC7002521.
5. Murthy R, Gupta H, Krishnatry R, Laskar S. Electron beam radiotherapy for the management of recurrent extensive ocular surface squamous neoplasia with orbital extension. Indian J Ophthalmol. 2015;63(8):672–4.
6. Nair AG, Kaliki S, Mishra DK, Reddy VA, Naik MN. Neoadjuvant chemotherapy for invasive squamous cell carcinoma of the conjunctiva: a case report. Indian J Ophthalmol. 2015;63(12):927–9.
7. Shields JA, Shields CL, Demirci H, Honavar SG, Singh AD. Experience with eyelid-sparing orbital exenteration: the 2000 Tullos O. Coston lecture. Ophthalmic Plast Reconstr Surg. 2001;17(5):355–61.

Uveal Melanoma with Extraocular Spread

48

Andrew W. Stacey, Mahmud Mossa-Basha, and Ido Didi Fabian

Contents

1 **Signs and Symptoms** 369
2 **Differential Diagnosis** 370
3 **Diagnosis** 370
4 **Treatment** 370
5 **Figures and Captions** 371
References 374

Abstract

- Uveal melanoma can invade the sclera and grow into the extrascleral space.
- When this occurs with anterior uveal tumors, the underlying ciliary body melanoma will create subconjunctival pigmentation in the perilimbal region that can be confused for conjunctival pigmentation.
- Posterior uveal melanomas that grow through the sclera may present with orbital signs and an orbital mass or they may be seen on routine evaluations of newly diagnosed intraocular melanomas.
- Imaging characteristics demonstrate a choroidal mass within the globe adjacent to the extrascleral lesion.
- Melanomas often demonstrate spontaneous hyperintensity on T1 weighted images and routinely show contrast enhancement.
- Ultrasound can be performed readily in clinic and can often lead to a presumptive diagnosis.
- Computed tomography and magnetic resonance imaging are important in the diagnosis and surgical planning of larger lesions.

Keywords

Uveal melanoma · Orbital melanoma · Extrascleral · Exophytic

1 Signs and Symptoms

Floaters, flashing lights, decreased visual acuity, and/or visual field defect in the affected eye. A pigmented mass under the conjunctiva in case of anterior uveal melanoma, often with an engorged feeder vessel. Often there are no characteristic signs for extraocular tumor spread in case of small posterior uveal melanoma. Large extraocular extension of posterior uveal melanoma may present with proptosis, diplopia, vision loss, or pain [1, 2].

A. W. Stacey
Department of Ophthalmology, University of Washington, Seattle, WA, USA

M. Mossa-Basha
Department of Radiology, University of Washington, Seattle, WA, USA
e-mail: mmossab@uw.edu

I. D. Fabian (✉)
Ocular Oncology Service, The Goldschleger Eye Institute, Sheba Medical Center, Tel Hashomer, Tel Aviv University, Tel Aviv, Israel
e-mail: didi@didifabian.com

© Springer Nature Switzerland AG 2022
G. Ben Simon et al. (eds.), *Atlas of Orbital Imaging*,
https://doi.org/10.1007/978-3-030-62426-2_39

2 Differential Diagnosis

Bulging uvea through thin sclera can be seen in cases of chronic elevated intraocular pressure, radiated and controlled ciliary body melanoma with thin overlying sclera, conjunctival melanoma and choroidal lymphoma with extraocular spread, and primary orbital melanoma.

3 Diagnosis

Diagnosis is based on typical clinical findings and ultrasonography. Adjunct MR scans are useful in the evaluation of the extraocular portion and involvement of adjacent structures. Uveal melanoma often shows spontaneous hyperintensity on T1-weighted MR scans and routinely shows enhancement with contrast [3].

4 Treatment

In case of small extraocular extension of a uveal melanoma, shave biopsy and plaque radiotherapy may be attempted. For larger extraocular spread, the treatment includes enucleation or modified enucleation (i.e., removal of some of the affected conjunctiva). In case of massive spread, exenteration may be considered after ruling out distant metastatic spread. Adjuvant orbital radiotherapy may be required in case of incomplete tumor resection.

5 Figures and Captions

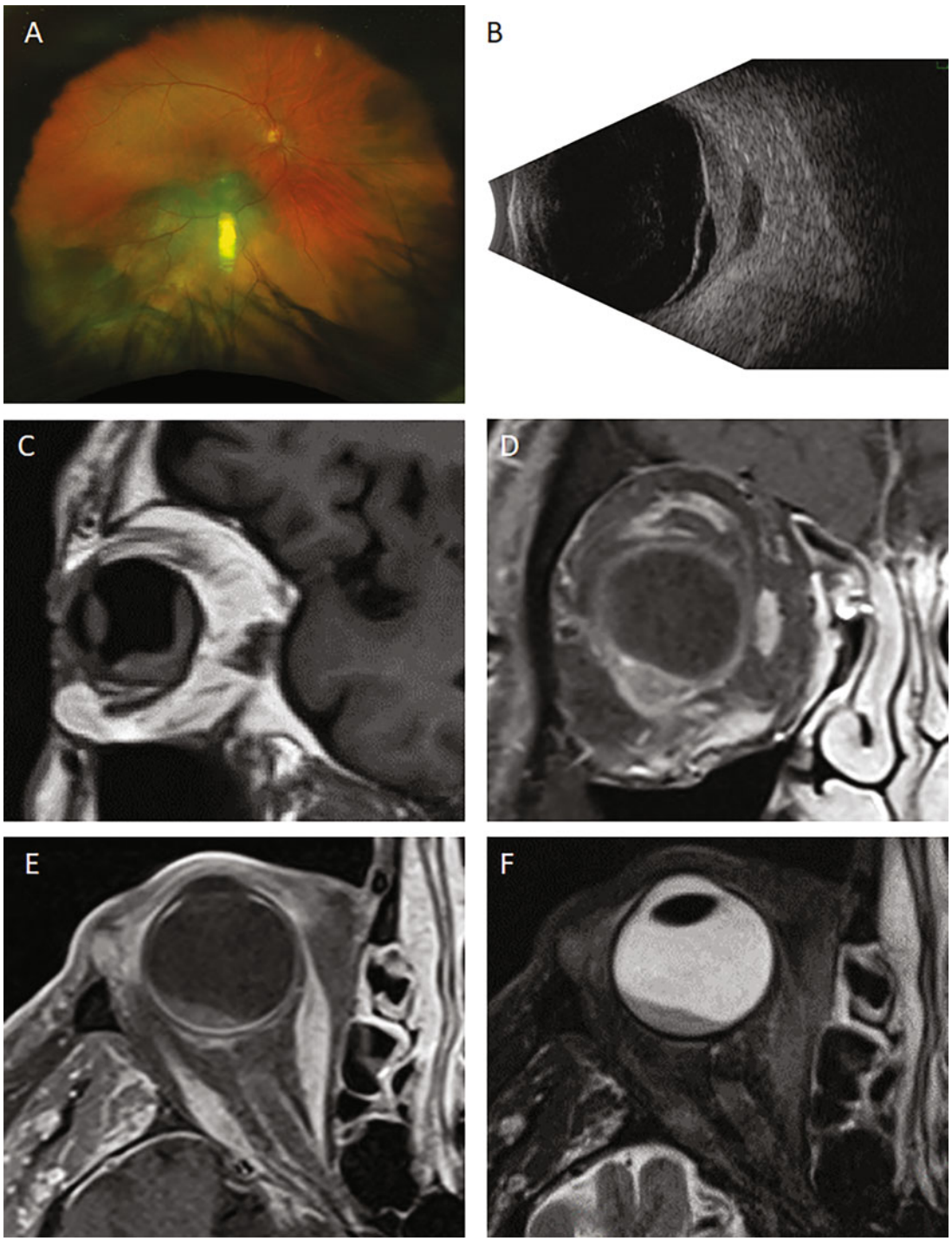


Fig. 1 Extra-scleral extension of a posterior uveal melanoma. **Color ocular fundus photo** (**a**) demonstrating pigmented mass extending from the inferior retinal periphery into the inferior macula. **B-scan ocular ultrasound with 40 MHz probe** (**b**) demonstrating inferior choroidal mass with low internal reflectivity and markedly hypoechoic area of extra-scleral extension at the inferior equator. **Sagittal T1 pre-contrast sequence** (**c**). In the right globe, the posterior and inferior choroidal soft tissue shows thickening with intermediate to slightly hyperintense signal within the lesion. **Coronal T1 post-contrast acquisition** (**d**) demonstrating enhancement and extraocular extension along the inferior margin of the globe. **Axial T1 post-contrast sequence** (**e**) demonstrating mild enhancement within the lesion. **Axial T2-weighted fat saturating acquisition** (**f**) demonstrating low T2 signal within the lesion

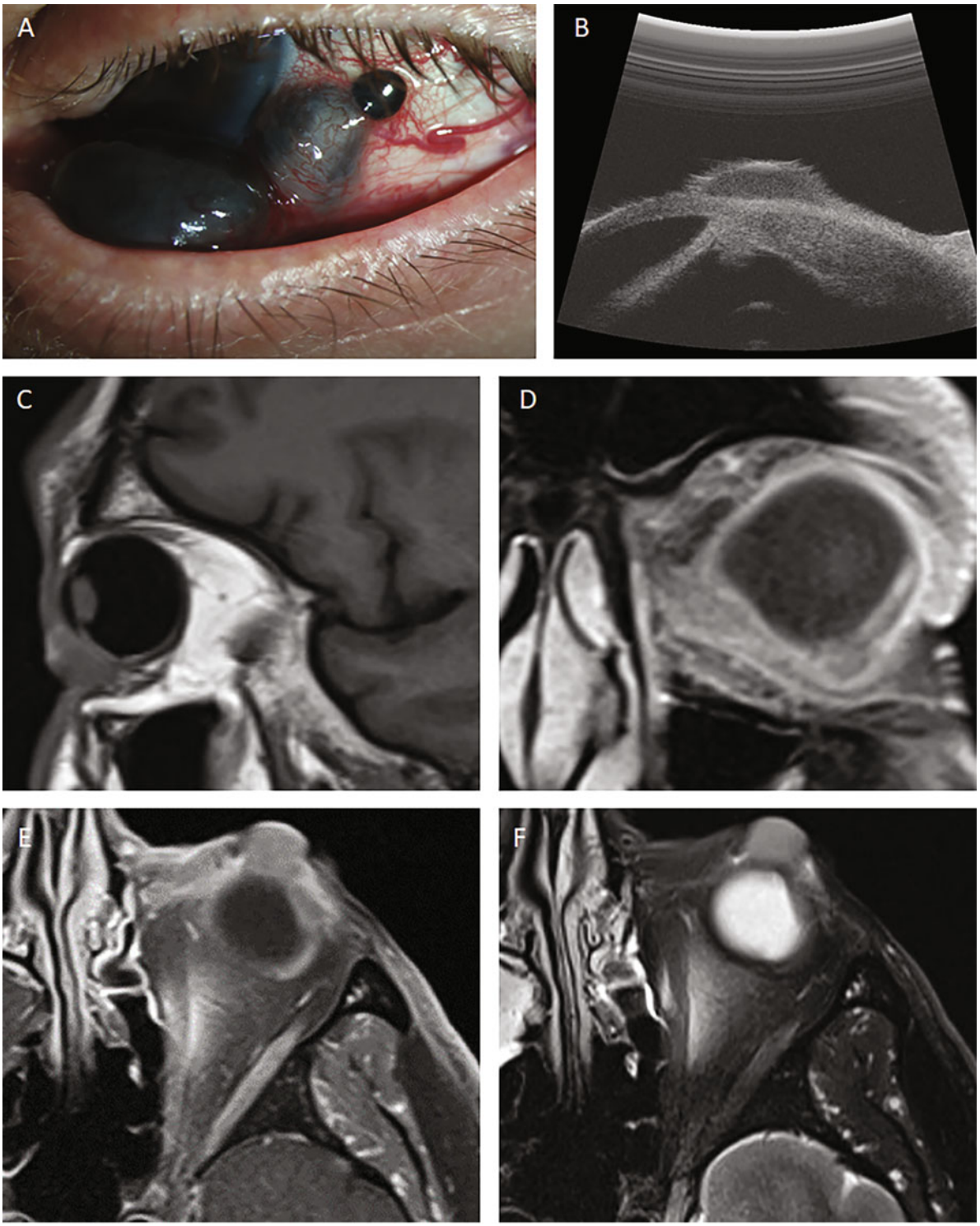


Fig. 2 Extra-scleral extension of an anterior uveal melanoma. **External photograph** (**a**) demonstrating a bullous extra-scleral extension of a ciliary body melanoma emanating from inferior to the corneal limbus. The lesions at 4 o'clock show the sub-conjunctival location of the pigmented lesion as evidenced by the normal appearing vessels overlying the pigment. **Ultrasound biomicroscopy with 20 MHz probe** (**b**) demonstrating the underlying ciliary body melanoma with medium internal reflectivity and the extra-scleral extension at the inferior corneal limbus demonstrating a lower echogenicity than the ciliary body portion. **On sagittal T1 FLAIR image** (**c**), there is focal choroidal thickening along the inferior aspect of the left globe, which is slightly hyperintense in signal, and shows mild enhancement on **coronal** (**d**) and **axial** (**e**) **fat-saturated T1 post-contrast sequences**. These scans contain dental hardware that may cause pseudo-infiltration of the left orbital fat. **On axial T2-weighted fat saturated acquisition** (**f**), the lesion has intermediate signal

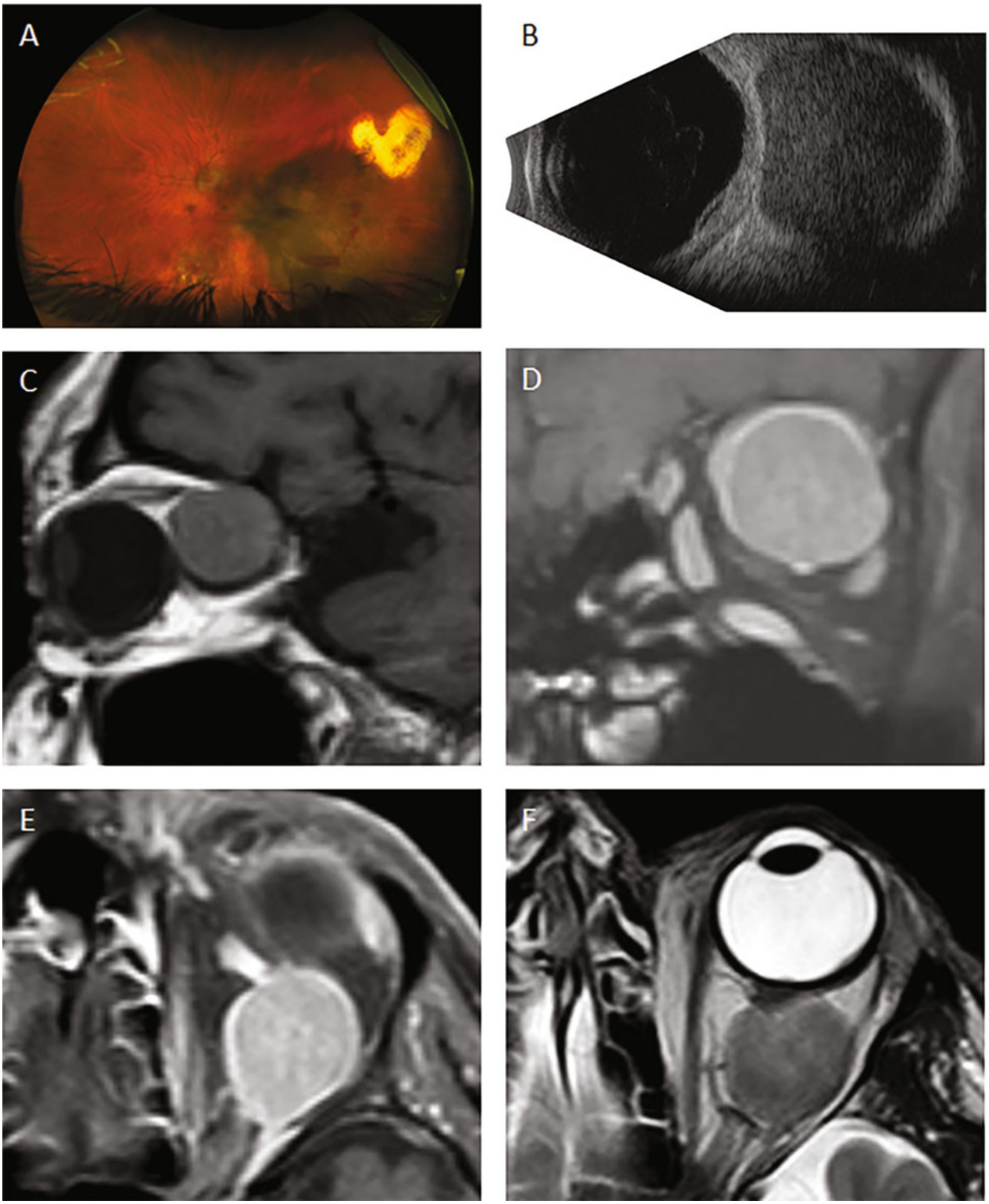


Fig. 3 Extra-scleral extension of a recurrent uveal melanoma after plaque brachytherapy. **Fundus photo (a)** nine years after plaque brachytherapy demonstrating no evidence of local recurrence in the eye. **B-scan ultrasound with 40MHz probe (b)** at the same time as image 3A demonstrating a large hypoechoic mass emanating from the superior border of the treated choroidal melanoma. **Sagittal T1 pre-contrast image (c)** demonstrating mildly hyperintense lesion projecting exophytically from the posterior aspect of the left globe. **Coronal (d)** and **axial (e) fat-suppressed T1-weighted post-contrast images** show the lesion with central, diffuse, mildly heterogeneous enhancement and a rim of intense enhancement. **Axial T2-weighted image (f)** showing the lesion with hypointense T2 signal within the orbit, the posterior border of the globe demonstrates mild irregularities that may be compatible with post-treatment changes

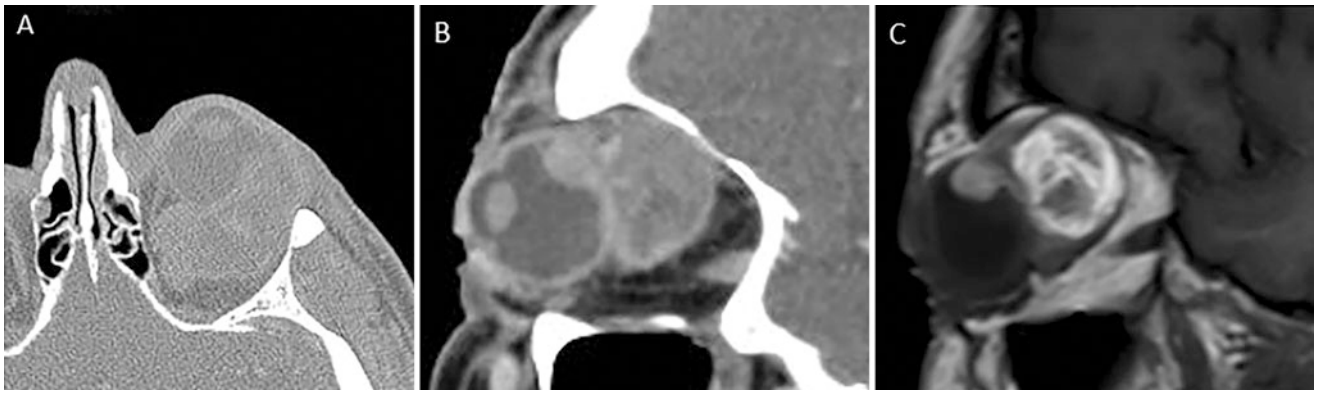


Fig. 4 Massive extra-scleral extension of a posterior uveal melanoma. **On post-contrast axial** (**a**) and **sagittal** (**b**) CT, there is a large, heterogeneously enhancing exophytic lesion involving the posterior and left lateral aspect of the left globe, which results in mass effect, deformity and displacement of the globe. The lesion extends into both the retrobulbar space and posterior chamber. **Sagittal T1-weighted pre-contrast image** (**c**) shows heterogeneous T1 hyperintense signal, likely due to melanin and/or blood products. **Axial T1-weighted fat-suppressed post contrast image** (**d**) shows likely small areas of lesional enhancement though a majority of the lesion bright signal is secondary to T1 shortening. **Axial STIR image** (**e**) Demonstrates the massive orbital extension of the uveal melanoma

References

1. Coupland SE, Campbell I, Damato B. Routes of extraocular extension of uveal melanoma: risk factors and influence on survival probability. Ophthalmology. 2008;115(10):1778–85. https://doi.org/10.1016/j.ophtha.2008.04.025.
2. Bellmann C, Lumbroso-Le Rouic L, Levy C, et al. Uveal melanoma: management and outcome of patients with extraocular spread. Br J Ophthalmol. 2010;94(5):569–74. https://doi.org/10.1136/bjo.2009.165423.
3. Ferreira TA, Grech Fonk L, Jaarsma-Coes MG, van Haren GGR, Marinkovic M, Beenakker J-WM. MRI of uveal melanoma. Cancers. 2019;11(3). https://doi.org/10.3390/cancers11030377

Retinoblastoma

49

Vikas Khetan, Pim de Graaf, Devjyoti Tripathy, and Ido Didi Fabian

Contents

1 **Signs and Symptoms** 376
2 **Differential Diagnosis** 376
3 **Diagnosis** 376
4 **Treatment** 376
5 **Figures with Captions** 377
References 384

Abstract

- Retinoblastoma is the most common intraocular childhood malignancy.
- A positive family history of retinoblastoma is present in less than 10% of cases, and bilateral disease in about 30%.
- Diagnosis of intraocular retinoblastoma is based on clinical examination via indirect ophthalmoscopy and portable fundus camera imaging, usually under general anesthesia.
- Ultrasound examination shows a Hyperechoic mass lesion with shadowing due to intra-lesional calcifications, and heterogeneity due to hemorrhage and necrosis.
- Extraocular retinoblastoma, which is rare in high-income countries, presents as swelling of periorbital soft tissues or proptosis.
- MRI of orbits is the study of choice in diagnosing and staging of extraocular retinoblastoma. It provides vital information regarding optic nerve and orbital invasion and is not associated with radiation exposure.
- MRI findings include intermediate signal intensity on T1 and low signal intensity on T2 with marked, usually heterogeneous, enhancement.
- Trilateral retinoblastoma is a rare variant of the disease that consists of hereditary retinoblastoma associated with an intracranial neuroblastic tumor. MRI is the study of choice to detect intracranial involvement, usually in the pineal gland region.

Keywords

Retinoblastoma · Intraocular childhood malignancy

V. Khetan
Sankara Nethralaya, Chennai, India

P. de Graaf
Department of Radiology and Nuclear Medicine, Amsterdam UMC, Vrije Universiteit Amsterdam, Cancer Center Amsterdam, Amsterdam, The Netherlands
e-mail: p.degraaf@amsterdamumc.nl

D. Tripathy
Ophthalmic Plastics, Orbit & Ocular Oncology Services, MTC Campus, LV Prasad Eye Institute, Bhubaneswar, India

I. D. Fabian (✉)
Ocular Oncology Service, The Goldschleger Eye Institute, Sheba Medical Center, Tel Hashomer, Tel Aviv University, Tel Aviv, Israel
e-mail: didi@didifabian.com

© Springer Nature Switzerland AG 2022
G. Ben Simon et al. (eds.), *Atlas of Orbital Imaging*,
https://doi.org/10.1007/978-3-030-62426-2_40

1 Signs and Symptoms

The most common initial presenting sign of intraocular retinoblastoma is leukocoria, followed by strabismus. For extraocular retinoblastoma, common signs include eyelid swelling, protruding extraocular mass or proptosis. In case of bilateral disease (~30% of cases), asymmetrical presentation is common, i.e., intraocular retinoblastoma in the fellow eye. Extraocular retinoblastoma is often a result of delayed diagnosis [1].

2 Differential Diagnosis

For intraocular retinoblastoma, Coats' disease, persistent fetal vasculature, vitreous hemorrhage, ocular toxocariasis, familial exudative vitreoretinopathy, rhegmatogenous retinal detachment, coloboma, astrocytic hamartoma, combined hamartoma of retina and retinal pigment epithelium, and endogenous endophthalmitis [2]. For extraocular retinoblastoma, other childhood orbital lesions of neoplastic, vascular, infectious and inflammatory conditions, such as optic nerve glioma, metastatic neuroblastoma, rhabdomyosarcoma, leukemia, and lymphoma. Other advanced-stage intraocular lesions causing proptosis, such as (teratoid) medulloepithelioma.

3 Diagnosis

Based mainly on clinical, but also radiological findings. Ocular ultrasound can demonstrate a hyperechoic lesion with shadowing due to intra-lesional calcifications, and heterogeneity due to intra-lesional hemorrhage and necrosis. It may also show intra-vitreous lesions, which represent vitreous retinoblastoma seeds. High-resolution contrast-enhanced MRI of orbits and brain is the study of choice for extraocular retinoblastoma [3–8]. Typical intraocular findings in the fellow eye, if present, may disclose the diagnosis. Biopsy from an extraocular lesion is rarely needed and strongly prohibited in case of suspected intraocular lesion with no extraocular extension. Although MRI may be inaccurate in assessment of early stage of optic nerve involvement, the high negative predictive value allows a reliable exclusion of advanced tumor invasion [3].

4 Treatment

Enucleation for advanced intraocular retinoblastoma or chemotherapy by various techniques of administration, to preserve an eye. In case of massive orbital retinoblastoma, neoadjuvant chemotherapy followed by enucleation, radiotherapy, and adjuvant chemotherapy [4]. In case of intraocular retinoblastoma with suspected retrolaminar invasion, primary enucleation is the treatment of choice. According to histopathology findings, adjuvant chemotherapy with or without radiotherapy may be indicated.

5 Figures with Captions

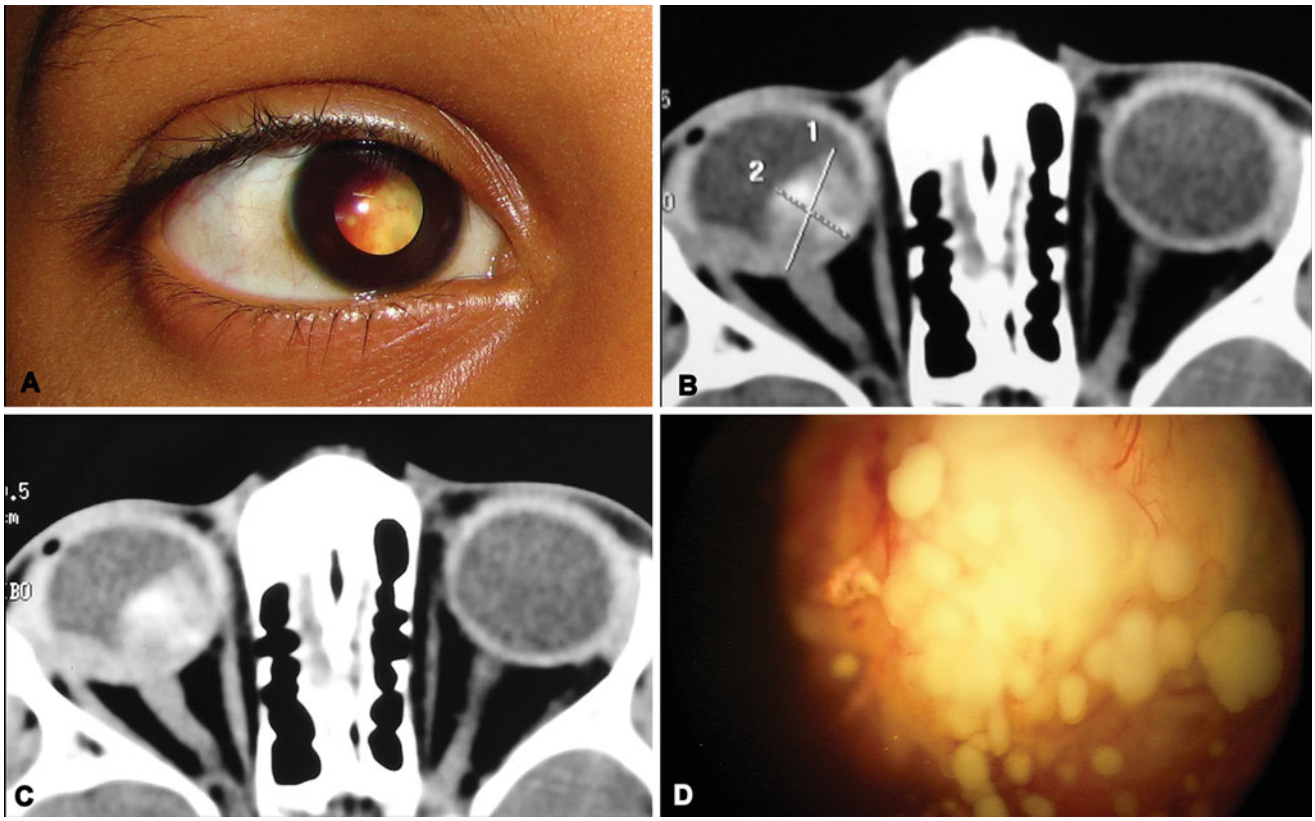
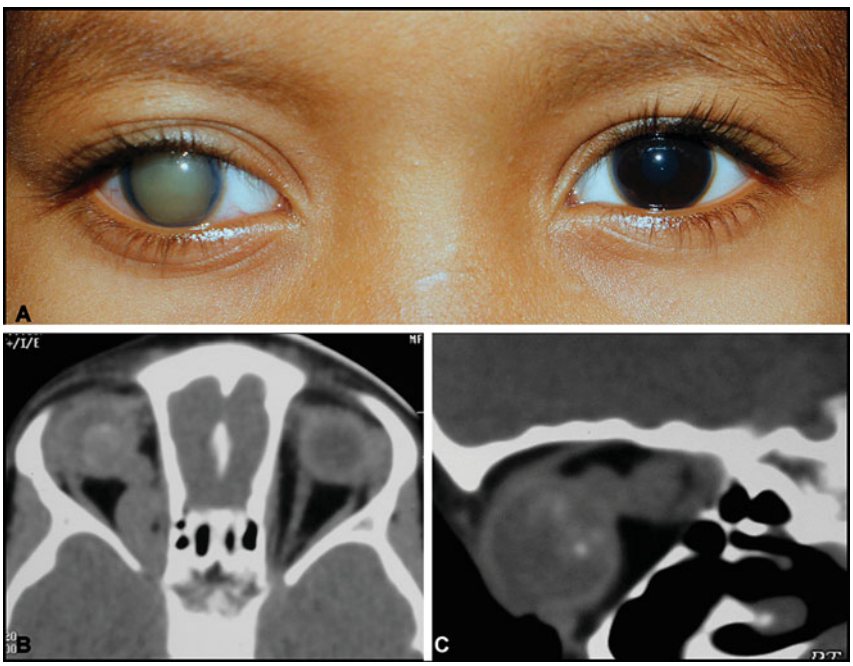


Fig. 1 **A color photo** of a 6-year-old boy with right side leukocoria (**a**). **Axial CT scan** shows an intraocular mass with calcific foci (**b**). **Axial CT scan with contrast** shows mass enhancement that appears on the optic nerve head with an underlying thickened optic nerve, suggestive of tumor extension (**c**). **Fundus photography (RetCam) under anesthesia** shows that the mass completely obscures the optic disc and is associated with multiple vitreous seeds shaped as "spheres" and "clouds" (**d**)

Fig. 2 **A color photo** of a 5-year-old girl with subtle right-side proptosis and corneal haze (**a**). **Axial and sagittal CT scans** show a grossly thickened optic nerve due to tumor infiltration on the right side (**b** and **c**). Optic nerve infiltration is noted to extend up to the optic chiasma



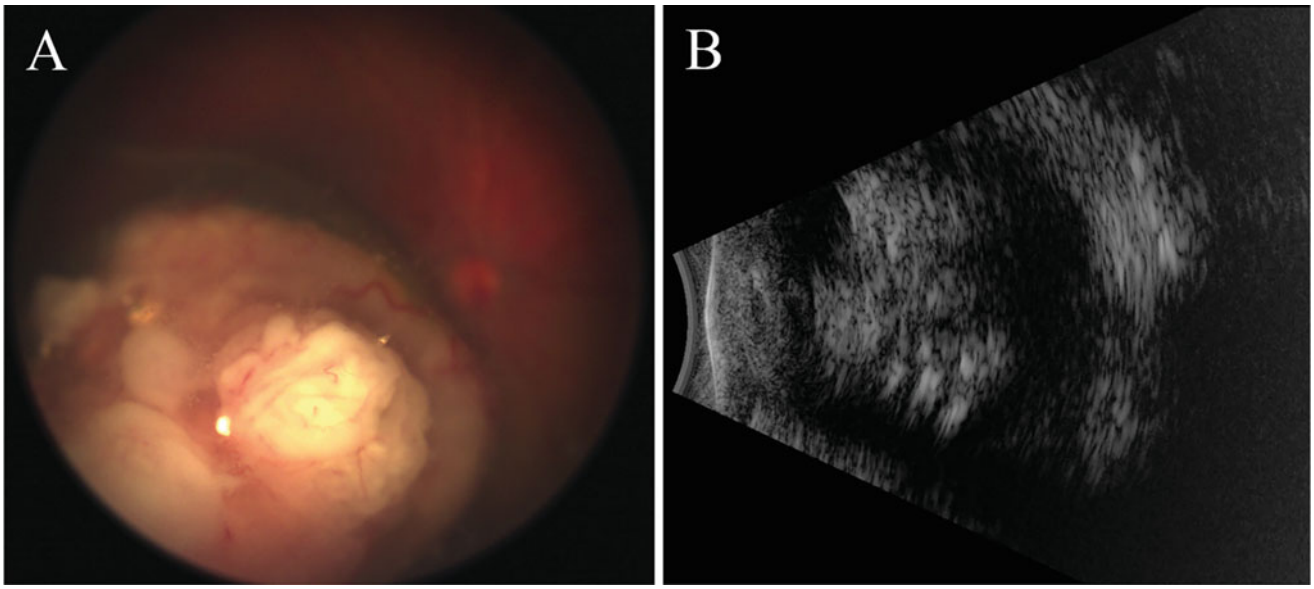


Fig. 3 **Fundus photography using a portable camera** demonstrating a right eye macular tumor (**a**) with overlying retinal detachment in a 1-year-old child. Note the optic disc adjacent to the mass. The mass shown on B-scan ultrasonography (**b**). Hyperechoic lesions within the mass suggest intra-lesional calcifications

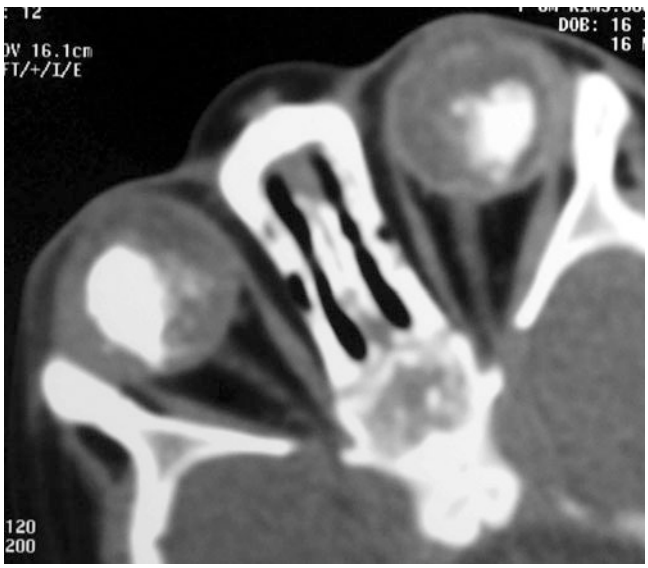


Fig. 4 **Axial CT scan** of an 8-month-old girl demonstrates bilateral intraocular soft tissue masses with large chunks of calcification. The globe contours and optic nerves are normal bilaterally and there is no evidence of extraocular tumor extension

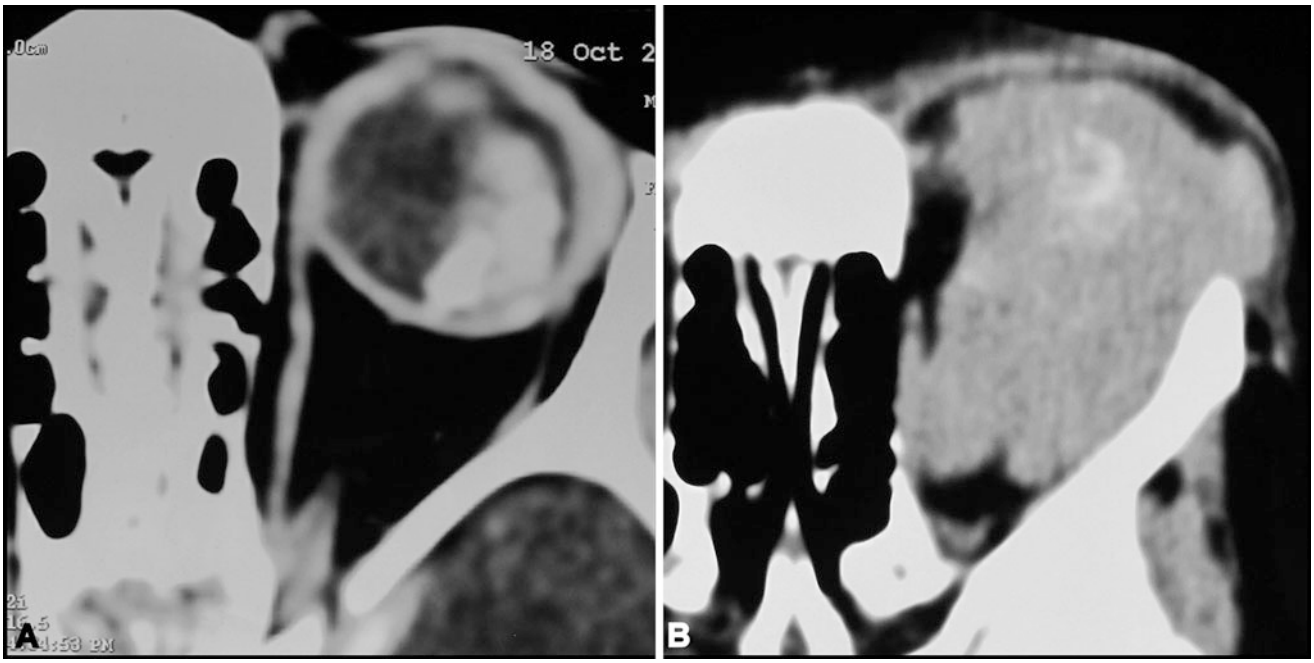


Fig. 5 **Axial CT scan** of a 2-year-old girl showing a contrast-enhancing intraocular mass with calcification (**a**) within the left eyeball. There is no evidence of optic nerve or extraocular extension. Significant delay in follow-up by the parents resulted in the tumor spreading beyond the eye wall, demonstrated by a large, contrast-enhancing mass occupying the left orbit (**b**). Note the intraocular calcification still discernible in the anterior portion of the orbital mass

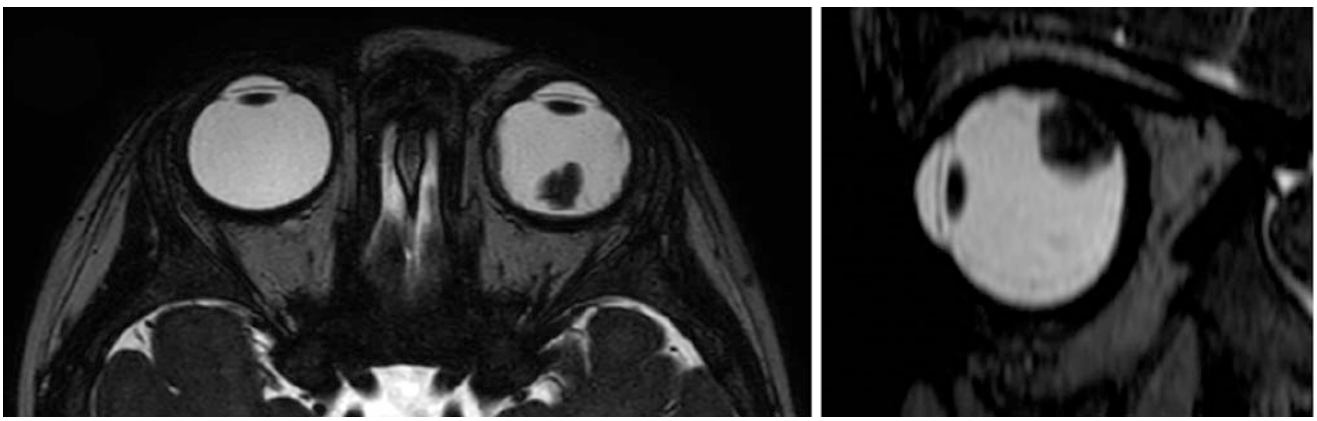


Fig. 6 **T2WI MRI** of a 1.7-year-old child with left eye group D multifocal retinoblastoma. Note a dominant lesion on the posterior-superior aspect of the globe and smaller nasal and temporal tumors, all hypointense on T2

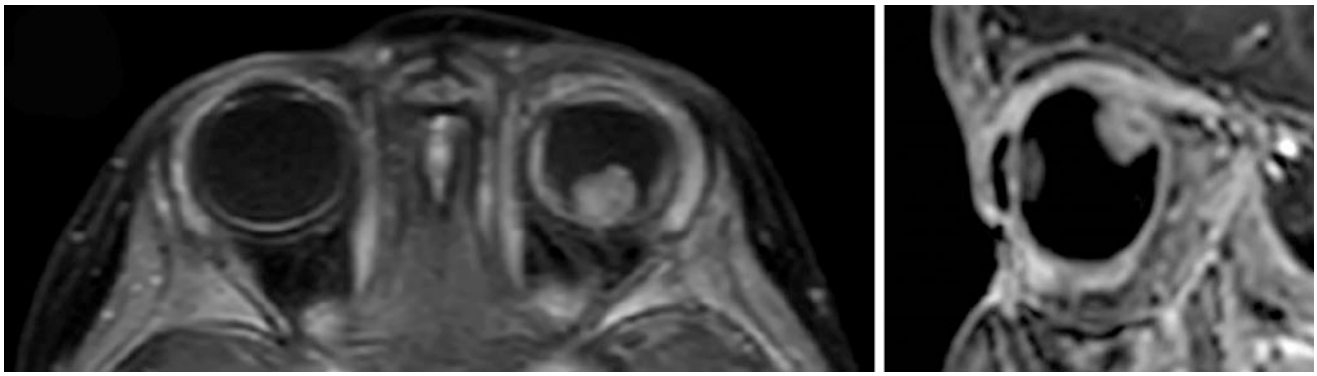


Fig. 7 **Same patient, CE T1 WI MRI**, axial FS (*left*) and sagittal 3D T1 TFE (*right*) views showing a heterogenous enhancement of the mass with choroidal extension

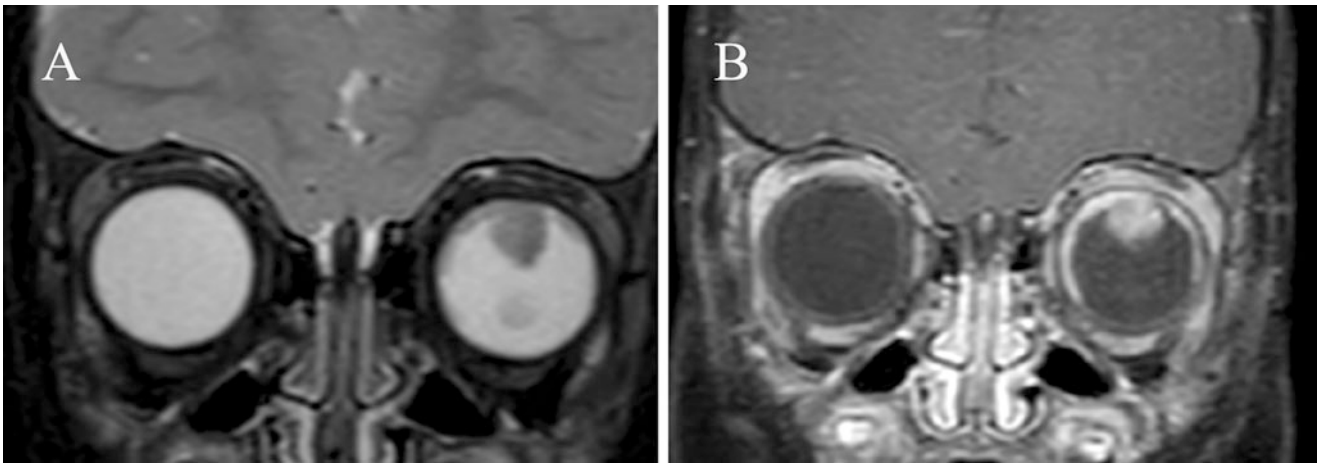


Fig. 8 **Coronal MRI** (A, T2, B, CE T1WI) of the same patient demonstrates the extent of intra-ocular involvement of retinoblastoma

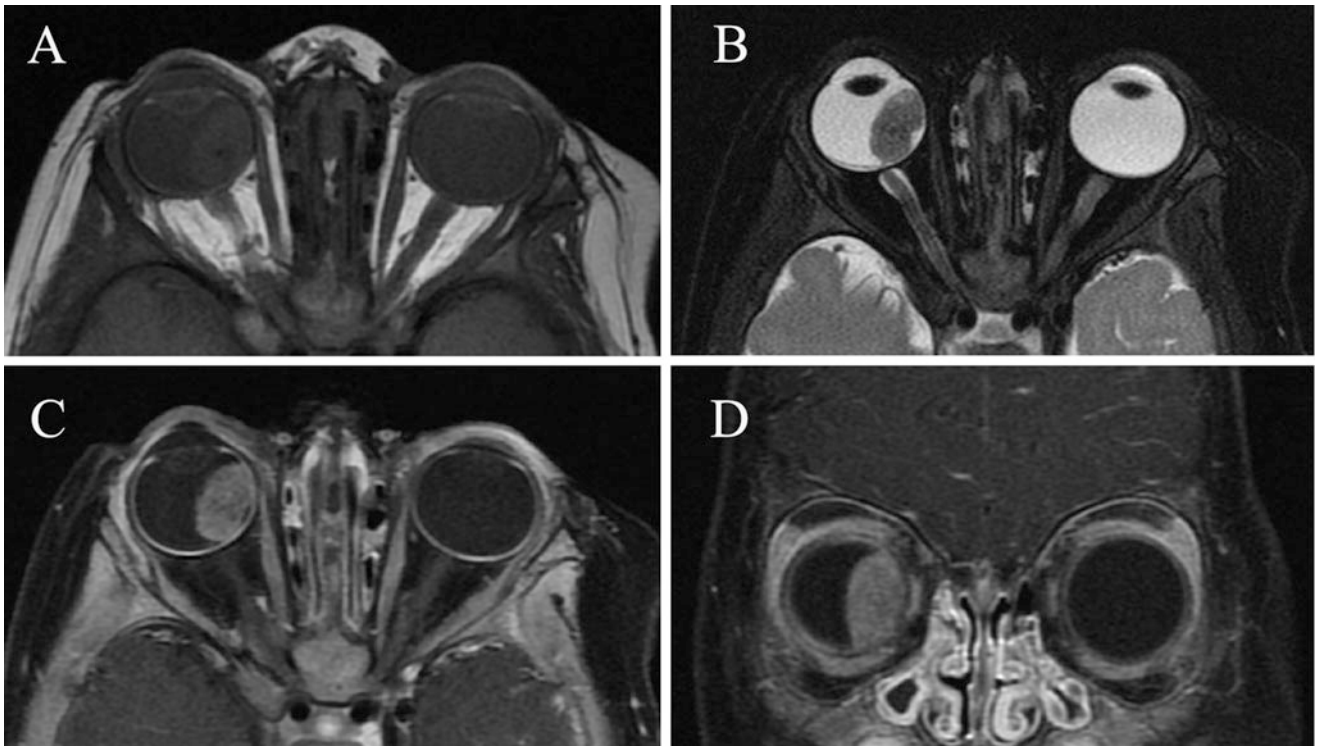


Fig. 9 **MRI of a child** with unifocal right eye intraocular retinoblastoma, located within the nasal half of the globe. The tumor is isointense on T1 (**a**), and hypointense on T2 (**b**), showing mildly heterogenous enhancement post-contrast administration (**c**, axial and **d**, coronal)



Fig. 10 **Clinical image** of a different child showing a right buphthalmic (i.e., enlarged) eye, with necrosis at anterior aspect



Fig. 11 **Axial T2-weighted image** through the orbits (child shown in Fig. 10) shows an enlarged right eye secondary to a heterogeneous intraocular tumor mass with anterior extraocular extension into the eyelids (**a**). The **contrast-enhanced fat-suppressed T1-weighted image** (**b**) shows a thickening and enhancement of the most distal part of the optic nerve (arrow) suspicious for extensive post-laminar tumor infiltration

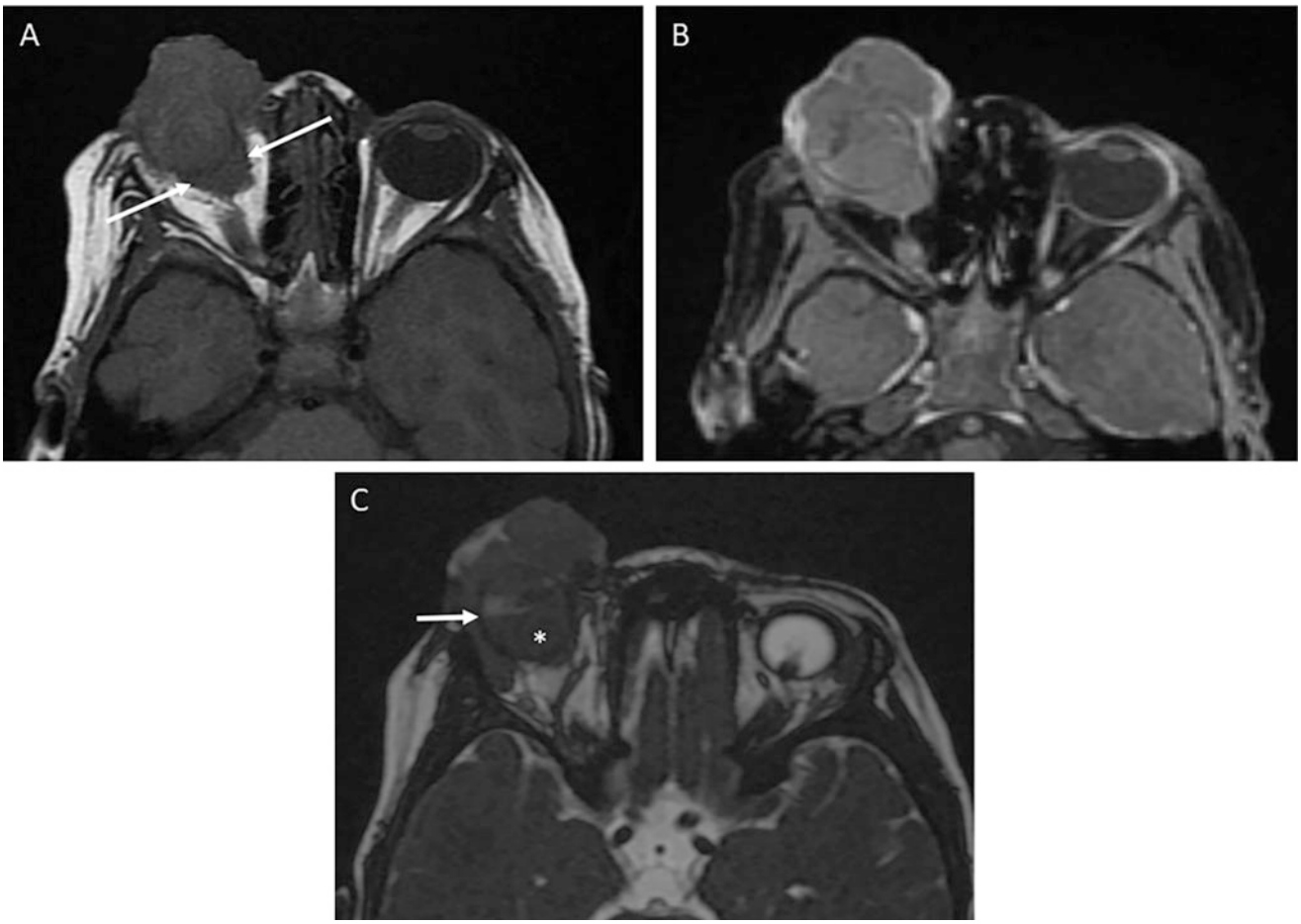


Fig. 12 **Axial T1-weighted (a) and contrast-enhanced fat-suppressed T1 weighted (b)** images (child shown in Fig. 10) show trans-scleral tumor growth with orbital fat invasion (in between arrows) as well as massive anterior extension into the eyelids. **Axial 3D-FIESTA image (c)** through the orbits shows a dependent fluid-fluid level (arrow) in the right eye from a subacute intraocular hemorrhage combined with the retinoblastoma (asterisk). The left eye also contains a hypo-intense intraocular tumor

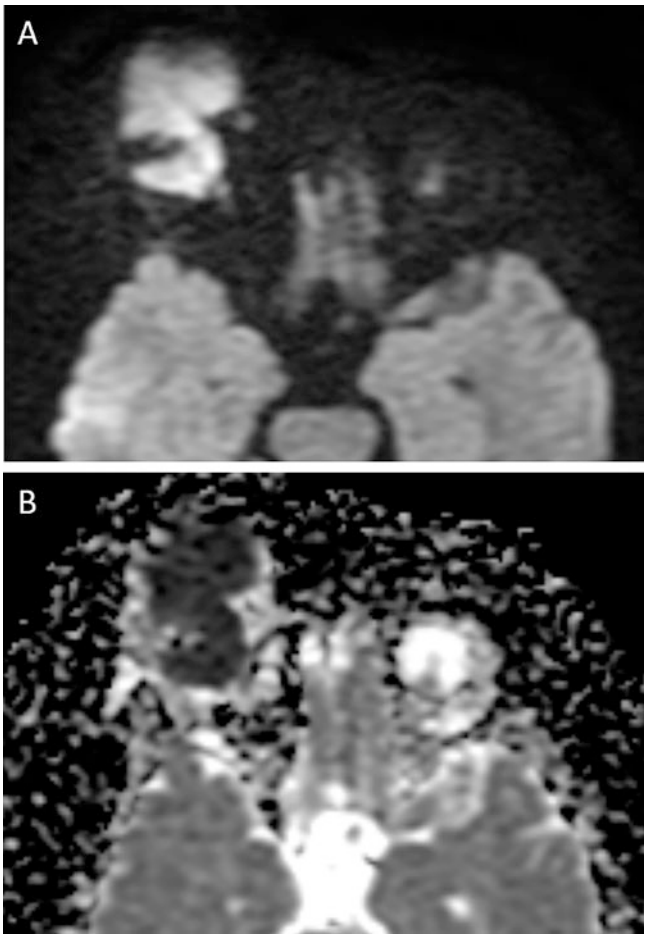


Fig. 13 **Axial diffusion-weighted image** (b-value of 1000) (**a**) **with corresponding ADC map** (**b**) (child shown in Fig. 10) shows a high signal intensity of the intra- and extraocular parts of the tumor in the right eye as well as linear high signal in the left eye. The ADC map shows corresponding low values within the tumor confirming its high cellularity

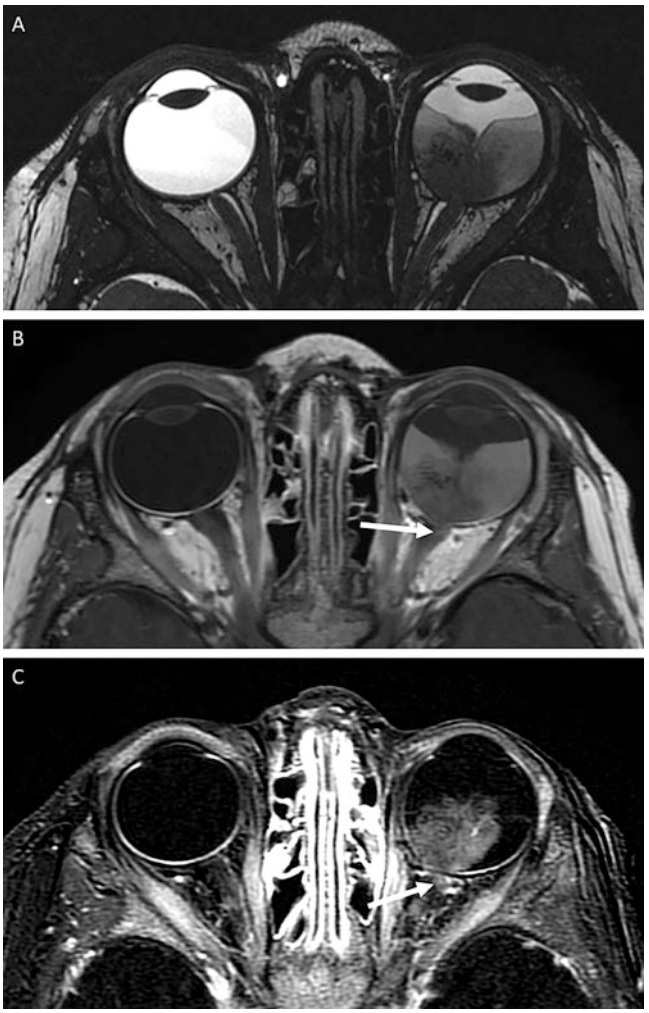


Fig. 14 **Axial 3D-FIESTA image** of a different child (**a**) (obtained at a 3 Tesla system combined with a 32-channel head coil) shows a large (exophytic) retinoblastoma combined with a retinal detachment and subretinal hemorrhage. (**b**) Contrast-enhanced axial T1-weighted image (without fat suppression) shows an irregular aspect of the papilla with enhancement in the retrolaminar optic nerve (arrow) as a sign of tumor invasion. (**c**) The tumor invasion (arrow) is even more conspicuous on the subtracted image (contrast-enhanced T1-weighted image minus the native T1-weighted image)

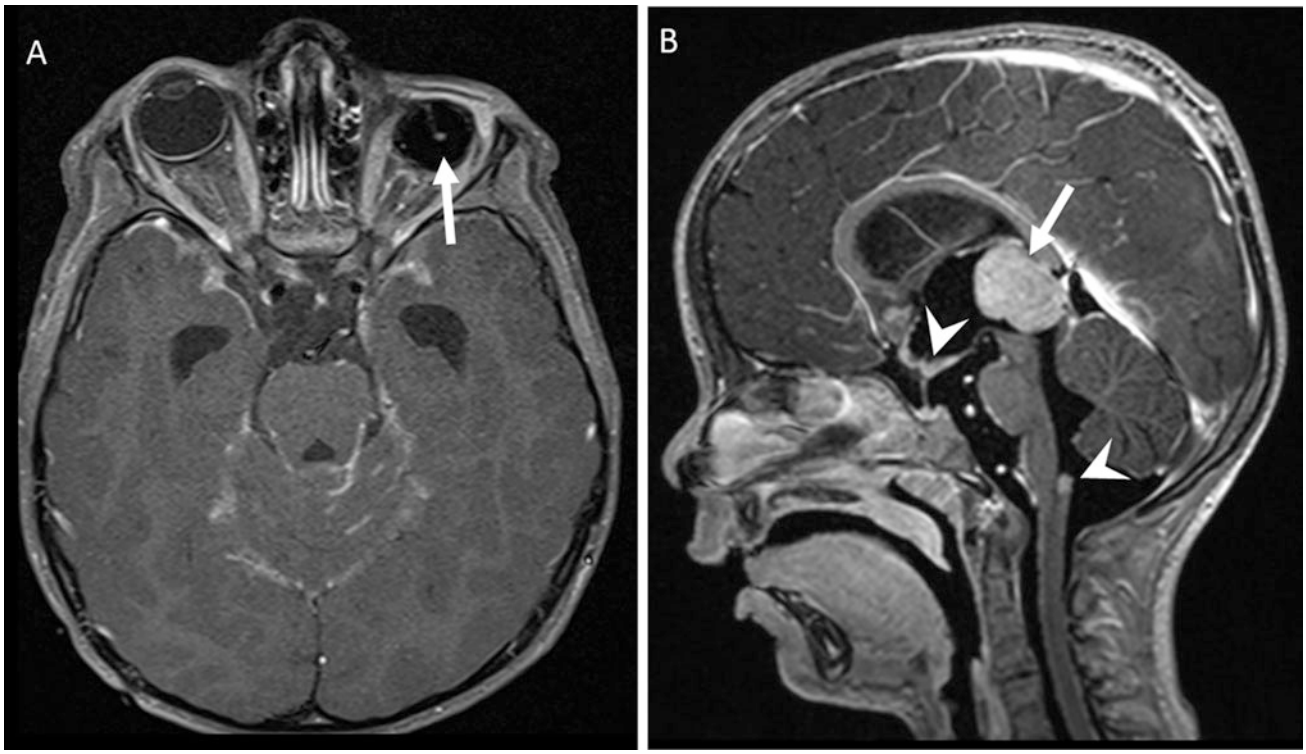


Fig. 15 **Axial contrast-enhanced fat-suppressed T1-weighted** (**a**) image shows an enucleation of the left eye with an orbital implant (arrow). The **Sagittal 3D contrast-enhanced T1-weighted** (**b**) image shows a midline intracranial mass within the pineal gland (arrow) combined with extensive leptomeningeal seeding (arrowheads)

References

1. Global Retinoblastoma Study Group. Global retinoblastoma presentation and analysis by National Income Level. JAMA Oncol. 2020;6(5):1–12. https://doi.org/10.1001/jamaoncol.2019.6716.
2. Shields CL, Schoenberg E, Kocher K, Shukla SY, Kaliki S, Shields JA. Lesions simulating retinoblastoma (pseudoretinoblastoma) in 604 cases: results based on age at presentation. Ophthalmology. 2013;120(2):311–6. https://doi.org/10.1016/j.ophtha.2012.07.067. Epub 2012 Oct 27. PMID: 23107579.
3. Brisse HJ, de Graaf P, Galluzzi P, et al. Assessment of early-stage optic nerve invasion in retinoblastoma using high-resolution 1.5 Tesla MRI with surface coils: a multicentre, prospective accuracy study with histopathological correlation. Eur Radiol. 2015. https://doi.org/10.1007/s00330-014-3514-1.
4. Honavar SG, Manjandavida FP, Reddy VAP. Orbital retinoblastoma: an update. Indian J Ophthalmol. 2017. https://doi.org/10.4103/ijo.IJO_352_15.
5. Gizewski ER, Wanke I, Jurklies C, Güngör AR, Forsting M. T1 Gd-enhanced compared with CISS sequences in retinoblastoma: superiority of T1 sequences in evaluation of tumour extension. Neuroradiology. 2005;47(1):56–61. https://doi.org/10.1007/s00234-004-1316-x. Epub 2005 Jan 14. PMID: 15650830.
6. de Jong MC, de Graaf P, Noij DP, Göricke S, Maeder P, Galluzzi P, Brisse HJ, Moll AC, Castelijns JA, European Retinoblastoma Imaging Collaboration (ERIC). Diagnostic performance of magnetic resonance imaging and computed tomography for advanced retinoblastoma: a systematic review and meta-analysis. Ophthalmology. 2014;121(5):1109–18. https://doi.org/10.1016/j.ophtha.2013.11.021. Epub 2014 Mar 1. PMID: 24589388.
7. Jansen RW, de Jong MC, Kooi IE, Sirin S, Göricke S, Brisse HJ, Maeder P, Galluzzi P, van der Valk P, Cloos J, Eekhout I, Castelijns JA, Moll AC, Dorsman JC, de Graaf P. MR imaging features of retinoblastoma: association with gene expression profiles. Radiology. 2018;288(2):506–15. https://doi.org/10.1148/radiol.2018172000. Epub 2018 May 1. PMID: 29714679.
8. Dimaras H, Corson TW. Retinoblastoma, the visible CNS tumor: a review. J Neurosci Res. 2019;97(1):29–44. https://doi.org/10.1002/jnr.24213. Epub 2018 Jan 3. PMID: 29314142; PMCID: PMC6034991.

Metastatic Orbital Lesions: Breast Cancer

50

Oded Sagiv, J. Matthew Debnam, and Bita Esmaeli

Contents

1 **Signs and Symptoms** 385
2 **Differential Diagnosis** 386
3 **Diagnosis** 386
4 **Treatment** 386
5 **Figures with Captions** 386
References 388

Abstract

- An infiltrative orbital mass.
- The most common primary cancer to cause orbital metastasis is breast cancer.
- Nonspecific on CT: there is usually soft tissue attenuation; may be well defined but also infiltrative patterns are not uncommon; may cause bone destruction. Contrast enhancement is a common feature.
- MRI – T1 – soft tissue iso-intense, contrast enhancement. Slightly hype-intense relative to EOM on T2. DWI may vary depending on the cellularity of the lesion with no definite ADC threshold.
- In certain subtypes (scirrhous/cicatrizing) relative enophthalmos can be seen on axial view.
- Orbital fat and EOM involvement is typical.

Keywords

Orbital Metastasis · Metastatic Breast Cancer

1 Signs and Symptoms

Metastatic cancer to the orbit occurs mainly in adults and is commonly unilateral. Symptoms tend to progress rapidly over weeks to months. Mass effect of the metastasis can cause proptosis or globe displacement, depends on its exact location in the orbit. Pain, inflammation, conjunctival chemosis and eyelid swelling, and erythema can also occur. Orbital functions may be disturbed as well resulting in restriction in eye movements, diplopia, ptosis, and compressive optic neuropathy. Presentation may vary considerably between patients and various primary cancers, and Goldberg et al. suggested to categorized them into: infiltrative (53%), mass (37%), inflammatory (5%), functional (3%), and silent (rare).

Orbital metastasis from breast cancer typically infiltrates the orbital fat and extraocular muscles. It may cause proptosis but has a unique scirrhous adenocarcinoma variant which can present as enophthalmos.

O. Sagiv
The Goldschleger Eye Institute, Sheba Medical Center, affiliated to the Sackler Faculty of Medicine, Tel-Aviv University, Tel Aviv, Israel
e-mail: Oded.sagiv@sheba.health.gov.il

J. M. Debnam
Department of Neuroradiology, The University of Texas MD Anderson Cancer Center, Houston, TX, USA
e-mail: Matthew.Debnam@mdanderson.org

B. Esmaeli (✉)
Ophthalmic Plastic Surgery, Department of Plastic Surgery, The University of Texas MD Anderson Cancer Center, Houston, TX, USA
e-mail: besmaeli@mdanderson.org.il

© Springer Nature Switzerland AG 2022
G. Ben Simon et al. (eds.), *Atlas of Orbital Imaging*,
https://doi.org/10.1007/978-3-030-62426-2_41

2 Differential Diagnosis

Unilateral proptosis in an adult with a history of cancer should raise the suspicion of a metastasis. This is also true for patients with no history of cancer since 19–25% of cases of orbital metastases happen in patients with no previously known cancer. Metastasis is therefore included in the differential diagnosis of many other orbital lesions.

The most common primary cancer to cause orbital metastasis is breast cancer.

3 Diagnosis

Diagnosis is made with an orbital biopsy of the metastasis.

4 Treatment

Breast cancer has seen in recent years new biologic and hormonal treatments with improved response rates and less toxicity compared with traditional chemotherapy. Orbital metastasis is preferably treated as a systemic disease with systemic treatment as directed by the treating oncologist. Metastases that do not respond or cause significant mass effect can also be treated with external beam radiation therapy which can stabilize the disease locally.

5 Figures with Captions

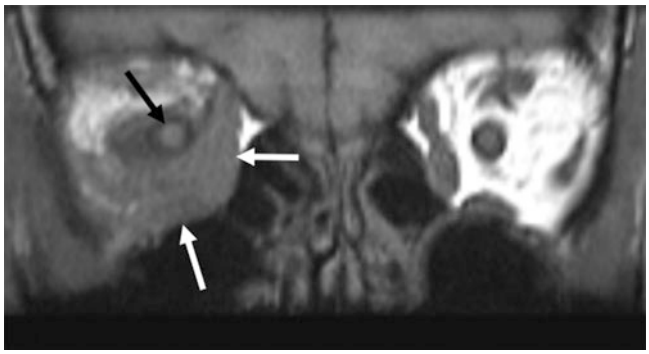


Fig. 2 Coronal T1 pre-contrast image (same patient) demonstrates that the tumor is located in the inferior and medial orbit (arrows) below the optic nerve (black arrow)

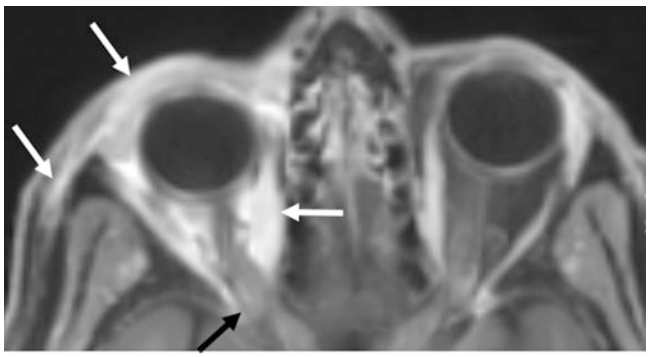


Fig. 3 Axial T1 post-contrast fat-saturated image shows enhancing tumor in the periorbital soft tissues, eyelid, and post-septal space (arrows) with involvement of the orbital apex (black arrow). Relative enophthalmos can be noted on the right side

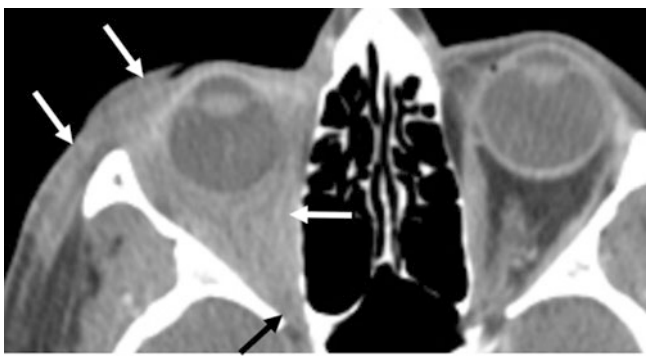


Fig. 1 Axial post-contrast CT orbit, soft tissue window shows enhancing tumor in the periorbital soft tissues, eyelid and post-septal space (arrows) extending posteriorly to the orbital apex (black arrow). Relative enophthalmos can be noted on the right side

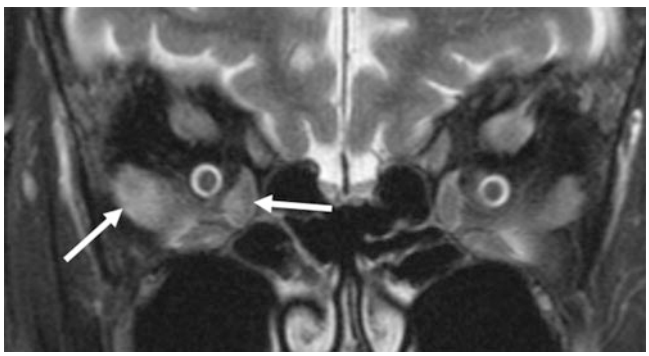


Fig. 4 Coronal T2 fat-saturated image (different patient) with hyperintense thickening in the medial and lateral rectus muscles (arrows) more obvious in the latter. Bilateral inferior intraconal fat stranding may be related to dental hardware rather than tumoral involvement

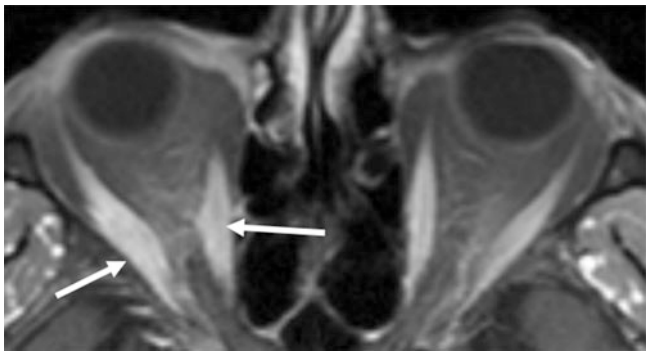


Fig. 5 **Axial T1 post-contrast fat-saturated image** shows fusiform enlargement and enhancement of both MR and LR muscles evidence of metastases (arrows)

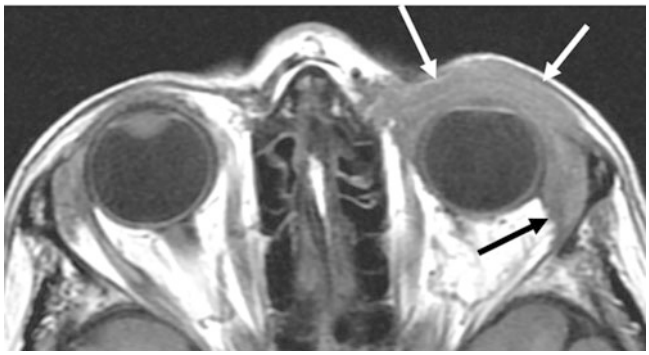


Fig. 6 **Axial T1 pre-contrast** (different patient) with tumor in the left eyelid (arrows) with extension into the lacrimal fossa and post-septal space (black arrow)



Fig. 7 T1-Fat Suppressed axial MRI of a 63-years old female patient with a right orbital breast cancer metastasis (**a**). The tumor is involving the intraconal space, extraocular muscles and extending intra-cranially to the cavernous sinus (white arrows, **a** & **b**). Note gradual improvement post medical treatment with near complete resolution (**b** & **c**)

References

1. Goldberg RA, Rootman J, Cline RA. Tumors metastatic to the orbit: a changing picture. Surv Ophthalmol. 1990;35(1):1–24.
2. Esmaeli B. Ophthalmic oncology, vol. 6. Boston: Springer Science & Business Media; 2011.
3. Sepahdari AR, Politi LS, Aakalu VK, Kim HJ, Razek AAKA. Diffusion-weighted imaging of orbital masses: multi-institutional data support a 2-ADC threshold model to categorize lesions as benign, malignant, or indeterminate. AJNR. 2014;35:170–5.
4. Salinas-Botrán A, Guarín-Corredor MJ. Orbital metastasis in breast cancer. N Engl J Med. 2019;381(12):e26. https://doi.org/10.1056/NEJMicm1814570.
5. Raap M, Antonopoulos W, Dämmrich M, Christgen H, Steinmann D, Länger F, Lehmann U, Kreipe H, Christgen M. High frequency of lobular breast cancer in distant metastases to the orbit. Cancer Med. 2015;4(1):104–11. https://doi.org/10.1002/cam4.331. Epub 2014 Oct 30. PMID: 25355547; PMCID: PMC4312124.
6. Tamura M, Tada T, Tsuji H, Tamura M, Yoshimoto M, Takahashi K, Tada K, Tanabe M, Kutomi G, Sekine Y, Kasumi F. Clinical study on the metastasis to the eyes from breast cancer. Breast Cancer. 2004;11(1):65–8. https://doi.org/10.1007/BF02968005.
7. Orr CK, Cochran E, Shinder R. Metastatic scirrhous breast carcinoma to orbit causing enophthalmos. Ophthalmology. 2016;123(7):1529. https://doi.org/10.1016/j.ophtha.2016.04.012.
8. Pinto Proença R, Fernandes J, Burnier MN, Proença R. Orbital metastasis from an occult breast carcinoma (T0, N1, M1). BMJ Case Rep. 2018;2018:bcr2017223542. https://doi.org/10.1136/bcr-2017-223542. PMID: 29643136; PMCID: PMC5898278.
9. Ahmad SM, Esmaeli B. Metastatic tumors of the orbit and ocular adnexa. Curr Opin Ophthalmol. 2007;18(5):405–13. https://doi.org/10.1097/ICU.0b013e3282c5077c.
10. Esmaeli B. Ophthalmology as a specialty at comprehensive cancer centers in the United States. Am J Clin Oncol. 2008;31(4):390–2. https://doi.org/10.1097/COC.0b013e3181660bc0.

Metastatic Orbital Lesions: Lung Cancer, Prostate Cancer, and Renal Cell Carcinoma (RCC) 51

Oded Sagiv, J. Matthew Debnam, and Bita Esmaeli

Contents

1 Signs and Symptoms 389

2 Differential Diagnosis 390

3 Diagnosis 390

4 Treatment 390

5 Figures with Captions 390
5.1 Metastatic Lung Cancer 390
5.2 Metastatic Prostate Cancer 392
5.3 Metastatic RCC 393

References 394

Abstract

Lung Cancer

- In most cases well-circumscribed orbital lesion with mass effect.
- CT can show bony infiltration and destruction with invasion to the brain or masticator space.
- Post-contrast images can show variable enhancement.

Prostate Cancer

- CT shows a sclerotic lesion in an orbital bone.
- Hypointense on T1 and T2 due to its sclerotic nature.
- Post-contrast T1 shows heterogenous enhancement.

RCC

- Diffuse orbital mass or localized lesion to bone, fat, or muscle.
- Post-contrast T1 enhancement.

Keywords

Orbital metastasis · Metastatic lung cancer · Metastatic prostate cancer · Metastatic RCC

O. Sagiv
The Goldschleger Eye Institute, Sheba Medical Center, affiliated to the Sackler Faculty of Medicine, Tel-Aviv University, Tel Aviv, Israel
e-mail: Oded.sagiv@sheba.health.gov.il

J. M. Debnam
Department of Neuroradiology, The University of Texas MD Anderson Cancer Center, Houston, TX, USA
e-mail: Matthew.Debnam@mdanderson.org

B. Esmaeli (✉)
Ophthalmic Plastic Surgery, Department of Plastic Surgery, The University of Texas MD Anderson Cancer Center, Houston, TX, USA
e-mail: besmaeli@mdanderson.org.il

© Springer Nature Switzerland AG 2022
G. Ben Simon et al. (eds.), *Atlas of Orbital Imaging*,
https://doi.org/10.1007/978-3-030-62426-2_98

1 Signs and Symptoms

Signs and symptoms are similar to that elaborated under ▶ Chap. 50, "Metastatic Orbital Lesions: Breast Cancer." Orbital metastasis from lung cancer tend to happen early after diagnosis of the primary cancer and have an aggressive presentation. Orbital metastasis from prostate cancer have

affinity to bone and indeed the majority of metastatic lesions have an osteoblastic component and pain is a more common symptom. Metastatic renal cell carcinoma (RCC) can involve muscle, fat, or bone. It generally appears as a diffuse orbital mass but can less commonly occur as a localized lesion. Conjunctiva and eyelids can also be involved. Pulsating exophthalmos may be a feature due to the high vascularity of the lesion.

2 Differential Diagnosis

Same as for breast cancer. Lung cancer is the second most common carcinoma to cause orbital metastasis. For prostate carcinoma – an osteoblastic lesion in an orbital bone, the differential diagnosis should also include meningioma, specifically if it is in the sphenoid bone. Other osteosclerotic metastases like breast cancer can also be considered. Renal cell carcinoma is the most common urologic cancer to metastasize to the orbit.

3 Diagnosis

Diagnosis is made with an orbital biopsy of the metastasis. For prostate carcinoma diagnosis is based on imaging and systemic staging, and solitary metastasis may be biopsied. Serum levels of prostate-specific antigen may also be elevated. Regarding RCC orbital metastases may be the presenting lesion of an occult RCC but may also occur many years after diagnosis of a primary tumor; tissue diagnosis may also be necessary.

4 Treatment

Orbital metastases of lung cancer have been generally treated with palliative orbital radiotherapy as these patients had usually poor prognosis. New generation of anticancer drugs, such as the immune checkpoint inhibitors that have improved the treatment of lung cancer, may have a role also in the treatment of orbital metastases. Orbital metastases of prostate cancer can be treated with a combination of radiotherapy and hormonal or biologic treatment. Treatment of metastatic RCC is generally directed at treating the systemic metastatic cancer with chemotherapy, biologic, or immunotherapy. Local control is managed by systemic treatment, with judicious use of radiation therapy or surgery as palliative measures.

5 Figures with Captions

5.1 Metastatic Lung Cancer

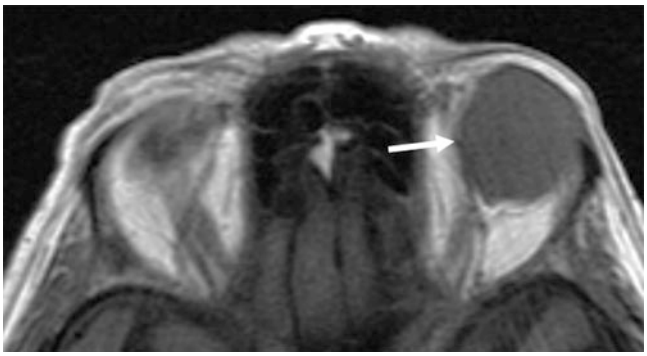


Fig. 1 **Axial T1 non-contrast image** shows a well-circumscribed mass in the superior left orbit (arrow)

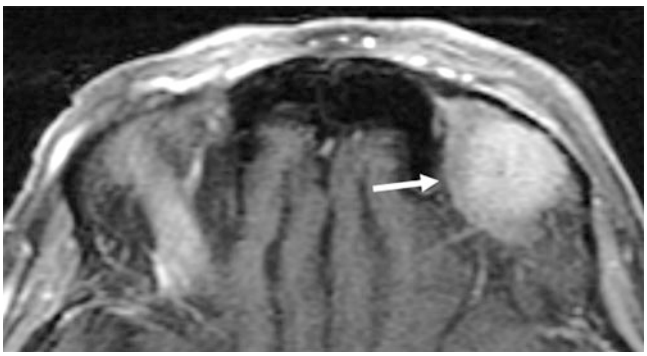


Fig. 2 **Axial T1 post-contrast fat-saturated image** (same patient as in Fig. 1) demonstrates homogeneous enhancement of the orbital mass (arrow)

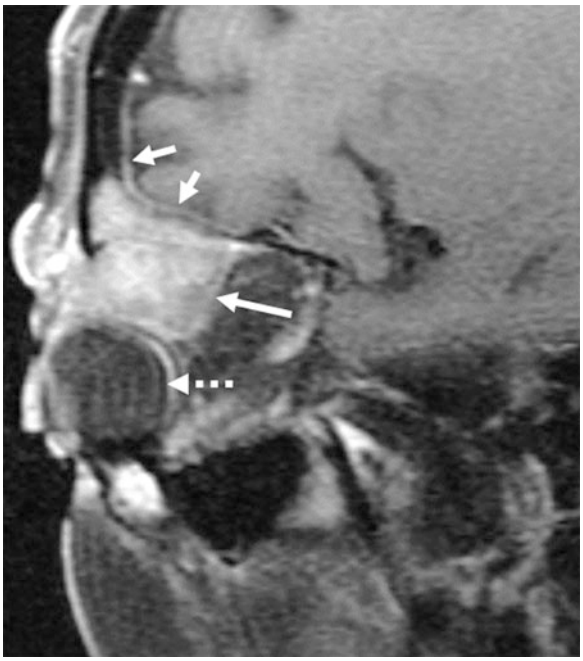


Fig. 3 Sagittal T1 post-contrast fat-saturated image (same patient as in Fig. 1) shows the mass in the superior orbit (arrow) with inferior displacement of the globe (dotted arrow). More superiorly the tumor is infiltrating the bony orbital roof with adjacent dural reaction (small arrows). Anteriorly the tumor is involving the brow and upper eyelid area

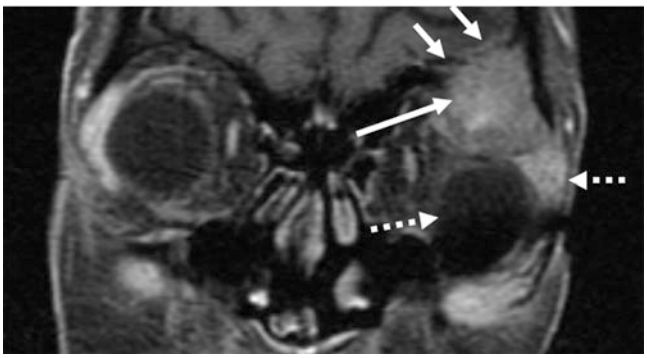


Fig. 4 Coronal T1 post-contrast fat-saturated image (same patient as in Fig. 1) shows the mass in the superior orbit (arrow) with inferior displacement of the globe and lacrimal gland (dotted arrows). More superiorly the tumor involves the orbital roof with adjacent dural reaction (small arrows)



Fig. 5 Axial non-contrast CT orbit, soft tissue window (different patient) with non-small-cell lung cancer involving the greater wing of sphenoid extending both to the lateral right extraconal space (arrow) as well as the masticator space (black arrow). There is suspected intracranial involvement. There is marked right proptosis

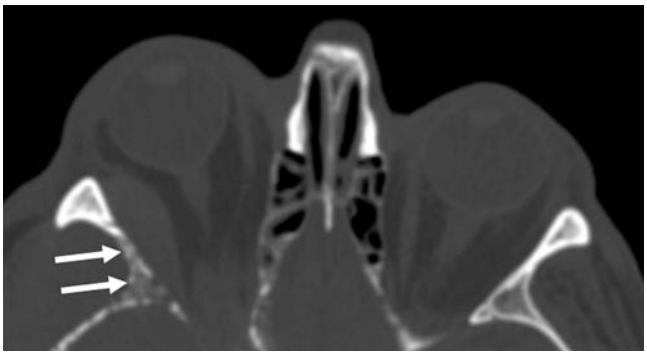


Fig. 6 Axial non-contrast CT orbit, bone window (same patient as in Fig. 5) demonstrates a mottled appearance of the posterior right lateral orbital wall and sphenoid bone (arrows) consistent with bone destruction

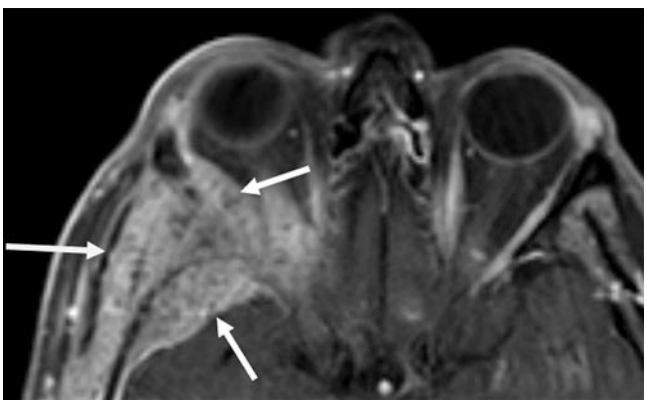


Fig. 7 Axial T1 post-contrast fat-saturated image (same patient as in Fig. 5) shows a heterogeneously enhancing tumor centered in the greater wing of the sphenoid bone and trilateral involvement including lateral orbit to the apex, masticator space, and middle cranial fossa (arrows)



Fig. 8 Coronal post-contrast CT chest image (same patient as in Fig. 5), lung window shows the primary tumor in the right lower lobe (arrow)

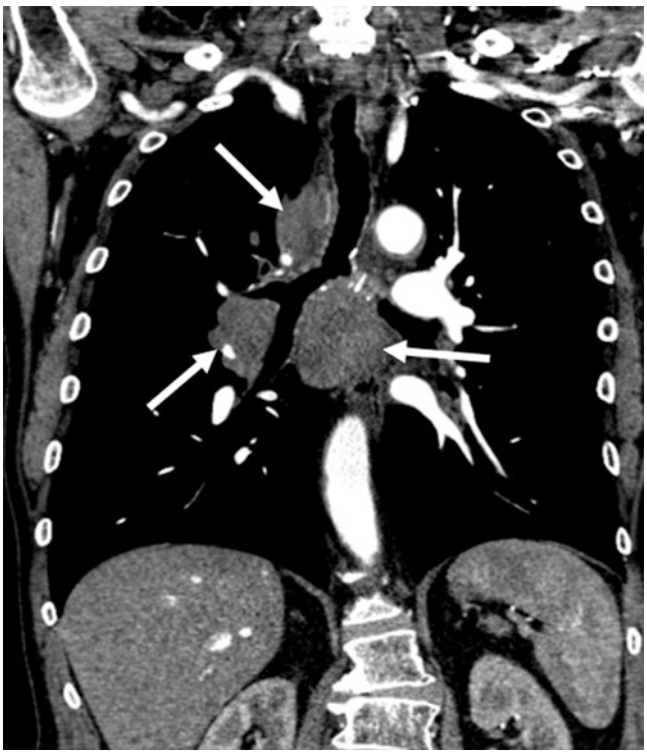


Fig. 9 Coronal post-contrast CT chest image, soft tissue window demonstrates mediastinal adenopathy (arrows)

5.2 Metastatic Prostate Cancer

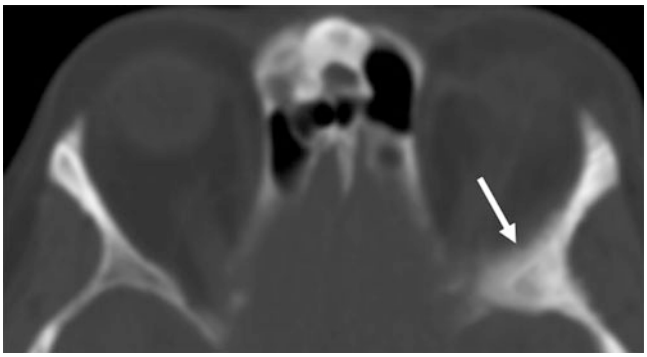


Fig. 10 Axial post-contrast CT orbit, bone window demonstrates a slightly expansile sclerotic lesion in the left sphenoid bone (arrow). There is irregular periosteal reaction around the lesion in all three compartments (orbit, infratemporal fossa, and middle cranial fossa)

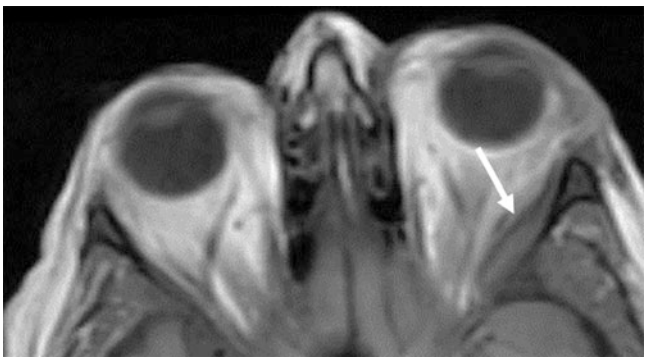


Fig. 11 Axial T1 pre-contrast image (same patient) shows an isointense mass centered about the greater wing of sphenoid, the white arrow is pointing at the lateral extraconal component of the lesion. There is secondary globe axial proptosis on the left side

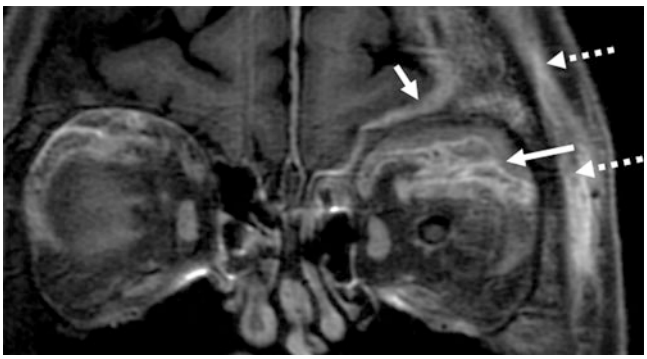


Fig. 12 Coronal T1 post-contrast fat-saturated image. A heterogeneously enhancing mass is located in the superior left orbit (arrow). Extension is seen superiorly into the intracranial compartment with adjacent dural thickening (small arrow) as well as the left periorbital and temporal regions (dotted arrows)

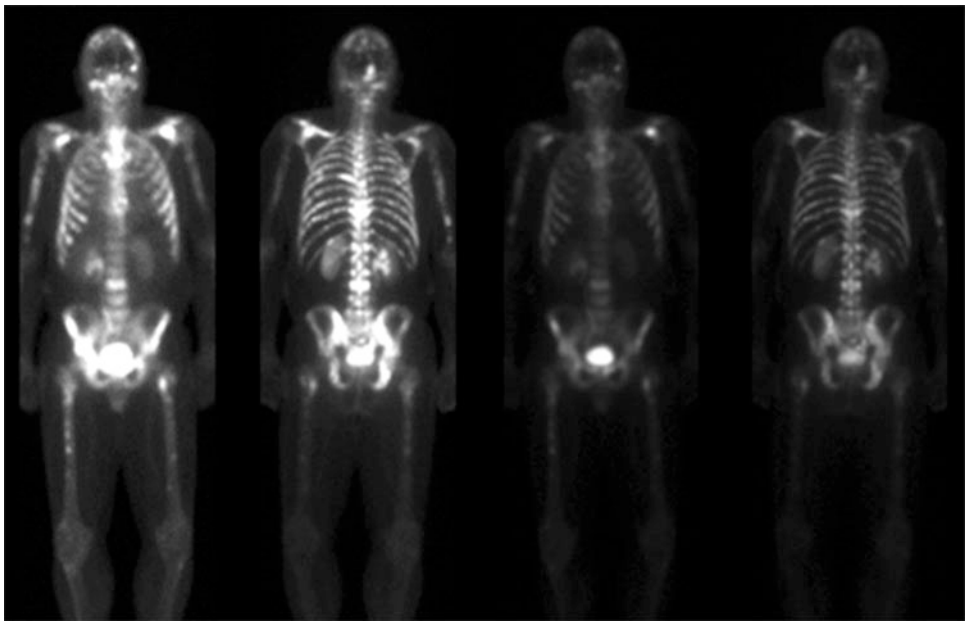


Fig. 13 Whole-body bone scan image shows multiple foci of increased uptake consistent with diffuse skeletal metastases

5.3 Metastatic RCC



Fig. 14 Axial non-contrast CT image, soft tissue window shows a large hyperdense lytic mass epicentered in the left sphenoid bone with involvement of the posterolateral left orbit, intracranial compartment (arrows), and infra-temporal/masticator space. There is secondary left axial proptosis

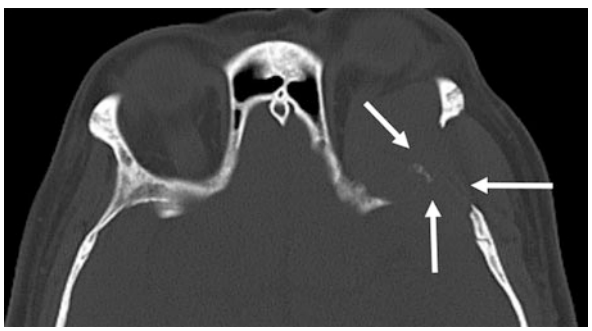


Fig. 15 Axial non-contrast CT image, bone window image reveals the extensive destruction of the lateral wall of the left orbit, sphenoid bone, and temporal calvarium (arrows). There is a small bony remnant within the extensive destruction

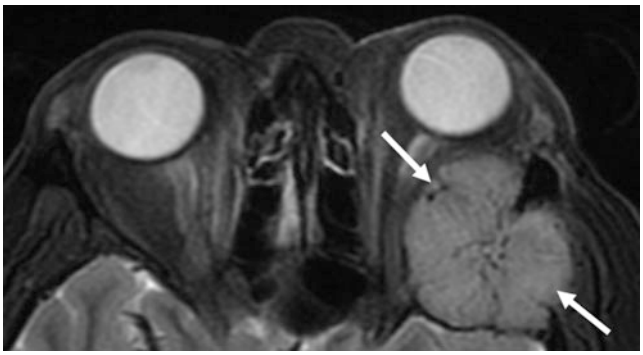


Fig. 16 Axial T2 fat-saturated image demonstrates a homogeneous relatively hyperintense mass in the posterolateral left orbit, the intracranial extradural compartment, and masticator space (delineated by the white arrows). Note the serpiginous flow voids within the mass representing the hyper-vascularity of the lesion (upper white arrow). There is mass effect upon the orbital content with stretching and displacement of the ON sheath complex



Fig. 17 Axial T1 post-contrast fat-saturated image shows intense homogeneous enhancement of the metastasis involving the left orbit (arrows). Note the dural reaction to the lesion with corresponding thickening



Fig. 18 Axial post-contrast CT soft tissue window image shows the primary tumor as a mass arising from the left kidney (arrows)

References

1. Esmaeli, B. Ophthalmic oncology, vol. 6. Springer Science & Business Media; 2011.
2. Shome D, et al. Metastasis to the eye and orbit from renal cell carcinoma-a report of three cases and review of literature. Surv Ophthalmol. 2007;52(2):213–23.

Metastatic Orbital Lesions: Melanoma

52

Oded Sagiv, J. Matthew Debnam, and Bita Esmaeli

Contents

1 **Signs and Symptoms** 395
2 **Differential Diagnosis** 395
3 **Diagnosis** 396
4 **Treatment** 396
5 **Figures with Captions** 396
References 398

Abstract

- Well-circumscribed orbital mass or several masses. May mimic a benign tumor.
- Affinity to extraocular muscles; however, all orbital compartments can be involved: the intraconal space, extraconal space, the lacrimal sac, and along the course of orbital veins.
- Often a discrete ovoid mass within the EOM may be seen.
- T1 heterogenous to high intensity signal. Areas of bright signal may represent melanin and/or hemorrhage.
- Low intensity signal on T2 WI.
- Metastatic mass is contrast enhancing and usually FDG-avid.
- Diffusion studies with low ADC may aid diagnosis.

Keywords

Orbital metastasis · Metastatic melanoma

1 Signs and Symptoms

Signs and symptoms are similar to that elaborated in ▶ "Metastatic Orbital Lesions: Breast Cancer". Orbital metastases from cutaneous melanoma have particular affinity to the extraocular muscles, and diplopia is a common presenting symptom. Proptosis and blepharoptosis are equally common presenting signs. Cutaneous melanoma can also send choroidal metastasis that may mimic uveal melanoma. Bilateral orbital involvement and multiple orbit and eyelid metastasis can occur in relatively low percent.

2 Differential Diagnosis

Similar to the differential in ▶ "Metastatic Orbital Lesions: Breast Cancer", these metastases are commonly seen as smooth enlargement of an extraocular muscle rather than as general infiltration to the orbit.

O. Sagiv
The Goldschleger Eye Institute, Sheba Medical Center, affiliated to the Sackler Faculty of Medicine, Tel-Aviv University, Tel Aviv, Israel
e-mail: Oded.sagiv@sheba.health.gov.il

J. M. Debnam
Department of Neuroradiology, The University of Texas MD Anderson Cancer Center, Houston, TX, USA
e-mail: Matthew.Debnam@mdanderson.org

B. Esmaeli (✉)
Ophthalmic Plastic Surgery, Department of Plastic Surgery, The University of Texas MD Anderson Cancer Center, Houston, TX, USA
e-mail: besmaeli@mdanderson.org

© Springer Nature Switzerland AG 2022
G. Ben Simon et al. (eds.), *Atlas of Orbital Imaging*,
https://doi.org/10.1007/978-3-030-62426-2_101

3 Diagnosis

Diagnosis is made via an orbital biopsy of the suspected lesion. A known primary cutaneous melanoma/metastatic disease may raise the suspicion of orbital involvement. The trunk is the most common primary site to send orbital metastasis followed by the upper and lower extremities. Head and neck cutaneous melanoma less commonly metastasize to the ocular structures. The left orbit is more commonly involved. Metastatic orbital melanoma represents 3–20% of all tumors that metastasize to the orbit and less than 5% of all orbital and ocular metastasis. Patients usually have known metastatic disease prior to presenting with orbital metastasis [1, 4, 5, 6, 7, 8].

4 Treatment

Treatment of metastatic cutaneous melanoma has been significantly improved over the past years since the approval of certain immune checkpoint inhibitors as first-line treatment. Orbital metastases have been shown to respond as well with complete resolution evident on MR imaging. New treatments may eliminate the need for local orbital therapy [1, 2, 3, 7, 8].

5 Figures with Captions

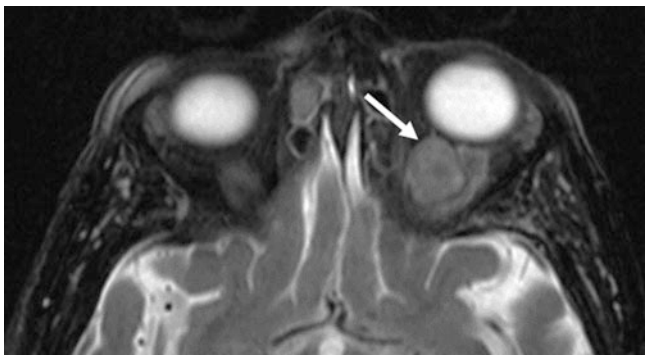


Fig. 1 CECT axial section of a patient with past history of cutaneous melanoma. He presented with right-sided axial proptosis. CT discloses a right orbital homogenous well-circumscribed hyperdense mass, inseparable from the lateral rectus muscle. The mass is located both in the extra- and intraconal compartments, medially displacing the orbital content and enveloping the globe with marked proptosis

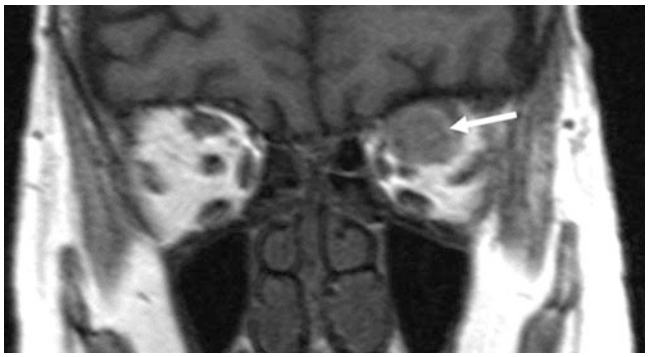


Fig. 2 CECT coronal view of the same patient showing the metastatic melanoma lesion filling the temporal orbit displacing both superior rectus muscle and the optic nerve. (Figs. 1 and 2 courtesy of the editors)

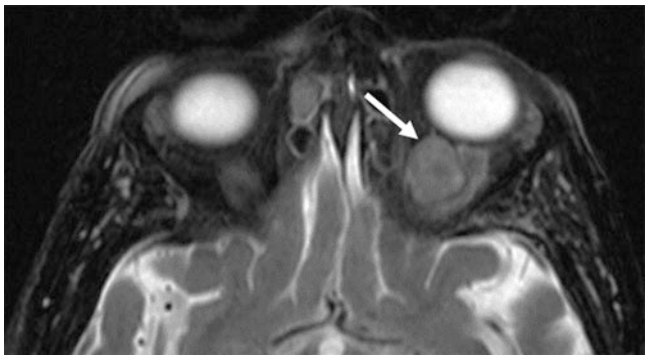


Fig. 3 **Axial T2 fat-saturated image** reveals a left nonhomogenous iso- to hypo-intense mass in the superior medial intraconal space (arrow)

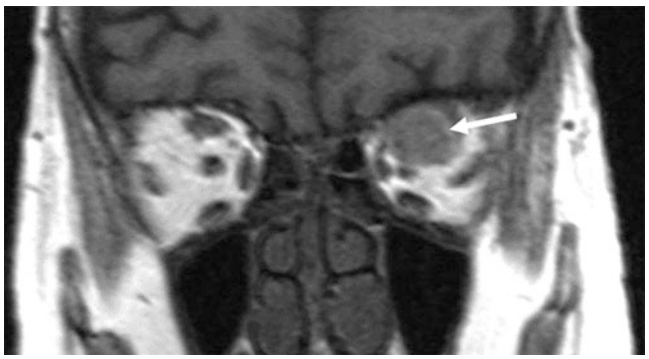


Fig. 4 **Coronal T1 noncontrast image** (same patient as in Fig. 3) demonstrates a heterogeneous mass in the superior left intraconal space (arrow). The mass is inseparable from the superior muscle complex and displacing the optic nerve/sheath complex downward and medially. Areas of bright signal may represent melanin and/or hemorrhage



Fig. 5 Axial PET/CT image (same patient as in Fig. 3) shows increased FDG activity in the left posterior orbital space (arrow)

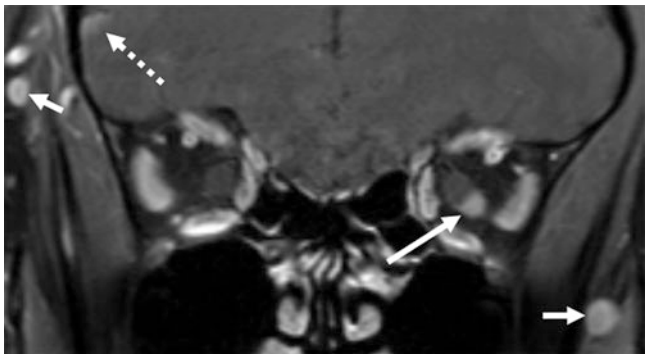


Fig. 8 Coronal T1 postcontrast fat-saturated image (same patient as in Fig. 6) depicting an enhancing metastasis abutting the left optic nerve (arrow). Note other metastases in the brain (dotted arrow), left cheek, and right temporal soft tissues (small arrows)

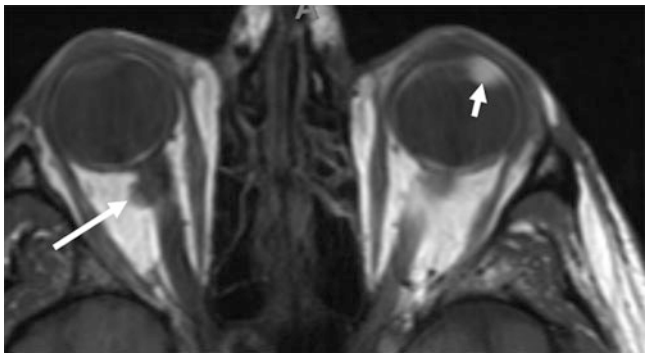


Fig. 6 Axial T1 precontrast image of a different patient with cutaneous melanoma and widespread metastases shows a small mass in the right intraconal space abutting the temporal surface of the optic nerve (arrow). A bright mass is also present in the left ciliary body of the globe (short arrow)



Fig. 9 Axial T1 precontrast image (different patient) depicting a bright lesion in the right orbital apex involving the posterior lateral recuts muscle (arrow). The bright signal is related to melanin

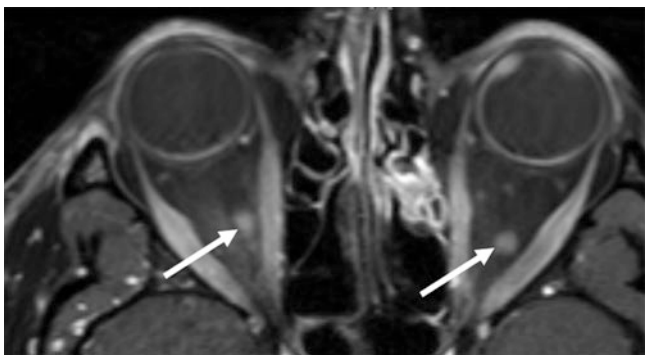


Fig. 7 Axial T1 postcontrast fat-saturated image (same patient as in Fig. 6) shows several enhancing metastases in bilateral intraconal spaces (arrows)



Fig. 10 Axial T1 postcontrast fat-saturated image shows the enhancing mass involving the right lateral rectus muscle (arrow)

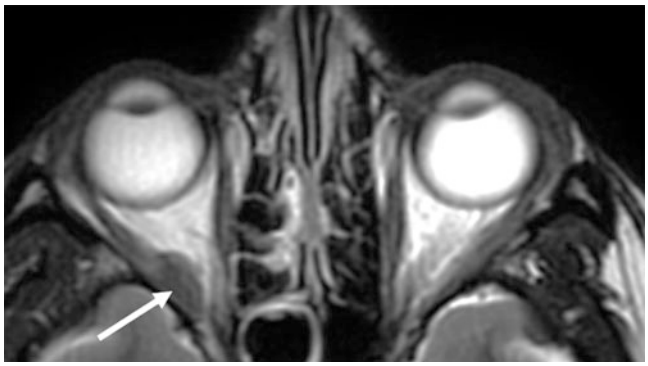


Fig. 11 **Axial T2 image** depicting a dark appearance of the metastasis due to melanin (arrow)

References

1. Esmaeli B. Ophthalmic oncology, vol. 6. Boston: Springer Science & Business Media; 2011.
2. Ford J, Thuro BA, Thakar S, Hwu WJ, Richani K, Esmaeli B. Immune checkpoint inhibitors for treatment of metastatic melanoma of the orbit and ocular adnexa. Ophthalmic Plast Reconstr Surg. 2017;33(4):e82–5. https://doi.org/10.1097/IOP.0000000000000790. PMID: 27662198.
3. Baroody M, Hartstein ME, Holds JB. Immunotherapy for melanoma metastatic to the orbit. Ophthalmic Plast Reconstr Surg. 2003;19(4):270–4. https://doi.org/10.1097/01.IOP.0000075015.65210.B4. PMID: 12878874.
4. Greene DP, Shield DR, Shields CL, Shields JA, Servat JJ, Lin CJ, Douglass AM, Fulco EA, Levin F. Cutaneous melanoma metastatic to the orbit: review of 15 cases. Ophthalmic Plast Reconstr Surg. 2014;30(3):233–7. https://doi.org/10.1097/IOP.0000000000000075. PMID: 24811686.
5. Everett L, Damato BE, Bloomer MM, Palmer JD, Kao AA, Stewart JM, Afshar AR. Metastatic cutaneous melanoma presenting with choroidal metastasis simulating primary uveal melanoma. Ocul Oncol Pathol. 2019;5(2):135–8. https://doi.org/10.1159/000488708. Epub 2018 Aug 8. PMID: 30976593; PMCID: PMC6422132.
6. Zografos L, Ducrey N, Beati D, Schalenbourg A, Spahn B, Balmer A, Othenin-Girard CB, Chamot L, Egger E. Metastatic melanoma in the eye and orbit. Ophthalmology. 2003;110(11):2245–56. https://doi.org/10.1016/j.ophtha.2003.05.004. PMID: 14597536.
7. Rosenberg C, Finger PT. Cutaneous malignant melanoma metastatic to the eye, lids, and orbit. Surv Ophthalmol. 2008;53(3):187–202. https://doi.org/10.1016/j.survophthal.2008.02.003. PMID: 18501266.
8. Rose AM, Cowen S, Jayasena CN, Verity DH, Rose GE. Presentation, treatment, and prognosis of secondary melanoma within the orbit. Front Oncol. 2017;7:125. https://doi.org/10.3389/fonc.2017.00125. PMID: 28690979; PMCID: PMC5481311.

Orbital Extension of Tumors from the Paranasal Sinuses: Squamous Cell Carcinoma

53

Oded Sagiv, J. Matthew Debnam, and Bita Esmaeli

Contents

1 **Signs and Symptoms** 399
2 **Differential Diagnosis** 399
3 **Diagnosis** 400
4 **Treatment** 400
5 **Figures with Captions** 400
References 401

Abstract

- A continuous destructive mass from the paranasal sinuses to the orbit.
- CT and MRI may show a heterogenous mass due to necrotic changes. Associated bony destruction is better seen on CT while marrow involvement is better delineated on MRI.
- Perineural invasion should be ruled out.
- Restricted diffusion on DWI / ADC is a common imaging hallmark.
- Tumor is FDG-avid on PET/CT.

Keywords

Squamous cell carcinoma of the sinuses · Head and neck squamous cell carcinoma · Orbital extension of tumors from the paranasal sinuses

1 Signs and Symptoms

Squamous cell carcinoma of the sinuses is the most common epithelial tumor with secondary orbital invasion, with maxillary sinus being the most common, followed by the ethmoids. In many cases orbital invasion will be the presenting symptom of the sinus disease. Typical signs include pain, paresthesia, local swelling of the malar and lower eyelid area, globe displacement, diplopia with limitation in eye movements, and even optic neuropathy.

2 Differential Diagnosis

The differential diagnosis includes other tumors of sinus or nasopharyngeal origin such as squamous papillomas, adenoid cystic carcinoma, and sarcomas. Osteomas and fibrous

O. Sagiv
The Goldschleger Eye Institute, Sheba Medical Center, affiliated to the Sackler Faculty of Medicine, Tel-Aviv University, Tel Aviv, Israel
e-mail: Oded.sagiv@sheba.health.gov.il

J. M. Debnam
Department of Neuroradiology, The University of Texas MD Anderson Cancer Center, Houston, TX, USA
e-mail: Matthew.Debnam@mdanderson.org

B. Esmaeli (✉)
Ophthalmic Plastic Surgery, Department of Plastic Surgery, The University of Texas MD Anderson Cancer Center, Houston, TX, USA
e-mail: besmaeli@mdanderson.org.il

© Springer Nature Switzerland AG 2022
G. Ben Simon et al. (eds.), *Atlas of Orbital Imaging*,
https://doi.org/10.1007/978-3-030-62426-2_42

dysplasia may involve the orbit and mimic soft tissue mass; however, imaging features are different.

3 Diagnosis

Tissue biopsy is mandatory for diagnosis and may be taken from the orbital part or the sino-nasal cavity depending on accessibility. Imaging evidence of vertical orbital involvement may be a poor prognostic sign.

4 Treatment

Treatment is determined by the stage and extension of the disease. Radical surgery with adjuvant chemo-radiation can be performed for resectable disease. Regional metastatic disease (regional lymph nodes) may also be curable with neck dissection and adjuvant radiation therapy. Distant metastatic disease is treated with systemic therapy or combination of the above. In the past, orbital and ocular sparing procedures were advocated only when the periorbita was not eroded by the tumor. Today, multidisciplinary therapy, consisting of minimally invasive resection, irradiation, regional chemotherapy, yield good patient prognosis, and quality of life.

5 Figures with Captions



Fig. 1 Axial post-contrast CT orbit, soft tissue window shows a large destructive necrotic mass probably emanating from the ethmoid sinuses protruding into the soft facial tissues: nasal bridge, glabella, medial canthi and forehead. The lesion is eccentric to the left, with obvious medial orbital involvement (arrows). There is left proptosis with temporal globe displacement

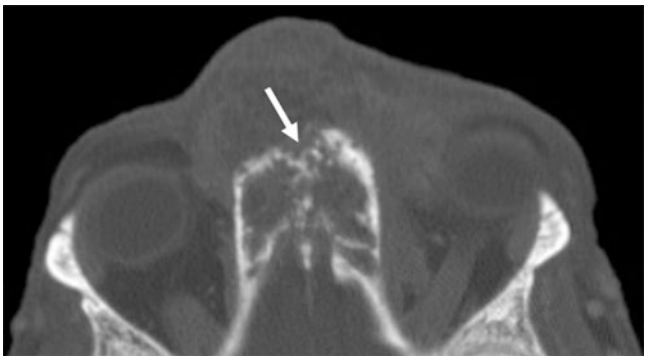


Fig. 2 Axial post-contrast CT orbit, bone window better demonstrates destruction of the ethmoids and nasal bridge (arrow)



Fig. 3 Coronal post-contrast CT orbit, soft tissue window shows bilateral orbital tumor involvement (left more than right) – arrows; there is left nasal cavity extension (short arrow). Note absence of the nasal septum and conchi from prior surgery of a nasal basal cell carcinoma (dotted arrow). Note opacification of both frontal sinuses most likely due to frontonasal recess obstruction. Similarly, the maxillary sinuses are opacified probably due to OMC obstruction by the tumor

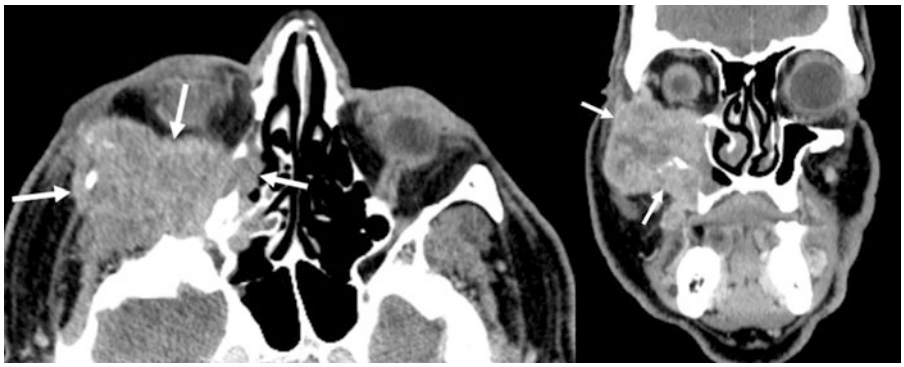


Fig. 4 Axial post-contrast CT orbit, soft tissue window (different patient) showing a large heterogenous soft tissue mass with internal necrotic changes originating in the right maxillary sinus invading adjacent structures. The mass is causing significant bone destruction of the maxillary sinus walls and ridge, malar bones, ethmoids, and sphenoids. The tumor is invading the masticator space, buccal region (lower arrow), the floor of the orbit (upper arrow), the inferior orbital fissure, as well as the posterior ethmoids. The tumor is causing axial globe proptosis

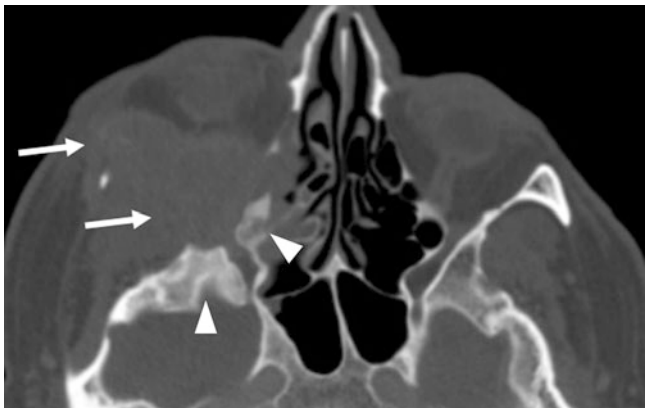


Fig. 5 Axial post-contrast CT orbit, bone window demonstrates near complete destruction of the lateral orbital wall (arrows). Note the osteosclerotic bony involvement of the greater wing of sphenoid and the posterior ethmoid bones (arrowheads)

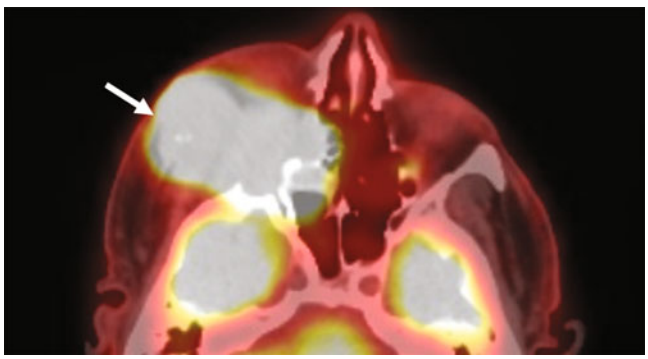


Fig. 6 Axial PET/CT image showing intense FDG avidity of the mass

References

1. Esmaeli, B., Ophthalmic oncology, vol. 6. Springer Science & Business Media; 2011.
2. Lau A, Yang WF, Li KY, Su YX. Systemic therapy in recurrent or metastatic head and neck squamous cell carcinoma – a systematic review and meta-analysis. Crit Rev Oncol Hematol. 2020;153:102984.
3. Carrau RL, Segas J, Nuss DW, Snyderman CH, Janecka IP, Myers EN, D'Amico F, Johnson JT. Squamous cell carcinoma of the sinonasal tract invading the orbit. Laryngoscope. 1999;109(2 Pt 1):230–5. https://doi.org/10.1097/00005537-199902000-00012. PMID: 10890772.
4. Johnson TE, Tabbara KF, Weatherhead RG, Kersten RC, Rice C, Nasr AM. Secondary squamous cell carcinoma of the orbit. Arch Ophthalmol. 1997;115(1):75–8. https://doi.org/10.1001/archopht.1997.01100150077013. PMID: 9006429.
5. Nibu K, Sugasawa M, Asai M, Ichimura K, Mochiki M, Terahara A, Kawahara N, Asato H. Results of multimodality therapy for squamous cell carcinoma of maxillary sinus. Cancer. 2002;94(5):1476–82. https://doi.org/10.1002/cncr.10253. PMID: 11920504.
6. Morice A, Ostertag A, Sahli-Amor M, Goudot P, Bertolus C, Schouman T. Prognostic factors of gingival-alveolar squamous cell carcinoma of the maxilla. Surg Oncol. 2016;25(3):263–8. https://doi.org/10.1016/j.suronc.2016.05.011. Epub 2016 May 24. PMID: 27566032.
7. Nishino H, Takanosawa M, Kawada K, Kanazawa T, Ichimura K, Takahashi S, Nakazawa M. Multidisciplinary therapy consisting of minimally invasive resection, irradiation, and intra-arterial infusion of 5-fluorouracil for maxillary sinus carcinomas. Head Neck. 2013;35(6):772–8. https://doi.org/10.1002/hed.23030. Epub 2012 Jun 23. PMID: 22730109.
8. Porceddu S, Martin J, Shanker G, Weih L, Russell C, Rischin D, Corry J, Peters L. Paranasal sinus tumors: Peter MacCallum Cancer Institute experience. Head Neck. 2004;26(4):322–30. https://doi.org/10.1002/hed.10388. PMID: 15054735.
9. Mani N, Shah JP. Squamous cell carcinoma and its variants. Adv Otorhinolaryngol. 2020;84:124–36. https://doi.org/10.1159/000457932. Epub 2020 Jul 30. PMID: 32731225.
10. Thompson LDR, Franchi A. New tumor entities in the 4th edition of the World Health Organization classification of head and neck tumors: nasal cavity, paranasal sinuses and skull base. Virchows Arch. 2018;472(3):315–30. https://doi.org/10.1007/s00428-017-2116-0. Epub 2017 Apr 25. PMID: 28444451.

Differential Diagnosis of Malignant Tumors of the Lacrimal Sac

54

Oded Sagiv, J. Matthew Debnam, and Bita Esmaeli

Contents

1 **Signs and Symptoms** 403
2 **Differential Diagnosis** 404
3 **Diagnosis** 404
4 **Treatment** 404
5 **Figures with Captions** 404
References 406

Abstract

- Mass in the lacrimal sac that classically extends superior to the medial canthal tendon can cause hemolacrima, epistaxis, and obstructive or functional epiphora.
- Can involve nasal cavity, sinuses, or orbit.
- Imaging evaluation of lacrimal sac tumors can define the location and extent of the lesion including distant metastases, and aid in narrowing the differential diagnosis based on the tumor's imaging characteristics.

Keywords

Carcinoma of the lacrimal sac · Malignant epithelial tumors of the lacrimal sac

1 Signs and Symptoms

Signs and symptoms suspicious of a mass in the lacrimal sac can be nonspecific and mimic a lacrimal duct obstruction with epiphora or chronic or acute dacryocystitis. However, some features should raise the suspicion for a mass in the lacrimal sac: palpable mass at the level superior to the medial canthal tendon, hemolacrima, and signs of chronic dacryocystitis with free irrigation. Lacrimal sac masses are mostly firm and immobile. Telangiectatic blood vessels and ulcerations or epistaxis are additional features to raise concern for a malignancy. Cervical, preauricular, or submandibular lymphadenopathy should be sought on physical examination [1].

O. Sagiv
The Goldschleger Eye Institute, Sheba Medical Center, affiliated to the Sackler Faculty of Medicine, Tel-Aviv University, Tel Aviv, Israel
e-mail: Oded.sagiv@sheba.health.gov.il

J. M. Debnam
Department of Neuroradiology, The University of Texas MD Anderson Cancer Center, Houston, TX, USA
e-mail: Matthew.Debnam@mdanderson.org

B. Esmaeli (✉)
Ophthalmic Plastic Surgery, Department of Plastic Surgery, The University of Texas MD Anderson Cancer Center, Houston, TX, USA
e-mail: besmaeli@mdanderson.org.il

© Springer Nature Switzerland AG 2022
G. Ben Simon et al. (eds.), *Atlas of Orbital Imaging*,
https://doi.org/10.1007/978-3-030-62426-2_102

2 Differential Diagnosis

The differential diagnosis for small nonpalpable tumors includes any type of acquired nasolacrimal duct obstruction. The differential diagnosis of a mass in the lacrimal sac includes dacryocystitis, as well as epithelial and nonepithelial tumors. Epithelial tumors are more common and include: papillomas (exophytic or endophytic/inverted), oncocytoma, squamous cell carcinoma, adenocarcinoma, adenoid cystic carcinoma, mucoepidermoid carcinoma, and transitional cell carcinoma. Common nonepithelial tumors include: lymphoma, leukemia, fibrous histiocytoma (and overlapping pathologies including solitary fibrous tumor, hemangiopericytoma, and giant-cell angiofibroma), and melanoma.

3 Diagnosis

In many patients the presence of a tumor is detected only during a dacryocystorhinostomy surgery in which case a biopsy is advised, and care should be taken not to perform a rhinostomy if possible before a diagnosis is made. Imaging is important in evaluation of a lacrimal sac tumor to demonstrate the extent of the lesion beyond the lacrimal sac. CT will show any bony erosions of the lacrimal fossa or invasion to the orbit, nasal cavity of sinuses. MRI will be superior in defining the extent of the soft tissue component and its qualities. However, in most cases a biopsy is needed to make the diagnosis.

4 Treatment

Treatment of various neoplasms of the lacrimal sac vary according to the type of tumor. Treatment of a lacrimal sac carcinoma includes an en bloc excision of the tumor and the tumor bed, and depending on its size will include a wide local excision of the lacrimal system, including the nasolacrimal duct using a medial maxillectomy/lateral rhinostomy. Eye-sparing surgery followed by adjuvant radiation therapy is the most common treatment approach; however, significant orbital involvement may require an orbital exenteration. Melanoma of the lacrimal sac is treated based on systemic evaluation and staging of the tumor. Local excision can be considered but rarely curative and will likely require additional systemic treatment such as immunotherapy. Treatment of lymphoma of the lacrimal sac will also be based on staging and type of lymphoma, similar to other cases of ocular adnexal lymphoma [2].

5 Figures with Captions

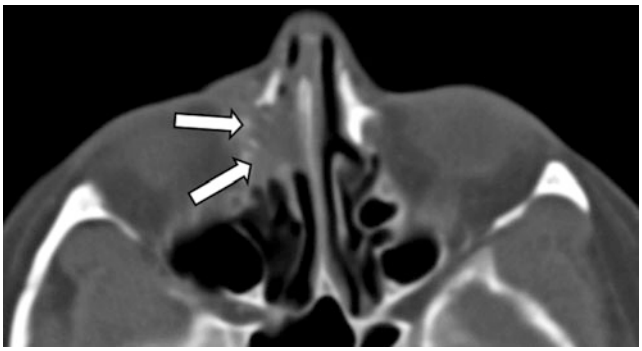


Fig. 1 Axial post-contrast CT of the orbits, bone window shows bone destruction of the right lacrimal fossa, lamina papyracea, and anterior ethmoid air cells caused by a squamous cell carcinoma in the right lacrimal sac (arrows)

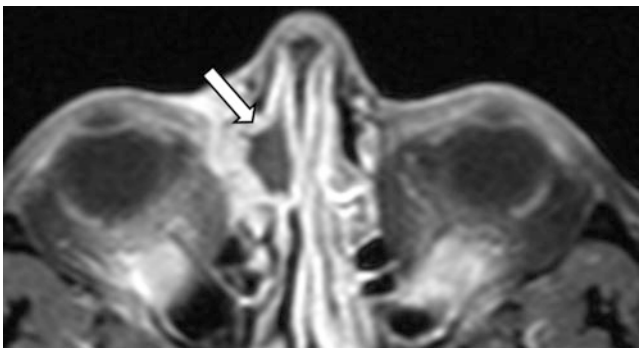


Fig. 2 Axial T1 post-contrast fat-saturated MRI image (same patient as Fig. 1) demonstrates a centrally necrotic squamous cell carcinoma in the right lacrimal fossa and anterior ethmoid air cells (arrow)

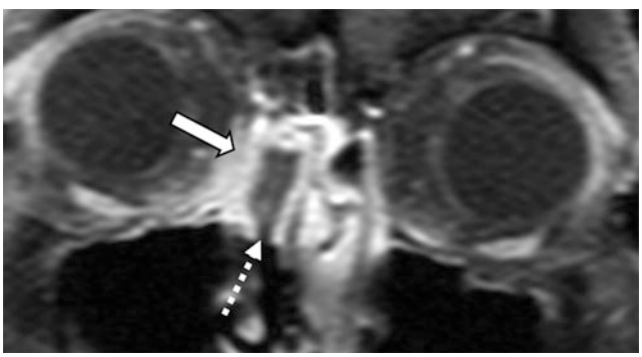


Fig. 3 Coronal T1 post-contrast fat-saturated image (same patient as Fig. 1) shows the necrotic mass in the right lacrimal sac (arrow) with inferior extension into the nasolacrimal duct (dotted arrow)



Fig. 4 Axial T1 pre-contrast image in a different patient with melanoma shows a heterogeneous T1 iso- to hyperintense mass in the right lacrimal fossa (arrow)



Fig. 5 Axial T1 post-contrast fat-saturated image (same patient as Fig. 4) demonstrates enhancement of the right lacrimal fossa mass (arrow)

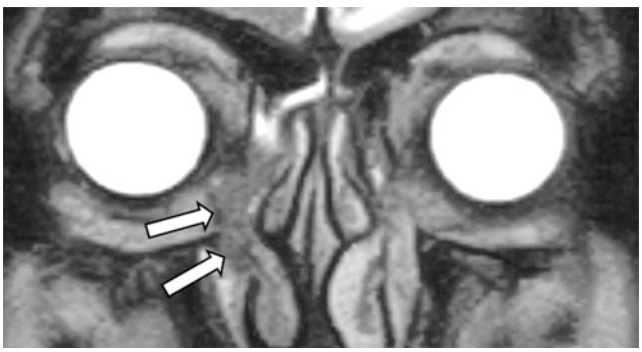


Fig. 6 Coronal T2 fat-saturated image (same patient as Fig. 4) shows a hypointense appearance of the melanoma in the right lacrimal fossa and proximal nasolacrimal duct (arrows)

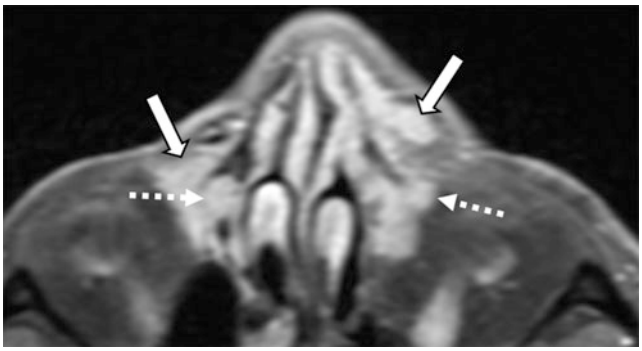


Fig. 7 Axial T1 post-contrast fat-saturated image in a different patient with diffuse large B-cell lymphoma demonstrates a multifocal enhancing lesion about the right orbit and left side of the nose (arrows). There is lymphoma present in the nasolacrimal ducts bilaterally (dotted arrows)

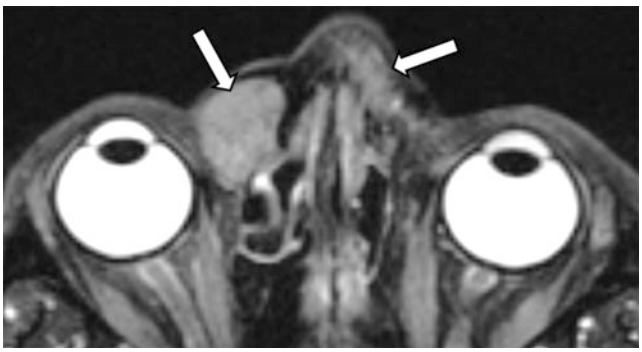


Fig. 8 Axial T2 fat-saturated image (same patient as Fig. 7) shows a hypointense appearance of the lymphoma in the right lacrimal fossa and about the left side of the nose (arrows)



Fig. 9 Axial PET/CT image (same patient as Fig. 7) shows FDG-avidity of lymphoma involving the right lacrimal fossa and the left side of the nose (arrows)

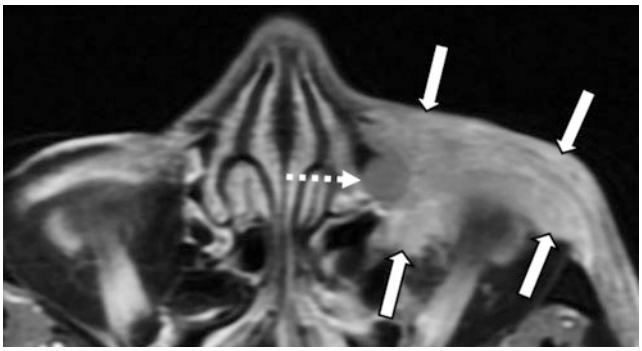


Fig. 10 Axial T1 post-contrast fat-saturated image in a different patient with left lacrimal sac high-grade adenocarcinoma shows an enhancing infiltrative mass involving the soft tissues of left face, lower eyelid, and medial left orbit (arrows) including the lacrimal fossa (dotted arrow)

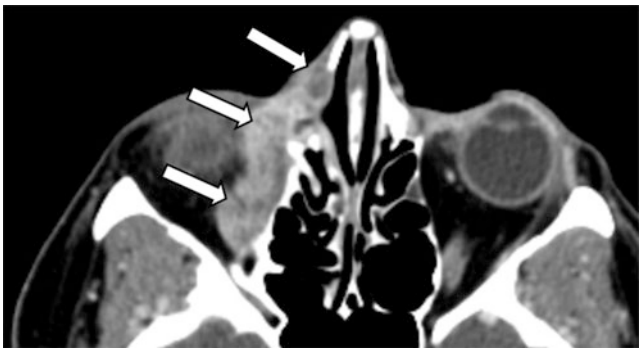


Fig. 13 Axial post-contrast CT orbit, soft tissue window in a different patient with right lacrimal sac adenoid cystic carcinoma shows a heterogeneously enhancing mass involving the right nose and lacrimal fossa with posterior extension into the inferomedial orbit (arrows)

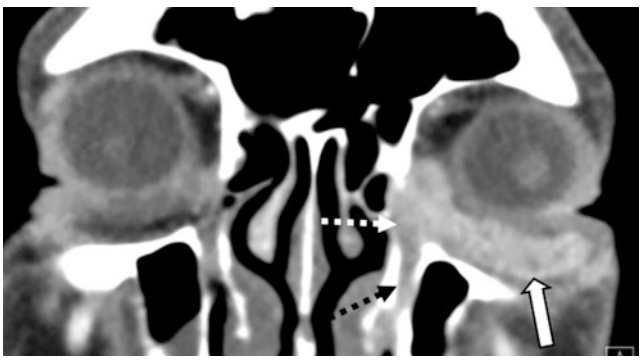


Fig. 11 Coronal post-contrast CT orbit, soft tissue window (same patient as Fig. 10) shows the heterogeneously enhancing mass in the left lower eyelid (arrow). Medially the tumor involves the lacrimal fossa and nasolacrimal duct (dotted arrows)

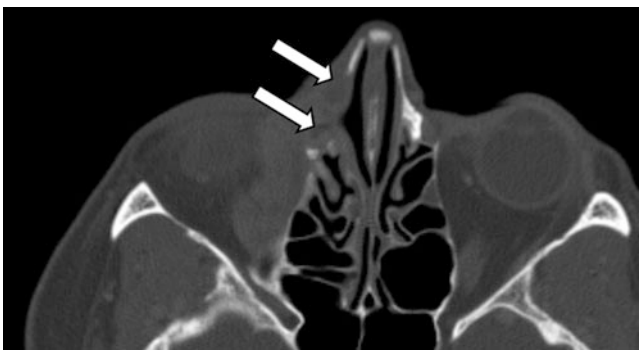


Fig. 14 Axial post-contrast CT orbit, bone window (same patient as Fig. 13) demonstrates destruction of the right nasal bone and lacrimal fossa (arrows)

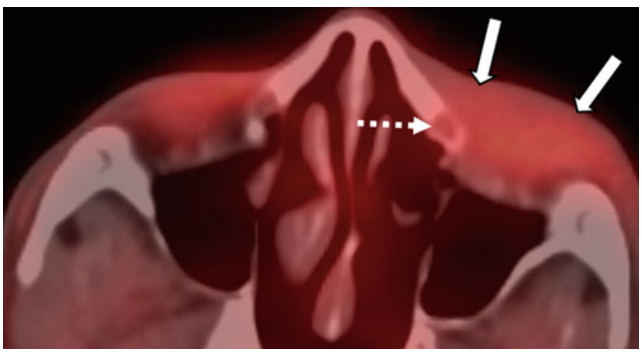


Fig. 12 Axial PET/CT image (same patient as Fig. 10) with mild FDG-avidity of the infiltrative mass in the left lower eyelid (arrows) and nasolacrimal duct (dotted arrow)

References

1. Esmaeli, B. Ophthalmic oncology, vol. 6. Springer Science & Business Media; 2011.
2. El-Sawy T, Frank SJ, Hanna E, Sniegowski M, Lai SY, Nasser QJ, Myers J, Esmaeli B. Multidisciplinary management of lacrimal sac/nasolacrimal duct carcinomas. Ophthalmic Plast Reconstr Surg. 2013;29(6):454–7.

Merkel Cell Carcinoma of Eyelid (MCC)

55

Soltan Khalaila, Rosa Novoa, Benzion Samueli, and Erez Tsumi

Contents

1 **Signs and Symptoms** 408
2 **Differential Diagnosis** 408
3 **Diagnosis** 408
4 **Histopathologic Features** 408
5 **Treatment** 408
6 **Prognosis** 408
7 **Figures with Captions** 409
References 414

Abstract

- Merkel cell carcinoma (MCC) of the eyelid is a highly aggressive malignant primary cutaneous neuroendocrine tumor.
- Risk factors include advanced age, male gender, fair-skinned, immunocompromise, sun exposure, polyomavirus infection.
- It usually presents as rapidly progressive violaceous nodule with or without ulceration.
- Differential diagnosis includes chalazion, cellulitis, capillary hemangioma, squamous cell carcinoma, basal cell carcinoma, sebaceous cell carcinoma.
- Biopsy is necessary for definitive diagnosis. Sentinel lymph node biopsy (SLNB) is required for detecting nodal metastases.
- Histopathologically, MCC is a small round blue cell tumor, positive for neuroendocrine markers (CD56, synaptophysin, chromogranin, and INSM1) and for cytokeratin 20.
- Surgical excision is the mainstay of treatment. Adjuvant radiotherapy is needed for local control, and chemotherapy is used in systemic involvement.
- MCC has a poor prognosis with relatively high mortality rate, especially in patients with distant metastases.
- On NECT, the mass is usually hyperdense due to its high cellular density, and enhancement varies depending on the aggressiveness of the tumor.
- The imaging features on MR also vary according to the literature. Some describe them as inhomogeneous on T1 and T2. These tumors usually enhance following contrast administration; the internal features may depend on the amount of necrosis and cystic degeneration.
- The hypercellular elements of the lesion will show restriction on DWI.
- Advanced disease may involve subcutaneous nodular spread and extra-capsular fatty stranding.

S. Khalaila (✉) · E. Tsumi
Ophthalmology, Soroka University Medical Center, Beer-Sheva, Israel
e-mail: ertsumi@post.bgu.ac.il

R. Novoa
Diagnostic Imaging, Soroka University Medical Center, Beer-Sheva, Israel

B. Samueli
Pathology, Soroka University Medical Center, Beer-Sheva, Israel
e-mail: benzis@post.bgu.ac.il

© Springer Nature Switzerland AG 2022
G. Ben Simon et al. (eds.), *Atlas of Orbital Imaging*,
https://doi.org/10.1007/978-3-030-62426-2_125

Keywords

Merkel cell carcinoma · Eyelid tumor · Polyomavirus infection · Violaceous nodule · Sentinel lymph node biopsy

1 Signs and Symptoms

Merkel cell carcinoma is a rare, highly aggressive primary malignant cutaneous neuroendocrine tumor with predilection for the head and neck area, with eyelid involvement in up to 5% of the cases. It originates from Merkel cells located in the basal layer of the epidermis that mediate fine touch sensation. Age, male gender, fair-skinned patients, immunocompromised states, history of sun exposure, polyomavirus infection, and immunosuppressive therapy are risk factors [1–6].

Merkel cell carcinoma is characterized by rapid growth to a significant size that occurs within few months and early lymph node metastasis. In the eyelid, it presents clinically as a painless reddish-blue indurated nodule with or without ulceration and madarosis, but presentation may vary. In the early course of the disease, it may have a clinical appearance of a benign lesion, such as a chalazion [1–6].

2 Differential Diagnosis

Chalazion, hordeolum, inflammatory lesion, infectious lesion (cellulitis), vascular (capillary hemangioma), malignant lesion (squamous cell carcinoma/basal cell carcinoma/sebaceous cell carcinoma) [1, 5].

3 Diagnosis

The clinical features of Merkel cell carcinoma of the eyelid are protean and nonspecific, meaning that the diagnosis cannot be made reliably based on clinical appearance. Tissue biopsy is mandatory for definitive diagnosis. In advanced cases, imaging modalities such as PET-CT are warranted to investigate local invasion and distant metastasis. Due to the aggressiveness of Merkel cell carcinoma, early detection of distant metastases is a cornerstone of early diagnostic practice and treatment plan. Sentinel lymph nodes should be obtained for all patients, and MRI, CT, and/or PET-CT is warranted in cases with positive nodes [2, 5, 8, 9].

4 Histopathologic Features

MCC is a "small round blue cell tumor," a description that has a differential diagnosis of a number of highly aggressive tumors. Superficially, there is usually a thin, uninvolved region of dermis, termed a Grenz zone. Histochemical features include positive staining for neuroendocrine markers (CD56, synaptophysin, chromogranin, and INSM1) and for cytokeratin 20 in a "dot-like" pattern [10].

5 Treatment

Management of Merkel cell carcinoma requires a multidisciplinary approach. The treatment modality of MMC of the eyelid in general is surgical with a wide 5 mm excision to ensure free margins. Adjuvant radiotherapy can be useful for local control, but its role in long-term survival is still controversial. Chemotherapy can be used in systemic involvement or as adjuvant therapy. In advanced cases, chemotherapy has been used as palliation treatment and not been shown to improve survival [1, 3, 5, 7].

6 Prognosis

MCC of the skin is a very aggressive tumor with poor prognosis and high mortality rate. The five-year survival rate for localized disease is 51%, decreases to 35% with lymph nodes involved, and further decreases to 14% for systemic involvement [2].

7 Figures with Captions



Fig. 1 Clinical photograph of a 73-YOF with recent history of a progressive painless violaceous indurated nodule of the left lower eyelid. Visual acuity and optic nerve function were preserved. (Courtesy of Eldad Silberstein; Plastic Surgery Department; Soroka University Medical Center, Beer-Sheva, Israel)

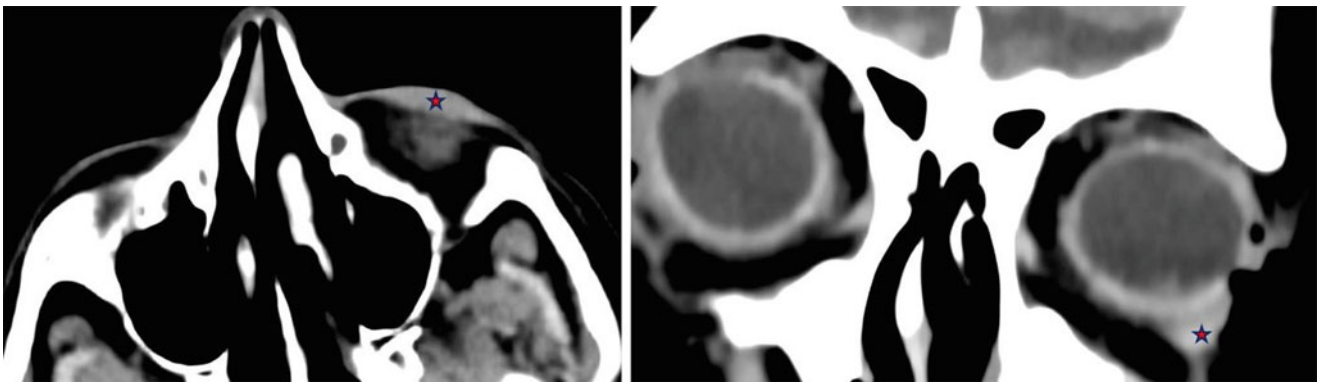


Fig. 2 NE axial CT of the same patient (*left*) and coronal reconstruction (*right*) shows a solid, relatively superficial, hyperdense, well-defined lesion of the left lower eyelid (*star*)

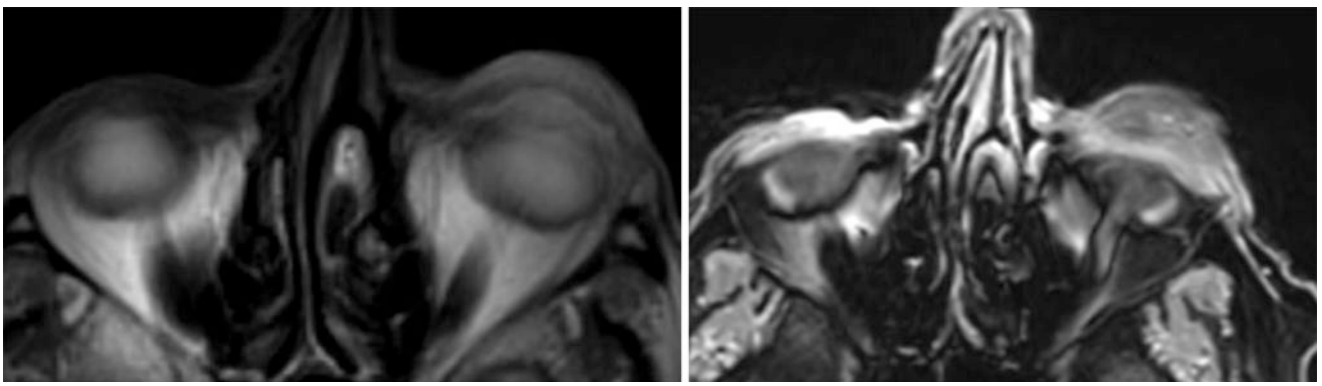


Fig. 3 Axial T2 MRI scan of the same patient shows a hyperintense mass infiltrating the left lower eyelid (*left*). T1 WI FS postgad shows diffuse enhancement (*right*)

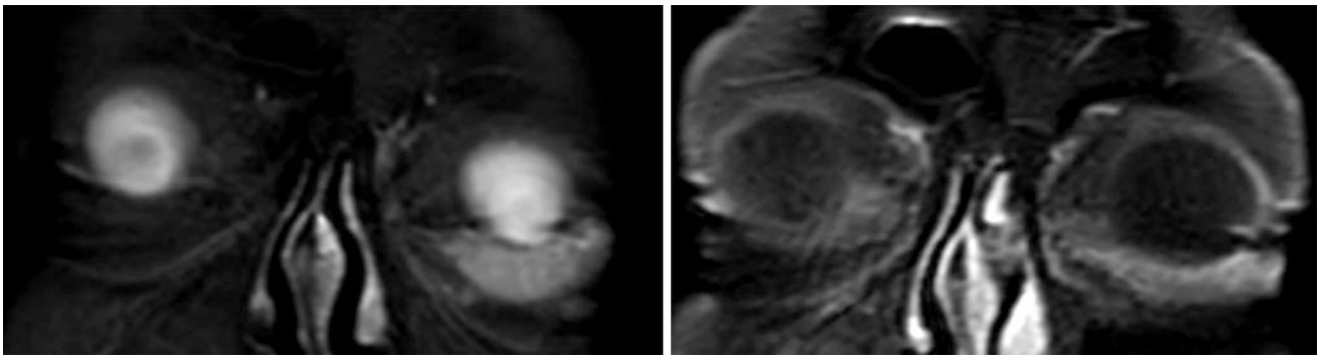


Fig. 4 T2 FS coronal view (*left*) showing the preseptal crescent-shape mass at the left lower eyelid with no obvious globe involvement. Homogeneous mild enhancement is demonstrated on T1 FS + Gad (*right*)

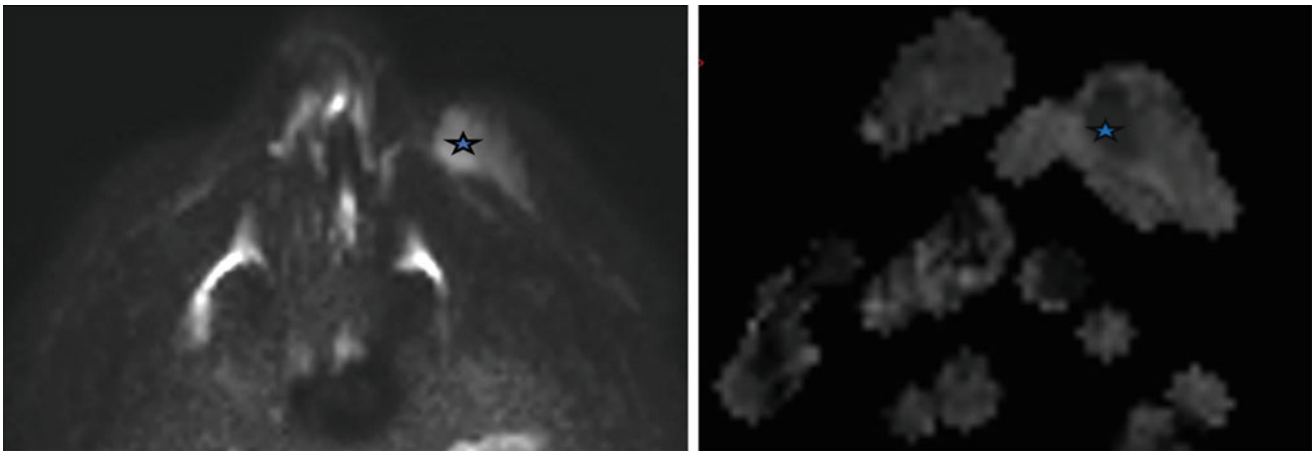


Fig. 5 Axial DWI (*left*) with corresponding ADC map (*right*) show restricted diffusion within the left lower eyelid mass (*star*) in keeping with a hypercellular tumor

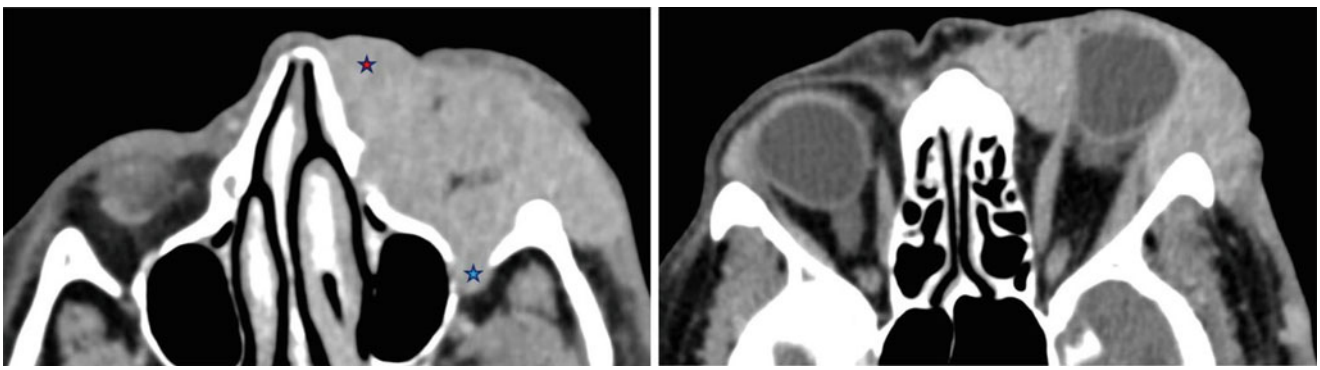


Fig. 6 NE CT axial view of the same patient taken 1 year after initial presentation shows a significant increase in tumor size, and extensive soft tissue involvement, now invading the orbit. The mass is protruding both anteriorly into the premaxillary tissues including the nasolabial fold (red star) and nasolacrimal apparatus and posteriorly to the infratemporal fossa through the inferior orbital fissure (blue star) (*left*). The mass is causing significant proptosis and compressing the globe bilaterally (*right*). The lesion remained homogenous without necrosis or calcifications

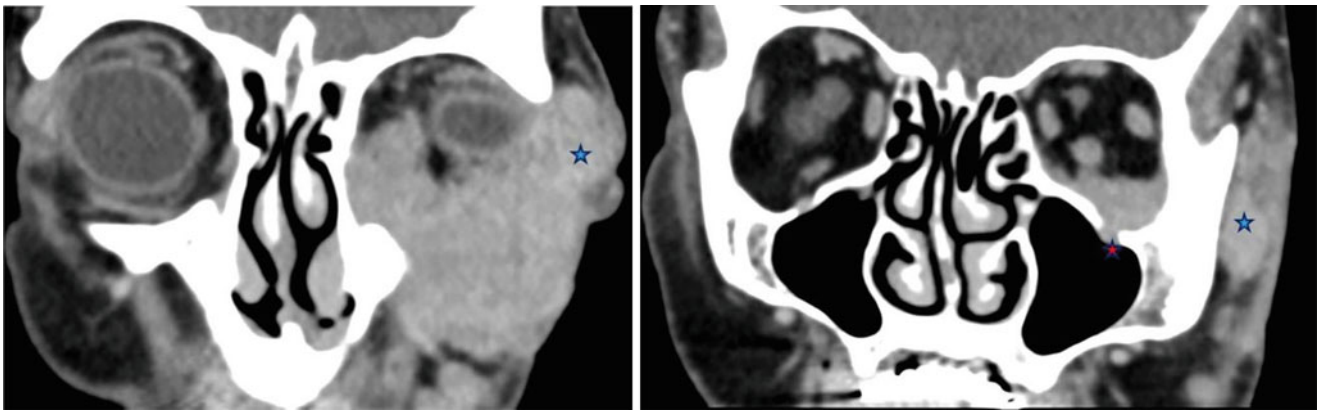


Fig. 7 CT Scan coronal reconstructions shows extensive intra and extraconal involvement as well as cheek and periorbital tissues (*blue stars*). A deeper section (*right*) shows the perineural invasion of the inferior orbital nerve (red star) and the extension of the tumor along the inferior third of the orbit. The tumor is encroaching the IR muscle but sparing the optic nerve



Fig. 8 CT Scan coronal reconstruction shows slight intraconal fat infiltration

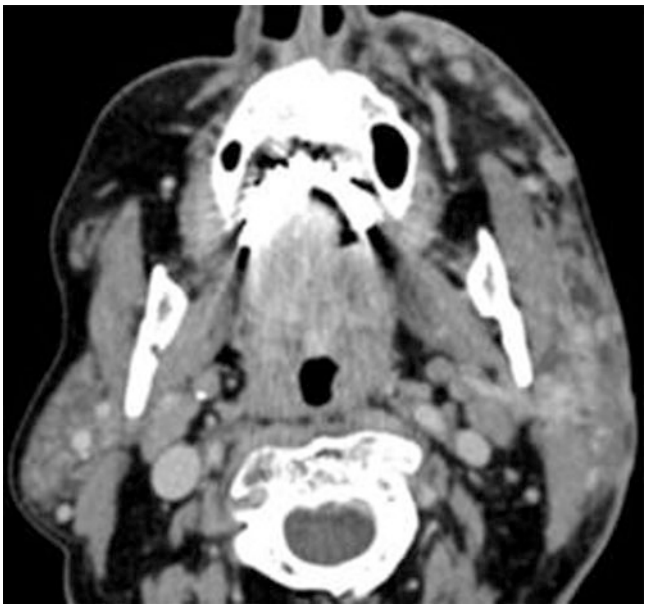


Fig. 9 CECT showing small multiple soft tissue lumps along the subcutaneous tissues of the cheek and left lateral face extending superficial to the masseter, and infiltrating the superficial left parotid gland. There is associated fatty stranding which may indicate extra-nodular spread

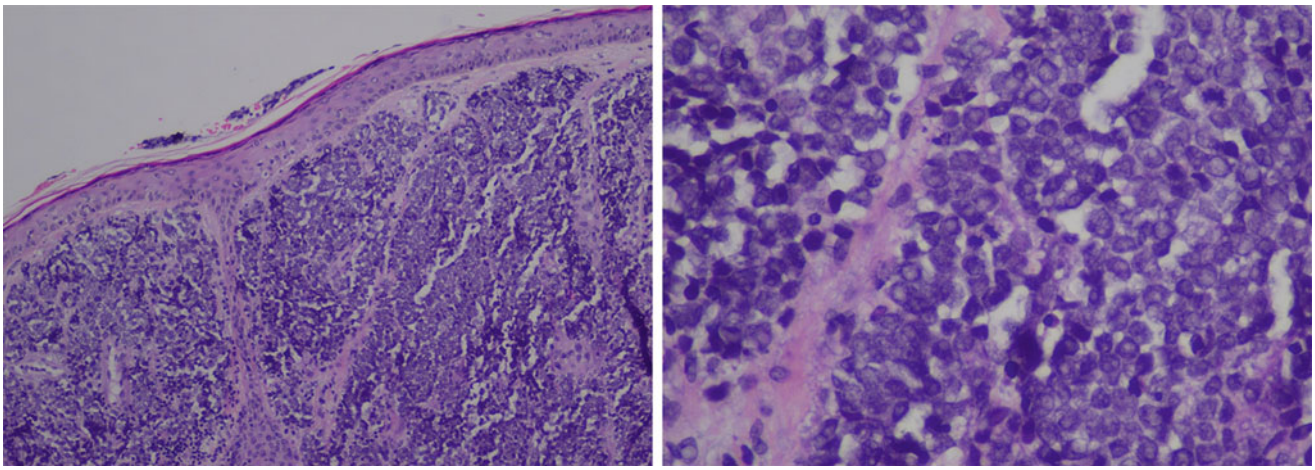


Fig. 10 Histologic images of the biopsy from the patient showing "small round blue cell tumor" diffusely infiltrate the epidermis. A thin Grenz zone (a small, uninvolved area of the superficial dermis, just deep to the epidermis) is present. The tumor cells have vesicular nuclei with some nuclear molding, inconspicuous nucleoli, and widespread mitotic figures and apoptotic bodies. (H&E, original magnification 10x *left*, 40x *right*)

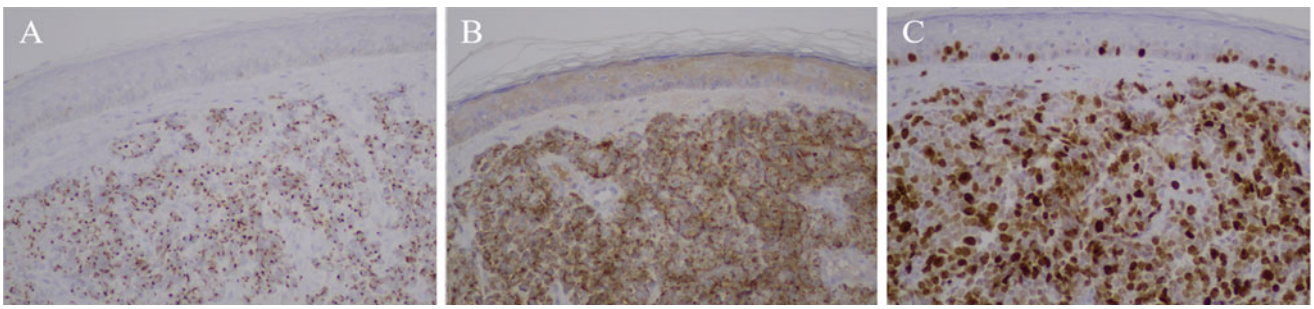


Fig. 11 Immunohistochemistry (IHC) in the tumor cells. CK20 (**a**) – Cytokeratin (CK) is a family intermediate filament expressed in epithelial cells; it is positive in carcinomas but not sarcomas, melanomas, or lymphomas. Specific keratins are numbered 1–20, and the expression of a combination of specific keratins narrows down the diagnosis. Merkel cell carcinoma expresses CK20 (shown here) but is negative for CK7 (not pictured). Further, tumors of neuroendocrine lineage demonstrate a dot-like pattern for keratin staining, as this one did. Chromogranin (**b**) – Cells of neuroendocrine lineage are positive for chromogranin (shown here) and synaptophysin (not pictured). Ki67 (**c**) – Ki67 is a protein marker expressed in cells in the cell cycle (G1, S, G2, and M) but not cells at rest (G0). In the overlying epidermis, scattered basal cells express Ki67, which is normal. This tumor has a very high Ki67 index, indicating aggressiveness

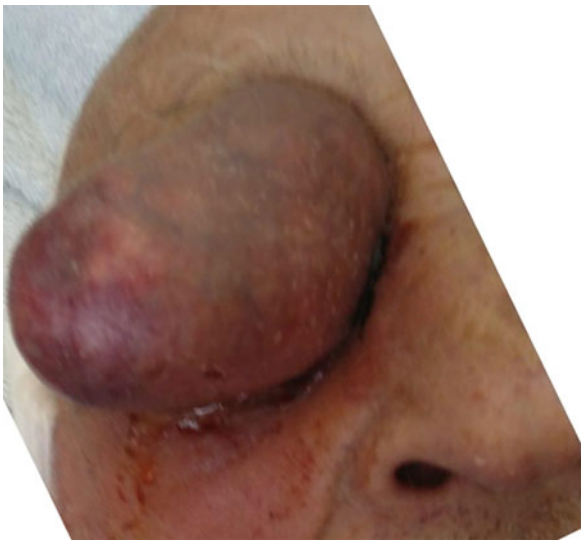


Fig. 12 Clinical photograph of a 95-year-old demented patient with a progressive right upper eyelid reddish-blue mass. The lesion had ulceration at its inferior border. The mass caused severe temporal displacement of the globe, enophthalmos, and ocular motility limitation. Visual acuity and optic nerve function could not be assessed

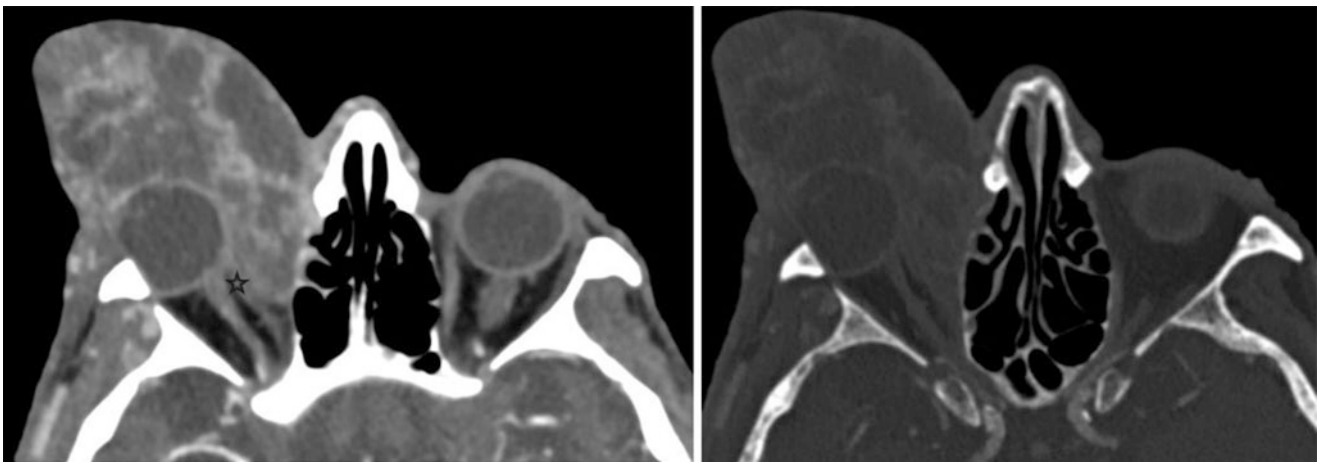


Fig. 13 CECT scan, soft tissue (*left*) and bone window (*right*), demonstrating a large intra- and extraconal space-occupying lesion in the right orbit with lobular boundaries. The lesion is immensely heterogeneous, containing multiple septa and blood vessels with intervening regions of nonenhancing tissue suggestive of necrosis. The medial rectus muscle is displaced temporally (*star*), the globe is displaced laterally and compressed against the lateral orbital wall

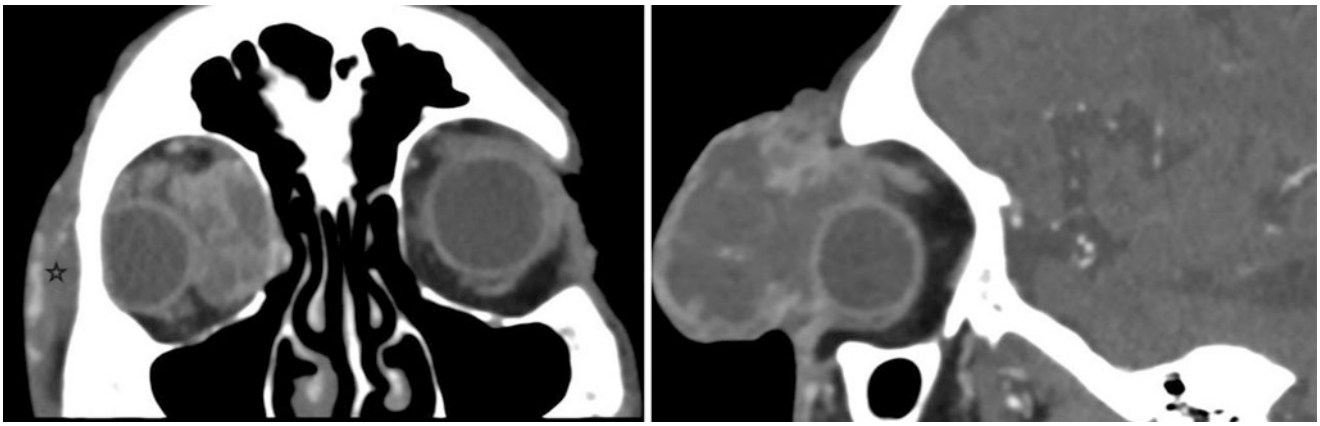


Fig. 14 CECT scan (coronal, *left*, sagittal, *right*) demonstrated mass extension to the right temple with multiple small vessels. On the sagittal view one can appreciate the excentric encroachment of the globe

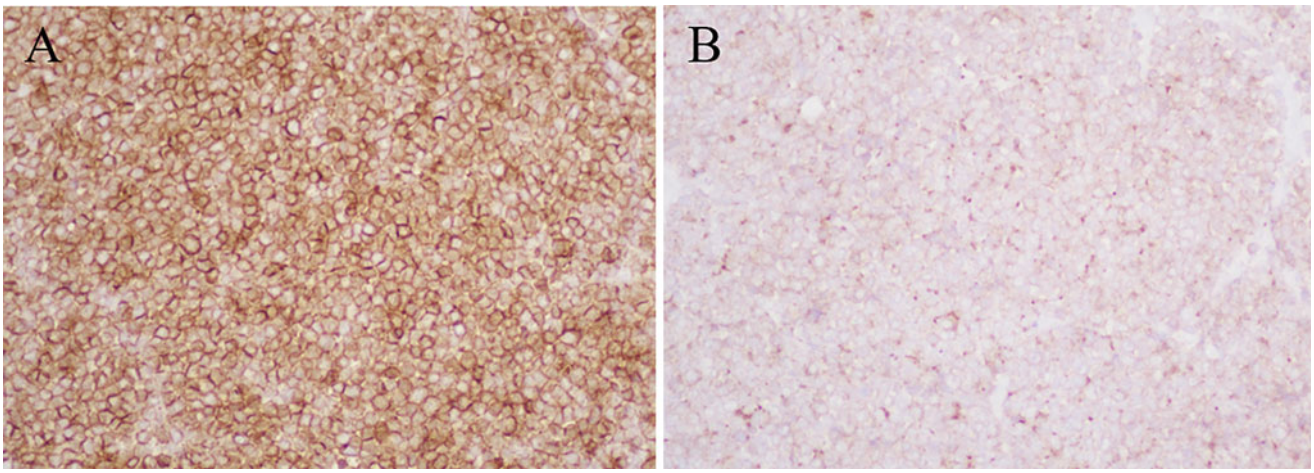


Fig. 15 CD56 (**a**) shows a membranous staining pattern. CD56 is positive in a wide variety of cell lineages, including neuroendocrine cells. The tumor is positive for synaptophysin (**b**) and chromogranin (not shown), both are neuroendocrine specific markers

References

1. Herbert HM, Sun MT, Selva D, et al. Merkel cell carcinoma of the eyelid: management and prognosis. JAMA Ophthalmol. 2014;132(2):197–204.
2. Coggshall K, Tello TL, North JP, Yu SS. Merkel cell carcinoma: an update and review: pathogenesis, diagnosis, and staging. J Am Acad Dermatol. 2018;78(3):433–42.
3. Tello TL, Coggshall K, Yom SS, Yu SS. Merkel cell carcinoma: an update and review: current and future therapy. J Am Acad Dermatol. 2018;78(3):445–54.
4. North VS, Habib LA, Yoon MK. Merkel cell carcinoma of the eyelid: a review. Surv Ophthalmol. 2019;64(5):659–67.
5. Merritt H, Sniegowski MC, Esmaeli B. Merkel cell carcinoma of the eyelid and periocular region. Cancers (Basel). 2014;6(2):1128–37.
6. Servat JJ, Black EH, Nesi FA, Gladstone GJ, Calvano CJ. Smith and Nesi's ophthalmic plastic and reconstructive surgery, 4th ed. Springer; 2020.
7. Peters GB 3rd, Meyer DR, Shields JA, Custer PL, Rubin PA, Wojno TH, Bersani TA, Tanenbaum M. Management and prognosis of Merkel cell carcinoma of the eyelid. Ophthalmology. 2001;108(9):1575–9.
8. Barrett RV, Meyer DR. Eyelid and periocular cutaneous Merkel cell carcinoma (aka. neuroendocrine or trabecular carcinoma). Int Ophthalmol Clin. 2009;49(4):63–75.
9. Harms KL, Healy MA, Nghiem P, Sober AJ, Johnson TM, Bichakjian CK, Wong SL. Analysis of prognostic factors from 9387 Merkel cell carcinoma cases forms the basis for the new 8th edition AJCC staging system. Ann Surg Oncol. 2016;23(11):3564–71.
10. Abbas O, Mahalingam M. The grenz zone. Am J Dermatopathol. 2013;35(1):83–91.

Part VIII

Osseous and Meninges Lesions

Imaging of Orbital Osteoma and Osteosarcoma

56

Alexandra Manta, Stefania B. Diniz, and Robert A. Goldberg

Contents

1 Signs and Symptoms 418
2 Differential Diagnosis 418
3 Diagnosis 418
4 Treatment 418
5 Figures with Captions 418
5.1 Osteoma 418
5.2 Osteosarcoma 418
References 422

Abstract

- Osteoma:
  - Benign tumor of the paranasal sinuses, frontal more than ethmoidal; only rarely primarily orbital; often associated with Gardner's syndrome
  - Slow growing, well-defined, most commonly invading the orbit through the supero-medial wall
  - Best imaged on CT scan, appears as a hyperintense, homogenous, bossellated, bone-like mass. Can have a central heterogeneous component of trabecular bone.
  - Causes a mass effect on orbital contents
- Osteosarcoma:
  - Most common primary neoplasm of the bone, can be primarily orbital but most commonly are metastatic lesions
  - CT scan shows an ill-defined, bone destructive, homogenous mass extending into the adjacent soft tissues
  - MRI is especially useful for assessing soft tissue involvement. Isointense on T1, hypointense on T2, markedly enhancing with contrast
  - Can express calcifications

Keywords

Sino-orbital osteoma · Benign osseous tumors of the orbit · Bony orbital tumor · Osteosarcoma · Orbital bone metastasis · Primary orbital osteosarcoma

A. Manta
Division of Orbital and Ophthalmic Plastic Surgery, Jules Stein Eye Institute, University of California, Los Angeles, CA, USA

S. B. Diniz · R. A. Goldberg (✉)
Division of Orbital and Ophthalmic Plastic Surgery, Stein and Doheny Eye Institutes, University of California, Los Angeles, CA, USA
e-mail: contato@stefaniadiniz.com; goldberg@jsei.ucla.edu

© Springer Nature Switzerland AG 2022
G. Ben Simon et al. (eds.), *Atlas of Orbital Imaging*,
https://doi.org/10.1007/978-3-030-62426-2_43

1 Signs and Symptoms

Osteoma causes slowly developing proptosis, globe dystopia, hard nodular mass felt under the skin, headache, sinusitis (secondary mucocele), facial or orbital pain, diplopia, restricted ocular motility, reduced vision, afferent pupillary defect, epiphora, dacryocystitis, orbital emphysema, and orbital cellulitis [1–6]. Osteosarcoma causes painful proptosis, globe dystopia, reduced vision, diplopia, extraocular motility restriction, facial swelling [7–9].

2 Differential Diagnosis

Other fibro-osseous or bone-forming benign or malignant lesions of the orbit like osteoblastoma, ossifying fibroma, fibrous dysplasia, osteosarcoma, and osteoblastic metastases [2, 3, 10].

3 Diagnosis

Clinical presentation and appearance on CT head and orbits are the principal modes of diagnosis for orbital osteoma. Tissue diagnosis usually confirms the radiologic and intraoperative findings and is important for histologic tumor typing [1]. In osteosarcoma, clinical and radiologic appearance may raise high suspicion of a bony malignancy especially if the patient has been previously diagnosed with adenocarcinoma (adult), embryonal tumors, or sarcomas (children), but histologic diagnosis is paramount. PET CT is warranted to identify a primary source and further metastatic lesions [8].

4 Treatment

For orbital osteoma, observation if asymptomatic. Multidisciplinary surgical approach with otolaryngology and neurosurgery if necessary. Surgical approaches include medial orbitotomy, endoscopic transnasal, lateral orbitotomy, upper eyelid crease, coronal or in most cases, a combination of these techniques. Recurrences are rare [2, 4–6]. For orbital osteosarcoma, clinical and radiologic appearance may raise high suspicion of a bony malignancy especially if the patient has been previously diagnosed with adenocarcinoma (adult), embryonal tumors, or sarcomas (children), but histologic diagnosis is paramount. PET CT is warranted to identify a primary source and further metastatic lesions [7].

5 Figures with Captions

5.1 Osteoma

5.2 Osteosarcoma



Fig. 1 Noncontrast CT scan, bone window, axial view (a), coronal view (b) Well-defined, homogeneous, lobulated, bone density mass growing into the left maxillary, ethmoid and frontal sinuses, nasal cavity and the orbit, displacing the globe forward by impinging on the orbital contents. It is also obscuring the structures of the nasal cavity and blocking the outlet of the left paranasal sinuses as evident by their opacification

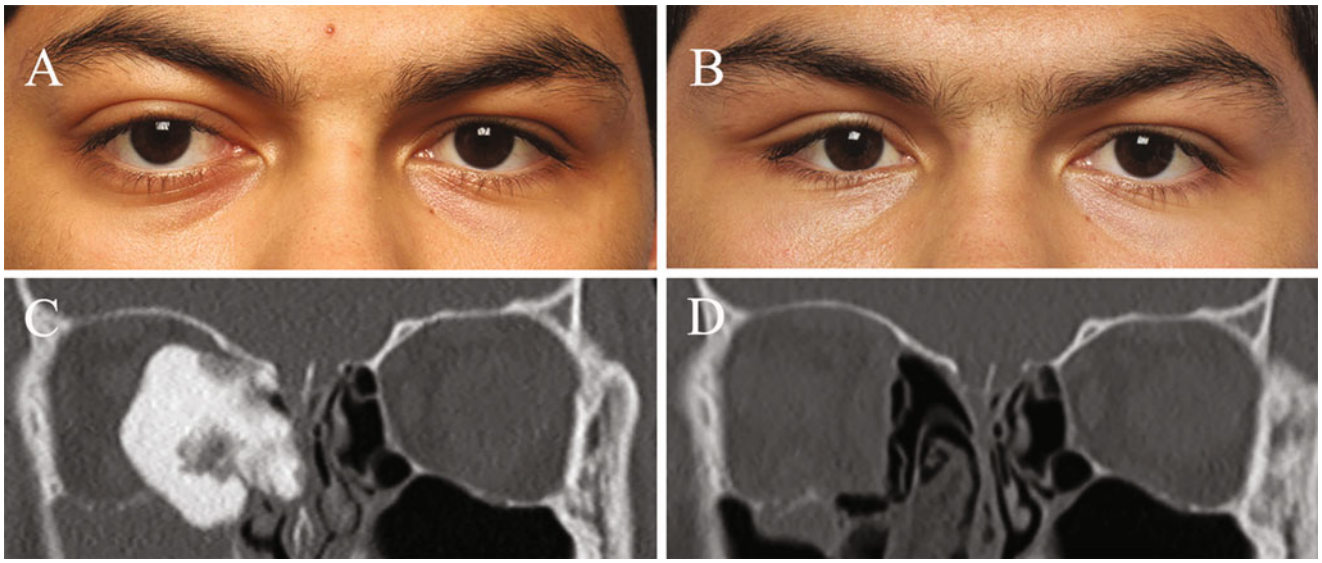


Fig. 2 Clinical images and orbital CT scans coronal view bone window pre- (**a** and **c**) and post- (**b** and **d**) surgical excision through transconjunctival approach

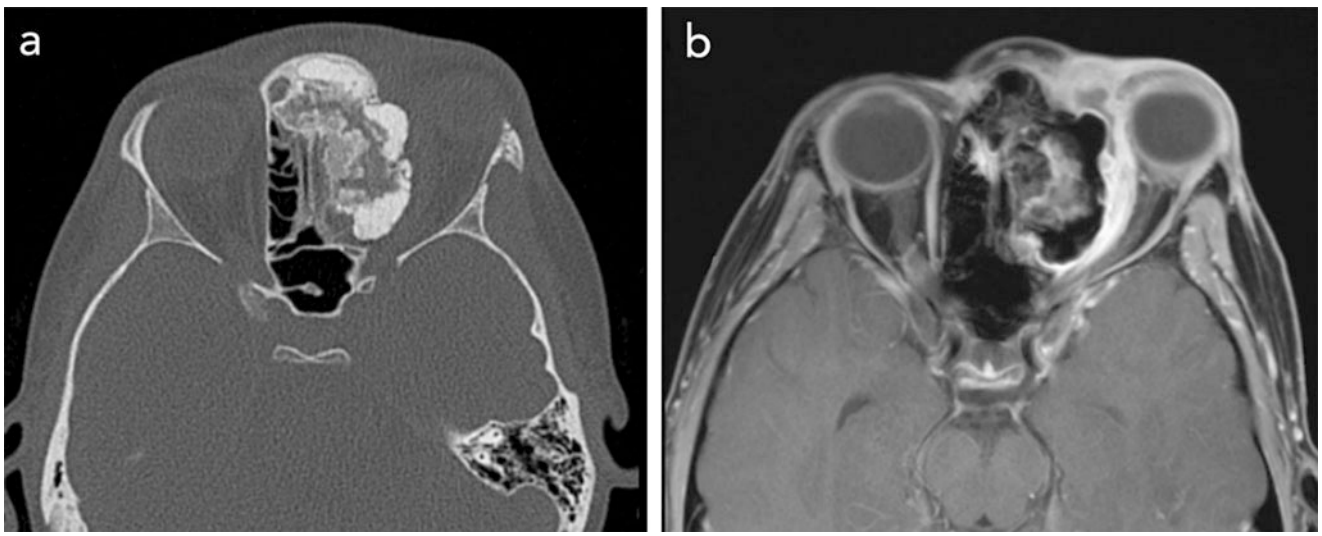


Fig. 3 Axial CT scan of the orbit bone window (**a**) and MR T1WI fat suppression (**b**) depicting a left ethmoid osteoma with mass effect upon the left orbital structures including the medial rectus muscle and left optic nerve. On MR, the signal of the lesion follows the signal of cortical bone

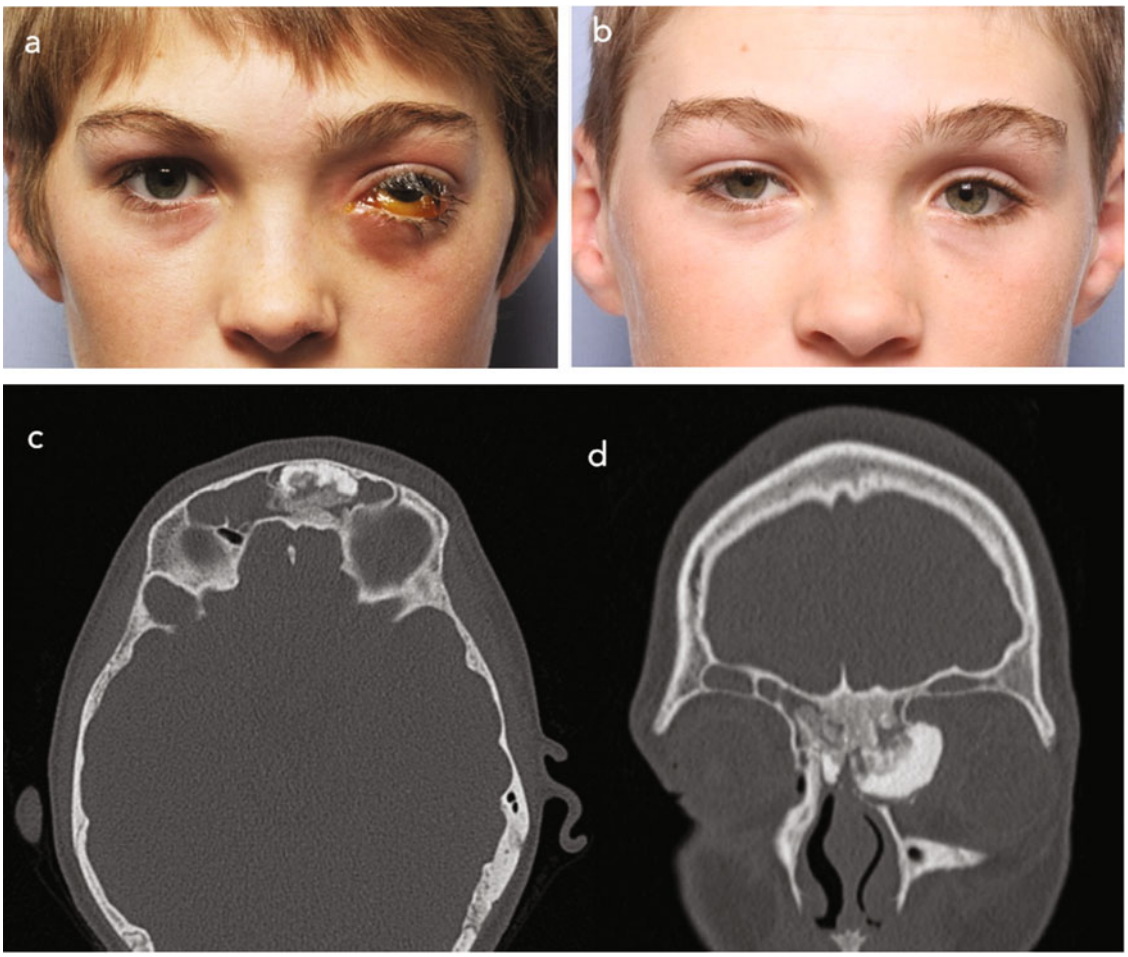


Fig. 4 A 13-year-old boy with previous diagnosis of left sino-orbital osteoma, presenting with left proptosis, globe displacement inferolaterally, sinusitis, and orbital cellulitis for one week (**a**). Orbital CT scans bone window, axial view (**c**) and coronal view (**d**) depict a lobulated heterogeneously ossified lesion centered in the left ethmoid sinus with a component extending into the left frontal sinus and a component extending laterally with significant mass effect on the orbit. Postoperative clinical photograph (**b**) of the patient post left orbital orbitotomy and excision of the bony lesion

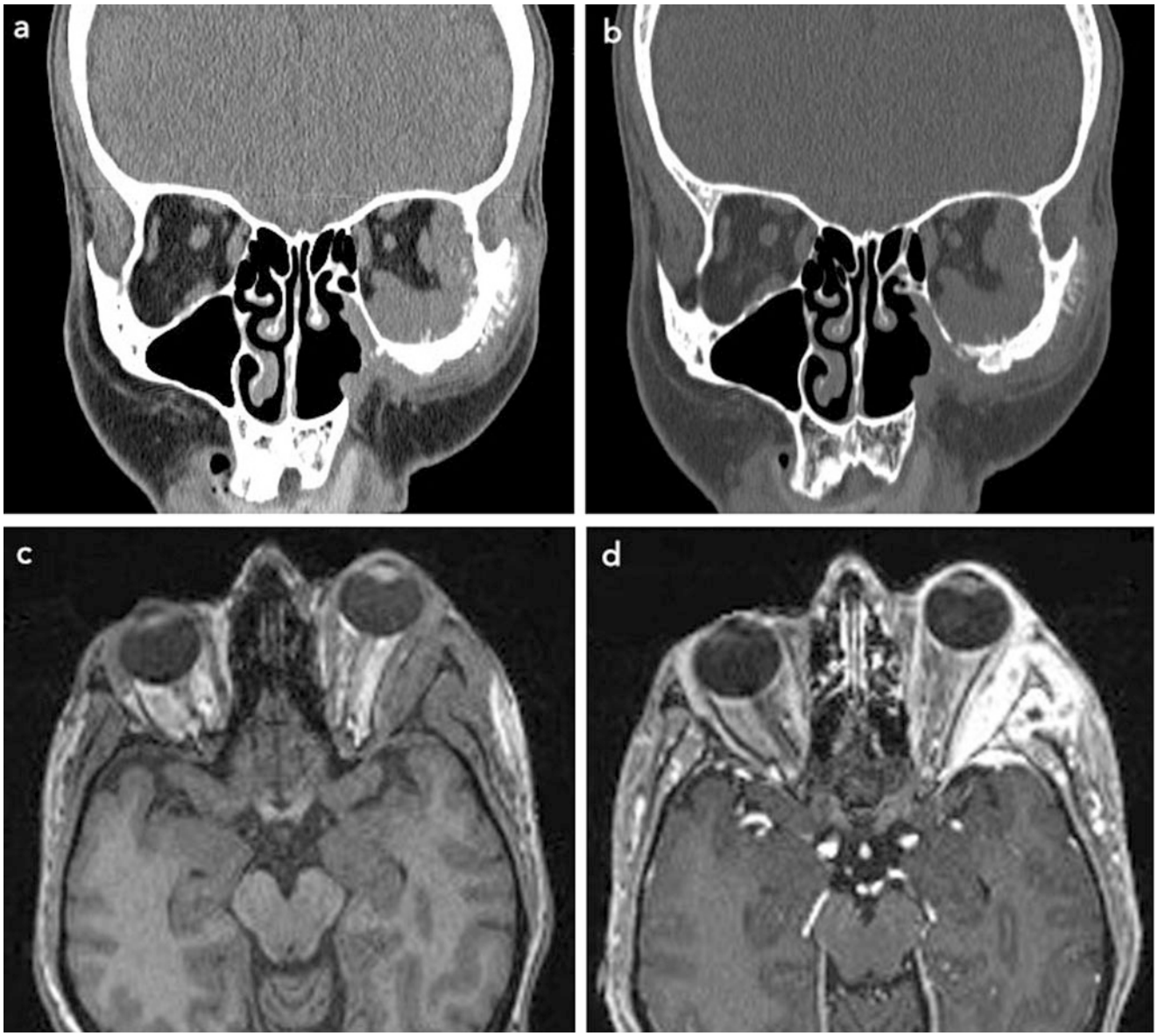


Fig. 5 48-year-old female with history of left maxillary osteosarcoma, for which she underwent surgery and radiation, with concurrent chemotherapy. Eight years later, she presented with left eye swelling, headache, and facial pain. Nonenhanced orbital **CT scan soft tissue (a) and bone window (b)** coronal view depict a poorly defined, soft tissue mass centered upon the lateral and inferior orbital walls with extension into the orbit, temple, and midface. There is irregular bone remodeling with aggressive periosteal reaction. Note the missing inferior turbinate and absent of the maxillary sinus. The mass is showing patchy alternating iso-, hypo-, and hyperintense areas representing the heterogeneous nature of the tumor. Biopsy was consistent with recurrent osteosarcoma. **Axial MRI T1WI nonenhanced (c) and enhanced (d)** depicting a large isointense mass with avid enhancement, centered in the greater wing of left sphenoid with left orbital extension and associated proptosis, as well as epidural extension into the left middle cranial fossa

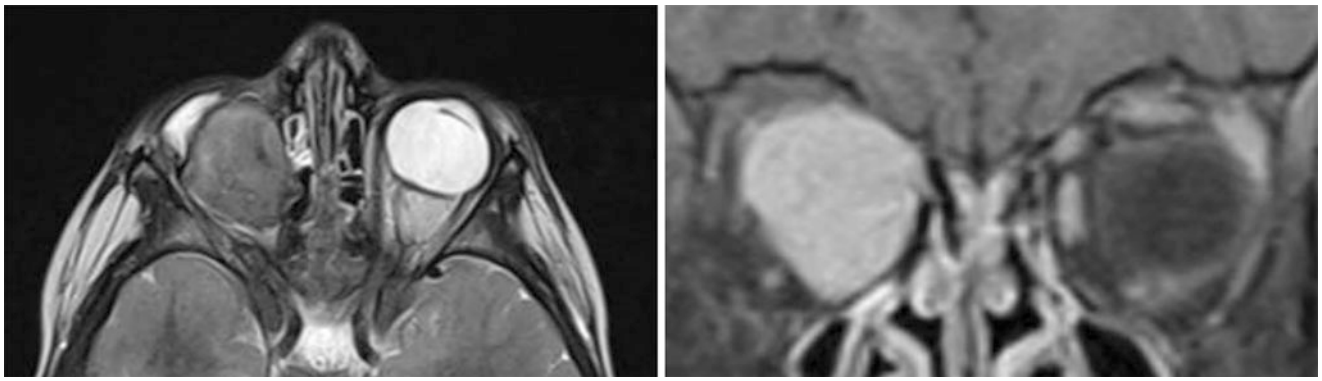


Fig. 6 MRI of an 11-YOF with past medical history of right eye retinoblastoma for which she underwent enucleation and RT. Axial T2 (*left)* showing a relatively homogenous isointense mass filling the right orbit. Coronal CE T1 WI (*right*) showing homogenous lesion enhancement. Orbital biopsy was consistent with extra-osseous osteosarcoma. The child underwent subtotal eyelid sparing exenteration, with radial fore-arm free flap, and managed to fit ocular prosthesis. (courtesy of the editors)

References

1. Selva D, White VA, O'Connell JX, Rootman J. Primary bone tumors of the orbit. Vol. 49, Survey of ophthalmology: Elsevier; 2004. p. 328–42.
2. Wei LA, Ramey NA, Durairaj VD, Ramakrishnan VR, Cruz AV, Dolman PJ, et al. Orbital Osteoma. Ophthal Plast Reconstr Surg [Internet]. 2014 [cited 2020 Apr 14];30(2):168–74. Available from: http://journals.lww.com/00002341-201403000-00015
3. McHugh JB, Mukherji SK, Lucas DR. Sino-orbital osteoma: a clinicopathologic study of 45 surgically treated cases with emphasis on tumors with osteoblastoma-like features. Arch Pathol Lab Med. 2009;133(10):1587–93.
4. Pons Y, Blancal J-P, Vérillaud B, Sauvaget E, Ukkola-Pons E, Kania R, et al. Ethmoid sinus osteoma: diagnosis and management. Head Neck [Internet]. 2013 [cited 2020 Apr 14];35(2):201–4. Available from: http://doi.wiley.com/10.1002/hed.22945
5. Jack LS, Smith TL, Ng JD. Frontal sinus osteoma presenting with orbital emphysema. Ophthal Plast Reconstr Surg. 2009;25(2):155–7.
6. A Unique Approach to Orbital Osteoma Removal – American Academy of Ophthalmology [Internet]. [cited 2020 Apr 14]. Available from: https://www.aao.org/clinical-video/unique-approach-to-orbital-osteoma-removal
7. Lin PY, Chen WM, Hsieh YL, Chen WYK, Chen TH. Orbital metastatic osteosarcoma. J Chin Med Assoc. 2005;68(6):286–9.
8. Rajabi MB, Saeedi-Anari G, Ramezani F, Tabatabaie S-Z, Rajabi MB, Amoli FA. Orbital metastatic osteosarcoma. Arch Iran Med. 2015;18:123.
9. Yip CC, Kersten RC, McCulley TJ, Ballard ET, Kulwin DR. Osteogenic sarcoma after orbital radiation rhabdomyosarcoma. Ophthalmology. 2003;110(10):1996–9.
10. Morita R, Shimada K, Kawakami S. Low-grade central osteosarcoma of the orbit. J Craniofac Surg. 2012;23(3):e178–80.

Ossifying Fibroma and Chondromyxoid Fibroma of the Orbit

57

Alexandra Manta, Stefania B. Diniz, and Robert A. Goldberg

Contents

1 **Signs and Symptoms** 423
2 **Differential Diagnosis** 423
3 **Diagnosis** 424
4 **Treatment** 424
5 **Figures with Captions** 424
References 426

Abstract

- Typically arising from paranasal sinuses (maxillary > ethmoid > sphenoid > frontal). Rarely primarily orbital.
- Three district subtypes: cemento-ossifying fibromas, juvenile psammomatoid ossifying fibroma, and juvenile trabecular ossifying fibroma.
- Slow growing mass developing within the affected bone, ground glass, or granular opacities with or without a defined hyperintense border on CT, depending on the subtype.
- Alternating osteolytic and osteoblastic areas give it a pebbled appearance, at times showing central, dense ossification or calcification areas.
- Homogenous or heterogenous on T1 and T2; the juvenile subtypes may have hyperintense areas on T2. The periphery enhances with Gadolinium contrast.
- Chondromyxoid fibroma (CMF) is a rare benign mesenchymal neoplasm that usually arises in the metaphyseal region of long bones in young adults. Adjacent cortical expansion, thinning, or destruction is typical and can be mistaken for malignant tumor.
- Imaging shows well-demarcated oval to lobulated eccentric metaphyseal lesion with a sclerotic rim, bone erosion or destruction. Soft tissue expansion is uncommon.

Keywords

Ossifying fibroma · Juvenile psammomatoid ossifying fibroma · Juvenile trabecular ossifying fibroma · Cementifying fibroma · Cemento-ossifying fibroma · Chondromyxoid fibroma

1 Signs and Symptoms

Mass effect due to its expansile nature can be aggressive in children causing significant facial deformity. Presentation may include proptosis, globe dystopia, facial pain, headache, sinusitis, diplopia with restricted ocular motility, periorbital inflammation, and orbital cellulitis [1–3].

2 Differential Diagnosis

Fibrous dysplasia, osteoma, osteoblastoma, osteosarcoma, chondrosarcoma, squamous cell carcinoma, odontogenic cysts with or without calcifications, aneurysmal bone cyst, and sphenoid wing meningioma [2, 4, 5].

A. Manta
Division of Orbital and Ophthalmic Plastic Surgery, Jules Stein Eye Institute, University of California, Los Angeles, CA, USA

S. B. Diniz · R. A. Goldberg (✉)
Division of Orbital and Ophthalmic Plastic Surgery, Stein and Doheny Eye Institutes, University of California, Los Angeles, CA, USA
e-mail: contato@stefaniadiniz.com; goldberg@jsei.ucla.edu

© Springer Nature Switzerland AG 2022
G. Ben Simon et al. (eds.), *Atlas of Orbital Imaging*,
https://doi.org/10.1007/978-3-030-62426-2_45

3 Diagnosis

Clinical presentation, age, and radiologic findings. Tissue diagnosis needed for subtyping.

4 Treatment

Complete surgical excision is recommended as recurrence rates have been reported in 30–56% of cases [4, 6, 7]. Multidisciplinary management with orbital and craniofacial reconstruction may be necessary in highly aggressive and facial deforming tumors [1, 8]. For CMF, there is a moderate risk of recurrence in 33% of cases, irrespective of margin status, with no reported occurrence of distant metastasis [9–12].

5 Figures with Captions

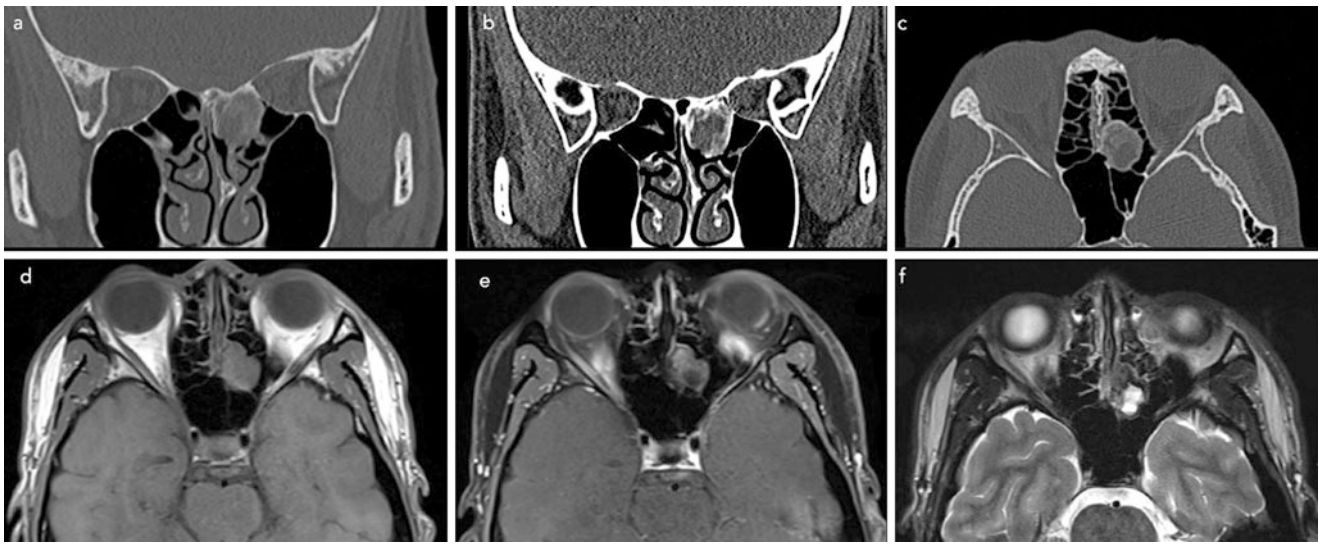


Fig. 1 **An** 18-year-old male with psammomatoid juvenile ossifying fibroma. **Noncontrasted CT scan, coronal view, bone window (a) soft tissue (b) and axial bone window (c)** depicting a well-defined iso/hypo dense mass arising from the left posterior ethmoid air cells with a sclerotic rim. Emphasis on the hyperdense border and the expansile nature of the lesion. Note the lesion is abutting the anterior skull base, essential for presurgical planning and assessing the risk of post-surgical CSF leak. **Axial MRI T1 (d), T1 post-contrast FS (e), and T2 (f) show** same mass with isointensity on T1, granular enhancement with contrast and a paracentral hyperintense area on T2 suggestive of a chondroid component associated with osteoclastic area

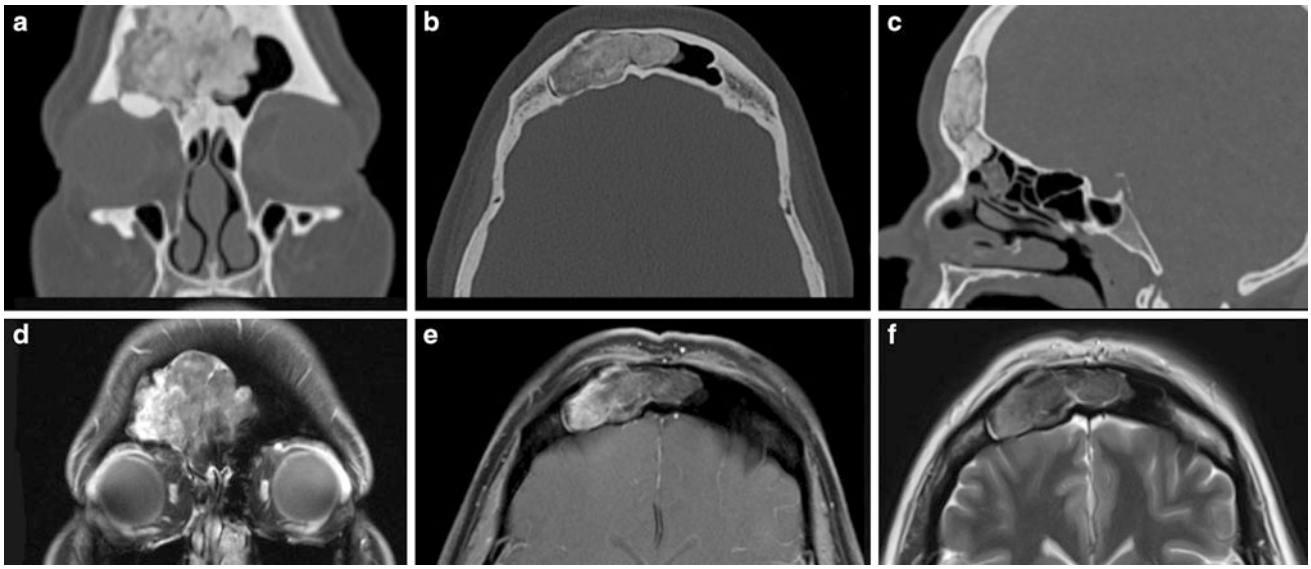


Fig. 2 A 39-year-old female with chronic frontal sinusitis. Non-enhanced **CT scans and** bone window **coronal (a), axial (b), and sagittal view (c)** depict heterogeneous mass centered in the right frontal sinus, with left frontal extension, and mass effect upon the right globe. **Coronal (d) and axial (e) T1WI** post contrast depict a heterogeneously enhanced mass filling the frontal sinus, mucosal thickening, and trace fluid. **T2Wi axial view (f)** depict posterior bowing of the right frontal sinus wall causing mild mass effect upon the frontal lobe, without evidence of edema.

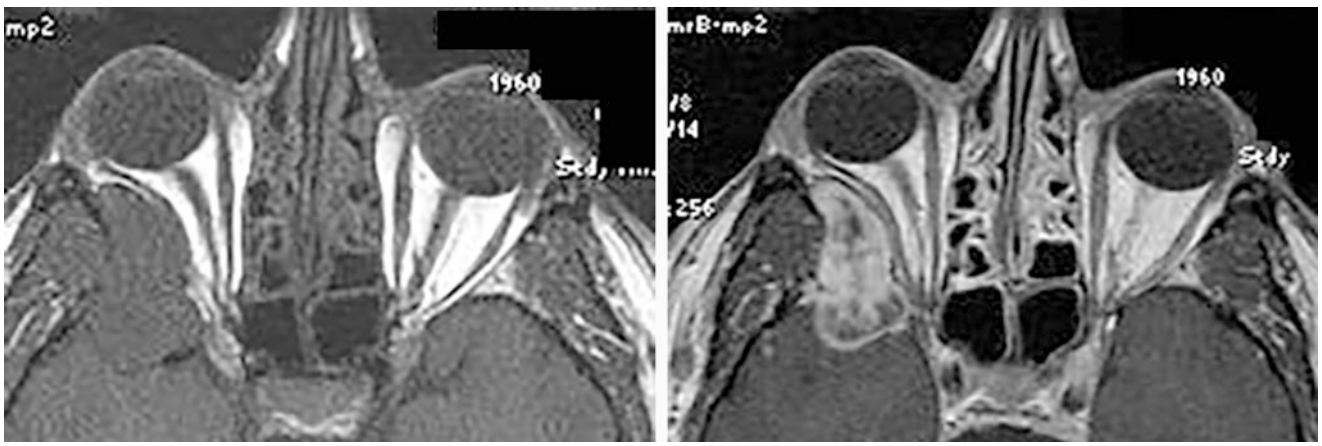


Fig. 3 MRI. Axial T1-weighted, non-fat-saturated, images of a different patient. Pre- (*left*) and post-contrast administration (*right*). There is a right sphenoid-wing expansile mass, with relatively defined contours, showing isointense signal on conventional T1, undergoing heterogeneous enhancement. The mass is displacing the orbital content medially and protruding towards the middle cranial fossae. Orbital biopsy was consistent with the diagnosis of chondromyxoid fibroma.

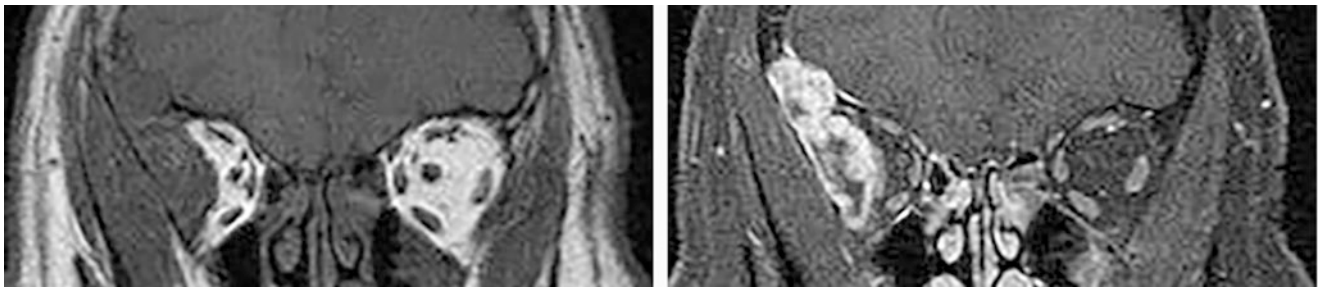


Fig. 4 MR coronal views, T1-weighted images, non-FS image (*left*), and post-contrast FS (*right*) of the same patient as Figs. 3 and 5. The coronal plane better demonstrates the vertical extension of the mass along with mild extra-dural involvement at the margins of the anterior cranial fossa.



Fig. 5 MRI axial non- FS T2 WI. The tumor portrays mixed signal intensities on T2 WI.

References

1. Hachach-Haram N, Benyon S, Maling S, Joshi N, Grant WE, Kirkpatrick WNA. Surgical management of two complex cases of large juvenile orbital ossifying fibroma. J Plast Reconstr Aesthetic Surg. 2011;64(12):1661–4.
2. Khanna M, Buddhavarapu SR, Hussain SA, Amir E. Cemento-ossifying fibroma of paranasal sinus presenting acutely as orbital cellulitis. J Radiol Case Rep. 2009;3(4):18–25.
3. Rabelo N, da Silva VTG, do Espírito Santo MP, Solla D, Oberman DZ, da Costa BS, et al. Orbit ossifying fibroma – case report and literature review. Surg Neurol Int. 2020;11:35.
4. Selva D, White VA, O'Connell JX, Rootman J. Primary bone tumors of the orbit. Vol. 49, survey of ophthalmology: Elsevier; 2004. p. 328–42.
5. Tunc M, Char DH. Ossifying fibroma of the lateral orbital wall in an adult. Orbit 2009 [cited 2020 Apr 16]. Available from: https://www.tandfonline.com/action/journalInformation?journalCode=iorb20
6. Wang M, Zhou B, Cui S, Li Y. Juvenile psammomatoid ossifying fibroma in paranasal sinus and skull base. Acta Otolaryngol [Internet]. 2017 [cited 2020 Apr 16];137(7):743–9. Available from: https://www.tandfonline.com/doi/full/10.1080/00016489.2016.1276302
7. Wakefield MJ, Ross AH, Damato EM, Salvi SM, Baker GRC. Review of lateral orbital wall ossifying fibroma. Orbit [Internet]. 2010 [cited 2020 Apr 15];29(6):317–20. Available from: http://www.tandfonline.com/doi/full/10.3109/01676830.2010.522299
8. Hartstein ME, Grove AS, Woog JJ, Shore JW, Joseph MP. The multidisciplinary management of Psammomatoid ossifying fibroma of the orbit. Ophthalmology. 1998;105(4):591–5.
9. Grewal AM, Singh M, Vishwajeet V, Thakur U, Das A, Gupta P. Primary chondromyxoid fibroma of the orbit: an orbital mass with calcification. Indian J Ophthalmol. 2019;67(12):2110–3. https://doi.org/10.4103/ijo.IJO_1275_19. PMID: 31755478; PMCID: PMC6896519.
10. Meredith DM, CDM F, Jo VY. Chondromyxoid fibroma arising in craniofacial sites: a clinicopathologic analysis of 25 cases. Am J Surg Pathol. 2018;42(3):392–400. https://doi.org/10.1097/PAS.0000000000001019. PMID: 29324473.
11. Ditta LC, Qayyum S, O'Brien TF, Choudhri AF, Wilson MW. Chondromyxoid fibroma of the orbit. Ophthalmic Plast Reconstr Surg. 2012;28(5):e105–6. https://doi.org/10.1097/IOP.0b013e31823bd1e0. PMID: 22743695.
12. Khalatbari MR, Hamidi M, Moharamzad Y. Chondromyxoid fibroma of the anterior skull base invading the orbit in a pediatric patient: case report and review of the literature. Neuropediatrics. 2012;43(3):140–5. https://doi.org/10.1055/s-0032-1307460. Epub 2012 Apr 2. PMID: 22473287.

Fibrous Dysplasia

58

Stefania B. Diniz and Robert A. Goldberg

Contents

1 **Signs and Symptoms** 427
2 **Differential Diagnosis** 428
3 **Diagnosis** 428
4 **Treatment** 428
5 **Figures with Captions** 428
References 431

Abstract

- Poorly circumscribed, heterogeneous bone proliferation typically arising from the frontal bone and less frequently from the sphenoid and ethmoid sinuses.
- Plain radiography shows smooth and homogenous bone lesions with endosteal scalloping and cortical thinning.
- The involved bone is thickened, sclerotic, and ground glass opacities are characteristic in CT scans.
- Increased density and regions of cystic lucencies may be seen.
- On MRI, involved bone is thickened and with heterogeneous signal.
- MRI is not specific, as the lesion may mimic more aggressive pathologies. Many times, reverting to CT may be needed for confirmation. MRI is a biomarker of tissue activity for fibrous dysplasia. Active lesions show avid enhancement, while inactive lesions show mild enhancement.
- *Patients presenting with visual loss may benefit of enhanced MRI* to rule out *compressive optic neuropathy.* Injury results in atrophy of the intracanalicular segment of the optic nerve.

Keywords

Fibrous dysplasia · Bone diseases · Hyperostosis

1 Signs and Symptoms

Clinically, the most common presentation is swelling [1]; other manifestations include progressive orbital dystopia, facial asymmetry, proptosis, hypoglobus, and eyelid ptosis. Insidious visual loss, cranial nerve palsies, and trigeminal neuralgia can occur in case of constriction of orbital fissures and canals of the skull base [2]. There is a remote risk of malignant transformation.

The monostotic variant of fibrous dysplasia (FD) accounts for approximately 70–85% of cases and manifests later in life, commonly affecting the femur or the ribs. In contrast, the polyostotic form affects several bones, manifests earlier in the first decade of life, and has a more serious prognosis. Lesions affecting craniofacial bones are likely to be polyostotic [3]. When associated with endocrine dysfunction and/or café-au-lait spots, it is termed as McCune-Albright syndrome.

S. B. Diniz · R. A. Goldberg (✉)
Division of Orbital and Ophthalmic Plastic Surgery, Stein and Doheny Eye Institutes, University of California, Los Angeles, CA, USA
e-mail: contato@stefaniadiniz.com; goldberg@jsei.ucla.edu

© Springer Nature Switzerland AG 2022
G. Ben Simon et al. (eds.), *Atlas of Orbital Imaging*,
https://doi.org/10.1007/978-3-030-62426-2_46

2 Differential Diagnosis

Hyperostotic meningioma; Paget's disease; Langerhans cell histiocytosis.

3 Diagnosis

Clinical characteristics and radiologic findings [4].

4 Treatment

Expectant management is advised if the symptoms are mild. Surgery is indicated for gross deformities, pain, functional deficits, or malignant transformation. Intravenous pamidronate has been reported to increase bone remodeling, offering some help in severe forms of the disease [5].

Surgical intervention with bone debulking may provide aesthetic improvement of the dystopia and proptosis. Prophylactic decompression of the optic nerve is not indicated if there is no visual loss associated. However, when visual impairment begins, it tends to be progressive, thus requiring an optic canal decompression [6].

5 Figures with Captions



Fig. 1 External photograph of a 27-YOF with McCune Albright Syndrome with left hypoglobus and prominent forehead (same patient as in Figs. 2 and 3).

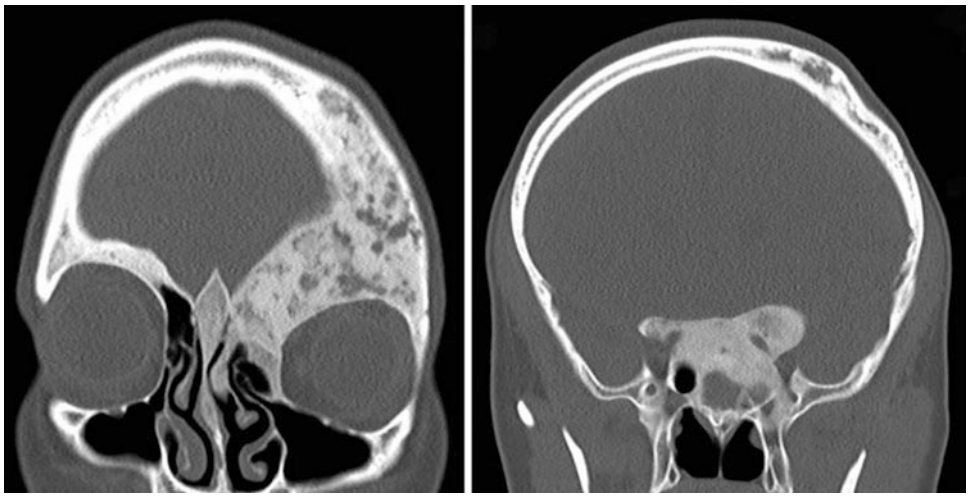


Fig. 2 **Nonenhanced CT scan** of the orbit in a 27-YOF patient with McCune Albright Syndrome (Fig.4), bone window depicting a heterogenous, dense and sclerotic bone expansion. **Anterior coronal view (left)** with areas of lucency and sclerosis (pagetoid lesion) involving the left frontal bone and anterior skull. **Coronal image through the anterior skull base (right)** depicting the posterior extension along the planum sphenoidale and the anterior clinoids with bilateral optic canal narrowing.

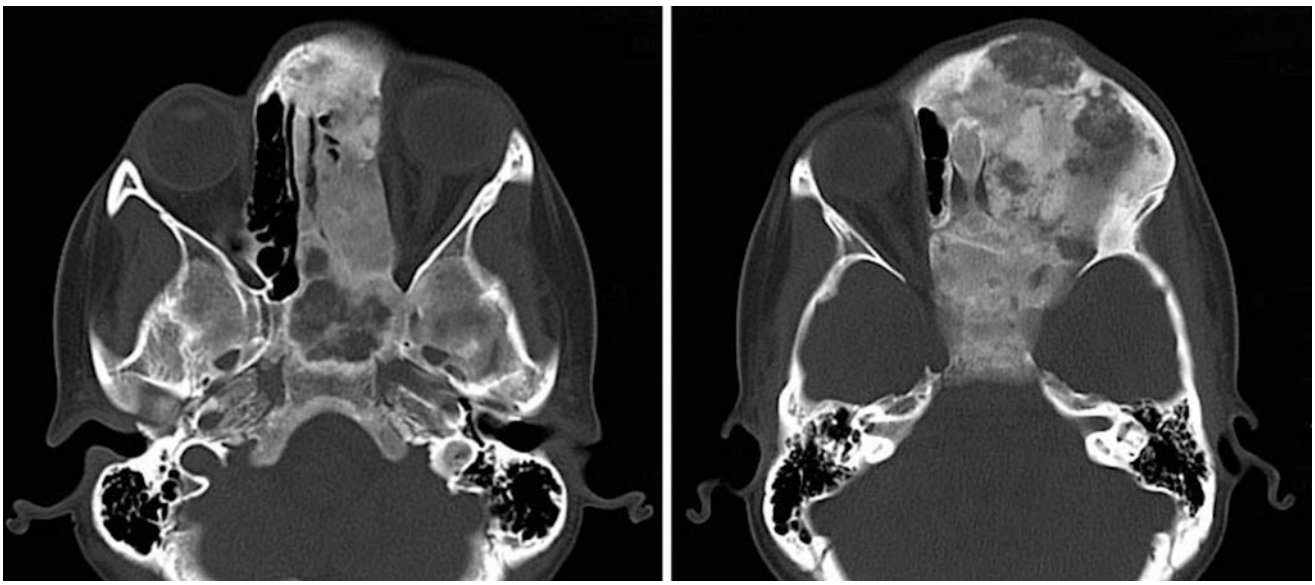


Fig. 3 **Axial nonenhanced CT scan** of the left orbit, bone window depicting a heterogenous expansion of the ethmoid and sphenoid sinus **(left).** Mixed sclerotic bone expansion of the frontal bone through the left orbit and skull base. **(right).** A typical ground glass appearance is demonstrated.



Fig. 4 **Bone window CT scans** of a 16 YOM with fibrous dysplasia, demonstrating a diffuse homogenous "ground glass" appearance of the frontal bone and greater wing of the sphenoid in **coronal (left), axial (center),** and **sagittal (right)** views

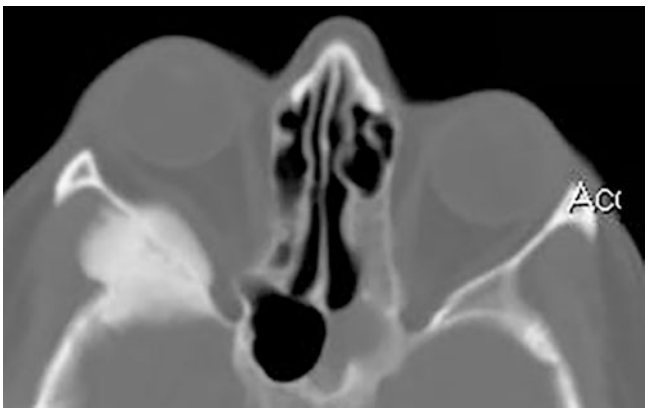


Fig. 5 Axial NE CT (bone window) of a different patient with monostotic FD of the right sphenoid bone showing "tri-lateral" compartment involvement (orbit, temporal fossa, middle cranial fossa)

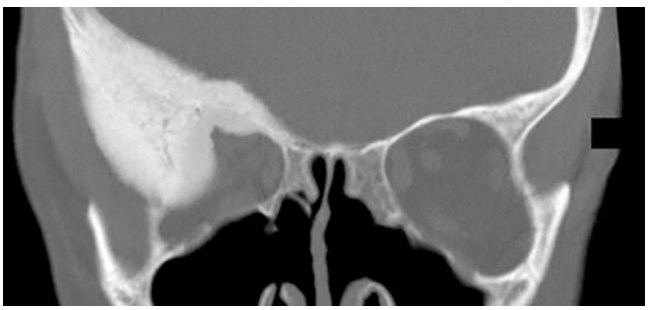


Fig. 6 NE CT, coronal view (bone window) of the same patient as in Fig. 5 showing the bony extension into the orbital roof, deep lateral (zygomatic) wall, as well as the frontal bone

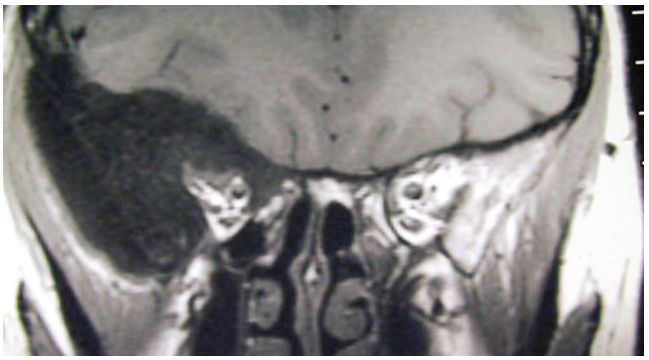


Fig. 7 T1 WI NE MR, coronal view of the same patient, the tumor-like process is hypointense, typical of sclerotic lesions

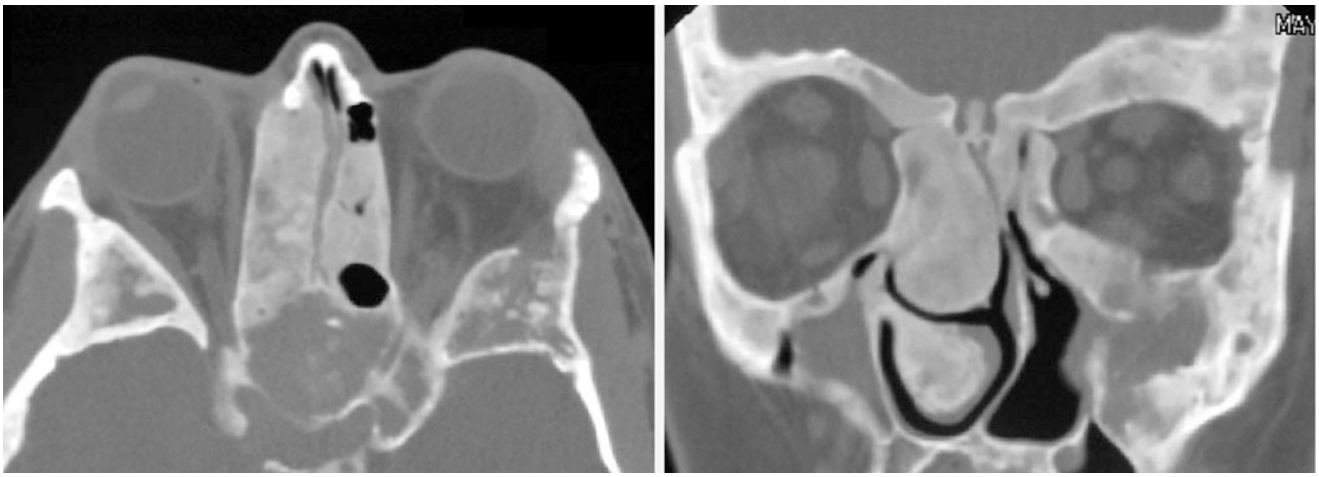


Fig. 8 40-YOF with polyostotic fibrous dysplasia (different patient). CT (bone window) axial (left) and coronal (right) views. There is extensive involvement of the facial and sinonasal bones together with the central skull base. The axial view shows the near-total obliteration of the ethmoid cavities by the lesion, as well as bilateral sphenoid wing involvement together with a more hypodense-appearing portion of the FD within the sphenoid body. The coronal view best demonstrates the extensive concentric involvement the left orbit, including the zygoma and maxillary bones, with narrowing of the SOF on the left side. This view also demonstrates the pronounced asymmetric expansion of the nasal turbinates on the right.

References

1. Ricalde P, Horswell BB. Craniofacial fibrous dysplasia of the fronto-orbital region: a case series and literature review. J Oral Maxillofac Surg. 2001;59(2):157–67. discussion 167–8.
2. Bibby K, McFadzean R. Fibrous dysplasia of the orbit. Br J Ophthalmol. 1994;78(4):266–70.
3. Adetayo OA, Salcedo SE, Borad V, Richards SS, Workman AD, Ray AO. Fibrous dysplasia: an overview of disease process, indications for surgical management, and a case report. Eplasty. 2015;15:e6. Published 2015 Feb 26.
4. Kushchayeva YS, Kushchayev SV, Glushko TY, et al. Fibrous dysplasia for radiologists: beyond ground glass bone matrix. Insights Imaging. 2018;9:1035–56.
5. Chapurlat R, Hugueny P, Delmas P, Meunier P. Treatment of fibrous dysplasia of bone with intravenous pamidronate: long-term effectiveness and evaluation of predictors of response to treatment. Bone. 2004;35(1):235–42.
6. Abe T, Satoh K, Wada A. Optic nerve decompression for orbitofrontal fibrous dysplasia: recent development of surgical technique and equipment. Skull Base. 2006;16(3):145–55.

Intraosseous Hemangioma and Cholesterol Granuloma of the Orbit

59

Liza M. Cohen, Stefania B. Diniz, and Robert A. Goldberg

Contents

1 Signs and Symptoms 434

2 Differential Diagnosis 434

3 Diagnosis 434

4 Treatment 434

5 Figures with Captions 434
5.1 Intraosseous hemangioma 434
5.2 Cholesterol granuloma 437

References 438

Abstract

1. Intraosseous Hemangioma
   - Well-circumscribed heterogeneous soft tissue lesion encased in bone, expands the inner and outer tables
   - CT with "corduroy sign" on coronal and sagittal images and "polka-dot" appearance on axial images created by replacement of normal cancellous bone by vertically-oriented thickened trabeculae surrounded by vascular lacunae [1]
   - Internal appearance also described as "honeycombed" [2]
   - T1 intensity depends on the fatty component of the lesion, ranging from isointense to hyperintense if high fat content [3]
   - Hyperintense on T2-weighted imaging
   - Heterogeneous contrast enhancement
2. Cholesterol Granuloma:
   - Orbital involvement nearly always occurs in the lateral region of the superior orbital ridge within the frontal diploic space.
   - Well-defined soft tissue mass associated with an expansile, osteolytic defect.
   - The lesion has homogeneous attenuation on CT scans, isodense with brain and muscle.
   - MRI is characterized by high signal intensity on T1- and varies on T2-weighted imaging according to the age of the blood products (intra- and extra-cellular methemoglobin content).
   - Usually there is no enhancement with contrast administration.

Keywords

Intraosseous hemangioma, hemangioma of bone · Cholesterol granuloma · Bone cyst · Cholesteatoma · Hematic cyst · Chocolate cyst

L. M. Cohen
Division of Orbital and Ophthalmic Plastic Surgery, Stein Eye Institute, University of California, Los Angeles, CA, USA
e-mail: cohenlizam@gmail.com

S. B. Diniz · R. A. Goldberg (✉)
Division of Orbital and Ophthalmic Plastic Surgery, Stein and Doheny Eye Institutes, University of California, Los Angeles, CA, USA
e-mail: contato@stefaniadiniz.com; goldberg@jsei.ucla.edu

© Springer Nature Switzerland AG 2022
G. Ben Simon et al. (eds.), *Atlas of Orbital Imaging*,
https://doi.org/10.1007/978-3-030-62426-2_47

1 Signs and Symptoms

For intraosseous hemangioma, slowly progressive mass effect with proptosis, globe displacement, and palpable mass. Gradual onset and progression. Predominance in 4th to 5th decades of life [1]. No known endocrine/hormonal influence. Spontaneous hemorrhage rare with only one case reported in the cranium [4–6].

For cholesterol granuloma, insidious history of painless unilateral axial proptosis and hypoglobus. Limited supraduction, eyelid ptosis, and diplopia may also occur.

2 Differential Diagnosis

For intraosseous hemangioma, other benign and malignant bony tumors including osteoma, osteosarcoma, osteochondroma, chondrosarcoma, fibrous dysplasia, ossifying fibroma, aneurysmal bone cyst, metastases, and chordoma.

For cholesterol granuloma: dermoid cyst; epidermoid cyst; Lacrimal gland carcinoma; Aneurysmal bone cyst.

3 Diagnosis

For intraosseous hemangioma, radiologic appearance. CT better demonstrates the classic internal stippled appearance. Nuclear medicine techniques such as Tc-99m tagged RBC scan have been shown to be a useful adjunct to differentiate atypical/aggressive vertebral intraosseous hemangiomas from metastasis [5–6]. Incisional biopsy should not be undertaken due to risk of uncontrolled hemorrhage.

For cholesterol granuloma, clinical presentation and radiological findings may help, but histopathological evaluation is imperative for a definitive diagnosis. It may be difficult to differentiate cholesterol granulomas from dermoid and epidermoid cysts on CT and MRI [7–10].

4 Treatment

For intraosseous hemangioma, en bloc resection including a rim of normal bone. This is critical in order to avoid excessive bleeding if the tumor is breached. Preoperative embolization may decrease intraoperative bleeding. A multidisciplinary approach to excision in conjunction with neurosurgery may be necessary.

For cholesterol granuloma, surgical resection followed by curettage or burring of residual tissue adherent to bone [7–10]. Recurrences have been reported in relation to the absence of sufficient bone drilling [9].

5 Figures with Captions

5.1 Intraosseous hemangioma

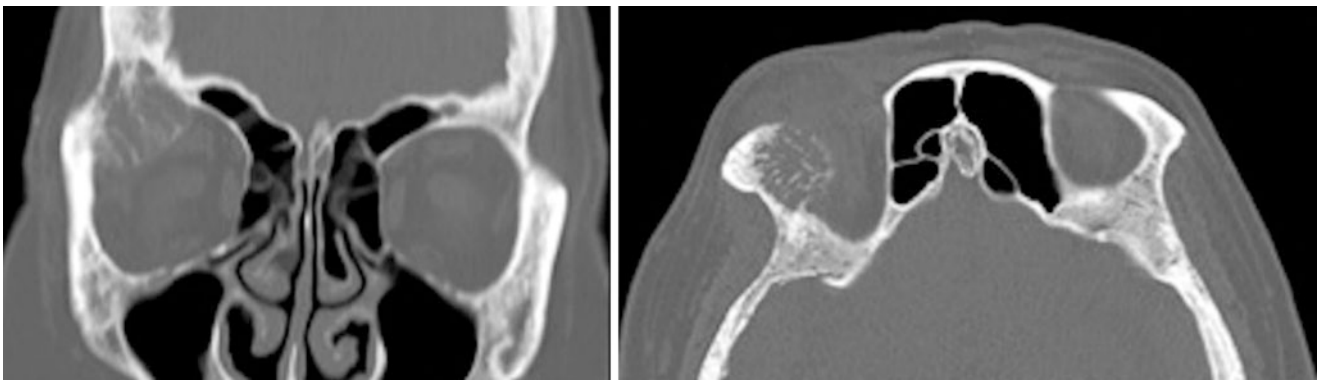


Fig. 1 **CT of the orbits, bone window, coronal view (left)** shows a well-defined expansile mass originating from within the right lateral orbital roof. Vertically-oriented trabeculae represent areas of normal bone replaced by vascular lacunae. This is referred to as the "corduroy sign." **Bone window, axial view (right).** Axial imaging demonstrates the "polka-dot" appearance due to these same trabeculae. The mass is displacing the orbital contents

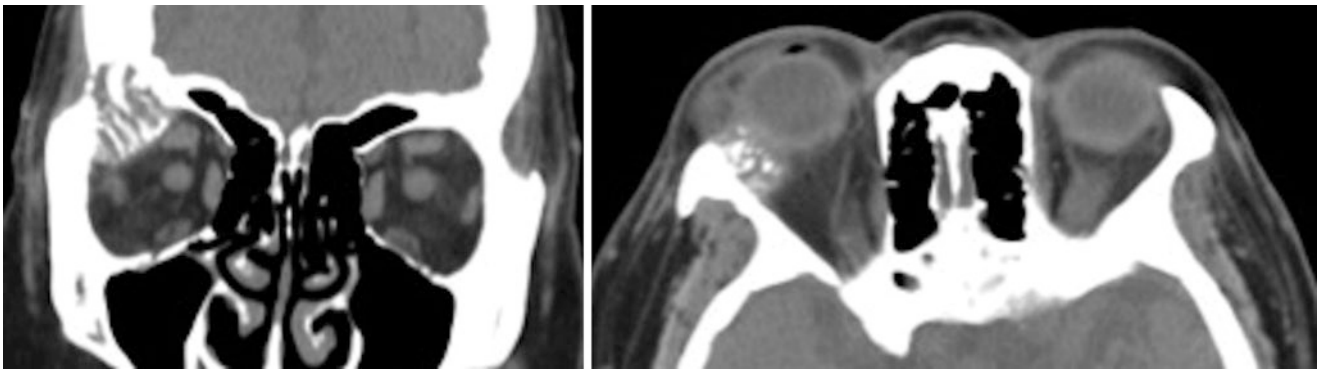


Fig. 2 Non-enhanced CT of the orbits, soft tissue window, coronal view (left) demonstrates a heterogeneous soft tissue mass encased in the right lateral orbital roof with vertical trabeculae "corduroy sign." **Soft tissue window, axial view (right).** There is mild mass effect on the right globe with proptosis

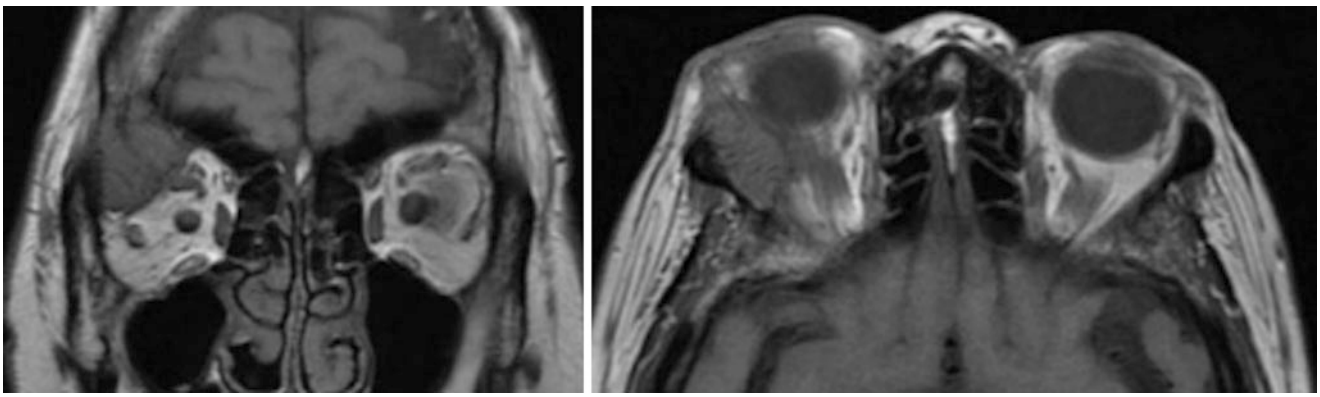


Fig. 3 Coronal (left) and axial (right) T1-weighted fast spin echo (FSE) MR images demonstrate an intraosseous isointense lesion within the superolateral bone of the right orbit. One can still appreciate the delicate trabeculae/dots within the lesion

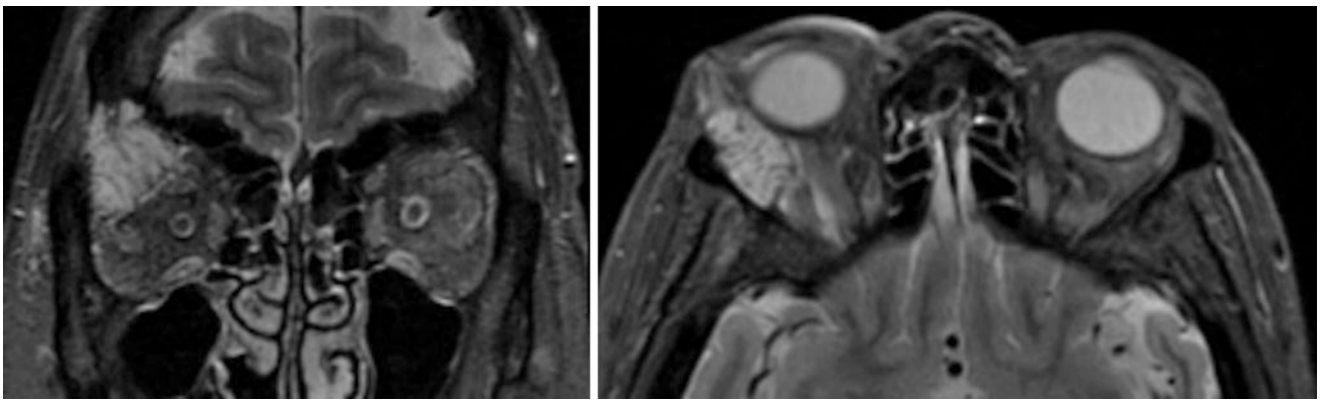


Fig. 4 Coronal (left) and axial (right) fast spin echo inversion recovery (FSE IR) T2-weighted MR images show the lesion is very hyperintense on T2 with fine traversing hypointense trabeculae

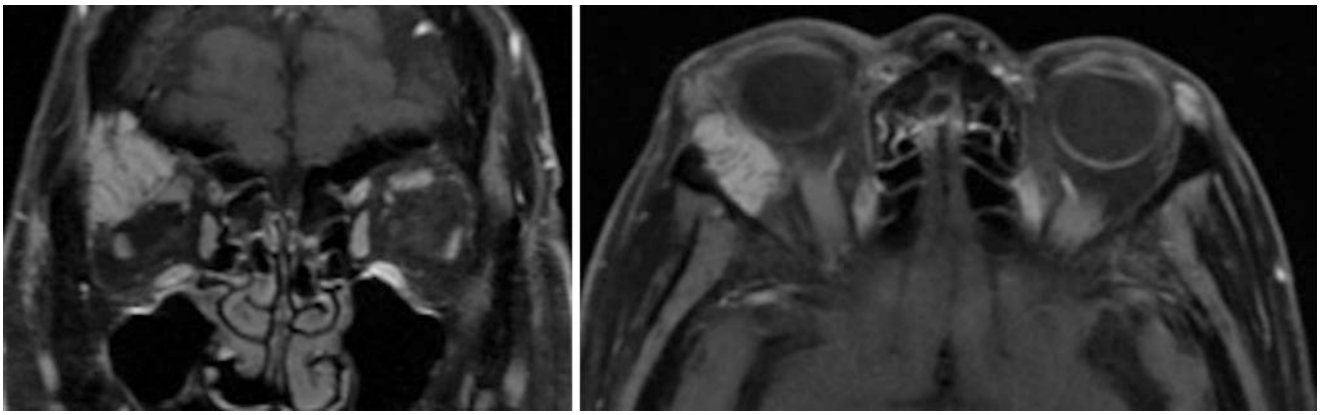


Fig. 5 Coronal (left) and axial (right) T1-weighted fast spin echo (FSE) fat-saturated postcontrast MR images demonstrate avid contrast enhancement, which appears heterogeneous due to vascular lacunae within the lesion (the trabeculae are non-enhancing)

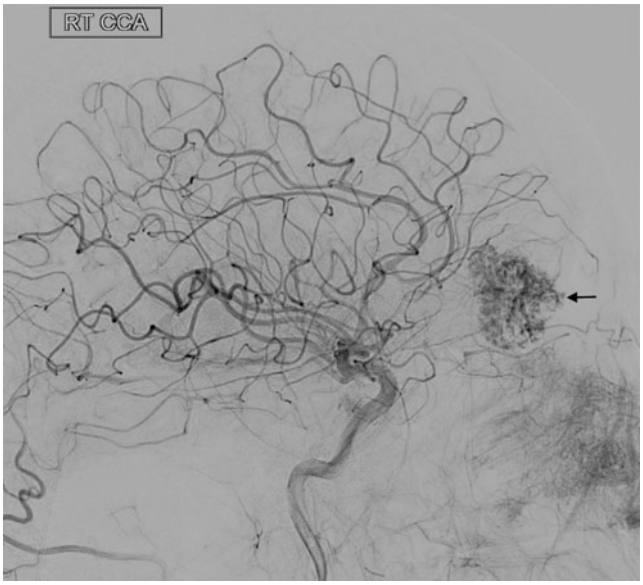


Fig. 6 Cerebral angiography demonstrates early and rapid arterial enhancement of the right superolateral orbital mass (arrow)

5.2 Cholesterol granuloma

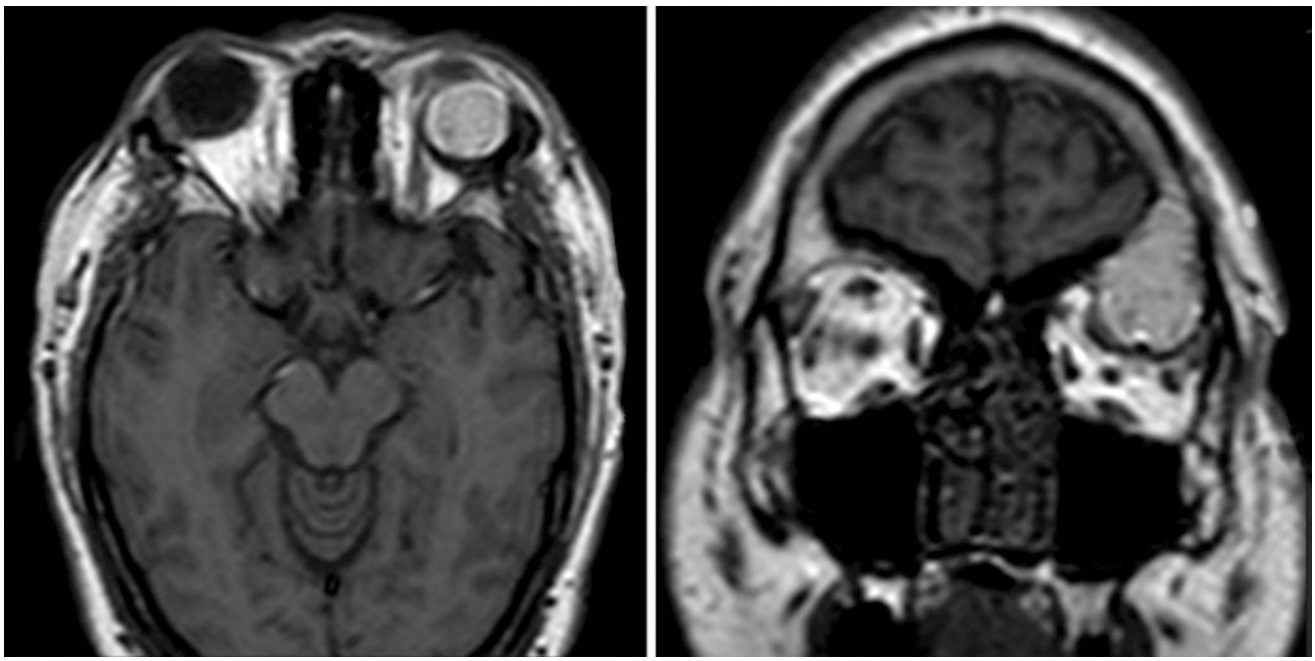


Fig. 7 Axial (left) and coronal (right) T1WI MR depicting a mostly hyperintense but heterogeneous signal within the left orbit

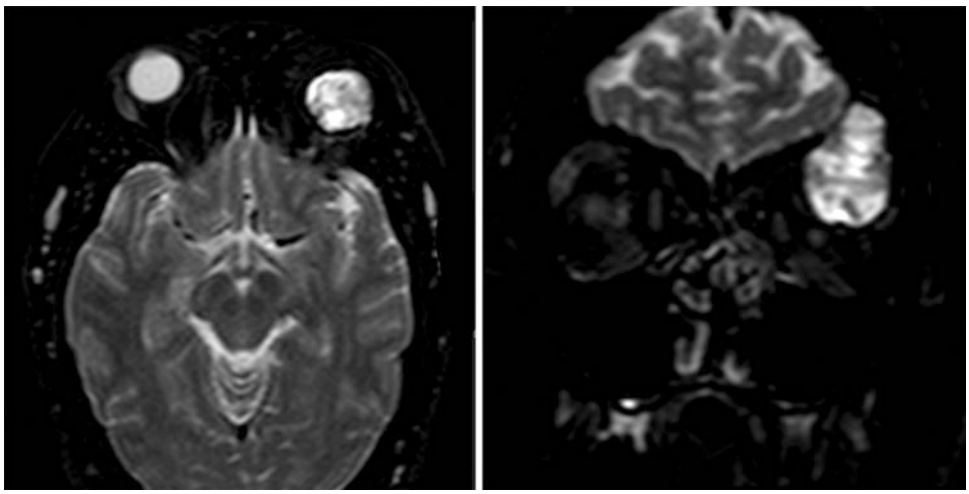


Fig. 8 Hyperintense T2WI axial (left) and coronal (right) depicting a large left frontal bone mass invading the superior-temporal quadrant of the orbit

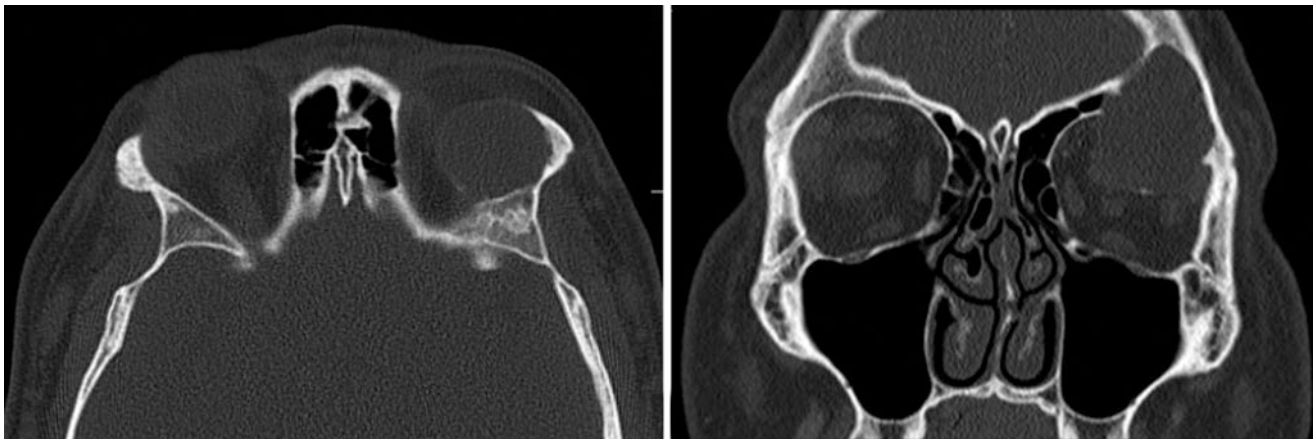


Fig. 9 Axial (left) and Coronal (right) non-enhanced orbital CT scans, bone window, showing the origin of the tumor from the diploic space of the left sphenoid wing and frontal bone

References

1. Garrity JA, Henderson JW, Cameron JD. Henderson's orbital tumors. 4th ed. Philadelphia: Lippincott Williams & Wilkins, 2007. Fibro-Osseous, Osseous, Cartilaginous, Vascular, and Inflammatory Tumors of Orbital Bone;111–3.
2. Rootman J. Diseases of the orbit: a multidisciplinary approach. 2nd ed. Philadelphia: Lippincott Williams & Wilkins, 2003. Chapter 9: Neoplasia;302.
3. Sweet C, Silbergleit R, Mehta B. Primary intraosseous hemangioma of the orbit: CT and MR appearance. AJNR Am J Neuroradiol. 1997;18(2):379–81.
4. Kessler LA, Lubic LG, Koskoff YD. Epidural hemorrhage secondary to cavernous hemangioma of the petrous portion of the temporal bone. J Neurosurg. 1957;14(3):329–31.
5. Elhelf IAS, Maheshwarappa RP, Hodgson J, Hodgson CK, Pollard J, Menda Y. Giant vertebral hemangioma masquerading as aggressive tumor: Tc-99m tagged RBC scan can help to solve the diagnostic conundrum! Radiol Case Rep. 2019;14(11):1360–3.
6. Choi JS, Bae YC, Kang GB, Choi KU. Intraosseous hemangioma of the orbit. Arch Craniofac Surg. 2018;19(1):68–71. https://doi.org/10.7181/acfs.2018.19.1.68. Epub 2018 Mar 20. PMID: 29609437; PMCID: PMC5894550
7. Rizvi SA, Hasan M, Alam MS. Cholesterol granuloma of the orbit: an atypical presentation. Indian J Ophthalmol. 2014;62(3):344–6. https://doi.org/10.4103/0301-4738.111187. PMID: 23619491; PMCID: PMC4061677
8. Hsu H-T, Liao W-C, Wu C-C, Lai P-H. Cholesterol granuloma of the orbit. Kaohsiung J Med Sci. 2017;33(8):422–3. https://doi.org/10.1016/j.kjms.2017.04.007.
9. Loeffler KU, Kommerell G. Cholesterol granuloma of the orbit-pathogenesis and surgical management. Int Ophthalmol. 1997;21(2):93–8.
10. Yan J, Cai Y, Liu R, Lin J, Li J. Cholesterol granuloma of the orbit. J Craniofac Surg. 2015;26(2):e124–6. https://doi.org/10.1097/SCS.0000000000001347. PMID: 25710742

Aneurysmal Bone Cyst and Ewing Sarcoma of the Orbit

60

Stefania B. Diniz, Liza M. Cohen, and Robert A. Goldberg

Contents

1 Signs and Symptoms 440

2 Differential Diagnosis 440

3 Diagnosis 440

4 Treatment 440

5 Figures with Captions 440
5.1 Aneurysmal Bone Cyst 440
5.2 Ewing Sarcoma 442

References 443

Abstract

Aneurysmal Bone Cyst (ABC)

- Nonneoplastic, reactive, multicystic and expansile lesion of the orbit.
- May follow trauma or arteriovenous anomalies of the bone cortex.
- Orbital roof is most commonly involved.
- CT scans show a multiloculated expansile, interdiploic lesion with cortical remodeling.
- Peripheral capsule and internal septations of the lesion are usually enhanced.
- MRI usually depicts a multiloculated isointense lesion on SE/T1, with areas of hyperintensity and high signal intensity on T2-weighted imaging. Fluid levels with heterogeneous signal intensities are the classic appearance, depending upon the state of the included blood.
- Some parts of the lesion may appear densely enhanced with contrast media.

Ewing Sarcoma

- Poorly circumscribed, heterogeneous lesion typically originating from bony wall of the orbit, most commonly the roof
- Osteolytic with mottled "moth-eaten" appearance due to erosion and destruction of bone [1]
- Associated soft tissue component may be present
- Patchy hypodense areas can indicate old hemorrhage and necrosis [2]
- Hypo- to isointense on T1-weighted MR imaging
- Heterogeneously high signal on T2-weighted imaging
- Heterogeneously contrast-enhancing on CT/MR imaging

Keywords

Aneurysmal bone cyst · Orbital tumor · Bone tumor · Proptosis · Ewing sarcoma · Osteolytic lesion

S. B. Diniz · R. A. Goldberg (✉)
Division of Orbital and Ophthalmic Plastic Surgery, Stein and Doheny Eye Institutes, University of California, Los Angeles, CA, USA
e-mail: contato@stefaniadiniz.com; goldberg@jsei.ucla.edu

L. M. Cohen
Division of Orbital and Ophthalmic Plastic Surgery, Stein Eye Institute, University of California, Los Angeles, CA, USA
e-mail: cohenlizam@gmail.com

© Springer Nature Switzerland AG 2022
G. Ben Simon et al. (eds.), *Atlas of Orbital Imaging*,
https://doi.org/10.1007/978-3-030-62426-2_48

1 Signs and Symptoms

Aneurysmal bone cyst's most common signs include axial proptosis and vertical orbital dystopia. Progressive pain is due to stretching of the overlying periosteum. There may be diplopia, local swelling and numbness. Onset of symptoms may be sudden or insidious over months or years. Permanent visual compromise is unusual.

For Ewing sarcoma, mass effect with unilateral proptosis, globe displacement and palpable mass. Signs of infiltration such as pain, decreased vision and motility restriction may be present. Subacute onset and progression. Typically presents in late childhood. Orbital lesions commonly represent metastases, but primary orbital Ewing sarcoma can occur [3].

2 Differential Diagnosis

For ABC, differential diagnosis includes chondroblastoma, telangiectatic osteosarcoma, giant cell tumor, fibrous dysplasia, osteoblastoma and tumoral calcinosis.

For Ewing sarcoma, other solid bony tumors of the orbit including Langerhans cell histiocytosis, plasmacytoma, aneurysmal bone cyst, osteogenic sarcoma, fibrosarcoma, and metastases, as well as pediatric tumors involving bone including epidermoid/dermoid cyst, neuroblastoma, rhabdomyosarcoma and leukemia.

3 Diagnosis

For both entities, diagnosis is based on clinical characteristics and radiologic findings. In patients with ABC, orbital CT scan with contrast enhances the features of the expansile lesions with thick sclerotic borders; fluid levels are better appreciated on MRI. Histopathological evaluation is imperative for a definitive diagnosis for both. Primary orbital Ewing sarcoma is rare; systemic work-up is necessary to evaluate for metastatic disease.

4 Treatment

In ABC, complete surgical curettage to prevent recurrence. May require eburnation of the bone cavity. Surgery is indicated due to mass effect consequences and risk of sudden hemorrhage [4, 5].

For Ewing sarcoma, multidisciplinary including surgical resection, radiation, and adjuvant chemotherapy. A regimen consisting of a combination of vincristine, doxorubicin, cyclophosphamide, etoposide, ifosfamide, adriamycin and actinomycin may be used [6, 7].

5 Figures with Captions

5.1 Aneurysmal Bone Cyst

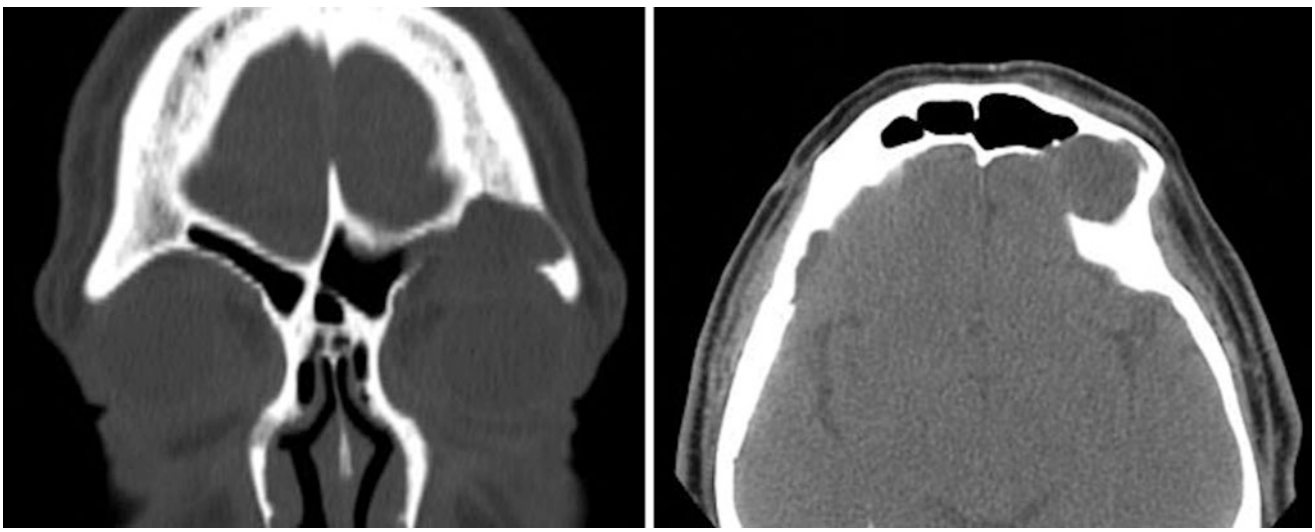


Fig. 1 Coronal bone window (left) and axial soft tissue window (right) nonenhanced CT scans of the head, depicting a superior and lateral lytic bone lesion of the left orbit, causing deep erosion of the orbital roof from within the diploic space and cortical thinning. The lesion is displacing orbital structures inferiorly

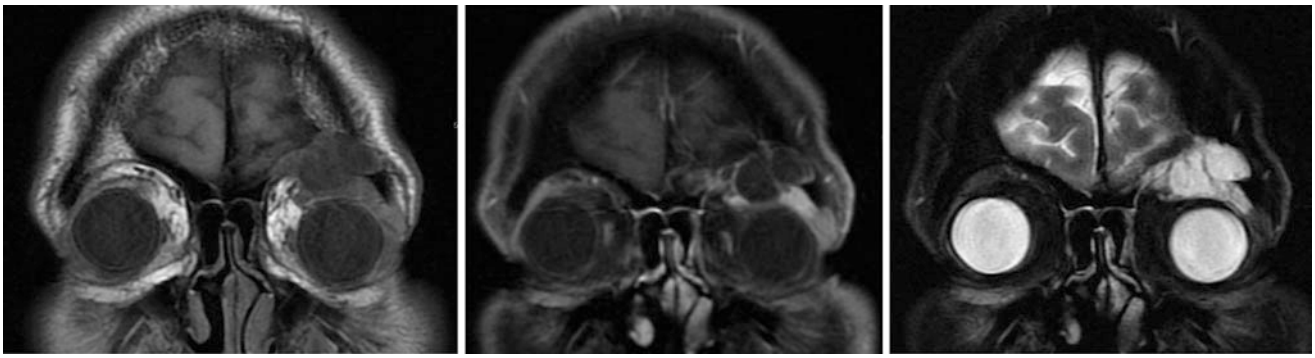


Fig. 2 Coronal MR images of the orbit depicting a multiloculated interdiploic lesion isointense on **T1WI non-FS (left)**, **T1WI CI (middle),** and hyperintense on **T2WI FS (right).** Note the delectae septi within the mass which are better depicted on MR

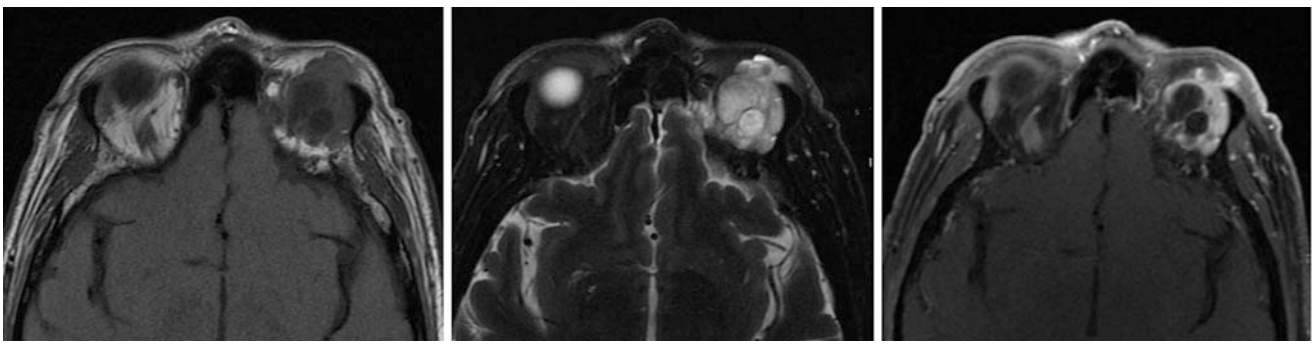


Fig. 3 Axial MR image of the orbit demonstrating a left septated lesion with variable signal intensity on **T1WI (left)**, where hypointense areas stand for the cystic fluid component and the isointense areas represents the soft tissue component. On **T2WI (middle)**, the cystic fluid component is hyperintense. **T1WI CI (right)** depicts enhancement of the cystic septae

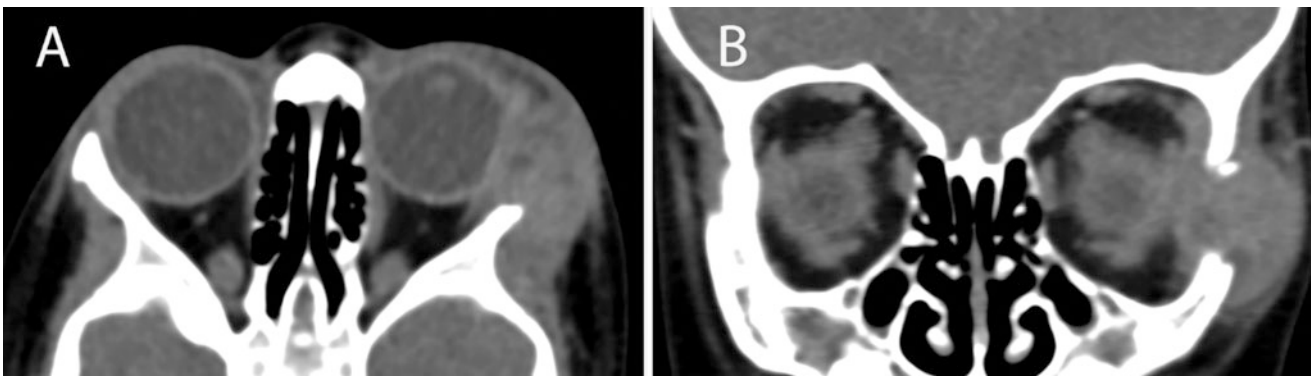


Fig. 4 Orbital CT scan (axial (A) and coronal (B), with contrast) of a 2-YOM with Langerhans cell histiocytosis (LCH) and secondary aneurysmal bone cyst (ABC) in the left frontozygomatic suture showing heterogeneous densities, mixed iso and hypo; the lesion is both intra- and extra-orbital with bone destruction. The lesion is indenting the left border of the globe

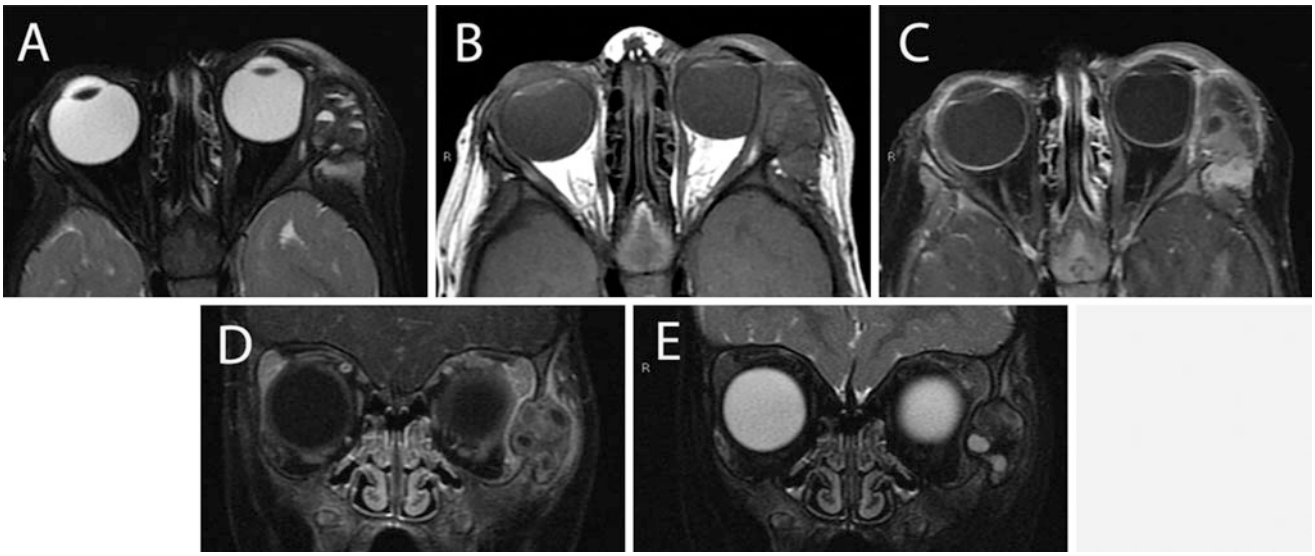


Fig. 5 Corresponding MR images of the same patient, axial sections, **A. T2 FS**, showing the fluid-fluid levels suggestive of ABC formation within the LCH lesion. **B. T1, non-FS nonenhanced image**, portraying the heterogenous intensities within the lesion. **C. T1, FS, with contrast**, better demonstrating the soft tissue and cystic component, as well as the peripheral enhancement. **D and E** showing the same lesion in coronal view, fluid-fluid levels are not demonstrated since the MR acquisition is performed in supine position

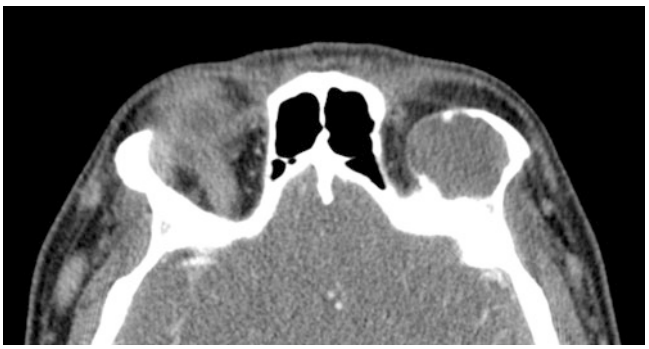


Fig. 6 Axial soft tissue enhanced CT of the orbit depicting a left ABC with peripheral uptake and less activity in the center of the lesion

5.2 Ewing Sarcoma

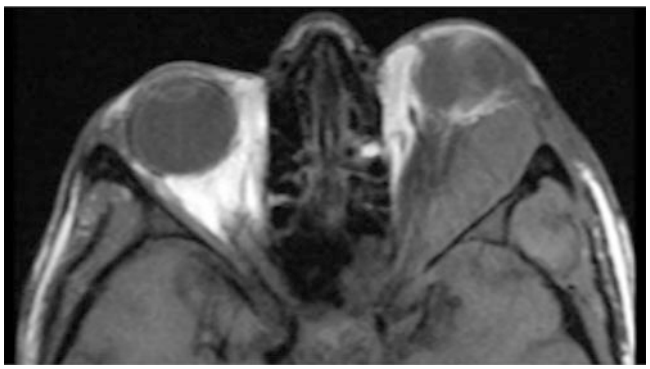


Fig. 7 **Axial T1-weighted MR image (NC, non-FS) of the orbits** demonstrates a poorly circumscribed isointense lesion originating from the greater wing of the left sphenoid with associated soft tissue component involving the left superolateral orbit and temporal fossa with intracranial extension. There is mass effect on the globe with left sided proptosis

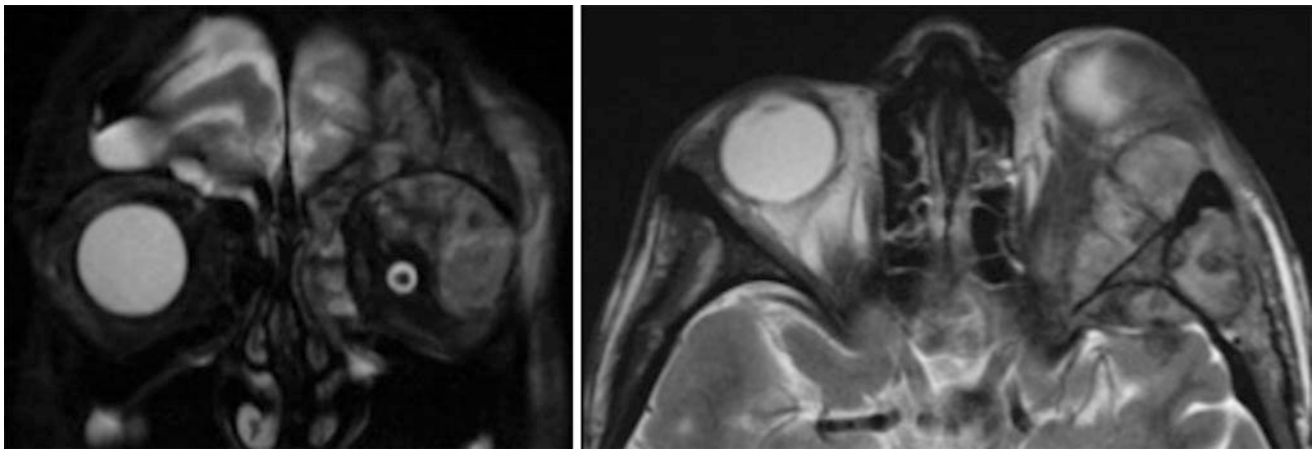


Fig. 8 **T2-weighted MR imaging of the orbits, coronal view FS (*left*) and axial view non-FS (*right*)** demonstrating mostly hyperintense but heterogeneous signal within the lesion

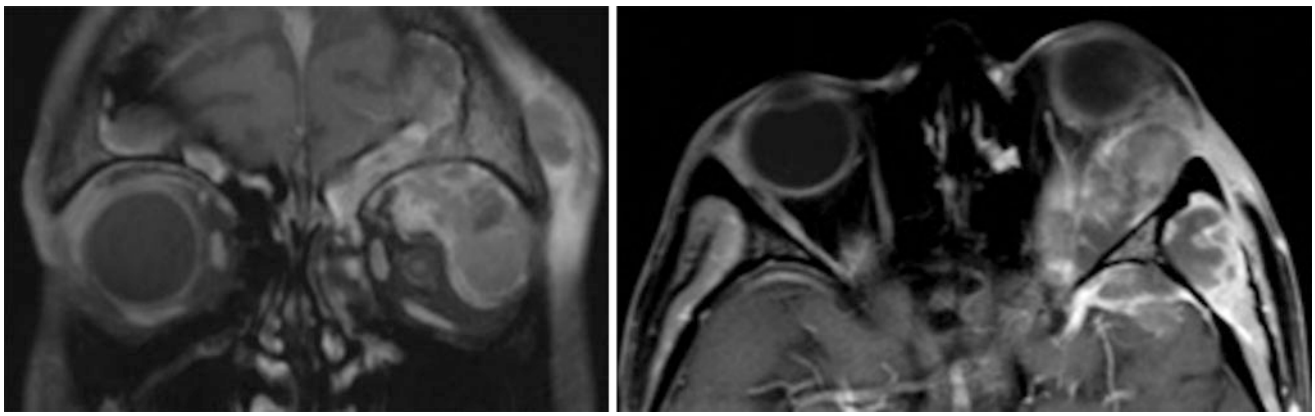


Fig. 9 **T1 FS postcontrast MRI of the orbits, coronal view (*left*) and axial view (*right*)** highlight the osteolytic mottled appearance of the involved bone. There is heterogeneous contrast enhancement of the lesion with scattered para-central nonenhancing areas representing central necrosis. The tumor is infiltrating the periorbital vicinity including the temporalis muscle, fascial planes, and intracranially the dura mater

References

1. Marcol W, Mandera M, Malinowska I, Pajak J, Wlaszczuk P, Kluczewska E. Aneurysmal bone cyst of the orbit. Pediatr Neurosurg. 2006;42:325–7.
2. Wang JC, Zhang M, Zhao XX. Aneurysmal bone cyst of the orbit. Chin Med J (Engl). 2015;128(4):562–3. https://doi.org/10.4103/0366-6999.151120. PMID: 25673465; PMCID: PMC4836266.
3. Rootman J. Chapter 9: Neoplasia. In: Diseases of the orbit: a multidisciplinary approach. 2nd ed. Philadelphia: Lippincott Williams & Wilkins; 2003. p. 299–301.
4. Lomoro P, Simonetti I, Vinci G, Fichera V, Tarotto L, Trovato P, Prevedoni Gorone MS. Secondary aneurysmal bone cyst in Langerhans cell histiocytosis: case report, literature review. Eur J Radiol Open. 2019;6:97–100.
5. Garrity JA, Henderson JW, Cameron JD. Henderson's Orbital Tumors. 4th ed. Philadelphia: Lippincott Williams & Wilkins; 2007. Fibro-osseous, osseous, cartilaginous, vascular, and inflammatory tumors of orbital bone; 101–3.
6. Dutton JJ, Rose JGJR, DeBacker CM, Gayre G. Orbital Ewing's sarcoma of the orbit. Ophthalmic Plast Reconstr Surg. 2000;16(4):292–300.
7. Alfaar AS, Zamzam M, Abdalla B, Magdi R, El-Kinaai N. Childhood Ewing sarcoma of the orbit. J Pediatr Hematol Oncol. 2015;37(6):433–7.

Meningioma of the Orbit and Orbital Vicinity

61

Justin N. Karlin and Robert A. Goldberg

Contents

1 Signs and Symptoms 446

2 Differential Diagnosis 446

3 Diagnosis 446

4 Treatment 446

5 Figures with Captions 447
5.1 Sphenoid Wing Meningioma 447
5.2 Olfactory Groove Meningioma 450
5.3 Extradural meningioma (Recurrent) 450

References 452

Abstract

- *Sphenoid Wing Meningioma*:
  - Classic clinical triad [1] – temporalis fossa fullness, visual field deficit, ophthalmoplegia
  - Anatomically may arise from medial (clinoid), middle, or lateral aspect of sphenoid
  - Extra-axial, often sharply demarcated – spherical, lobulated or "en plaque" (flat) – and may exhibit adjacent dural invasion
  - On nonenhanced CT, appear isodense to brain parenchyma; occasionally may appear slightly hyperdense, and may contain calcifications [4, 5]
    - Typically exhibit intense homogeneous enhancement with contrast administration (as they lack blood–brain barrier)
    - Varying degrees of peritumoral parenchymal vasogenic edema may be seen
    - Commonly associated with hyperostosis, less commonly bony erosion
    - This type of meningioma is usually not confined solely to bone (as it is with metastasis), and is typically seen with an adjacent soft tissue lesion
  - Usually Iso- or hypointense relative to gray matter on nonenhanced T1w and T2w sequences, occasionally hyperintense on T2w sequences [4, 5]
    - Internal signal voids represent tumoral vessels or calcifications, adjacent low signal may be due to hyperostosis (i.e., cortical bone)
    - Heterogeneity may be due to tumor necrosis, heme breakdown products, lipid
    - Homogeneous enhancement with Gd – may appear in adjacent meninges – the so-called "dural tail" (not pathognomonic)
  - Meningiomas have intrinsic lower diffusivity; atypical meningiomas may have even lower ADC values. Diffusion-weighted imaging has not been shown to correlate with histologic behavior or tumor subtype [2]

J. N. Karlin
Division of Orbital and Ophthalmic Plastic Surgery, Stein Eye Institute, University of California, Los Angeles, CA, USA
e-mail: jkarlin@mednet.ucla.edu

R. A. Goldberg (✉)
Division of Orbital and Ophthalmic Plastic Surgery, Stein and Doheny Eye Institutes, University of California, Los Angeles, CA, USA
e-mail: goldberg@jsei.ucla.edu

© Springer Nature Switzerland AG 2022
G. Ben Simon et al. (eds.), *Atlas of Orbital Imaging*,
https://doi.org/10.1007/978-3-030-62426-2_51

- *Olfactory Groove Meningioma*:
  - Olfactory groove meningiomas may displace the chiasm inferiorly and posteriorly, unlike tuberculum sella meningiomas, which displace the chiasm superiorly [3]
  - Extra-axial, often sharply demarcated
  - On nonenhanced CT, appear isodense to brain parenchyma; occasionally may appear slightly hyperdense, and may contain calcifications [4, 5]
    - Typically exhibit intense homogeneous enhancement with contrast administration (as they lack blood–brain barrier)
    - Varying degrees of peritumoral parenchymal vasogenic edema may be seen
    - Hyperostosis is best seen on CT; paranasal sinus invasion can be seen on both modalities
  - Usually iso- or hypointense relative to gray matter on nonenhanced T1w and T2w sequences, occasionally hyperintense on T2w sequences [4, 5]
    - Internal signal voids represent tumoral vessels or calcifications, adjacent low signal may be due to hyperostosis (i.e., cortical bone)
    - Heterogeneity may be due to tumor necrosis, heme breakdown products, lipid
    - Homogeneous enhancement with Gd

Keywords

Sphenoid wing meningioma · Sphenoid ridge meningioma · Meningioma *en plaque* of the sphenoid wing · Orbito-sphenoid meningioma · Sphenoid wing meningioma with osseous involvement · Meningioma *en masse* · Intraosseous meningioma · Clinoidal meningioma · Olfactory groove meningioma · Cribriform plate · OGM

1 Signs and Symptoms

Sphenoid Wing Meningioma: Headache, seizure, facial pain, numbness/paresthesia, temporal fullness with facial asymmetry, unilateral proptosis, eyelid fullness, ptosis, visual field deficit, cranial nerve (oculomotor, trochlear, abducens) palsy, Horner's syndrome, cranial nerve aberrant regeneration, cavernous sinus syndrome, increased intracranial pressure with or without papilledema, transient visual obscurations. Gradual onset and progression. Associated with neurofibromatosis type II.

Olfactory Groove Meningioma: Headache, personality changes, akinesia, apathy, anosmia (not typically a primary complaint), visual field deficit, Foster-Kennedy syndrome. Gradual onset and progression. Often large at the time of presentation

2 Differential Diagnosis

For sphenoid wing meningioma: Fibrous dysplasia, osteoma, Paget disease of bone, aneurysmal bone cyst, Brown tumor, osteogenic sarcoma, metastatic carcinoma (ex. prostate), myeloma/plasmacytoma, giant cell tumor, neurosarcoidosis, fungal or tuberculous granulomatous disease, epidermoid/dermoid cyst, lymphoma, hemangiopericytoma (of bone), sarcoma

For olfactory groove meningioma: Tuberculum sellae meningioma, subfrontal schwannoma, solitary fibrous tumor or hemangiopericytoma, lymphoma, esthesioneuroblastoma

3 Diagnosis

Clinical characteristics, demographics, and radiologic findings. Diagnosis confirmed by tissue biopsy.

4 Treatment

Observation for small, asymptomatic lesions, especially in elderly patients and poor surgical candidates. For middle and lateral meningiomas, transcranial or transorbital resection (or combined approach) may be employed. Resection of clinoidal meningiomas requires craniotomy. Radiosurgery, radiation, hormone therapy, and chemotherapy have been used.

5 Figures with Captions

5.1 Sphenoid Wing Meningioma

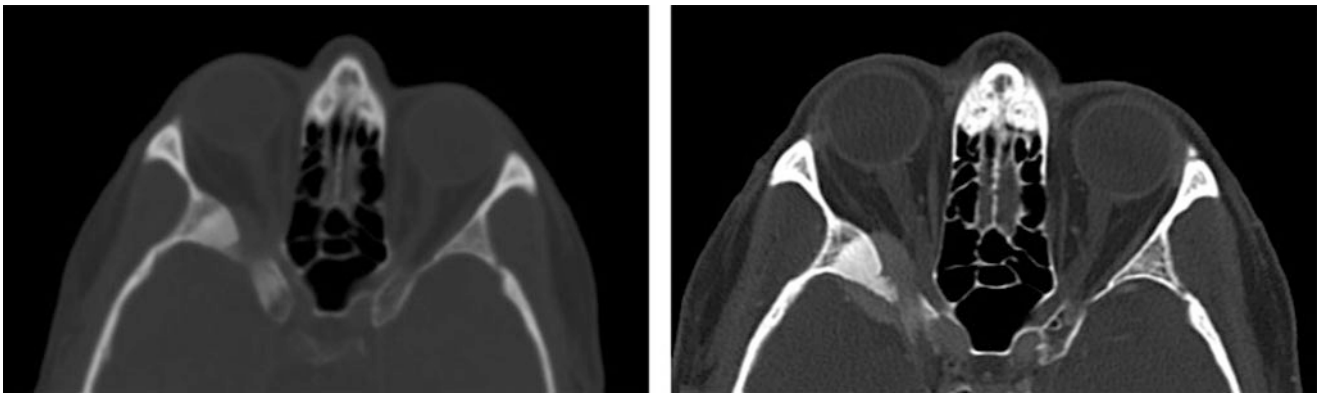


Fig. 1 Pre- (left) and post-contrast (right) axial orbit CT. Bone window. *En plaque* meningioma of the middle portion of the right greater sphenoid wing causing right proptosis. There is soft tissue involvement on both the orbital side and the middle cranial fossa, and associated hyperostosis

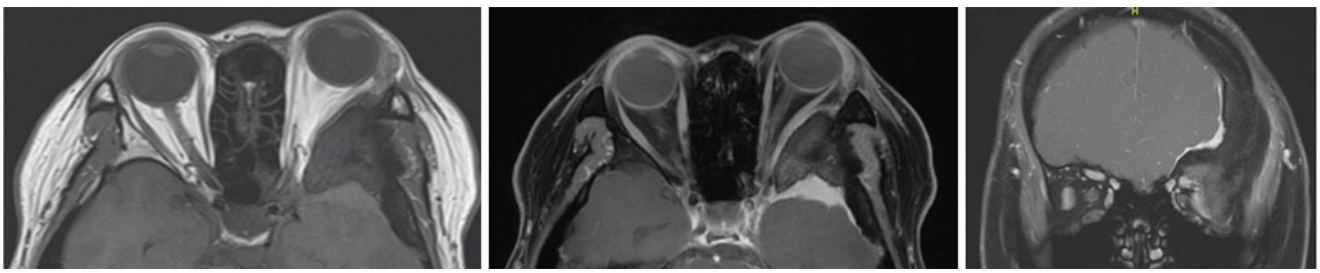


Fig. 2 Left image – Conventional non-contrast axial T1w MRI orbit showing a hypointense intraosseous lesion of the middle- and lateral thirds of the greater wing of the sphenoid, resulting in left proptosis. **Middle image – Gd contrast axial T1w MRI orbit with fat saturation** showing the same lesion with temporal dural enhancement and thickening, as well as lateral sub-periorbital enhancement. **Right image – Gd contrast coronal T1w MRI orbit with fat saturation** showing enhancement of orbital component with inferomedial displacement of orbital apex, and superior extent of intraosseous tumor

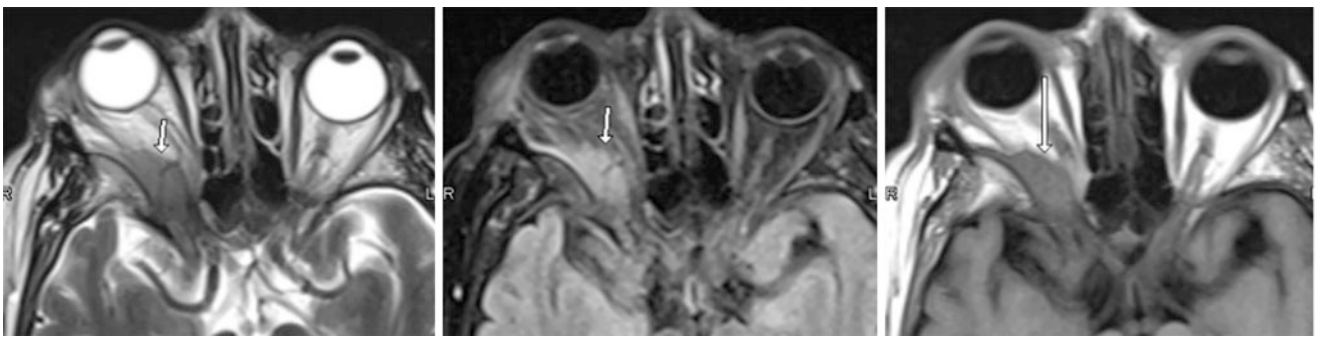


Fig. 3 Left image – non-contrast axial T2w MRI orbit demonstrating a right isointense orbital soft tissue component of meningioma emanating from the middle third of the greater sphenoid wing, causing proptosis. **Middle image – Gd contrast T2w FLAIR MRI orbit** showing homogeneous contrast enhancement of the lesion. **Right image – non-contrast axial T1w FLAIR MRI orbit** showing isointense lesion of right middle sphenoid wing causing displacement and compression of optic nerve

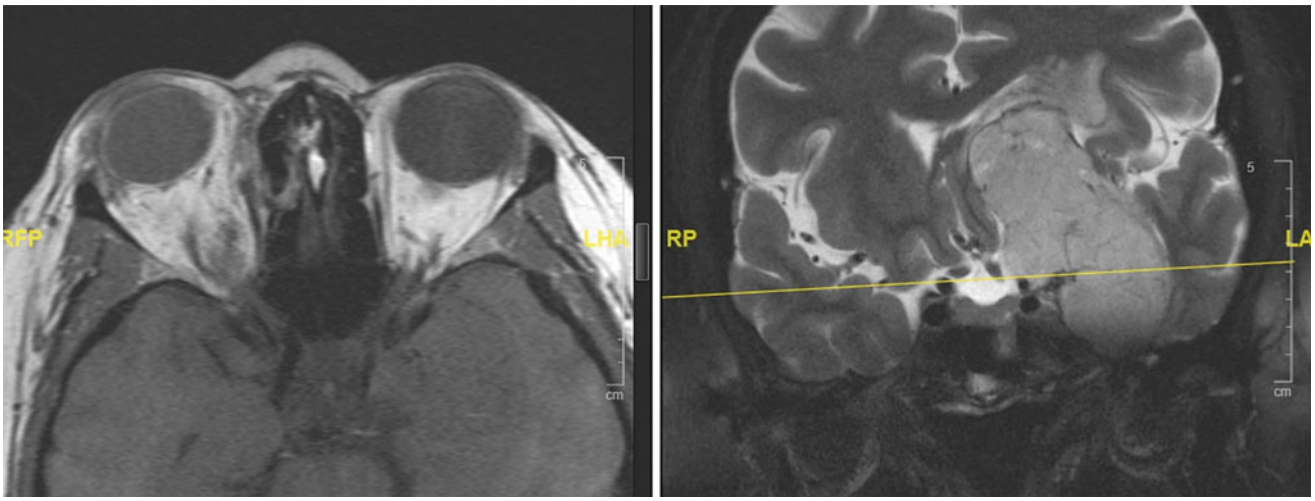


Fig. 4 **Left image – non-contrast axial T1w MRI orbit** through the superior third of the orbit showing a subtle left isointense medial meningioma emanating from the anterior clinoid. **Right image – non-contrast axial T2w MRI brain** demonstrating a hyperintense lesion emanating from the anterior clinoid causing significant mass effect on both temporal and fronto-basal lobes with accompanying midline shift and compression of the left lateral ventricle. The heterogeneity of the superior aspect of the tumor may be due to tumoral vessels or calcifications or both. Vasogenic edema is seen superior to the tumor. The yellow line demonstrates the plane of the left image

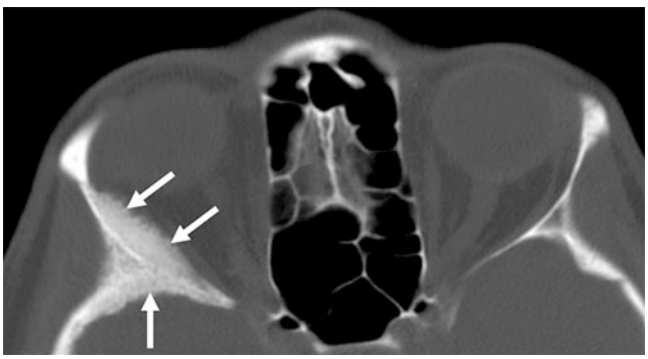


Fig. 5 **Axial post-contrast CT orbit, bone window**. This is a 64-year-old female who presented with a gradual onset of right painless proptosis. There is a hyperostotic expansion of the right sphenoid bone and lateral orbital wall with irregular margins (arrows)

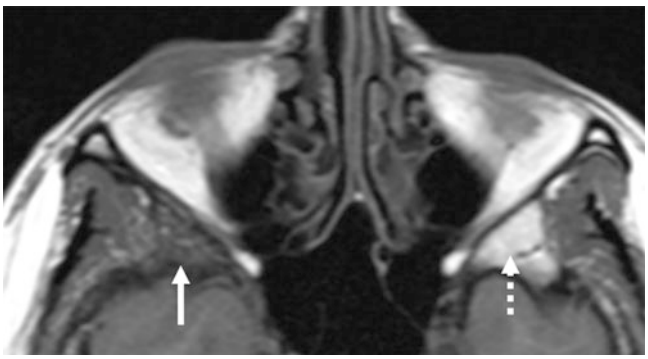


Fig. 6 **Axial T1 pre-contrast image** (same patient as in Fig. 5) shows replacement of the normal marrow signal in the right sphenoid bone (arrow). Note the normal fatty marrow signal in the contralateral left sphenoid bone (dotted arrow)

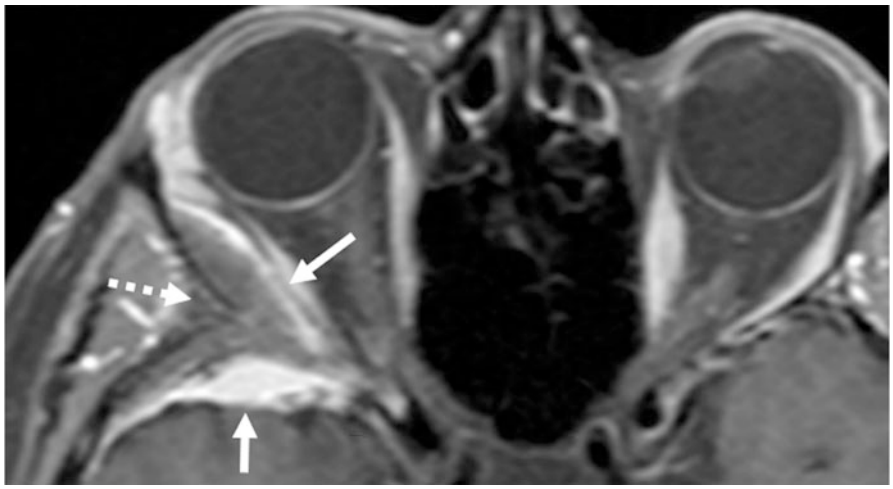


Fig. 7 Axial T1 post-contrast fat-saturated image (same patient as in Fig. 5) demonstrates enhancement of the soft tissue component of the meningioma in the lateral right orbit and middle cranial fossa (arrows) at the edges of the hyperostotic bone (dotted arrow)



Fig. 8 Axial T1 post-contrast fat-saturated image (different patient). This image shows an enhancing mass epicentered in the left sphenoid bone and involving both extraconal space of the left orbit and the middle cranial fossa (arrows). There is secondary globe proptosis and crowding of the orbital apex

(Figs. 5, 6, 7, 8, and 9 *courtesy of Oded Sagiv, J. Matthew Debnam, and Bita Esmaeli)*

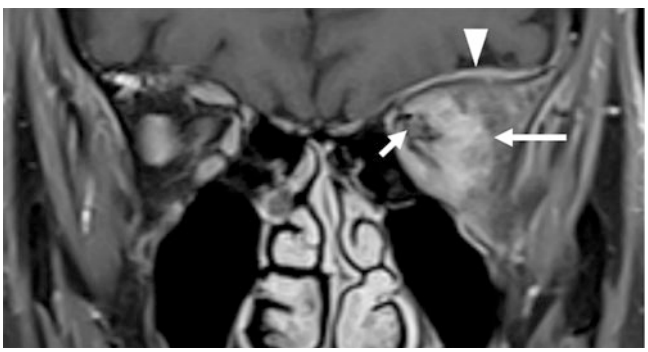


Fig. 9 Coronal T1 post-contrast fat-saturated image (same patient as in Fig. 8) demonstrates the orbital component of the mass (arrow). Note medial displacement of the left optic nerve (small arrow). There is medial cranial fossa dural involvement (meningioma en plaque, arrowhead)

5.2 Olfactory Groove Meningioma

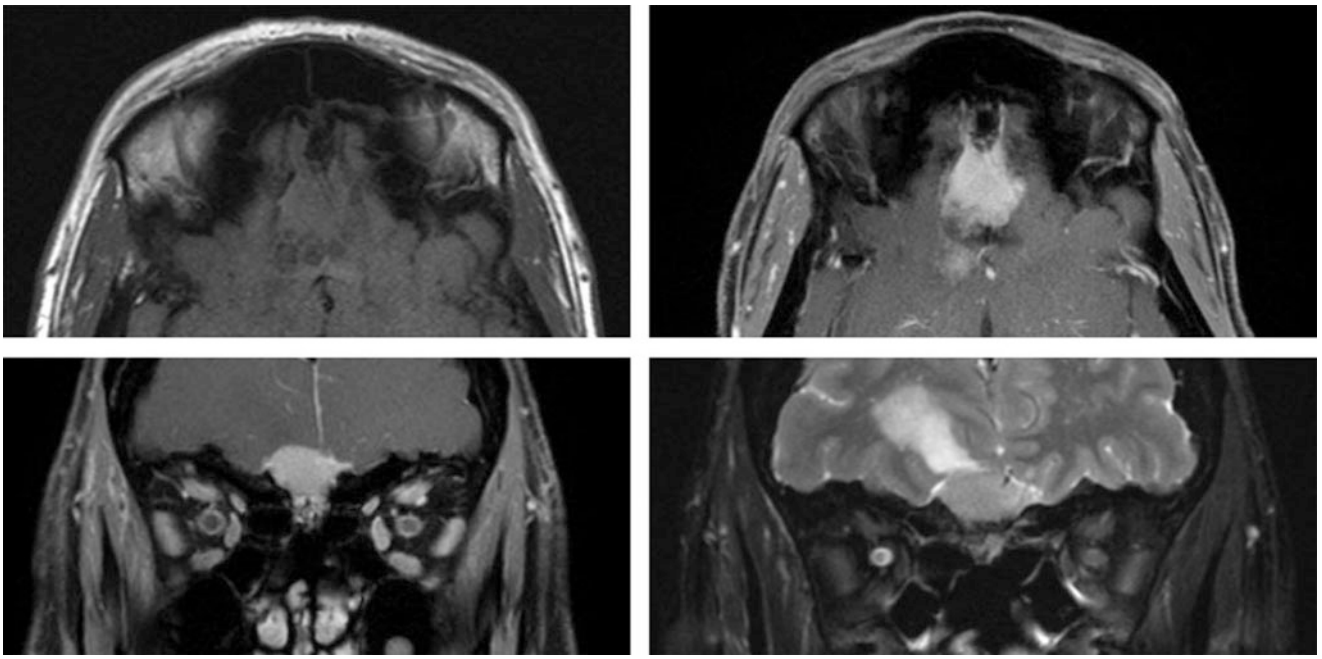


Fig. 10 MRI orbit. Upper left non-contrast axial T1w with fat suppression image shows an olfactory groove meningioma, an isointense lesion of the midline abutting ethmoid sinuses. **Upper right T1w with Gd contrast axial** and **bottom left T1w with Gd contrast coronal** images highlight the same lesion. The **bottom right non-contrast coronal T2w MRI orbit with fat saturation** shows the lesion isointense to gray matter, crossing midline, with vasogenic edema extending to the right gyrus rectus and frontal white matter. The tumor is also invading the anterior skull base through the cribriform plate

5.3 Extradural meningioma (Recurrent)

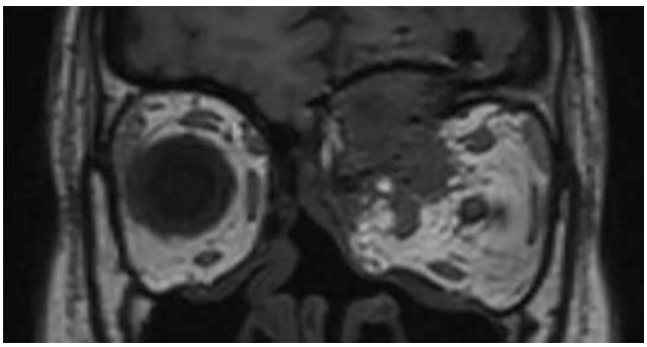


Fig. 11 NE MR T1, coronal view of an 18-YOF with recurrent left fronto-ethmoid meningioma and orbital involvement. The tumor has soft tissue intensity, is poorly defined and invading the superomedial orbit displacing the SR and the MR muscles and the ON. Note the previous orbital decompression, and metallic mesh at the superior border of the tumor

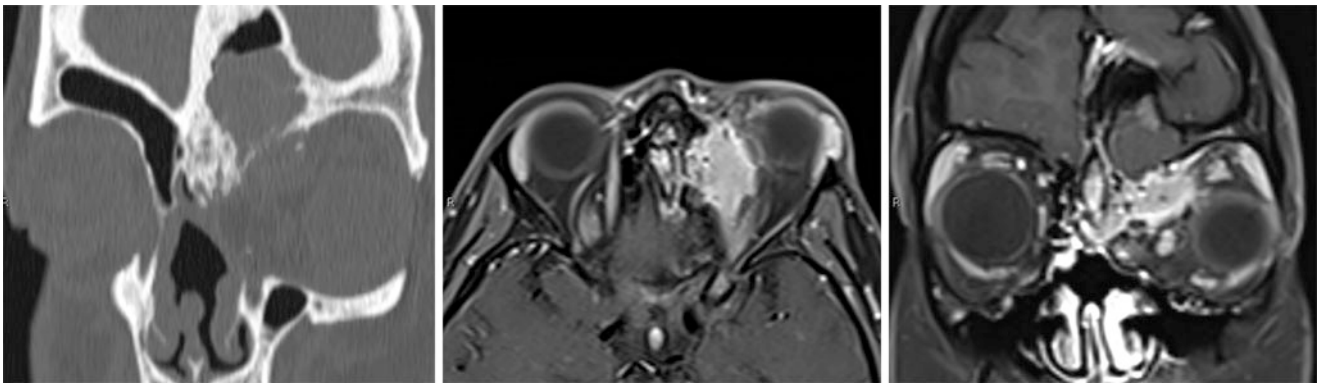


Fig. 12 Coronal CT (*left*), CE FS T1 MR axial (*middle*) and coronal (*right*) showing the tumor has bony and soft tissue components, and is invading the superomedial orbit displacing the orbital content. The MR shows contrast enhancement typical of meningiomas

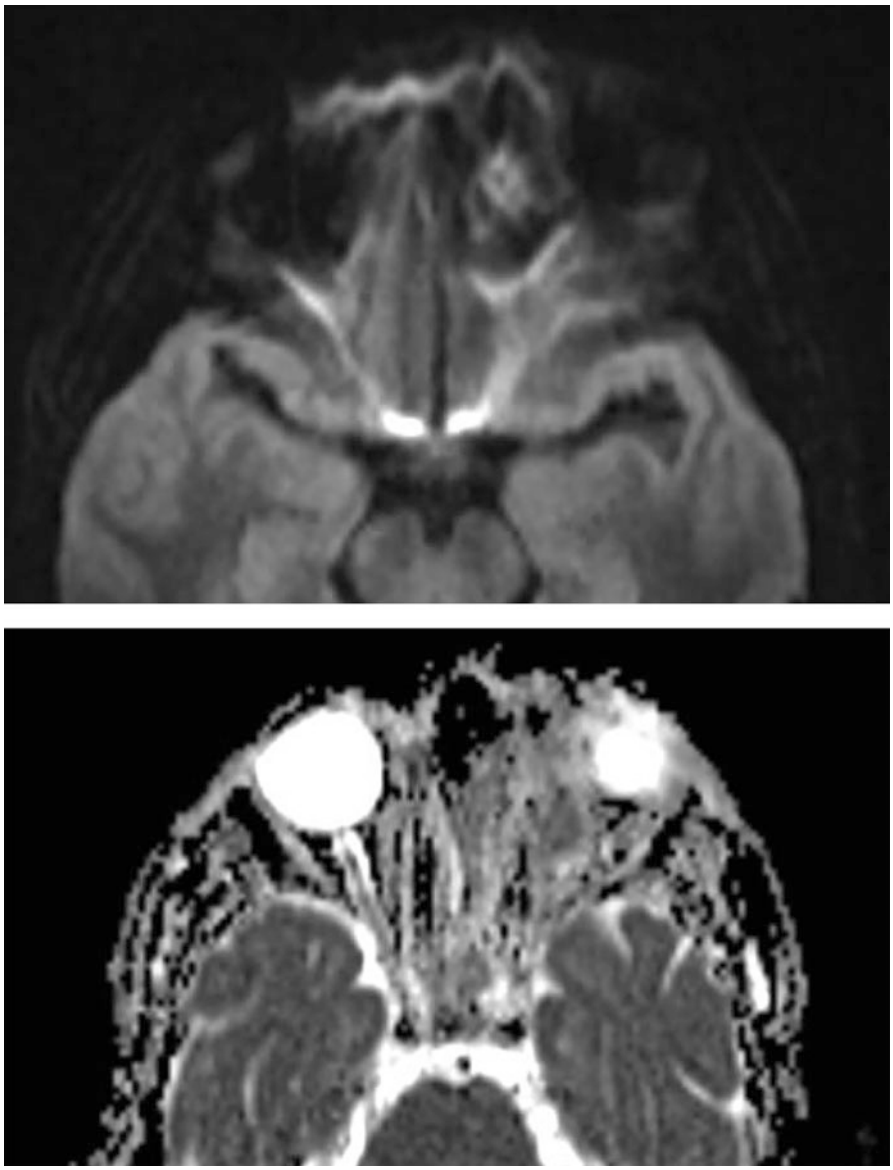


Fig. 13 DWI (*upper*) with corresponding ADC map (*lower*) of the patient demonstrates restriction in keeping with the hypercellular nature of the meningioma. (Figs. 11, 12, and 13 courtesy of the editors) Extradural meningioma

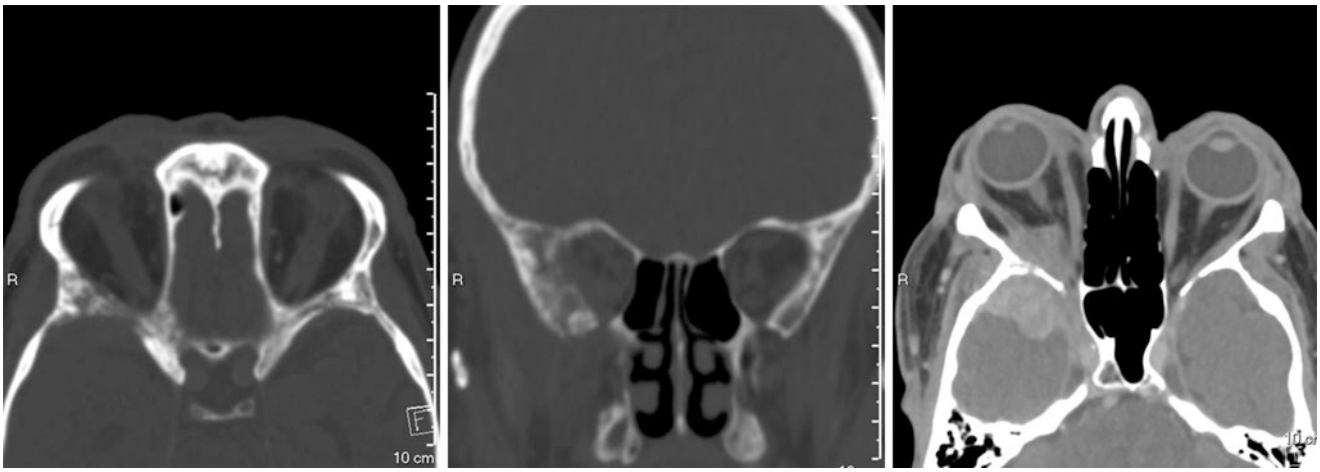


Fig. 14 Axial and coronal CT images, bone window (*left* and *middle*) demonstrating the less common osteolytic/permeative pattern of a presumptive primary intraosseous meningioma in the right sphenoid wing. An axial post contrast image with soft tissue windowing (right) shows the full extent of the lesion

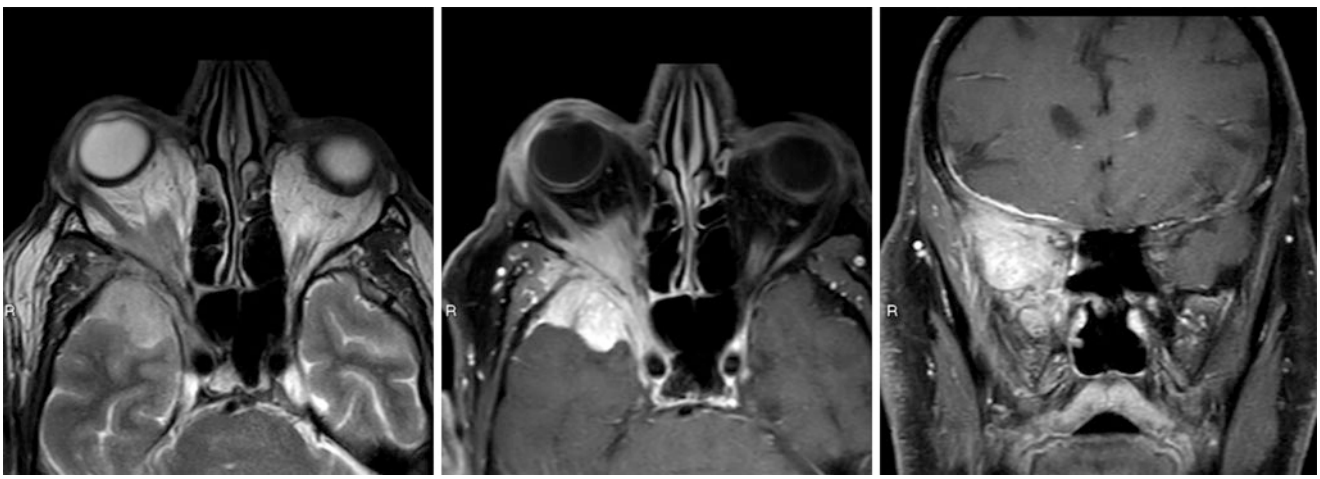


Fig. 15 MRI images of the same patient (Ax T2-*left* image, Ax T1 FS post Gd-*middle* image) portraying the enhancing expansile lobular mass with classic trilateral involvement including orbit, middle cranial fossa and extracranial temporal fossa. The coronal T1 FS contrast enhanced image on the right depicts the typical enhancing "dural tail" along the anterior cranial fossa

References

1. Lee JH. Meningiomas: diagnosis, treatment, and outcome. London: Springer; 2008. p. 639. xxiii.
2. Sanverdi SE, et al. Is diffusion-weighted imaging useful in grading and differentiating histopathological subtypes of meningiomas? Eur J Radiol. 2012;81(9):2389–95. https://doi.org/10.1016/j.ejrad.2011.06.031.
3. Hentschel SJ, DeMonte F. Olfactory groove meningiomas. Neurosurg Focus. 2003;14(6):E4.
4. Lyndon D, et al. Dural masses: meningiomas and their mimics. Insights Imaging. 2019;10(1):11.
5. Huang RY, et al. Imaging and diagnostic advances for intracranial meningiomas. Neuro-Oncology. 2019;21(Suppl 1):i44–61.

Part IX

Optic Nerve

Optic Nerve Glioma: Pilocytic Astrocytoma

62

Yoon-Duck Kim

Contents

1 **Signs and Symptoms** 455
2 **Differential Diagnosis** 455
3 **Diagnosis** 455
4 **Treatment** 455
5 **Figures with Captions** 456
References 465

Abstract

- Optic nerve glioma (ONG) is the most common primary tumor of the optic nerve.
- On CT and MRI, gliomas present as fusiform or tubular enlargement of optic nerve with smooth, well-defined dural margins, often with kinking of the optic nerve.
- CT scan demonstrates the tumor of similar density to normal optic nerve with heterogeneous and variable enhancement after contrast infusion. Calcification is rare. Widening of optic canal and cystic degeneration can be seen.
- On MRI, gliomas are isointense on T1W images, hyperintense on T2W images, and show variable enhancement. ONG can grow in two distinct patterns: intraneural glial proliferation and perineural arachnoidal gliomatosis, which is more typical but not exclusive of NF-1.

Keywords

Enlargement · Fusiform · Tubular · Optic nerve

Y.-D. Kim (✉)
Oculoplastic and Orbital Surgery Division, Nune Eye Hospital, Seoul, South Korea
e-mail: ydkimoph@skku.edu

1 Signs and Symptoms

Proptosis, visual loss, optic disc swelling or pallor, strabismus [1, 2]. Rarely optociliary shunts. There is an association with neurofibromatosis type 1 [3].

2 Differential Diagnosis

Optic nerve sheath meningioma, medulloepithelioma.

3 Diagnosis

Clinical findings and characteristic radiologic findings. Tissue biopsy is rarely needed [4].

4 Treatment

Regular follow-up with clinical, functional, and imaging studies. Surgical removal is reserved for patients with severe disfiguring proptosis or progressive posterior extension of the tumor with neuroimaging [6]. Radiotherapy and chemotherapy for aggressive tumors [5, 8].

© Springer Nature Switzerland AG 2022
G. Ben Simon et al. (eds.), *Atlas of Orbital Imaging*,
https://doi.org/10.1007/978-3-030-62426-2_54

5 Figures with Captions

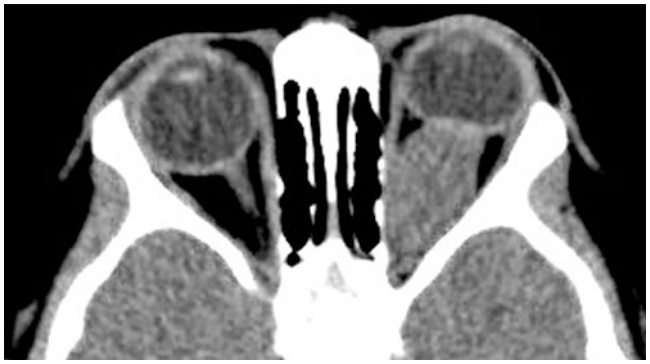


Fig. 1 Pre-contrast axial CT scan shows a fusiform enlargement of the left optic nerve/sheath complex with a smooth, well-defined margin produced by the intact dura. The mass is causing axial proptosis and flattening of the posterior globe

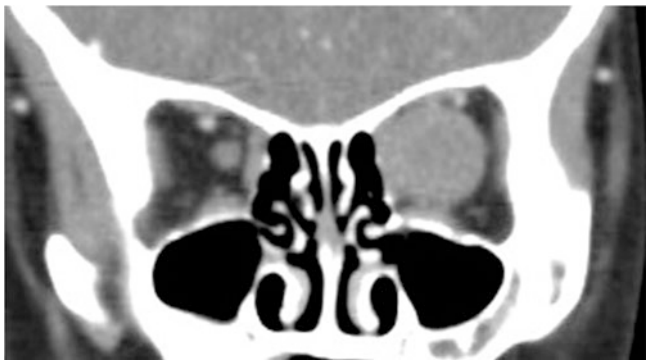


Fig. 2 Post-contrast coronal CT scan shows a left intraconal mass inseparable from the optic nerve with uniform mild enhancement



Fig. 3 Axial T1-weighted MR image showing a well-defined, isointense fusiform mass, connected with the optic nerve (arrow)

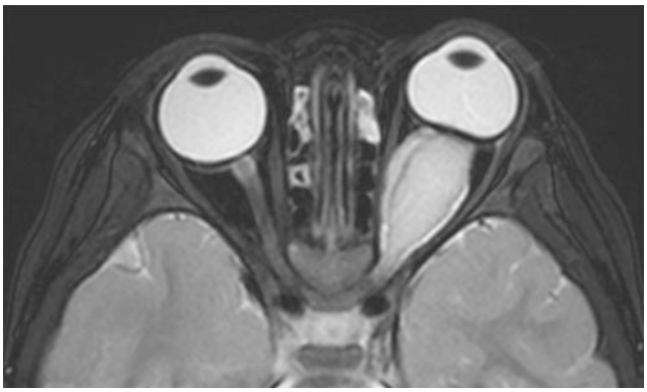


Fig. 4 Axial T2-weighted MR image showing a hyperintense, fusiform enlargement of the optic nerve. Asymmetrical thickening of the medial border of the mass may suggest perineural arachnoidal gliomatosis

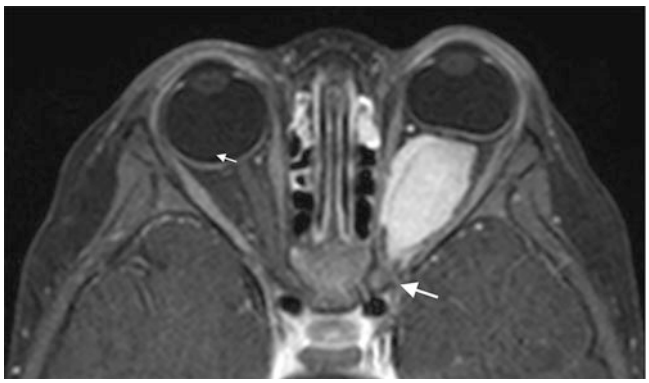


Fig. 5 Post-contrast axial T1 fat-saturated image showing a well-defined enhancing intraconal mass. The tumor does not involve the proximal optic nerve (arrow). MRI is useful for assessing the range of tumor involvement in the optic nerve and intracranial extension [7]

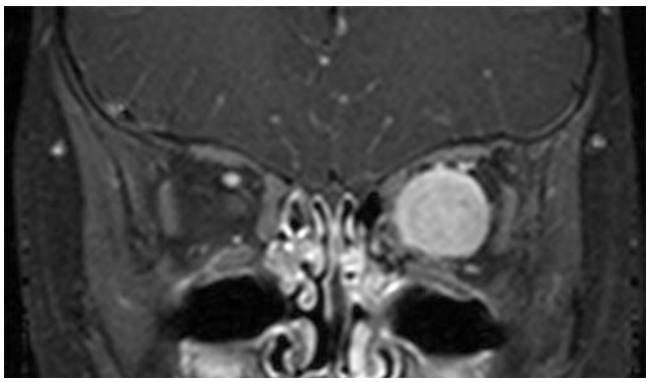


Fig. 6 Post-contrast coronal T1 fat-saturated image showing a well-enhancing intraconal mass. The optic nerve is not distinguished from the tumor, which is an imaging feature differentiating processes originating in the nerve vs the optic nerve sheath, e.g., meningioma



Fig. 7 Axial T1-weighted MR image of different patient showing a well-defined, tubular enlargement of the right optic nerve

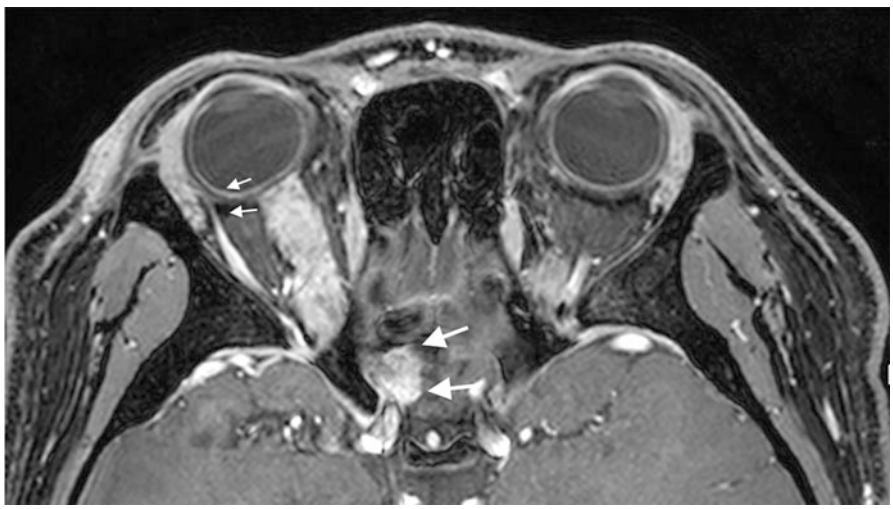


Fig. 8 Post-contrast axial T1 fat-saturated image showing a well-defined enhancing intraconal mass with intracranial extension to the pre-chiasmatic segment of the optic nerve (arrows)

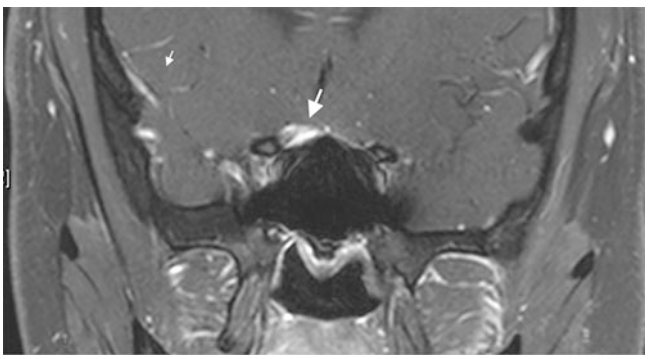


Fig. 9 Post-contrast coronal T1 fat-saturated image showing intracranial extension to the pre-chiasmatic segment of the optic nerve (arrow)

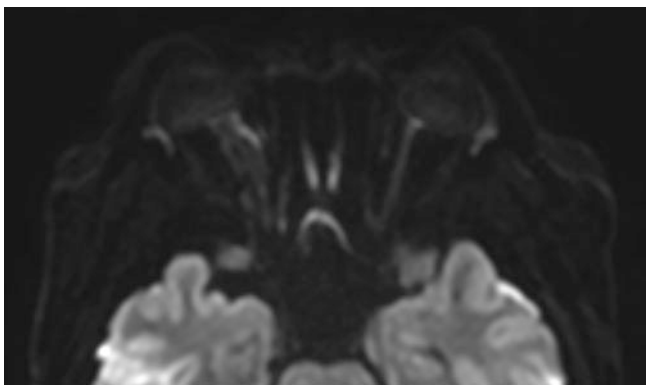


Fig. 10 Axial DWI image of this patient showing high signal of glioma along the right optic nerve [1]

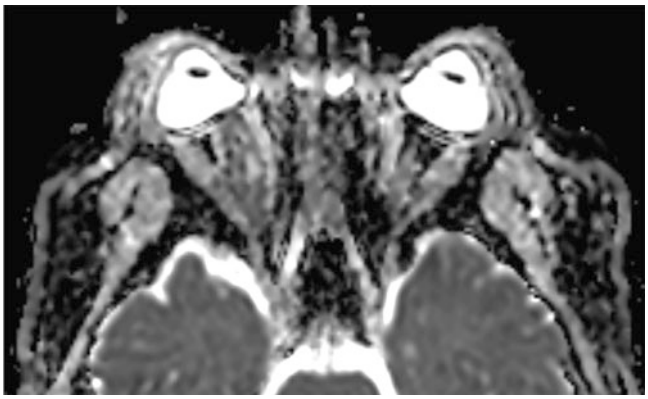


Fig. 11 Axial ADC map showing low ADC values of glioma along the optic nerve. When compared with meningioma, glioma shows a relatively brighter lesion on the ADC map and higher mean ADC values

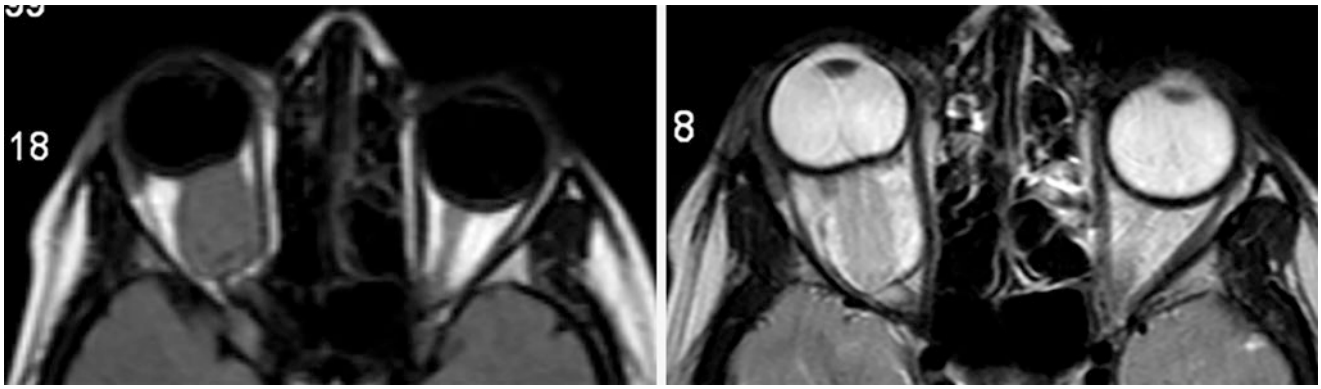


Fig. 12 MRI of a 9-year-old child with recent onset right side painless proptosis. He had decreased vision with signs of optic neuropathy. T1 axial view (*left*) showing tubular enlargement of the intra-orbital optic nerve with right side proptosis. The tumor is isointense on T1 and mixed signal on T2WI – centrally iso – with peripheral hyperintensity (*right*). Suggestive of optic nerve glioma

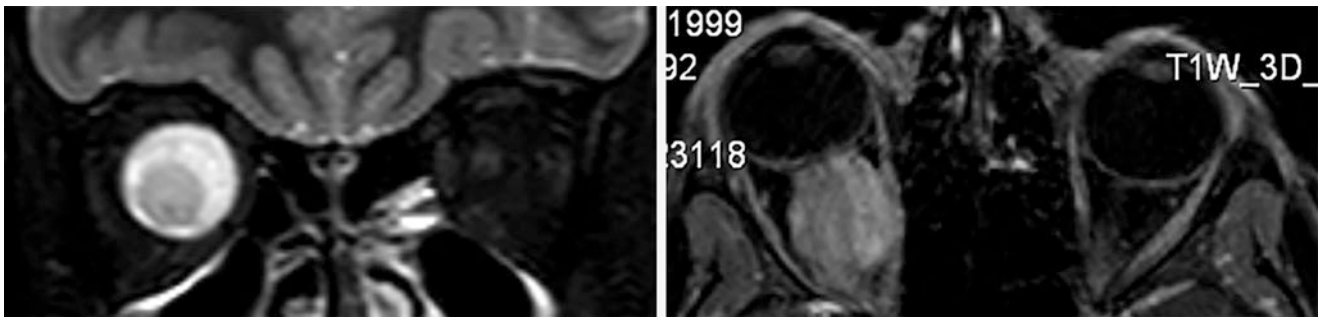


Fig. 13 STIR coronal view (*left*) and T1 FS CE axial MR (*right*) of the same patient showing optic nerve enlargement and hyperintense ONS thickening evident of perineural arachnoid gliomatosis typical of optic nerve glioma. The tumor shows solid enhancement as seen on the axial section (*right*)



Fig. 14 Clinical photograph of a 12-year-old child with right side axial proptosis and inferior temporal globe displacement with near-blind eye secondary to long standing optic nerve glioma

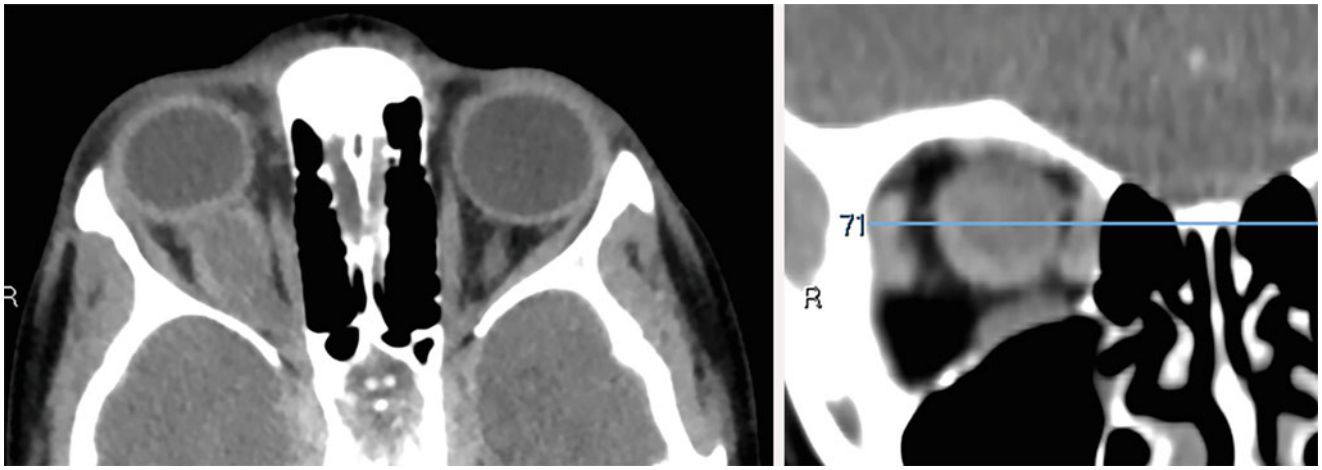


Fig. 15 CECT of the same child at 7 years of age, showing fusiform isodense enlargement of the right optic nerve with mild contrast enhancement at the vicinity of the nerve typical of optic nerve glioma. Axial (*left*) and coronal (*right*)

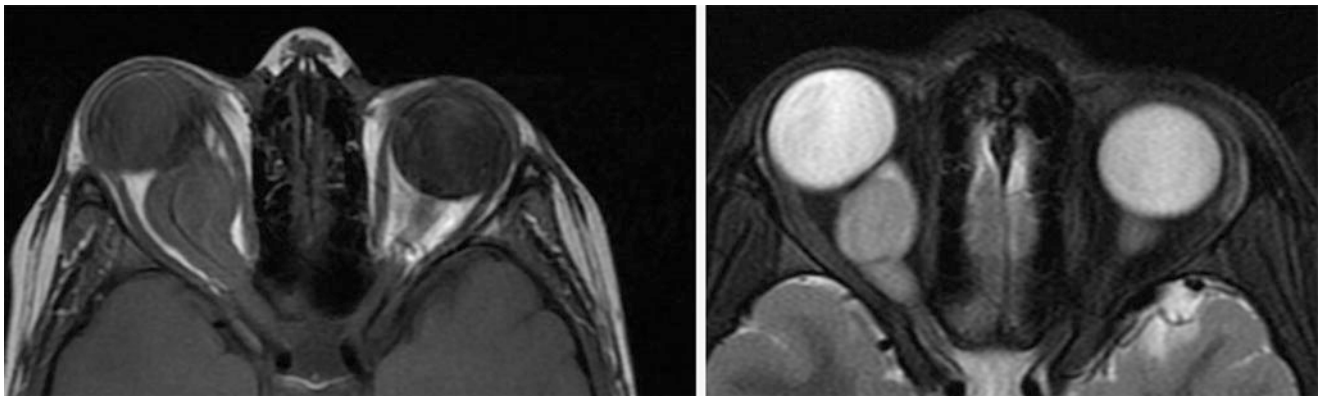


Fig. 16 MRI T1WI (*left*) and T2 FS WI (*right*) axial view of the same patient showing bulbous/fusiform thickening and tortuosity of the right optic nerve, isointense on T1 and iso-hyperintense on T2, with minor perineural thickening. The appearances are typical of optic nerve pilocytic astrocytoma. There is marked axial proptosis

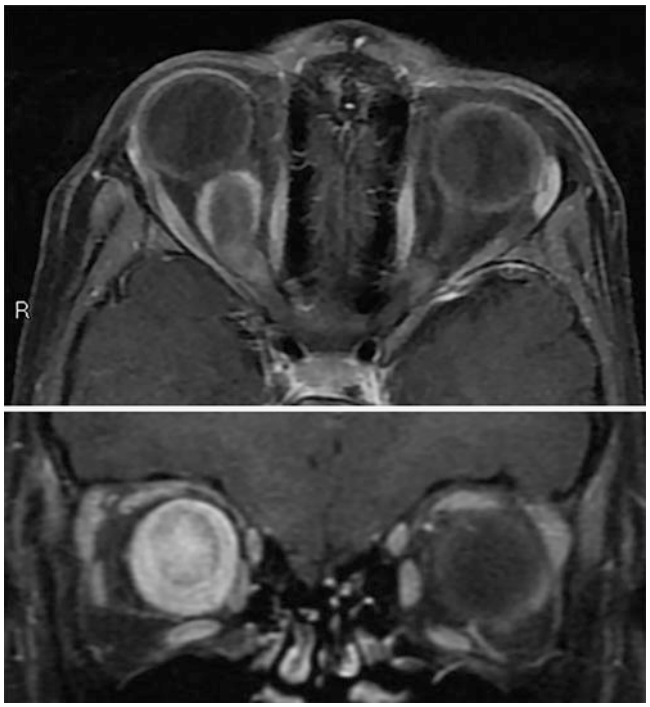


Fig. 17 T1 FS CE axial (*upper*) and coronal (*lower*) views of the same patient showing the enlarged right optic nerve and thickened optic nerve sheath. The child underwent orbital biopsy confirming the diagnosis of ON glioma prior to decision on biological treatment

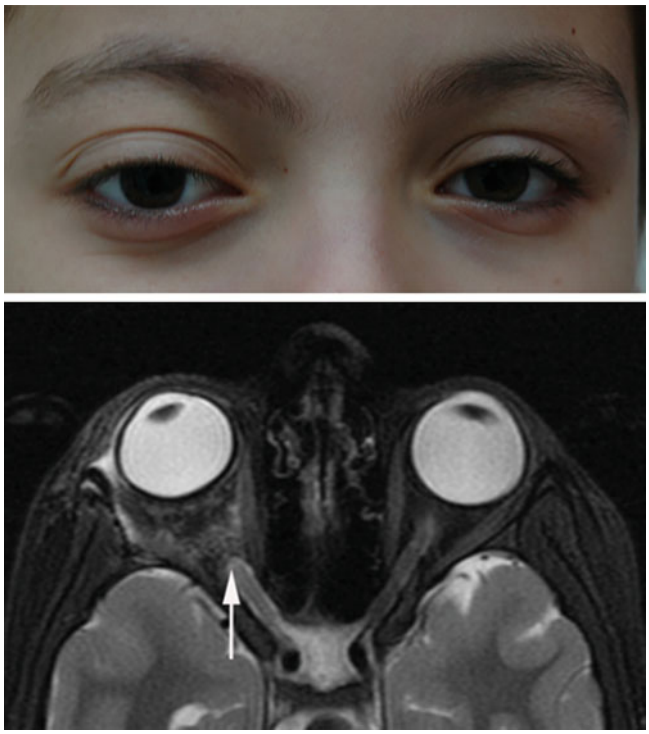


Fig. 18 Clinical photograph (*upper*) and T2 FS WI axial MR (*lower*) of the same child 2 months after "inside out" optic nerve glioma removal via lateral orbitotomy (Rootman's method). The image shows complete removal of the tumor with mild postoperative edematous changes within the surgical bed, note the remaining atrophic intra-canalicular optic nerve stump (*arrow*). She had an excellent cosmetic outcome with good ocular motility, mild ptosis, which resolved on follow-up and the pupil remained round and constricted. Six years postoperative there was no evidence of tumor recurrence



Fig. 19 Clinical photograph of a 2.5-year-old boy (*left*) with left eye marked proptosis and globe dystopia (superior temporal displacement) secondary to optic nerve glioma. The child underwent trans-orbital optic nerve glioma removal (Rootman's technique) with excellent cosmetic outcome (*right*)

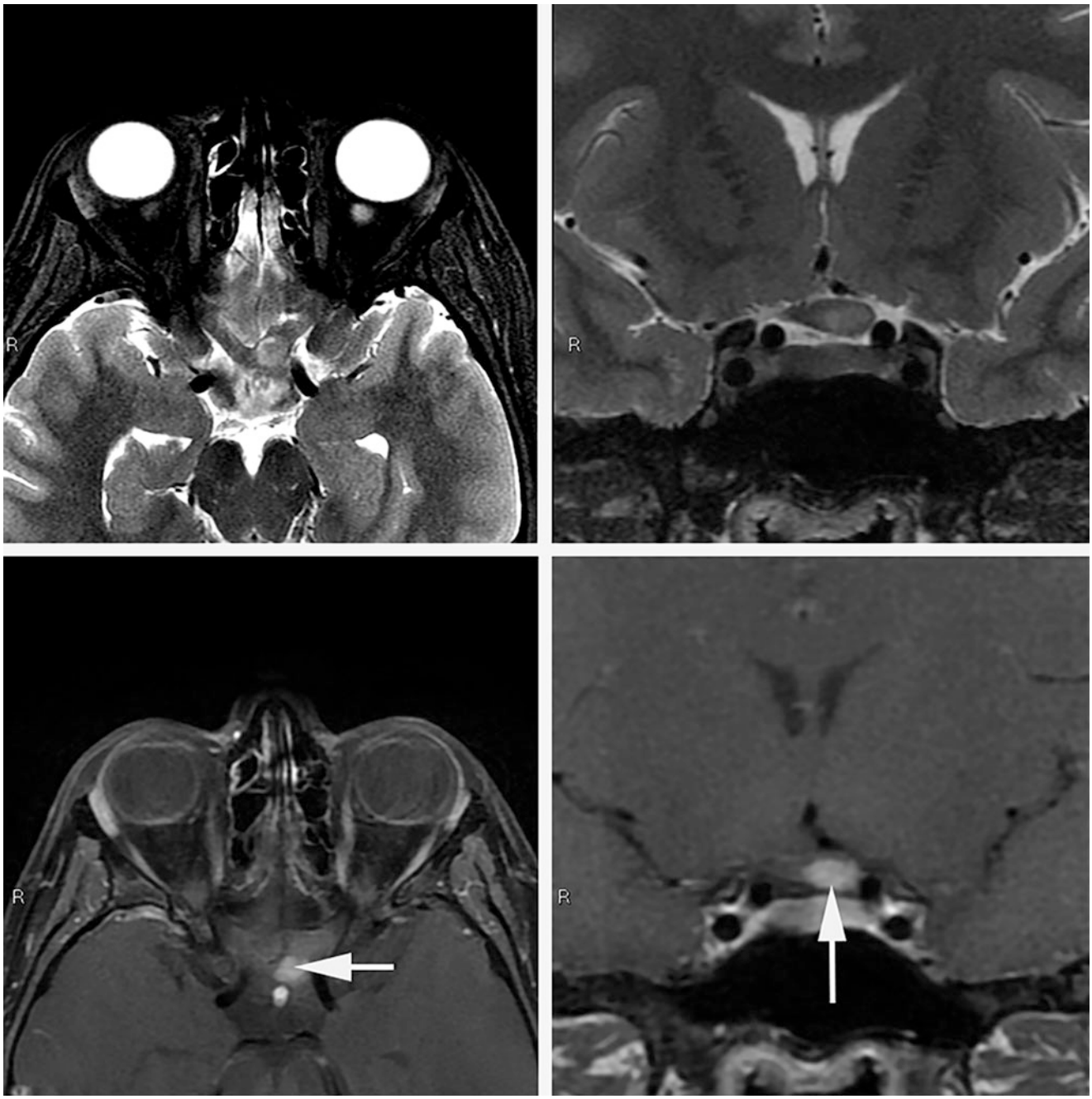


Fig. 20 MR of a 24-year-old female with left pre-chiasmal optic nerve glioma (arrows). Note the tumor has mixed intensity on T2 WI axial (*upper left*) and coronal (*upper right*) views, and is enhancing post-contrast administration on T1FS WI axial (*lower left*) and coronal (*lower right*) sections

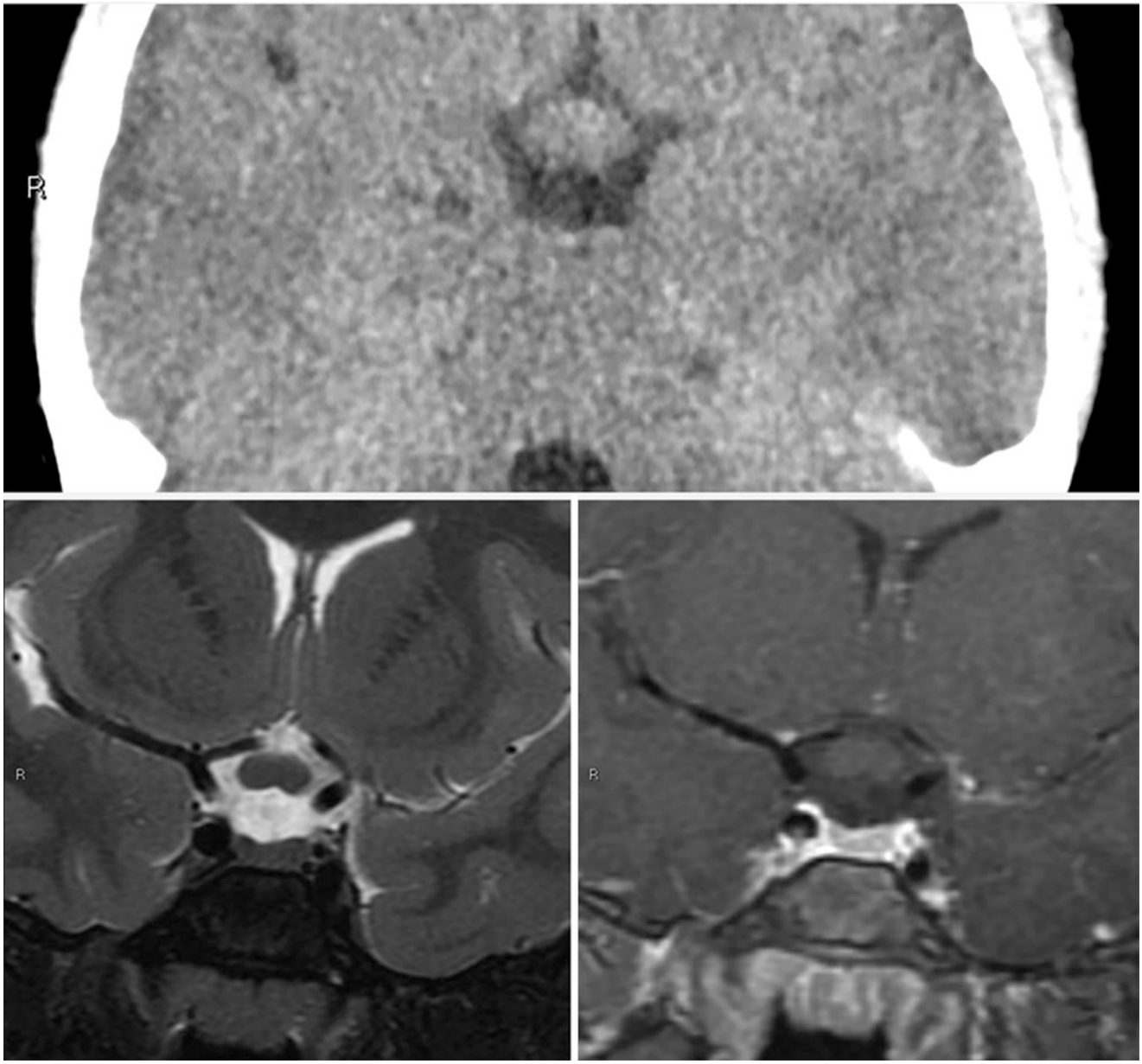


Fig. 21 NECT (*upper image*) and MR (*lower images*) of a 10-year-old female with glioma of the optic chiasma. Note the tumor is isodense on CT image, hypointense on T2 WI (*lower left*), and shows no enhancement post-contrast administration on T1WI (*lower right*)



Fig. 22 NECT of a 7-year-old male with complex optic chiasmatic-hypothalamic glioma. Note calcifications within the tumor mass and the extensive cystic component filled with proteinaceous material. The tumor cannot be distinguished from craniopharyngioma

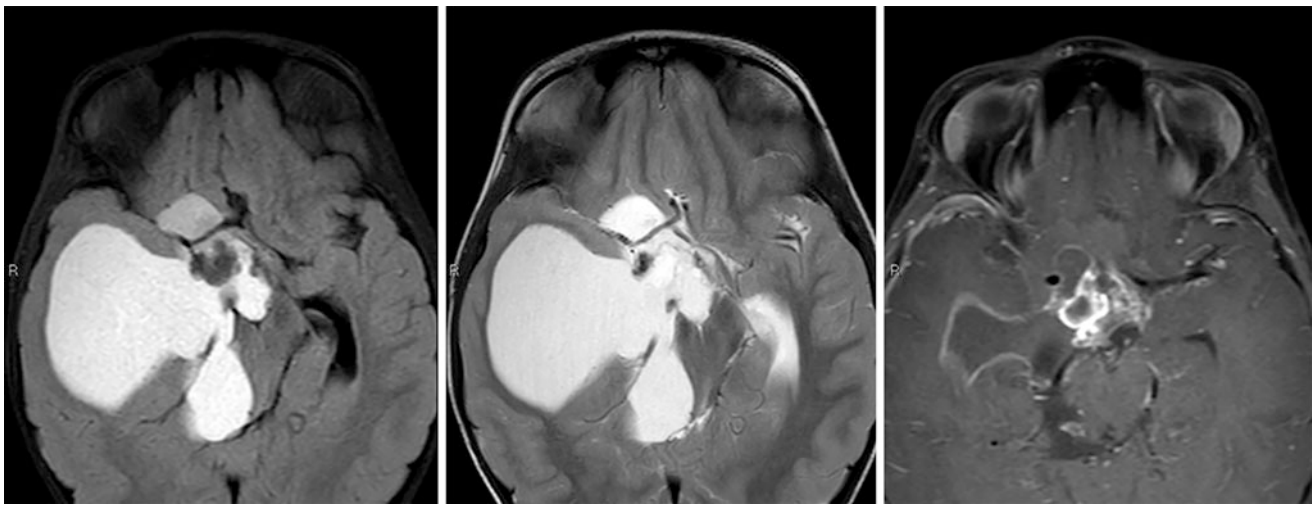


Fig. 23 MR of the same patient as in Fig. 22, T2 FLAIR (*left*), T2 (*middle*), and T1 FS CE (*right*) showing central tumor mass with extensive cystic components. The right scan is taken after surgical intervention with evacuation of the cystic component

(Figs. 12, 13, 14, 15, 16, 17, 18, 19, 20, 21, 22, and 23 courtesy of the editors)

References

1. Miller NR. Primary tumours of the optic nerve and its sheath. Eye. 2004;18:1026–37.
2. Purohit BS, Vargas MI, Ailianou A, Merlini L, Poletti P-A, Platon A, Delattre BM, Rager O, Burkhardt K, Becker M. Orbital tumours and tumour-like lesions: exploring the armamentarium of multiparametric imaging. Insights Imaging. 2016;7:43–68.
3. Tailor TD, Gupta D, Dalley RW, Keene DC, Anzai Y. Orbital neoplasms in adults: clinical, radiologic, and pathologic review. Radiographics. 2013;33:1739–58.
4. Rasool N, Odel JG, Kazim M. Optic pathway glioma of childhood. Curr Opin Ophthalmol. 2017;28(3):289–95. https://doi.org/10.1097/ICU.0000000000000370. PMID: 28257299.
5. Farazdaghi MK, Katowitz WR, Avery RA. Current treatment of optic nerve gliomas. Curr Opin Ophthalmol. 2019;30(5):356–63. https://doi.org/10.1097/ICU.0000000000000587. PMID: 31246635; PMCID: PMC7410088.
6. Calixto NC, Simão GN, Dos Santos AC, de Oliveira RS, Junior LGD, Valera ET, Cintra MB, Mello AS. Monitoring optic chiasmatic-hypothalamic glioma volumetric changes by MRI in children under clinical surveillance or chemotherapy. Childs Nerv Syst. 2019;35(1):63–72. https://doi.org/10.1007/s00381-018-3904-9. Epub 2018 Aug 4. PMID: 30078056.
7. Spicer GJ, Kazim M, Glass LR, Harris GJ, Miller NR, Rootman J, Sullivan TJ. Accuracy of MRI in defining tumor-free margin in optic nerve glioma surgery. Ophthalmic Plast Reconstr Surg. 2013;29(4):277–80. https://doi.org/10.1097/IOP.0b013e318291658e. PMID: 23715516.
8. Fatima A, Ichikawa T, Ishigame K, Motosugi U, Waqar AB, Hori M, Iijima H, Araki T. Orbital masses: the usefulness of diffusion-weighted imaging in lesion categorization. Clin Neuroradiol. 2014;24:129–34.

Optic Nerve Sheath Meningioma

63

Yoon-Duck Kim

Contents

1 **Signs and Symptoms** 467
2 **Differential Diagnosis** 467
3 **Diagnosis** 467
4 **Treatment** 467
5 **Figures with Captions** 468
References 474

Abstract

- Meningioma manifests as a tubular, globular, fusiform, or focal enlargement of the optic nerve.
- On contrast-enhanced CT or MR imaging, a hypodense area of the optic nerve surrounded by an enhancing tumor typically produces a "tram-track" sign (axial) or a "target" sign (coronal).
- The CT scan is superior for assessing calcification.
- Contrast-enhanced MR imaging is the study of choice for evaluation of soft tissue involvement in the orbit as well as intracranial extension.
- A dural tail may be a typical finding with intracranial extension of tumor, particularly on MR.
- PET CT shows typical ^{68}Ga-DOTATATE avidity.

Keywords

Tram-track sign · calcification · tubular enlargement · optic nerve

1 Signs and Symptoms

Decreased vision, transient visual obscurations, duction-induced visual change, proptosis, strabismus, optic disc swelling, disc atrophy, optociliary shunt vessels [1, 2].

2 Differential Diagnosis

Optic nerve glioma, optic neuritis, lymphoma, leukemia, sarcoidosis, inflammatory pseudotumor, metastatic tumors [3].

3 Diagnosis

Clinical findings and characteristic radiologic findings. Usually tissue biopsy is not necessary.

4 Treatment

Regular follow-up with clinical, functional, and imaging studies. Conformal fractionated radiation therapy [4], or gamma knife stereotactic radiosurgery [5] is the optimum therapy in patients with progressive loss of vision. For

Y.-D. Kim (✉)
Oculoplastic and Orbital Surgery Division, Nune Eye Hospital, Seoul, South Korea
e-mail: ydkimoph@skku.edu

© Springer Nature Switzerland AG 2022
G. Ben Simon et al. (eds.), *Atlas of Orbital Imaging*,
https://doi.org/10.1007/978-3-030-62426-2_55

cases of intracranial spread, the intracranial portion can be removed through a craniotomy to prevent tumor spread to the contralateral optic nerve.

5 Figures with Captions



Fig. 1 Pre-contrast axial CT scan shows a globular enlargement of the optic nerve/sheath complex with a well-defined margin. The lesion is isodense to cortical gray matter



Fig. 2 Post-contrast axial CT scan demonstrates a central lucent area of the optic nerve surrounded by marked homogeneous enhancement of the tumor producing a tram-track sign [6]. This characteristic finding is useful for differentiating meningioma from glioma, in which the nerve itself cannot be distinguished from the tumor

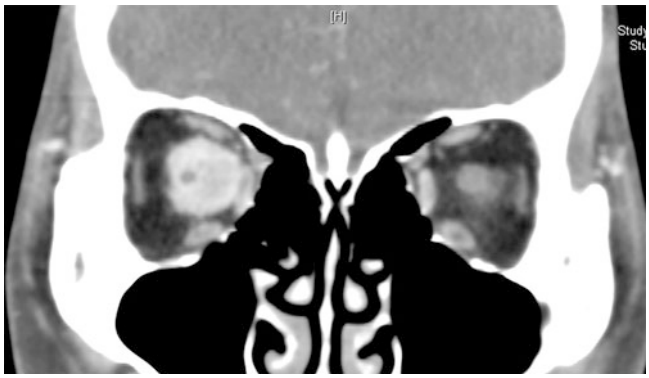


Fig. 3 Post-contrast coronal CT scan demonstrates marked homogeneous enhancement of the tumor with a central zone of lower density representing the optic nerve, similar to a target or a donut configuration. Note that the tumor is enveloping the ON in an eccentric fashion

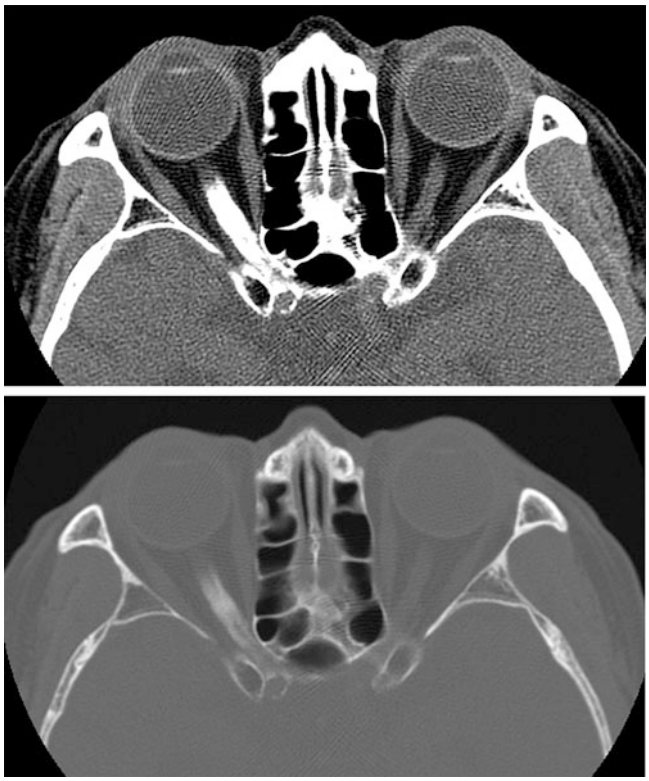


Fig. 4 Pre-contrast axial CT, different patient. Soft tissue window (left) demonstrates dense calcification of tubular meningioma along the optic nerve. Bone window (right) allows better visualization of calcification surrounding the nerve. Diffuse calcification tends to be associated with very slow growth of meningioma

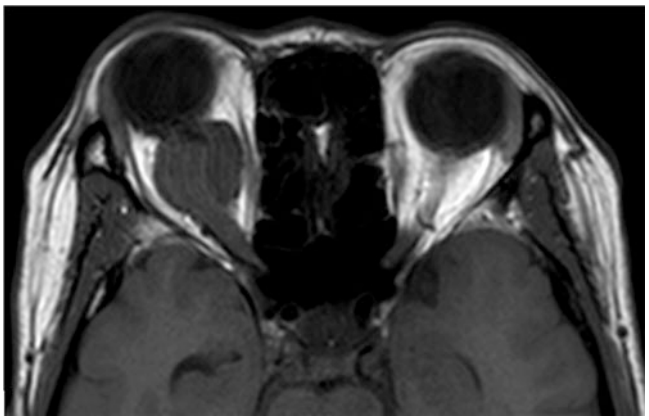


Fig. 5 Axial T1-weighted MR image showing a well-defined, isointense mass of the optic nerve, same patient as in Figs. 1, 2, and 3

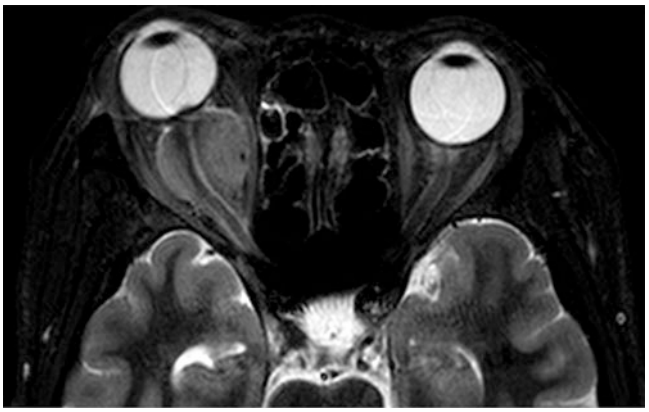


Fig. 6 Axial T2-weighted MR image showing a hyperintense mass surrounding the optic nerve. There is a notable axial proptosis, flattening of the posterior globe, and bulging of the papilla

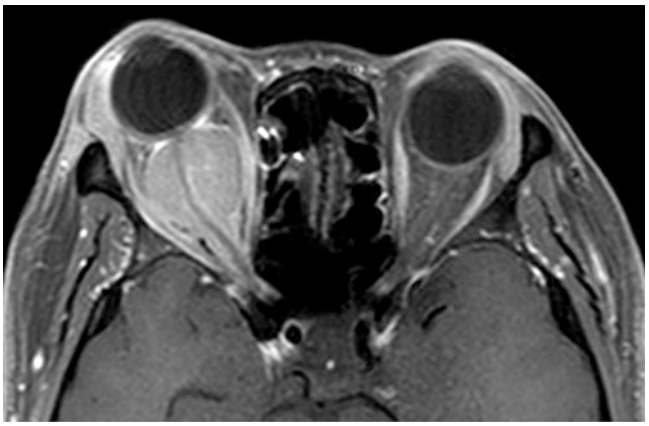


Fig. 7 Post-contrast axial T1 fat-saturated image, same patient 2 years later, demonstrates a central hypointense structure representing the optic nerve, surrounded by markedly enhancing tumor, producing a tram-track sign. A lacrimal gland prolapse is caused by the anterior globe displacement

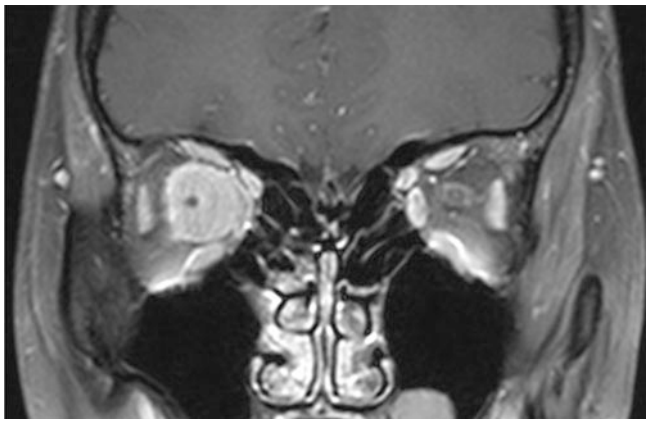


Fig. 8 Post-contrast coronal T1 fat-saturated image demonstrates marked homogeneous enhancement of the tumor with a central zone of lower intensity representing the optic nerve similar to a target or a donut configuration

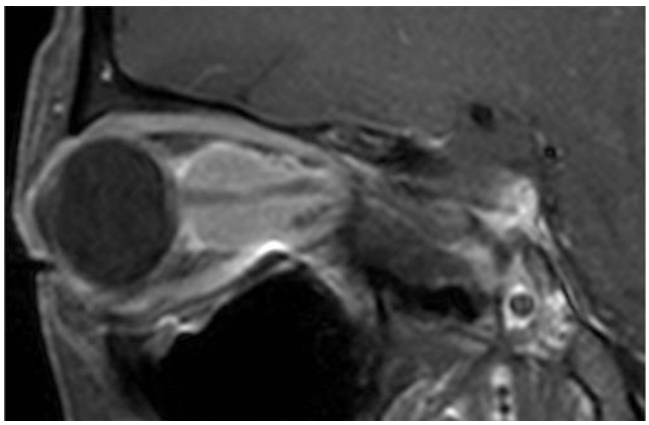


Fig. 9 Post-contrast sagittal-oblique T1 fat-saturated image demonstrates marked homogeneous enhancement of the tumor with a central zone of lower intensity representing the optic nerve

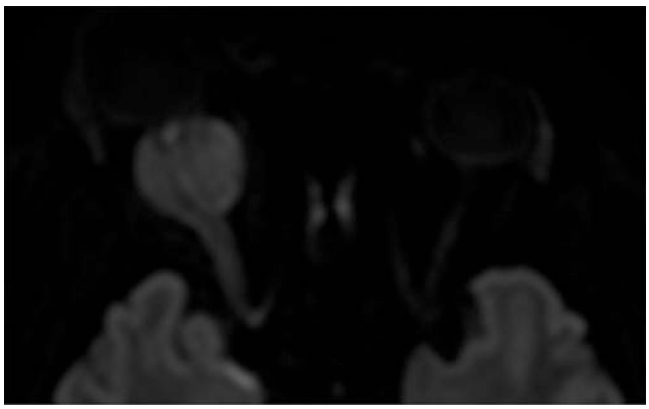


Fig. 10 Axial DWI image showing high signal of meningioma

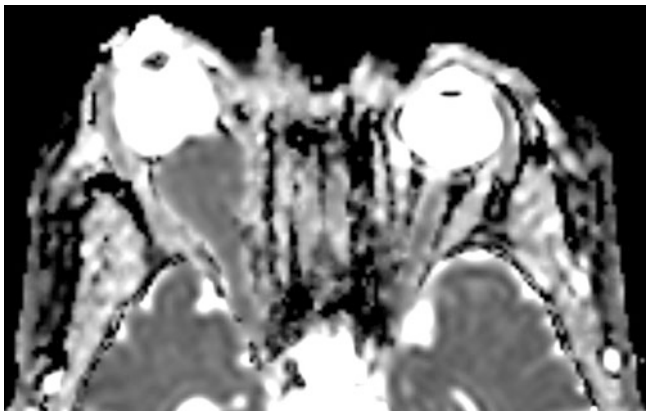


Fig. 11 Axial ADC map showing restricted diffusion with low ADC values because of hypercellular nature of the tumor. When compared with glioma, meningioma shows lower mean ADC values [7]

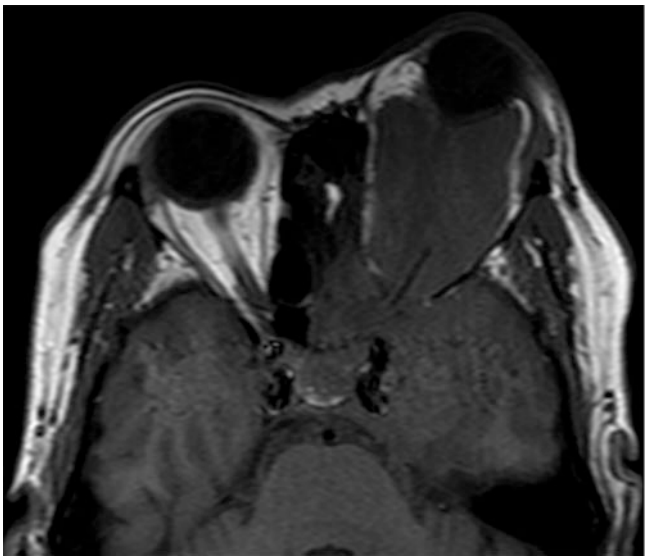


Fig. 12 Axial T1-weighted MR image of 55-year-old woman showing a huge, isointense mass occupying the entire left orbit with severe exophthalmos

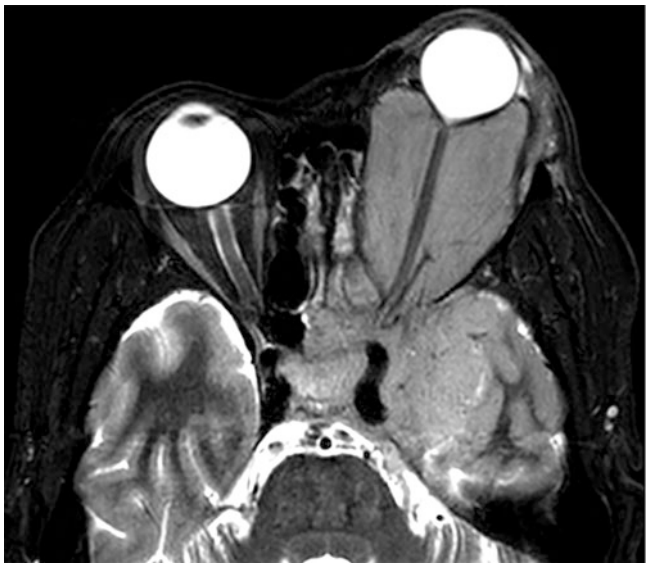


Fig. 13 Axial T2-weighted MR image showing a hyperintense, huge mass surrounding the stretched optic nerve and tenting of the eyeball from severe axial proptosis

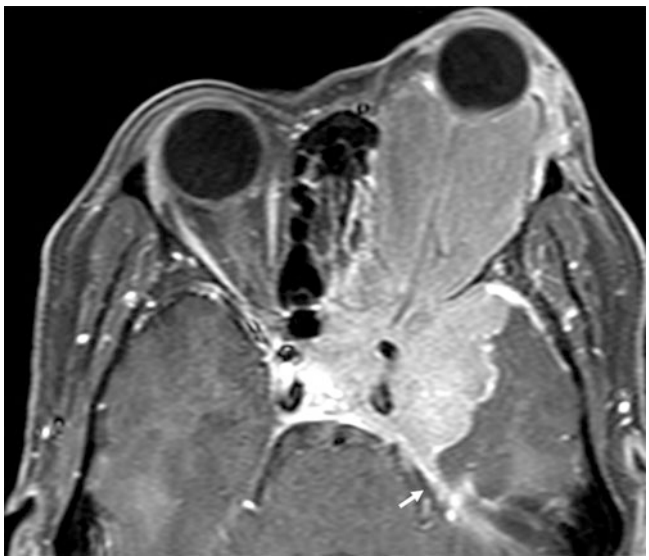


Fig. 14 Post-contrast axial T1 fat-saturated image demonstrates a central hypointense structure representing the optic nerve, surrounded by markedly enhancing huge tumor. Intracranial extension to the cavernous sinus, anterior cranial fossa, and middle cranial fossa is well delineated by contrast enhancement with dural thickening along the tentorium (dural tail, arrow)

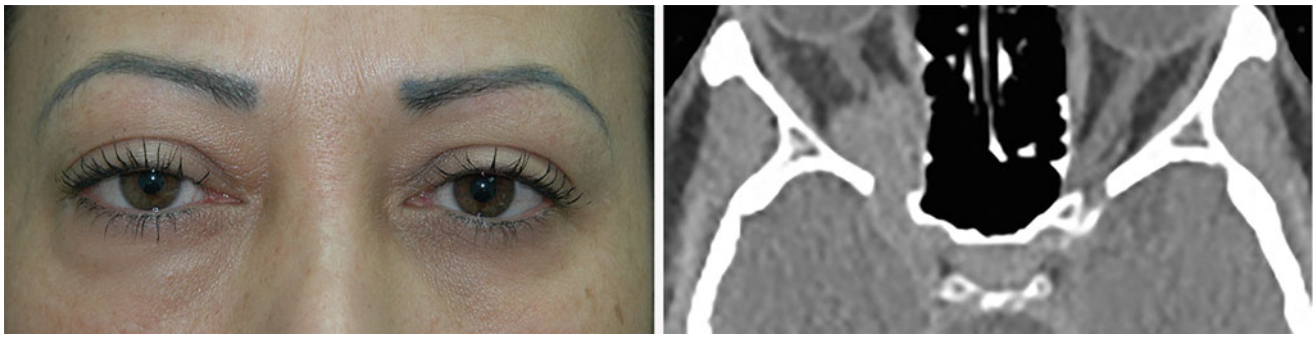


Fig. 15 Clinical photograph (*left*) and NECT (*right*) of a 40-YOF with mild right eye proptosis, mild ptosis and decreased vision function. Note homogenous soft tissue density mass encroaching the posterior aspect of the right optic nerve, extending into the SOF. (Courtesy: Editors)

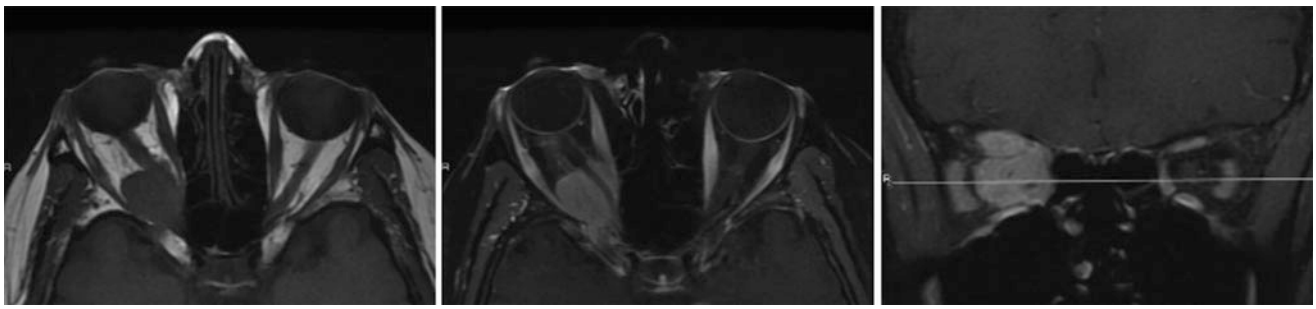


Fig. 16 MRI of the same patient, Axial T1 non-FS)*left* (and post contrast axial and coronal T1 FS views (*middle* and *right*) showing the tumor is isointense on T1WI and enhancing vividly following contrast administration. Note the mass is enveloping and displacing the ON (reference line) rather than causing ON expansion, typical of ONS tumors. (Courtesy: Editors)

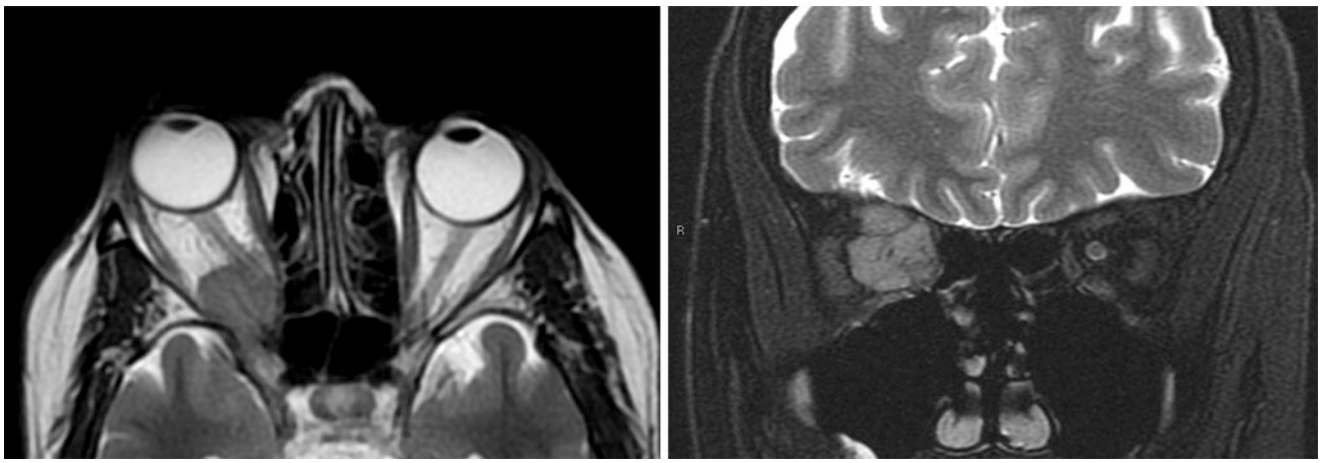


Fig. 17 T2 WI axial (*left*) and with fat suppression coronal (*right*) of the same patient as in Figs. 15 and 16 also demonstrating ON displacement and SOF involvement. The tumor is iso-intense on T2. (Courtesy: Editors)

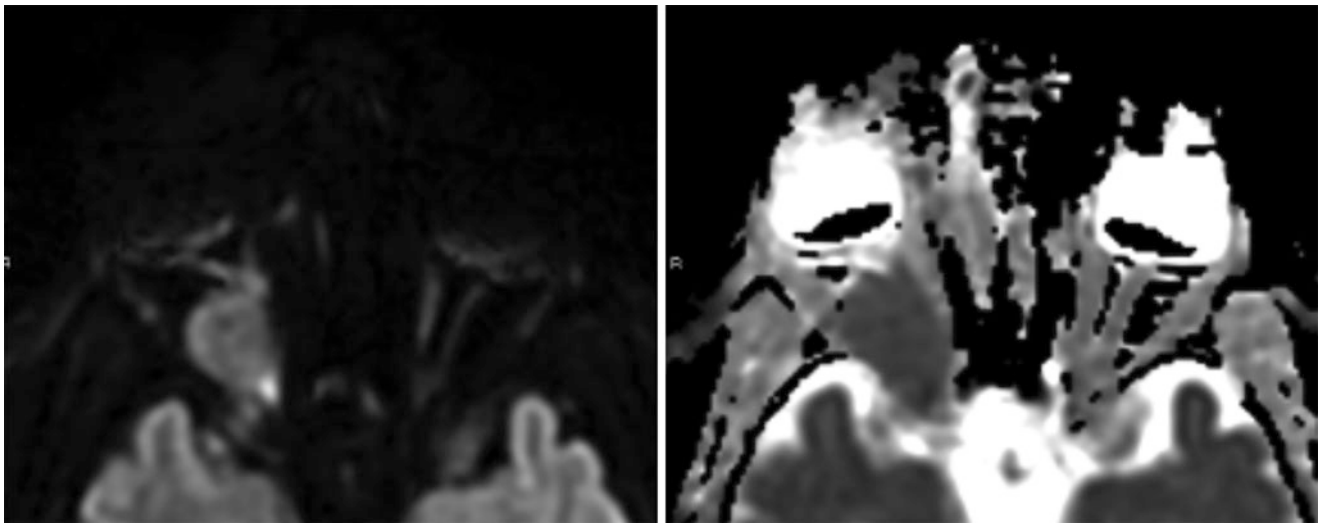


Fig. 18 MR diffusion, DWI (*left*) and corresponding ADC map (*right*) showing restricted diffusion within the tumor, a common feature in meningiomas due to cell density. (Courtesy: Editors)

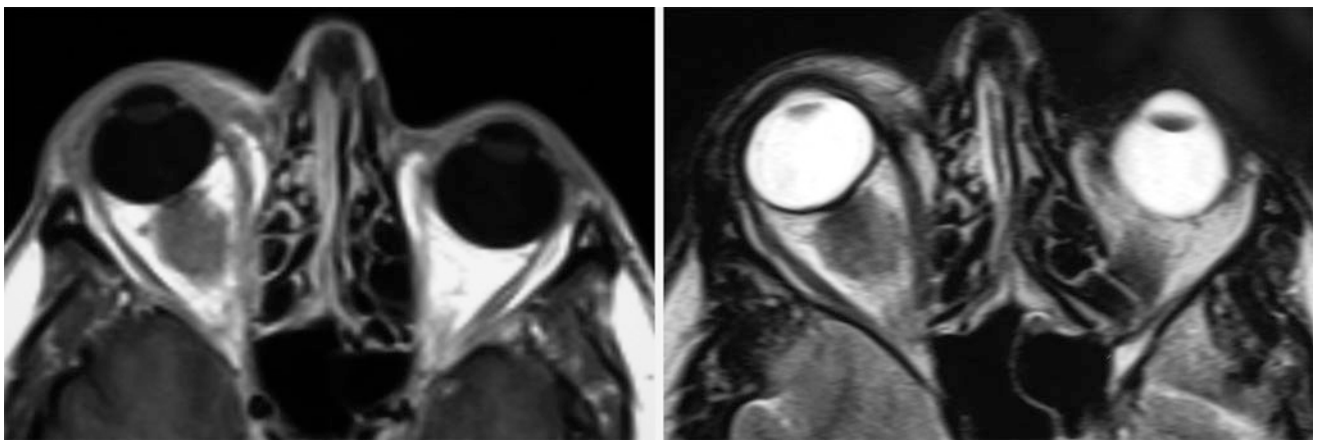


Fig. 19 MR, axial view of a different patient with right ONSM, note the tumor is iso to hyper intense on T1WI (*left*) and hypointense on T2WI (*right*). There is marked axial proptosis on the right side. (Courtesy: Editors)

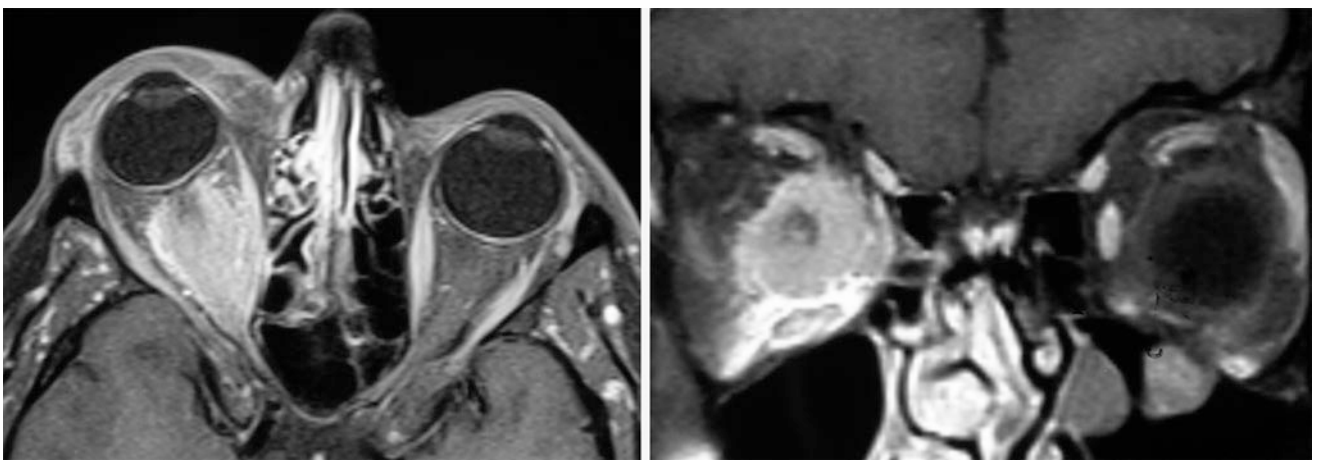


Fig. 20 T1 FS CE axial MRI (*left*) and coronal view (*right*) of the same patient with ONS meningioma on the right side, note perineural thickening with normal nerve, and homogenous contrast enhancement. Typical tram track sign and dural tail is demonstrated on the axial section and target sign on the coronal section. (Courtesy: Editors)

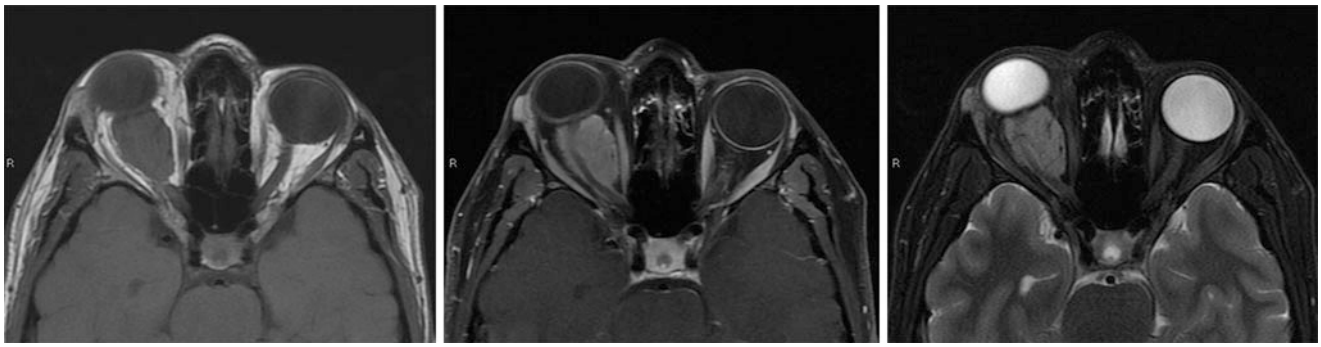


Fig. 21 Axial MR of a 41-YOF (different patient) with right ONS meningioma. Note the tumor is isointense on T1WI (*left*), enhancing with contrast administration (*middle*) and iso to somewhat hyper-intense on T2WI (*right*). (Courtesy: Editors)

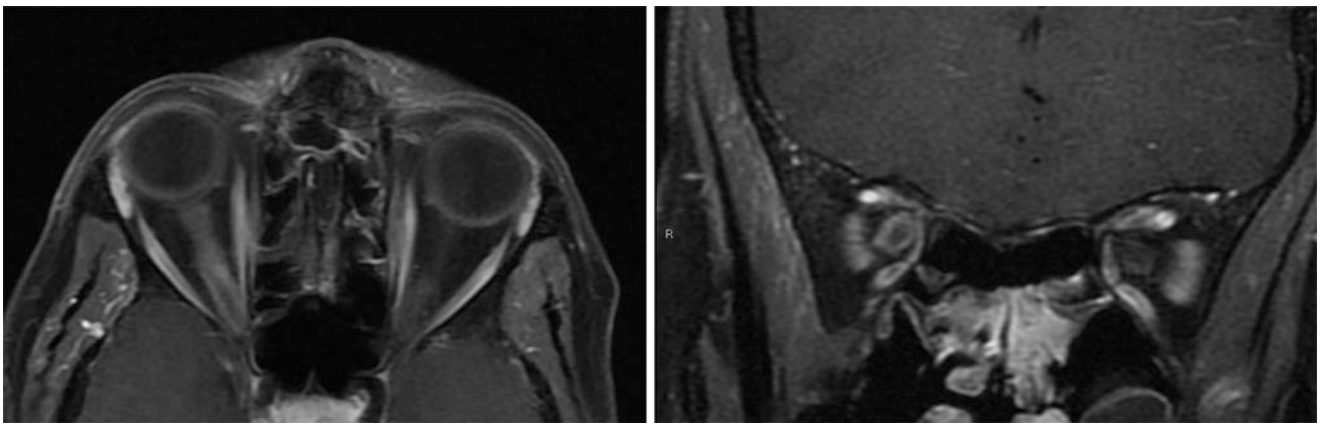


Fig. 22 T1 CE FS MRI of a 49-YOF with right ONS meningioma. Note typical tram-track sign on the axial view (*left*) with corresponding target sign on coronal view (*right*). (Courtesy: Editors)

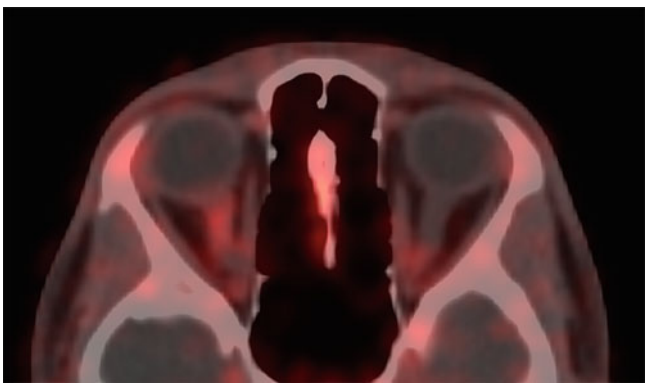


Fig. 23 PET CT of a 15-YOM with presumed clinoid meningioma extending into the right ONS with ^{68}Ga-DOTATATE avidity [8]. The child underwent orbital biopsy which was inconclusive most likely due to too anterior sampling. (Courtesy: Editors)

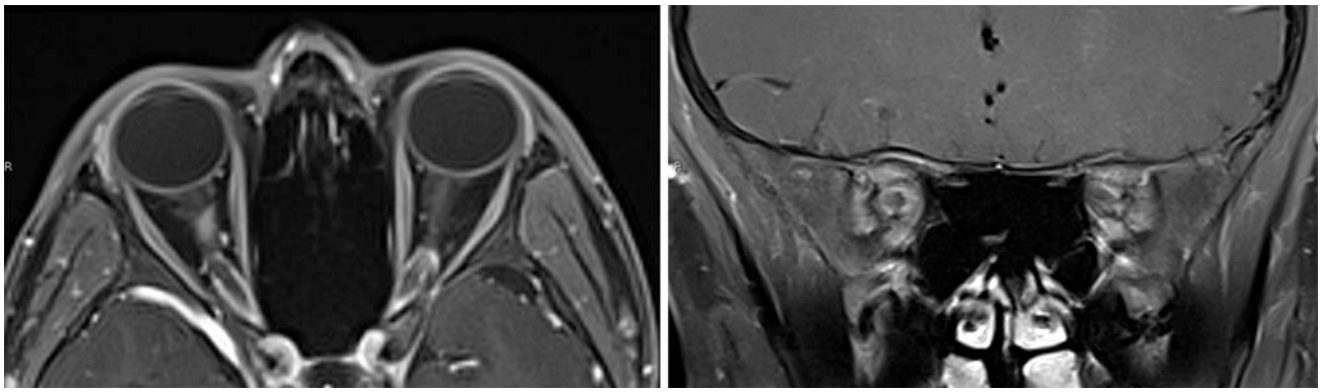


Fig. 24 T1 CE FS MR of the same patient as in Fig. 23 showing typical tram track sign on the axial scan (*left*) with corresponding target sign on the coronal view (*right*). (Courtesy: Editors)

References

1. Miller NR. Primary tumours of the optic nerve and its sheath. Eye. 2004;18:1026–37.
2. Douglas VP, Douglas KAA, Cestari DM. Optic nerve sheath meningioma. Curr Opin Ophthalmol. 2020;31(6):455–61. https://doi.org/10.1097/ICU.0000000000000700.
3. Purohit BS, Vargas MI, Ailianou A, Merlini L, Poletti P-A, Platon A, Delattre BM, Rager O, Burkhardt K, Becker M. Orbital tumours and tumour-like lesions: exploring the armamentarium of multiparametric imaging. Insights Imaging. 2016;7:43–68.
4. Jin J, Joo JD, Han JH, Yang HK, Hwang JM, Kim YJ, Kim IA, Kim CY. Optic nerve sheath meningioma: preliminary analysis of the role of radiation therapy. Brain Tumor Res Treat. 2018;6(1):8–12. https://doi.org/10.14791/btrt.2018.6.e2. Epub 2018 Apr 2. PMID: 29644809; PMCID: PMC5932300
5. K-l J, Im YS, Kong D-S, Seol HJ, Nam D-H, Kim Y-D, Lee J-I. Multisession gamma knife surgery for benign orbital tumors. J Neurosurg (Suppl). 2012;117:102–7.
6. Tailor TD, Gupta D, Dalley RW, Keene DC, Anzai Y. Orbital neoplasms in adults: clinical, radiologic, and pathologic review. Radiographics. 2013;33:1739–58.
7. Fatima A, Ichikawa T, Ishigame K, Motosugi U, Waqar AB, Hori M, Iijima H, Araki T. Orbital masses: the usefulness of diffusion-weighted imaging in lesion categorization. Clin Neuroradiol. 2014;24:129–34.
8. Al Feghali KA, Yeboa DN, Chasen B, Gule MK, Johnson JM, Chung C. The use of ^{68}Ga-DOTATATE PET/CT in the non-invasive diagnosis of optic nerve sheath meningioma: a case report. Front Oncol. 2018;8:454. https://doi.org/10.3389/fonc.2018.00454. PMID: 30386741; PMCID: PMC6198069

Intrinsic and Extrinsic Etiologies of Optic Nerve Damage

64

Ofira Zloto, Nina Borissovsky, Judith Luckman, and Nitza Goldenberg Cohen

Contents

1 **Introduction** 475
2 **Imaging Features** 476
3 **Figures with Captions** 476
References 488

Abstract

Optic neuropathy can be caused by hereditary, mechanical, infiltrative, inflammatory, and ischemic pathologies.

The location of the damage, the amount of optic nerve involved, laterality, and adjunctive findings, especially in the central nervous system, can help in diagnosis.

We present few examples of the multiple etiologies leading to optic neuropathy.

Keywords

Optic neuritis · optic perineuritis · MS · ADEM · Demyelinating diseases · Infiltration · Compressive optic neuropathy · Thyroid eye disease · Fibrous Dysplasia · Traumatic optic neuropathy · Optic atrophy · Meningioma · Sarcoidosis · Optic nerve metastasis · Primary and secondary tumours infiltrating the optic nerve · Lymphoma · Glioma · Leber's hereditary optic neuropathy · Optic disc drusen

1 Introduction

- Diagnosis of optic nerve pathologies can be challenging. Not uncommonly, joint effort of multidisciplinary team is required including neuro-ophthalmologists, neuroradiologists, neurologists, oculoplastic surgeons, and oncologists.
- Optic nerve pathologies include [1, 2]:
  - Acute disseminated encephalomyelitis (ADEM), demyelinated multiple sclerosis, neuromyelitis optica, neuromyelitis optica spectrum disorder (NMOSD), myelin oligodendrocyte glycoprotein (MOG) optic neuritis

O. Zloto
Department of Ophthalmology, Créteil, France

Goldschleger Eye Institute, Sheba Medical Center, Tel Hashomer, Israel

Sackler Faculty of Medicine, Tel Aviv University, Tel Aviv, Israel

N. Borissovsky
Imaging Department, Bnai-Zion Medical Center, Rappaport Faculty of Medicine, Technion, Haifa, Israel
e-mail: nina.borissovsky@b-zion.org.il

J. Luckman
Radiology Department, Rabin Medical Center-Beilinson Hospital, Petah Tikva, Israel

N. G. Cohen (✉)
Krieger Eye Research Laboratory, Bnai-Zion Medical Center, Haifa, Israel

Department of Ophthalmology, Bnai-Zion Medical Center, Haifa, Israel

Rappaport Faculty of Medicine, Technion, Israel Institute of Technology, Haifa, Israel

© Springer Nature Switzerland AG 2022
G. Ben Simon et al. (eds.), *Atlas of Orbital Imaging*,
https://doi.org/10.1007/978-3-030-62426-2_114

- Inflammatory/infectious diseases – thyroid eye disease, sarcoidosis, tuberculosis, syphilis
- Compressive – osteoma, meningioma, fibrous dysplasia
- Infiltrative – lymphoproliferative, glioma, metastasis, etc.
- Traumatic – traumatic optic neuropathy, apex syndrome, orbital hematoma
- Vascular – anterior and posterior ischemic optic neuropathy, nonarteritic and arteritic anterior ischemic optic neuropathy, vascular malformations
- Genetic – Autosomal dominant optic atrophy, Leber's hereditary optic neuropathy, other mitochondrial diseases
- Metabolic/toxic – B12 deficiency, B1, amiodarone, tamoxifen, alcohol induced, etc.
- Degenerative, atrophic optic neuropathy
- ICP induced papilledema, pseudotumor

2 Imaging Features

- Rarely the etiology of the optic nerve diseases can be made on the basis of a single clinical finding. Therefore, in addition to the history, visual function tests and ophthalmoscopy, specific ancillary testing (autofluorescence, optical coherence tomography, ultrasound) [3], and imaging tests (magnetic resonance imaging (MRI) and/or computed tomography (CT)) are essential [4, 5].
- CT is the dominant imaging modality in the evaluation of orbital trauma, in primary bone lesions, and in pathologies with clacifications [6].
- In almost all other cases, MRI is considered a better tool to diagnose optic nerve pathologies because of its superior soft tissue contrast compared to CT [6].
- Coronal MRI of normal human eyes showed an average optic nerve sheath diameter range of 4.0–6.0 mm and an average optic nerve diameter range of 2.6–4.0 mm [7–9].
- Few signs are considered specifically indicative or "pathognomonic" of particular neuropathy, for example: "tram-track" sign in axial view can be present in any optic nerve sheath pathology, such as optic nerve sheath meningiomas, optic nerve kink of NF1, and more [10].
- Regarding MR technique, a comprehensive orbit protocol should include FAT SAT images in at least two plains, thin slice T2W millimeters or submillimeters images (e.g., FIESTA, CISS, TSE, DRIVE dependent on MR vendor). DWI aids in depicting tumor cellularity and acute infectious/inflammatory processes as well as ischemic changes.

3 Figures with Captions

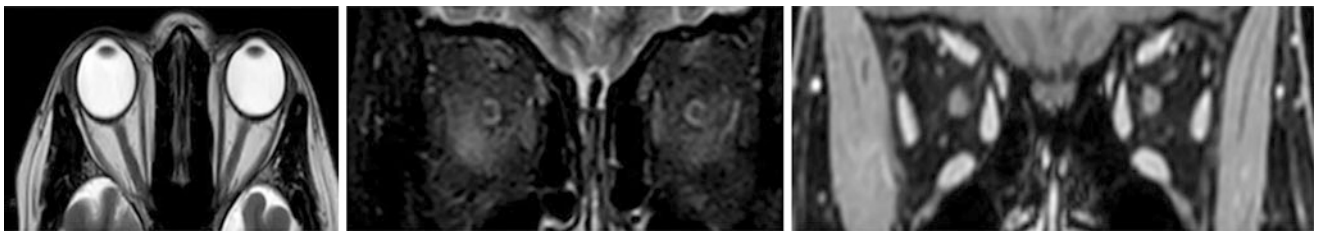


Fig. 1 MRI of normal optic nerve – axial view T2 (*left*), coronal view T2 FAT SAT (*middle*), coronal view T1 FAT SAT, CE (*right*)

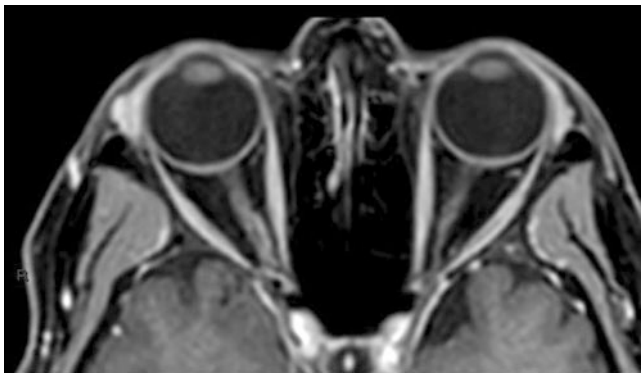


Fig. 2 MRI left atrophic optic nerve – axial view T1 FAT SAT, CE

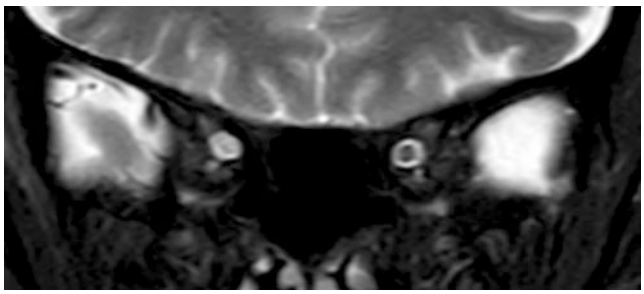


Fig. 3 T2WI FS, coronal section of a 70-YOF with right optic atrophy, note higher signal as evidence of reduced neuronal tissue and increased hyperintense CSF signal surrounding the optic nerve

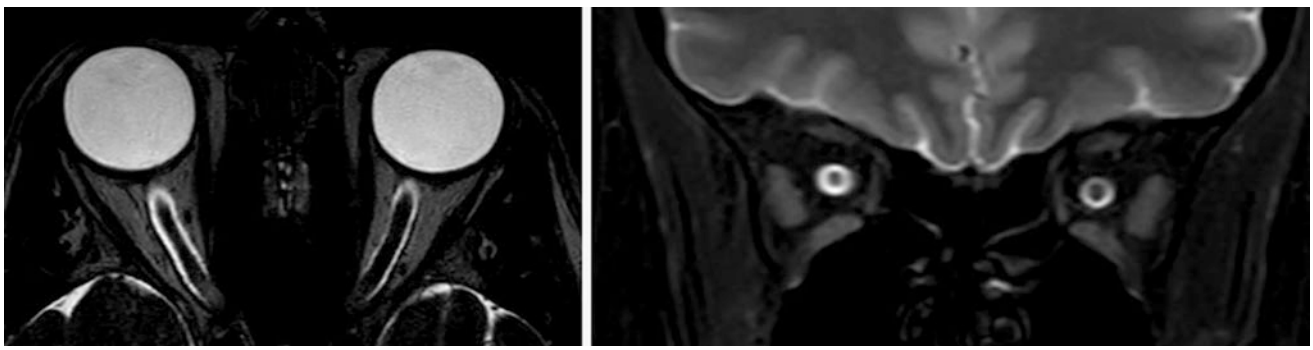


Fig. 4 T2WI , axial (left) and coronal FS (right) of a 50-YOF with right optic atrophy, again note the increased fluid signal on the right compared with the normal left optic nerve

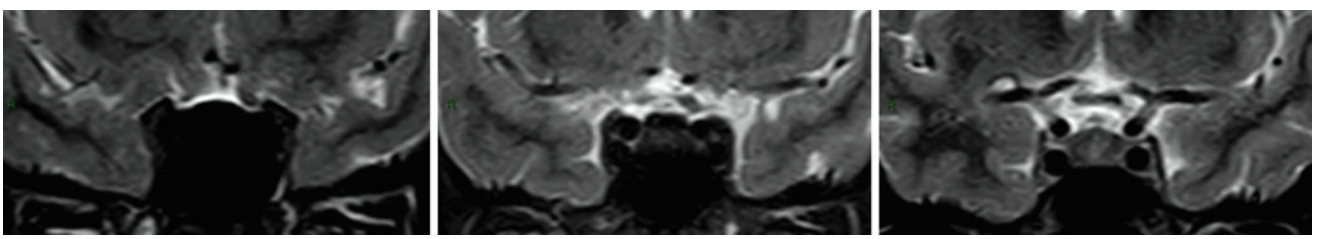


Fig. 5 Idiopathic prechiasmatic right optic atrophy coronal imaging**,** showing the atrophy of the right optic nerve in the prechiasmatic region, as compared to normal left optic nerve

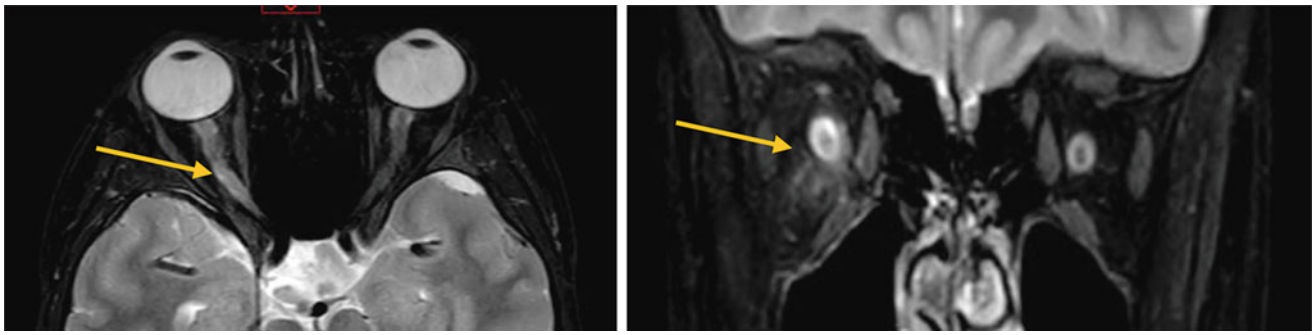


Fig. 6 MRI of a 15-year-old boy with right optic nerve sheath meningioma. Axial T2 (*left*): effacement of the right bulbar optic nerve borders and mild thickening of the right anterior clinoid. Coronal view T2 enlargement of the right optic nerve sheath, note typical "doughnut" sign

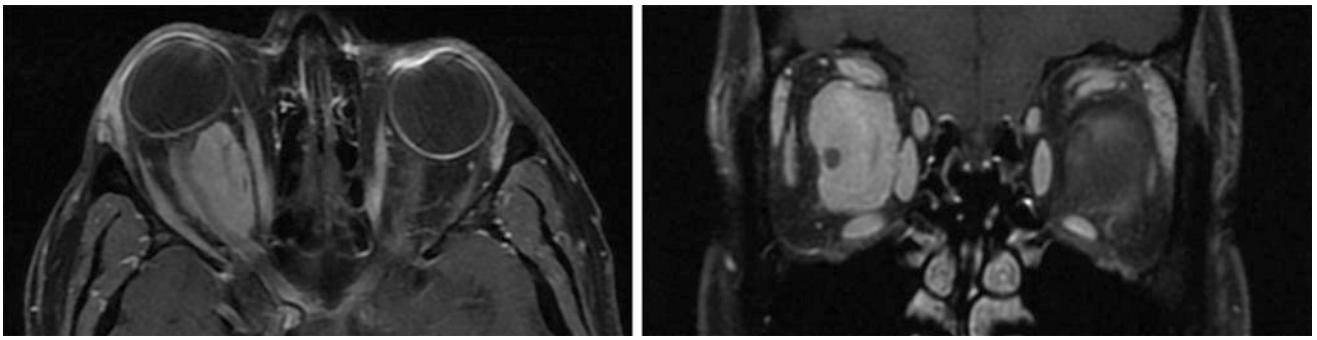


Fig. 7 MRI postcontrast of a 44-year-old-woman with a large right optic nerve meningioma – axial view, T1 FAT SAT, CE (*left*) – an enhancing, homogeneous mass surrounding the right optic nerve complex in an eccentric fashion, nasal more than temporal. Coronal view, T1 FAT SAT, CE (*right*) – homogeneous intraorbital mass surrounding the optic nerve and encasing it. It may be difficult to evaluate the intrinsic characteristics of the optic nerve

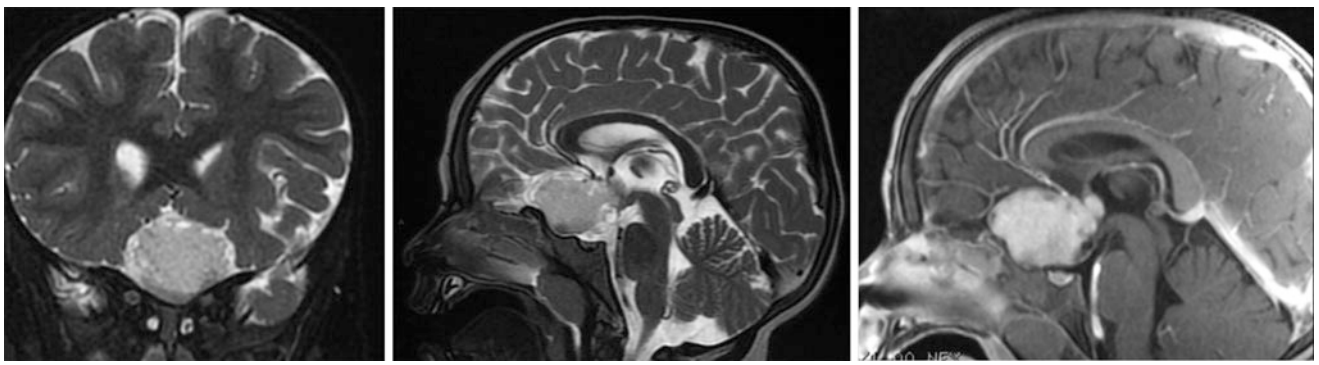


Fig. 8 MRI postcontrast of a patient with tuberculum sella meningioma. Coronal view, T2 (*left*) – homogenous mass, extra axial with compression of bilateral basal frontal lobes. Sagittal view, T2 (*middle*) – homogenous slightly hyperintense mass in extra axial location extending from Tuberculum Sella causing chiasmal compression. Sagittal view (*right*) – a large extra axial enhancing mass compressing the chiasm

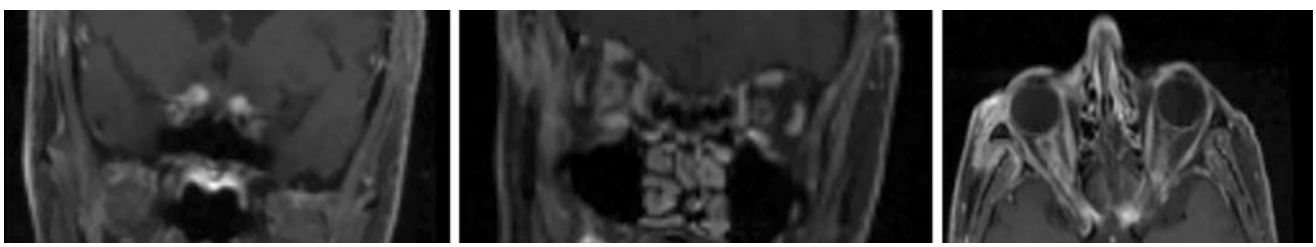


Fig. 9 MRI postcontrast of a patient with glioblastoma. Coronal (*middle and left*) and axial (*left*) views, T1 FAT SAT bilateral enhancing lesions within the bilateral retrobulbar optic nerves and chiasm consistent with malignant optic nerve tumor

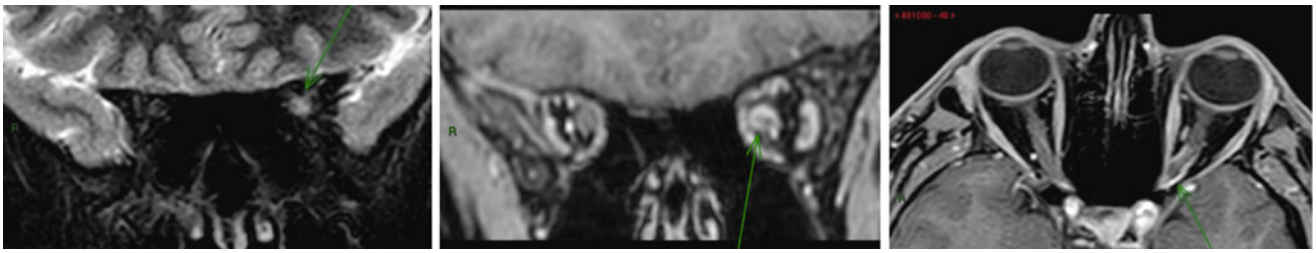


Fig. 10 MRI of a patient with left optic perineuritis – coronal view, T2 (*left*) FAT SAT – high signal within the left optic nerve, a doughnut sign. Coronal view, T1 FAT SAT CE (*middle*) – enhancement of the optic nerve sheath. Axial view, T1 FAT SAT CE (*right*) enhancement of the optic nerve sheath. A tram-track sign

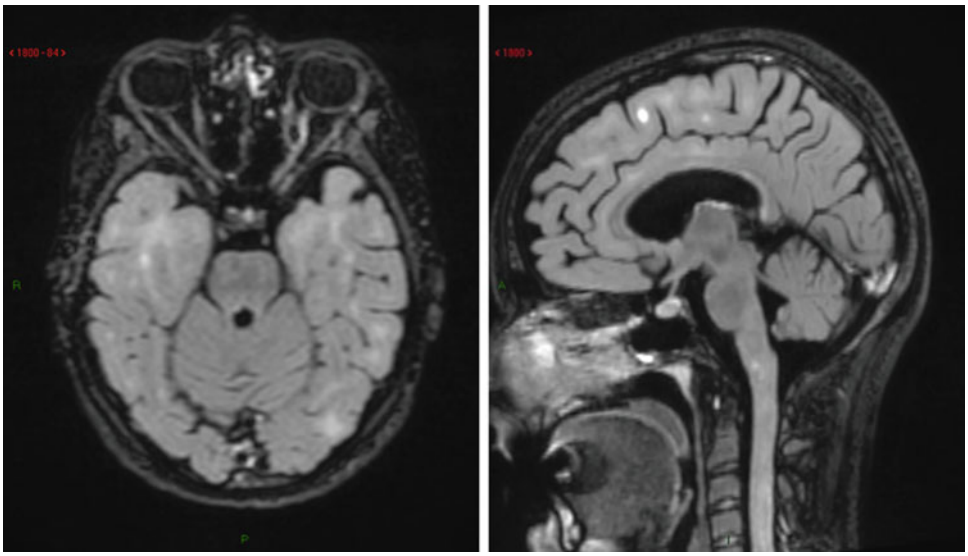


Fig. 11 MRI postcontrast of a patient with multiple sclerosis (MS) – axial view (*left*) and sagittal view (*right*) FLAIR – multiple confluent white matter lesions. The left optic nerve shows high signal consistent with optic neuritis

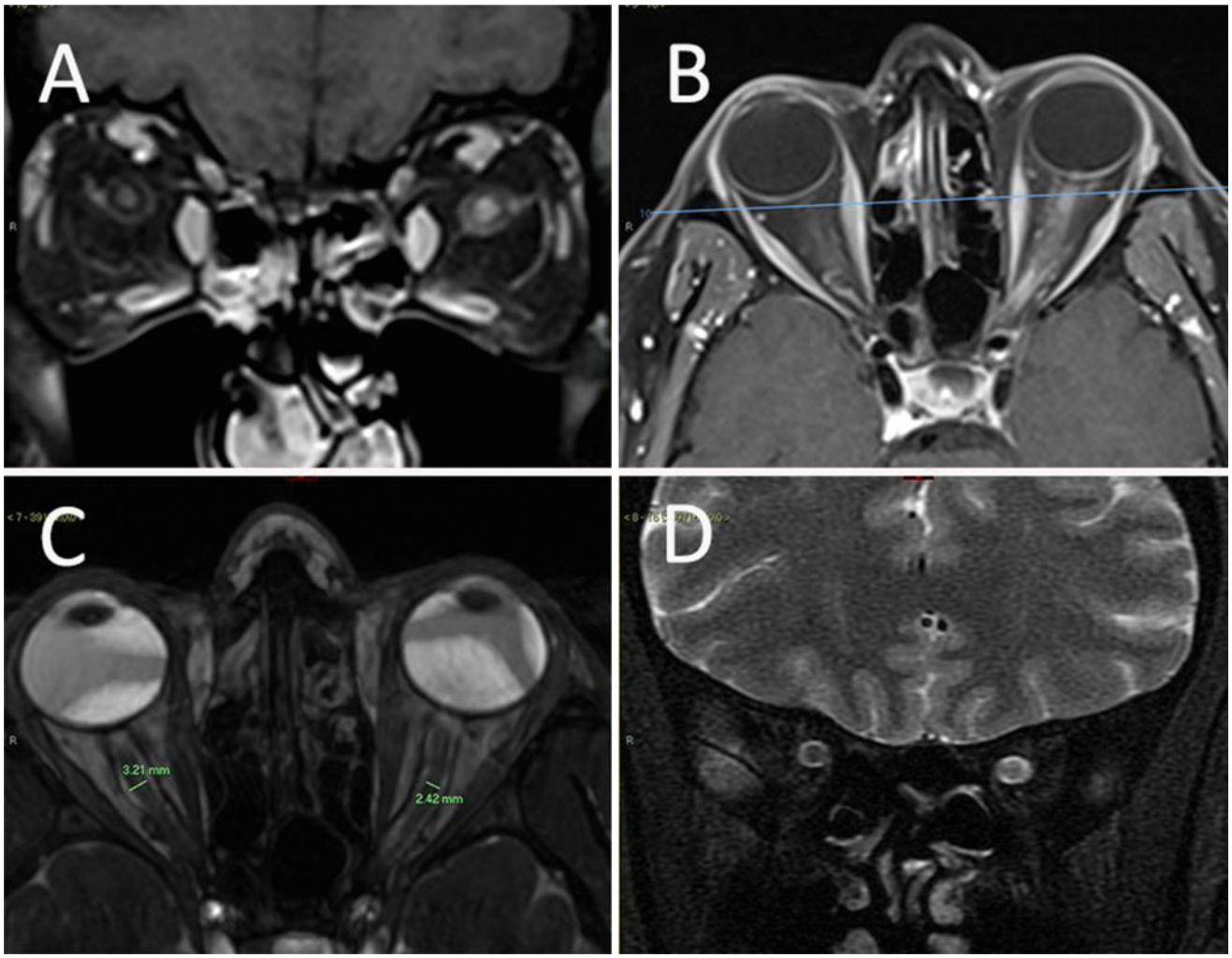


Fig. 12 T1WI-CE MR scan of a 59-year-old patient with MS and left optic neuritis (coronal **a** and axial **b**) note the high signal and enhancement within the left optic nerve as evident of the inflammatory process. Two years after treatment there is left optic atrophy (axial FIESTA – **c** and coronal T2 FAT SAT – **d**), note left optic nerve thinning (**c**) with hyperintense signal (**d**) as evident of "central pallor"

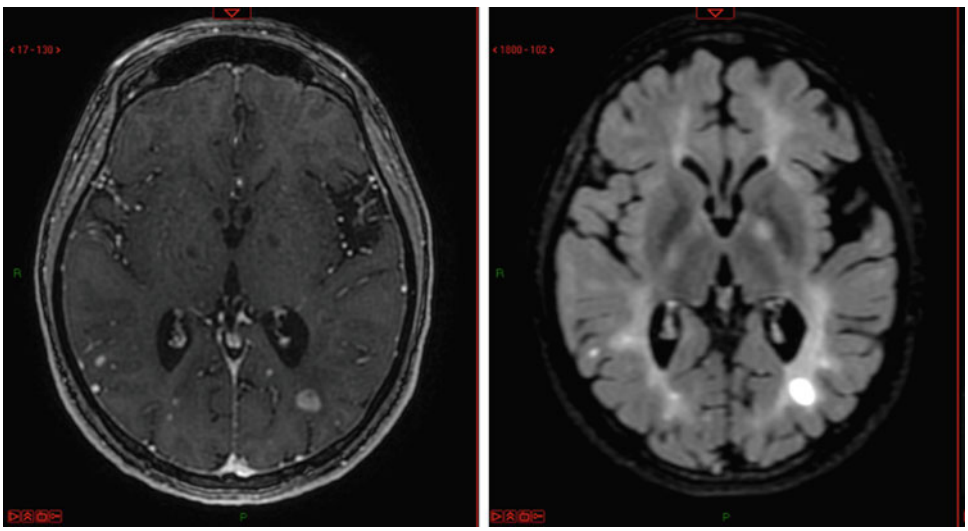


Fig. 13 MRI postcontrast of a different MS patient axial view T1 (*left*) and axial view FLAIR (*right*) – a few enhancing lesions on both sides. The most prominent is within the left parietal lesion consistent with acute demyelinating lesion

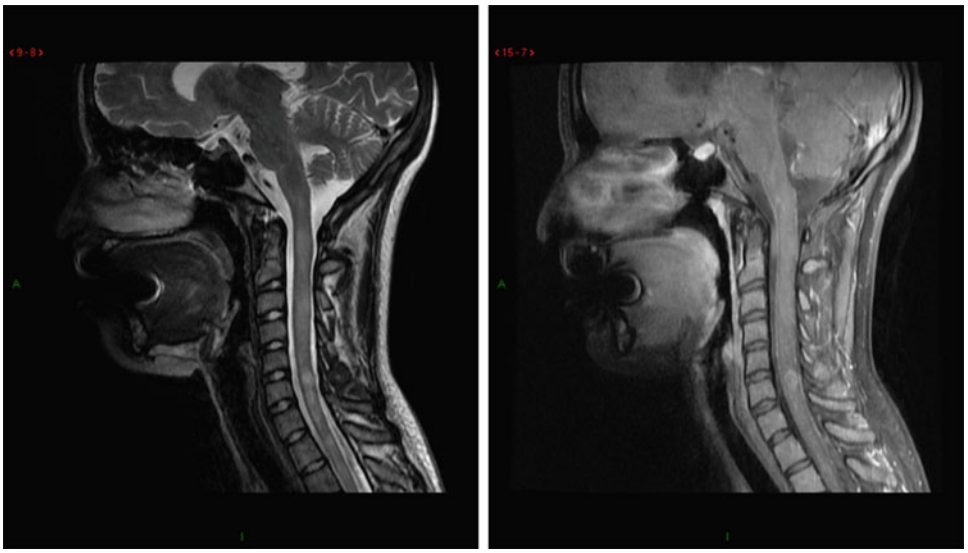


Fig. 14 MRI postcontrast multiple sclerosis (MS) – sagittal view T2 of cervical spine (*left*) and sagittal view T1 FAT SAT of cervical spine (*right*) – multiple confluent lesions within the cervical spine with an enhancing lesion at the C6 level consistent with acute demyelinating lesion

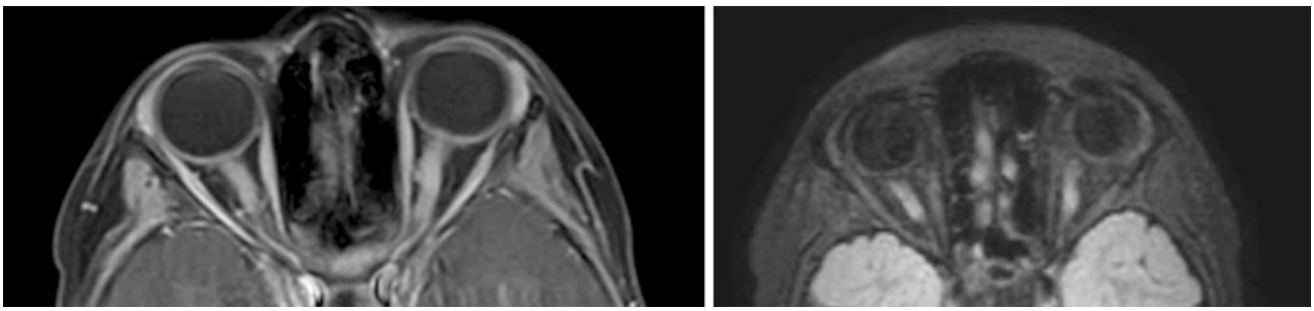


Fig. 15 MRI of a patient with bilateral optic neuritis axial view, T1 FAT SAT CE (*left*) – enhancement of both optic nerves Axial view, FLAIR (*right*) – hyperintense signal in both optic nerves

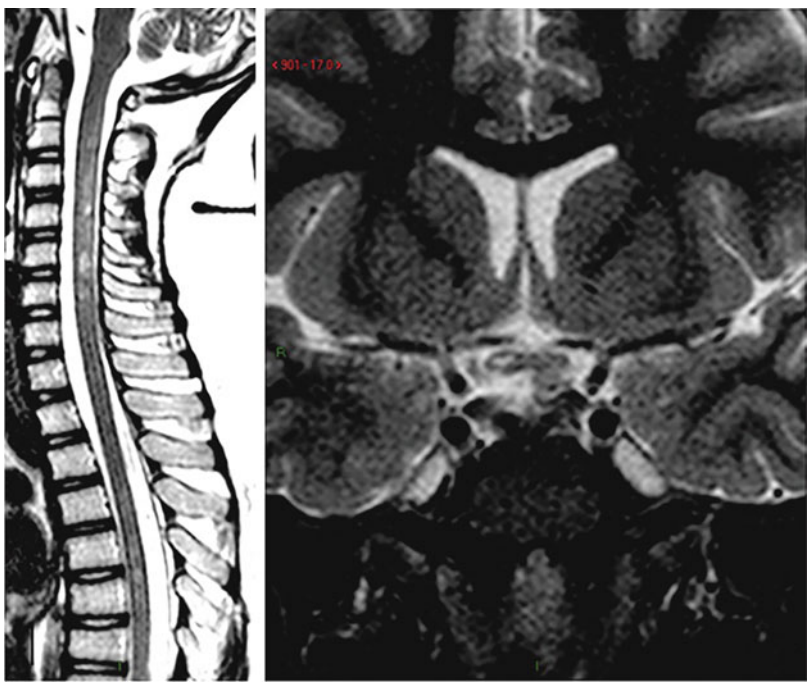


Fig. 16 MRI of the cervical and upper thoracic spine and brainT2. Neuromyelitis Optica (NMO) – sagittal view, T2 (*left*) – hyperintense long confluent lesion of the cord. Coronal view, T2 (*right*) – hyperintensity within the right chiasm



Fig. 17 Sagittal STIR image of the thoracic spine demonstrating a longitudinal hyperintense spinal cord lesion (white arrow) evident of NMO

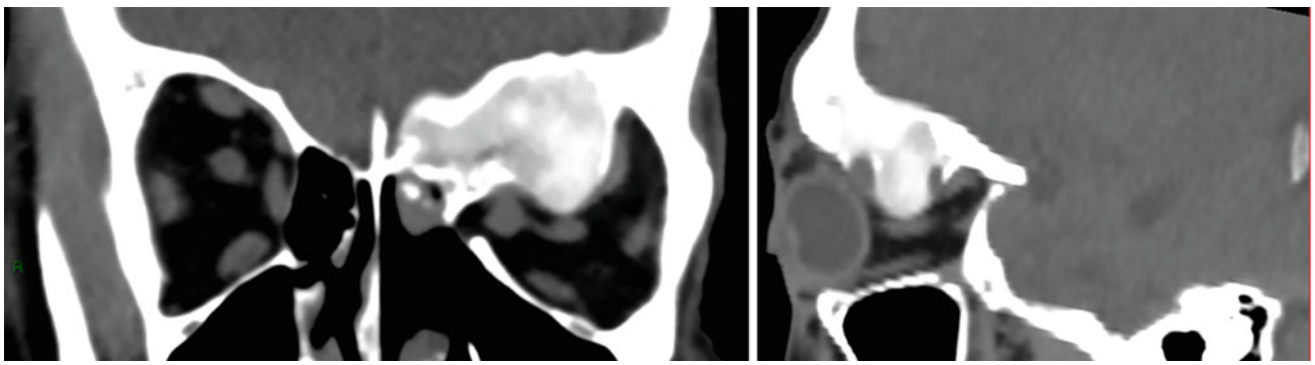


Fig. 18 CECT. Compression of the optic nerve due to orbitofrontal fibrous dysplasia (extrinsic optic nerve pathology) – coronal view, soft tissue window (*left*) – sclerotic fibrous dysplasia lesion involving the left orbital roof with inferior expansion of the lesion toward the orbit and compression of the optic nerve. Sagittal reformat, soft tissue window (*right*) – optic nerve compression due to fibrous dysplasia lesion involving the orbital roof



Fig. 19 3D reconstruction of the same patient with orbitofrontal fibrous dysplasia causing left optic nerve compression

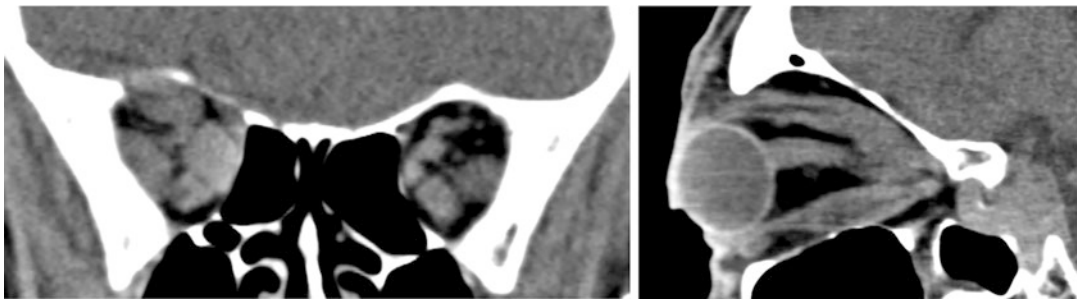


Fig. 20 CT of a patient with dysthyroid optic neuropathy (DON) – coronal, soft tissue view (*left*) – severe extra-ocular muscles enlargement of the right orbit with crowding of the orbital apex and optic nerve compression. Sagittal, soft tissue view (*right*) – fusiform enlargement of the superior and inferior rectus of the right orbit

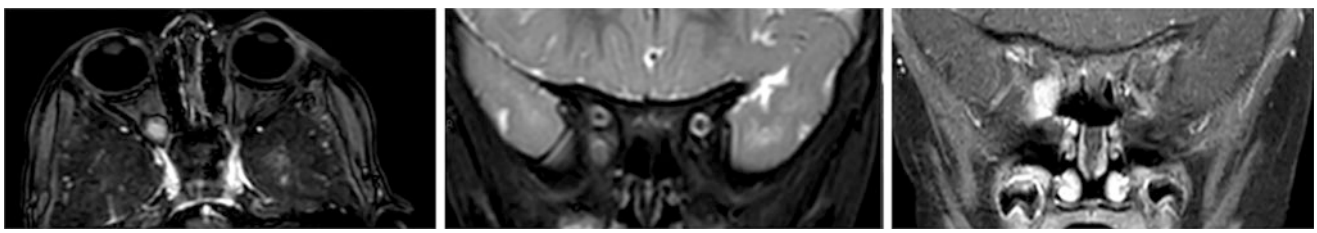


Fig. 21 MRI postcontrast – Orbital apex syndrome involving optic nerve and leads to right hypotropia – axial view, T1 FAT SAT (*left*) – an enhancing lesion inferior to the right optic nerve. Coronal view, T2 (*middle*) – probable inferior rectus muscle lesion causing compression of the right optic nerve. Coronal view (*right*) – enhancing lesion within the inferior rectus muscle. No biopsy proven diagnosis. Lost to follow up. Differential diagnosis is pseudotumor orbit and primary or secondary malignancy involving the inferior rectus muscle



Fig. 22 CT scan axial soft tissue window, left globe traumatic proptosis with retrobulbar fat stranding and apical soft tissue thickening consistent with orbital apex hemorrhage

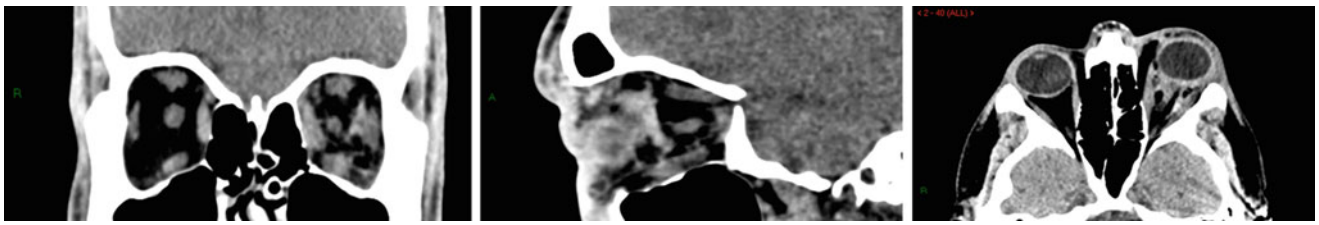


Fig. 23 CT scan coronal and sagittal views (*left* and *middle*) – left acute intraconal orbital traumatic hemorrhage. Axial view (*right*) – acute hemorrhage at left orbit, proptosis, and stranding of retrobulbar fat

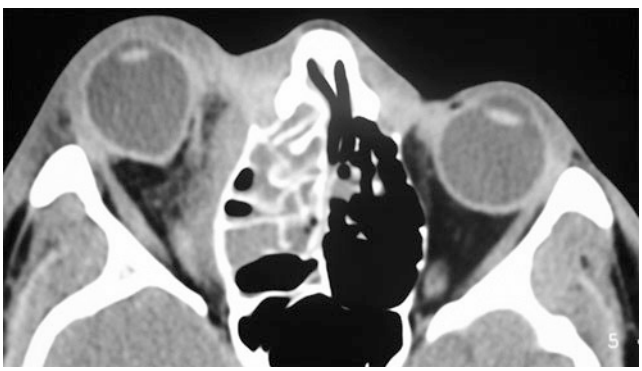


Fig. 24 NECT of a young male with right orbital cellulitis and SPA secondary to ethmoid sinusitis. The patient presented with periocular swelling, right proptosis, and decreased optic nerve function. Note significant proptosis with globe tenting on the right side (posterior globe angle of less than 130°)

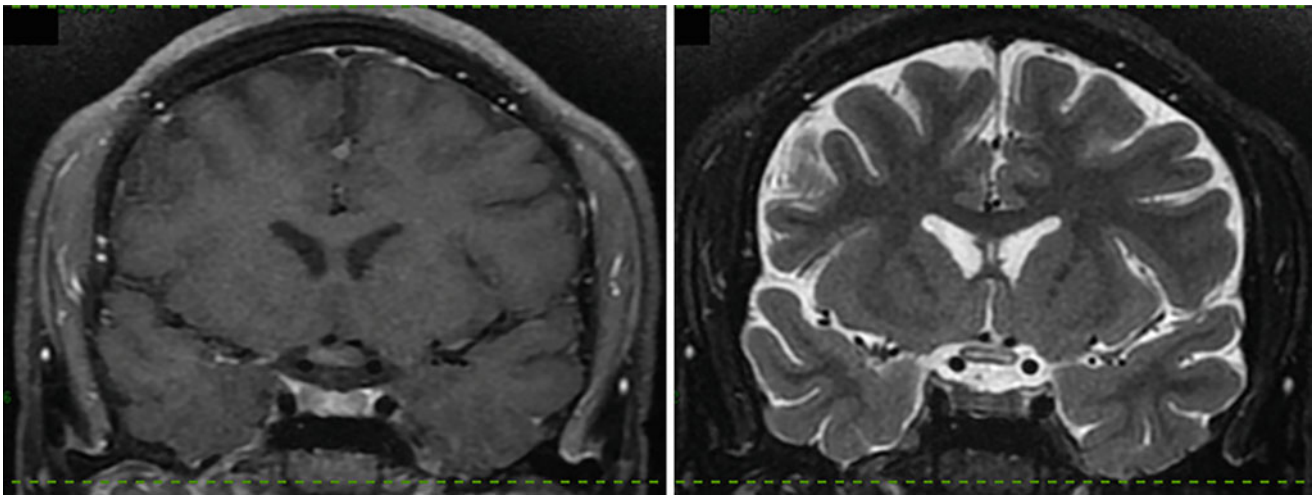


Fig. 25 MRI postcontrast – Leber's hereditary optic neuropathy (LHON) – coronal view, T1 (*left*) – slight enhancement of optic chiasm. Coronal view, T2 (*right*) – faint high signal within the chiasm early stage before optic atrophy



Fig. 26 Clinical appearance of the optic disc (color fundus photograph). Right eye swollen disc consistent with papillitis (*left*), left eye normal appearance of the optic nerve (*right*)

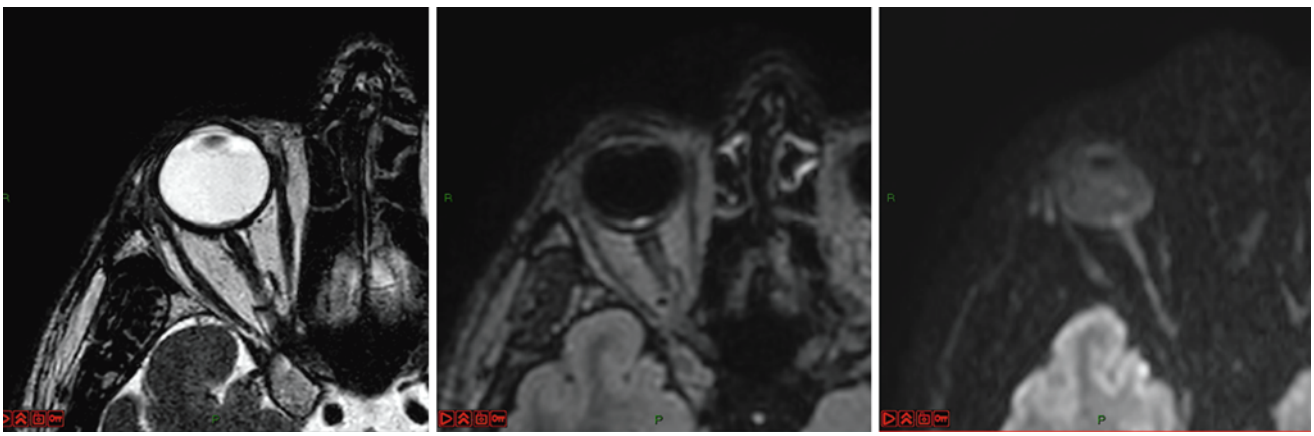


Fig. 27 MRI right optic nerve papillitis, axial T2 high resolution (*left*), FLAIR (*middle*), DWI (*right*). There is bulging of the right optic nerve head with high signal consistent with radiologic papillitis

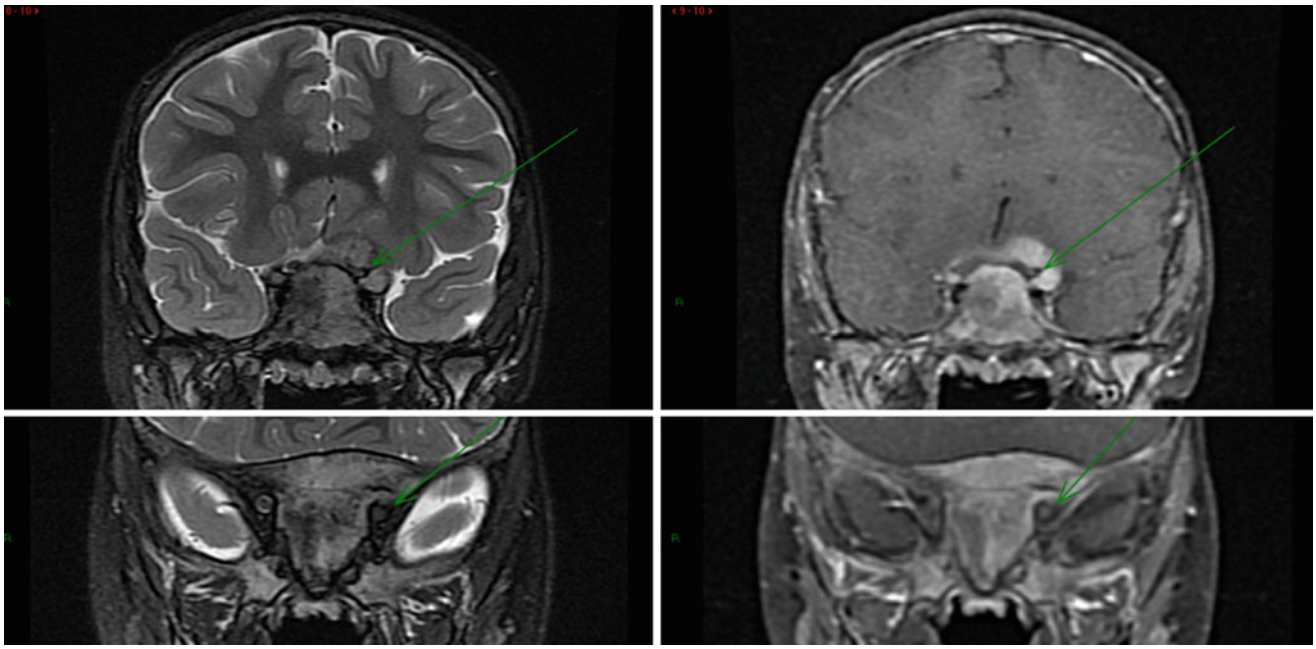


Fig. 28 MRI postcontrast of a 2.5-year-old girl with neuroblastoma metastasis to the sphenoid (extrinsic optic nerve pathology); T2 WI coronal view (*left* images), T1 WI + gad coronal view (*right* images) – there is thickening of the left sphenoid bone with soft tissue enhancement and involvement of the left clinoid causing compression of the left optic nerve within the orbital apex. The child was diagnosed with metastasis of neuroblastoma from the adrenal gland, he presented with left eye vision loss, new onset strabismus, and left sensory exotropia

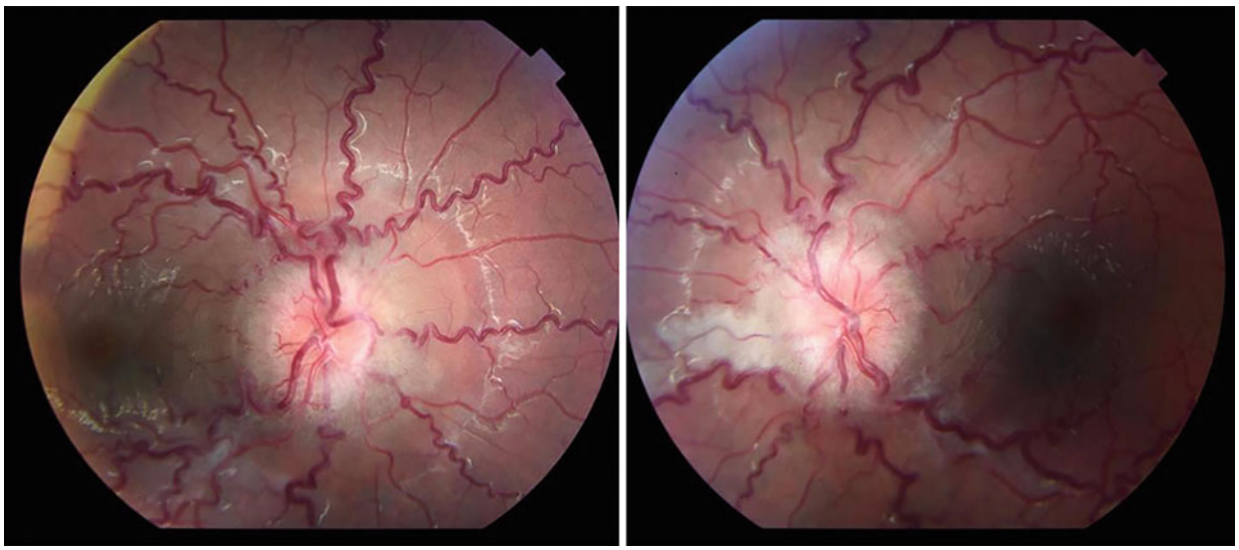


Fig. 29 Fundus photograph of a patient with bilateral optic disc edema secondary to papilledema

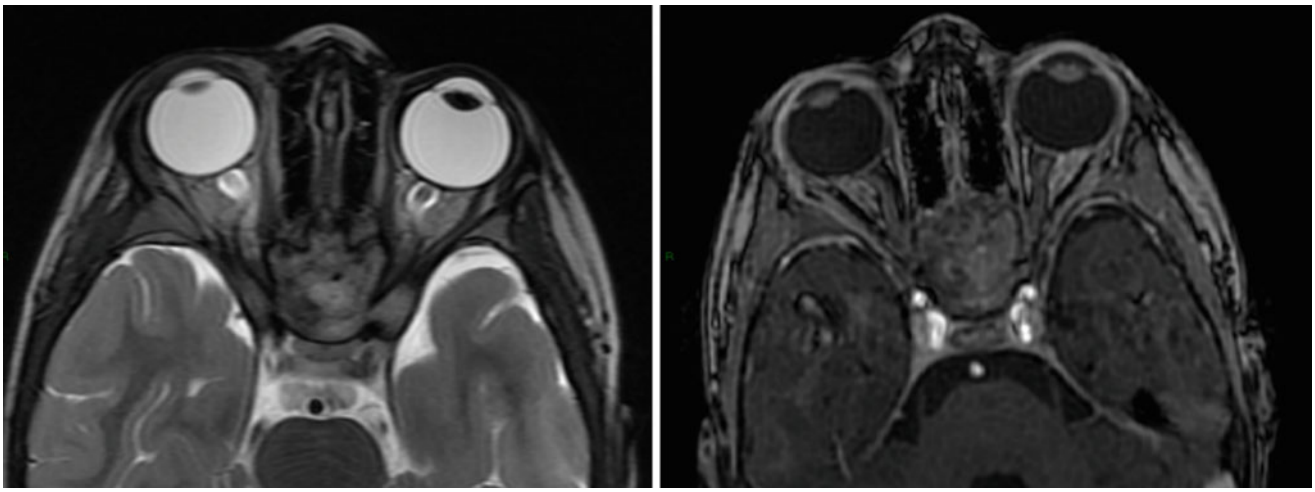


Fig. 30 MOG – MRI axial T2 (*left*) and axial T1 FS CE (*right*) with bilateral optic nerve edema and enhancement with bulging of the optic disc-consistent with papilledema (different patient). The patient tested positive for MOG antibodies

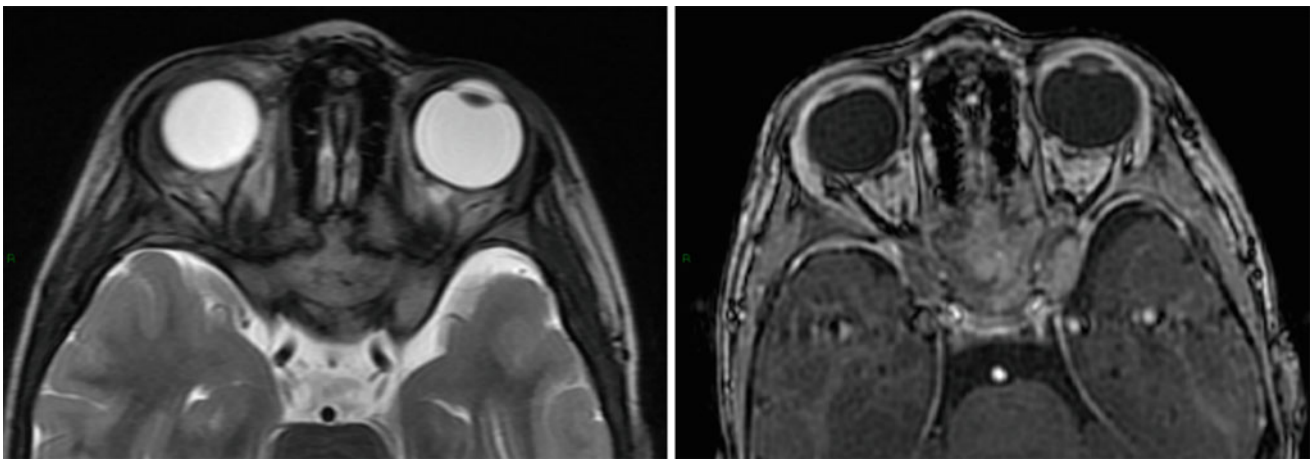


Fig. 31 MRI of the same patient, 2 years apart with bilateral optic atrophy. The contrast enhancement and papilledema resolved. T2 axial (*left*) and T1 axial CE FAT SAT (*right*)

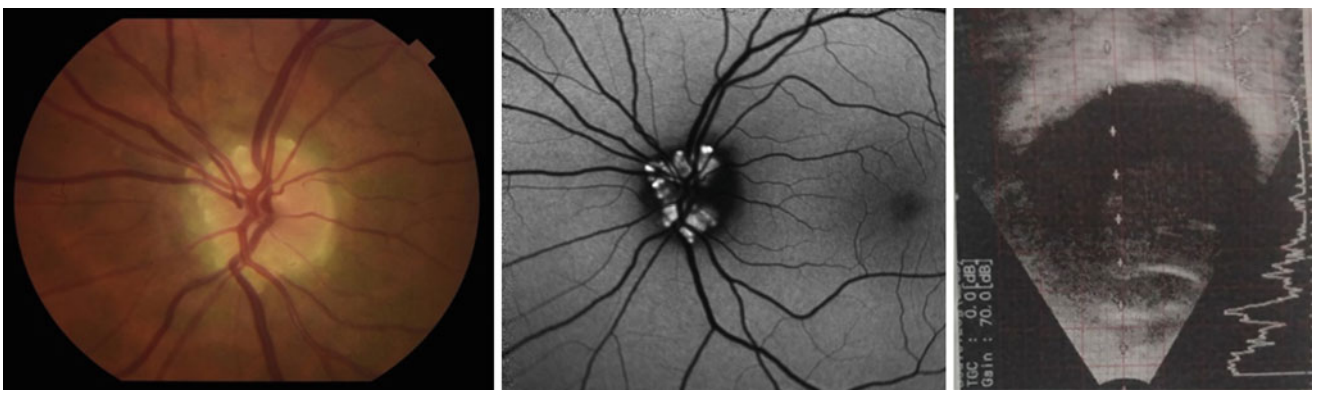


Fig. 32 Optic disc drusen – color fundus photography (*left*) – refractile, pale, rounded foci, and lobulated clusters occupying sectors of the nerve head. Fundus autofluorescence (*middle*) – bright hyper-auto-fluorescent foci in the disc. B-scan ultrasound (*right*) – a hyperechogenic appearance at the optic disc that persists at low gain



Fig. 33 Axial CT, soft tissue window of a patient with left optic disc drusen. Note a small focus of calcification within the left optic disc

References

1. Jäger HR, Miszkiel KA. Pathology of the optic nerve. Neuroimaging Clin N Am. 2008;18(2):243–59. https://doi.org/10.1016/J.NIC.2007.10.001.
2. Rebhun WC. Retinal and optic nerve diseases. Vet Clin North Am Equine Pract. 1992;8(3):587–608. https://doi.org/10.1016/s0749-0739(17)30443-1.
3. Riordan-Eva P. Clinical assessment of optic nerve disorders. Eye. 2004;18(11):1161–8. https://doi.org/10.1038/sj.eye.6701575.
4. Becker M, Masterson K, Delavelle J, Viallon M, Vargas M-I, Becker CD. Imaging of the optic nerve. Eur J Radiol. 2010;74(2):299–313. https://doi.org/10.1016/J.EJRAD.2009.09.029.
5. Menjot de Champfleur N, Leboucq N, Menjot de Champfleur S, Bonafé A. Imaging of the pre-chiasmatic optic nerve. Diagn Interv Imaging. 2013;94(10):973–84. https://doi.org/10.1016/J.DIII.2013.06.001.
6. De Potter P. Advances in imaging in oculoplastics. Curr Opin Ophthalmol. 2001;12(5):342–6. https://doi.org/10.1097/00055735-200110000-00003.
7. Tailor TD, Gupta D, Dalley RW, Keene CD, Anzai Y. Orbital neoplasms in adults: clinical, radiologic, and pathologic review. Radiographics. 2013;33(6):1739–58. https://doi.org/10.1148/rg.336135502.
8. Shokoohi H, Pyle M, Kuhl E, et al. Optic Nerve Sheath Diameter Measured by Point-of-Care Ultrasound and MRI. J Neuroimaging. 2020;30(6):793–799. https://doi.org/10.1111/jon.12764.
9. Kim DH, Jun JS, Kim R. Measurement of the Optic Nerve Sheath Diameter with Magnetic Resonance Imaging and Its Association with Eyeball Diameter in Healthy Adults. J Clin Neurol. 2018;14(3):345–350. https://doi.org/10.3988/jcn.2018.14.3.345
10. Association for Research in Vision and Ophthalmology. JD, Garcia JPS, Baxter AB, Garcia PMT, Holliday RA, Rosen RB. Investigative Ophthalmology & Visual Science. Vol 45. C.V. Mosby Co; 1977. https://iovs.arvojournals.org/article.aspx?articleid=2407938. Accessed November 22, 2020.

Part X

Vascular Malformations

Lymphatic Malformations

65

Kasturi Bhattacharjee, Nirod Medhi, and Shyam Sundar Das Mohapatra

Contents

1 **Signs and Symptoms** 492
2 **Differential Diagnosis** 492
3 **Diagnosis** 492
4 **Treatment** 492
5 **Figures with Captions** 493
References 497

Abstract

- Lymphatic malformations (LM) are low-flow vascular lesions of orbit and classified under simple vascular malformations based on the International Society for the Study of Vascular Anomalies (ISSVA) classification of vascular anomalies, which was expanded upon Mulliken and Glowaki's classification based on pathologic features.
- LMs can be macrocystic, microcystic, or mixed and all of them may have solid stromal components.
- LM is a benign vascular lesion of the lymphatic system, which is characterized by abnormal endothelial-lined channels and frequently affects the orbit.
- Orbital LM is probably congenital, but generally does not become clinically apparent for months or years after birth. In some cases, LM may be familial and can present as diffuse or multifocal lesions.
- Orbital LM may appear in children in the first few years of life or may be delayed for years after birth.
- The patient may present with abrupt onset of proptosis, ptosis, periocular soft tissue swelling and ecchymosis resulting from spontaneous or traumatic hemorrhage.
- Conjunctival components, such as multiple clear or hemorrhagic cysts, are commonly present along with underlying orbital lesion. Blood-filled cysts are known as chocolate cyst.
- In most cases, orbital LM can be diagnosed on the basis of its typical clinical course and clinical findings. However, imaging is mandatory to rule out a venous component.
- On CT, the orbital lesion appears as a low-density cystic, intra- and/or extraconal mass.
- On MRI, the lesion is hypointense on T1 and hyperintense on T2, but may be variable depending on the state of hemoglobin degeneration.
- The hemorrhagic cyst-like spaces are best seen on T2-weighted MRI. These cysts sometimes contain blood–plasma levels, which is highly suggestive of the diagnosis. On T1-weighted MRI, subacute hemorrhages in the range of intra- and extra-cellular methemoglobin will appear hyperintense.
- Complete surgical resection is often not possible and may not be necessary due to poorly defined nature of the lesion and excessive bleeding at the time of surgical manipulation.

K. Bhattacharjee (✉)
Department of Ophthalmic Plastic and Reconstructive Surgery, Sri Sankaradeva Nethralaya, Guwahati, India

N. Medhi
Primus Imaging, Guwahati, India

S. S. D. Mohapatra
Sri Sankaradeva Nethralaya, Guwahati, India

© Springer Nature Switzerland AG 2022
G. Ben Simon et al. (eds.), *Atlas of Orbital Imaging*,
https://doi.org/10.1007/978-3-030-62426-2_105

- Aspiration of large hemorrhagic cysts can be performed through the eyelid or conjunctiva as a temporary treatment modality.
- During surgical resection, the mass should be debulked as much as possible without damaging surrounding structures. The carbon dioxide laser can be used in some cases to control bleeding and to facilitate tumor removal.
- Recently, aspiration with intralesional injection of sclerosing agents or tissue glue has become a popular modality of treatment and gives longer lasting action. Oral sildenafil has been found to soften and involute LM.
- Bleomycin has become one of the most popular agents in treating orbital LM.

Keywords

Lymphatic malformations · Low-flow vascular lesions · Simple vascular malformations · Endothelial-lined channels · Proptosis · Hemorrhage · Chocolate cyst · Aspiration · Sclerosing agents · Bleomycin

1 Signs and Symptoms

Orbital LMs generally appear in children in the first few years of life. In a few instances, it is recognized in the teenage years, when the patient presents with abrupt proptosis, ptosis, periocular soft tissue swelling, and ecchymosis resulting from spontaneous or traumatic hemorrhage. LM may also become apparent in adulthood and even in old age. Conjunctival components, such as multiple clear or hemorrhagic cysts, are commonly present and these findings indicate the presence of underlying orbital lesion. These cystic structures are often filled with blood and seen clinically or at the time of surgery and known as chocolate cyst. Patients with orbital LM may have LMs elsewhere in the body, commonly on the palate. Presence of such findings should suggest the orbital diagnosis. The abrupt hemorrhage in the orbit may resolve gradually, but can also recur. The size of the lesions may change with upper respiratory tract infections [1–11].

2 Differential Diagnosis

The differential diagnosis includes other orbital tumors or malformations including orbital venous malformation, capillary malformation, malignant rhabdomyosarcoma, lymphoma, chloroma, neuroblastoma, orbital cysts, pseudotumor, and cellulitis.

3 Diagnosis

In most instances, orbital LM can be diagnosed on the basis of its typical clinical course and clinical findings as described. Additionally, imaging modalities like CT and MRI scan help to establish the diagnosis without resorting to an immediate biopsy. The orbital lesion appears as a low-density cystic, intra- and/or extraconal mass. On MRI, the lesion appears hypointense on T1 and hyperintense on T2, but may be variable depending on the state of hemoglobin degeneration. The hemorrhagic cyst-like spaces are best seen on T2-weighted MRI. These cysts sometimes contain blood–fluid levels within, which is very suggestive of the diagnosis. However, it should be interpreted with caution because orbital malignant tumors, such as rhabdomyosarcoma, can also present with hemorrhagic cysts. LM shows variable enhancement with contrast agent. No vascular component is seen on angiography. Deep orbital LM can sometimes present as well defined, round or oval mass simulating cavernous venous malformations, however typical diffuse enhancement of the latter will distinguish between these two.

4 Treatment

Management of orbital LM can be difficult. Complete surgical resection is often not possible because of poorly defined nature of the lesion and excessive bleeding at the time of surgical manipulation. Observation is more suitable in young children if the visual acuity is not threatened. Acute hemorrhage may resolve over time with observation alone. If massive tumor and hemorrhage cause extreme proptosis or causes optic nerve compression, then immediate treatment should be considered. Aspiration of large hemorrhagic cysts can be performed through the eyelid or conjunctiva as a temporary treatment modality. Exploration with open biopsy is warranted if malignancy, such as orbital rhabdomyosarcoma, is suspected. During surgical resection, the tumor should be debulked as much as possible with taking care not to damage the optic nerve or extraocular muscles. The carbon dioxide laser can be used in some cases to control bleeding and to facilitate tumor removal. Recently, aspiration with intralesional injection of sclerosing agents (commonly bleomycin) or tissue glue has become a popular modality of treatment. Sclerosing agents are longer lasting, but may require interventional neuroradiologist for localization. Oral sildenafil has been found to soften and involute LM [12, 13].

5 Figures with Captions



Fig. 1 Clinical photograph showing facial appearance of a 29-year-old female patient with proptosis of the right eye



Fig. 2 Clinical photograph showing conjunctival involvement by anterior extension of orbital LM with hemorrhagic cysts in conjunctiva (same patient as in Fig. 1)



Fig. 3 Clinical photograph showing facial appearance of a 21-year-old female patient with ptosis, proptosis, and inferotemporal displacement of the left eye

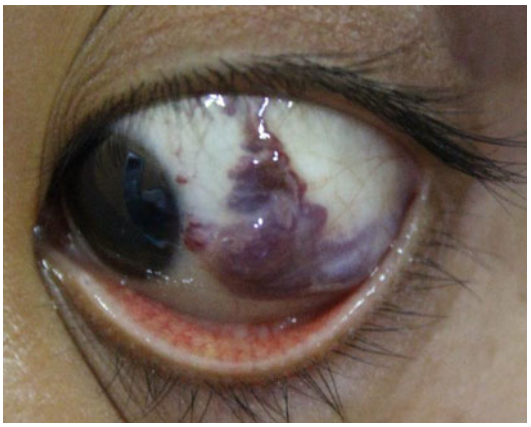


Fig. 4 Clinical photograph showing hemorrhagic cyst in conjunctiva (same patient as in Fig. 3)

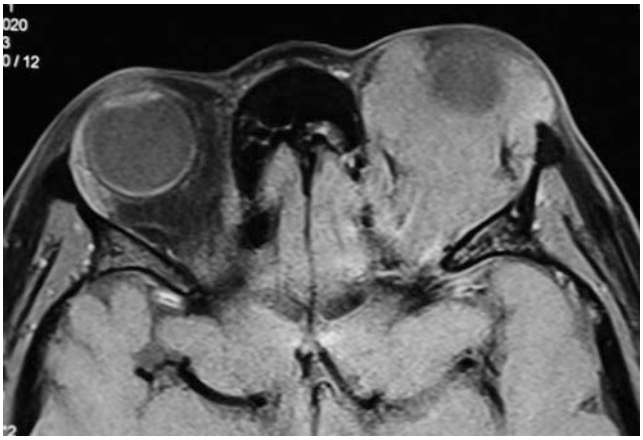


Fig. 5 MRI scan axial section (T1-weighted FS) showing lobulated isointense lesion involving the intra- and extraconal space in the left orbit (same patient as in Fig. 3)

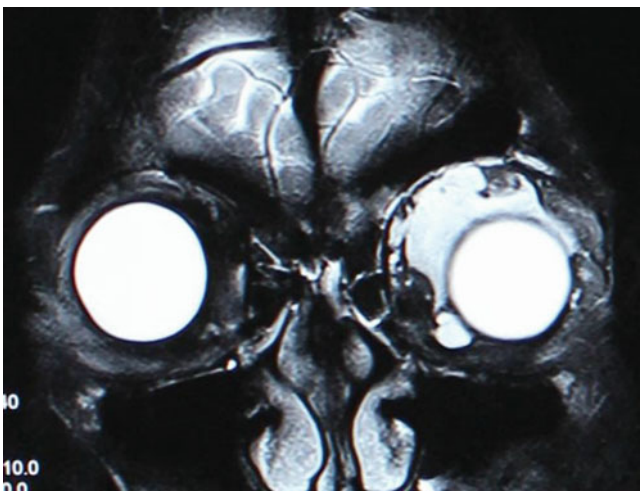


Fig. 6 MRI scan coronal section (T2-weighted FS) showing lobulated hyperintense lesion in the left orbit (same patient as in Fig. 3)

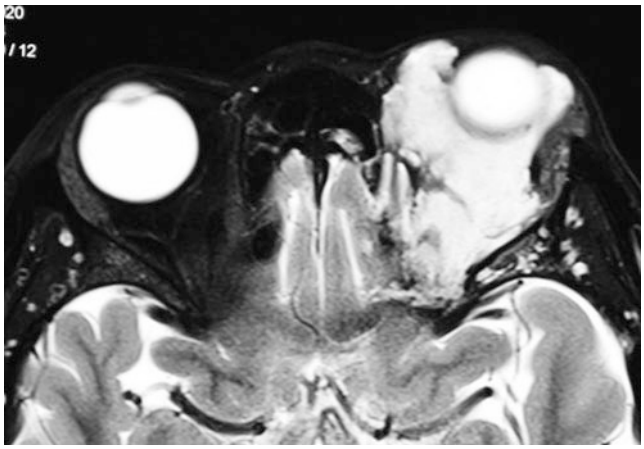


Fig. 7 MRI scan axial section (T2 weighted) showing lobulated hyperintense lesion involving the intra- and extraconal space in the left orbit (same patient as in Fig. 3)



Fig. 8 Clinical photograph showing facial appearance of a 50-year-old female patient with minimal proptosis of the right eye

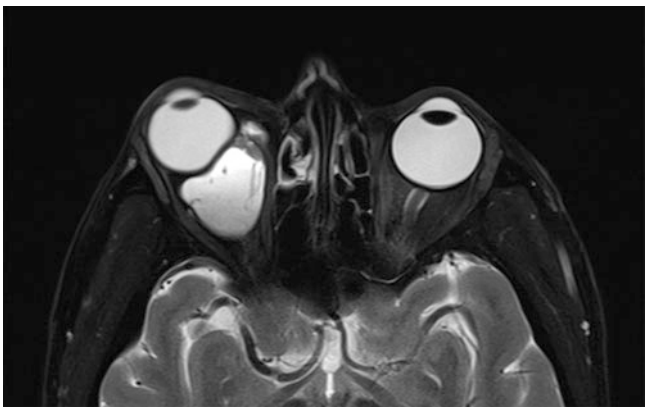


Fig. 9 MRI scan axial section (T2-weighted FS) showing lobulated mixed intensity lesion with gradual fluid-fluid levels in the retrobulbar space of right eye (same patient as in Fig. 8)



Fig. 10 MRI scan axial section (T1 weighted with fat suppression) showing dominant hyperintense signal suggesting subacute hemorrhage, methemoglobin is in the dependent part (same patient as in Fig. 8)

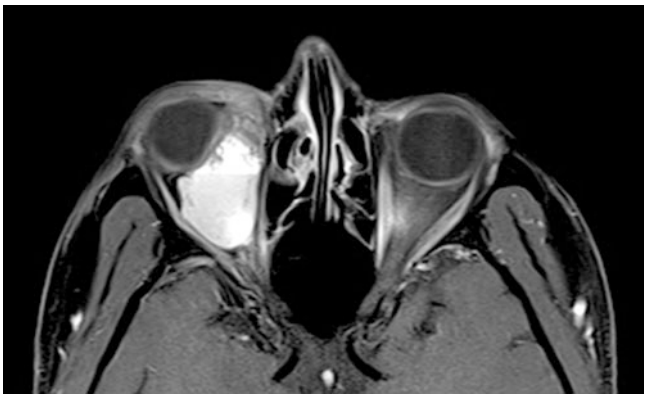


Fig. 11 MRI scan axial section (T1 weighted with fat suppression) showing no evidence of any enhancement in post-contrast study. The LM is indenting the posterior aspect of the right globe (same patient as in Fig. 8)



Fig. 12 Clinical photograph showing facial appearance of a 28-year-old male patient with hemorrhagic proptosis of the left eye



Fig. 13 Clinical photograph showing facial appearance after aspiration with intralesional injection of sclerosing agents (same patient as in Fig. 12)

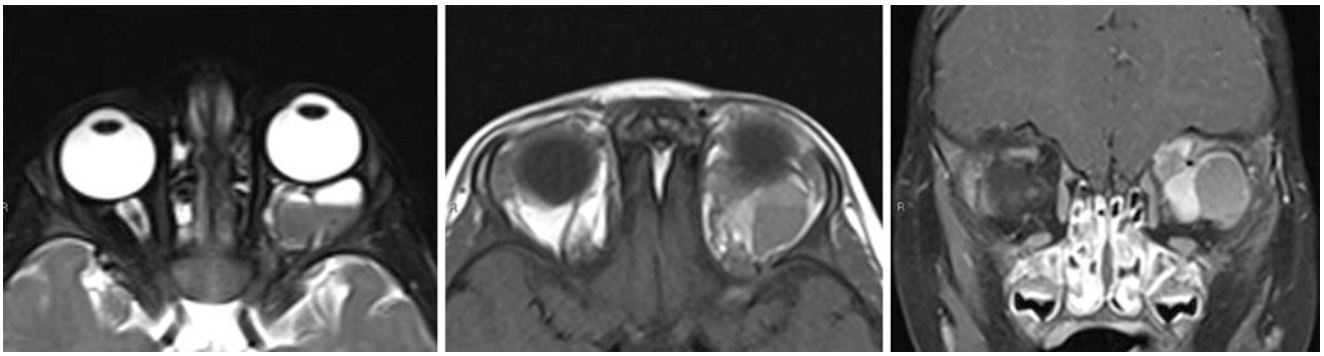


Fig. 14 MR of a 1.5-year-old male with left orbital LM. Axial T2-weighted FS image (*left*) showing fluid–fluid levels, axial conventional T1 (*middle*) and coronal CE-T1-FS (*right*) showing the multi-lobulated nature of the LM and the variable intensities depending on the age of the blood

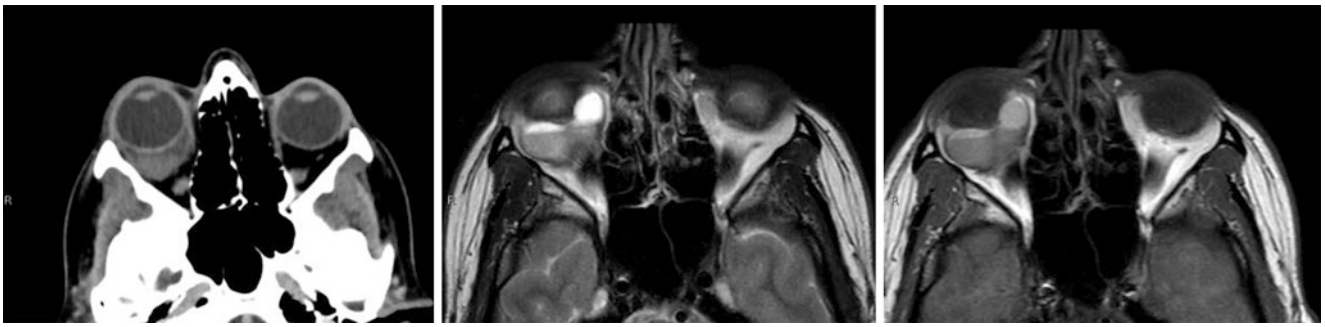


Fig. 15 Imaging studies of a 35-year-old female with right orbital LM. CECT axial view (*left*) demonstrating mixed density nonenhancing anterior intraconal mass. Axial T2-weighted (*middle*) and axial T1-weighted CE (*right*) images showing the fluid–fluid levels and variable intensities

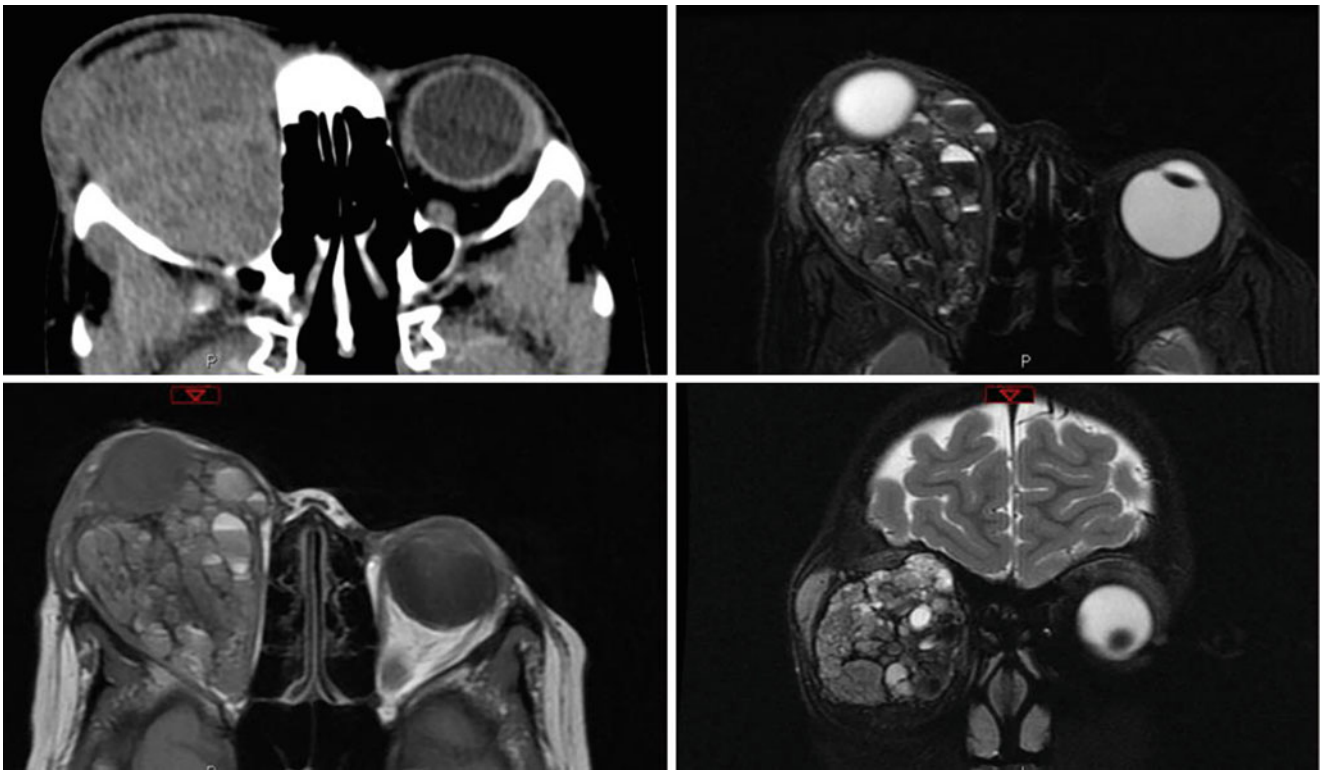


Fig. 16 Axial CT (*upper left*) of a 19-year-old female with right orbital extensive LM and blind eye, note the mixed density signal of the malformation. Axial T1 (lower left) and T2-weighted FS (*upper right*) images showing the fluid–fluid levels of the cystic components. T2-weighted FS coronal image (*lower right*) demonstrates the heterogeneity of the LM



Fig. 17 Axial CT of the same patient as in Fig. 16 after right eye evisceration and extensive lesion debulking. Note the hyperdense glass beads (*black arrow*) used to fill the scleral pocket and the hypodense porous polyethylene orbital implant (*gray arrow*)

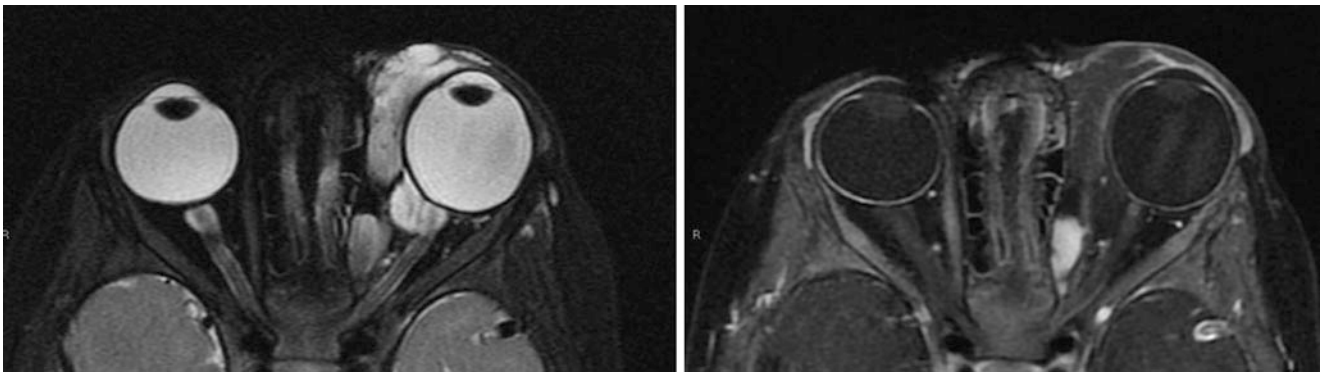


Fig. 18 MR of a 2-year-old female with left orbital LVM. T2-weighted FS image (*left*) showing the multispatial nature of the anterior lymphatic component. T1-weighted FS CE image (*right*) demonstrating the hypointensity of the anterior LM with peripheral enhancement in comparison with the bright homogeneous enhancement of the posterior medial venous component. Note the relatively large left globe due to axial myopia and amblyopia

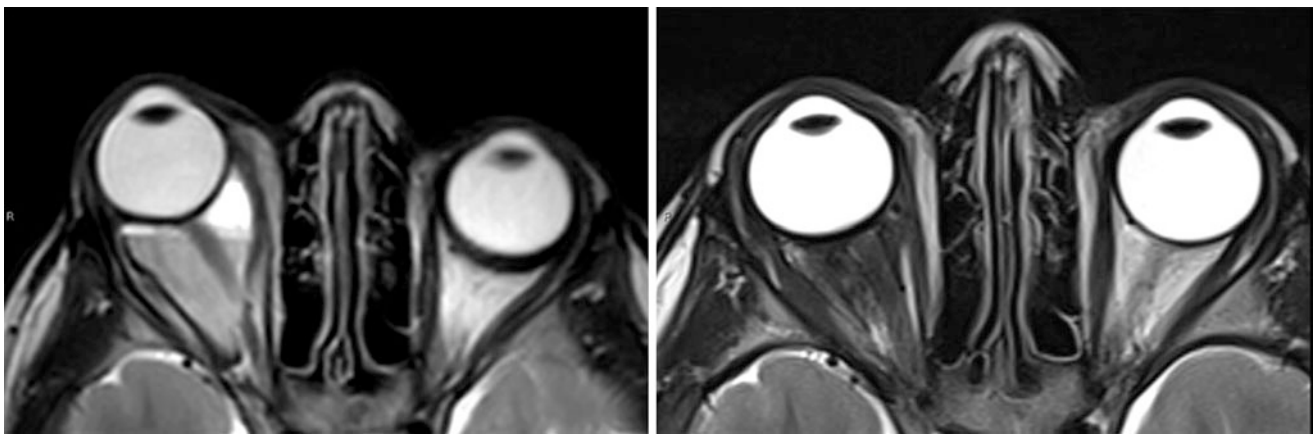


Fig. 19 T2-weighted axial MRI of a 9-year-old female with right orbital macrocystic LM and fluid–fluid levels (*left*). The patient underwent LM aspiration and bleomycin injection with excellent response and involution of the LM (*right*); note the mixed hypointense signal after treatment. (Figs. 14, 15, 16, 17, 18, and 19*: Courtesy of the editors*)

References

1. Rootman J, Heran MK, Graeb DA. Vascular malformations of the orbit: classification and the role of imaging in diagnosis and treatment strategies. Ophthalmic Plast Reconstr Surg. 2014;30(2):91–104.
2. ISSVA. Classification of vascular anomalies ©2018. International Society for the Study of Vascular Anomalies. Available at http://issva.org/classification. Accessed 17 Nov 2020.
3. Mulliken JB, Glowacki J. Hemangiomas and vascular malformations in infants and children: a classification based on endothelial characteristics. Plast Reconstr Surg. 1982;69(3):412–22.
4. Shields JA, Shields CL, Scartozzi R. Survey of 1264 patients with orbital tumors and simulating lesions: the 2002 Montgomery lecture, part 1. Ophthalmology. 2004;111:997–1008.
5. Guinto G, Guinto-Nishimura Y. Orbital lymphangiomas. World Neurosurg. 2014;81(5–6):708–9.
6. Woo YJ, Kim CY, Sgrignoli B, Yoon JS. Orbital lymphangioma: characteristics and treatment outcomes of 12 cases. Korean J Ophthalmol. 2017;31(3):194–201.
7. Seca M, Borges P, Reimão P, Gomes M, Meireles A. Conjunctival lymphangioma: a case report and brief review of the literature. Case Rep Ophthalmol Med. 2012;2012:836573.
8. Kennerdell JS, Maroon JC, Garrity JA, et al. Surgical management of orbital lymphangioma with the carbon dioxide laser. Am J Ophthalmol. 1986;102:308–14.
9. Hill RH, Shiels WE, Foster JA, et al. Percutaneous drainage and ablation as first line therapy for macrocystic and microcystic orbital lymphatic malformations. Ophthal Plast Reconstr Surg. 2012;28:119–25.
10. Gandhi NG, Lin LK, O'Hara M. Sildenafil for pediatric orbital lymphangioma. JAMA Ophthalmol. 2013;131:1228–30.
11. Prat D, Gomel N, Zloto O, Anne M, BenSaid A, Bhattacharjee K, Yassur I, Sagiv O, Ben Simon GJ. Low-dose bleomycin injections for orbital lymphatic and lymphatic-venous malformations: a multicentric case series study. Ophthalmic Plast Reconstr Surg. 2020. Epub ahead of print.
12. Danial C, Tichy AL, Tariq U, et al. An open-label study to evaluate sildenafil for the treatment of lymphatic malformations. J Am Acad Dermatol. 2014;70(6):1050–7.
13. Wang S, Zhang J, Ge W, Liu Y, Guo Y, Liu Y, et al. Efficacy and safety of oral sildenafil in treatment of pediatric head and neck lymphatic malformations. Acta Otolaryngol. 2017 Jun;137(6):674–8.

Venous Malformations (VM) Distensible/ Lymphatico-Venous Malformations (LVM)

66

Kasturi Bhattacharjee, Shyam Sundar Das Mohapatra, and Aditi Mehta

Contents

1 **Signs and Symptoms** 500

2 **Differential Diagnosis** 500

3 **Diagnosis** 500

4 **Treatment** 500

5 **Figures with Captions** 501
5.1 Capillary Malformation 501
5.2 Orbital Venous Malformation 503

References 505

Abstract

- Capillary malformations (CM) and venous malformations (VM) of the orbit are low-flow lesions and classified as simple vascular malformations based on the International Society for the Study of Vascular Anomalies (ISSVA) classification of vascular anomalies, which was expanded upon Mulliken and Glowaki's classification [1–3] based on cellular characteristics.
- CMs and VMs are distensible in nature.
- CM, also known as capillary hemangioma, benign hemangioendothelioma or strawberry hemangioma, is a common vascular tumor of childhood, usually occurs on the eyelid, and can involve the orbit also [4].
- CM of orbit can be present at birth or shortly after birth or within the first few months of life. The lesions generally enlarge for the first 1 to 2 years of life and then gradually regress, similar to eyelid or superficial CMs.
- Large CMs may be associated with a condition known as Kasabach–Merritt syndrome [5], which causes sequestration of platelets by large visceral hemangiomas.
- VM is caused by dilation of one or more veins and can produce mass effect in the orbit.
- The classic VM usually becomes apparent in young adults and causes positional proptosis.
- In VM, the proptosis increases with the head bent downward or during Valsalva maneuver [6]. This sign can be observed in CM also, but it is not pathognomonic for it [7]
- Orbital CM appears as a round or ovoid circumscribed mass or an irregular or diffuse mass in the intraconal or extraconal space on computed tomography (CT) imaging and homogeneous to heterogeneous, commonly being hypointense on T1 and hyperintense on T2 weighted magnetic resonance imaging (MRI) imaging. Moderate to marked homogeneous enhancement occurs with contrast agents
- Orbital VM appears as a round or irregular mass on CT and MRI, which may become more prominent with Valsalva maneuver performed during the scanning procedure.
- Systemic or local corticosteroids can help in regression of the tumor, but risk of potential complications is there [8]. Interferon-α2b has also been found to be effective in hastening tumor regression [9]. Recently, beta

K. Bhattacharjee (✉) · A. Mehta
Department of Ophthalmic Plastic and Reconstructive Surgery, Sri Sankaradeva Nethralaya, Guwahati, India

S. S. D. Mohapatra
Sri Sankaradeva Nethralaya, Guwahati, India

© Springer Nature Switzerland AG 2022
G. Ben Simon et al. (eds.), *Atlas of Orbital Imaging*,
https://doi.org/10.1007/978-3-030-62426-2_104

blocker (propranolol) given orally or topically has been shown to cause significant involution over a relatively shorter period of time [10]. Well-circumscribed tumors can be treated with surgical excision. The prognosis is generally excellent for vision and life.

- Orbital VM can be observed if not symptomatic or may require surgical excision in symptomatic cases. Vascular clips can also be used. Recently, embolization of orbital varices with cyanoacrylate glue has been utilized to make the surgical resection more facile [11].

Keywords

Capillary malformation · Venous malformation · Low-flow lesions · Simple vascular malformations · Kasabach–Merritt syndrome · Proptosis · Valsalva maneuver · Corticosteroids · Beta blocker

1 Signs and Symptoms

CM of orbit is usually noticed shortly after birth, within first few months of life or present at birth also. Orbital lesions give rise to proptosis and displacement of the globe. The lesion appears as a soft mass deep to the skin, which becomes more pronounced when the child strains or cries. Pulsation and bruit are generally absent. The lesion can occur in the deeper orbit without any associated eyelid or superficial lesions, although these superficial lesions may facilitate in making the orbital diagnosis. Amblyopia and strabismus are the main complications. Lesions with diameter more than 10 mm are more likely to cause these complications, whereas lesions with diameter less than 10 mm are less likely to do so [12]. The lesion usually enlarges for the first 1 to 2 years of life and then gradually regresses, similar to eyelid or superficial CMs. Large lesions may be associated with large visceral hemangiomas, which may sequester platelets, a condition known as Kasabach–Merritt syndrome [1–11].

Orbital VMs commonly present at any time from early childhood to late middle age, but occasionally can be acquired later secondary to a local high-flow vascular lesion or trauma. It can be apparent at birth and can present with extreme neonatal proptosis. VMs typically present with slowly progressive intermittent proptosis. Ophthalmoplegia and pain are variable depending on the size and location. Symptoms frequently are exacerbated by changes in head position, bending forward, or by Valsalva maneuver. Orbital VM can be located more anteriorly and can present as a subconjunctival mass or lacrimal sac mass. Complications include acute orbital hemorrhage, thrombosis (pain, proptosis, decreased vision) and optic nerve compression. Patients with long-standing lesions may develop atrophy of surrounding fat, giving enophthalmos with a deepened superior sulcus.

2 Differential Diagnosis

CM is one of the most common benign orbital tumors of infancy. The differential diagnosis includes other orbital vascular tumors including orbital varices and cavernous venous malformation, malignant rhabdomyosarcoma, lymphatic malformation, chloroma, neuroblastoma, orbital cysts, and cellulitis.

Differential diagnosis for venous malformation includes other orbital vascular malformations such as capillary hemangioma and other lesions as mentioned above as its differential diagnosis.

3 Diagnosis

CM can largely be diagnosed clinically, though some cases are difficult to distinguish. Orbital imaging is performed for identification of CM and also to rule out other orbital diseases. Orbital ultrasound (USG) shows medium internal reflectivity of the lesions. With computed tomography (CT) and magnetic resonance imaging (MRI), orbital CM appears as a round or ovoid circumscribed mass or an irregular or diffuse mass in the intraconal or extraconal space. On MRI, the lesion appears to be homogeneous to heterogeneous, generally being hypointense on T1 and hyperintense on T2 images. Moderate to marked homogeneous enhancement occurs with contrast agents.

Orbital venous malformation appears as a round or irregular mass on CT and MRI, which may not be apparent until Valsalva maneuver is performed during the scanning procedure. Color Doppler imaging can also be used to demonstrate an orbital varix.

4 Treatment

Treatment of CM consists of observation because many lesions will involute, while others may disappear completely. Initial management should be directed at prevention or treatment of associated amblyopia with correction of refractive error and occlusive patching if necessary. If there is no threat to vision, the lesion can be cautiously observed. Systemic or topical treatment with beta blockers can hasten regression of the lesion. Local injection of corticosteroids can be performed under ultrasound guidance to accurately place the needle within the tumor. Risk of potential complications is the major drawback of corticosteroid usage. For large lesions or if amblyopia is present, local radiotherapy (500 cGy) or corticosteroids (systemic or local) may be indicated. Interferon-α2b has also been reported to be effective in hastening tumor regression. Recently, use of the beta blocker propranolol, given orally

or topically, has been shown to cause significant involution over a relatively shorter period of time for tumors in the proliferative phase. Well-circumscribed tumors can be treated with surgical excision. The prognosis is generally excellent for vision and life.

Management of orbital VM is difficult and controversial. Minimally symptomatic lesions can be observed and more symptomatic ones may require surgical excision. Exposure of the lesion and embolization with coils has been used to minimize the extent of surgical resection. Vascular clips can be used near the orbital apex to manage orbital varix. More recently, embolization of orbital varices with cyanoacrylate glue has been utilized to make the surgical resection more facile.

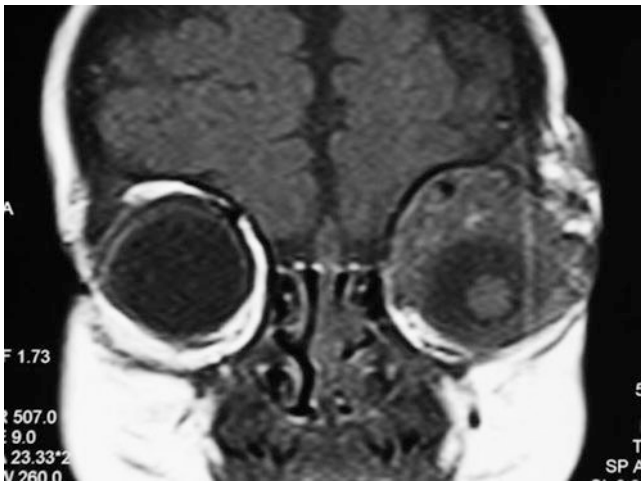


Fig. 2 MRI scan coronal section (T1 weighted) showing extensive isointense lesion involving the superior extraconal space of left orbit (same patient as in Fig. 1)

5 Figures with Captions

5.1 Capillary Malformation



Fig. 1 Clinical photograph showing facial appearance of a female infant with orbital capillary hemangioma and involvement of eyelid, anterior orbit, and forehead with displacement of the globe inferiorly

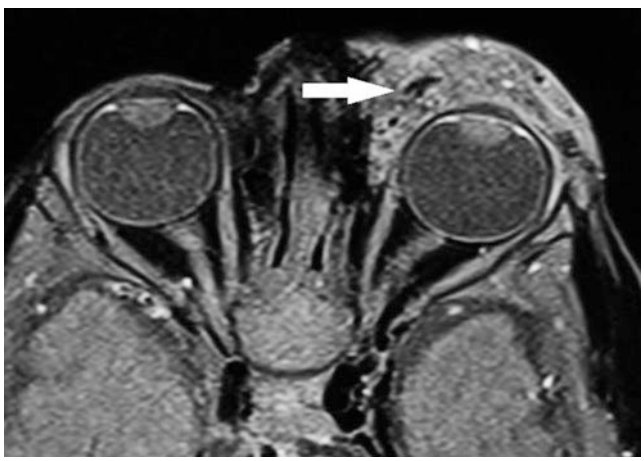


Fig. 3 MRI scan axial section (T1 weighted, FS, CE) showing an extensive enhancing lesion involving the medial extraconal space of left orbit and periocular soft tissues; note the flow voids (arrow) representing high flow intra-tumoral vessels (same patient as in Fig. 1)

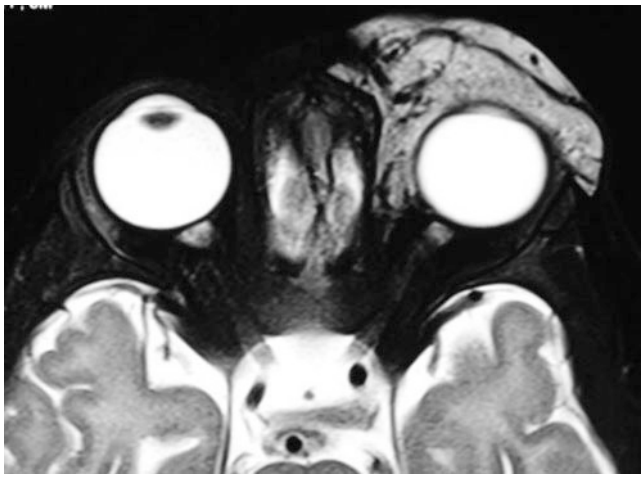


Fig. 4 MRI scan axial section (T2 weighted, FS) showing an extensive hyperintense lesion involving the extraconal space of left orbit and periocular soft tissues (same patient as in Fig. 1)

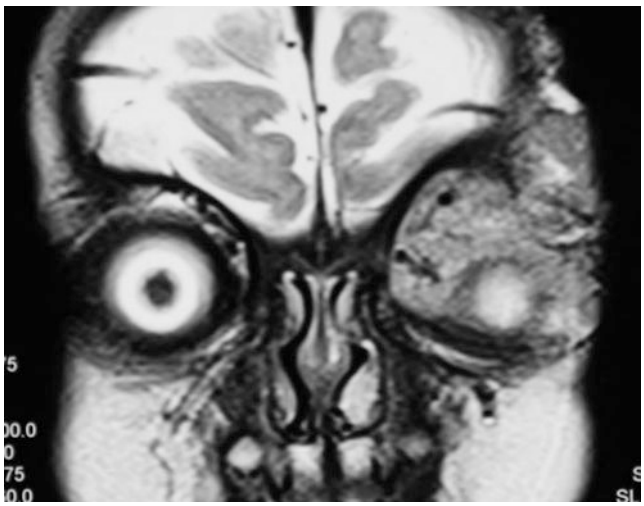


Fig. 5 MRI scan coronal section (T2 weighted) showing an extensive hyperintense lesion involving the extraconal space of left orbit (same patient as in Fig. 1)



Fig. 6 Clinical photograph showing regression of the lesions following 3 months treatment with systemic beta blocker (oral propranolol) (same patient as in Fig. 1)



Fig. 7 Clinical photograph showing facial appearance of a 14-year-old male with inferolateral displacement of the left globe

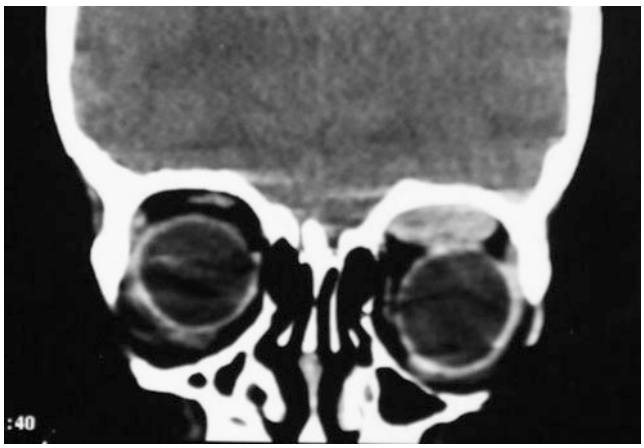


Fig. 8 CT scan coronal section showing a well defined lobulated homogenous iso- to mild hyperdense lesion in superior extraconal compartment of the left orbit causing mild inferolateral displacement of the globe (same patient as in Fig. 7)

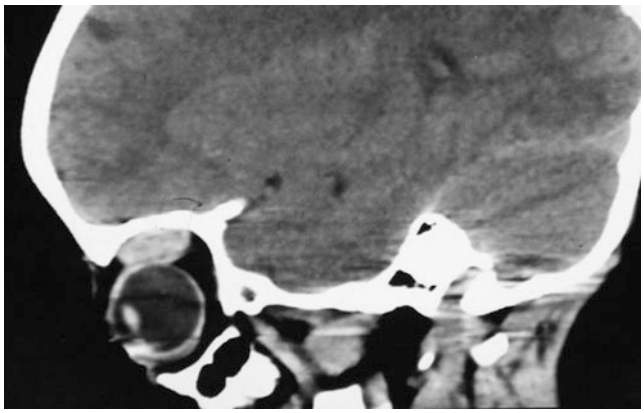


Fig. 9 CT scan sagittal section showing a well defined lobulated homogenous iso- to mild hyperdense lesion in superior extraconal compartment of the left orbit (same patient as in Fig. 7)

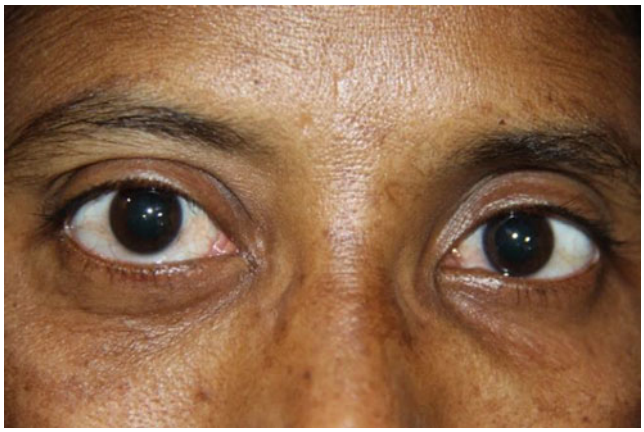


Fig. 12 Clinical photograph showing close up view with proptosis of the right eye following Valsalva maneuver (same patient as in Fig. 11)



Fig. 10 Clinical photograph showing facial appearance in the immediate post-operative period following surgical removal of the lesion, proven as capillary malformation on histopathological examination (same patient as in Fig. 7)

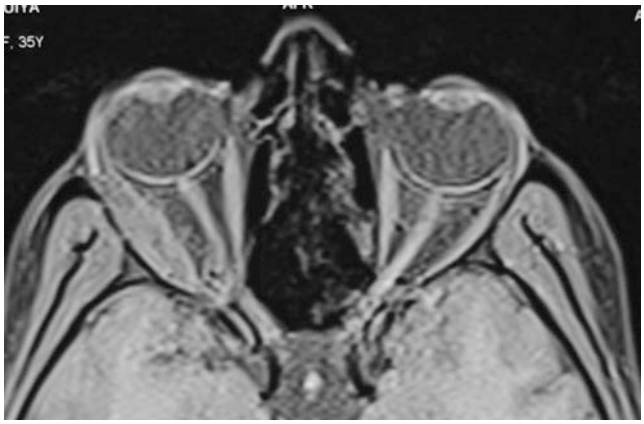


Fig. 13 MRI scan axial section (T1 weighted, FS) showing an iso to hypointense lesion in the extraconal space of the right orbit (same patient as in Fig. 11)

5.2 Orbital Venous Malformation



Fig. 11 Clinical photograph showing facial appearance of a 35-year-old female with very minimal proptosis of the right eye with complaints of feeling of fullness behind the right eye while straining or bending over

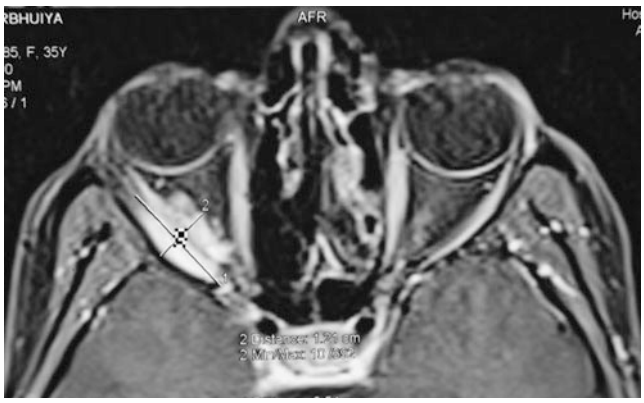


Fig. 14 MRI scan axial section (T1 weighted FS with contrast enhancement during Valsalva maneuver) showing increased dimension of the lesion with marked enhancement (same patient as in Fig. 11)

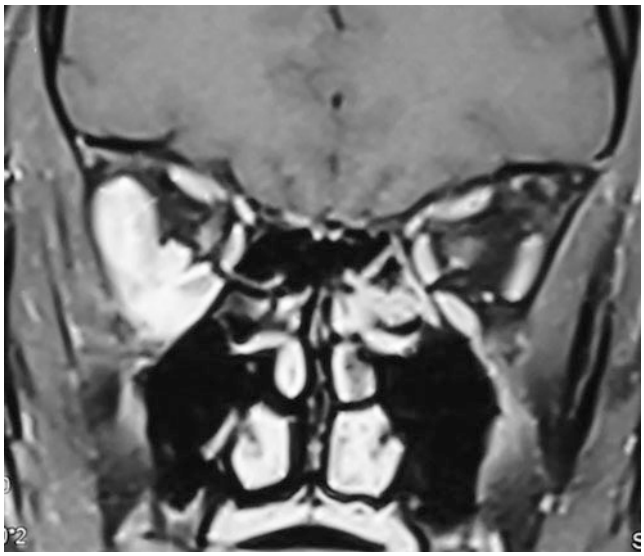


Fig. 15 MRI scan coronal section (T1 weighted FS with contrast enhancement during Valsalva maneuver) showing larger dimension of the lesion with marked enhancement (same patient as in Fig. 11)



Fig. 16 Clinical photograph showing facial appearance of an 8-year-old male with very minimal proptosis of the right eye with fullness over the supero-medial part of right eye while straining or bending over



Fig. 17 Clinical photograph showing close up view with fullness of the supero-medial part of right eye following Valsalva maneuver (same patient as in Fig. 16)

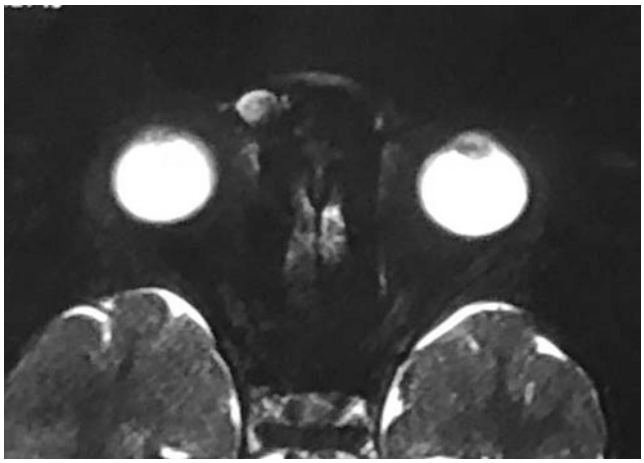


Fig. 18 MRI scan axial section (T2 weighted FS) showing a round mostly hyperintense lesion in the supero-medial part of right anterior orbit (same patient as in Fig. 16)

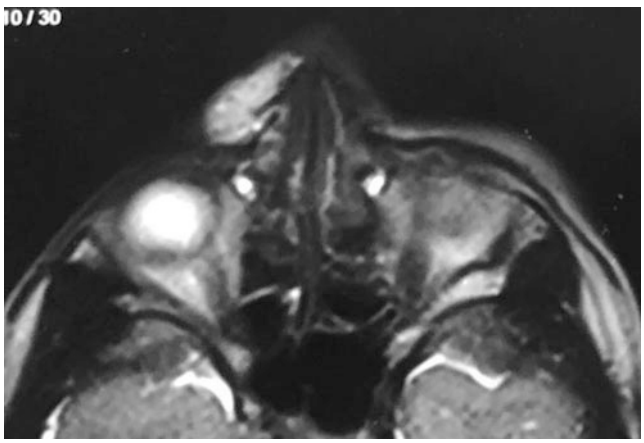


Fig. 19 MRI scan axial section (T2 weighted FS during Valsalva maneuver) showing larger dimension of the lesion (same patient as in Fig. 16)

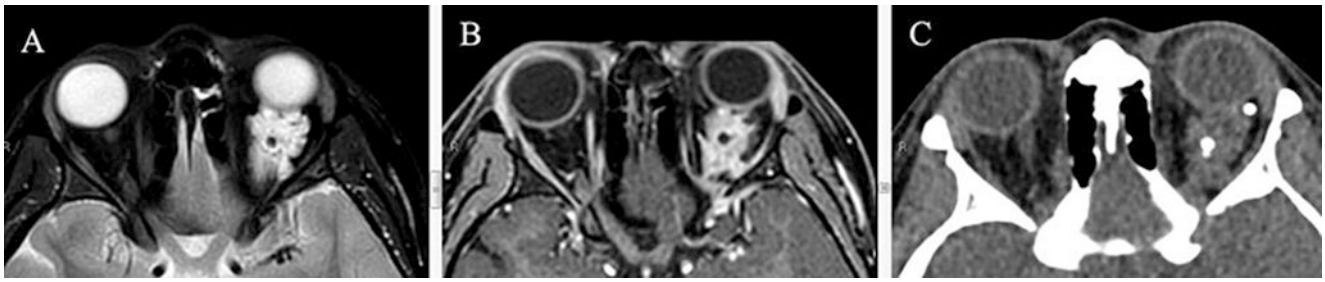


Fig. 20 Axial scans of a 16-year-old female with left orbital venous malformation (VM); A. MRI T2WI FS, showing a diffuse venous malformation, located in the intraconal space, heterogenous signal mostly hyperintense, and areas of low signal within the lesion. B, MRI T1-weighted FS CE image showing the bright enhancement of the VM. C. NECT scan showing hyperdense round foci evidence of phleboliths. (*Courtesy of the editors*)

References

1. Rootman J, Heran MK, Graeb DA. Vascular malformations of the orbit: classification and the role of imaging in diagnosis and treatment strategies*. Ophthalmic Plast Reconstr Surg. 2014;30(2):91–104.
2. ISSVA Classification of vascular anomalies ©2018. International Society for the Study of Vascular Anomalies. Available at http://issva.org/classification. Accessed on 17 Nov 2020.
3. Mulliken JB, Glowacki J. Hemangiomas and vascular malformations in infants and children: a classification based on endothelial characteristics. Plast Reconstr Surg. 1982;69(3):412–22.
4. Shields JA, Shields CL, Scartozzi R. Survey of 1264 patients with orbital tumors and simulating lesions: the 2002 Montgomery lecture, part 1. Ophthalmology. 2004;111:997–1008.
5. Hall GW. Kasabach-Merritt syndrome: pathogenesis and management. Br J Haematol. 2001;112(4):851–62.
6. Yeatts RP, Driver PJ. Orbital varix. Arch Ophthalmol. 1993;111(5):702–3.
7. Haik BG, Jakobiec FA, Ellsworth RM, Jones IS. Capillary hemangioma of the lids and orbit: an analysis of the clinical features and therapeutic results in 101 cases. Ophthalmology. 1979;86(5):760–92.
8. Egbert JE, Paul S, Engel WK, et al. High injection pressure during intralesional injection of corticosteroids into capillary hemangiomas. Arch Ophthalmol. 2001;119:677–83.
9. Wilson MW, Hoehn ME, Haik BG, et al. Low-dose cyclophosphamide and interferon alfa 2a for the treatment of capillary hemangioma of the orbit. Ophthalmology. 2007;114(5):1007–11.
10. Thoumazet F, Léauté-Labrèze C, Colin J, et al. Efficacy of systemic propranolol for severe infantile haemangioma of the orbit and eyelid: a case study of eight patients. Br J Ophthalmol. 2012;96(3):370–4.
11. Couch SM, Garrity JA, Cameron JD, et al. Embolization of orbital varices with N-butyl cyanoacrylate as an aid in surgical excision: results of 4 cases with histopathologic examination. Am J Ophthalmol. 2009;148(4):614–8.
12. Ceisler E, Blei F. Ophthalmic issues in hemangiomas of infancy. Lymphat Res Biol. 2003;1:321–30.

Orbital Venous Malformations (VM): Nondistensible

67

Kasturi Bhattacharjee, Nirod Medhi, and Shyam Sundar Das Mohapatra

Contents

1 **Signs and Symptoms** 508
2 **Differential Diagnosis** 508
3 **Diagnosis** 508
4 **Treatment** 508
5 **Figures with Captions** 508
References 511

Abstract

- The cavernous venous malformations (CVMs) of the orbit, previously called cavernous hemangioma, are venous malformations and the most common intraconal mass of the orbit in adults [1, 2].
- CVMs are nondistensible in nature.
- This vascular malformation presents commonly at the early middle age, and females are more frequently affected than males [3].
- It produces painless proptosis and late motility restriction due to its mass effect. Because it arises most often in the muscle cone, it usually produces axial proptosis. Large cavernous venous lesions may cause decrease in vision due to choroidal folds, optic disc edema, and optic nerve compression. It may grow during pregnancy [4–7].
- CVM appears as a well-defined round to oval lesion, usually within the muscle cone on CT and MRI scan. On MRI, it appears isointense on T1 and hyperintense on T2 with respect to the extraocular muscle. It shows moderate to marked nonhomogeneous enhancement with contrast agents, typically early stippled enhancement with gradual centrifugal filling reaching diffuse homogenous enhancement on late images [8, 9].
- CVM is usually well encapsulated and relatively easier for complete surgical removal. Meticulous surgery and complete excision are important to avoid recurrence.
- In cases of inaccessible or nonresectable CVMs, alternative therapy such as radiotherapy can be considered in the treatment.
- Gamma knife radiosurgery (GKS), a representative method of stereotactic radiosurgery (SRS), has become an established alternative treatment modality for CVMs located at orbital apex [10, 11].
- GKS has been performed in a single session of irradiation; however, multisession treatment reduces the risk of visual morbidity especially in perioptic lesions [12].
- The prognosis is generally excellent for vision and life.

Keywords

Cavernous venous malformation · Cavernous hemangioma · Intraconal mass · Nondistensible · Proptosis · Encapsulated · Surgical removal · Stereotactic radiosurgery · Gamma knife radiosurgery

K. Bhattacharjee (✉)
Department of Ophthalmic Plastic and Reconstructive Surgery, Sri Sankaradeva Nethralaya, Guwahati, India

N. Medhi
Primus Imaging, Guwahati, India

S. S. D. Mohapatra
Sri Sankaradeva Nethralaya, Guwahati, India

© Springer Nature Switzerland AG 2022
G. Ben Simon et al. (eds.), *Atlas of Orbital Imaging*,
https://doi.org/10.1007/978-3-030-62426-2_56

1 Signs and Symptoms

CVM is a benign, slowly progressive lesion of orbit. Although congenital, it typically becomes symptomatic in adults, generally between the second and fourth decades of life. Symptoms relate to its mass effect, which produces painless proptosis and late motility restriction. Because it arises most often in the muscle cone, it usually produces axial proptosis. Large CVM may be associated with choroidal folds, optic disc edema, and optic nerve compression, which may result in decreased vision.

2 Differential Diagnosis

The differential diagnosis of orbital CVM are other well-circumscribed, round to ovoid, solid orbital tumors of orbit including peripheral nerve sheath tumors (schwannoma and neurofibroma), hemangiopericytoma (solitary fibrous tumor), fibrous histiocytoma, and melanoma.

3 Diagnosis

Certain imaging properties on CT or MRI may be highly suggestive of CVM. CVM appears as a well-defined round to oval lesion, usually located within the muscle cone on CT and MRI scan. On MRI, it appears isointense on T1 and hyperintense on T2 with respect to the extraocular muscle. It shows moderate to marked heterogeneous enhancement with contrast agents, typically early stippled enhancement with gradual centrifugal filling reaching diffuse homogenous enhancement on late images. Although less commonly used, orbital ultrasound (USG) can also be a useful imaging modality for relatively superficial lesions.

4 Treatment

In many instances, CVMs are detected incidentally on scans performed for unrelated reasons. For such asymptomatic cases, observation alone is often appropriate. Symptomatic lesions require surgical excision in most cases because they gradually enlarge. CVM is usually well encapsulated and relatively easier for complete surgical removal. Alternative therapy such as radiotherapy can be considered in the treatment of inaccessible and unresectable CVMs, especially those in close proximity to the optic nerve. Stereotactic radiosurgery (SRS) has the advantage of delivering high-dose radiation to the intended target in a single session with minimal collateral damage in contrast to traditional fractionated radiotherapy. Thus, gamma knife radiosurgery (GKS), a representative method of SRS, has become an established alternative treatment modality for CVMs located at orbital apex. Traditionally, GKS has been performed in a single session of irradiation; however, the risk of visual morbidity might be high with the treatment of peri-optic lesions; hence, multisession treatment can be attempted to minimize the risk. The prognosis is excellent for vision and life.

5 Figures with Captions



Fig. 1 Clinical photograph showing facial appearance of a 34-year-old female patient with minimal proptosis of the left eye



Fig. 2 Clinical photograph showing minimal proptosis of the left eye in worm's-eye view (same patient as in Fig. 1)

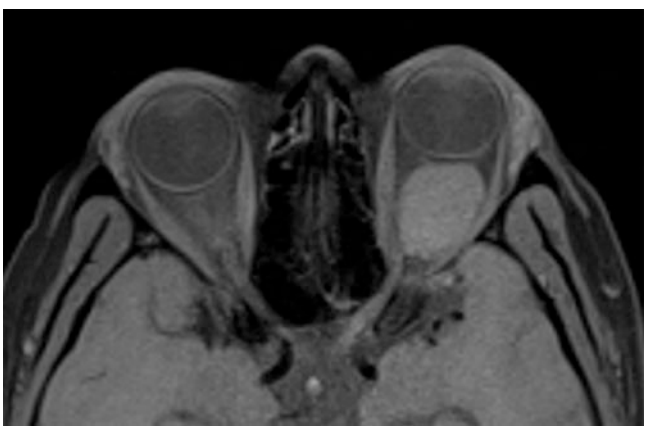


Fig. 3 MRI scan axial section (T1 weighted FS with fat suppression) showing a well-defined isointense lesion in the intraconal space in the left orbit with mild indentation of the globe (same patient as in Fig. 1)

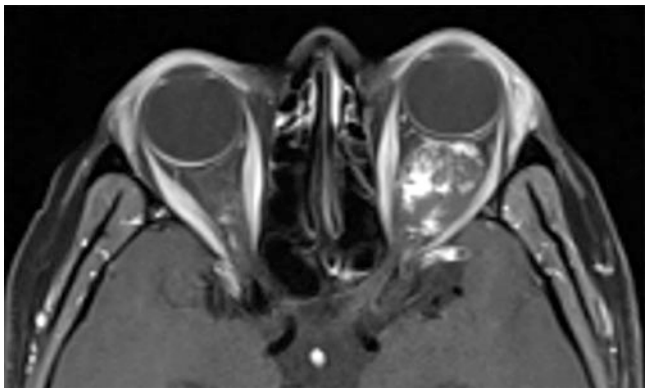


Fig. 4 MRI scan axial section (T1 weighted FS with contrast enhancement) showing strong heterogeneous enhancement of the lesion (same patient as in Fig. 1)

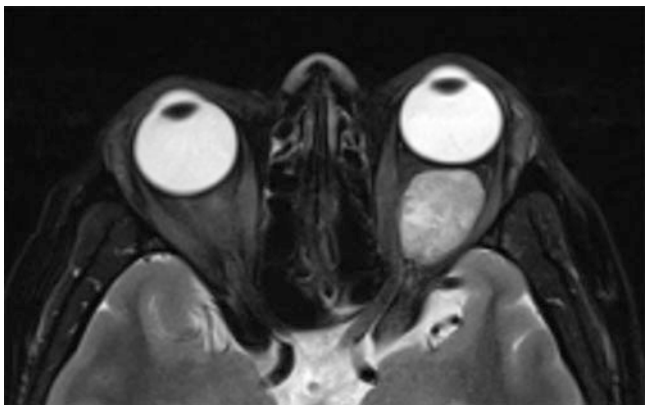


Fig. 5 MRI scan axial section (T2 weighted with fat suppression) showing a well-defined hyperintense lesion with thin internal septations (same patient as in Fig. 1)

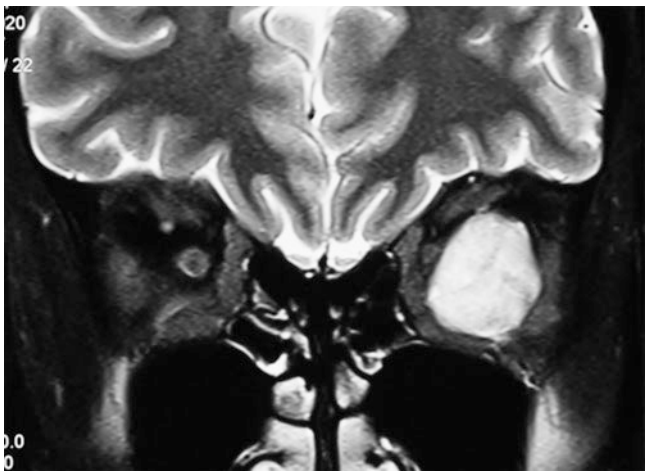


Fig. 6 MRI scan coronal section (T2 weighted with fat suppression) showing a well-defined intraconal hyperintense lesion with thin internal septations, the lesion is displacing the optic nerve superonasal (same patient as in Fig. 1)



Fig. 7 CT scan axial section showing a well-defined lesion of soft tissue density in the intraconal space in the left orbit displacing the optic nerve medially (same patient as in Fig. 1)

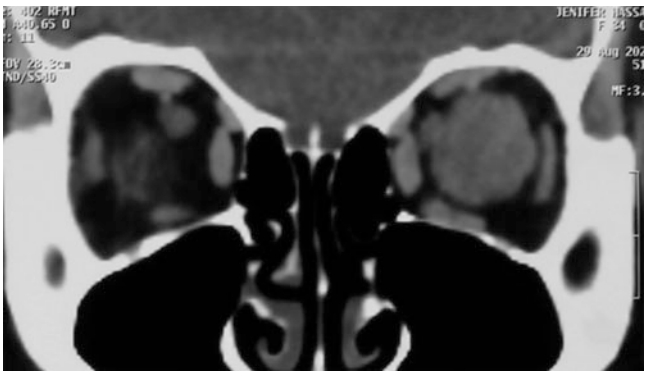


Fig. 8 CT scan coronal section showing a well-defined isodense lesion in the intraconal space in the left orbit displacing the optic nerve medially (same patient as in Fig. 1)

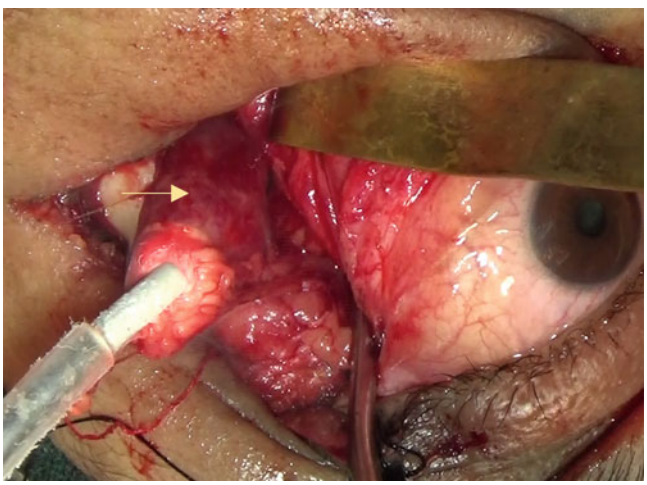


Fig. 9 Intraoperative image showing cryo-assisted tumor removal (reddish-blue-colored, yellow arrow) via inferolateral orbitotomy by transconjunctival approach (same patient as in Fig. 1)



Fig. 10 Clinical photograph showing facial appearance of a 52-year-old female patient with minimal proptosis of the right eye

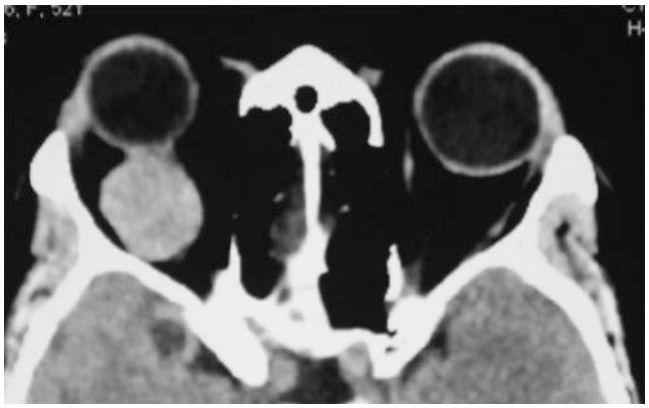


Fig. 11 CT scan axial section showing a well-defined isodense lesion in the intraconal space in the right orbit (same patient as in Fig. 10)

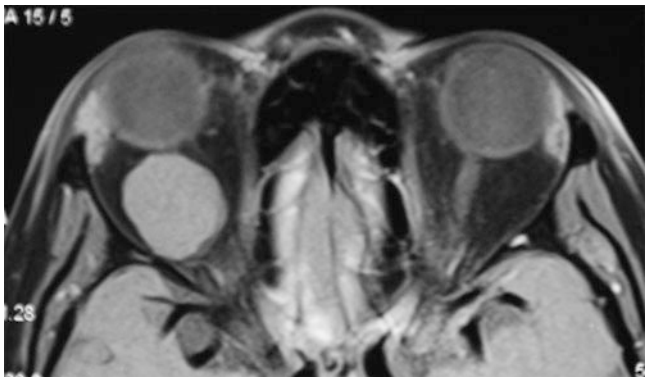


Fig. 12 MRI scan axial section (T1 weighted with fat suppression) showing a well-defined isointense lesion in the intraconal space of the right orbit (same patient as in Fig. 10)

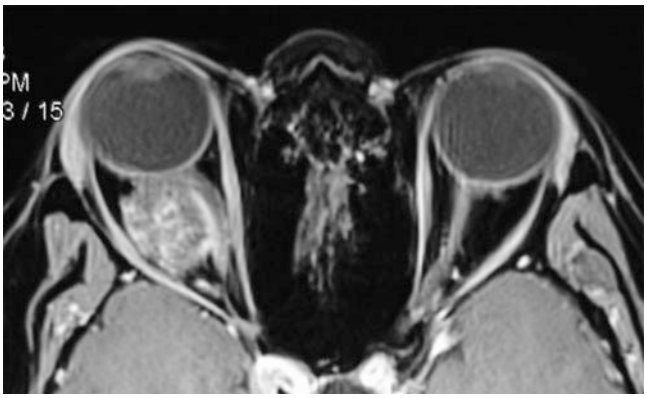


Fig. 13 MRI scan axial section (T1 weighted FS with contrast enhancement) showing heterogeneous enhancement of the lesion (same patient as in Fig. 10)

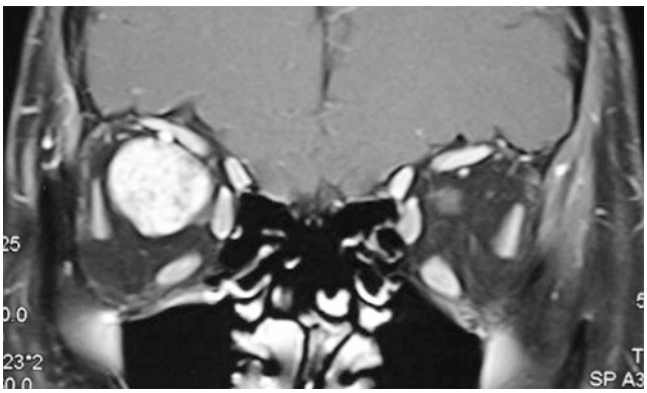


Fig. 14 MRI scan coronal section (T1 weighted FS with contrast enhancement) showing strong heterogeneous enhancement of the lesion (same patient as in Fig. 10)

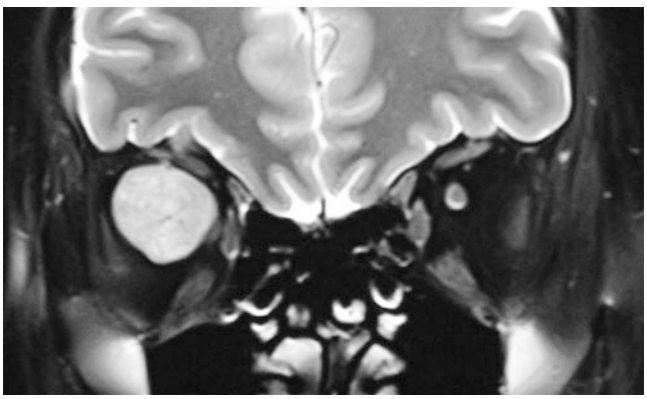


Fig. 15 MRI scan coronal section (T2 weighted with fat suppression) showing a well-defined hyperintense lesion with thin internal septations in the intraconal space in the right orbit (same patient as in Fig. 10)

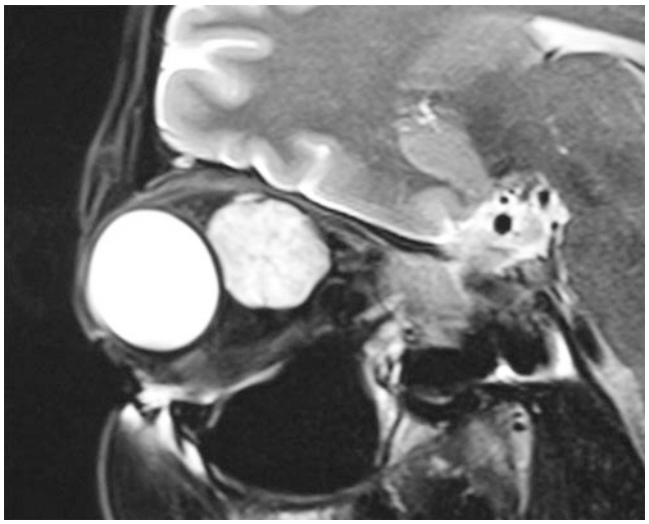


Fig. 16 MRI scan sagittal section (T2 weighted with fat suppression) showing a well-defined hyperintense lesion with thin internal septations in the intraconal space in the right orbit (same patient as in Fig. 10)



Fig. 17 Clinical photograph showing the tumor (reddish-blue colored) following surgical removal (same patient as in Fig. 10)

References

1. Shields JA, Shields CL, Scartozzi R. Survey of 1264 patients with orbital tumors and simulating lesions: the 2002 Montgomery lecture, part 1. Ophthalmology. 2004;111:997–1008.
2. Shields JA, Bakewell B, Augsburger JJ, et al. Classification and incidence of space-occupying lesions of the orbit. A survey of 645 biopsies. Arch Ophthalmol. 1984;102:1606–11.
3. Harris GJ, Jakobiec FA. Cavernous hemangioma of the orbit. J Neurosurg. 1979;51(2):219–28.
4. Osaki TH, Fay A, Waner M. Vascular malformations. In: Fay A, Dolman PJ, editors. Diseases and disorders of the orbit and ocular adnexa. Edinburgh: Elsevier; 2017.
5. Osaki TH, Jakobiec FA, Mendoza PR, et al. Immunohistochemical investigations of orbital infantile hemangiomas and adult encapsulated cavernous venous lesions (malformation versus hemangioma). Ophthal Plast Reconstr Surg. 2013;29:183–95.
6. Dutton JJ, Bryne SF, Proia AD. Diagnostic atlas of orbital disease. 1st ed. Philadelphia: W.B. Saunders Company; 2000. p. 66.
7. Shields JA, Shields CL. Eyelid, conjunctival and orbital tumors. 2nd ed. Philadelphia: Lippincott, Williams & Wilkins; 2008. p. 522.
8. Harris GJ. Cavernous hemangioma of the orbital apex: pathogenetic considerations in surgical management. Am J Ophthalmol. 2010;150(6):764–73.
9. Kahana A, Lucarelli MJ, Grayev AM, Van Buren JJ, Burkat CN, Gentry LR. Noninvasive dynamic magnetic resonance angiography with Time-Resolved Imaging of Contrast KineticS (TRICKS) in the evaluation of orbital vascular lesions. Arch Ophthalmol. 2007;125(12):1635–42.
10. Rootman DB, Rootman J, Gregory S, Feldman KA, Ma R. Stereotactic fractionated radiotherapy for cavernous venous malformations (hemangioma) of the orbit. Ophthal Plast Reconstr Surg. 2012;28(2):96–102.
11. Chen HC, Hu CJ, Pan DH. Stereotactic gamma knife radiosurgery for orbital cavernous hemangioma: clinical outcome and visual function protection. J Neuro-Oncol. 2021;152:183–93. Epub ahead of print.
12. Kim BS, Im YS, Woo KI, Kim YD, Lee JI. Multisession gamma knife radiosurgery for orbital apex tumors. World Neurosurg. 2015;84(4):1005–13.

Carotid-Cavernous Fistula

68

Kasturi Bhattacharjee, Nirod Medhi, and Shyam Sundar Das Mohapatra

Contents

1 **Signs and Symptoms** 514
2 **Differential Diagnosis** 514
3 **Diagnosis** 514
4 **Treatment** 515
5 **Figures with Captions** 515
References 519

Abstract

- Carotid-Cavernous Fistulas (CCF) are classified as simple vascular malformations based on the International Society for the Study of Vascular Anomalies (ISSVA) classification of vascular anomalies [1].
- CCF is an abnormal shunt from the carotid artery to the cavernous sinus [2].
- Anatomically, they can be direct or indirect with high-flow or low-flow fistulas.
- Etiologically, they can be classified as post-traumatic or spontaneous [3].
- Barrow (1985) classified CCF into four subtypes based on their communication: [4]
  - Type A: Direct communication between ICA and cavernous sinus.
  - Type B: Communication between dural ICA branches and cavernous sinus.
  - Type C: Communication between dural external carotid artery branch and cavernous sinus.
  - Type D: Communication from dural branches of ICA and external carotid artery branches to cavernous sinus.
- Direct CCF commonly occur secondary to a traumatic tear in the artery from a skull base fracture, from the acceleration-deceleration force of a traumatic injury or from an iatrogenic injury following an endovascular intervention or a trans-sphenoidal procedure. It can also occur spontaneously following an ICA aneurysm rupture or weakening of the arteries from a genetic condition [5].
- Indirect CCF result from rupture of the dural branches of the carotid artery due to weakness as a result of genetic condition or comorbidities including hypertension [2].
- Direct CCF presents early following head injury with a classic triad of pulsatile proptosis, conjunctival chemosis, and a whooshing noise in the head [6, 7].
- A bruit that is audible to the patient, may also be audible to the examiner.
- Indirect CCF presents with a more gradual onset of redness in one or both eyes due to conjunctival vascular engorgement. Patients generally present with proptosis, arterialization of conjunctival vessels (corkscrew appearance), elevated intraocular pressure, oculomotor palsies, ptosis, bruit, venous stasis retinopathy, visual field defects, pain, chemosis, and lid swelling [8].

K. Bhattacharjee (✉)
Department of Ophthalmic Plastic and Reconstructive Surgery, Sri Sankaradeva Nethralaya, Guwahati, India

N. Medhi
Primus Imaging, Guwahati, India

S. S. D. Mohapatra
Sri Sankaradeva Nethralaya, Guwahati, India

© Springer Nature Switzerland AG 2022
G. Ben Simon et al. (eds.), *Atlas of Orbital Imaging*,
https://doi.org/10.1007/978-3-030-62426-2_107

- CT and MRI may demonstrate prominence of the superior ophthalmic vein and diffuse enlargement of extraocular muscles, proptosis, and fat stranding and asymmetric engorgement of the involved cavernous sinus. CT and MRI angiography and selective catheter digital subtraction angiography (DSA) are useful diagnostic modalities. CTA has been shown to be more sensitive than MRA. Time-resolved imaging of contrast kinetics (TRICKS) is a recently introduced technique that improves temporal resolution with respect to contrast-enhanced MRA technique. By TRICKS, dynamic images can be obtained during the arterial, capillary, and venous phases. Using this sequence, three-dimensional volumes can be acquired during the passage of gadolinium (GD), to detect the vascularization of the region of interest over time, similar to DSA [9]. DSA is the gold standard for showing the rapid shunting and assessment of the extent and location of feeding vessels [10].
- On MRI, one should search for the internal signal void on T2 weighted image (indicative of high flow) and change in contour of the involved cavernous sinus.
- Surgery is indicated if the fistula does not close spontaneously [11, 12]. Transarterial or sometimes transvenous embolization with platinum coils or liquid embolic material such as cyanoacrylate or parent artery occlusion can be performed [13, 14].

Keywords

Carotid-Cavernous Fistula · AVM · Carotid artery · Cavernous sinus · Direct or indirect · High-flow or low-flow · Post-traumatic or spontaneous · Pulsatile proptosis · Conjunctival chemosis / vascular engorgement · Corkscrew appearance · Bruit · Angiography · Embolization

1 Signs and Symptoms

Ocular manifestations occur as a result of venous and arterial stasis around the eye and orbit, increased episcleral venous pressure and decreased arterial blood flow to the cranial nerves within the cavernous sinus.

Direct CCF presents early, within hours to several days or weeks after head injury, classic triad of pulsatile proptosis, conjunctival chemosis, and a whooshing noise in the head. The clinical signs include pulsatile exophthalmos, eyelid swelling, conjunctival chemosis, arterialization of conjunctival vessels, elevated intraocular pressure (often pulsatile), restriction of extraocular muscle movements, cranial neuropathies, and intraocular signs including optic disc swelling and venous stasis retinopathy. A bruit that is audible to the patient may also be audible to the examiner. Proptosis occurs due to congestion of the orbital tissues as well as due to displacement of the globe by the dilated superior ophthalmic vein. Ocular pulsation could be visible and/or palpable, but may be absent if the orbit is too rigid from hemorrhage and edema. Arterialization of conjunctival and episcleral vessels occur and the vessels have a corkscrew appearance and their tortuosity and dilation extends to the limbus.

Indirect CCF has a more gradual onset of redness in one or both eyes, caused by conjunctival vascular engorgement. Patients generally present with proptosis, arterialization of conjunctival vessels, elevated intraocular pressure, oculomotor palsies, ptosis, bruit, venous stasis retinopathy, visual field defects, pain, chemosis, and lid swelling. The onset is typically insidious, which often causes delay in diagnosis and with patients often treated as nonspecific red eyes. Bruits are less commonly reported by patients and audible to the examiners. Pain is infrequent and usually mild. Arterialization of conjunctival and episcleral vessels occur and the vessels have a characteristic appearance known as limbal loops in which vessels have an acute angulation near the limbus. Intraocular pressure elevation can occur as a result of episcleral venous pressure elevation and the patients often develop glaucomatous visual field defects. Posterior segment complications include venous stasis retinopathy, vitreous hemorrhage, proliferative retinopathy, disc swelling, ischemic optic neuropathy, and exudative retinal detachments can also occur.

2 Differential Diagnosis

Differential diagnoses for CCF include vascular lesions such as arteriovenous malformation and cavernous sinus thrombosis, cavernous sinus tumors, skull base tumors, mucocele, thyroid ophthalmopathy (the arterialization of blood vessels in CCF is usually diffuse and extends to the limbus, while in thyroid eye disease (TED) there is a clear zone between the conjunctival erythema over the EOM insertion and the limbus), nonspecific orbital inflammation, superior orbital fissure syndrome, orbital apex syndrome, orbital infection, orbital tumors, and orbital hemorrhage.

3 Diagnosis

Neuroimaging methods including CT and MRI may demonstrate prominence of the superior ophthalmic vein and diffuse enlargement of extraocular muscles as well as other radiological signs (see above). CT and MRI angiography can be useful diagnostic modalities. Although MRI offers the advantage of identifying other lesions such as arteriovenous malformation, cavernous sinus tumors, or thrombosis, CTA has

been shown to be more sensitive than MRA. Definitive diagnosis may involve selective catheter DSA, which remains the gold standard for assessment and documentation of the extent and location of feeding vessels. Color Doppler ultrasound can document abnormal flow patterns, particularly reversal of flow in the superior ophthalmic vein.

4 Treatment

Direct CCFs generally require treatment in order to restore normal flow and occlude the fistula. The post-traumatic CCFs have higher blood flow and much less likely to close on their own than a spontaneous CCF. Surgery is indicated if the fistula does not close spontaneously. Preferred treatment modalities for direct CCFs are transarterial or sometimes transvenous embolization with platinum coils or liquid embolic material such as cyanoacrylate or parent artery occlusion. Craniotomy, although rarely required, helps in arterial repair under direct visualization following successful closure of a direct CCF, prognosis is usually excellent with full recovery occurring within weeks.

Spontaneous closure or occluding thrombosis sometimes occurs in indirect CCFs. Intermittent carotid compression under specialist supervision has been reported to increase the likelihood of spontaneous closure. These conservative measures can be applied upon asymptomatic patients. If conservative measures fail, treatment usually involves transvenous occlusion of the involved sinus. However, treatment by embolization with liquid agents or coils is recommended for patients who have ophthalmic symptoms. Alternatively, a trans-internal carotid procedure may be necessary if transvenous attempts have failed. Rarely, direct surgery on the cavernous sinus can be performed. Ocular symptoms generally start to improve within days of treatment and usually resolve completely within 6 months.

5 Figures with Captions



Fig. 1 Clinical photograph showing facial appearance of a 50-year-old female patient with ptosis and proptosis of the left eye following head injury



Fig. 2 Arterialization of conjunctival and episcleral vessels with corkscrew appearance and extension of their tortuosity and dilation to the limbus (same patient as in Fig. 1)

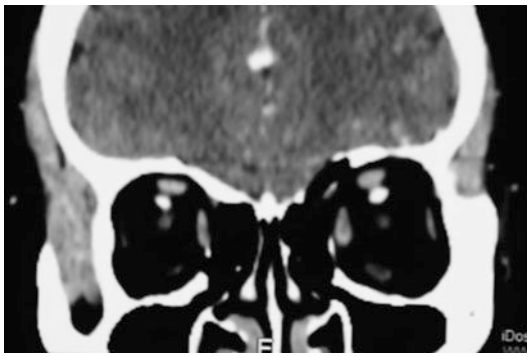


Fig. 3 CT scan sagittal section (contrast enhanced) showing the mildly dilated superior ophthalmic vein on the left side (same patient as in Fig. 1)

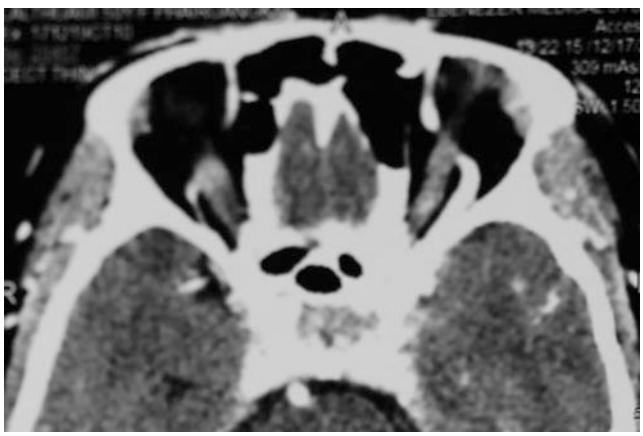


Fig. 4 CT scan axial section (contrast enhanced) showing dilated superior ophthalmic vein on the left side (same patient as in Fig. 1)

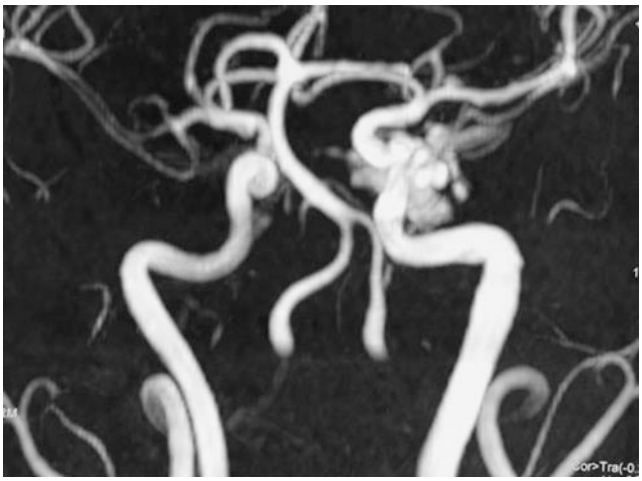


Fig. 5 MRI scan with angiography showing left Carotid-Cavernous Fistula with communication between the cavernous sinus and the left internal carotid artery resulting in arterialization of the cavernous sinus (same patient as in Fig. 1)

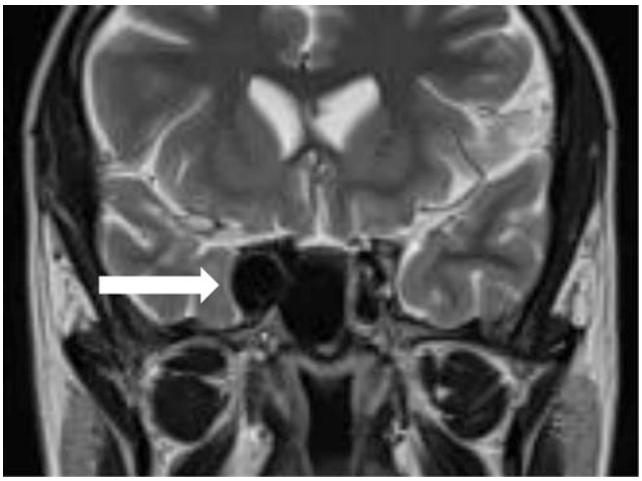


Fig. 7 MRI scan coronal section (T2 weighted) showing enlarged right cavernous sinus with rounding of the lateral CCF border (arrow) and prominent signal void (same patient as in Fig. 6)

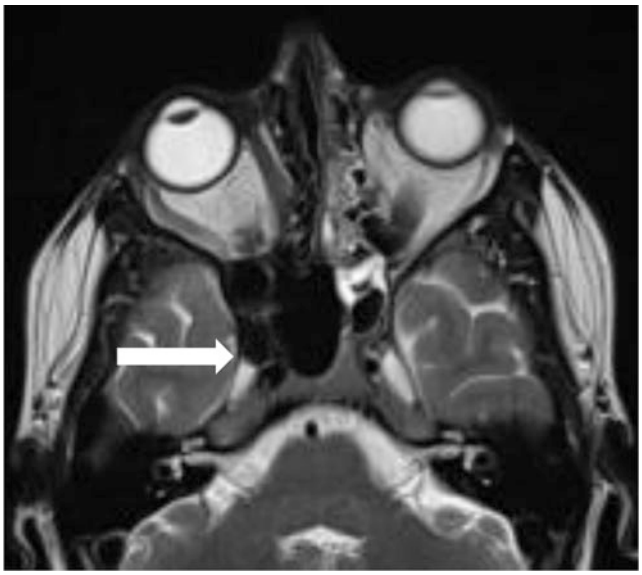


Fig. 6 MRI scan axial section (T2 weighted) showing enlarged right cavernous sinus with prominent signal void (arrow) and retrobulbar heterogeneity, prominent extraocular muscles and proptosis in a 28 years old male patient following head injury

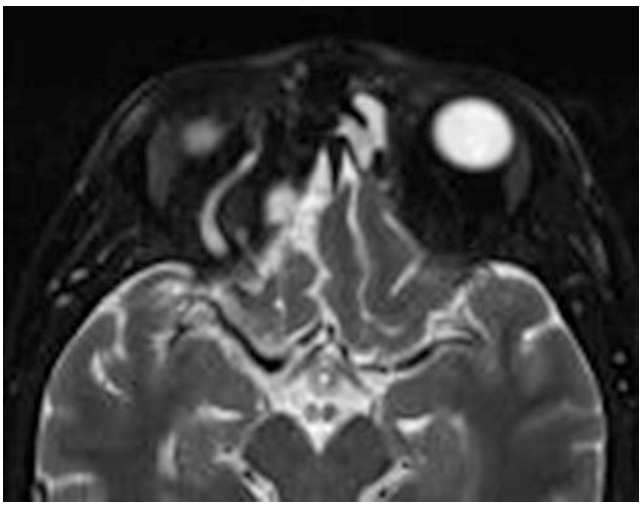


Fig. 8 MRI scan axial section (T2 weighted with fat suppression) showing dilated right superior ophthalmic vein in the right orbit (same patient as in Fig. 6)

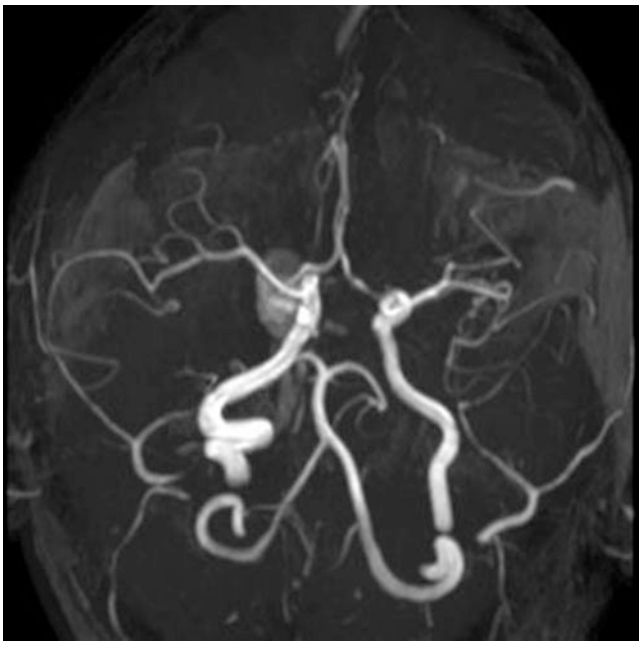


Fig. 9 MR Angiography time of flight study shows the enlarged right cavernous sinus (same patient as in Fig. 6)



Fig. 11 MRI scan axial section (T1 weighted with contrast) showing dilated right superior ophthalmic vein and enlarged right cavernous sinus (same patient as in Fig. 10)

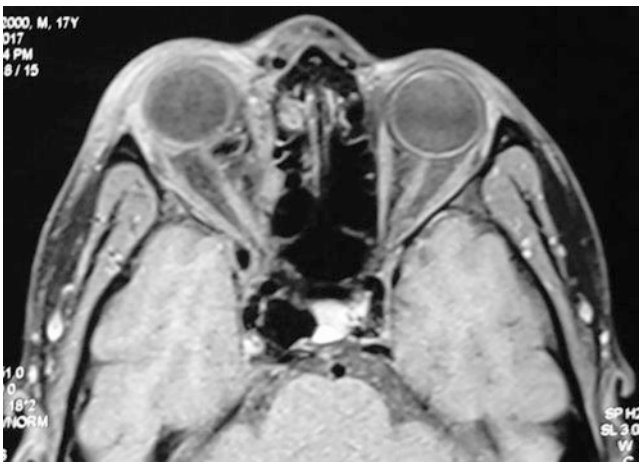


Fig. 10 MRI scan axial section (T1 weighted FS) showing enlarged right cavernous sinus with prominent extraocular muscles, congestion of retrobulbar fat and proptosis in a 17-year-old female patient following head injury



Fig. 12 MR Angiography time of flight study shows right Carotid-Cavernous Fistula with enlarged right cavernous sinus and dilated right superior ophthalmic vein (same patient as in Fig. 10)



Fig. 13 Clinical photograph showing facial appearance of a 32-year-old male patient with proptosis, congestion and chemosis of the right eye following head injury. (Courtesy of Firdaus Ahmed, Radiologist, GNRC Hospital, Guwahati, India)

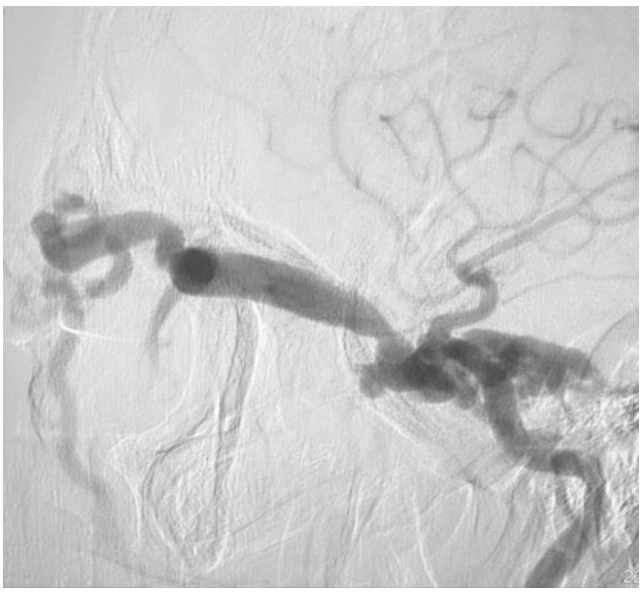


Fig. 14 DSA image showing right direct Carotid-Cavernous Fistula (same patient as in Fig. 13). (Courtesy of Firdaus Ahmed, Radiologist, GNRC Hospital, Guwahati, India)

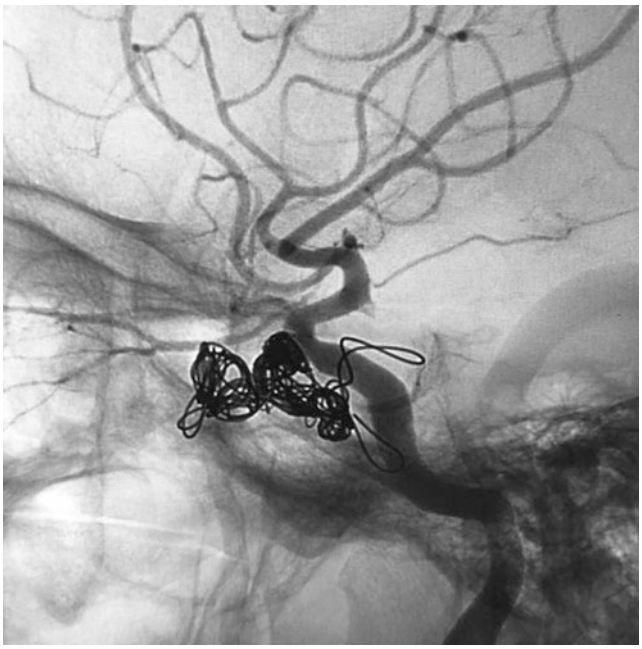


Fig. 15 DSA image showing the post coil embolization of the Carotid-Cavernous Fistula (same patient as in Fig. 13). (Courtesy of Firdaus Ahmed, Radiologist, GNRC Hospital, Guwahati, India)



Fig. 16 Post coil embolization check DSA image showing complete exclusion of the Carotid-Cavernous Fistula from the circulation (same patient as in Fig. 13). (Courtesy of Firdaus Ahmed, Radiologist, GNRC Hospital, Guwahati, India)



Fig. 17 Clinical photograph showing complete resolution of the proptosis, congestion and chemosis of the right eye by 4 weeks after treated with coiling (same patient as in Fig. 13). (Courtesy of Firdaus Ahmed, Radiologist, GNRC Hospital, Guwahati, India)

References

1. ISSVA Classification of vascular anomalies ©2018 International Society for the Study of Vascular Anomalies. issva.org/classification. Accessed on 17 Nov 2020.
2. Ellis JA, Goldstein H, Connolly ES Jr, Meyers PM. Carotid-cavernous fistulas. Neurosurg Focus. 2012;32(5):E9.
3. Chaudhry IA, Elkhamry SM, Al-Rashed W, Bosley TM. Carotid cavernous fistula: ophthalmological implications. Middle East Afr J Ophthalmol. 2009;16(2):57–63.
4. Barrow DL, Spector RH, Braun IF, Landman JA, Tindall SC, Tindall GT. Classification and treatment of spontaneous carotid-cavernous sinus fistulas. J Neurosurg. 1985;62(2):248–56.
5. Henderson AD, Miller NR. Carotid-cavernous fistula: current concepts in aetiology, investigation, and management. Eye (Lond). 2018;32(2):164–72.
6. Miller NR. Diagnosis and management of dural carotid-cavernous sinus fistulas. Neurosurg Focus. 2007;23(5):E13.
7. Goldberg RA, Goldey SH, Duckwiler G, Vinuela F. Management of cavernous sinus-dural fistulas. Indications and techniques for primary embolization via the superior ophthalmic vein. Arch Ophthalmol. 1996;114(6):707–14.
8. Farouk MM, Mostafa EM, Mounir A. Central retinal vein occlusion complicating spontaneous dural carotid-cavernous fistula after phacoemulsification. GMS Ophthalmol Cases. 2019;9:Doc28. Published 2019 July 16.
9. Romano A, Tavanti F, Rossi Espagnet MC, et al. The role of time-resolved imaging of contrast kinetics (TRICKS) magnetic resonance angiography (MRA) in the evaluation of head-neck vascular anomalies: a preliminary experience. Dentomaxillofac Radiol. 2015;44(3):20140302.
10. Chen CC, Chang PC, Shy CG, Chen WS, Hung HC. CT angiography and MR angiography in the evaluation of carotid cavernous sinus fistula prior to embolization: a comparison of techniques. AJNR Am J Neuroradiol. 2005;26(9):2349–56.
11. Meena US, Gupta P, Shrivastava T, Purohit D. Spontaneous closure of posttraumatic high-flow carotid-cavernous fistula following cerebral angiography. Asian J Neurosurg. 2016;11(2):172.
12. Iampreechakul P, Tirakotai W, Tanpun A, Wattanasen Y, Lertbusayanukul P, Siriwimonmas S. Spontaneous resolution of direct carotid-cavernous fistulas: case series and literature review. Interv Neuroradiol. 2019;25(1):71–89.
13. Alexander MD, Halbach VV, Hallam DK, Cooke DL, Ghodke BV, Dowd CF, Amans MR, Hetts SW, Higashida RT, Meyers PM. Long-term outcomes of endovascular treatment of indirect carotid cavernous fistulae: superior efficacy, safety, and durability of transvenous coiling over other techniques. Neurosurgery. 2019;85(1):E94–E100.
14. Nishizawa T, Terada K, Matsuyama N. Transvenous detachable coil embolization of direct & high-flow carotid-cavernous fistula. Alternative of transarterial detachable balloon embolization. Interv Neuroradiol. 2000;6 (Suppl 1):117–24.

Arteriovenous Malformations of the Orbit

69

Kasturi Bhattacharjee and Aditi Mehta

Contents

1 Signs and Symptoms 522
1.1 Orbital and Periorbital AVMs 522
1.2 Retinal AVMs 522
1.3 Intracranial AVMs 523

2 Differential Diagnosis 523

3 Diagnosis 523
3.1 Computed Tomography (CT) 523
3.2 Magnetic Resonance Imaging (MRI) 523
3.3 Digital Subtraction Angiography (DSA) 523

4 Treatment 524

5 Figures with Captions 524

References 528

Abstract

- Arteriovenous malformations (AVMs) are considered to be congenital hamartomas which involve multiple organ systems; the head and neck region is predominantly affected.
- Orbital AVMs may be sporadic and isolated to the orbit or involve the periorbital, cerebral, and facial regions, usually syndromic. The cerebrofacial arteriovenous metameric syndrome (CAMS) spectrum is diagnosed when AVMs have intracranial and maxillofacial components.
- Enlargement may occur at puberty or be precipitated by trauma-induced intralesional hemorrhage, leading to symptoms. Visual loss can occur due to the orbital component or the involvement of the visual pathway.
- Patients commonly present to the ophthalmologist. Based on clinical suspicion, a prompt neuroimaging confirms the diagnosis.
- Contrast-enhanced computed tomography (CT) and CT angiography demonstrate feeder arteries and draining veins with an intervening nidus having a "bag of worms" appearance.
- On magnetic resonance imaging (MRI), fast flow voids are noted on T2-weighted scans. Either phase contrast or time-resolved MR angiography are useful in delineating the lesions complicated by acute hemorrhage.
- Digital subtraction angiography (DSA) is the gold standard and can detail the location, number of feeding vessels, and pattern of drainage.
- Hemodynamically, there is high flow with direct shunting of blood without an intervening capillary bed. Shunting is demonstrated by abnormal opacification of the dilated veins during the arterial phase of the angiography.

Arteriovenous fistulas including the carotico-cavernous fistulas also bypass the capillary system and have a similar radiological pattern. However, these lesions do not have a dysplastic nidus, are *usually* acquired in nature (due to degenerative or traumatic changes), and are hence not included in this discussion.

K. Bhattacharjee (✉) · A. Mehta
Department of Ophthalmic Plastic and Reconstructive Surgery, Sri Sankaradeva Nethralaya, Guwahati, India

© Springer Nature Switzerland AG 2022
G. Ben Simon et al. (eds.), *Atlas of Orbital Imaging*,
https://doi.org/10.1007/978-3-030-62426-2_106

Keywords

High-flow lesions · Arteriovenous malformations · Nidus · Arterial feeder · Pulsatile proptosis

1 Signs and Symptoms

Nontraumatic arteriovenous malformations (AVMs), also known as orbital aneurysms, are thought to be congenital hamartomas, though their presentation may be delayed till they enlarge or develop intralesional hemorrhage [1]. The International Society for the Study of Vascular Anomalies (ISSVA) in their updated 2018 classification describes high-flow lesions which include simple AVMs, arteriovenous fistulas (AVFs), and combined capillary AVMs with or without a venous or lymphatic component [2]. All these lesions may involve the orbit and present as pulsatile masses with proptosis and congestive orbitopathy.

Embryologically, AVMs may arise from the arterial system, the venous system, or both and are characterized as progressively enlarging high-flow communications between arteries and veins bypassing the intervening normal capillary bed [3]. The presence of a central nidus of dysplastic vessels differentiates these lesions from AVFs. Histologic examination demonstrates thick-walled, irregular arterial, and venous channels with or without intrastromal hemorrhage [4]. Clinically, these lesions may be purely orbital, orbital and periorbital, or orbital with retinal or cerebral AVMs.

The cerebrofacial arteriovenous metameric syndrome (CAMS) spectrum is diagnosed when the AVMs have both an intracranial and a maxillofacial component. This includes the Wyburn Mason syndrome (WMS), also known as the Bonnet-Dechaume-Blanc syndrome, comprising of arteriovenous aneurysms of midbrain and retina along with cutaneous angiomas [5].

Ophthalmic symptoms can occur due to growth and hemorrhage in the orbital lesion (pulsatile proptosis), due to retinal lesions (visual loss) and cerebral lesions involving the visual pathway (visual loss/field defects). Neurological symptoms from the coexisting intracranial AVMs include signs of raised intracranial pressure (headache and nausea), hydrocephalus, seizures, cranial nerve palsies, stroke, and hemiplegia. Coexisting cutaneo-facial AVMs lead to facial hemangiomas causing cosmetic concern, epistaxis, gum and oral bleeds, etc.

Isolated orbital AVMs are much less common than isolated cerebral AVMs. Retinal AVMs, as a part of the WMS, can present early due to posterior pole involvement. Secondary type of orbital AVM is a term proposed to describe orbital symptoms, in the absence of any orbital lesion, developing due to congestion from cerebral AVMs because of atypical venous drainage into the orbital veins [6]. All three types of lesions commonly present to the ophthalmologist. Based on clinical suspicion, a prompt neuroimaging confirms the diagnosis. We describe the ophthalmic symptoms of orbital, retinal, and cerebral AVMs.

1.1 Orbital and Periorbital AVMs

Superficial (palpebral) AVMs involve the eyelid and may be isolated or be associated with hemifacial AVMs. Though congenital, patients present in early childhood due to visible pink or blue masses, at puberty when there is growth in the lesions or after trauma. Pulsatile palpebral mass, mechanical blepharoptosis, decrease in visual acuity due to induced astigmatism, and bleeding following trauma are common clinical signs. Surface of the mass is warm on palpation and may show dilated blood vessels. Schöbinger's classification subdivides superficial AVMs into four grades – quiescent pink or blue cutaneous warm lesions (I), expansive pulsatile lesions with thrill (II), necrosis, infection. or hemorrhage leading to pain (III), and associated cardiac failure (IV) [7].

Orbital AVMs are deeper in location. Although the lesions are large in size, mass effect is uncommon till there is rapid growth or an intralesional hemorrhage. These lesions may present as periocular swelling and fullness progressively increasing in size, pulsatile proptosis, or with conjunctival congestion with dilated corkscrew vessels. Associated signs include pain, elevated intraocular pressure (due to raised episcleral venous pressure), restricted ocular motility, and reduced visual acuity. A thrill may be palpable and bruit can be detected on auscultation. Recurrent pain is associated with intralesional hemorrhage occurring after trivial trauma or spontaneously. Some patients may give history of debulking procedure(s) with incomplete resolution and recurrences.

1.2 Retinal AVMs

Retinal AVMs are congenital, sporadic vascular anomalies usually involving the posterior pole. Small lesions may be asymptomatic and in preverbal children may be incidentally detected by the presence of unilateral dilated tortuous retinal vessels. Growth is slow, though may be accelerated with menarche, pregnancy, and trauma. Presence of coexisting AVMs in the brain, mandible, skin, or orbit – the Wyburn-Mason syndrome (WMS), may lead to an earlier presentation. Severe vision loss occurs due to central retinal vein occlusions, hemorrhage, retinal ischemia (due to shunting), retinal detachment, optic disk oedema, rubeosis iridis, and neovascular glaucoma. Patients of WMS may present with either acute or slowly progressive loss of visual acuity. Acute vision loss usually occurs secondary to spontaneous hemorrhage, whereas the gradual progressive reduction results from ischemia because of impaired perfusion or due to damage to nerve fibers by mechanica1 compression of the optic nerve, chiasm, or tract [8]. Diagnostic features on fundus examination are the presence of a large AVM with massive dilation and tortuosity of the involved vasculature. Associated peripheral perivascular sheathing may be noted. Fluorescein angiography of the fundus shows direct rapid transit in early frames along with

peripheral nonperfusion, secondary to shunting of blood within the lesion. Archer et al. have categorized retinal AVMs into three types. Group 1 includes typically asymptomatic isolated retinal AVM containing a major artery and vein with an abnormal capillary plexus in between. Group 2 includes AVM without any capillary network in between. These lesions are at a risk of retinal complications. Group 3 are complex and extensive AVMs with large vessels without a capillary plexus in between. These have a high risk for retinal complications and are more likely to have syndromic associations with intracranial malformations [9].

1.3 Intracranial AVMs

The emergent neurological presentation occurs due to intracranial bleed and stroke-related complications. In the absence of these complications, intracranial AVMs may present to the ophthalmologist with visual field defects and visual loss due to involvement of the cerebral visual pathways. Gibo et al. have described visual field defects secondary to a cerebral AVM involving the optic chiasm with vascular anomaly in the left maxillary region. In their case, the lesion demonstrated tortuous dilated vessels running over the optic nerve with strong adhesions. The lesion had several large feeders and draining veins passing through the chiasm. They attempted a partial removal, to avoid the devastating consequence of bilateral vision loss [10]. Orbital symptoms also develop secondary to orbital venous congestion from cerebral AVMs. This leads to proptosis, conjunctival chemosis, congestion, and dilated corkscrew episcleral vessels, in the absence of an orbital AVM.

2 Differential Diagnosis

Simple AVMs may occur sporadically, or in association with syndromes (Wyburn Mason syndrome). Combined AVMs are those with two or more vascular malformations within the same lesion. These include capillary-arteriovenous malformation (CAVM), capillary-lymphatic-arteriovenous malformation (CLAVM), capillary-venous-arteriovenous malformation (CVAVM), and the capillary-lymphatic-venous-arteriovenous malformation (CLVAVM).

Various eponymous syndromes with vascular malformations may have a similar presentation, though pulsatility is not noted in the absence of an arterial feeder. These include the Sturge-Weber (capillary venous or venolymphatic), Turner/Noonan (lymphatic), Maffucci and Rendu-Osler-Weber (venous), and Klippel-Trenaunay (capillary lymphaticovenous) syndromes among others.

Some other syndromes to be considered in the list of differentials have now included the CAMS syndrome. Besides the WMS syndrome, cases have been described by various authors – the neuro-retinal and encephalic angiomatosis by Fishgold (1952), Paillas (1959), Theron (1974), and Troost (1978); mesencephalo-oculo/retinal and facial angiomatosis by Bufford (1963) and Rubinstein (1972); and the ophthalmofacial-hypothalamic AVM by Morgan (1985) [11].

Arteriovenous fistulas (AVF) form the most important differential diagnosis. These lesions are usually acquired (traumatic or spontaneous/degenerative). They also present with pulsatile proptosis and dilated corkscrew episcleral vessels. Angiographically, they are also high-flow lesions with arterial feeders and dilated veins but they do not have the dysplastic central nidus which is characteristic of AVMs.

Another orbital lesion which has antegrade flow from arterial through to the venous side is the cavernous hemangioma, as described by Rootman [4]. However, as per the updated ISSVA classification, cavernous hemangioma is reclassified as a cavernous venous malformation which consists of dilated vascular channels with a fibrous capsule, low vascular flow, mild contrast enhancement on CT, and few flow voids on MRI [2].

3 Diagnosis

Clinical findings of warm pulsatile palpebral mass, pulsatile proptosis, dilated corkscrew episcleral vessels, vision loss, and/or dilated tortuous retinal vessels provide the ophthalmologist a clue for suspecting AVMs. Noninvasive in-office doppler sonography may demonstrate the high-flow arteriovenous connection. A prompt orbital and neuroimaging helps confirm the diagnosis and also helps detect associated craniofacial lesions.

3.1 Computed Tomography (CT)

On CT scan, there is presence of a diffuse isodense lesion with prominent contrast enhancement. CT angiography demonstrates feeder arteries and draining veins with an intervening nidus having a “bag of worms” appearance.

3.2 Magnetic Resonance Imaging (MRI)

On MRI, the lesion is isointense on T1-weighted images, unless complicated by hemorrhage. It demonstrates a mixed signal with multiple flow voids on T2-weighted scans. The superior ophthalmic vein and other orbital veins may be dilated. Either time-resolved or phase-contrast MR - angiography are useful in delineating the lesions complicated by acute hemorrhage.

3.3 Digital Subtraction Angiography (DSA)

DSA is the gold standard and can detail the location, number of feeding vessels, and pattern of drainage. AVMs demonstrate rapid filling with multiple feeder arteries, a central nidus, and numerous draining veins, which are dilated.

4 Treatment

The management of AVMs is challenging and needs a multidisciplinary approach. Angiography is essential for planning the management of orbital AVMs. Treatment depends on clinical symptoms. As the lesions are slow growing, watchful observation may suffice in some patients. Regression has been described in cerebral AVMs but not in orbital lesions. DSA with embolization may be offered as a primary treatment though the lesion may recur. Surgical excision should be combined with preoperative embolization as there is a high risk of perioperative hemorrhage leading to complications and poor outcome.

The Spetzler-Martin AVM scale is a grading system based on angiographic features of cerebral AVMs to predict morbidity/mortality risk of surgery [12]. However, no such system exists for orbital AVMs.

Mukherjee et al. have described combined management of a preseptal AVM with feeders from branches of both the external and internal carotid arteries and drainage into the superior ophthalmic vein. Their case (6-year-old female) underwent endovascular embolization with *N*-butyl 2-cyanoacrylate glue into the feeder as well as intralesionally (fluoroscopy guided) followed by surgical excision through an eyelid crease incision, 72 h later. Their method enabled complete surgical excision without any excessive intraoperative bleeding [13].

Other authors have also recommended a combined approach of embolization prior to surgery, which changes the hemodynamics to a static state, lowering the risk of hemorrhage and reduced perioperative morbidity. Lesions isolated to the posterior orbit may benefit from embolization alone, as they pose a high surgical risk. It is important to keep in mind that AVMs have a propensity to reform collaterals and thus recur [3, 14, 15].

5 Figures with Captions

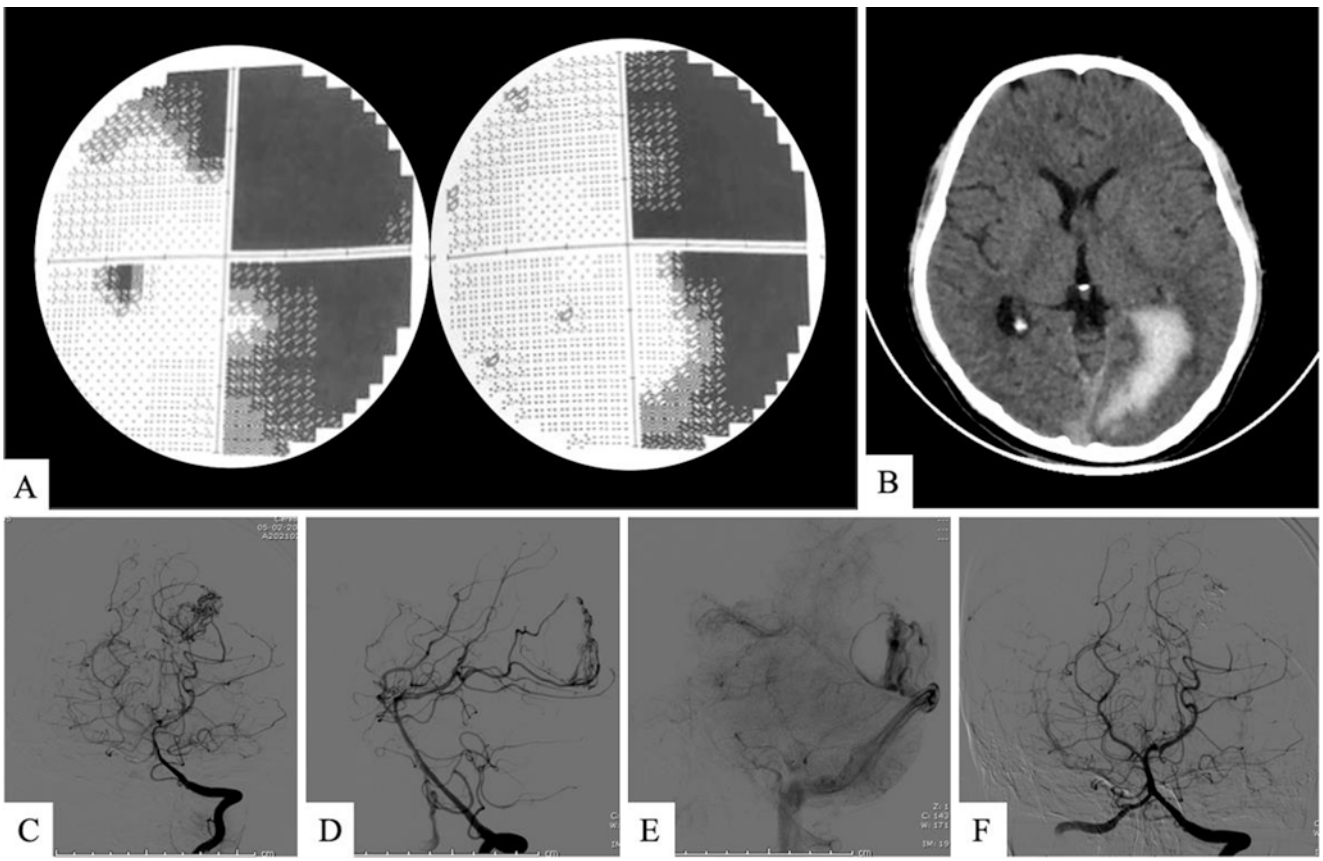


Fig. 1 A: Patient presented with chief complaint of inability to perceive objects in the right peripheral visual field. Of note was history of recurrent headache. His visual acuity was 20/20 OU, pupillary reactions and color vision were normal. Intraocular pressure of the left eye on noncontact tonometry was raised (right: 20 and left: 26 mmHg). Visual field testing confirmed a right-sided homonymous hemianopia. B: Neuroimaging with computed tomography revealed a large hematoma in the left occipital lobe. C, D: Diagnostic cerebral angiography showed an AVM supplied primarily by the calcarine branches of left posterior cerebral artery (PCA) and also the parieto-occipital branches of left PCA (lateral projection and anteroposterior projection). E: Venous phase showed the superficial venous drainage of the AVM and displacement of vessels from mass effect from the hematoma. F: Post-embolization left vertebral angiogram showed a near complete obliteration of the AVM with few residual fine feeders from parieto-occipital artery

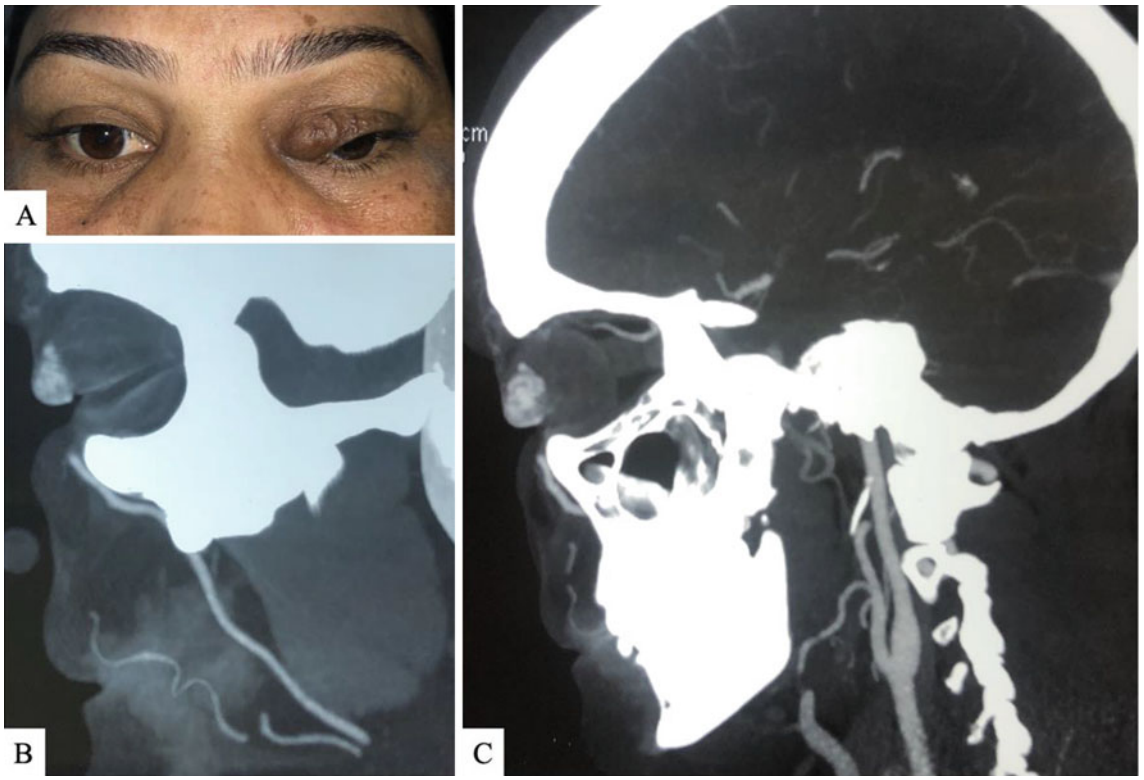


Fig. 2 A: Young female patient presented with left upper eyelid mass progressively increasing in size for the past two decades. On evaluation, surface dilated vessels were noted with raised temperature and pulsatility. The lesion was extending into the medial orbit and the visual acuity, eye ball, and motility were unaffected. B: CT angiography demonstrated an AVM in the medial aspect of the left orbit and eyelid with arterial supply from the angular branch of the left facial artery and drainage into the left anterior jugular vein. C: The sagittal section of CT angiography demonstrating the dilated superior ophthalmic vein in the left orbit, and absence of any associated intracranial or facial AVMs

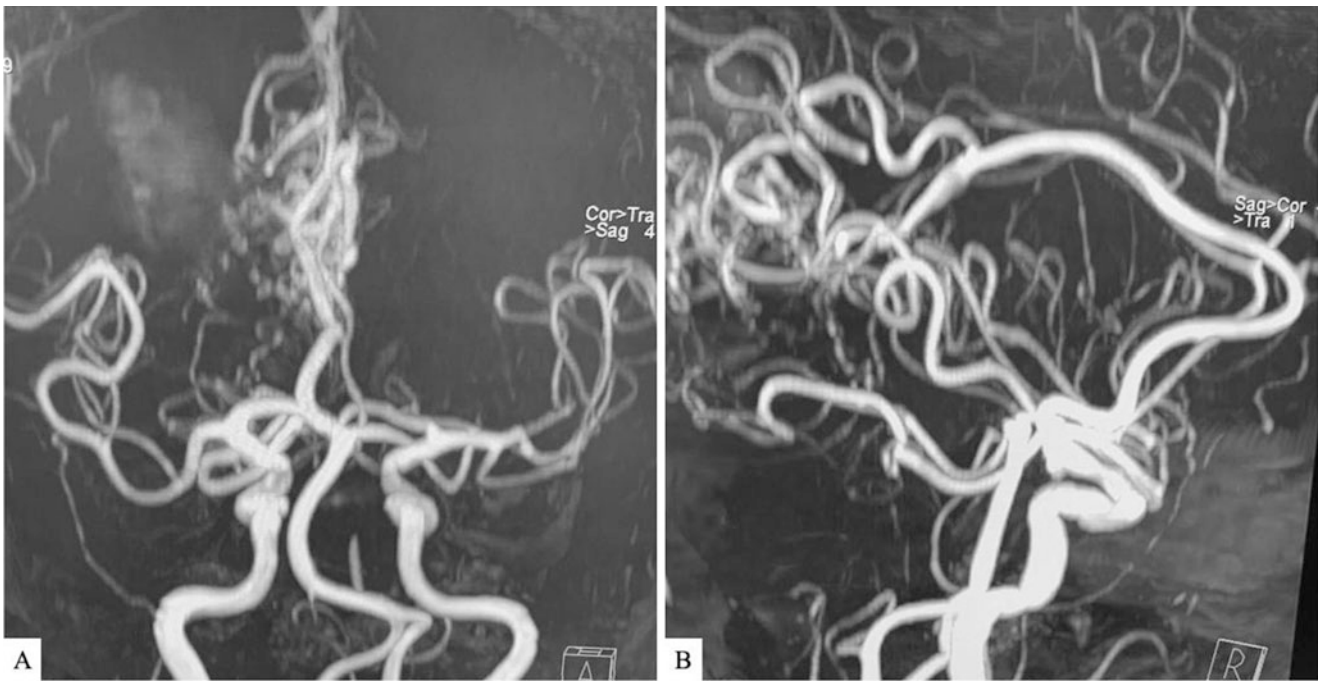


Fig. 3 Magnetic resonance angiography image (A: coronal and B: sagittal) showing an intracerebral arteriovenous malformation with feeders from both distal anterior cerebral arteries

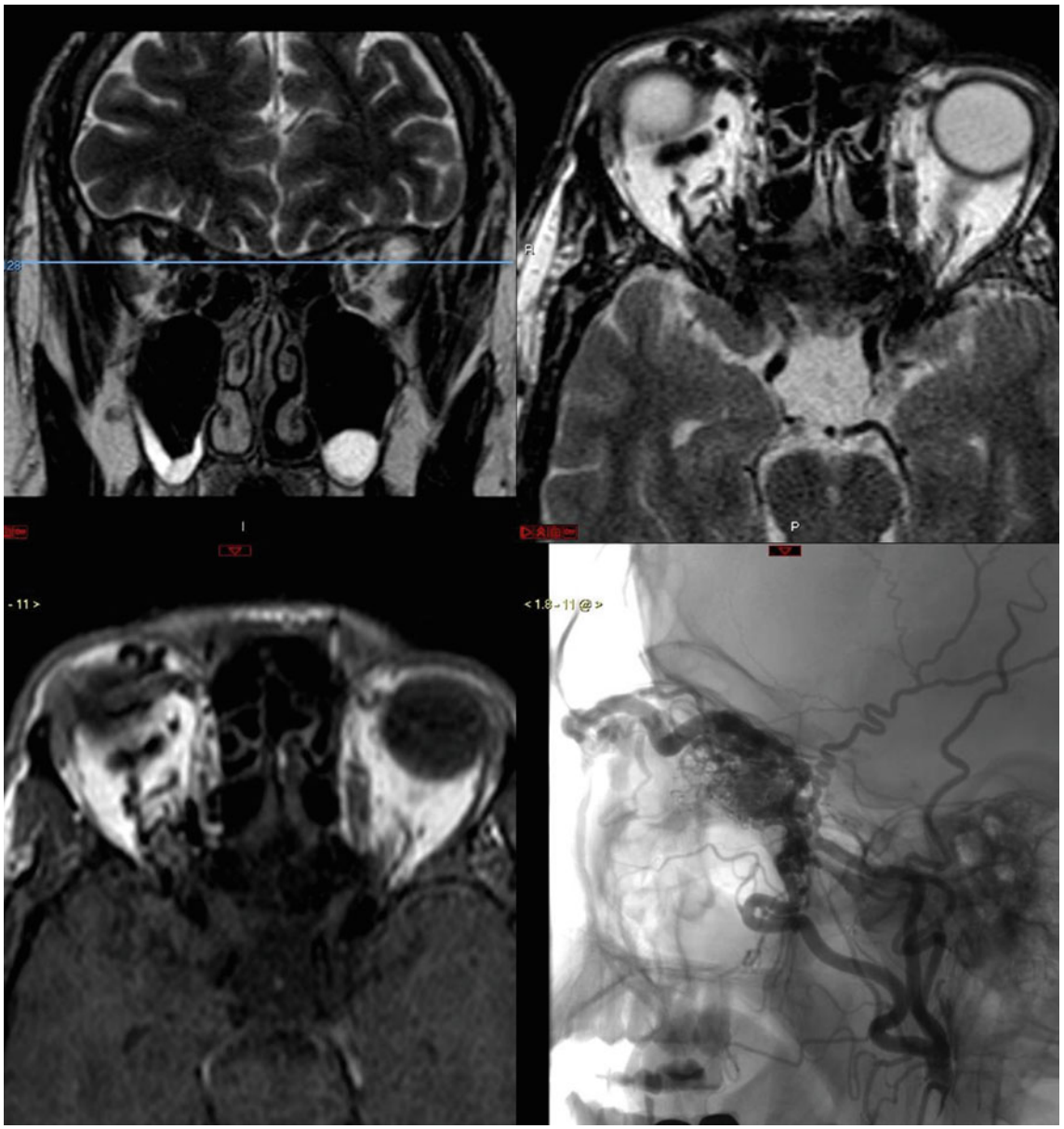


Fig. 4 MR of a 37-year-old male with right orbital AVM, non-FS T2 (*upper images*) and T1 (*lower left image*). Note the posterior medial location of the nidus encroaching the right medial rectus muscle. DSA lateral view (*lower right*) showing the full extent of the lesion along with its feeder external carotid artery and draining superior ophthalmic vein

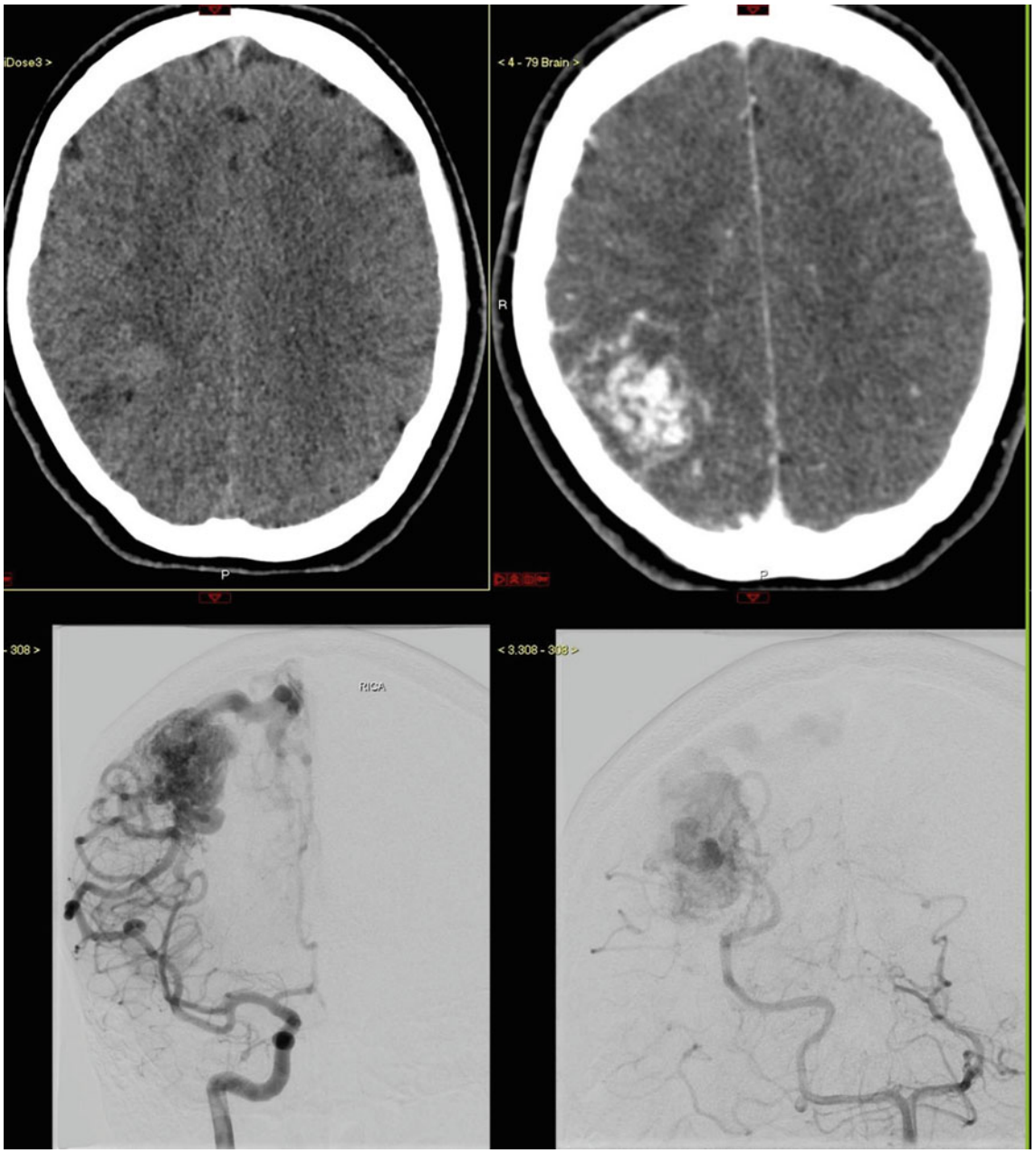


Fig. 5 CT (*upper images*) and DSA (*lower images*) of a 19-year-old female with a right parietal lobe AVM. The malformation is isodense on NECT (*upper left*) and shows bright enhancement post-contrast administration (*upper right*). It has double feeder vessels from the MCA and PCA as demonstrated by the angiography images (*lower left and lower right, respectively*)

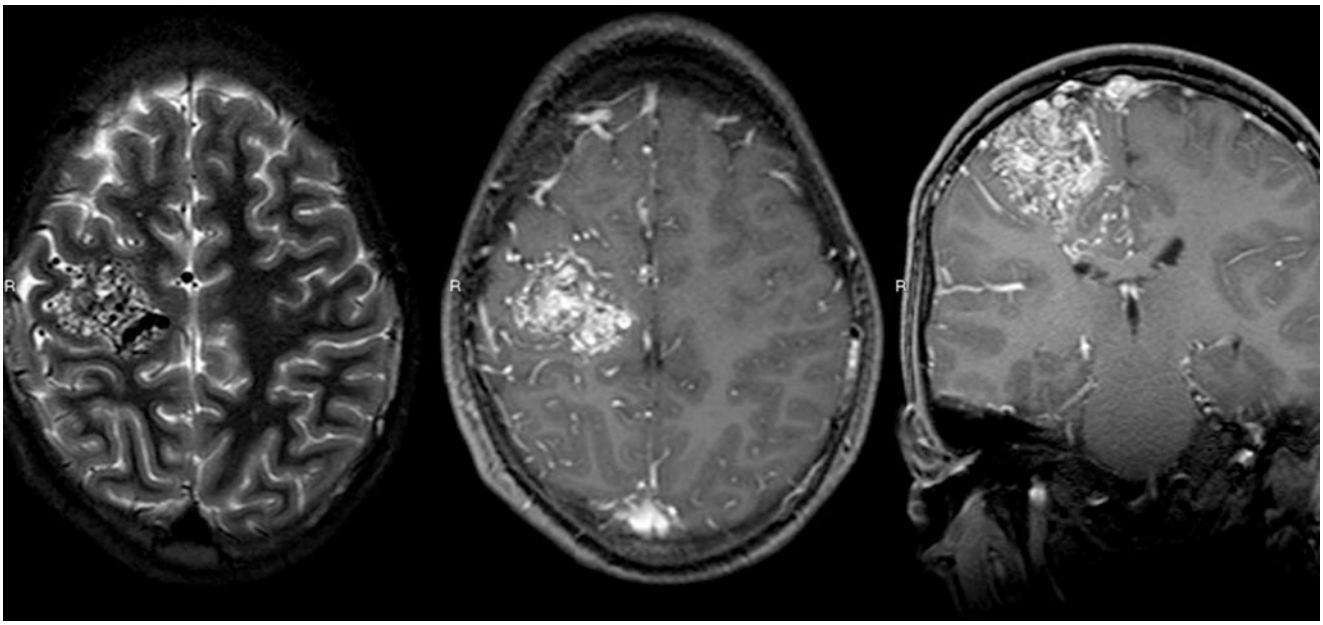


Fig. 6 MR of a 12-year-old female with right frontal lobe AVM. Axial T2 (*left*) and post-gad T1 (*middle and right*) images depicting the mixed intensity and bright enhancement of the malformation (Figs. 4, 5, and 6 *Courtesy of the editors)*

References

1. Kim AW, Kosmorsky GS. Arteriovenous communication in the orbit. J Neuroophthalmol. 2000;20(1):17–9.
2. ISSVA. Classification of vascular anomalies ©2018. International Society for the Study of Vascular Anomalies Available at http://issva.org/classification. Accessed 12 Feb 2021.
3. Hayes BH, Shore JW, Westfall CT, Harris GJ. Management of orbital and peri- orbital arteriovenous malformations. Ophthalmic Surg. 1995;26(2):145–52.
4. Rootman J. Vascular malformations of the orbit: hemodynamic concepts. Orbit. 2003;22(2):103–20.
5. O'Loughlin L, Groves ML, Miller NR, Pearl MS. Cerebrofacial arteriovenous metameric syndrome (CAMS): a spectrum disorder of craniofacial vascular malformations. Childs Nerv Syst. 2017;33(3):513–6. https://doi.org/10.1007/s00381-016-3277-x. Epub 2016 Oct 27. PMID: 27787648.
6. Garrity JA, Henderson JW, Cameron JD. Henderson's orbital tumors. 4th ed. Philadelphia: Lippincott Williams & Wilkins; 2007.
7. Schöbinger R. In: Proceedings of international society for the study of vascular anomalies congress, Rome, Italy. June 23–26, 1996.
8. Hopen G, Smith JL, Hoff JT, Quencer R. The Wyburn-Mason syndrome. Concomitant chiasmal and fundus vascular malformations. J Clin Neuro Ophthalmol. 1983;3:53–62.
9. Archer DB, Deutman A, Ernest JT, Krill AE. Arteriovenous communications of the retina. Am J Ophthalmol. 1973;75:224–41.
10. Gibo H, Watanabe N, Kobayashi S, Sugita K. Removal of an arteriovenous malformation in the optic chiasm. Surg Neurol. 1989;31(2):142–8. https://doi.org/10.1016/0090-3019(89)90329-7.
11. Kang H, Han MH, Kwon BJ, Yoon B, Chang K. Cerebellopontomandibular vascular malformation: a rare type of cerebrofacial arteriovenous metameric syndrome. J Neurosurg. 2005;102(1):156–60.
12. Spetzler RF, Martin NA. A proposed grading system for arteriovenous malformations. J Neurosurg. 1986;65(4):476–83. https://doi.org/10.3171/jns.1986.65.4.0476.
13. Mukherjee B, Vijay V, Halbe S. Combined approach to management of periocular arteriovenous malformation by interventional radiology and surgical excision. Indian J Ophthalmol. 2018;66:151–4.
14. Goldberg RA, Garcia GH, Duckwiler GR. Combined embolization and surgical treatment of arteriovenous malformation of the orbit. Am J Ophthalmol. 1993;116(1):17–25.
15. Warrier S, Prabhakaran VC, Valenzuela A, Sullivan TJ, Davis G, Selva D. Orbital arteriovenous malformations. Arch Ophthalmol. 2008;126(12):1669–75. https://doi.org/10.1001/archophthalmol.2008.501.

Other Rare Vascular Tumors of the Orbit

70

Kasturi Bhattacharjee and Vatsalya Venkatraman

Contents

1 Signs and Symptoms 530
1.1 Orbital solitary fibrous tumor 530
1.2 Angiosarcoma 530
1.3 Hemangioblastoma 530

2 Differential Diagnosis 530
2.1 Orbital solitary fibrous tumor 530
2.2 Angiosarcoma 530
2.3 Hemangioblastoma 531

3 Diagnosis 531
3.1 Orbital solitary fibrous tumor 531
3.2 Angiosarcoma 531
3.3 Hemangioblastoma 531

4 Treatment 532
4.1 Orbital solitary fibrous tumor 532
4.2 Angiosarcoma 532
4.3 Hemangioblastoma 532

5 Figures with Captions 532

References 534

Abstract

Hemangiopericytoma

- Hemangiopericytoma, now referred to as Solitary fibrous tumor, is an uncommon tumor arising from spindle cells of mesenchymal origin. Though the most common site of origin of such a tumor is pleura, these tumors can also be observed in the extra pleural locations of the body such as, the lung, mediastinum, peritoneum, pericardium, retro peritoneum, pelvis, adrenals, kidney, periosteum, salivary gland, thyroid, breast, and orbit. On histopathological studies, it shows a patternless growth pattern characterized by bland spindle-cell proliferation with alternating hyper- and hypo-cellular areas and a focal hemangiopericytoma-like vascular pattern.
- On computed tomography, it appears as a well-defined soft tissue mass which is low or isodense compared to the extra ocular muscles but shows bright contrast enhancement.
- Magnetic resonance imaging depicts iso intensity on T1 weighted and iso to hypo intensity on T2 weighted images, but some lesions may show heterogeneous hyper intensity or cystic appearance also. As mentioned above, it shows intense enhancement.
- Immunohistochemistry can confirm the diagnosis, following which, complete tumor resection is the treatment of choice.

K. Bhattacharjee (✉)
Department of Ophthalmic Plastic and Reconstructive Surgery, Sri Sankaradeva Nethralaya, Guwahati, India

V. Venkatraman
Sri Sankaradeva Nethralaya, Guwahati, India

© Springer Nature Switzerland AG 2022
G. Ben Simon et al. (eds.), *Atlas of Orbital Imaging*,
https://doi.org/10.1007/978-3-030-62426-2_108

Angiosarcoma

- Angiosarcoma is a rare, frequently misdiagnosed vascular tumor which is a deadly masquerader and bears high propensity for local recurrence and metastasis.
- It is a moderately differentiated tumor with nuclear atypia, distinct vascular channels of irregular size and shape, communicating focally to form a reticular network of sinusoids which dissect through the collagen of dermis.
- Computed tomography of angiosarcoma can mimic other vascular tumors and thus is useful only to determine the extent of the lesion and does not aid in diagnosis.
- Treatment aims at complete surgical resection to prevent recurrence and metastases, but due to its multifocal and aggressive nature, this goal might not be achieved. It is relatively resistant to other adjuvant modalities like chemotherapy and radiotherapy.

Hemangioblastoma

- Hemangioblastoma is a benign vascular tumor, chiefly of capillary size vessels which account for 1–2% of primary tumors in the central nervous system in the posterior fossa or the spinal cord. It is frequently associated with von Hippel-Lindau syndrome.
- It usually involves the retina and the optic nerve with rare orbital manifestations. It is a soft solid lesion arising from the substance of the nerve and not the overlying neural sheaths.
- Computed tomography shows a homogenous mass hyperdense to the vitreous and hypodense to the extra ocular muscles.
- Magnetic resonance imaging shows the mass to be isointense on T1 weighted scan and hyper intense on both T2 weighted scans and in fluid-attenuated inversion recovery imaging. The lesion also takes up contrast in a moderately homogenous to heterogenous fashion.
- For lesions associated with the optic nerve, the mainstay of treatment remains surgical resection following which the patient must be evaluated for other associated tumors in the von Hippel-Lindau umbrella such as cerebellar hemangioblastoma and renal cell carcinoma.

Keywords

Solitary fibrous tumor · Hemangiopericytoma · Cutaneous angiosarcoma · Hobnail hemangioendothelioma · Pediatric epitheloid angiosarcoma · Hemangioblastoma · von Hippel-Lindau syndrome

1 Signs and Symptoms

1.1 Orbital solitary fibrous tumor

Patients with orbital solitary fibrous tumor often present with a gradually progressing unilateral painless proptosis with a palpable mass, which can cause severe facial asymmetry along with eyelid swelling, visual disturbances, tearing, and ptosis [1]. It is usually seen in the fifth decade with a slight male predilection [1]. According to the recent literature, there have been 90 reported cases of orbital solitary fibrous tumor [2, 3]. There has been an increase in the number of reported cases due to advances in the field of immunohistochemistry.

1.2 Angiosarcoma

Angiosarcoma usually presents as a cutaneous lesion of the scalp and face which can secondarily involve the orbit and periocular structures [4]. It is known to mimic several benign and malignant tumors and other reactive processes. It evolves rapidly into a violaceous mass that can be mistaken for inflammation, edema, or hematoma [5]. It can at times have a fleshy appearance which can be misunderstood for an epithelial carcinoma or metastases. Hobnail hemagioendothelioma is an intermediate grade tumor that is considered as a variant of low-grade angiosarcoma seen in middle-aged adults [5].

1.3 Hemangioblastoma

Hemangioblastoma often presents as a unilateral mass between 15 and 67 years of age with a slight male preponderance [6]. Since optic nerve is a common site of involvement, they present with exophthalmos [7], diagnoses of which can be confirmed with neuro imaging along with decreased visual acuity [6].

2 Differential Diagnosis

2.1 Orbital solitary fibrous tumor

The differential diagnosis for an orbital solitary fibrous tumor include hemangiomas, fibrous histiocytomas, nerve sheath meningiomas and schwannomas, liposarcoma, synovial sarcoma, neurofibroma [8, 9].

2.2 Angiosarcoma

Angiosarcoma is a great masquerader and can be mistaken for inflammatory eyelid conditions with associated ecchymosis, edema, and ulceration [5]. Other differentials are intravascular

papillary endothelial hyperplasia, Mason's low grade pseudoangiosarcoma, Kaposi sarcoma, angiolymphoid hyperplasia, metastatic skin or renal carcinoma, amelanotic melanoma, idiopathic inflammation of the orbit, trauma, and benign hemangio-endothelioma-pericytoma [10, 11].

2.3 Hemangioblastoma

Hemangioblastomas when not in concurrence with von Hippel-Lindau syndrome and involving the optic nerve have to be differentiated from optic nerve meningioma, optic nerve glioma, and other conditions [7].

3 Diagnosis

3.1 Orbital solitary fibrous tumor

Orbital solitary fibrous tumor is often benign and non-aggressive. Within the orbit, it may involve the intra- or extraconal space, lacrimal fossa, or sac area and eyelids with noted preference to superolateral extraconal space [12, 13].

The diagnosis can be solidified with immunohistochemistry as this tumor shows strong immunopositivity for CD34, vimentin, bcl-2, CD99, STAT6, and early growth response protein 1, but is negative for cytokeratin, EMA, S100 protein, αSMA, factor VIII-related antigen, and desmin. Its vascular structure shows staghorn configuration characterized by irregular, angular, thin-walled, and branching blood vessels and frequently hyalinized thick blood vessels.

Some authors believe solitary fibrous tumor and hemangiopericytoma to be different entities. It thus has been emphasized that they must be differentiated. Orbital hemangiopericytoma is prone to recurrence and metastases and located typically in the extraconal space, adjacent to paranasal sinuses. They are well circumscribed, lobulated lesions of aggressive nature displaying bony erosion, whereas solitary fibrous tumor can remodel adjacent bones but usually do not cause bone destruction [12]. Hemangiopericytomas show weak and patchy staining for CD34 while solitary fibrous tumors show positive staining for CD34 but they can be negative in malignant cases.

Hemangiopericytomas show marked arterial enhancement with early venous enhancement and rapid washout in computed tomography [14]. Magnetic resonance imaging shows the lesion isointense and isointense to hypointense to cerebral cortex or the extra ocular muscles on both T1 and T2 weighed imaging [9]. They also show signal intensity void tubular structures suggestive of fast flowing vessels within the tumor [9]. Since both hemangiopericytomas and solitary fibrous tumor have similar soft tissue characteristics on radiological imaging, it doesn't form a diagnostic tool for differentiating the two from each other.

3.2 Angiosarcoma

Angiosarcoma is a clinical challenge to diagnose. It is classically a moderately differentiated lesion with moderate nuclear atypia. It has distinct vascular channels that form anastomotic branching network of sinusoidal spaces [5]. On the other hand, it can have solid sheet like epithelioid areas suggestive of high grade neoplasia.

It is important to differentiate hobnail hemangioendothelioma from angiosarcoma. Hobnail hemangioendothelioma has poorly circumscribed proliferation of long, well-formed retiform blood vessels lined by protuberant endothelial cells (hobnail) with papillary tufts and hyaline cores inside the lumen. Although in some cases, they also show focally solid areas of monomorphic spindle cells in the form of sinusoids bearing resemblance to angiosarcoma, the dissection of collagen planes with endothelial cells and prominent endothelial multilayering is not seen which is often seen in angiosarcoma. Both the tumors are positive for immunohistochemical markers of vascular and lymphatic endothelial differentiation. They show immunopositivity for CD31, CD34, VE-cadherin, FLI-1, and factor VIII related antigen with special preponderance for CD31 [5, 15]. It also shows a high Ki-67 level (>10%) [15].

3.3 Hemangioblastoma

Hemangioblastomas are characterized microscopically by reddish mass along the margin of the vessel with vacuolar interstitial cells and abundant capillary networks [7]. Literature states that from a total of 35 cases reported in a study, 71% were associated with von Hippel-Lindau syndrome [16]. In case of an optic nerve hemangioblastoma, other nerves of the body must be evaluated to rule out syndromic association.

On magnetic resonance imaging, these lesions are solid or cystic, iso to hypo intense on T1 and hyperintense on T2 weighted images. It also shows multiple flow voids in case of a cystic morphology with high vascularity. They show marked contrast enhancement in the solid part of the nerve which segregates it from optic sheath meningiomas that displace the nerve to one side and show enhancement in the surrounding dural sheath [6]. These lesions also show a peculiar feature of large amounts of edema around the tumor extending from the optic nerve up to the optic radiation [7]. Magnetic resonance imaging, non-contrast and contrast form the most sensitive tools for the diagnosis of this lesion. On computed tomography, there is no bony destruction or hyperostosis [6].

4 Treatment

4.1 Orbital solitary fibrous tumor

The standard treatment for solitary fibrous tumors is surgical excision, but it usually follows an incomplete initial excision [9, 12]. Biopsy of these lesions is not recommended due to expected massive bleeding from feeding arteries. The recurrence is rare. Chemotherapy and radiotherapy can be performed after surgical excision in locally invasive lesions. These tumors must be preoperatively differentiated from other spindle cell tumors of the orbit.

4.2 Angiosarcoma

The desired goal in the management of angiosarcoma is complete tumor resection but it is a multifocal lesion making surgical excision of the lesion in entirety extremely difficult. It is important to differentiate it from hobnail hemangioendothelioma which is an intermediate grade neoplastic lesion with propensity for regional recurrence but very low risk of metastases, whereas the former shows high propensity for metastases necessitating adjuvant radiotherapy and chemotherapy. Wide local excision with or without radiotherapy is the accepted current mode of treatment for hobnail hemangioendothelioma [17]. Angiosarcoma is recalcitrant to most therapeutic modalities with frequent metastases to liver, lung and lymph nodes. Patients with angiosarcoma involving the eyelids and adjacent facial structures have been recorded to have a 3-year survival of 57% [4].

4.3 Hemangioblastoma

Surgical resection is currently the best method of treatment for optic nerve hemangioblastoma. Turel et al. suggested that early surgical treatment was needed when the tumor was far away from the optic disc and did not involve the optic nerve [18]. Stereotactic radiosurgery is an important tool for management of carefully selected patients of hemangioblastoma. It can be used for deep seated tumors, for von Hippel-Lindau patients with recurrent tumors, for residual tumors of patients who have undergone subtotal resection and as salvage therapy for progressive cases [19]. Orbital hemangioblastomas are extremely rare but richly vascular. Wu et al. [20] suggested that the hypervascularity of the lesion predisposes for torrential bleeding intraoperatively while resection and thus preoperative embolization with N-butyl cyanoacrylate has been tried with acceptable results.

5 Figures with Captions



Fig. 1 Hemangiopericytoma. A 55-year-old female patient presented with left axial proptosis and upper eyelid fullness. T1 weighted FS post contrast coronal scan (*upper image*) demonstrated the lesion (*arrow*) to be avidly enhancing. T2 weighted fat suppressed axial scan (*lower image*) demonstrated a moderately homogenous texture of the lesion (*arrow)* with internal flow voids

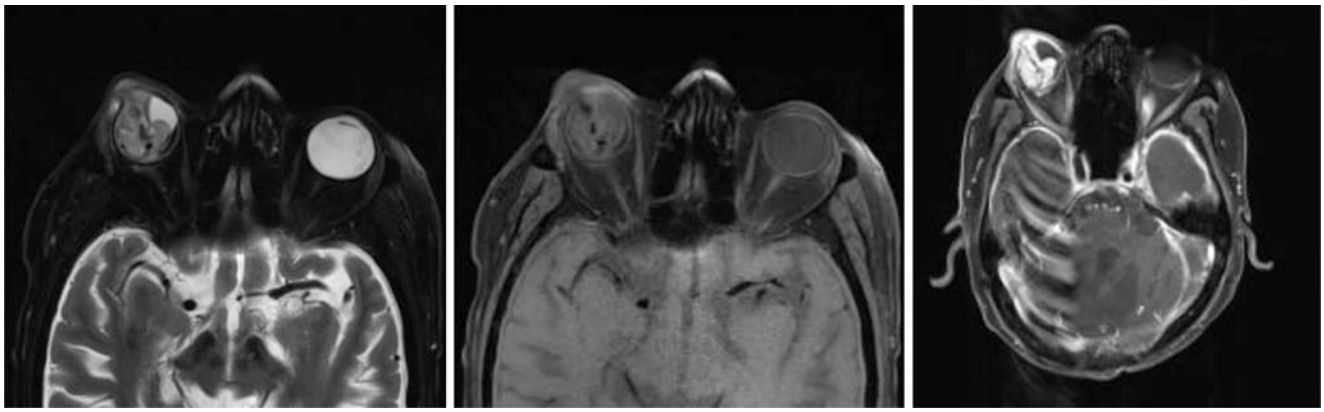


Fig. 2 Hemangioblastoma. 51-year-old male patient with right proptosis and visual disturbances.T2 weighted axial FS image (*left*) reveals a moderate hyperintense lesion in the posterior globe wall extending to the vitreous with prominent flow void signals. The lesion is isointense on T1 FS WI (*middle*) and shows heterogeneous enhancement post-contrast administration (*right*)

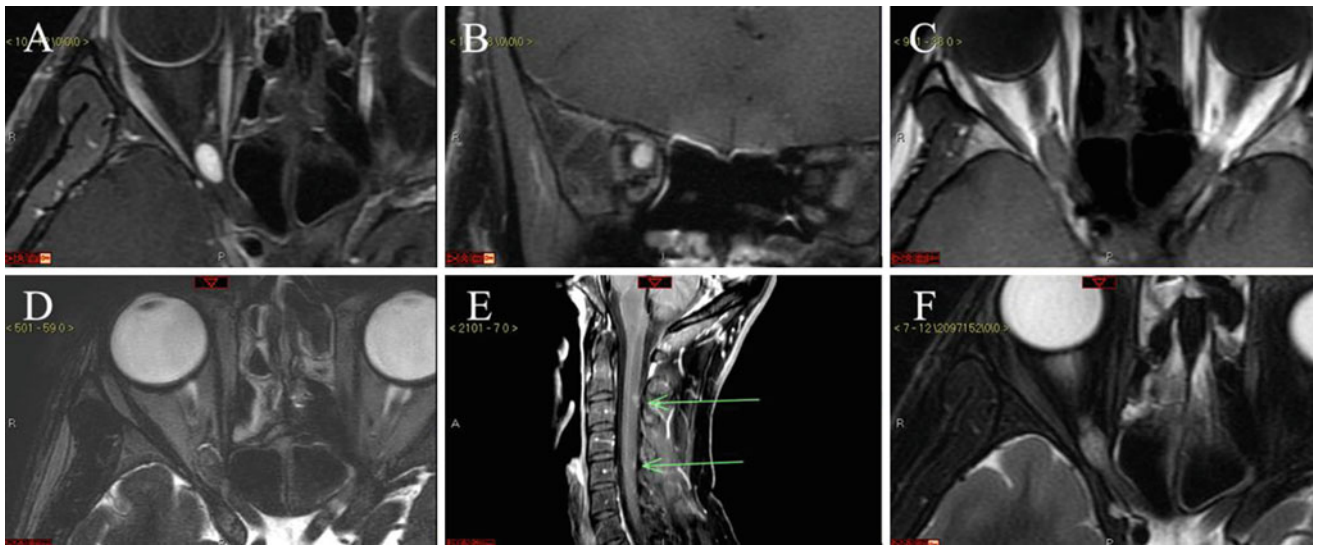


Fig. 3 MRI scans of a 26-YOM with Von Hippel-Lindau (VHL) disease, multiple hemangioblastomas and presumed bilateral optic nerve involvement. (**a**) T1WI FS CE, axial view, showing homogenous enhancement of the tumor at the apical portion of the optic nerve. (**b**) Coronal view. (**c**) Conventional T1 showing the tumor is isointense to EOM. (**d**) Heavily T2-WI better delineates the hemangioblastoma from the normal optic nerve tissue. (**e**) Multiple spinal cord hemangioblastomas, at the level of C2-C3 and C5 (green arrows) typical of VHL. (**f**) T2 WI FS showing the hyperintensity of the lesion typical T2 feature of vascular tumors. The left ON hemangioblastoma, located more caudally at the intracanalicular portion is not shown. (Courtesy of the editors)

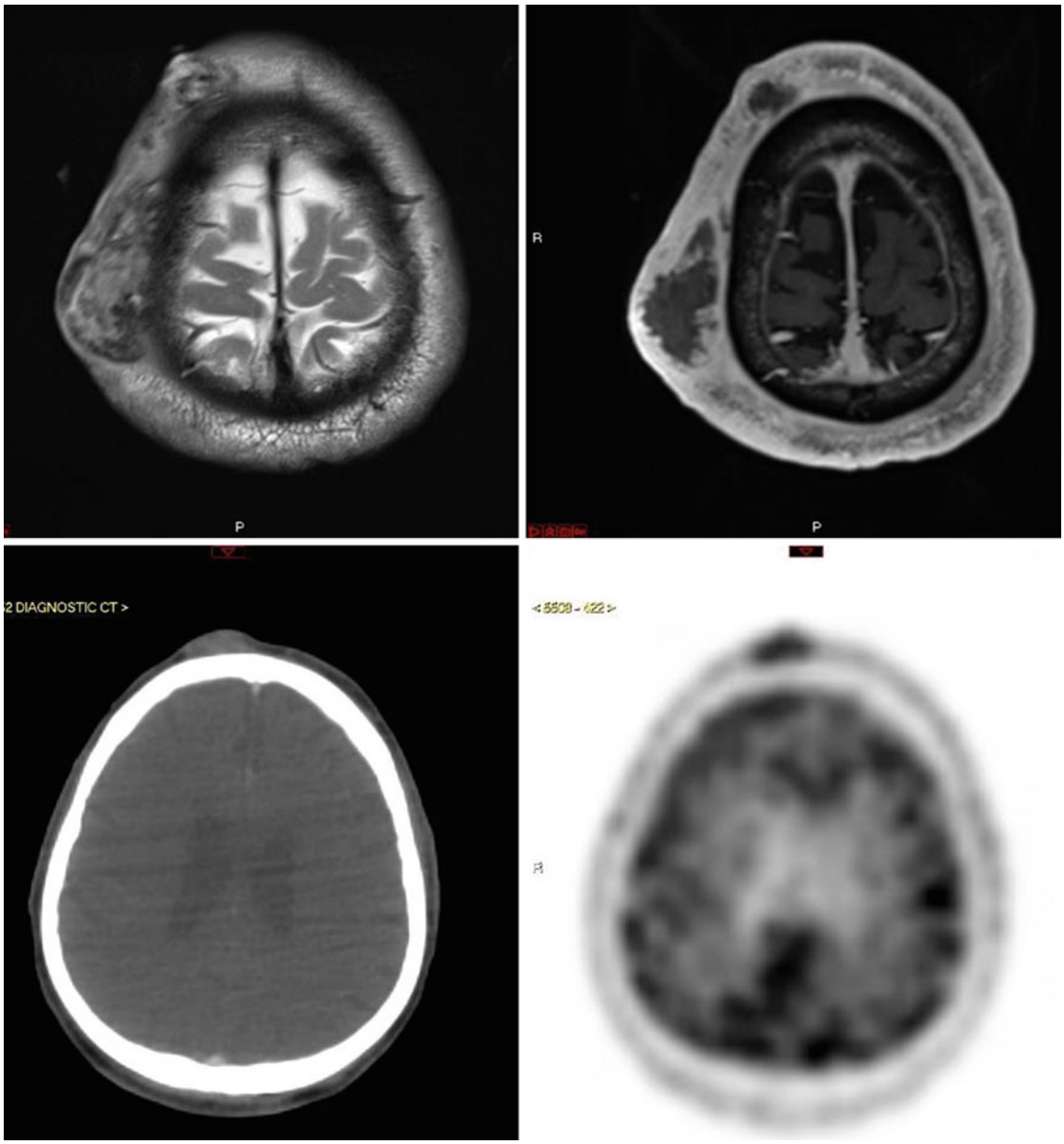


Fig. 4 A 75-year-old male with right superficial frontotemporal angiosarcoma. MRI scans (*upper left,* T2-WI; *upper right*, T1 CE) demonstrate a heterogenous lesion with presumed central necrosis. CE CT (*lower left*) better demonstrates the lack of bony involvement of the tumor which is FDG-avid on PET scan (*lower right*). (Courtesy of the editors)

References

1. Le CP, Jones S, Valenzuela AA. Orbital solitary fibrous tumor: a case series with review of the literature. Orbit. 2014;33:145–51.
2. Furusato E, Valenzuela IA, Fanburg-Smith JC, Auerbach A, Furusato B, Cameron JD, Rushing EJ. Orbital solitary fibrous tumor: encompassing terminology for hemangiopericytoma, giant cell angiofibroma, and fibrous histiocytoma of the orbit: reappraisal of 41 cases. Hum Pathol. 2011;42(1):120–8. https://doi.org/10.1016/j.humpath.2010.05.021. Epub 2010 Nov 5. PMID: 21056898.
3. Shen J, Li H, Feng S, Cui H. Orbital solitary fibrous tumor: a clinicopathologic study from a Chinese tertiary hospital with a literature review. Cancer Manag Res. 2018;10:1069–78. https://doi.org/10.2147/CMAR.S165218. Published 2018 May 9.
4. Papalas JA, Manavi CK, Woodward JA, San-gueza OP, Cummings TJ. Angiosarcoma of the eyelid: a clinicopathologic comparison between isolated unilateral tumors and tumors demonstrating extrapalpebral involvement. Am J Dermatopathol. 2010;32:694–9.
5. Milman T, Shields CL, Brooks JSJ, Lally SE, Shields JA, Tuluc M, Eagle RC Jr. Primary cutaneous angiosarcoma of the eyelid: a diagnostic and therapeutic challenge. Ocul Oncol Pathol. 2018;4(4):230–5. https://doi.org/10.1159/000485427. Epub 2018 Jan 12. PMID: 30643767; PMCID: PMC6322085.
6. Darbari S, Meena RK, Sawarkar D, Doddamani RS. Optic nerve hemangioblastoma: review. World Neurosurg. 2019;128:211–5.

https://doi.org/10.1016/j.wneu.2019.04.224. Epub 2019 May 1. PMID: 31054346.
7. Xu S, Li Q, Bian B, Zhou H, Li D. Optic nerve Hemangioblastoma with bilateral frontal lobe Oedema: a case report. BMC Ophthalmol. 2020;20(1):437. https://doi.org/10.1186/s12886-020-01706-4. PMID: 33143685; PMCID: PMC7640410.
8. Ha JK, Park BJ, Kim YH, Lim YJ. Orbital solitary fibrous tumor: a case report and diagnostic clues. J Korean Neurosurg Soc. 2009;46: 77–80.
9. Mitamura M, Kase S, Suzuki Y, Sakaguchi T, Suimon Y, Dong Y, Hatanaka KC, Sinohara T, Kase M, Ishida S. Solitary fibrous tumor of the orbit: a clinicopathologic study of two cases with review of the literature. In Vivo. 2020;34(6):3649–54. https://doi.org/10.21873/invivo.12211. PMID: 33144480; PMCID: PMC7811632.
10. De Keizer RJW, de Wolff-Rouendaal D. Angiosarcoma of the eyelid and periorbital region. Experience in Leiden with Iridium192 brachytherapy and low-dose doxorubicin chemotherapy. Orbit. 2008;27:5e12.
11. Lemanski N, Farber M, Carruth BP, Wladis EJ. Primary adnexal angiosarcoma masquerading as periorbital hematoma. Surv Ophthalmol. 2014;59(6):655–9. https://doi.org/10.1016/j.survophthal.2014.06.005. Epub 2014 Jul 2. PMID: 25444365.
12. Sayit AT, Elmali M, Gul A, Sullu Y. Solitary fibrous tumor of the orbit: computed tomography and histopathological findings. J Cancer Res Ther. 2019;15(3):719–21. https://doi.org/10.4103/jcrt.JCRT_1194_16. PMID: 31169250.
13. Genc A, Toktas Z, Azman C, Bozkurt SU, Kilic T. Solitary fibrous tumor of the orbit: a case report and review of the literature. Turk Neurosurg. 2015;25:984–7.
14. Tailor TD, Gupta D, Dalley RW, Keene CD, Anzai Y. Orbital neoplasms in adults: clinical, radiologic, and pathologic review. Radiographics. 2013;33:1739–58.
15. Duarte AF, Valera E, Chahud F, Cruz AA. Infantile primary orbital angiosarcoma. Pediatr Blood Cancer. 2016;63(4):752–3. https://doi.org/10.1002/pbc.25846. Epub 2015 Nov 24. PMID: 26599256.
16. McGrath LA, Mudhar HS, Salvi SM. Hemangioblastoma of the optic nerve. Surv Ophthalmol. 2019;64(2):175–84.
17. Al-Faky YH, Al-Mosallam AR, Al-Rikabi AC, Al-Sohaibani MO: Medial canthus retiform hemangioendothelioma. Indian J Ophthalmol. 2014:491–93.
18. Turel MK, Kucharczyk W, Gentili F. Optic nerve Hemangioblastomas? A review of visual outcomes. Turk Neurosurg. 2017;27(5):827–31.
19. Johnson S, Niranjan A, Kano H, Lunsford LD. Leksell radiosurgery for the 3 H tumors: Hemangiomas, Hemangioblastomas, and Hemangiopericytomas. Prog Neurol Surg. 2019;34:223–31. https://doi.org/10.1159/000493068. Epub 2019 May 16. PMID: 31096251.
20. Wu YM, Wong HF, Ng SH. Direct intratumoral pre-surgical embolization of orbital Hemangioblastoma. A Case Report Neuroradiol J. 2008;21(5):693–7. https://doi.org/10.1177/197140090802100514. Epub 2008 Dec 17. PMID: 24257013.

Part XI

Orbital Inflammation

Idiopathic Orbital Inflammation (IOI)

71

Alan A. McNab

Contents

1 **Symptoms and Signs** 539
2 **Differential Diagnosis** 539
3 **Diagnosis** 540
4 **Treatment** 540
5 **Figures with Captions** 540
References 544

Abstract

- Idiopathic orbital inflammation (once called orbital pseudotumor) is a diagnosis of exclusion.
- Imaging features depend on the anatomical site affected, but generally show mass effect with indistinct borders and contrast enhancement.
- Biopsy should be obtained in most cases to exclude specific forms of inflammation and mimicking lesions.
- Inflammation may be acute, subacute, or sclerosing.
- Specific anatomical patterns may occur such as dacryoadenitis, orbital myositis, scleritis, and Tolosa Hunt syndrome.
- Treatment is generally with corticosteroids and immunosuppressants.

Keywords

Idiopathic orbital inflammation · Acute inflammation · Subacute inflammation · Sclerosing inflammation · Orbit

1 Symptoms and Signs

Idiopathic orbital inflammation (IOI, previously called pseudotumor) is a diagnosis of exclusion. The inflammatory process can be acute, subacute, chronic, granulomatous, or sclerosing, and can affect any orbital tissue. Anatomically localized forms include idiopathic dacryoadenitis, orbital myositis, and Tolosa Hunt syndrome (involvement of the orbital apex and superior orbital fissure). Symptoms vary depending on the above factors, but in acute IOI, classical symptoms and signs of inflammation (pain, redness, swelling, loss of function) are common. Chronic and sclerosing forms may show no signs of acute inflammation

2 Differential Diagnosis

Differential diagnosis depends on the anatomical site. Any infiltrative process can mimic IOI including other specific forms of inflammation (IgG4-RD, sarcoidosis, granulomatosis with polyangiitis, Sjögren's syndrome), and lymphoma

A. A. McNab (✉)
Orbital Plastic and Lacrimal Clinic, Royal Victorian Eye and Ear Hospital, Melbourne, VIC, Australia

© Springer Nature Switzerland AG 2022
G. Ben Simon et al. (eds.), *Atlas of Orbital Imaging*,
https://doi.org/10.1007/978-3-030-62426-2_58

3 Diagnosis

In most cases, a definitive diagnosis is only possible with a tissue biopsy. Appropriate immunohistochemistry and blood tests are required to exclude specific forms of inflammation and lymphoma.

4 Treatment

Acute IOI is usually treated with a tapering course of oral steroids. Chronic and sclerosing forms of IOI may require steroid-sparing agents or biologic agents.

5 Figures with Captions



Fig. 1 A young woman with subacute onset of painful left upper eyelid swelling and erythema, with ptosis and pain on eye movement



Fig. 2 (same patient as in Fig. 1) An axial non-contrast CT shows an ill-defined hyperdense intraconal lesion molding to the globe. The patient had subacute onset symptoms of swelling, diplopia, and ptosis. Biopsy confirmed chronic IOI

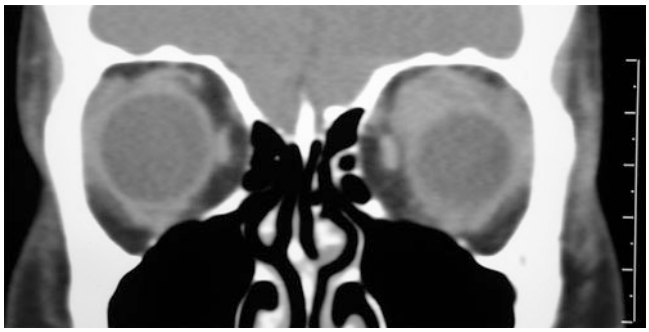


Fig. 3 A coronal non-contrast CT (same patients as Figs. 1, 3, and 4) shows a superior orbital lesion molding to the globe and causing inferior globe dystopia

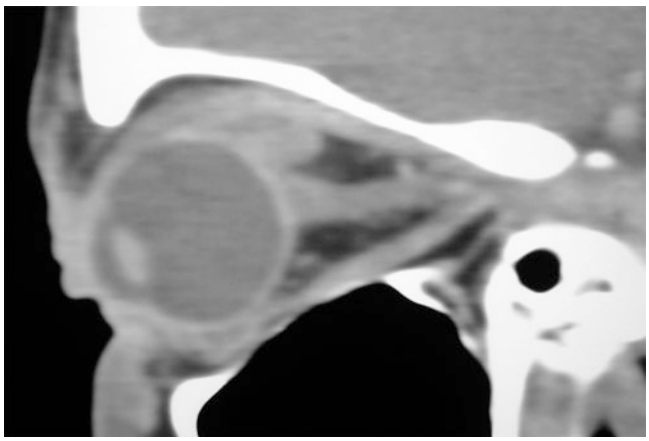


Fig. 4 A sagittal non-contrast CT (same patient as in Figs. 1, 2, and 3) shows a lesion lying between the globe and superior rectus

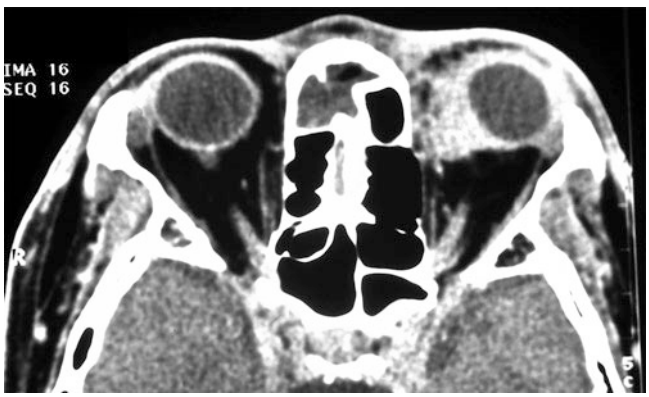


Fig. 5 An axial contrast-enhanced CT in a man with acute onset IOI shows an ill-defined supero-medial enhancing orbital lesion molding to the globe, also seen as a component encircling the superior globe. Biopsy confirmed acute IOI, and he responded well to a course of oral steroids

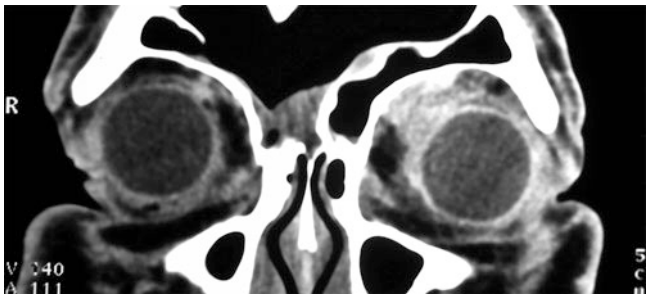


Fig. 6 A coronal contrast-enhanced CT (same patient as Fig. 5) shows an ill-defined supero-medial mass, molding to the globe with some globe dystopia, and possible mild flattening of the globe

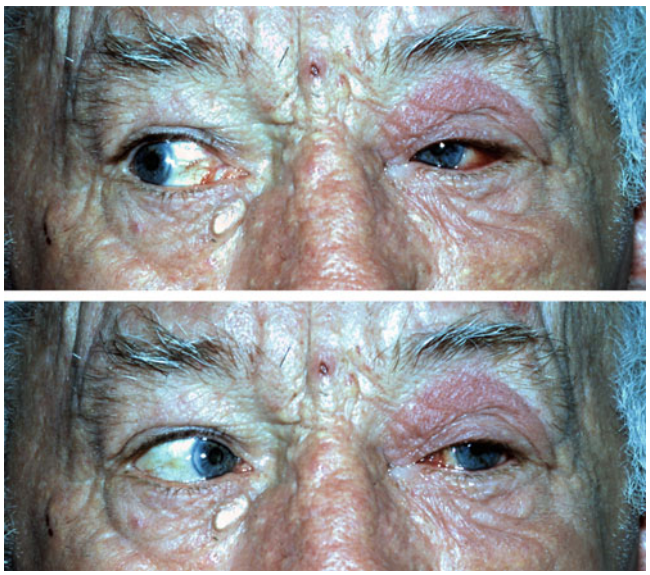


Fig. 7 An elderly man with acute onset of left eye swelling, erythema, optic neuropathy, and limited eye movements



Fig. 8 (Same patient as Figs. 7, 8, and 10). An axial contrast-enhanced CT shows a widely infiltrating largely intraconal left orbital lesion, which enhances modestly. The elderly male had an acute onset of inflammatory signs with optic neuropathy and reduced motility. A biopsy diagnosed acute IOI



Fig. 9 An axial contrast-enhanced CT (same patient as in Figs. 7 and 8) shows an enhancing intraconal lesion surrounding the optic nerve, and causing optic neuropathy with ptoptosis and mild flattening of the posterior globe. In addition, the image demonstrates involvement of the medial and lateral rectus muscles, with fusiform enlargement of the medial, and diffuse enlargement of the lateral rectus including tendon involvement



Fig. 10 A young adult male with chronic left proptosis, hyperglobus, lower lid retraction, and restricted eye movements

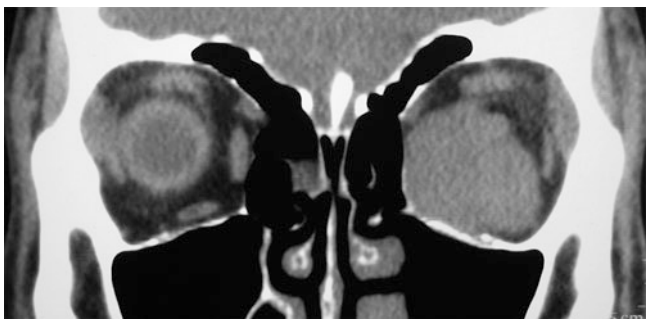


Fig. 11 A coronal non-contrast CT of the patient in Fig. 10 shows a large medial intra- and extraconal lesion extending to and partially surrounding the optic nerve. The medial and inferior rectus muscles are inseparable from the lesion. Biopsy showed sclerosing IOI. There was no response to a variety of immune-suppressants and Rituximab



Fig. 12 A coronal non-contrast CT (same patient as in Figs. 10, 11, and 13) shows a large lesion medially extending into the intraconal space, obscuring the extra-ocular muscles and causing superolateral globe displacement. There is some bone breach inferomedially raising the possibility of Granulomatosis with Polyangiitis (GPA) but there were no features of this on biopsy

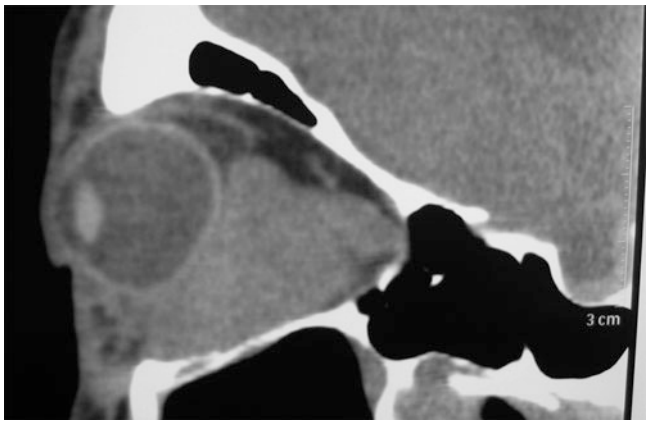


Fig. 13 A sagittal non-contrast CT (same patient as Figs. 10, 11, and 12) shows an extensive extra- and intraconal mass lesion causing globe dystopia and flattening



Fig. 14 Computed tomography scan axial section of a 71-year-old patient who referred with palpable orbital mass in the supero-temporal region. Note homogeneous enlargement of her right lacrimal gland and eyelid tissue. The patient underwent orbital biopsy that was consistent with the diagnosis of idiopathic orbital inflammation (orbital pseudotumor)

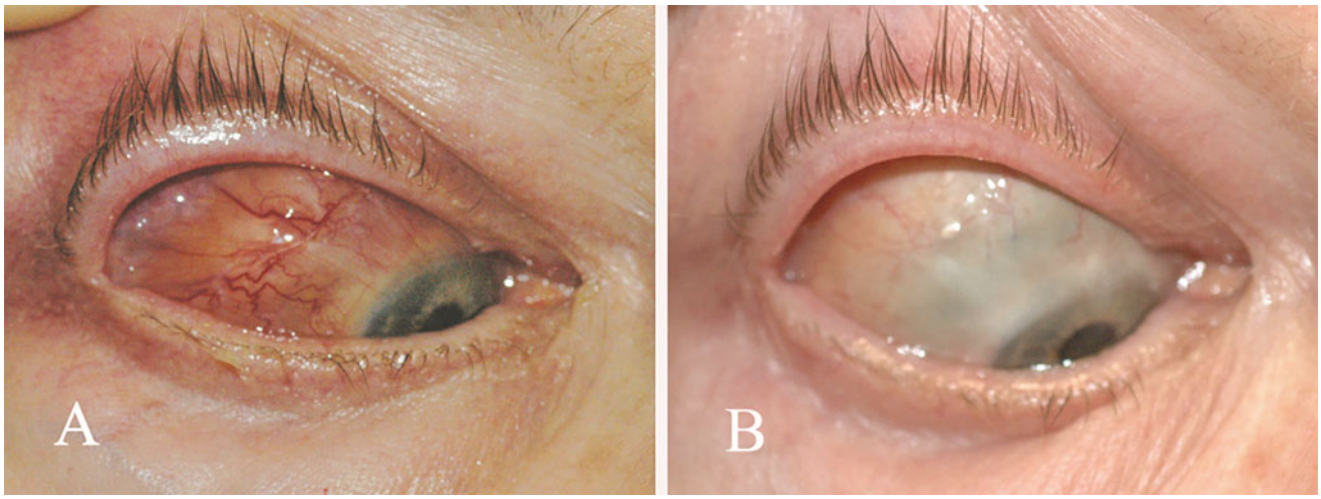


Fig. 15 Clinical image of the same patient as in Fig. 14 before (*A*) and after (*B*) triamcinolone acetonide injection with near complete resolution

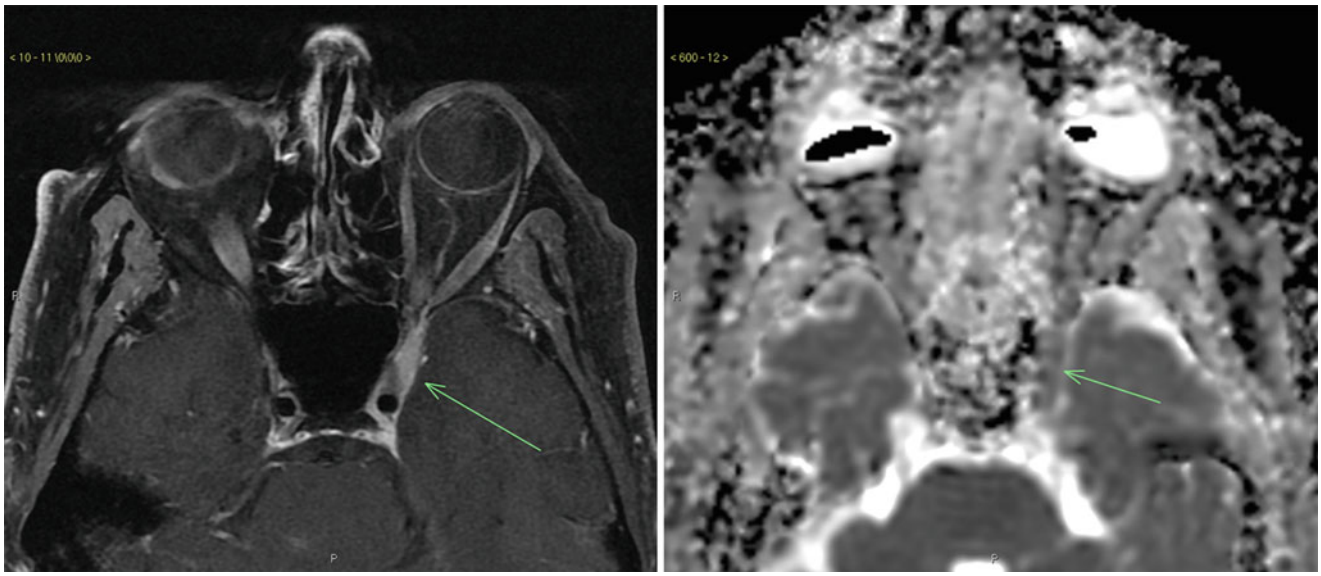


Fig. 16 Axial T1WI fat sat with Gad (*left*) of a different patient, showing left para-cavernous soft tissue-enhancing process abutting the orbital apex (arrow). The ADC map (*right*) showing low signal indicative of restricted diffusion typical of inflammation. The patient was diagnosed with Tolosa-Hunt syndrome

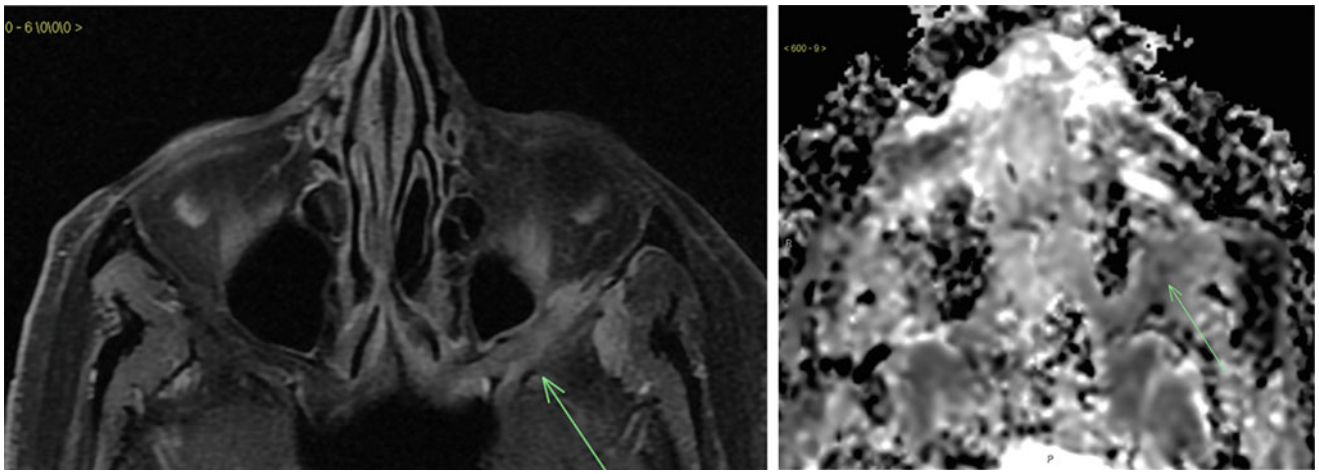


Fig. 17 Axial T1WI fat sat with gad (left) showing inferior orbital fissure-enhancing lesion involving the left temporal fossa and the sphenopalatine foramen medially. The patient was diagnosed with Tolosa Hunt syndrome. The corresponding ADC map (right) depicts restricted diffusion

References

1. Yuen SJ, Rubin PA. Idiopathic orbital inflammation. Distribution, clinical features and treatment outcome. Arch Ophthalmol. 2003;121:491–9.
2. Hsuan JD, Selva D, McNab AA, Sullivan TJ, Saeed P, O'Donnell BA. Idiopathic sclerosing orbital inflammation. Arch Ophthalmol. 2006;124:1244–50.
3. Mombaerts I, Bilyk JR, Rose GE, McNab AA, Fay A, Dolman PJ, Allen RC, Devoto MH, Harris GJ, Expert Panel of the Orbital Society. Consensus on diagnostic criteria of idiopathic orbital inflammation using a modified Delphi approach. JAMA Ophthalmol. 2017;135(7):769–76. https://doi.org/10.1001/jamaophthalmol.2017.1581. PMID: 28570731; PMCID: PMC5710199.
4. Mombaerts I, Rose GE, Garrity JA. Orbital inflammation: biopsy first. Surv Ophthalmol. 2016;61(5):664–9. https://doi.org/10.1016/j.survophthal.2016.03.002. Epub 2016 Mar 17. PMID: 26994870.

Orbital Myositis

72

Alan A. McNab

Contents

1 **Symptoms and Signs** 545
2 **Differential Diagnosis** 545
3 **Diagnosis** 545
4 **Treatment** 546
5 **Figures with Captions** 546
References 550

Abstract

- Orbital myositis occurs in typical acute forms and atypical forms (multiple muscles, bilateral disease, and poor response to corticosteroids) and may be associated with systemic inflammatory and auto-immune diseases.
- Acute single muscle disease presents with painful diplopia in young adult females, and usually responds well to oral steroids.
- Atypical cases should be considered for biopsy.
- Fusiform enlargement of the muscle is typical, with tendon sparing, but tendon involvement may occur. More than one muscle may be affected.
- Contrast enhancement is usually seen.

Keywords

Extraocular muscle · Orbital myositis · Orbit · Inflammation · Systemic inflammatory disorders

1 Symptoms and Signs

Inflammation of extraocular muscle (EOM) is most commonly due to thyroid orbitopathy, but that is excluded from the term orbital myositis (OM). OM occurs in a typical and atypical form [1]. Typically, OM presents with acute onset painful diplopia in young adult females, with usually one (sometimes more than one) swollen EOM with pain on eye movement, partial paresis, or restriction of the muscle, and associated eyelid and conjunctival swelling (worse over the muscle insertion) [2]. It usually responds to a course of oral steroids [3]. Atypical forms are recurrent [4, 5], bilateral, or occurring with specific inflammatory and auto-immune disorders, or in response to some drugs.

2 Differential Diagnosis

Any cause of EOM swelling, including lymphoma, metastasis, and congestion as occurs with carotid-cavernous fistula and orbital apex lesions, but the commonest differential is with thyroid orbitopathy.

3 Diagnosis

In typical cases, the symptoms, signs, and imaging are sufficient to make a diagnosis. In atypical or unresponsive cases, a muscle biopsy may be required to establish a diagnosis and exclude other pathologies [6, 7].

A. A. McNab (✉)
Orbital Plastic and Lacrimal Clinic, Royal Victorian Eye and Ear Hospital, Melbourne, VIC, Australia

© Springer Nature Switzerland AG 2022
G. Ben Simon et al. (eds.), *Atlas of Orbital Imaging*,
https://doi.org/10.1007/978-3-030-62426-2_59

4 Treatment

Treatment is usually with a course of oral steroids. Relapse or atypical cases may require other forms of immunosuppression including biologics, especially when OM occurs in association with other inflammatory or autoimmune conditions.

5 Figures with Captions



Fig. 1 An axial contrast-enhanced CT of a young woman with acute onset orbital myositis of the left medial rectus muscle, with relative sparing of the muscle tendon, which is less common than tendon involvement

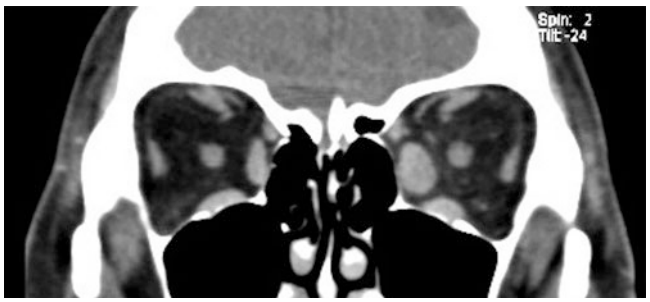


Fig. 2 A coronal contrast-enhanced CT (same patient as Fig. 1) shows smooth enlargement and mild enhancement of the left medial rectus muscle belly. There is mild infiltration of the orbital fat



Fig. 3 An axial contrast-enhanced CT of a different patient with acute orbital myositis affecting the left medial rectus muscle, with involvement of the muscle tendon, unlike the previous case with tendon sparing

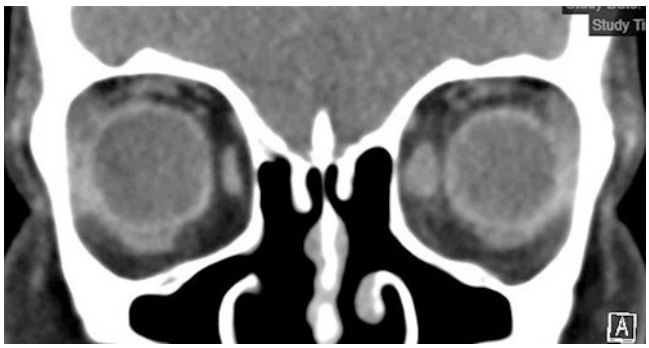


Fig. 4 A coronal CT (same patient as in Figs. 3 and 5) shows swelling of the anterior belly of medial rectus on the left

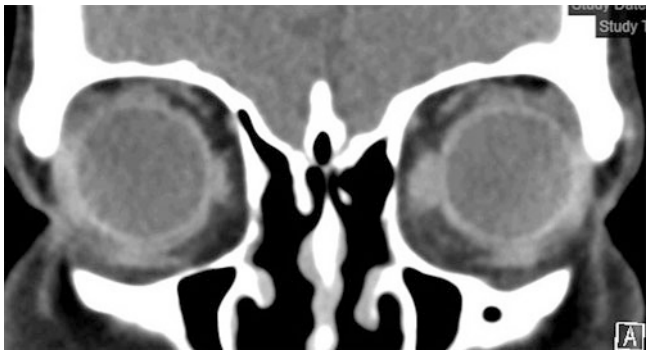


Fig. 5 A coronal CT scan (same patient as Figs. 3 and 4) shows the muscle swelling of the left medial rectus extends anteriorly to involve the muscle belly and tendon junction. Mild anterior orbital fat stranding is also seen



Fig. 6 An axial contrast-enhanced CT of a patient with acute orbital myositis of the right medial rectus muscle, with tendon involvement

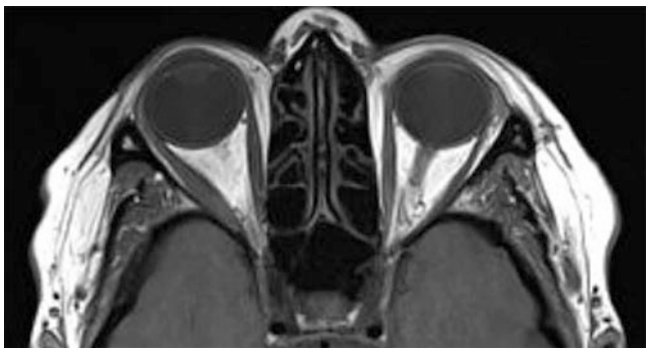


Fig. 7 An axial T1 MRI of the same patient as in Figs. 6, 8, and 9, but 4 years later when she presented with acute orbital myositis of the right lateral rectus on this occasion (recurrent migratory orbital myositis)

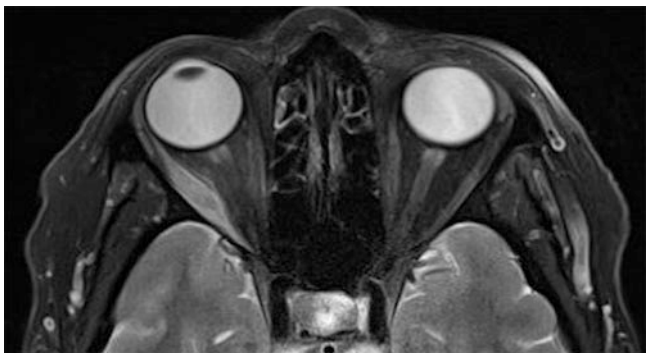


Fig. 8 An axial fat-sat T2 MRI (same patient as in Figs. 6, 7, and 9) shows hyperintense, edematous swelling of the belly of the right lateral rectus muscle

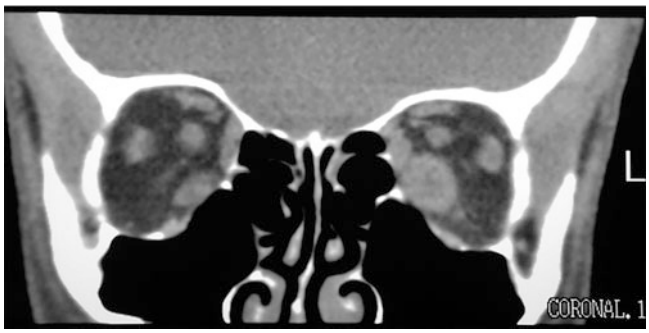


Fig. 9 A coronal CT of a patient with acute orbital myositis affecting the left inferior rectus muscle, with orbital fat stranding

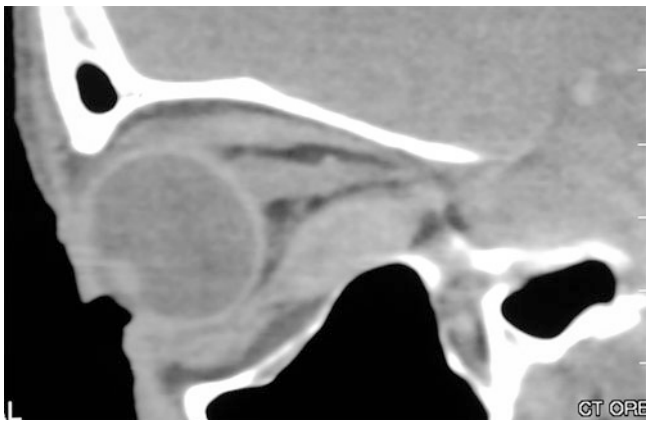


Fig. 10 A sagittal CT scan (same patient as in Fig. 9) shows fusiform swelling of the left inferior rectus muscle belly due to acute orbital myositis

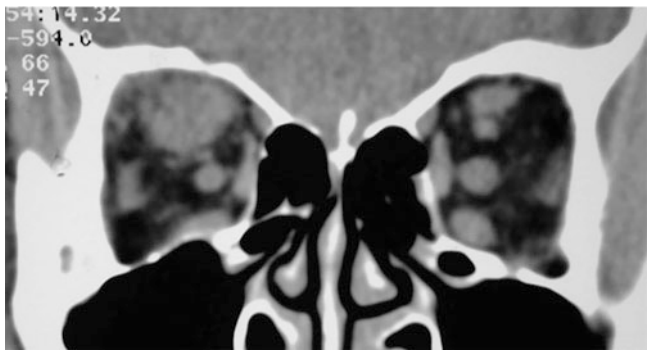


Fig. 11 A coronal CT of a patient with subacute myositis of the right levator and superior rectus muscles (atypical). While thyroid eye disease could present with this appearance, the patient had loss of function of the levator with ptosis rather than lid retraction



Fig. 12 An axial CT (same patient as in Fig. 11) shows swelling of the right superior rectus and levator muscle complex due to subacute orbital myositis

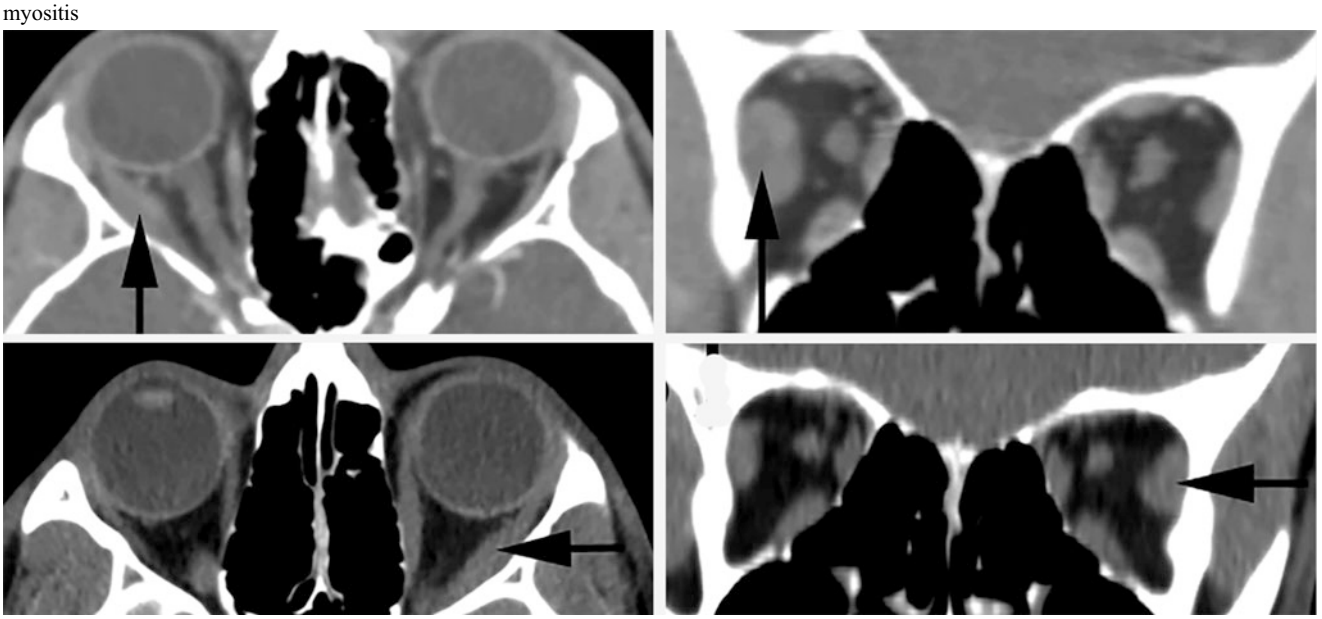


Fig. 13 Axial computed tomography (CT) scans of the orbit during first episode of myositis in an 18-year-old male showing right lateral rectus enlargement (*upper left*) – axial scan, (*upper right*) – coronal scan (vertical black arrows). Lower images showing CT scan of the orbit during second relapse involving the left orbit, (*lower left*) – left lateral rectus enlargement axial scan, (*lower right*) – left lateral rectus enlargement coronal scan (horizontal black arrows). The patient was diagnosed with migratory polymyositis

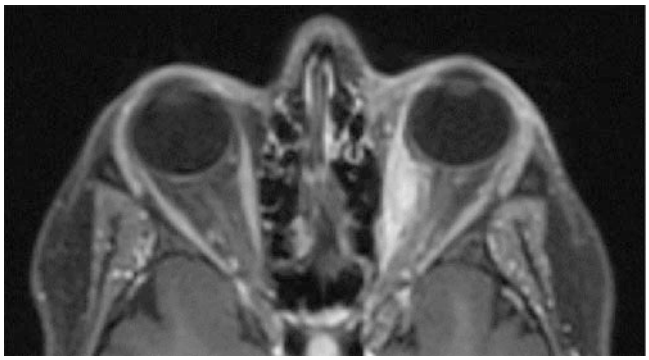


Fig. 14 Axial T1WI contrast-enhanced FS of a different patient with left orbital myositis showing fusiform enlargement and enhancement of the left MR muscle and its vicinity; there is also mild globe proptosis on the same side

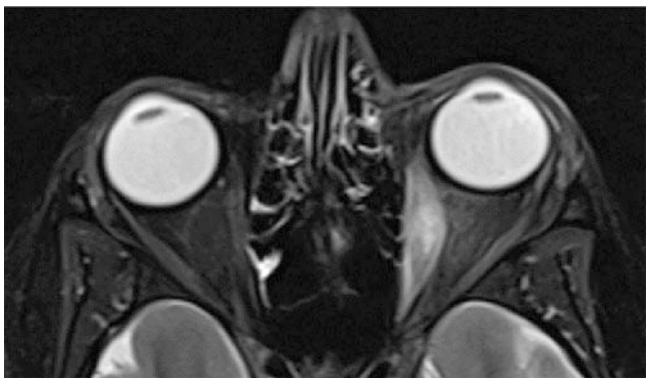


Fig. 15 Axial T2WI FS of the same patient as in Figs. 13, 15, and 16 depicts heterogenous but mostly hyperintense signals within the muscle and its sheath

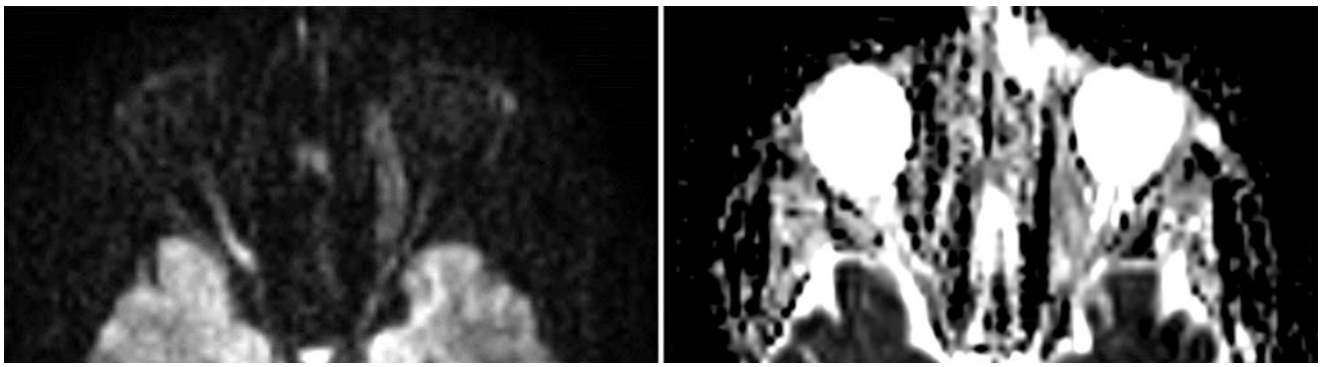


Fig. 16 On DWI the inflamed MR muscle shows mixed signals (*left*) with corresponding partially restrictive (dark) area on the ADC map (*right*), consistent with an inflammatory process

References

1. McNab AA. Orbital myositis: a comprehensive review and reclassification. Ophthalmic Plast Reconstr Surg. 2020;36:109–17.
2. Scott IU, Siatkowski RM. Idiopathic orbital myositis. Curr Opin Rheumatol. 1997;9:504–12.
3. Mombaerts I, Koornneef L. Current status in the treatment of orbital myositis. Ophthalmology. 1997;104:402–8.
4. Mannor GE, Rose GE, Moseley IF, et al. Outcome of orbital myositis. Clinical features associated with recurrence. Ophthalmology. 1997;104:409–13.
5. Avni-Zauberman N, Tripathy D, Rosen N, Ben Simon GJ. Relapsing migratory idiopathic orbital inflammation: six new cases and review of the literature. Br J Ophthalmol. 2012;96(2):276–80. https://doi.org/10.1136/bjo.2010.191866. Epub 2011 Apr 27. PMID: 21527417.
6. Mombaerts I, Rose GE, Garrity JA. Orbital inflammation: biopsy first. Surv Ophthalmol. 2016;61(5):664–9. https://doi.org/10.1016/j.survophthal.2016.03.002. Epub 2016 Mar 17. PMID: 26994870.
7. Mombaerts I, Bilyk JR, Rose GE, McNab AA, Fay A, Dolman PJ, Allen RC, Devoto MH, Harris GJ, Expert Panel of the Orbital Society. Consensus on diagnostic criteria of idiopathic orbital inflammation using a modified Delphi approach. JAMA Ophthalmol. 2017;135(7):769–76. https://doi.org/10.1001/jamaophthalmol.2017.1581. PMID: 28570731; PMCID: PMC5710199.

Dacryoadenitis

73

Alan A. McNab

Contents

1 **Signs and Symptoms** 551
2 **Differential Diagnosis** 552
3 **Diagnosis** 552
4 **Treatment** 552
5 **Figures with Captions** 552
References 555

Abstract

- Inflammation of the lacrimal gland may be infective (bacterial or viral), due to specific forms of inflammation, or idiopathic, and unilateral or bilateral.
- Imaging (CT or MRI) will show diffuse homogeneous enlargement of the lacrimal gland, with contrast enhancement; fat stranding can be seen.
- DWI may show restriction due to the inflammatory nature of the disease, which may mimic a lymphoproliferative process.
- In cases of bacterial dacryoadenitis, an abscess may form with a central cystic component (hypointense on T1, hyperintense on T2, and low density on CT) and ring enhancement [1].
- With specific forms of inflammation such as IgG4-related disease and sarcoidosis, there may be associated radiological signs such as enlargement of the infraorbital nerve (IgG4-RD) or rhino-sinusitis (IgG4-RD, GPA, or sarcoidosis) [3, 4].

Keywords

Dacryoadenitis · IgG4-related disease · Sarcoidosis · Sjögren's syndrome · Idiopathic orbital inflammation · Lacrimal gland inflammation

1 Signs and Symptoms

Dacryoadenitis produces signs of inflammation in the region of the lacrimal gland – swelling, redness, ptosis of the lateral upper eyelid (S-shaped lid), and in some cases pain. The clinical presentation will depend on the etiology. Bacterial dacryoadenitis may be associated with purulent discharge, and an abscess may develop within the gland [1]. Many forms of dacryoadenitis such as sarcoidosis and IgG4-related disease will not typically present with significant oedema, redness, or pain. The lacrimal gland can be palpated in the superior sulcus and can sometimes be visualized on eyelid eversion. Conjunctival injection is common. Mass effect from the enlarged gland can cause inferonasal displacement of the globe. Inflammation may involve other orbital structures and therefore cause proptosis, limitation and pain with eye movement, and double vision. Various etiologies can typically present unilaterally or bilaterally.

A. A. McNab (✉)
Orbital Plastic and Lacrimal Clinic, Royal Victorian Eye and Ear Hospital, Melbourne, VIC, Australia

© Springer Nature Switzerland AG 2022
G. Ben Simon et al. (eds.), *Atlas of Orbital Imaging*,
https://doi.org/10.1007/978-3-030-62426-2_60

2 Differential Diagnosis

For unilateral lacrimal gland swelling, the differential may include lymphoma or epithelial tumors, or specific forms of inflammation such as sarcoidosis, IgG4-RD, Sjögren's syndrome, or granulomatosis with polyangiitis. For bilateral lacrimal gland swelling, all of the above may be responsible, except for epithelial tumors, which are unilateral. Thyroid eye disease may sometimes be associated with lacrimal gland enlargement and inflammation.

3 Diagnosis

A careful history and thorough examination looking for clues to the cause of the lacrimal gland swelling is essential. For acute bilateral dacryoadenitis, viral serology (EBV, mumps) is helpful. Blood tests for specific forms of inflammation may help make a diagnosis. For cases other than bacterial or viral infection, a biopsy of the gland is essential to establish whether there is a specific form of inflammation, idiopathic dacryoadenitis [2], or lymphoma [5].

4 Treatment

Treatment will depend on the specific diagnosis, and varies from supportive care for viral infection, anti-infective agents for bacterial and fungal etiology, and anti-inflammatory drugs for noninfectious etiologies.

5 Figures with Captions



Fig. 1 Clinical photo of a 69-year-old woman who presented with acute right painful periorbital swelling and erythema, together with marked chemosis

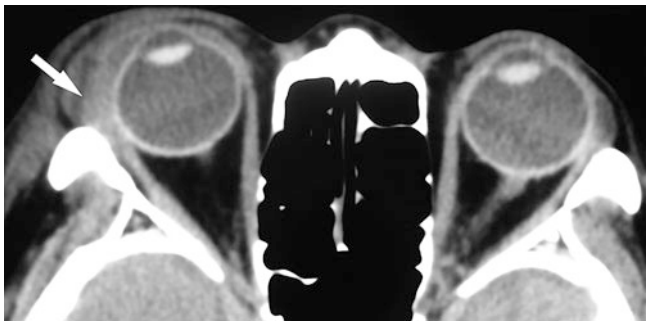


Fig. 2 Axial CT of the same patient shows diffuse enlargement of the right lacrimal gland (arrow), with associated soft tissue swelling and mild proptosis, suggestive of dacryoadenitis



Fig. 3 Clinical photo of the patient after intravenous antibiotic treatment and oral steroids with marked improvement



Fig. 4 Clinical photo of a different patient, with left upper eyelid ptosis, tender swelling, and erythema

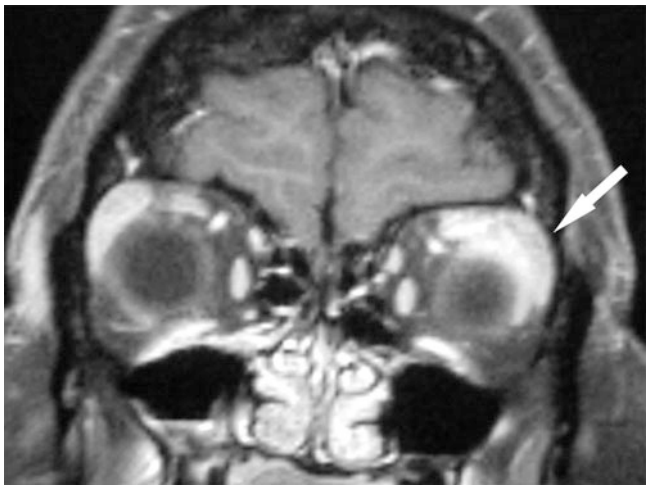


Fig. 5 Coronal T1 post-contrast fat-saturated image of the patient in Fig. 4, showing diffuse homogenous enlargement and enhancement of the left lacrimal gland (arrow) compared to the normal appearing lacrimal gland on the right (Figs. 1, 2, 3, 4, and 5 *courtesy of the editors*)

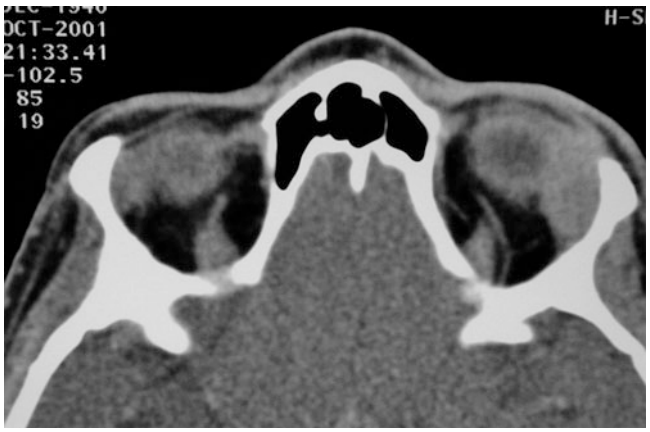


Fig. 6 Axial contrast CT in a different patient with subacute left lacrimal gland inflammation shows enlargement of the orbital portion of the gland. A biopsy showed nonspecific inflammation

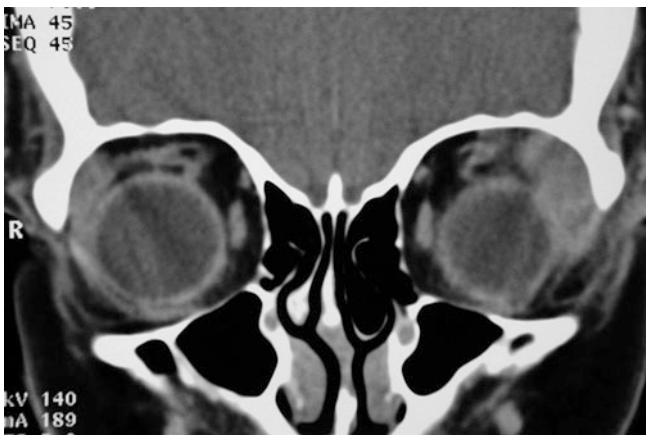


Fig. 7 A coronal noncontrast CT in a patient with subacute left dacryoadenitis shows diffuse enlargement of the gland with globe dystopia



Fig. 8 An axial noncontrast CT in a patient with symptomatically unilateral left-sided lacrimal gland swelling shows probable bilateral lacrimal gland enlargement with slightly indistinct edges, indicating spillover of the pathological process into the adjacent orbital fat. A biopsy showed features of nonspecific dacryoadenitis

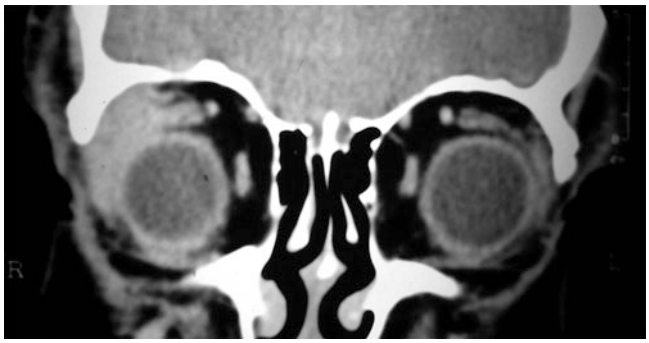


Fig. 9 A coronal contrast-enhanced CT of a patient with right dacryoadenitis shows an enlarged gland with mild enhancement abutting the levator-superior rectus complex. There is mild globe dystopia

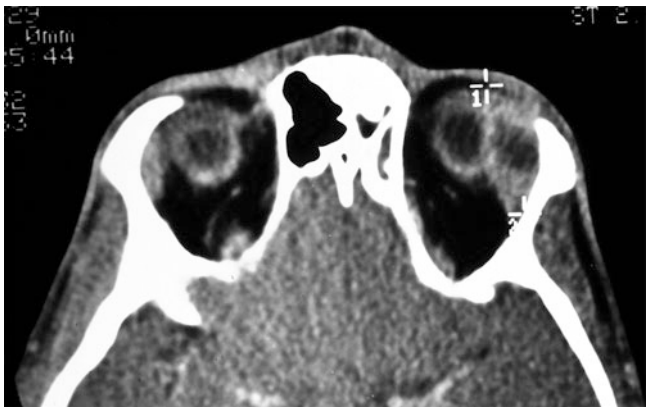


Fig. 10 An axial contrast-enhanced CT in a patient who had developed bacterial dacryoadenitis after conjunctivitis, treated with antibiotics. The swelling failed to resolve, and the scan showed an enlarged left gland with a central low density and peripheral enhancement of the adjacent gland. An abscess was drained

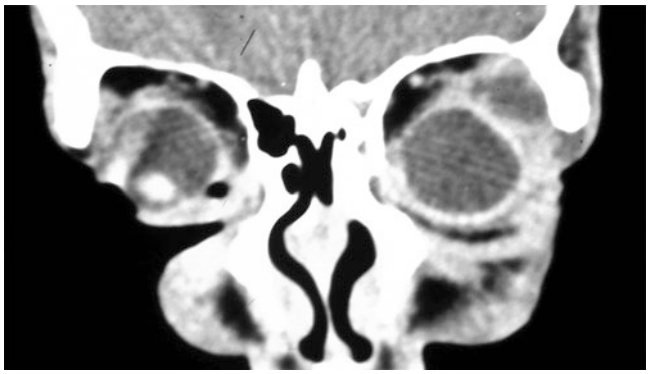


Fig. 11 A coronal contrast-enhanced CT of the same patient in Fig. 5 shows the gland with abscess displacing and flattening the globe



Fig. 12 Pre- (left) and post-contrast (*right*) T1 axial MRIs in a young patient with severe bacterial left dacryoadenitis shows marked enlargement of the gland with soft tissue swelling extending over the upper lid and anterior temple. There is marked globe dystopia and compression There is a lower intensity area centrally suggesting an abscess cavity. The right figure shows marked contrast enhancement of the inflamed tissues which surround a bilocular abscess



Fig. 13 A coronal noncontrast CT in a patient with chronic bilateral lacrimal gland swelling. A biopsy showed features of IgG4-related disease. There is possible enlargement of the left infra-orbital nerve, as well as patchy paranasal sinus disease



Fig. 14 A coronal T1-weighted contrast-enhanced MRI of a patient with bilateral lacrimal gland enlargement from biopsy-proven IgG4-related disease who also demonstrated marked enlargement of the left infra-orbital nerve (arrow)

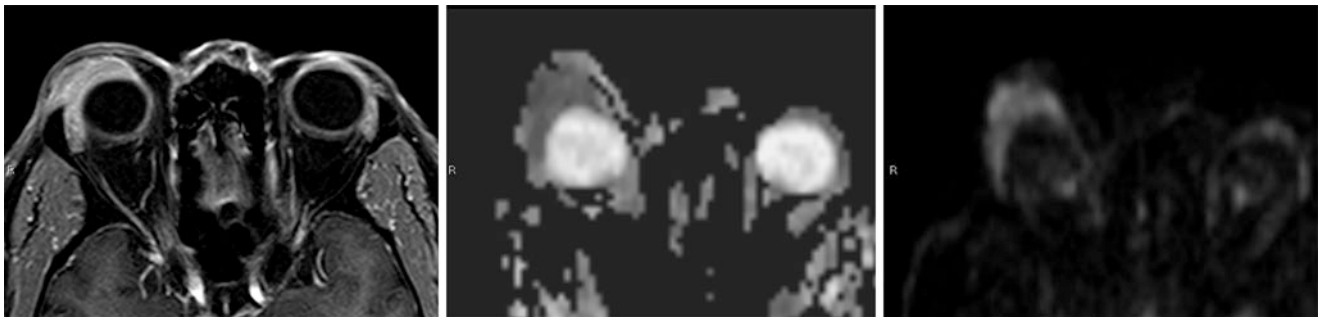


Fig. 15 T1 FS CE MR (*left*) of a young male with right orbit dacryoadenitis. ADC (*middle*) and DWI (*right*) maps demonstrate restricted diffusion, typical of the inflammatory process

References

1. Goold LA, Madge SN, Au A, Leibovitch I, McNab A, Tumuluri K, Selva D. Acute suppurative bacterial dacryoadenitis: a case series. Br J Ophthalmol. 2013;97:735–8.
2. Andrew NH, Kearney D, Sladden N, McKelvie P, Wu A, Sun MT, McNab A, Selva D. Idiopathic dacryoadenitis: clinical features, histopathology, and treatment outcomes. Am J Ophthalmol. 2016;163:148–53.
3. McNab AA, McKelvie P. IgG4-related ophthalmic disease. Part II: clinical aspects. Ophthalmic Plast Reconstr Surg. 2015;31:167–78.
4. McNab AA, McKelvie P. IgG4-related ophthalmic disease. Part I: background and pathology. Ophthalmic Plast Reconstr Surg. 2015;31:83–8.
5. Luemsamran P, et al. The role of biopsy in lacrimal gland inflammation: a clinicopathologic study. Orbit. 2017;36(6):411–8.

Scleritis

74

Alan A. McNab

Contents

1 **Signs and Symptoms** 557
2 **Differential Diagnosis** 558
3 **Diagnosis** 558
4 **Treatment** 558
5 **Figures with Captions** 558
References 560

Abstract

- Scleritis is a generalized term to describe inflammation of the sclera from any etiology.
- Scleral inflammation anterior to the ora serrata is categorized as anterior while inflammation posterior to it defines posterior scleritis.
- Anterior scleritis may be divided according to the clinical presentation as diffuse or nodular, sclerosing, necrotizing without inflammation (scleromalacia perforans), or necrotizing with inflammation.
- A relatively rare condition, typically affects women more than men, and older individuals (fifth or sixth decades of life). It is commonly associated (one-third to one-half of patients) with systemic autoimmune or vasculitic disease while infectious causes are relatively rare (less than 10%).
- Typically painful.
- B-mode ultrasound may show scleral thickening, sometimes with fluid suprachoroidal effusions giving rise to the typical T sign.
- CT and MRI typically show scleral thickening with feathery soft tissue change in the adjacent orbital tissues.
- Chronic cases may show marked nodular thickening of the sclera.
- High-dose steroids or immunosuppression may be required.

Keywords

Scleritis · Vasculitis · Autoimmune disease · Pain · Orbit

1 Signs and Symptoms

Scleritis is inflammation of the sclera of the eye (anterior, posterior, diffuse or nodular, sclerosing, or ulcerative), and about half of cases are associated with a systemic disease (vasculitic diseases, auto-immune processes). Some are infective (less than 10%) [1–3]. Patients present usually acutely with redness, pain, often severe, and reduced vision. Anterior scleritis can involve the cornea (sclera-keratitis). Posterior scleritis is relatively common among all other subtypes of scleritis in children [8].

A. A. McNab (✉)
Orbital Plastic and Lacrimal Clinic, Royal Victorian Eye and Ear Hospital, Melbourne, VIC, Australia

© Springer Nature Switzerland AG 2022
G. Ben Simon et al. (eds.), *Atlas of Orbital Imaging*,
https://doi.org/10.1007/978-3-030-62426-2_61

2 Differential Diagnosis

The main differential is episcleritis, inflammation of the layer of tissue lying against the sclera, which is a much more benign disease.

3 Diagnosis

The diagnosis is usually made on the basis of the clinical features with supportive evidence from imaging. Since in one-third to one-half of patients it may be associated with systemic disease, in patients who present with a new diagnosis of scleritis performing a thorough diagnostic workup is of utmost importance [1]. Tissue diagnosis is rarely required.

4 Treatment

Treatment is directed at the cause and, in noninfectious cases, usually involves nonsteroidal anti-inflammatory drugs (NSAIDs), corticosteroids, immunomodulatory therapy (IMT), or biologic agents depending on the etiology and severity of the disease [4–7]. If left untreated, it can lead to devastating ocular complications such as globe perforation, endophthalmitis, or even loss of the eye. Infectious causes require topical and often systemic antibiotics.

5 Figures with Captions

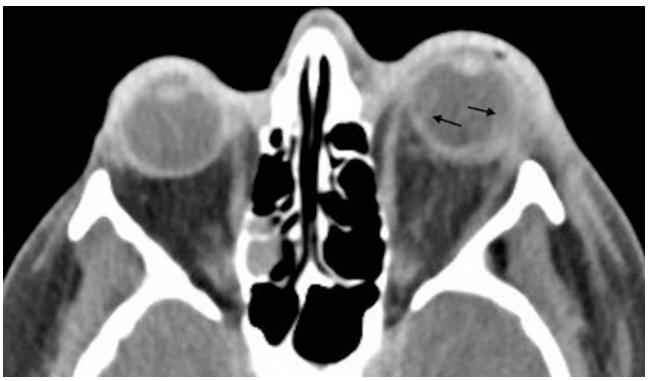


Fig. 1 An axial noncontrast CT scan of a patient with acute left posterior scleritis. There is asymmetric thickening of the sclera with indistinct edges, worse temporally. Within the eye, faint shadows showing choroidal effusions can just be seen (arrows). There is preseptal involvement as well as intraconal fat stranding and secondary proptosis

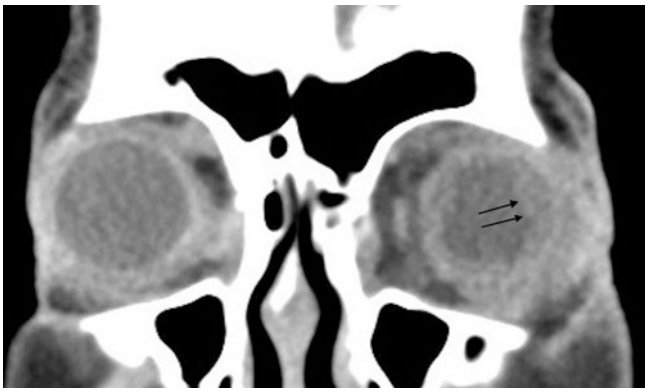


Fig. 2 A coronal noncontrast CT of the same patient as in Fig. 1, with diffuse left scleritis. There is soft tissue change laterally, and thickening of the sclera with elevation of the retina and choroid within the eye (arrows)

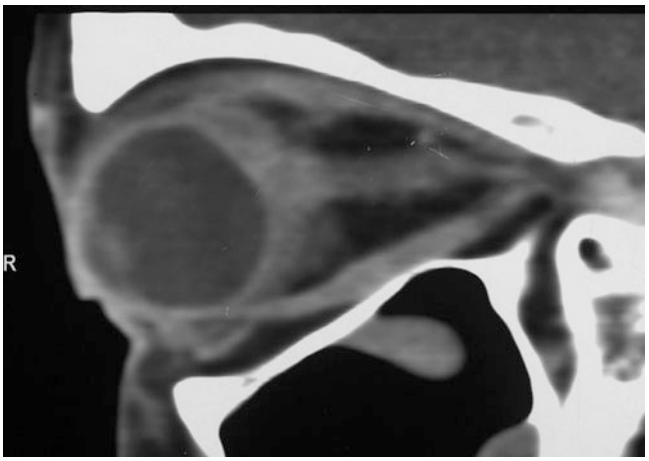


Fig. 3 A sagittal noncontrast CT scan of a patient with posterior scleritis. There is thickening of the sclera and indistinct soft tissue changes adjacent to the sclera with some flattening of the globe superiorly. The inflammatory process is also involving the retrobulbar orbital fat

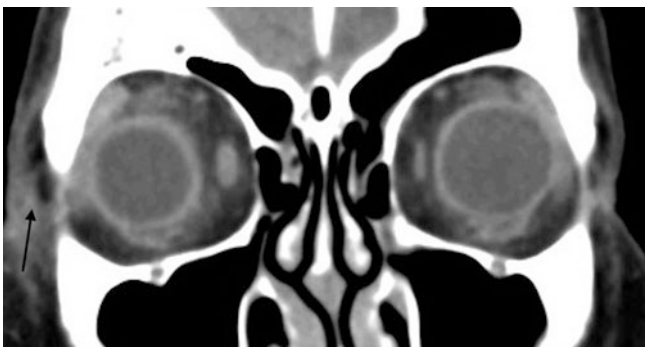


Fig. 4 A coronal noncontrast CT scan of a patient with diffuse right scleritis shows thickening of the sclera and some infiltration of the adjacent orbital fat. There is mild right eye proptosis with hypoglobus, and inflammation in the right temple region (arrow)



Fig. 5 An axial contrast-enhanced CT of a patient with diffuse right scleritis. There is thickening of the sclera with mild enhancement, as well as some soft tissue changes in the eyelids. In addition, there is mild proptosis with very mild fat stranding. The patient had infective scleritis due to pseudomonas infection of a necrotic anterior scleral ulcer

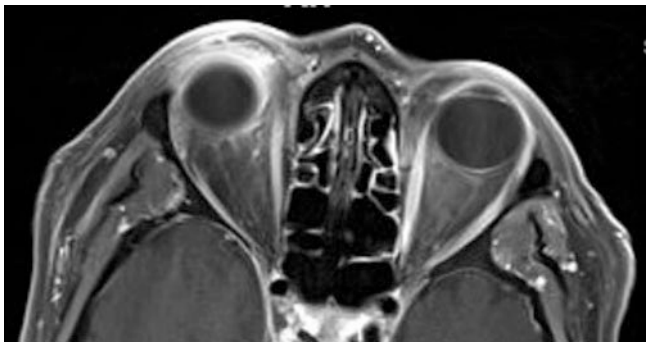


Fig. 6 An axial T1-weighted fat-suppressed MRI with contrast (same patient as in Fig. 5) shows marked enhancement of thickened sclera and eyelid soft tissues. The hyperintense signal of the left nasal intraconal fat is probably related to dental artifact

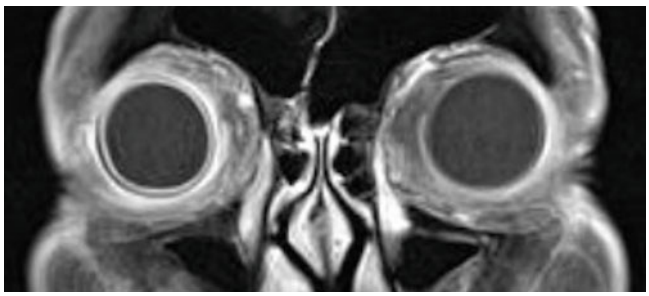


Fig. 7 A coronal T1-weighted fat-suppressed contrast-enhanced MRI (same patient as in Figs. 5 and 6) shows thickening and enhancement of the sclera and adjacent soft tissues

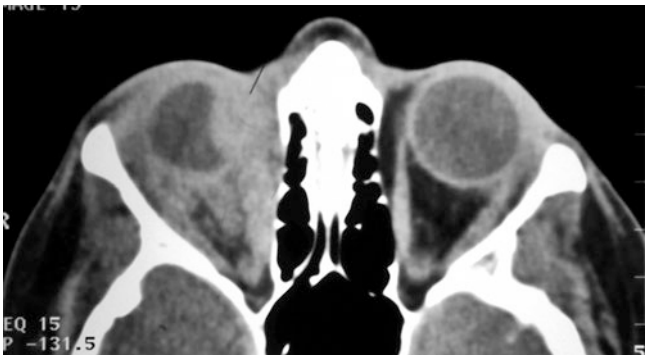


Fig. 8 An axial noncontrast CT of a patient with granulomatosis and polyangiitis (GPA). In addition to patchy inflammatory changes within the right orbit, involving the medial rectus and adjacent tissues mainly, there is marked thickening of the medial sclera

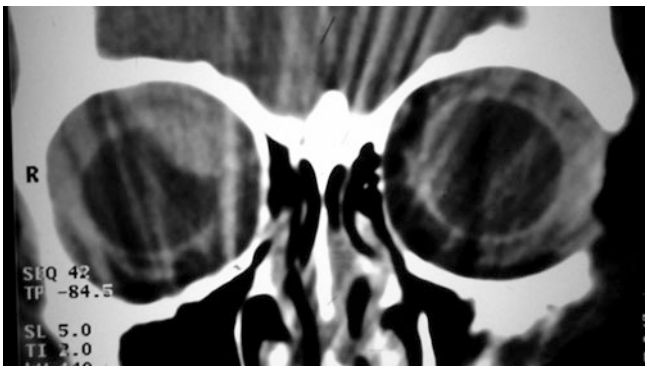


Fig. 9 A direct coronal CT with streaking secondary to dental artifacts (same patient as in Fig. 8) shows an area of marked thickening in the right superonasal sclera in this patient with GPA



Fig. 10 T1 WI postcontrast of a 58 YOM with posterior scleritis on the left side; note contrast-enhancing ring surrounding the posterior globe, nasal more than temporal, representing subtenon effusion (arrow)



Fig. 11 T2 WI fat sat of the same patient as in Fig. 10; note the subtenon effusion (arrow)

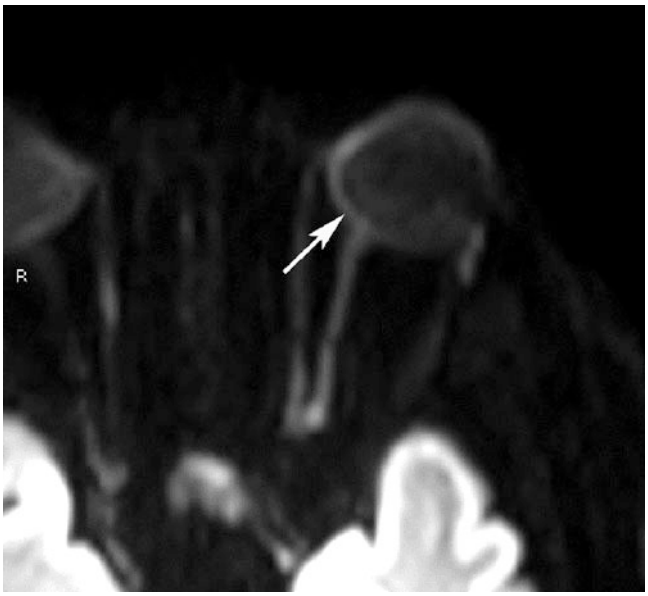


Fig. 12 DWI of the same patient as in Figs. 10 and 11 showing restricted diffusion evidence of the inflammatory process (arrow)

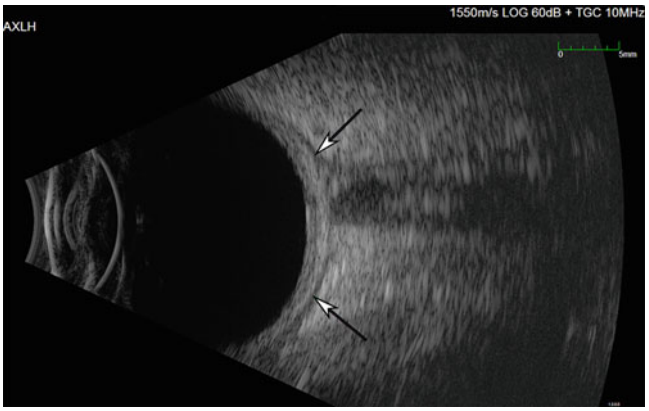


Fig. 13 Ultrasound of the right globe of a 14-YOM with recurrent episodes of both sides posterior scleritis; note the thickening of the choroid-sclera complex with subtenon effusion (arrows) and typical T sign. (Courtesy of Iris Moroz, MD)

References

1. Okhravi N, Odufuwa B, McCluskey P, Lightman S. Scleritis. Surv Ophthalmol. 2005;50:351–63.
2. Daniel Diaz J, Sobol EK, Gritz DC. Treatment and management of scleral disorders. Surv Ophthalmol. 2016;61(6):702–17.
3. Sen HN, Sangave AA, Goldstein DA, Suhler EB, Cunningham D, Vitale S, Nussenblatt RB. A standardized grading system for scleritis. Ophthalmology. 2011;118(4):768–71. https://doi.org/10.1016/j.ophtha.2010.08.027. Epub 2010 Nov 20. PMID: 21093921; PMCID: PMC3070789.
4. Stem MS, Todorich B, Faia LJ. Ocular pharmacology for scleritis: review of treatment and a practical perspective. J Ocul Pharmacol Ther. 2017;33(4):240–6. https://doi.org/10.1089/jop.2016.0127. Epub 2017 Mar 29. PMID: 28355124.
5. Ingaralingam S, Rauz S, Murray PI, Barry RJ. Effectiveness of pharmacological agents for the treatment of non-infectious scleritis: a systematic review protocol. Syst Rev. 2020;9(1):54. https://doi.org/10.1186/s13643-020-01314-9. PMID: 32164765; PMCID: PMC7068966.
6. McCluskey P, Wakefield D. Prediction of response to treatment in patients with scleritis using a standardised scoring system. Aust N Z J Ophthalmol. 1991;19(3):211–5. https://doi.org/10.1111/j.1442-9071.1991.tb00663.x. PMID: 1958366.
7. Hankins M, Margo CE. Histopathological evaluation of scleritis. J Clin Pathol. 2019;72(5):386–90. https://doi.org/10.1136/jclinpath-2018-205360. Epub 2019 Feb 5. PMID: 30723093.
8. Majumder PD, Ali S, George A, Ganesh S, Biswas J. Clinical profile of scleritis in children. Ocul Immunol Inflamm. 2019;27(4):535–9. https://doi.org/10.1080/09273948.2017.1423333. Epub 2018 Jan 25. PMID: 29370565.

Orbital Manifestations of Granulomatosis with Polyangiitis

75

Alan A. McNab

Contents

1 **Symptoms and Signs** 561
2 **Differential Diagnosis** 561
3 **Diagnosis** 561
4 **Treatment** 562
5 **Figures with Captions** 562
References 565

Abstract

- Granulomatosis with polyangiitis frequently involves the eye and orbit.
- ANCA is often negative in the "limited" form of GPA affecting sinuses and the orbit.
- Inflammatory masses may occur adjacent to affected paranasal sinuses.
- CT can demonstrate an iso-/hyperdense mass with indistinct margins.
- Loss of bone is characteristic [1], including in some cases the nasal septum which can lead to a "saddle-nose" deformity. Bone loss is best seen on bone-window CT.
- MRI shows usually isointense lesions with some contrast enhancement; it is frequently hypointense on T2.
- Treatment is with immunosuppression.

Keywords

Granulomatosis with polyangiitis · GPA · Vasculitis · Orbit

A. A. McNab (✉)
Orbital Plastic and Lacrimal Clinic, Royal Victorian Eye and Ear Hospital, Melbourne, VIC, Australia

1 Symptoms and Signs

GPA can present with a "limited" form of disease affecting largely the upper airways, often with orbital involvement, or more widespread disease affecting the lower airways and kidneys. Sclerokeratitis and uveitis may also occur. Chronic nasal and sinus inflammation with tissue loss and middle ear disease are common presentations. Orbital disease often occurs adjacent to involved sinuses, although dacryoadenitis may also occur [2]. Orbital inflammation is often sclerosing. Involvement of the lacrimal drainage apparatus is common [3].

2 Differential Diagnosis

Infiltrative orbital lesions such as idiopathic and specific inflammatory processes, as well as sclerosing orbital inflammation and dacryoadenitis.

3 Diagnosis

ANCA is often negative with orbital disease and "limited" disease, but a positive ANCA is very helpful. Biopsy is essential but the full-blown features of the disease with vasculitis (usually medium and small vessel arteritis) and

© Springer Nature Switzerland AG 2022
G. Ben Simon et al. (eds.), *Atlas of Orbital Imaging*,
https://doi.org/10.1007/978-3-030-62426-2_62

necrotizing granulomatous inflammation are not always seen. On imaging, infiltrative lesions, especially medially, are often seen, and bone loss is characteristic.

4 Treatment

Treatment is with a combination of corticosteroid and immunosuppressants such as cyclophosphamide. Resistant cases often respond well to Rituximab.

5 Figures with Captions

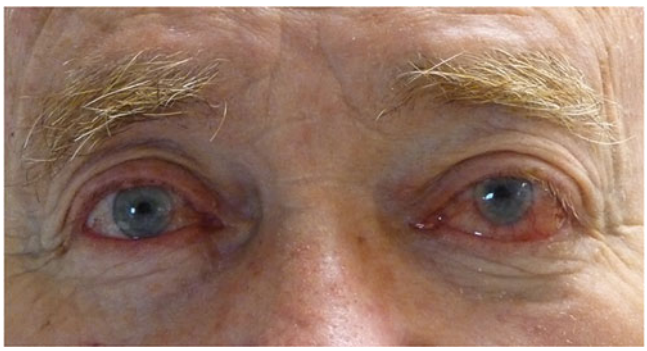


Fig. 1 An elderly man with many months of left epiphora, swelling and redness of the left eye, had complete lacrimal obstruction, restricted left eye movements, a firm mass inferomedially in the orbit, left scleral-keratitis, and left globe dystopia. Biopsies confirmed GPA (same patient as in Figs. 2 and 3)

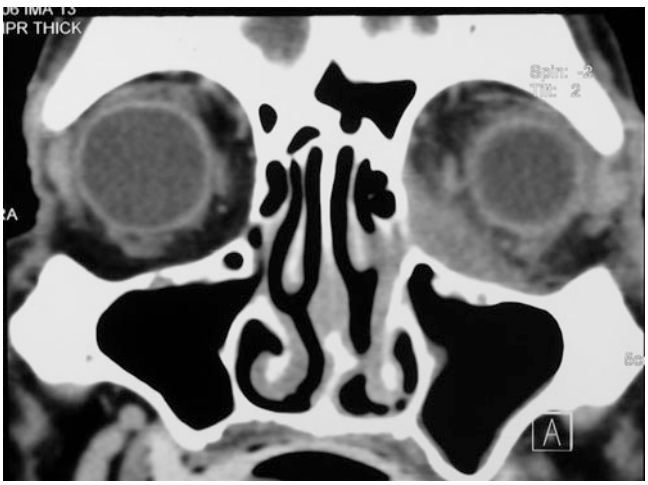


Fig. 2 A coronal noncontrast CT shows an infiltrative infero-medial hyperdense orbital mass lesion on the left with indistinct margins. The surrounding supero-medial and infero-temporal orbital fat is infiltrated

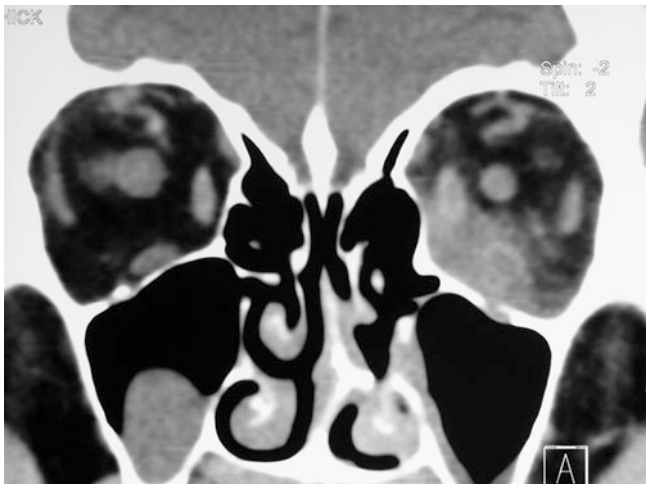


Fig. 3 A coronal noncontrast CT shows an infiltrative lesion in the infero-medial orbit surrounding the inferior and medial recti muscles. There is no apparent bone erosion or loss of intranasal structures (same patients as in Figs. 1 and 2). Biopsy was consistent with GPA, but ANCA was negative

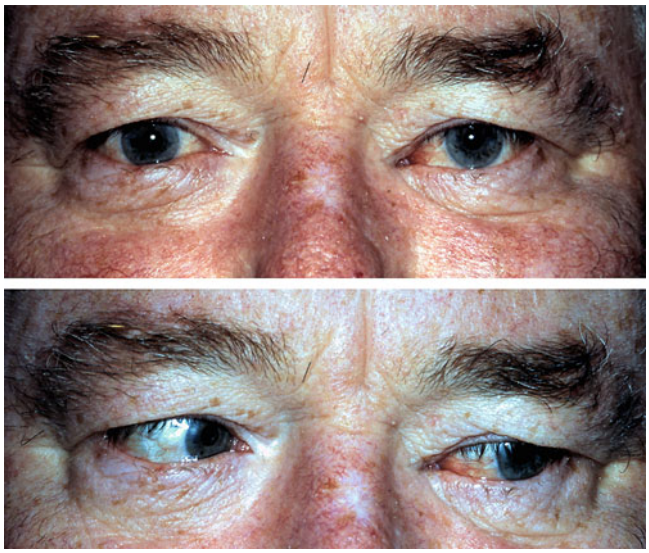


Fig. 4 A 60-year-old man with chronic left epiphora had previously undergone a DCR and placement of a Lester Jones tube. He then developed increasing diplopia on left gaze and had a palpable hard mass inferomedially in the left orbit. A biopsy was consistent with GPA, in its "limited" form. Same patient as in Figs. 5, 6, 7, 8, and 9

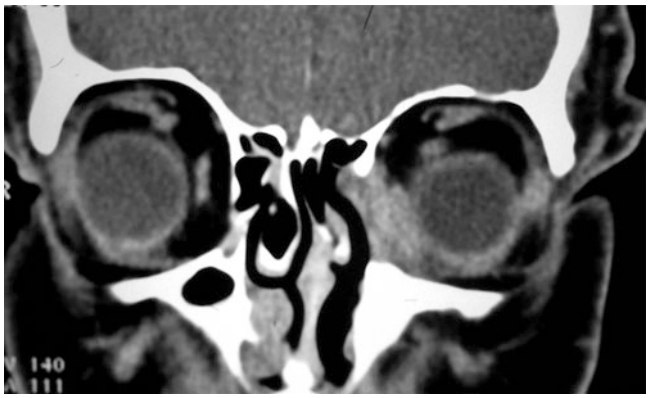


Fig. 5 A direct coronal noncontrast CT shows an infero-medial infiltrating mass lesion with loss of adjacent medial orbital wall and inferior turbinate due to destructive inflammation with vasculitis. There was restrictive strabismus



Fig. 6 A coronal noncontrast CT (same patient as in Figs. 4, 5, 6, 7, 8, and 9) further posteriorly shows more extensive loss of normal sinus and nasal tissues adjacent to the infiltrative orbital lesion. Only part of the bone and tissue loss is postsurgical, with most of it due to the disease process



Fig. 7 An axial postcontrast CT (same patient as in Figs. 4, 5, 6, 7, 8, and 9) shows a medial orbital infiltrative lesion with loss of adjacent bone

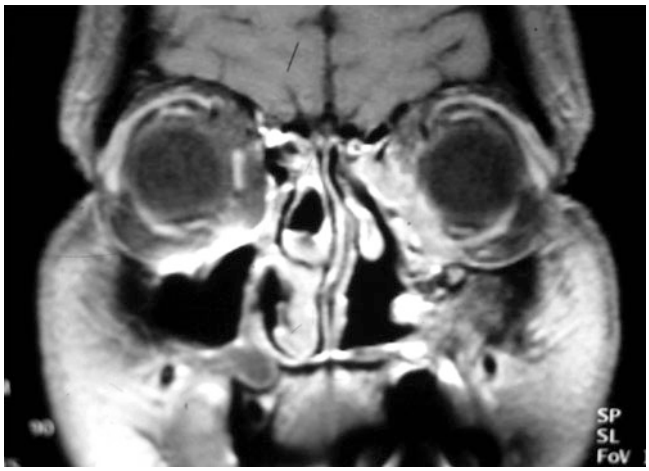


Fig. 8 A coronal T1 weighted contrast-enhanced scan (same patient as Figs. 4, 5, 6, 7, 8, and 9) shows an enhancing infero-medial orbital mass with loss of left sided intranasal structures. Note that the fat suppression is partial due to dental artifacts

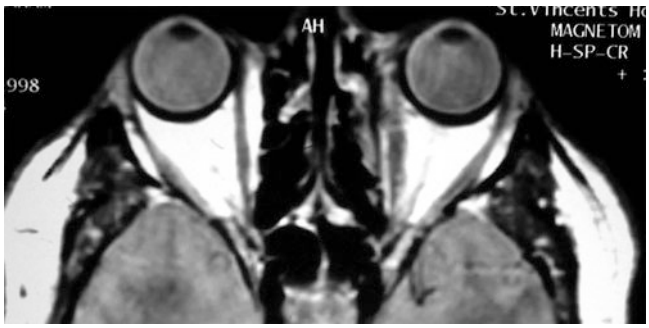


Fig. 9 An axial noncontrast T1 MRI (same patient as Figs. 4, 5, 6, 7, 8, and 9) shows an iso-intense anterior medial orbital infiltrate involving the medial rectus



Fig. 10 An axial noncontrast CT, soft tissue window, in a patient with long-standing treated GPA shows a large infiltrative mass involving the extra- and intraconal space with obliteration of the normal medial anatomy. The mass is obliterating the optic nerve sheath and causes right eye proptosis. She had a right optic neuropathy with poor vision



Fig. 11 An axial noncontrast bone window CT in a man with right-sided long-standing treated GPA shows soft tissue loss as well as a medial infiltrative and sclerosing mass with loss of adjacent bone and ethmoid sinuses. There was tethering of the globe with restrictive strabismus. There is a risk of sino-orbital fistula developing

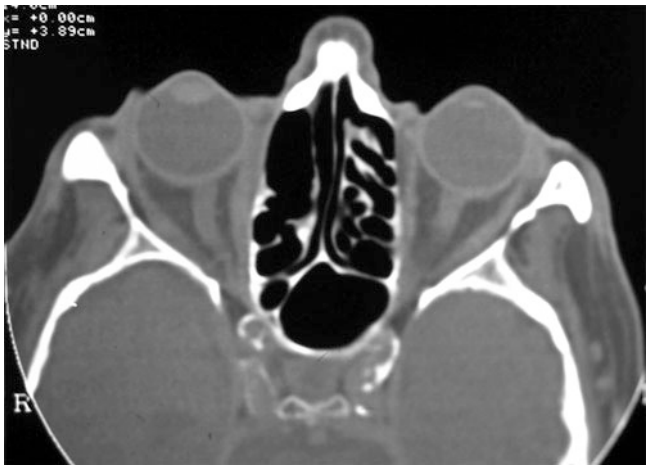


Fig. 12 An axial noncontrast bone window CT (same patient as in Fig. 11) shows some infiltrative soft tissue in the medial orbit adjacent to some bone loss and loss of normal ethmoid air cells

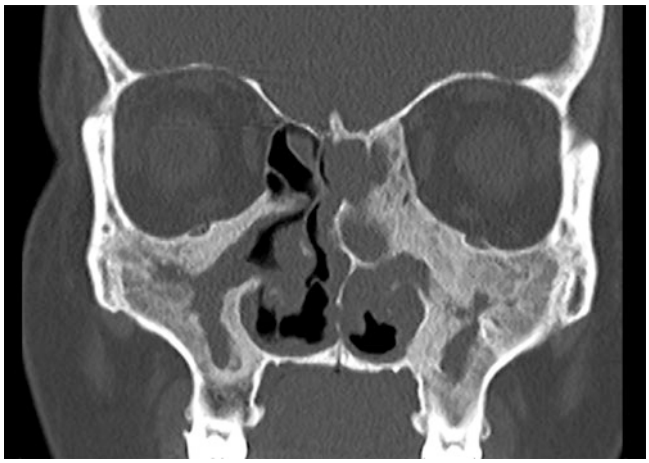


Fig. 13 A coronal bone window CT of a patient with long-standing treated "limited" GPA shows extensive sinus disease with secondary hyperostosis of the sinus walls representing extensive muco-periosteal reaction, causing gross distortion of the intranasal anatomy

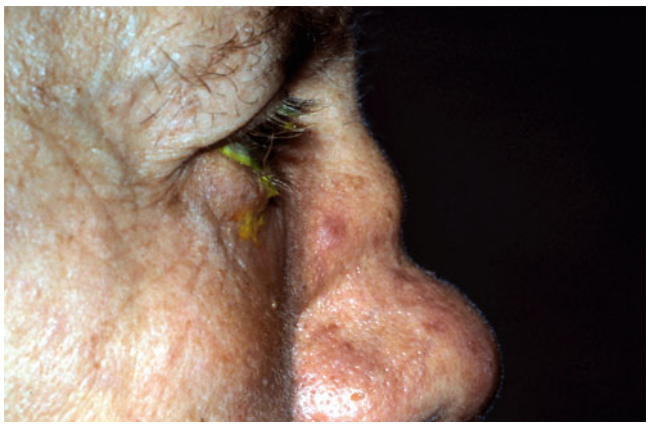


Fig. 14 An older man with long-standing GPA with a "saddle nose" deformity due to loss of nasal septum (see Fig. 15)



Fig. 15 A coronal bone-window setting CT scan (same patient as in Fig. 15) shows gross intranasal and sinus disease. The nasal septum is absorbed, a typical finding in GPA. The patient also had left nasolacrimal duct obstruction, as noted by the widening and obliteration of the left nasolacrimal canal

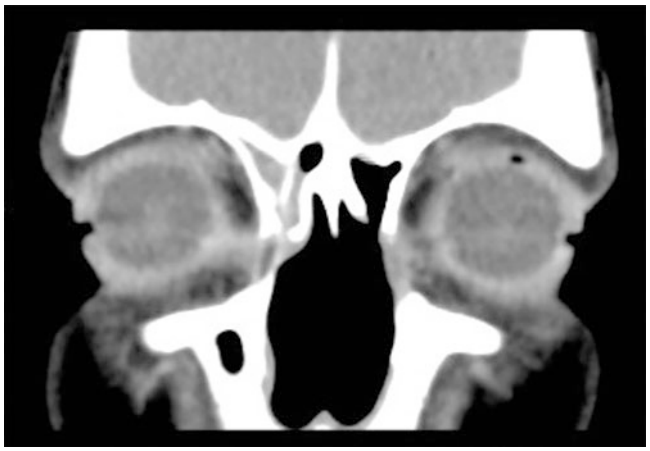


Fig. 16 A coronal noncontrast CT in a patient with diagnosed and treated GPA shows loss of intranasal structures (turbinates and septum) and loss of the left medial orbital wall. The tissue loss was almost entirely due to the disease, and not surgical excision

References

1. Tan LT, Davagnanam I, Isa H, et al. Clinical and imaging features predictive of orbital granulomatosis with polyangiitis and the risk of systemic involvement. Ophthalmology. 2014;121:1304–9.
2. Tan LT, Davagnanam I, Isa H, et al. Clinical and imaging features of lacrimal gland involvement in granulomatosis with polyangiitis. Ophthalmology. 2015;122:2125–9.
3. Woo TL, Francis IC, Wilcsek GA, Coroneo MT, McNab AA, Sullivan TJ. Australasian orbital and adnexal Wegener's granulomatosis. Ophthalmology. 2001;108:1535–43.

IgG-4 Related Orbital Disease

76

Alan A. McNab

Contents

1 **Signs and Symptoms** 567
2 **Differential Diagnosis** 567
3 **Diagnosis** 567
4 **Treatment** 568
5 **Figures with Captions** 568
References 571

Abstract

- IgG4-related disease (IgG4-RD) commonly affects the orbit.
- Common patterns are dacryoadenitis (usually bilateral) associated with salivary gland disease; infraorbital nerve enlargement with paranasal sinus disease and extraocular muscle enlargement; and orbital fat involvement.
- Lesions on both CT and MRI tend to be well defined.
- CT shows lesions with mild-to-moderate contrast enhancement, and some bone remodeling of the infraorbital canal if the nerve is enlarged, or enlargement of other nerve canals or foramina.
- MRI shows the lesions as homogeneous and iso-intense on T1 images, and hypo-intense on T2 images, with contrast enhancement.
- PET scanning is useful to assess systemic disease.
- Biopsy is required to establish the diagnosis.
- Treatment is with corticosteroids, other immunosuppressants, or Rituximab.
- In approximately 10% of patients with IgG4-ROD, low-grade marginal zone MALT lymphoma will develop.

A. A. McNab (✉)
Orbital Plastic and Lacrimal Clinic, Royal Victorian Eye and Ear Hospital, Melbourne, VIC, Australia

© Springer Nature Switzerland AG 2022
G. Ben Simon et al. (eds.), *Atlas of Orbital Imaging*,
https://doi.org/10.1007/978-3-030-62426-2_63

Keywords

IgG4-related disease · IgG4-related ophthalmic disease · Lacrimal gland · Infraorbital nerve · Orbit

1 Signs and Symptoms

Common patterns of disease include bilateral (less often unilateral) lacrimal gland swelling (often with fibrosis), extraocular muscle swelling (often without much strabismus), infraorbital nerve (less often frontal nerve) swelling (without sensory loss), or any other orbital site may be involved [1, 2].

2 Differential Diagnosis

With lacrimal gland or orbital fat disease, other causes of dacryoadenitis (idiopathic, sarcoidosis, Sjögren's syndrome, and granulomatosis with polyangiitis) or generalized infiltrative inflammatory disease.

3 Diagnosis

Tissue diagnosis is essential to identify lymphoplasmacytic infiltrates, often with storiform fibrosis and increased numbers of IgG4+ plasma cells according to diagnostic criteria [3],

in combination with possible other organ involvement (any site, but commonly salivary glands, lymph nodes, pancreas, hepatobiliary tract, retroperitoneum, and upper or lower airways), and an elevated serum IgG4 and circulating IgG4 plasmablasts. PET scan is useful for determining systemic involvement [5].

4 Treatment

The mainstay of treatment is corticosteroids, with long-term low-dose maintenance to minimize recurrence. Rituximab and other immunosuppressants are often needed as steroid-sparing agents [4].

5 Figures with Captions

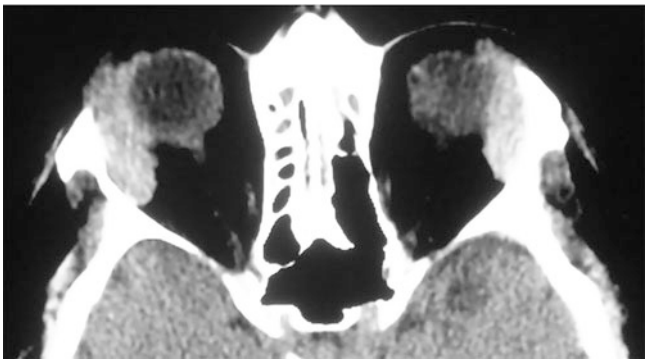


Fig. 1 Noncontrast axial CT demonstrates bilateral symmetrical lacrimal gland enlargement. The patient also had bilateral submandibular and parotid gland enlargement (Mikulicz pattern of disease)

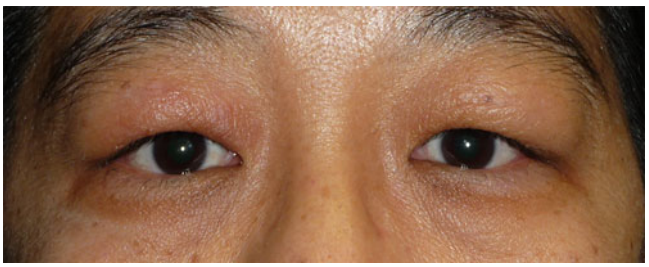


Fig. 2 A 40-year-old woman presented with several months of bilateral upper eyelid swelling and nasal obstructive symptoms. She had bilateral lacrimal gland enlargement. A lacrimal gland biopsy revealed features of IgG4-RD

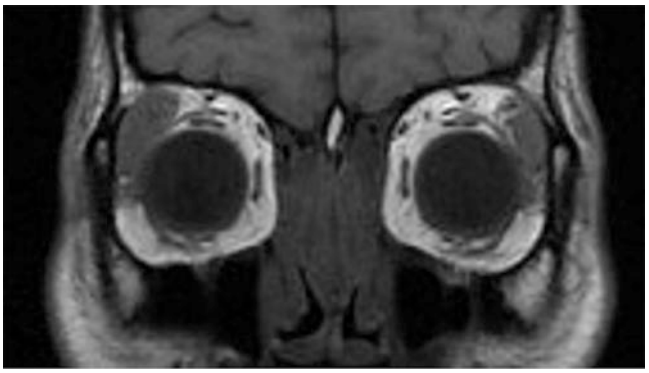


Fig. 3 Coronal T1 MRI of a patient with bilateral lacrimal gland enlargement due to IgG4-ROD (same patient as in Figs. 2, 3, 4, 5, 6, 7, and 8). There is also paranasal sinus disease

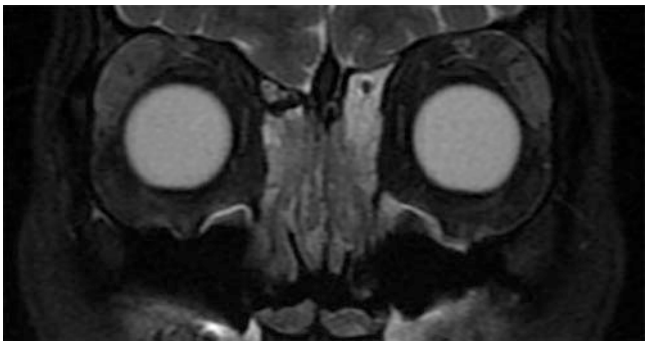


Fig. 4 Coronal T2 fat sat MRI shows bilateral lacrimal gland enlargement and paranasal sinus disease



Fig. 5 Axial T2 FLAIR noncontrast MRI shows bilateral symmetrical lacrimal gland enlargement and some patchy paranasal sinus disease. The patient also had lower airway disease and cervical lymphadenopathy and an elevated serum IgG4

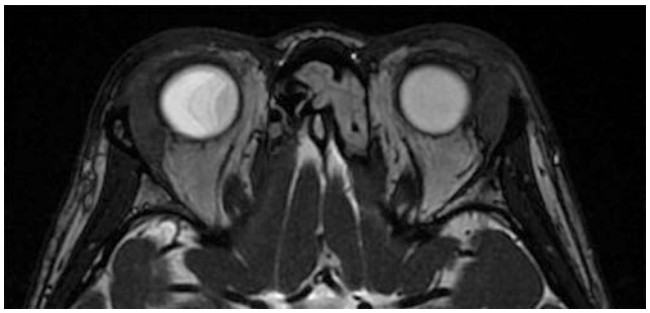


Fig. 6 Axial T2WI MRI shows bilateral lacrimal gland enlargement and patchy paranasal sinus disease (same patient as Figs. 2, 3, 4, 5, 6, 7, and 8)

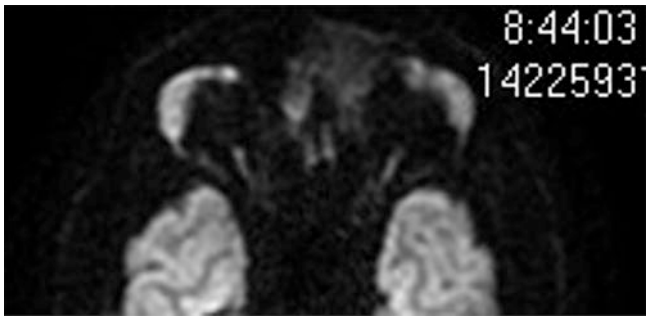


Fig. 7 DWI MRI of patient with bilateral lacrimal gland enlargement due to IgG4-ROD shows high signal in the lacrimal glands

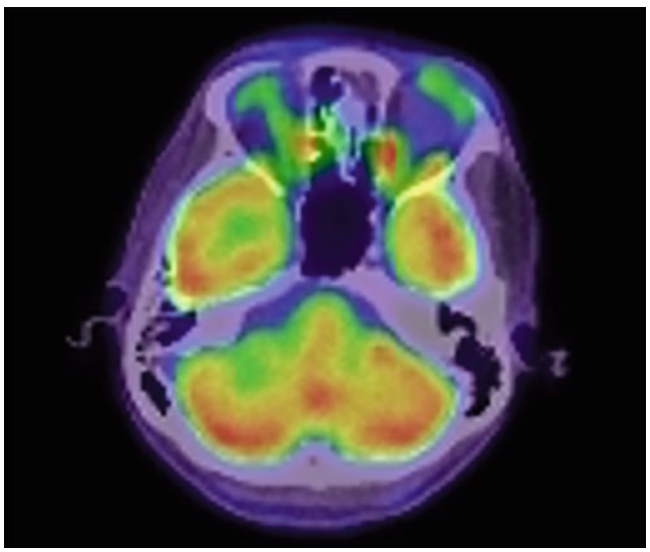


Fig. 8 PET scan of patient in Figs. 2, 3, 4, 5, and 6 shows FDG avidity in both lacrimal glands and some extraocular muscle

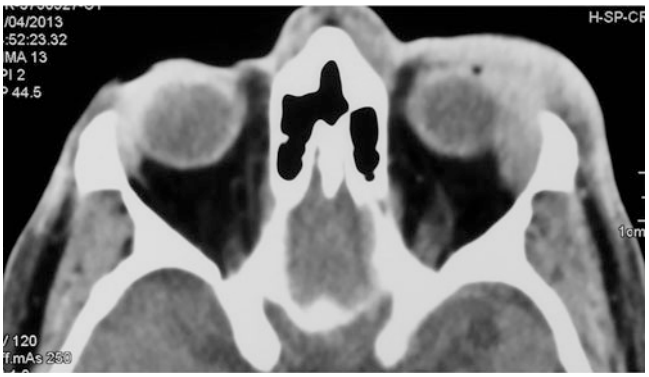


Fig. 9 Noncontrast axial soft tissue window CT shows an enlarged left lacrimal gland with associated pre-septal hyperdense soft tissue thickening (which is atypical for IgG4-RD)



Fig. 10 A 50-year-old man with a several year history of sclerosing cholangitis, lacrimal, and salivary gland enlargement, presented with worsening bilateral eyelid swelling and proptosis, and diplopia in peripheral gaze. Biopsies showed features of IgG4-ROD (same patient as in Figs. 11 and 12)

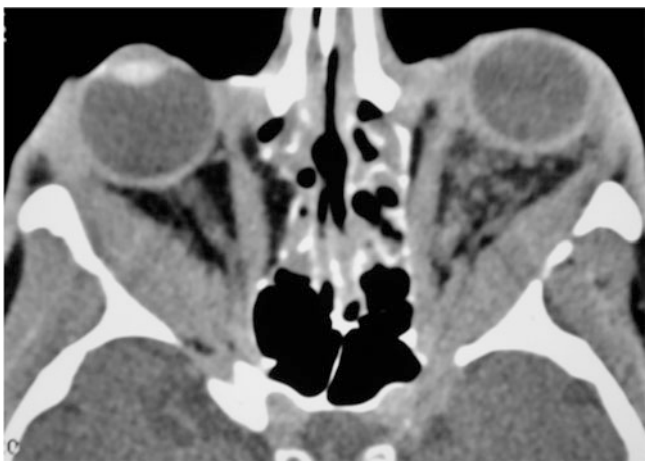


Fig. 11 Axial noncontrast CT shows infiltrative disease involving both lateral recti and lateral orbits extending to the superior orbital fissures. The patient had marked bilateral proptosis. There is patchy intraconal infiltrate on the left and paranasal sinus disease. The patient had presented some years earlier with lacrimal gland and salivary gland enlargement



Fig. 12 Noncontrast direct coronal CT shows enlargement of right inferior rectus; left inferior, lateral, and superior rectus/levator; and extraconal superior orbital disease (left more than right and continuous with bilateral lacrimal gland disease seen on other sections). There is marked enlargement of the left infraorbital nerve (arrow) and patchy paranasal sinus disease. Streak artifact is due to dental fillings

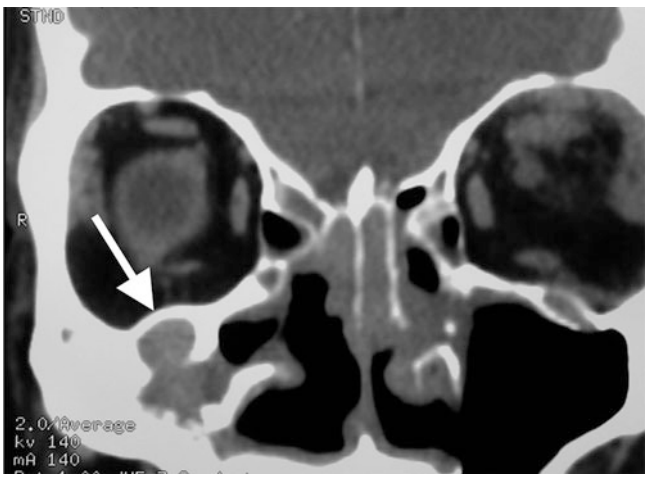


Fig. 13 Coronal noncontrast CT shows marked enlargement of the right infraorbital canal by enlarged infraorbital nerve (ION) (arrow). The left ION is also mildly enlarged. There is left superior extraconal disease continuous with enlarged lacrimal gland (not imaged here) and widespread paranasal sinus disease (previous surgery)

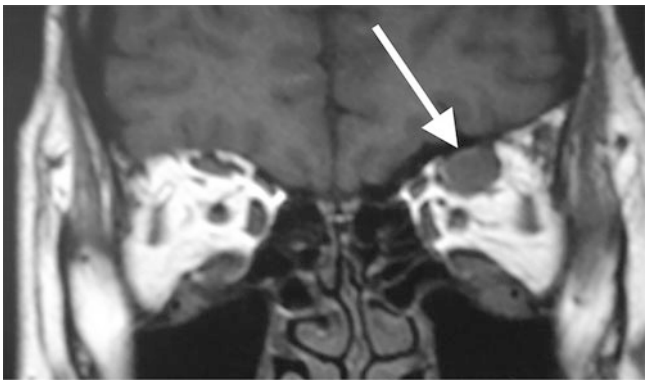


Fig. 14 Coronal T1 noncontrast MRI shows enlargement of the left frontal nerve (V1) (arrow) which extended through the superior orbital fissure into the cavernous sinus. Both infraorbital nerves are also enlarged. Involvement of the first division of the trigeminal nerve or other nerves is less common than infraorbital nerve involvement

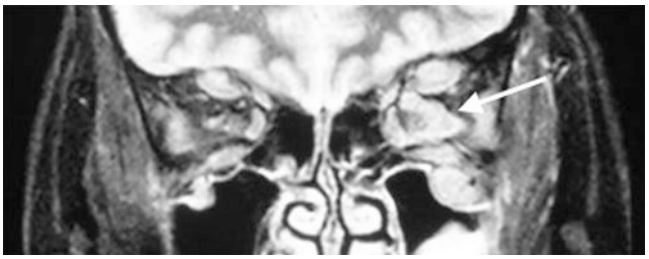


Fig. 15 The same patient as in Figs. 2 and 14 years later, when she presented with left optic neuropathy. This coronal T2 MRI shows persistent frontal nerve and infraorbital nerve enlargement, but now also disease surrounding the left optic nerve (arrow). A repeat biopsy showed transformation to marginal zone MALT lymphoma, treated with low-dose radiotherapy

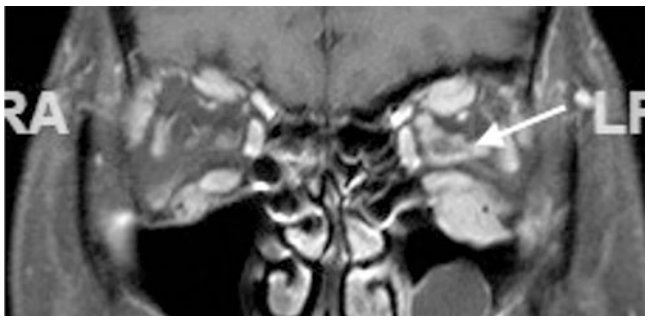


Fig. 16 The same patient as in Fig. 15. A coronal contrast-enhanced T1 MRI shows bilateral infraorbital nerve enlargement, left frontal nerve enlargement, and left perioptic nerve disease (arrow), which showed transformation to marginal zone MALT lymphoma

References

1. McNab AA, McKelvie P. IgG4-related ophthalmic disease. Part II: clinical aspects. Ophthalmic Plast Reconstr Surg. 2015;31:167–78.
2. McNab AA, McKelvie P. IgG4-related ophthalmic disease. Part I: background and pathology. Ophthalmic Plast Reconstr Surg. 2015;31:83–8.
3. Wallace ZS, Naden RP, Chari S, et al. The 2019 American College of Rheumatology/European league against rheumatism classification criteria for IgG4-related disease. Arthrit Rheumatol. 2020;72:7–19.
4. Bledsoe JR, Della-Torre E, Rovati L, Deshpande V. IgG4-related disease: review of the histopathologic features, differential diagnosis, and therapeutic approach. APMIS. 2018;126(6):459–76. https://doi.org/10.1111/apm.12845. PMID: 29924455.
5. Kurowecki D, Patlas MN, Haider EA, Alabousi A. Cross-sectional pictorial review of IgG4-related disease. Br J Radiol. 2019;92(1103):20190448. https://doi.org/10.1259/bjr.20190448. Epub 2019 Jul 29. PMID: 31335170; PMCID: PMC6849681.

Granulomatous Orbital Inflammation: Orbital Sarcoidosis

77

Alan A. McNab

Contents

1 **Symptoms and Signs** 573
2 **Differential Diagnosis** 573
3 **Diagnosis** 573
4 **Treatment** 574
5 **Figures with Captions** 574
References 576

Abstract

- Sarcoidosis may present in patients with known sarcoidosis or as the first manifestation
- Lacrimal gland involvement is common, as well as adjacent orbital tissues, the inferior orbit or extraocular muscle
- Orbital involvement may be by diffuse infiltrative disease or a well-defined discrete mass
- CT shows soft tissue lesions, sometimes with indistinct edges and moderate contrast enhancement
- On MRI, the lesions tend to be hypo-intense on T2, but with marked contrast enhancement
- Biopsy helps to make the diagnosis, or may be made on the basis of disease elsewhere (typically mediastinal or hilar lymphadenopathy)
- Treatment is usually with oral corticosteroids or other immunosuppressants

Keywords

Sarcoidosis · Granulomatous inflammation · Lacrimal gland · Orbit

A. A. McNab (✉)
Orbital Plastic and Lacrimal Clinic, Royal Victorian Eye and Ear Hospital, Melbourne, VIC, Australia

© Springer Nature Switzerland AG 2022
G. Ben Simon et al. (eds.), *Atlas of Orbital Imaging*,
https://doi.org/10.1007/978-3-030-62426-2_109

1 Symptoms and Signs

Sarcoidosis may present with chronic lacrimal gland swelling (usually bilateral), infiltrative masses anywhere in the orbit, but more commonly the inferior orbit, extraocular muscle swelling, usually with lacrimal gland and orbital fat involvement, or rarely optic nerve involvement (neurosarcoidosis) [1–7]. Most patients will have features of systemic sarcoidosis [3]. Uveitis is uncommon in patients with ocular adnexal sarcoidosis [1, 3].

2 Differential Diagnosis

For lacrimal gland swelling, the differential diagnosis includes all causes of lacrimal gland inflammation and lymphoma, or in unilateral cases, epithelial tumors of the lacrimal gland.

3 Diagnosis

Diagnosis can be established with a tissue biopsy. Other causes of granulomatous inflammation need to be excluded (TB, granulomatosis with polyangiitis, fungal infection, foreign body). Serum ACE and calcium and a chest x-ray or CT scan may be helpful.

4 Treatment

Corticosteroids are the mainstay of treatment but other immunosuppressants such as methotrexate may be required in resistant cases or as steroid sparing agents.

5 Figures with Captions

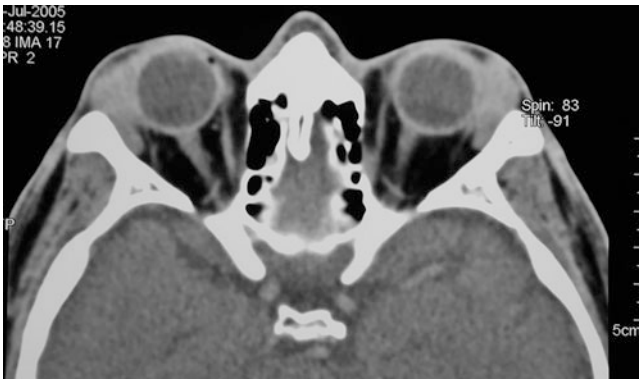


Fig. 1 An axial non-contrast CT in a man with bilateral lacrimal gland swelling, S-shaped upper lid ptosis and a chronic cough. There is bilateral lacrimal gland swelling. A biopsy diagnosed sarcoidosis



Fig. 2 A young adult man from India presented with swelling in both upper eyelids with S-shaped ptosis. He also had marked nasal obstruction and epididymo-orchitis. A lacrimal gland biopsy confirmed sarcoidosis. Tissue cultures for TB were negative (same patient as Fig. 3)



Fig. 3 (same patient as Fig. 2) An axial contrast-enhanced CT in a man with chronic bilateral lacrimal gland swelling, nasal obstruction, and epididymo-orchitis. He had bilateral proptosis and S-shaped upper eyelid ptosis. Both lacrimal glands are enlarged and showed mild enhancement. There was severe paranasal sinus disease. A lacrimal gland biopsy showed sarcoidosis

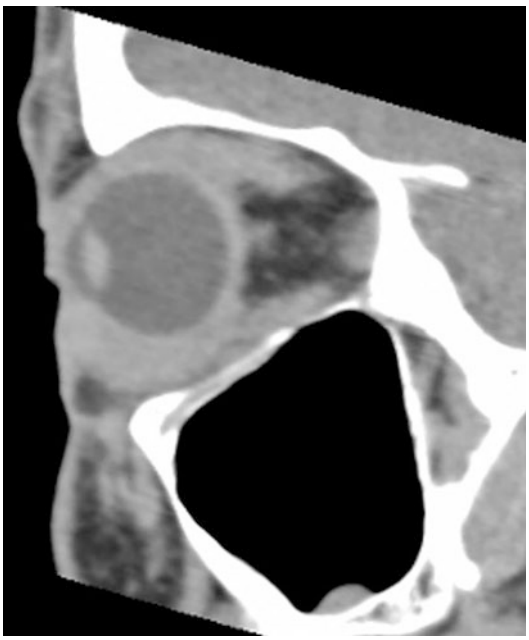


Fig. 4 A sagittal non-contrast CT in a man with right-sided upper and lower eyelid swelling, ptosis, and mild restricted ocular motility shows an infiltrative process in the lower eyelid, anterior orbital tissues superiorly and inferiorly extending into the superior rectus-levator complex and the inferior rectus. A biopsy found sarcoidosis

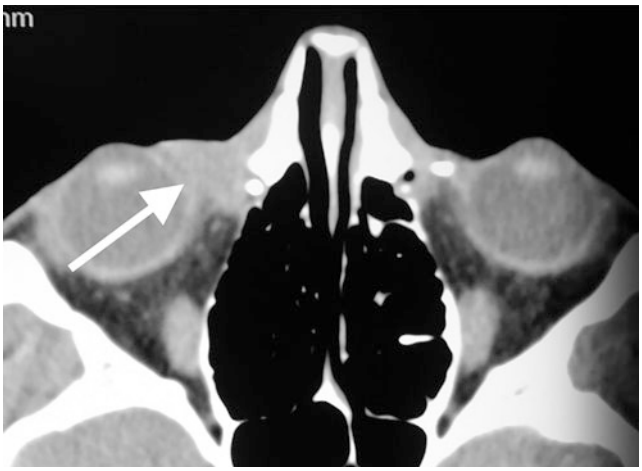


Fig. 5 An axial CT with contrast injected into both lacrimal systems (CT-DCG) in a man with right lacrimal obstruction and swelling of the medial lower eyelid and a palpable mass, shows an infiltrative process in the medial eyelid and adjacent anterior orbit surrounding the lacrimal sac. A biopsy established sarcoidosis as the diagnosis. Contrast material passed into the lacrimal sac on the right, but no further



Fig. 6 A young adult female presented with sub-acute left optic neuropathy with markedly reduced vision. An axial non-contrast CT showed the left optic nerve to be expanded in a tubular manner. There was mild contrast-enhancement

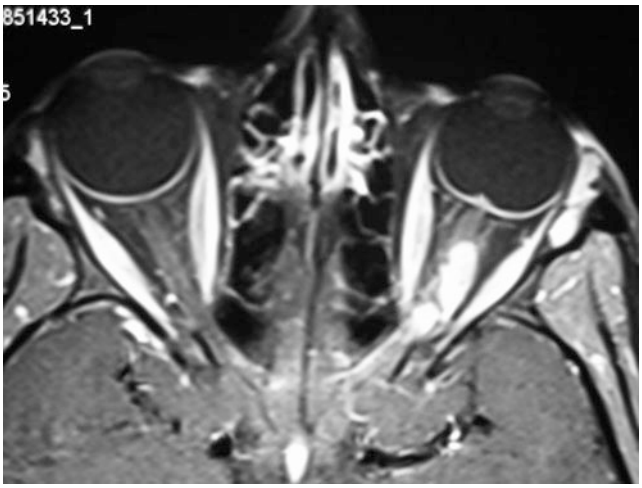


Fig. 7 An axial T1 contrast-enhanced fat suppressed MRI of the patient in Fig. 6 shows patchy enhancement of the left optic nerve and/or sheath. There is left sided optic disc swelling and flattening of the back of the globe

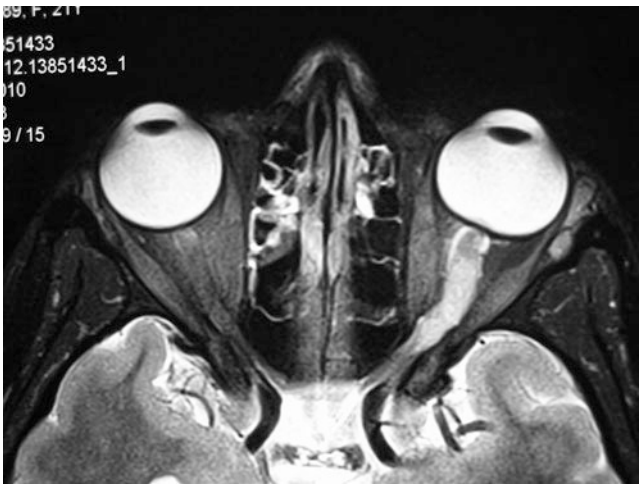


Fig. 8 An axial T2 contrast enhanced MRI shows enlargement and enhancement of the left optic nerve and sheath. A biopsy of the sheath and adjacent optic nerve showed neuro-sarcoidosis. There was no other central nervous system or meningeal involvement

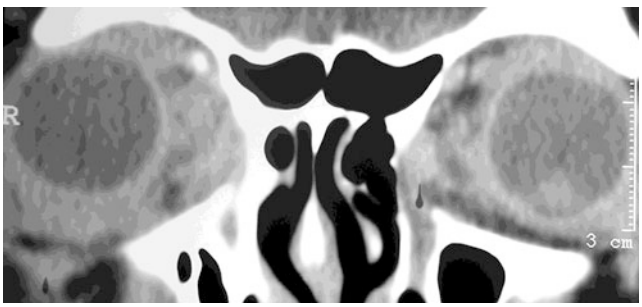


Fig. 9 CT scan coronal view of a 48-YOF with bilateral diffuse orbital infiltrates, right more than left. Orbital biopsy was consistent with sarcoidosis. (Courtesy of the editors)

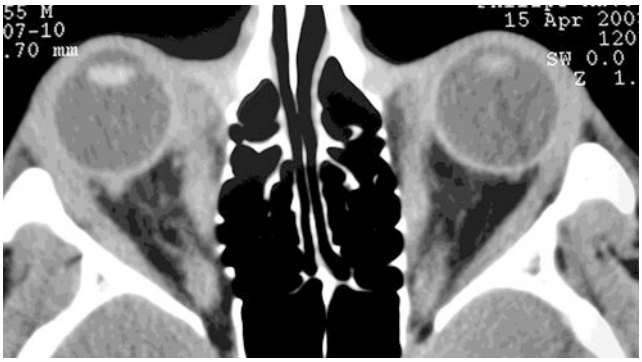


Fig. 10 CECT, axial view of the same patient as in Fig. 9, showing bilateral ill-defined, relatively homogenous infiltrates involving the anterior compartment (preseptal and periocular) of both orbits, more so on the right. Intra-conal fat stranding is also demonstrated, more pronounced on the right side. The patient was treated with oral steroids and methotrexate. (Courtesy of the editors)



Fig. 11 Clinical photograph of a 59-YOF with gradual onset right periocular swelling, edema and inflammation, accompanied by blurred vision and right globe proptosis for the past year. There was mild optic neuropathy on the right with decreased vision. (Courtesy of the editors)



Fig. 12 NE CT axial view of the same patient as in Fig. 11, showing an ill-defined, iso-to-hyperdense, intra-conal mass, with periocular soft tissue swelling on the right side. The infiltrative process is extending through the orbital apex and SOF, with contiguous involvement of the inferior cavernous sinus and part of Meckel's cave on the right. Orbital biopsy was consistent with sarcoidosis. (Courtesy of the editors)

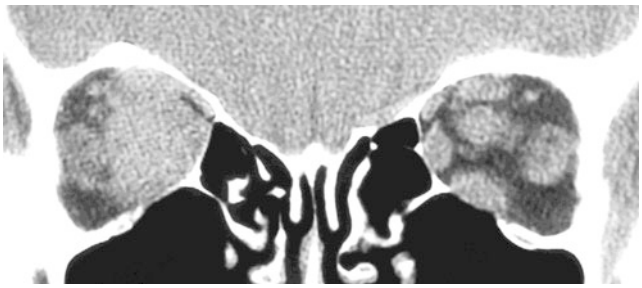


Fig 13 NE CT coronal section of the same patient, showing the inflammatory process occupying most of the intra-conal space (mainly central and nasal portion), and cannot be distinguished from the adjacent extra-ocular muscles and optic nerve. (Courtesy of the editors)

References

1. Prabhakaran VC, Saeed P, Esmaeli B, Sullivan TJ, McNab A, Davis G, Valenzuela A, Leibovitch I, Kesler A, Sivak-Callcott J, Hoyama E, Selva D. Orbital and adnexal sarcoidosis. Arch Ophthalmol. 2007;125:1657–62.
2. Mavrikakis I, Rootman J. Diverse clinical presentations of orbital sarcoid. Am J Ophthalmol. 2007;144:769–75.
3. Demiric H, Christianson MD. Orbital and adnexal involvement in sarcoidosis: an analysis of clinical features and systemic disease in 30 cases. Am J Ophthalmol. 2011;151:1074–80.
4. Tugal-Tutkun I. Systemic vasculitis and the eye. Curr Opin Rheumatol. 2017;29(1):24–32. https://doi.org/10.1097/BOR.0000000000000345. PMID: 27662569.
5. Rosenbaum JT, Choi D, Wilson DJ, Grossniklaus HE, Sibley CH, Harrington CA, Planck SR, Orbital Disease Consortium. Molecular diagnosis of orbital inflammatory disease. Exp Mol Pathol. 2015;98(2):225–9. https://doi.org/10.1016/j.yexmp.2015.01.009. Epub 2015 Jan 14. PMID: 25595914; PMCID: PMC4388776.
6. Marinò M, Ionni I, Lanzolla G, Sframeli A, Latrofa F, Rocchi R, Marcocci C. Orbital diseases mimicking graves' orbitopathy: a long-standing challenge in differential diagnosis. J Endocrinol Invest. 2020;43(4):401–11. https://doi.org/10.1007/s40618-019-01141-3. Epub 2019 Nov 5. PMID: 31691261.
7. McNab AA. The 2017 Doyne Lecture: the orbit as a window to systemic disease. Eye (Lond). 2018;32(2):248–61. https://doi.org/10.1038/eye.2017.224. Epub 2017 Nov 10. PMID: 29125145; PMCID: PMC5811731.

Xanthogranulomatous Disease of the Orbit

78

Alan A. McNab

Contents

1 **Symptoms and Signs** 577
2 **Differential Diagnosis** 577
3 **Diagnosis** 578
4 **Treatment** 578
5 **Figures with Captions** 578
References 580

Abstract

- Xanthogranulomatous disease of the orbit occurs in four types: adult onset xanthogranuloma (AOX), adult onset asthma and periocular xanthogranuloma (AAPOX), necrobiotic xanthogranuloma (NBX, NXG), and Erdheim Chester disease (ECD).
- These are non-Langerhans histiocytic disorders. Histopathologic features include the presence of foamy histiocytes, Touton giant cells, and varying degrees of fibrosis and possible necrosis.
- Yellowish discoloration of the eyelids and anterior orbital tissues occur in AOX, AAPOX, and NXG. Posterior infiltrative masses are seen in ECD.
- NXG is associated with haematological disease.
- Biopsy is required for diagnosis.
- Imaging shows infiltrative masses of the preseptal tissues, anterior orbit, as well as lacrimal glands in AOX and AAPOX, often with paranasal sinus disease in AAPOX.
- Treatment is with immunosuppression or Rituximab; BRAF inhibitors may help ECD.

Keywords

Xanthogranulomatous disease · Adult onset xanthogranuloma (AOX) · Adult onset asthma and periocular xanthogranuloma (AAPOX) · Necrobiotic xanthogranuloma (NBX) · and Erdheim Chester disease (ECD) · Orbit

1 Symptoms and Signs

Xanthogranulomatous diseases of the ocular adnexa comprise four entities: adult onset xanthogranuloma (AOX), adult onset asthma and periocular xanthogranuloma (AAPOX), necrobiotic xanthogranuloma (NBX), usually associated with haematological disease, and Erdheim Chester disease (ECD, which has many systemic manifestations, and can be fatal. Patients with AOX, AAPOX, and NXG have infiltrative lesions of the eyelids and anterior orbit which have a distinct yellowish-red appearance, whereas ECD characteristically has bilateral intraconal infiltrative masses [1–5].

2 Differential Diagnosis

These diseases may be confused with exuberant xanthelasma, or other infiltrative inflammatory processes, but the yellowish discoloration of the eyelids and tissues is characteristic.

A. A. McNab (✉)
Orbital Plastic and Lacrimal Clinic, Royal Victorian Eye and Ear Hospital, Melbourne, VIC, Australia

© Springer Nature Switzerland AG 2022
G. Ben Simon et al. (eds.), *Atlas of Orbital Imaging*,
https://doi.org/10.1007/978-3-030-62426-2_118

3 Diagnosis

A tissue diagnosis is required, with mixed inflammatory infiltrates, foamy macrophages, and Touton giant cells present [1].

4 Treatment

Many treatments have been tried for AOX and AAPOX, including corticosteroids and other immunosuppressants. Rituximab works very well [5]. For NXG, treatment of the underlying haematological disorder is important plus local or systemic steroids. For ECD, which in many cases has a BRAF mutation, BRAF inhibitors can be used [3].

5 Figures with Captions



Fig. 1 A young man presented with chronic bilateral symmetrical yellow and red swelling of the upper eyelids, and some conjunctival injection and swelling over the insertions of both lateral rectus muscles. Biopsy confirmed adult onset xanthogranuloma (AOX)



Fig. 2 (Same patient as Figs. 1 and 3) An axial contrast CT of a patient with AOX shows marked bilateral symmetrical preseptal swelling and infiltration plus gross lacrimal gland enlargement



Fig. 3 An axial contrast-enhanced CT (same patient as Figs. 1 and 2) shows the infiltrative disease extending along the lateral walls of both orbits



Fig. 4 An elderly man with long-standing yellowish swelling of the left upper and lower lids and some minor changes on the right. He also had adult onset asthma and rhinosinusitis. Biopsy confirmed xanthogranulomatous disease (AAPOX)



Fig. 5 An axial noncontrast CT of the patient with markedly asymmetric AAPOX with preseptal swelling, lacrimal gland enlargement, and infiltrative disease extending along the left lateral orbital wall, and possibly involving lateral rectus which is inseparable from the lesion. However, he had normal eye movements. There is also patchy paranasal sinus disease

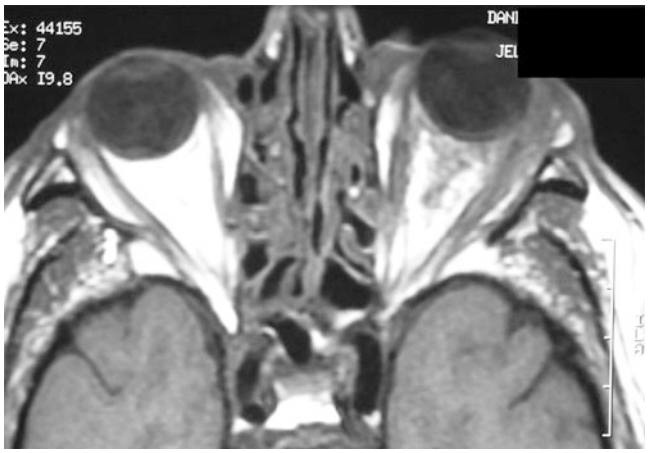


Fig. 6 An axial noncontrast T1 MRI (same patient as Figs. 4, 5, and 7) shows an infiltrative process in the anterior left intraconal space and in the region of the lacrimal gland, and the LR tendon attachments

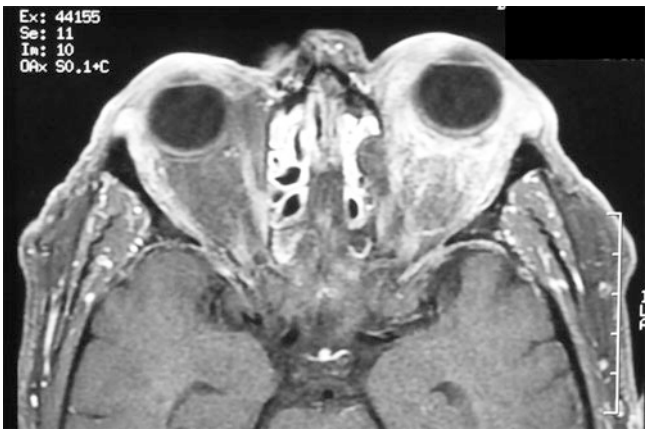


Fig. 7 A contrast-enhanced axial T1 MRI (same patient as Figs. 4, 5, and 6) shows marked contrast enhancement of the infiltrative process in the left preseptal and anterior orbital soft tissues, with mild changes on the right, and paranasal sinus disease. The MRI was taken only a few weeks after the CT scan above (Fig. 3)



Fig. 8 A 40-year-old man with yellowish swelling of the upper eyelids and also swelling of the lower lids and conjunctival redness and swelling over the lateral rectus muscle insertions. He also had rhinosinusitis and asthma. Biopsy confirmed xanthogranulomatous disease (AAPOX)

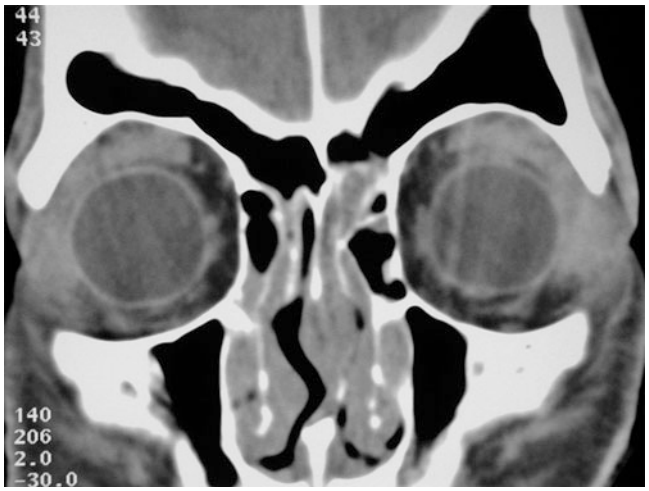


Fig. 9 A coronal noncontrast CT of a man with AAPOX (same patient as Figs. 8 and 10) shows a bilateral infiltrative process in the superior and lateral extraconal areas plus paranasal sinus disease

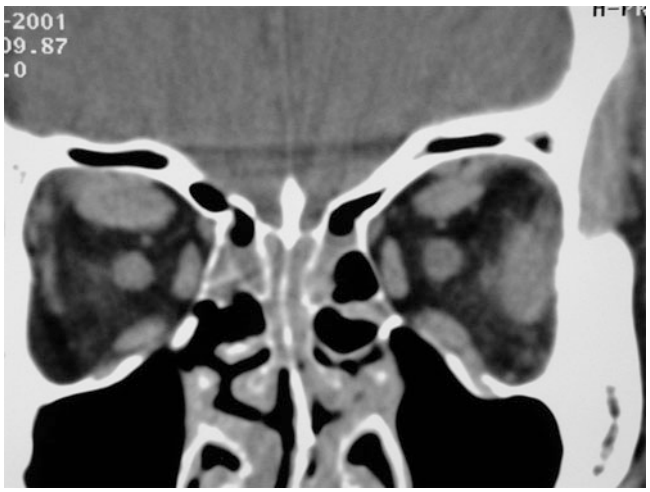


Fig. 10 A coronal noncontrast CT further posterior than Fig. 9 (same patient) shows enlargement of the right superior rectus-levator complex and the left lateral rectus and the patchy paranasal sinus disease



Fig. 11 A 45-year-old man with gradual onset of bilateral proptosis, worse on the right. He also had bone, pericardial, and meningeal disease. Biopsy confirmed Erdheim-Chester disease

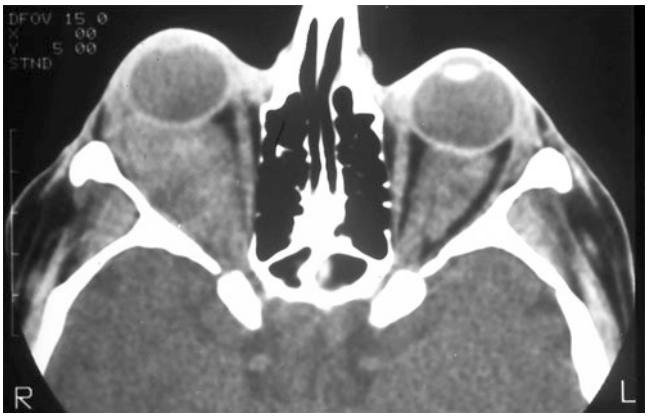


Fig. 12 A noncontrast axial CT of a patient with Erdheim Chester disease (Fig. 11). There is extensive intraconal infiltrative disease on the right and milder disease on the left. There is bilateral globe proptosis more significant on the right and mild globe compression on the left. There is a faint delineation of the ON/sheath complex on the right

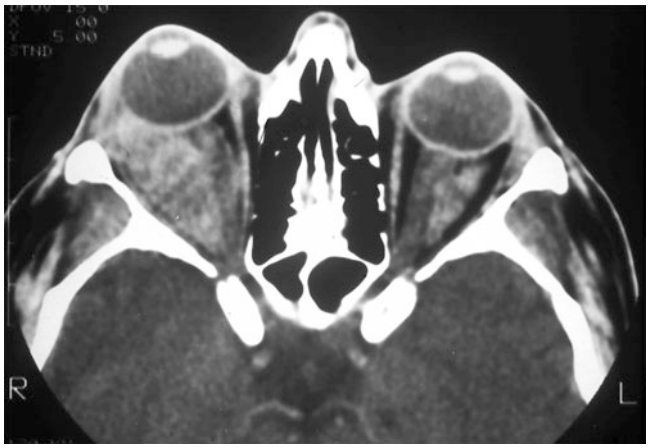


Fig. 13 An axial contrast-enhanced CT (same patient as Figs. 11 and 12) shows the intraconal disease enhances. He had disease of the long bones, pericardium, and meninges

References

1. Sivak-Callcott JA, Rootman J, Rasmussen SL, Nugent RA, White VA, Paridaens D, Currie Z, Rose G, Clark B, McNab AA, Buffam FV, Neigel JM, Kazim M. Adult xanthogranulomatous disease of the orbit and ocular adnexa: new immunohistochemical findings and clinical review. Br J Ophthalmol. 2006;90:602–8. https://doi.org/10.1136/bjo.2005.085894. PMID: 16622091; PMCID: PMC1857051.
2. McKelvie P, McNab AA, Hardy T, Rathi V. Comparative study of clinical, pathological, radiological and genetic features of patients with adult ocular adnexal xanthogranulomatous disease, Erdheim-Chester disease, and IgG4-related disease of the orbit/ocular adnexa. Ophthalmic Plast Reconstr Surg. 2017;33:112–9.
3. Goyal G, Heaney ML, Collin M, et al. Erdheim-Chester disease: consensus recommendations for evaluation, diagnosis, and treatment in the molecular era. Blood. 2020;135:1929–45.
4. Hidayat AA, Mafee MF, Laver NV, Noujaim S. Langerhans' cell histiocytosis and juvenile xanthogranuloma of the orbit. Clinicopathologic, CT, and MR imaging features. Radiol Clin North Am. 1998;36(6):1229–40, xii. https://doi.org/10.1016/s0033-8389(05)70242-6. PMID: 9884699.
5. Sagiv O, Thakar SD, Morrell G, Tetzlaff MT, Esmaeli B. Rituximab monotherapy is effective in treating orbital necrobiotic xanthogranuloma. Ophthalmic Plast Reconstr Surg. 2018;34(1):e24–7. https://doi.org/10.1097/IOP.0000000000000988. PMID: 28863117.

Thyroid Eye Disease

79

Kelsey A. Roelofs and Ezekiel Weis

Contents

1 **Signs and Symptoms** 582
2 **Differential Diagnosis** 582
3 **Diagnosis** 582
4 **Treatment** 582
5 **Figures with Captions** 582
References 587

Abstract

- Findings of thyroid eye disease (TED) detected on computed tomography and/or magnetic resonance imaging are bilateral in 90% and symmetric in 70% of cases.
- Patients with TED may have prominent expansion of orbital fat with no apparent extraocular muscle (EOM) enlargement (type 1) while others demonstrate fusiform enlargement of EOMs (type 2). Although most cases demonstrate tendon sparing, EOM enlargement with tendon involvement is seen not infrequently in TED.
- While inferior rectus enlargement often occurs early in patients with TED, the medial and lateral recti volumes appear to increase proportionally to disease severity. Enlargement of the superior complex (superior rectus and levator palpebra superioris) can also be seen.
- Findings on MRI may be helpful in detecting disease activity in the deeper orbit when clinical signs may be equivocal.
- Apical crowding and maximum medial rectus diameter measured on a coronal scan are important radiologic predictors of dysthyroid optic neuropathy.
- Identification of variations in anatomy of the cribriform plate are critical in avoiding operative injury during decompression of the medial wall, which can result in dural laceration and cerebrospinal fluid rhinorrhea.
- In instances where deep lateral orbital decompression is required, pre-operative computed tomography allows assessment of the thickness of the diploic trigone to optimize surgical planning.

Keywords

Thyroid eye disease · Autoimmune dysthyroidism · Dysthyroid optic neuropathy · EOM enlargement · Exophthalmos

K. A. Roelofs
Division of Orbital and Ophthalmic Plastic Surgery, Stein and Doheny Eye Institutes, University of California, Los Angeles, CA, USA
e-mail: roelofs@ualberta.ca

E. Weis (✉)
Department of Ophthalmology and Visual Sciences, University of Alberta, Edmonton, AB, Canada

Department of Surgery, University of Calgary, Calgary, AB, Canada

© Springer Nature Switzerland AG 2022
G. Ben Simon et al. (eds.), *Atlas of Orbital Imaging*,
https://doi.org/10.1007/978-3-030-62426-2_65

1 Signs and Symptoms

Eyelid retraction typified by temporal flare, signs of inflammation, unilateral or bilateral exophthalmos, extraocular muscle enlargement, often but not always with sparing of the tendons [1], secondary restrictive strabismus, and occasionally optic nerve dysfunction.

2 Differential Diagnosis

Inflammation, infections, and infiltrating masses involving the orbital soft tissue, predominantly the rectus muscles, can mimic TED. These include nonspecific and specific orbital inflammatory syndromes (e.g., IgG4, granulomatosis with polyangiitis, sarcoidosis), most commonly in the form of a myositis. Infiltrations include metastatic solid tumors, lymphoproliferative deposits, and primary tumors. Rarely, low-grade infections can present with a sub-acute onset making diagnosis difficult. In contrast to the smooth EOM expansion seen in TED, many inflammatory and neoplastic processes result in irregular enlargement/borders.

3 Diagnosis

While there is no pathognomonic clinical, laboratory, or radiologic finding to diagnose TED, a constellation of clinical findings such as bilateral eyelid retraction with temporal flare, proptosis with a history of dysthyroidism, or elevated thyroid antibodies are highly suggestive.

4 Treatment

Management of TED is guided by both disease activity and severity. A variety of medical therapies (corticosteroids, steroid-sparing agents [ciclosporin, methotrexate, azathioprine], biologics [teprotumumab, Rituxan, and tocilizumab], and external beam radiotherapy) may be used for patients with significant activity/inflammation; while surgical interventions (decompression, strabismus and eyelid surgery) are often required for those with moderate to severe inactive/fibrotic disease.

5 Figures with Captions

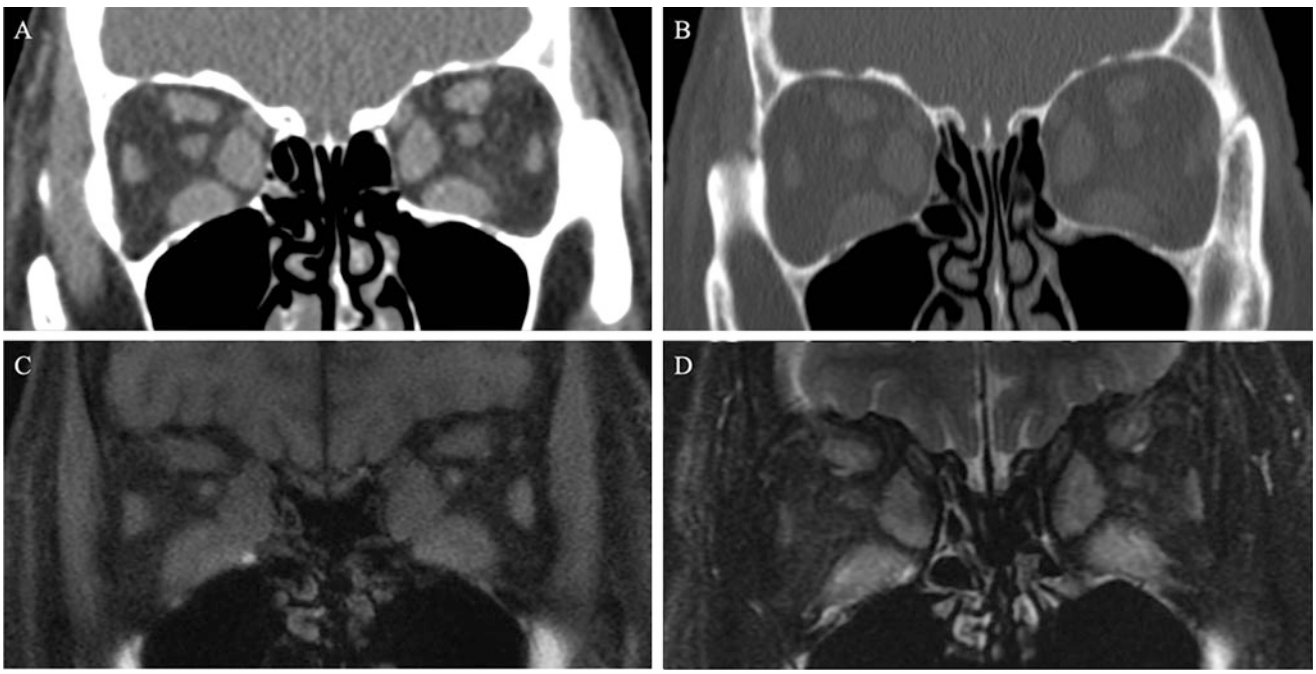


Fig. 1 Extraocular muscle enlargement in thyroid eye disease often follows a pattern, involving the inferior rectus most commonly, followed by the medial, superior and lateral rectus muscles. This figure demonstrates a typical case of bilateral extraocular muscle enlargement involving primarily the inferior and medial rectus, and to a lesser degree the superior muscle complex (superior rectus and levator muscle), on (**a** and **b**) coronal CT using the soft tissue and bone windows, and (**c** and **d**) coronal T1- and T2-weighted MRI with fat suppression

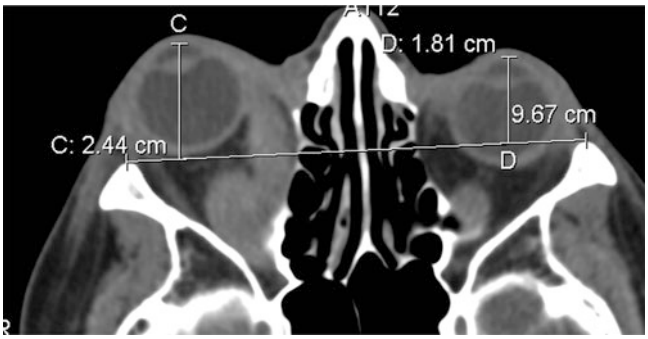


Fig. 2 (**a**) Axial CT demonstrating proptosis measured using the interzygomatic method, which involves drawing a reference line between the anterior portion of both zygomatic bones and measuring to the anterior globe surface

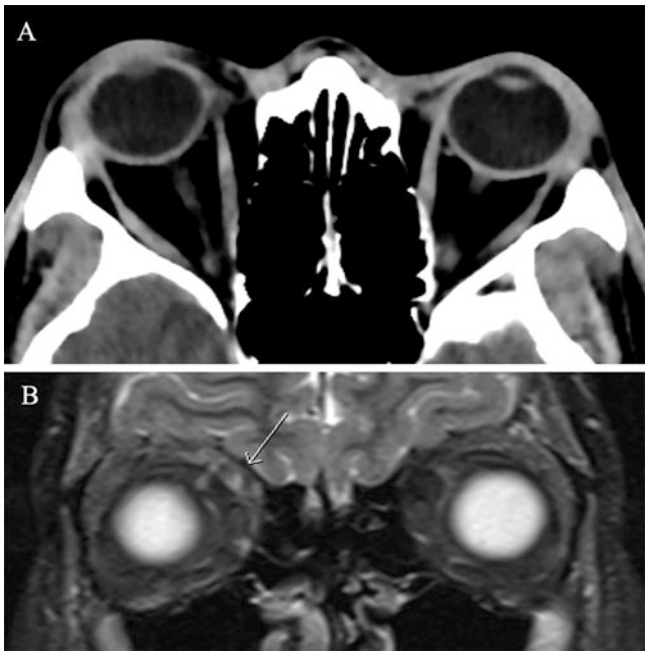


Fig. 3 (**a**) On axial CT proptosis in the absence of EOM enlargement with a significant increase in fat volume (FV) in a 25-year-old male with TED. (B) Coronal T2 fat suppression of the same patient demonstrating a faint increased T2 signal along small segment of the right superior oblique muscle (white arrow). The pattern of disease appreciated on orbital imaging may vary with age, with younger patients tending to have more expansion in FV compared to their older counterparts who are more likely to have increases in MV. Other risk factors, such as smoking, have been associated with an increase in MV. Preoperative CT identifies patients with predominant increases in FV, allowing for optimal case selection for orbital fat decompression without bone removal [2]. Finally, as demonstrated in this case, EOM involvement in TED is not limited to the rectus muscles and superior oblique enlargement may be an under recognized finding [3]

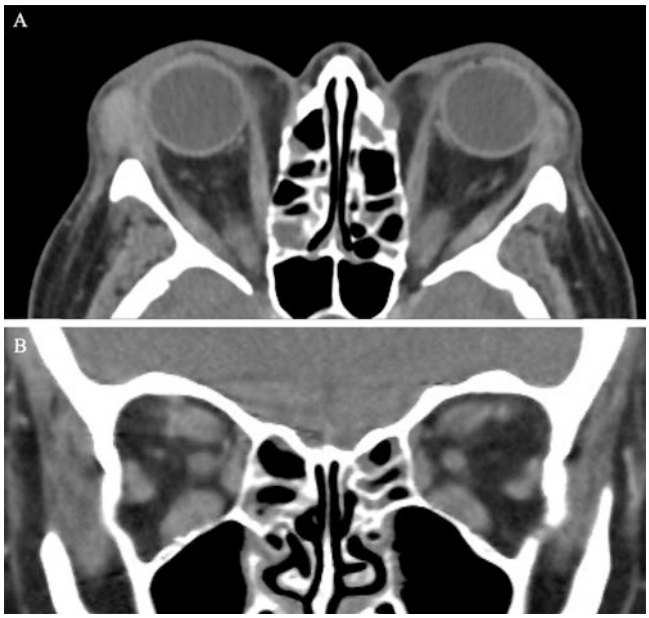


Fig. 4 Lacrimal gland enlargement has been reported in patients with TED [4] and may correlate with subjective tearing and proptosis [5, 6]. (**a**) Axial computed tomography demonstrating bilateral lacrimal gland enlargement and prolapse, right > left and (**b**) coronal images highlighting bilateral extraocular muscle enlargement, right > left

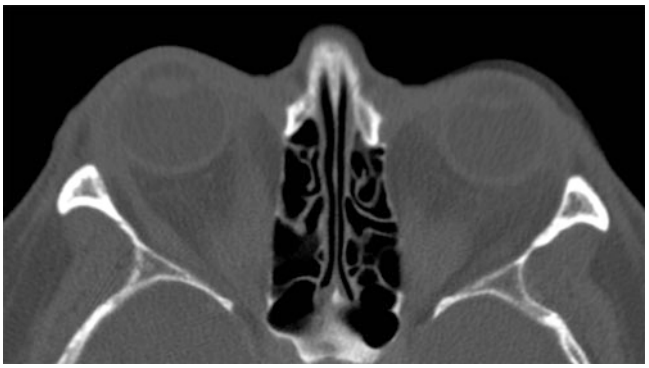


Fig. 5 Axial CT bone window demonstrating subtle bowing of the left medial orbital wall. Medial wall bowing has been reported to occur in 12% of patients, and may serve as a useful predictor for severe disease given its association with more proptosis, greater restriction of extraocular movements, higher CAS [7] and larger medial rectus size [8]. Rarely, spontaneous decompression of the medial orbital wall can occur [9]

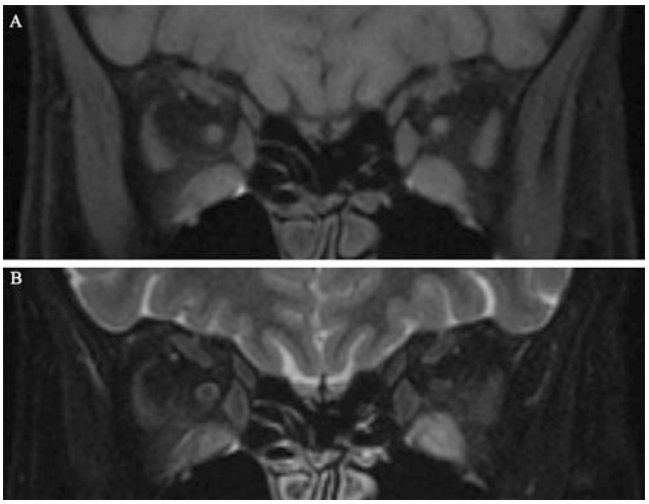


Fig. 6 Coronal (**a**) T1-weighted non-enhanced fat saturation showing enlargement of inferior and medial rectus muscles, left slightly more prominent than right and (**b**) T2 fat saturation images showing increased T2 signal within the inferior rectus muscles bilaterally, slightly more prominent on the left side. Prolonged T2-weighted MRI relaxation time (high signal / hyperintensity) of extraocular muscles[10–13] is indicative of active disease, and correlates well with both CAS and response to corticosteroids in patients with TED

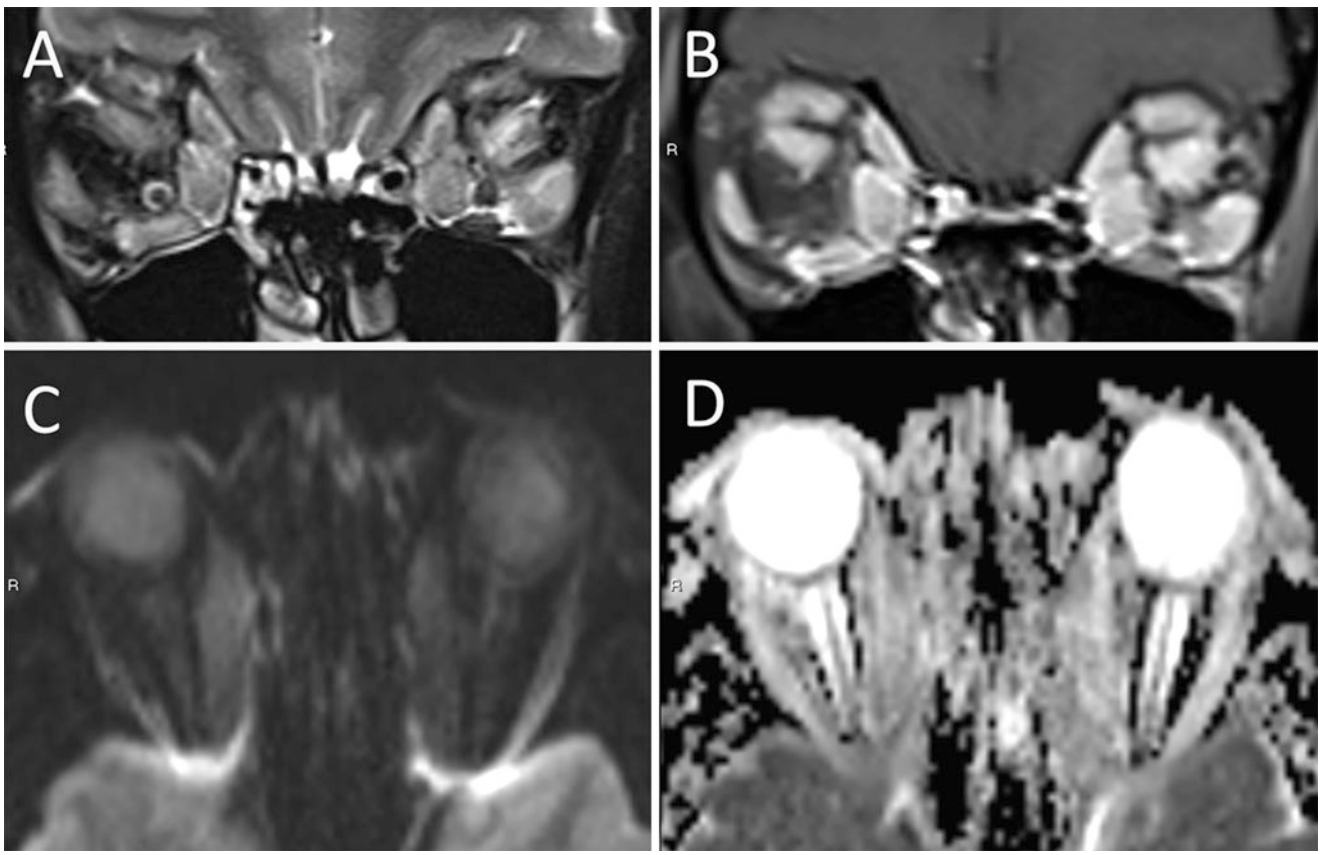


Fig. 7 A MRI of a 51-year-old female with active TED and bilateral EOM enlargement (IR, MR, SO and superior complex). (**a**) The EOM are hyperintense on T2-weighted fat saturation images, (**b**) demonstrate enhancement on T1, (**c**, **d**) and show no restriction on DWI / ADC

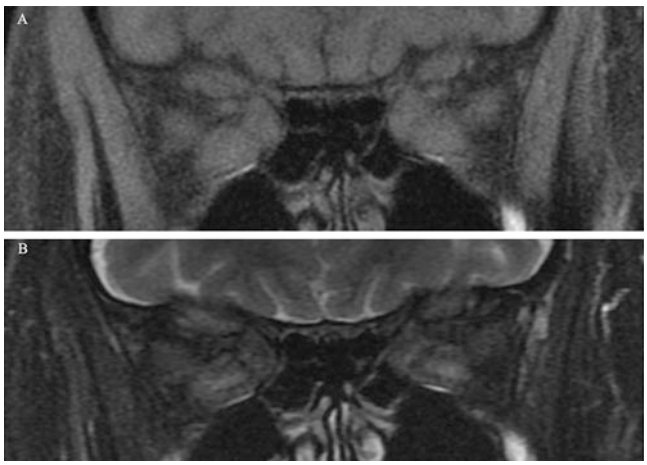


Fig. 8 Apical crowding is an important risk factor for DON. This figure demonstrates a coronal (**a**) T1- and (**b**) T2-weighted non-enhanced fat saturation showing enlargement of the extraocular muscles, predominantly the inferior and medial recti, causing crowding of the orbital apices without any definitive evidence of optic nerve compression. Weis et al. conducted a retrospective consecutive case series of patients with TED to determine which clinical and soft-tissue CT findings at presentation best predict the risk of developing DON [14]. On multivariate analysis, significant clinical and radiologic features included: decreased total ductions, decreased marginal reflex distance (MRD1) and apical crowding on CT

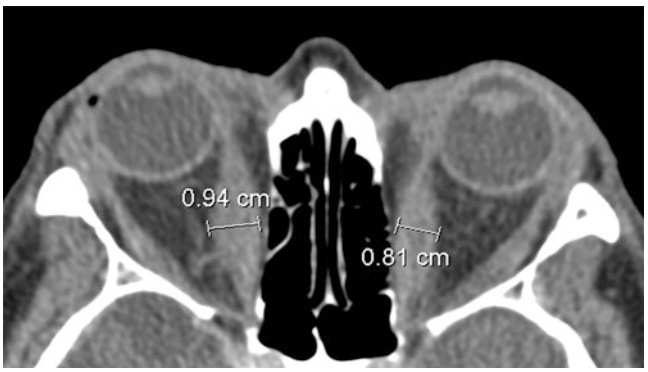


Fig. 9 Axial CT demonstrating measurement of maximal medial rectus size. The medial rectus size appears to be predictive of DON, perhaps due to its closer proximity to the optic nerve at the orbital apex. Weis et al. found the predictive value of maximum medial rectus diameter, simply measured on an axial scan, to be non-inferior to the more complex and time-consuming medial rectus volumetric calculation. These authors did not find an association between orbital bony anatomical configuration or orbital volume and DON [15]. Also note the fusiform pattern of enlargement with sparing of the tendinous insertion characteristic of thyroid eye disease



Fig. 10 (**a**) Axial computed tomography demonstrating a enlarged left medial rectus with (**b**) corresponding apical crowding noted on coronal cuts

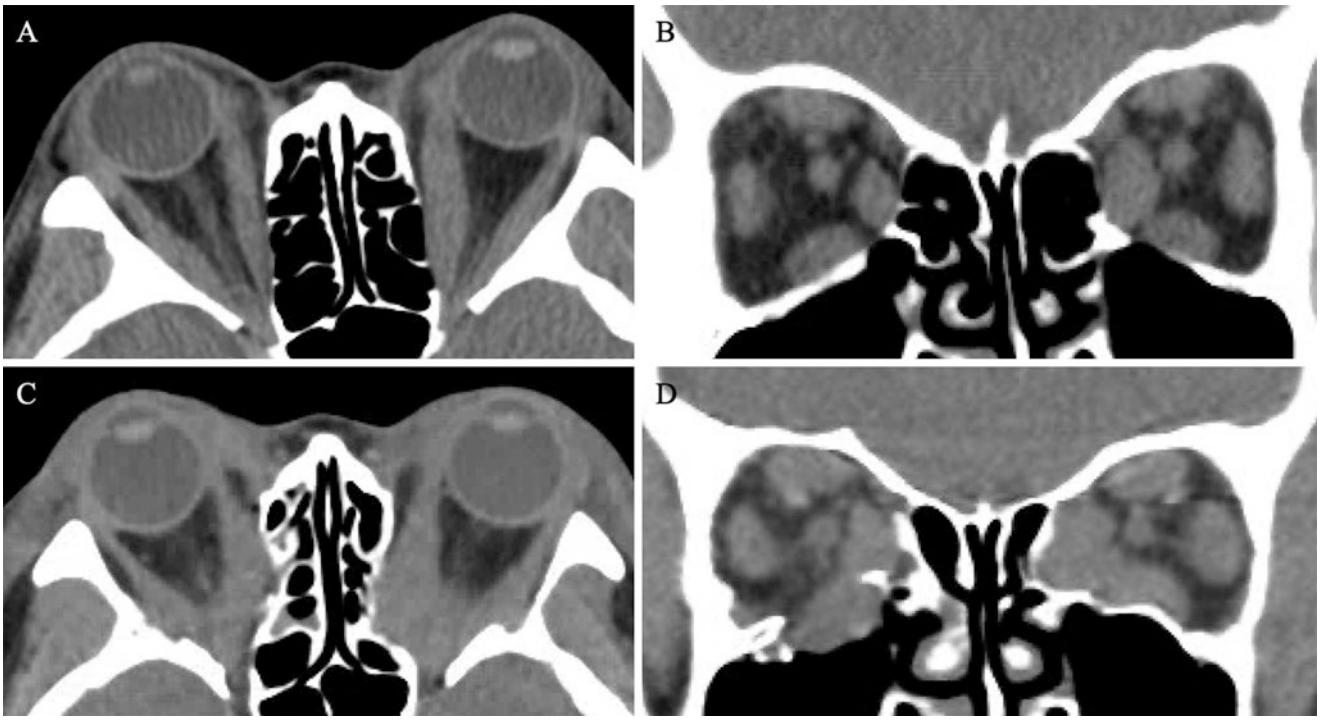


Fig. 11 An increase in either medial [16] or lateral rectus [17] muscle volume may be observed following various decompression techniques, possibly due to alterations in hydrostatic pressure after expansion of orbital volume and/or alteration of muscle vector pathways following removal of adjacent bone. These figures further expand on the case depicted in Fig. 10, to highlight imaging differences pre- and post-bilateral orbital floor, medial and lateral wall and fat decompression. (**a** and **b**) Axial and coronal computed tomography demonstrating enlargement of the extraocular muscles, left >right. (**c** and **d**) Axial and coronal computed tomography showing significant increase in the medial rectus (L > R), inferior rectus, and to a lesser degree, lateral rectus

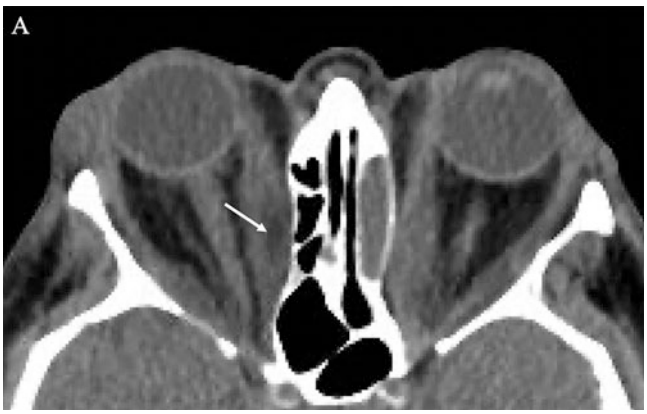


Fig. 12 A 65-year-old-female with Graves hyperthyroidism and a longstanding history of thyroid eye disease. On axial computed tomography there is evidence of EOM enlargement with intramuscular hypodensity in keeping with possible fatty degeneration

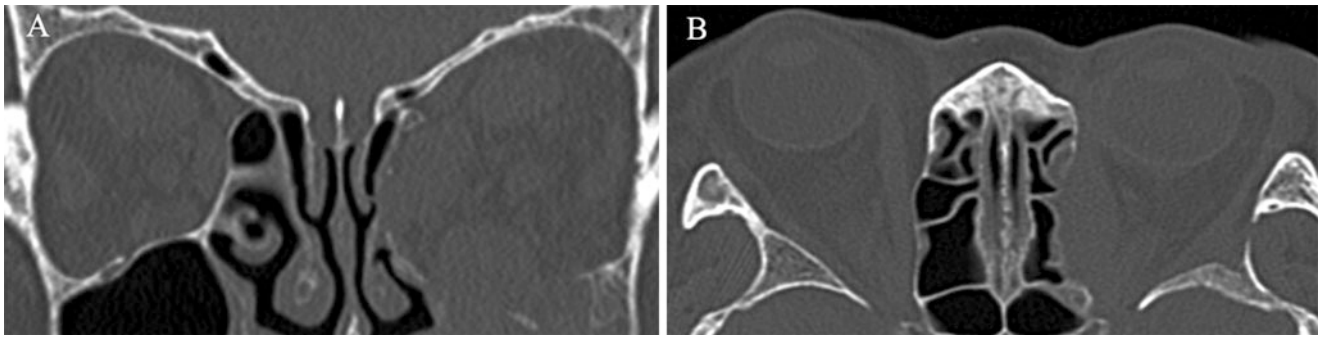


Fig. 13 (**a**) Coronal and (**b**) axial computed tomography of a patient with asymmetrical enlargement of extraocular muscles, left greater than right, following left three wall decompression

References

1. Ben Simon GJ, Syed HM, Douglas R, McCann JD, Goldberg RA. Extraocular muscle enlargement with tendon involvement in thyroid-associated orbitopathy. Am J Ophthalmol. 2004;137(6):1145–7.
2. Prat MC, Braunstein AL, Dagi Glass LR, Kazim M. Orbital fat decompression for thyroid eye disease: retrospective case review and criteria for optimal case selection. Ophthalmic Plast Reconstr Surg. 2015;31(3):215–8.
3. Del Porto L, Hinds AM, Raoof N, et al. Superior oblique enlargement in thyroid eye disease. J AAPOS. 2019;23(5):252.e251–4.
4. Harris MA, Realini T, Hogg JP, Sivak-Callcott JA. CT dimensions of the lacrimal gland in Graves orbitopathy. Ophthalmic Plast Reconstr Surg. 2012;28(1):69–72.
5. Huh HD, Kim JH, Kim SJ, Yoo JM, Seo SW. The change of lacrimal gland volume in Korean patients with thyroid-associated ophthalmopathy. Korean J Ophthalmol. 2016;30(5):319–25.
6. Bingham CM, Harris MA, Realini T, Nguyen J, Hogg JP, Sivak-Callcott JA. Calculated computed tomography volumes of lacrimal glands and comparison to clinical findings in patients with thyroid eye disease. Ophthalmic Plast Reconstr Surg. 2014;30(2):116–8.
7. Bokman CL, Ugradar S, Rootman DB. Measurement of medial wall bowing and clinical associations in thyroid eye disease. Ophthalmic Plast Reconstr Surg. 2018;34(6):557–9.
8. Tan NYQ, Leong YY, Lang SS, Htoon ZM, Young SM, Sundar G. Radiologic parameters of orbital bone remodeling in thyroid eye disease. Invest Ophthalmol Vis Sci. 2017;58(5):2527–33.
9. Kang EM, Yoon JS. Clinical and radiological characteristics of Graves' orbitopathy patients showing spontaneous decompression. J Craniomaxillofac Surg. 2015;43(1):48–52.
10. Tachibana S, Murakami T, Noguchi H, et al. Orbital magnetic resonance imaging combined with clinical activity score can improve the sensitivity of detection of disease activity and prediction of response to immunosuppressive therapy for Graves' ophthalmopathy. Endocr J. 2010;57(10):853–61.
11. Ohnishi T, Noguchi S, Murakami N, et al. Extraocular muscles in Graves ophthalmopathy: usefulness of T2 relaxation time measurements. Radiology. 1994;190(3):857–62.
12. Kirsch EC, Kaim AH, De Oliveira MG, von Arx G. Correlation of signal intensity ratio on orbital MRI-TIRM and clinical activity score as a possible predictor of therapy response in Graves' orbitopathy – a pilot study at 1.5 T. Neuroradiology. 2010;52(2):91–7.
13. Das T, Roos JCP, Patterson AJ, Graves MJ, Murthy R. T2-relaxation mapping and fat fraction assessment to objectively quantify clinical activity in thyroid eye disease: an initial feasibility study. Eye (Lond). 2019;33(2):235–43.
14. Weis E, Heran MK, Jhamb A, et al. Clinical and soft-tissue computed tomographic predictors of dysthyroid optic neuropathy: refinement of the constellation of findings at presentation. Arch Ophthalmol. 2011;129(10):1332–6.
15. Weis E, Heran MK, Jhamb A, et al. Quantitative computed tomographic predictors of compressive optic neuropathy in patients with thyroid orbitopathy: a volumetric analysis. Ophthalmology. 2012;119(10):2174–8.
16. Hu WD, Annunziata CC, Chokthaweesak W, et al. Radiographic analysis of extraocular muscle volumetric changes in thyroid-related orbitopathy following orbital decompression. Ophthalmic Plast Reconstr Surg. 2010;26(1):1–6.
17. Gupta A, Nobori A, Wang Y, Rootman D, Goldberg R. Lateral rectus muscle expands more than medial rectus following maximal deep balanced orbital decompression. Ophthalmic Plast Reconstr Surg. 2018;34(2):140–2.

Part XII

Orbital Infection

Pre-septal Orbital Cellulitis

80

Kelsey A. Roelofs and Ezekiel Weis

Contents

1 **Signs and Symptoms** 592
2 **Differential Diagnosis** 592
3 **Diagnosis** 592
4 **Treatment** 592
5 **Figures with Captions** 592
References 598

Abstract

- The orbital septum is a membranous tissue that extends from the tarsal plate to the orbital rim, where it fuses with the periorbita in a fibrous condensation known as the arcus marginalis.
- On imaging, evidence of pre-septal soft tissue swelling and inflammation in the absence of post-septal/orbital involvement is in keeping with the diagnosis of pre-septal cellulitis.
- CT is an adequate modality for assessing periorbital cellulitis. Administration of contrast is very helpful in cases of suspected infection as it optimizes visualization of pre-septal abscesses, and highlights intraorbital inflammation/infiltration. A pre-septal abscess would typically demonstrate a hypodensity in the subcutaneous space with adjacent rim enhancement.
- Thickening of the palpebral portion of the lacrimal gland may also serve as an adjunct imaging feature.
- Since CT would be the initial imaging modality used in most cases, exclusion of post-septal involvement can rely on more than "eyeballing," as the IC fat measurements of Hounsfield units (HU) is very useful. Fat typically measures in the range of −50 to −150. Inflammation/edema results in asymmetric values between the involved and uninvolved orbits.
- Imaging in cases of pre-septal cellulitis may provide additional evidence as to the origin of infection, for example, concurrent sinus disease or evidence of an odontogenic source.
- We recommend obtaining imaging if there are any clinical or serum markers suggestive of orbital cellulitis, any clinical features or medical history suggestive of other causes (e.g., history of high-grade lymphoma such as diffuse large B cell lymphoma) or a lack of response to antibiotics over 48 h.

Keywords

Pre-septal cellulitis · Periorbital inflammation

K. A. Roelofs
Division of Orbital and Ophthalmic Plastic Surgery, Stein and Doheny Eye Institutes, University of California, Los Angeles, CA, USA
e-mail: roelofs@ualberta.ca

E. Weis (✉)
Department of Ophthalmology and Visual Sciences, University of Alberta, Edmonton, AB, Canada

Department of Surgery, University of Calgary, Calgary, AB, Canada

© Springer Nature Switzerland AG 2022
G. Ben Simon et al. (eds.), *Atlas of Orbital Imaging*,
https://doi.org/10.1007/978-3-030-62426-2_66

1 Signs and Symptoms

Patients with pre-septal cellulitis most commonly present with eyelid edema and erythema. Occasionally a fluctuant pre-septal abscess can be palpated on clinical examination. Fever may be seen, more commonly in children (71%) than adults (32%) [1]; however, its presence should raise the suspicion for orbital involvement [2]. In cases of pre-septal cellulitis, there should be no limitation of extraocular movements, proptosis, chemosis, restriction of extraocular motility, change in visual acuity or color vision, or relative afferent pupillary defect. General indications for obtaining orbital imaging (typically contrast-enhanced computed tomography) include: suspicion of foreign body (FB) material, uncooperative patient with limited clinical examination, failure to improve despite appropriate initial treatment, severe eyelid edema, proptosis, ophthalmoplegia, conjunctival chemosis, deteriorating visual acuity, change in color vision, and a septic patient [3, 4].

2 Differential Diagnosis

The differential diagnosis includes inflammatory entities (idiopathic and specific orbital inflammations), ruptured dermoid cysts [5], fulminant chalazions with leakage of oil into surrounding tissues, dacryocystitis, allergic reaction, or acquired mass lesions including high-grade malignancies (for example, diffuse large B cell lymphoma), or periorbital dermal fillers with associated inflammation.

3 Diagnosis

The diagnosis of periorbital cellulitis is typically made based on clinical features. Fever, and laboratory investigations, including c-reactive protein (CRP), erythrocyte sedimentation rate (ESR), and complete blood count (CBC) often provide useful information. When there is evidence of fever, leukocytosis, and a neutrophilia or elevation of CRP/ESR, the diagnosis of orbital cellulitis (rather than pre-septal cellulitis) becomes more likely [2] and appropriate imaging should be obtained [6].

4 Treatment

While mild cases of pre-septal cellulitis can be managed with oral antibiotics, severe cases may require broad-spectrum intravenous antibiotics. Overall, the most common pathogens are *Staphylococcus aureus* and *Streptococcus pneumoniae* [7, 8]. Although *Haemophilus influenzae* was previously a common cause of pre-septal cellulitis in young children, the incidence has decreased significantly since the implementation of routine immunization with the *H. influenzae* type b vaccine [9]. Pre-septal cellulitis can arise following bug bites or local skin breakdown (especially in children) or may occur as a sequelae of dacryocystitis or sinus disease (often in adults). Therefore, empiric antibiotic choices vary by geographic area, underlying cause, and patient age. Younger children are more likely to have infections caused by a single pathogen versus older children/adults who are more likely to have polymicrobial/mixed aerobic and anaerobic pathogens [10].

5 Figures with Captions

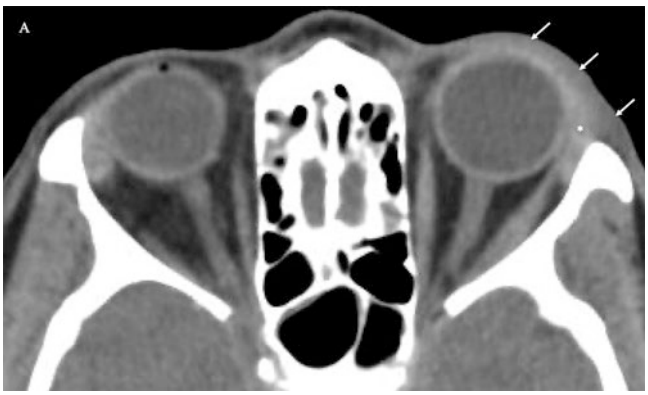


Fig. 1 A 68-year-old female presented with a two-day history of worsening left periorbital edema, erythema, and pain. (**a**) Axial noncontrast computed tomography demonstrating pre-septal tissue edema (arrows) and slight enlargement of the palpebral lobe of the lacrimal gland (asterix), consistent with pre-septal cellulitis on the left side

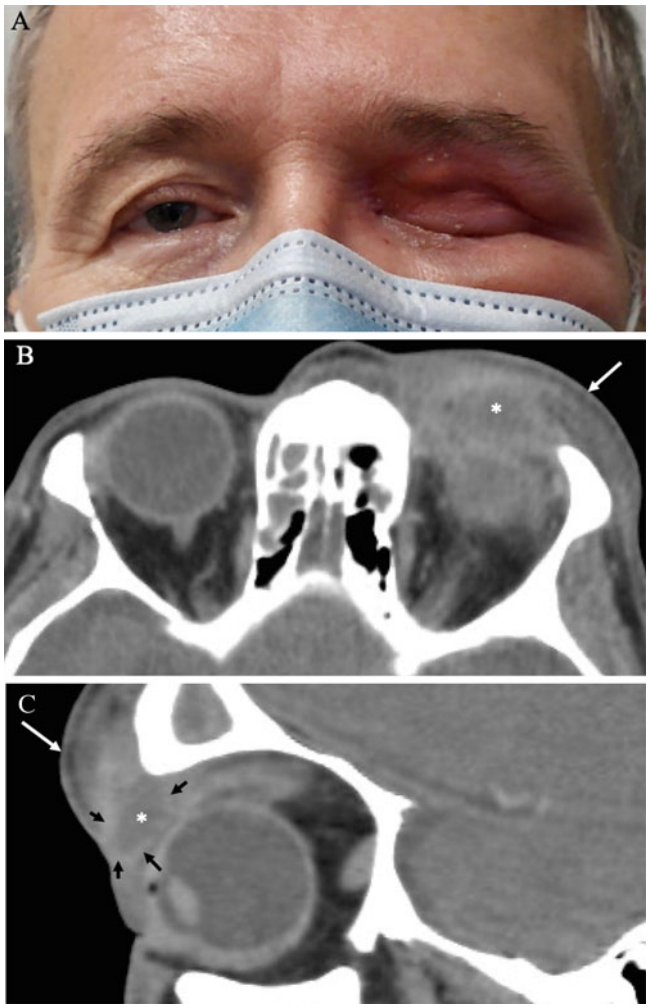


Fig. 2 (**a**) A 60-year-old male presented with a four-day history of progressive left periorbital edema, erythema, and pain. (**b**) Axial and (**c**) sagittal CE computed tomography demonstrate a moderate-sized circular hypodense fluid collection in the left superior pre-septal region (asterix) with associated adjacent soft tissue edema (white arrows) and ring enhancement (black arrows). The post-septal structures and lacrimal gland are unremarkable. These findings are in keeping with a pre-septal abscess associated with cellulitis

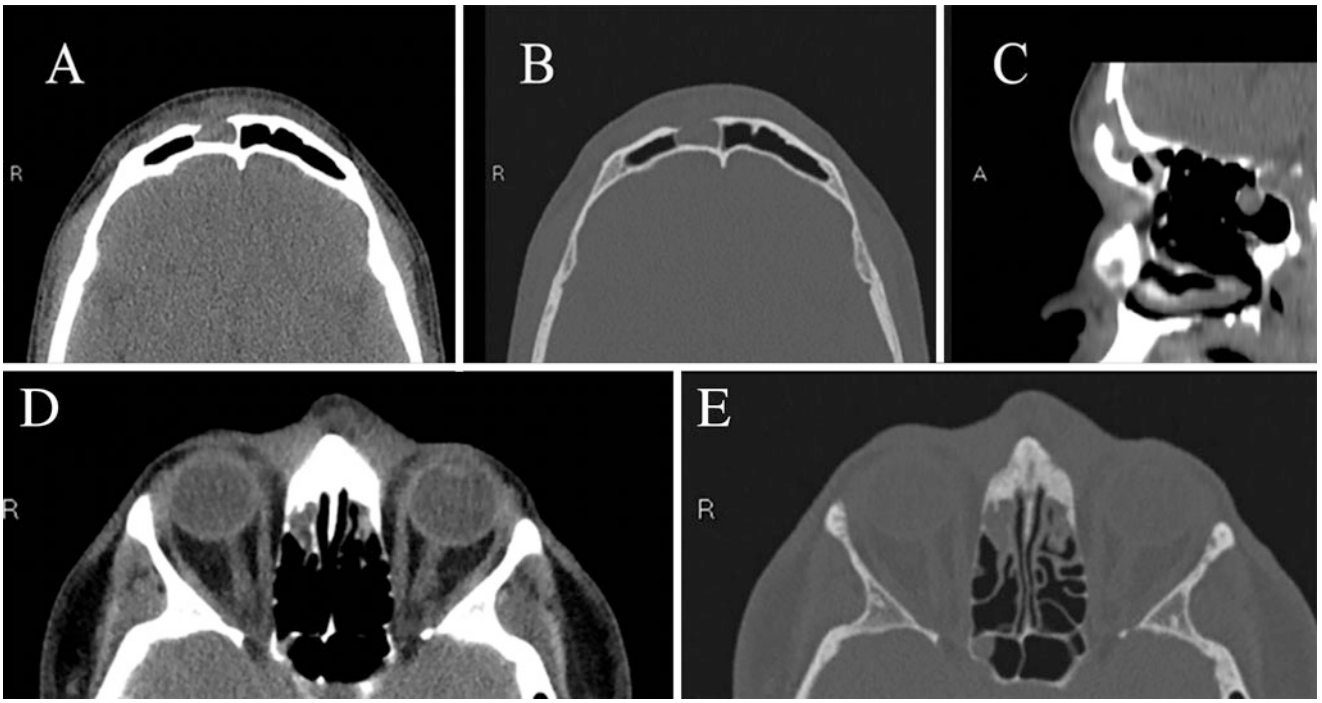


Fig. 3 Computed tomography of a 50-year-old male with Pott's puffy tumor of the right frontal sinus, subperiosteal abscess, bone destruction (**a**–**c**), and bilateral central periorbital cellulitis (**d**, **e**). Pott's puffy tumor is characterized by the triad of subperiosteal abscess, osteomyelitis, and frontal sinusitis. Patients often present with headache, periorbital/eyelid or scalp swelling, fever, and purulent nasal discharge [11, 12]. It is important for clinicians to be aware of this potentially life-threatening diagnosis and to have an appropriately low threshold to obtain neuroimaging [13] by way of contrast-enhanced CT and/or MRI, as a high proportion (72–85%) of patients will develop intracranial complications [14, 15]

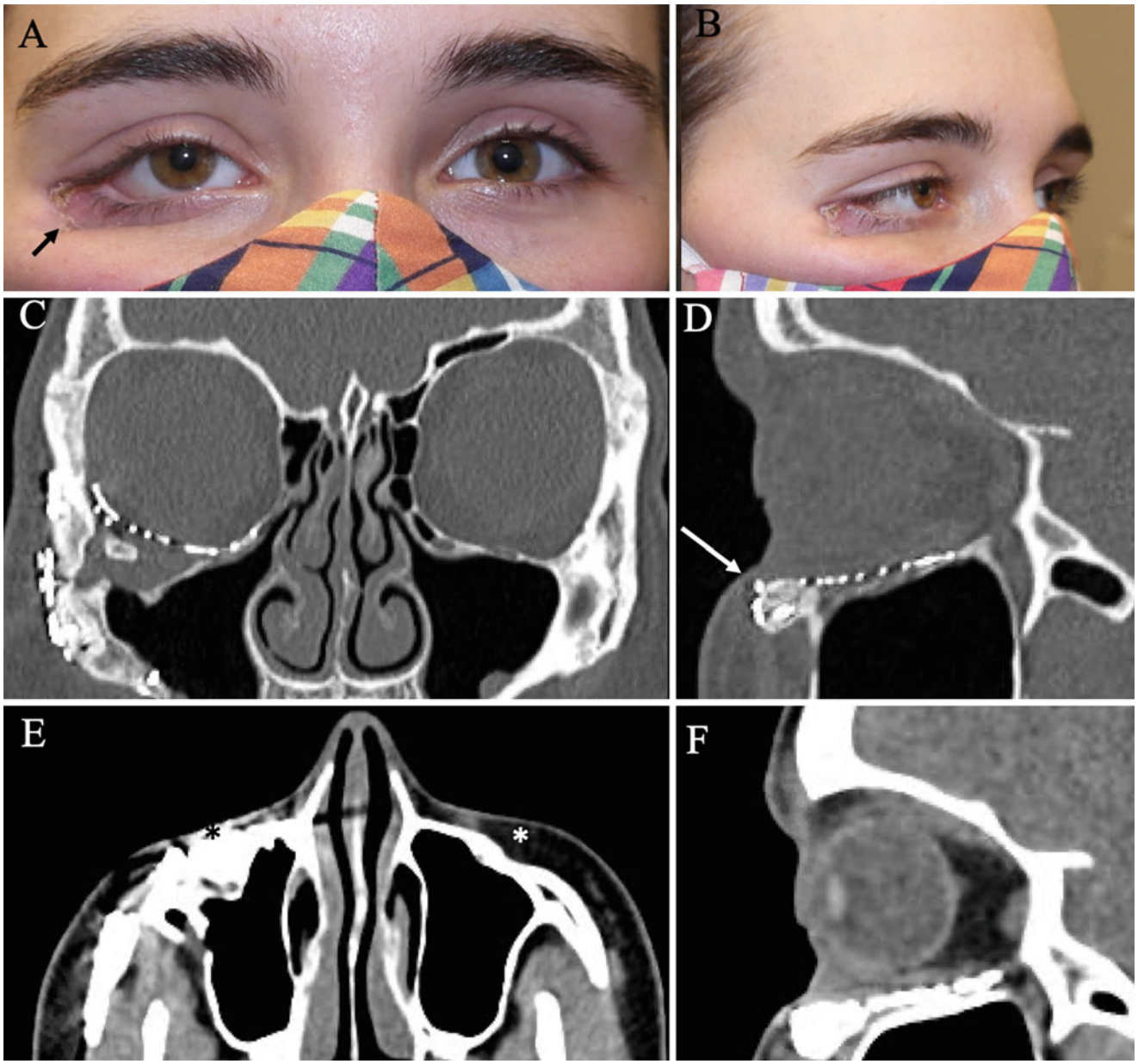


Fig. 4 A 23-year-old female presented with recurrent periorbital inflammation and discharge 2 years following facial trauma. (**a** and **b**) External photographs demonstrate right lower eyelid retraction with evidence of a draining fistula (arrow). (**c**) Coronal and (**d**) sagittal computed tomography images demonstrate previous repair of right maxillary, zygomatic, and orbital floor. On the sagittal image, the plate is noted to be very close and possibly contiguous with the skin (arrow). (**e** and **f**) Axial and sagittal soft tissue windows highlight asymmetric loss of subcutaneous space (asterix) consistent with chronic cellulitis and osteomyelitis. Clinically, a draining fistula was noted, likely secondary to infected hardware and osteomyelitis. The implant was subsequently removed along with debridement of the fistulous tract, bone, and reconstruction of the lower eyelid

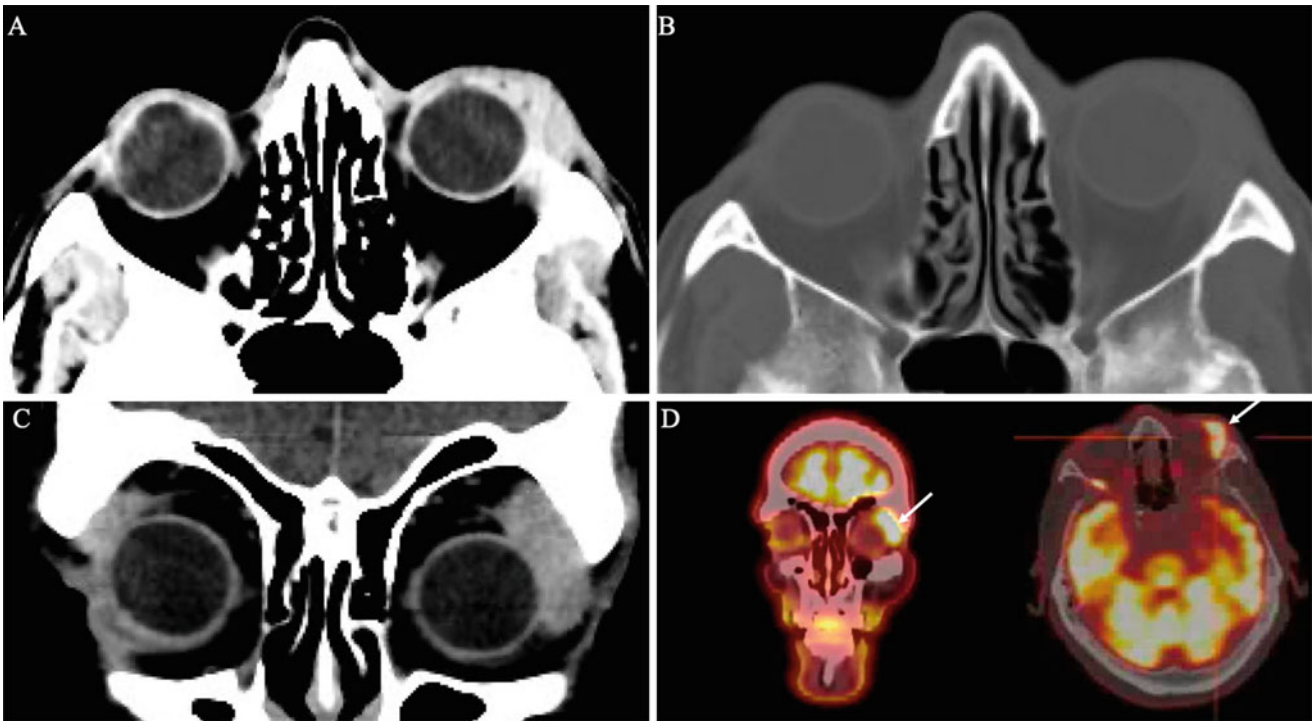


Fig. 5 An 83-year-old male presented with a progressive left periorbital fullness. He denied pain or diplopia. (**a** and **b**) Axial and (**c**) coronal computed tomography demonstrate a soft tissue mass arising within the left lacrimal fossa with homogenous intense contrast enhancement. An incisional biopsy of the mass was consistent with mucosa-associated lymphoid tissue (MALT) lymphoma. (**d**) Staging workup with PET-CT shows hypermetabolism in the left lacrimal gland and also identified multiple hypermetabolic peri-esophageal lymph nodes and pulmonary nodules

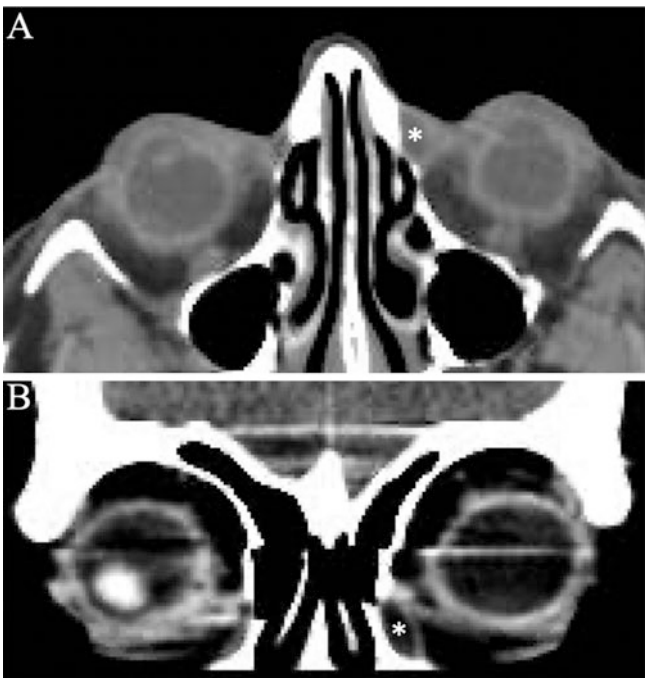


Fig. 6 A 73-year-old female presented with a five-year history of recurrent left periorbital swelling and persistent epiphora. (**a**) Axial and (**b**) coronal computed tomography demonstrates enlargement of the left nasolacrimal sac (asterix) in keeping with formation of an acquired dacryocystocele secondary to nasolacrimal duct obstruction and chronic dacryocystitis

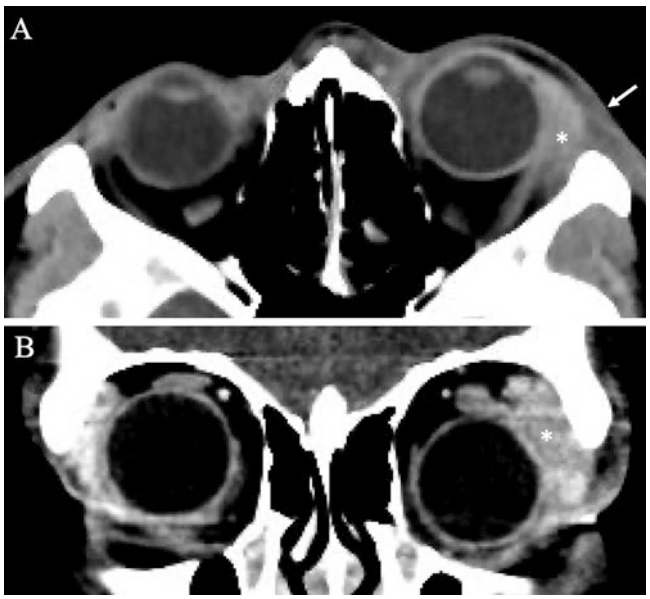


Fig. 7 A 25-year-old male presented with a three-week history of left periorbital swelling and pain. (**a**) On axial and (**b**) coronal computed tomography, diffuse enlargement of the left lacrimal gland (asterix) is appreciated, along with overlying pre-septal edema (arrow). This patient underwent incision biopsy which revealed evidence of chronic sclerosing inflammation treated successfully with a course of oral corticosteroids

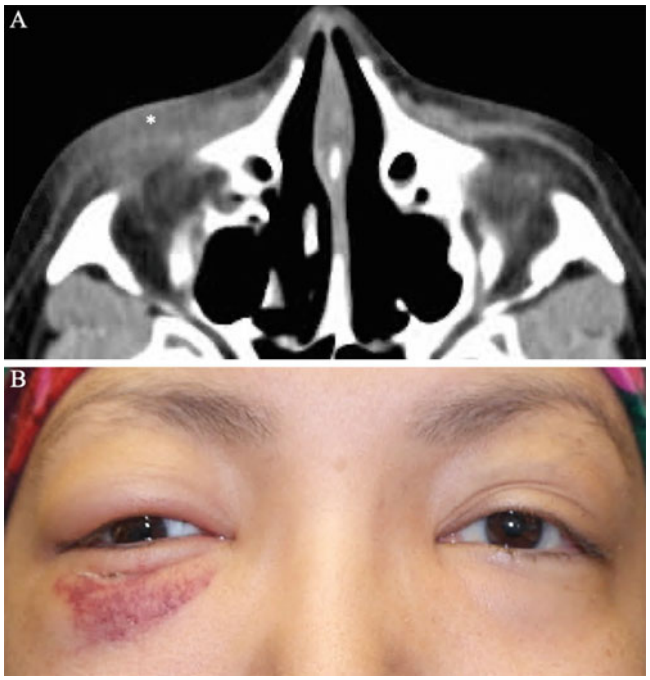


Fig. 8 A 34-year-old female was referred for painless right periorbital edema and erythema which were present for 4 months. (**a**) Axial computed tomography show thickening and hyperdensity of the right pre-septal and mid-face soft tissue. (**b**) Following incisional biopsy, the diagnosis of cutaneous T cell lymphoma was confirmed

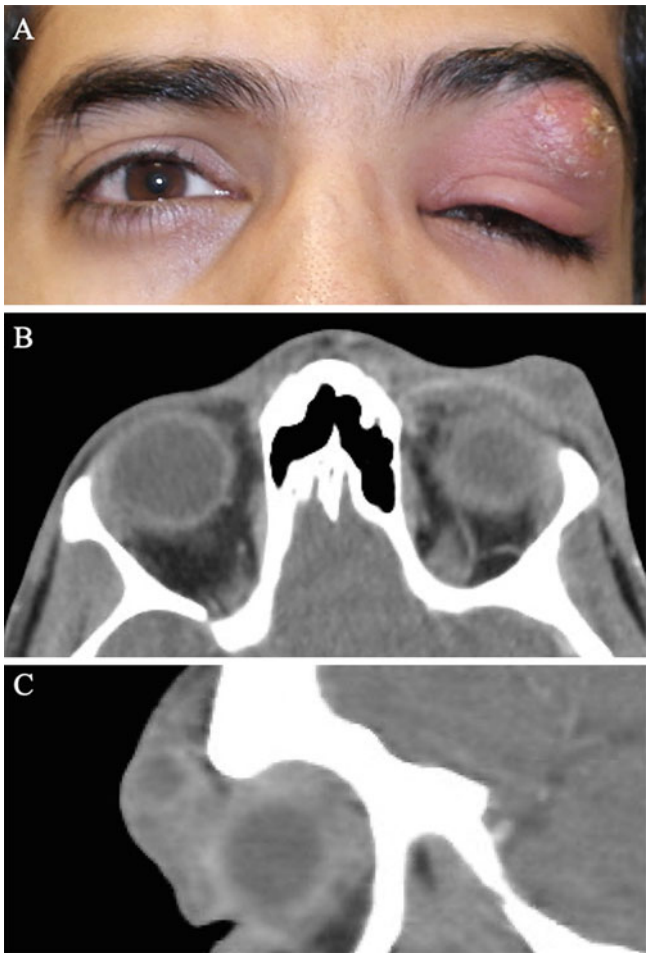


Fig. 9 A 40-year-old male was referred with a history of a left eyebrow lesion present for 1 month with increasing erythema, edema, and pain over the past 5 days. (**a**) On examination, there was evidence of left periocular erythema and edema, and a cystic lesion with an overlying fistula. (**b**) Axial and (**c**) sagittal contrast-enhanced computed tomography demonstrate pre-septal soft tissue thickening and a focal mass-like bulge superolateral to the left globe with mixed fat and soft tissue density. Excisional biopsy was performed and on histopathology, the lesion was found to be in keeping with a pilomatrixoma

References

1. Ferguson MP, McNab AA. Current treatment and outcome in orbital cellulitis. Aust N Z J Ophthalmol. 1999;27(6):375–9.
2. Santos JC, Pinto S, Ferreira S, Maia C, Alves S, da Silva V. Pediatric preseptal and orbital cellulitis: a 10-year experience. Int J Pediatr Otorhinolaryngol. 2019;120:82–8.
3. Tsirouki T, Dastiridou AI, Ibanez Flores N, et al. Orbital cellulitis. Surv Ophthalmol. 2018;63(4):534–53.
4. Goldberg F, Berne AS, Oski FA. Differentiation of orbital cellulitis from preseptal cellulitis by computed tomography. Pediatrics. 1978;62(6):1000–5.
5. Dizon M, Ozturk A, Redett RJ, Izbudak I. Neuroimaging findings in a child with dumbbell-shaped frontosphenoidal dermoid cyst presenting as preseptal cellulitis. Pediatr Radiol. 2009;39(8):850–3.
6. Ohana-Sarna-Cahan L, Hurvitz N, Gross I, Cohen A, Hashavya S. Factors associated with increased risk of pediatric orbital cellulitis-who should be scanned? Pediatr Emerg Care. 2020.
7. Chaudhry IA, Shamsi FA, Elzaridi E, Al-Rashed W, Al-Amri A, Arat YO. Inpatient preseptal cellulitis: experience from a tertiary eye care Centre. Br J Ophthalmol. 2008;92(10):1337–41.
8. Botting AM, McIntosh D, Mahadevan M. Paediatric pre- and post-septal peri-orbital infections are different diseases. A retrospective review of 262 cases. Int J Pediatr Otorhinolaryngol. 2008;72(3):377–83.
9. Ambati BK, Ambati J, Azar N, Stratton L, Schmidt EV. Periorbital and orbital cellulitis before and after the advent of *Haemophilus influenzae* type B vaccination. Ophthalmology. 2000;107(8):1450–3.
10. Garcia GH, Harris GJ. Criteria for nonsurgical management of subperiosteal abscess of the orbit: analysis of outcomes 1988–1998. Ophthalmology. 2000;107(8):1454–6; discussion 1457–58.
11. Avcu G, Belet N, Kurnaz SC, Karli A, Sensoy G. Pott's puffy tumor in a 12-year-old boy. Pediatr Int. 2015;57(1):163–5.
12. Linton S, Pearman A, Joganathan V, Karagama Y. Orbital abscess as a complication of Pott's puffy tumour in an adolescent male. BMJ Case Rep. 2019;12(7):e229664.
13. Palabiyik FB, Yazici Z, Cetin B, Celebi S, Hacimustafaoglu M. Pott puffy tumor in children: a rare emergency clinical entity. J Craniofac Surg. 2016;27(3):e313–6.
14. Ketenci I, Unlu Y, Tucer B, Vural A. The Pott's puffy tumor: a dangerous sign for intracranial complications. Eur Arch Otorhinolaryngol. 2011;268(12):1755–63.
15. Nisa L, Landis BN, Giger R. Orbital involvement in Pott's puffy tumor: a systematic review of published cases. Am J Rhinol Allergy. 2012;26(2):e63–70.

Orbital Cellulitis

81

Kelsey A. Roelofs and Ezekiel Weis

Contents

1 **Signs and Symptoms** 600
2 **Differential Diagnosis** 600
3 **Diagnosis** 600
4 **Treatment** 600
5 **Figures with Captions** 600
References 603

Abstract

- Contrast enhanced CT is the preferable modality of choice for detecting both the soft tissue component (cellulitis and abscess formation, presence of gas) as well as bony involvement (thinning, destruction, signs of osteomyelitis, detecting dental origin).
  - Computed tomography may also be advantageous in certain patients, including young children, who may be able to avoid a general anesthetic required for MRI.
- Postseptal fat stranding is one of the hallmark features of orbital cellulitis. It is useful to measure the fat density in comparison to the contralateral orbit (normal fat measures in the negative range of −50 to −150, inflammation/edema will cause a relative increase in HU values)
- MRI is beneficial in cases where intracranial complications are suspected: cavernous sinus involvement/thrombosis, meningeal involvement, intracranial empyema, and abscess formation. The protocol must include both T1 and T2 fat-saturated images and DWI. T2 FLAIR postcontrast is highly sensitive for depicting meningeal involvement.
- When the cavernous sinus is involved, CTA/V may show the thrombosed sinus as well as vasculitis/vasospasm.
- Both nonaxial and axial globe displacement can occur – occasionally this is severe enough to cause tenting of the optic-nerve globe junction (<130°).
- The presence of gas foci on CT (or signal void on MRI) should raise the suspicion for an anaerobic pathogen and when found within a subperiosteal abscess, is an indication for surgical drainage.
- In cases of orbital cellulitis arising from an odontogenic source, abnormal periapical lucency and widening of the periodontal ligament space can be seen on CT.
- Orbital cellulitis can present with or without an associated abscess, and abscesses may be located in either the intraconal soft tissues or subperiosteal plane.
- The risk of intracranial complications is highest when the frontal sinus is involved as infection can spread through the thin bone of the anterior cranial fossa.
- Rarely, in atypical cases, proton magnetic resonance spectroscopy may be helpful to provide information and narrow the differential diagnosis [1].

K. A. Roelofs
Division of Orbital and Ophthalmic Plastic Surgery, Stein and Doheny Eye Institutes, University of California, Los Angeles, CA, USA

E. Weis (✉)
Department of Ophthalmology and Visual Sciences, University of Alberta, Edmonton, AB, Canada

Department of Surgery, University of Calgary, Calgary, AB, Canada
e-mail: ezekiel_weis@post.harvard.edu

© Springer Nature Switzerland AG 2022
G. Ben Simon et al. (eds.), *Atlas of Orbital Imaging*,
https://doi.org/10.1007/978-3-030-62426-2_67

- Compared to orbital inflammation and lymphoid lesions, orbital cellulitis tends to have a higher ADC ratio [2].

Keywords

Orbital cellulitis · Meningitis · Septic cavernous sinus thrombosis

1 Signs and Symptoms

Pain with extra-ocular movements (EOM), chemosis, diplopia and EOM limitation, globe displacement and/or proptosis, a relative afferent pupillary defect/compressive optic neuropathy are often seen in cases of orbital cellulitis and not commonly seen in preseptal cellulitis. Occasionally, intraorbital pressure may rise high enough to cause a central retinal artery and/or cilioretinal artery occlusion [3].

All cases with clinical findings suggestive of orbital cellulitis should undergo imaging. Repeat imaging is recommended in the setting of clinical deterioration, or if symptoms develop to suggest a septic cavernous sinus thrombosis, including bilateral progression of ocular symptoms, involvement of cranial nerves III–VI, V1, and/or V2, altered mental status and visual loss [4]. Following the initiation of broad spectrum intravenous antibiotics, some degree of early clinically improvement, such as a decrease in pain, swelling, erythema, is usually observed within 36–72 h. A failure to improve should prompt re-consideration of the differential diagnosis and is another indication for repeat orbital imaging.

2 Differential Diagnosis

The differential diagnosis is broad and includes inflammatory entities (idiopathic orbital inflammation, sarcoidosis, Kawasaki disease [5]), mass lesions (mucocele [6]) xanthogranulomatous disease [7], and neoplastic entities [8], including orbital lymphoma [9] and rhabdomyosarcoma [10]. Occasionally intraocular tumors (retinoblastoma [11, 12] or choroidal melanoma [13]) can incite a similar clinical presentation of fulminant orbital inflammation. Imaging can be particularly helpful in these cases, as an intact ocular wall with no intraocular abnormality visualized on MRI favors inflammation over tumor invasion [11].

3 Diagnosis

Most cases of orbital cellulitis can be diagnosed clinically; however, imaging allows for both increased diagnostic sensitivity and optimization of therapeutic planning [14]. When CT is inconclusive, MRI may be more sensitive at detecting postseptal soft tissue involvement.

4 Treatment

Broad-spectrum intravenous antibiotics form the mainstay of management for most cases of orbital cellulitis. When a subperiosteal abscess is present, initial treatment with IV antibiotics may be considered in children <9 years of age; however, if the abscess occurs in a non-medial location, is large (>3.8 mL) or is associated with frontal sinusitis, evidence of intracranial complications, findings on imaging which are suspicious for an anaerobic pathogen (ie. gas) or evidence of optic nerve dysfunction, urgent surgical intervention is required.

5 Figures with Captions

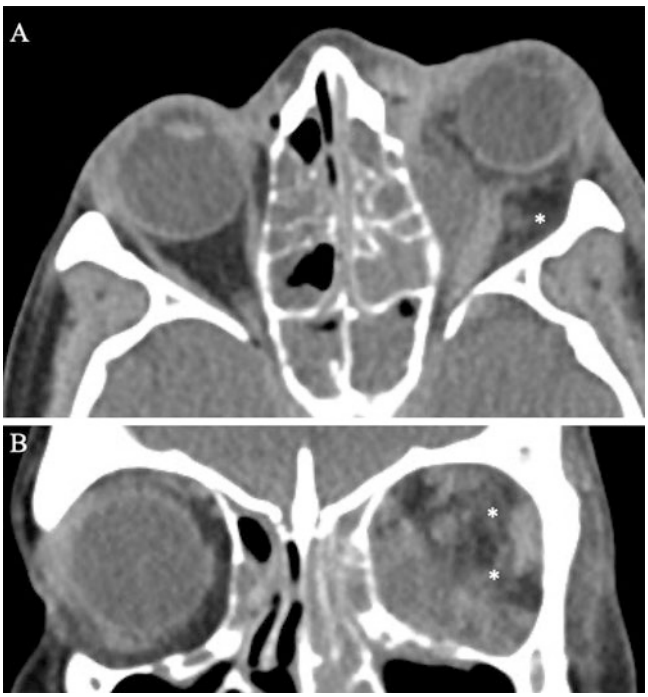


Fig. 1 (**a**) Axial and (**b**) coronal NE computed tomography demonstrating significant left proptosis. There is extensive mucosal thickening along with heterogenous content in the adjacent ethmoid, sphenoid sinuses, and medially there is a subperiosteal intermediate-density fluid collection measuring 2.2 cm in greatest dimension. Moreover, there is evidence of diffuse postseptal fat stranding (asterix), a hallmark feature of orbital cellulitis [16]

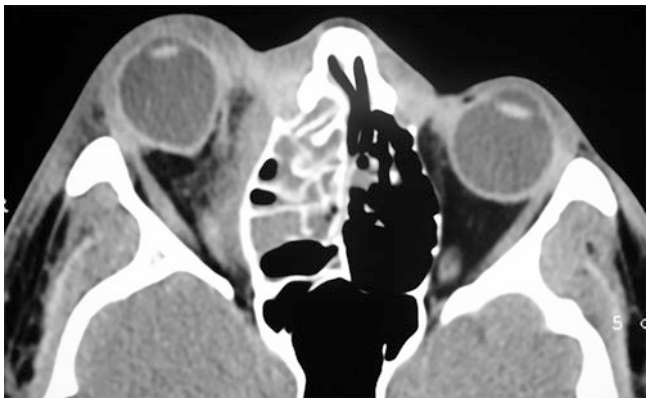


Fig. 2 Computed tomography demonstrating tenting of the optic-nerve globe junction (<130°) 2nd to right orbital cellulitis with medial subperiosteal collection and concurrent ethmoid sinusitis [17]. (Courtesy of the editors)

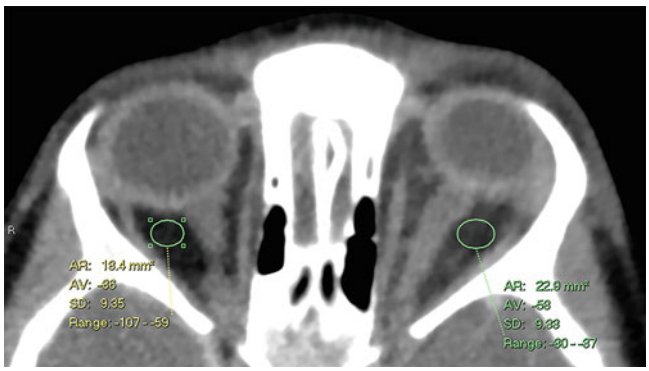


Fig. 3 NECT of a 3-YOM with left orbital cellulitis, note higher HU measurements (less negative) on the involved side evident of IC fat stranding. (Courtesy of the editors). When measuring try to avoid adjacent structures such as vessels or EOM in order to get a more accurate measurement

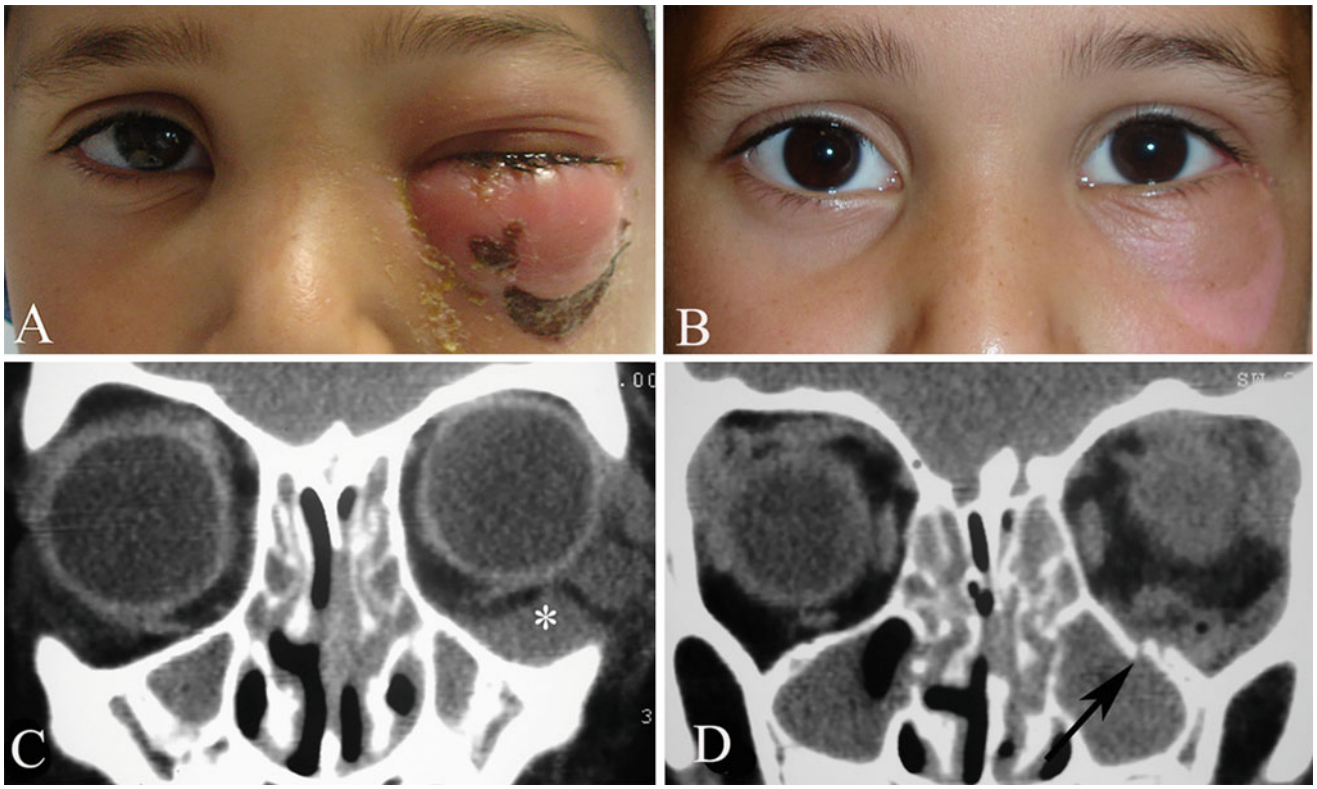


Fig. 4 (**a**) Pre- and (**b**) post-treatment clinical photographs of a 6-year-old male with nonresolving orbital cellulitis, several days after blunt trauma. History was notable for a recent upper respiratory tract infection. (**c** and **d**) Coronal NECT demonstrates a soft tissue collection along the inferotemporal orbital floor along with an orbital floor fracture. The patient had coexistent pan-sinusitis, and most likely the fracture served as port of entry to the orbit. (Courtesy of the editors)

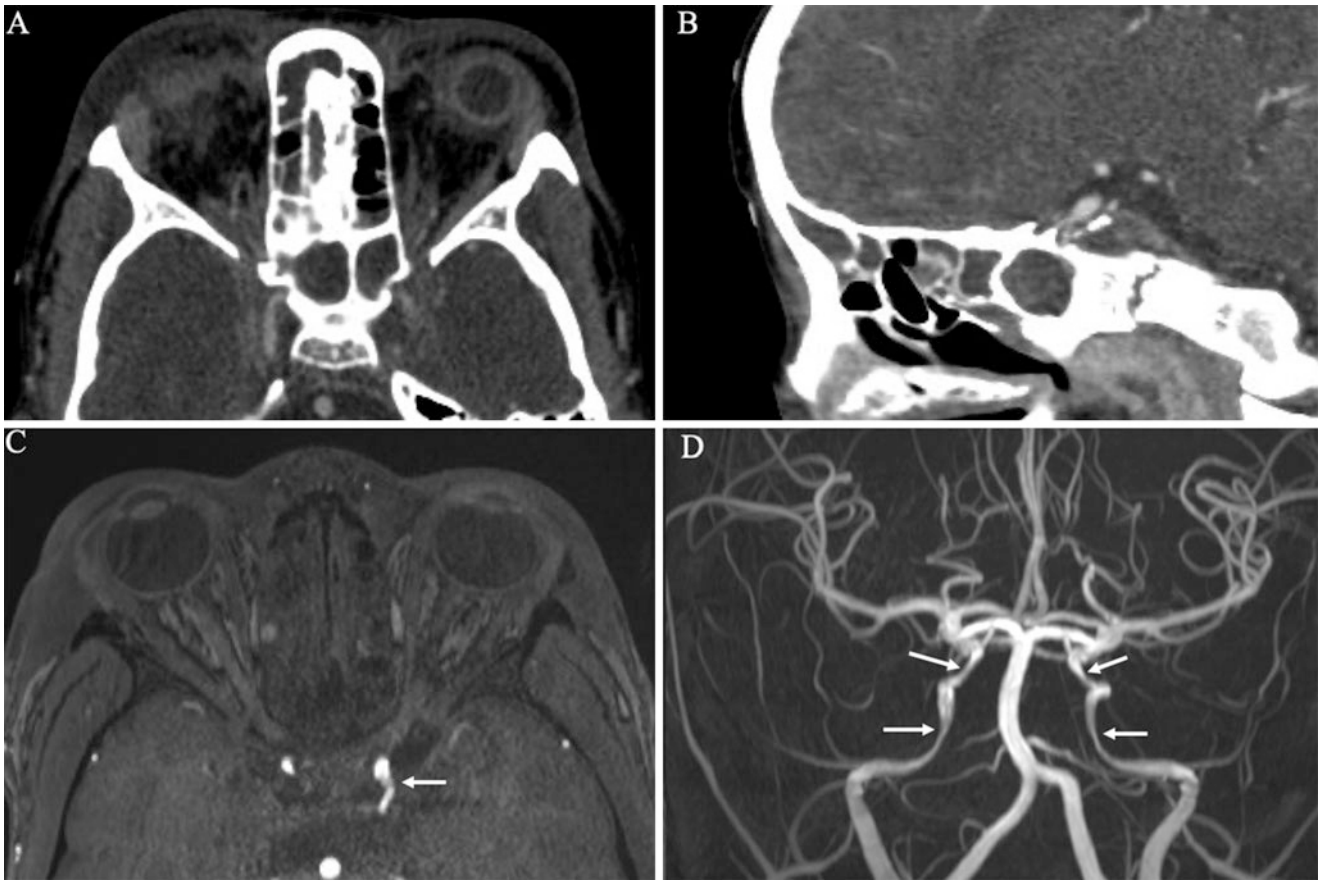


Fig. 5 (**a**) Axial and (**b**) sagittal computed tomography demonstrating bilateral sphenoid sinusitis with expansion of the lateral walls of the cavernous sinus and narrowing of the intracavernous carotid artery, presumably secondary to vasospasm or infectious arteritis [4]. On magnetic resonance imaging, (**c**) axial time of flight sequences and (**d**) maximum intensity projection images demonstrate severe narrowing of the distal lacerum and cavernous segments of the internal carotid artery (arrows)

References

1. Pakdel F, Hadizadeh H, Pirmarzdashty N, Kiavash V. Masquerading orbital abscess following attempted Hydrogel Scleral Buckle removal: diagnostic value of orbital magnetic resonance spectroscopy. Orbit. 2015;34(4):179–82.
2. Kapur R, Sepahdari AR, Mafee MF, et al. MR imaging of orbital inflammatory syndrome, orbital cellulitis, and orbital lymphoid lesions: the role of diffusion-weighted imaging. AJNR Am J Neuroradiol. 2009;30(1):64–70.
3. Keorochana N, Vongkulsiri S, Choontanom R. Combined central retinal vein, central retinal artery and cilioretinal artery occlusion with ischemic macular hole secondary to severe orbital cellulitis after black fly bite. Int Med Case Rep J. 2019;12:125–34.
4. Branson SV, McClintic E, Yeatts RP. Septic cavernous sinus thrombosis associated with orbital cellulitis: a report of 6 cases and review of literature. Ophthalmic Plast Reconstr Surg. 2019;35(3):272–80.
5. Cerman E, Eraslan M, Turhan SA, Usta SA, Akalin F. Orbital cellulitis presenting as a first sign of incomplete kawasaki disease. Case Rep Ophthalmol. 2013;4(3):294–8.
6. Ch'ng SW, Pillai MB, Morton C. Frontal sinus mucoceles presenting in the upper eyelid: an easily missed diagnosis. BMJ Case Rep. 2012;2012
7. Das A, Gupta A, Naina HVK. Orbital cellulitis as the initial presentation of Langerhans cell histiocytosis in an adult patient. Am J Hematol. 2017;92(6):591–2.
8. Atik A, Krilis M, Shannon K. Small cell neuroendocrine carcinoma masquerading as cellulitis and causing blindness via bilateral orbital involvement. Orbit. 2013;32(3):197–9.
9. Moon HR, Park GH, Jung JM, et al. A case of anaplastic large-cell lymphoma mimicking preseptal cellulitis. Clin Exp Dermatol. 2014;39(1):77–8.
10. Shields CL, Shields JA, Honavar SG, Demirci H. Clinical spectrum of primary ophthalmic rhabdomyosarcoma. Ophthalmology. 2001;108(12):2284–92.
11. Chawla B, Duraipandi K, Sharma S. MRI in retinoblastoma with orbital cellulitis. *Ophthalmology.* 2013;120(6):1308-1309 e1301-1304.
12. Mullaney PB, Karcioglu ZA, Huaman AM, Al-Mesfer S. Retinoblastoma associated orbital cellulitis. Br J Ophthalmol. 1998;82(5):517–21.

13. Singh P, Sen S, Banerjee M, Meel R. Choroidal melanoma masquerading as orbital cellulitis. BMJ Case Rep 2018 Dec 9;11 (1):e227486. https://doi.org/10.1136/bcr-2018-227486
14. Younis RT, Anand VK, Davidson B. The role of computed tomography and magnetic resonance imaging in patients with sinusitis with complications. Laryngoscope. 2002;112(2):224–9.
15. Wong SJ, Levi J. Management of pediatric orbital cellulitis: a systematic review. Int J Pediatr Otorhinolaryngol. 2018;110:123–9.
16. Pahwa S, Sharma S, Das CJ, Dhamija E, Agrawal S. Intraorbital Cystic Lesions: An Imaging Spectrum. Curr Probl Diagn Radiol. 2015;44(5):437–48.
17. Lindsay RA, Weiss AH, Kelly JP, Anderson VC, Lindsay TH, Cabrera MT. Clinical Outcomes in Children With Orbital Cellulitis and Radiographic Globe Tenting. Ophthalmic Plast Reconstr Surg. 2018;34(4):329–32.

Mucocele with Orbital Involvement

82

Kelsey A. Roelofs and Ezekiel Weis

Contents

1 **Signs and Symptoms** 605
2 **Differential Diagnosis** 606
3 **Diagnosis** 606
4 **Treatment** 606
5 **Figures with Captions** 606
References 610

Abstract

- On imaging, virtually all cases of mucoceles with orbital involvement will have evidence of sinus opacification and 80% have evidence of bone loss between the involved sinus and orbit.
- On computed tomography imaging, mucoceles appear as a cystic expansion of the involved sinus with heterogenous content, ranging in densities depending on viscosity of the secretion. Proteinaceous and inspissated material usually appear hyperdense and may overlap with blood or fungal disease (mycetoma).
- Similarly, on magnetic resonance imaging, T1 and T2 intensities rely on the content and chronicity. Hence, mucoceles can appear hypointense on T1 and hyperintense on T2; however, if the mucinous secretions become desiccated or purulent, their intensity can increase on T1 and decrease on T2. Dark signal on both sequences should raise the possibility of fungal infection.
- Mucoceles most commonly arise from the frontal sinus (70%), erode through the orbital roof and cause inferior displacement of the globe.
  - Mucoceles arising from the ethmoid sinus (12%) result in lateral globe displacement and resultant hypertelorism.

Keywords

Mucocele · Paranasal sinus obstruction · Globe displacement · Mucocele

1 Signs and Symptoms

Most patients (93%) have a history of prior sinus surgery, chronic sinusitis, or trauma [1]. Presenting symptoms of mucoceles directly relate to the underlying sinus pathology and the mechanical effects on the orbital contents. Symptoms may include a history of nasal congestion, hyposmia, and periorbital pain [2]. On examination, periorbital [3] or facial swelling [4], axial or nonaxial globe displacement [5], reduced ocular motility, and signs of optic nerve compression may be seen [1, 6, 7]. Rarely, frontal sinus mucoceles may present with spontaneous eyelid ecchymosis [8]. Although mucoceles of the sphenoid sinus are relatively uncommon,

K. A. Roelofs
Division of Orbital and Ophthalmic Plastic Surgery, Stein and Doheny Eye Institutes, University of California, Los Angeles, CA, USA

E. Weis (✉)
Department of Ophthalmology and Visual Sciences, University of Alberta, Edmonton, AB, Canada

Department of Surgery, University of Calgary, Calgary, AB, Canada
e-mail: ezekiel_weis@post.harvard.edu

© Springer Nature Switzerland AG 2022
G. Ben Simon et al. (eds.), *Atlas of Orbital Imaging*,
https://doi.org/10.1007/978-3-030-62426-2_68

they are more likely to present with cranial nerve palsies due to their close proximity to critical structures at the orbital apex and cavernous sinus [9].

2 Differential Diagnosis

The differential diagnosis for a mucocele includes solid masses, infectious etiologies (pre-septal or orbital cellulitis and fungal infection), congenital entities (dermoid cyst, cephalocele, and meningocele), acquired lesions (varix and optic nerve sheath meningocele), and parasitic cysts (hydatid cyst) [10].

3 Diagnosis

Diagnosis is confirmed on CT and/or MRI.

4 Treatment

Surgical intervention is required for most mucoceles and imaging is necessary for diagnosis and management planning [11]. Preoperative imaging is essential to minimize the risk of iatrogenic injury as mucoceles can significantly distort normal anatomy [12]. The choice of surgical approaches depends on both the extent and location of the lesion. Many mucoceles can be successfully managed with endoscopic marsupialization [13, 14]; however, in some instances, a combined transorbital and transnasal endoscopic approach is required [15, 16]. Image-guided navigational systems are particularly helpful in these cases, especially when bony landmarks are missing [17]. In cases with both intraorbital and intracranial components [18], or mucoceles arising secondary to sinus ostium obstruction from a tumor [19], an open surgical techniques may be preferred. Correcting the underlying obstruction is imperative to preventing recurrences.

5 Figures with Captions

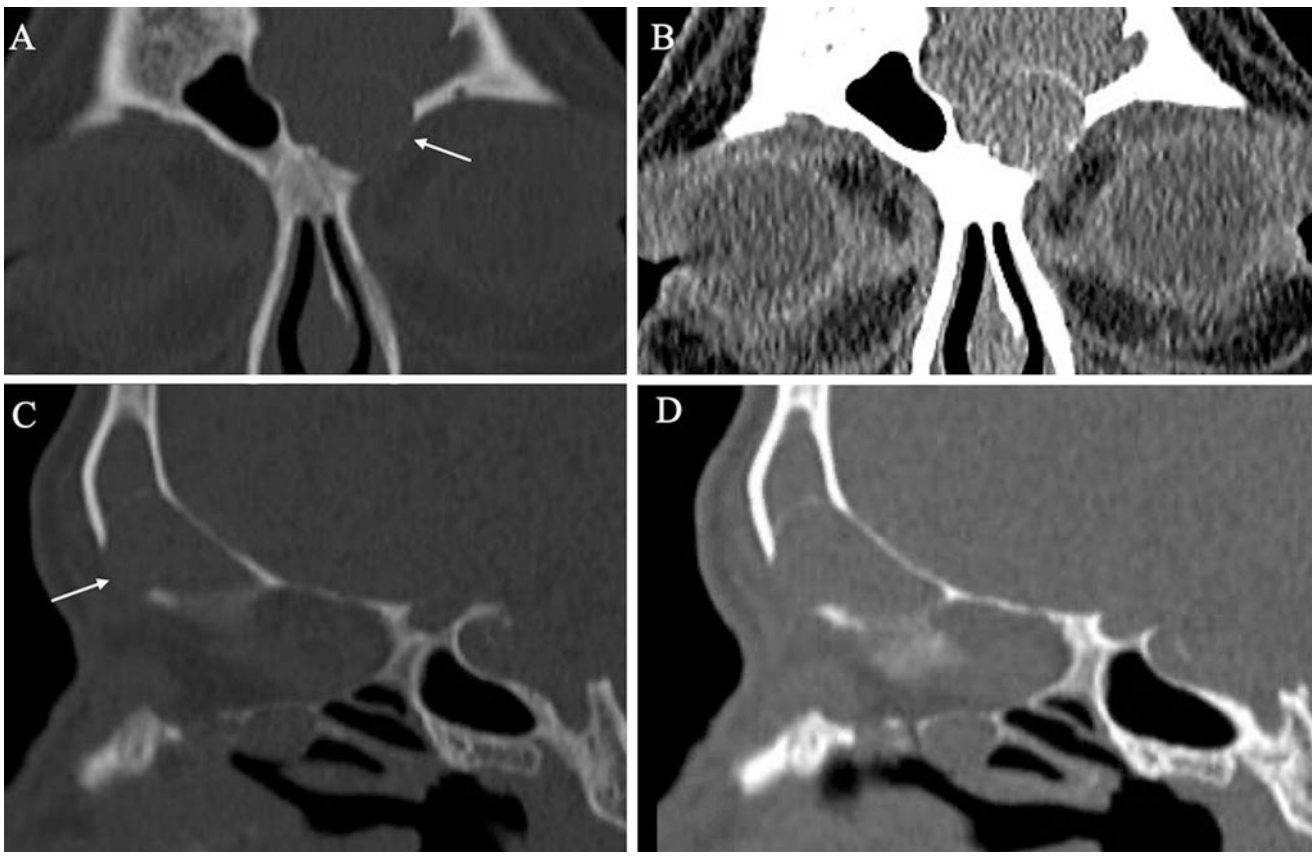


Fig. 1 (**a** and **b**) Coronal and (**c** and **d**) sagittal computed tomography demonstrating a frontal sinus mucocele with minimal involvement of the left orbit (arrows)

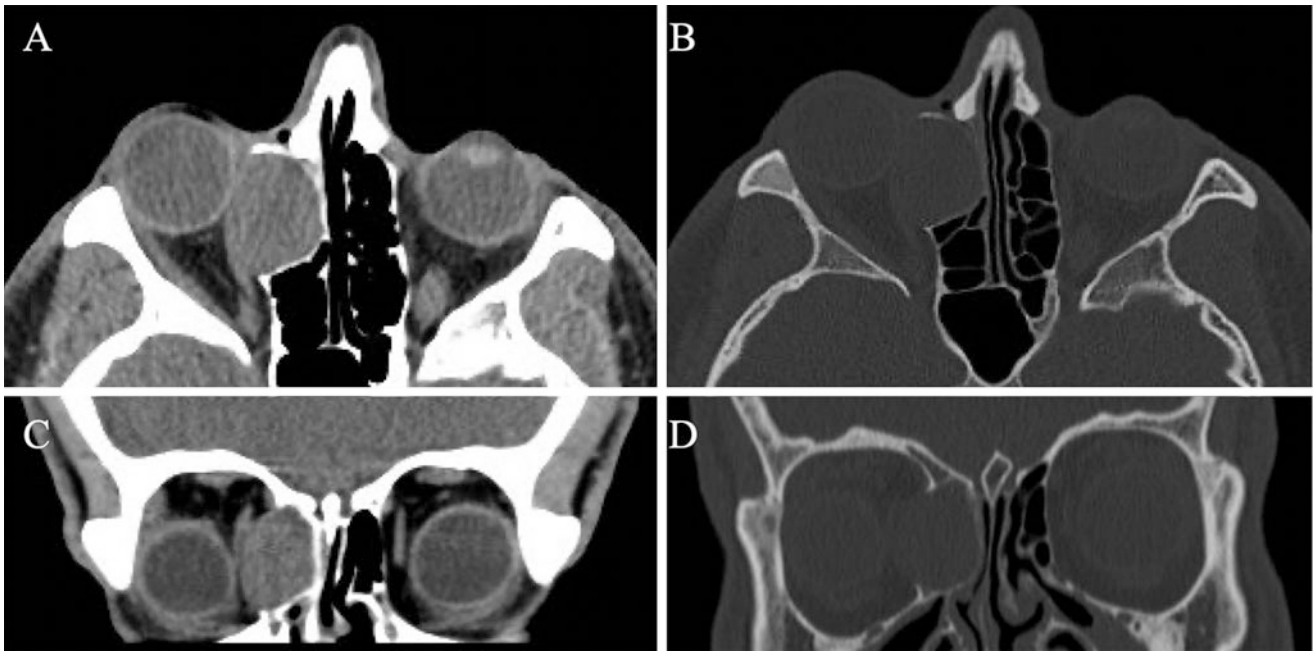


Fig. 2 (**a** and **b**) Axial and coronal (**c** and **d**) NE computed tomography images demonstrating right ethmoid sinus mucocele with thinning of medial orbital wall and lateral displacement of the globe. Note the heterogenous appearance of the lesion, with a density resembling soft tissue. The apparent absence of the medial orbital wall on bone window does not necessarily imply bone destruction, but rather marked thinning and remodeling with intact periorbita. Smooth remodeling is suggestive of a benign lesion

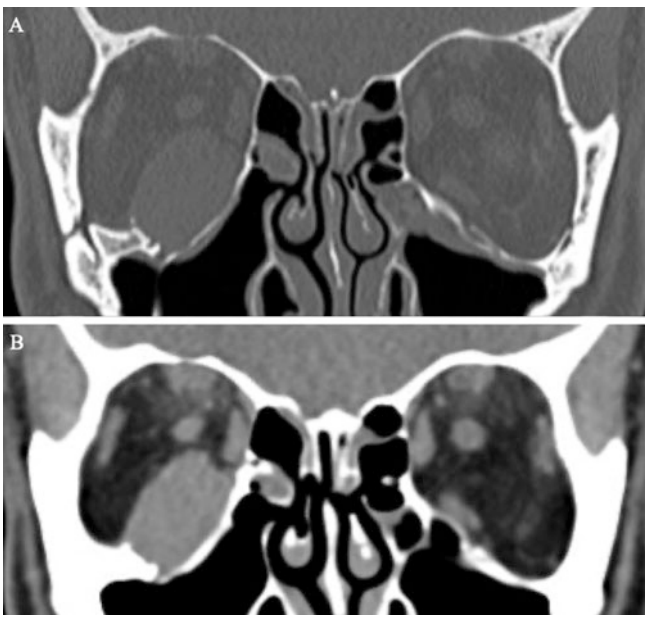


Fig. 3 Coronal computed tomography on (**a**) bone and (**b**) soft tissue windows demonstrating maxillary sinus mucocele arising in a patient with a prior history of trauma and previous orbital floor fracture. While the maxillary sinus is well aerated; intraoperatively, this lesion was found to be filled with thick, mucinous secretions and a cystic lining connecting the lesion to the maxillary sinus was identified in keeping with a mucocele

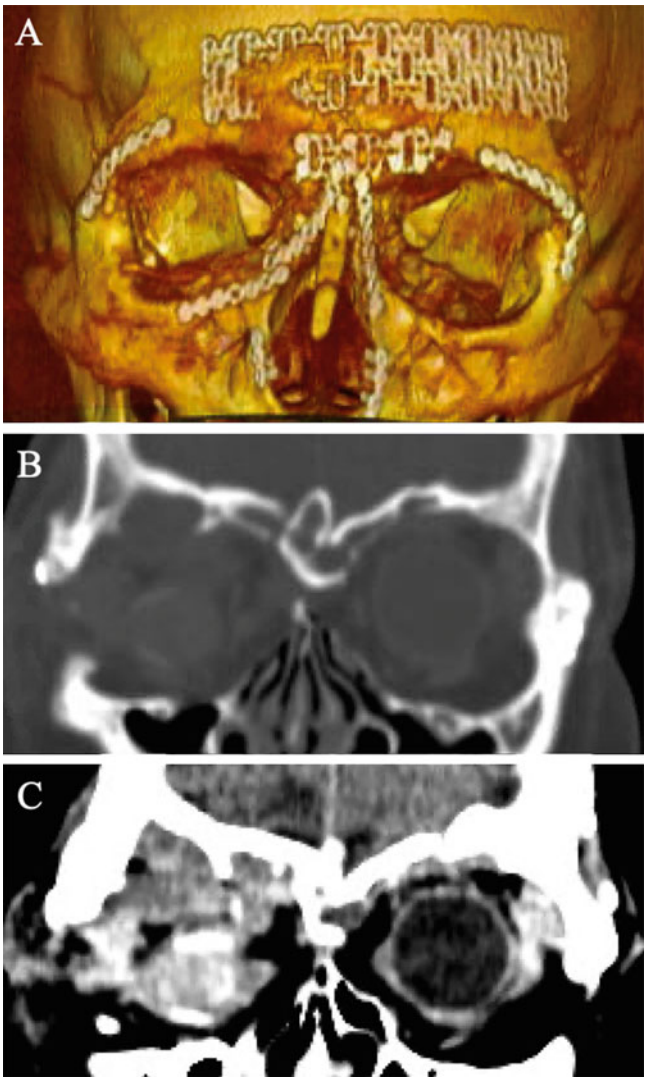


Fig. 4 Computed tomography with (**a**) three-dimensional reconstruction and (**b** and **c**) coronal scans showing evidence of previous extensive facial and frontal skull injuries and an anophthalmic socket with an orbital implant on the right side. The right frontal sinus is completely opacified and a mucocele is expanding into the orbit

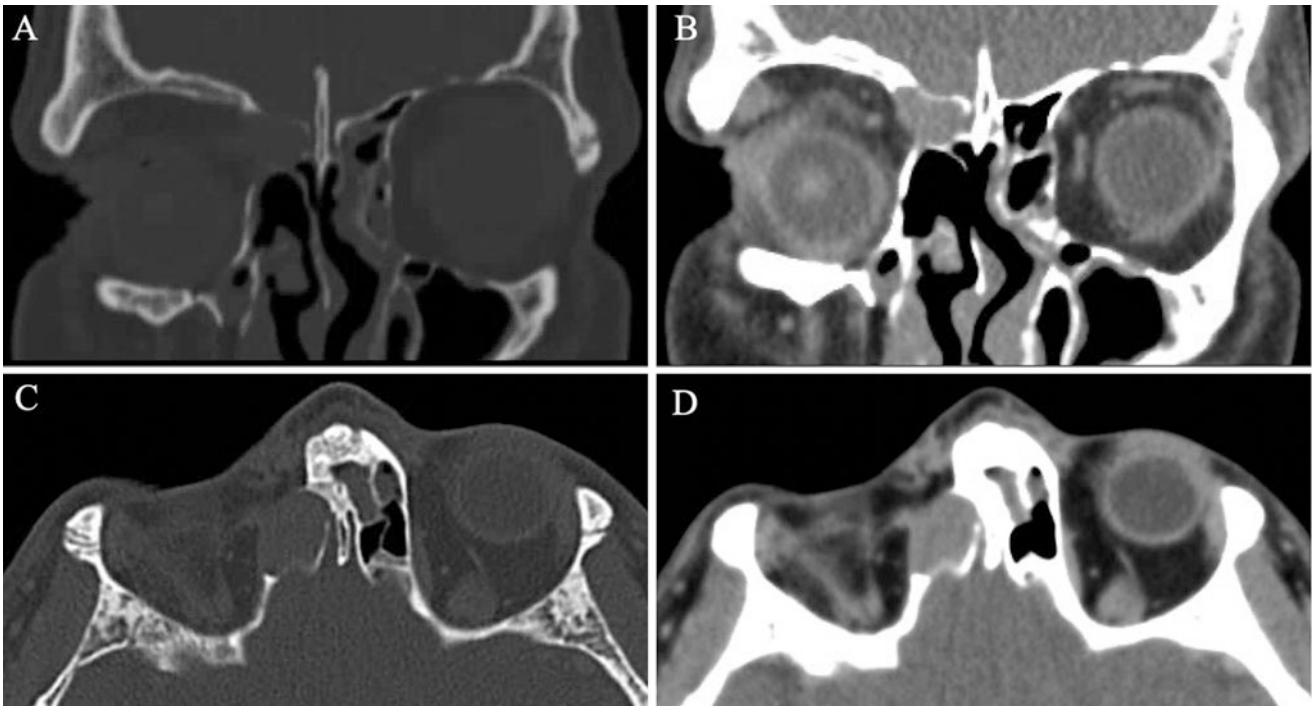


Fig. 5 Twenty years following surgical resection of a cementoblastoma, (**a** and **b**) coronal and (**c** and **d**) axial CT images demonstrate a largely absent right maxillary sinus and resultant defect of the orbital floor causing inferior displacement of the globe. A mucocele arising from the ethmoid sinus extending into the right orbit is noted. Patient subsequently underwent insertion of a custom-made PEEK implant, excision of the mucocele, and functional endoscopic sinus surgery

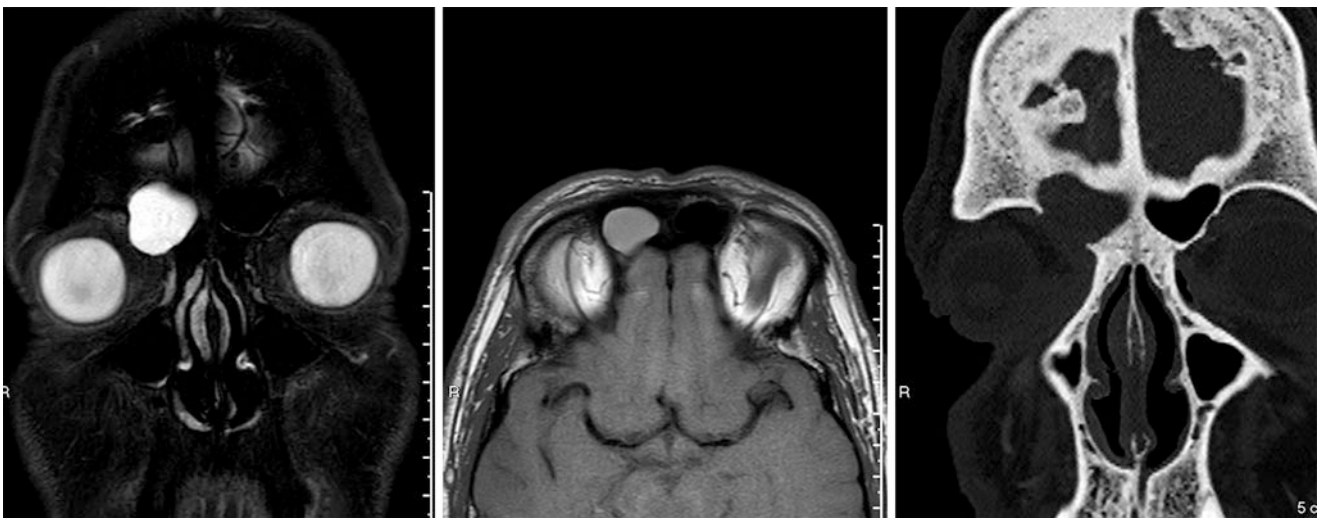


Fig. 6 Coronal T2 FS image (*left*) showing a right-sided frontal mucocele bulging into the superonasal orbit with high T1 content (*middle*) in keeping with proteinaceous secretions. Coronal CT reformat, bone window (*right*) demonstrating the long-standing pressure erosion occurring at the medial orbital roof with a thin imperceptible bony wall

References

1. Khong JJ, Malhotra R, Wormald PJ, Selva D. Endoscopic sinus surgery for paranasal sinus mucocoele with orbital involvement. Eye (Lond). 2004;18(9):877–81.
2. Desjarlais EB, Jovanovic N, Teo HMT, Kahana A. Surgical management of a recurrent orbit-eroding mucocele associated with frontal-ethmoidal sinus inverted papilloma. Ophthalmic Plast Reconstr Surg. 2019;35(6):e136–8.
3. Sadiq SA, Lim MK, Jones NS. Ophthalmic manifestations of paranasal sinus mucocoeles. Int Ophthalmol. 2009;29(2):75–9.
4. Shahi S, Devkota A, Bhandari TR, Pantha T, Gautam D. Rare giant maxillay mucocele: a rare case report and literature review. Ann Med Surg (Lond). 2019;43:68–71.
5. Tailor R, Obi E, Burns J, Sampath R, Durrani OM, Ford R. Fronto-orbital mucocele and orbital involvement in occult obstructive frontal sinus disease. Br J Ophthalmol. 2016;100(4):525–30.
6. Hejazi N, Witzmann A, Hassler W. Ocular manifestations of sphenoid mucoceles: clinical features and neurosurgical management of three cases and review of the literature. Surg Neurol. 2001;56(5):338–43.
7. Ting MYL, Shan M, Gantz O, Zhang-Nunes S, Wrobel B. Optic neuropathy due to an ethmoid mucocele: a case report and literature review. Case Rep Ophthalmol. 2019;10(2):227–34.
8. Mehta AA, Wagner LH, Blace N. Spontaneous upper eyelid ecchymosis: a rare presenting sign for frontal sinus mucocele. Orbit. 2017;36(3):183–7.
9. Sethi DS, Lau DP, Chan C. Sphenoid sinus mucocoele presenting with isolated oculomotor nerve palsy. J Laryngol Otol. 1997;111(5):471–3.
10. Pahwa S, Sharma S, Das CJ, Dhamija E, Agrawal S. Intraorbital cystic lesions: an imaging spectrum. Curr Probl Diagn Radiol. 2015;44(5):437–48.
11. Samil KS, Yasar C, Ercan A, Hanifi B, Hilal K. Nasal cavity and paranasal sinus diseases affecting orbit. J Craniofac Surg. 2015;26(4):e348–51.
12. Dutta M. Ethmoid pneumatization and a large frontal-orbital-ethmoid mucocele. Radiol Case Rep. 2019;14(3):419–22.
13. Erdogan BA, Unlu N, Aydin S, Avci H. Frontal mucocele extended Orbita and endoscopic marsupialization technique. J Craniofac Surg. 2018;29(4):e408–9.
14. Sautter NB, Citardi MJ, Perry J, Batra PS. Paranasal sinus mucoceles with skull-base and/or orbital erosion: is the endoscopic approach sufficient? Otolaryngol Head Neck Surg. 2008;139(4):570–4.
15. Hicks KL, Moe KS, Humphreys IM. Bilateral transorbital and transnasal endoscopic resection of a frontal sinus osteoblastoma and orbital mucocele: a case report and review of the literature. Ann Otol Rhinol Laryngol. 2018;127(11):864–9.
16. Miller C, Berens A, Patel SA, Humphreys IM, Moe KS. Transorbital approach for improved access in the management of paranasal sinus mucoceles. J Neurol Surg B Skull Base. 2019;80(6):593–8.
17. Casale M, Costantino A, Sabatino L, Cassano M, Moffa A, Rinaldi V. Image-guided endoscopic marsupialization technique for frontal sinus mucocele with orbital extension: a case report. Int J Surg Case Rep. 2019;61:259–62.
18. Severino R, Severino P. Fronto-orbital mucocele with intracranial extension: a case report. J Surg Case Rep. 2017;2017(6):rjx107.
19. Bassily R, Wallace D, Liolios V, Prinsely P, Beigi B. Ethmoidal air cell schwannoma presented as a fronto-ethmoidal mucocele. Orbit. 2013;32(3):187–9.

Subperiosteal Orbital Abscess

83

Kelsey A. Roelofs and Ezekiel Weis

Contents

1 **Signs and Symptoms** 611
2 **Differential Diagnosis** 612
3 **Diagnosis** 612
4 **Treatment** 612
5 **Figures with Captions** 612
References 614

Abstract

- Subperiosteal abscess (SPA) typically assumes a flat or lentiform configuration with enhancement of the rim following administration of contrast.
- It is important to note the size of SPA on imaging, as several studies have found larger size to be predictive of the need for surgical intervention in pediatric patients [1, 2].
- Imaging is mandatory in all cases of nonresolving orbital cellulitis or any signs of optic nerve dysfunction. Contrast-enhanced CT is the appropriate modality of choice in most cases since it provides useful information regarding coexistent sinus disease, intraorbital foreign body, and bony defects/erosion.
- Imaging to evaluate for recurrence of SPA may be indicated if rapid resolution does not occur following surgical intervention or conservative (antibiotic) management.
- Magnetic resonance imaging is appropriate in cases with concern for cavernous sinus involvement, or other intracranial complications.

Keywords

Orbital cellulitis · Sinusitis · Pott's puffy tumor · Subperiosteal abscess · SPA

1 Signs and Symptoms

Subperiosteal abscess most commonly arises in the setting of orbital cellulitis, particularly in the pediatric population, and hence, typically presents with orbital signs and symptoms. In addition to proptosis, extraocular motility restriction,

K. A. Roelofs
Division of Orbital and Ophthalmic Plastic Surgery, Stein and Doheny Eye Institutes, University of California, Los Angeles, CA, USA

E. Weis (✉)
Department of Ophthalmology and Visual Sciences, University of Alberta, Edmonton, AB, Canada

Department of Surgery, University of Calgary, Calgary, AB, Canada
e-mail: ezekiel_Weis@post.harvard.edu

© Springer Nature Switzerland AG 2022
G. Ben Simon et al. (eds.), *Atlas of Orbital Imaging*,
https://doi.org/10.1007/978-3-030-62426-2_69

chemosis, and nonaxial globe displacement in the direction opposite the location of the SPA may be seen. The presence of a compressive optic neuropathy (decreased color vision, presence of a relative afferent pupillary defect) or evidence of orbital compartment syndrome necessitates urgent intervention. In most cases, coexisting rhinosinusitis is expected on imaging. In general, nearly two-third of patients with orbital cellulitis-related SPA and normal vision function can be managed conservatively and do not require surgical intervention.

2 Differential Diagnosis

The differential diagnosis of SPA includes mucocele, subperiosteal hematoma, orbital inflammation, and high grade malignancies including leukemia (granulocytic sarcoma). Enhancement of the rim on contrast CT, the presence of an infectious source (i.e., sinusitis), evidence of concurrent orbital inflammatory signs, and general signs of infection including an elevated white blood cell count aid in the differentiation of SPA from the other entities.

3 Diagnosis

The diagnosis of SPA is most commonly reached when the classical clinical presentation of an infection are present with involvement of the orbit and a subperiosteal collection confirmed on imaging.

4 Treatment

There are important differences in the management of children (< 9 years old) compared to adolescents/adults with orbital cellulitis and sub-periosteal abscess. In the absence of a large SPA (>1250 mm^3), frontal sinusitis, suspicion of anaerobic SPA, and recurrent SPA after drainage or a compressive optic neuropathy, initial conservative management with IV antibiotics and observation is usually indicated for children <9 years of age [4]. Surgical drainage is more commonly required in those >9 years of age; however, the volume of SPA (≥ versus <1250 mm^3) plays an important role in determining management [3].

5 Figures with Captions

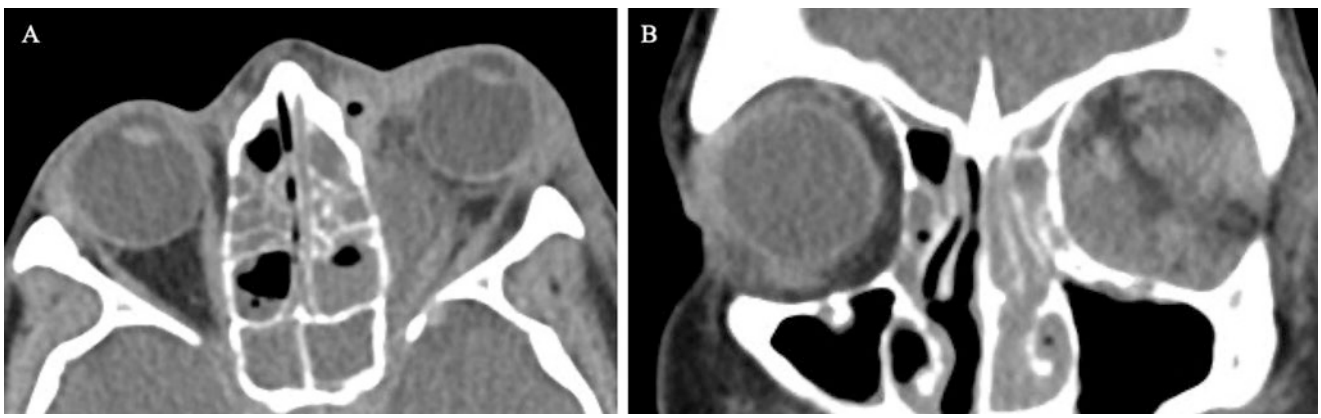


Fig. 1 (**a**) Axial and (**b**) coronal nonenhanced computed tomography demonstrating opacification and mucosal thickening of the ethmoid and sphenoid sinuses with evidence of an inferomedial subperiosteal abscess in the left orbit. Note preseptal thickening on the left side on the axial section

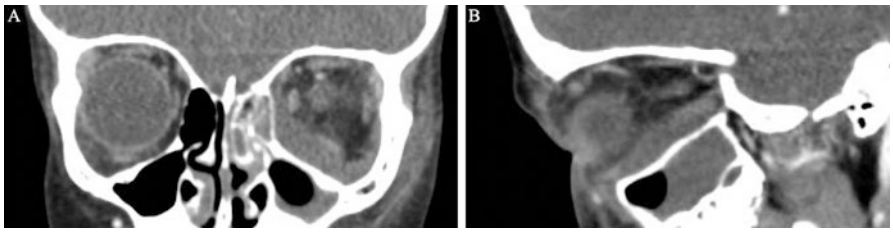


Fig. 2 (**a**) Axial and (**b**) sagittal computed tomography showing an inferior subperiosteal abscess in the context of mucosal thickening and partial opacification of the maxillary and ethmoid sinuses. Many times, no evident bone destruction is seen, since infectious agents can gain access to the orbit via vascular channels which are valveless

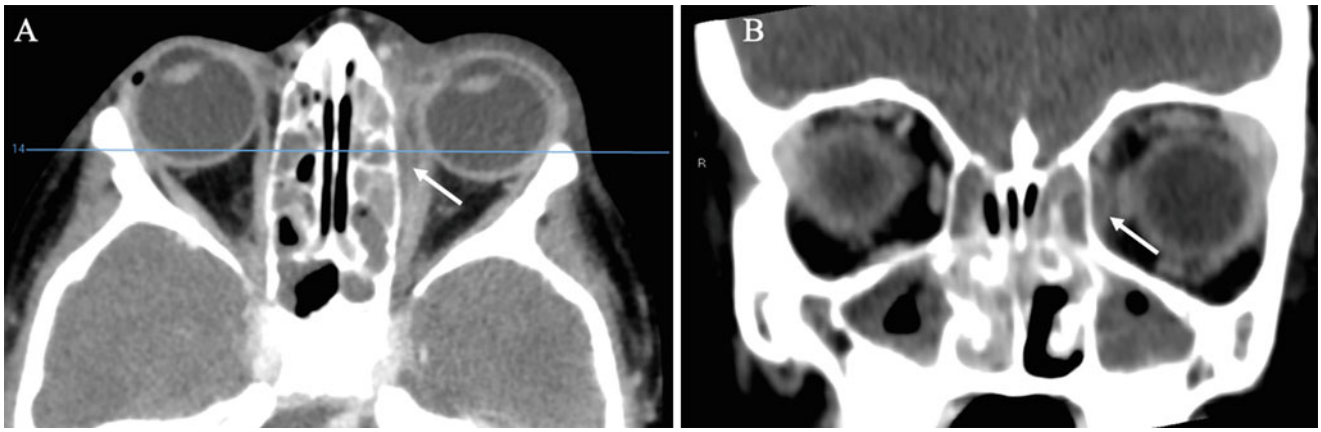


Fig. 3 (**a**) Axial and (**b**) coronal contrast-enhanced CT of a 5-year-old male with left orbital cellulitis and medial SPA with a typical lentiform shape (arrows). Note pansinusitis, mild preseptal thickening on the left. The patient had good ON functions and improved solely on IV antibiotic treatment (courtesy of the editors)

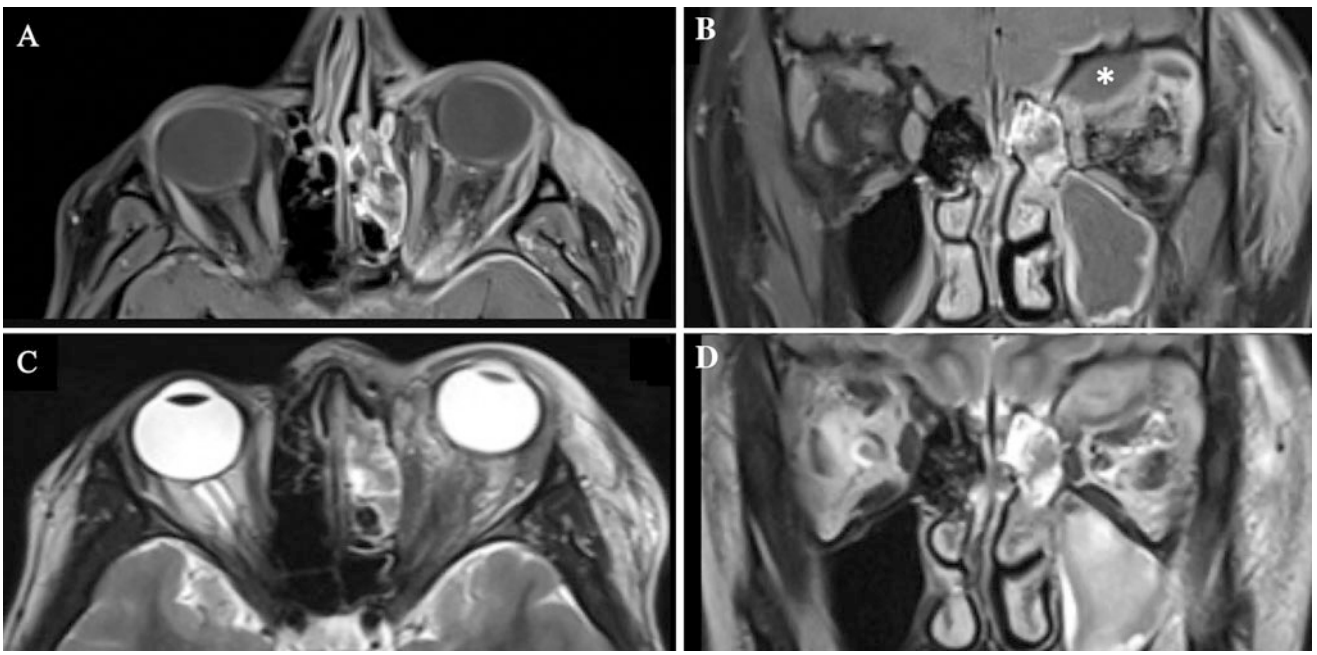


Fig. 4 (**A** and **B**) Axial and coronal T1 (**C** and **D**) and T2-weighted gadolinium-enhanced magnetic resonance imaging. Soft tissue swelling, and a discrete rim-enhancing fluid collection, is noted along the superomedial aspect of the posterior orbit in keeping with an abscess (astrix). There is near complete fluid filling of the left maxillary, ethmoidal, and frontal sinuses. Significant fat stranding is noted within the orbit, in keeping with orbital cellulitis. Smooth dural enhancement is seen along the left anterior and middle cranial fossa, which most likely represents reactive change

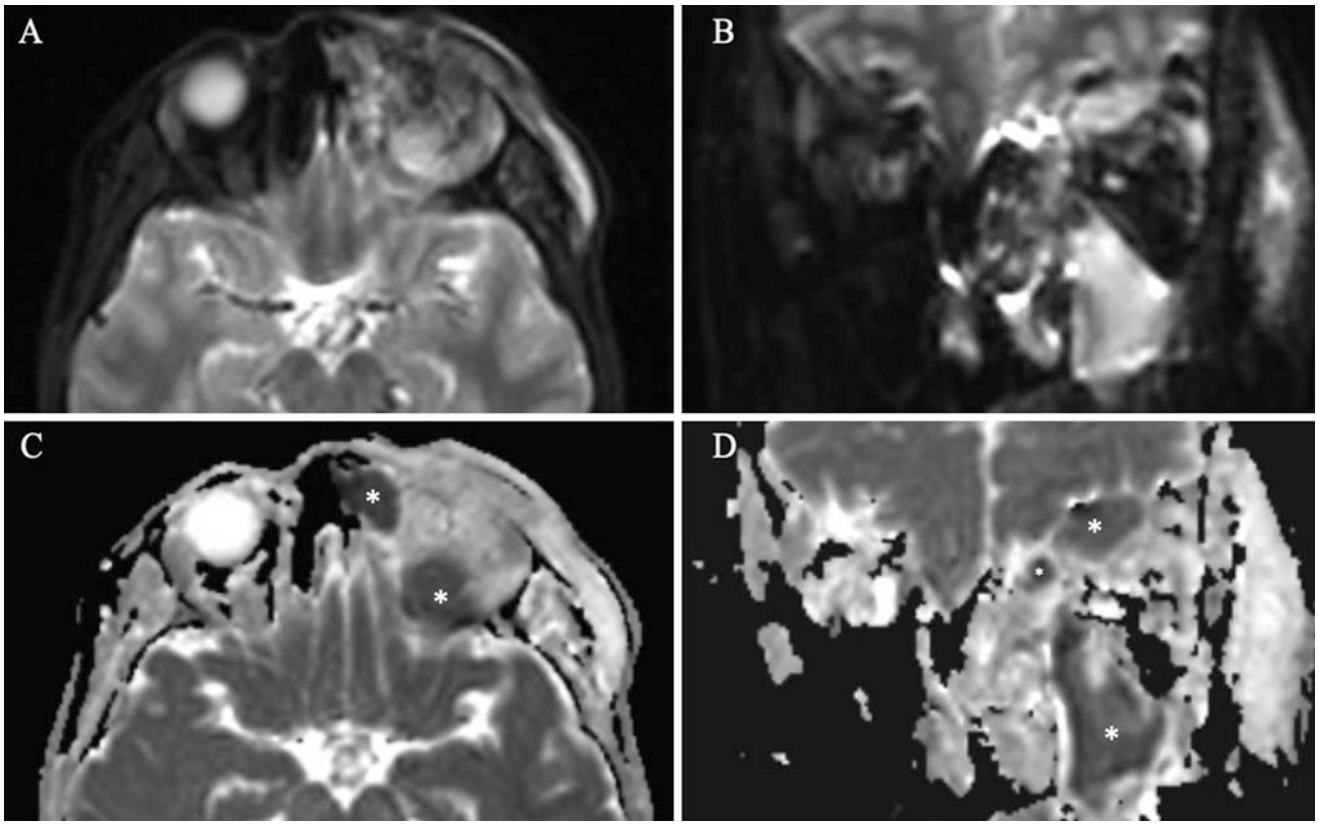


Fig. 5 (**a** and **b**) Axial and coronal b0 ("b-zero" T2-weighted) images and (**c** and **d**) apparent diffusion coefficient images showing restricted diffusion within the left supero-medial posterior subperiosteal abscess, maxillary ethmoidal and frontal sinuses (asterix) indicative of purulent material

References

1. Le TD, Liu ES, Adatia FA, Buncic JR, Blaser S. The effect of adding orbital computed tomography findings to the Chandler criteria for classifying pediatric orbital cellulitis in predicting which patients will require surgical intervention. J AAPOS. 2014;18(3):271–7.
2. Sharma A, Liu ES, Le TD, et al. Pediatric orbital cellulitis in the *Haemophilus influenzae* vaccine era. J AAPOS. 2015;19(3):206–10.
3. Wong SJ, Levi J. Management of pediatric orbital cellulitis: a systematic review. Int J Pediatr Otorhinolaryngol. 2018;110:123–9.
4. Garcia GH, Harris GJ. Criteria for nonsurgical management of subperiosteal abscess of the orbit: analysis of outcomes 1988–1998. Ophthalmology. 2000;107(8):1454–6. https://doi.org/10.1016/s0161-6420(00)00242-6; discussion 1457–8. PMID: 10919887.

Aspergillosis

84

Kelsey A. Roelofs, Erin D. Wright, and Ezekiel Weis

Contents

1 **Signs and Symptoms** 616
2 **Differential Diagnosis** 616
3 **Diagnosis** 616
4 **Treatment** 616
5 **Figures with Captions** 617
References 621

Abstract

- Orbital aspergillosis is commonly encountered in immunocompromised hosts but can also occur in immunocompetent patients. On computed tomography, invasive orbital aspergillosis appears as an often ill-defined, heterogenous iso-, or hypodense lesion.
- On magnetic resonance imaging, orbital aspergillosis often appears as a heterogenous lesion typically iso- or hyperintense on T1- and patchy hypo- and hyperintense on T2-weighted images.
- Intense gadolinium enhancement can be seen and is often particularly prominent around the periphery of the lesion.
- Invasive orbital aspergillosis can present with evidence of surrounding tissue destruction and bone erosion whereas noninvasive disease tends to show remodeling changes secondary to chronic inflammation and mass effect.
- The presence of dense, sinus concretions >2000 Hounsfield units are suggestive of noninvasive/extramucosal aspergillosis, which most commonly arises in the maxillary and sphenoid sinuses.
- Fat-saturating sequences are essential in depicting skull base, neural foramina, cavernous sinus, and meningeal involvement.
- Imaging can be suggestive of invasive fungal disease but cannot differentiate between subtypes.

Keywords

Aspergillus · Eyelid swelling · Proptosis

K. A. Roelofs
Division of Orbital and Ophthalmic Plastic Surgery, Stein and Doheny Eye Institutes, University of California, Los Angeles, CA, USA
e-mail: roelofs@ualberta.ca

E. D. Wright
Department of Surgery, University of Alberta, Edmonton, AB, Canada

E. Weis (✉)
Department of Ophthalmology and Visual Sciences, University of Alberta, Edmonton, AB, Canada

Department of Surgery, University of Calgary, Calgary, AB, Canada

© Springer Nature Switzerland AG 2022
G. Ben Simon et al. (eds.), *Atlas of Orbital Imaging*,
https://doi.org/10.1007/978-3-030-62426-2_71

1 Signs and Symptoms

Orbital aspergillosis can be divided into noninvasive (allergic bronchopulmonary aspergillosis and aspergilloma) and invasive (chronic necrotizing aspergillosis and invasive aspergillosis) disease. Although invasive disease is more common in immunocompromised individuals, orbital aspergillosis can occur in immunocompetent individuals as well. In immunocompromised individuals, orbital aspergillosis often presents as an acutely progressive entity, whereas in those who are immunocompetent, disease typically follows a chronic, indolent course. Chronic invasive disease typically occurs in older individuals and may be due in part to a local suppression of the immune response by a toxin released by aspergillus that inhibits macrophage activity and complement activation [1].

Patients with sino-orbital aspergillosis may report a history of preceding nasal discharge or sinusitis [2], a vague history of retro-orbital pain that eventually becomes sharp and persistant [3] and/or gradually progressive proptosis [4]. On examination, eyelid swelling, proptosis, and findings in keeping with orbital apex syndrome, including restriction of extraocular movements and visual disturbance, may be seen [2, 5–7].

2 Differential Diagnosis

Invasive aspergillosis may behave similar to a malignant or inflammatory condition, as bone invasion and destruction of nearby structures can occur. On the other hand, noninvasive orbital aspergillosis presents with a more chronic appearance with changes in adjacent structures secondary to mass effect and chronic inflammation, rather than fungal invasion (i.e., remodeling of sinus and orbital bones). The differential diagnosis in these cases includes more indolent infections and benign lesions.

3 Diagnosis

Elucidation of risk factors for aspergillosis on history, including environmental exposure and/or recent travel to an endemic area (i.e., Sudan), is helpful when considering the diagnosis of orbital aspergillosis. However, incisional biopsy with multiple specimens is often obtained to confirm the diagnosis [8]. Early diagnosis is critical so that efforts can be made to prevent intracranial involvement.

4 Treatment

An appropriate workup for, and treatment of, any reversible underlying immunosuppression should be initiated. Compared to mucormycosis, a more conservative approach is often preferred for aspergillosis. Surgical debridement of the involved sinuses and orbit may be required, and systemic treatment with amphotericin B, itraconazone, or voriconazole is usually indicated. Retrobulbar injections of amphotericin B have also been used with some success in cases of sino-orbital aspergillus [9]. In cases of aspergilloma, surgical excision alone is usually curative.

5 Figures with Captions

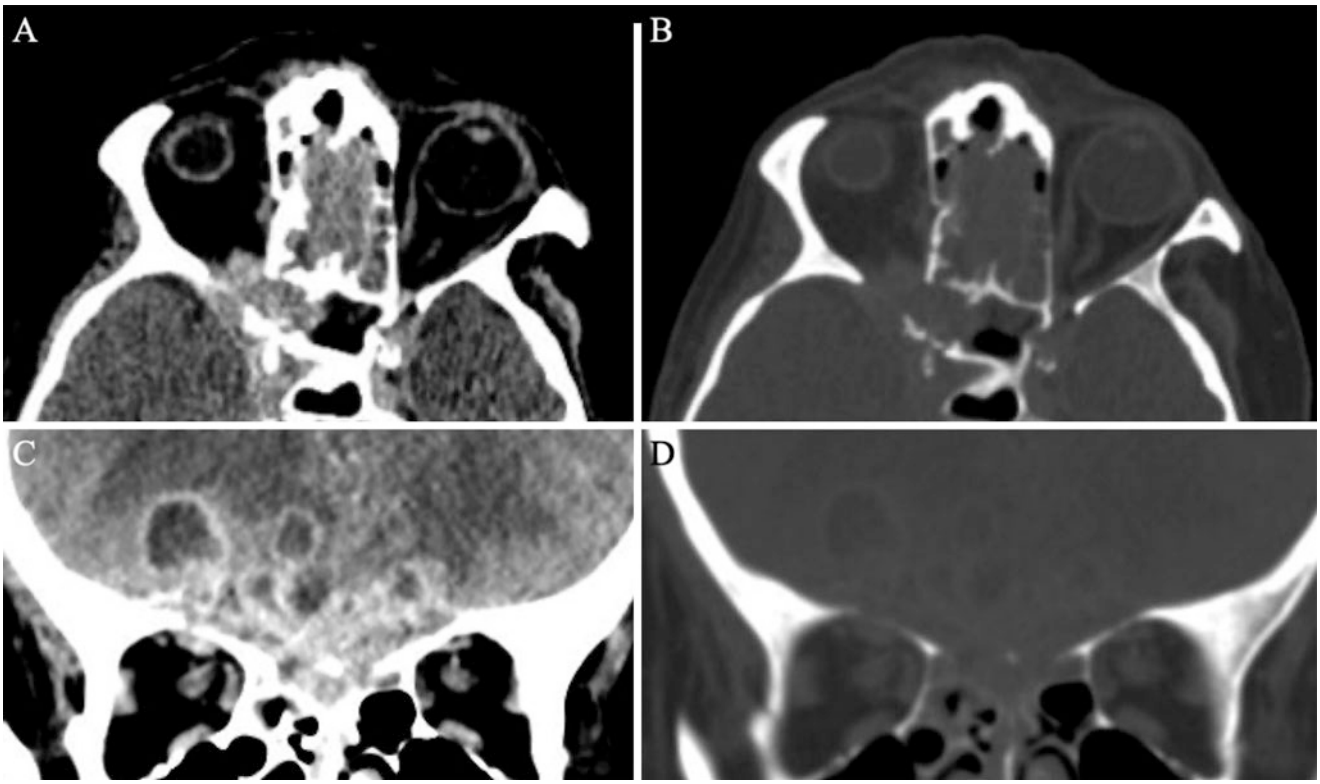


Fig. 1 A 69-year-old insulin-dependent diabetic presented with a history of pain and progressive vision loss, beginning in the right and left eyes 4 and 1 week prior to presentation, respectively. On computed tomography, invasive aspergillosis typically presents as a heterogenous, ill-defined lesion with focal hypodense areas and bony erosion. (**a** and **b**) Axial CT reveals a heterogeneously enhancing soft tissue mass centered within the ethmoid sinuses extending posteriorly to encase the right sphenoid sinus, right cavernous sinus, and right superior orbital fissure. (**c** and **d**) On coronal images, the infectious process extends intracranially, breaching the cribriform plate into the right and left anterior/inferior frontal lobes. The parenchymal invasion is heterogeneously enhancing and contains multiple rim-enhancing cystic components in keeping with multiple abscesses

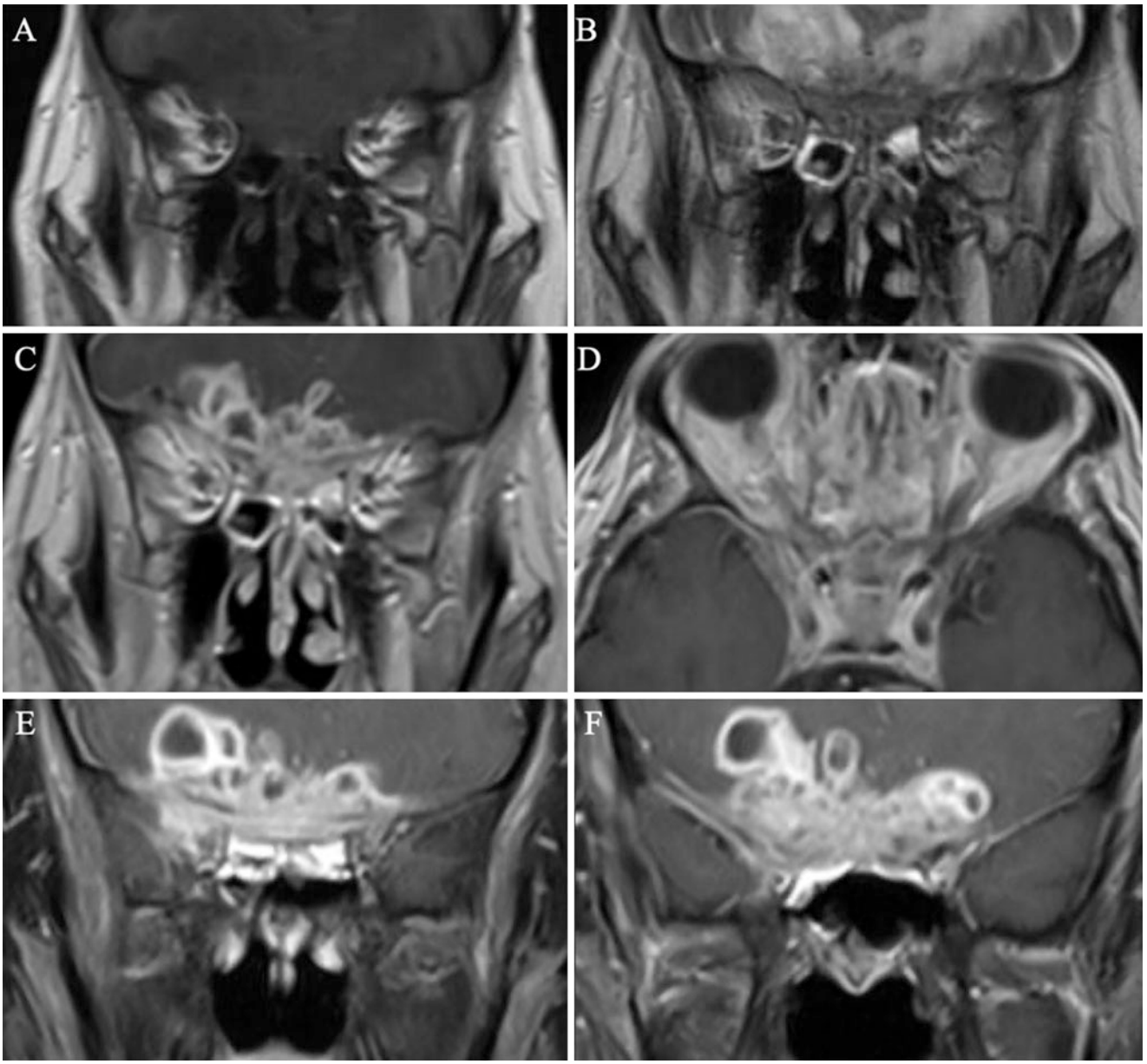


Fig. 2 Given that the early findings on imaging may be subtle, magnetic resonance imaging is often helpful [3]. This figure highlights the MRI findings of the same patient shown in Fig. 1. (**a** and **b**) Coronal T1- and T2-weighted images show a hypointense plate of tissue along the floor of the anterior cranial fossa originating from the middle ethmoid air cells. Cephalad to this and invading brain parenchyma are multiple loculated areas of increased T2 signal representing cystic masses and accompanying edema. (**c** and **d**) There is intense gadolinium enhancement of the plate tissue along the floor of the anterior cranial fossa, along the dura of the right middle cranial fossa and around the periphery of the multiple locules/abscesses. (**e** and **f**) There is enhancement and possibly invasion of the orbital apices and involvement back to the chiasm

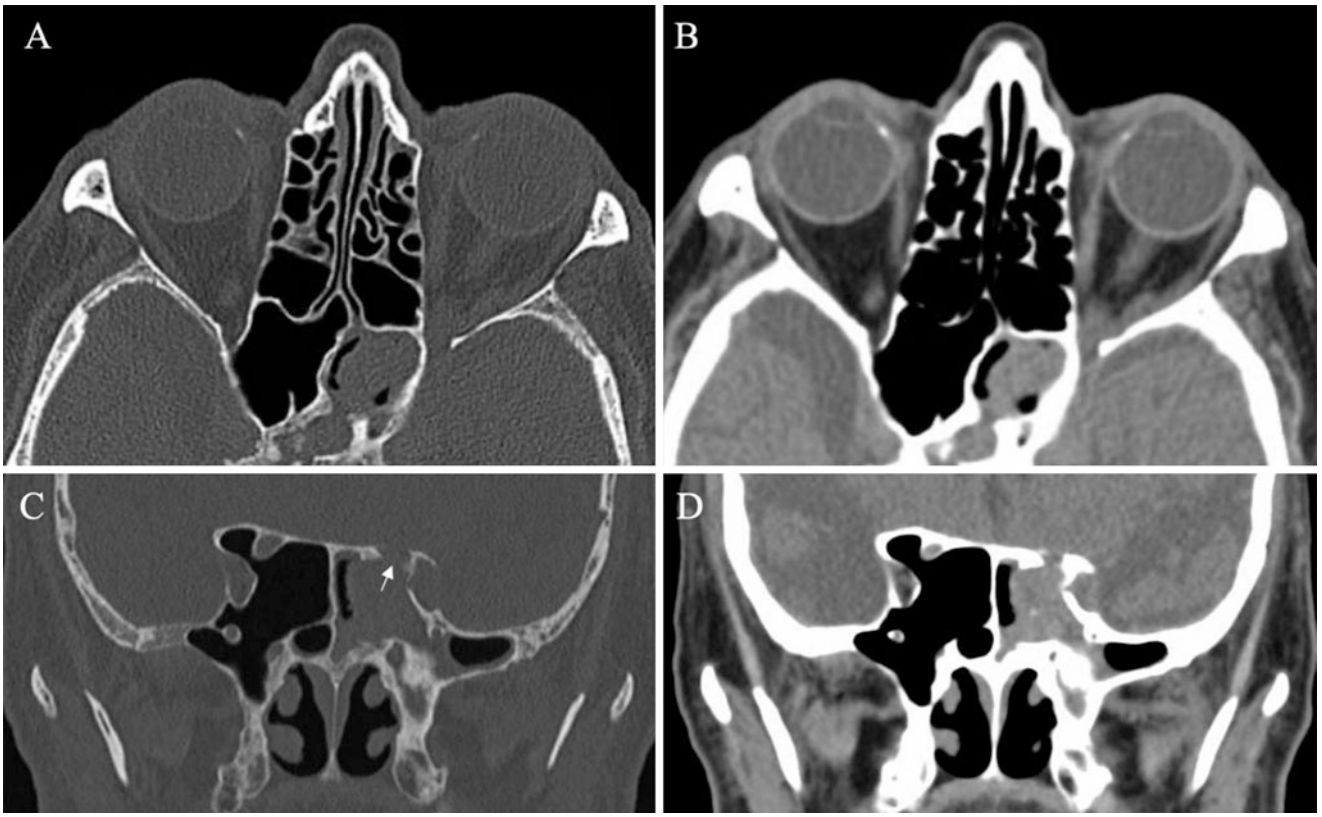


Fig. 3 A 85-year-old otherwise healthy male presented with a 1-month history of left orbital pain, progressive vision loss, and new onset of sixth nerve palsy. Axial and coronal CT (**a**, **c** bone and **b**, **d**, soft tissue windows) show a collection of heterogenous material with small foci of mineralization within the left sphenoid sinus. A small osseous defect (arrow) is noted at the anterosuperior aspect of the left sphenoid sinus which appears to extend between the sinus and the optic nerve canal

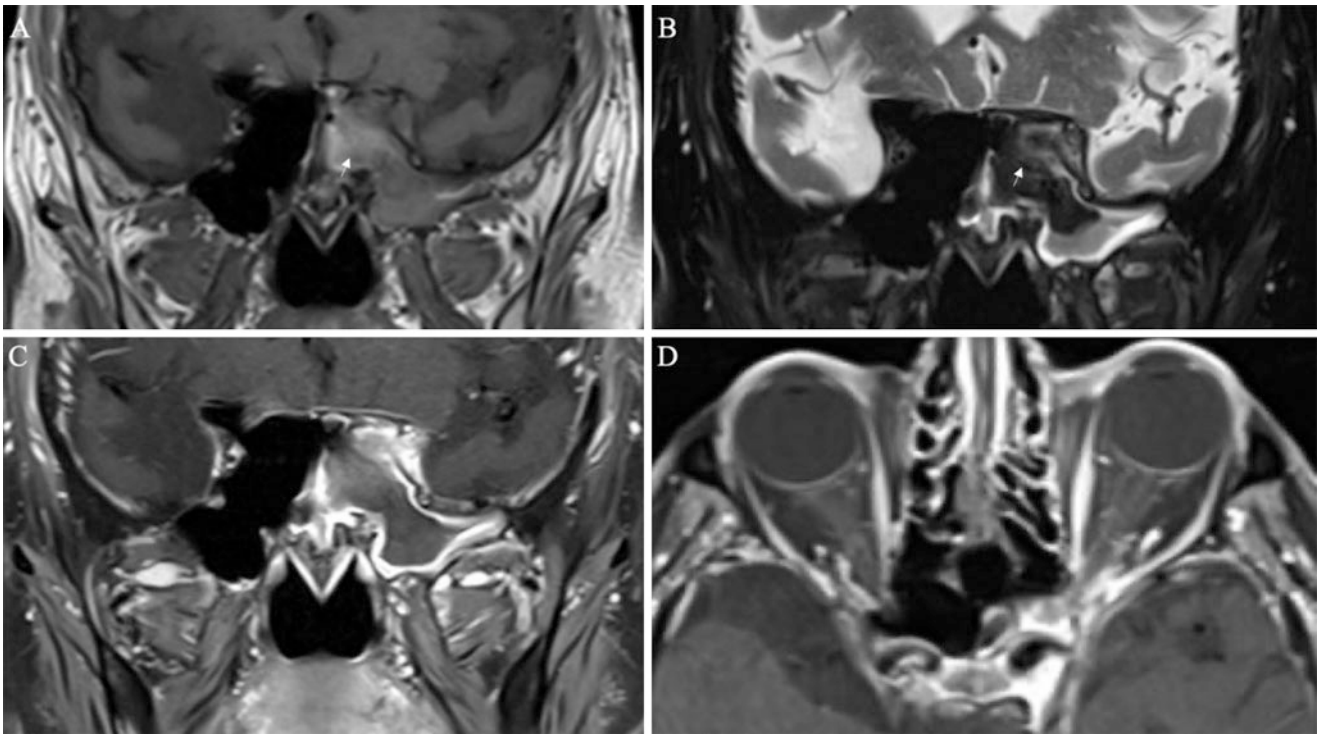


Fig. 4 Magnetic resonance imaging of the same patient presented in Fig. 3 demonstrates heterogenous-appearing material which is predominantly (**a**) hyperintense on T1- and (**b**) centrally hypointense on T2-weighted images (arrows). Following administration of gadolinium, (**c** and **d**) coronal and axial T1-weighted fat saturation images demonstrate peripheral enhancement within the left sphenoid sinus extending into the region of the optic strut/anterior clinoid process. MRI is superior to CT in identifying invasive disease, particularly for subtle disease within the cavernous sinus or involvement of the intracranial structures

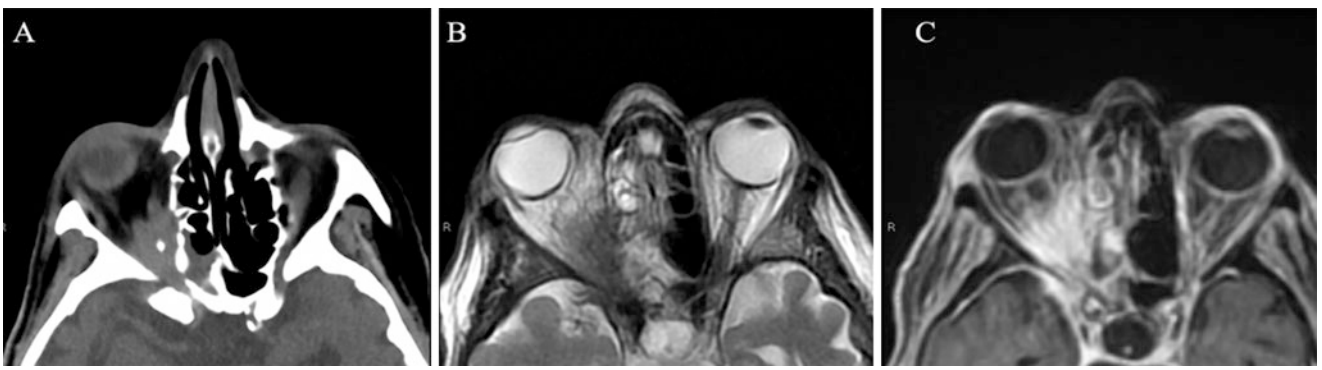


Fig. 5 (**a**) Nonenhanced axial CT of an 87-year-old female with right sino-orbital aspergillosis, demonstrating sphenoid sinus and orbital apex involvement. (**b**) On T2-weighted MRI, the lesion appears hypointense (**c**) and exhibits moderate enhancement on T1-weighted fat saturation sequences following administration of gadolinium, typical of fungal infection. There are motion artifacts in the MR images. (Courtesy of the editors)

References

1. Rhodes J. Aspergillosis. In: Murphy J, Friedman H, Bendinelli M, editors. Fungal infections and immune responses (infectious agents and pathogenesis). New York: Springer; 1993.
2. Lee AS, Sullivan TJ. Orbital mycoses in a pediatric subtropical population: a case series. J AAPOS. 2019;23(5):270.e271–7.
3. Sivak-Callcott JA, Livesley N, Nugent RA, Rasmussen SL, Saeed P, Rootman J. Localised invasive sino-orbital aspergillosis: characteristic features. Br J Ophthalmol. 2004;88(5):681–7.
4. Mody KH, Ali MJ, Vemuganti GK, Nalamada S, Naik MN, Honavar SG. Orbital aspergillosis in immunocompetent patients. Br J Ophthalmol. 2014;98(10):1379–84.
5. Aggarwal E, Mulay K, Menon V, Sundar G, Honavar SG, Sharma M. Isolated orbital aspergillosis in immunocompetent patients: a multicenter study. Am J Ophthalmol. 2016;165:125–32.
6. Choi HS, Choi JY, Yoon JS, Kim SJ, Lee SY. Clinical characteristics and prognosis of orbital invasive aspergillosis. Ophthalmic Plast Reconstr Surg. 2008;24(6):454–9.
7. Lee AS, Lee PWY, Allworth A, Smith T, Sullivan TJ. Orbital mycoses in an adult subtropical population. Eye (Lond). 2019;34:1640–7.
8. Asanad S, Lo C, Ugradar S, Rootman DB. Invasive cavernous sinus aspergillosis: an orbitocranial approach for diagnosis and management. Can J Ophthalmol. 2020;55(1):e33–6.
9. Colon-Acevedo B, Kumar J, Richard MJ, Woodward JA. The role of adjunctive therapies in the management of invasive sino-orbital infection. Ophthalmic Plast Reconstr Surg. 2015;31(5):401–5.

Mucormycosis

85

Kelsey A. Roelofs and Ezekiel Weis

Contents

1 **Signs and Symptoms** 624
2 **Differential Diagnosis** 624
3 **Diagnosis** 624
4 **Treatment** 624
5 **Figures with Captions** 624
References 628

Abstract

- Rhino-sino-orbital mucormycosis, a subtype of zygomycoses, is an aggressive opportunistic infection that tends to affect poorly controlled diabetic and immunocompromised patients.
- Initial features may be subtle on imaging; however, disease often progresses rapidly from sinus to orbit involvement, so repeat imaging should be performed if the clinical picture changes. Concomitant sinus disease is seen in 60–90% of cases.
- On computed tomography, disease often appears as an ill-defined infiltration with orbital fat stranding, advancing into a homogenous hyperdense lesion.
- Occasionally, associated bone remodeling and/or erosion can be seen.
- On magnetic resonance imaging, fungal disease appears isointense on T1 and hypointense on T2, compared to extraocular muscles.
- On contrast-enhanced studies, there may be patchy enhancement of the mass. The necrotic portions of the infectious process do not enhance (e.g., "dark/black turbinate sign" in the nasal cavity).
- There is often a lag time between tissue involvement and enhancement on contrast magnetic resonance imaging, resulting in an underestimation of the true pathological extent.
- Imaging is suggestive of invasive fungal disease but cannot differentiate between subtypes.

Keywords

Mucormycosis · Immunocompromised · Ischemia · Fungal infection

K. A. Roelofs
Division of Orbital and Ophthalmic Plastic Surgery, Stein and Doheny Eye Institutes, University of California, Los Angeles, CA, USA

E. Weis (✉)
Department of Ophthalmology and Visual Sciences, University of Alberta, Edmonton, AB, Canada

Department of Surgery, University of Calgary, Calgary, AB, Canada
e-mail: ezekiel_weis@post.harvard.edu

© Springer Nature Switzerland AG 2022
G. Ben Simon et al. (eds.), *Atlas of Orbital Imaging*,
https://doi.org/10.1007/978-3-030-62426-2_121

1 Signs and Symptoms

On examination, proptosis and findings in keeping with orbital apex syndrome, including restriction of extraocular movements and visual disturbance, may be seen [1–4]. Soft tissue swelling, eyelid edema, and conjunctival injection are also possible. Fungal sino-orbital infections with mucormycosis can result in profound ischemia and tissue necrosis; resultantly, when the maxillary sinus is involved, a painful, black necrotic eschar may be seen on the hard palate [5].

2 Differential Diagnosis

The differential diagnosis of sino-orbital fungal disease includes other infectious agents (bacteria, parasitic), inflammatory conditions (orbital apex syndrome, thyroid eye disease, sarcoidosis, and granulomatosis polyangiitis), neoplastic lesions (primary orbital tumor, metastatic lesion, and lymphoma), and vascular malformations (carotid-cavernous fistula) [6].

3 Diagnosis

As the features of sino-orbital fungal disease can be somewhat nonspecific, both clinically and on imaging, the diagnosis is often reached following biopsy [7]. Multiple biopsies may be needed for diagnosis due to the patchy nature of the fungal infection. Early diagnosis is critical so that efforts can be made to prevent intracranial involvement.

4 Treatment

Due to the high mortality associated with intracranial spread, in some centers, invasive sino-orbital fungal disease is the commonest nonneoplastic reason for exenteration [8]; however, more recent literature suggests that exenteration may not affect patient survival in certain cases [9]. Given that fungal infection incites ischemia and tissue infarction, systemic drug delivery alone is insufficient. When globe sparing surgery is performed, the goal is often to debride all infected, ischemic, or necrotic tissue followed by medical management with either amphotericin B, voriconazole, or itraconazole [1, 10, 11].

5 Figures with Captions

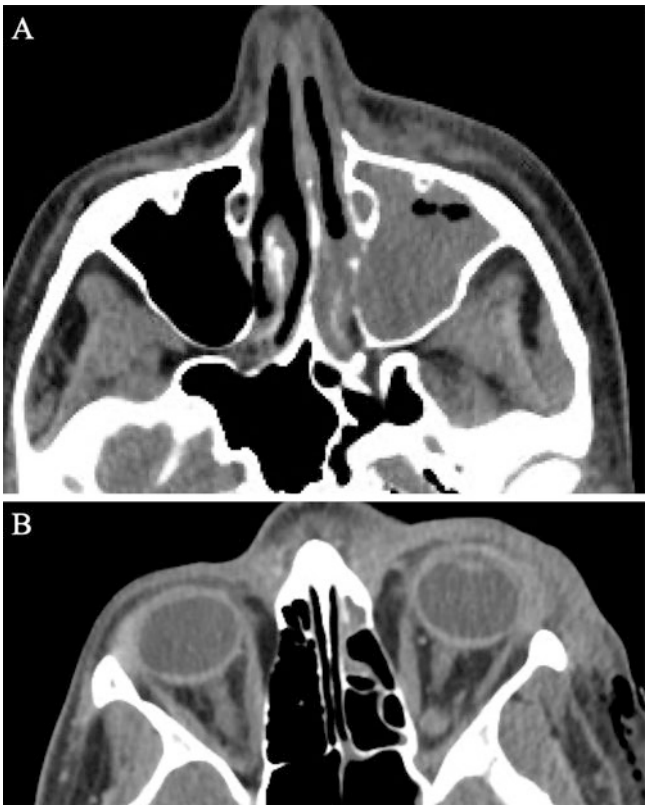


Fig. 1 A 25-year-old poorly controlled diabetic presented with paresthesia, facial pain, and diplopia. (**a**) Axial nonenhanced computed tomography imaging demonstrating near complete opacification of the left maxillary sinus and (**b**) inflammation of the left periorbital region and lacrimal gland that is ill-defined, homogenous, and hyperdense in appearance, consistent with a diagnosis of mucormycosis

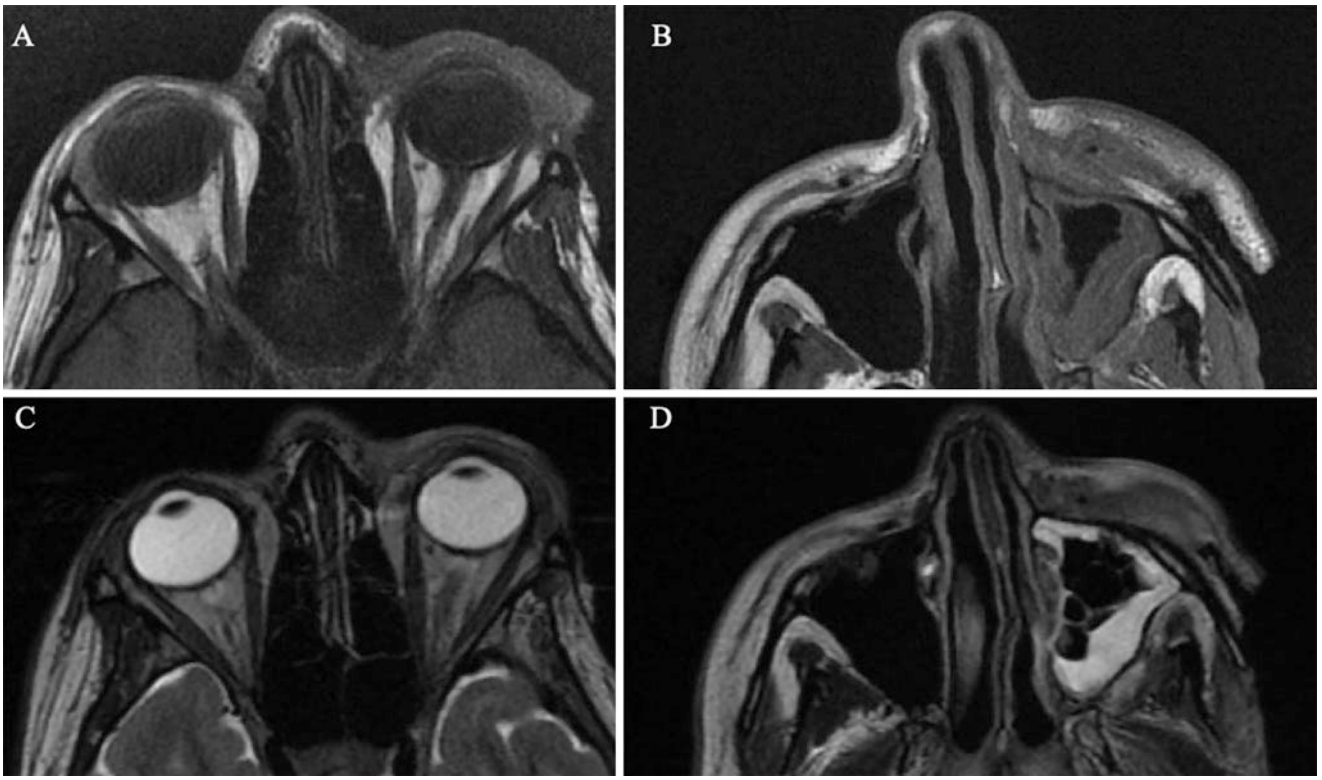


Fig. 2 Axial (**a** and **b**) T1- and (**c** and **d**) T2-weighted fat suppression magnetic resonance images. Fungal material appears isointense on T1 and hypointense on T2, compared to the extraocular muscles [10]. This patient required extensive debridement of necrotic tissue resulting in a large cutaneous defect overlying the left cheek and temple region. Unfortunately, she was too unwell to receive contrast; however, in cases where contrast is administered, there may be mild to moderate, patchy enhancement [1]

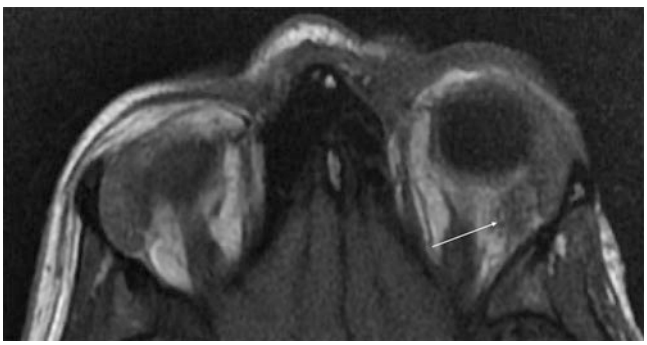


Fig. 3 Axial T1-weighted magnetic resonance image demonstrating early intraorbital extension (arrow)

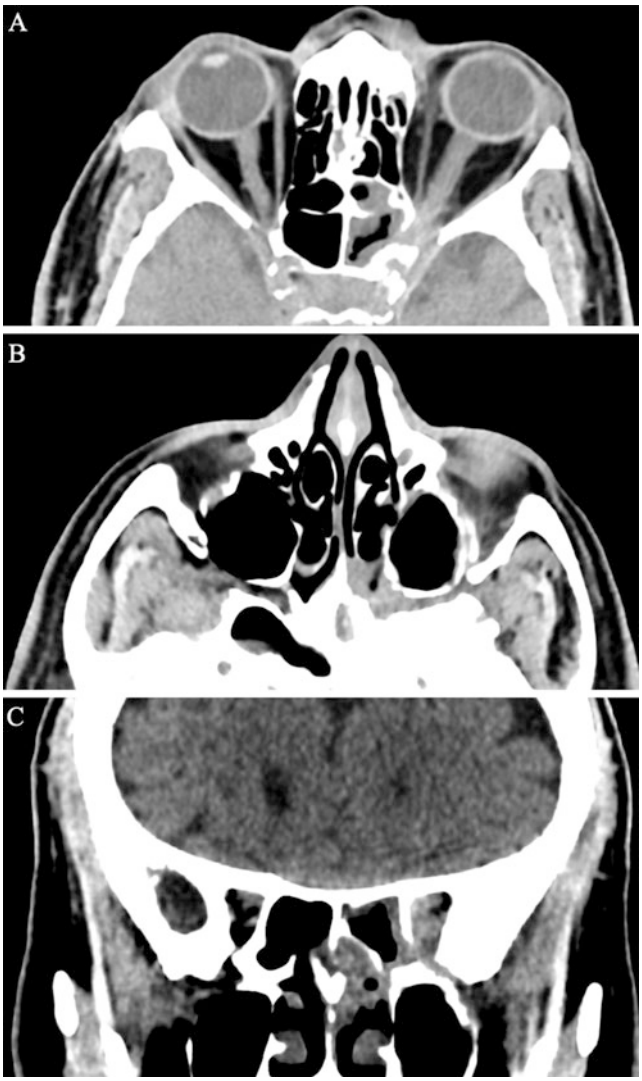


Fig. 4 (**a**) A 62-year-old male with left sino-orbital mucormycosis. (**a** and **b**) Axial and (**c**) coronal nonenhanced computed tomography demonstrates involvement of the left sphenoid sinus, orbital apex, inferior orbital fissure, and pterygopalatine fossa. (Courtesy of the editors)

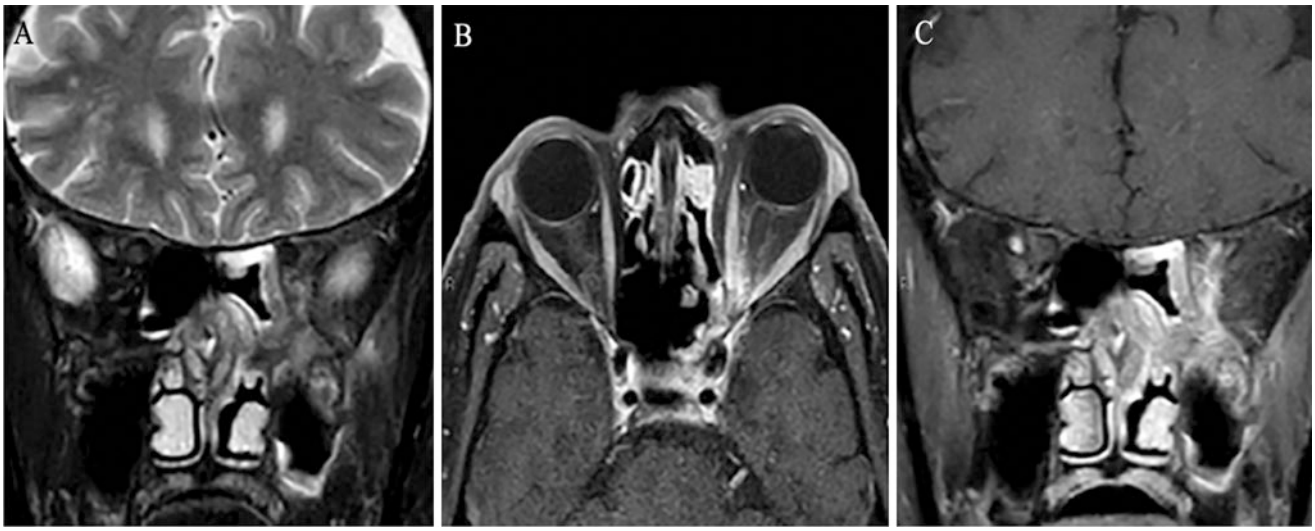


Fig. 5 Magnetic resonance imaging of the same patient illustrated in Fig. 4. (**a**) T2-weighted fat saturation demonstrates a hypointense signal along the left sphenoid sinus and orbital apex typical of mucormycosis. (**b**) Axial and (**c**) coronal T1-weighted fat saturation images show marked contrast enhancement of the infection. (Courtesy of the editors)

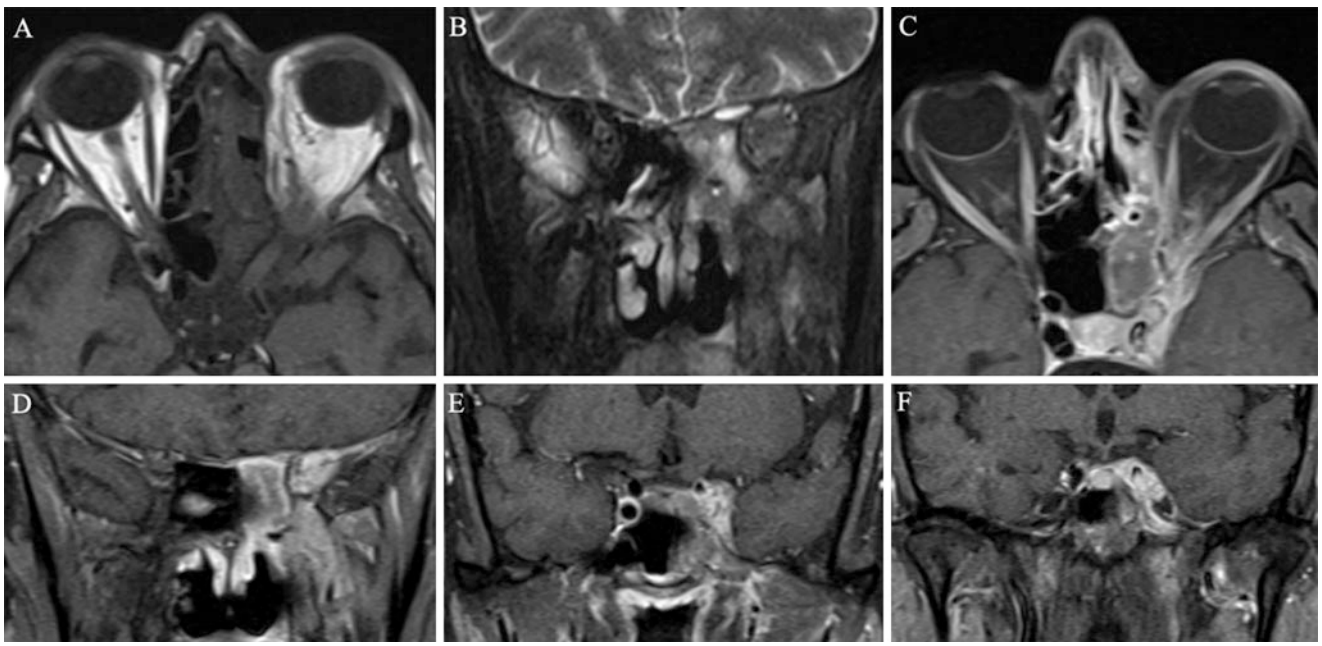


Fig. 6 A 56-year-old poorly controlled type 2 diabetic patient presented with a 4-day history of progressive proptosis, diplopia, and vision loss in the left eye. Nonenhanced (**a**) axial T1-weighted image shows a hypointense lesion involving the left paranasal sinuses, orbital apex, and skull base (**b**) that has heterogenous hyper- and hypo-intense regions on coronal T2-weighted fat saturation sequences. Following administration of gadolinium, (**c**) axial and (**d**–**f**) coronal T1-weighted fat saturation images show moderate, heterogenous enhancement of the mass involving the left paranasal sinuses, orbital apex, and pterygopalatine fossa. (**e**) The lesion extends posteriorly to the cavernous sinus, with narrowing of the left intracavernous internal carotid artery and (**f**) extends along V2 to the level of Meckel's cave. Debridement of the sinuses confirmed the diagnosis of mucormycosis

References

1. Aggarwal E, Mulay K, Menon V, Sundar G, Honavar SG, Sharma M. Isolated orbital aspergillosis in immunocompetent patients: a multicenter study. Am J Ophthalmol. 2016;165:125–32.
2. Choi HS, Choi JY, Yoon JS, Kim SJ, Lee SY. Clinical characteristics and prognosis of orbital invasive aspergillosis. Ophthalmic Plast Reconstr Surg. 2008;24(6):454–9.
3. Lee AS, Lee PWY, Allworth A, Smith T, Sullivan TJ. Orbital mycoses in an adult subtropical population. Eye (Lond). 2019;34:1640–7.
4. Lee AS, Sullivan TJ. Orbital mycoses in a pediatric subtropical population: a case series. J AAPOS. 2019;23(5):270.e271–7.
5. Gamaletsou MN, Sipsas NV, Roilides E, Walsh TJ. Rhino-orbital-cerebral mucormycosis. Curr Infect Dis Rep. 2012;14(4):423–34.
6. Levin LA, Avery R, Shore JW, Woog JJ, Baker AS. The spectrum of orbital aspergillosis: a clinicopathological review. Surv Ophthalmol. 1996;41(2):142–54.
7. Asanad S, Lo C, Ugradar S, Rootman DB. Invasive cavernous sinus aspergillosis: an orbitocranial approach for diagnosis and management. Can J Ophthalmol. 2020;55(1):e33–6.
8. Ali MJ, Pujari A, Dave TV, Kaliki S, Naik MN. Clinicopathological profile of orbital exenteration: 14 years of experience from a tertiary eye care center in South India. Int Ophthalmol. 2016;36(2):253–8.
9. Kashkouli MB, Abdolalizadeh P, Oghazian M, Hadi Y, Karimi N, Ghazizadeh M. Outcomes and factors affecting them in patients with rhino-orbito-cerebral mucormycosis. Br J Ophthalmol. 2019;103(10):1460–5.
10. Pushker N, Meel R, Kashyap S, Bajaj MS, Sen S. Invasive aspergillosis of orbit in immunocompetent patients: treatment and outcome. Ophthalmology. 2011;118(9):1886–91.
11. Seiff SR, Choo PH, Carter SR. Role of local amphotericin B therapy for sino-orbital fungal infections. Ophthalmic Plast Reconstr Surg. 1999;15(1):28–31.

Orbital Hydatid Cysts

86

Milind N. Naik and Dilip K. Mishra

Contents

1 **Signs and Symptoms** 629
2 **Differential Diagnosis** 629
3 **Diagnosis** 630
4 **Treatment** 630
5 **Figures with Captions** 630
References 632

Abstract

- Hydatid cyst disease is an infection caused by *Echinococcus granulosus*, and is seen more commonly in certain endemic areas. Liver, lungs, and abdominal cavity are more commonly involved.
- Orbital hydatid cysts are rare, and mostly affect children and young adults.
- The history is often long standing, and insidious, with no symptoms apart from proptosis and globe dystopia.
- Imaging reveals a homogenous, thin-walled, well-defined cystic lesion, with rare polycystic nature. Orbital volume expansion due to bony excavation is common.
- Intact surgical removal, systemic screening for additional cysts, and oral albendazole in case of ruptured cysts are the mainstay of treatment.

Keywords

Orbital hydatid · Hydatid cyst · Orbital cyst

1 Signs and Symptoms

- Symptoms are often insidious, with proptosis and pressure symptoms leading to impaired motility, diplopia, papilledema, and optic atrophy (Fig. 1) [1].
- The cyst can be intra- or extraconal, with a predilection for supero-medial orbit [2].
- Rarely, the cyst may rupture, and the patient may present with fulminant orbital inflammation (Fig. 2).

2 Differential Diagnosis

Hydatid is rare within the orbit, and hence other cystic lesions are often considered as a possibility [3]. Circumscribed lymphangioma, cystic schwannoma, colobomatous cyst, orbital dermoid cyst, epidermoid cyst, teratoma, encephalocoele, and hematinic cyst are some of the differentials to be considered. Not uncommonly, it is an intraoperative diagnosis based on the classic finding of the cyst wall.

M. N. Naik (✉) · D. K. Mishra
LV Prasad Eye Institute, Hyderabad, India
e-mail: milind@drmilindnaik.com

© Springer Nature Switzerland AG 2022
G. Ben Simon et al. (eds.), *Atlas of Orbital Imaging*,
https://doi.org/10.1007/978-3-030-62426-2_72

3 Diagnosis

- Orbital ultrasonography can identify the cyst as unilocular well-circumscribed anechoic lesion [4]. However, it is of limited value in differentiating between various cystic lesions of the orbit.
- Computed tomography of the orbit shows the cyst as a hypodense, unilocular, well-defined, thin-walled, homogenous mass with a hyperdense rim [5]. Contrast administration will show a typical rim enhancement.
- Magnetic resonance imaging of the orbit shows a cystic lesion with a low-intensity signal on T1-weighted images and a high-intensity signal on T2-weighted images [4].
- CT scan and MRI of the orbit are diagnostic of the internal architecture of the cyst, and also provide information about surrounding important orbital structures. Rarely, polycystic nature of the cyst is revealed by imaging [6].
- Casoni intradermal test: Counter immuno-electrophoresis, double-diffusion tests, and indirect hemagglutination have also been used. These tests are simple with high sensitivity but have a low specificty, and are difficult to standardize. Positivity rates with orbital cycts are low, due to the localized nature of the cyst and lack of protoscolices.

4 Treatment

Radical surgery is curative. Complete removal of the endocyst with its contents is important. Endocystectomy can be performed with or without prior aspiration of the cyst. Meticulous aspiration of the cyst fluid, without spillage, followed by a hydrogen peroxide wash and subsequent removal of the endocyst wall, is curative.

5 Figures with Captions

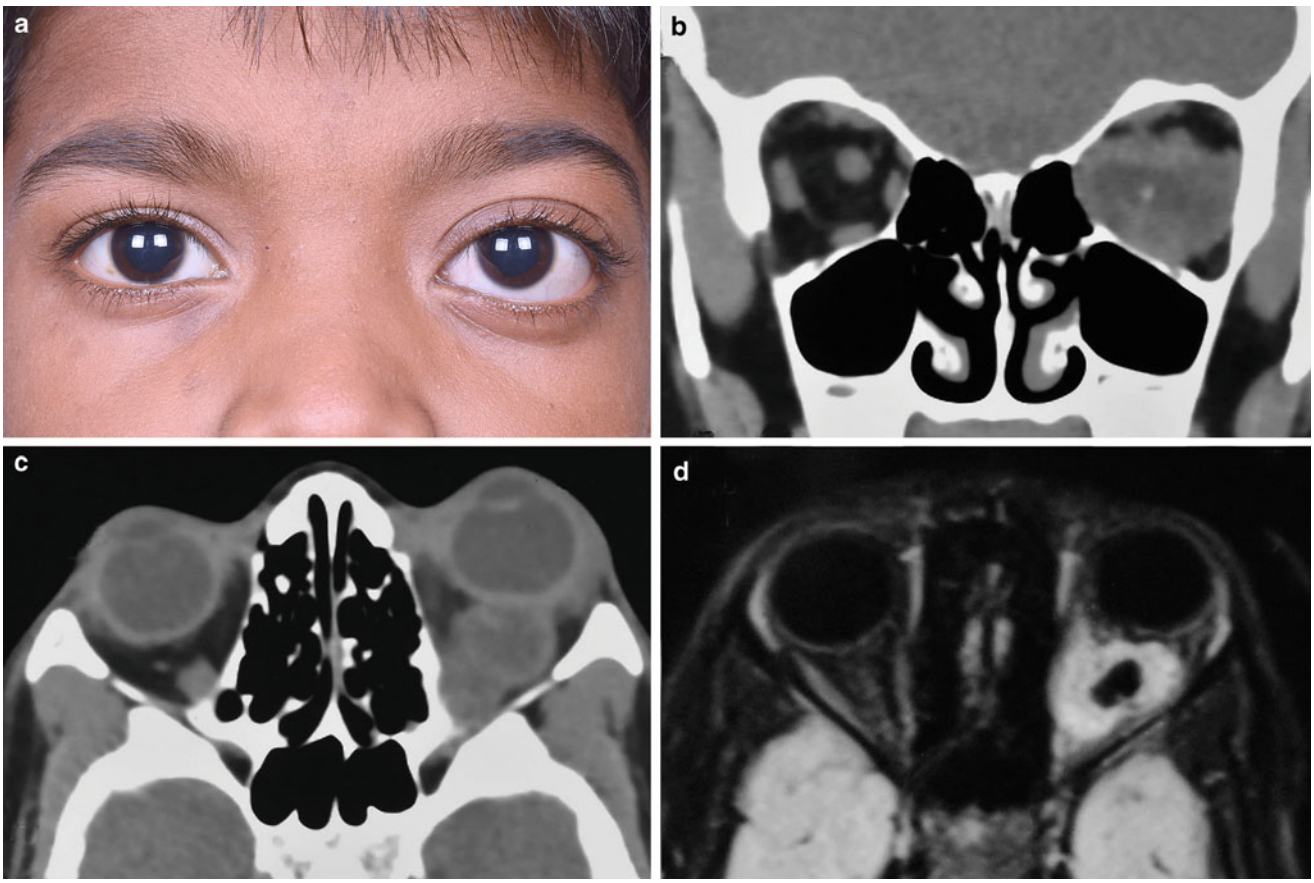


Fig. 1 A 13-year-old boy presented with two-years history of left proptosis (**a**). Recently, he noted blurring in the left eye. Vision was 6/60, left eye showed 4 mm proptosis with Grade I RAPD and blurring of disc margin. CT scan of the orbit (**b**, **c**) showed a large intraconal cystic mass, displacing the optic nerve superiorly, with ill-defined soft tissue density around the cyst representing the cyst wall. Note the central calcification within the cyst. MRI orbit showing FLAIR with fat suppression sequence (**d**) confirmed the cystic nature, with the thick pseudocapsule around the cyst, the low signal intensity in the center corresponds with the internal calcification. Multiple septae within the cyst or calcification may suggest polycystic or long-standing lesion to suggest the rare possibility of hydatid. An inferior transconjunctival approach was taken, and the endocyst was delivered intact after incising the soft tissue capsule around it

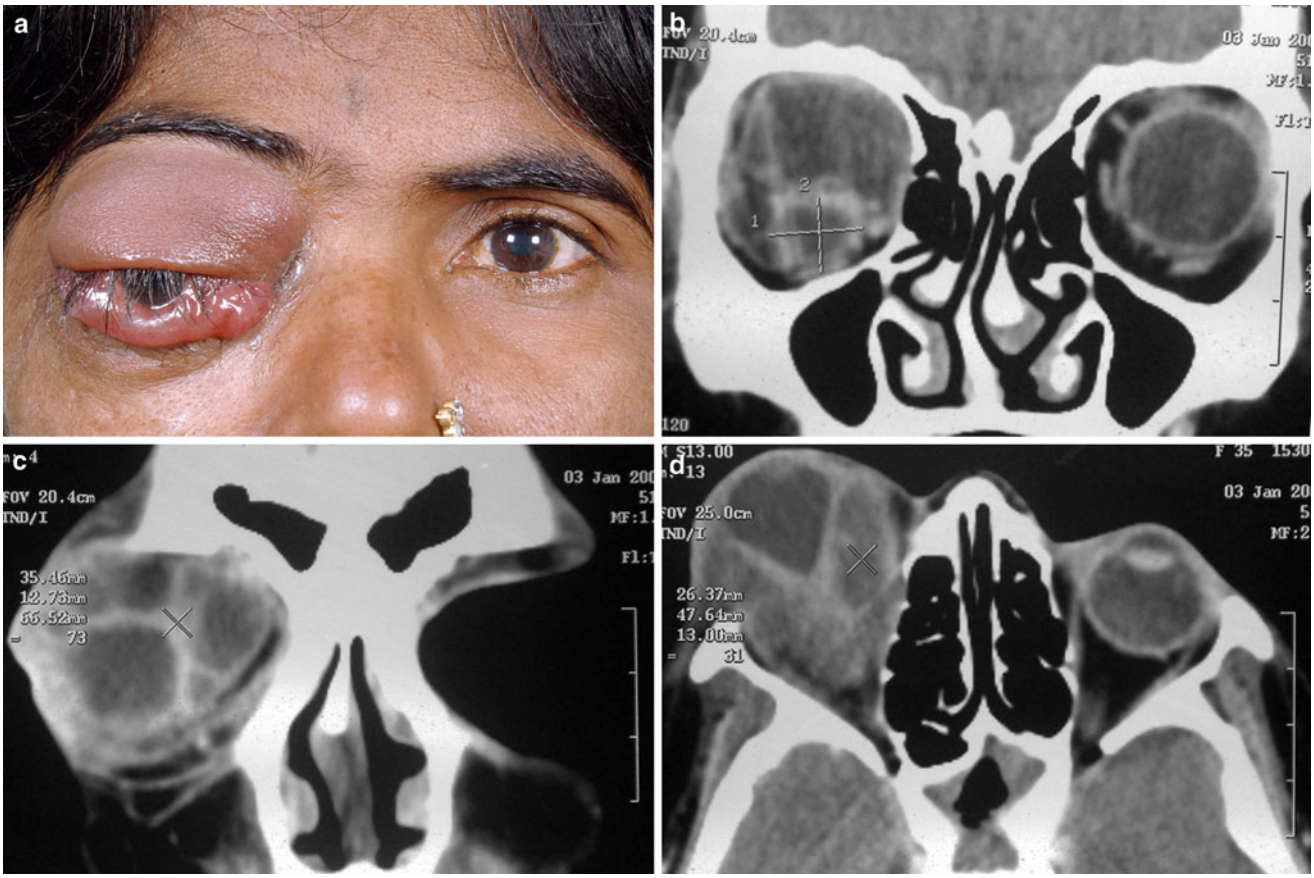


Fig. 2 A 35-year-old female presented with acute right proptosis, with referral diagnosis of orbital cellulitis (**a**). She reported a prominent right eye since 5 years. Orbital CT scan (**b**–**d**) showed a polycystic lesion in the intraconal space, leading to extreme proptosis and tenting of the eyeball. Image b shows the dimensions of the inferior cyst. A possible rupture of the cyst was suspected, explaining the acute inflammation. Surgical removal under steroid cover followed by albendazole therapy was given

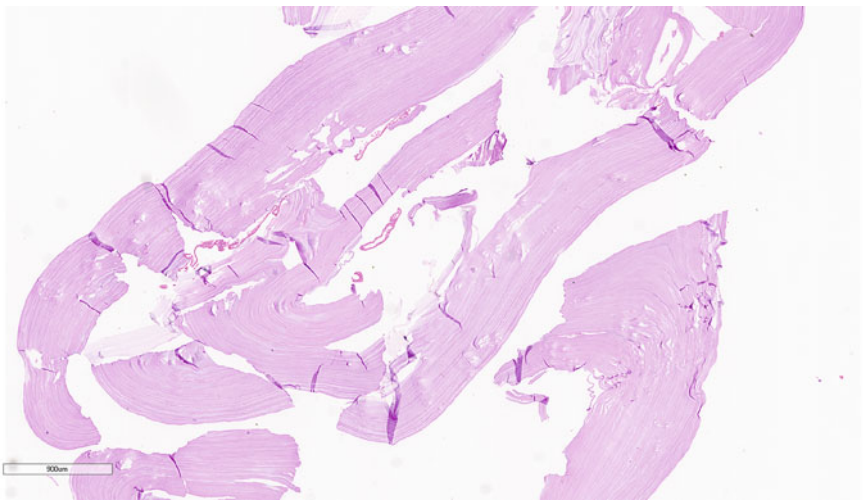


Fig. 3 Photomicrograph showing eosinophilic chitinous avascular laminated membrane like cyst wall of the hydatid cyst (Hematoxylin and Eosin stain, 8× digital scanner)

References

1. Gomez Morales A, Croxatto JO, Crovetto L, Ebner R. Hydatid cysts of the orbit. A review of 35 cases. Ophthalmology. 1988;95(8):1027–32. https://doi.org/10.1016/s0161-6420(88)33067-8.
2. Xiao A, Xueyi C. Hydatid cysts of the orbit in Xinjiang: a review of 18 cases. Orbit. 1999;18(3):151–5. https://doi.org/10.1076/orbi.18.3.151.2705.
3. Günalp I, Gündüz K. Cystic lesions of the orbit. Int Ophthalmol. 1996;20(5):273–7. https://doi.org/10.1007/BF00131923.
4. Hanioglu S, Saygi S, Yazar Z, Saltik G, Gürsel E. Orbital hydatid cyst. Can J Ophthalmol. 1997;32(5):334–7.
5. Kars Z, Kansu T, Ozcan OE, Erbengi A. Orbital echinococcosis. Report of two cases studied by computerized tomography. J Clin Neuroophthalmol. 1982;2(3):197–9.
6. Murthy R, Honavar SG, Vemuganti GK, Naik M, Burman S. Polycystic echinococcosis of the orbit. Am J Ophthalmol. 2005;140(3):561–3. https://doi.org/10.1016/j.ajo.2005.03.048.

Orbital Cysticercosis

87

Jaee M. Naik and Milind N. Naik

Contents

1 **Signs and Symptoms** 633
2 **Differential Diagnosis** 634
3 **Diagnosis** 634
4 **Treatment** 634
5 **Figures with Captions** 634
References 636

Abstract

- Orbital cysticercosis is a relatively common orbital parasitic infection in the developing world, and typically affects young individuals.
- Majority of the cysts lodge in the extraocular muscle (myocysticercosis), although isolated orbital cyst may rarely occur.
- Medical management with antiparasitic drugs (albendazole or praziquantel) under steroid cover (prednisolone) for a duration of 2–4 weeks is a highly effective treatment.
- Resolution of symptoms and signs may take a few weeks to months, and residual sequelae (extreme gaze diplopia or ptosis) may persist in 20% cases.

Keywords

Orbital cysticercosis, Myocysticercosis

1 Signs and Symptoms

- Commonest symptoms are: periocular swelling, proptosis, ptosis, and double vision [1].
- Commonest signs: motility restriction, diplopia, and proptosis (Fig. 1)
- Average duration of symptoms: 2 months
- Cyst location in decreasing order of frequency: anterior orbit, subconjunctival space, and posterior orbit
- Myocysticercosis: 80%; Orbital (free from muscle): 20%
- Frequency of muscles involved: superior rectus, inferior rectus, medial rectus, lateral rectus, and superior oblique
- Subconjunctival cysts are usually anterior, and lead to anterior orbital inflammation rather than motility restriction (Fig. 2)

J. M. Naik
St. John's Medical College, Bangalore, India

M. N. Naik (✉)
LV Prasad Eye Institute, Hyderabad, India
e-mail: milind@drmilindnaik.com

© Springer Nature Switzerland AG 2022
G. Ben Simon et al. (eds.), *Atlas of Orbital Imaging*,
https://doi.org/10.1007/978-3-030-62426-2_73

2 Differential Diagnosis

- Idiopathic myositis
- Orbital dermoid
- Cystic schwannoma
- Hydatid cyst
- Tumors metastatic to the extraocular muscle (for example, carcinoma breast cancer)

3 Diagnosis

- Clinical signs and symptoms
- Serology: indirect hemagglutination, indirect immunofluorescence, and enzyme-linked immunosorbent assay (ELISA)
- Radiological diagnosis:
  - (i) B scan ultrasonography: well-defined cyst with hyperechoic scolex [2].
  - (ii) A scan ultrasonography: high-amplitude spikes
  - (iii) Computed tomography scan: hypodense cystic mass with central hyperdense scolex

4 Treatment

- Medical therapy is preferred for myocysticercosis and orbital or retrobulbar cysticercosis. Oral albendazole (15 mg/kg body weight per day) for 4 weeks and oral prednisolone (1 mg/kg per day) for 4–6 weeks (Fig. 3).
- Surgical removal is preferred for subconjunctival and eyelid cysticercosis (Fig. 2).

5 Figures with Captions

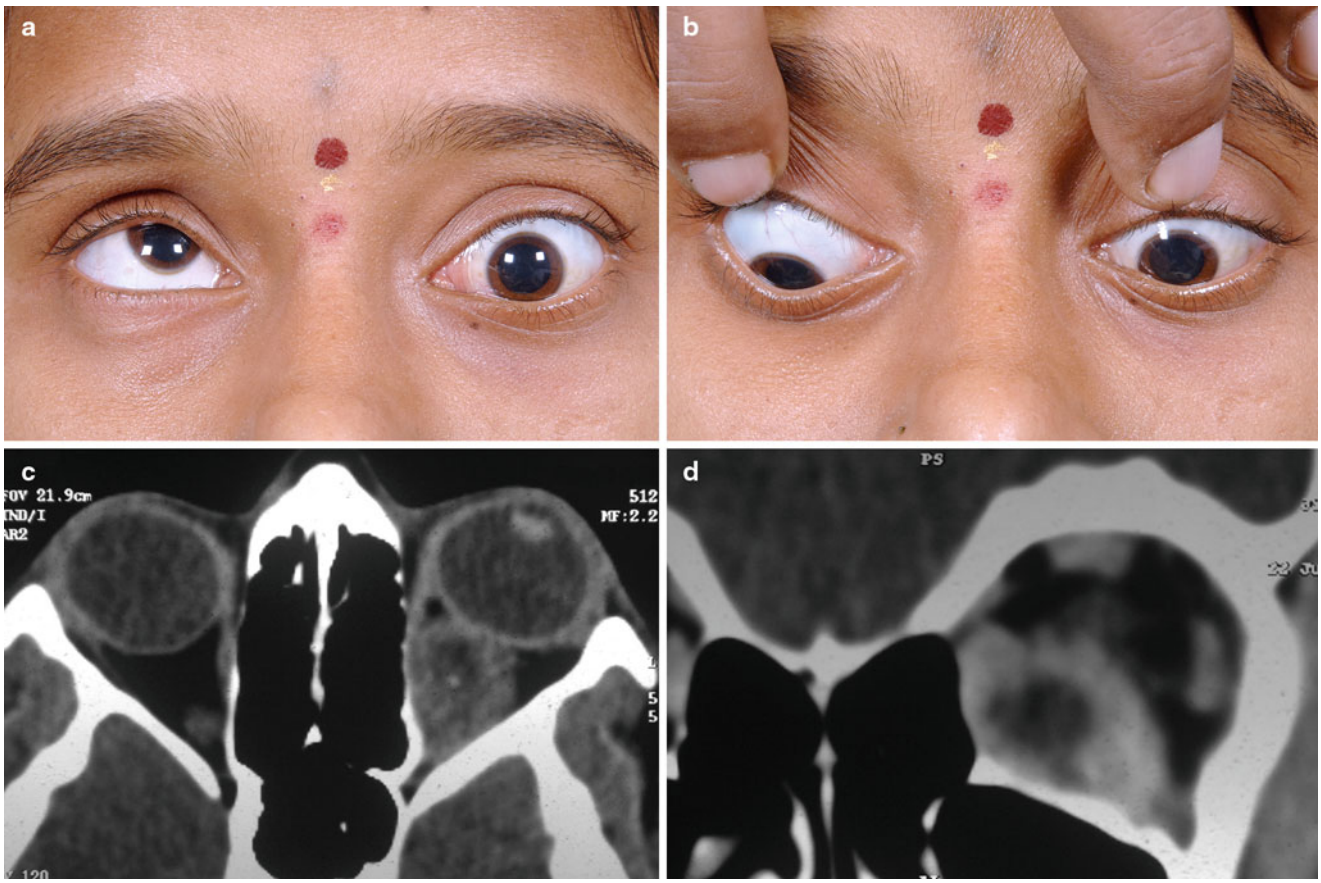


Fig. 1 A 13-year-old girl presented with left proptosis, and diplopia of 2 months duration. On examination she had gross upgaze restriction (a) and moderate downgaze restriction (b). Computed tomography plain scan axial section showed cystic lesion within the body of inferior rectus muscle, with a central hyperdense spot suggestive of scolex (c). Coronal section showing the cystic lesion along the inferior rectus muscle (d)

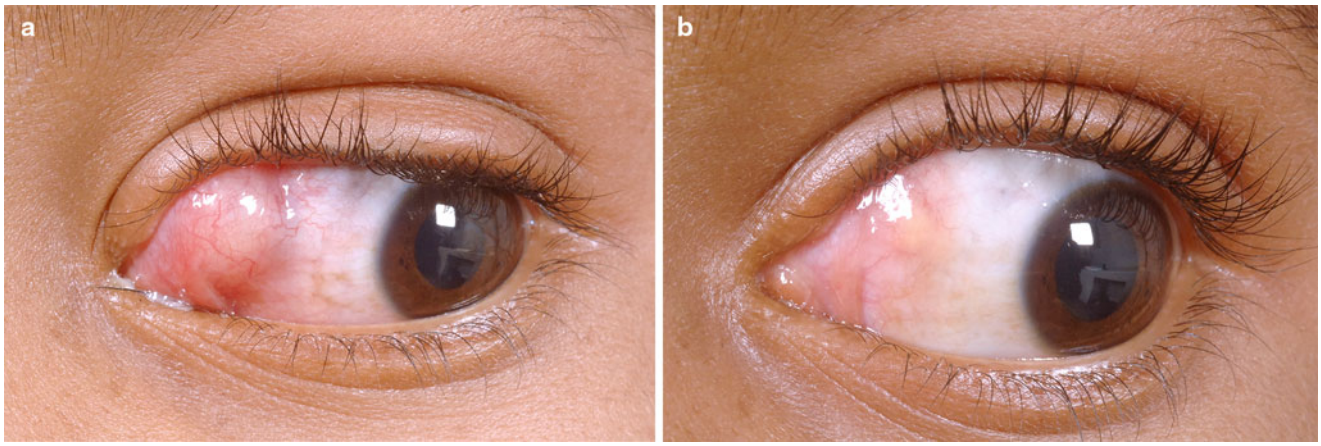


Fig. 2 A 15-year-old boy with left eye subconjunctival cystic mass within the medial fornix (a). There was no motility restriction, and the lesion could be removed via medial transconjunctival incision leading to a good recovery (b)

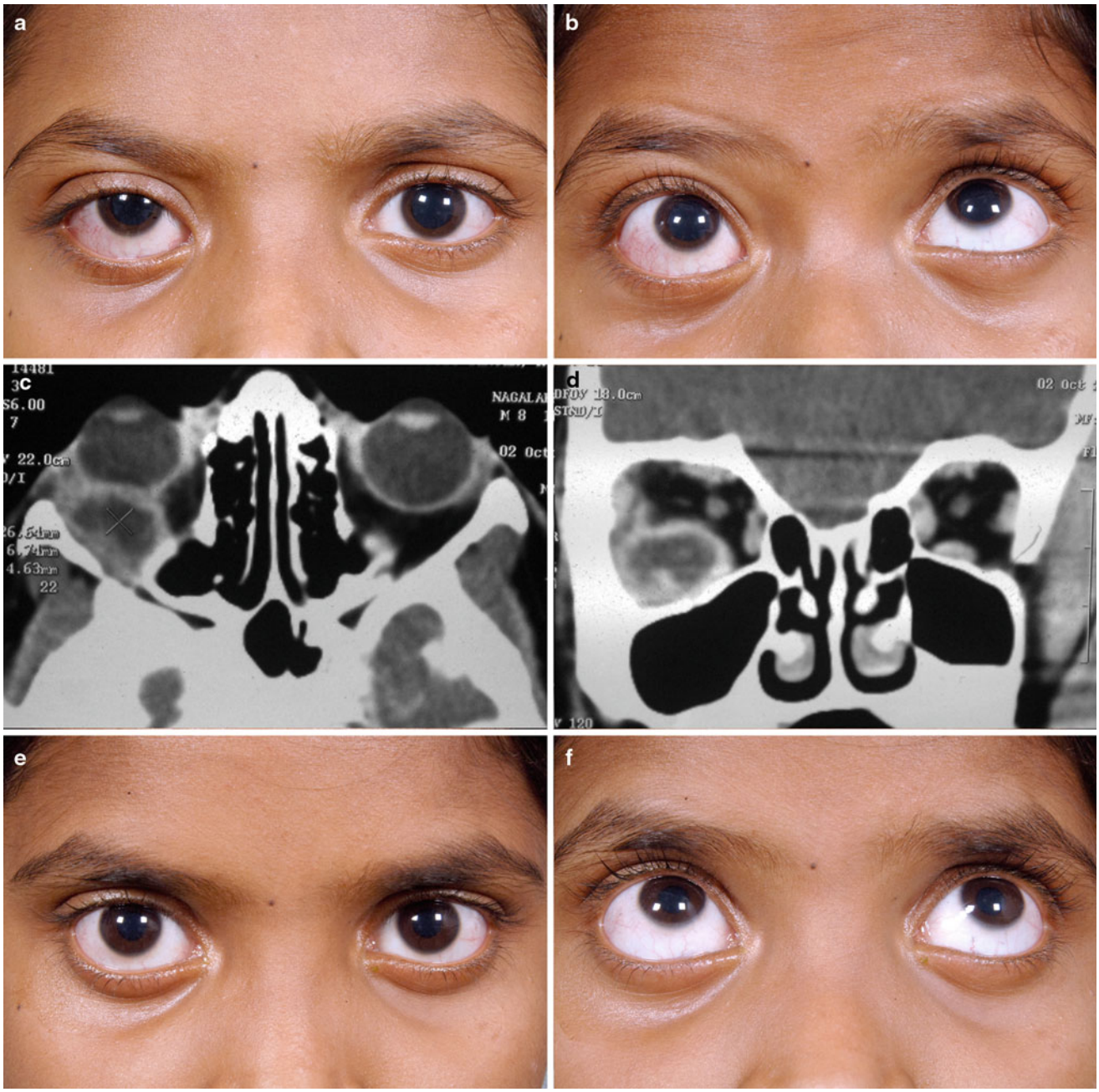


Fig. 3 A 22-year-old male presented with 6-week history of diplopia, pain around the right eye, and proptosis (a). Upgaze was restricted in the right eye (b). Computed tomography scan showed a cystic lesion within the right inferior rectus muscle (c, d), with a thickened hyperdense wall and a central hyperdense spot (scolex) that was better appreciated in the coronal scan. The patient received oral albendazone and prednisolone for 4 weeks, following which the proptosis resolved and upgaze improved (e, f)

References

1. Rath S, Honavar SG, Naik M, Anand R, Agarwal B, Krishnaiah S, Sekhar GC. Orbital cysticercosis: clinical manifestations, diagnosis, management, and outcome. Ophthalmology. 2010;117(3):600–5.
2. Honavar SG, Sekhar GC. Ultrasonological characteristics of extra-ocular cysticercosis. Orbit. 1998;17(4):271–84.

Granulomatous Orbital Inflammation: Orbital Tuberculosis (TB)

88

Milind N. Naik and Joveeta Joseph

Contents

1 **Signs and Symptoms** 637
2 **Differential Diagnosis** 638
3 **Diagnosis** 638
4 **Treatment** 638
5 **Figures with Captions** 639
References 645

Abstract

- Orbital tuberculosis (OTB) represents a rare form of extrapulmonary TB.
- Orbital involvement is either by hematogenous spread to orbital soft tissues, or by direct spread from the paranasal sinuses.
- It can involve the orbital bones, soft tissues, or both. Lacrimal system and overlying skin may also be involved.
- Coexisting systemic infection is common and should be ruled out.
- Clinical diagnosis is difficult and often necessitates an orbital biopsy.
- Microbiological evidence of infection (Acid fast bacilli) or characteristic histopathology clinches the diagnosis.
- Treatment with oral antituberculous therapy (ATT) is curative

Keywords

Orbital tuberculosis · Cold abscess · Mycobacteria

M. N. Naik (✉) · J. Joseph
LV Prasad Eye Institute, Hyderabad, India
e-mail: milind@drmilindnaik.com; joveeta@lvpei.org

1 Signs and Symptoms

- Risk factors to acquire orbital Tb include contact with an index case, lower socio-economic status, drug abusers, and some health care workers [1].
- The condition presents in one of the five forms [2]:
  - (i) Orbital tuberculoma or cold abscess without bone involvement: Presenting features include proptosis, palpable orbital mass lesion, diplopia, and pain (Fig. 1). Lesion can either be well-defined, or diffuse, with intracranial extension.
  - (ii) Classic periostitis: Chronic ulceration or discharging sinus in the periorbital region, with skin tethering to the surrounding bone, often leading to ectropion (Fig. 1). CT scan shows bony erosion, with irregular thickening of the bone, most commonly seen to affect the orbital margin.
  - (iii) Tuberculoma with bony involvement: Proptosis with bony involvement is seen in this category, and intracranial extension may also occur (Fig. 2)
  - (iv) Sino-orbital disease: Proptosis with globe dystopia is common, with maxillary sinus being most commonly involved (Figs. 3 and 4).
  - (v) Tuberculous dacryoadenitis: Presenting features include ptosis, proptosis, and a mass in the region of the lacrimal gland, with or without regional lymphadenopathy (Fig. 5).

© Springer Nature Switzerland AG 2022
G. Ben Simon et al. (eds.), *Atlas of Orbital Imaging*,
https://doi.org/10.1007/978-3-030-62426-2_110

2 Differential Diagnosis

Sarcoidosis, idiopathic orbital inflammation, sino-orbital fungal granulomas, and sinus/orbital malignancies are some of the close differentials to be considered. For lesions involving only the lacrimal gland, lacrimal gland tumors and infiltrative disorders form the possible differentials. Orbital tuberculosis involving the bone can mimic sphenoid wing meningioma, especially when there is surrounding bony sclerosis. Orbital lesions with surrounding osteolytic activity should also suggest histiocytic lesions as a possible differential.

3 Diagnosis

- Diagnostic criteria: Orbital tuberculosis can be established based on one or more of the following criteria [3]:
  (i) Clinical, radiological, and histological features of the orbital lesion with the presence of a tuberculous lesion elsewhere in the body
  (ii) Demonstration of acid fast bacilli
  (iii) Positive culture using tissue sample/fluid
  (iv) PCR evidence of *Mycobacterium tuberculosis*
- Biopsy: Any patient who presents with one of the five classic presenting types described above and supported by radiologic evidence should be subjected to biopsy confirmation. And all patients should also be investigated for systemic TB.
- Presence of AFB: Direct smear examination of orbital pus aspirate can show AFB with Gram stain or Ziehl Neelsen stain (Fig. 6).
- Histology: The histological hallmark of TB is the epitheloid granuloma with Langerhans giant cells and caseation necrosis (Fig. 7). The presence of AFB can be missed in formalin-fixed tissue; hence, immunohistochemical techniques may increase the specificity of histologic assessment.
- Culture: Culture of mTB remains the gold standard to clinch the diagnosis. Traditional media like Lowenstein Jensen can be used, although it may take weeks for the growth (Fig. 6). Recent automated commercial broth culture systems use colorimetric or radiometric methods of mycobacterial growth detection and can give positive results in 1–3 weeks [4].
- Nucleic acid amplification techniques: Polymerase Chain Reaction (PCR) is a rapid test for the diagnosis of TB, with high specificity (93.7–100), but low sensitivity (27–100%) [5].
- Ancillary tests: Mantoux or tuberculin skin testing can be performed, but has very limited diagnostic role in endemic areas or for Orbital TB. Interferon-based immunological tests, such as measurement of interferon-gamma (IFN-y), are available as commercial kits, with sensitivity similar to Mantoux, but a higher specificity. Chest radiography can reveal pulmonary TB in at least 50% of cases [2].

4 Treatment

Surgery in Orbital TB is mostly diagnostic. It is therapeutic when surgical debridement of involved soft tissue and bone is performed. Treatment of Orbital TB is with 6–9 months of antitubercular treatment (ATT) [4, 6]. Treatment regimen comprises of a two-month initial phase (rifampicin, isoniazid, pyrazinamide, and ethambutol, followed by a four-month continuation phase (rifampicin and isoniazid). Formation of nonhealing sinuses is a frequent complication, if surgical debridement is not accompanied with ATT.

5 Figures with Captions

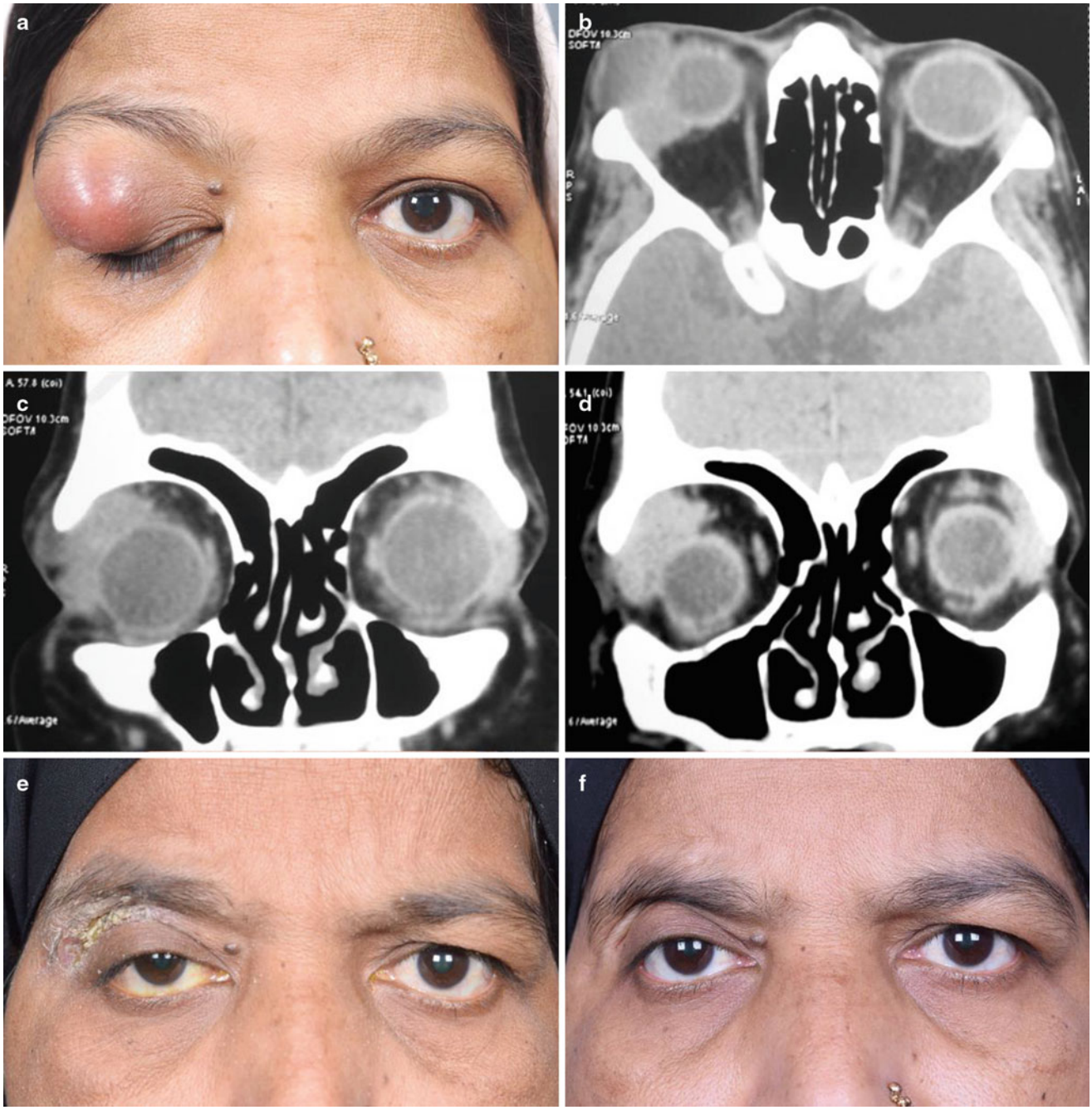


Fig. 1 A 48-year-old lady with 4 months history of right periorbital swelling with minimal pain (**a**). Computed tomography plain axial scan of the right orbit showed a large lobulated mass within the right lacrimal fossa, with a pronounced preseptal nonlucid cystic component suggestive of an abscess and a posterior more solid intraorbital component (**b**). Precontrast (**c**) and post-contrast (**d**) coronal CT scan of the mid-orbit shows diffuse enhancement of the superolateral extraconal mass. Following abscess drainage, she continued to have a discharging sinus, which led to the suspicion of tubercular etiology (**e**) and also demonstrated periosteitis, with orbital rim bony resorption that persisted even after complete cure (**f**)

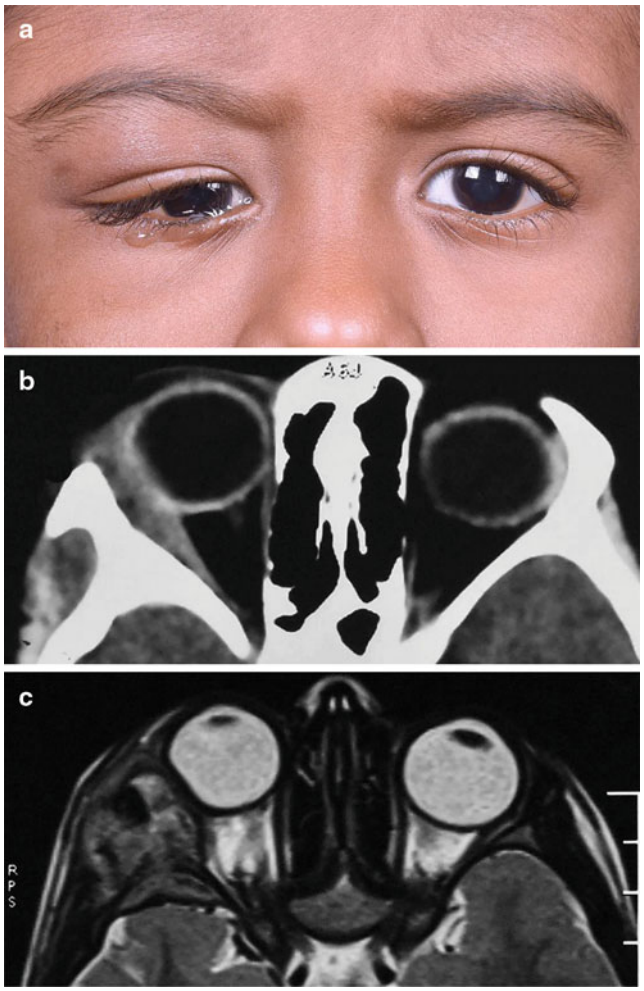


Fig. 2 An 8-year-old child with right periorbital fullness with nonaxial proptosis and globe compression (**a**). CT scan (**b**) and MRI of the orbit (**c**) revealed a diffuse, ill-defined sclerotic expansile bony lesion centered upon the greater wing of sphenoid with tri-lateral extension including temporal fossa, extra-conal orbit, and extra-dural middle cranial fossa involvement. An incisional biopsy with culture and smears proved tubercular etiology

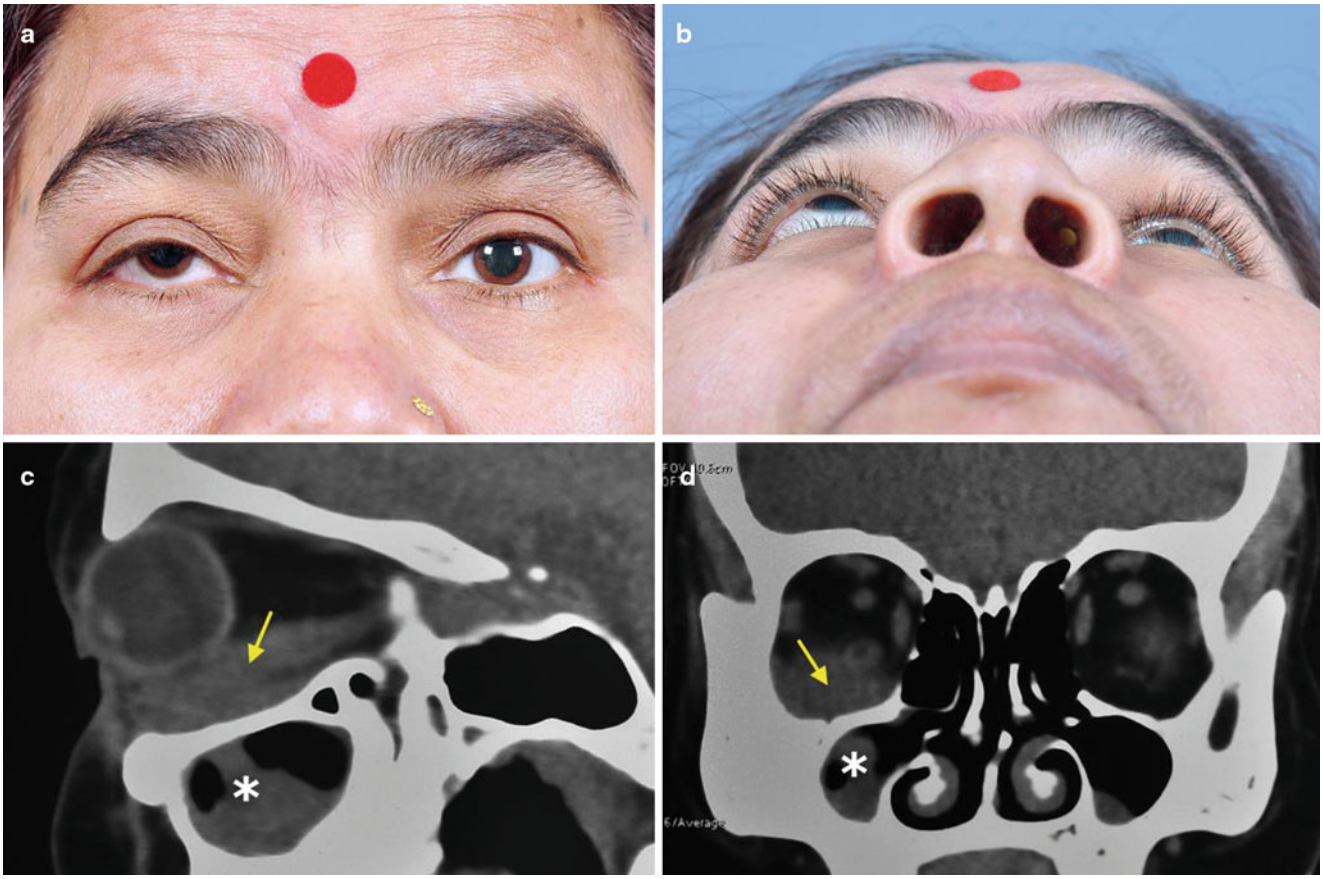


Fig. 3 A 50-year-old lady presented with right insidious nonaxial proptosis and hyperglobus (**a.b**). CT scan of the orbit (**c, d**) revealed a diffuse-ill-defined inferior extra-conal orbital mass (arrow) with coexisting paranasal sinus opacities (asterix). IOI/tumor mass, fungal granuloma, and sino-orbital tuberculosis were the differential diagnoses. Incisional biopsy revealed tubercular etiology

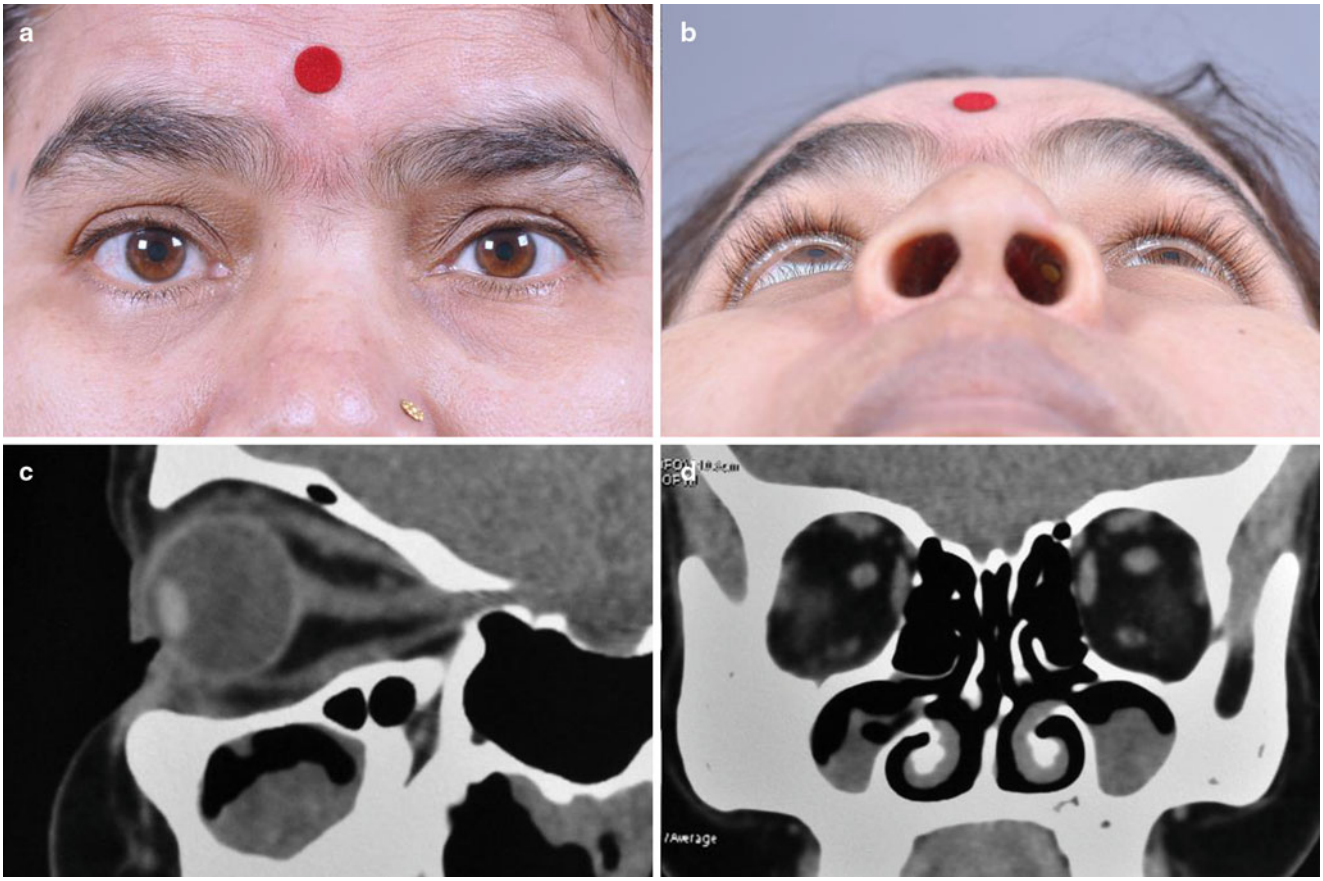


Fig. 4 Clinical photographs of the same patient with right orbital tuberculosis following 6 months of antitubercular therapy (**a, b**). Note the reduction in proptosis and hyperglobus as well as resolution of the inferior orbital mass on the right side (**c, d**)

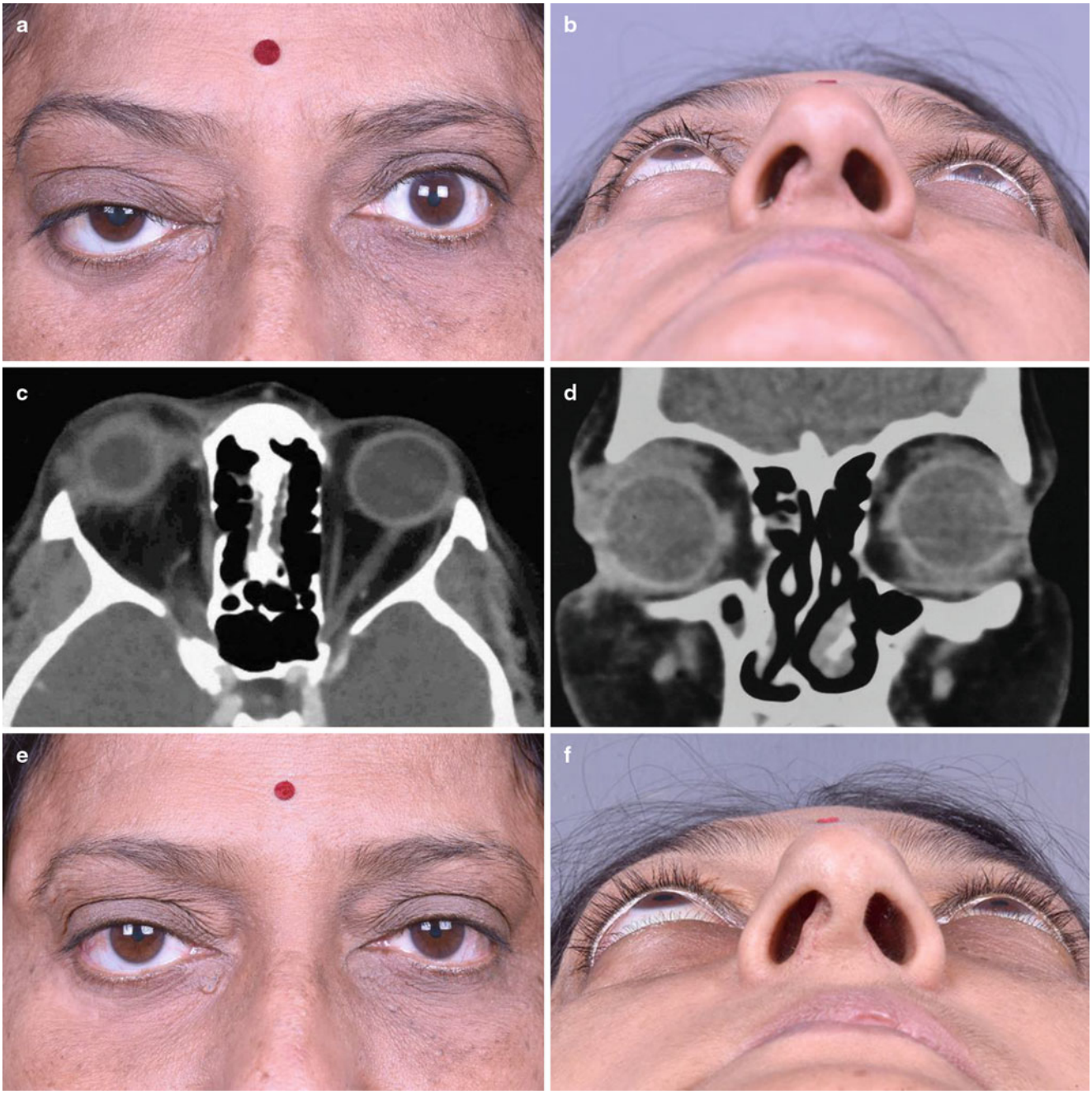


Fig. 5 A 47-year-old lady with right nonaxial proptosis and hypoglobus (**a, b**). CT scan of the orbit showed diffuse, ill-defined superotemporal soft tissue mass involving the lacrimal gland (**c, d**). Some component of the mass extended behind the equator of the globe, leading to proptosis. This classic dacryoadenitis like presentation of orbital tuberculosis responded well to antitubercular therapy (**e, f**)

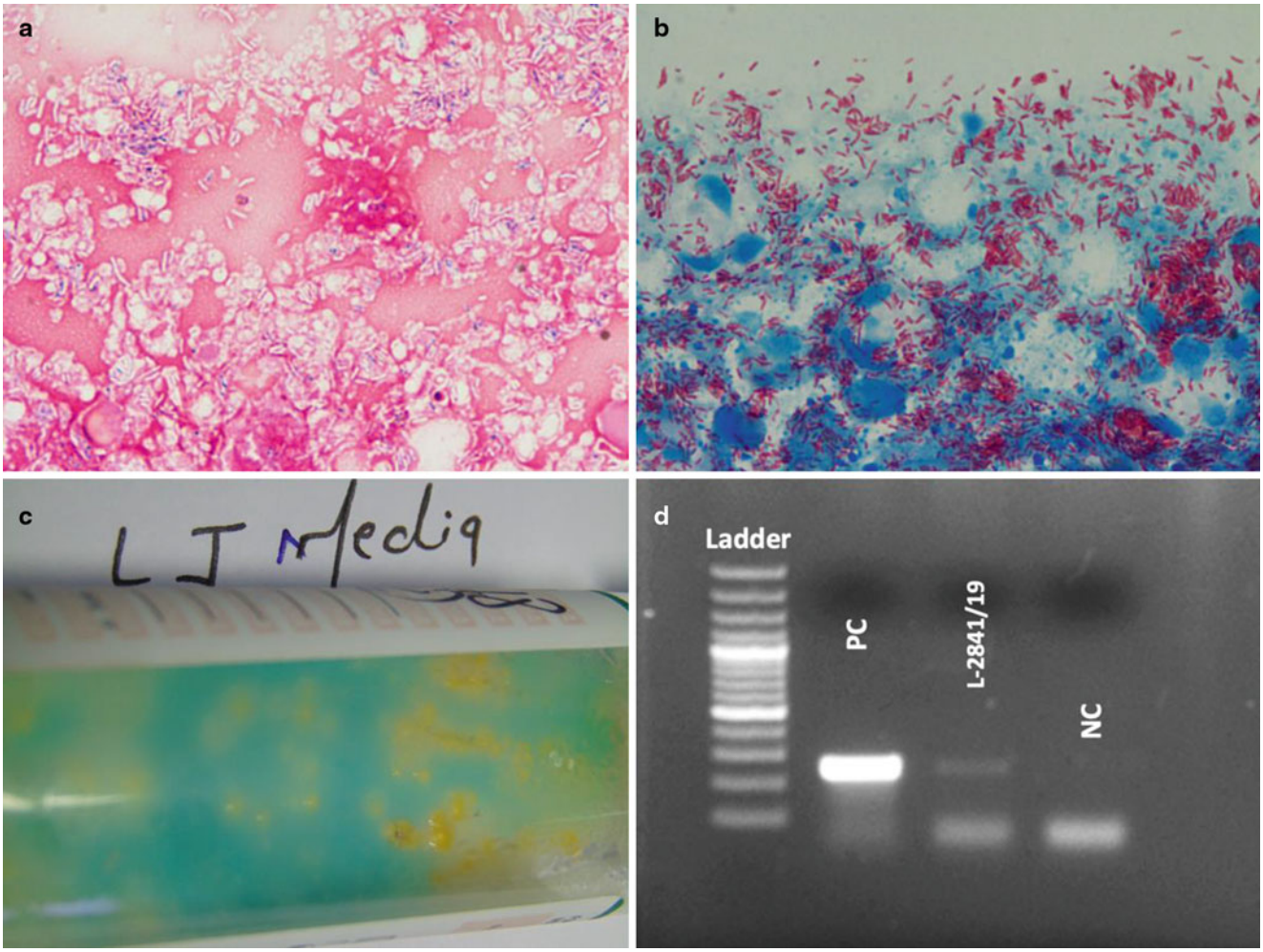


Fig. 6 Gram stain smear of orbital pus sample (magnification ×1000), showing plenty of unstained to poorly stained Gram positive beaded bacilli (**a**). Ziehl Neelsen stain smear of the purulent material (magnification ×1000) showing long, slender acid fast bacilli taken from the same patient (**b**). Culture of purulent material on LJ medium (Day 34, 37 °C, aerobic) showing typical non pigmented, rough, dry colonies which were creamy-white initially, becoming yellowish or buff-colored after prolonged incubation (**c**). Ethidium bromide stained gel electrophoresis picture showing results of one round of PCR amplification using primers for target gene MPB64 of *Mycobacterium tuberculosis* on DNA isolated from orbital biopsy of the patient (**d**). Amplified DNA of 240 bp size is seen in lane 2 containing PCR product from orbital biopsy (NC, negative control; ladder, base pair size marker; PC, positive control)

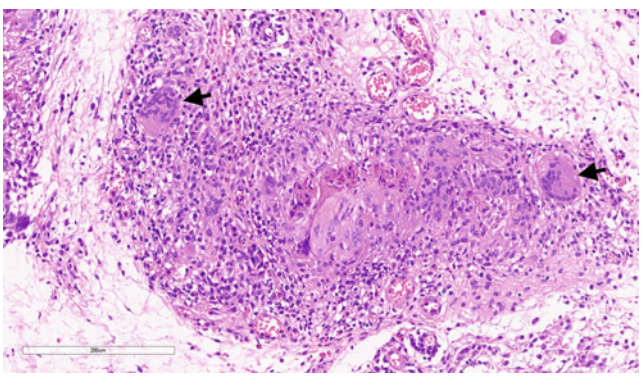


Fig. 7 Photomicrograph (Hematoxylin and Eosin stain, 20× Digital scanner) showing epithelioid granuloma formed of multinucleated giant cells (Black arrow), epithelioid cells, chronic inflammatory cells, and histiocytes. (Photo courtesy: Dr Dilip Mishra, MD, Ocular Pathologist, LV Prasad Eye Institute, Hyderabad, India)

References

1. Marks SM, Taylor Z, Qualls NL, Shrestha-Kuwahara RJ, Wilce MA, Nguyen CH. Outcomes of contact investigations of infectious tuberculosis patients. Am J Respir Crit Care Med. 2000;162(6):2033–8. https://doi.org/10.1164/ajrccm.162.6.2004022.
2. Madge SN, Prabhakaran VC, Shome D, Kim U, Honavar S, Selva D. Orbital tuberculosis: a review of the literature. Orbit. 2008;27(4):267–77. https://doi.org/10.1080/01676830802225152.
3. Sen DK. Tuberculosis of the orbit and lacrimal gland: a clinical study of 14 cases. J Pediatr Ophthalmol Strabismus. 1980;17(4):232–8.
4. Powell DA, Hunt WG. Tuberculosis in children: an update. Adv Pediatr Infect Dis. 2006;53:279–322. https://doi.org/10.1016/j.yapd.2006.04.014.
5. Cheng VC, Yew WW, Yuen KY. Molecular diagnostics in tuberculosis. Eur J Clin Microbiol Infect Dis. 2005;24(11):711–20. https://doi.org/10.1007/s10096-005-0039-1.
6. Golden MP, Vikram HR. Extrapulmonary tuberculosis: an overview. Am Fam Physician. 2005;72(9):1761–8.

Part XIII

Orbital Trauma and Other Inferred Changes

Orbital Trauma: Orbital Soft Tissue Injuries and Intraorbital Foreign Bodies

89

Gangadhara Sundar

Contents

1 **Introduction** 649

2 **Signs and Symptoms** 650

3 **Differential Diagnosis** 650

4 **Treatment** 650

5 **Diagnosis** 650

6 **Soft tissue injuries** 651
6.1 Globe injuries 651
6.2 Orbital Soft Tissue Injuries 652
6.3 Extraorbital Soft Tissue Changes 654
6.4 Foreign Bodies 654

7 **Conclusion** 659

References 660

Abstract

In addition to diagnosing orbital and orbitofacial fractures, recognizing and managing soft tissue injuries, which include the globe, the optic nerve, the extraocular muscles and other soft tissues are essential in ophthalmic trauma. Also, in penetrating, blunt, and blast injuries, recognizing and addressing orbital and periorbital foreign bodies which may cause significant structural and functional deformity is also very important. We herewith share important radiological features of globe, ocular adnexal, and periorbital soft tissue injuries including unique imaging characteristic of foreign bodies.

Keywords

Orbital trauma · Periorbital trauma · Orbital fractures · Orbital hematoma · Orbital emphysema · Orbital compartment syndrome · Open globe injuries · Closed globe injuries · Orbital foreign bodies · CT scan · MRI

1 Introduction

Orbital and orbitofacial injuries are common and may be classified into orbital contusions, penetrating injuries with or without orbital foreign bodies, and orbit and orbitofacial fractures. In this section, we shall focus on orbital, globe, periorbital soft tissue injuries, and orbital foreign bodies. These injuries should always be considered and comanaged along with underlying orbit and orbitofacial fractures if and when present.

G. Sundar (✉)
Orbit & Oculofacial Surgery, Department of Ophthalmology, National University Hospital, National University of Singapore, Singapore, Singapore
e-mail: Gangadhara_sundar@nuhs.edu.sg

© Springer Nature Switzerland AG 2022
G. Ben Simon et al. (eds.), *Atlas of Orbital Imaging*,
https://doi.org/10.1007/978-3-030-62426-2_122

2 Signs and Symptoms

Common symptoms of orbital soft tissue injury include pain, periorbital swelling, blurring or loss of vision, double vision, bleeding from the nose, and occasionally loss of consciousness as well from intracranial injuries.

Early signs often include periorbital ecchymosis, eyelid, periorbital or facial lacerations, proptosis from orbital hemorrhage, crepitus from emphysema, tenderness with or without orbital rim step deformity, infraorbital and/or supraorbital paresthesia, reduced visual acuity, diplopia in primary or other gazes from ocular motility limitation.

Late signs may include eyelid and periorbital scarring, variable degrees of visual loss, smoldering orbital infections especially in the presence of retained or contaminated foreign bodies, persistent ocular motility limitation with diplopia, abnormal globe position, or even phthisis bulbi.

3 Differential Diagnosis

With a history of significant trauma and the above signs, the diagnosis of significant orbital tissue disruption with or without fractures is usually straightforward. Visual loss may result from either closed globe, open globe injuries, or traumatic optic neuropathy. Monocular diplopia may result from dislocated lens. Binocular diplopia may result from contusion of one or more extraocular muscles, entrapment of the EOM/IMS complex or cranial neuropathies. Moderate to severe proptosis with visual loss with or without RAPD may represent an Orbital Compartment Syndrome (OCS) and should be managed as an emergency. Rarely an absent globe may be present from displacement into one of the adjacent paranasal sinuses – maxillary or ethmoid or rarely into the anterior cranial fossa as well [1].

4 Treatment

Most orbital injuries may be managed conservatively with symptomatic and medical management after ruling out vision threatening globe or orbital injuries, significant entrapment, and large fractures. Significantly displaced orbital or orbitofacial fractures, especially those with entrapment of the extraocular muscle – intermuscular septum complex (EOM/IMS complex) or large soft tissue herniation often require surgical management. Open globe injuries should be managed urgently after stabilizing the patient. Orbital compartment syndrome may warrant an urgent bedside canthotomy, cantholysis, and septolysis. Orbital foreign bodies may be observed or removed based on the nature, the location, the morbidity caused, and patient preference.

5 Diagnosis

Orbital and orbitofacial imaging may be performed with ultrasound scan, plain x-ray, CT scan, and occasionally MRI. CT angiography is nowadays considered in patients presenting with acute craniofacial trauma to rule out intracranial vascular and soft tissue abnormalities concomitantly. Noncontrast fine cut CT scans are the imaging modality of choice in orbitofacial trauma for both bony and soft tissue injuries [2]. Ultrasound is only minimally useful for orbital injuries, but very useful in the assessment and follow-up of suspected closed globe injuries with limited intraocular visualization or gently in open globe injuries following repair. Some common indications, contraindications, advantages, and limitations of various imaging modalities are shown in Table 1.

It should be remembered that orbital imaging is not only essential for diagnosis and helps detect and localize foreign bodies, but the imaging data is also useful for preoperative treatment planning, intraoperative guidance and may be compared to postoperative imaging as well.

In this chapter, we shall present the soft tissue changes from orbital and orbitofacial trauma and highlight characteristics of intraocular and intraorbital foreign bodies [3] highlighting relevant features on CT scan and MRI.

Table 1 Imaging modalities and their relevance to ophthalmic trauma

Imaging modality	Indications	Contraindications	Advantages	Disadvantages
Ultrasound	Closed globe injury with limited posterior segment view	Open globe injury	Availability in ophthalmic practices Inexpensive	Technician dependent Can miss superficial/ anterior segment pathology
Plain x-ray	Screening for radioopaque foreign bodies	None	Availability in most medical centers/ emergency rooms Inexpensive Low dose radiation	Poor sensitivity Poor specificity Limited use intraoperatively (poor localization)
CT scan	All significant soft tissue and bony injuries	Pregnancy (relative)	Fast acquisition High resolution Reliable localization Bony and soft tissue imaging Orbital fat – natural contrast Hounsfield units measurement	Radiation exposure
MRI	Suspected wooden & other organic foreign bodies Traumatic optic neuropathy without optic canal fractures, optic nerve/nerve sheath hematoma	Ferromagnetic foreign bodies RF incompatible pacemakers	Better soft tissue resolution Better visualization of vegetative matter	Expensive Time consuming Motion artifacts
CT Angiogram	Severe craniofacial and suspect intracranial injuries	Anaphylactic reaction to iodine, Renal failure, Pregnancy (relative)	Orbital, facial and intracranial visualization Vascular pathology	Less soft tissue resolution
MR Angiogram	Suspect CCF	Uncooperative patient Incompatible pacemakers Ferromagnetic foreign bodies		Motion artifacts

6 Soft tissue injuries

6.1 Globe injuries

Soft tissues relevant to midfacial trauma include the globe, the orbital and periorbital soft tissues, the facial soft tissues, and intracranial spaces.

1. **Globe injuries:** These include closed globe injuries, open globe injuries, globe luxation, and avulsions [4] (Fig. 1). Open globe injuries include penetrating injuries, perforating injuries with/without intraocular foreign bodies [5], and ruptured globes. These may be recognized by the presence of an enlarged or distorted globe with extrusion of intraocular contents (Figs. 2 and 3a, b).

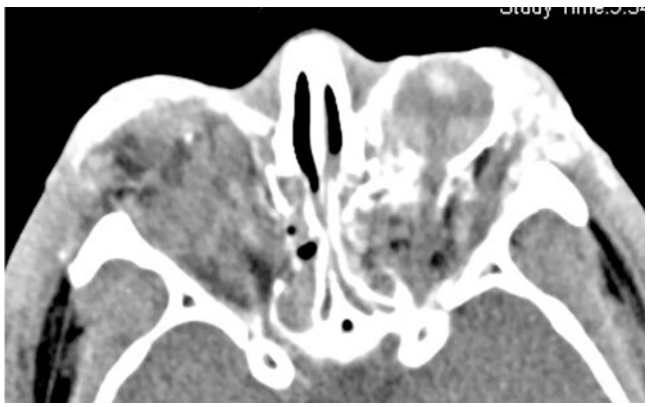


Fig. 1 Axial CT scan soft tissue window image of a blast injury patient: Dense orbital hemorrhage with absent globe in the right orbit, bilateral medial wall fractures, globe injury with vitreous hemorrhage, and dislocated lens on the left side

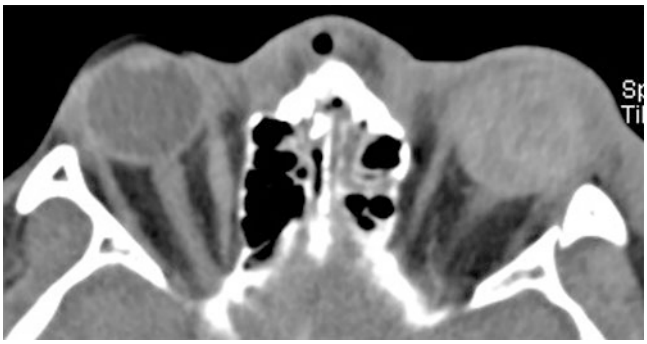


Fig. 2 Axial CT scan soft tissue window: Enlarged left globe with intraocular opacification (hemorrhage) and absence (extrusion) of the crystalline lens. Note incidental left ZMC fracture, ethmoidal sinus opacification, and emphysema of nasal bridge

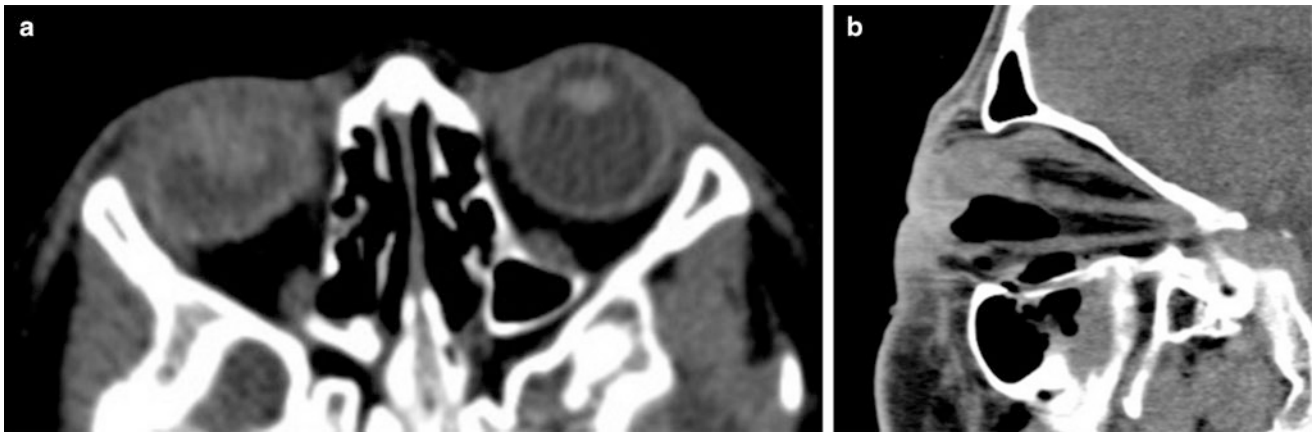


Fig. 3 Axial and sagittal CT scan soft tissue windows: Right globe deformation with dislocated lens from severe open globe injury (Flat tire sign)



Fig. 4 Coronal CT scan bone window: Left medial orbital wall fracture with emphysema of the superior and medial orbit

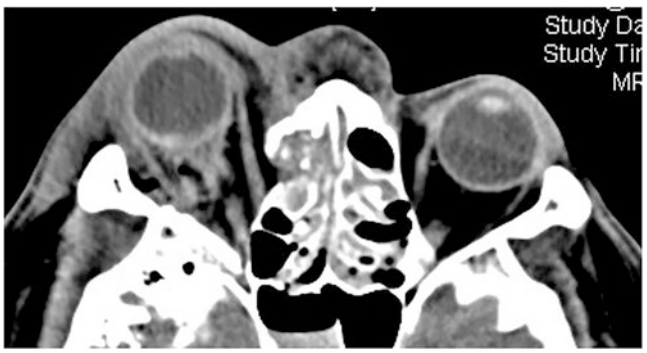


Fig. 5 Axial Ct scan soft tissue window: Right optic nerve/nerve sheath hematoma with severe proptosis, soft tissue swelling of the nasal bridge, and opacification of ethmoid sinuses. Note that discontinuity of optic nerve may be an artefact due to volume averaging or sinuous course of optic nerve

6.2 Orbital Soft Tissue Injuries

Other orbital soft tissue radiologic changes include orbital emphysema [6] (Fig. 4), orbital foreign bodies, optic nerve

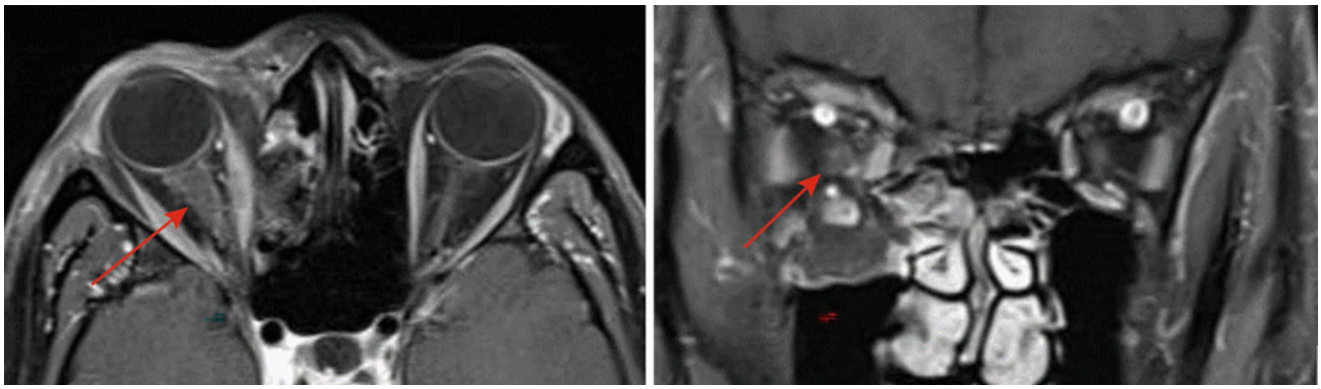


Fig. 6 Axial and coronal MRI Orbits fat saturated T1 weighted sequence with gadolinium: Right optic nerve sheath swelling in a patient with traumatic optic neuropathy

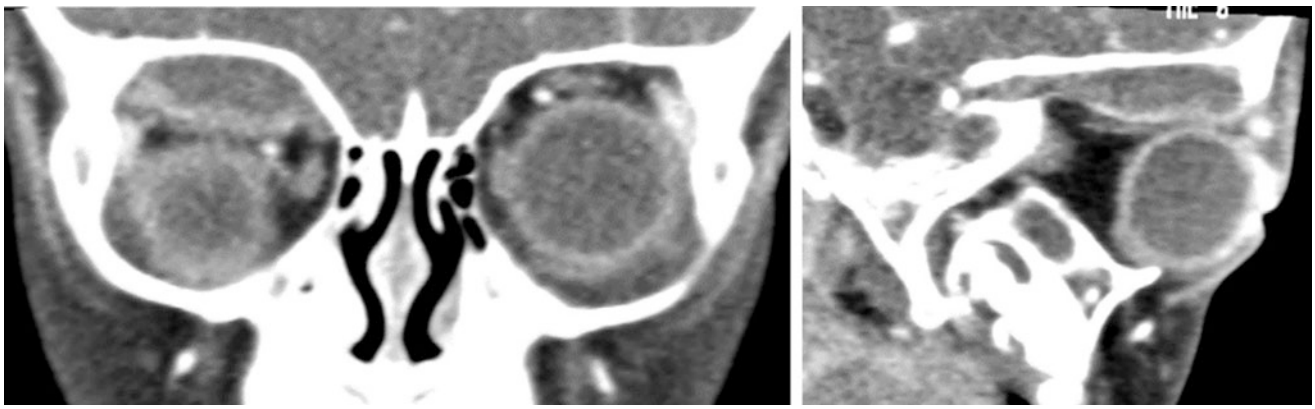


Fig. 7 CT scan coronal and sagittal soft tissues windows: 5-year-old child with orbital roof fracture and superior orbital subperiosteal hematoma

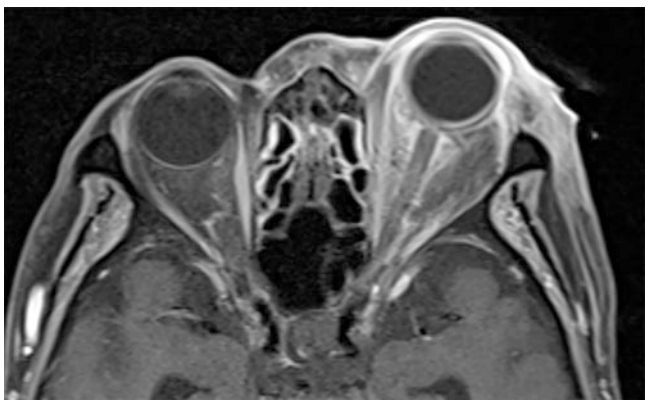


Fig. 8 T1 weighted axial MRI with fat saturation showing diffuse left orbital and periorbital hemorrhage with straightening of the optic nerve, orbital compartment syndrome, and visual loss



Fig. 9 Sagittal CT scan soft tissue window: Orbital soft tissue (inferior rectus and orbital fat) prolapse into the maxillary sinus



Fig. 10 Severe comminuted displaced left cranioorbitofacial fracture with intracranial hemorrhage



Fig. 11 Coronal bone window CT scan: Intracranial emphysema from frontal sinus involvement in a patient with right cranioorbital fracture

injuries (contusion, optic nerve/nerve sheath hematoma (Fig. 5, Fig. 6a, b) or optic nerve avulsion), orbital hemorrhage – subperiosteal or intraorbital hematoma (Fig. 7a, b) causing orbital compartment syndrome [7] (Fig. 8) and prolapse of orbital contents into adjacent paranasal sinuses (Fig. 9).

6.3 Extraorbital Soft Tissue Changes

Soft tissue changes may also be seen in adjacent soft tissues that include the facial soft tissues and intracranial cavity that may range from minimal to severe consequences. Common soft tissue intracranial radiologic features include intracerebral hemorrhage, pneumocephalus (Fig. 10), and occasionally a traumatic high flow carotid-cavernous fistula (CCF) [8] (Figs. 11 and 12). For the latter a selective angiogram is often helpful to identify feeders and direct treatment planning.

6.4 Foreign Bodies

Orbital foreign bodies may be present following crush injuries as well as penetrating injuries, blast injuries and falls. A high degree of suspicion should be maintained in all such injuries [9]. While radiopaque foreign bodies may be detected on plain x-rays [10] (Fig. 13), CT scan is the imaging of choice for both intraocular (IOFB) (Fig. 14) and intraorbital (IOrbFB) (Figs. 15–20) foreign bodies. Detection and localization are ideally performed with sub-mm Image Guidance Surgery (IGS) protocol, which may also be used intraoperatively [11]. Apart from history, the nature of foreign body may also be confirmed using the radiologic characteristics of the outline and the Hounsfield Units on CT scan [12, 13] (Table 2). Organic animal material and vegetative foreign bodies may be missed on CT scans or incompletely visualized. In such situations, MRI is often indicated when



Fig. 12 Axial and coronal CTscans: Left proptosis with dilated superior ophthalmic vein (*arrow*) and cavernous sinus (*arrow*) in a patient with traumatic high flow carotid-cavernous fistula

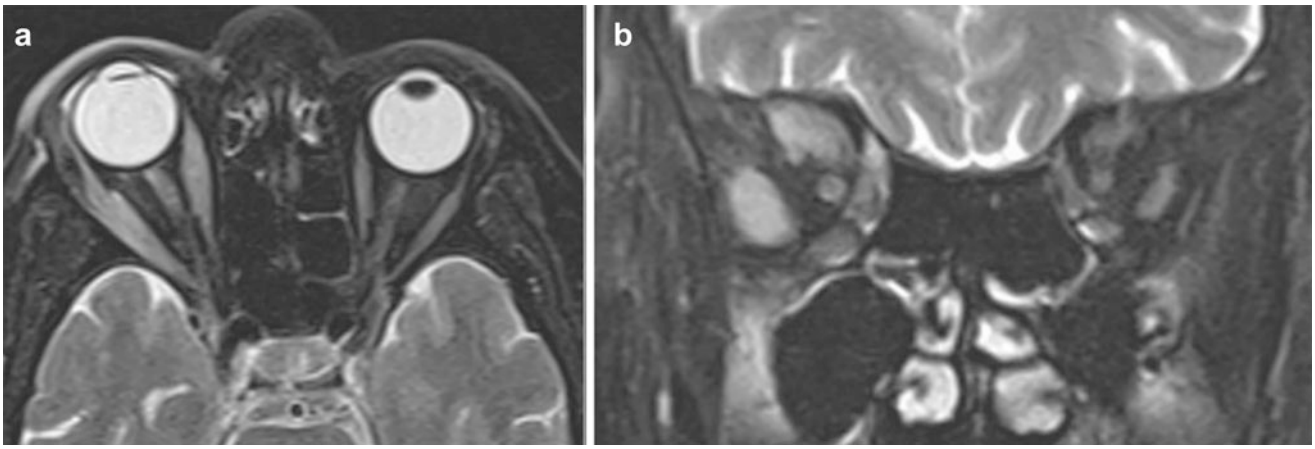


Fig. 13 MRI T2 weighted sequence, axial (*left*) and coronal (*right*): Right proptosis from congestive enlargement of all extraocular muscles in a patient with low flow carotid-cavernous fistula in a pseudophakic eye

Table 2 Hounsfield characteristics of foreign bodies and soft tissues on CT scan. In daily practice, region of interest (ROI) measurements are usually within a range of Hounsfield Units (HU) rather than an accurate number

Material	Hounsfield units (HU)
Metal	4000
Glass	2407
Stone	1876
Tooth	1881
Bone	700 to 3000
Graphite	742
Acrylic resin	193
Plastic	112 to 133
Muscle	71
Wood	60
Blood/hematoma	40 to 90
Water	0
Fat	−50 to −100
Air	−1000

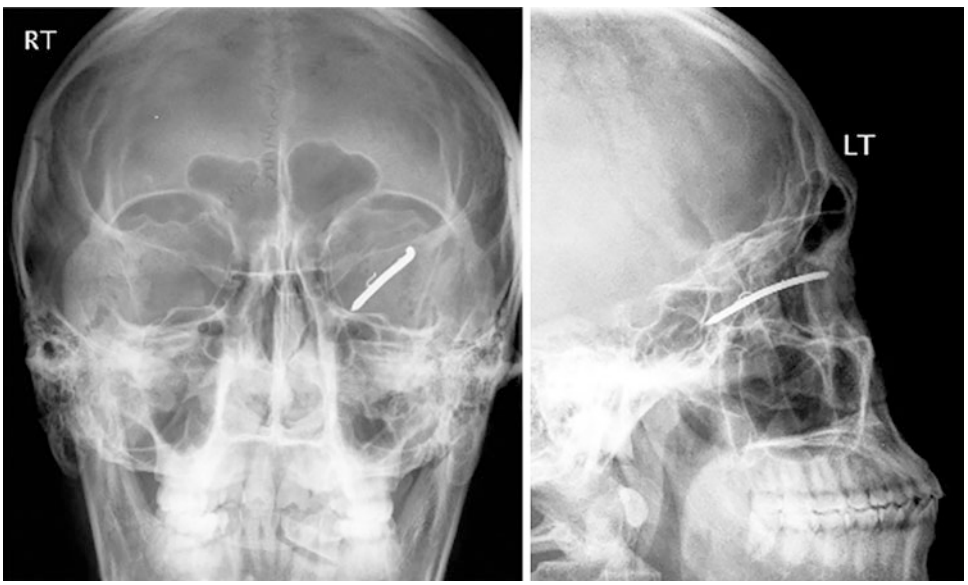


Fig. 14 Plain x-skull demonstrating linear radioopaque foreign body left orbit

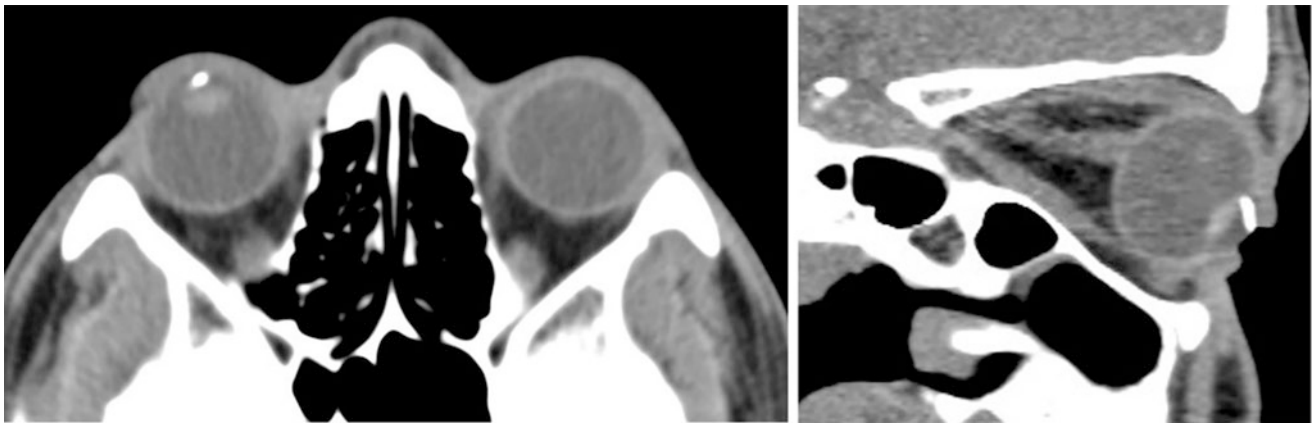


Fig. 15 Axial and sagittal CT scan soft tissue windows: Radiopaque intraocular foreign body in the anterior segment of the right eye

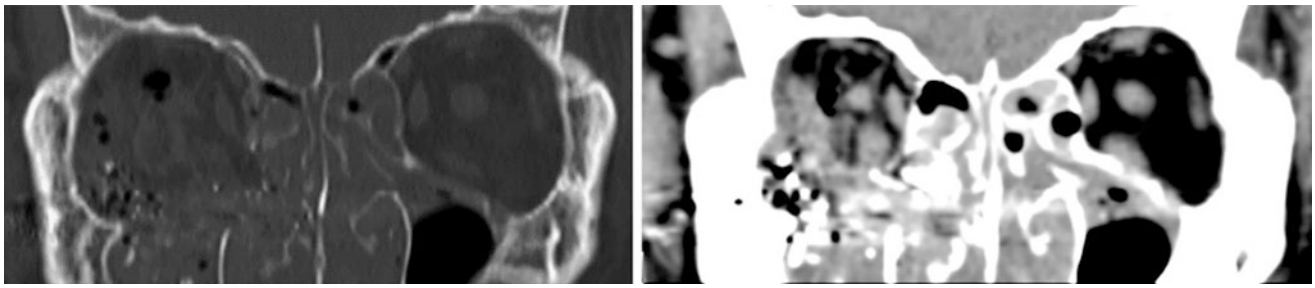


Fig. 16 Coronal CT scan bone and soft tissue windows in a gunshot wound: Multiple radiopaque opacities (Shattered bone) and soft tissue opacification of the right orbit and maxillary sinus with disruption of the medial wall and orbital floor

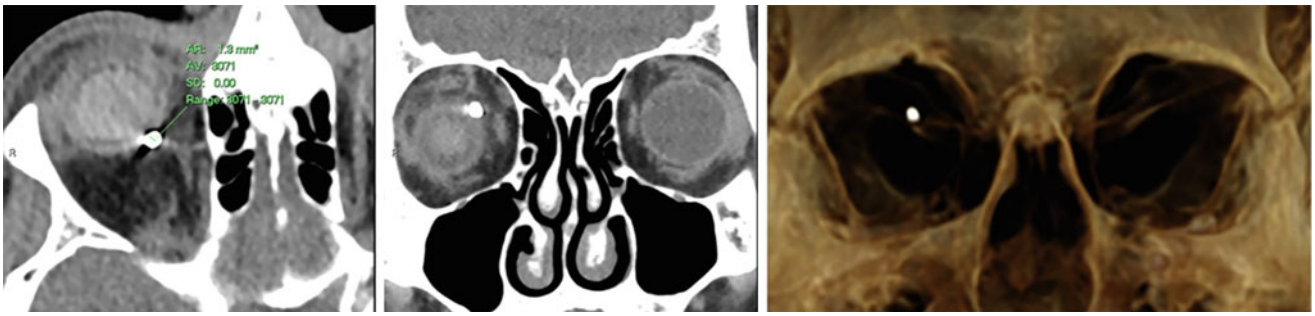


Fig. 17 Axial (*left*) and coronal (middle) CT scan soft tissue windows. Metallic posterior ocular foreign body with ROI measurements of 3071 HU compatible with a high density metal. Note hyperdense opacity filling the right eye evident of silicone oil post vitrectomy. 3D reconstruction (*right*) showing spatial resolution (Courtesy Dr Guy Ben Simon)

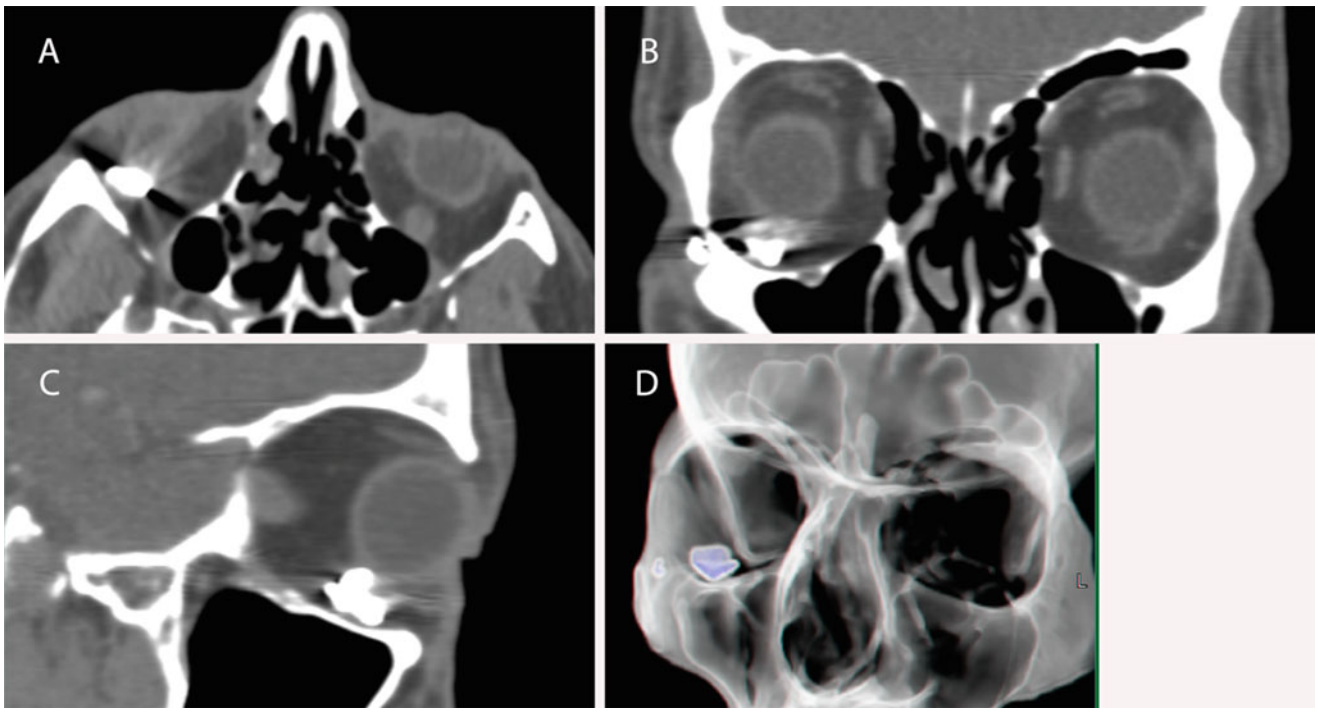


Fig. 18 CT scan soft tissue window (**a**, axial, **b**, coronal, **c**, sagittal) and 3D reconstruction (**d**) in a patient with a history of explosive injury: Note beam hardening artifact in all axial, coronal, and sagittal sections. 3D x-ray reconstruction (**d**) better demonstrates spatial location of the object (Courtesy Dr Guy Ben Simon)

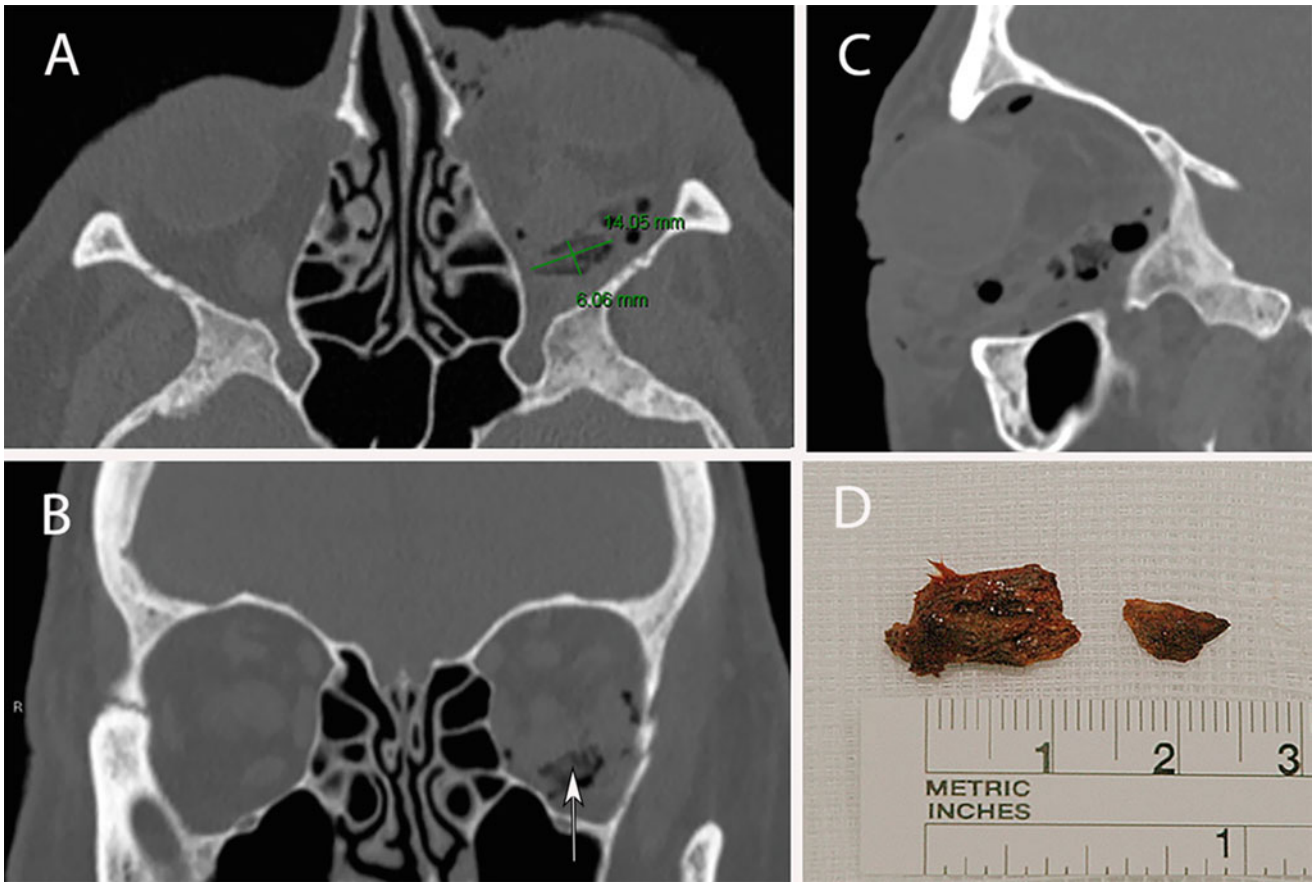


Fig. 19 CT Scan orbits bone windows **a**. axial, **b**. coronal, **c**. sagittal , masking radiolucent foreign body (**d**) in the inferotemporal intraoconal space with emphysema. (Courtesy Dr Guy Ben Simon)

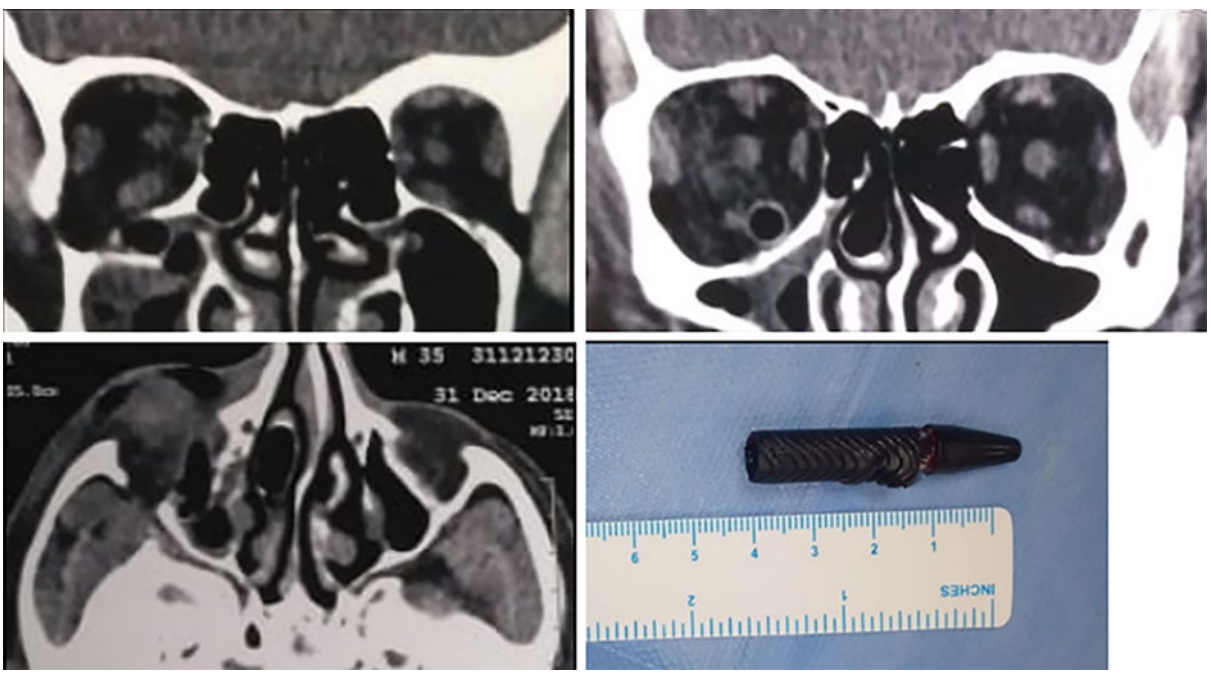


Fig. 20 CT scan soft tissue windows showing right orbital floor fracture with well circumscribed radiolucent plastic foreign body. (Courtesy Dr. Varsha Backiavathy)

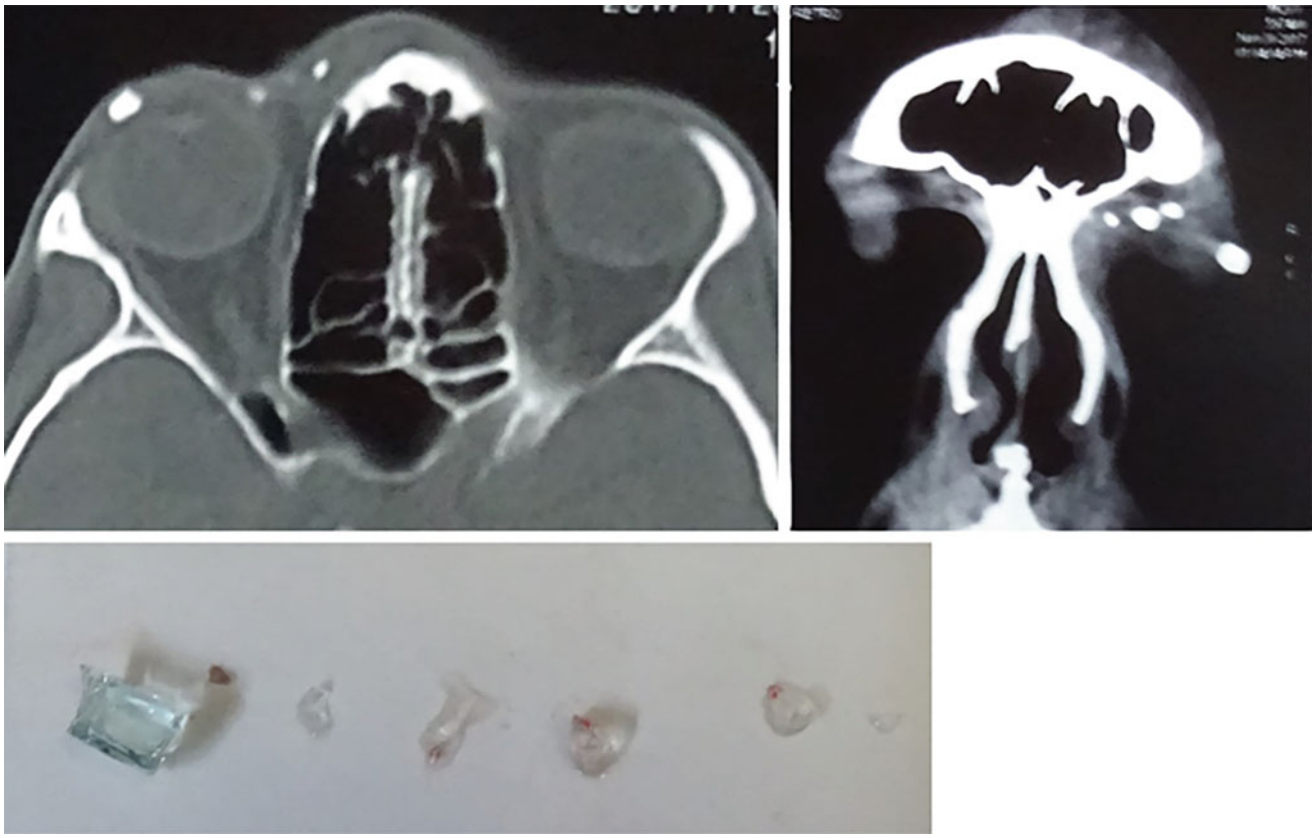


Fig. 21 Noncontrast CT scan bone (axial) and soft tissue (coronal) windows: radiopaque well delineated foreign bodies with high ROI of 2500 suggestive of glass. (Courtesy Dr. Raghuraj Hegde)

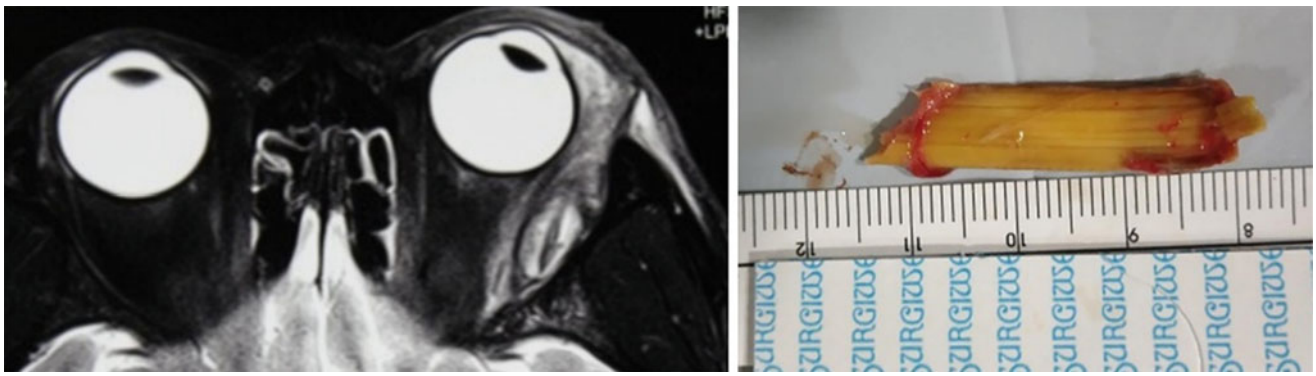


Fig. 22 MRI Axial T2 weighted fat saturated imaging: Residual foreign body after previous CT scan and exploration showing variably intense linear foreign body against left lateral rectus representing wooden foreign body. (Courtesy Dr JK Das)

organic foreign bodies are suspected and for imaging residual organic foreign bodies [14, 15] (Fig. 21).

7 Conclusion

In summary, imaging of the globe, adnexa, and periorbital tissues plays a very important and complementary role in the management of periorbital trauma. Patient counseling, treatment planning and execution are often dependent on accurate

interpretation of features on various imaging modalities. The clinician should thus be well versed with the above, with a good communication with the radiologist who can further provide input which may have both medical and medicolegal consequences.

References

1. https://eyewiki.org/Traumatic_Globe_Luxation
2. Almousa R, Amrith S, Mani AH, Liang S, Sundar G. Radiologic signs of periorbital trauma – the Singapore experience. Orbit. 2010;29(6):307–12.
3. https://eyewiki.org/Imaging_in_Ocular_and_Ocular_adnexal_trauma
4. Ting E. Imaging in orbital & orbitofacial fractures, in orbital fractures – principles, concepts & techniques. In: Imaging science today. LLC. ISBN: 13:978-0997781922.
5. Kuhn F, Pieramici DJ. Ocular trauma, principles and practice: Thieme; 2002.
6. Attoya KA, Mirvis SE. Radiological evaluation of the craniofacial skeleton. In: Dorafshar AH, Rodriguez ED, Manson PN, editors. Facial trauma surgery – from primary repair to reconstruction: Elsevier; 2020. ISBN: 978-0-323-49755-8.
7. Meltzer DE, Mirbagheri S, Aygun N. Subperiosteal hematoma of the orbit: a variety of presentations. J Radiol Case Rep. 2019;13(6):13–23.
8. Henderson AD, Miller NR. Carotid-cavernous fistula: current concepts in aetiology, investigation, and management. Eye (Lond). 2018;32(2):164–72. https://doi.org/10.1038/eye.2017.240.
9. Rao R, Honavar SG. Orbital foreign bodies, in orbital fractures – principles, concepts & management. In: Sundar G, editor. Imaging science today. New York: LLC.
10. Seymour EQ, Bane DB. A comparison of the accuracy of the Comberg and Sweet techniques of orbital foreign-body localization. Radiology. 1970;96(1):75–6.
11. Momoniat HT, England A. An investigation into the accuracy of orbital x-rays, when using CR, in detecting ferromagnetic intraocular foreign bodies. Radiography (Lon). 2017;23(1):55–9.
12. Moisseiev E, Barequet D, Zunz E, Barak A, Mardor Y, Last D, Goez D, Segal Z, Loewenstein A. Validation of an algorithm for nonmetallic intraocular foreign bodies' composition identification based on computed tomography and magnetic resonance imaging. Retina 2015;35:1898–1904.
13. Javadrashid R, Golamian M, Shahrzad M, Hajalioghli P, Shahmorady Z, Fouladi DF, Sadrarhami S, Akhoundzadeh L. Visibility of different intraorbital foreign bodies using plain radiography, computed tomography, magnetic resonance imaging and cone-beam computed tomography: an in vitro study. Can Assoc Radiol J. 2017;68(2):194–201.
14. Di Gaeta A, Giurazza F, Capobianco E, Diano A, Muto M. Intraorbital wooden foreign body detected by computed tomography and magnetic resonance imaging. Neuroradiol J. 2017;30(1):88–91.
15. Nagae LM, Katowitz WR, Bilaniuk LT, Anninger WV, Pollock AN. Radiological detection of intraorbital wooden foreign bodies. Pediatr Emerg Care. 2011;27(9):895–6.

Orbital Trauma: Orbital and Orbitofacial Fractures

90

Kavya Sundar and Gangadhara Sundar

Contents

1 Introduction 662

2 Signs and Symptoms 662

3 Differential Diagnosis 662

4 Treatment 662

5 Diagnosis 662

6 Figures with Captions 662
6.1 X-rays 662
6.2 CT Scans 663
6.3 Other Orbital Fracture Considerations 668
6.4 MRI in Orbital Fractures 669

7 Summary 675

References 675

Abstract

Imaging of the orbitofacial skeleton and soft tissues – including the globe, the face, and intracranial structures, is an essential component in the diagnosis, counseling, prognostication, management, and follow-up of patients afflicted by trauma to the craniofacial region, which has both medical and medicolegal consequences. We herewith provide an overview of the various imaging modalities (ultrasound, CT scan, Magnetic resonance imaging, angiography), and common radiologic features. A thorough knowledge is thus paramount to the practicing ophthalmologist managing these complex conditions.

In general, Computed Tomography (CT scan) is the imaging modality of choice for orbital trauma and foreign bodies. However, Magnetic Resonance Imaging (MRI) may be considered in special circumstances as it may be more sensitive in the detection and assessment of nonmetallic/organic intra-orbital foreign bodies. Black bone MRI is increasingly being used nowadays or orbital imaging, especially in children, who need repeated imaging of the soft tissues and the bone.

Keywords

Orbital trauma · Orbital fractures · Blow-out fractures · Trapdoor fractures · Blow-in fractures · Orbital compartment syndrome · Open globe injuries · Closed globe injuries · Zygomatico-maxillary complex fractures · Naso-orbito-ethmoidal fractures · Cranio-orbital fractures · Orbitofacial fractures · Panfacial fractures · Orbital foreign bodies · Cone beam CT (CBCT)

K. Sundar
Faculty of Dentistry, National University Centre for Oral Health, National University of Singapore, Singapore, Singapore

G. Sundar (✉)
Orbit & Oculofacial Surgery, Department of Ophthalmology, National University Hospital, National University of Singapore, Singapore, Singapore
e-mail: Gangadhara_sundar@nuhs.edu.sg

© Springer Nature Switzerland AG 2022
G. Ben Simon et al. (eds.), *Atlas of Orbital Imaging*,
https://doi.org/10.1007/978-3-030-62426-2_116

1 Introduction

Orbital injuries are common and may be classified into orbital contusions, orbital and orbitofacial fractures, and penetrating injuries with or without orbital foreign bodies. In this section we shall focus on orbital and orbitofacial fractures. However, A variable amount of soft tissue injuries, e.g., to the globe, extraocular muscles, and the optic nerve [1] is often present in patients with fractures and should be addressed simultaneously. Imaging of the globe, the adnexa, and periorbital structures is thus essential for both a complete diagnosis of orbital and orbitofacial fractures and guide management.

2 Signs and Symptoms

Common symptoms of orbital fractures include periorbital discomfort or pain, often with swelling, blurring or loss of vision, double vision, numbness of the cheek or upper gums, bleeding from the nose, etc.

Early signs often include periorbital ecchymosis, associated periorbital or facial lacerations, variable degrees of proptosis from orbital hemorrhage, crepitus from emphysema, tenderness with or without step-off at the orbital rims, infraorbital and/or supraorbital paresthesia with orbital floor/roof involvement, respectively, reduced visual acuity, diplopia in primary or other gazes with limitation of ocular motility.

Late signs include variable degrees of visual loss, ocular motility limitation dependent on the degree and location of entrapment of extraocular muscles/intermuscular septum (EOM/IMS) complex, abnormal globe position in any of the three axes- horizontal, vertical, and anteroposterior, canthal and other midfacial deformities.

3 Differential Diagnosis

With a history of significant trauma and the above signs, the diagnosis of fractures may usually be straightforward especially with significant deformity. Visual loss may result from either closed globe injuries, open globe injuries, or traumatic optic neuropathy. Monocular diplopia may result from dislocated intraocular lens. Binocular diplopia may result from contusion and limited cooperation of the patient, entrapment of the EOM/IMS complex, or cranial neuropathies from fractures of the superior orbital fissure. Moderate to severe proptosis with visual loss with or without RAPD may represent an Orbital Compartment Syndrome (OCS) and should be managed as an emergency. Rarely acute severe orbital fractures may present with enophthalmos or even globe prolapse – externally or within the adjacent paranasal sinuses.

4 Treatment

Most orbital fractures may require just symptomatic management after ruling out vision threatening globe or orbital injuries, significant entrapment and large fractures. Significantly displaced orbital or orbitofacial fractures, especially those with entrapment of the extraocular muscle – intermuscular septum complex (EOM/IMS complex) or large soft tissue herniation often require surgical management. An open reduction with internal fixation (ORIF) either by the orbital surgeon alone or along with a craniomaxillo-facial (CMF) surgeon is often indicated in such cases.

5 Diagnosis

Orbital and orbitofacial imaging may be performed with x-ray, CT scan, occasionally MRI, and even, less frequently, specialized imaging (MR Angiography (MRA), CT Angiography (CTA), etc.). CT angiography is nowadays considered in patients presenting with acute craniofacial trauma to rule out intracranial vascular and soft tissue abnormalities concomitantly. Non-contrast fine cut CT scans are the imaging modality of choice in orbitofacial trauma for both bony and soft tissue injuries [2]. Ultrasound is only minimally useful for orbital injuries, but very useful in the assessment and follow-up of closed globe injuries with limited intraocular visualization and is beyond the scope of this chapter.

It should be remembered that orbital imaging is not only essential for diagnosis but also the imaging data is useful for preoperative treatment planning, intraoperative and postoperative imaging as well, some of which are highlighted below.

In this chapter, we shall present the bony changes from orbital and orbitofacial trauma. Soft tissue signs and orbital foreign bodies shall be discussed elsewhere.

6 Figures with Captions

6.1 X-rays

These are only used as a screening tool to detect gross disruptions of the orbitofacial skeleton and to rule out radiopaque (metallic) foreign bodies prior to MR Imaging. Advantages include relatively easy access in the emergency department setting, ease and brevity of image acquisition with least radiation exposure. Limitations include false negative and thus missed orbital fractures and poor details of orbital bone and soft tissue structures. As a screening tool it may demonstrate a “tear drop sign” in orbital floor blow-out fractures (Fig. 1).



Fig. 1 Plain x-ray Water's view (occipitomental, angled PA skull radiograph): Tear drop sign from a left orbital floor blow-out fracture (orbital soft tissue expansion into the maxillary sinus)

6.2 CT Scans

This is the imaging modality of choice, usually performed without contrast, for suspected orbital and orbitofacial fractures, suspected and occult globe disruptions, orbital and ocular foreign bodies, traumatic optic neuropathy, and to rule out intracranial injuries [3]. It is often viewed in both a bone window (to visualize orbital bones and fractures, intraocular and orbital foreign bodies) and soft tissue windows (to visualize globe and other soft tissue structures) in the axial, coronal, and sagittal sections. Foreign bodies are often analyzed in both windows, with attention to their Hounsfield Units (HU). Conventional CT scans offer high resolution images with sub-mm cuts and the DICOM data is utilized not just for preoperative treatment planning but also for custom implant designing and intraoperative navigation. Cone beam CT scans (CBCTs) are often used for postoperative analysis of orbital implants and volumes with significantly reduced radiation exposure, acquisition time, and cost [4]. An intraoperative O-arm may also be used for intraoperative confirmation of adequate reconstruction in some centers globally.

An overview of the Practical Classification of Orbital and Orbitofacial fractures [5], their approximate incidence and radiologic features are shown below (Table 1).

Table 1 Practical Classification of Orbit and Orbitofacial fractures and their frequency[7]

"Simple"/Pure orbital fracture	"Complex" orbitofacial fracture
1. Linear fractures 2. Blow-out fractures (a) 1 Wall fractures (21%) (i) Floor blow-out fractures (ii) Medial wall blow-out fractures (iii) Roof blow-out fractures (iv) Trapdoor fracture (b) 2 Wall fractures (10%) (i) Floor and medial wall blow-out fractures 3. Blow-in fractures.	1. Zygomatico-maxillary complex fractures (ZMC) Type I-III (18%) 2. Naso-orbito-ethmoidal fractures (NOE) Type I-III (3%) 3. Cranio-orbital fractures (10%) 4. Orbitofacial fractures Le Fort II fracture (5%) Le Fort III fracture (14%) 5. Cranio-orbitofacial fracture (14%) 6. Panfacial fracture (5%)

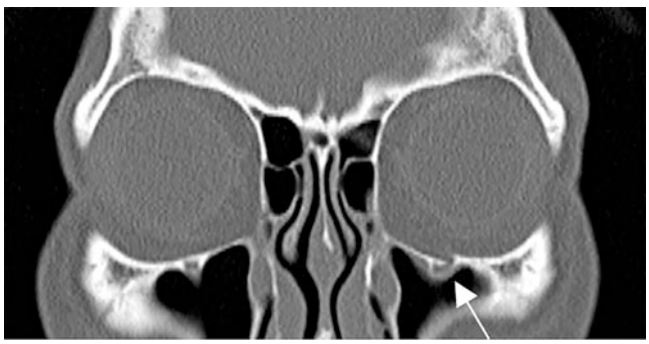


Fig. 2 Coronal bone window: Left orbital floor linear fracture along infraorbital groove from sports injury

I. **Simple Orbital Fractures:** These are isolated orbital wall fractures without orbital rim or other craniofacial bone involvement or displacement.

A. Linear Orbital Fracture: These are crack or minimally displaced fractures, usually of one wall without significant orbital content prolapse or entrapment (Fig. 2) and thus managed conservatively.

B. Blow Out Fractures: These are fractures of either one wall or more than one wall of the orbit without orbital rim involvement. They may involve the floor (Fig. 3), medial wall (Fig. 4). or roof (Fig. 5) or may present as trapdoor.

These trapdoor fractures are a form of blow-out fractures typically seen in children and young adults. Following blunt trauma, a momentary prolapse of orbital contents into the adjacent paranasal sinuses with the displaced bone springing back results in entrapment, often with severe consequences [6] (Figs. 6 and 7). In 10% of orbital fractures, combined

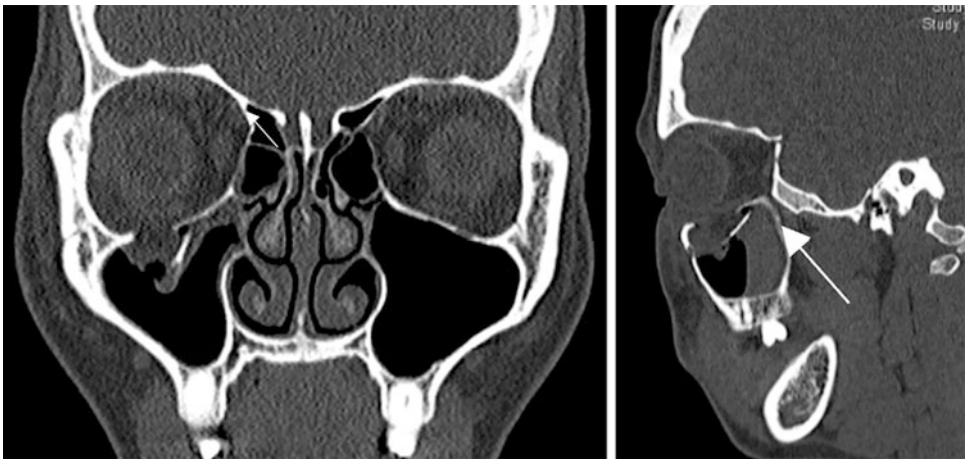


Fig. 3 CT scan, coronal and sagittal bone windows: Right orbital floor blow-out fracture, the posterior ledge (arrow), with orbital soft tissue herniation and blood in the maxillary sinus

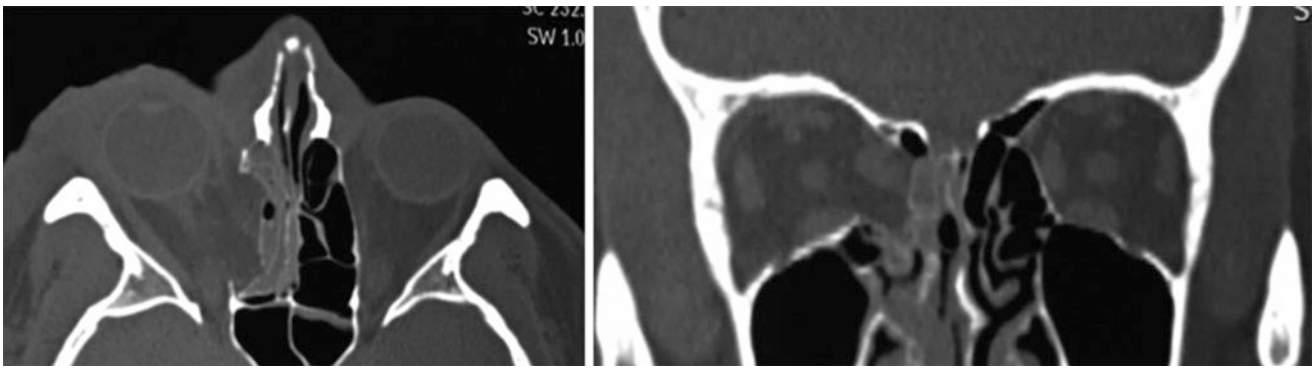


Fig. 4 CT scan, axial and coronal bone windows: Large right medial wall blow-out fracture with orbital fat and medial rectus prolapse and opacification of the ethmoid sinus

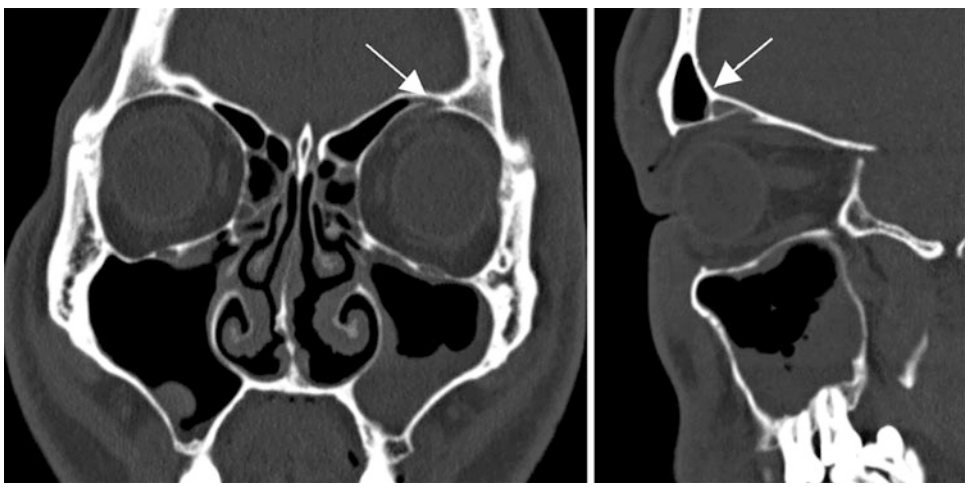


Fig. 5 CT scan coronal and sagittal bone windows: Left orbital roof blow-out fracture with minimal prolapse into the frontal sinus

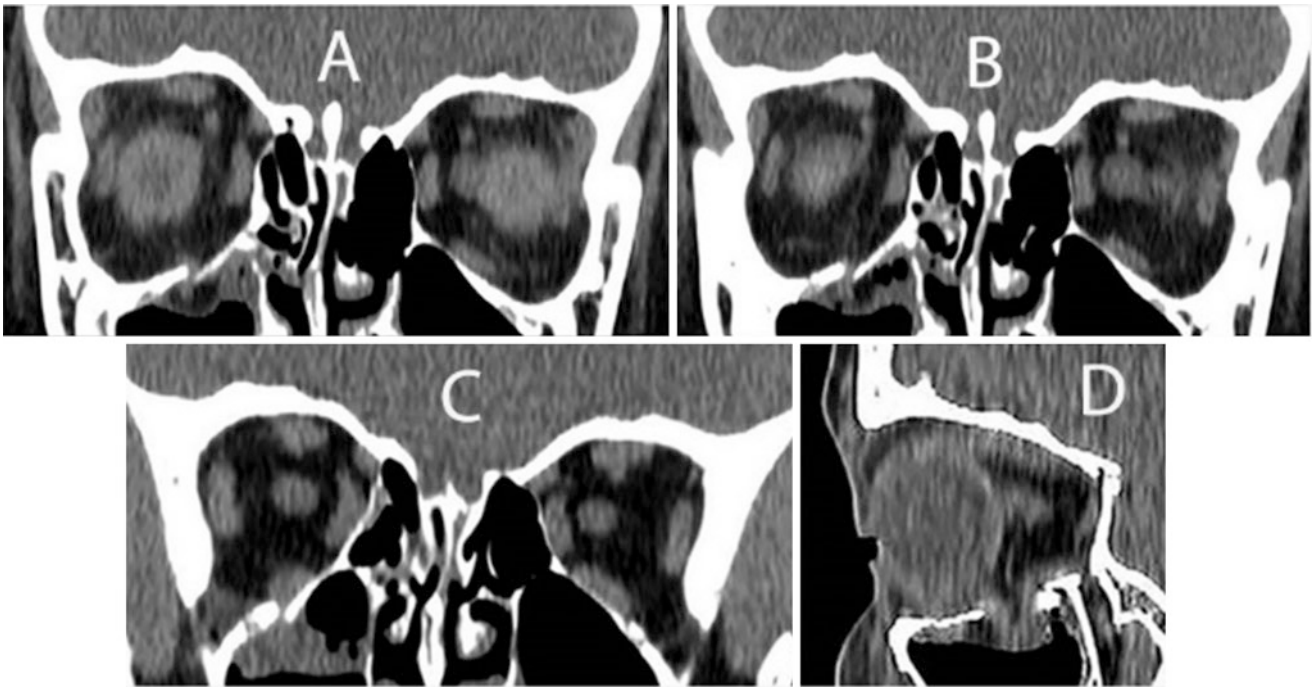


Fig. 6 CT soft tissue window: Trapdoor fracture of the right orbital floor with inferior rectus herniation and entrapment. Serial anterior to posterior coronal sections (**a**–**c**): Note the IR is not visible intraorbitally in figures A and B, but visible posteriorly (**c**, **d**). (*Courtesy: Dr Guy Ben Simon*)

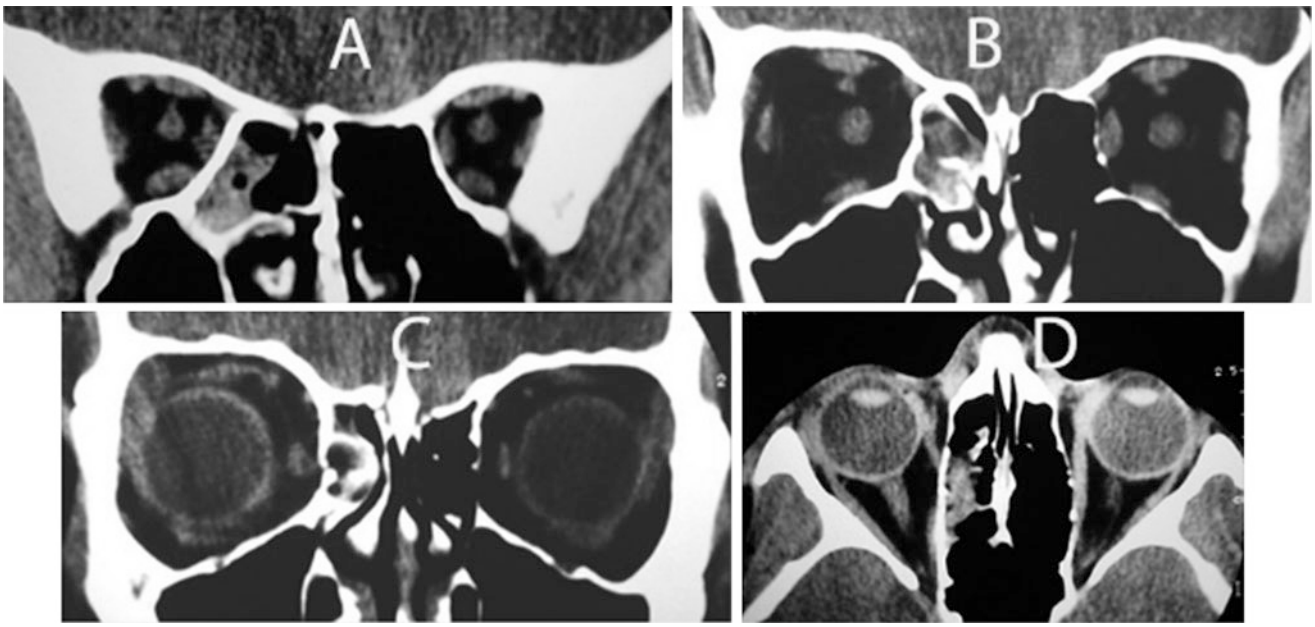


Fig. 7 CT scan soft tissue window: Right medial wall fracture with medial rectus entrapment. Medial rectus present in the anterior section that disappears in the mid-posterior sections but visualized in the ethmoidal sinus (**a**, **b**, **d**)

orbital floor and medial wall fractures are seen with disruption of the inferomedial orbital strut.

C. Blow-in Fractures: These are orbital wall fractures sparing the orbital rim, with bony fragment displacement toward the orbital soft tissue structures which may affect the roof (Fig. 9) or medial wall (Fig. 10).

II. **Complex Orbitofacial Fractures:** These are orbital fractures, usually from high impact injuries, involving the orbit walls, its rims, and variable components of the facial skeleton – the upper face (fronto-temporal injuries), the midface (the maxilla, zygoma, pterygoids), and the lower face (mandible). They often require multidisciplinary intervention [7].

A. Zygomatico-maxillary complex fracture: The second most common type of facial fracture, these are fractures of the zygoma, involving the lateral wall of the orbit and variable component of the orbital floor. The three types include Types I (Simple tripod fractures), Type II (Complex tetrapod fractures) (Fig. 11), and Type III (Comminuted severely displaced fractures) (Fig. 12).



Fig. 8 CT scan coronal bone (*left*) and soft tissue (*right*) windows: Combined right orbital floor and medial wall fracture with disruption of the inferomedial orbital strut, the Angle of Inferomedial Orbital Strut (AIOS) and soft tissue prolapse with hematoma of the ethmoid and maxillary sinus

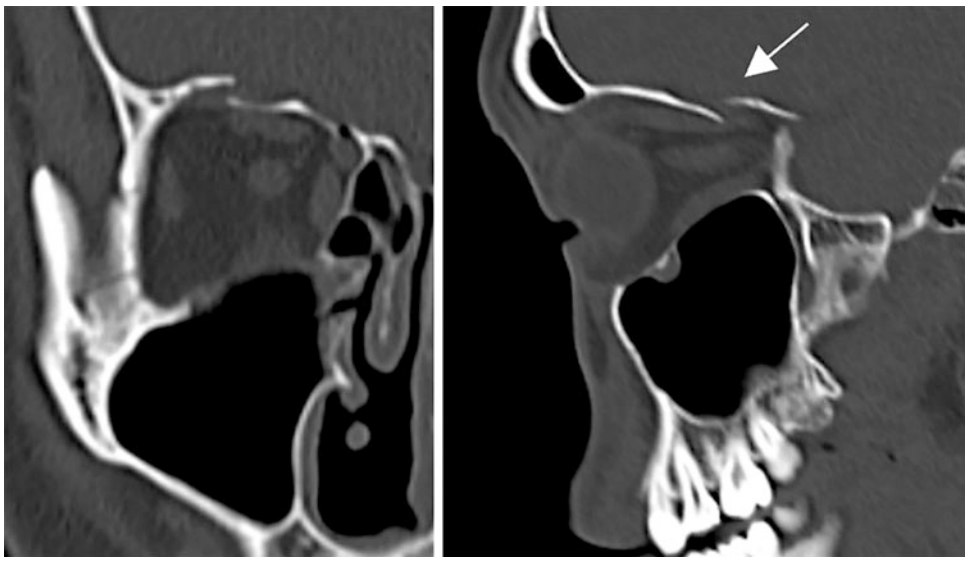


Fig. 9 Coronal and sagittal bone windows: Right orbital roof blow-in fracture with impingement against the Levator palpebrae superioris/Superior rectus (LPS-SR complex)



Fig. 10 CT scan axial bone window: Right medial wall blow-in fracture with impingement against medial rectus and orbital structures

B. Naso-orbito-ethmoidal (NOE) Fracture: Very uncommon in isolation, these are fractures of the central midface often involving the nasal bones, the medial walls of the orbit and variable damage to the medical canthal tendon and its attachments caused by high velocity high impact injuries. They may be unilateral or bilateral. Markowitz-Manson classification include Type I (single central fragment with attached MCT), Type II (comminuted central fragment), and Type III (comminuted often disorganized central fragment without significant MCT attachment, Fig. 13).

C. Craniorbital fracture: These are fractures of the orbital roof involving the anterior cranial fossa (Fig. 14) and often require comanagement with the neurosurgeons.

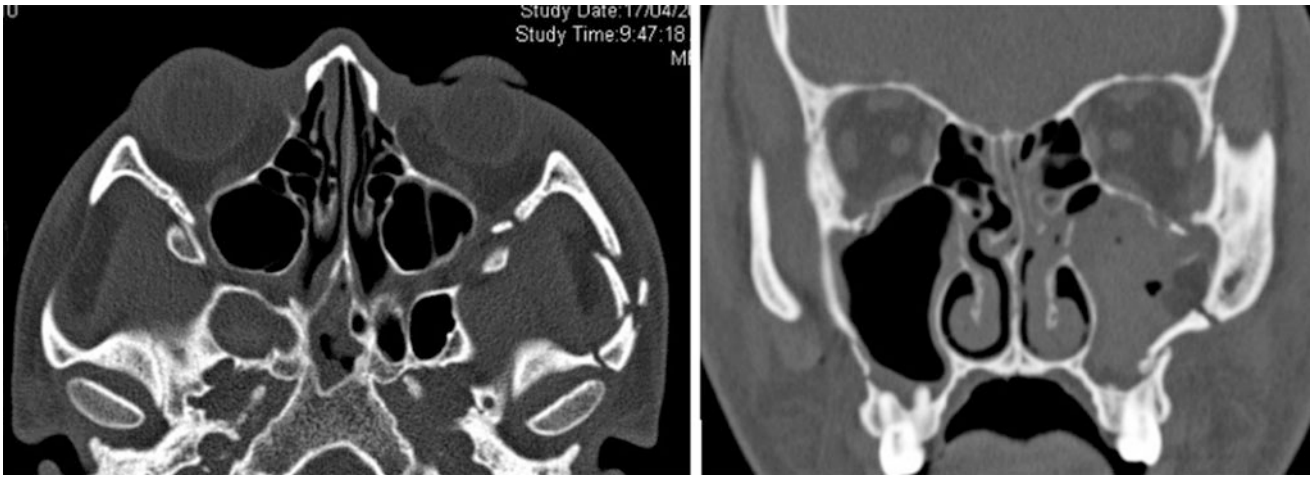


Fig. 11 CT scan axial and coronal bone windows: Minimally displaced comminuted left ZMC fracture with involvement of the lateral orbital wall, floor, and the zygomatic arch



Fig. 12 3D CT reconstruction: Comminuted displaced right ZMC fracture from blast injury

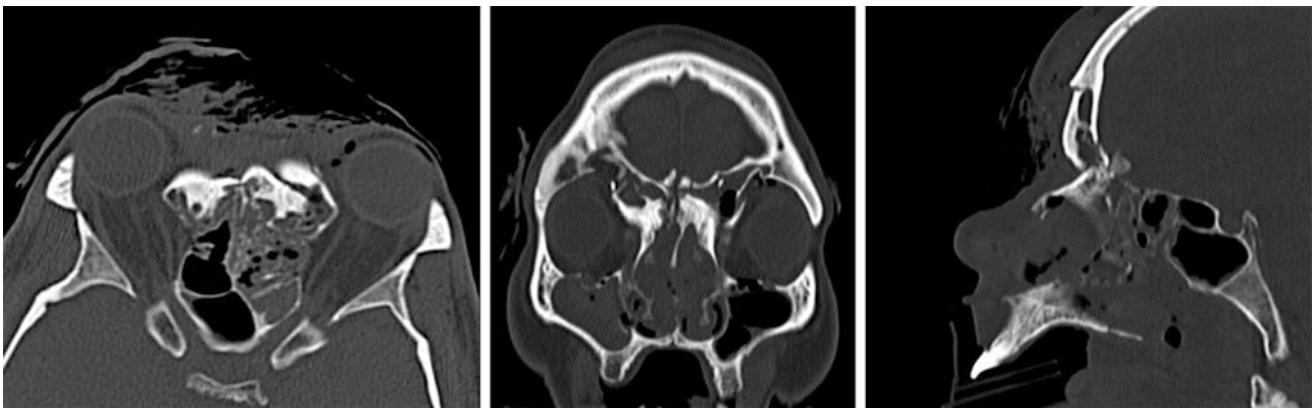


Fig. 13 CT scan axial, coronal and sagittal bone windows: Bilateral severe Type III NOE fractures with telescoping and comminution of the naso-orbito-ethmoidal complex and medial walls of the orbit

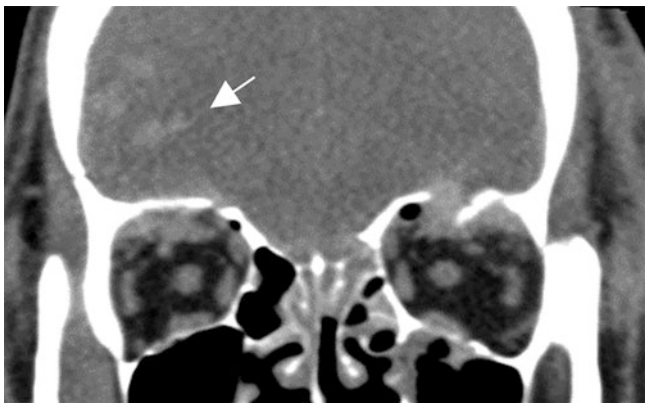


Fig. 14 CT scan coronal soft tissue windows: Bilateral orbital roof fractures, more on the left, with anterior cranial fossa involvement and frontal lobe hemorrhage (arrow)

D. Orbitofacial fractures: These are fractures of the orbit involving other bones of the midface (lower maxilla with or without zygoma) (Fig. 15a). Le Fort Type I fractures do not involve the orbit. Le Fort II fractures are midfacial fractures involving the medial wall and floor of orbit (Fig. 15a, b). Le Fort III fractures are midfacial fractures with medial wall and lateral walls of the orbit (craniofacial dysjunction) (Fig. 15a, c).

E. Cranio-orbitofacial fracture: These are fractures involving the skull base, orbits and the midface (Fig. 16).

F. Panfacial fracture: These are fractures involving the upper facial skeleton (skull base and orbital roof), midface (orbit, zygoma, and maxilla), and the lower face (mandible) (Fig. 17). These fractures often require a multidisciplinary approach, more meticulous treatment planning, and occasionally staged reconstruction.

6.3 Other Orbital Fracture Considerations

A. Apical Orbital Fractures: These are fractures of either the superior orbital fissure (Fig. 18), Optic canal fractures (Fig. 18), or both. They are important anatomical bony landmarks with vital structures coursing through them. Fracture of superior orbital fissure may present with a complete ptosis with poor or absent levator function, globe elevation with supraorbital paresthesia. Fractures of the optic canal may present with visual loss and gross relative afferent pupillary defect.

B. Lacrimal Drainage System Fractures: These are commonly seen (around 15%) in fractures of the midface (Le Fort II, Le Fort III, and NOE fractures) (Fig. 20a). Occasionally surgeries of the midface may also result in damage and disruption of lacrimal drainage apparatus primarily or iatrogenically (Fig. 20b, c).

C. DICOM Data in Orbital Fractures

Apart from diagnostic imaging, the DICOM data from sub-mm imaging of orbital fractures may also be utilized for preoperative treatment planning (segmentation with mirroring), intraoperative navigation, postoperative verification, and quality control with image fusion [8] (Fig. 21a–e). DICOM data from conventional or cone beam CT scans [9] can also be used for volumetric analysis both preoperatively and in patients with posttraumatic enophthalmos for treatment planning and implant fabrication.

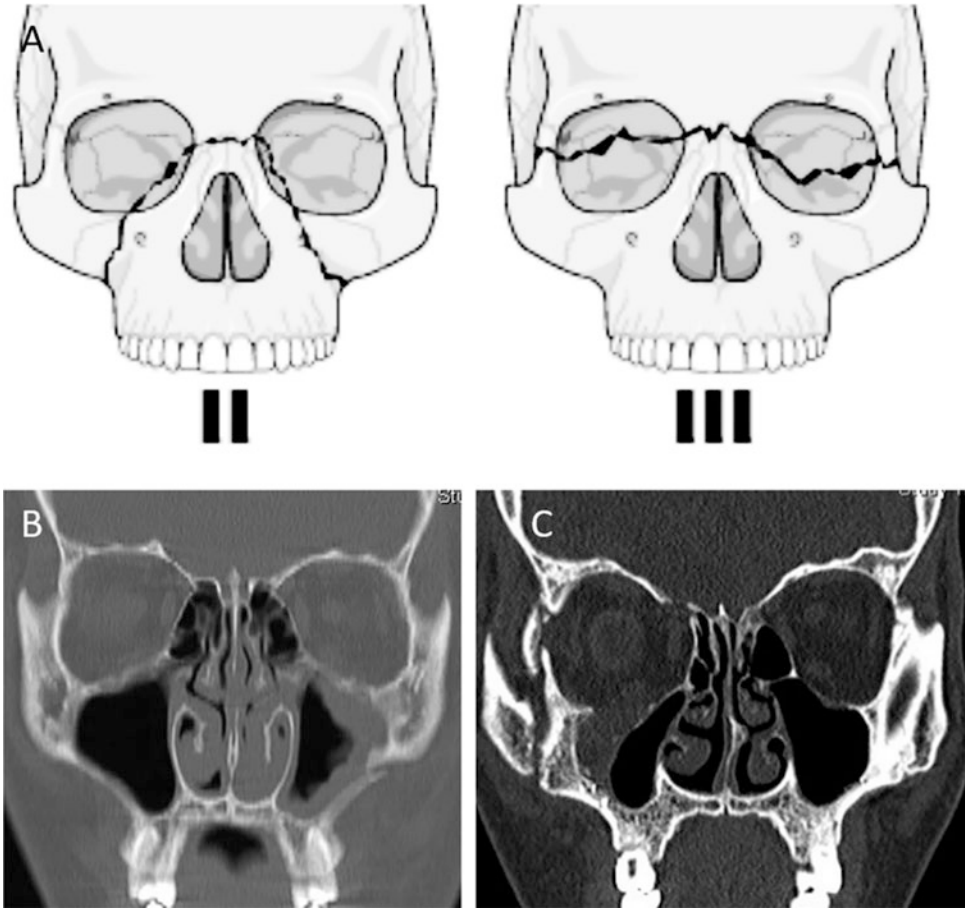


Fig. 15 (A) Le Fort II (Pyramidal) fracture and Le Fort III (Craniofacial dysjunction) fractures. (B) Coronal bone window: Left-sided Le Fort II fracture with involvement of the orbital floor and medial wall along with lateral maxillary wall fracture. (C) Coronal bone window: Right-sided Le Fort III fracture with involvement of the superomedial wall of the orbit including the skull base and the lateral wall – craniofacial dysjunction

D. Postoperative Imaging of Orbital Implants: Image Characteristics and Implant Positioning.

Every implant biomaterial has different imaging characteristics. These include clarity of visibility in soft tissue and bone windows. Silicone and titanium implants are readily visible on both bone and soft tissue windows (Figs. 22 and 23). Polyethylene (Medpor®) implants are radiolucent on CT scans (Fig. 24). Bioresorbable implants are ideally visualized on soft tissue window (e.g., polylactides (Fig. 25), polycaprolactones (Fig. 26)). The surgeon should be familiar with these, especially when patients have postoperative complications and when operative notes are unavailable.

We herewith demonstrate some imaging characteristics of commonly used implants and their complications. Early postoperative imaging may confirm adequate reduction of orbital contents and either proper (Fig. 23) or improper implant placement (Fig. 27). In patients with bioresorbable implant placement, late postoperative imaging, typically performed 18 months postop, may help confirm complete resorption of implant with bone healing (Fig. 28).

6.4 MRI in Orbital Fractures

Traditionally, MRI has been contraindicated in acute head and neck injuries and has been considered a poor imaging modality for structural defects of the bony skeleton. However, since the description of "black bone MRI" by Eley et al. in 2012 [10], it is now being considered for various conditions including pediatric head injuries. Novel sequences with short echo time (TE of 4.2 ms) and repetition time (TR of 8.6 ms) along with low flip angle of 5° enables a high resolution depiction of bone with excellent contrast between bone, soft tissue, and air. While this may still not aid diagnosis of fracture of the bone next to paranasal sinuses (orbital floor, medial wall), it may be useful for the orbital roof and lateral wall, in addition to identifying soft tissue changes such as orbital fat, extraocular muscle and intermuscular septal prolapse, and/or incarceration [11] (Fig. 29).



Fig. 16 CT scan coronal soft tissue window: Left cranio-orbitofacial fracture from high impact construction site injury with displaced fractures of the left orbital roof/anterior cranial fossa, floor of the orbit, and the maxilla with globe dystopia

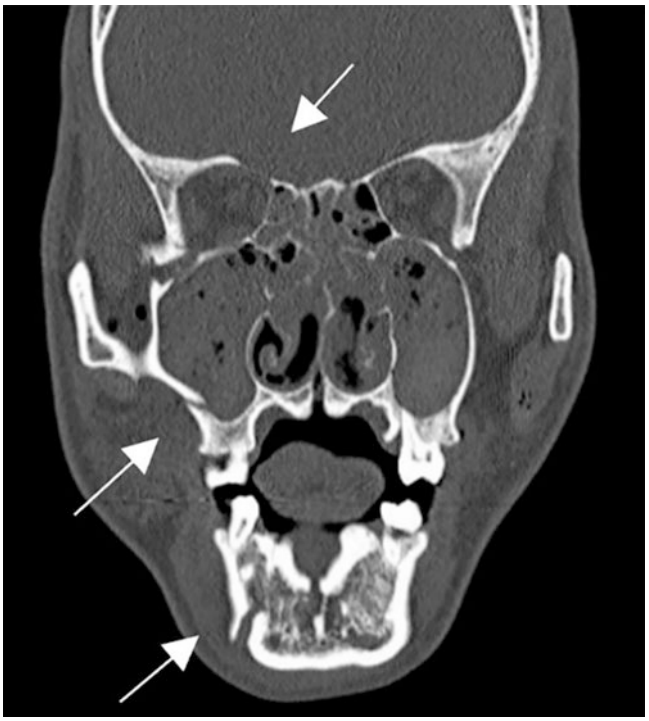


Fig. 17 CT scan coronal bone window: Right panfacial fracture with fractures of the upper face (Frontal bone/orbital roof), midface(maxilla), and lower face (mandible)



Fig. 18 CT scan coronal bone windows image of orbital apex: Displaced fracture of left posterior greater wing of sphenoid near the superior orbital fissure, which may present as ophthalmoplegia or ptosis

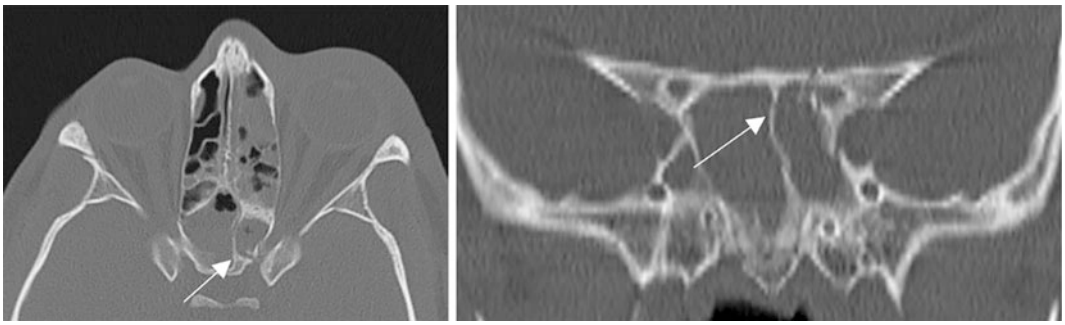


Fig. 19 CT scan axial and coronal bone windows: Left optic canal fracture presenting as traumatic optic neuropathy

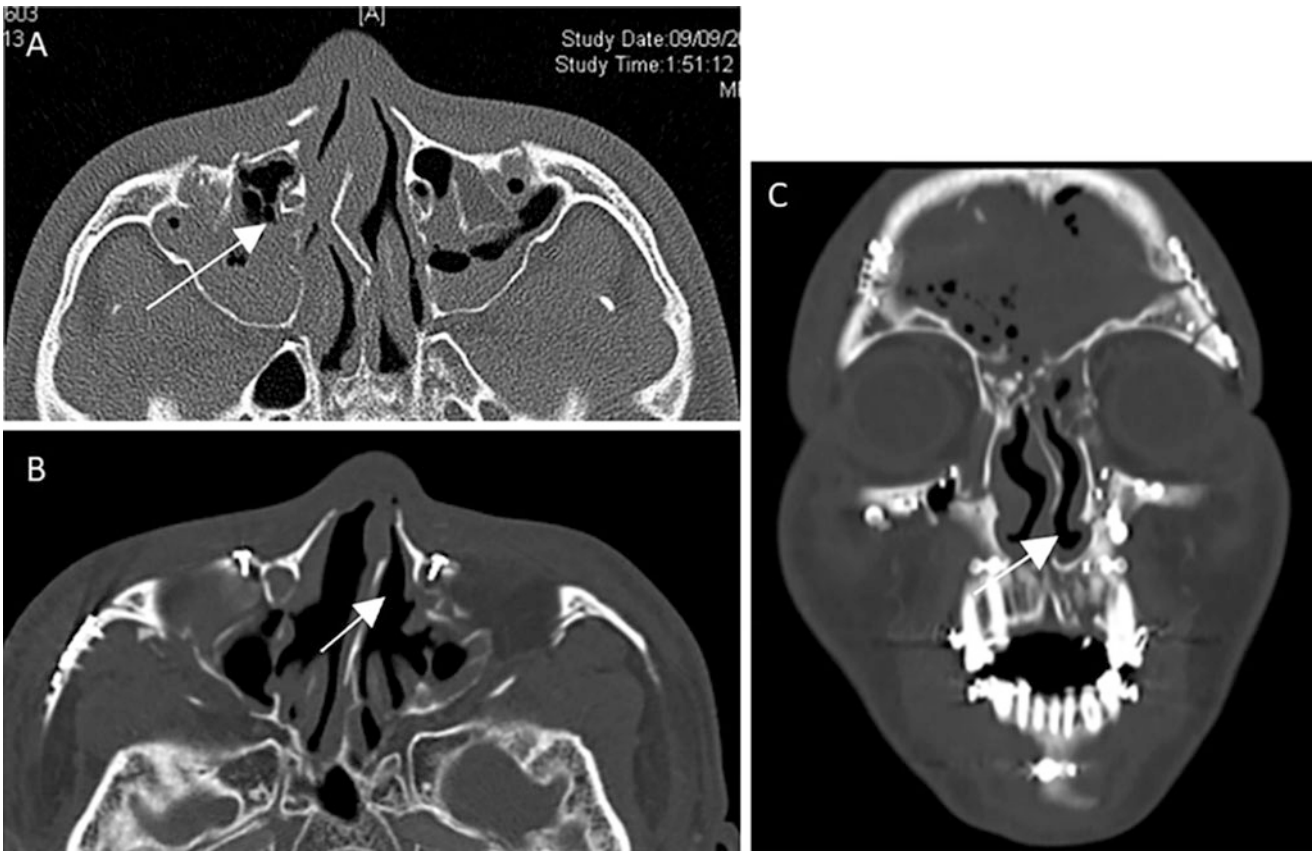


Fig. 20 (**a**) Axial bone window: Fracture of the right bony nasolacrimal duct in midfacial trauma. (**b**, **c**) Axial and coronal bone windows in a postoperative scan: Accidental placement of fixation screw through left nasolacrimal duct

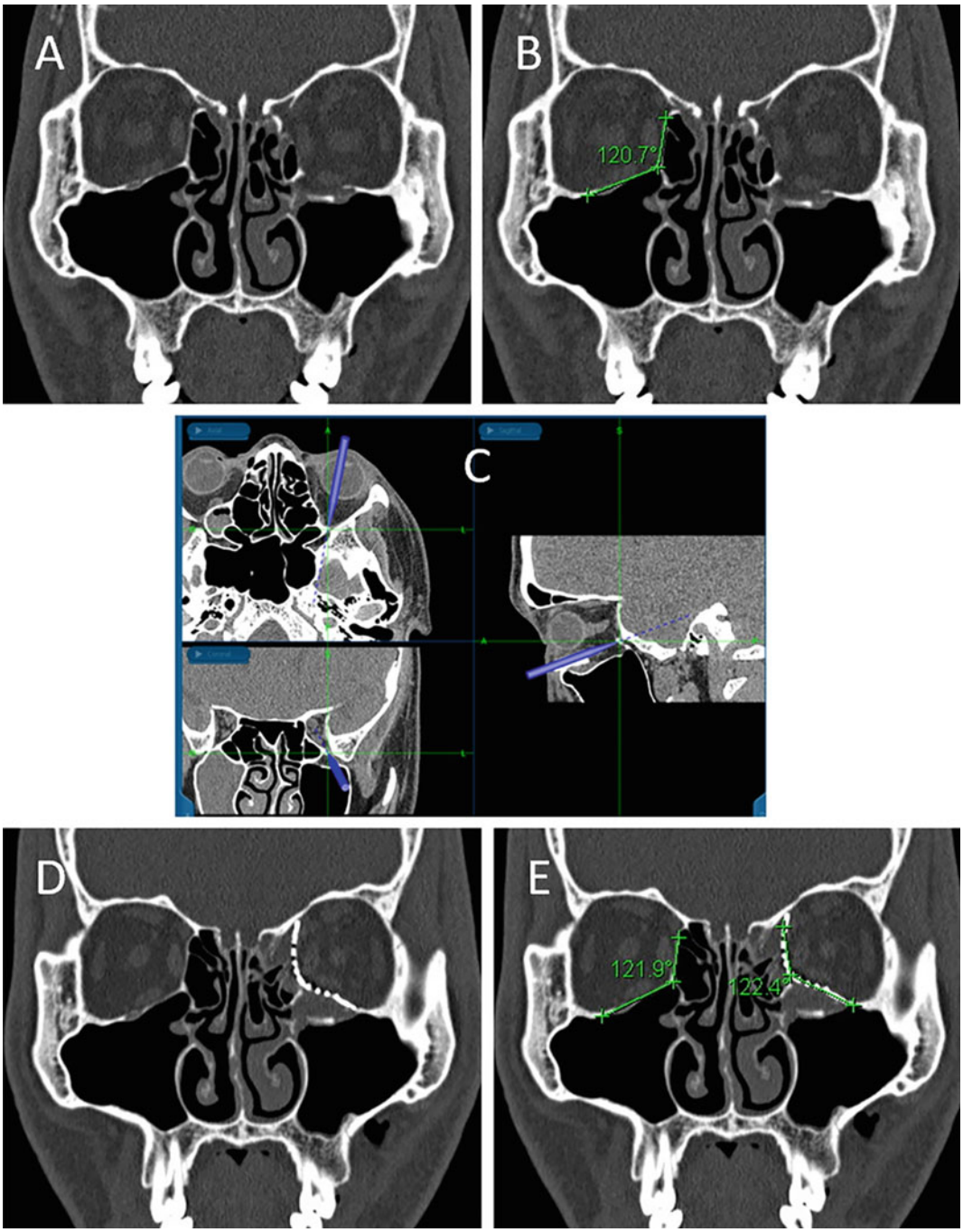


Fig. 21 (**a**) Preoperative imaging of unilateral left combined orbital floor – medial wall fracture with disruption of the inferomedial orbital strut. (**b**) Preoperative treatment planning with measurement of contralateral Angle of the Inferomedial Orbital Strut (AIOS). (**c**) Intraoperative navigation of posterior ledge for placement of implant. (**d**) Reconstruction of the left orbit with a prebent (AIOS) prefabricated anatomical titanium plate. (**e**) Postoperative verification of reconstructed orbit including AIOS

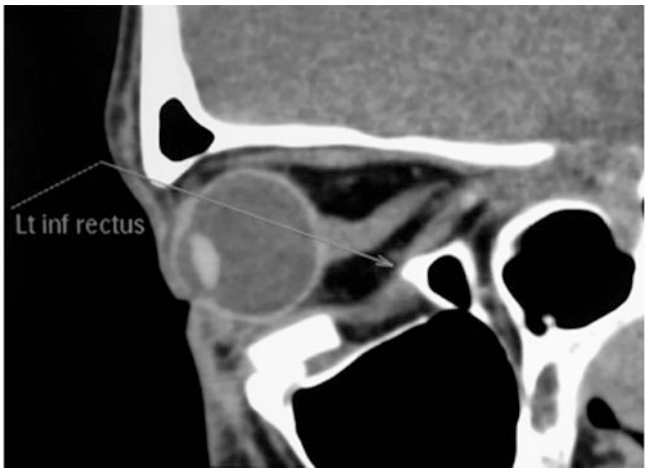


Fig. 22 Sagittal soft tissue window: Silicone block placed in the anterior orbit with incomplete reconstruction of orbital floor and residual prolapse of inferior rectus

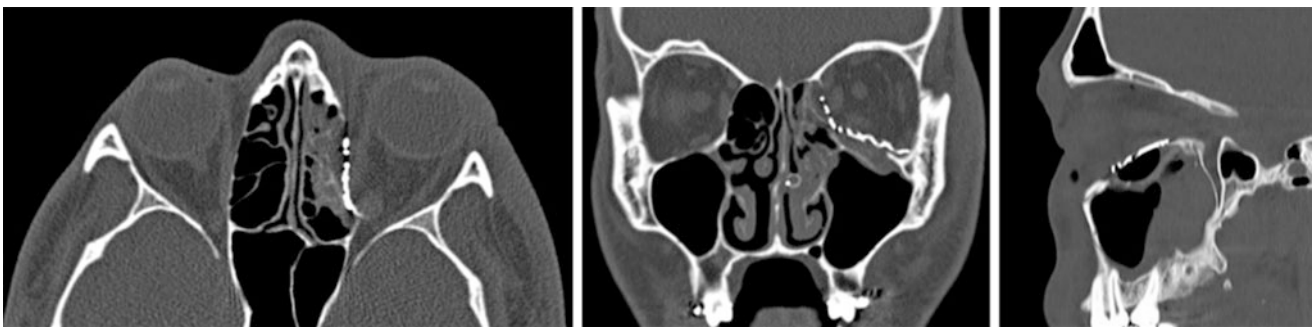


Fig. 23 Axial, coronal and sagittal bone window postoperative CT Scan: Ideally placed prebent (AIOS) prefabricated anatomic titanium plate for combined left orbital floor-medial wall fracture. Note reconstruction of the inferomedial orbital strut, with posterior convexity with implant resting against the posterior ledge restoring symmetry with the contralateral orbit

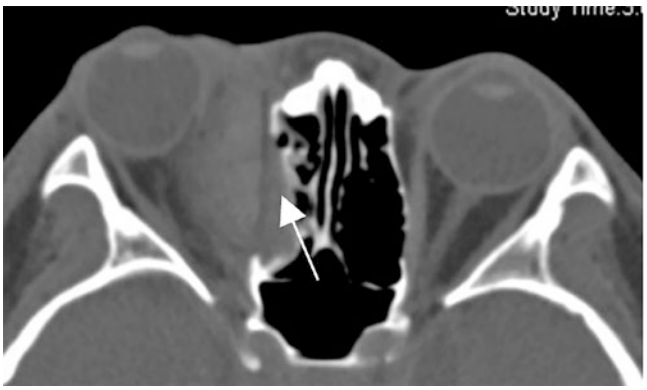


Fig. 24 Axial CT scan soft tissue window: Porous polyethylene (Medpor®) implant visualized as a linear radiolucency (arrow) along the right medial orbit with secondary hematoma causing globe displacement

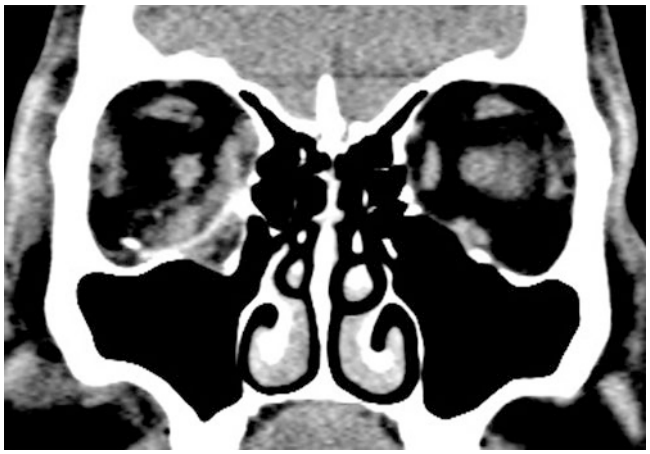


Fig. 25 Early postoperative CT scan coronal soft tissue window showing bioresorbable (Rapidsorb®) along right floor of orbit

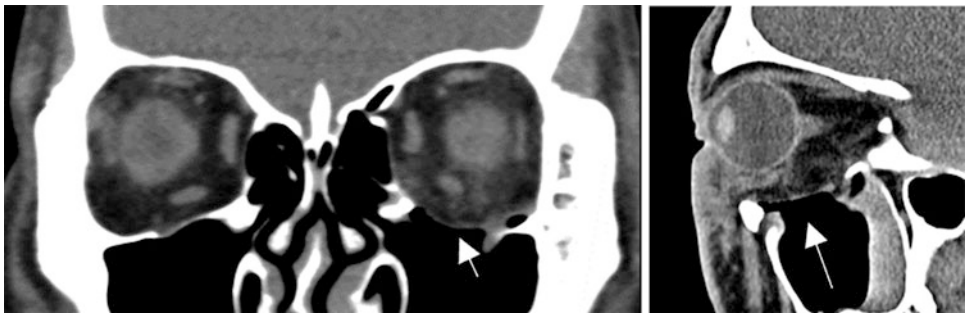


Fig. 26 Early postoperative CT scan, coronal and sagittal views: Radiolucent polycaprolactone (Osteomesh®) implant along left orbital floor (arrows)



Fig. 27 *Upper row*, postoperative A coronal and sagittal bone window CT scans: Superiorly mispositioned radio-opaque Titanium prefabricated implant along left orbital floor impinging upon inferior rectus muscle.
Lower row, postoperative coronal and sagittal scans: Inferiorly positioned Titanium implant below the posterior ledge (arrow) of the left orbit into the maxillary sinus with incomplete reduction of orbital contents

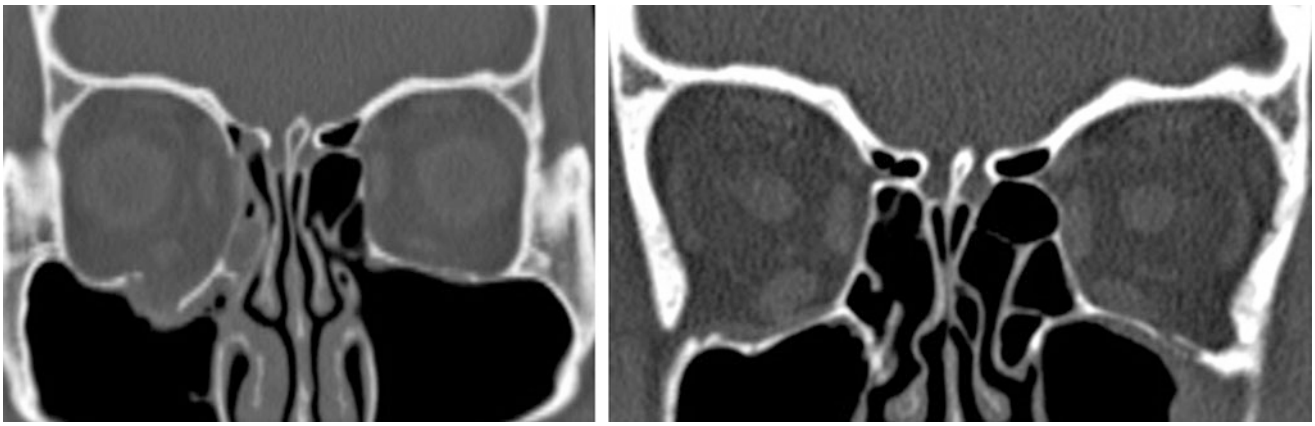


Fig. 28 Late postoperative CT scan coronal and sagittal bone windows: Completely healed left orbital floor fracture with implant resorption

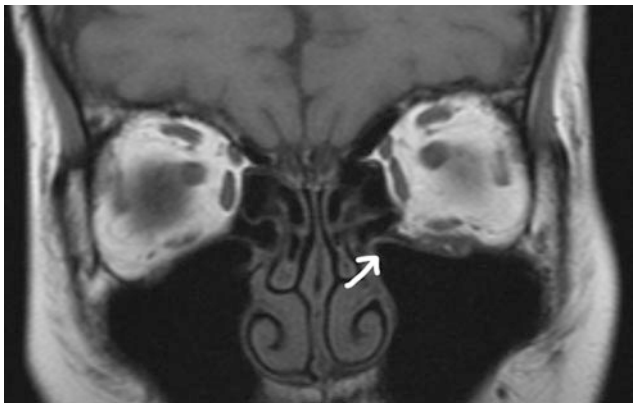


Fig. 29 Coronal MRI demonstrating inferior displacement of the inferior rectus in an orbital floor fracture

7 Summary

In summary, a thorough understanding of the indications for imaging in globe and ocular adnexal trauma, the various modalities, and accurate interpretation goes a long way in making a proper diagnosis and treatment planning. Occasionally, postoperative imaging may also be indicated, which helps the surgeon confirm optimal surgical management.

References

1. Almousa R, Amrith S, Mani AH, Liang S, Sundar G. Radiologic signs of periorbital trauma – the Singapore experience. Orbit. 2010;29(6):307–12.
2. https://eyewiki.org/Imaging_in_Ocular_and_Ocular_adnexal_trauma
3. Ting E. Imaging in orbital & orbitofacial fractures. In Orbital fractures – principles, concepts & techniques. Imaging Science Today LLC. ISBN-13:978-0997781922.
4. Shintaku W, Venturin J, Azevedo B, Noujeim M. Applications of cone-beam computed tomography in fractures of the maxillofacial complex. Dental Traumatol. 2009;25:358–66.
5. Practical classification of Orbital & Orbitofacial Fractures. In: Sundar G, editor. Orbital fractures – principles, concepts & management. Imaging Science Today LLC. ISBN-13: 978-0997781922.
6. Kakizaki H, Zako M, Katori N, Iwaki M. Adult medial orbital wall trapdoor fracture with missing medial rectus muscle. Orbit. 2006;25(1):61–3.
7. Attoya KA, Mirvis SE. Radiological evaluation of the craniofacial skeleton. In: Dorafshar AH, Rodriguez ED, Manson PN, editors. Facial trauma surgery – from primary repair to reconstruction. Elsevier; 2020. ISBN: 978-0-323-49755-8.
8. Udhay P, Bhattacharjee K, Ananthanarayanan P, Sundar G. Computer-assisted navigation in orbitofacial surgery. Indian J Ophthalmol. 2019;67:995–1003.
9. Friedrich RE, Bruhn M, Lohse C. Cone-beam computed tomography of the orbit and optic canal volumes. J Craniomaxillofac Surg. 2016;44(9):1342–9.
10. Eley KA, McIntyre AG, Watt-Smith SR, Golding SJ. "Black bone" MRI: a partial flip angle technique for radiation reduction in craniofacial imaging. Br J Radiol. 2012;85(1011):272–8.
11. Freund M, Hähnel S, Sartor K. The value of magnetic resonance imaging in the diagnosis of orbital floor fractures. Eur Radiol. 2002;12:1127–33.

Ocular Trauma and Intrinsic Pathology

91

Ofira Zloto

Contents

1 **Overview** 677
2 **Diagnosis** 678
3 **Figures with Captions** 678
References 681

Abstract

- Computed tomography (CT) is the preferred modality in the setting of ocular trauma and intraorbital or intraocular foreign bodies.
- Magnetic resonance imaging (MRI) is preferred when suspecting organic intraocular foreign bodies.
- Blunt trauma can cause anteroposterior compression with expansion in the equatorial plane. This may result in various injuries including dislocated lens, vitreous hemorrhage, choroidal and/or retinal detachment, optic nerve avulsion, and ruptured globe, most can be demonstrated on CT.

Keywords

Anterior chamber perforation · Dislocated lens · Intraocular foreign body · Ruptured globe · Retinal detachment · Senile calcific scleral plaques

1 Overview

Ocular trauma constitutes 7% of all bodily injuries and 10–15% of all ocular insults [1, 2]. The most important factor in determining the severity and the treatment of ocular trauma is the mechanisms of injury. Three major injury mechanisms exist [3, 4]:

- Blunt trauma – the impact is transferred to the globe in an anteroposterior compression with expansion in the equatorial plane. This can cause orbital blowout fractures, and ocular injuries such as hyphema, traumatic mydriasis, stellate or rosette-shaped cataract, subluxation or dislocation of the lens, traumatic optic neuropathy, retinal dialysis, commotio retina, and retinal detachment. In severe cases, globe rupture can occur.
- Sharp objects – foreign bodies that cause penetrating or perforating trauma. Usually foreign bodies lose momentum on penetrating the cornea and reaching the anterior chamber, high velocity foreign bodies may injure the posterior segment. The reaction that the foreign body causes depends on the nature of the particle. Ferrous metals usually cause an inflammatory response in the eye while organic materials may be associated with severe bacterial or fungal infection.

O. Zloto (✉)
Department of Ophthalmology, Créteil, France
Goldschleger Eye Institute, Sheba Medical Center, Tel Hashomer, Israel
Sackler Faculty of Medicine, Tel Aviv University, Tel Aviv, Israel

© Springer Nature Switzerland AG 2022
G. Ben Simon et al. (eds.), *Atlas of Orbital Imaging*,
https://doi.org/10.1007/978-3-030-62426-2_115

- Chemical injuries – alkali or acid burns may cause ocular surface injury with limbal stem cell insufficiency, corneal opacities, conjunctival and corneal scarring.

2 Diagnosis

- A comprehensive history regarding the mechanism of injury, the time of onset, and symptoms is essential.
- The ocular and orbital examination should be systematic and thorough. The visual function should be assessed by visual acuity, visual fields to confrontation, eye movement, and checking for a relative afferent pupillary defect. A thorough anterior and posterior segment exam should be done.
- Computed tomography (CT) is the most diagnostic tool utilized in cases of ocular trauma. However, most of the intraocular pathologies can be diagnosed by direct ocular examination.
- Radio-opaque intraocular foreign bodies as well as facial fractures and intraocular hemorrhage/retinal detachment can be visualized by a CT scan.
- Magnetic resonance imaging (MRI) is usually used for detection of nonmetallic intraocular foreign bodies (IOFB), optic nerve sheath hematoma, and traumatic cortico-cavernous fistula. However, MRI should be avoided if there is any suspicion of a metallic foreign body [5].
- The integration of information available from T1, T2, and gradient-echo sequence-MRI and CT images may be used to identify the composition of such IOFBs.
- Ultrasound is considered to be contraindicated when an open-globe injury is suspected.

3 Figures with Captions

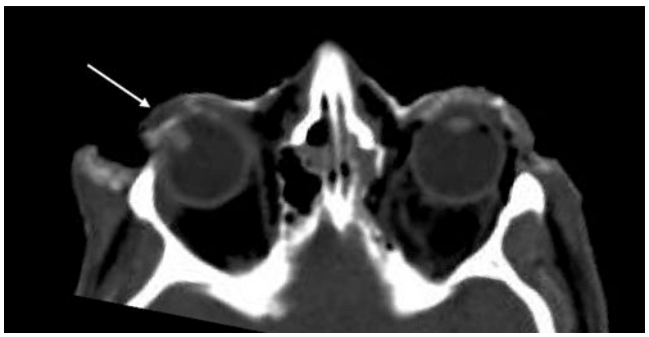


Fig. 1 NE CT bone window axial view – anterior segment perforation and lens dislocation. An 18-year-old male following multi-trauma injury. Anterior segment perforation in both eyes and lens dislocation (*arrow*) on the right eye are observed. Note the bilateral intraorbital emphysema and left orbital blowout medial wall fracture

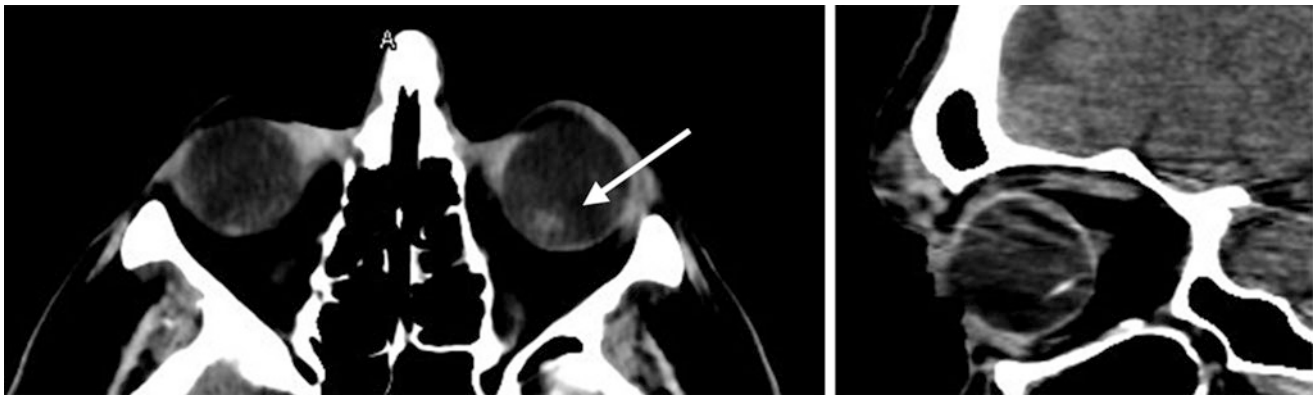


Fig. 2 NE CT soft tissue window axial view (*left*) – intraocular lens (IOL) dislocation. A 74-year-old pseudophakic female after a recent fall. A posterior intravitreal left IOL dislocation is seen (*arrow*). Sagittal view (*right*) demonstrates soft tissue edema overlying the left orbit representing forehead hematoma; notice the slit-like appearance of the posterior dislocated IOL. (*Courtesy of Sara Sella, MD*)

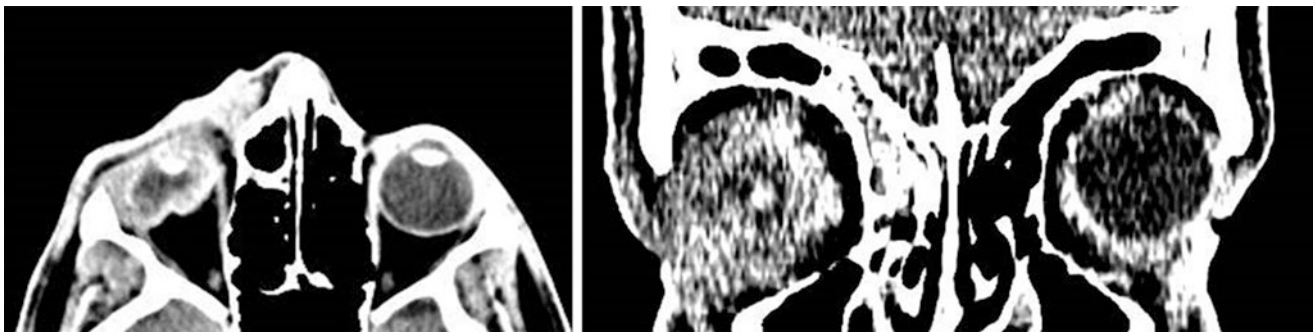


Fig. 3 NE CT soft tissue window, axial view (*left image*) – ruptured globe. A 20-year-old male after head injury. Notice periorbital soft tissue thickening, an abnormal contour, and content of the right globe consistent with globe rupture. Coronal view (*right image*) demonstrating orbital hematoma. Hyperdense content in the frontal and ethmoidal sinuses in keeping with hemorrhage is caused by frontal bone fracture (not demonstrated)

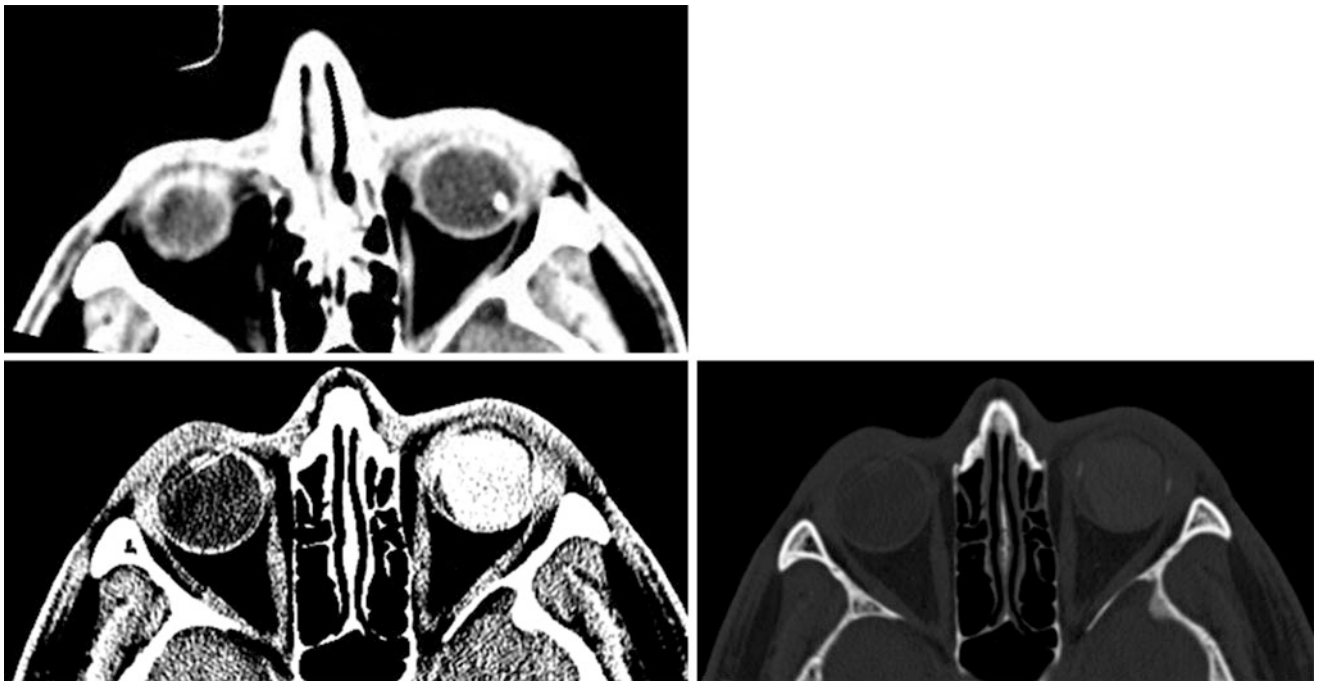


Fig. 4 NE CT, brain window, axial view (*upper image*) – a 46-year-old male after gunshot injury with intraocular metallic foreign body in the posterior segment of the left eye. Note the preseptal thickening. Post-operative scans (*lower images*): the patient underwent band-vitrectomy with foreign body removal and silicon oil injection, seen as a hyperdense material. Note the high-attenuation scleral band that encircles the globe (*right lower)*

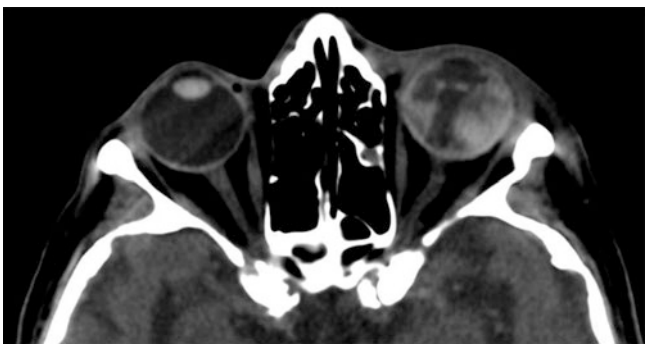


Fig. 5 NE CT, brain window, axial view – retinal detachment. An 86-year-old female after a fall. Hyperdense fluid collection in the posterior segment of the left globe, a finding consistent with traumatic retinal detachment. Note that the detachment spares the optic disk

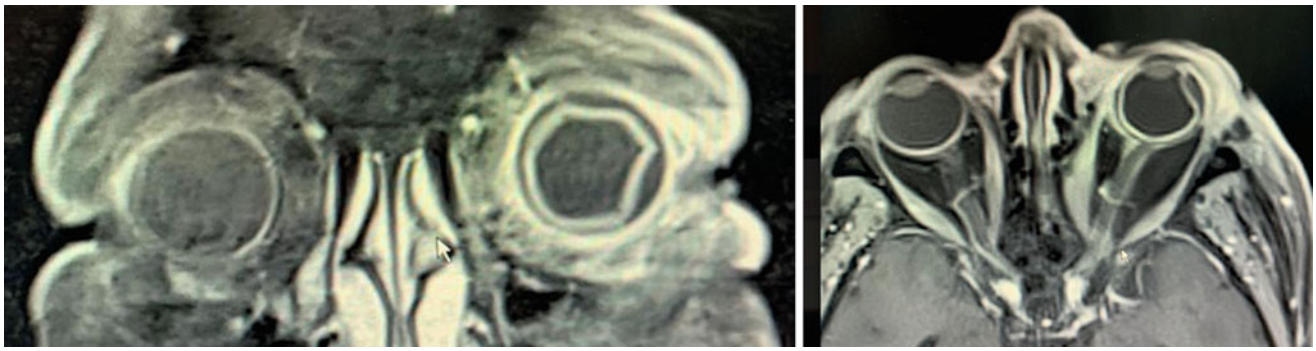


Fig. 6 MRI T1 FS post-contrast of a 70-year-old female with choroidal detachment. Coronal view (*left*) and axial view (*right*) demonstrate hypointense signal, compared to the retinal detachment, the choroidal detachment is not limited anteriorly by the ora serrata and posteriorly by the optic disc

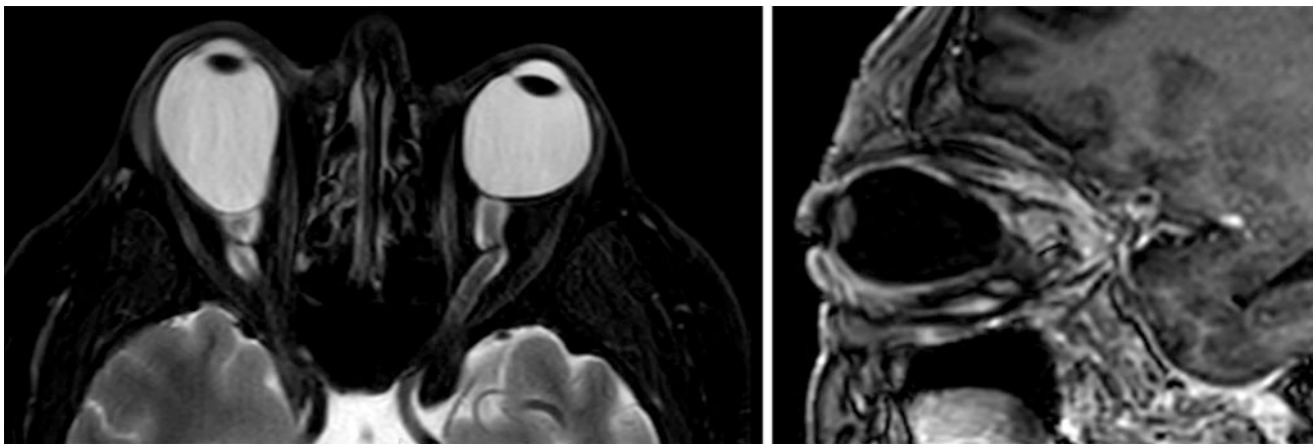


Fig. 7 MRI of a 55-year-old patient with high myopia and staphyloma – T2 axial view (*left*), T1 CE sagittal view (*right*) – an increased anteroposterior diameter and sphero-elliptical shape of the right eye compared to the left eye

References

1. Acar U, Tok OY, Acar DE, Burcu A, Ornek F. A new ocular trauma score in pediatric penetrating eye injuries. Eye (Lond). 2011;25(3):370–4. https://doi.org/10.1038/eye.2010.211.
2. Parver LM, Dannenberg AL, Blacklow B, Fowler CJ, Brechner RJ, Tielsch JM. Characteristics and causes of penetrating eye injuries reported to the National Eye Trauma System Registry, 1985-91. Public Health Rep. 1993;108(5):625–32. http://www.ncbi.nlm.nih.gov/pubmed/8210260. Accessed 6 June 2020.
3. Kuhn F, Morris R, Witherspoon CD, Heimann K, Jeffers JB, Treister G. A standardized classification of ocular trauma. Ophthalmology. 1996;103(2):240–3. https://doi.org/10.1016/s0161-6420(96)30710-0.
4. Kuhn F, Maisiak R, Mann LR, Mester V, Robert M, Douglas Witherspoon C. The ocular trauma score (OTS). Ophthalmol Clin North Am. 2002;15(2):163. https://doi.org/10.1016/S0896-1549(02)00007-X.
5. Moisseiev E, Last D, Goez D, Barak A, Mardor Y. Magnetic resonance imaging and computed tomography for the detection and characterization of nonmetallic intraocular foreign bodies. Retina. 2015;35(1):82–94. https://doi.org/10.1097/IAE.0000000000000266.

Nontraumatic Orbital Hemorrhage (NTOH)

92

Daphna Landau Prat, Gahl Greenberg, Alan A. McNab, and Guy Ben Simon

Contents

1 Signs and Symptoms 684

2 Differential Diagnosis 684

3 Diagnosis 684

4 Treatment 684

5 Figures with Captions 685
5.1 IR/EOM-Related Hemorrhage 685
5.2 Peri-Implant Hemorrhage 688
5.3 Subperiosteal Hemorrhage 689
5.4 Hemorrhage Related to Vascular Malformations 691

References 693

Abstract

- Non-traumatic orbital hemorrhage (NTOH) occurs in several distinct patterns:
  - (1) subperiosteal hemorrhage (NTSOH), usually due to a sudden rise in cranial venous pressure, almost always in the superior orbit.
  - (2) hemorrhage related to extraocular muscles or their sheath, most commonly the inferior rectus.
  - (3) hemorrhage within the capsule surrounding alloplastic implants, usually in the orbital floor.
  - It can also occur diffusely within the orbital soft tissues, or secondary to vascular malformations.

D. Landau Prat · G. Ben Simon (✉)
Ophthalmic Plastic and Lacrimal Surgery Institute, Department of Ophthalmology, The Goldschleger Eye Institute, Sheba Medical Center, Tel Hashomer, Israel

G. Greenberg
Department of Diagnostic Imaging, Sheba Medical Center, Tel Hashomer, Israel
e-mail: gahl.greenberg@sheba.health.gov.il

A. A. McNab
Orbital Plastic and Lacrimal Clinic, Royal Victorian Eye and Ear Hospital, Melbourne, VIC, Australia

© Springer Nature Switzerland AG 2022
G. Ben Simon et al. (eds.), *Atlas of Orbital Imaging*,
https://doi.org/10.1007/978-3-030-62426-2_82

- Hemorrhage related to the inferior rectus or its sheath is seen as a well-defined orbital mass, with smooth enlargement of the belly of the IR muscle or its sheath or the intermuscular septum, in a tear-drop configuration, tapering towards the orbital apex.
- Inferiorly located hemorrhages have been described as having the appearance of a beached whale.
- Subperiosteal hemorrhages have a characteristic lenticular or "D" shape.
- Hyperacute hemorrhage (within minutes) can appear hypodense on CT.
- Acute hemorrhage is markedly hyperdense on CT in relation to muscle (blood will usually measure between 50 and 70 H.U).
- Recent/subacute hemorrhage appears iso/hypodense, and an old clot will have similar CSF density as it liquefies.
- On MR scan, the appearance of hemorrhage is dependent on the age of the hemorrhage and the stages of the clot, though it can be variable particularly in extracranial location like the orbit:

Clot Stage	Timing	T1	T2
Oxyhemoglobin	(<2 days)	iso	hypo
Methemoglobin intracellular	(<2 weeks)	hyper	hypo
Methemoglobin extra-cellular	(<2 months)	hyper	hyper
Hemosiderin	(>2 months)	hypo	hypo

- A fresh clot containing deoxyhemoglobin appears iso-hypointense on T1 and hypointense on T2 imaging; as it changes to methemoglobin, the signal becomes hyperintense from the periphery to the center of the hemorrhage, eventually producing a homogenous high signal. The intensity lessens as the methemoglobin breaks down to hemosiderin and ferritin.
- Blood will show susceptibility (blooming effect) on SWI sequences; blood products may cause restriction on DWI
- Fluid level can be observed within the clot as it liquifies
- CT/MR with contrast help to rule out vascular anomaly related hemorrhage
- Enhancement is dependent on the status of the hemorrhage ranging from no enhancement, homogenous enhancement to peripheral ring enhancement

Keywords

Orbital hemorrhage · IR enlargement / EOM enlargement · Peri-implant hemorrhage · Sub-periosteal hematoma · Orbital roof hemorrhage · Acute proptosis · Nontraumatic orbital hemorrhage

1 Signs and Symptoms

Non-traumatic orbital hemorrhage is rare, can occur with no underlying pathology or secondary to hemorrhage associated with orbital tumor, vascular malformation or inflammation. Its clinical presentation is related to the confined anatomical space of the hemorrhage. It can occur in association with arterial hypertension or following ocular or orbital surgery. It can occur in defined anatomical spaces such as the sub-periosteal space of the orbital roof or around alloplastic materials used in orbital fractures repair. It can rarely be confined to a rectus muscle or its sheath, more commonly in the inferior rectus muscle. In most cases, it resolves spontaneously within weeks without long-term sequelae. Mild thickening of the IR muscle when involved may be anticipated in the minority of cases; however, this has no clinical impact. Systemic coagulopathies are not usually present in cases related to extraocular muscles, but some sub-periosteal hematomas occur with coagulopathies or more commonly with an acute rise in intra-cranial venous pressure.

Clinical signs and symptoms include acute onset of unilateral orbital pain, diplopia with restricted ocular motility, proptosis and globe displacement, depending on the anatomical site of hemorrhage. Nausea and vomiting can occur, probably as a result of acute rise in intra-orbital pressure. IOP is not normally elevated, i.e., the episcleral venous pressure is not raised.

Most of the time the acute onset and radiological appearance make a strong presumptive diagnosis of idiopathic NTOH possible. Search for a soft tissue component to rule out an underlying tumor.

2 Differential Diagnosis

Vascular malformation such as venous-lymphatic malformation, orbital tumors, infection, trauma, orbital implant infection, or peri-implant hemorrhage.

Enlarged EOM: neoplastic, metastasis (melanoma, lymphoma), IOI (myositis), TED, acromegaly – however, these have more gradual onset and are associated with systemic and orbital distinct features.

3 Diagnosis

The sudden onset of symptoms is highly suggestive of hemorrhage. Diagnostic imaging features per CT / MRI or both are required to diagnose the hemorrhage and to rule-out orbital mass or vascular malformation. MRI is helpful in dating the hematoma.

4 Treatment

Treatment is usually conservative, as spontaneous resolution is common. If persistent or ON function is affected, i.e., vision threatening hematoma, consider intra-orbital pressure lowering procedures. Surgical evacuation / aspiration of hematoma when possible can be performed such as in the case of peri-orbital implant hematoma, albeit in IR muscle-related hematoma this may not be possible.

5 Figures with Captions

5.1 IR/EOM-Related Hemorrhage



Fig. 1 Clinical photograph of a 79-YOM with acute onset right eye proptosis, orbital pain, nausea and vomiting. There were OM limitations with 6 mm of right eye proptosis and 3 mm of hyperglobus. Visual acuity and other optic nerve functions were preserved, IOP was increased to 23 mmHg



Fig. 2 Axial CT scan, soft tissue window, without contrast, demonstrating a right intra-conal well-defined hyperdense relatively homogenous mass extending from the posterior pole of the globe to the orbital apex and protruding to the superior orbital fissure. The mass is displacing the inferior rectus muscle medially (white arrow) and causing axial proptosis. Note anterior ethmoid opacity on the right side and posterior ethmoid on the left as evidence of chronic inflammation; these findings are not related to the orbital mass

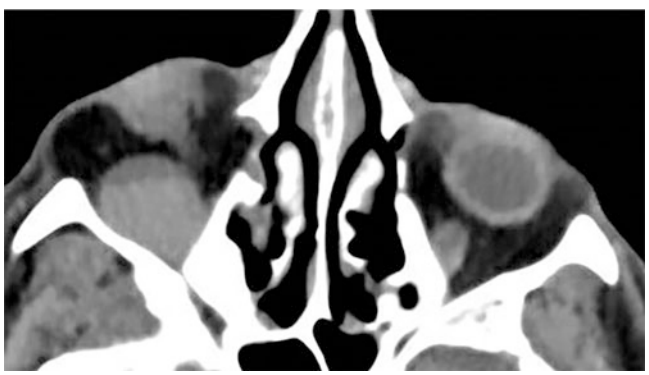


Fig. 3 Axial section at an inferior level of the orbit showing fluid level as evidence of recent orbital hemorrhage. Such fluid levels may be more common in acute/subacute hemorrhage



Fig. 4 Coronal section showing that the hemorrhage is emanating from within the lateral IR sheath filling the extra-conal inferior temporal compartment, displacing the IR medially, the LR superiorly, and the ON supero-medially

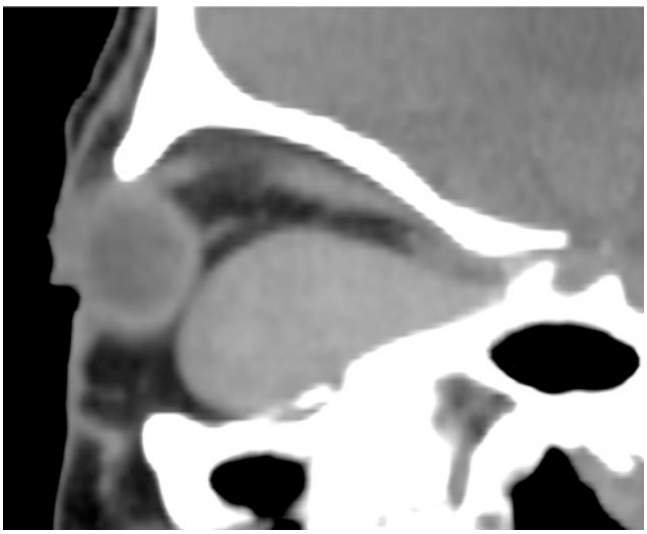


Fig. 5 Sagittal section denoting the posterior extent of the hematoma in a "beached whale" appearance. The hematoma was measured 10 cc in volume

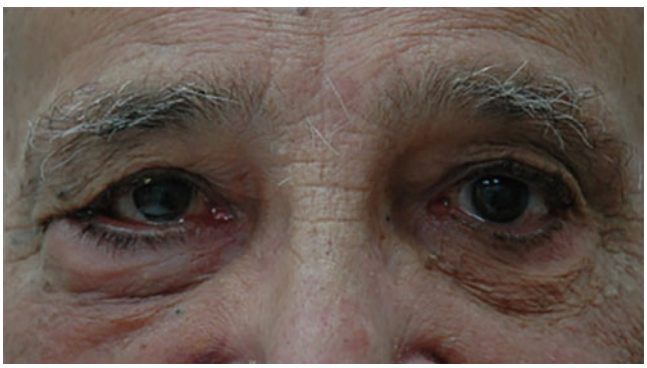


Fig. 6 Clinical photograph of the patient one week after surgical evacuation of the orbital hematoma which was connected to the sheath of the IR muscle. Note marked improvement of right globe proptosis and hyperglobus. Lower eyelid swelling is related to normal post-operative course



Fig. 7 Post-operative axial CT scan, soft tissue window, showing marked decrease in the volume of the hematoma and axial proptosis with a residual homogenous mass confined to the inferior orbital apex region

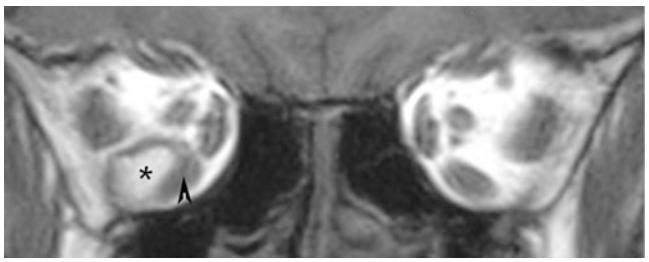


Fig. 8 Non-contrast, non-FS coronal T1WI MR scan of a 39-YOM (different patient) with acute onset painful right proptosis and vomiting. There is a hyperintense homogenous mass (Asterix) related to the IR muscle sheath, at its superior-temporal border. The muscle itself (arrowhead) is compressed medially but is of normal size and signal

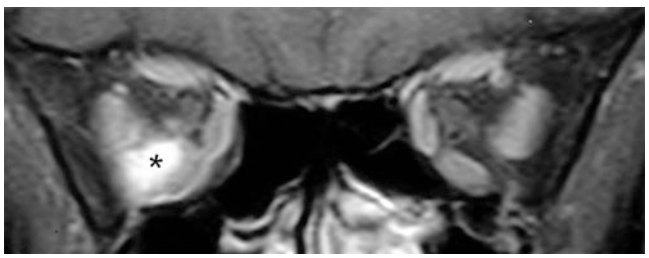


Fig. 9 T1-WI fat sat +gad showing homogenous enhancement of the lesion (Asterix), characteristic of recent clot with methemoglobin. The enhancement may be 2nd to contrast extravasation

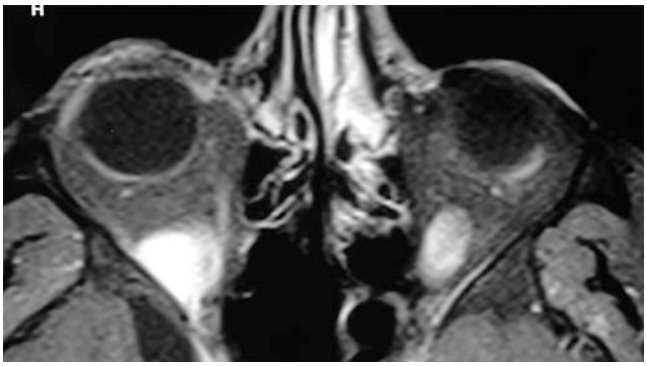


Fig. 10 T1-WI fat sat +gad emphasizing the epicenter of the mass at the posterior half of the IR muscle

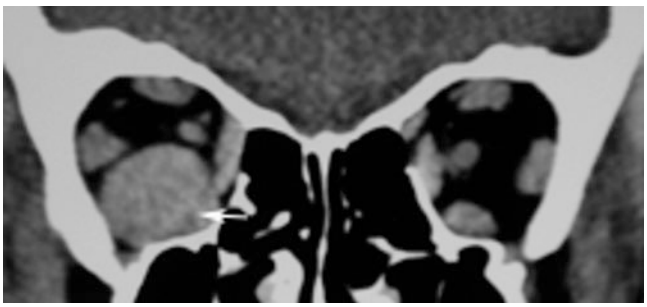


Fig. 11 Post contrast CT scan, soft tissue window, of the same patient showing the right orbital homogenously enhancing hematoma related to the IR muscle sheath. There is a subtle demarcation line between the muscle and the hematoma (white arrow)

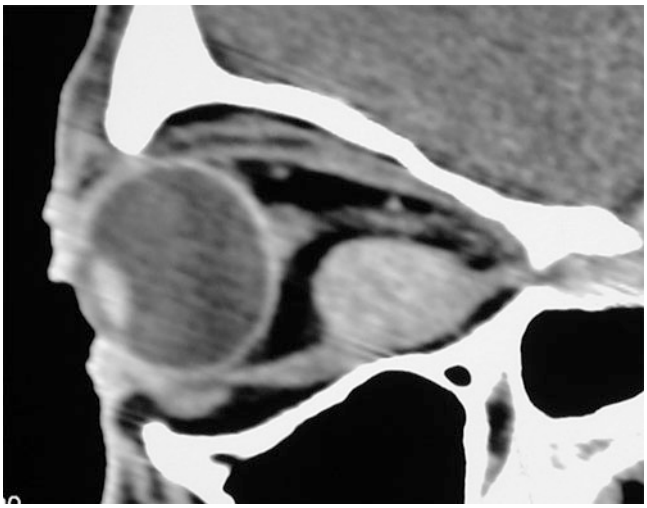


Fig. 12 A sagittal oblique CT reconstruction of the same patient showing the mass located within the posterior half of the IR muscle sheath giving the typical appearance of "beached whale"

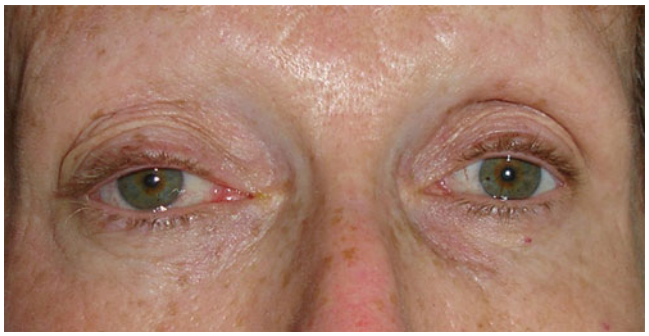


Fig. 13 Clinical photograph of a 55-year-old female with 5 days history of right eye throbbing pain and proptosis associated with migraine headaches. Visual acuity was normal, there was mild upgaze limitation with no diplopia

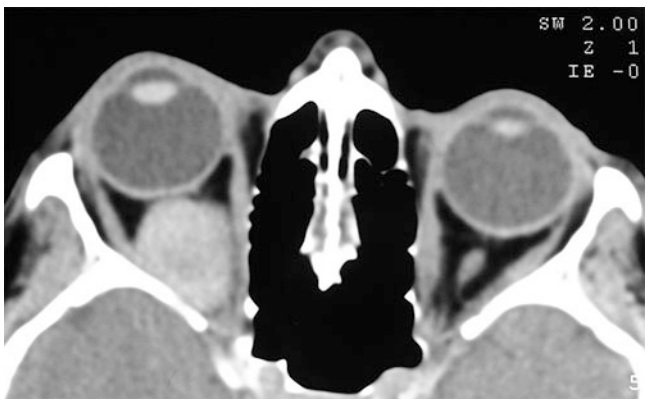


Fig. 14 Post contrast axial CT scan, soft tissue window, disclosed a posteriorly intra-conal, homogenously enhanced mass related to the right IR muscle. The mass was indenting the globe



Fig. 15 CT axial section of a 73-YOM with acute onset left IR-related orbital hemorrhage. Note the homogenous hyperdense well delineated intra-conal mass extending to the orbital apex



Fig. 16 MRI T1-WI Fat sat with Gadolinium of the same patient showing the isointense mass within the IR muscle sheath and peripheral enhancement

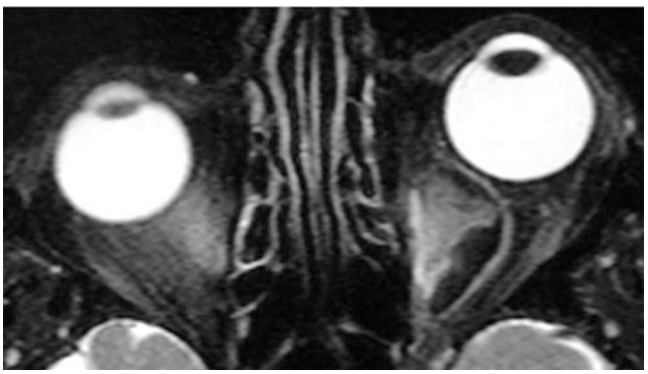


Fig. 17 The IR related hemorrhage is of mixed signal intensities on T2-WI

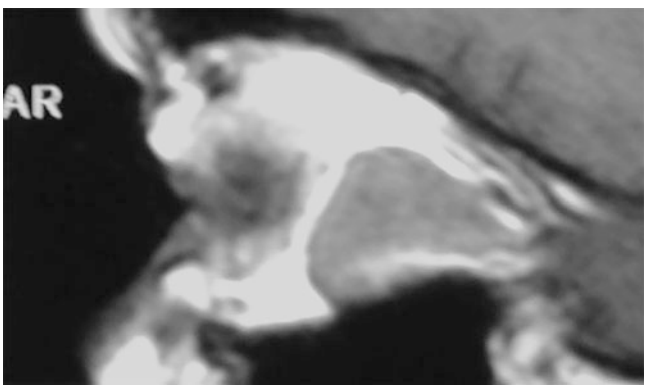


Fig. 18 Sagittal T1-WI without contrast in a typical beached whale appearance; the mass is slightly hyperintense to brain gray matter

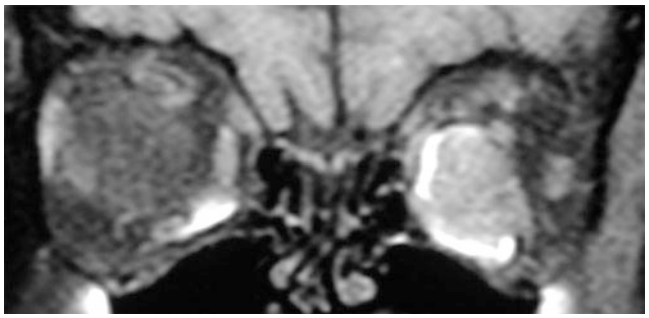


Fig. 19 Coronal section T1WI fat sat with contrast demonstrating the superior-temporal displacement of the left optic nerve. Note the peripheral enhancement on the medial and inferior aspects of the hematoma

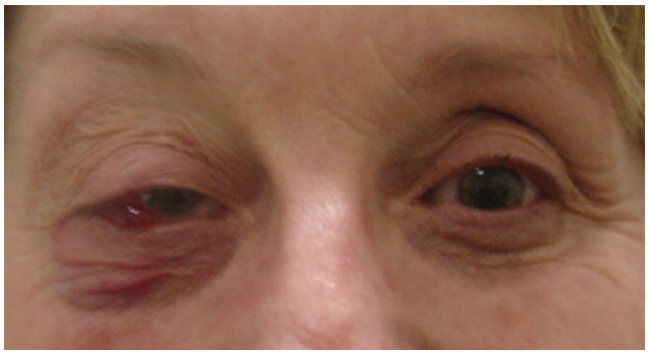


Fig. 20 Clinical photograph of a woman with one day history of right ocular pain, double vision, proptosis, periocular redness and swelling. There were OM limitations in abduction and infra-duction, decreased VA to 20/60, with no APD

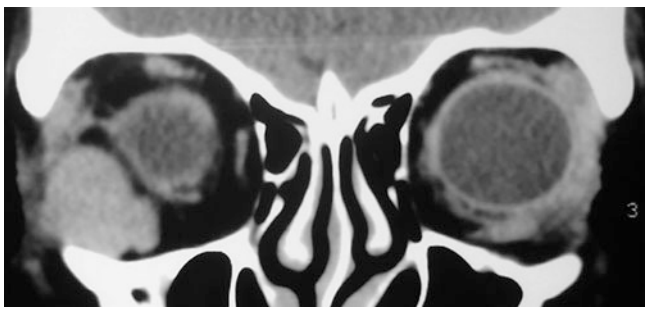


Fig. 21 Coronal CT scan showing right inferior temporal hyperdense orbital mass, circumscribed, homogenous, indenting the globe. Findings consistent with spontaneous orbital hemorrhage most likely IR related

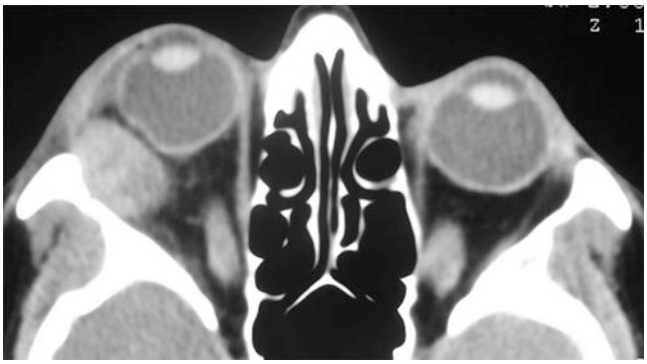


Fig. 22 Axial scan showing the posterior extent of the hemorrhage and globe indentation. The patient showed marked improvement within 24 hours with normal VA of 20/20 and less OM limitations

5.2 Peri-Implant Hemorrhage

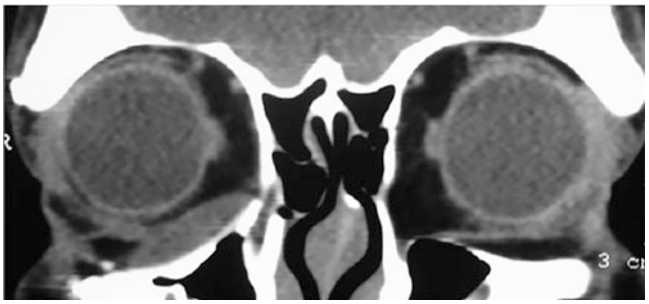


Fig. 23 Coronal NECT scan of a 31-YOM with 3 weeks history of binocular vertical diplopia. Two years prior to admission he underwent right orbital blow-out fracture repair using alloplastic material. The scan shows an iso-hyperdense relatively homogenous well-defined extra-conal mass, lentiform shaped, at the orbital floor in line with the implant configuration. The patient was diagnosed with orbital hemorrhage surrounding the implant

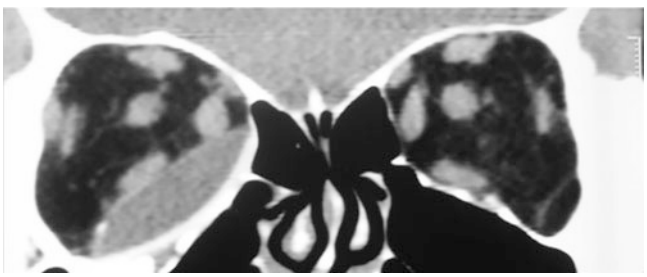


Fig. 24 Coronal section further posterior into the orbit showing the expansion of the hemorrhage keeping parallel to the orbital floor and implant. The bleeding is confined to the capsule of the orbital floor implant bearing a biconvex configuration

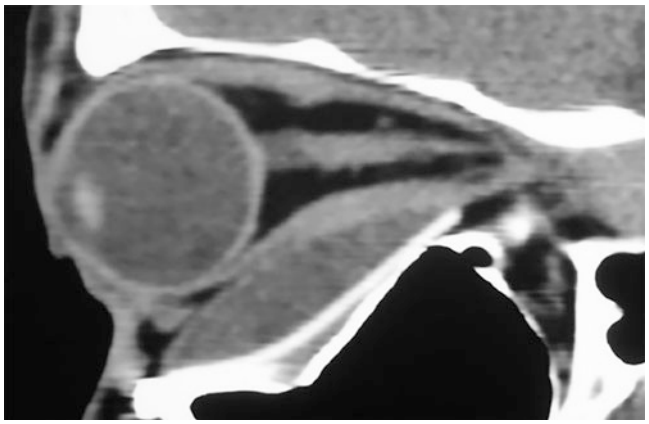


Fig. 25 Sagittal oblique reconstruction scan showing the extent of the hemorrhage, the old fracture plate, good position of the floor implant covering the posterior fracture edge and the hemorrhage within the capsule. The patient underwent surgical evacuation of the hemorrhage along with extirpation of the implant's capsule

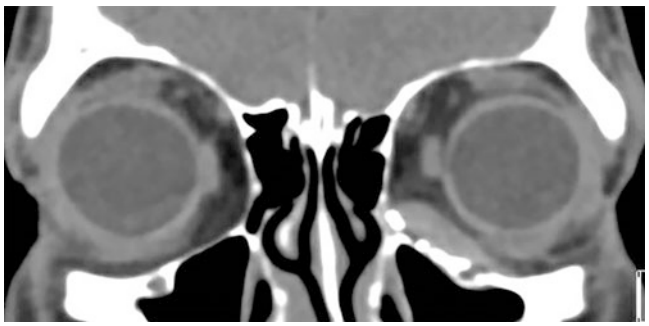


Fig. 26 Coronal CT scan of a 24-year-old patient 7 years after repair of left orbital floor fracture and recent history of left globe proptosis, and binocular vertical diplopia in upgaze. CT showed left peri-implant hemorrhage as hyperdense homogenous mass in the configuration of the capsule

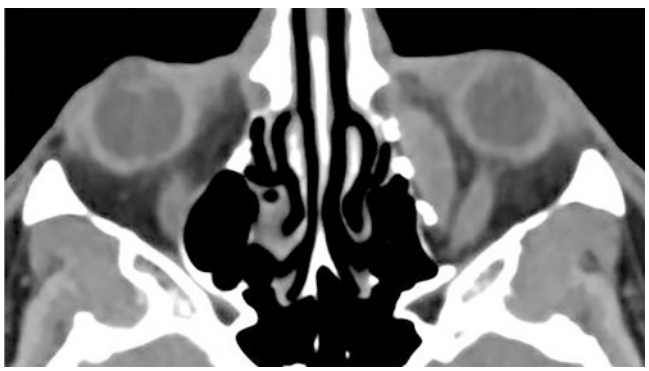


Fig. 27 Axial section showing the hemorrhage extending to the medial orbital wall as the implant is bent gaping the inferior-medial fracture

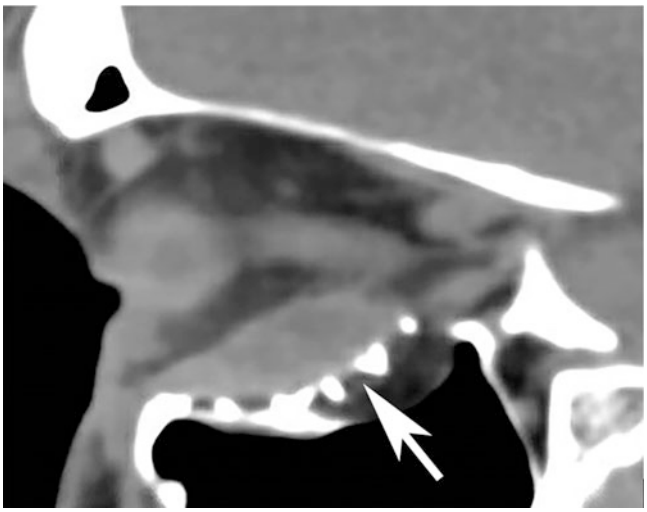


Fig. 28 Sagittal reformat of the same patient showing the lentiform shape of the hemorrhage around the implant and within the capsule. The white dotted line (white arrow) represents the porous polyethylene implant

5.3 Subperiosteal Hemorrhage



Fig. 29 A young woman awoke in the morning after an episode of vomiting with left eyelid swelling, vertical diplopia and proptosis

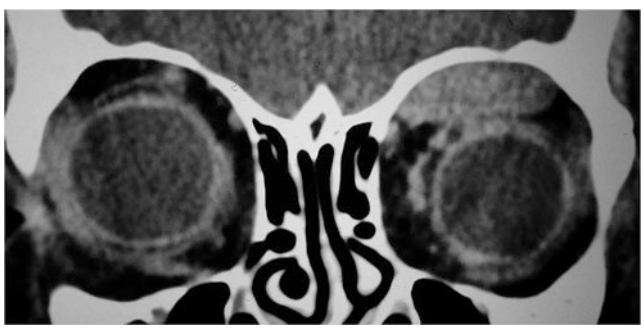


Fig. 30 A coronal CT non-enhanced scan shows a hyperdense extraconal lesion consistent with a hematoma in the superior subperiosteal space of typical lenticular shape

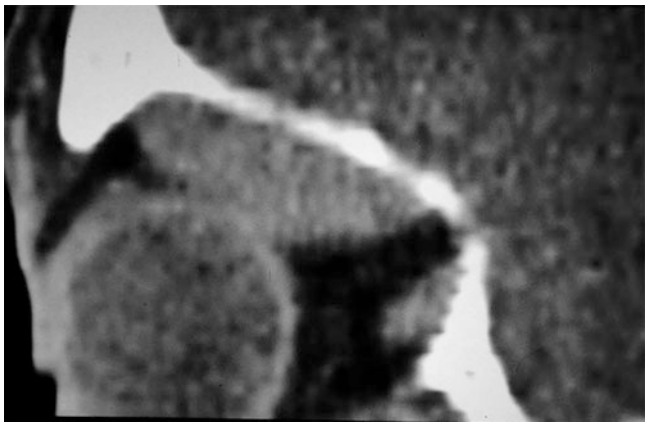


Fig. 31 A sagittal CT reformat shows the typical lenticular shape of the hematoma

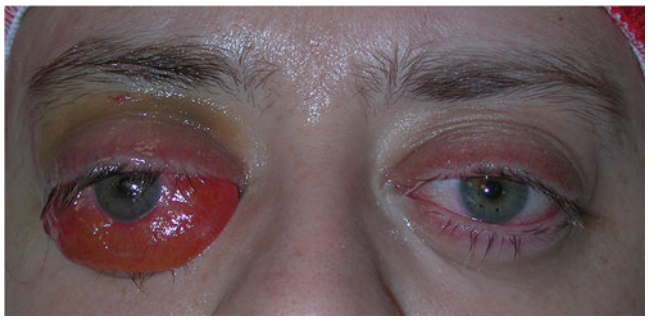


Fig. 32 Clinical photograph of a 30-YOF with recent history of massive pulmonary embolus secondary to thrombophilia. The patient had a cardiopulmonary arrest and was resuscitated (CPR), intubated and anticoagulated with placement of an inferior vena cava filter. In ICU she was noted to have bilateral proptosis and asymmetric chemosis with reduced vision

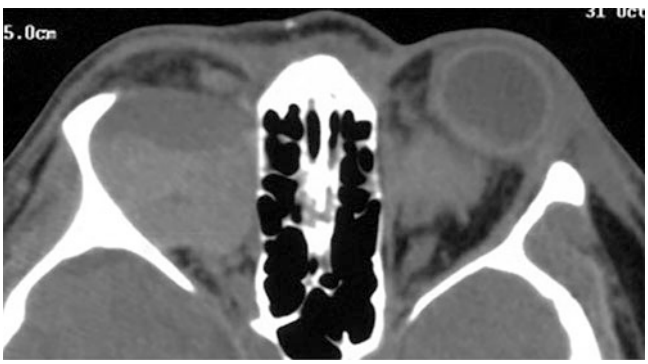


Fig. 33 Axial CT scan showing a right superior orbital inhomogeneous mass with fluid level, and less organized smaller mass on the left side as evidence of subperiosteal bilateral orbital hemorrhage

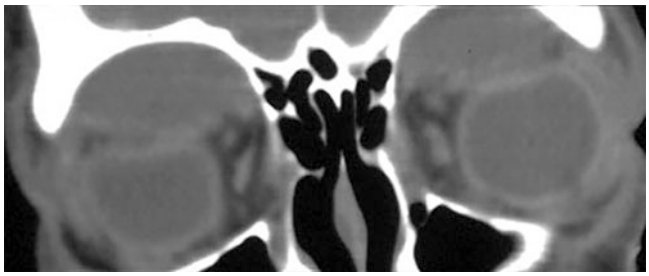


Fig. 34 CT scan, coronal view (same patient) showing bilateral superior orbital mass compressing the posterior aspect of the globe

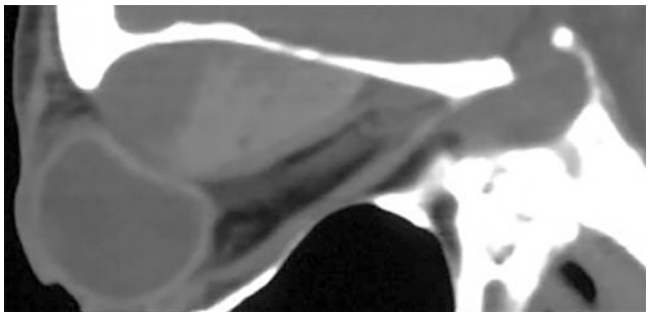


Fig. 35 Sagittal section, beautifully demonstrating typical lenticular shape superior subperiosteal hemorrhage, a posterior hyperdense part and anterior hypodense part representing layering of blood products. The mass is compressing the posterior superior part of the globe. Both sides collections were drained, and the patient made a full recovery

5.4 Hemorrhage Related to Vascular Malformations

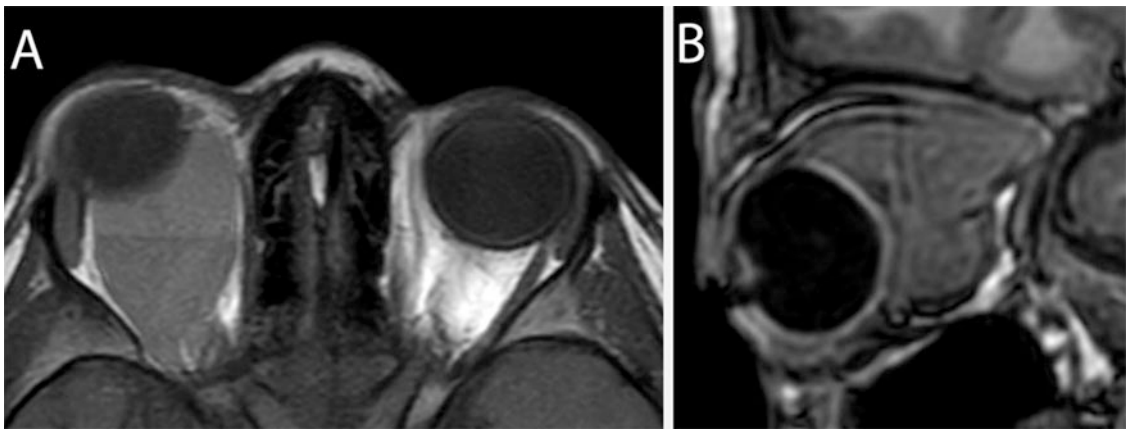


Fig. 36 MRI NE NFS (**a**, axial and **b**, sagittal) T1WI of an 8-YOF with right orbital lymphatic malformation (LM) and new onset pain and proptosis secondary to orbital hemorrhage. There is a large IC hemorrhagic sac containing fluid-fluid levels of different intensities, indicating subacute blood products within LM. Note mild globe proptosis on the axial image

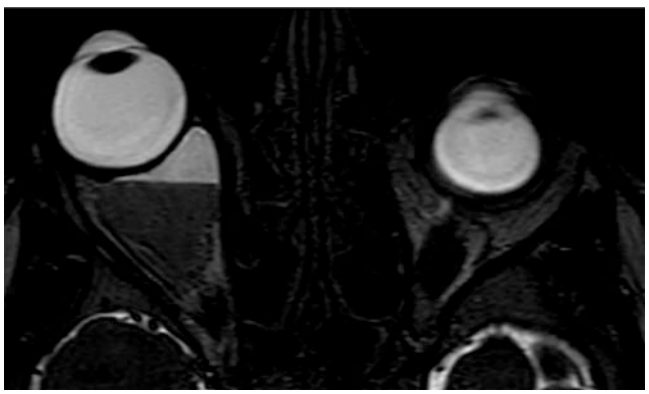


Fig. 37 Axial 3D T2 TSE of the same patient again showing a nice demarcation of the fluid-fluid levels within the hemorrhage

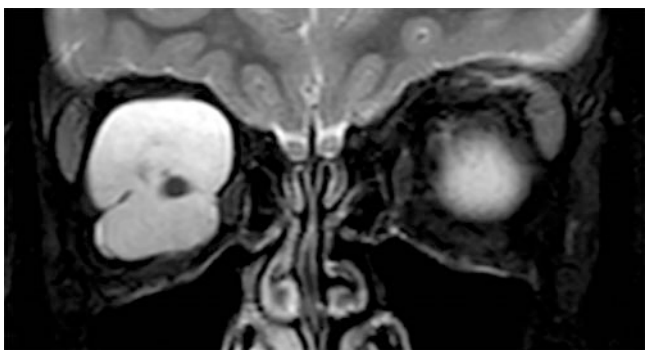


Fig. 38 Coronal T2WI showing how the malformation is engulfing the ONS in a concentric fashion and fully occupying the intra-conal space

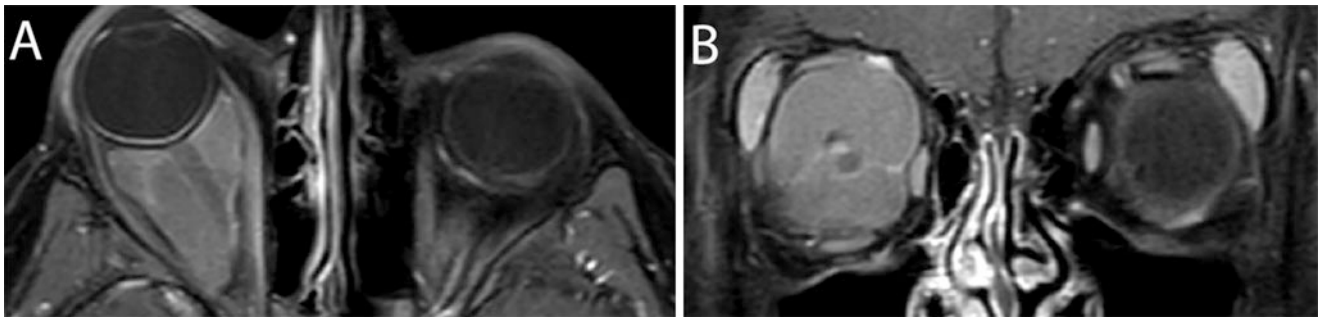


Fig. 39 T1WI-CE-FS images (A, axial and B, coronal) showing a lack of an enhancing venous components excluding a LVM; note mild rim enhancement and delicate septae within the malformation

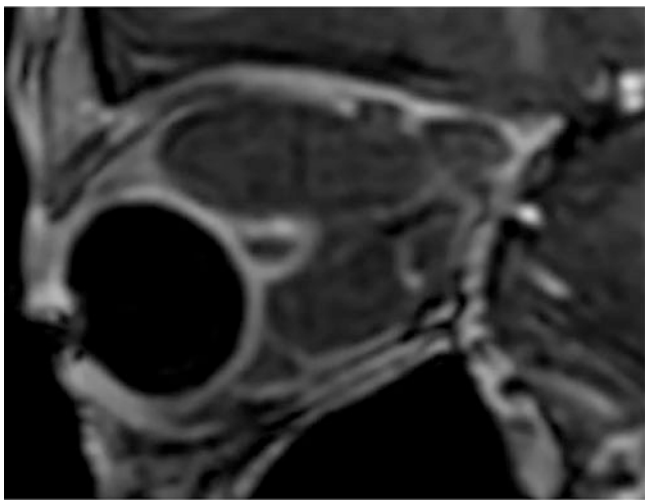


Fig. 40 Sagittal T1 3D TFE CE showing the anterior-posterior extent of the LM

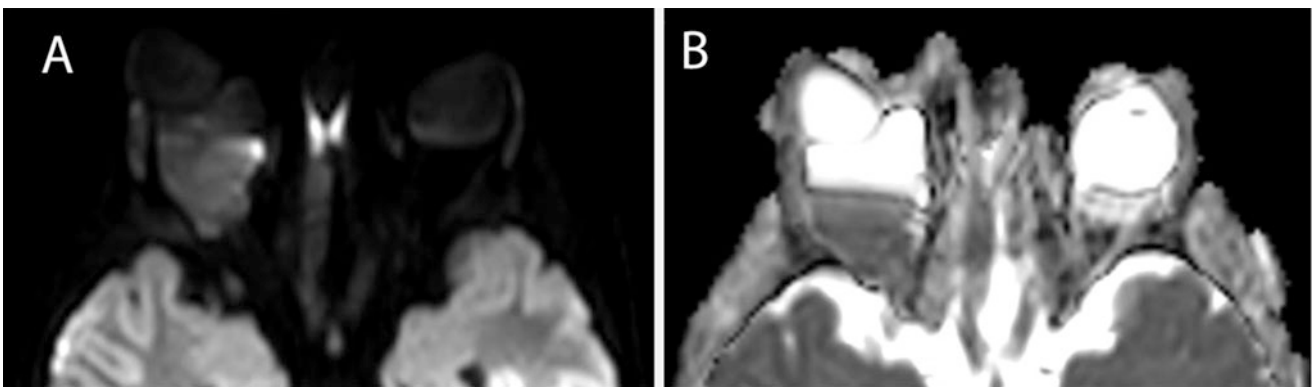


Fig. 41 Axial DWI (**a**) and corresponding ADC map (**b**) showing mild restrictive features within the hematoma typical for blood products

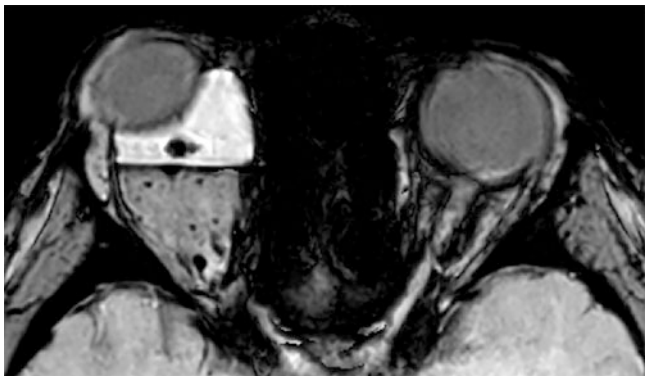


Fig. 42 Axial SWI depicts the variety of blood products ranging from methemoglobin (intermediate to high signal) to hemosiderin (multiple dark or hypointense signals contained within the hemorrhage)

References

1. McNab AA. Nontraumatic orbital hemorrhage. Surv Ophthalmol. 2014;59:166–84.
2. Chan HHL, Hardy TG, McNab AA. Spontaneous orbital hemorrhage related to the extraocular muscles. Ophthal Plast Reconstr Surg. 2019;35:256–61.
3. Ben Simon GJ, McNab AA. Idiopathic orbital hemorrhage related to the inferior rectus muscle. A rare cause for acute-onset diplopia and unilateral proptosis. Ophthalmology. 2005;112:1838–43.
4. Ryu YA, Park JB, Kyung HW, Song SH, Kang NH. Delayed orbital hemorrhage around alloplastic implants after blowout fracture reduction. Arch Craniofac Surg. 2015;16:35–8.
5. Gupta S, Aakalu VK, Ahmad AZ. Late-onset orbital hematoma secondary secondary to alloplastic orbital implant mimicking transient transient ischemic attacks. OPRS. 2011;27:18–20.
6. Prendes MA, Gudgel B, Kassa EB, Todd AM, Fu R, Abou-Jaoude M, Timoney PJ, Shipchandler TZ, Nunery WR, Lee HBH. Intracapsular hemorrhage rates in non-fixated nylon sheet orbital implants for orbital fracture management. Am J Otolaryngol. 2019;40:509–11.
7. Gilhotra JS, McNab AA, McKelvie P, O'Donnell BA. Late orbital haemorrhage around alloplastic orbital floor implants: a case series and review. Clin Exp Ophthalmol. 2002;30:352–5.
8. Rose GE, Verity DH. Acute presentation of vascular disease within the orbit-a descriptive synopsis of mechanisms. Eye (Lond). 2013;27:299–307.

Postoperative Changes

93

Ofira Zloto

Contents

1 **Overview** 695
2 **Figures with Captions** 696
References 703

Abstract

Imaging is an integral part of the assessment of orbital disorders; ocular and orbital surgery may involve the use of various implants within the globe or at its vicinity. These may include intraocular lenses in cataract surgery, scleral encircling/radial bands for vitreo-retinal pathologies, glaucoma filtering devices located partially adjacent to the globe and partially at the anterior chamber, orbital implants for fractures repair, lacrimal bypass tubes for naso-lacrimal obstructions, and eyelid metallic weights for lagophthalmos. It is important that physicians will be aware of such devices and/or possible ocular changes with surgery, as the radiologic appearance can be confusing and potentially mimic other pathologies. In this chapter, we will present different ocular and orbital postoperative imaging changes along with commonly used implants.

Keywords

Lester Jones tube · Orbital wall fractures · Gold weight · Vitrectomy · Ahmed glaucoma valve · Cataract extraction · Intraocular lens

1 Overview

- There are numerous surgical procedures involving the globe and adnexa, in part implants and devices may be used.
- Modalities such as CT or MRI are not routinely implemented following ocular surgeries.
- Imaging can be performed for evaluating the outcome of orbital surgery, and in many cases, the orbits are included when imaging the brain, face, or paranasal sinuses.
- Clinicians should be familiar with the spectrum of orbital postoperative findings on CT and MRI because radiologic appearance can be confusing and potentially mimic pathologic entities.
- Knowledge of the MRI safety of the implanted devices is mandatory as well as the ability to distinguish them from foreign bodies.

O. Zloto (✉)
Department of Ophthalmology, Créteil, France

Goldschleger Eye Institute, Sheba Medical Center, Tel Hashomer, Israel

Sackler Faculty of Medicine, Tel Aviv University, Tel Aviv, Israel

© Springer Nature Switzerland AG 2022
G. Ben Simon et al. (eds.), *Atlas of Orbital Imaging*,
https://doi.org/10.1007/978-3-030-62426-2_123

2 Figures with Captions

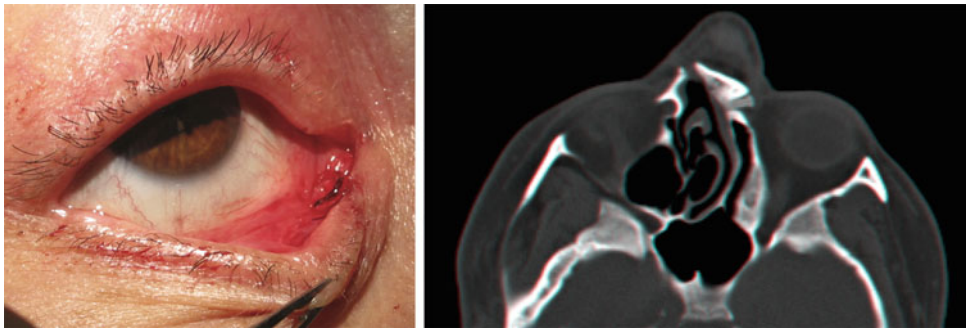


Fig. 1 **Lester Jones tube (LJT)** is a small polished Pyrex tube that creates a bypass to an obstructed upper lacrimal system, allowing direct flow of tears from the ocular surface into the nose. The tube is inserted during conjunctivodacryocystorhinostomy surgery [1]. **Clinical picture** – right side Lester Jones Tube. **Bone window, axial view** demonstrating a left side LJT, note the deviated nasal septum and thickening of the posterior medial orbital wall and the frontal process of the maxilla. The optimal position of the tube should be within the middle meatus space, with its tip at least 2 mm away from the nasal septum to prevent mucosal erosion, bleeding, and tube obstruction

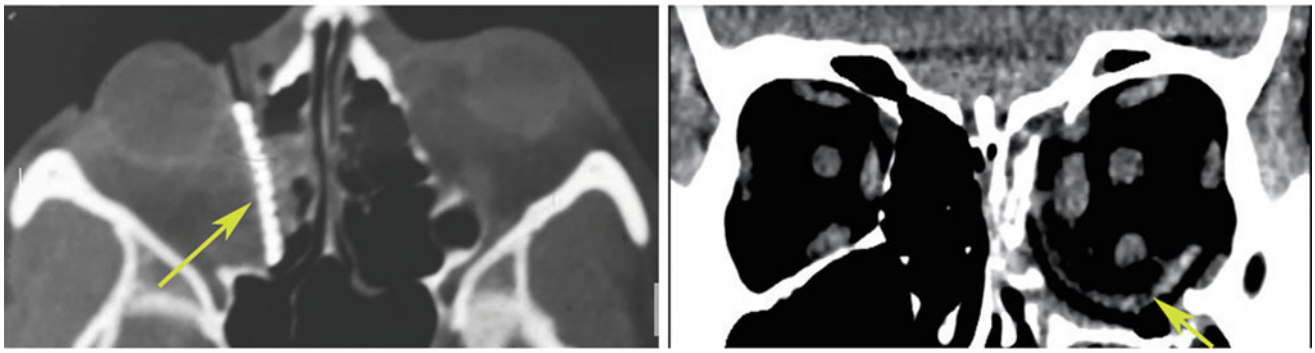


Fig. 2 Maloriented implants of orbital blowout fractures repair. Orbital fractures are among the most common facial fractures; high-energy impact may require orbital reconstruction surgery. The goal of surgical repair is to restore internal contour, volume, function, and aesthetics. Imaging is commonly recommended for presurgical planning and post-surgical assesment [2–4]. CT Bone window, axial view (*left*) demonstrating medial wall fracture with a medial wall titanium mesh implant (*arrow*). The implant is maloriented, with anterior displacement towards the globe, and posterior displacement towards the ethmoid sinus. Ideal implant position should bridge the entire extent of the fracture, from stable bone to stable bone (as shown in the following Fig. 3). CT Brain window, coronal view (*right*) – left orbital floor porous polyethylene implant (*arrow*) that covers the inferior fracture but does not reach the superior medial end of the fracture and partially positioned in the ethmoid sinus

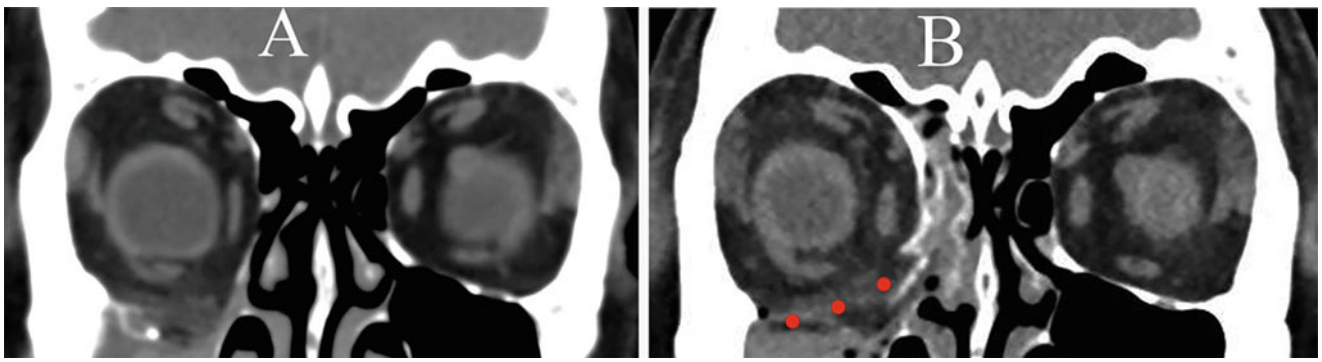


Fig. 3 NECT coronal scan of a 63-YOF with right orbital blow-out floor fracture secondary to fall injury (**a**). The patient underwent fracture repair with porous polyethylene implant (**b**) which is relatively radiolucent. The implant is marked by the dotted red line. Note good internal contour and implant position bridging the full extent of the fracture

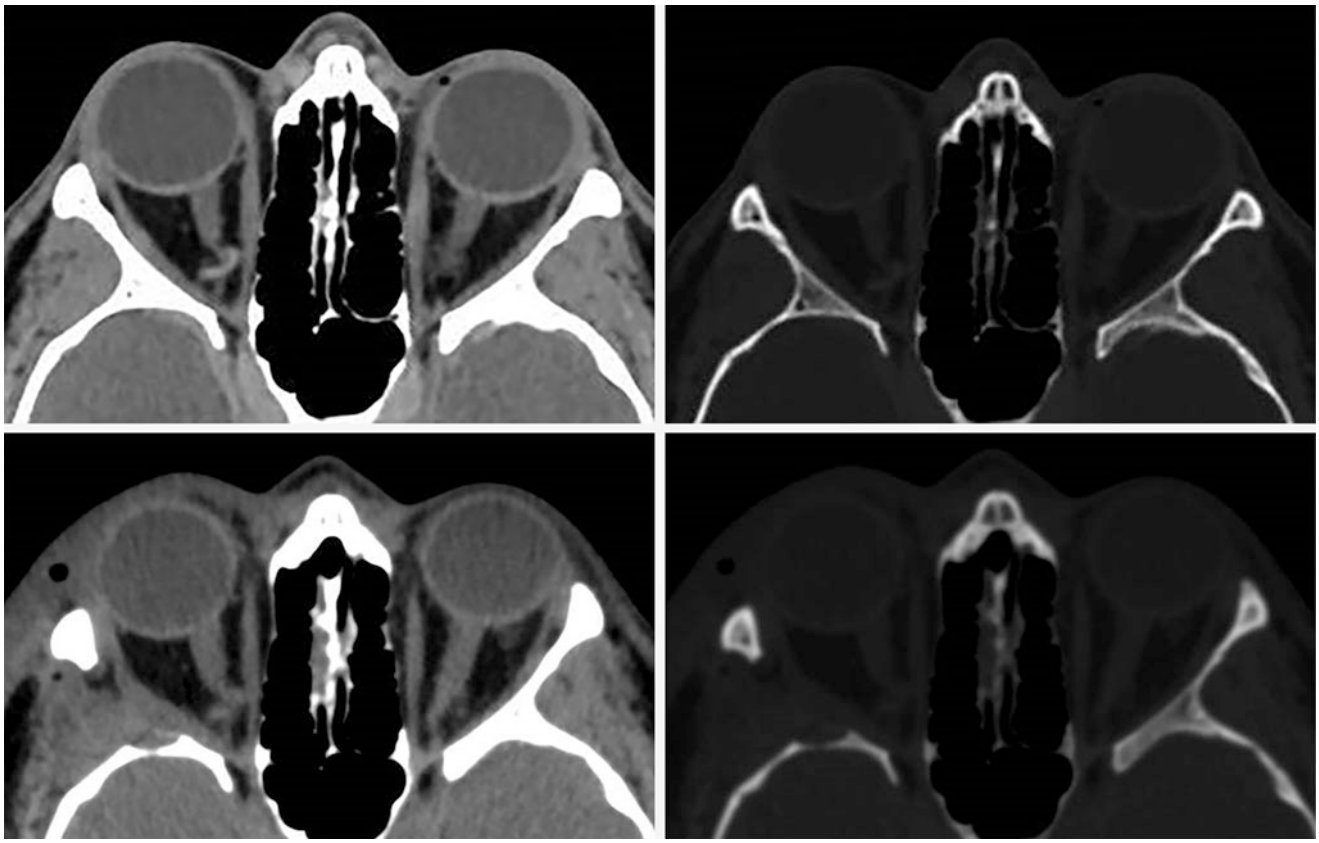


Fig. 4 Pre- (*upper*) and postoperative (*lower images*) CT scan of a 43-YOM with right eye physiologic proptosis. Soft tissue (*left*) and bone window (*right*). The patient underwent right deep lateral wall orbital decompression with intraconal fat debulking. One day postoperative scans show absence of the deep lateral wall, lateral rectus muscle prolapse with orbital expansion, and soft tissue swelling in the infratemporal fossa. Deep sphenoid bone (trigone) is drilled out to allow axial posterior displacement of the globe and improved position

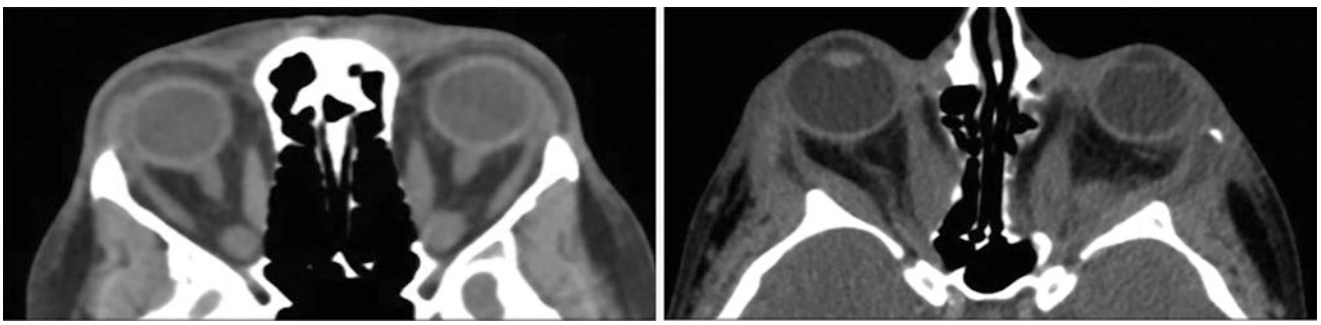


Fig. 5 Pre- (*left*) and postoperative (*right*) NECT of a 30-YOM who underwent rim-off balanced (medial and lateral) bilateral orbital decompression. Note the absence of orbital rim in the postoperative scans along with medial orbital expansion and MR muscles displacement into the ethmoidal sinuses. The EOM muscles are enlarged in a fusiform configuration typical of TED

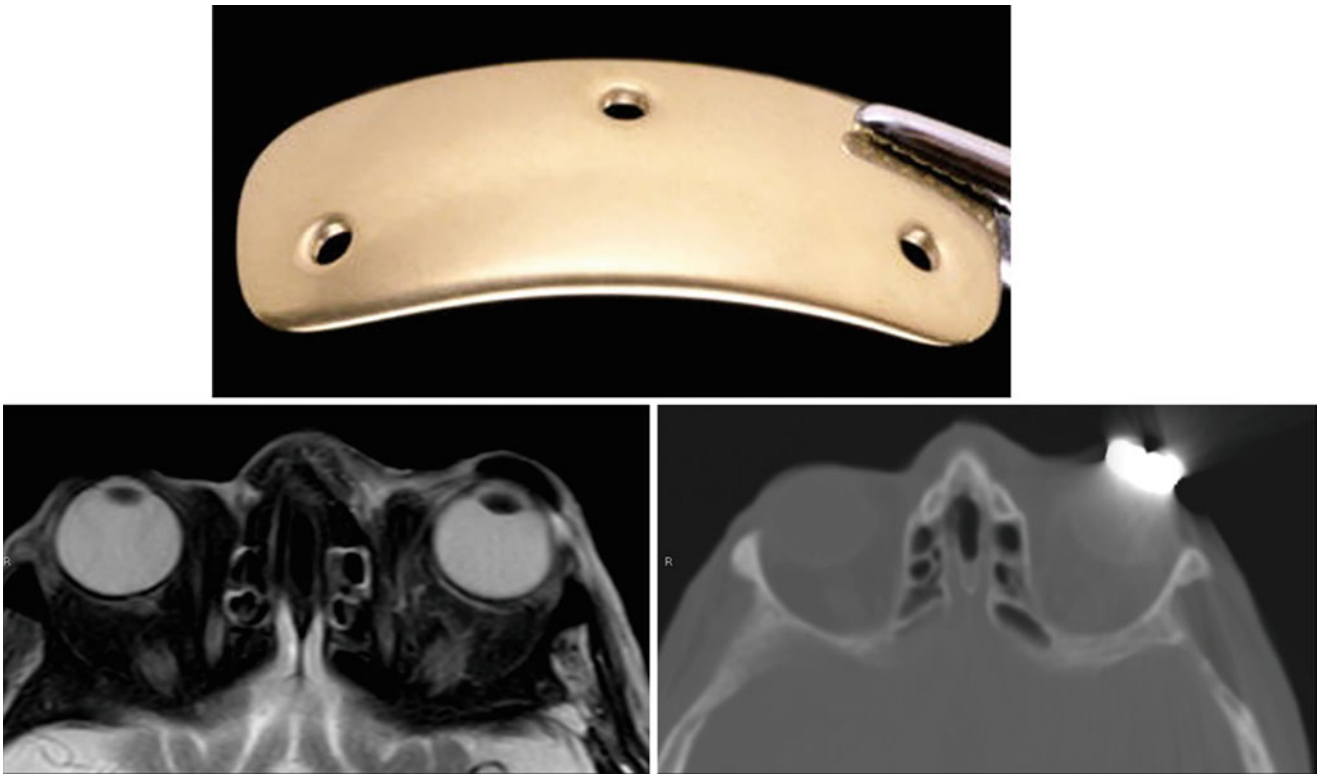


Fig. 6 Upper eyelid gold weight implantation is a common treatment for lagophthalmos (*upper image*). It improves blinking and eyelid closure, thus protects the ocular surface [5]. MRI axial T2 view (*lower left*) – gold is a noble metal, hence MRI-safe in static magnetic field of 3-Tesla or less. CT bone window axial view (*lower right*) – image artifact caused by the gold weight

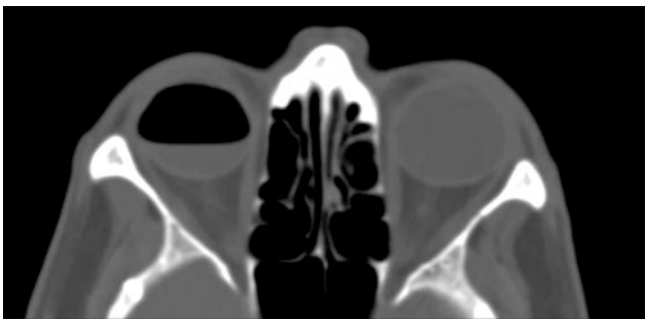


Fig. 7 An air and gas mixed after vitrectomy. During vitrectomy surgery, a fluid/air exchange is performed to remove the intraocular fluid from the posterior segment of the globe and in some cases air/gas (typically mixed gas and air) exchange is done to provide internal tamponade and prevent retinal detachment. The mixed gases disappear spontaneously and the posterior segment re-fills with fluid. CT Bone window, axial view demonstrates intraocular air within the right eye

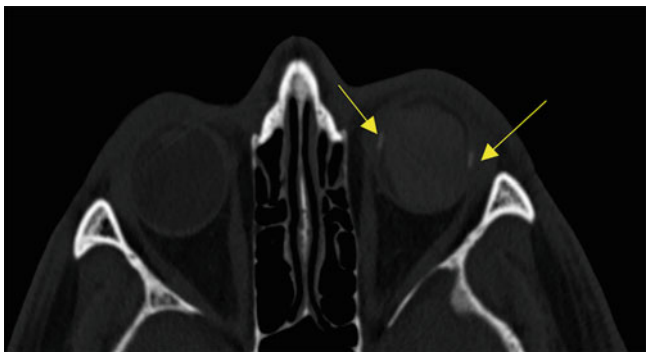


Fig. 8 Intraocular silicone oil after vitrectomy. Liquid silicone has been used for vitreous replacement and internal tamponade for complex retinal detachment. CT bone window axial view – left intraocular high attenuation fluid representing the silicone oil, accompanied with a scleral buckle (*arrows*)

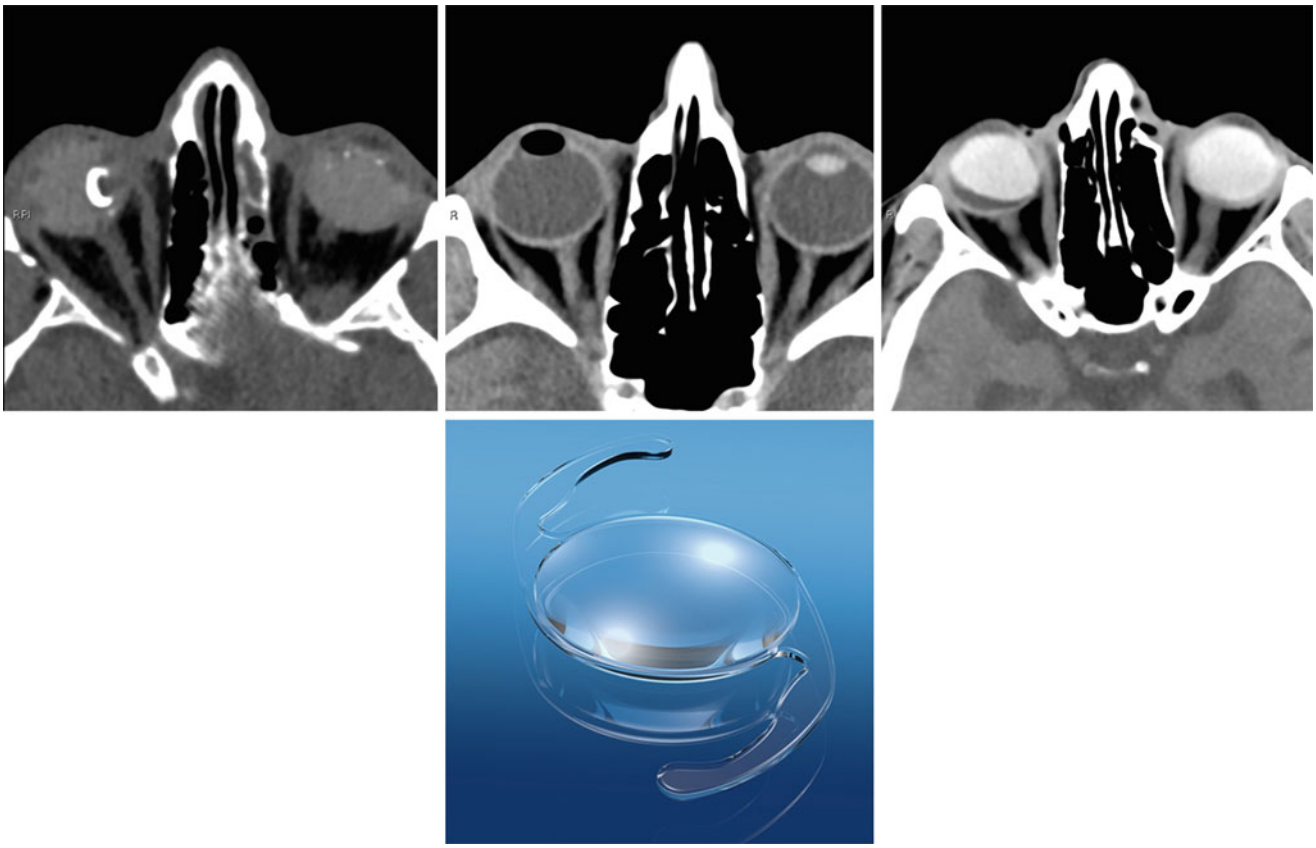


Fig. 9 NE-CT axial view, of three different patients post vitrectomy surgery. *Left*, 49-YOM, bilateral surgery with right posteriorly dislocated IOL. *Middle*, 79-YOM right vitrectomy with air/gas bubble in the anterior chamber (patient in supine position). *Right* image, 53-YOM postbilateral vitrectomy. *Lower image* shows a typical foldable modern IOL

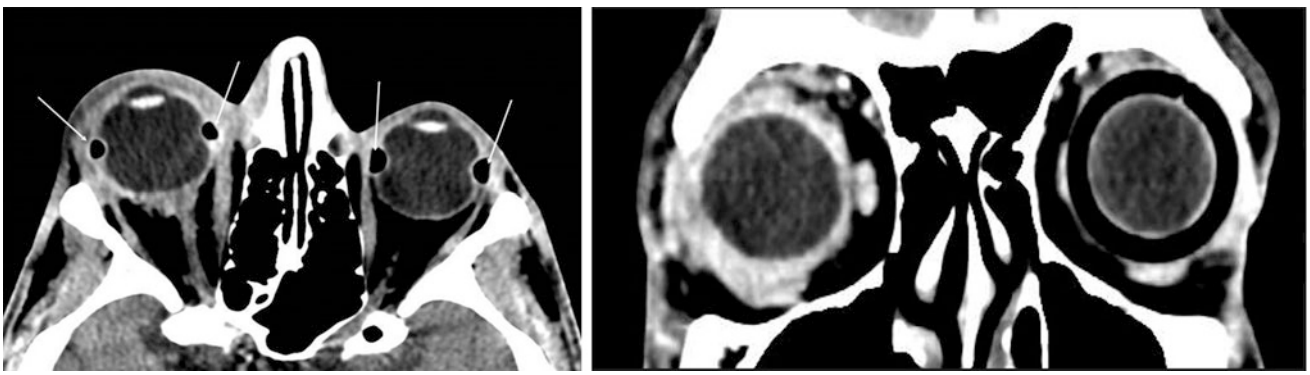


Fig. 10 Scleral buckle for retinal detachment. Scleral buckles are small, rounded bands often made from silicone or sponge. CT bone window, axial view, and coronal view (*left and right images*) – a thin hyperattenuating structure (*arrows*) encircling both sides. The patient underwent successive bilateral surgeries for high myopia related retinal detachment. He developed postoperative subconjunctival hemorrhage as noted in the thickened preseptal tissue on the right side. Note the typical globe appearance postencircling buckle surgery with mild globe elongation

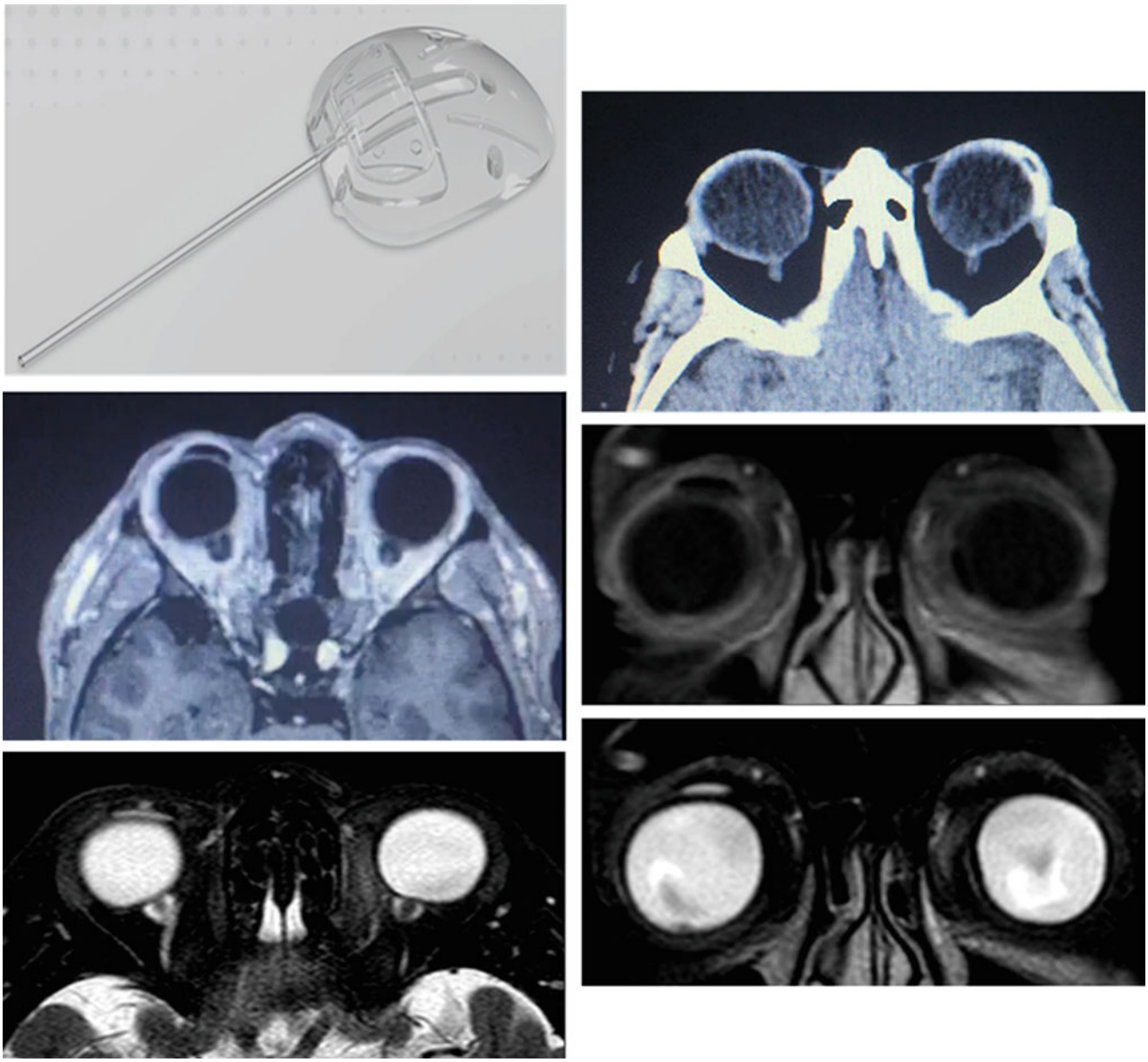


Fig. 11 Ahmed glaucoma valve (*upper left*) is used to reduce medically uncontrolled intraocular pressure. It comes in different sizes, single or double plate, and can be manufactured from polypropylene or silicone [6]. CT brain window, axial view (*upper right*) – Ahmed glaucoma valve on the superior temporal quadrant of the left eye, appears as a hyperdense crescent structure with a central lucency representing the aqueous humor. MRI T1 postcontrast nonfat-sat axial view and coronal view (*middle right* and *left*) – a valve located in the superonasal quadrant of the right eye. The hypointense center on T1 WI and hyperintense on T2 (*lower left* and *right*) represents the aqueous fluid

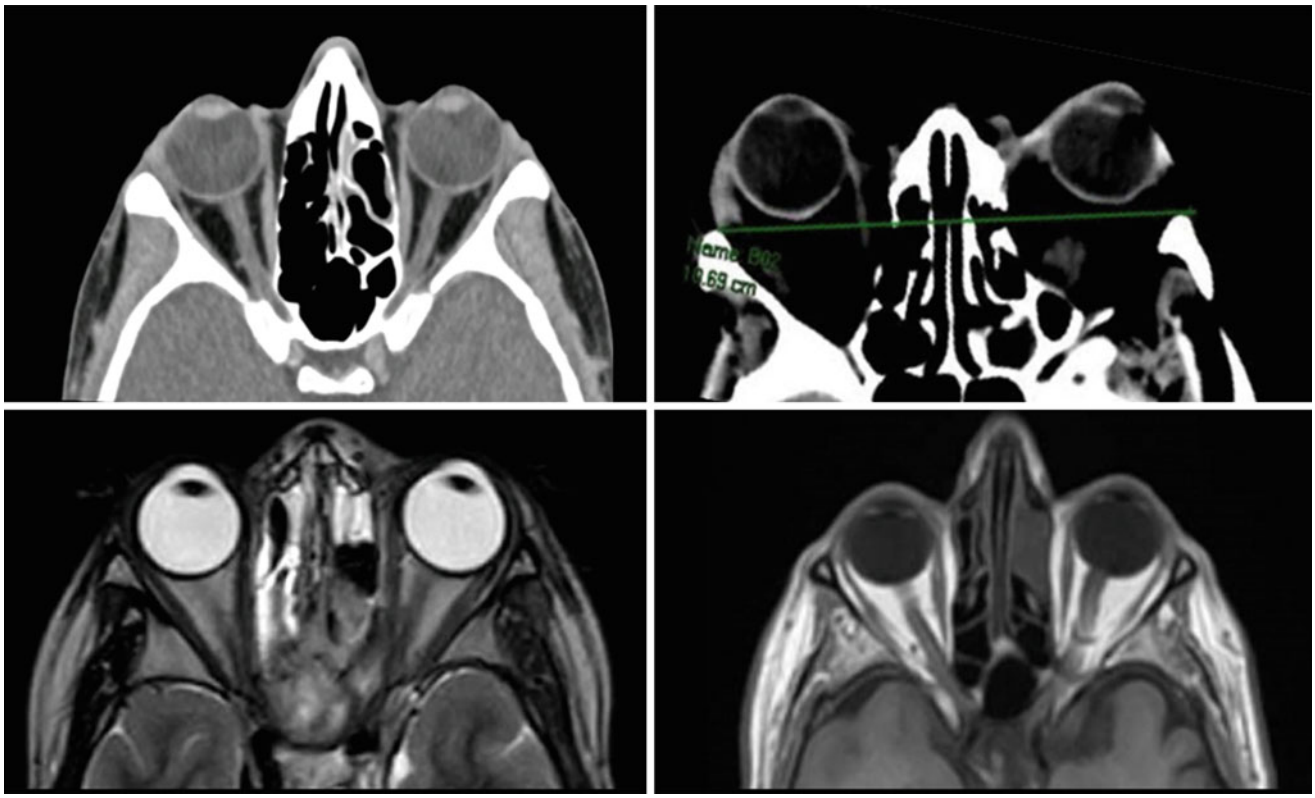


Fig. 12 Pseudophakia. Cataract extraction with implantation of an artificial intraocular lens (IOL) is the most common ocular surgery in the developed world [7]. CT soft tissue view, axial (*upper left*) demonstrates the hyperdense crystalline lenses (before cataract surgery); brain window (*upper right*) demonstrates hyperattenuating linear IOL implants. MRI before (*lower left, T2*) and after (*lower right, T1 non-FS CE*) cataract surgery. Note the hyperintense anterior chamber IOL in the right eye and posterior chamber IOL in the left eye (*lower right*)

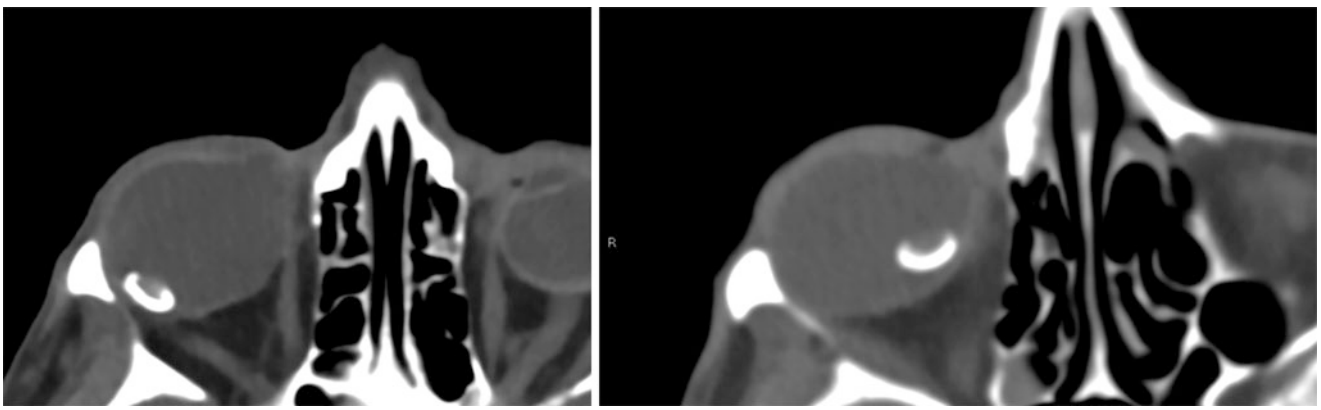


Fig. 13 NECT of an 83-YOM with right eye dislocated IOL (*left*). The IOL flows freely in the liquid vitreous space as seen in the *right* image taken 3 years apart, at the age of 86

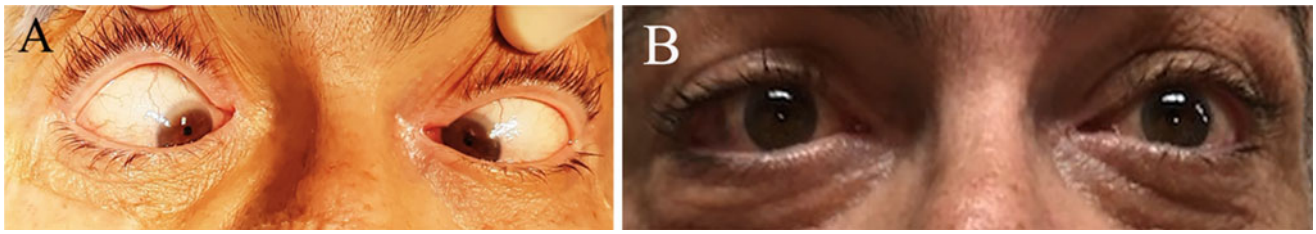


Fig. 14 Clinical photograph of a 66-YOM with heavy eye syndrome, axial length of 35 mm and -17 diopters glasses correction, pre (**a**) and post (**b**) strabismus repair. The patient presented with esotropia and hypotropia and underwent bilateral medial rectus muscle recession and loop myopexy of the superior rectus muscle to the lateral rectus muscle and achieved excellent postoperative results. (Courtesy: Tamara Wygnanski-Jaffe, MD)

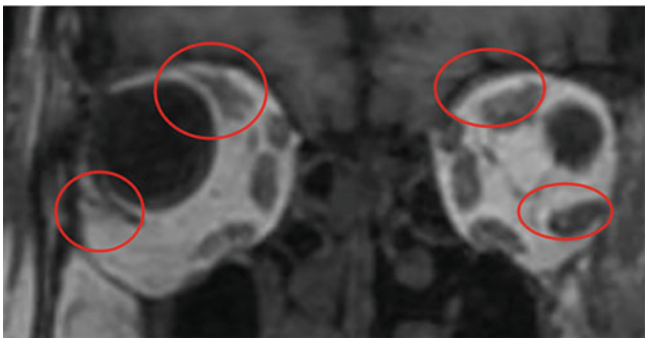


Fig. 15 Preoperative T2WI MR coronal scan of the same patient showing herniation of the posterior globe through the superior and lateral recti muscles in both eyes (red circles). (Courtesy: Tamara Wygnanski-Jaffe, MD)

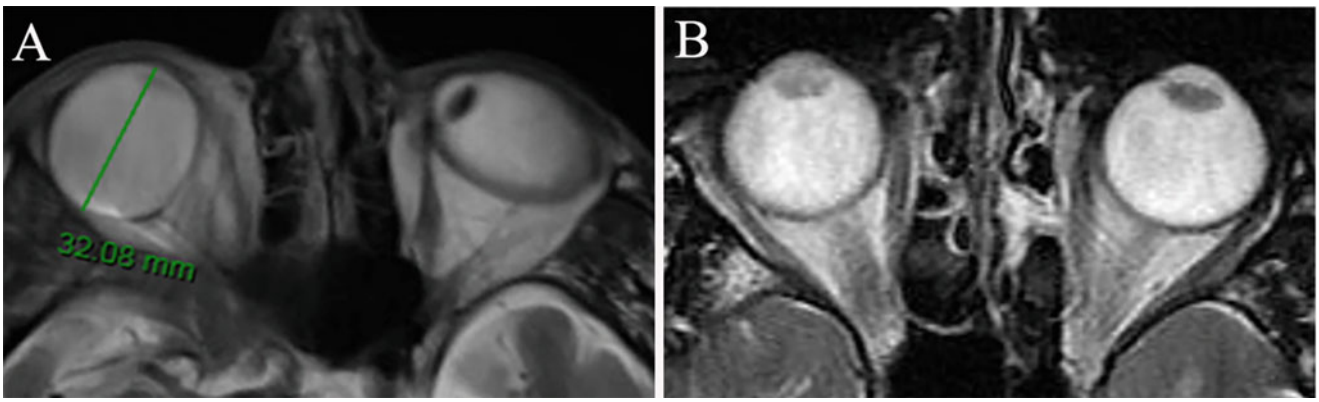


Fig. 16 Pre- (**a**) and postoperative (**b**) T2 MR axial scans of the same patient showing preoperative inward rotations of the elongated globes (esotropia) and the excellent alignment of both eyes after surgery. (Courtesy: Tamara Wygnanski-Jaffe, MD)

References

1. Liarakos VS, Boboridis KG, Mavrikakis E, Mavrikakis I. Management of canalicular obstructions. Curr Opin Ophthalmol. 2009;20(5):395–400.
2. Grob S, Yonkers M, Tao J. Orbital Fracture Repair. Semin Plast Surg. 2017;31(1):31–9.
3. Burnstine MA. Clinical recommendations for repair of orbital facial fractures. Curr Opin Ophthalmol. 2003;14(5):236–40.
4. Manolidis S, Weeks BH, Kirby M, Scarlett M, Hollier L. Classification and surgical management of orbital fractures: experience with 111 orbital reconstructions. J Craniofac Surg. 2002;13(6):726–37; discussion 738.
5. Allen RC. Controversies in periocular reconstruction for facial nerve palsy. Curr Opin Ophthalmol. 2018;29(5):423–7.
6. Riva I, Roberti G, Katsanos A, Oddone F, Quaranta L. A review of the Ahmed glaucoma valve implant and comparison with other surgical operations. Adv Ther. 2017;34(4):834–47.
7. Micieli JA, Arshinoff SA. Cataract surgery. CMAJ. 2011;183(14):1621.

Periocular Fillers

94

Ayelet Priel, Don Kikkawa, Gahl Greenberg, Dana Niry, and S. Cohen

Contents

1 **Imaging Features** 705
2 **Differential Diagnosis** 706
3 **Diagnosis** 706
4 **Treatment** 706
5 **Figures with Captions** 707
References 712

Abstract

- Injectable fillers are commonly used for periorbital rejuvenation and correction of postenucleation socket syndrome.
- HA-based fillers are the most commonly used filler in the periocular area.
- Most often, periocular fillers are incidental findings on imaging.
- Fillers have characteristic imaging features on CT, MRI, and on PET-CT scans.
- Acquaintance with the imaging features of the commonly used injectable fillers is of paramount importance especially in circumstances where patients deny, forget, or otherwise are unaware of the filler used.
- This chapter presents key imaging features of the commonly used periocular fillers.

Keywords

Periocular filler · Imaging features

A. Priel (✉)
Department of Ophthalmology, Goldschleger Eye Institute, Sheba Medical Center, Ramat-Gan, Israel

Sackler Faculty of Medicine, Tel Aviv University, Tel Aviv, Israel

D. Kikkawa
Division of Oculofacial Plastic and Reconstructive Surgery, Department of Ophthalmology, University of California San Diego, La Jolla, CA, USA
e-mail: dkikkawa@ucsd.edu

G. Greenberg
Department of Diagnostic Imaging, Sheba Medical Center, Tel Hashomer, Israel
e-mail: gahl.greenberg@sheba.health.gov.il

D. Niry
Department of Radiology, Sourasky Medical Center, Tel Aviv University, Tel Aviv, Israel

S. Cohen
Department of Plastic and Reconstructive Surgery, Assaf Harofeh Medical Center, Zerifin, Israel

1 Imaging Features

Injectable fillers are a heterogeneous group of medical device materials that differ based on their chemical composition, source (biological/synthetic), and biodegradability. Subgroup classification is based on their rheological properties (i.e., cohesivity, viscosity). Hence, their imaging properties differ (Table 1).

© Springer Nature Switzerland AG 2022
G. Ben Simon et al. (eds.), *Atlas of Orbital Imaging*,
https://doi.org/10.1007/978-3-030-62426-2_83

Table 1 MRI/CT characteristics of the commonly used dermal-fillers

	MRI T1W	MRI T2/STIR	CT
Biodegradability			
Rapidly resorbable			
Hyaluronic acid	Hypointense	Hyperintense (strong)	Soft tissue attenuation
Collagen	Hypointense	Hyperintense	Soft tissue attenuation
Slowly resorbable			
PLLA	Hypointense		Fluid attenuation
CaHA	Low-intermediate signal intensity	Low-intermediate signal intensity	Hyper attenuation, calcific like pattern
Nonbiodegradable			
PAAG	Hypointense	Hyperintense	Soft tissue attenuation
Silicone – low viscosity	Slightly hyperintense	Iso-/slightly hypointense	Slightly hyper attenuated
Silicone – high viscosity	Hyperintense	Hypointense	Slightly hyper attenuated

PLLA = poly-l-lactic acid, CaHA = calcium hydroxyapatite, PAAG = polyalkylimide and polyacrylamide hydrogels (Bio-alcamid = polyalkylimide and Aquamid = polyacrylamide)

MRI has an excellent soft tissue discrimination capability and the perceived signal intensity can identify the injected filler with high sensitivity. Silicone and hyaluronic acid have distinct MRI appearances, corresponding to the low and high water content, respectively. Most fillers (HA, collagen, PAAG) have signal intensity patterns compatible with high water content [1, 2].

2 Differential Diagnosis

Enhancement/increased uptake on MRI/FDG PET-CT may represent a physiologic inflammatory response elicited by most commonly used fillers (i.e., collagen, HA, CaHA, especially in the early post-injection period) or mimic true pathology (primary/recurrent tumor). Restricted diffusion on DWI and atypical location for filler injection should prompt a potential for infection/malignancy and may warrant biopsy

3 Diagnosis

1. MRI is an excellent diagnostic modality for filler type characterization. It enables precise anatomic localization and quantification of the injected filler and illustrates filler-related complications.
2. CT is superior to MRI in identifying calcifications, which are pathognomonic of certain filler (CaHA) and certain filler related complications. It also demonstrates linear stranding typical of HA and other dermal fillers.

4 Treatment

Please see corresponding section in the following chapter of treatment related complications.

5 Figures with Captions

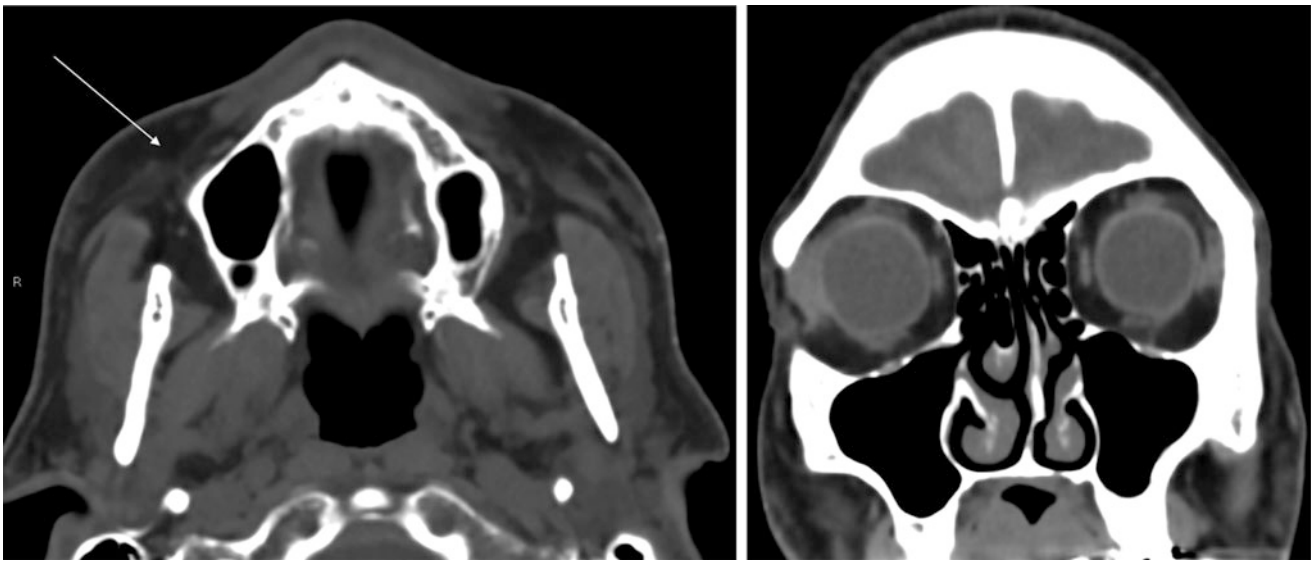


Fig. 1 Axial and coronal reformat NECT images showing subtle densities in both cheeks, mostly superficial to the zygomaticus muscles (*arrow*)

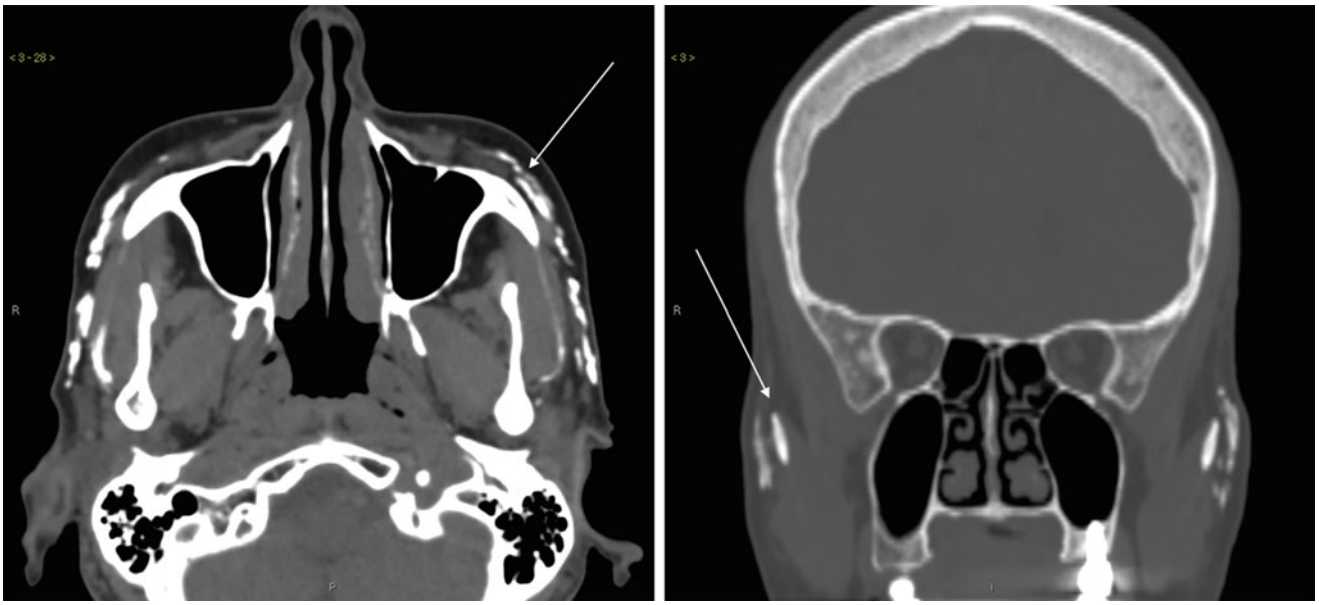


Fig. 2 Axial NECT image, soft tissue windowing (*left*) at the level of the malar bones, and coronal reformat, bone windowing (*right*), showing scattered hyperdensities measuring as calcifications in both cheeks as shown by arrows

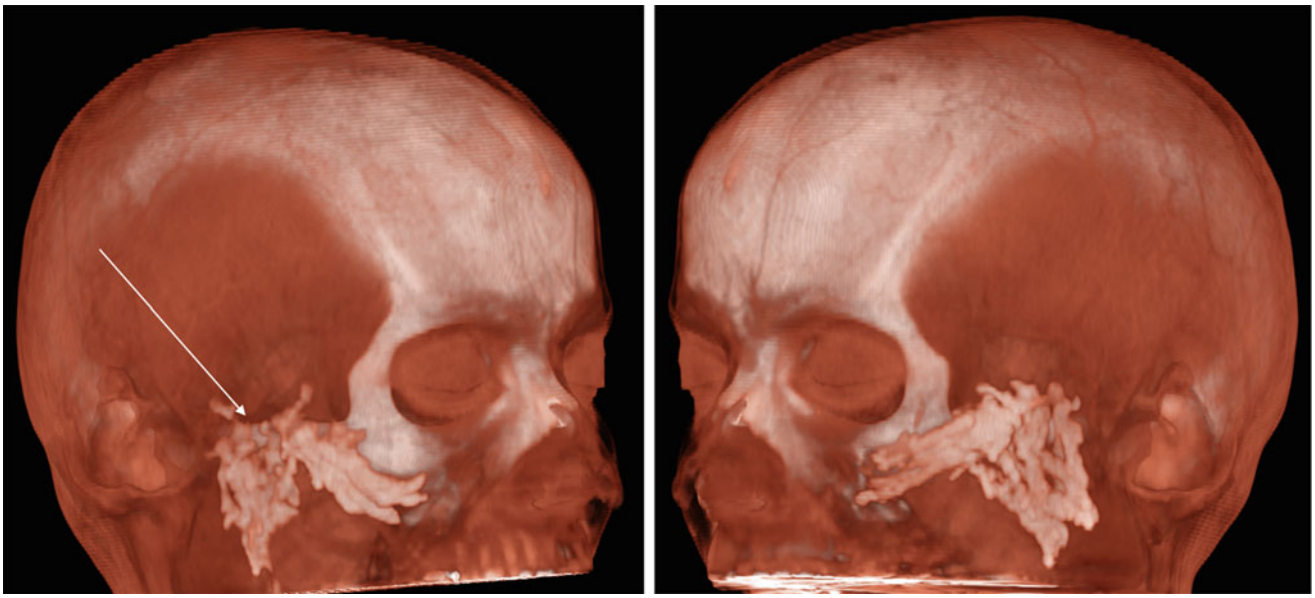


Fig. 3 Same patients as Fig. 2, 3D reconstructions are able to portray the streak-like appearances of the dermal fillers projected upon the superficial cheek fat

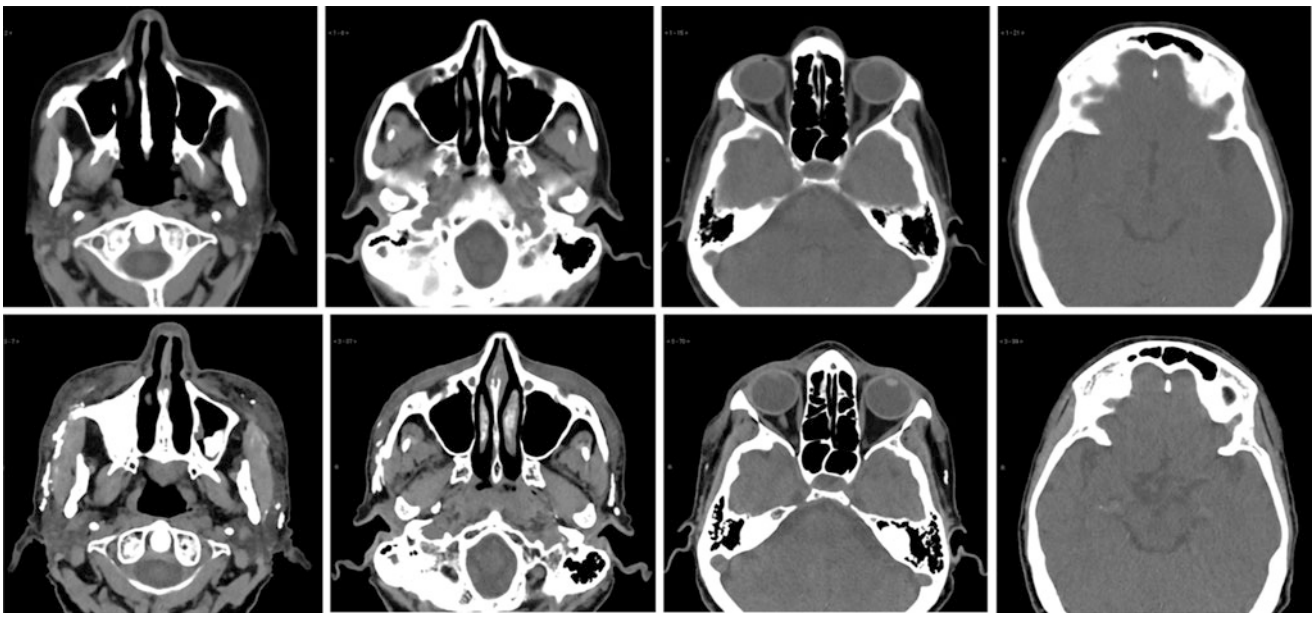


Fig. 4 NECT images of a 55-year-old patient – upper row, and 8 years after, following dermal filler – lower row. Axial consecutive NECT images showing the changes in the fatty planes before and after the treatment, demonstrating a combination of soft tissue densities and calcifications within the injected sites (CA Hydroxylapatite)

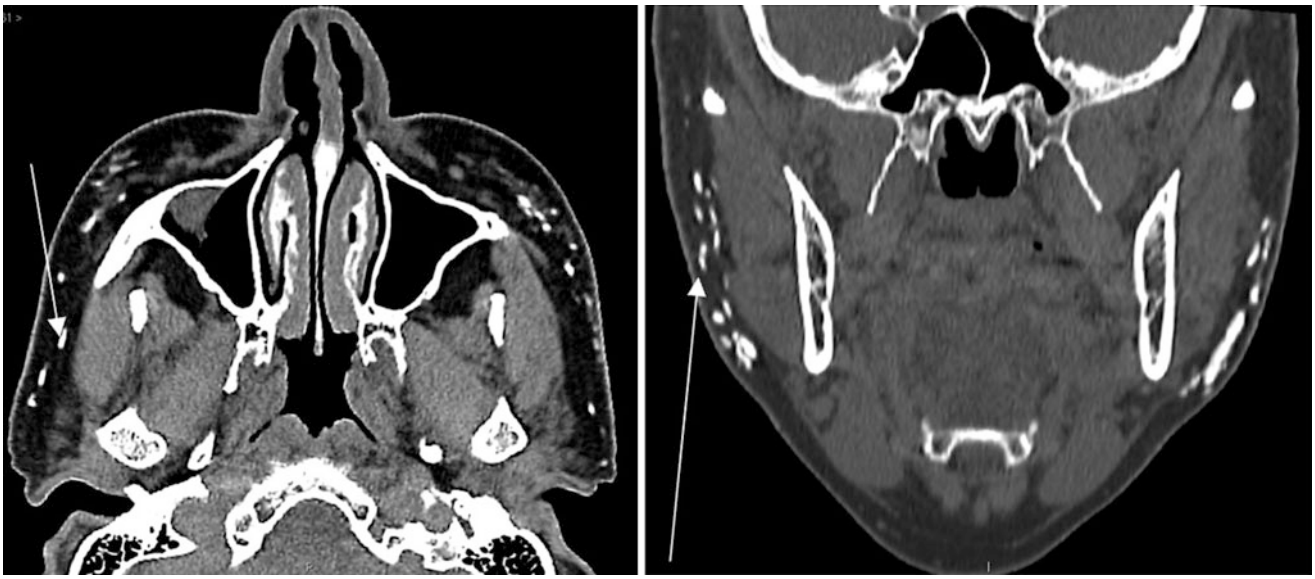


Fig. 5 Axial and coronal NECT images showing a combination of soft tissue densities mixed with more opaque linear densities (arrows) that may represent cosmetic threads

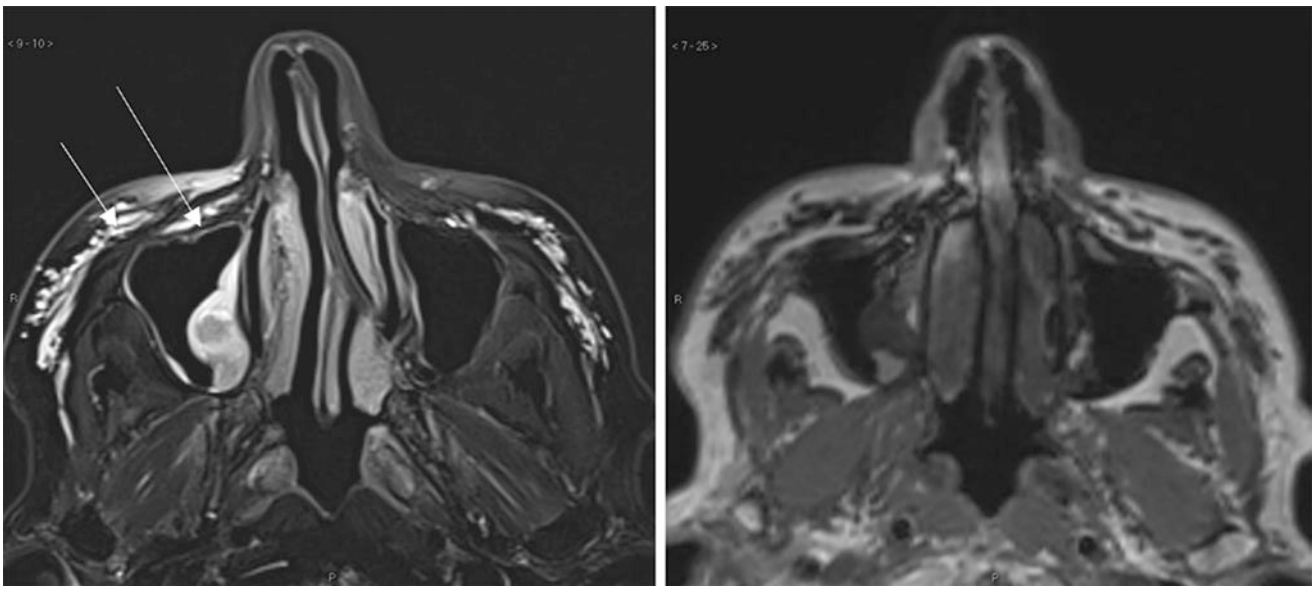


Fig. 6 Axial MR images acquired at the level of the nose showing subdermal deposits scattered in the middle and medial superficial cheek fat. The material is hyperintense on T2 FS weighted imaged (*left*) and hypointense on T1 weighted scans (*right*). Distribution is somewhat asymmetrical towards the right cheek. Long arrow – pointing at the SOOF (suborbicularis oculi fat), showing that the dermal filler (short arrow) is in the superficial fat layer, although some of the filler is directly deeper to the SOOF

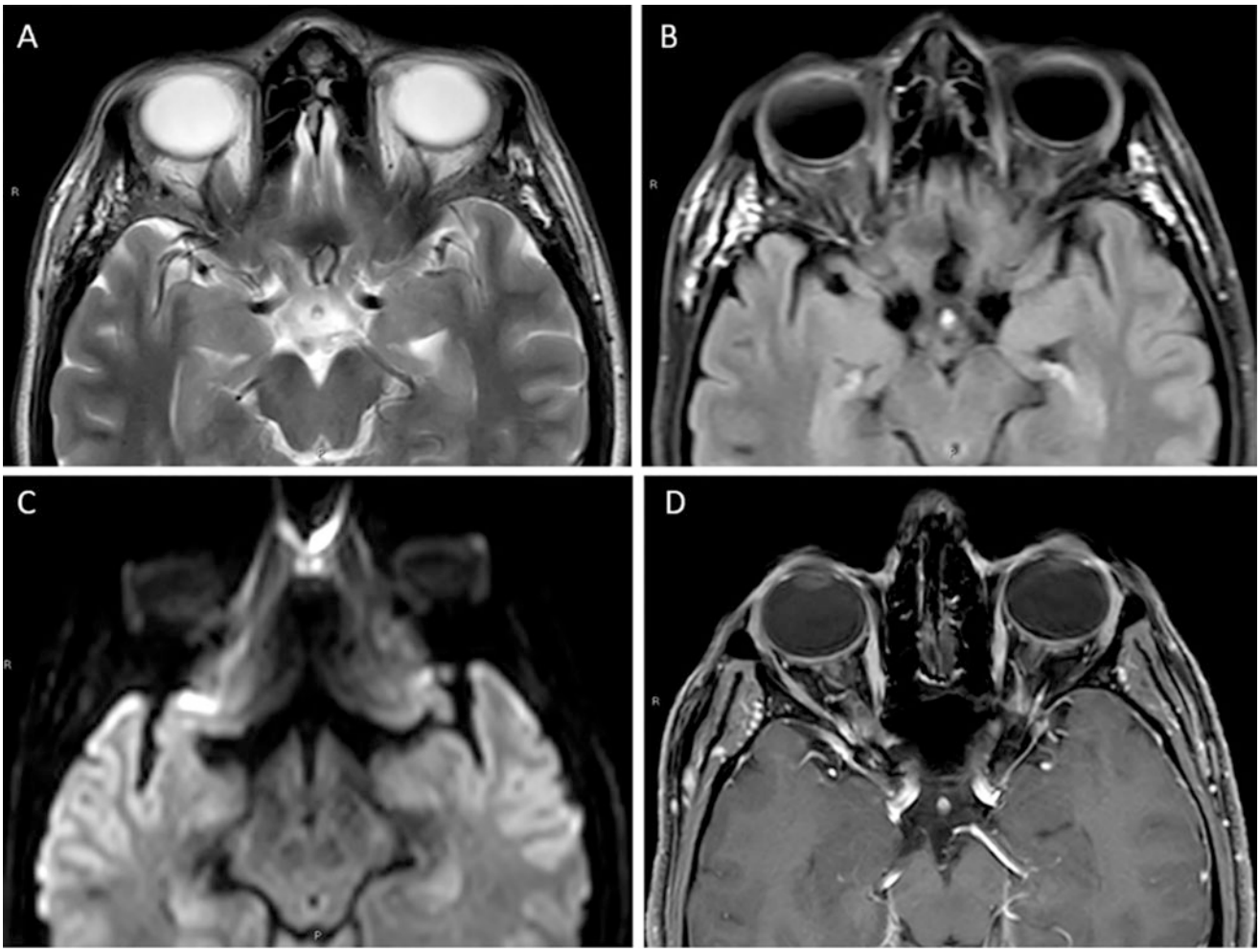


Fig. 7 Axial MR images at the level of the orbits, depict dermal filler material dispersed within the temporalis muscles in both temples (asymmetric towards the right). The infiltrations appear hyperintense on conventional T2 weighted images (**a**) but far more conspicuous on the T2 FLAIR fat saturated scan (**b**). The filler material has no intrinsic restriction properties on diffusion weighted images (**c**) and shows no associated enhancement following contrast (**d**) (albeit in cases of inflammation or granuloma formation)

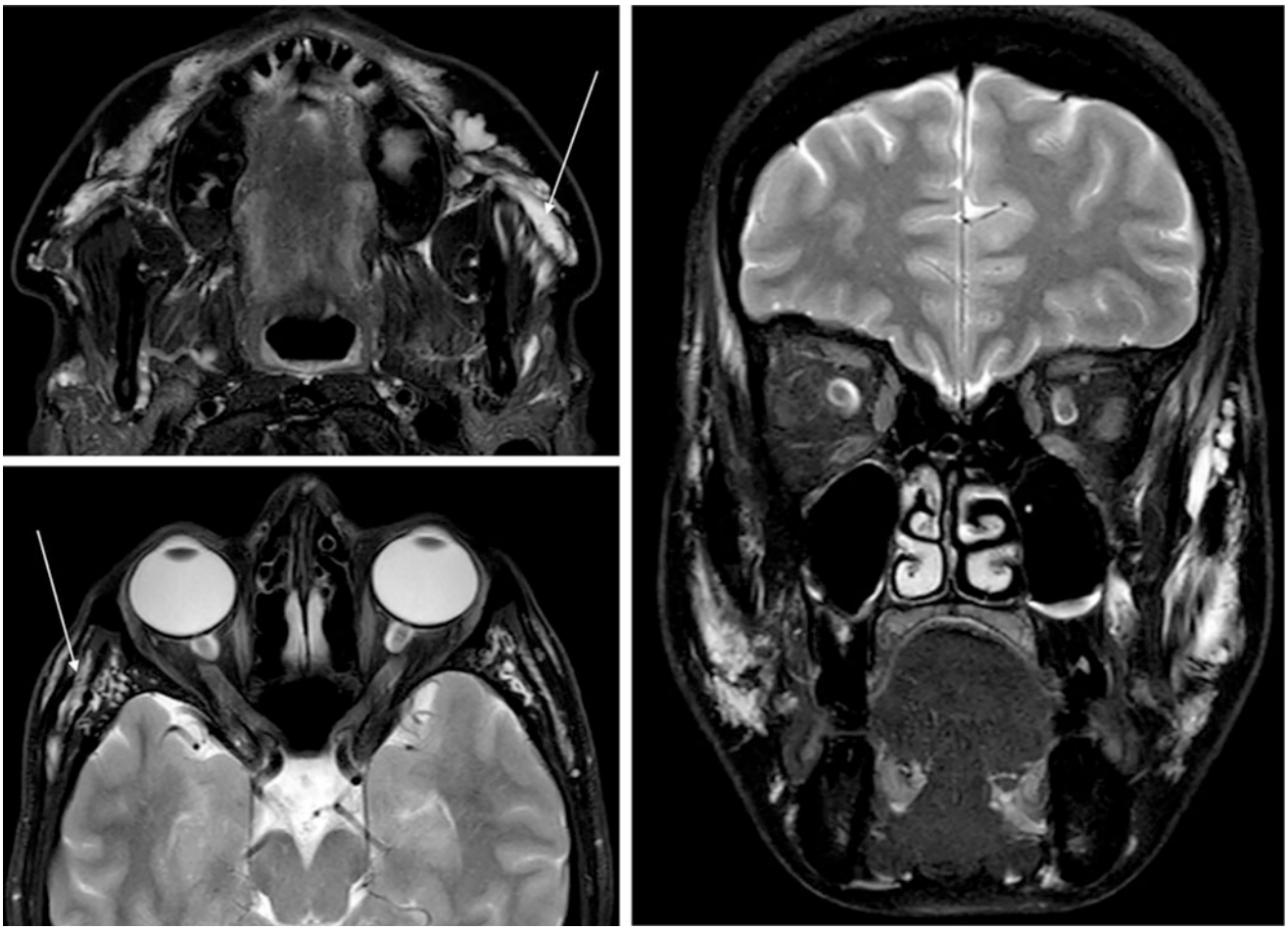


Fig. 8 Axial and coronal T2 fat-saturated imaged showing typical anatomical distribution and appearances of the facial fillers (buccal – arrow, upper left image, nasolabial, temples – arrow, lower left image, periorbital locations)

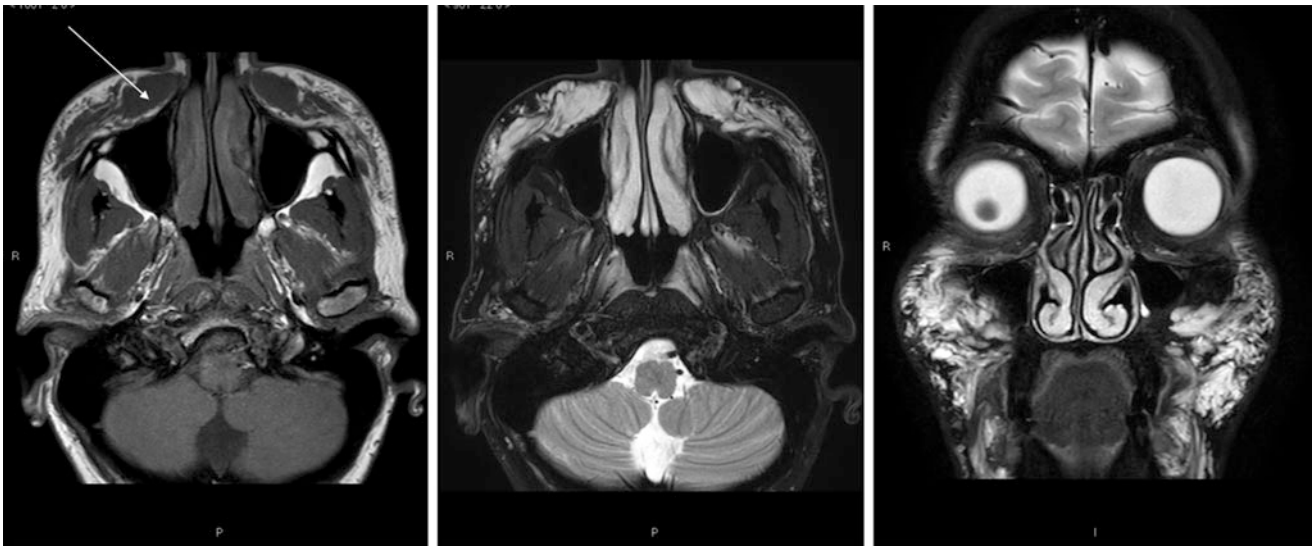


Fig. 9 Axial T1 FS WI (*left*), axial (*middle*) and coronal (*right*) T2 FS images showing a bulkier appearance of the facial fillers as marked by arrows. On T1WI the fat serves as a good contrast background to the relatively hypointense dermal filler, for the same reason fat saturation on T2WI enhances the fluid like appearances of the filler

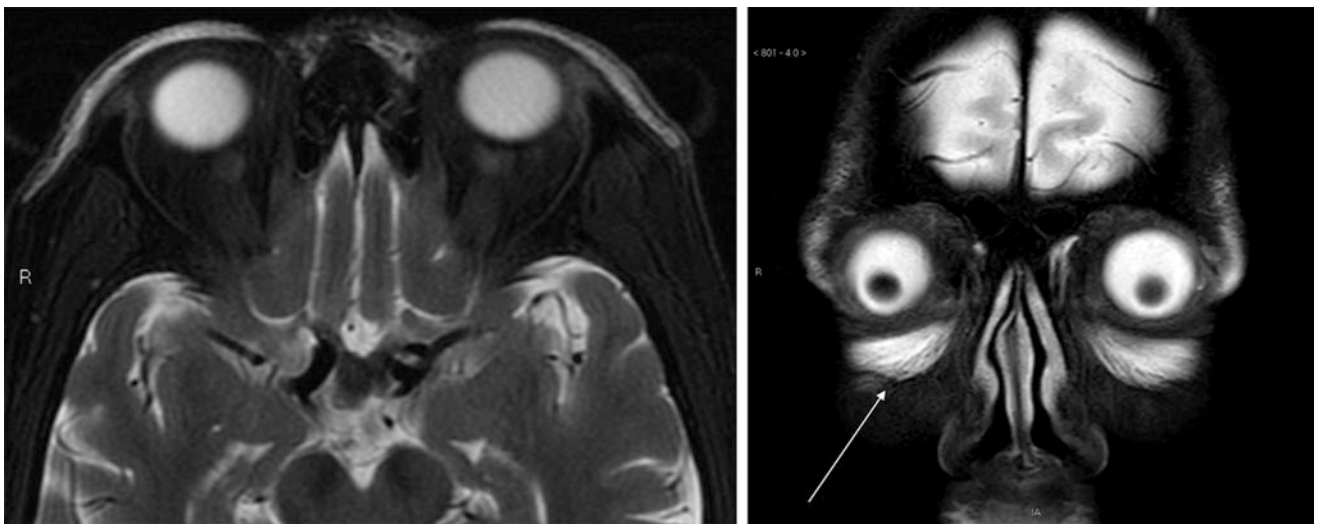


Fig. 10 Axial and coronal MR T2 fat-saturated images depicting dermal fillers within the inferior orbital fat abutting the lower eye lids

References

1. Mundada P, et al. Injectable facial fillers: imaging features, complications, and diagnostic pitfalls at MRI and PET CT. Insights Imaging. 2017;8:557–72.
2. Ginat D, Schatz CJ. Imaging features of midface injectable fillers and associated complications. Am J Neuroradiol. 2013;34:1488–95.

Periocular Fillers–Related Complications: Imaging Features

95

S. Cohen, Dana Niry, and Ayelet Priel

Contents

1 **Signs and Symptoms** 714
2 **Differential Diagnosis** 714
3 **Diagnosis** 714
4 **Treatment** 714
5 **Figures with Captions** 715
References 718

Abstract

- The surge in popularity of periocular fillers has heralded an increase in filler-related complications.
- Short-term complications are usually mild and require no/minimal intervention. However, rare devastating vascular complications can occur. Long-term complications pose a diagnostic challenge and may require radiologic evaluation [1, 2].
- The chapter presents clinical-radiological manifestations of the commonly encountered periocular filler–related complications including intravascular embolism of the injected material, foreign body granuloma, chronic malar edema, and filler migration.
- Acquaintance with the key imaging features of periocular filler–related complications is of paramount importance to avoid misdiagnosis and an unnecessary biopsy [3–5].
- Most commonly used fillers (i.e., collagen, HA, and CaHA) induce a physiologic inflammatory response, especially in the early postinjection period. The consequent mild enhancement/increased uptake on FDG PET–CT/MRI is attributed to vascularization and increased glycolysis in activated inflammatory cells and is not, by itself, indicative of infection.
- Cellulitis appears as stranding and enhancement of the subcutaneous tissue adjacent to the injected filler (resembling inflammatory reactions).
- Abscess formation appears as a rim-enhancing collection. On DWI abscess shows restricted diffusion whereas infected filler collections do not show restricted diffusion.
- Foreign body granuloma may show a variable degree of enhancement on MRI. Definitive diagnosis requires histopathological evaluation.

Keywords

Periocular filler · Filler complications · Imaging features · MRI

S. Cohen (✉)
Department of Plastic and Reconstructive Surgery, Assaf Harofeh Medical Center, Zerifin, Israel

D. Niry
Department of Radiology, Sourasky Medical Center, Tel Aviv University, Tel Aviv, Israel

A. Priel
Department of Ophthalmology, Goldschleger Eye Institute, Sheba Medical Center, Ramat-Gan, Israel

Sackler Faculty of Medicine, Tel Aviv University, Tel Aviv, Israel

© Springer Nature Switzerland AG 2022
G. Ben Simon et al. (eds.), *Atlas of Orbital Imaging*,
https://doi.org/10.1007/978-3-030-62426-2_120

1 Signs and Symptoms

Each complication has its own distinctive features; these commonly include local swelling and inflammation. In cases of vascular compromise, pain, paresthesia, erythema, blisters, skin necrosis, and vision loss can occur.

2 Differential Diagnosis

Filler-related complications may mimic:

1. True pathology (primary/recurrent tumor). Both may demonstrate enhancement/increased uptake on FDG PET-CT/MRI. Restricted diffusion on DWI and atypical location for filler injection should prompt a potential for malignancy and warrant biopsy
2. Dermatological entities, including sarcoidosis, cutaneous lymphoma, and dermatomyositis

3 Diagnosis

- MRI is the preferred modality for diagnosis, anatomic delineation, and differential diagnosis of filler-related complications especially in unclear cases and in long-term filler-related complications.
- CT is superior for identification of calcifications, which are pathognomonic of certain filler (CaHA) and certain filler-related complications.

4 Treatment

- Early onset noninflammatory nodules can be monitored and massaged or treated with hyaluronidase (in HA-based fillers).
- Inflammatory nodules should be treated with appropriate antibiotics. Filler removal may occasionally be the only cure. Intralesional 5-FU injections and RF are other methods to reduce/remove the injected filler.
- FBG is usually treated with intralesional corticosteroid injection, systemic steroid therapy, and occasionally surgical excision.
- Chronic malar edema may respond to hyaluronidase and if fibrosis is suspected, addition of 5-FU and corticosteroids is recommended.
- In the event of impending retinal ischemia, the injection should be stopped immediately, high-dose hyaluronidase should be injected, the globe should be massaged, and the patient should be urgently referred to ophthalmic surgeon. Similarly, in the event of cutaneous/other tissues ischemia hyaluronidase should be infiltrated at the injection site.

5 Figures with Captions

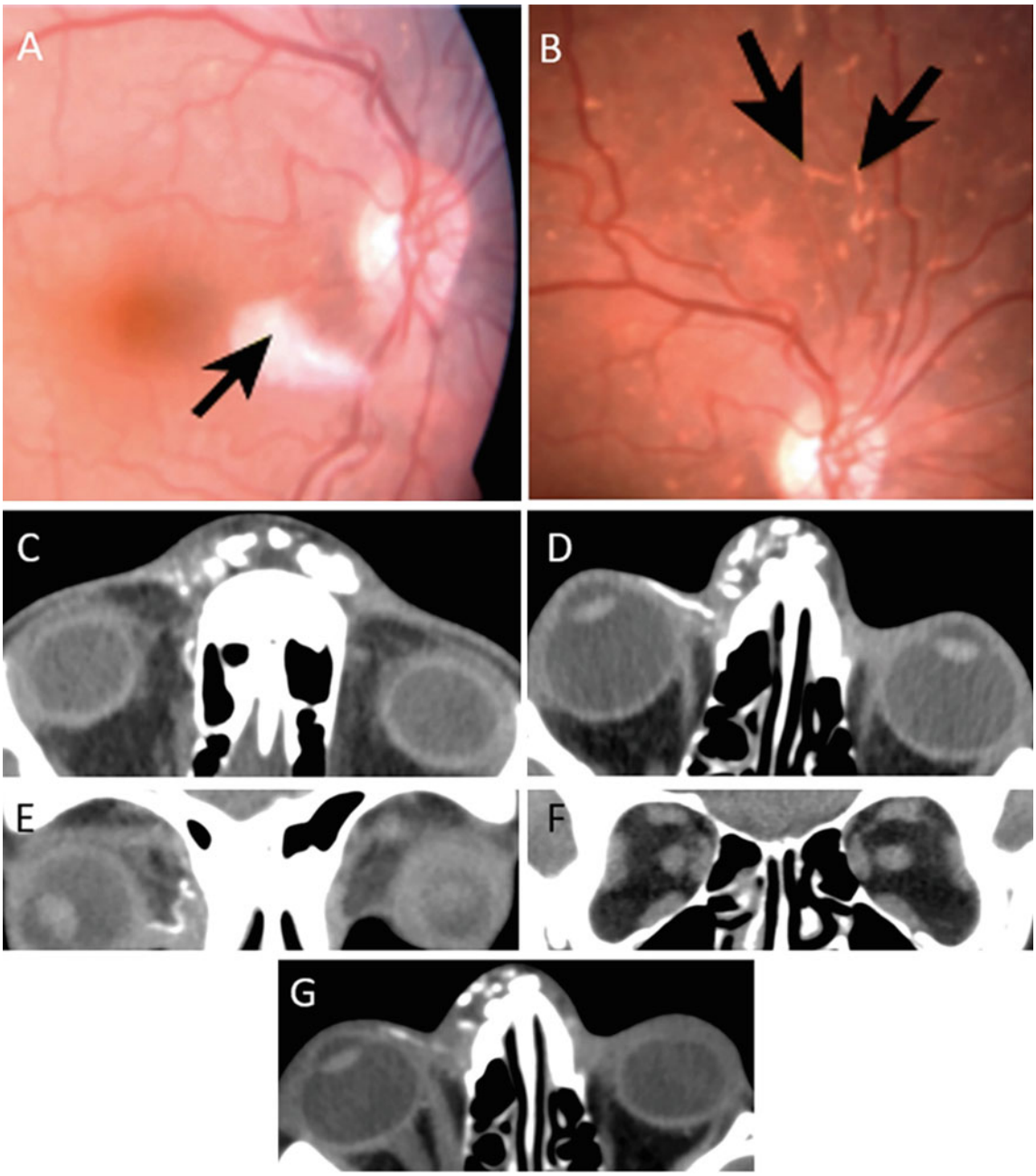


Fig. 1 Retinal artery occlusion. A 24-year-old woman presented with RE periocular pain and blurred vision immediately following calcium hydroxyapatite (CaHA) injection to the nasal dorsum. RE examination revealed periorbital hematoma, exophthalmos exotropia, ptosis and ophthalmoplegia, and a dilated pupil (RAPD+). Fundus examination revealed retinal ischemia (**a**, cotton wool spot, arrow) secondary to vascular occlusion effecting both retina and choroidal vasculature (**b**). Unenhanced orbit CT, soft tissue window, axial view through the superior third of the orbit demonstrates multiple foci of hyperattenuated material, of calcific density embedded within the subcutaneous tissue in the nasoglabellar region. There is serpiginous hyperdensity, of similar attenuation, anchored to the medial wall of the right orbit (**c**). Axial view through the middle third of the orbit demonstrates that the hyperattenuated material extends to the right medial canthus region. There is linear hyperdensity along the medial right superior eyelid (**d**). In both images the vessel-like hyperdensity is consistent with intravasation of filler material. Coronal view at the anterior third of the orbit reveals hyperdense tortuous structures at the superomedial aspect of the right orbit nicely illustrating the intravascular filler material within terminal branches of the ophthalmic artery (**e**). An enlargement of the right medial rectus muscle with fat stranding in the retrobulbar fat is shown in the coronal view at the level of the middle third of the optic nerve (**f**). At a follow-up CT angiogram, soft tissue window, axial view, there is contrast filling within the linear structure containing the hyperdense filler material, confirming it is arterial (**g**)

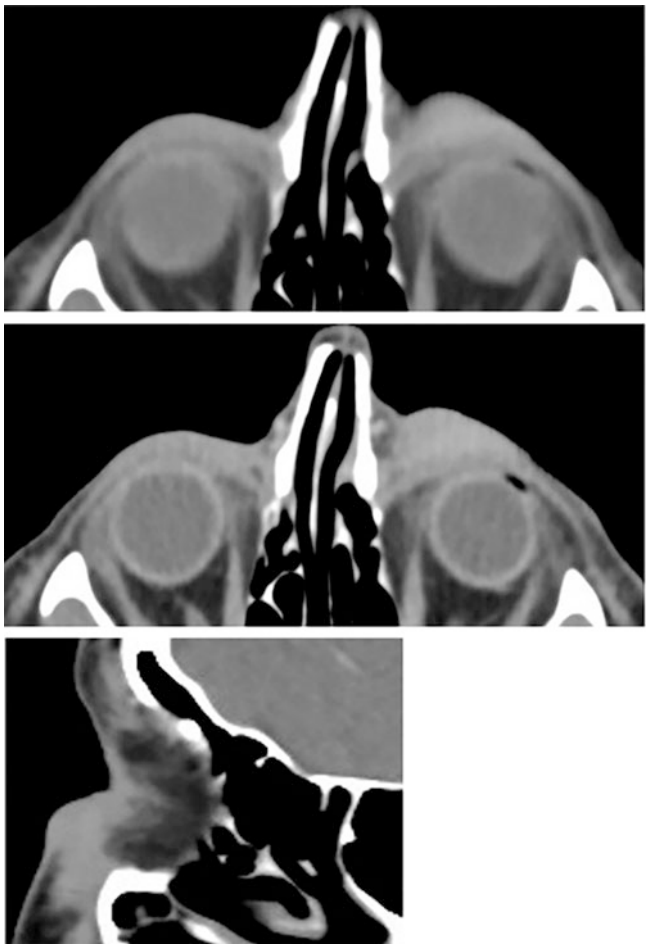


Fig. 2 **Foreign body granuloma (FBG)**. A 69-year-old woman with unknown filler injection 5 years back presented with palpable induration and swelling in the left lower lid. Histopathological findings were consistent with FBG. Unenhanced orbit CT, soft tissue window, axial view, shows a left preseptal hyperdense soft tissue lesion in the nasal aspect of the left lower eyelid. There are no calcifications, nor post-septal involvement (**a**). Post-contrast axial view demonstrates mild enhancement of the lesion (**b**). Post-contrast sagittal oblique view at a level medial to the left eyeball and through the ethmoid air cells demonstrates the location of the lesion in the lower eyelid, inseparable from the orbicularis oculi muscle, with fat stranding around it (**c**)

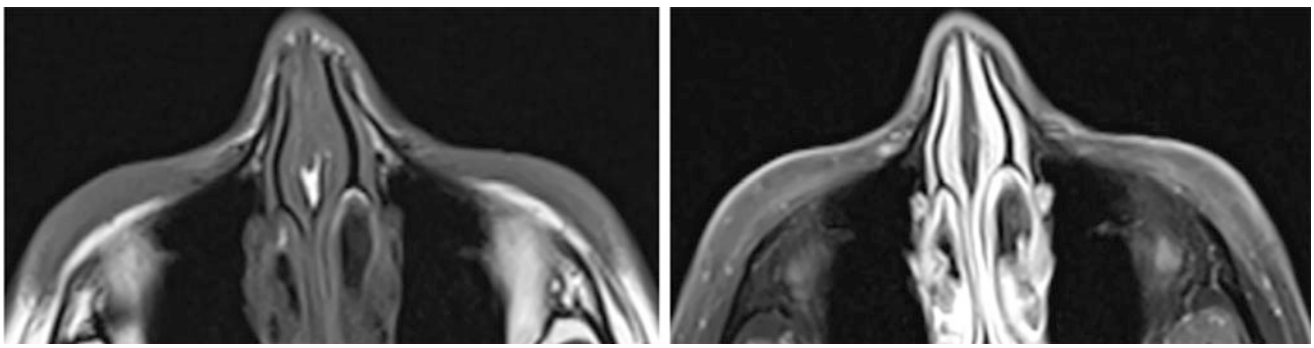


Fig. 3 **Chronic malar edema**. A 66-year-old woman presented with disfiguring bilateral chronic malar and lower lids edema 6 years after HA filler injection. Axial MRI images at the level of the upper maxilary sinus demonstrate bilateral subcutaneous lesions located in the inferior orbital fat anterior to the orbicularis oculi muscle. The lesions appear homogenously hypointense on T1 (*left*) and heterogenous with mild-to-moderate enhancement on fat-saturated T1 post-contrast image (*right*)

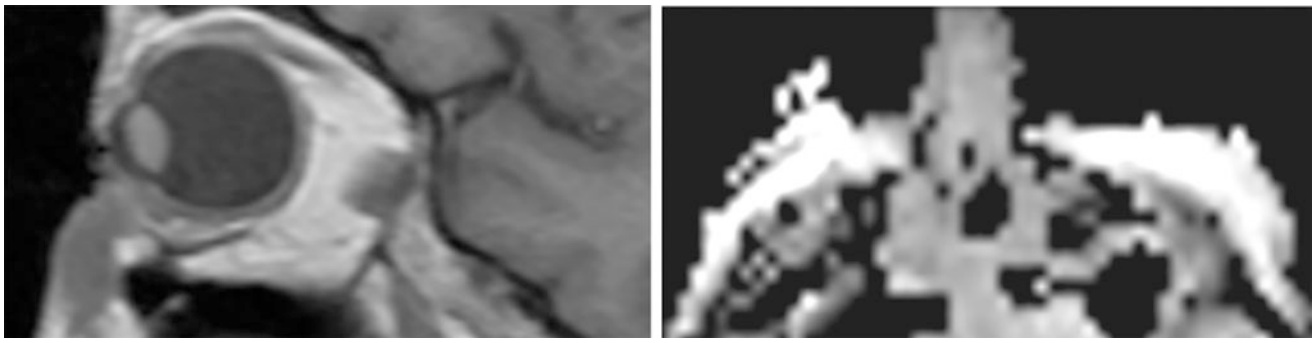


Fig. 4 (Same patient as in Figs. 3 and 5) The cranio-caudal extent of the hypointense lesion, located inferior to the left lower eyelid, is seen in the sagittal unenhanced unsaturated T1 image (*left*). Axial ADC map reveals a hyperintense signal with no obvious restriction, suggesting low cellularity (*right*)

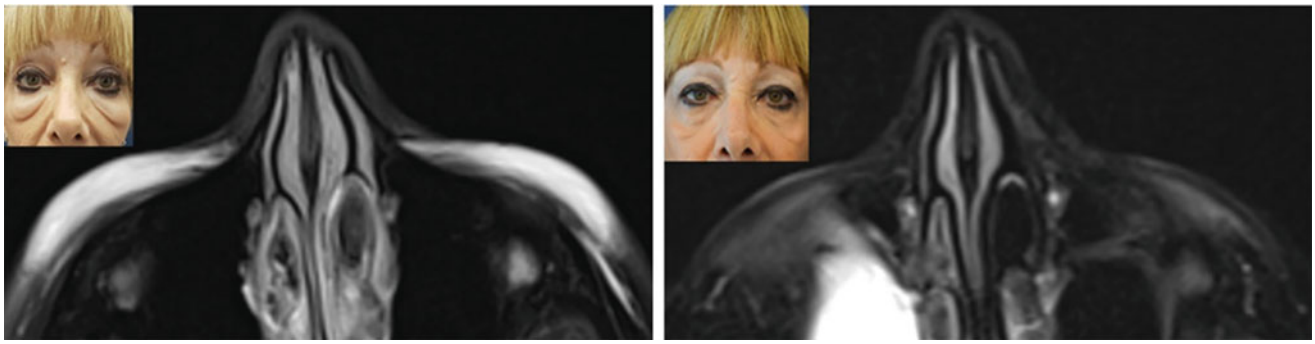


Fig. 5 (Same patient as in Figs. 3 and 4) The lesions appear homogenously hyperintense on fat-saturated T2W images (*left*). Chronic malar edema, possibly due to compromised lymphatic drainage, was diagnosed. Marked resolution of edema was clinically apparent following intralesional injection of hyalorunidase, 5-flurouracil (5-FU), and triamicinolone. Posttreatment T2 fat-saturated view (*right*) shows remarkable decrease in signal intensity compared to the corresponsing pretreatment view (*left*), correlating well with the clinical improvement (pretreatment: left upper window, posttreatment: right upper window)



Fig. 6 Migration. A 38-year-old female presented with newly appearing subcutaneous mass in the right superomedial eyelid. The lesion was suspected clinically as space occupying lesion of the lacrimal apparatus. The patient denied filler injection to the nasoglabellar region. Upon further questioning, she recalled filler injection to the malar region, 6 months before presentation. Unenhanced orbit CT, soft tissue window, axial view, at the mid orbital level shows a cystic hypodense lesion in the right nasoglabellar region causing subcutaneous swelling

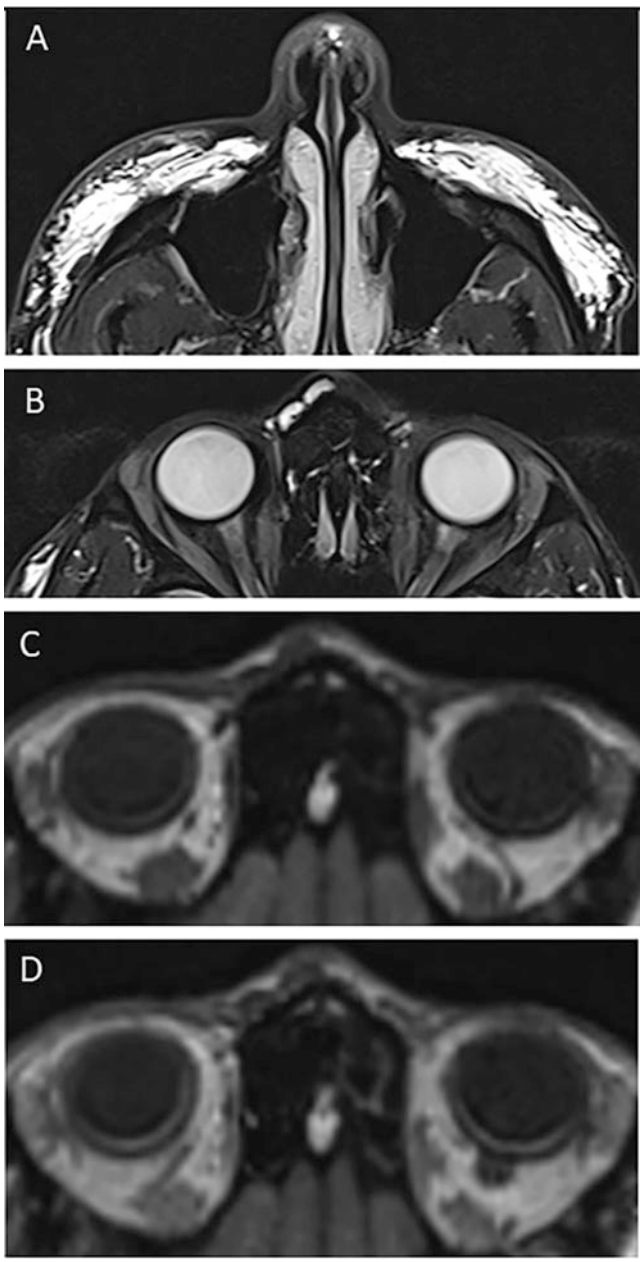


Fig. 7 (Same patient as in Fig. 6) Axial T2 fat-saturated views demonstrate hyperintense T2 signal; at the level of the maxillary sinus, in the malar region (encompassing the medial and middle subcutaneous cheek fat compartments bilaterally as well as the right deep medial cheek fat compartment) compatible with filler injections (**a**) and at the mid orbital level (**b**). The multiloculated cystic lesions (**b**) are of similar intensity to the malar filler injection material. Axial unsaturated T1 images demonstrates that the lesions are of hypointense T1 signal (**c**) and show no enhancement on post-godalinum T1W image (**d**). Based on the radiological findings, filler migration was diagnosed.The patient was closely followed up clinically and the lesion was self-resorbed within a year

References

1. Funt D, Pavicic T. Dermal fillers in aesthetics: an overview of adverse events and treatment approaches. Clin Cosmet Investig Dermatol. 2013;6:295–316.
2. Chiang YZ, Pierone G, Al-Niaimi F. Dermal fillers: pathophysiology, prevention and treatment of complications. J Eur Acad Dermatol Venereol. 2017;31(3):405–13.
3. Mundada P, Kohler R, Boudabbous S, Toutous Trellu L, Platon A, Becker M. Injectable facial fillers: imaging features, complications, and diagnostic pitfalls at MRI and PET CT. Insights Imaging. 2017;8(6):557–72.
4. Ginat DT, Schatz CJ. Imaging features of midface injectable fillers and associated complications. AJNR Am J Neuroradiol. 2013;34(8):1488–95.
5. Di Girolamo M, Mattei M, Signore A, Grippaudo FR. MRI in the evaluation of facial dermal fillers in normal and complicated cases. Eur Radiol. 2015;25(5):1431–42.

Acquired Anophthalmus

96

Yoav Vardizer, Nina Borissovsky, and Daphna Landau Prat

Contents

1 **Introduction** 720
2 **Signs and Symptoms** 720
3 **Treatment** 720
4 **Diagnosis** 720
5 **Figures with Captions** 721
References 726

Abstract

- Anophthalmic socket is the term used to describe the orbital content and structure when no globe is present, including the bony structure, soft tissues and the remaining potential space.
- When investigating anophthalmic socket imaging, one should look for the following:
  - The position of the prosthesis in the orbit
  - The presence or absence of an orbital implant, implant type
  - Evaluation of the orbital implant integration (vascular ingrowth)
  - The anatomic relations between the implant and the prosthesis; the implant and EOM
  - The volumetric effect of the implant and prosthesis on the presumed orbital symmetry between the two sides
- CT imaging key points:
  - Ocular prosthesis is observed as a semilunar hyperdense structure better viewed on axial and sagittal images.
  - Orbital implants are usually hyperdense, except for integrated implants immediately after implantation, seen as hypodense round structures with possible internal air bubbles.
  - Non-integrated Implant and ocular prosthesis internal characteristics are not affected by contrast administration
- MRI imaging key points:
  - There is no advantage for MRI over CT scan to demonstrate non-integrated implants.
  - For integrated implants, T1 weighted MRI images demonstrate low to intermediate signal, while T2 demonstrate high to intermediate signal.
  - MRI is advantageous in evaluating integrated orbital implants since this modality has better tissue discrimination and allows better visualization of the immediate vicinity (the high signal disturbance from the implant itself is less evident).

Y. Vardizer (✉)
Ophthalmology Department, Bnai-Zion Medical Center, Rappaport Faculty of Medicine, Technion, Haifa, Israel

N. Borissovsky
Imaging Department, Bnai-Zion Medical Center, Rappaport Faculty of Medicine, Technion, Haifa, Israel

D. Landau Prat
Ophthalmic Plastic and Lacrimal Surgery Institute, Department of Ophthalmology, The Goldschleger Eye Institute, Sheba Medical Center, Tel Hashomer, Israel

© Springer Nature Switzerland AG 2022
G. Ben Simon et al. (eds.), *Atlas of Orbital Imaging*,
https://doi.org/10.1007/978-3-030-62426-2_117

- T1 weighted MRI images with GAD of integrated orbital implants demonstrate enhancement of the periphery of the implant depending on the time elapsed from surgery. The implants enhance in a concentric fashion from the edges of the implant inwards.
- DWI has no additive value in differentiating implant types.

Keywords

Anophthalmic socket · Post enucleation socket syndrome (PESS) · Orbital implant · Prosthesis

1 Introduction

Anophthalmia refers to either congenital or acquired absence of the eye. As opposed to congenital anophthalmia, acquired anophthalmia is caused by a globe removal procedure due to various conditions, among them ocular trauma, malignancies or blind painful eye due to glaucoma or any other pathology.

Globe removal procedures are categorized into three types: (1) evisceration (removal of the globe contents alone, with preservation of the sclera); (2) enucleation (removal of the globe itself with the sclera); (3) exenteration (removal of the entire contents of the orbit, including the globe, extraocular muscles and periorbita, with or without the eyelid and adjacent bony structures [extended exenteration]). The selection of the appropriate procedure is based on patient, ocular and orbital characteristics.

"Anophthalmic socket" is the term used to describe the orbital content and structure when no globe is present, including the bony structure, soft tissues, and the remaining potential space. This condition may involve unique complications, and its management requires a comprehensive understanding of this entity and the knowledge of the various tools for enabling optimal management.

2 Signs and Symptoms

Various complications are associated with anophthalmic socket, most commonly including enophthalmos, deep superior sulcus deformity and prosthesis tilting, ptosis, lower lid laxity, contracted socket, orbital implant migration, exposure and extrusion, implant infection and Post Enucleation Socket Syndrome (PESS – deep superior sulcus, enophthalmos, upper eyelid ptosis and lower eyelid ectropion). Each complication has its unique signs and symptoms.

3 Treatment

In socket reconstruction, treatment target is to add volume to the orbit. Orbital implants, autologous grafts, and ocular prosthesis can help restore orbital volume and architecture. Intra-conal ball implant is the most popular in use. There are several types of synthetic orbital implants that can be categorized by different features: primary or secondary, porous–integrated (interconnected channels that permit fibrovascular ingrowth) or nonporous-nonintegrated, buried or exposed, and differences in materials, sizes, and shapes. Complications are diagnosed and managed individually.

4 Diagnosis

Diagnosis of most disorders associated with anophthalmos is primarily clinical and does not require imaging (PESS, extrusion, contracted socket, etc.). However, when preparing for socket reconstruction, non-contrast CT scan is useful in demonstrating the orbital anatomy thus enables proper pre-operation planning [1, 2]. Contrast-enhanced imaging can demonstrate vascular ingrowth into integrated orbital implants. If additional orbital pathology is suspected, i.e., implant infection, contrast enhanced imaging is mandatory. MRI is mostly used to demonstrate blood vessels ingrowth into integrated orbital implants.

Both CT and MRI scan can aid to differentiate between different orbital implants [3]. On CT, orbital implants are usually hyperdense. Some implants, e.g., hydroxyapatite, are more hyperdense than others, e.g., silicone. However, integrated orbital implants immediately after implantation are commonly hypodense, with possible air bubbles inside the implants [4]. On MRI, integrated implants have low to intermediate signal on T1 and high to intermediate signal on T2, while non-integrated implants have low to intermediate signal both on T1 and T2. With fibrovascular ingrowth, integrated implants enhance in a non-homogenous fashion from the edges of the implant inwards.

5 Figures with Captions

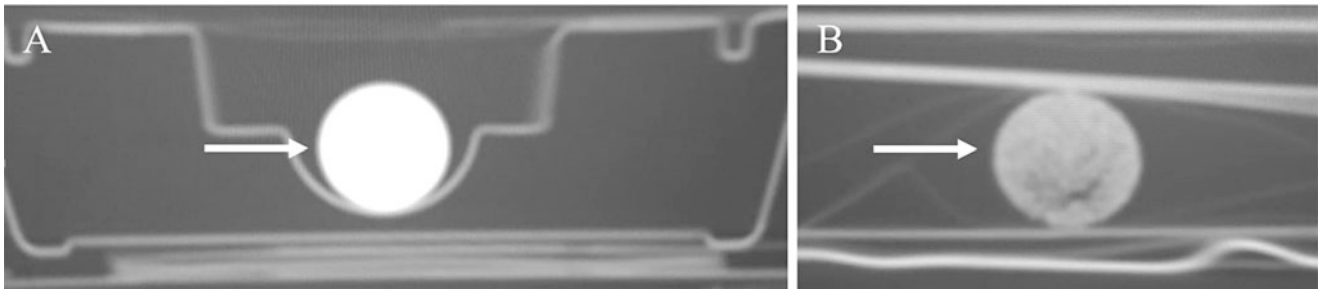


Fig. 1 High resolution CT scan of spherical orbital implants in their original package. A, silicone ball implant, B, porous polyethylene implant (*arrows*). Note the homogenously hyperdense silicone implant versus the somewhat stippled appearance of the porous polyethylene implant

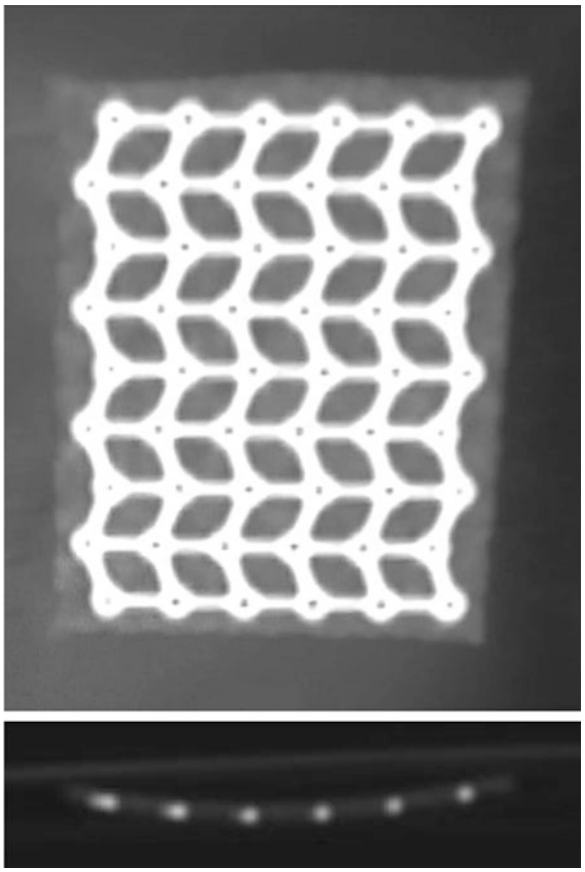


Fig. 2 High resolution CT scan, high-res window, of a Medpor-Titan® surgical implant (Stryker Leibinger Freiburg/Germany) for orbital wall reconstruction in its original package. Enface (*upper image*) and transverse (*lower image*) cut. Note the faint signal from the porous polyethylene part of the implant, versus the high density of the embedded titanium mesh



Fig. 3 Clinical photo of a patient with right Post Enucleation Socket Syndrome (PESS), demonstrating deep upper eyelid sulcus, enophthalmos, ptosis, and mild lower lid ectropion

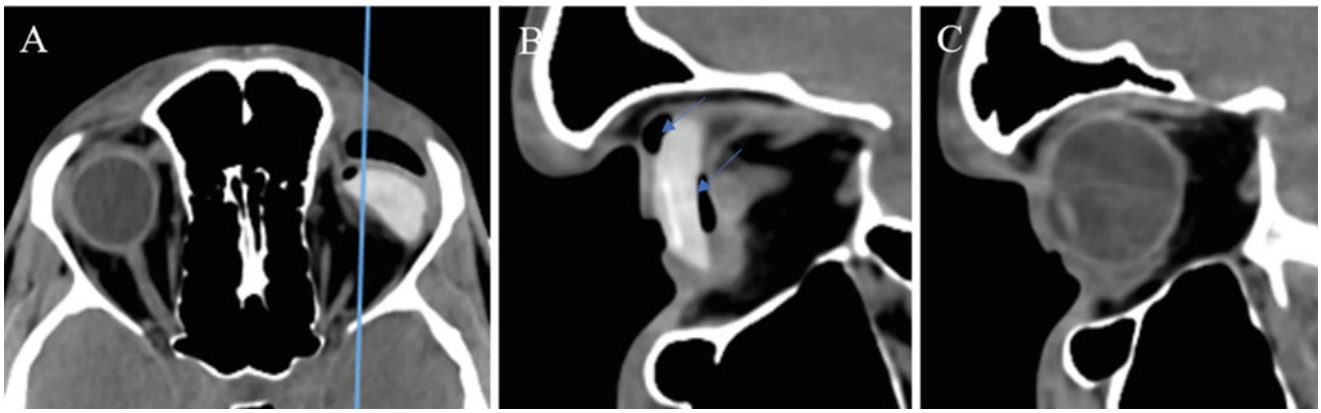


Fig. 4 NCE CT images of A 24 YO patient who had his left eye enucleated at the age of 3YO secondary to retinoblastoma. No implant was inserted during primary surgery. The patient was concerned about asymmetric appearance and lack of prosthesis movement. On examination, he had a typical post enucleation socket syndrome (PESS) appearance: enophthalmos, deep superior eyelid sulcus, ptosis and mild lower eyelid ectropion. (**a**) Axial CT, NCE, soft tissue window demonstrates left relative enophthalmos of the prosthesis secondary to lack of an intraconal implant. Note the air anterior to the superior eyelid representing the deep sulcus and the trapped air bubble superficial and deep to the prosthesis (air bubbles are marked in sagittal view by 2 blue arrows). Sagittal view (**b**) demonstrates the relative enophthalmos in comparison with the right side (**c**). Note the difference in distances from the orbital edge to the prosthesis and the orbital edge to the normal eye demonstrating the shortening of the superior muscle complex. The prosthesis is tilted backwards superiorly, secondary to orbital fat shift down and forward, pushing the prosthesis forwards inferiorly



Fig. 5 16 YO patient with acute leukemia was referred to the ophthalmology department after being diagnosed with mucormycosis. On her ophthalmological examination on the left: exophthalmia, near total ophthalmoplegia, VA of 6/48, RAPD with normal appearing retina. Axial NCE CT scan (**a**) demonstrates s/p turbinectomy, maxillary sinus opacity, and pre-maxillary soft tissue infiltration. (**b**) Left exophthalmia with pre-septal soft tissue infiltration and orbital fat stranding up to the orbital apex together with left MR thickening (in keeping with an aggressive process that does not respect the orbital anatomical borders). Coronal NCE CT (**c**) demonstrates fat stranding, exophthalmos and hypoglobus of the left orbit

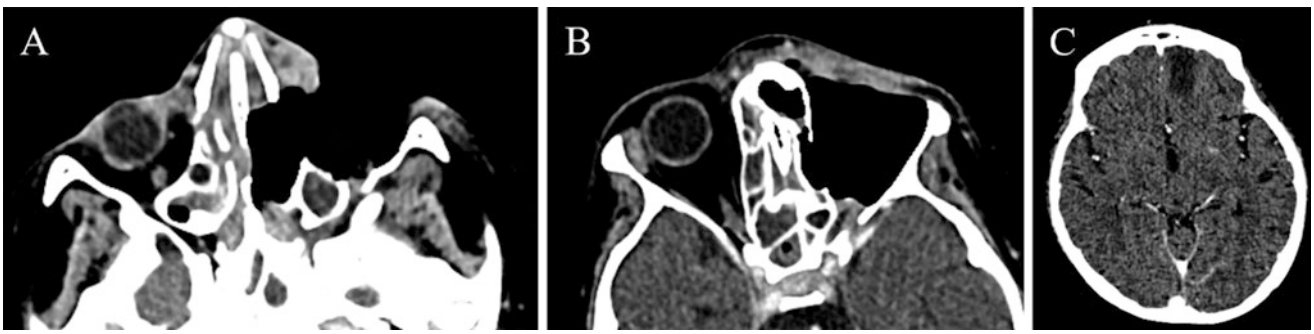


Fig. 6 Same patient as in Fig. 5, seven days post exenteration. Axial CE CT (A,B) demonstrates extensive post-surgical changes: the absence of the orbital soft tissue and the nasal orbital wall including left sided ethmoidectomy. Right ethmoidal and sphenoidal mucosal thickening and fluid can be seen. A follow-up brain axial CE CT (C) shows a hypo-dense area in the left frontal lobe indicative of infiltrative mucormycosis

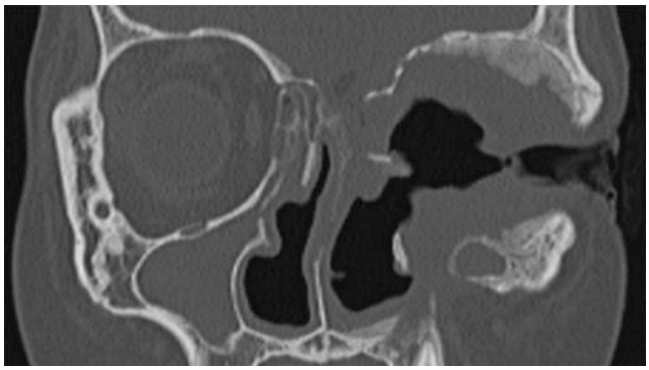


Fig. 7 Same patient as in Figs. 5 and 6, one-year post exenteration. Coronal NCE CT, bone window s/p craniotomy demonstrates missing medial and inferior orbital walls with soft tissue growth from the nasal cavity, bone remodeling of the superior and inferior-lateral walls. Mucosal thickening and fluid can be seen in the right maxillary and ethmoidal sinuses

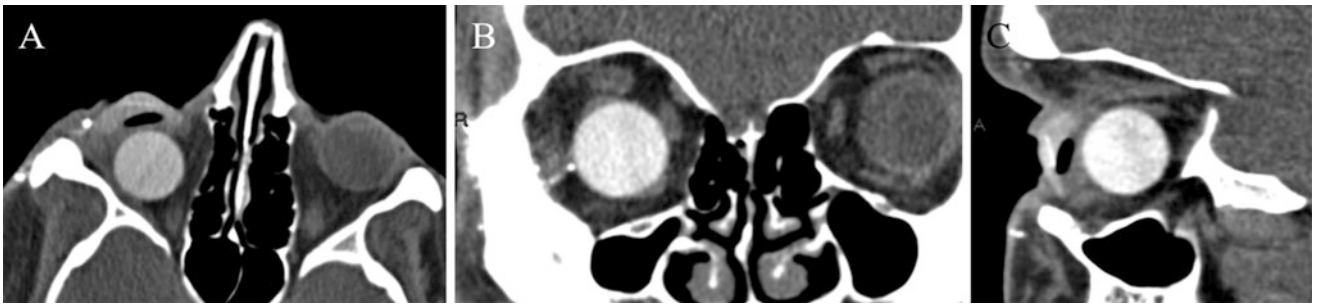


Fig. 8 29-YO after a gunshot injury to the right orbit. A PMMA ball was implanted into the intraconal space. Axial (**a**), coronal (**b**), and sagittal (C) NCE CT complement the differences in size of the two orbits with right vertical expansion secondary to the floor fracture. Right zygomatic bone thickening with lobular changes can be seen (**a**). Bone fragments can be seen around the right zygoma and in the inferolateral quadrant of the right orbit in the axial and coronal cuts. Intraconal ball implant is demonstrated as a hyperdense sphere with clear edges. The prosthesis is demonstrated in the axial and sagittal images as a hyperdense semilunar structure anterior to the orbital implant. The hypodense area representing air between the prosthesis and the implant is a common and normal finding

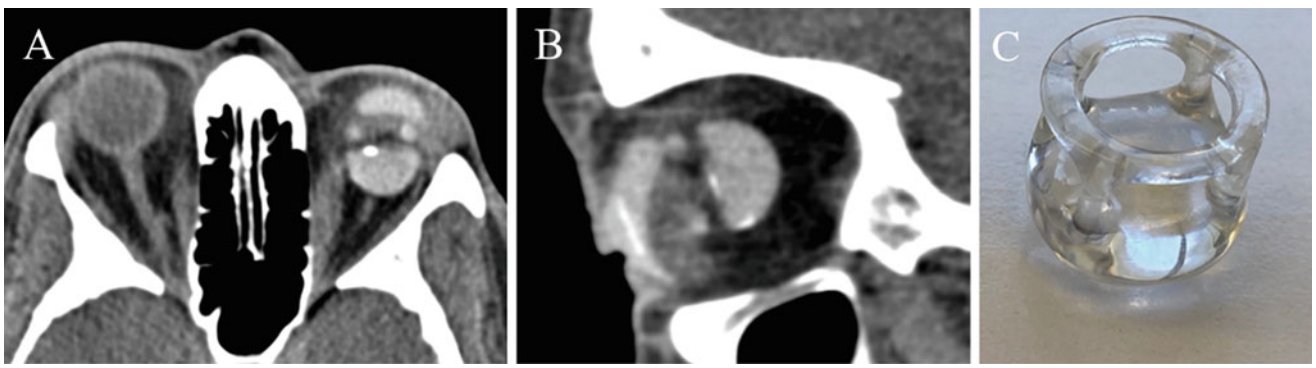


Fig. 9 Axial NCE orbital CT (**a**) demonstrates a posterior intraconal hyperdense semicircular implant (Allen ring implant). The ring is demonstrated as two hyperdense foci. The horizontal extraocular muscles can be seen entering the space between the implant and the ring. On the sagittal cut (**b**), the prosthesis has a hyper-dense semilunar shape in front of the ring of the implant. (**c**) Allen ring implant

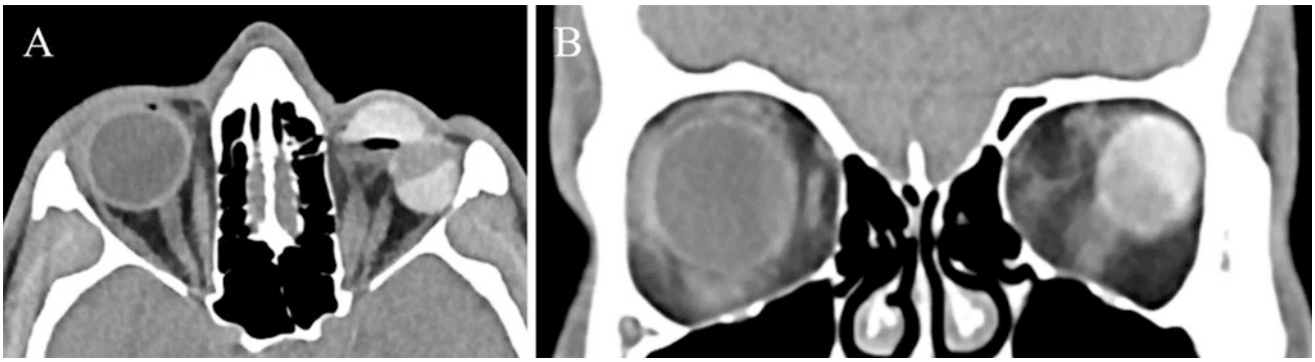


Fig. 10 A left anophthalmic patient addressed the oculoplastic clinic due to an ongoing worsening pain in his anophthalmic socket, especially in left gaze. On examination the bulging temporal edge of an Allen ring PMMA implant could be seen through an intact conjunctiva. Axial orbital NCE CT (**a**) demonstrates a temporally migrated hyperdense semicircular Allen ring implant that has migrated from the central intraconal space to the temporal extraconal space. On the coronal cut (**b**), note that the implant has direct contact with the zygomatic-sphenoid junction

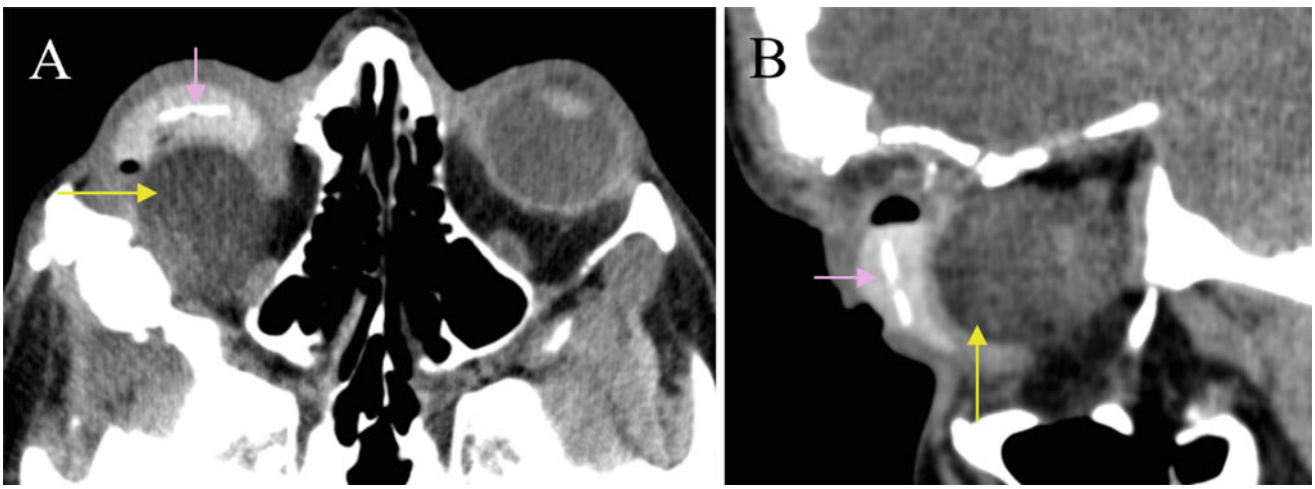


Fig. 11 22-YO female after multiple reconstructive operations following a blast injury to the right side of her face. Axial NCE CT (**a**) demonstrates an oval heterogeneous mostly hypodense structure representing a porous polyethylene integrated implant (Medpor®) filling most of the intraconal space of the orbit (*yellow arrows*). Sagittal view (**b**) demonstrates titanium mesh reconstruction of the orbital roof. The prosthesis is seen as a hyperdense intraorbital object. The painted iris (*pink arrows*) is demonstrated as a hyperdense interrupted line inside the ocular prosthesis

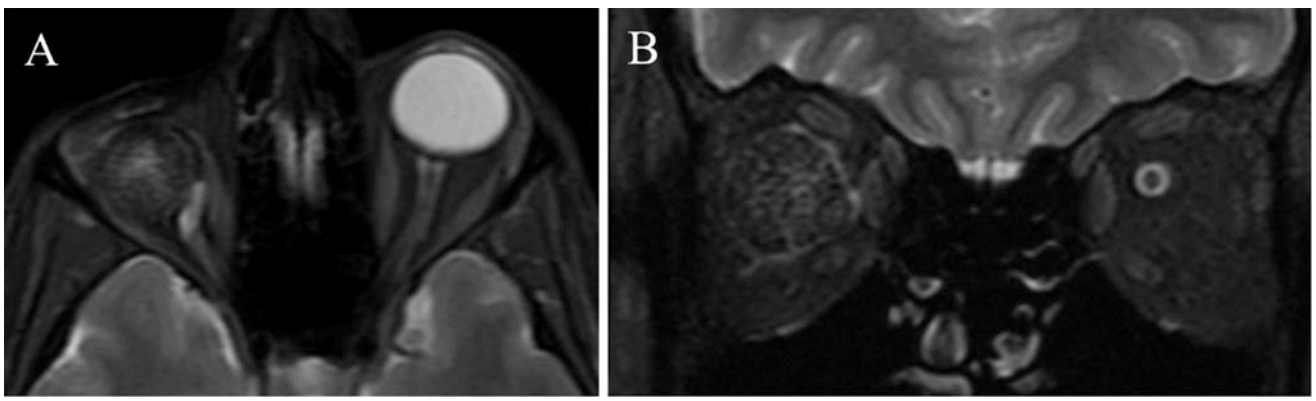


Fig. 12 Six months post enucleation, T2 weighted FS Orbital MRI images, axial (**a**) and coronal (**b**) images. The right intraconal space is mostly filled by an integrated orbital ball implant without prosthesis. The implant is non homogenous showing mixed signals with high intensity dots in keeping with its porous texture . Note the relative posterior position of the implant

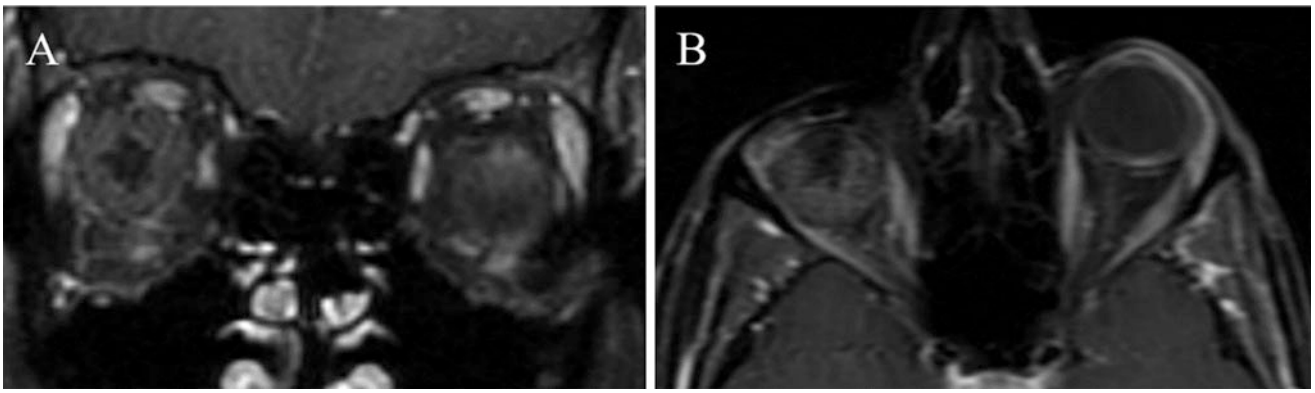


Fig. 13 Same patient as in Fig. 11, T1-weighted FS orbital MRI with GAD (coronal view, **a**; axial view, **b**) shows interval enhancement in the periphery of the implant indicating fibrovascular ingrowth, according to the time elapsed from surgery (one year)

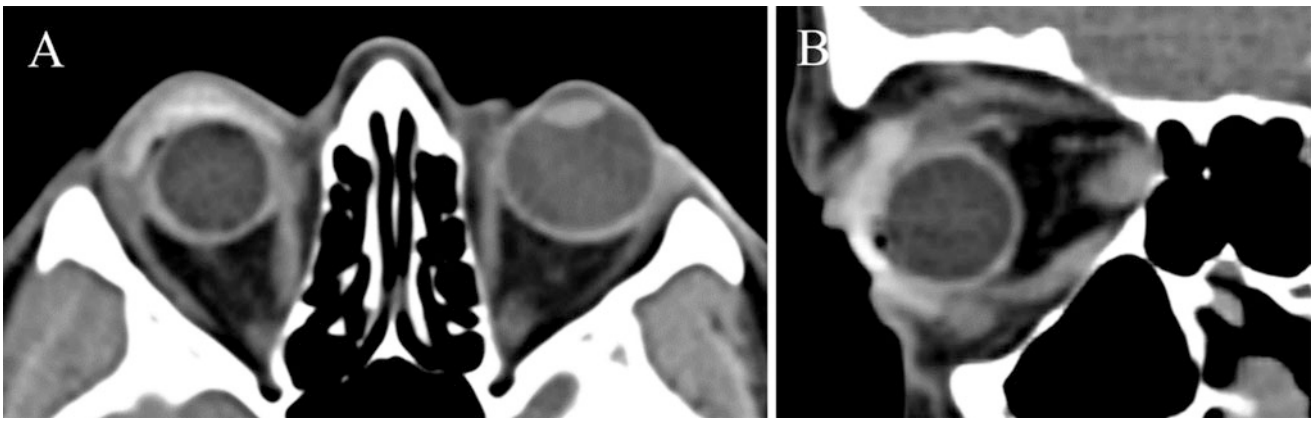


Fig. 14 Axial (**a**) and sagittal (**b**) CE CT of an intraconal integrated implant does not add information over MRI, as seen in the previous case

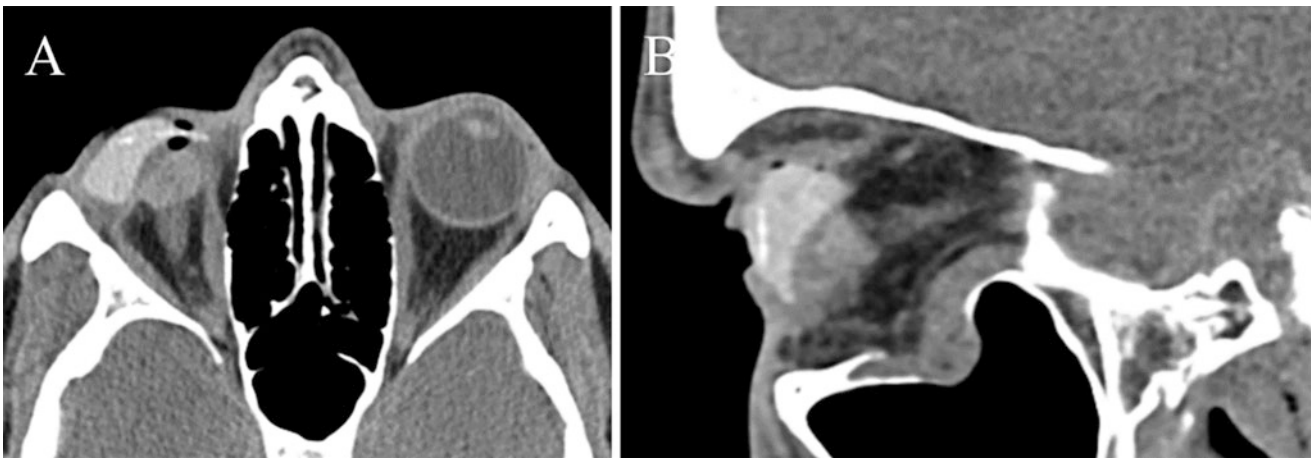


Fig. 15 A 50-YO patient with right phthisis bulbi after blunt trauma. He wears a scleral shell to cover the small and disfigured eye. Axial CT (**a**) shows the prosthesis lying on top of the slightly hyperdense small bulbi. Sagittal view (**b**) shows orbital floor fracture with fat and inferior rectus prolapse into the maxillary sinus. The prosthesis is demonstrated lying on top of the phthisical eye in an attempt to masquerade the enophthalmos and deep superior sulcus

References

1. Smit TJ, Koornneef L, Zonneveld FW, Groet E, Otto AJ. Computed tomography in the assessment of the postenucleation socket syndrome. Ophthalmology. 1990;97(10):1347–51. https://doi.org/10.1016/s0161-6420(90)32411-9.
2. Tyers AG, Collin JR. Orbital implants and post enucleation socket syndrome. Trans Ophthalmol Soc U K. 1982;102(Pt 1):90–2.
3. Themes UFO. Imaging after oculoplastic surgery. Radiology Key. Published September 17, 2016. Accessed August 17, 2020. https://radiologykey.com/imaging-after-oculoplastic-surgery/
4. Handler LF, Heher KL, Katowitz JA. Congenital and acquired anophthalmia. Curr Opin Ophthalmol. 1994;5(5):84–90. PMID: 10172408.

Index

A
Acid fast bacilli, 638
Acquired anophthalmia, 720, 724
  diagnosis, 720
  signs and symptoms, 720
  treatment, 720
Acute bilateral dacryoadenitis, 552
Acute dacryocystitis, 290
  AS-OCT, 283–285
  diagnosis, 284
  differential diagnosis, 284
  enlarged lacrimal sac, 284, 286
  image-guided dacryolocalization, 284, 287
  signs and symptoms, 284
  treatment, 284
Acute disseminated encephalomyelitis (ADEM), 475
Acute inflammation, 541
Acute IOI, 539, 540
Adenocarcinoma, 406
Adenoid cystic carcinoma, 141, 146, 263–266, 406
  diagnosis, 168
  differential diagnosis, 142, 168
  PET/CT, 169–170
  symptoms of, 168
  treatment, 168
  ultrasound, 141–144
Adjuvant orbital radiotherapy, 370
Adnexa, 36
Adult onset asthma and periocular xanthogranuloma (AAPOX), 577–579
Adult onset xanthogranuloma (AOX), 577, 578
Ahmed glaucoma valve, 700
Albendazole, 634, 636
Allen ring implant, 723, 724
Amphotericin B, 616
Anastomoses, 26
Aneurysmal bone cyst
  CT scan and MRI, 440
  cystic fluid component, 441
  differential diagnosis, 440
  formation, 344
  Langerhans cell histiocytosis, 441, 442
  multiloculated interdiploic lesion, 441
  peripheral uptake and less activity in center, 442
  superior and lateral lytic bone lesion, 440
  treatment, 440
Angel's kiss, 240
Angiography, 121, 122, 514, 516, 517
Angiosarcoma
  diagnosis, 531
  differential diagnosis, 530–531
  signs and symptoms, 530
  treatment, 532
Anophthalmia, 720
  bilateral, 210, 211
Anophthalmic socket, 720, 724
Anterior orbitotomy surgery, 232, 597
Anterior scleritis, 557
Anterior segment optical coherence tomography (ASOCT), 279, 280
Apert syndrome, 196
Apex syndrome, 476, 483
Apparent diffusion coefficients (ADC), 104
Arterial anatomy
  anastomoses, 26
  external carotid circulation, 26
  internal carotid circulation, 25–26
Arterial feeder, 523
Arterial hypertension, 684
Arterial spin labeling RA, 118
Arterial supply, 27
Arteriovenous fistulas (AVF), 522, 523
Arteriovenous malformations (AVMs), 120, 150–151, 525–527
  computed tomography, 523
  diagnosis, 523
  differential diagnosis, 523
  digital subtraction angiography, 523
  intracranial AVMs, 523
  magnetic resonance imaging, 523
  orbital and periorbital AVMs, 522
  retinal AVMs, 522–523
  right frontal lobe AVM, 528
  signs and symptoms, 522
  superficial venous drainage, 524
  treatment, 524
AS-OCT, 283, 284
Aspergillosis
  differential diagnosis, 616
  invasive, 616–618
  non-invasive, 616
  osseous defect, 619
  signs and symptoms, 616
  sino-orbital, 620
  treatment, 616
Aspergillus, 616
Aspiration, 492, 495, 497
Autoimmune disease, 557
Axial diffusion weighted imaging (DWI), 300

© Springer Nature Switzerland AG 2022
G. Ben Simon et al. (eds.), *Atlas of Orbital Imaging*,
https://doi.org/10.1007/978-3-030-62426-2

B
Bacterial dacryoadenitis, 551, 553
Basal cell carcinoma tumor
  differential diagnosis, 350
  iso-intense soft tissue mass, 350
  left superior eyelid and frontal sinus involvement, 350
  left superior nasal area, 350
  medial canthus with deep bone erosion, 351
  radiologic findings, 350
  signs and symptoms, 349
  soft tissue window and bone window, 350
  tissue biopsy, 350
  treatment, 350
Benign epithelial tumors, lacrimal gland, *see* Lacrimal gland pleomorphic adenoma
Benign lymphoid hyperplasia
  asymmetric homogeneous enlargement of right lacrimal gland, 272
  diagnosis, 272
  differential diagnosis, 271
  homogeneous symmetrical lacrimal gland enlargement, 272
  normal appearing lacrimal glands, 272
  PET/CT, 272
  signs and symptoms, 271
  treatment, 272
Benign osseous tumors of orbit, 418
Beta blockers, 500, 502
Bicoronal craniotomy approach, 229
Bilateral disease, 172
Bilateral infiltrative tumor, 305
Bilateral lacrimal gland enlargement, 553, 568
  and paranasal sinus disease, 568
  and patchy paranasal sinus disease, 569
Bilateral lacrimal gland swelling, 574
Bilateral optic atrophy, 487
Bilateral proptosis, 574
Bilateral retinoblastomas, 110
Bilateral sphenoid sinusitis, 603
Binocular vertical diplopia, 688
Bioresorbable implants, 669
Bleomycin, 492, 497
Blow in fractures, 663, 666, 667
Blow out fractures, 662–664
Blunt trauma, 677, 725
Bone erosion, 340, 341
Bones of the orbit
  adjacent skeletal structures, 6
  adjacent spaces, 5
  ethmoid bone, 18, 19
  frontal bone, 18
  globe and optic nerves, 11
  human skull, 6–10
  inferior medial orbital wall and lacrimal drainage apparatus, 22
  infraorbital canal, 14
  maxillae and lacrimal bones, 19
  missing lacrimal bone, 8
  orbital bony structures, 5
  orbital floor and related structures, 21
  orbital roof and related structures, 21, 22
  sphenoid bone, 15
  sphenoid sinus, 15
Bony cyst, 434
Bony nasolacrimal duct (NLD), 280–282
Bony orbital tumor, 420
Brachycephaly, 197
Breast cancer, *see* Metastatic breast cancer
Bright blood sequences, 117
Bruit, 514
B-scan screening exam, 130
Bulla ethmoidalis, 48
Buphthalmos, 200

C
Capillary malformation
  beta blocker, 502
  diagnosis, 500
  differential diagnosis, 500
  hemangioma, 501
  on histopathological examination, 503
  hyperintense lesion, 502
  inferolateral displacement of left globe, 502
  signs and symptoms, 500
  treatment, 500
Carcinoma ex-pleomorphic adenoma
  diagnosis, 268
  differential diagnosis, 268
  heterogeneous enhancement, 269
  isointense orbital mass, 269
  orbital exenteration, 269
  signs and symptoms, 268
  thinning of orbital roof, 269
  treatment, 268
Carotid artery, 516
Carotid-cavernous fistulas (CCF), 114, 654
  cavernous sinus, 516
  diagnosis, 514–515
  differential diagnosis, 514
  dilated right superior ophthalmic vein, 516
  direct CCF, 514
  enlarged right cavernous sinus, 516, 517
  indirect CCF, 514
  left internal carotid artery, 516
  post coil embolization, 518
  signs and symptoms, 514
  treatment, 515
Carotid siphon, 25, 28
Casoni intradermal test, 630
Cataract extraction, 701
Catheter-based angiography, 122
Cavernous sinus, 86–88, 95
  syndrome, 446
  thromboses, 114
Cavernous venous malformation (CVM), 135, 146, 151–152
  cryo-assisted tumor removal, 509
  CT and MRI scan, 508
  differential diagnosis, 135, 508
  facial appearance, 508, 510
  heterogeneous enhancement, 509, 510
  hyperintense lesion with thin internal septation, 510
  intraconal hyperintense lesion with thin internal septations, 509
  intraconal space, 509
  isodense lesion in intraconal space, 509, 510
  isointense lesion in intraconal space, 508, 510
  minimal proptosis, 508
  orbital ultrasound, 508
  primary hyperintense lesion with thin internal septation, 509
  radiotherapy, 508
  signs and symptoms, 508
  surgical removal, 511
  ultrasound, 135–136
Cavernous venous vascular malformation, 119

CD34, 531
Cementoblastoma, 609
Cemiplimab, 354
Central nidus, 522, 523
Cerebrofacial arteriovenous metameric syndrome (CAMS), 522
Cervical adenopathy, 175
Chocolate cyst, 492
Cholesterol granuloma
  clinical presentation and radiological findings, 434
  differential diagnosis, 434
  signs and symptoms, 434
  superior-temporal orbit quadrant invasion, 437
  treatment, 434
Chondromyxoid fibroma (CMF), 424, 425
Choroidal detachment, 681
Chronic bilateral lacrimal gland swelling, 574
Chronic invasive aspergillosis, 616
Chronic malar edema, 714, 716, 717
Chronic nasal and sinus inflammation, 561
Chronic sclerosing inflammation, 596
Classic periostitis, 637
Clinoidal meningiomas, 446
Closed globe injuries, 650, 651, 662
Cold abscess, 637
Coloboma, 211
  bilateral, 213
  chorioretinal, 212
  cyst after enucleation, 213
Compressive optic neuropathy, 612
Computed tomography (CT), 99, 289, 650–655, 657, 678
  axial bone algorithm CT, 100
  axial soft tissue CT with contrast, 101
  coronal bone algorithm CT, 100
  coronal CT without contrast, 101, 102
  coronal soft tissue CT with contrast, 101
  indications, 100
  sagittal soft tissue CT with contrast, 101
  technique and protocol considerations, 100
Computed tomography angiography (CTA)
  carotid cavernous fistula, 114
  indications, 113
  orbital floor defect, 115
  recurrent sphenoid wing meningioma, 115
  technique and protocol considerations, 113
  uses, 113
Computed tomography dacryocystography (CT-DCG), 280–281
Computed tomography venography (CTV)
  cavernous sinuses, 114
  technique and protocol considerations, 113
  uses, 113
Cone beam CT scans (CBCTs), 663
Congenital hamartomas, 522
Conjunctival chemosis, 514
Constructive interference in steady state (CISS), 104
Contrast-enhanced MRA, 117
Corkscrew appearance, 514, 515
Corkscrew vessels, 522
Corticosteroids, 500, 568, 574
Cranial bones, 3
Craniofacial trauma, 650
Cranio-orbital fracture, 654, 667–668
Cranio-orbital teratoma, 222
Cranio-orbitofacial fracture, 668–670
Craniosynostosis
  diagnosis, 192
  differential diagnosis, 192
  gradual expansion of skull, 194
  head with elongation, 194
  nonsyndromic sagittal, 194
  signs, 192
  symptoms, 192
  treatment, 192
Crbital capillary hemangioma, 501
Cutaneous melanoma, 160, 395–397
Cystic lesions of orbit
  encephalocele (*see* Encephalocele)
  teratoma, 221–223
Cytokeratin, 412

D
Dacryoadenitis
  ADC and DWI, 555
  bacterial, 553
  bilateral lacrimal gland enlargement, 554
  chronic bilateral lacrimal gland swelling, 554
  differential diagnosis, 552
  diffuse gland enlargement with globe dystopia, 553
  eyelid ptosis, tender swelling, and erythema, 552
  gland enlargement with soft-tissue swelling, 554
  gland with abscess and flattening the globe, 554
  homogenous enlargement and left lacrimal gland enhancement, 553
  intravenous antibiotic treatment and oral steroids, 552
  lacrimal gland enlargement with soft tissue swelling and mild proptosis, 552
  mild globe dystopia, 553
  periorbital swelling and erythema, 552
  signs of inflammation, 551
  sub-acute left lacrimal gland inflammation, 553
  treatment, 552
  unilateral left sided lacrimal gland swelling, 553
Dacryocystitis, 234, 403
Dacryocystocele
  asymmetric, 238
  bilateral, 234–236
  bilateral asymmetric, 235
  diagnosis, 234
  differential diagnosis, 234
  intranasal cysts, 234
  post bilateral nasal cyst microdebridement with drainage of, 235
  signs, 233
  treatment, 234
  ultrasound of, 238
Dacryocystorhinostomy surgery, 404
Dacryops (lacrimal gland ductal cysts), 249
Dark blood sequences, 117
Deep upper eyelid sulcus, 721
Demyelinating lesion, 480, 481
Dermoid cyst, 133, 146, 153–154
  configuration to, 216
  diagnosis, 216
  differential diagnosis, 133, 216
  history of, 216
  leaking/rruptured, 215
  orbital, 215, 218
  signs, 215
  symptoms, 215
  treatment, 216
  ultrasound, 133–134
Diffuse large B-cell lymphoma, 405
Diffusion tensor imaging (DTI), 104, 106, 107

Diffusion weighted imaging (DWI), 104, 105
Digital subtraction angiography (DSA), 28, 30, 118, 124, 125, 515, 518, 523, 524, 526, 527
Dilated right superior ophthalmic vein, 516
Dilated superior ophthalmic vein, 515
Direct CCF, 514, 515
Disc drusen, 488
Discreet neurofibroma, 200
Dumbbell shape, 216
Dural reaction, 184
Dynamic fluoroscopy, 122
Dysptopia, 227
Dysthyroidism, 582
Dysthyroid optic neuropathy (DON), 483

E
Embolization, 515, 518
Encapsulated CVM, 508
Encephalocele
  anterior extension of, 229
  anterior orbitotomy surgery, 232
  bicoronal craniotomy approach, 229
  diagnosis, 226
  dysptopia, 227
  facial reconstruction, 230
  medial mass, 231
  mucocele, 231
  nasal, 229, 230
  orbital dystopia, 230
  proptosis, 228
  signs and symptoms, 225
  treatment, 226
Endocystectomy, 630
Endocyst removal, 630
Endophthalmitis, 558
Endoscopic dacryocystorhinostomy (DCR), 284
Endovascular embolization, 524
Enlarged right cavernous sinus, 516, 517
Enophthalmos, 386, 721
Epidermoid cyst, 216
Epididymo-orchitis, 574
Epithelioid granuloma, 644
Epitheloid granuloma, 638
Erdheim-Chester disease (ECD), 577–580
Esotropia, 216
Ethmoidal foramina, 29
Ethmoid bone, 18, 19
Ethmoid sinus, 60
  mucocele, 607
Ethmoid sinusitis, 484
Ewing sarcoma
  differential diagnosis, 440
  histopathological evaluation, 440
  MR imaging, 443
  osteolytic mottled appearance, 443
  signs and symptoms, 440
  treatment, 440
Exophthalmos, 582
Exophytic lesion, 373, 374
External beam radiation therapy, 386
External carotid circulation, 26
Extradural meningioma, 450–451
Extranodular marginal zone lymphoma (EMZL), 272
Extra-ocular movements (EOM), 600
Extraocular muscle (EOM), 34–35, 39, 40, 42–44, 130, 545
  enlargement, 582, 587
  swelling, 567
Extraocular retinoblastoma
  differential diagnosis, 376
  high-resolution contrast-enhanced MRI, 376
  high signal intensity, 383
  signs, 376
Extraocular spread, 370
Extraorbital soft tissue changes, 654–655
Extra-scleral extension
  anterior uveal melanoma, 372
  posterior uveal melanoma, 371, 374
  recurrent uveal melanoma, 373
Eye, 366–368
Eyelid(s), 33–34
  edema, 592
  swelling, 616
Eye-sparing surgery, 404

F
Facial dysmorphism, 200
Fascia of the eyeball, 34
Fast imaging employing steady-state acquisition (FIESTA), 104
Fat-saturating sequences, 184
Fatty lesions, 187
FDG-PET, 301
Fibrolipoma, *see* Lipomas
Fibrous dysplasia (FD), 180, 181, 400, 476, 482, 483
  bony extension, 430
  clinical characteristics, 428
  differential diagnosis, 428
  ground glass appearance, 429
  heterogenous, dense and sclerotic bone expansion, 429
  left hypoglobus and prominent forehead, 428
  monostotic variant, 427
  polyostotic, 431
  sclerotic lesions, 430
  signs and symptoms, 427
  treatment, 428
  tri-lateral compartment involvement, 430
Filler related complications, 714
Fluid attenuated inversion recovery (FLAIR), 104, 109
Fluorescein angiography, 522
Fluoroscopy, 121, 122
Fontanelles, of fetal skull, 192
Foramen of Magendie, 245
Foramen rotundum, 75
Forehead melanoma, 161
Foreign bodies, 654–659
Foreign body granuloma (FBG), 714, 716
Fractionated radiation therapy, 272
Frontal bone, 3, 4, 18
Frontal sinus, 47, 59
Frontal sinus mucocele, 605
Frontoethmoidal bony defect, 226
Fungal infection, 624

G
^{68}Ga-dotatate PET/CT, metastasis, 172
Gamma knife radiosurgery (GKS), 508
Gamma knife stereotactic radiosurgery, 467

Gasserian ganglion, 92
Glioblastoma, 478
Glioma, 200, 476
Gold weight, 698
Granulomatosis with polyangiitis (GPA), 552, 559
  ANCA, 561
  chronic left epiphora, 562
  differential diagnosis, 561
  enhancing infero-medial orbital mass, 563
  epiphora, swelling and redness, 562
  extensive loss of normal sinus and nasal tissues, 563
  extensive sinus disease with secondary hyperostosis, 564
  infero-medial infiltrating mass lesion, 563
  infiltrative lesion in infero-medial orbit, 562
  infiltrative mass with extra-and intraconal space, 563
  infiltrative soft tissue in medial orbit, 564
  intranasal and sinus disease, 565
  iso-intense anterior medial orbital, 563
  loss of intranasal structures and left medial orbital wall, 565
  medial orbital infiltrative lesion with adjacent bone loss, 563
  saddle nose deformity, 564
  soft tissue loss and sclerosing mass, 564
  supero-medial and infero-temporal orbital fat, 562
  symptoms and signs, 561
  treatment, 562
Granulomatous orbital inflammation
  orbital sarcoidosis (*see* Orbital sarcoidosis)
  orbital tuberculosis (*see* Orbital tuberculosis (OTB))
Grave's disease, 172
Graves hyperthyroidism, 586
Greater sphenoid wing (GSW), 183

H
Head and neck squamous cell carcinoma, *see* Squamous cell carcinoma of the sinuses
Head injury, 515
Hemangioblastoma, 533
  diagnosis, 531
  differential diagnosis, 531
  signs and symptoms, 530
  treatment, 532
Hemangioma
  of bone (*see* Intraosseous hemangioma)
  infantile, 240
  non-involuting capillary, 240
  rapidly involuting capillary, 240
  See also Cavernous venous malformation (CVM)
Hemangiopericytoma, 153, 531, 532
  spectrum (*see* Solitary fibrous tumor (SFT))
Hemifacial microsomia, 194, 195
Hemorrhage, 494
Hemorrhagic proptosis, 494
Herniation of brain tissue, 230
High-flow lesions, 522, 523
Hobnail hemangioendothelioma, 530–532
Horner's syndrome, 446
Hydatid cysts, 629
Hypercellular tumor, 410
Hyperechoic scolex, 634
Hyperostosis, 428
Hypophysis gland, 63
Hypoplasia, 197

I
Idiopathic orbital inflammation (IOI), 138, 552
  chronic left proptosis, 541
  differential diagnosis, 140, 539
  extra and intraconal mass lesion, 542
  hyperdense intraconal lesion, 540
  inferior orbital fissure enhancing lesion, 544
  largely intraconal left orbital lesion, 541
  lesion between globe and superior rectus, 540
  lesion medial extending into intraconal space, 542
  medial intra-and extraconal lesion, 541
  optic neuropathy with ptoptosis and mild flattening, 541
  palpable orbital mass in the supero-temporal region, 542
  para-cavernous soft tissue enhancing process, 543
  superior orbital lesion, 540
  supero-medial enhancing orbital lesion, 540
  supero-medial mass moulding with dystopia and mild flattening, 541
  swelling, erythema, optic neuropathy and limited eye movements, 541
  swelling and erythema, with ptosis, 540
  symptoms and signs, 539
  tissue biopsy, 540
  treatment, 540
  ultrasound, 138–139
Idiopathic pre-chiasmatic right optic atrophy, 477
IgG4-related disease (IgG4-RD), 551, 552, 554
  bilateral symmetrical lacrimal gland enlargement, 568
  CT, 175–176
  diagnosis, 175
  differential diagnosis, 567
  DWI MRI, 569
  enlarged infra-orbital nerve, 570
  FDG avidity, 569
  infiltrative disease involving lateral recti and orbits, 569
  infra-orbital nerve and patchy paranasal sinus disease, 570
  left frontal nerve enlargement, 570
  left optic neuropathy, 570
  marginal zone MALT lymphoma, 570
  PET scan, 175–176, 568
  pre-septal hyperdense soft tissue thickening, 569
  sclerosing cholangitis, lacrimal and salivary gland enlargement, 569
  signs and symptoms, 174, 567
  tissue diagnosis, 567
  treatment, 175, 568
  upper eyelid swelling and nasal obstructive symptoms, 568
IgG4-related ophthalmic disease, *see* IgG4-related disease (IgG4-RD)
IL-6/JAK/STAT3 pathways, 268
Image-guided dacryolocalization, 284, 287
Immune checkpoint inhibitors, 390
Immunohistochemical staining, 332
Immunohistochemistry (IHC), 412
Immunomodulatory therapy (IMT), 558
Immunotherapy, 160
Incisional biopsy, 314, 320
Indirect CCF, 514, 515
Infantile hemangioma, 134, 146, 234
  ADC map, 243
  axial MR angiography, 246
  axial T1-weighted MRI, 244
  coronal T1-weighted MR imaging, 242
  coronal T2-weighted MRI, 245
  diagnosis, 240
  differential diagnosis, 135, 240
  diffusion weighted imaging, 242
  flow voids within, 241
  large orbital mass, 240

Infantile hemangioma (*cont.*)
Meckel's cave, 241
MRA image, 243
oral beta blocker treatment, 243
orbital component of, 245
PHACES syndrome, 244
pterygopalatine fossa through right foramen rotundum, 241
signs, 240
supra-zygomatic infra-temporal/soft tissue involvement, 240
symptoms, 240
T2-weighted MR imaging, 242
treatment, 240
ultrasound, 134–136
ultrasound with doppler flow studies, 244
Inferior oblique, 45
Inferior ophthalmic vein, 69
Inferior orbital fissure (IOF), 69, 71, 73
Infiltrating carcinoma, 268
Infiltrative disease, 173, 578
Infiltrative process, 579
Inflammatory disorders, 545
Infra-orbital nerve (ION)
enlargement, 570
swelling, 567
Infratemporal fossa (ITF), 17, 69, 76, 80, 81, 83
Injectable fillers, 705
Insidious, 629
Internal carotid circulation, 25–26
International Society for the Study of Vascular Anomalies (ISSVA), 522, 523
Intra-arterial neoadjuvant chemotherapy, 124
Intraconal disease, 580
Intraconal orbital traumatic hemorrhage, 484
Intracranial AVMs, 523
Intracranial emphysema, 654
Intracranial structures, 39
Intranasal cyst
bilateral, 234
dacryocystocele, 234
nasal endoscopy, 234
respiratory distress, 233
Intraocular foreign body, 656, 678
Intraocular lens (IOL), 699, 701
dislocation, 679
Intraocular metallic foreign body, 680
Intraocular retinoblastoma
biopsy, 376
differential diagnosis, 376
high signal intensity, 383
leukocoria, 376
MRI, 381
primary enucleation, 376
Intraoperative dynamic imaging, 121
axial CTA, 125
catheter-based angiography, 122
cone-beam CT, 122
coronal CTA, 125
dynamic fluoroscopy, 122
indications, 122
technique and protocol considerations, 122
Intraorbital hematoma, 654
Intraosseous hemangioma
avid contrast enhancement, 436
corduroy sign, 434
isointense lesion within superolateral bone, 435
nuclear medicine techniques, 434
polka-dot appearance, 434
traversing hypointense trabeculae, 435
Intraosseous meningioma, 447
Intravenous pamidronate, 428
Invasive aspergillosis, 616
IR/EOM related hemorrhage, 685–688
beached whale appearance, 687
epicenter of the mass, 686
fluid levels, 685
globe indentation, 688
hematoma, 685, 686
homogenous enhancement of lesion, 686
homogenous hyperdense well delineated intra-conal mass, 687
hyperdense relatively homogenous mass, 685
lower eyelid swelling, 685
superior-temporal displacement of optic nerve, 688
upgaze limitation, 687
Ischemia, 624

J
Jugum sphenoidale, 63

K
Kasabach–Merritt syndrome, 500
K-space, 104, 105

L
Lacrimal bone, 4, 8, 19
Lacrimal drainage system, 54
anatomical flow, 283, 285
ASOCT, 280
CT-DCG, 280–281, 283, 285
imaging modalities, 279
mispositioned Lester-Jones tube, 283, 286
naso-orbitoethmoid fracture repair, 286
NLD, 281–282
surgical anatomy, 280, 282
Lacrimal fossa (LF), 279
Lacrimal gland, 34, 45, 131, 175
adenoid cystic carcinoma, 169
enlargement, 578, 583
enlargement of bilateral, 175
epithelial tumors of, 140–142
fossa, 339
inflammation, 551–553
swelling, 567, 573, 574
Lacrimal gland carcinoma, 268
adenoid cystic carcinoma and tissue, 265
bony destruction, 265
cavernous sinus and Meckel's cave, 266
clinical suspicion, 264
defect in lateral orbital wall, 264
differential diagnosis, 263
enhancing mass in superotemporal left orbit, 265
heterogeneous mass enhancement, 264
hypointense mass in superotemporal right orbit, 264
incisional biopsy, 264
left foramen rotundum, 266
orbital roof with dural enhancement, 266
PET/CT, 265
superior and lateral rectus muscles, 265
superotemporal left orbit, 265

superotemporal right orbital mass with inferior displacement, 264
symptoms, 263
treatment, 264
tumor recurrence, 266
Lacrimal gland pleomorphic adenoma
axial post-contrast CT orbit, 254
axial SWI image, 257
axial T1 post-contrast fat-saturated image, 254, 255
axial T2 fat-saturated image, 254, 256
coronal post-contrast CT orbit, 254
diagnosis, 254
differential diagnosis, 253
diffusion ADC map, 256
diffusion DWI image, 256
early post-contrast coronal FSPGR T1 partially saturated image, 256
post-contrast axial T1 fat-saturated image, 256
post-contrast coronal FSPGR T1, 256
post-contrast orbit CT, 255
sagittal T2 fat-saturated image, 254
signs, 253
symptoms, 253
treatment, 254
Lacrimal gland prolapse, 469
axial T1 post-contrast fat-saturated image, 252
axial T2 fat-saturated image, 251
cyst's margin, 252
diagnosis, 250
differential diagnosis, 250
homogenous enlargement of right palpebral lacrimal gland, 251
inferotemporal and anterior prolapse, 251
mild temporal ptosis, 251
normal diffuse enhancement of, 251
signs, 249
in superotemporal fornix, 251
symptoms, 249
treatment, 250
Lacrimal mucocele, 237
Lacrimal punctum and canaliculi, 279
Lacrimal sac carcinoma
diagnosis, 404
differential diagnosis, 404
treatment, 404
See also Malignant epithelial tumors of the lacrimal sac
Lacrimal sac tumor
adenocarcinoma, 292
CT scan, 291
differential diagnosis, 290
malignancies, 289
MRI, 289–291
muco-epidermoid carcinoma, 293, 294
signs and symptoms, 290
sino-nasal malignancy, 290
tissue biopsy, 290
treatment, 290
Lagophthalmos, 200
Langerhans cell histiocytosis (LCH), 441
aneurysmal bone cyst formation, 344
differential diagnosis, 339
enlarged left lateral rectus muscle, 341
extra-conal orbital component, 343
eyelid edema and mechanical ectropion, 343
irregular bone erosion, 340
left postero-lateral orbit and middle cranial fossa, 341
local bone destruction at superolateral orbital roof, 342
mild central areas of restriction, 344
mixed diffusivity signals, 343
PET-CT and whole-body MRI, 340
postero-lateral orbit, middle cranial fossa and temporal fossa, 341, 342
post-surgical curettage, 345
relatively intense, inhomogeneous, enhancement of lesion, 342
soft tissue infiltration in lacrimal fossa region, 340
soft tissue infiltration in posterior lateral orbit, 341
soft tissue lesion in left superior orbit, 340
symptoms and signs, 339
tissue diagnosis, 339
treatment, 340
Langerhans giant cells, 638
Lateral pterygoid muscle (LPM), 79, 80
Leber's hereditary optic neuropathy (LHON), 476, 485
Le Fort II fracture, 668
Left acute intraconal orbital traumatic hemorrhage, 484
Left eye multifocal retinoblastoma, 124
Left maxillary sinus, 624
Left middle cranial fossa, 93
Left orbit, 42
Left sided optic disc swelling, 575
Left sino-orbital mucormycosis, 626
Left sphenoid sinus, 627
Lens dislocation, 678
Lester Jones tube (LJT), 696
Leukocoria, 376
Levator palpebrae superioris, 34
Li-Fraumeni familial cancer syndrome, 314
Linear orbital fracture, 663
Linear radiopaque foreign body, 655
Lipomas
bone window, 326
crescent-shaped lesion, 327
differential diagnosis, 326
hyperintense T1 signal, 327
intraorbial and subcutaneous fat, 326
left upper eyelid, 328
MRI image, 328
no contrast enhancement, 327
non-enhancing lesion, 327
radiological findings, 326
signs and symptoms, 326
soft tissue window, 326
treatment, 326
unenhanced fat-saturated T1 axial image, 326
well-defined homogenous hypoindense mass, 329
well-defined hypodense lesion, 327
Liposarcoma
diagnosis, 314
heterogeneous internal enhancement, 317
homogeneously enhancing mass at left intraconal space, 316
hyperintense homogeneous mass, 317
hyperintense mass at left orbit, 316
hyperintense retrobulbar mass, 316
inferolateral extraconal extension, 316
inflammatory causes, 314
large hypointense right orbital mass, 316
mass at the left intraconal space, 315
MRI, 314–318
neoplastic causes, 314
patchy enhancement, 317
short-tau inversion recovery MRI, 317
signs and symptoms, 314
treatment, 314
well circumscribed homogeneous intraconal mass, 315
well-circumscribed hyperintense mass, 314

Lobulated hyperintense lesion, 493, 494
Lobulated hypointense lesion, 493
Longitudinal hyperintense spinal cord lesion, 482
Lung cancer
  homogeneous enhancement of orbital mass, 390
  mediastinal adenopathy, 392
  non-small cell, 391
  well-circumscribed mass, 390
Lymphatic malformations (LM), 495–497
  diagnosis, 492
  differential diagnosis, 492
  hemorrhagic cyst in conjunctiva, 493
  infero-temporal displacement of left eye, 493
  lobulated hyperintense lesion, 493, 494
  lobulated hypointense lesion, 493
  proptosis, 493, 494
  sclerosing agents, 495
  signs and symptoms, 492
  treatment, 492
Lymphoma, 140, 271
  apparent diffusion coefficient (ADC), 275
  diagnosis, 164
  differential diagnosis, 164
  diffusion weighted image, 275
  homogenous enlargement of lacrimal gland, 273
  isointense, homogenous partially lobulated mass, 275
  magnetic resonance imaging scan, 274
  mild enhancement of enlarged lacrimal glands, 273
  mild enhancement of left lateral mass, 275
  palpebral and lacrimal segments of lacrimal glands, 273
  PET/CT, 164, 274
  proptosis, hypoglobus, normal visual acuity and preserved ocular motility, 273
  treatment, 164
Lymphoproliferative disease, *see* Orbital lymphoma
Lymphoproliferative disorders, of lacrimal gland, 271

M

Magnetic resonance angiography (MRA)
  arteriovenous malformation, 120
  benefits of, 118
  cavernous venous vascular malformation, 119
  contrast-enhanced, 117
  indications, 117
  non-contrast-enhanced, 118
Magnetic resonance dacryocystography (MR-DCG), 279
Magnetic resonance imaging (MRI), 103, 289, 531, 650, 651, 653, 654, 659, 678
  DTI, 106, 107
  DWI, 104, 105
  FLAIR, 104, 109
  k-space, 104, 105
  longitudinal relaxation, 104
  T1 and T2 relaxation curves, 105
  transversal relaxation, 104
Magnetic resonance venography (MRV)
  arteriovenous malformation, 120
  cavernous venous vascular malformation, 119
  indications, 117
  techniques, 118
Malignant epithelial lacrimal gland tumor, 263
Malignant epithelial tumors of the lacrimal sac
  adenocarcinoma, 406
  adenoid cystic carcinoma, 406
  diagnosis, 404
  diffuse large B-cell lymphoma, 405
  lymphoma, 405
  melanoma, 405
  signs and symptoms, 403
  squamous cell carcinoma, 404
  treatment, 404
Malignant lacrimal tumors, 290
Malignant skin tumors, 350
Mantoux, 638
Marginal zone MALT lymphoma, 570
Maxillary nerve (V_2), 69
Maxillary sinus, 48, 50, 54, 59
  mucocele, 607
McCune Albright syndrome, 427, 428
Meckel's cave, 86, 92–96
Medial pterygoid muscle (MPM), 80
Mediastinal adenopathy, 392
Medpor®, 669
Medpor-Titan® surgical implant, 721
Medulloepithelioma, 455
Melanin, 398
Melanoma
  in bilateral intraconal spaces, 397
  diagnosis, 160, 396
  differential diagnosis, 160, 395
  due to melanin, 398
  ^{18}F-FDG PET/CT, 160–163
  nodal metastases, 161
  signs and symptoms, 160, 395
  treatment, 160, 396
Meningioma, 476, 478
  En plaque of the sphenoid wing, 447
Meningocele, 226
Meningoencephalocele, 226
Merkel cell carcinoma of eyelid (MCC)
  diagnosis, 408
  differential diagnosis, 408
  histopathologic features, 408
  homogeneous mild enhancement, 410
  intra and extraconal involvement, 411
  large intra-and extraconal space-occupying lesion, 413
  membranous staining pattern, 414
  prognosis, 408
  progressive right upper eyelid reddish-blue mass, 413
  signs and symptoms, 408
  slight intraconal fat infiltration, 411
  treatment, 408
Mesenchymal tumors, 332
Metallic posterior ocular foreign body, 657
Metastatic breast cancer, 171
  biologic and hormonal treatments, 386
  differential diagnosis, 386
  fusiform enlargement and muscle enhancement, 387
  hyperintense thickening in medial and lateral rectus muscles, 386
  lacrimal fossa and post-septal space, 387
  located in inferior and medial orbit, 386
  MRI, 387
  orbital biopsy, 386
  post-septal space with orbital apex involvement, 386
  signs, 385
  symptoms, 385
Metastatic neuroblastoma, 339
Metastatic orbital lesions, *see* Metastatic breast cancer
Metastatic renal cell carcinoma (RCC), 393–394
Methemoglobin, 494
Methotrexate, 172

Microphthalmia, 211
bilateral colobomas and, 213
persistent hyperplastic primary vitreous with, 212
Microphthalmos with orbital cyst, 131
differential diagnosis, 132
ultrasonograpphy, 132
Migration, 717, 718
Mild lower lid ectropion, 721
Mucocele(s), 231
diagnosis, 606
differential diagnosis, 606
ethmoidal, 231
ethmoid sinus, 607
frontal sinus, 608
maxillary sinus, 607
pressure erosion, 609
signs and symptoms, 605
sinus, 226
treatment, 606
Mucormycosis, 627
diagnosis, 624
differential diagnosis, 624
early intraorbital extension, 625
left sino-orbital mucormycosis, 626
orbital apex typical, 627
signs and symptoms, 624
treatment, 624
Mucosa associated B cell lymphoma, 273
Mucosa-associated lymphoid tissue (MALT) lymphoma, 596
Multidisciplinary approach, 524
Multiple myeloma (MM)
adjacent bony orbit preservation, 310
bony destruction, 308
CT, 308–309
diagnosis, 308
DWI and ADC, 310
homogeneous mass at left posterior intraconal space, 309
hypercellularity, 309
ill-defined left anterior orbital mass, 310
inferolateral displacement, 310
infiltrative soft tissue pattern, 310
inflammatory differentials, 308
left posterior intraconal mass, 309
movement artefact, 311
MRI, 309
neoplastic differentials, 308
signs and symptoms, 308
superior rectus involvement, 309
superotemporal orbit, 308
trans-spatial/multi-compartment nature, 310
treatment, 308
Multiple sclerosis (MS), 475, 479–481
Mycobacterial growth, 638
Myeloma, *see* Multiple myeloma (MM)
Myocysticercosis, 633, 634
Myopia, 681
Myositis, 582

N
Nasal encephalocele, 229, 230
Nasal (ethmoidal) turbinates, 50, 51
Nasal obstruction, 574
Nasolacrimal duct obstruction (NLDO), 283, 284
Naso-orbito-ethmoidal (NOE) fracture, 667–668
Necrobiotic xanthogranuloma (NBX), 577
Necrotising sialmetaplasia, 290
Neoplasm, 153
Neuritis, 475, 479, 480
Neuroblastoma, 145, 146
differential diagnosis, 145
metastasis, 486
ultrasound, 145
Neuroendocrine carcinoma, 172
Neurofibromatosis
diagnosis, 200
signs, 200
symptoms, 200
treatment, 200
type 1, 200–202
type 2, 200
Neuromyelitis optica, 475, 481
Neuro-sarcoidosis, 575
Nevus simplex, 240
Nidus, 522, 523, 526
"bag of worms" appearance, 523
Non-contrast-enhanced MRA, 118
Non-involuting capillary hemangioma (NICH), 240
Non-small cell lung cancer, 391
Non-steroidal anti-inflammatory drugs (NSAIDs), 558
Non-traumatic orbital hemorrhage (NTOH)
clinical presentation, 684
diagnosis, 684
IR enlargement/EOM related hemorrhage, 685–688
peri-implant hemorrhage, 688–689
signs and symptoms, 684
sub-periosteal hematoma, 689–690
treatment, 684
vascular malformation, 691–693

O
Ocular adnexal lymphoma, 163
Ocular prosthesis, 720, 724
Ocular surface squamous neoplasia (OSSN)
computed tomography (CT) scan, 367
differential diagnosis, 366
exenteration with/without adjuvant radiotherapy, 366
histopathology analysis, 366
medial bulbar conjunctiva, plica semilunaris, and caruncle, 368
MRI, 367
orbital imaging, 366
orbital involvement, 365
signs and symptoms, 365
systemic chemotherapy and radiotherapy, 366
temporal scleral thinning and thickened surrounding conjunctiva, 366
tissue biopsy, 366
Ocular trauma, 677
blunt trauma, 677
chemical injuries, 678
diagnosis, 678
sharp objects, 677
Olfactory groove meningioma
cribriform plate, 450
differential diagnosis, 446
midline abutting ethmoid sinuses, 450
signs and symptoms, 446
tissue biopsy, 446
treatment, 446
Open globe injuries, 650, 651, 662
Open reduction with internal fixation (ORIF), 662
Ophthalmic artery, 25, 26, 28, 29, 32

Optic atrophy, 477, 480, 485, 487
Optic canal, 71
Optic chiasm, 46
Optic chiasmatic-hypothalamic glioma, 464
Optic disc drusen, 487, 488
Optic nerve, 28, 29, 66, 409
  compression, 482, 483
  diagnosis, 475
  imaging features, 476
  left atrophic, 477
  pathologies, 475
Optic nerve glioma
  ADC, 458
  bulbous/fusiform thickening and tortuosity, 459
  chiasmatic-hypothalamic glioma, 464
  clinical and radiologic findings, 455
  cystic components, 464
  differential diagnosis, 455
  DWI, 457
  enhancing intraconal mass, 456
  fusiform enlargement, 456, 459
  intracranial extension to pre-chiasmatic segment, 457
  MR image, 456
  NECT and MR, 463
  orbital biopsy, 460
  painless proptosis, 458
  peri-neural arachnoid gliomatosis, 458
  proptosis and inferior temporal globe displacement, 459
  radiotherapy and chemotherapy, 455
  removal via lateral orbitotomy, 460
  Rootman's technique, 461
  sheath, 456
  signs and symptoms, 455
  surgical removal, 455
  tissue biopsy, 455
  tubular enlargement, 457
  uniform mild enhancement, 456
Optic nerve sheath meningioma (ONSM), 304, 455
  ADC, 470
  axial proptosis, 472
  calcification of tubular meningioma, 468
  clinical and radiologic findings, 467
  clinoid meningioma, 473
  conformal fractionated radiation therapy, 467
  differential diagnosis, 467
  donut configuration, 468, 469
  DWI, 469
  globular enlargement, 468
  homogeneous enhancement, 469
  hyperintense mass, 469
  hypointense structure, 470
  isointense mass, 469
  mild proptosis, mild ptosis and decreased vision function, 471
  MRI, 471
  ON displacement and SOF involvement, 471
  perineural thickening and homogenous contrast enhancement, 472
  restricted diffusion, 472
  severe axial proptosis, 470
  severe exophthalmos, 470
  signs and symptoms, 467
  tram-track sign, 468, 469, 473, 474
Optic neuritis, 475, 479, 480
Optico-carotid recess, 25
Optic perineuritis, 479
Oral chlorambucil, 272
Oral sildenafil, 492
Orbital apex, 43, 77, 86
Orbital arterial supply, 27
Orbital AVMs, *see* Arteriovenous malformations (AVMs)
Orbital bones, *see* Bones of the orbit
Orbital bony walls, 130
Orbital cellulitis, 612, 613
  after blunt trauma, 602
  bilateral sphenoid sinusitis, 603
  clinical diagnosis, 600
  differential diagnosis, 600
  IC fat stranding, 601
  management, 600
  post-septal fat stranding, 600
  proptosis, 600
  signs and symptoms, 600
Orbital compartment syndrome (OCS), 612, 650, 653, 654, 662
Orbital cysticercosis
  diagnosis, 634
  differential diagnosis, 634
  medical therapy, 634
  signs and symptoms, 633
  surgical removal, 634
  upgaze restriction and downgaze restriction, 634
Orbital dystopia, 440
Orbital emphysema, 652
Orbital floor defect, 115
Orbital foramina, 70
Orbital foreign bodies, 649, 650, 652, 654, 662, 663
Orbital fractures, 696
  apical orbital fractures, 668
  blow in fractures, 666–667
  blow out fractures, 663
  DICOM data, 668
  lacrimal drainage system fractures, 668–671
  linear, 663
  MRI, 669
  postoperative imaging of orbital implants, 669
Orbital hydatid cysts
  diagnosis, 630
  differential diagnosis, 629
  eosinophilic chitinous avascular laminated membrane like cyst wall, 631
  signs and symptoms, 629
  treatment, 630
Orbital imaging
  contrast enhanced T2 FLAIR, 185
  CT, 180, 181
  fat-saturating sequences, 184
  metastatic RCC, axial T1W post contrast FS image, 184
  NECT, 181
  normal/physiologic changes, 181–187
  safety and technical issues, in MRI, 181
  steady-state gradient echo sequence, 185
  T1 weighted non-enhanced, non-fat suppressed images, 182
  T2 fat saturated images, 185
Orbital implant, 720, 723
Orbital inflammation, 561
Orbital inflammatory diseases, 137–140
Orbital inflammatory syndrome, 582
  diagnosis, 172
  differential diagnosis, 172
  PET/CT, 173–174
  signs and symptoms, 172
  treatment, 172
Orbital injuries, 650
Orbital lesions, 440

Orbital lipomas, *see* Lipomas
Orbital liposarcoma, *see* Liposarcoma
Orbital lymphoma, 108, 140, 163
  bilateral and multifocal nature, 302
  bilateral anterior orbital mass, 302
  diagnosis, 298
  differential diagnosis, 140
  DWI, 300, 303
  FDG-PET scan, 301
  homogeneous enhancement of the intraconal mass, 305
  homogeneously enhancing mass at medial anterior orbits, 302
  hypointense right intraconal mass, 303
  infiltrative lesion, 298
  infiltrative pattern, 305
  intraconal enhancing mass, 303
  intraconal mass with homogeneous enhancement, 304
  intraconal mass with slightly ill-defined margins, 302
  intraconal tumor, 298
  lacrimal gland, 298
  lobulated heterogeneous and hypointense right intraconal orbital mass, 303
  metastasis, 303
  MRI, 298–300, 304
  multifocal and bilateral, 305
  muscle involvment, 298
  plasmablastic, 301
  preseptal component, 301
  preservation of adjacent bony structures, 305
  proptosis and subtle tenting of globe, 301
  signs and symptoms, 298
  treatment, 298
  ultrasound, 140–141
Orbital malformations, 240
Orbital melanoma, 370
Orbital metastasis
  diagnosis, 390
  diagnosis, 170
  differential diagnosis, 170, 390
  lung cancer, 390–392
  melanoma, 395–398 (*see* Metastatic breast cancer)
  metastatic RCC, 393–394
  PET/CT, 171–172
  prostate cancer, 392–393
  signs and symptoms, 389
  symptoms, 170
  treatment, 170, 390
Orbital mucocele, 134
  differential diagnosis, 134
  ultrasound, 134–135
Orbital multiple myeloma, *see* Multiple myeloma (MM)
Orbital myositis
  anterior belly swelling of medial rectus, 546
  differential diagnosis, 545
  DWI, 549
  edematous belly swelling, 547
  fusiform enlargement and enhancement, 549
  fusiform swelling, 547
  hyperintense signals within muscle, 549
  lateral rectus enlargement, 548
  left inferior rectus muscle with orbital fat stranding, 547
  left medial rectus muscle,, 546
  medial rectus muscle with tendon involvement, 547
  muscle biopsy, 545
  muscle swelling of left medial rectus, 546
  relative sparing of muscle tendon, 546
  right levator and superior rectus muscles, 547
  right superior rectus and levator muscle complex, 548
  smooth enlargement and mild enhancement, 546
  symptoms and signs, 545
  treatment, 546
Orbital osteoma, *see* Osteoma
Orbital osteosarcoma, *see* Osteosarcoma
Orbital plasmacytoma, 140
  differential diagnosis, 140
  ultrasound, 140–142
Orbital pseudo-tumor, *see* Idiopathic orbital inflammation (IOI)
Orbital radiotherapy, 320
Orbital rhabdomyosarcoma, 172
Orbital RMS, *see* Rhabdomyosarcoma (RMS)
Orbital sarcoidosis
  bilateral diffuse orbital infiltrates, 575
  bilateral lacrimal gland swelling, 574
  chronic bilateral lacrimal gland swelling, 574
  diagnosis, 573
  differential diagnosis, 573
  edema and inflammation, 576
  epididymo-orchitis, 574
  gradual onset right periocular swelling, 576
  infiltrative process, 574–576
  inflammatory process, 576
  intra-conal fat stranding, 576
  nasal obstruction, 574
  palpable mass, 575
  right lacrimal obstruction and swelling, 575
  S-shaped upper lid ptosis, 574
  symptoms and signs, 573
  treatment, 574
Orbital scan, 183
Orbital septa, 38
Orbital soft tissue injuries, 651–653
Orbital soft tissue sarcomas, *see* Liposarcoma
Orbital solitary fibrous tumor
  diagnosis, 531
  differential diagnosis, 530
  signs and symptoms, 530
  treatment, 532
Orbital trauma
  complex orbitofacial fractures, 666–670
  CT scans, 663
  diagnosis, 662
  differential diagnosis, 662
  signs and symptoms, 662
  simple orbital fractures, 663–667
  treatment, 662
  X-rays, 662–663
Orbital tuberculosis (OTB)
  ancillary tests, 638
  anti-tubercular therapy, 642
  axial and vertical proptosis and globe compression, 640
  biopsy, 638
  culture, 638
  diagnostic criteria, 638
  differential diagnosis, 638
  histology, 638
  large lobulated mass, 639
  non-axial proptosis and hyperglobus, 641
  non-axial proptosis and hypoglobus, 643
  nucleic acid amplification techniques, 638
  presence of AFB, 638
  signs and symptoms, 637
  superolateral extraconal mass, 639
  treatment, 638

Orbital tumor, 440
Orbital tumor extension from paranasal sinuses, *see* Squamous cell carcinoma of the sinuses
Orbital ultrasound, with Doppler
  arteriovenous malformation, 150–151
  cavernous venous malformation, 152
  dermoid cysts, 153–154
  probe and image conventions, 149
  solitary fibrous tumor (hemangiopericytoma), 152–153
  venolymphatic malformation, 151–152
Orbital venolymphatic malformation, 123
Orbital venous congestion, 523
Orbital venous-lymphatic malformation, 135–137
Orbitofacial fractures, 662, 663, 666, 668
  cranio-orbital fracture, 667–668
  cranio-orbitofacial fracture, 668–670
  NOE fracture, 667–668
  panfacial fracture, 668–670
  ZMC fracture, 666–667
Orbito-sphenoid meningioma, 448, 449
Ossifying fibroma
  chronic frontal sinusitis, 425
  differential diagnosis, 423
  mild extra-dural involvement at anterior cranial fossa, 426
  MRI, 425, 426
  signs and symptoms, 423
  tissue diagnosis, 424
  treatment, 424
Osteolytic lesion, 443
Osteoma, 399
  CT scan, 418, 419
  diagnosis, 418
  signs and symptoms, 418
  surgical excision through transconjunctival approach, 419
  treatment, 418
Osteomesh®, 674
Osteosarcoma
  biopsy, 421
  chemotherapy, 421
  diagnosis, 418
  MRI, 422
  signs and symptoms, 418
  treatment, 418

P
Painless orbital dystopia, 225
Palatine bone, 4
Palpebral fissure, 36
Panfacial fracture, 668, 670
Papilledema, 476, 487
Papillitis, 485
Paranasal sinuses, 48
  disease, 568
  ethmoid sinus, 60
  frontal sinus, 47, 59
  maxillary sinus, 48, 50, 59
  opacities, 641
  sinus structures, 49
  sphenoid sinus, 55–57, 60
Paraocular approach, 130–131
Patchy paranasal sinus disease, 554
PD-1 inhibitors, 354, 360
Pediatric glaucoma, 200
Pembrolizumab, 360
Peri-implant hemorrhage, 688–689
  hyperdense homogenous mass, 689
  orbital floor and implant, 688
  porous polyethylene implant, 689
Perineural disease, 175
Perineuritis, 479
Periocular basal cell carcinoma, *see* Basal cell carcinoma tumor
Periocular fillers
  bulkier appearance of facial fillers, 712
  CT, 706
  imaging properties, 705
  MRI, 706
  soft tissue densities and calcifications, 708
  subdermal deposits, 709
  temporalis muscles, 710
Periocular fillers related complications
  chronic malar edema, 716
  diagnosis, 714
  differential diagnosis, 714
  FBG, 716
  migration, 717
  retinal artery occlusion, 715
  signs and symptoms, 714
  treatment, 714
Periocular sebaceous cell carcinoma, *see* Sebaceous cell carcinoma tumor
Periocular squamous cell carcinoma, *see* Squamous cell carcinoma tumor
Periorbital soft tissue thickening, 679
Periosteitis, 639
Pfeiffer syndrome, 197
PHACES syndrome, 244, 245
PHACE syndrome, 240
Pilocytic astrocytoma, 459
Pituitary gland, 28
Plaque radiotherapy, 370
Plasmablastic lymphoma, 301
Plasmacytoma, 140, 146, 308
Pleomorphic adenoma, 140, 146
  ultrasound, 140–143
Plexiform neurofibroma, 200
Pneumatized anterior clinoid, 58
Polymicrogyria, 228
Polyomavirus infection, 408
Polyostotic fibrous dysplasia, 431
Porous polyethylene implant, 696, 721
Positron emission tomography/computed tomography (PET/CT)
  adenoid cystic carcinoma, 169–170
  IgG4-related disease, 176
  lymphoma, 164
  melanoma, 160–163
  orbital inflammatory syndrome, 173–174
  orbital metastases, 171–172
  squamous cell carcinoma, 157–159
Post coil embolization, 518
Post enucleation socket syndrome (PESS), 720–722
Posterior cerebral artery (PCA), 524
Posterior intraconal hyperdense semicircular implant, 723
Posterior scleritis, 557–560
Post-operative changes
  Ahmed glaucoma valve, 700
  bilateral orbital decompression, 697
  cataract extraction, 701
  IOL, 699
  lateral rectus muscle prolapse, 697
  LJT, 696

maloriented implants, 696
porous polyethylene implant, 696
scleral buckle for retinal detachment, 699
upper eyelid gold weight implantation, 698
vitrectomy, 698
Postoperative radiotherapy/chemotherapy, 332
Post-traumatic CCFs, 515
Pott's puffy tumor, 594
Prednisolone, 634, 636
Pre-septal abscess, 592, 593
Pre-septal cellulitis
diagnosis, 592
differential diagnosis, 592
left eyebrow lesion erythema and edema, 597
left periorbital edema, erythema and pain, 592, 593
left periorbital swelling and pain, 596
periorbital edema and erythema, 597
Pott's puffy tumor, 594
progressive left periorbital fullness, 596
recurrent left periorbital swelling, 596
recurrent periorbital inflammation, 595
signs and symptoms, 592
treatment, 592
Primary acquired nasolacrimal duct obstruction (PANDO), 283, 285
Primary adenocarcinoma, 291
Primary extramedullary plasmacytoma (PEP), 308
Primary liposarcoma, *see* Liposarcoma
Primitive mesoderm, 142–145
Primitive neuroectodermal tumors, 145
Progressively enlarging high-flow communications, 522
Proptosis, 200, 215, 216, 440, 492–494, 500, 515, 518, 519, 630, 631
and hyperglobus, 240
painless eyelid mass, 240
soft lesion, 240
Prostate cancer, 392–393
Prosthesis, 720, 722–725
Psammomatoid juvenile ossifying fibroma, 424
Pseudophakia, 701
Pseudotumor, *see* Idiopathic orbital inflammation (IOI)
Pterygoid muscle, 81
Pterygoid venous plexus, 69
Pterygomaxillary fissure, 76, 78, 80
Pterygopalatine fossa (PPF), 69, 75–78
Pterygopalatine ganglion, 75, 76
Ptosis, 721
Pulsatile palpebral mass, 522
Pulsatile proptosis, 200, 514, 522, 523
Pulse sequences, 104

R
Radiation therapy, 350
Radio-frequency (RF), 103, 104, 181
Radiotherapy and chemotherapy, 314
Rapidly involuting capillary hemangioma (RICH), 240
Reactive follicular hyperplasia, 173
Reactive lymphoid hyperplasia, *see* Benign lymphoid hyperplasia
Recti muscles, 44
Recurrent lacrimal gland pleomorphic adenoma (RLGPA)
diagnosis, 260
differential diagnosis, 259
hyperintense nodules, 260
hyperostotic sclerotic changes, 261
lesion in left lacrimal fossa, 260
signs and symptoms, 259
soft tissue mass, 261
treatment, 260
Recurrent solitary fibrous tumor, 332
Recurrent sphenoid wing meningioma, 115
Respiratory epithelial cysts of the orbit, 133
differential diagnosis, 133
ultrasound features, 133
Retinal artery occlusion, 715
Retinal AVMs, 522–523
Retinal detachment, 677, 678, 680, 681
Retinoblastoma
axial diffusion-weighted image with ADC, 383
bilateral intraocular soft tissue masses with large chunks of calcification, 378
buphthalmic eye with necrosis, 381
chemotherapy, 376
contrast-enhancing intraocular mass with calcification, 379
differential diagnosis, 376
fundus photography, 378
intraocular tumor mass with anterior extraocular extension, 382
left eye enucleation with orbital implant, 384
leukocoria, 377
MRI, 379, 380
optic nerve infiltration, 377
pineal gland with leptomeningeal seeding, 384
proptosis and corneal haze, 377
retinal detachment and subretinal hemorrhage, 383
signs and symptoms, 376
trans-scleral tumor growth with orbital fat invasion, 382
ultrasound, 376
Retrobulbar optic nerve, 130
Rhabdomyosarcoma (RMS), 142, 146, 339
axial apparent diffusion coefficient, 322
bone window, 321
coronal STIR image, 322
CT, 323
differential diagnosis, 145, 320
diffusion-weighted imaging, 322
enhanced fat-saturated T1 coronal image, 322
histopathology, 320
hyperintense orbital fat, 321
PET-CT, 320
signs and symptoms, 320
soft tissue window, 321
treatment, 320
ultrasound, 142–144
Rhinosinusitis, 612
Right cavernous sinus, 125
Right internal carotid artery, 124
Right maxillary sinus, 50
Right optic atrophy, 477
Right optic nerve sheath meningioma, 478
Right orbit, 40, 42, 44
Right periorbital swelling, 639
Right proptosis, 125
Right superficial frontotemporal angiosarcoma, 534
Rituximab, 568
Ruptured globe, 679

S
Saethre-Chotzen syndrome, 198
Salmon patch infiltrate, 163
Sarcoidosis, 476, 551, 552, 638
bilateral diffuse orbital infiltrates, 575
bilateral lacrimal gland swelling, 574
chronic bilateral lacrimal gland swelling, 574

Sarcoidosis (*cont.*)
diagnosis, 573
differential diagnosis, 573
edema and inflammation, 576
epididymo-orchitis, 574
gradual onset right periocular swelling, 576
infiltrative process, 574–576
inflammatory process, 576
intra-conal fat stranding, 576
nasal obstruction, 574
palpable mass, 575
right lacrimal obstruction and swelling, 575
S-shaped upper lid ptosis, 574
symptoms and signs, 573
treatment, 574
Schwannoma, 200
Schwannomatosis, 200
Scleritis
asymmetric thickening, 558
diagnosis, 558
differential diagnosis, 558
elevation of retina and choroid, 558
eye proptosis with hypoglobus and inflammation, 558
GPA, 559
hyperintense signal of left nasal intra-conal fat, 559
restricted diffusion, 560
sclera thickening and enhancement and adjacent soft tissue, 559
sclera thickening with mild enhancement, 559
signs and symptoms, 557
sub-tenon effusion, 560
thickening in right superonasal sclera, 559
treatment, 558
Sclerosing agents, 492, 495
Sclerosing IOI, 540, 541
Sclerotic lesion, 392
Sebaceous cell carcinoma tumor
CE CT, 361
differential diagnosis, 360
DWI, 360
hyperintense soft tissue mass, 362
ill-defined enhancing mass, 362
MRI, 360, 362
palpebral conjunctiva, protruding on eversion of the upper eyelid, 360
PET CT, 361
restrictive diffusion, 363
signs and symptoms, 360
tissue and map biopsies, 360
treatment, 360
Sensory fibers, 76
Septic cavernous sinus thrombosis, 600
Shave biopsy, 370
Silicone ball implant, 721
Sinonasal melanoma, 160, 162
Sinonasal SCC, 156
Sino-orbital aspergillosis, 616, 620
Sino-orbital disease, 637
Sino-orbital fungal disease, 624
Sino-orbital osteoma, 420
Sinusitis, 612
Sjögren's syndrome, 552
Skull base defect repair, 229
Small round blue cell tumor, 412
Soft tissue(s), 38, 130
sarcoma (*see* Rhabdomyosarcoma (RMS))
tumor, 332
Soft tissue injuries
extraorbital soft tissue changes, 654–655
globe injuries, 651–652
orbital soft tissue injuries, 652–653
symptoms, 650
Solitary extramedullary plasmacytoma, 308
Solitary fibrous tumor (SFT), 291, 530–532
axial apparent diffusion coefficient, 334
CT angiogram, 332
diffusion-weighted image, 334
heterogeneous T2 signal, 333
histopathology, 336
homogenous tumor enhancement, 333
immunohistochemical staining, 332
intense enhancement, 337
left eye axial proptosis and hyperglobus, 334
left optic nerve sheath complex, 333
metastatic breast cancer, 337
MRI orbit, 336
MR scan, 335
radiologic imaging, 332
signs and symptoms, 332
soft tissue window, 335
superior rectus muscle, 333
treatment, 332
well-defined lobulated mass in superior aspect, 333
Sonidegib, 350
Sphenoidal mucosal thickening, 722
Sphenoid bone, 3, 4, 15, 63, 64
Sphenoid sinus, 28, 48, 55–57, 60
Sphenoid wing dysplasia, 200
Sphenoid wing meningioma
cranial fossa dural involvement, 449
differential diagnosis, 446
emanating from anterior clinoid, 448
hyperostotic bone, 449
proptosis, 447
signs and symptoms, 446
tissue biopsy, 446
treatment, 446
Spherical orbital implants, 721
Spontaneous CCF, 515
Squamous cell carcinoma (SCC), 293, 404
clinical presentation, 156
diagnosis, 156
and orbital extension, 157
PET/CT, 157–159
treatment, 156
Squamous cell carcinoma of sinuses
bilateral orbital tumor involvement, 400
complete destruction of lateral orbital wall, 401
destructive necrotic mass, 400
differential diagnosis, 399
ethmoids and nasal bridge destruction, 400
FDG avidity, 401
heterogenous soft tissue mass with internal necrotic changes, 401
signs and symptoms, 399
tissue biopsy, 400
treatment, 400
Squamous cell carcinoma tumor
bony erosion on left supraorbital foramen, 355
cavernous carotid artery, 356
clinical signs, 354
CT, 354, 357
deep invasion, 354
differential diagnosis, 354

FDG avid, 357
full extent along orbital roof / SON, 356
left cavernous sinus, 356
left frontal sinus along supra-orbital canal, 355
MRI, 354, 355, 357
soft tissue window and bone window, 354
at superior orbital fissure and cavernous sinus, 355
tissue biopsy, 354
treatment, 354
S-shaped upper lid ptosis, 574
Staghorn configuration, 531
Staphyloma, 681
STAT6, 531
Steady-state free precession (SSFP), 118
Stereotactic radiosurgery (SRS), 508, 532
Steroid treatment, 272
Strabismus, 200, 215
Subacute inflammation, 540
Sub-acute left optic neuropathy, 575
Subconjunctival and eyelid cysticercosis, 634, 635
Sub-conjunctival cysts, 633
Submandibular gland, 176
Subperiosteal abscess (SPA)
diagnosis of, 612
differential diagnosis of, 612
diffusion coefficient images, 614
inferior, 613
inferomedial, 612
orbital cellulitis and medial, 613
signs and symptoms, 611
in supero-medial posterior orbit, 613
treatment, 612
Sub-periosteal hematoma, 684, 689–690
bilateral proptosis and asymmetric chemosis, 690
layering of blood products, 690
lenticular shape of the hematoma, 690
Superior oblique muscle, 45, 46
Superior ophthalmic vein, 523
Superior orbital fissure (SOF), 43, 63–66
Superior orbital subperiosteal hematoma, 653
Superior rectus, 46, 633
Supero-medial orbit, 629
Superotemporal soft tissue mass, 643
Surgical debridement, 638
Surgical excision, 314, 524
Swollen disc, 485
Systemic chemotherapy and radiotherapy, 320

T
T1, 104, 105, 108
T2, 104, 105, 109
Temporal fossa, 70
Temporalis fascia, 81
Teratoma
cranio-orbital, 222
diagnosis, 222
differential diagnosis, 221
proptosis, 222
solid cystic mass with internal septations, 222
stroke, 223
symptoms, 221
treatment, 222
Thyroid eye disease (TED), 137, 138, 146, 476, 552
apical crowding, 585
asymmetrical enlargement of extraocular muscles, 587
bilateral EOM enlargement, 584
bilateral eyelid retraction, 582
decompression techniques, 586
differential diagnosis, 138, 582
enlarged left medial rectus, 585
enlargement of inferior and medial rectus muscles, 584
EOM enlargement, 582
Graves hyperthyroidism, 586
interzygomatic method, 583
lacrimal gland enlargement, 583
management, 582
medial rectus size, 585
medial wall bowing, 583
medical therapies, 582
proptosis, 582, 583
risk factors, 583
signs and symptoms, 582
surgical interventions, 582
ultrasound, 138
Time-of-flight (TOF) MRA, 118
Tolosa-Hunt syndrome, 543
Transitional cell carcinoma, 290
Transocular approach, 130
Transorbital and transnasal endoscopic approach, mucoceles, 606
Trapdoor fracture, 663, 665
Traumatic optic neuropathy, 476
Traumatic proptosis, 484
Treacher-Collins syndrome, 193
Trigeminal ganglion, 92
Trigeminal nerve, 84, 86, 92, 95
Tuberculosis (TB)
diagnosis, 638
differential diagnosis, 638
signs and symptoms, 637
treatment, 638
Tuberculous dacryoadenitis, 637
Tuberculum sella meningioma, 478

U
Ultrasound, 128
adenoid cystic carcinoma, 141–144
axial scan, 129
B-scan screening exam, 130
cavernous venous malformation, 135–136
dermoid cyst, 133–134
idiopathic orbital inflammation, 138–139
infantile hemangioma, 134–136
longitudinal scan, 129
microphthalmos with orbital cyst, 132
neuroblastoma, 145
normal ultrasound anatomy, of orbit and periorbital region, 130–131
orbital lymphoma, 140–141
orbital mucocele, 134–135
orbital plasmacytoma, 140–142
paraocular approach, 130–131
pleomorphic adenoma, 140–143
probe orientation, 129–130
probe position, 130–131
respiratory epithelial cysts of the orbit, 133
rhabdomyosarcoma, 142–144
technique of examination, 129
thyroid eye disease, 138
transducers and frequencies, 128–129
transocular approach, 130
transverse scan, 129, 130
venous-lymphatic malformation, 137

Unilateral proptosis, 386
Uveal melanoma
  anterior, 372
  differential diagnosis, 370
  heterogeneously enhancing exophytic lesion, 374
  MR scans, 370
  posterior, 371
  recurrent, 373
  signs and symptoms, 369
  treatment, 370
  ultrasonography, 370

V
Valsalva maneuver, 500, 504
Vascular anatomy
  arterial anatomy, 25–26
  venous anatomy, 27
Vascular anomalies, 134–137
Vascular clips, 501
Vascular engorgement, 514
Vascular malformation, 500, 684, 691–693
Vascular tumors, of infancy, 240
Vasculitis, 557, 561, 563
Venolymphatic malformation (VLM), 151–152
Venous anatomy, 27
Venous drainage, 27, 31
Venous-lymphatic malformation, 135, 146
  differential diagnosis, 137
  ultrasound, 137
Venous malformation
  diagnosis, 500
  differential diagnosis, 500
  diffuse, 505
  hypointense lesion, 503
  management of, 501
  proptosis, 503, 504
  signs and symptoms, 500
Vismodegib, 350
Visual acuity, 409
Visual field defects, 523
Visual loss, 653
Visual pathways, 523
Vitrectomy, 698, 699
Von Hippel-Lindau syndrome, 531
Voxel, 103, 104, 106

W
Wegener's granulomatosis, *see* Granulomatosis with polyangiitis (GPA)
Wyburn-Mason syndrome (WMS), 522

X
Xanthogranulomatous disease
  AAPOX, 578, 579
  AOX, 578
  diagnosis, 578
  differential diagnosis, 577
  ECD, 579, 580
  symptoms and signs, 577
  treatment, 578

Z
Ziehl Neelsen stain, 638, 644
Zygomatic arch, 81
Zygomatic bone, 4
Zygomaticofrontal process, 76
Zygomatico-maxillary complex (ZMC) fractures, 666–667